

IV International Conference on Particle-based Methods

PARTICLES 2015

28 - 30 September 2015, Barcelona, Spain



PARTICLE-BASED METHODS IV

Fundamentals and Applications

Proceedings of the IV International Conference on Particle-Based Methods – Fundamentals and Applications
held in Barcelona, Spain
28 - 30 September 2015

Edited by:

E. Oñate

CIMNE / Universitat Politècnica de Catalunya, Spain

M. Bischoff

Universität Stuttgart, Germany

D.R.J. Owen

Swansea University, United Kingdom

P. Wriggers

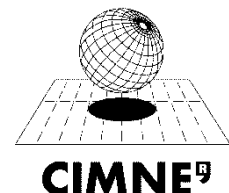
Leibniz Universität Hannover, Germany

T. Zohdi

University of California, Berkeley, USA

A publication of:

**International Center for Numerical
Methods in Engineering (CIMNE)**
Barcelona, Spain



**International Center for Numerical Methods in Engineering
(CIMNE)**

Gran Capitán s/n, 08034 Barcelona, Spain
www.cimne.com

**Particle-based Methods IV – Fundamentals and
Applications**

E. Oñate, M. Bischoff, D.R.J. Owen, P. Wriggers and T. Zohdi (Eds.)

First edition, September 2015

© The authors

Printed by: Artes Gráficas Torres S.A., Huelva 9, 08940 Cornellà de Llobregat, Spain

ISBN: 978-84-944244-7-2

TABLE OF CONTENTS

Preface	7
Acknowledgements	9
Organizers and Committees	10
SUMMARY	11
CONTENTS	13
Invited Sessions	22
Contributed Sessions	214
Authors Index	1117

PREFACE

This volume contains the full papers presented at the IV International Conference on Particle-based Methods (PARTICLES 2015), held in Barcelona on 28 - 30 September, 2015. The first three conferences of the series were held in Barcelona, Spain, in the years 2009 and 2011, and in Stuttgart, Germany, in September 2013.

Particles 2015 addresses fundamentals and applications of particle-based computational methods, including both *discrete* modeling concepts and *discretization* methods. Full papers included cover discrete element methods, smoothed particle hydrodynamics, material point methods, moving particle simulations and meshless methods as well as aspects of parallel computing for solid und fluid mechanics, multi-scale and multi-phase problems, damage, fracture and fragmentation, granular materials, soft matter, geo- and bio-mechanics, micro-macro transitions, coupling of discrete and continuous models and discretizations, fluid-structure interaction and industrial applications.

The conference is held under the auspices of the European Community on Computational Methods in Applied Sciences (ECCOMAS) and the International Association for Computational Mechanics (IACM). The organizers would like to thank all authors for submitting their contributions and the supporting organizations for their help in making PARTICLES 2015 possible.

PARTICLES 2015 Organizers

Eugenio Oñate (Chair)

*CIMNE / Universitat Politècnica de Catalunya (UPC)
Barcelona, Spain*

M. Bischoff

Universität Stuttgart, Germany

D.R.J. Owen

Swansea University, United Kingdom

P. Wriggers

Leibniz Universität Hannover, Germany University of California, Berkeley, USA

T. Zohdi

ACKNOWLEDGEMENTS

The conference organizers acknowledge the support towards the organization of PARTICLES 2015 to the following organizations:



International Center for Numerical Methods in Engineering (CIMNE)



Universitat Politècnica de Catalunya (UPC)



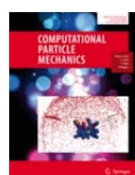
European Community on Computational Methods in Applied Sciences (ECCOMAS)



International Association for Computational Mechanics (IACM)



European Research Council (ERC)



Computational Particle Mechanics, a Springer Journal

We thank the **Plenary Speakers**, the **Invited Sessions Organizers** and the **Authors** for their help in the setting up of a high standard Scientific Programme.

ORGANIZERS AND COMMITTEES

Conference Chair

E. Oñate, *Universitat Politècnica de Catalunya, Spain*

Conference Co-Chairs

M. Bischoff, *Universität Stuttgart, Germany*

D. R. J. Owen, *Swansea University, United Kingdom*

P. Wriggers, *Leibniz Universität Hannover, Germany*

T. Zohdi, *University of California, Berkeley, USA*

Local Organizing Committee

E. Oñate, *LOC Chair*

P. Dadvand

A. Larese, *LOC Co-Chair*

R. Rossi

S. Idelsohn

F. Zárate

Scientific Committee

N. Adams, Germany	H. Herrmann, Switzerland	A. Munjiza, UK
P. Alart, France	C. Holm, Germany	F. Nicot, France
M. Alnaggar, USA	G. Horrigmoe, Norway	X. Oliver, Spain
N. Bicanic, UK	X. Hu, Germany	J. Ooi, UK
S. Amini, Italy	A. Huerta, Spain	M. Pastor, Spain
J. Bonet, UK	S. Idelsohn, Spain	T. Poeschel, Germany
J.M. Carbonell, Spain	H. Jaeger, USA	F. Radjaï, France
J.S. Chen, USA	K. Kamrin, USA	S. Radl, Austria
Z. Chen, USA	C. Kloss, Austria	C. Recarey, Cuba
P. Cleary, Australia	E. E. Knight, USA	V. Richefeu, France
G. Combe, France	S. Koshizuka, Japan	J. Rojek, Poland
M. Crapper, UK	P. Koumoutsakos, Switzerland	R. Rossi, Spain
G. Cusatis, USA	F. Kun, Hungary	E. Rougier, USA
P. Dadvand, Spain	C. Labra, UK	R. Seifried, Germany
A. Daouadji, France	A. Larese, Spain	A. Serra, Spain
F. Darve, France	C. Leonardi, Australia	M. Shirazaki, Japan
P. Eberhard, Germany	S. Li, China	D. Simkins, USA
W. Ehlers, Germany	M. Liu, China	D. Sulsky, USA
M. Ellero, Germany	W.K. Liu, USA	A. Thornton, Netherlands
Y.T. Feng, UK	R. Löhner, USA	M.A. Toledo, Spain
J. Foster, USA	S. Luding, Netherlands	T. Weinhart, Netherlands
J.M. García-Aznar, Spain	V. Magnanimo, Netherlands	J.R. Williams, USA
C. Goniva, Austria	J. Martí, Spain	F. Wittel, Switzerland
J. Goddard, USA	L. McCue-Weil, USA	G. Yagawa, Japan
T. Hagelien, Norway		F. Zárate, Spain
S. Hagihara, Japan		X. Zhang, China

SUMMARY

PREFACE	9
ACKNOWLEDGEMENTS	11
ORGANIZERS AND COMMITTEES	12
SUMMARY	13
CONTENTS	15

INVITED SESSIONS

Fracture and Fragmentation with DEM	
Organized by Falk Wittel and Ferenc Kun	
From Discrete Particles to Continuum Models of Granular Mechanics:	
Part I. Elasticity and Wave Propagation	
Organized by Ken Kamrin and Vanessa Magnanimo	
From Discrete Particles to Continuum Models of Granular Mechanics:	
Part II. Quasi-static Elastoplastic Flows	
Organized by Stefan Luding and Farhang Radjaï	
From Discrete Particles to Continuum Models of Granular Mechanics:	
Part III. Rapid Granular Flows	
Organized by Joe Goddard and Thomas Weinhart	
High Performance Computing for Particle Methods: New Trends,	
Algorithms and Applications	
Organized by Peter Wriggers, Eugenio Oñate, Bircan Avci and Pooyan Dadvand	
Multi-Scale Modelling of Reactive Particle-Based Processes	
Organized by Christoph Kloss, Stefan Radl, Christoph Goniva, Thomas Hagelien and Shahriar Amini	
MuMoLaDe (Multiscale Modelling of Landslides and Debris Flows)	
Organized by Sergio Idelsohn, Eugenio Oñate and Pablo Becker	
Particle Methods for Fluid-Structure Interactions at Different Scales	
Organized by Moubin Liu	
The Material Point Method and Other Meshfree and Particle Methods	
Organized by J.S. Chen, Zhen Chen, Daniel Simkins, Xiong Zhang	

CONTRIBUTED SESSIONS

Composites
Contact Problems
Coupled Problems
Damage, Fracture and Fatigue
Environment and Geosciences
Geomechanics
Granulation Processes
Industrial Applications
Material Point Method (MPM) and the Lattice-Boltzmann-Method (LBM)
Meshless Methods
Mixing Processes
Modelling of Granular Materials
Molecular Dynamics (MD) or Discrete (Distinct) Element Method (DEM)
Moving Particle Simulation (MPS)
Multi-fracturing Solids Systems
Multiphase Flows
Multi-scale Material Models
Parallel Computing
Particle Finite Element Method (PFEM)
Smoothed Particles Hydrodynamics (SPH)

CONTENTS

INVITED SESSIONS

IS - Fracture and Fragmentation with DEM

An important role of elastic vortices in unsteady propagation of longitudinal shear cracks in brittle materials.....	22
<i>E.V. Shilko*, S.G. Psakhie, V.L. Popov</i>	
Representation of bulk and surface crushing phenomenon in DEM model of railway ballast.....	34
<i>R. Dubina*, J. Eliáš</i>	
Time-dependent DEM based fracture simulations at the grain size level for brittle heterogeneous solids	41
<i>H. Konietzky*, W. Chen</i>	

IS - From Discrete Particles to Continuum Models of Granular Mechanics: Elasticity and Wave Propagation

A rigid body spring network model for the simulation of hysteretic behavior of materials	53
<i>C. Sofianos*, V. Koumousis</i>	

IS - From Discrete Particles to Continuum Models of Granular Mechanics: Quasi-static Elastoplastic Flows

From elasto-plasticity to visco-elasto-plasticity for saturated granular materials	60
<i>B. Chareyre*, D. Marzougui, J. Chauchat</i>	

IS - From Discrete Particles to Continuum Models of Granular Mechanics: Rapid Granular Flows

Granular flow through an orifice: solving the free fall arch paradox.....	71
<i>S.M. Rubio-Largo, A. Janda, I. Zuriguel, D. Maza, R.C. Hidalgo*</i>	

IS - High Performance Computing for Particle Methods: New Trends, Algorithms and Applications

Validation of the GPU based BLAZE-DEM framework for hopper discharge	81
<i>N. Govender*, P. Pizette, D.N. Wilke, N-E. Abriak</i>	

IS - Multi-Scale Modelling of Reactive Particle-Based Processes

DEM particle characterization by artificial neural networks and macroscopic experiments	93
<i>L. Benvenuti*, C. Kloss, S. Pirker</i>	

Optimal particle parameters for CLC and CLR processes – predictions by intra-particle transport models and experimental validation	105
<i>T. Forgber, J.R. Tolchard, A. Zaabout, P.I. Dahl, S. Radl*</i>	
ParScale - An open-source library for the simulation of intra particle heat and mass transport processes in coupled simulations	117
<i>S. Radl, T. Forgber*, A. Aigner, C. Kloss</i>	

IS - MuMoLaDe (Multiscale Modelling of Landslides and Debris Flows)

Hydro-mechanical continuum modelling of an experimental slope with a material stability criterion	128
<i>E. Kakogiannou*, M. Lora, L. Sanavia</i>	
Mixed finite element formulation for non-isothermal porous media in dynamics...	140
<i>T.D. Cao*, Y. Wang, L. Sanavia, B.A. Schrefler</i>	
Multiphase analysis of strain localization with regularized models	149
<i>M. Lazari*, L. Sanavia, B.A. Schrefler</i>	
What is wrong in Love-Weber stress for unsaturated granular materials?.....	161
<i>C. Chalak*, B. Chareyre, F. Darve</i>	

IS - Particle Methods for Fluid-Structure Interactions at Different Scales

Numerical simulation of shaped charge jet penetrating a plate using Smoothed Particle Hydrodynamics	171
<i>Z. Zhifan*, M. Furen, Z. Aman</i>	
Numerical study of fluid-structure interaction with macro-scale particle methods	183
<i>G. Zhou*</i>	

IS - The Material Point Method and Other Meshfree and Particle Methods

Application of kinetic damping in dynamic material point method for static problems	192
<i>Y. Sun*, E. Song, J. Yang</i>	
Improving accuracy in particle methods using null spaces and filters	202
<i>C. Gritton, M. Berzins*, R.M. Kirby</i>	

CONTRIBUTED SESSIONS

Composites

Implementation and application of vector form intrinsic finite element in pushover analysis for reinforced concrete buildings.....	214
<i>F.P. Hsiao*, H. Ho, R.Z. Wang, Y.C. Ou</i>	
Numerical simulation analysis of reinforced concrete structure using VFIFE fiber-element model	226
<i>R-Z. Wang*, B-C. Lin, C-H. Huang</i>	

Contact Problems

Discrete element analysis of cohesive granular bulk solid materials	237
<i>L.I. Del Cid*, G. Mustoe</i>	
Molecular dynamics modelling of boundary migration in bicrystals under nanoburnishing	248
<i>A.I. Dmitriev*, A.Y. Nikonov</i>	
Role of vertex-like motion in contact loading of strengthening coating.	
Movable cellular automaton modeling.....	255
<i>A.Y. Smolin*, G.M. Eremina, S.G. Psakhie</i>	

Coupled Problems

Coupling of particle-based and grid-based methods within object-oriented multi-physics CFD framework.....	263
<i>R. Steijl*, S. Colonia, G.N. Barakos</i>	
Hybrid thermo-mechanical contact algorithm for 3D SPH-FEM multi-physics simulations.....	275
<i>K.A. Fraser*, L. St-Georges, L.I. Kiss, Y. Chircota</i>	
Numerical simulation of heat and mass transfer under the conditions of phase transitions and chemical reaction during ignition of condensed substances by single hot particles.....	287
<i>D.O. Glushkov, P.A. Strizhak*, O.V. Vysokomornaya</i>	
Radiation heat transfer within the discrete element method – relevance, implementation and examples -	298
<i>S. Wirtz*, J. Wiese, F. Wissing, V. Scherer</i>	
Two-phase modeling of conduction mode laser welding using Smoothed Particle Hydrodynamics	308
<i>H. Hu*, P. Eberhard</i>	

Damage, Fracture & Fatigue

Adaptive refinement technique for discrete static models of fracture.....	320
<i>J. Eliáš*</i>	
Comparison of wear models using a Lagrangian approach	333
<i>F. Beck, P. Eberhard*</i>	

Modelling of concrete fracture at aggregate level using DEM based on x-ray µCT images of internal structure.....	343
<i>M. Nitka, J. Tejchman*</i>	
Modelling plasticity by non-continuous deformation	355
<i>Y. Ben-Shmuel*, E. Altus</i>	
Virtual concrete specimens: discrete element simulations of the quasistatic and dynamic material behavior and failure mechanisms of concrete and mortar	367
<i>D.S. Reischl*, M. Curbach</i>	

Environment and Geosciences

Adaptive methods for the simulation of Multiscale Fluid Dynamic Phenomena using Vortex Particle Methods with applications to civil structures.....	379
<i>D. Milani*, G. Morgenthal</i>	
Application of the lattice Boltzmann method in acoustics.....	391
<i>E. Salomons*, W.J.A. Lohman, H. Zhou</i>	
Bridges wash out simulation during tsunami by a stabilized ISPH method.....	403
<i>Y. Miyagawa*, M. Asai, N.A.B. Idris</i>	
Snow property modeling and its application to particulate ice-snow flow computing in snowblower	410
<i>Y. Yamamoto*, J. Ishimoto, N. Ochiai</i>	

Geomechanics

A discrete approach to describe the elastic-plastic behaviour of snow	419
<i>B. Peters*, M. Michael, F. Nicot</i>	
A novel systematic method to estimate the contact parameters of particles in discrete element simulations of soil	430
<i>R. Lichtenheldt*</i>	
A theoretical investigation of a mechanical response of fluid-saturated porous materials based on a coupled discrete-continuum approach.....	442
<i>A.V. Dimaki*, E.V. Shilko, S.V. Astafurov, S.G. Psakhie</i>	
Clarification of soil scour and seepage flow by using a particle method.....	451
<i>T. Nogami*, M. Asai, A. Abdelraheem</i>	
Comparisons of shear strength of particulate materials determined by the direct shear test and DEM simulations	460
<i>X. Wang*, C. Niklasch, P-M. Mayer</i>	
Discrete element modelling of grain size segregation in bi-disperse granular flows down chute.....	474
<i>L. Jing*, F.C.Y. Kwok, A.Y.F. Leung</i>	
Discrete modeling of geotextile-wrapped soil under simple shear	485
<i>H. Cheng*, H. Yamamoto</i>	
Effect of wall roughness on interface behavior of DEM-simulated granular material	497
<i>K.A. El Cheikh, S. Rémond, C. Djelal, P. Pizette, Y. Vanhove</i>	

Investigations of vortex structures in granular materials under earth pressure conditions by DEM	507
<i>M. Nitka*, J. Tejchman</i>	
Micromechanical analysis of the surface erosion of a cohesive soil by means of a coupled LBM-DEM model	519
<i>P. Cuéllar*, P. Philippe, S. Bonelli, N. Benahmed, F. Brunier-Coulin, J. Ngoma, J-Y. Delenne, F. Radjaï</i>	
Numerical simulation of free surface seepage in saturated soil using Smoothed Particle Hydrodynamics	529
<i>C. Peng*, W. Wu, H.S. Yu, C. Wang</i>	
PS-MRT Lattice Boltzmann model for direct simulation of granular soils and seepage flow	537
<i>Y. Fukumoto*, S. Ohtsuka, A. Murakami</i>	
Real grain shape analysis: characterization and generation of representative virtual grains. Application to railway ballast	545
<i>N. Ouhbi*, C. Voivret, G. Perrin, J-N. Roux</i>	
Transient regime to fluidized chimney within a granular bed by means of a 2D DEM/LBM modeling.....	558
<i>J. Ngoma, P. Philippe*, S. Bonelli, P. Cuéllar, J-Y. Delenne, F. Radjaï</i>	

Granulation Processes

DEM simulations of particle dynamics in a spheronization process to describe the pelletization mechanisms.....	567
<i>D. Weis*, D. Thäte, M. Thommes, S. Antonyuk</i>	

Industrial Applications

Application of the Lattice-Boltzmann method for modeling All-Vanadium Redox Flow Batteries.....	579
<i>D. Maggiolo*, F. Picano, A. Marion, M. Guarnieri</i>	
Investigation of green water in FPSO by a particle-based numerical offshore tank	590
<i>C.A. Bellezi*, D.T. Fernandes, L-Y. Cheng, K. Nishimoto</i>	
Modelling centrifugal membrane deployment of solar sails with the discrete element method	602
<i>Z. Xu, D. Zhang*, W. Chen, F. Peng</i>	
Theoretical investigation of the dynamics of friction stir welding process by movable cellular automaton method	612
<i>S.V. Astafurov*, E.V. Shilko, E.A. Kolubaev, A.I. Dmitriev, A.Y. Nikonov, S.G. Psakhie</i>	

Material Point Method (MPM) and the Lattice-Boltzmann-Method (LBM)

Effect of boundary condition applying type on heat transfer modeling via double species lattice Boltzmann method	623
<i>M. Mohammadi-Amin*, M. Bustanchy</i>	
Effects of the MPM discretisations on the soil-structure problems	635
<i>S. Fatemizadeh*, F. Hamad, C. Moormann</i>	
Simulations of dense snow avalanches with generalized interpolation material point method: preliminary outcomes.....	646
<i>W.T. Solowski*, D. Baroudi, M. Ghobakhloou, L. Korkiala-Tanttu</i>	

Meshless Methods

Solution of the stationary Stokes and Navier-Stokes equations using the modified finite particle method in the framework of a least square residual method	657
<i>D. Asprone, F. Auricchio, A. Montanino*, A. Reali</i>	
The algorithm for 3D vortex sheet influence computation in meshless vortex method	670
<i>I.K. Marchevsky*, G.A. Shcheglov</i>	
The modified numerical scheme for 2D flow-structure interaction simulation using meshless vortex element method	680
<i>K.S. Kuzmina*, I.K. Marchevsky</i>	
Using the dipole particles for simulation of 3D vortex flow of a viscous incompressible fluid	692
<i>D. Syrovatskiy*, G. Dynnikova, S. Guvernyuk, G. Arutunyan</i>	

Mixing Processes

Modelling the formation and breakup of particle clusters in metal melt subjected to external fields	702
<i>A. Manoylov*, V. Bojarevics, K. Pericleous</i>	
Resolving lateral segregation effects of static blenders.....	714
<i>B.T. Ton*, R.J. Farnish, S. Zigan</i>	
Simulating mixing processes with water addition using DEM – From bulk material to suspension	722
<i>K. Krenzer*, V. Mechtcherine, U. Palzer</i>	

Modelling of Granular Materials

Active-set based quadratic programming algorithm for solving optimization problems arising in granular dynamics simulations	732
<i>L. Pospisil*, Z. Dostal, D. Horak</i>	

Molecular Dynamics (MD) or Discrete (Distinct) Element Method (DEM)

A general method for modelling deformable structures in DEM.....	744
<i>A. Effeindzourou*, K. Thoeni, B. Chareyre, A. Giacomini</i>	
A molecular dynamics study on the effects of wall-fluid interaction strength and fluid density on thermal resistance of graphene/argon interface.....	755
<i>A. Amani, S.M.H. Karimian, M. Seyednia*</i>	
An investigation in the effect of particle platyness on the strength of granular materials using the discrete element method	767
<i>M. Potticary*, A. Zervos, J. Harkness</i>	
Correction of the gas flow parameters by molecular dynamics	779
<i>V. Podryga*, S. Polyakov</i>	
Discrete element simulation of wet granular materials: plastic compression.....	789
<i>V-D. Than*, J-N. Roux, A-M. Tang, J-M. Pereira</i>	
Experimental and numerical investigation of the behaviour of complex particles in a model scale fluidized bed	801
<i>K. Vollmari*, H. Kruggel-Emden</i>	
Internal states, stress-strain behavior and elasticity in oedometrically compressed model granular materials	810
<i>M.H. Khalili*, J-N. Roux, J-M. Pereira, M. Vandamme, S. Brisard, M. Bornert</i>	
Investigations of tire-soil-interactions using the Discrete-Element- Method	822
<i>O. Zieher, M. Meywerk*</i>	
Microdynamic analysis of ellipsoidal particle flow in a shear cell	833
<i>M. Hossain*, H. Zhu, A. Yu</i>	
Non Smooth Contact Dynamic approach for railway engineering: investigation of ballast behaviour under stabilisation process.....	842
<i>J-F. Ferellec*, R. Perales, P-E. Laurens, M. Wone, J. Plu, G. Saussine</i>	
Parametric evaluation for powder flowability using a Freeman rheometer: a discrete element method study	854
<i>Z. Yan*, S.K. Wilkinson, S.A. Turnbull, E.H. Stitt, M. Marigo</i>	
Powder compaction with polygonal particles built from radially extending one-dimensional frictional devices.....	866
<i>F.A. Lülf*, P. Wriggers</i>	
Tribological effects in granular materials and their impact on the macroscopic material behaviour	878
<i>B. Suhr*, K. Six</i>	
Using Delaunay triangulations to investigate the effect of interparticle friction on critical-state DEM simulations.....	890
<i>K.J. Hanley*, X. Huang, C. O'Sullivan</i>	

Moving Particle Simulation (MPS)

Analysis of airborne fines in cylindrical biomass storage silos	900
<i>L.L. Lulbadda Waduge*, S. Zigan</i>	
Back from the solid temperature to kinetic energy of its macro-molecules	909
<i>S.V. Arinchev*</i>	

Multi-fracturing Solids Systems

An application of the finite-discrete element method in the simulation of ceramic breakage: methodology for a validation study for alumina specimens	921
<i>A. Farsi*, J. Xiang, J. P. Latham, A. D. Pullen, M. Carlsson, E.H. Stitt, M. Marigo</i>	
Development of higher order particle discretization scheme for analysis of failure phenomena	933
<i>M.K. Pal, L. Wijerathne*, M. Hori, T. Ichimura, S. Tanaka</i>	
Inclusion of pore pressure effects in discrete element modeling of rock cutting ...	945
<i>R.L.J. Helmons*, S.A. Miedema, C. van Rhee</i>	

Multiphase Flows

A pore-scale approach of two-phase flow in granular porous media	957
<i>C. Yuan*, B. Chareyre, F. Darve</i>	
Aerodynamic properties of particles in the gravitational flow of a chuted bulk material	969
<i>I.N. Logachev, K.I. Logachev, O.A. Averkova*, V.A. Uvarov, A.K. Logachev</i>	
Deformation of a droplet in Couette flow subject to an external electric field simulated using ISPH	981
<i>N. Tofighi, M. Ozbulut*, M. Yildiz</i>	
Numerical simulation of water and water emulsion droplets evaporation in flames with different temperatures	991
<i>P.A. Strizhak*, R.S. Volkov, A.O. Zhdanova</i>	
Particle contact laws and their properties for simulation of fluid-sediment interaction with coupled SPH-DEM model	998
<i>D.F. Vetsch*, F. Fleissner, A. Mueller, R.M. Boes</i>	
Particle tracking numerical methods for nanoparticle transport in heterogeneous porous media	1010
<i>D.V. Papavassiliou*, N. Pham</i>	
The aerodynamics of a jet of particles in a channel.....	1016
<i>I.N. Logachev, K.I. Logachev*, O.A. Averkova, V.A. Uvarov, A.K. Logachev</i>	

Multi-scale Material Models

A Master equation for force distributions in polydisperse frictional particles.....	1028
<i>K. Saitoh*, V. Magnanimo, S. Luding</i>	
Modeling of elasto-plastic behaviour of granular materials using multi-particle finite element simulations	1040
<i>N. Abdelmoula*, B. Harthong, D. Imbault, P. Dorémus</i>	

Parallel Computing

Vortex particle method for aerodynamic analysis: parallel scalability and efficiency.....	1052
<i>K. Ibrahim*, G. Morgenthal</i>	

Particle Finite Element Method (PFEM)

Numerical modeling of metal cutting processes using PFEM and a physical based model	1066
<i>J.M. Rodríguez *, P. Jonsén, A. Svoboda</i>	
Numerical simulation of penetration problems in geotechnical engineering with the Particle Finite Element Method (PFEM)	1073
<i>L. Monforte*, J.M. Carbonell, M. Arroyo, A. Gens</i>	
On some drawbacks and possible improvements of a Lagrangian finite element approach for simulating incompressible flows	1081
<i>M.L. Cerquaglia*, G. Deliége, R. Boman, L. Papeleux, V. Terrapon, J-P. Ponthot</i>	
Vertical natural modes of gravel aggregate in the ballasted railway track.....	1093
<i>A. Aikawa*</i>	

Smoothed Particles Hydrodynamics (SPH)

Regular or random: a discussion on SPH initial particle distribution.....	1105
<i>J. Young*, I. Alcântara, F. Teixeira-Dias, J.Y. Ooi, F. Mill</i>	

AUTHOR INDEX	1095
---------------------------	------

AN IMPORTANT ROLE OF ELASTIC VORTICES IN UNSTEADY PROPAGATION OF LONGITUDINAL SHEAR CRACKS IN BRITTLE MATERIALS

EVGENY V. SHILKO^{1,2}, SERGEY G. PSAKHIE^{1,2} AND VALENTIN L. POPOV^{1,3}

¹Institute of Strength Physics and Materials Science SB RAS (ISPMS SB RAS)
2/4, pr. Akademicheskii, 634021 Tomsk, Russia
shilko@ispms.tsc.ru, <http://www.ispms.ru>

²Tomsk State University
36 Lenin prospect, 634050 Tomsk, Russia
shilko@ispms.tsc.ru, <http://ff.tsu.ru>

³Berlin University of Technology (TU Berlin)
Sekr. C 8-4, Str. Des 17. Juni 135, D-10623 Berlin, Germany
v.popov@tu-berlin.de, <http://www.tu-berlin.de/reibungsphysik>

Key words: crack, dynamic fracture, elastic vortex, DEM, movable cellular automata.

Abstract. The paper is devoted to the numerical study of some fundamental aspects of longitudinal shear crack propagation in sub-Rayleigh and supershear regimes. The simulation was carried out with use of particle-based movable cellular automaton method. It is shown that a well-known phenomenon of shear crack acceleration towards longitudinal wave speed is explained by the formation and development of elastic vortex traveling ahead of the crack tip at a shear wave velocity. The stress concentration area ahead of the crack tip revealed by different authors is connected with the elastic vortex. Shear crack accelerates towards the longitudinal wave speed through the formation of a daughter crack by the mechanism of shearing (the daughter crack is formed in the center of elastic vortex). Analysis of sub-Rayleigh-to-intersonic transition showed that the condition of this transition can be expressed in terms of dimensionless geometrical crack parameter.

1 INTRODUCTION

Dynamic crack propagation has been studied both experimentally and numerically for many years. Nevertheless some fundamental questions concerning the material deformation in the vicinity of the crack tip are still not fully understood. In particular, why the near-circular or elliptical area with high stress concentration is formed near the tip of propagating longitudinal shear crack? This question is of fundamental importance because under mode II loading (longitudinal shear) the effect of stress concentration ahead of the crack tip is most pronounced and determines the main features of dynamic crack development [1-3]. Continuum mechanics based analytical and numerical solutions explain such stress concentration by elastic strain energy transport/influx from unloaded material behind the crack tip. However a satisfactory physical explanation of processes and the mechanism

leading to the formation of relatively small (localized) elliptical region with high stress concentration near the tip of dynamically growing mode II crack has not yet been given.

Formation of a maximum of shear stresses ahead of mode II crack growing in unstable regime was first shown analytically by Burridge [1]. In the following decades the evolution of such stress peak was studied in detail by numerical modeling and laboratory experiments [2,4-7]. In particular, it was shown that this stress peak forms at the initial stage of unstable crack growth and then propagates ahead of the rupture front at a shear wave velocity [2]. Moreover, during the course of dynamic crack propagation an area of concentration of shear stresses ahead of the crack tip is enlarged, and the magnitude of the stress peak increases. Under certain conditions stress peak magnitude can reach the shear strength of the material. In this case small fracture ahead the shear crack tip is nucleated (it was called by Abraham and Gao [8] a daughter crack). This daughter crack is capable to propagate faster than the shear wave speed (in intersonic regime). An effect of stress peak induced acceleration of mode II cracks towards the longitudinal wave speed is quite general as it was observed numerically or instrumentally at various spatial scales from the atomic one [8] to the scale of tectonic faults [9,10]. It was found that important features of shear crack growth in supershear regime are many times higher values of velocity and displacement amplitudes, as well as duration of the oscillations, as compared to the conventional sub-Rayleigh regime.

Therefore, understanding of physical causes of formation of elliptical region of stress concentration ahead of longitudinal shear crack and the conditions providing the ability of the shear crack to develop faster than the speed of transverse elastic wave are the keys to identify general features of dynamic fracture of solids at different spatial scales under shear dominated loading. Presented study is devoted to the numerical analysis of this problem.

2 PROBLEM STATEMENT

Analysis of the results of theoretical and experimental studies of unstable development of mode II cracks gave the reason to believe that the formation and development of a localized region of maximum shear stress ahead of the crack tip has to be a consequence of the collective vortex-like elastic displacement of material particles near the tip. Note that circular (vortex-like) motion profile of material particles in a certain plane is conventionally associated with surface waves (Raleigh, Love or Lamb waves) and waves propagating along the interfaces between different phases (Stoneley wave). The trajectories of material particle motion in such waves have pronounced vortex nature. We can assume that in the case of propagating longitudinal shear crack the opposite direction of motion of the material layers separated by a crack will provide conditions for the formation of elastic circular motion of material points near the crack tip in much the same way as dynamic vortex structures form in liquids or gases at flow past an obstacle.

One of the most important characteristics of elastic waves is the concentration of elastic energy concerned with volume strain (in longitudinal waves) or shear strain (in shear waves). In the case of collective vortex-like elastic motions (in particular, in surface waves), which are often considered as the result of interference of a large number of differently oriented shear waves, the concentration of the elastic strain energy must be related, primarily, with elastic strain energy of distortion (in other words, with shear stresses). Therefore it is logically to

assume that the area of concentration of shear stresses in elastic vortex should have a circular or elliptical shape.

To study the question of whether collective vortex-like elastic motions of material points could be the real physical mechanism of formation of elliptical stress concentration region ahead of the mode II crack tip (formation of such a region was shown by different authors [10,11]), we have performed computer-aided simulations.

The simulation was carried out with use of particle-based movable cellular automaton (MCA) method. The MCA method belongs to the group of *distinct element methods* within a wide class of discrete element methods (DEM). The DEM treats the solid as an ensemble of linked (chemically bonded) or contacting interacting particles and hence is an efficient tool to simulate fracture phenomena (including multiple fracture) accompanied by contact interaction of surfaces [12,13]. These advantages have determined the choice of this numerical technique for analysis of shear crack propagation. The main advantage of the MCA method as being compared to other representatives of the group of distinct element methods is multi-body formulation of element-element interaction forces [14,15]. Such a formulation makes possible to interconnect average strains and stresses in the volume of distinct element with forces of element interaction with neighbours (such approximation to description of element deformation is called approximation of *simply deformable element*). This allows implementation of various constitutive laws of solids (each automaton behaves following applied constitutive law and hence the mechanical response of the whole ensemble of elements corresponds to applied constitutive equations) and overcoming some critical limitations of the distinct element method including packing related artificial anisotropy and fundamental problems in correct simulation of irreversible strain accumulation in ductile materials.

To treat the considered problem the model of many-body interaction, which provide macroscopically isotropic linear-elastic response of particle ensemble, was applied [14,15]. Equivalent stress criterion was used as a criterion of breaking the bond between linked particles (i.e. as a fracture criterion) [14].

The numerical study was carried out with use of the two-dimensional model slab (Fig. 1). It consists of two bonded parts. Parts have the same properties and are isotropic, linear-elastic and high-strength. The following mechanical properties of material of the plates were used in the study: Young modulus $E=200$ GPa, Poisson's ratio $\nu=0.3$, density $\rho=5700$ kg/m³. Ideal bonding between the parts was assumed. This assumption means that thickness of the interface zone is much smaller than automaton (element) size. In the framework of such assumption the only interface property taken into account in the model is interface strength. In the study we assumed much smaller interface strength (critical value of equivalent stress σ_{eq}^{is} was assigned to be 250 MPa) in comparison to strength of plates themselves ($\sigma_{eq}^{ps}=2000$ MPa). A short initial section (preliminary crack) at the interface was cut by means of breaking bonds between corresponding linked elements belonging to different parts of the slab. Note that such kind of models with "weak" (low-strength) interface is typically used in studies of shear crack development because shear cracks always tend to kink into the plate or branch out [3].

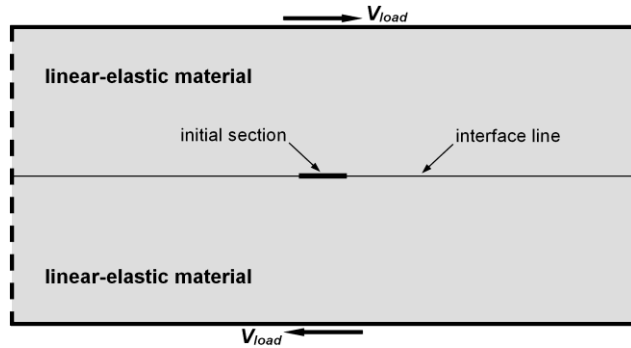


Figure 1: Schematic representation of the geometry of two-dimensional plane-strain model and the loading conditions. Horizontal solid bold lines delineate the upper and the lower external boundaries. Vertical dashed bold lines mark the side boundaries subjected to periodic boundary conditions in horizontal direction. Longitudinal shear loading is modelled by displacement of the upper and the lower external boundaries in horizontal direction at a constant velocity V_{load} . Vertical positions of these boundaries are fixed.

To simulate shear loading, the upper and the lower layers of elements defining the opposite horizontal faces of the slab were displaced in opposite directions along the interface line with very low constant velocity V_{load} (Fig. 1). This loading scheme models the condition of simple shear of the system in quasi-static regime. Periodic boundary conditions in horizontal direction (along the interface line) were applied to opposite vertical (side) faces to avoid the influence of contortions at these faces of the slab. Plane strain state approximation was used as a boundary condition in the normal direction to the considered plane. The applied loading and boundary conditions remained unchanged during the simulation.

Under such a loading the course of deformation of the slab consists of two stages. In the first stage the slab is elastically deformed and accumulates elastic energy. Maximum shear stresses in the specimen are concentrated at the crack tip. Upon reaching the threshold value of shear stress τ_0 (shear strength τ_0 , which depends on the length of the initial crack and amounts a portion of the shear strength of intact interface) the second stage related to the dynamic crack propagation at the interface begins.

3 SIMULATION RESULTS AND DISCUSSION

3.1 Formation and development of elastic vortices

Fig. 2 shows several consecutive snapshots of distribution of element velocities in the area surrounding the right tip of dynamically propagating shear crack. It is clearly seen that at the beginning of unstable crack growth the collective vortex-like elastic motion of material particles (hereinafter referred to as elastic vortex) is formed ahead of the tip of growing crack. As the crack develops the elastic vortex occupies a larger area in front of the crack. The development of an elastic vortex is inseparably linked with development of a crack. During the short initial period of crack propagation the crack velocity rapidly increases to the value comparable with Raleigh wave speed (this period depends on material and geometrical parameters of the sample and crack and takes several microseconds in the example shown in Fig. 2) and then changes slightly [3,4,8]. During this period the elastic vortex is formed as a self-dependent dynamic structure.

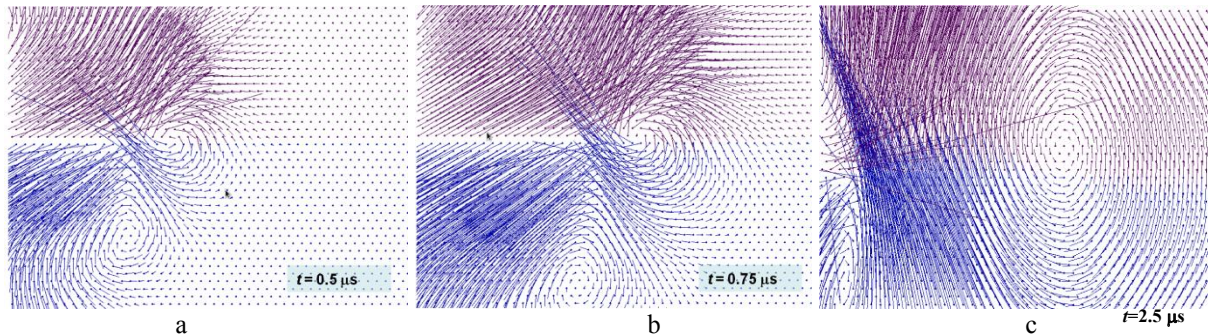


Figure 2: Fields of velocities of distinct elements near the right tip of growing shear crack 0.5 μ s (a), 0.75 μ s (b) and 2.5 μ s (c) after propagation beginning. Crack is propagating from the left to the right. In the shown example initial crack length was 0.6 mm, the height of the slab was 14 mm, the size of the distinct element was 0.1 mm. Transition to steady-state regime of vortex and crack propagation takes just about several microseconds.

Formation of such a vortex at the beginning of dynamic crack propagation is not surprising. Previous study by the authors have shown that dynamic loading or dynamic change of specimen stress state can lead to formation of elastic vortices near grain or interphase boundaries as well as near free surfaces [16]. In the considered case the formation of a vortex is also concerned with a presence of free surfaces. These are surfaces of the initial crack which provide conditions for bending around the crack tip.

Formation and propagation of elastic vortices is an important mechanism of dynamic redistribution of elastic strain energy in the material. In the considered case of unstable propagation of a shear crack the elastic strain energy comes ahead of the crack tip from unloading material behind the tip. Crack tip advancement is accompanied by divergence of surfaces behind the tip (crack opening). Such opening leads to increase in crack normal (tensile) component of crack tip strain. Fracture is accompanied by dynamic liberation of elastic strain energy accumulated in material of slab parts behind the crack tip (elastic energy transforms to kinetic energy). Due to the opening of growing mode II crack the dominating part of this kinetic energy in a short segment behind the crack tip is concerned with transversal or crack normal component of particle velocities. This can be illustrated by Fig. 3 showing typical distributions of crack normal and crack parallel components of kinetic energy density along the interface at different time moments after crack propagation beginning. Distributions are built for the thin horizontal layer of the upper part of the slab adjoining the interface. It is seen that around the crack tip the crack normal component of kinetic energy is order of magnitude larger than crack parallel. Maximum values of crack normal velocities are strongly localized within the thin vertical layer containing the crack tip. Horizontal gradient of crack normal (vertical) component of velocity vectors reaches here the maximum values as well. This indicates high shear strain rate in the thin vertical layer containing the crack tip and leads to intensive transfer of elastic energy ahead of the crack tip by the transverse (shear) elastic wave. Note that the magnitude of crack normal component of velocity vector gradually decreases with distance from the crack tip in vertical (crack normal) direction. This causes the vertical gradient of the strain rates. Strong horizontal and vertical gradients of velocities (and elastic displacements) in the slab parts at and behind the crack tip leads to the formation of collective vortex-like elastic motion ahead of the crack tip.

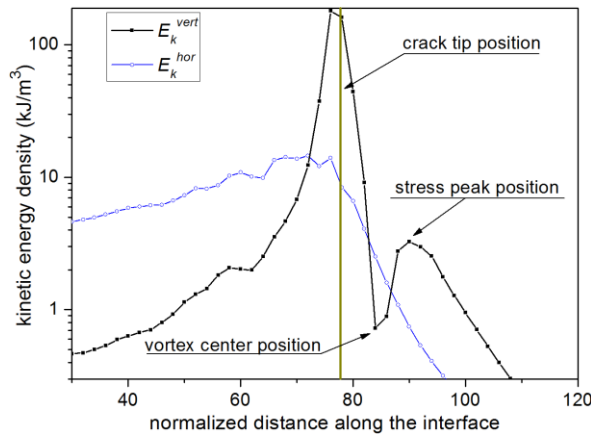


Figure 3: Typical distributions of crack normal (E_k^{vert}) and crack parallel (E_k^{hor}) components of kinetic energy density along the interface. An example shown in Fig. 2 is presented. The plot corresponds to the time moment shown in Fig. 2c. The abscissa is the distance to the initial position of the crack tip, divided by the distinct element size. Crack is propagating from the left to the right. Bold vertical line in the center of plot indicates instantaneous position of the crack tip.

Localized collective circular displacements of material points in elastic vortex indicate the concentration of shear stresses. Fig.4 shows typical equivalent stress distributions near the right tip of growing mode II crack at different stages of vortex development. Strongly pronounced elliptical region of high shear stresses (compared to background value far from the crack) accompanies the vortex-like collective behavior of material ahead of the crack tip. This elliptical region is situated in the frontal part of the vortex. Horizontal coordinate of the center of this region (maximum of equivalent stress distribution) corresponds to the coordinate of the maximum value of crack normal component of element velocities in the frontal part of the vortex (see Fig. 3). Note that this coordinate corresponds to position of stress peak ahead of the crack tip described by Burridge [1] and Andrews [2]).

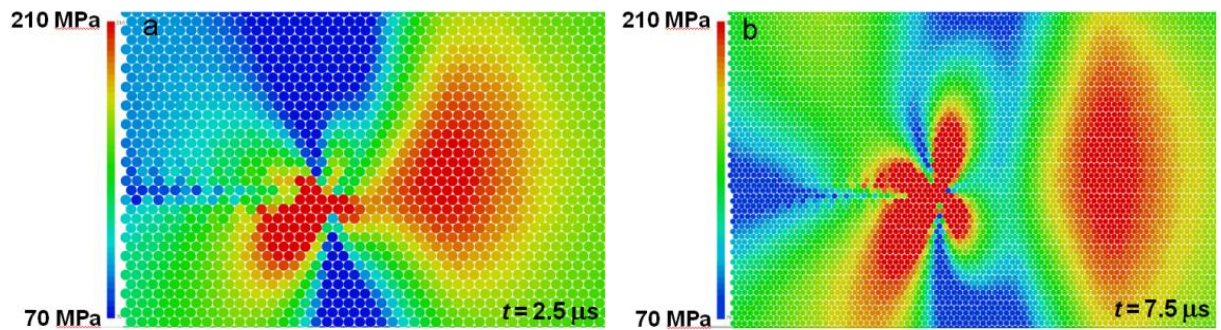


Figure 4: Snapshots of the distributions of equivalent stress near the right tip of dynamically growing shear crack 2.5 μ s (a) and 7.5 μ s (b) after growth start. An example shown in Fig. 2 is presented. Stress distribution in Fig. 4a corresponds to the time moment shown in Fig. 2c. Pictures demonstrate stress patterns before (a) and after (b) detaching of elastic vortex from the crack.

Since the formation of the elastic vortex is due to the influx of elastic energy, during the course of dynamic crack propagation the vortex increases in size (it occupies larger area ahead of the crack tip), and the concentration of shear stress in the vortex increases as well.

The velocity of propagation of the vortex rapidly approaches the shear wave speed V_S . At the same time the crack advances at a velocity lower than Raleigh wave speed V_R . So, during the course of propagation the vortex gradually moves away from the crack tip and finally detaches from it. Two snapshots in Fig. 4 show equivalent stress distributions before (Fig. 4a) and after (Fig. 4b) vortex detaching from the crack. The elastic strain energy in the vortex increases until the moment of its separation from the crack (i.e. while the vortex has energy supply). After separation the elastic vortex becomes a self-dependent dynamic object, which propagates independently on the source of its origin. During the course of subsequent (independent) vortex propagation the concentration of shear stresses gradually decreases.

Intensive transfer of elastic strain energy of distortion ahead of the tip of advancing mode II crack by the shear elastic waves (i.e. at a shear wave speed) provides the conditions for the formation of a new vortex at the crack tip after separation of the first one. The history of new vortex development and direction of rotation are similar to those for the first vortex. Fig. 5 shows an example of equivalent stress distribution near the right tip of the mode II crack after the second vortex formation. Note that the second vortex repeats the “fate” of the first one. The maximum concentration of equivalent stress in the second vortex is achieved to the moment of separation from the crack tip (this moment is shown in Fig. 5). After that the second vortex moves independently (it follows the first one) and gradually attenuates.

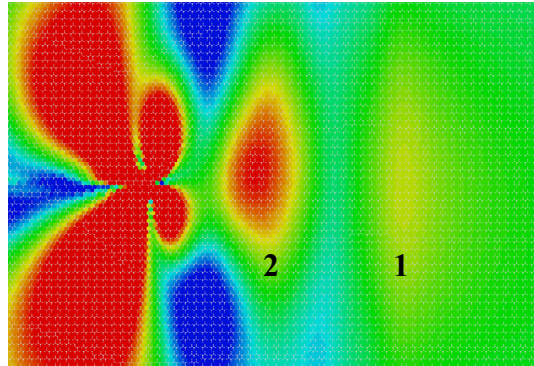


Figure 5: Snapshot of the distribution of equivalent stress near the right tip of growing shear crack after formation of the second vortex. An example shown in Fig. 2 is presented. The first and the second elliptical areas of shear stress concentration concerned with elastic vortices are shown by numbers 1 and 2 correspondingly.

So, mode II crack propagating in conventional sub-Raleigh regime generates a chain of elastic vortices moving ahead of the tip at a shear wave speed V_S . The main feature of these vortices is stress concentration in their frontal parts. In this study the limiting rheological model of material (namely, the elastic-brittle material) was considered. In the framework of this model fracture is not preceded by plastic deformation connected with motion of crystal lattice defects or accumulation of low rank damages. In fracture mechanics models inelastic deformation ahead of the crack tip in real materials is taken into account by means of introduction of a process zone composed of fracture process zone and hardening plasticity zone. Simulation results give grounds to suggest that plastic deformation of material strip (including interface segment) ahead of the tip of unstable growing mode II crack can realize in quasi-periodic manner (by series of elastic vortices).

In conventional analytical models of dynamic propagation of longitudinal shear cracks the

steady-state regime of this process is considered as a self-similar [1]. This means that the elastic vortices propagating ahead of the crack tip need to be scale-invariable objects.

This assumption was confirmed by a specially conducted numerical simulations on geometrically similar slabs with initial sections (cracks), obtained by spatial scaling of the sample in Fig. 1 within several orders of magnitude. Scaling was done by means of increasing the size of the distinct elements and corresponding increasing the size of the sample while maintaining the aspect ratio (the initial crack was scaled as well as the slab). Spatial scaling is characterized by dimensionless coefficient which is the ratio of size of scaled distinct element to the original element size. Simulation results showed that the extensive parameters of elastic vortices (including the time from vortex nucleation to separation from the crack, the geometric characteristics of vortex at different stages of development, stress and strain gradients) in scaled samples are scaled along with spatial scaling, while the intensive vortex parameters (values of stresses and velocities in corresponding areas) remain the same in all cases. This demonstrates the scale-invariable nature of elastic vortices propagating ahead of the tip of mode II cracks growing in sub-Rayleigh regime

3.2 Conditions of sub-Rayleigh-to-supershear transition

We have also made an extension to this study. Simulation results showed that stress concentration in frontal part of elastic vortex is determined by the density of elastic strain energy of distortion E_0 accumulated in the slab to the moment of crack propagation beginning. Such a relation is clear because liberation and redistribution of elastic strain energy during dynamic crack propagation is realized at the expense of preliminary accumulated energy. The concentration of elastic energy in elastic vortex is characterized, in particular, by the magnitude of equivalent stress peak at the interface ahead of the crack tip. This stress peak is situated at the central point of the imaginary section of elliptical region of high shear stresses (examples of such a region are shown in Fig. 4 and Fig. 5) by interface line.

Note that an interest to stress peak magnitude is determined by its “responsibility” for crack acceleration towards the supershear propagation regime [2]. The maximum magnitude of the equivalent stress peak σ_{eq}^{max} is achieved to the moment of detaching of the elastic vortex from the crack. The study has shown that σ_{eq}^{max} is proportional to the shear strength τ_0 of the slab with initial crack, or, what is the same, to the root of accumulated elastic strain energy E_0 ($\tau_0 = \sqrt{2E_0G}$, where G is shear modulus of material):

$$\sigma_{eq}^{max} = a + b(\tau_0 - \tau_\infty), \quad (1)$$

where a and b are constants depending on material properties, τ_∞ is an asymptotic shear strength of the interface with semi-infinite crack. Parameters E_0 and τ_0 are directly connected to geometrical characteristics of initial crack (particularly, E_0 is inversely proportional to its length). It is clear that due to scale invariance of crack and vortex propagation the parameters E_0 and τ_0 (and hence the maximum magnitude of the stress peak σ_{eq}^{max}) should be the functions not of individual dimensional geometrical characteristics of initial crack but of dimensionless parameter connecting dimensional geometrical characteristics.

In the partial case of simple shape of initial crack (section or rectangular notch) the most

important dimensional characteristics of the crack are the length L_0 and thickness D . Note that for section-like cracks the physical meaning of the parameter D is roughness of crack surfaces (when modelling material with a section by the ensemble of distinct elements the regular artificial roughness of the crack surfaces is determined by distinct element size). For rectangular notch-shaped cracks the parameter D has the meaning of the distance between notch surfaces. Special study has been conducted with the purpose to analyze the dependence of τ_0 on D and L_0 for these two types of cracks (in the case of section-like initial cracks the value of roughness parameter D varied by changing the size of distinct elements simulating the slab). Simulation results showed that the set of two-parameter dependences $\tau_0(D, L_0)$ for initial cracks with various effective thicknesses D can be reduced to a unified (general for all the cracks) dependence of τ_0 on the dimensionless geometrical parameter $P=L_0/D$ [17]. The existence of a dimensionless parameter P , which determines the influence of the geometrical characteristics of a crack on τ_0 (and, consequently, on the equivalent stress peak σ_{eq}^{max}) confirms the scale invariant nature of dynamic growth of mode II cracks.

Revealed dependence $\sigma_{eq}^{max}(P)$ is of fundamental importance for understanding of necessary geometrical condition of shear crack acceleration towards the P-wave speed. As was shown by different authors, the crack accelerates if the stress peak at the interface segment ahead of the crack tip reaches interface strength and a daughter crack is nucleated [2,5]. Simulation results showed that the possibility of reaching a critical value of the stress peak is determined by the value of the parameter P . The initial crack is characterized by the magnitude of dimensionless parameter $P>P_{critical}$ (where $P_{critical}$ is a critical/maximum value providing the conditions for reaching the interface strength σ_{eq}^{is} by the stress peak at the interface ahead of dynamically growing crack), it is able to propagate in conventional sub-Rayleigh regime only. Otherwise ($P<P_{critical}$) it has the potential to overcome Rayleigh wave velocity barrier. This particularly means that only crack whose initial length is $L_0 < L_{critical}=D \cdot P_{critical}$ is capable of propagating in intersonic regime.

Simulation results showed that for elastic-brittle materials the quantity $P_{critical}$ varies from 1 to 10. For elastic-plastic materials the quantity $P_{critical}$ should be much smaller.

Thus, the effective thickness of the crack D (roughness of the section surfaces, the distance between the surfaces of the notch and so on) determines the maximum value of the initial crack length $L_{critical}$ such that a crack may potentially propagate at a supershear velocity. Such an effect of the parameter D is defined by the features of displacement and strain distributions around the crack at the stage of stable deformation (prior to unstable crack propagation). In particular, displacement field ahead of the stable shear crack is contorted and the crack is open. The contortion and crack opening both decrease with increase in the height of crack surface asperities (for section-like cracks) or gap between surfaces of notch (i.e. as the parameter D increases). This results in a lower concentration of shear stresses at the interface near the crack tip and consequently in an increase in the value of the density of elastic strain energy of distortion E_0 accumulated in the slab to the moment of crack propagation beginning.

The dependence of the critical value of a dimensionless geometric parameter P on the magnitude of the elastic constants and the density was analyzed for the partial case of elastic-brittle materials. The dynamics of unstable crack propagation is controlled by elastic energy fluxes Therefore from physical point of view stress concentration in the elastic vortex is

determined by the following differences between speeds of different elastic waves:

1. Difference between shear wave speed V_S and Rayleigh wave speed V_R (which is an upper limit of crack propagation in sub-Rayleigh regime). The difference $(V_S - V_R)$ characterizes time interval between the moments of elastic vortex nucleation and separation from the crack. The longer time interval the higher stress concentration in the vortex and vice versa (the larger speed difference the smaller stress concentration in the vortex).

2. Difference between longitudinal wave speed V_P and shear wave speed V_S . During the course of elastic vortex propagation a fraction of its elastic strain energy outflows in surrounding areas by longitudinal elastic waves. So, this difference characterizes energy loss by elastic vortex.

From this point of view the critical value of the dimensionless geometrical crack parameter (or what is the same the critical value of shear strength) should depend on the sum of these two differences, namely on the difference between longitudinal and Rayleigh wave speeds ($V_P - V_R$). Elastic wave speeds depend on the ratios of elastic moduli to material density. Hence they are material parameters.

Fig. 6a shows examples of numerically determined dependences of dimensionless geometrical parameter P on elastic wave difference. Here each set of points connected by line was obtained by varying the density and Young modulus of the slab material while maintaining constant value of Poisson ratio. Different sets correspond to different Poisson ratios. All the sets corresponding to different Poisson ratios are parallel to each other (they are shifted along the vertical axis). The offset is proportional to the Poisson ratio.

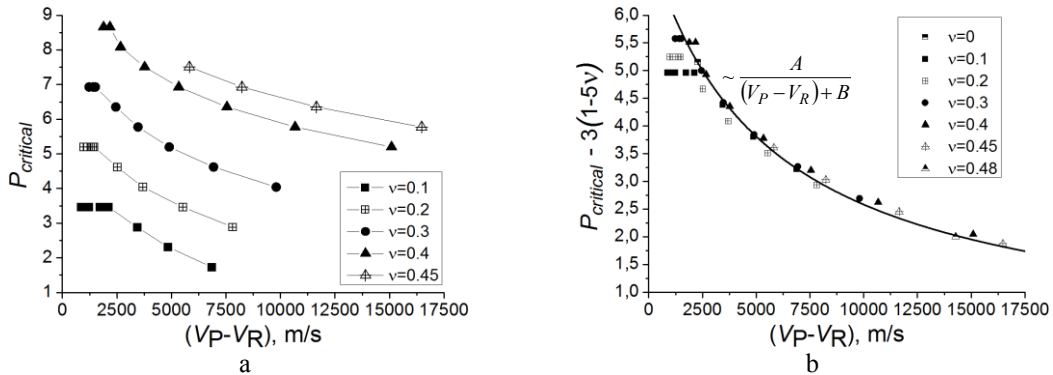


Figure 6: Dependences of the value of critical geometrical parameter $P_{critical}$ on elastic wave difference for slab materials characterized by different ratios E/ρ and Poisson ratios v (a) and the “master curve” (b).

Therefore these curves can be merged into one so-called “master curve” when using derived geometrical parameter instead of original one (Fig. 6b). Total set of points corresponding to different values of elastic constants (E, v) and densities ρ is approximated well by the following empirical equation, which is inverse proportion to elastic wave difference:

$$P_{critical} \approx \frac{A}{(V_P - V_R) + B} + 3(5v - 1), \quad (2)$$

where A and B are constants. Expression (2) determines critical value of dimensionless

geometrical crack parameter and hence the critical shear strength via elastic wave velocity difference and Poisson's ratio. The relation is valid in the very wide ranges of elastic constants and densities except the region of very small values of velocity difference. This region corresponds to extremely heavy or soft material. Here the dependence $P_{critical}(V_P-V_R)$ tends to saturation.

4 CONCLUSIONS

- The paper nicely complements numerous numerical and laboratory studies of dynamic mode II fracture and explains the concentration of high shear stresses at some distance from the crack tip by formation of a collective circular motion (elastic vortex) ahead of the shear crack. Elastic vortex in solid is a scale-invariable dynamic object. This feature explains the generality of regularities of longitudinal shear crack propagation at different spatial scales and, in particular, the well-known fact that supershear regime of shear crack propagation is observed at all scales. Moreover the importance of the results is related to their predictive ability. Numerically derived dependence (2) makes it possible to estimate critical value $P_{critical}$ for the considered brittle material. This allows one to forecast an ability of pre-existing crack (characterized by geometrical parameter P) in the considered material to propagate in supershear regime under shear-dominated loading.
- Note that elastic vortex related mechanism of stress redistribution in solids can determine not only the regularities of dynamic crack growth but peculiarities of deformation of materials under dynamic loading as well. For example the papers [18,19] describe the results of experimental observation of the formation of "a transient, short range periodicity in the direction of shear band growth in the form of an array of intense "hot spots" reminiscent of the well-known, shear-induced hydrodynamic instabilities in fluids". The results of the present study suggest that experimentally revealed small-scale localized shear regions may arise in the areas involved in intensive (high-speed) elastic vortex-like motion. Moreover the vortex related mechanism can be responsible for grain boundary migration under high-rate shear loading [20,21].

5 ACKNOWLEDGEMENTS

E.V.S. gratefully acknowledges financial support from the Russian Science Foundation grant 14-19-00718 (Russia). V.L.P. acknowledges financial support from The Tomsk State University Academic D.I. Mendeleev Fund Program (research grant No. 8.2.19.2015).

REFERENCES

- [1] Burridge, R. Admissible speeds for plane-strain self-similar shear cracks with friction but lacking cohesion. *Geophys. J. R. Astr. Soc.* (1973) **35**:439-455.
- [2] Andrews, D.J. Rupture velocity of plane strain shear cracks. *J. Geophys. Res.* (1976) **81**:5679-5687.

- [3] Shi, Z., Ben-Zion, Y. and Needleman, A. Properties of dynamic rupture and energy partition in a solid with frictional interface. *J. Mech. Phys. Solids* (2008) **56**:5-24.
- [4] Hao, S., Liu, W.K., Klein, P.A. and Rosakis, A.J. Modeling and simulation of intersonic crack growth. *Int. J. Solids Struct.* (2004) **41**:1773-1799.
- [5] Geubelle, P.H. and Kubair, D.V. Intersonic crack propagation in homogeneous media under shear-dominated loading: numerical analysis. *J. Mech. Phys. Solids* (2001) **49**:571-587.
- [6] Rosakis, A.J. Intersonic shear cracks and fault ruptures. *Adv. Phys.* (2002) **51**:1189-1257.
- [7] Dunham, E.M. Conditions governing the occurrence of supershear ruptures under slip-weakening friction. *J. Geophys. Res.* (2007) **112**:B07302.
- [8] Abraham, F.F. and Gao, H. How fast can crack propagate? *Phys. Rev. Lett.* (2000) **84**:3113-3116.
- [9] Xia, K., Rosakis, A.J. and Kanamori H. Laboratory earthquakes: the sub-Rayleigh-to-supershear rupture transition. *Science* (2004) **303**:1859-1861.
- [10] Mello, M., Bhat, H.S., Rosakis, A.J. and Kanamori, H. Identifying the unique ground motion signatures of supershear earthquakes: theory and experiments. *Tectonophysics* (2010) **493**:297-326.
- [11] Broberg, K.B. Differences between mode I and mode II crack propagation. *Pure Appl. Geophys.* (2006) **163**:1867-1879.
- [12] Mustoe, G.G.W. A generalized formulation of the discrete element method. *Eng. Computation.* (1992) **9**:181-190.
- [13] Jing, L. and Stephansson, O. *Fundamentals of Discrete Element Methods for Rock Engineering*. Elsevier, (2007).
- [14] Psakhie, S.G., Shilko, E.V., Grigoriev, A.S., Astafurov, S.V., Dimaki, A.V. and Smolin, A.Yu. A mathematical model of particle-particle interaction for discrete element based modelling of deformation and fracture of heterogeneous elastic-plastic materials. *Eng. Fract. Mech.* (2014) **130**:96-115.
- [15] Shilko, E.V., Psakhie, S.G., Schmauder, S., Popov, V.L., Astafurov, S.V. and Smolin, A.Yu. Overcoming the limitations of distinct element method for multiscale modeling of materials with multimodal internal structure. *Comp. Mat. Sci.* (2015) **102**:267-285.
- [16] Psakhie, S.G., Zolnikov, K.P., Dmitriev, A.I., Smolin, A.Yu. and Shilko, E.V. Dynamic vortex defects in deformed material. *Physical Mesomechanics* (2014) **17**:15-22.
- [17] Psakhie, S.G., Shilko, E.V., Popov, M. and Popov, V.L. The key role of elastic vortices in the initiation of intersonic shear cracks. *Phys. Rev. E* (2015) (*in print*).
- [18] Guduru, P.R., Ravichandran, G. and Rosakis, A.J. Observations of transient high temperature vortical microstructures in solids during adiabatic shear banding. *Phys. Rev. E* (2001) **64**:036128.
- [19] Li, S., Liu, W.K., Rosakis, A.J. et al. Mesh-free Galerkin simulations of dynamic shear band propagation and failure mode transition. *Int. J. Solids Struct.* (2002) **39**:1213-1240.
- [20] Psakh'e, S.G. and Zol'nikov, K.P. Anomalously high rate of grain boundary displacement under fast shear loading. *Tech. Phys. Lett.* (1997) **23**:555-556.
- [21] Psakh'e, S.G. and Zol'nikov, K.P. Possibility of a vortex mechanism of displacement of the grain boundaries under high-rate shear loading. *Combust. Expl. Shock+* (1998) **34**:366-368.

REPRESENTATION OF BULK AND SURFACE CRUSHING PHENOMENON IN DEM MODEL OF RAILWAY BALLAST

R. DUBINA AND J. ELIÁŠ

Institute of Structural Mechanics, Faculty of Civil Engineering Brno University of Technology
Veveří 331/95, Brno, 602 00, Czech Republic
dubina.r@fce.vutbr.cz, <http://www.fce.vutbr.cz/STM/dubina.r>
elias.j@fce.vutbr.cz, <http://www.fce.vutbr.cz/STM/elias.j>

Key words: Railway ballast, Discrete Element Method (DEM), bulk crushing, oedometric test

Abstract. To simulate ballast behaviour in railway track using Discrete Element Models (DEM), it is reasonable to take into account the crushing and the abrasion of grains. Nowadays, two approaches have been used in discrete modelling. The first approach represents each grain as an assembly of smaller particles with cohesive contacts between them. The crushing is represented by rupturing of contacts between particles. Such approach is universal, but demands very high computational resources. Therefore, the second approach is utilized here. At the beginning every ballast grain is modelled as one rigid body and may be replaced by several smaller particles later. Both crushing and abrasion is considered. Crushing is studied on model of oedometric test of railway ballast.

1 INTRODUCTION

Both crushing and abrasion can affect behaviour of the railway track. Therefore it is reasonable to include them in the discrete model. The grains can be crushed during the tamping of the ballast or during the cyclic loading. The Discrete Element Method (DEM) [5] has been recognized as an effective tool for studying the micromechanical behaviour of granular materials. Recently, DEM has been used to model particle fracture and crushable materials. At first the 2D models, that study the fragmentation process under compression were developed [1, 13] and compared with experiments. Nowadays, two approaches have been used in 3D discrete modelling. The first approach represents each grain as an assembly of smaller units with cohesive contacts between them [3, 7, 14]. The crushing proceeds by rupturing contacts between the particles. This approach is universal, but it demands extreme computational resources from the beginning of the simulation, because the time step is dictated by the minimum grain size. Therefore it could be better to use another approach [4, 6, 10], which is subject of our study. At the beginning every ballast grain is modelled as one rigid body, due to crushing, it might be

replaced by smaller units. In work [11] it was found that the surface fracture (abrasion) rather than bulk fracture (crushing) may dominate, therefore it is desirable to consider the abrasion too. Therefore, both crushing and abrasion models are considered. Only spherical body shapes are considered to keep the model computationally efficient.

2 BULK CRUSHING

The condition that indicate crushing is based on some equivalent stress, σ_e , in the grain, which is compared to the size depending material strength, f_t . The crushing occurs when the equivalent stress exceeds material strength.

$$\sigma_e > f_t \quad (1)$$

The equivalent stress is computed as von Mises stress (2)

$$\sigma_e = \sqrt{\frac{(\sigma_I - \sigma_{II})^2 + (\sigma_{II} - \sigma_{III})^2 + (\sigma_I - \sigma_{III})^2}{2}} \quad (2)$$

where σ_I , σ_{II} , σ_{III} are the principal stresses, which are calculated from fabric stress tensor [2]. The fabric stress tensor is expressed as

$$\sigma_{ij} = \frac{1}{V} \sum_c l_i^{(c)} F_j^{(c)} \quad (3)$$

where V is the volume of the particle, the vector $l_i^{(c)}$ connects the centroid of the grains with the c -th contact point and $F_j^{(c)}$ is the vector of contact forces. The material strength f_t is expressed as

$$f_t = \frac{f_{t0}}{r_{eq}} \quad (4)$$

where f_{t0} is the reference material strength and r_{eq} is the radius of a spherical particle. If the condition (1) is satisfied, then the grain is replaced by several smaller bodies, pieces. These pieces must have the spherical shape as the original grain, therefore their assembly cannot form the exact shape as the original grain. Also no overlapping of them and no protrusion from the original grain shape is allowed. Therefore, there is significant loss of volume. Three variants of the replacement are implemented and studied (Fig. 1). These three variants seem to be sufficient for our purpose. Considering even finer debris would lead to undesirable slowdown of the simulation due to decrease of the critical time step Δt_{cr} (5).

$$\Delta t < \Delta t_{cr} = \frac{1}{w_n} \Rightarrow r \sqrt{\frac{\rho}{E}} \quad (5)$$

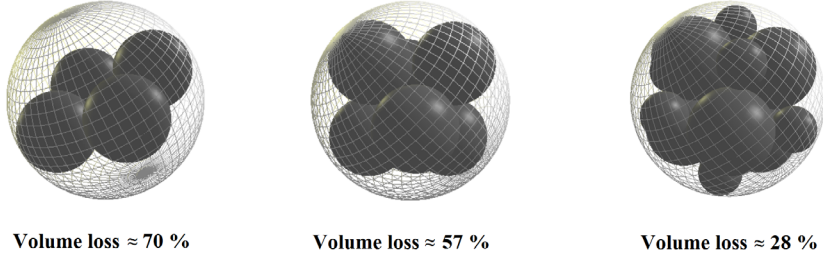


Figure 1: Three variants of replacement of the original spherical particle; the first option is replacement by four identical spheres (about 70 % of the volume is lost), the second option by six identical spheres (about 57 % of the volume is lost), the third option by fourteen spheres (more than 28 % of the volume is lost).

3 SURFACE CRUSHING

The surface crushing (abrasion) is another possibility of the railway ballast degradation. The abrasion in the model occurs when the surface pressure, p_0 , here presented by maximum Hertzian pressure [8], exceeds the material strength f_{t0} .

$$p_0 > f_{t0} \quad (6)$$

The maximum Hertzian pressure is given by

$$p_0 = \frac{3F_N}{2\pi a^2} \quad (7)$$

where F_N is normal force, $a = (Ru_N)^{\frac{1}{2}}$, with R being effective radius of spheres in the contact and u_N is penetration depth of spheres. For two spheres the effective radius is $R = \frac{R_1 \cdot R_2}{R_1 + R_2}$, where R_1, R_2 are the radii of spheres. The abraded grain has to be spherical too, because the model is limited to spherical shape only. The abrasion is represented by reduction of grain radius, see Fig. 2, $r_{\text{new}} = \gamma \cdot r_{\text{old}}$, where parameter γ is the reduction factor. For convenience, only sufficiently large grains are subjected to bulk and surface

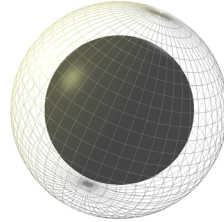


Figure 2: The surface crushing (abrasion) is managed by the reduction of radius of the spherical particle.

crushing. Whenever grain radius decreases under chosen minimal value r_{\min} , it cannot crush anymore.

4 SIMULATION OF OEDOMETRIC TEST

The procedures of grain degradation described above were tested on the oedometric test which was made at the University of Nottingham by Lim [9].

The dimension of the oedometric test are 300 mm in diameter and the 150 mm in height. The boundary condition are denoted in the Fig. 3 (markers \perp , \odot or dots in floor projection).

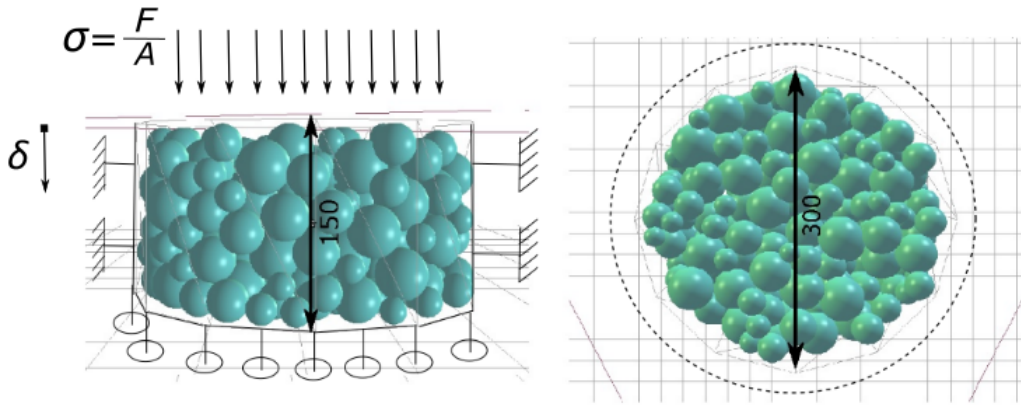


Figure 3: Scheme of the oedometric test; The diameter is 300 mm and height is 150 mm. The mean diameter of spherical grains is 32.5 mm, the standard deviation is 7 mm.

The simulation proceeds as follows. The oedometer is filled by grains, which diameter is randomly sampled from uniform distribution between 20.5 and 44.5 mm. Then the sample is vibrated by horizontal acceleration to provide sufficient number of contact between grains. The subsequent compressive cycle loaded the sample by force up to 1500 kN and then unload, the loading is defined by sinus function

$$F(t) = \frac{1500}{2} \left[\sin\left(2\pi ft - \frac{\pi}{2}\right) + 1 \right] \quad (8)$$

where f is loading frequency and t is the loading time. The material properties were set according to the literature. The oedometer material was made from steel, its density was set to 7850 kg/m³, the Poisson number to 0.25 and the friction angle to 0.0 rad [12]. The Young's modulus of the steel was considered 10 times than the Young's modulus of ballast. The ballast density was 2600 kg/m³, the Poisson number 0.3 and the friction angle 0.8 rad [10]. The Young's modulus of ballast is set to $3 \cdot 10^{11}$ Pa based on our previous research and according to Lim [9].

5 RESULTS OF THE SIMUALTION

The results are presented using loading force F and movement of the loading plate δ . The effect of several input parameters were investigated for both modes of grain

degradation. Namely type of the replacement of the origin sphere, the minimal radius r_{\min} , reference value of material strength f_{t0} and the reduction factor γ in surface crushing (abrasion). All these investigated parameters have the expected influence on the $F - \delta$ diagram. The most significant influence had the volume loss (type of replacement).

Two studies are selected and presented here in detail. The first parameter is the loading frequency f . Six different values of loading frequency are used 0.25, 0.5, 1.0, 2.0, 4.0 and 8.0 Hz. The results are presented in Fig. 4. Five realizations of oedometric test for

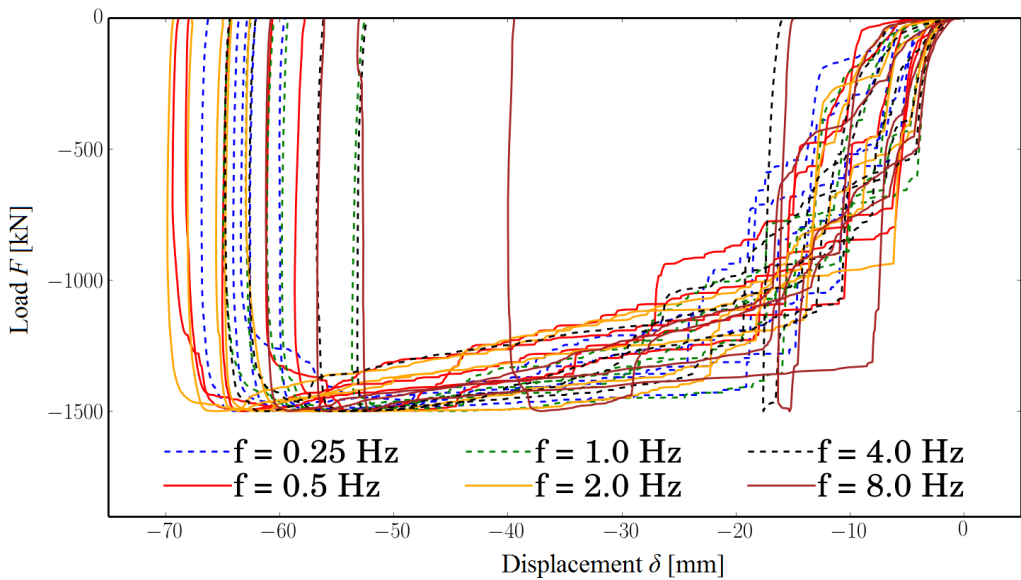


Figure 4: The Load - Displacement diagram of oedometric test simulation; Six values of loading frequency are investigated, for each frequency five realizations are computed.

each loading frequency are calculated. These realization differ in initial configuration of spheres inside the oedometer. Particle crushing is in the graph represented by horizontal jumps. The majority of simulations has the maximum displacement about 60 mm and similar shape of the loading curve. There are however also curves which have substantially smaller displacements (dashed black and solid red), where it almost does not occur particle crushing due better force redistribution. From the study we conclude that loading frequency (in range 0.25 - 8.0 Hz) has almost no effect on results.

The other investigated parameter is so-called crushing period, T_c . The crushing period represents a time period, after which the crushing condition is checked. The purpose of crushing period is to save a computational time comparing to simulation when crushing condition is checked every time step. Sixty realization of oedometric test were computed for different crushing periods. The displacements at the peak force are shown in Fig. 5. In the most left part of Fig. 5 are results, when the control of crushing is checked in every time step. In the right part of the graph the crushing condition is checked every 0.04 s.

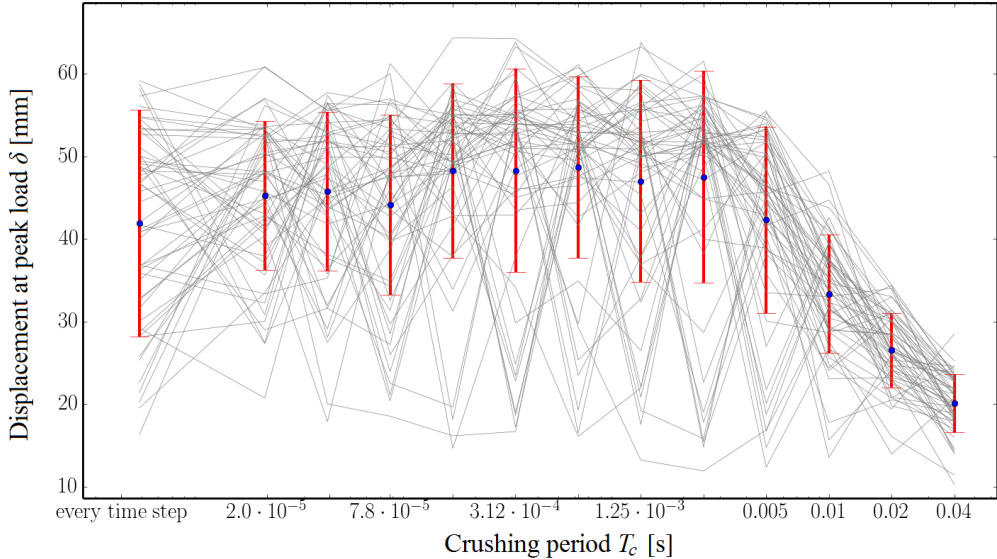


Figure 5: The dependence of displacement at peak load, δ , on crushing period, T_c ; Sixty realization for each crushing period are shown by solid grey lines; Errorbars show mean value and standard deviation.

We expect that there would exist a certain crushing period, from which the mean values of displacement (blue points in Fig. 5) will be constant. The first five largest crushing periods have an expected trend and by increasing crushing period the number of crushed particles grows and the displacement grows. As well in range $T_c = 2.5 \cdot 10^{-3}$ to $3.12 \cdot 10^{-4}$ s the mean displacement is almost constant. This was expected to remain for even smaller crushing periods. However, in range for smaller crushing periods decrease of mean value of displacement occurs. This decreasing is undesirable and the reason of this behaviour is the object of future research.

6 CONCLUSIONS

The developed algorithm of particle crushing suffers by large volume loss. Therefore its application is more convenient for problems where the crushing has local character. In studied range of loading frequencies, the crushing model is independent on the loading frequency. The observed dependence on crushing period will be subject of further research.

ACKOWLEDGEMENT

This outcome has been achieved with the financial support of Brno University of Technology under project No. FAST-J-15-2849. The support is gratefully acknowledged.

REFERENCES

- [1] Astrm, J. A. and Herrmann, H. J. Fragmentation of grains in a two-dimensional packing. *Eur. Phys. J. B.* (1998) **5**:551–554.
- [2] Bagi, K. Stress and strain in granular assemblies. *Mechanics of Materials.* (1996) **22**:165–177.
- [3] Cheng, Y. P., Nakata, Y. and Bolton, M. D. Discrete element simulation of crushable soil. *Géotechnique.* (2003) **53**:633–641.
- [4] Cleary, P.W. DEM prediction of industrial and geophysical particle flows. *Particulology.* (2010) **8**:106–118.
- [5] Cundall, P.A. and Strack, O.D.L. A discrete numerical model for granular assemblies. *Géotechnique.* (1979) **29**:47–65
- [6] Eliáš, J. Simulation of railway ballast using crushable polyhedral particles. *Powder Technology.* (2014) **264**:458–465.
- [7] Ergenzinger, Ch., Seifried, R. and Eberhard. A discrete element model predicting the strength of ballast stones. *Computers and Structures.* (2012) **3-13**:108–109.
- [8] Hertz, H. *Ueber die berhrung fester elastischer krper (on the contact of rigid elastic solids).* J. reine und angewandte Mathematik, **92**:156–171, (1882), (translated and reprinted in English in Hertz's Miscellaneous Papers (Macmillan & Co., London), (1896)).
- [9] Lim, W. L. and McDowell G. R. Discrete element modelling of railway ballast. *Granular Matter.* (2005) **7**:19–29.
- [10] Lobo-Guerrero, S. and Vallejo, L. E. Discrete element method analysis of railtrack ballast degradation under cycling loading. *Granular Matter.* (2006) **8**:195–204.
- [11] McDowell, G. R. and Amon, A. The application of Weibull statistics to the fracture of soil particles. *Soils and foundation.* (2000) **40**:133–141.
- [12] McDowell, G. R. and De Bono, J. P. On the micro mechanics of one-dimensional normal compression. *Géotechnique.* (2013) **63**:895–908.
- [13] Thakur, P. K. Vinod, J. S. and Indraratna, B. Effect of particle breakage on cyclic densification of ballast: a DEM approach. *Materials Science and Engineering.* (2010) **10**:1–7.
- [14] Wang, J. F. and Yan, H. B. 3D DEM Simulation of Crushable Granular Soils under Plane Strain Compression Condition. *Procedia Engineering.* (2011) **14**:1713–1720

TIME-DEPENDENT DEM BASED FRACTURE SIMULATIONS AT THE GRAIN SIZE LEVEL FOR BRITTLE HETEROGENEOUS SOLIDS

HEINZ KONIETZKY¹, WEI CHEN²

¹ Chair for Rock Mechanics, Geotechnical Institute, TU Bergakademie Freiberg, Germany
09599 Freiberg, Germany
e-mail: Heinz.Konietzky@ifgt.tu-freiberg.de
web page: <http://tu-freiberg.de/fakult3/gt/feme/mitarb/konietz.en.html>

² Chair for Rock Mechanics, Geotechnical Institute, TU Bergakademie Freiberg, Germany
09599 Freiberg, Germany
e-mail: chenwei.csu@foxmail.com
web page: <http://tu-freiberg.de/fakult3/gt/feme/mitarb/chen.html>

Key words: Discrete Element Method, Heterogeneous Granite, Time-dependent Fracture.

Abstract. A discrete element numerical model for Lac du Bonnet granite is built for time-dependent fracture simulations. The heterogeneity is considered by different mineral components randomly distributed inside the rock. The minerals are represented by elastic Voronoi cells connected by elasto-plastic contacts. The Hillig-Charles equation is implanted in the numerical model for analyzing time-dependent damage due to subcritical crack growth. The damage processes during uniaxial compressive creep tests are investigated. The numerical simulations reveal not only reasonable lifetime of the specimens under different loads, but also show primary, secondary and tertiary creep stages until final failure characterized by macroscopic fracturing. The simulation results of crack growth and damage index evolution deliver a deeper insight into the microscopic damage process.

1 INTRODUCTION

Time-dependent damage of rocks is especially important for long-term stability and safety of geotechnical structures such as mines, tunnels, and nuclear waste repositories. The time-dependent damage in brittle rocks has a close relationship to subcritical crack growth. Analysis of time-dependent damage of brittle rocks has been carried out by many scientists using both, continuum and discrete element based methods.

For a continuum based method: According to theory of subcritical crack growth, Konietzky et al. [1] proposed a numerical model to simulate the lifetime of rocks under static loads by growing microcracks. Li and Konietzky [2,3,4] developed this approach further by taking into account stochastic distributions for initial length and orientation of microcracks and different crack growth models.

For discrete element method: Kemeny [5] developed a fracture mechanical model, considering the degradation of cohesive strength of rocks due to subcritical crack growth, to simulate time-dependent failure of rock bridges along discontinuities. Lee [6] analyzed the time-dependent stability of Coconino rock slope using UDEC based on the method proposed

by Kemeny [5]. Park [7] introduced a numerical method in PFC to investigate time-dependent fracture growth in rocks. Potyondy [8] used PFC to simulate static fatigue of granite due to stress corrosion.

In this paper, the explicit consideration of time-dependent damage evolution due to subcritical crack growth until final failure is analyzed. UDEC is adopted to perform the numerical simulations utilizing the embedded constitutive laws for elastic grains and elasto-plastic contacts, but extended by incorporating own developed routines to simulate subcritical crack growth.

2 THEORY OF SUBCRITICAL CRACK GROWTH

The relationship between subcritical crack growth velocity and stress intensity factor is illustrated in Figure 1. As discussed by many researchers [8,9,10,11], K_{I0} is the lower limit stress intensity factor, below which the crack is stable. K_{Ic} is the Mode I fracture toughness at the time when the velocity of crack growth suddenly approaches critical values and causes failure. In region 1 (Figure 1), the velocity is controlled by the rate of stress corrosion reactions at the crack tips. In region 2, the velocity is controlled by the rate of transport of reactive species to the crack tips and in region 3, crack growth is mainly ruled by mechanical rupture and is relatively insensitive to the environment.

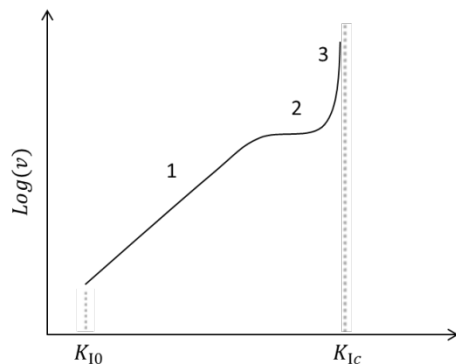


Figure 1: Crack growth velocity versus stress intensity factor [10]

Hillig-Charles equation (exponential law) is frequently used to describe the subcritical crack growth (region 1 of Figure 1). Hillig and Charles [12] made the hypothesis that the static fatigue in glass follows the rule of chemical reaction between the glass and the environment, but they have also recognized that the process is stress-sensitive. According to their findings, they proposed a quantitative equation for describing crack velocity:

$$v = v_0 \exp[(-E + V\sigma - V_m\gamma/\rho)/RT] \quad (1)$$

where E is the stress free activation energy, V is the activation volume, σ is the tensile stress at the crack tip, V_m is the molar volume of the material, γ is the interfacial surface energy between the glass and the reaction products, ρ is the radius of the curvature of the crack tip, R is the gas constant and T is the absolute temperature.

Wiederhorn and Bolz [13] have re-written Eq. (1) by introducing the two-dimensional Griffith crack term $\sigma = 2K_1/\sqrt{\pi\rho}$:

$$\begin{cases} v = v_0 \exp\left[(-E_* + 2VK_1/\sqrt{\pi\rho})/RT\right] \\ E_* = E + V_m\gamma/\rho \end{cases} \quad (2)$$

Based on Eq. (2), Wiederhorn et al. [14] have proposed an empirical relation by fitting lab test data from glass with least square method:

$$v = v_0 \exp[(-E_* + bK_1)/RT] \quad (3)$$

where b is empirical constant obtained from the fitting curve.

Eq. (3) was successfully used to analyze subcritical crack growth in rocks [8,10,15].

3 NUMERICAL MODEL

3.1 Grain-based heterogeneous model

The mineral composition of Lac du Bonnet (LdB) granite is characterized by 7.1% biotite, 51.1% K-feldspar, 31.8% quartz and 10% plagioclase. The smallest grains have a diameter of about 1 mm. They are randomly distributed within a piece of rock. The numerical model was created by Voronoi cells with equivalent diameter of about 1 mm. The percentages of the mineral components were considered and the allocation was performed in a random manner, so that the model matches the grain size distribution in an approximate manner and also bigger grain clumps (mineral clumps) were automatically produced (Figure. 2). The Voronoi cells itself are unbreakable and behave elastically. The height and the diameter of numerical model are 63.4mm and 31.7mm, respectively. The parameters for the mineral components and Voronoi cells, respectively, are given in Table 1.

Table 1: Grain parameters [16,17,18]

Mineral	Elastic Modulus (GPa)	Poisson's Ratio
Biotite	35	0.25
K-feldspar	62	0.27
Quartz	91	0.20
Plagioclase	69	0.23

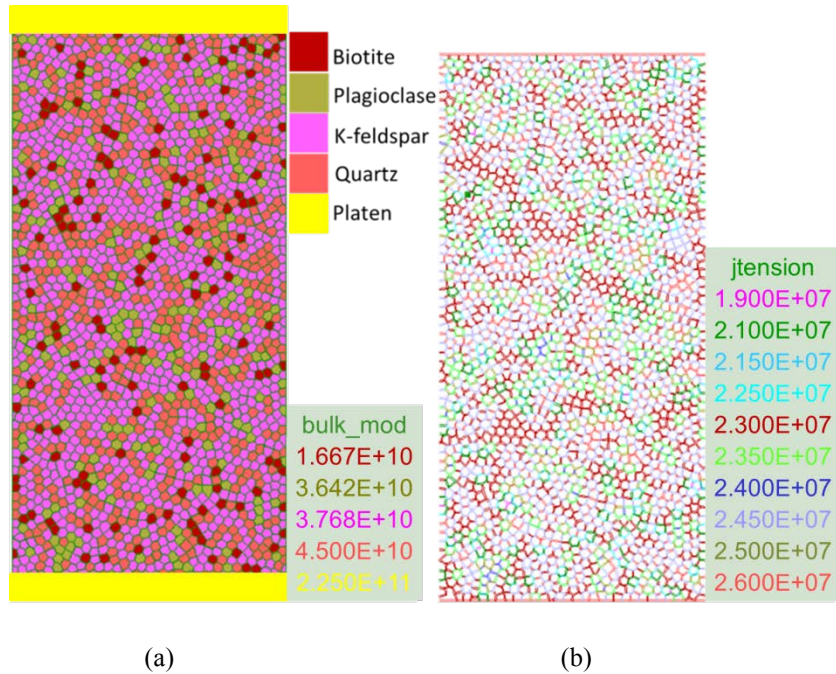


Figure 2: Model set-up: (a) Voronoi blocks representing different minerals, (b) contacts between minerals

The contact behavior is elasto-plastic and characterized by a Mohr-Coulomb failure criterion with tension cut-off and softening (Figure. 3). For each mineral component, a corresponding set of contact parameters is specified (Table 2). At the contacts between the grains, the arithmetic average of the parameters is applied. Parameters shown in Table 2 are obtained by numerical back-analysis of time-independent loading tests. The simulated and experimental uniaxial compressive strength is 234.5 MPa and 200±22 (n=81) MPa [19], respectively. In the normal and shear direction, the stress-displacement relation below the strength limit at the contacts is assumed to be linear and governed by the normal stiffness k_n and the shear stiffness k_s . If the tensile strength is reached, the contact breaks and the tensile strength is set to zero. If the shear strength is reached, sudden softening takes place and cohesion and friction of the contact are set to residual values. Eqs. (4) and (5) describe the contact behavior:

$$\begin{cases} \sigma_n = -k_n u_n \\ \text{if } \sigma_n < -J^T, \sigma_n = J_r^T = 0 \end{cases} \quad (4)$$

$$\begin{cases} \tau_s = k_s u_s \\ \tau_{\max} = J^C + \sigma_n \tan \varphi \\ \text{if } |\tau_s| \geq \tau_{\max}, \tau_s = \text{sign}(\Delta u_s) \cdot (J_r^C + \sigma_n \tan \varphi_r) \end{cases} \quad (5)$$

where σ_n and τ_s are normal stress and shear stress, respectively, u_n and u_s are normal displacement and shear displacement, respectively, J^T and J_r^T are tensile strength and residual

tensile strength, respectively, τ_{\max} is shear strength, J^C and J_r^C are cohesive strength and residual cohesive strength, respectively, φ and φ_r are friction angle and residual friction angle, respectively, and Δu_s is the incremental contact shear displacement.

Within the model the damage and fracture process associated with plastic deformations is controlled by the breakage of contacts and relative movement along or across them.

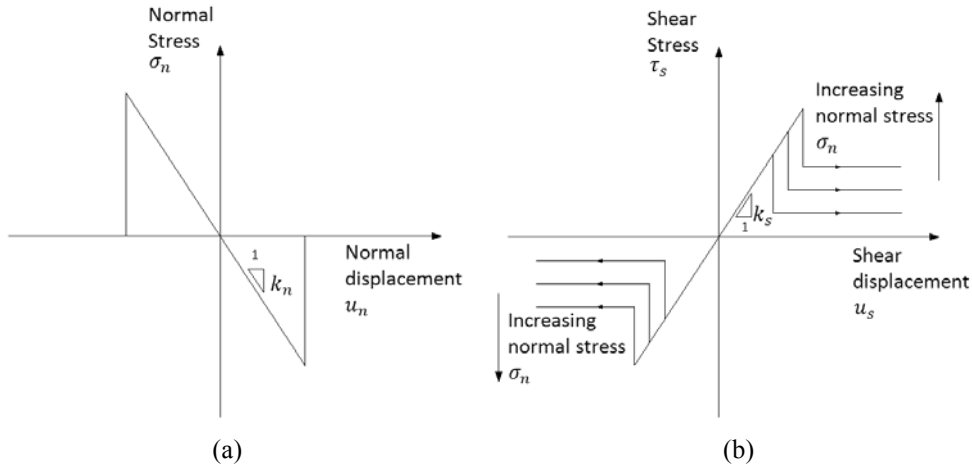


Figure 3: Elasto-plastic contact behaviour with softening: (a) in normal direction, (b) in shear direction

Table 2: Contact parameters (result of own calibration)

Contact	k_n (Pa/m)	$\frac{k_s}{k_n}$	J^T (MPa)	J_r^T (MPa)	J^C (MPa)	J_r^C (MPa)	φ (°)	$\frac{\varphi_r}{\varphi}$
Biotite/Biotite	4.20E+14	1	19	0	37	0	48	0.5
K-feldspar/K-feldspar	7.75E+14	1	23	0	52	0	55	0.5
Quartz/Quartz	1.01E+15	1	26	0	62	0	62	0.5
Plagioclase/Plagioclase	8.00E+14	1	24	0	57	0	59	0.5
Biotite/K-feldspar	5.97E+14	1	21	0	44.5	0	51.5	0.5
Biotite/Quartz	7.16E+14	1	22.5	0	49.5	0	55	0.5
Biotite/Plagioclase	6.10E+14	1	21.5	0	47	0	53.5	0.5
K-feldspar/Quartz	8.93E+14	1	24.5	0	57	0	58.5	0.5
K-feldspar/Plagioclase	7.87E+14	1	23.5	0	54.5	0	57	0.5
Quartz/Plagioclase	9.06E+14	1	25	0	59.5	0	60.5	0.5

3.2 Implementation Hillig-Charles equation into the numerical model

In order to consider subcritical crack growth, Hillig-Charles equation was implemented into UDEC under the assumption, that stress corrosion only affects contacts and not the rock matrix. Therefore, subcritical cracks can only propagate along the edges of the Voronoi cells. This leads to a time-dependent reduction of tensile and cohesive strength at the corresponding contacts. The degradation rates at the contacts are stress-dependent. The degradation for tensile strength

and cohesive strength of the contact is only influenced by tensile and shear stress in the contact.

Taking into account the above-mentioned assumptions and Eq. (1), the degradation rates can be described as follows:

$$\begin{cases} \frac{dJ_i^T}{dt} = -\lambda_r v_t = -(\lambda_r v_0 e^{-(E+V_m\gamma/\rho)/RT}) e^{V\bar{\sigma}_i/RT} \\ \frac{dJ_i^C}{dt} = -\lambda_r v_c = -(\lambda_r v_0 e^{-(E+V_m\gamma/\rho)/RT}) e^{V\bar{\tau}_i/RT} \end{cases} \quad (6)$$

where J_i^T and J_i^C are tensile and cohesive strengths at the contact i , respectively, λ_r is a constant describing the proportionality between strength degradation and subcritical crack growth velocity, v_t and v_c are crack growth velocities governed by the level of tensile and shear stress at the contact, respectively, $\bar{\sigma}_i = F_i^n/L_i$ and $\bar{\tau}_i = F_i^s/L_i$ are average tensile and shear stresses at the contact, respectively, F_i^n and F_i^s are normal and shear forces at the contact, respectively, and L_i is the contact length.

Assuming that $\beta_1 = \lambda_r v_0 e^{-(E+V_m\gamma/\rho)/RT}$ and $\beta_2 = V/RT$, and considering the constitutive model of the contacts, Equation (6) can be re-written into the following simple form:

$$\begin{cases} \frac{dJ_i^T}{dt} = \begin{cases} -\beta_1 e^{\beta_2 \bar{\sigma}_i}, & \bar{\sigma}_i < J_i^T \\ -\infty, & \bar{\sigma}_i \geq J_i^T \end{cases} \\ \frac{dJ_i^C}{dt} = \begin{cases} -\beta_1 e^{\beta_2 \bar{\tau}_i}, & \bar{\tau}_i < \tau_{\max(i)} \\ -\infty, & \bar{\tau}_i \geq \tau_{\max(i)} \end{cases} \end{cases} \quad (7)$$

where $\tau_{\max(i)}$ is the shear strength at the contact i .

The contact strength decreases with time elapsing are ruled by Eq. (7). After a certain period of time, the contact strength degrading velocity approaches infinite, meaning that sudden failure at the contact occurs. The stresses around this failed contact will be redistributed and may cause further local stress concentrations, so that strength degrading at neighboring contacts will accelerate.

4 TIME-DEPENDED DAMAGE SIMULATIONS

4.1 Uniaxial compressive creep test simulations

Schmidtke and Lajtai [20] have used 126 specimens of LdB granite to perform uniaxial compressive creep tests. The cylindrical specimen with a diameter of 37.1 mm was saturated before testing and kept submerged during testing at a temperature of 25°C. The numerical modelling approach implemented in Eq. (7) was used to simulate uniaxial compressive creep tests. The subcritical crack growth parameters are $\beta_1 = 0.001 \text{ Pa/s}$ and $\beta_2 = 1.0 \times 10^{-7}$. The other parameters are taken from Tables 1 and 2.

To minimize CPU time and to guarantee that the damage process is followed with sufficient precision, a changeable time step scheme is used for the simulations:

$$\begin{cases} \Delta t_{\min} \leq \Delta t_b \leq \Delta t_{\max} \\ \text{if } F_u < 100N, \Delta t_b = 2 * \Delta t_{b-1} \\ \text{if } F_u \geq 100N, \Delta t_b = \Delta t_{\min} \end{cases} \quad (8)$$

where Δt_{\min} , Δt_b and Δt_{\max} are the minimum, actual and maximum time steps respectively, and F_u is the unbalance force, b is the corresponding step number. For one-edged crack growth simulations we specified $\Delta t_{\min} = 1.0 \times 10^{-5}$ s and $\Delta t_{\max} = 1.0 \times 10^4$ s.

Results from lab tests [20] and numerical simulations with respect to lifetime (time to failure) for LdB granite under different driving-stress ratios are shown in Figure 4. The driving-stress ratio is defined by σ/σ_c (σ and σ_c are uniaxial actual compressive stress and uniaxial compressive strength, respectively). The data show, that lifetime of specimens decrease with increasing driving-stress ratio. For different specimens under the same driving-stress ratio, there are variations in lifetime due to the heterogeneity of rock samples.

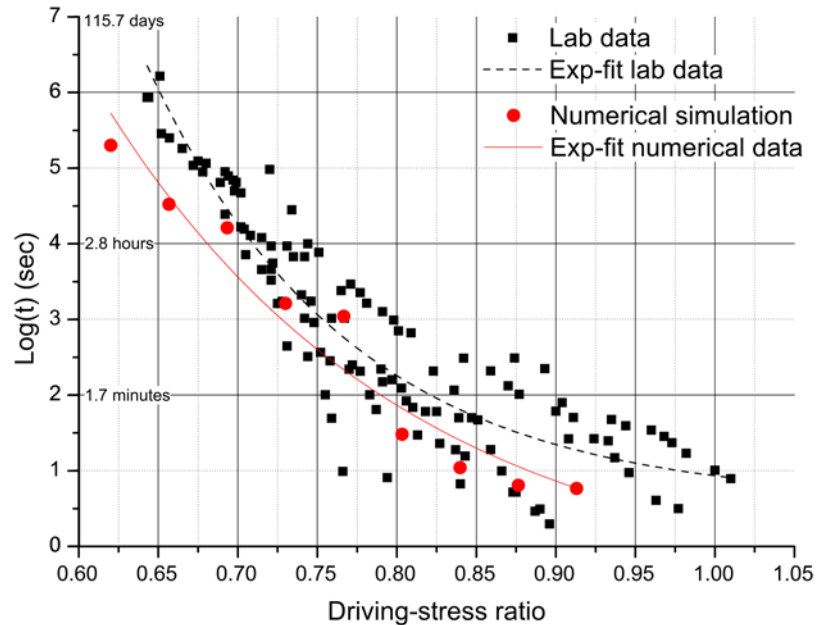


Figure 4: Lab test [20] and numerical simulation results for lifetime of LdB granite under different driving-stress ratios

Figure 5 shows simulation results of uniaxial compressive creep tests, which reveal primary, secondary and tertiary creep phases. The curves in Figure 5b is smoother than those in Figure 5a, because time steps change automatically in one case (Figure 5a) and are constant, that means equal to Δt_{\min} , in the other case (Figure 5b). The introduction of changeable time steps is necessary whenever huge lifetime is expected, which is the case for low load levels. Lifetime increases in a strong non-linear manner with decreasing load.

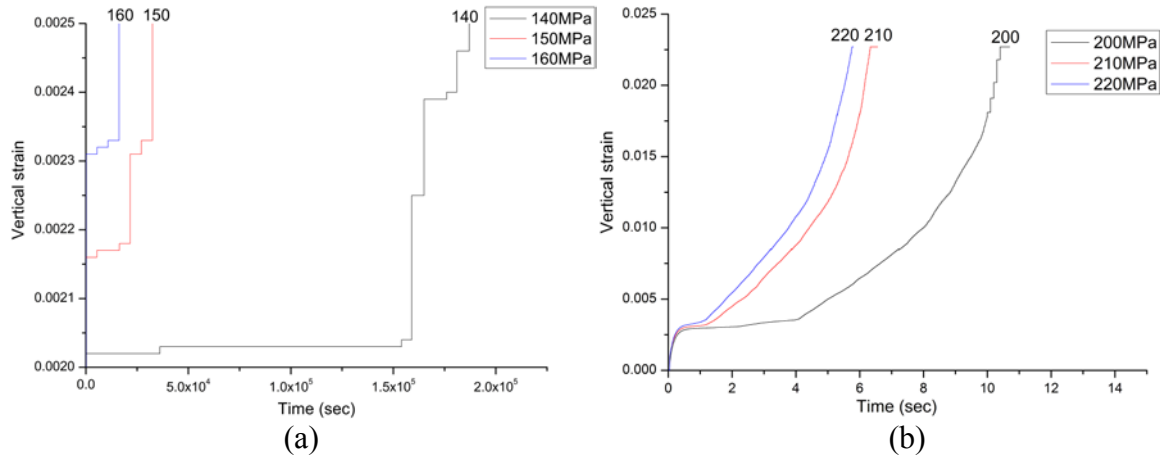


Figure 5: Uniaxial creep simulation results for strain versus time: (a) load range 140-160 MPa, (b) load range 200-220 MPa

Figure 6 shows how contact failure (microcracks) and strain develop with ongoing time under constant load of 160 MPa. The rate of contact bond breakage (microcrack development) shows some correlation to the creep phases: the rate is relatively low within the secondary creep phase, but shows stronger values at the primary and tertiary creep phases.

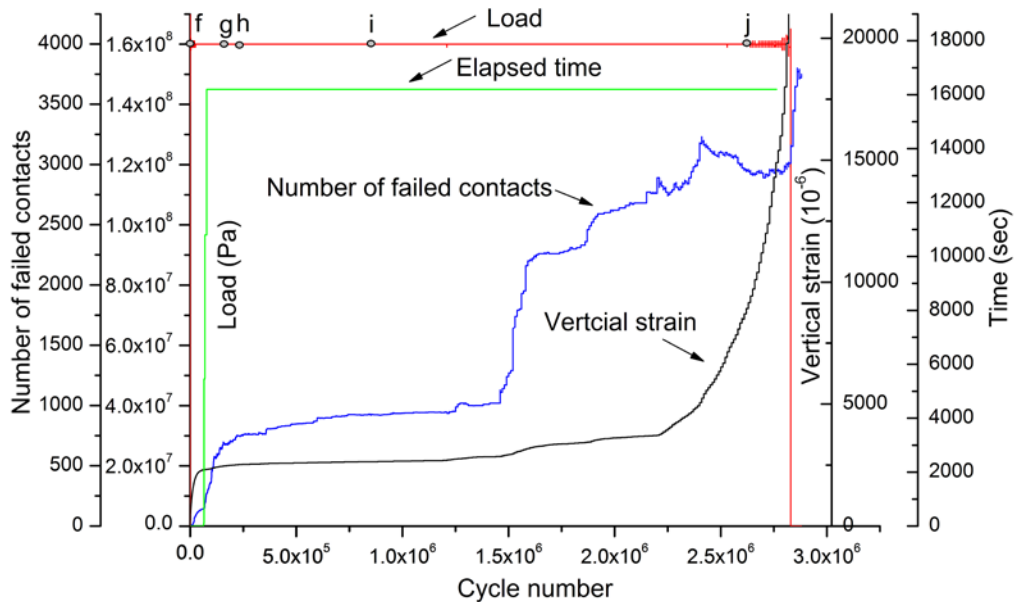


Figure 6: Simulation results of uniaxial creep tests under 160 MPa

Exemplary, macrocrack (totally detached contacts) distribution inside the specimen for a load level of 160 MPa for different points in time according to Figure 6 is shown in Figure 7. During the primary phase cracks emerge in a more random manner within the specimen (Figure 7g). Later, within the secondary creep phase, cracks grow further, interact with each other and form larger cracks mainly parallel to the maximum stress direction (Figure 7h-j). Finally, within the tertiary creep phase, massive crack interactions are observed and, in addition to large

vertical cracks, shear band formation is observed until final macroscopic failure is noticed (Figure 7 j).

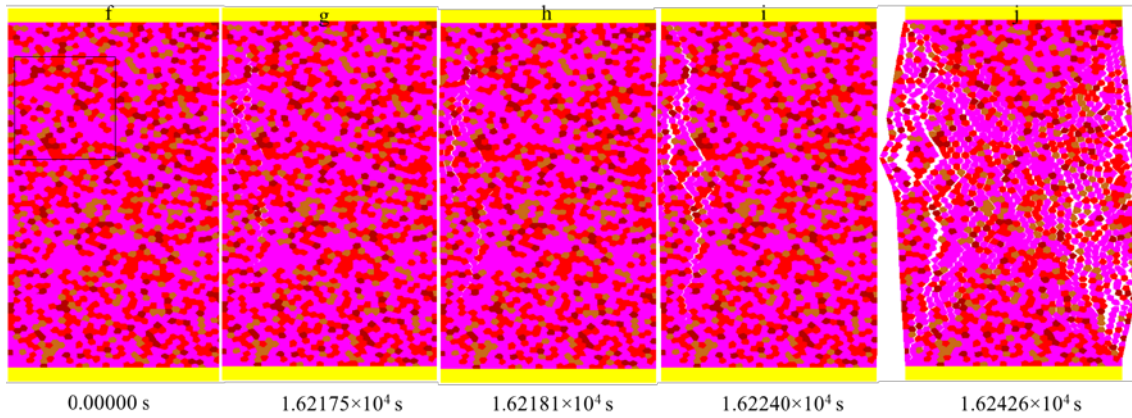


Figure 7: Macrocracks distribution under 160 MPa uniaxial compressive load for different points in time according to Figure 6

4.2 Crack growth and damage characteristic

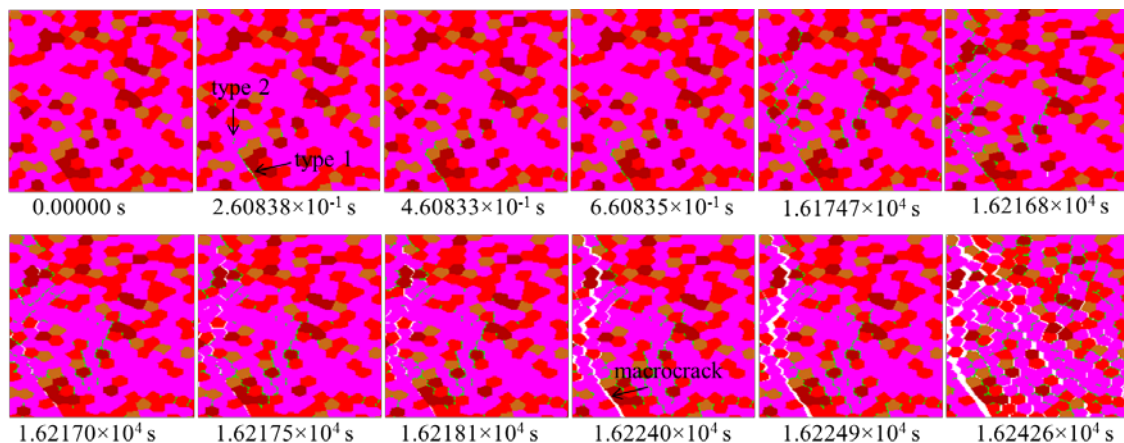


Figure 8: Microcrack and macrocrack distribution with time elapsing in a magnified viewing area indicated by black quadrangle in Figure 7f

Microcrack and macrocrack distribution with time elapsing in a magnified viewing area indicated by black quadrangle in Figure 7f is shown in Figure 8. The green lines and white space represent microcracks (position of failed contacts) and macrocracks (totally detached contacts which are the result of progressive crack development), respectively. At first the microcracks are randomly distributed within the specimen, but preferred occurring at the contacts between different minerals (type 1: inter-granular microcrack at 2.60838×10^{-1} s) and with less preference in the contacts between the same minerals (type 2: intra-granular microcrack at 2.60838×10^{-1} s). With time elapsing, more and more microcracks emerge, coalesce and form networks. Finally, this leads to occurrence of macrocracks, which is

illustrated by type 1 microcrack at 2.60838×10^{-1} s, and which develops further towards a totally opened macrocrack at 1.62240×10^4 s. As shown in Figure 8a, initially, the propagation of subcritical crack due to stress corrosion is very time consuming (from 0 s to 1.62170×10^4 s). But once the microcrack network has formed (that means stress concentration phenomenon is serious), the speed of subcritical crack growth increases suddenly, and soon the macrocrack network is created and cause failure of the specimen (from 1.62170×10^4 s to 1.62426×10^4 s).

The damage index evaluated by number of failed contacts is defined as:

$$D_n = \frac{N_{ct}}{N_{c \max t}} \quad (9)$$

where N_{ct} is the instantaneous number of failed contacts at elapsed time t and $N_{c \max t}$ is the maximum number of failed contacts at t_f (time to failure).

Simulation results in terms of damage index evolution versus normalized time elapsing is shown in Figure 9. The damage index evolution under high and low loadings is different. For the specimen under 160 MPa load, the damage index increases slowly with time elapsing during secondary creep stage (very time consuming) and then accelerates suddenly causing failure of specimen with typical tertiary creep phenomena. But for the specimen under 200 MPa load, the damage index develops quickly from beginning until failure occurs.

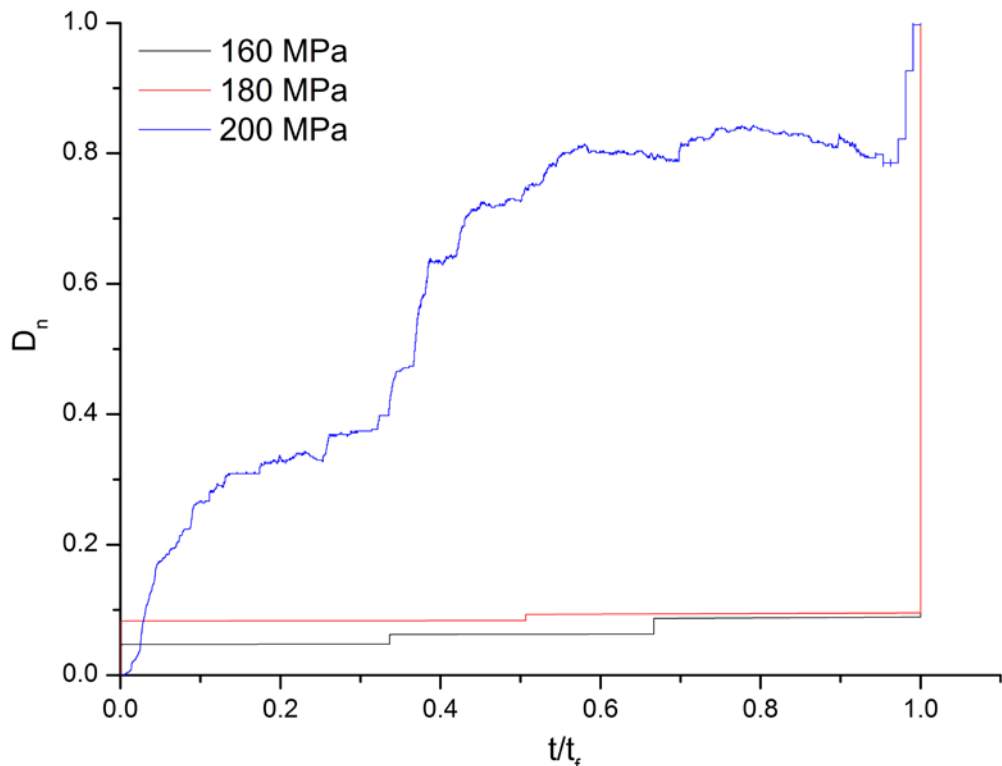


Figure 9: Damage index evaluated by number of failed contacts

5 CONCLUSIONS

- A modeling approach is presented, where the heterogeneity of the rock is realized by explicit considering the mineral components with different block and contact parameters.
- Uniaxial compressive creep of the rock has been analyzed by this numerical approach which has incorporated the Hillig-Charles equation for taking into account subcritical crack growth.
- The time-dependent fracture and damage evolution of rock samples under uniaxial compressive load has been studied at the grain size level in detail by the proposed numerical approach and shown satisfying agreement in terms of fracture pattern and time-dependent failure.

REFERENCES

- [1] Konietzky, H. Heftenberger, A. and Feige, M. Life time prediction for rocks under static compressive and tensile loads - a new simulation approach. *Acta Geotechnica* (2009) 4, 73-78.
- [2] Li, X. and Konietzky, H. Time to Failure Prediction Scheme for Rocks. *Rock Mech Rock Eng* (2014) 47, 1493-1503.
- [3] Li, X. and Konietzky, H. Simulation of time-dependent crack growth in brittle rocks under constant loading conditions. *Engineering Fracture Mechanics* (2014) 119, 53-65.
- [4] Li, X. and Konietzky, H. Numerical simulation schemes for time-dependent crack growth in hard brittle rock. *Acta Geotechnica* (2014) DOI 10.1007/s11440-014-0337-9.
- [5] Kemeny, J. Time-dependent drift degradation due to the progressive failure of rock bridges along discontinuities. *International Journal of Rock Mechanics & Mining Sciences* (1995) 42(1), 35-46.
- [6] Lee, J.S. Time-dependent crack growth in brittle rocks and field applications to geologic hazards. PhD dissertation (2007), The University of Arizona.
- [7] Park, N. Discrete element modeling of rock fracture behavior: fracture toughness and time-dependent fracture growth. PhD dissertation (2006), The University of Texas at Austin.
- [8] Potyondy, D.O. Simulation stress corrosion with a bonded-particle model for rock. *International Journal of Rock Mechanics & Mining Sciences* (2007) 44, 677-691.
- [9] Freiman, S.W. Effect of chemical environments on slow crack growth in glasses and ceramics. *J Geophys Res* (1984) 89(B6):4072–6.
- [10] Atkinson, B.K. Subcritical crack growth in geological materials, *J. Geophys. Res* (1984) 89, 4077–4114.
- [11] Rinne, M. Fracture mechanics and subcritical crack growth approach to model time-dependent failure in brittle rock. PhD dissertation (2008), Helsinki University of Technology.
- [12] Hillig, W.B. and Charles R.J. In *High-Strength Materials*. Edited by V.F.Zackey. John Wiley & Sons, Inc., New York, (1965) pp.682-705.
- [13] Wiederhorn, S.M. and Bolz, L.H. Stress Corrosion and Static Fatigue of Glass. *J. Am. Cer. Soc.* (1970) 53, 544-548.
- [14] Wiederhorn, S.M. Fuller, E.R. Jr. and Thomson, R. Micromechanisms of Crack Growth

- in Ceramics and Glasses in Corrosive Environments, Metal Science (1980) August-September, pp. 450-458.
- [15] Amitrano, D. and Helmstetter, A. Brittle creep, damage and time-to-failure in rocks. Journal of Geophysical Research B: Solid Earth 111 (2006) (B11201 DOI:10.1029/2005JB004252).
 - [16] Bass, D.J. Elasticity of minerals, glasses and melts, in Mineral Physics and Crystallography, Ref. Shelf Ser., vol. 2, edited by T. J. Ahrens, pp. 45– 63, AGU, Washington, D. C (1995).
 - [17] Chen, S. Yue, Z.Q. and Tham, L.G. Digital image-based numerical modeling method for prediction of inhomogeneous rock failure. International Journal of Rock Mechanics & Mining Sciences (2004), 41(2004), 939-957.
 - [18] Yu, Q. Zheng, C. Yang, T. Tang, S. Wang, P. and Tang, C. Meso-structure characterization based on coupled thermal-mechanical model for rock failure process and applications. Chinese Journal of Rock Mechanics and Engineering (2012), Vol.31 No.1, pp. 42-51 (in Chinese).
 - [19] Potyondy, D.O. and Cundall, P.A. A bonded-particle model for rock. International Journal of Rock Mechanics & Mining Science (2004) 41, 1329-1364.
 - [20] Schmidtke, R.H. and Lajtai, E.Z. The Long-Term Strength of Lac du Bonnet Granite. Int J Rock Mech Min Sci & Geomech Abstr (1985) 22(6):461-465.

A RIGID BODY SPRING NETWORK MODEL FOR THE SIMULATION OF HYSTERETIC BEHAVIOR OF MATERIALS

SOFIANOS CHRISTOS¹, KOUMOUSIS VLASIS¹

¹National Technical University of Athens
Institute of Structural Analysis & Aseismic Research
Zografou Campus, 15780, Athens, Greece
e-mails: sofianoschristos@yahoo.gr, vkoum@central.ntua.gr

Key words: RBSN, Hysteresis, Elastoplastic, Discrete models.

Abstract. In this work, a discrete numerical approach is presented to model the hysteretic behavior of materials. Rigid Body Spring Network models (RBSN) that were first proposed by Kawai ^[1] are extended to account for hysteretic elastoplastic behavior. Discretization is based on Voronoi tessellation, as proposed by Bolander ^[2]. The domain is discretized into convex polygons that will form the discrete rigid bodies of the model. These are connected with three zero length springs in the middle of their common interfaces. The springs are following the smooth hysteretic Bouc-Wen model which efficiently incorporates classical plasticity with no direct reference to the yield surface. Numerical results both for static and dynamic loading are presented that validate the proposed formulation and verify its computational efficiency as compared to the standard elastoplastic finite element method.

1 INTRODUCTION

The rigid-body-spring-network model was proposed by Kawai ^[1] who developed a physical model rather than a mathematical one, as a way of reducing computational time and mathematical complexity without losing essential characteristics of the behavior of deformable bodies. The main idea was to divide the structure in a finite number of rigid parts that are connected by springs in their common boundaries. This way structure deformation and internal forces are based solely on the deformation and forces of internal springs respectively.

Bolander and Saito ^[2] employed the Voronoi tessellation method to discretize the structure into convex polygons. Based on a random distribution of points they developed formulae to ensure elastic uniformity and maximize the degree of isotropy regarding crack propagation in homogeneous isotropic materials. Bolander and Berto ^[6] used Voronoi discretization of the domain in three-dimensional irregular lattices to model the cohesive zone of fracture while Bolander, Moriizumi and Kunieda ^[7] used the rigid-body-spring-network approach to analyze quasi-brittle fracture using a stress retrieval algorithm. Finally Kim et al. ^[8] presented a rate dependent viscoplastic model to simulate dynamic fracture under different loading rates. In this work the Bouc-Wen rate independent hysteretic model is employed in the rigid-body-spring-network framework to model hysteretic behavior of plane structures.

2 PROBLEM FORMULATION

According to Bolander and Saito [2] in a 2d rectangular domain the maximum number of points that can be placed using a random distribution process is $\hat{n} \approx 0.68ab/d_m^2$ where a and b are dimensions of the domain and d_m is the minimum allowable distance between points. By choosing $n \rightarrow \hat{n}$ particles the mesh becomes more regular and the points more uniformly distributed. These points or nuclei are now the computational points of the model and are used to define the Voronoi diagram (Preparata and Shamos [3]). The Voronoi diagram mainly divides the domain into convex polygons that define the rigid particles of the model. Each element consists of two rigid particles and their common boundary as shown in Figure 1.

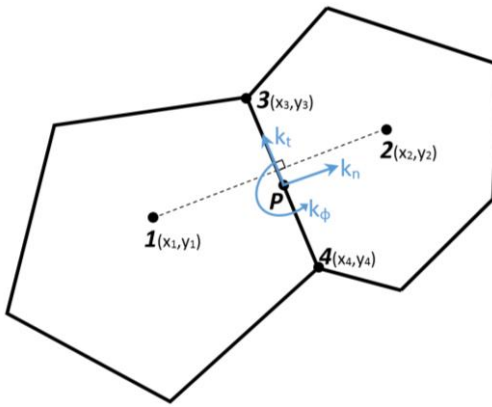


Figure 1: Rigid body spring network element.

Let the coordinates of the computational points be (x_1, y_1) and (x_2, y_2) for the two particles and (x_3, y_3) , (x_4, y_4) the coordinates of the common boundary. At the middle of the interface (point P) three zero length springs are considered with stiffness (in the local coordinate system) k_n , k_t and k_ϕ in the normal, tangential and rotational local degrees of freedom respectively. If we consider the relative displacements at point P in the facet local system:

$$\{d\}^T = [\delta_n \quad \delta_t \quad \varphi] \quad (1)$$

and the nodal displacements of the two computational points:

$$\{u_e\}^T = [u_1 \quad v_1 \quad \theta_1 \quad u_2 \quad v_2 \quad \theta_2] \quad (2)$$

These are connected through the relation:

$$\{d\} = [B]\{u_e\} \quad (3)$$

where:

$$[B] = \frac{1}{l_{43}} \begin{bmatrix} y_{43} & -x_{43} & (-x_{43}x_{P1} - y_{43}y_{P1}) & -y_{43} & x_{43} & (x_{43}y_{P2} + y_{43}y_{P2}) \\ x_{43} & y_{43} & (y_{43}x_{P1} - x_{43}y_{P1}) & -x_{43} & -y_{43} & (-y_{43}x_{P2} + x_{43}y_{P2}) \\ 0 & 0 & -l_{43} & 0 & 0 & l_{43} \end{bmatrix} \quad (4)$$

And $x_{ij}=x_i-x_j$, $y_{ij}=y_i-y_j$, l_{ij} is the Euclidean distance between points i and j, $x_{Pi}=(x_{4i}+x_{3i})/2$, $y_{Pi}=(y_{4i}+y_{3i})/2$. In addition we can derive the internal forces through the local displacements using relation:

$$\{q\} = [D]\{d\} \quad (5)$$

where D is a diagonal matrix with entries the normal, tangential and rotational spring stiffness to approximate the elastic properties of a continuum medium:

$$\begin{aligned} k_n &= E'tl_{43} / h \\ k_t &= E''tl_{43} / h \\ k_\phi &= k_n l_{43}^2 / 12 \end{aligned} \quad (6)$$

For plane stress conditions we have $E' = E/(1 - \nu^2)$ and $E'' = E/(2(1 + \nu))$, E being the elastic modulus, ν the Poisson ratio, t the thickness and h the distance of the two nodes. In order to obtain the element stiffness matrix the principle of virtual work theorem is applied:

$$[K]_e = B^T DB \quad (7)$$

All the elemental stiffness matrices are then combined using the direct stiffness method to form the stiffness matrix of the structure.

3 BOUC-WEN MODEL IN RBSN

In this work the Bouc-Wen hysteretic model is employed. It is a smooth hysteretic model that was first proposed by Bouc ^[4] and was later modified by Wen ^[5]. Its mathematical description for a Single Degree of Freedom (sdof) system is as follows:

$$\begin{cases} m\ddot{u} + c\dot{u} + a\dot{u} + (1-a)kz = p \\ \dot{z} = \dot{u} \left[1 - \left| \frac{z}{z_y} \right|^n (\gamma + \beta \operatorname{sgn}(z\dot{u})) \right] \end{cases} \quad (8)$$

where $a=K_{pl}/K_{el}$ and sgn is the signum function. The model consists of a first order non linear differential equation and z is the hysteretic parameter. For this single degree of freedom system the restoring force is given as the sum of an elastic and an inelastic hysteretic force as seen in Figure 2:

$$F(t) = \alpha \frac{F_y}{u_y} u(t) + (1-\alpha) F_y z(t) \quad (9)$$

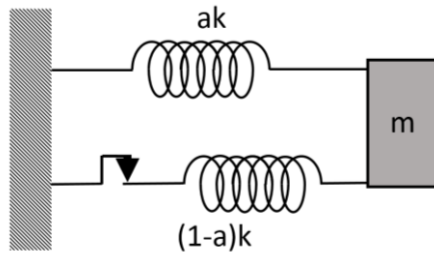


Figure 2: Bouc-Wen model.

Considering Figure 1 the forces of the zero length springs of the facet and the end actions at the computational nodes are connected through the relation:

$$\begin{Bmatrix} N_1 \\ Q_1 \\ M_1 \\ N_2 \\ Q_2 \\ M_2 \end{Bmatrix} = [B]^T \begin{Bmatrix} F_n \\ F_t \\ M \end{Bmatrix} \quad (10)$$

According to Bouc-Wen model spring forces are the sum of an elastic and an hysteretic part:

$$\begin{aligned} F_n &= ak_n \delta_n + F_n^p \\ F_t &= ak_t \delta_t + F_t^p \\ M &= ak_\theta \varphi + M^p \end{aligned} \quad (11)$$

or in matrix form:

$$\begin{Bmatrix} F_n \\ F_t \\ M \end{Bmatrix} = \begin{bmatrix} ak_n & 0 & 0 \\ 0 & ak_t & 0 \\ 0 & 0 & ak_\theta \end{bmatrix} \begin{Bmatrix} \delta_n \\ \delta_t \\ \varphi \end{Bmatrix} + \begin{Bmatrix} F_n^p \\ F_t^p \\ M^p \end{Bmatrix} \quad (12)$$

Now considering equations (3), (12) and substituting into (10) the following relation is obtained:

$$\begin{Bmatrix} N_1 \\ Q_1 \\ M_1 \\ N_2 \\ Q_2 \\ M_2 \end{Bmatrix} = [B]^T \begin{bmatrix} ak_n & 0 & 0 \\ 0 & ak_t & 0 \\ 0 & 0 & ak_\theta \end{bmatrix} [B] \begin{Bmatrix} u_1 \\ w_1 \\ \theta_1 \\ u_2 \\ w_2 \\ \theta_2 \end{Bmatrix} + [B]^T \begin{Bmatrix} F_n^p \\ F_t^p \\ M^p \end{Bmatrix} \quad (13)$$

where the hysteretic part of the forces follows the Bouc-Wen formulation:

$$\dot{F}^p = (1-a)k \left(1 - \left| \frac{F^p}{F_y} \right|^n \left(\beta + \gamma \operatorname{sgn}(F^p \dot{u}) \right) \right) \dot{u} \quad (14)$$

It is obvious that the hysteretic stiffness matrix is then given as:

$$[K_h] = [B]^T \begin{bmatrix} (1-a)k_n & 0 & 0 \\ 0 & (1-a)k_t & 0 \\ 0 & 0 & (1-a)k_\varphi \end{bmatrix} \quad (15)$$

The equation of motion has the following form:

$$[M]_s \{\ddot{u}\} + [C]_s \{\dot{u}\} + [K]_s \{u\} + [K_h]_s \{z\} = \{P(t)\} \quad (16)$$

where the hysteretic stiffness matrix is a rectangular matrix with $(3n \times 3n_{el})$ elements where n_{el} is the number of element and n is the number of nodes. Hysteretic parameter z represents the hysteretic part of displacements or curvature and follows the Bouc-Wen hysteretic equation. The equation of motion together with the differential equations of Bouc-Wen type should be solved simultaneously. This is facilitated by transforming the system into state-space form by introducing as auxiliary unknown the vector of nodal velocities.

4 NUMERICAL EXAMPLES

4.1 Single DOF verification

In this section results that verify the proposed model are presented. Consider a $1 \times 0.5\text{m}$ domain discretized with 2 nodes and 1 element as shown in Figure 3(a). Material is steel S235 and Poisson ratio is set to 0.3. The first node is fixed and a sinusoidal force is applied in the second node in the horizontal direction. The resulting force-displacement diagram is shown in Figure 3(b).

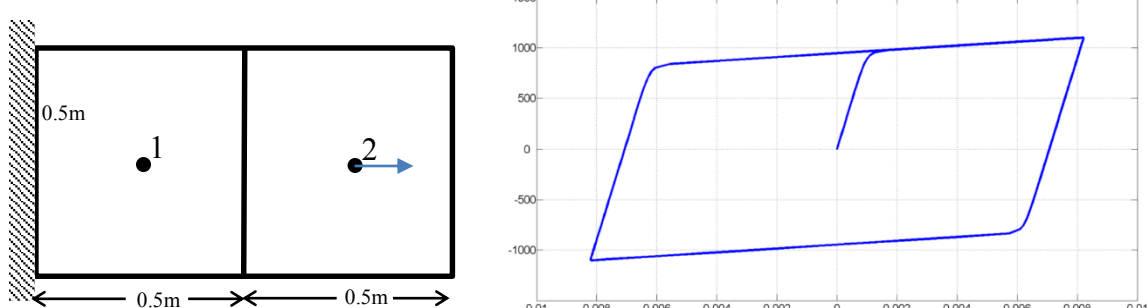


Figure 3: a) discretized model, b) Force- displacement diagram.

4.2 Beam with harmonic force

For the second example a beam with dimensions $1 \times 0.2\text{m}$ and 0.02m thickness is considered as seen in Figure 4. Material is steel S235 with 5% hardening. The force at the end

of the beam is harmonic with maximum value 75 kN. In the next Figures the results using rigid-body-spring-network with hysteretic approach are compared with those from inelastic finite element method. Results show good correlation considering the differences of the two methods.

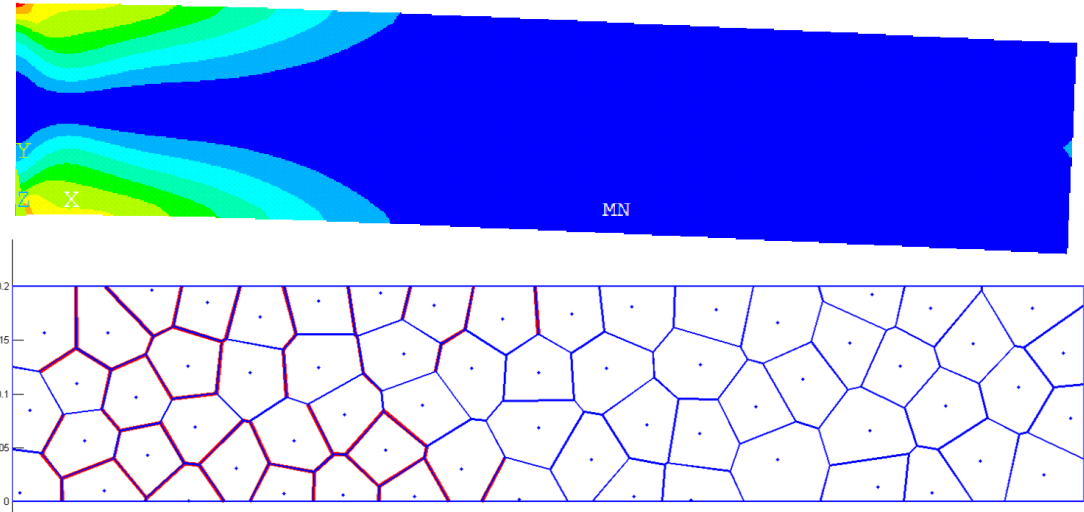


Figure 4: Comparison of Plastic regions.

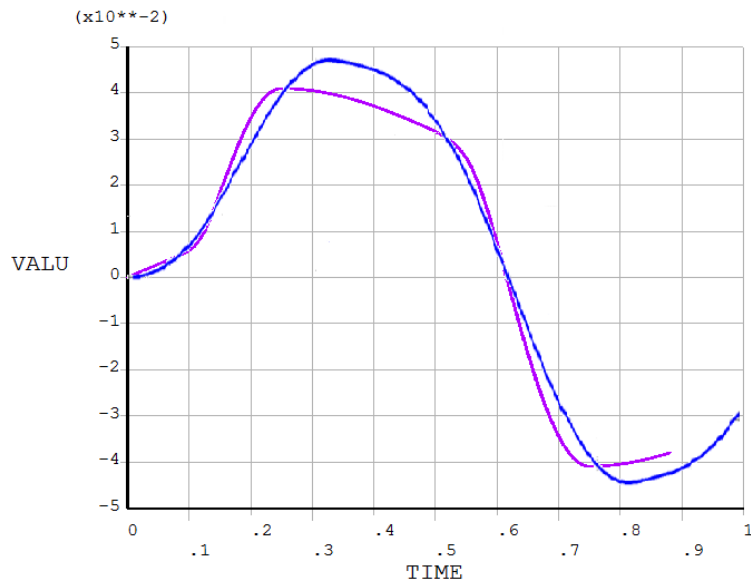


Figure 5: Free end displacement vs time.

5 CONCLUSIONS

- In this paper the rigid-body-spring-network model is extended to account for plasticity in rate-independent materials using the Bouc-Wen model.
- The numerical examples presented show the effectiveness of the model to simulate

- hysteretic behavior.
- Results are compared with the finite element method and show satisfactory agreement.

REFERENCES

- [1] Kawai T. *New discrete models and their application to seismic response analysis of structures*. Nuclear Engineering and Design. 48:207-209.
- [2] Bolander, J.E. & Saito, S., *Fracture analysis using spring networks with random geometry*. Engng Fracture Mech 61:569-591.
- [3] Preparata FP, Shamos MI. *Computational Geometry-An introduction*. 390. Springer, New York, 1985.
- [4] Bouc, R. *Forced vibration of mechanical system with hysteresis* (Abstract). Proc. 4th Conf. on Nonlinear Oscillation, Prague, Czechoslovakia.
- [5] Wen Y.K *Equivalent linearization for hysteretic system under random excitation*. Journal of Applied Mechanics 47:150-154.
- [6] Bolander, J.E.; Berton, S.: *Cohesive Zone Modeling of Fracture in Irregular Lattices* Fracture Mechanics of Concrete Structures, Proc. of FRAMCOS-5, (2004) pp.989- 994.
- [7] Bolander, J.E., Moriizumi, K., Kunieda, M., & Yip, M. 2001. *Rigid-Body-Spring Network modeling of cement-based composites*. In R. de Borst et al. (eds.), Fracture Mechanics of Concrete Structures. Lisse: Swets & Zeitlinger, 773-780.
- [8] Kim, K.; Bolander, J.E.; Lim, Y.M., *Rigid-Body-Spring Network with Visco-Plastic Damage Model for Simulating Rate Dependent Fracture of RC Structures*, Applied Mechanics and Materials, vol. 82, pp. 259-265

FROM ELASTO-PLASTICITY TO VISCO-ELASTO-PLASTICITY FOR SATURATED GRANULAR MATERIALS

BRUNO CHAREYRE¹, DONIA MARZOUGUI¹, JULIEN CHAUCHAT²

¹3SR, Univ. Grenoble Alpes, F-38000 Grenoble, France and
3SR, CNRS, F-38000 Grenoble, France

²LEGI, Univ. Grenoble Alpes, F-38000 Grenoble, France and
LEGI, CNRS, F-38000 Grenoble, France

Key words: Granular Materials, Lubrication, Poromechanics, Suspension, Viscoplasticity

Abstract. A recent extension of the discrete element method is reported for the simulation of dense mixtures of non-colloidal particles and viscous fluids in the non-inertial regime. The numerical model includes sphere-sphere contacts using a soft contact approach [2], short range hydrodynamic interactions defined by frame-invariant expressions of forces and torques in the lubrication approximation, and drag forces resulting from the poromechanical coupling computed with the DEM-PFV technique [3]. The proposed model is general and applies directly to sheared saturated granular media in which pore pressure feedback plays a key role. A partitioned solver makes the algorithm trivially parallel, which enables the coupled problems to be solved with nearly the same wall-clock time as uncoupled dry materials simulations. The shear stress in a dense suspension is analyzed, and decomposed into contact stress and hydrodynamic stress. Both contributions are shown to be increasing functions of a dimensionless shear rate Iv , in agreement with experimental results [4]. In contrast with a popular idea, the results suggest that lubrication may not necessarily reduce the contribution of contact forces to the bulk shear stress.

1 INTRODUCTION

Simulating the flow of saturated granular materials raises two challenging questions: 1) how to reflect the rheological properties of the moving materials in relevant constitutive laws and, 2) how to solve a boundary value problem when this constitutive law is used combined with very large deformations and a complex morphology of the run-out slope. Advances are needed on both points in order to provide the engineers with better tools, enabling namely numerical studies of gravitational flows from the triggering to the possible impact on structures and infrastructures.

Regarding the second question, the conventional FEM methods are helpless due to (namely) the moving free surface of the flow. The methods usually used for fluid dynamics (such as direct Navier-Stokes solvers or the Lattice-Boltzman method) may have less problems with the free surface but they make the implementation of complex visco-elasto-plastic models extremely difficult. To overcome these difficulties dedicated techniques have been developed in the recent years, using e.g. the SPH[10] (Smoothed Particle Hydrodynamics) or the FEMLIP[5] (FEM with lagrangian integration points). In this paper we focus on the first question: the rheology of flowing geomaterials, and we propose an approach of this question through micromechanical modeling as in [9]. Recent developments of the discrete element method (DEM) are explained in the first section and the results of simulated simple shear tests are summarized.

2 MICROMECHANICAL MODEL OF PARTICLES IN A VISCOUS FLUID

We assume that the flowing material can be conceptualized as a granular material. This assumption is relevant for the grain size of silts and above. Clayey materials (i.e. colloidal particles) are very different and exhibit much more complex interactions between particles, thus this study does not consider pure clays. For the mixtures of clay and coarser particles, the present approach may be valid as soon as the clay content and the pore water can be accounted for altogether as an equivalent viscous suspension carrying the bigger particles. Hereafter we introduce a numerical coupling between the DEM and a hydrodynamic model.

2.1 Discrete Element Model

An explicit finite difference scheme is employed for updating the position of each particle in a time-marching algorithm. The particles move according to the Newton's second law. The interactions between particles are governed by elastic-frictional contact forces defined using a soft contact approach [4]. The contact parameters are the normal and shear stiffnesses k_n and k_s , and the angle of contact friction ϕ . The contact forces are supplemented hereafter with forces coming from the interstitial fluid. A three-dimensional implementation of the DEM as found in the open source software YADE is used herein. For more details about the implementation, please refer to [13].

2.2 Long range interactions

The DEM-PFV method is used to solve a pore-scale version of the mass balance equation which appears in the continuous theory of porous media and leads to the so-called poromechanical coupling - leading to long range interactions between the particles. Only the main steps of the method are outlined hereafter since the details can be found in previous papers. We assume incompressible phases as in [3, 2] (for compressible phases see [11]). A tetrahedral decomposition of the pore space is introduced based on regular triangulation (figure 1), where that part of a tetrahedron occupied by the fluid is called

a pore. From now on V_i denotes the volume of pore i . It is uniquely defined by the positions \mathbf{x}_i and sizes of the solid particles, while the rate of change \dot{V}_i also depends on their velocities $\dot{\mathbf{x}}_i$.

An exchange of fluid between adjacent pores i and j is represented by the interface flux q_{ij} . The volume balance equation gives

$$\dot{V}_i = \sum_{j=1}^{j=4} q_{ij}. \quad (1)$$

A linear relationship between q_{ij} and the local pressure gradient $(p_i - p_j)/l_{ij}$ (where l_{ij} is a reference length [3]) leads to

$$\dot{V}_i = \sum_{j=1}^{j=4} k_{ij} (p_j - p_i)/l_{ij} = \sum_{j=1}^{j=4} K_{ij} (p_j - p_i). \quad (2)$$

In this equation K_{ij} is the local hydraulic conductivity. It reflects the small scale geometry of the packing. In details, the proposed expression of K_{ij} depends on a local hydraulic radius R_{ij}^h (area of the fluid-solid interface divided by the fluid volume - again see [3]) as

$$K_{ij} = \alpha \frac{S_{ij}^f R_{ij}^{h^2}}{2\eta l_{ij}} \quad (3)$$

where S_{ij}^f is the cross-sectional area of the pore-throat, η is the viscosity of the fluid, and α can be interpreted as a calibration parameter. $\alpha = 1$ is known to give good estimates of the actual permeability of glass beads [14] but we used $\alpha < 1$ in this study. This is further discussed in section 3.

Substituting \dot{V}_i by its expression in terms of particles velocity and writing equation 2 for every element gives a system of linear equations. At each time step in the motion integration, solving this system gives a discrete field of fluid pressure \mathbf{P} as function of the particles velocity.

The drag forces are deduced from the pressure field. They are the integrals of the pressure p and the viscous stress τ on the surface of the particle, i.e.

$$F_k^f = \int_{\partial\Gamma_k} p \mathbf{n} ds + \int_{\partial\Gamma_k} \tau \mathbf{n} ds \quad (4)$$

The F_k^f are introduced in Newton's second law together with the forces coming from solid contacts (\mathbf{F}^c) and lubrication effects (\mathbf{F}^L defined in the next section). I.e.

$$\mathbf{M}\ddot{\mathbf{x}} = \mathbf{F}^c + \mathbf{F}^L + \mathbf{F}^f, \quad (5)$$

The strong two-way coupling defined by equation 5 (remember that \mathbf{F}^f depends on $\dot{\mathbf{x}}$) is the poromechanical coupling. It is integrated with an explicit scheme whose accuracy has been verified in [2].

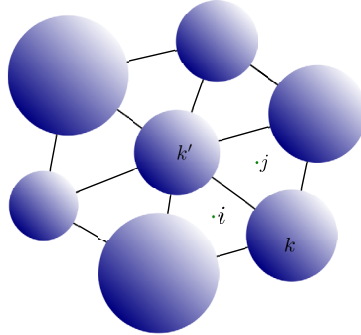


Figure 1: Regular triangulation in 2D.

2.3 Short range interactions

The lubrication forces are linked to the presence of the fluid and are only significant for nearly touching particles. We note particles k and k' with radii a_k and $a_{k'}$, linear velocities \mathbf{v}_k and $\mathbf{v}_{k'}$ and angular velocities $\boldsymbol{\omega}_k$ and $\boldsymbol{\omega}_{k'}$, respectively. Their average radius is defined as $a = (a_k + a_{k'})/2$ and h denotes the inter-particle distance (surface to surface). An arbitrary relative motion between two particles can be decomposed in four elementary motions corresponding to normal displacement (subscript n), shear displacement (s), rolling (r) and twisting (t). For full details see [9]. Noting $\boldsymbol{\omega}_n = (\mathbf{v}_{k'} - \mathbf{v}_k) \times \mathbf{n} / (a_k + a_{k'} + h)$ the angular velocity of the local frame attached to the interacting pair, lubrication forces and torques are defined as follow:

$$\mathbf{F}_n^L = \frac{3}{2} \pi \eta \frac{a^2}{h} \mathbf{v}_n \quad (6)$$

$$\mathbf{F}_s^L = \frac{\pi \eta}{2} \left[-2a + (2a + h) \ln \left(\frac{2a + h}{h} \right) \right] \mathbf{v}_t \quad (7)$$

$$\mathbf{C}_r^L = \pi \eta a^3 \left(\frac{3}{2} \ln \frac{a}{h} + \frac{63}{500} \frac{h}{a} \ln \frac{a}{h} \right) [(\boldsymbol{\omega}_k - \boldsymbol{\omega}_{k'}) \times \mathbf{n}] \quad (8)$$

$$\mathbf{C}_t^L = \pi \eta a^2 \frac{h}{a} \ln \frac{a}{h} [(\boldsymbol{\omega}_k - \boldsymbol{\omega}_{k'}) \cdot \mathbf{n}] \mathbf{n} \quad (9)$$

where $\mathbf{v}_n = ((\mathbf{v}_{k'} - \mathbf{v}_k) \cdot \mathbf{n}) \mathbf{n}$ is the normal relative velocity and $\mathbf{v}_t = (a_k(\boldsymbol{\omega}_k - \boldsymbol{\omega}_n) + a_{k'}(\boldsymbol{\omega}_{k'} - \boldsymbol{\omega}_n)) \times \mathbf{n}$ is an objective expression of the tangential relative velocity. In this set of equations, the normal and shear forces, \mathbf{F}_n and \mathbf{F}_s , are based on Frankel & Acrivos [6, 15] whereas C_r and C_t are based on Jeffrey & Onishi [8, 7]. The total lubrication force \mathbf{F}_k^L (resp. $\mathbf{F}_{k'}^L$) applied by particle k' on particle k (resp. by particle k on particle k') and the total torque \mathbf{C}_k^L (resp. $\mathbf{C}_{k'}^L$) applied by particle k' on particle k (resp. by particle k on particle k') relative to the particle center read:

$$\mathbf{F}_k^L = -\mathbf{F}_{k'}^L = \mathbf{F}_n + \mathbf{F}_s, \quad (10)$$

$$\mathbf{C}_k^L = (a_k + \frac{h}{2}) \mathbf{F}_s + \mathbf{C}_r + \mathbf{C}_t, \quad (11)$$

$$\mathbf{C}_{k'}^L = (a_{k'} + \frac{h}{2}) \mathbf{F}_s - \mathbf{C}_r - \mathbf{C}_t. \quad (12)$$

We account for the deformability of the particles near the contact region by combining the above normal lubrication model with the linear contact model via a Maxwell-type visco-elastic scheme ([9]. Lastly, we introduce a surface roughness such that the contact model and the lubrication model use slightly different values of h . The repulsive contact force appears even before $h = 0$ so that practically $h \leq 0$ never occurs in simulations.

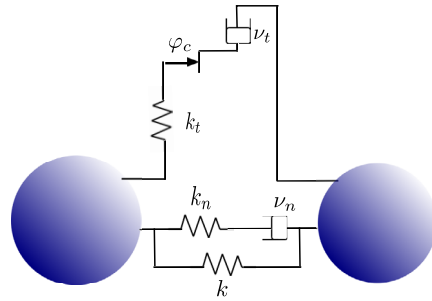


Figure 2: Visco-elastic scheme of the interaction between two elastic-like particles.

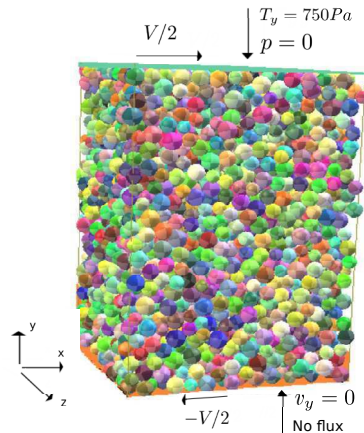


Figure 3: Simulation cell.

2.4 A note on computational cost

The time integration is done using a partitioned approach. At each step the contribution of contact forces and the fluid forces are summed, and the total force is used to update momentum using a classical (explicit) centered finite difference scheme. A purely sequential vision of this procedure is shown in figure 4(a). Both types of forces are uniquely defined by the positions and velocities of the previous step. It makes the algorithm pleasantly parallel, as contact interactions and fluid forces (including lubrication forces) can be computed simultaneously (fig. 4(b)). Virtually, it results in a fluid model which comes at no cost compared to the classical DEM without fluid. This is assuming that the computational resources are not limited and that the overhead coming from summing the fluid forces and the contact forces is negligible (practically it is). There is of course no restriction on how each branch in fig. 4(b) is further parallelized.

How close to this theoretical performance a concrete implementation can be depends on many factors. Namely, the performance of the original DEM code is a key factor. Indeed there is no merit in computing fluid forces faster than contact forces if the latter is initially slow. Also, the number of particles plays a role since the computational cost of contacts and fluid solver may scale differently (the fluid solver has to solve a sparse linear system). Our tests with the YADE-DEM code used in this study showed that assigning four cores to both the contact and the fluid parts leads to an increase of the computation time of the order of 50% for a range of problem sizes between 5,000 and 20,000 particles. Below 5,000, the cost of the fluid is almost negligible. Above 20,000 particles the fluid solver tend dominate the computation time. Further investigations will be done on this question.

3 SIMPLE SHEAR AT IMPOSED NORMAL PRESSURE

We simulate a saturated flowing material with bi-periodic boundary conditions, made of $N = 1000$ frictional spheres of average radius $a = 0.025 \pm 0.01$ m. The physical properties are roughness $\varepsilon = 0.035 a$, density $\rho = 2500$ kg/m³, normal contact stiffness $k_n/a = 5 \times 10^5$ Pa, shear stiffness $k_s = k_n/2$, and contact friction angle $\varphi = 30^\circ$. There is no gravity. The numerical sample is first confined between two parallel plates then sheared by moving the top and the bottom plates at constant velocity $\pm V/2 = 1.5$ m/s. The boundary conditions for the top plate are the velocities $v_x = V/2$, $v_z = 0$, the total normal stress $T_y = 750$ Pa and the fluid pressure $p = 0$. At the bottom plate, $v_x = -V/2$, $v_z = 0$ and the fluid velocity along the y axis $v_y^f = 0$ (impermeable boundary). Periodic boundary conditions are defined along the horizontal axis for both the particles and the fluid. The external stress vector is $\mathbf{T} = \mathbf{F}/S$ where \mathbf{F} is the total force on the top plate and S is the horizontal cross sectional area. T_y is kept constant during the deformation, while T_x is a result of the imposed shear.

Figure 6 shows the evolution of the shear stress T_x , the pressure p and the solid fraction ϕ function of the deformation $\gamma(T) = \int_0^T \dot{\gamma}(t)dt$ where $\dot{\gamma}(t) = V/H(t)$ is the shear rate.

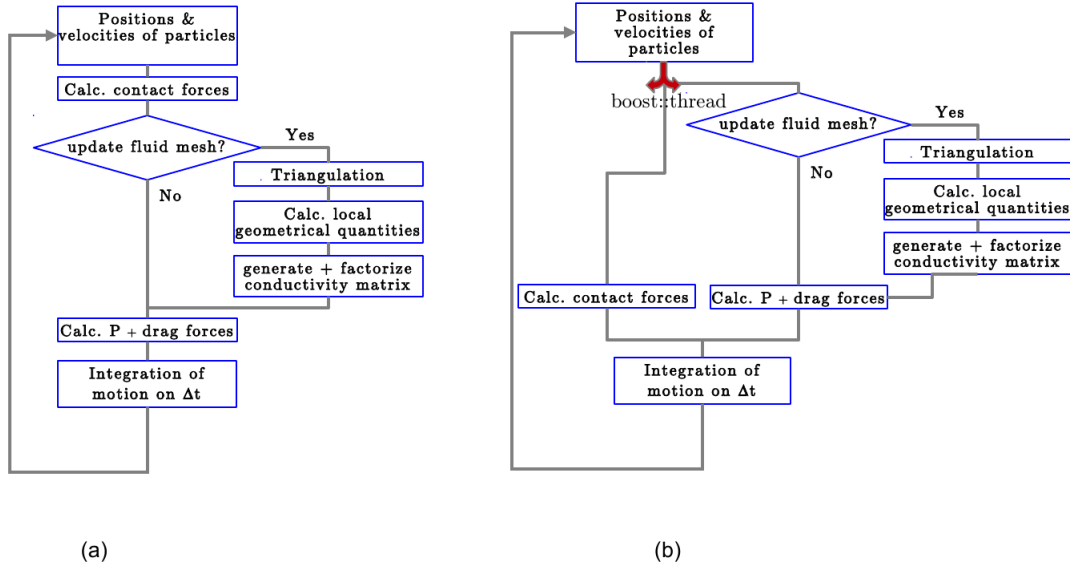


Figure 4: The time-stepping algorithm for the coupled problems, (a) purely sequential or (b) using task parallelism.

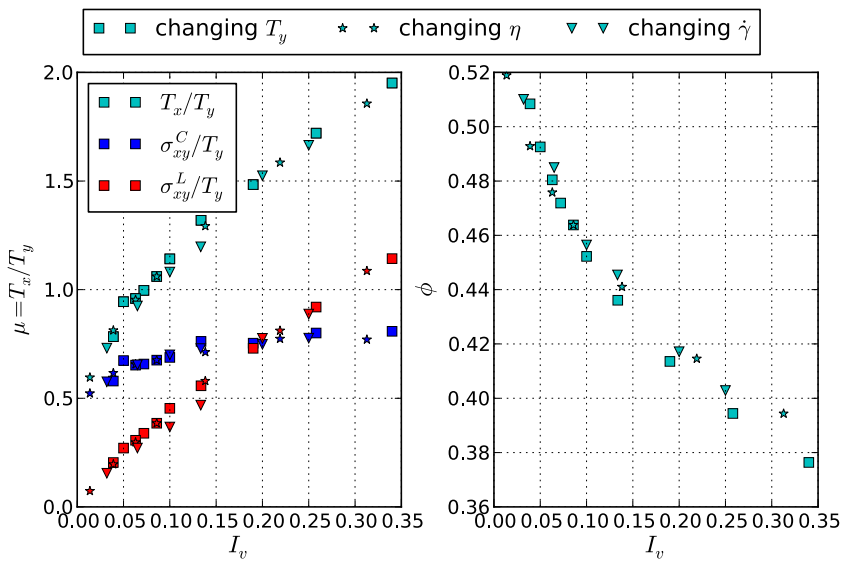


Figure 5: Normalized shear stress and solid fraction at steady state versus I_v . In each series the change of I_v is obtained by changing a different parameter: normal stress, viscosity, or shear rate.

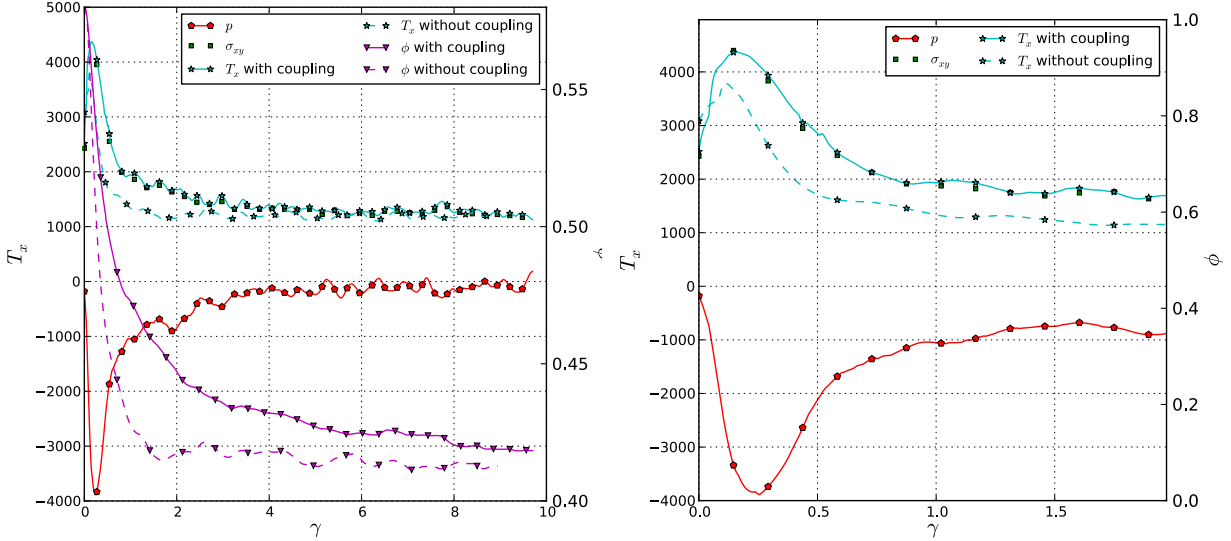


Figure 6: (left): The evolution of the shear stress and the solid fraction as a function of the deformation, with and without the poromechanical coupling. (right): Zoom on the transient regime.

The numerical results are presented for two cases: a first case where the poromechanical coupling (long range interactions) is included and another one where it is not (i.e. ignoring the last term in equation 5). In the early stage of deformation a transient regime is observed, reminiscent of the critical state theory. It is characterized by a peak stress, a decrease of the solid fraction and a negative pore pressure in the coupled case. This later effect entails a higher effective stress in the coupled problem, explaining why the shear stress reaches higher values. The system evolves toward a steady state for large deformations, in which the shear stress and the solid fraction are approximately constant and the pore pressure is nearly zero. The poromechanical coupling has no visible effect at steady state: the shear stress and the solid fraction reach similar values for both cases.

At steady state in non-inertial regimes the stress ratio $\mu = T_x/T_y$ and the solid fraction ϕ are entirely controlled by the viscous number I_v . I_v is a dimensionless form of the shear rate [1], reflecting the magnitude of viscous effects, and is defined as:

$$I_v = \frac{\eta |\dot{\gamma}|}{T_y}, \quad (13)$$

In other words, all possible combinations of confining pressure, fluid viscosity, and shear rate corresponding to a given value of I_v give the same result. It is easily confirmed by comparing simulations in which these control parameters are changed independently to produce different values of I_v (fig. 5).

Finally, a validation of our coupled model is obtained by comparing the normalized shear stress and the solid fraction at steady state with the empirical equation of [1] (fig. 7, the empirical relation is plotted for convenience, it goes through data points not shown in the figure).

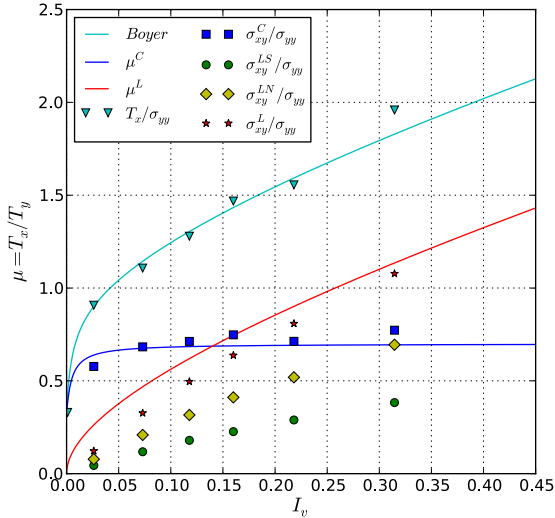


Figure 7: The stress ratio μ and the decomposition in contact stress, normal lubrication stress and shear lubrication stress. The solid line is the phenomenological law of [1].

4 DISCUSSION

The previous section reveals a key feature of saturated geomaterials which has implications on debris flow: the shear stress and the solid fraction (or porosity) at large deformations are no longer uniquely defined by the confining stress as in critical state theory. They are both dependent on the shear rate. The effect is relatively well known as an experimental fact in the rheology of suspensions. It is attributed to the short range lubrication effects.

A consequence rarely discussed, however, is that the rate dependent volume changes are strongly coupled with long range poromechanical effects. In rheometer tests, the shear rate is usually applied for a sufficiently long time period so that the measurements are done at steady state. The transient regime is disregarded and the pore pressure is not recorded in most cases. For debris flow in natural conditions however, the shear rate may not be constant if the material is flowing down a slope where the slope angle is not constant. In such case the flowing material may never reach the steady state and it may be strongly influenced by the pore pressure changes associated to the poromechanical coupling.

Let us recall that the poromechanical coupling entails long range effects in the system and, ultimately, a dependency on the problem size. Indeed the characteristic time of poromechanical effects scale with $\eta H^2/\kappa$ where κ is the intrinsic permeability and the problem size. Since κ scales with a^2 (squared particle size), the relaxation time of the transient regime is proportional to $\eta(H/a)^2$. A consequence is that the peak pore pressure and the peak stress in figure 6 scales with $(H/a)^2$. That is, they are much more significant

in large scale in-situ conditions than in small scale lab tests.

A key conclusion is that it is impossible to modelize a flowing suspension as an equivalent single-phase mixture. It is always necessary to solve a coupled problem. Promising steps in this direction can be found in [10], which provides an efficient computational techniques at the field scale. The micromechanical model we presented in this paper is complementary, in the sense that it hardly applies to large scale problems but it can provide insight into the rheology of the flowing materials and the coupling phenomena. It is freely available as part of Yade-DEM [12] and it can be used for further investigations.

References

REFERENCES

- [1] BOYER, F., GUAZZELLI, E., AND POULIQUEN, O. Unifying suspension and granular rheology. *Physical Review Letters* 107, 18 (2011), 188301.
- [2] CATALANO, E., CHAREYRE, B., AND BARTHÉLEMY, E. Pore-scale modeling of fluid-particles interaction and emerging poromechanical effects. *International Journal for Numerical and Analytical Methods in Geomechanics* 38, 1 (2014), 51–71.
- [3] CHAREYRE, B., CORTIS, A., CATALANO, E., AND BARTHÉLEMY, E. Pore-scale modeling of viscous flow and induced forces in dense sphere packings. *Transport in porous media* 94, 2 (2012), 595–615.
- [4] CUNDALL, P., AND STRACK, O. A discrete numerical model for granular assemblies. *Geotechnique* 29, 1 (1979), 47–65.
- [5] CUOMO, S., PRIME, N., IANNONE, A., DUFOUR, F., CASCINI, L., AND DARVE, F. Large deformation femlip drained analysis of a vertical cut. *Acta Geotechnica* 8, 2 (2013), 125–136.
- [6] FRANKEL, N., AND ACRIVOS, A. On the viscosity of a concentrated suspension of solid spheres. *Chemical Engineering Science* 22, 6 (1967), 847853.
- [7] JEFFREY, D., AND ONISHI, Y. Calculation of the resistance and mobility functions for two unequal rigid spheres in low-reynolds-number flow. *Journal of Fluid Mechanics* 139 (1984), 261–290.
- [8] JEFFREY, D., AND ONISHI, Y. The forces and couples acting on two nearly touching spheres in low-reynolds-number flow. *Zeitschrift für angewandte Mathematik und Physik ZAMP* 35, 5 (1984), 634–641.
- [9] MARZOUGUI, D., CHAREYRE, B., AND CHAUCHAT, J. Microscopic origins of shear stress in dense fluid–grain mixtures. *Granular Matter* (2015), DOI:10.1007/s10035-015-0560-6.

- [10] PASTOR, M., BLANC, T., HADDAD, B., DREMPETIC, V., MORLES, M., DUTTO, P., STICKLE, M., MIRA, P., AND MERODO, J. Depth averaged models for fast landslide propagation: Mathematical, rheological and numerical aspects. *Archives of Computational Methods in Engineering* 22, 1 (2015), 67–104.
- [11] SCHOLTÈS, L., CHAREYRE, B., MICHALLET, H., CATALANO, E., AND MARZOUGUI, D. Modeling wave-induced pore pressure and effective stress in a granular seabed. *Continuum Mechanics and Thermodynamics* 27, 1-2 (2015), 305–323.
- [12] SMILAUER, V., CATALANO, E., CHAREYRE, B., DOROFENKO, S., DURIEZ, J., GLADKY, A., KOZICKI, J., MODENESE, C., SCHOLTÈS, L., SIBILLE, L., STRANSKY, J., AND THOENI, K. Yade Reference Documentation. In *Yade Documentation*, V. Smilauer, Ed., 1st ed. The Yade Project, 2010. <http://yade-dem.org/doc/>.
- [13] SMILAUER, V., AND CHAREYRE, B. Yade DEM Formulation. In *Yade Documentation*, V. Smilauer, Ed., 1st ed. The Yade Project, 2010. <http://yade-dem.org/doc/>.
- [14] TONG, A.-T., CATALANO, E., AND CHAREYRE, B. Pore-Scale Flow Simulations: Model Predictions Compared with Experiments on Bi-Dispersed Granular Assemblies. *Oil & Gas Science and Technology-Revue d'IFP Energies Nouvelles* 67, 5 (2012), 743–752.
- [15] VAN DEN BRULE, B., AND JONGSCHAAP, R. Modeling of concentrated suspensions. *Journal of statistical physics* 62, 5 (1991), 12251237.

GRANULAR FLOW THROUGH AN ORIFICE: SOLVING THE FREE FALL ARCH PARADOX

S.M. Rubio-Largo¹, A. Janda², I. Zuriguel¹, D. Maza¹ and R.C. Hidalgo¹,

¹ Department of Physics and Applied Mathematics. University of Navarra. Navarra. Spain.

² School of Engineering. University of Edinburgh. Edinburgh. United Kingdom.

Key words: Granular Materials, DEM, Particle Flow

Abstract. Several theoretical predictions of the mass flow rate of granular flows through outlets are based on the existence of a *free fall arch* region covering the silo outlet. Early in the nineteenth century, it was suggested that the particles crossing this region lose their kinetic energy and start to fall freely under their own weight. However, there is not conclusive evidence of this hypothetical region. We examined experimentally and numerically the micro-mechanical details of the particle flow through an orifice placed at the bottom of a silo. Remarkably, the contact stress monotonously decreases when the particles approach to the exit and it only vanishes just at the outlet. The behavior of this magnitude was practically independent of the size of orifice indicating that particle deformation, is insensible to the size of the aperture. Contrary, the behavior of the kinetic stress puts on evidence that the outlet size controls the propagation of the velocity fluctuations inside the silo. Examining this magnitude, we conclusively argue that indeed there is a well-defined transition region where the particle flow changes its nature. Above this region, the particle motion is completely correlated with the macroscopic flow. Our outcomes clarifies why the *free fall arch* picture has served as an approximation to describe the flow rate in the discharge of silos.

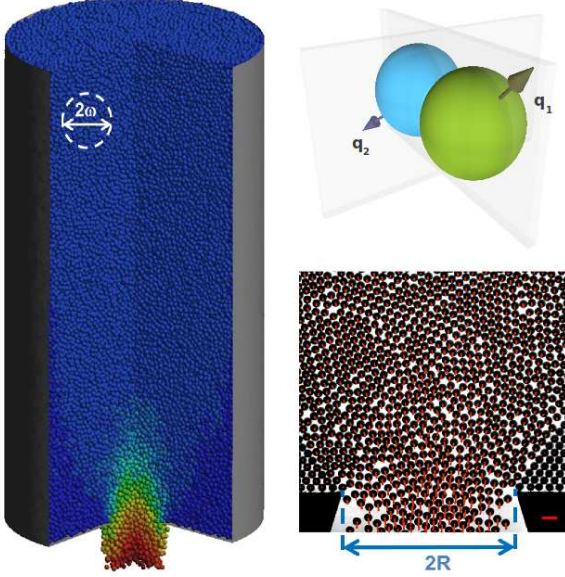


Figure 1: (a) Numerical three-dimensional silo, the color of the particles indicates the velocity in the vertical direction. (b) Sketch of the numerical interaction among two colliding particles. (c) A picture of the two-dimensional silo used in the experiments. The red arrows represent the velocity of each grain. The arrow at right bottom is equivalent to $500\text{mm}/\text{s}$.

1 INTRODUCTION

Predicting the mass flow rate during silo discharging has been thoroughly attempted in the past years [1, 2, 3]. In general, theoretical frameworks rest on the existence of region close to the orifice where the inter-particle forces diminish and, below this vault, fall due to gravity. Long time ago, this was postulated by Brown & Richards [2], who introduced the concept of *free-fall arch*. Nowadays, this conception is fully accepted and researchers commonly relate it with Beverloo' correlation [4]. However, the *free-fall arch* idea implies the strong formal inconsistency of a spatial stress discontinuity, which is difficult to justify. In addition, recent experimental efforts aimed on proving the existence of such a transition have provided inconclusive outcomes [5, 6].

When examining granular flows experimentally, there are several technical restrictions [7, 8, 9]. Hence, to capture the behavior of three dimensional flows and packings is generally not feasible. In this framework, there is a real need of performing numerical simulations. Discrete element modeling (DEM) is widely accepted as an effective method to address engineering problems concerning dense granular media [10]. Moreover, in applications the formulation of granular macroscopic fields is also necessary. The micro-mechanical details provided by DEM, *i.e.* velocity, position and contacts of individual particles, allow to determine the continuum field profiles, implementing coarse grained average techniques. In this work, we apply a post-processing methodology introduced by I. Goldhirsch [11] and generalized by Weinhart et al [12, 13]. We analyze the granular

flow through an orifice, thoroughly describing the kinetic and dynamic fields.

The paper is organized as follows: in Sec. 2, we describe the experimental setup, the numerical simulations and the theoretical framework of the coarse-grained formulation [11]. Then, in Sec. 3 we explain the implementation of the coarse-grained methodology, which has been used to process both numerical and experimental data, allowing to clarify the nature of the granular flow close to the orifice.

2 METHOD

2.1 Experimental Setup

The experimental setup consists of a quasi-bidimensional silo built with two glass sheets (height 800mm and width 200mm) separated by a steel frame which also conforms the lateral walls (see Fig. 1). The gap between the glass sheets is slightly larger than the particles diameter ($d = 2r_p = 1.0\text{mm}$) so the beads can only arrange themselves in a single layer. The particles flow out through a horizontal slit of a tunable aperture $D = 2R$ located at the flat bottom of the silo. The discharge process is recorded by a hight speed camera. The videos were analyzed using image processing techniques allowing a precise determination of the instantaneous position \vec{r} and velocity \vec{v} of each particle. A more detailed description of the experimental setup and image analysis techniques can be found in [14] and [9], respectively.

2.2 Numerical Simulations

In order to model a 3D silo, we have developed a hybrid CPU-GPU Discrete Element [15, 16] algorithm for a system of spheres with $r_p = 1/64\text{ m}$. Initially, we generate a granular column from a granular gas of particles, where particles are located at random positions, within a cylindrical container with flat bottom. Then they settle under the effect of gravity and are allowed to leave the system through a circular outlet, which is located at the bottom of the column. A snapshot of the silo of the numerical three-dimensional silo is shown in Fig. 1.

In the model, each particle ($i = 1\dots N$) has three translational degrees of freedom and a quaternion formalism has been implemented for describing the 3D angular rotations. The interaction between particle i and particle j is decomposed in normal and tangential directions (see Fig.1). In our approach, the normal interaction is defined by a linear contact and dissipation is introduced using a velocity dependent viscous damping. Our model has been used to simulate spheres with density $\rho = 7520\text{ kg/m}^3$, restitution coefficient $e_n = 0.5$ and $\Delta t = 10^{-6}\text{ s}$. More details about the numerical implementation can be found in [16, 17].

2.3 Coarse Graining Formulation

In order to explore the macromechanical properties of particle flow, a novel coarse graining methodology is used [11, 12]. In both cases, simulations and experiments, we

have accessed to the position and velocities of the particles. According to [11, 12], the microscopic mass density of a granular flow, $\rho(\vec{r})$, at time t is defined as,

$$\rho(\vec{r}) = \sum_{i=1}^N m_i \phi(\vec{r} - \vec{r}_i(t)) \quad (1)$$

where the sum runs over all the particles within the system and $\phi(\vec{r} - \vec{r}_i(t))$ is an integrable coarse-graining function. In the same way, the coarse grained momentum density field $P(\vec{r}, t)$ reads as,

$$P(\vec{r}, t) = \sum_{i=1}^N m_i \vec{v}_i \phi(\vec{r} - \vec{r}_i(t)) \quad (2)$$

where the \vec{v}_i represent the velocity of particle i . The macroscopic velocity field $\vec{V}(\vec{r}, t)$ is then obtained as the ratio of momentum and density fields,

$$\vec{V}(\vec{r}, t) = P(\vec{r}, t)/\rho(\vec{r}, t). \quad (3)$$

To calculate the macroscopic stress tensor we have used a mathematically consistent definition of the mean stress tensor $\sigma_{\alpha\beta}$ [11]. Following this approach the total stress field $\sigma_{\alpha\beta}$ can be decomposed by kinetic stress field $\sigma_{\alpha\beta}^k$ and contact stress field $\sigma_{\alpha\beta}^c$. The mean contact stress tensor reads as,

$$\sigma_{\alpha\beta}^c = -\frac{1}{2} \sum_{i=1}^N \sum_{j=1}^{N_{ci}} f_{ij\alpha} r_{ij\beta} \int_0^1 \phi(\vec{r} - \vec{r}_i + s\vec{r}_{ij}) ds \quad (4)$$

where the sum runs over all the contacting particles i, j , whose center of mass are at \vec{r}_i and \vec{r}_j , respectively. Moreover, f_{ij} accounts for the force exerted by particle j on particle i and $\vec{r}_{ij} \equiv \vec{r}_i - \vec{r}_j$.

The kinetic stress field reads as,

$$\sigma_{\alpha\beta}^k = - \sum_i m_i v'_{i\alpha} v'_{i\beta} \phi(\vec{r} - \vec{r}_i(t)), \quad (5)$$

where \vec{v}'_i accounts for the velocity fluctuation of particle i , respect to the mean field.

$$\vec{v}'_i(t, \vec{r}) = \vec{v}_i(t) - \vec{V}(\vec{r}, t). \quad (6)$$

Based on the previous theoretical framework, we have implemented a post-processing tool, which has allowed us to examine the 2D and 3D kinetic and dynamic fields obtained experimentally and numerically.

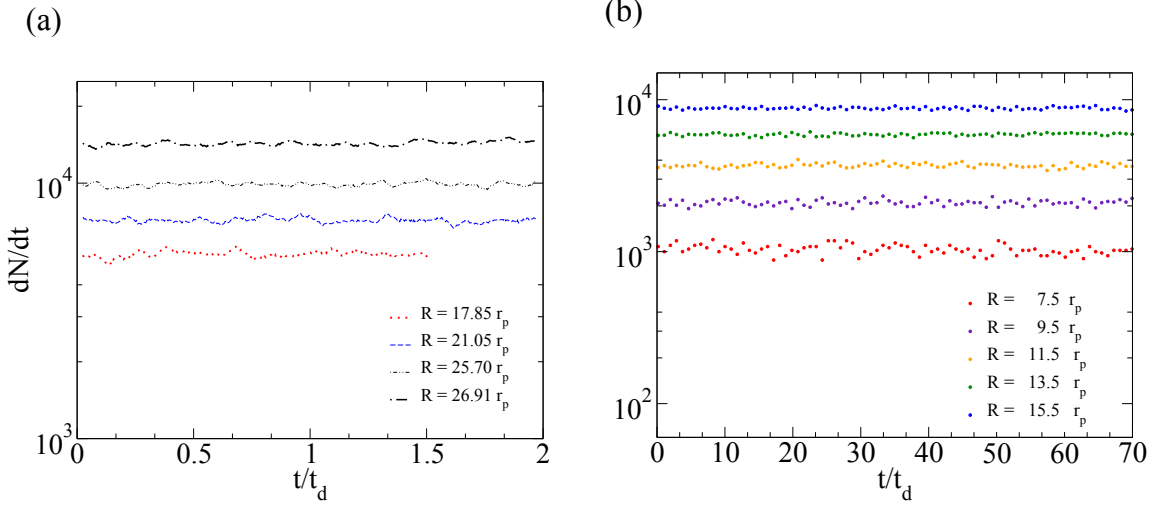


Figure 2: The time evolution of the flow rates in terms of the characteristic time $t_d = \sqrt{\frac{2r_p}{g}}$ are shown for different outlet sizes. In a) experimental and b) simulations

3 RESULTS AND DISCUSSION

Our aim is to determine the micro-mechanical properties of a granular flow during a silo discharge. Thus, the complexity of the particle flow was explored experimentally and numerically in a region close to the silo aperture. Additionally, the simulations give the micromechanical details and the contact forces of all particles within the silo.

First, we have determined the particle' flow rate through the surface of the outlet. Experimental and numerical outcomes are exposed for several apertures in Fig.2.3a and Fig.2.3b, respectively. The time evolution of the flow rate dN/dt in particles per second is shown in terms of the characteristic time scale $t_d = \sqrt{\frac{2r_p}{g}}$, i.e. the time elapse in which a particle moves its own diameter. In all cases, it is noticeable the system quickly evolves to a steady state characterized by a constant flow rate. This fact allows us to use the coarse-graining methodology, describing the micro-mechanical details of the particle flow [11, 12, 18].

As a second step, we have thoroughly examined the outcomes of the coarse-graining methodology described in Sec. 2.3. To this end, two different coarse-graining functions $\phi(\vec{r})$ have been studied. It is known that $\phi(\vec{r})$ should be an integrable normalized function. First, we have implemented the method with a Heaviside function

$$\phi_h(\vec{r}) = \frac{1}{\Omega_d(\omega)} H(\omega - |\vec{r}|). \quad (7)$$

and as second choice, we have used a Gaussian

$$\phi_g(\vec{r}) = \frac{1}{(\sqrt{2\pi}w)^3} \exp\left(-\frac{|\vec{r}|^2}{2w^2}\right). \quad (8)$$

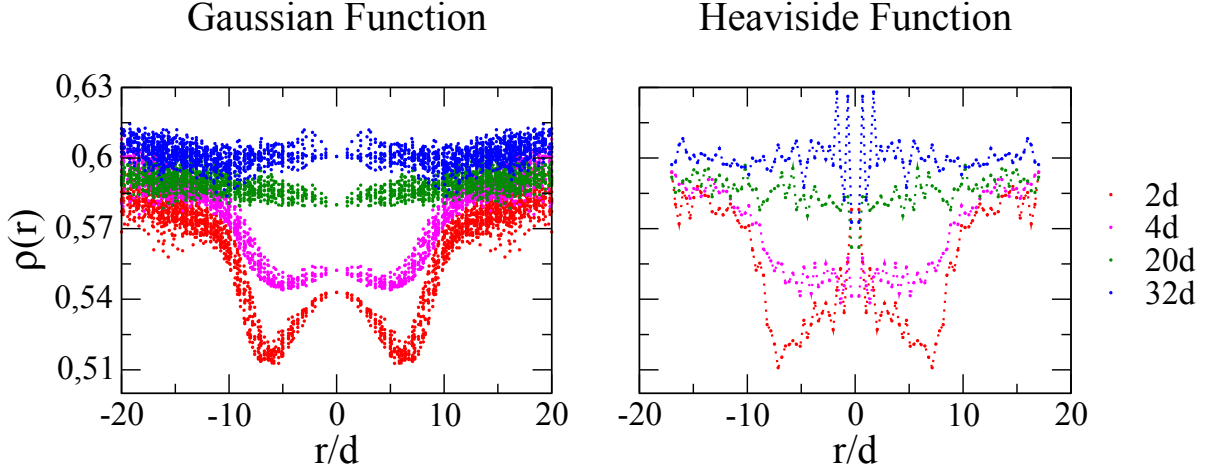


Figure 3: Mass density profiles of a granular flow, $\rho(\vec{r})$, using Gaussian (left) and (right) Heaviside coarse-graining functions. The measurement has been obtained at different heights from the base of the silo. The orifice size of the silo is $R = 16d$ and the coarse graining scale $w = d$.

In Fig.3, the mass density profiles $\rho(\vec{r})$ of a 3D numerical granular flow are shown. Outcomes obtained using two different integrable functions Heaviside Eq. 7 and Gaussian Eq. 8 are illustrated . Note, the measures were done at different heights respect to the silo outlet, covering from $z = 2d$ to $z = 32d$ where d is the particle diameter. As can be observed, both coarse-graining functions give equivalent outcomes for the density profiles. However, the Gaussian function produces smoother results for the same coarse graining scale $w = d$. In the following, the data processing has been done using the Gaussian function $\phi(\vec{r}) = \phi_g(\vec{r})$. At the end of this work, we will clarify the role of the coarse-graining scale w .

Given the positions and velocities of all particles, one can fully describe the steady state kinetic fields in the whole silo. In Fig. 4 we plot the average velocity fields obtained numerically in a 3D silo with an orifice of $R = 16d$. The profiles of the radial velocity $v_r(r)$ at different heights are shown in Fig. 4(right). As it can be expected, the radial absolute velocity field diminishes at the center of the silo, that is clearly explained by symmetry reasons. Note, that the magnitude $v_r(r)$ is comparable with the magnitude of $v_z(r)$ and the location of the maximum absolute radial velocity $|v_r(r)|$ only slightly changes with the height from the orifice. Additionally, in Fig. 4(left), the vertical velocity fields $v_z(r)$ are also illustrated. The Gaussian shape of the velocity profiles $v_z(r)$ is in excellent agreement with those experimentally obtained [19]. Moreover, in the past it has been proven that this behavior is compatible with the solution of a diffusive-like equation [20]

Additional macromechanical details of the particle flow can be extracted studying the changes in the stress field. In Fig.5a, we plot the spatial behavior of the *contact pressure*,

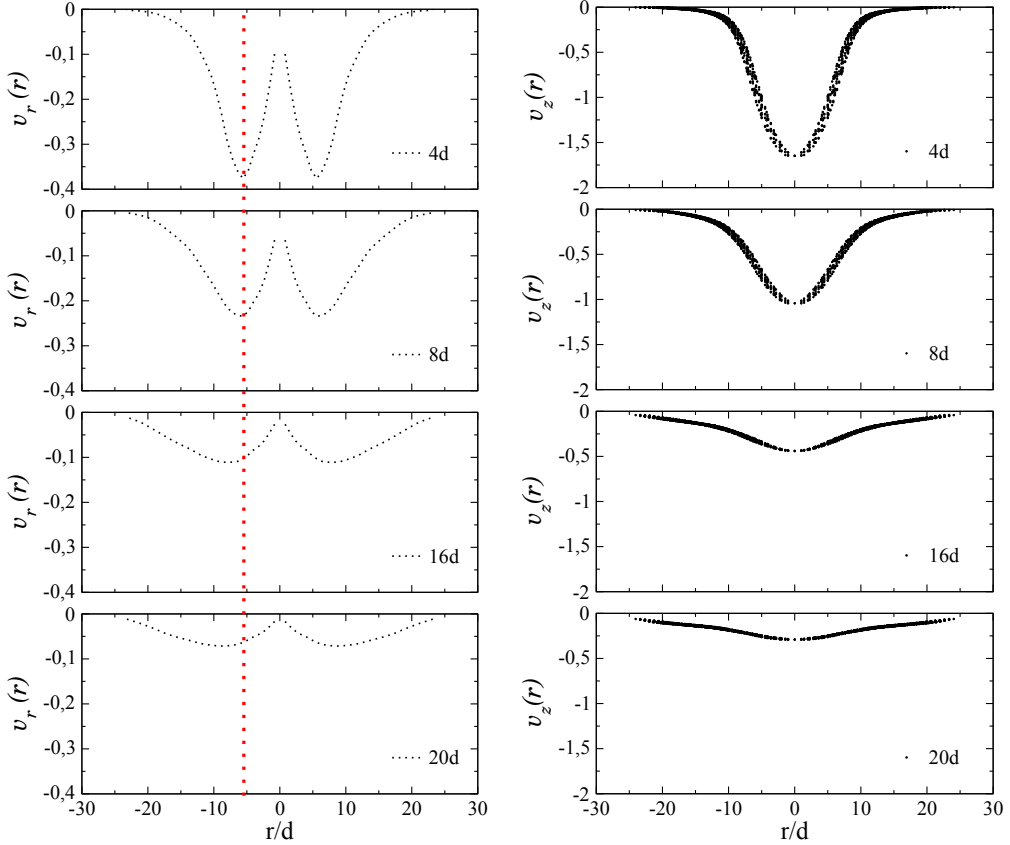


Figure 4: On the left, radial component of the velocity at different heights from the orifice (velocity measured in units of diameter of particle per second). On the right, vertical component of the velocity at different heights from the orifice. The measurements have been done for the simulation of a 3D silo with an orifice size of $R = 16d$ (heights of $z = 4d$, $z = 8d$, $z = 16d$ and $z = 20d$, respectively). In all cases, the units are diameter/sec.

which was estimated using trace and the deviatoric of the contact stress field σ^c . Note that the *contact pressure* results in a monotonous decreasing function that correlates with the increase of the dilatancy, which achieves a maximum at the outlet [9, 17]. Here, it is important to remark that the values of *contact pressure* were nearly independent on the outlet size [18]. Accordingly, a region resembling a *free-fall arch* (that should scale with R) can not be inferred from these findings.

Complementary, we have analyzed the strength of the *kinetic pressure* field calculating the trace and the deviatoric of the mean kinetic stress tensor σ^k , defined by Eq.(5) (see Fig. 5b). Although the strength of the *kinetic pressure* results several order of magnitude smaller than the *contact pressure*, its spatial pattern revealed novel micro-mechanical details. The *kinetic pressure* field evidenced conclusively the existence of a well defined transition region. Both, experimental and numerical outcomes suggest that above a well

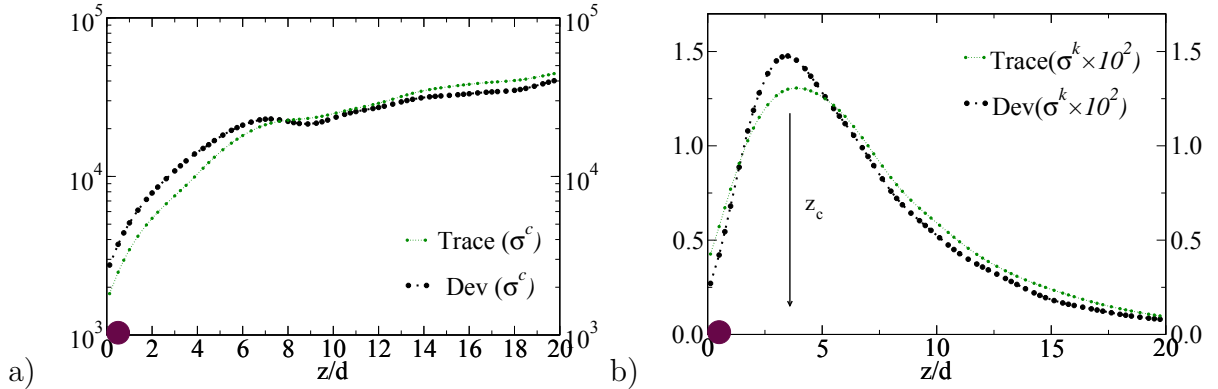


Figure 5: Trace and deviator of the a) contact stress mean field tensor $\sigma_{\alpha\beta}^c$ and b) kinetic stress mean field tensor, $\sigma_{\alpha\beta}^k$.

defined surface the particles follow the global macroscopic laminar flow [18]. The latter correlates with the diminishing of the *kinetic pressure* with the height and indicates the mass transport within the silo is mainly advective. However, as the particles get closer to the orifice their individual movement decorrelates respect to the global flow and, accordingly, the *kinetic pressure* shows a maximum value at the transition surface $z_c(r)$. After crossing, the particles start to fall by gravity and the contacting stress gradient slowly diminishes as one gets closer to the outlet.

In Fig.6, we present the universal surface z_c/R that characterizes the transition region. We illustrate outcomes corresponding to two different orifices obtained experimentally. Remarkably, we have found the transition surface is independent of the outlet size. For testing the consistency of our results, the post-processed experimental data was analyzed using different coarse-graining scales. As it noticeable the findings are totally compatible within our experimental errors. The data collapse clearly proves the existence of a parabolic transition arch. For comparison, two truncate paraboloids $\alpha(1 - (r/R)^2)$ have been included in the graph.

Astonishing, all the curves z_c/R obtained for different outlet sizes can be collapsed [18]. Moreover, we have found excellent qualitative agreement in wide domain of apertures for both experimental and numerical outcomes [18]. Hence, we have identified a region where the collisional part of the stress tensor starts to diminish and the dynamics becomes gradually dominated by the external field. The scaling of this surface with the size of the aperture links the observed dynamics in the discharge process with the stress fields inside the silo. This picture contrasts with the traditional view of the existence of a *free fall arch* region where the velocity is negligible and grains start a free fall.

Acknowledgements

This work has been supported by Projects FIS2011-26675 and FIS2014-57325 MINECO (Spain). S.M. Rubio-Largo thanks *Asociación de Amigos de la Universidad de Navarra*

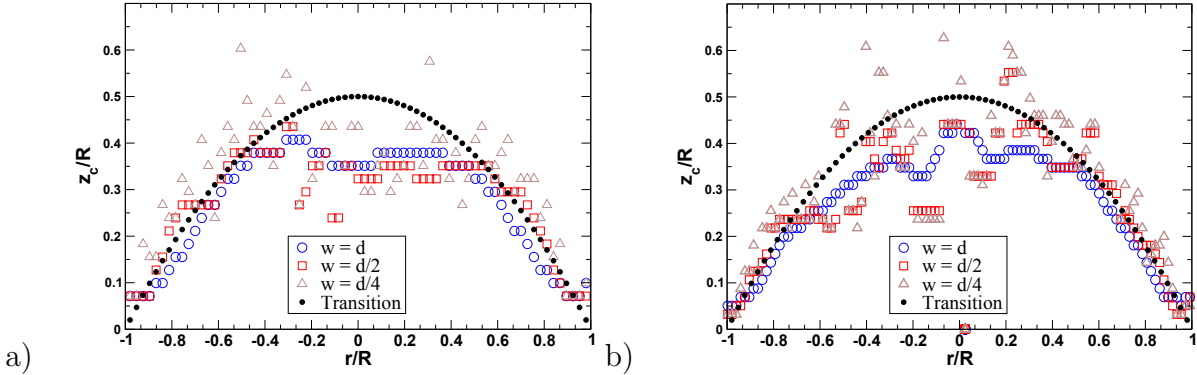


Figure 6: Position of the local maximum z_c/R of the *kinetic pressure* as a function of the radial distance. Experimental results are illustrated for (a) $R = 17d$ and (b) $R = 26d$. Testing the consistency, several values of the coarse-graning scale w has been used. For comparison, truncate paraboloids $\alpha(1 - (r/R)^2)$ have also shown.

for a scholarship.

REFERENCES

- [1] B.P Tighe and M. Sperl, *Granular Matter*, **9**, 141–144 (2007).
- [2] R. C. Brown and J. C. Richards, *Principles of Powder Mechanics*, Pergamon Press, 1970.
- [3] R. M. Nedderman, *Statistics and kinematics of granular materials*, Cambridge University Press, 1992.
- [4] W. A. Beverloo, H. A. Leniger, and J. J. Van de Velde, *Chem. Eng. Sci.* **15**, 260 (1961).
- [5] F. Vivanco, Sergio Rica and F. Melo, *Granular Matter* **14**, 563 (2012).
- [6] D.J. Van Zuilichem, N.D. Van Egmond, and J.G. De Swart, *Powder Technology* **10**, 161 (1974).
- [7] C. Mankoc, A. Janda, R. Arévalo, J. M. Pastor, I. Zuriguel, A. Garcimartn and D. Maza *Granular Matter* **9** 407 (2007).
- [8] I. Zuriguel, A. Garcimartín, D. Maza, L.A. Pugnaloni and J.M. Pastor. *Phys. Rev. E* **71** 051303 (2005)
- [9] A. Janda, I.Zuriguel, and D.Maza, *Phys. Rev. Lett.* **108**, 248001(2012).
- [10] T. Pöschel, T. Schwager, Computational Granular Dynamics, Springer-Verlag Berlin Heidelberg New York, 2005.

- [11] I. Goldhirsch, *Granular Matter* **12**, 239 (2010).
- [12] T. Weinhart, A. R. Thornton, S. Luding, and O. Bokhove, *Granular Matter* **14**, 531, (2012).
- [13] T. Weinhart, R. Hartkamp, A. R. Thornton, and S. Luding, *Phys. Fluids* **25**, 070605, (2013)
- [14] A. Janda, I.Zuriguel, I.A.Garcimartn, L.A.Pugnaloni and D.Maza, *Europhys. Lett.* **84**, 44002(2008).
- [15] J. Owens, M. Houston, D. Luebke, S. Green, J. Stone, and J. Phillips, *Proceedings of the IEEE* **96**, 879-899 (2008).
- [16] R. C. Hidalgo, T. Kanzaqui, T. Alonso-Marroquin and S. Luding *AIP Conf.Proc.* **1542**, 169-172 (2013).
- [17] D. Maza, A. Janda, S.M. Rubio-Largo, I. Zuriguel and R.C. Hidalgo, *AIP Conf. Proc.* **1542**, 674 (2013).
- [18] S.M. Rubio-Largo, A. Janda, I. Zuriguel, D. Maza and R.C. Hidalgo. *Phys. Rev. Lett.* (2015)
<http://journals.aps.org/prl/accepted/34076Y19Md515b4914c8754174498186553516e7f>
- [19] A. Garcimartín, I. Zuriguel, A. Janda and D. Maza. *it Phys. Rev. E* **84**, (2011), 031309
- [20] R. M. Nedderman and U. Tüzün, *Powder Technol.* **22**, 243 (1979)

VALIDATION OF THE GPU BASED BLAZE-DEM FRAMEWORK FOR HOPPER DISCHARGE.

Nicolin Govender¹, Patrick Pizette² AND Daniel N Wilke³ AND Nor-edine Abriak²

¹ Advanced Mathematical Modeling CSIR
Pretoria, 0001 South Africa
ngovender1@csir.co.za

² Mines Douai
LGCgE GCE, F-59508 Douai, France
patrick.pizette@mines-douai.fr

³ University of Pretoria, Department of Mechanical and Aeronautical Engineering
Pretoria, 0001, South Africa
nico.wilke@up.ac.za

Key words: Hoppers, Silos, Large scale DEM, GPU, Polyhedra

Abstract. Understanding the dynamical behavior of particulate materials is extremely important to many industrial processes, with typical applications that range from hopper flows in agriculture to tumbling mills in the mining industry. The discrete element method (DEM) has become the defacto standard to simulate particulate materials. The DEM is a computationally intensive numerical approach that is limited to a moderate amount (thousands) of particles when considering fully coupled densely packed systems modeled by realistic particle shape and history dependent constitutive relationships. A large number (millions) of particles can be simulated when the coupling between particles is relaxed to still accurately simulate lesser dense systems. Massively large scale simulations (tens of millions) are possible when particle shapes are simplified, however this may lead to oversimplification when an accurate representation of the particle shape is essential to capture the macroscopic transport of particulates. Polyhedra represent the geometry of most convex particulate materials well and when combined with appropriate contact models predicts realistic mechanical behavior to that of the actual system. Detecting collisions between polyhedra is computationally expensive often limiting simulations to only hundreds of thousands of particles. However, the computational architecture e.g. CPU and GPU plays a significant role on the performance that can be realized. The parallel nature of the GPU allows for a large number of sim-

ple independent processes to be executed in parallel. This results in a significant speed up over conventional implementations utilizing the Central Processing Unit (CPU) architecture, when algorithms are well aligned and optimized for the threading model of the GPU. We recently introduced the BLAZE-DEM framework for the GPU architecture that can model millions of spherical and polyhedral particles in a realistic time frame using a single GPU. In this paper we validate BLAZE-DEM for hopper discharge simulations. We firstly compare the flow-rates and patterns of polyhedra and spheres obtained with experiment to that of DEM. We then compare flow-rates between spheres and polyhedra to gauge the effect of particle shape. Finally we perform a large scale DEM simulation using 16 million particles to illustrate the capability of BLAZE-DEM to predict bulk flow in realistic hoppers.

1. Introduction

1.1. Hoppers

Simulating the dynamics of particulate materials is critical in the design and optimization of many industrial processes. The hopper configuration is one of the most studied configurations, either to increase the fundamental knowledge about the dynamics of granular flows or to design storage devices. Experimental, empirical [1], continuous [2] and discrete models [3] are typical approaches used to study either the granular intrinsic properties or the handling of granular media. The behavior of granular media is complex. For example, when a hopper is discharged by gravity the flow rate does not depend on the height of the material. Furthermore when the height of the material is ≥ 3.5 times the hydraulic radius of the silo, the pressure at the bottom saturates due to the Janssen effect, resulting in a flow rate that remains fairly constant. The design of the hopper and the stored material influence directly the flow rate and flow pattern. In particular, the hopper angle and the outlet size are calculated to allow bulk solid flow and prevent arch formation which restricts flow.

1.2. DEM

The discrete element method (DEM), which was first described by Cundall and Strack in 1979 [4], is one of the most successful discrete methods to simulate particulate materials. The DEM was originally developed for solving problems in geotechnical engineering, but has been employed to model particulate materials in a variety of fields [5, 6].

The DEM requires that all particles in the system need to be checked for contact at each time step. This involves a considerable number of calculations depending on the particle geometry and the number of particles [7] in the system. To reduce the computational cost, particle shape is often approximated by a sphere (Figure 1(a)). This approximation however

may result in the model exhibiting unrealistic mechanical behavior, as discussed by Latham and Munjiza [8]. The clumped-sphere (Figure 1(b)) approximation [9] provides a better description of shape by using a number of spheres to represent a particle. However, this approach is limited in the number of particles and introduces non-physical artifacts into the simulation, as discussed by Horner [10]. Polyhedral shaped particles, depicted in Figure 1(c), can capture details in particle shape well and hence exhibit realistic mechanical behavior to that of the actual system [11, 12]. However, the number of polyhedral particles that can be simulated on typical workstation computers in a realistic time frame is limited, as discussed by Mack et al. [13], in which only 322 polyhedra are simulated. This limitation is due primarily to complex collision detection and storage requirements of polyhedra.

The developed BLAZE-DEM code [14, 15] aims to address the computational limitations of modeling polyhedra, by efficiently implementing polyhedra contact algorithms on the GPU architecture. This paper gives a brief overview of the BLAZE-DEM framework and dedicates the rest of the effort to validate the utility of BLAZE-DEM to model hopper discharge for polyhedral and spherical particles.

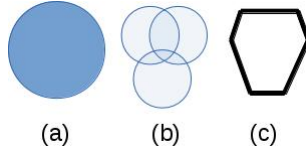


Figure 1: (a) Single sphere, (b) clumped sphere and (c) polyhedron representations of a corn kernel.

Once the particles that are in contact is determined, the resultant forces acting on the particles can be calculated. As with all numerical simulations there is a trade-off between model accuracy and computational speed. In [16, 17] the number of particles that can be modeled is limited due to the large computational cost of the associated FEM simulations and the solution of the coupled dynamic equilibrium problem associated with multiple bodies being simultaneously in contact. This allows for the simulation of strongly coupled problems associated with the compaction of particles, in addition to weakly coupled problems found in typical bulk flow analysis. The BLAZE-DEM framework focuses only on typical bulk flow problems that allows for some assumptions to be made without significant loss of accuracy but drastically benefit the computational efficiency of the numerical model. We only consider binary contact to resolve the associated contact forces on particles. In addition we consider the original contact force model proposed by Cundall et al. [17]. The constitutive model is described by a spring-dashpot coupled in parallel, which offers an appropriate model fidelity for the problems under consideration. The model is computationally efficient. This is in

contrast to the computational expense of the higher fidelity FEM-DEM model [16]. Once the forces are calculated an explicit integration scheme is used to determine the resultant motion of all particles in the system.

1.3. Computational Implementation

Since DEM computations are compute bound, the number and complexity of simulated particles has scaled with increased computational power over the past three decades. In the last few years the trend of increasing Central Processing Unit (CPU) clock speed has stopped due to the physical limits on the materials used in the manufacturing of computer hardware. While computational power still scales with Moore's Law, this scaling is now achieved through increasing the number of computing cores on a single chip as opposed to make a single core faster. Leading this evolution from multi-core to many core processing chips is the Graphical Processor Unit (GPU). Designed to convey information to screen that has millions of pixels which need to be updated simultaneously to render visual information to the user, the GPU is a massively parallel processor that can perform billions arithmetic operations in parallel (7.52 TFLOPS). The NVIDIA developed CUDA programming model [18] provides access to the GPU from a variety of high level programming languages such as C++, Java and Python.

An emerging trend in the past few years is the implementation of scientific and engineering solutions on GPU's [19, 20]. Utilizing the GPU for computation over the conventional GPU offers significant speed-ups when computations are well aligned for the parallel threading model of the GPU. Parallelism on the CPU is limited to domain decomposition [21] as depicted in Figure 2(a) [22]. The GPU however is a many core processor enabling parallelism at a particle level, with each particle having its own thread. Figure 2(b) depicts the theoretical performance of a Xeon CPU and Tesla GPU for task of performing computations for 10 millions particles. The CPU can only launch 12 threads (Particles are processed in a serial loop for each thread), while the GPU can launch 53284 threads per cycle. This gives the GPU an enormous edge over the CPU in DEM calculations which are data parallel resulting in a speed up of 500 when taking into consideration cost and power consumption.

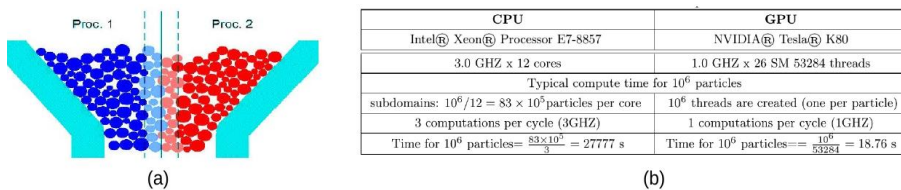


Figure 2: (a) Domain decomposition on CPUs [22] and (b) Comparison of CPU and GPU parallel solutions.

There has been little development in terms of simulations based on the DEM using the GPU from the both academic and commercial sectors. Although the GPU is an ideal match for certain DEM simulations the current learning curve associated with GPU development is high as the technology is fairly new compared to the traditional CPU platform. Furthermore only an efficiently implemented GPU DEM solution will yield significant performance benefits over the CPU.

The DEM code used in this paper is built on the BLAZE-DEM GPU framework developed by the authors [14]. The framework and its associated algorithms [15] has thus far been successfully used in the simulation of tumbling mills [23]. BLAZE-DEM can model (i) tens of millions of spherical particles and (ii) millions of polyhedral particles in a realistic time frame on a desktop computer using a single GPU. To the best of the author's knowledge there are no published works on large scale simulations of hoppers using the GPU.

2. OVERVIEW BLAZE-DEM CONTACT MODEL

A linear spring dash-pot model is used to calculate the normal force between particles given by :

$$\mathbf{F}_N = (K_n \delta) \bar{\mathbf{n}} - C_n (\mathbf{V}_R \cdot \bar{\mathbf{n}}) \bar{\mathbf{n}}, \quad (1)$$

where δ is the penetration depth, $\mathbf{V}_R = \mathbf{V}_1 - \mathbf{V}_2$ is the relative translational velocity, $K_n = \frac{m_{\text{eff}}}{t_{\text{contact}}^2} \ln(\epsilon)^2 + \pi^2$ is the spring stiffness, $C_n = \frac{2 \ln(\epsilon) \sqrt{K_n m_{\text{eff}}}}{\sqrt{\ln(\epsilon)^2 + \pi^2}}$ is the viscous damping coefficient, $\bar{\mathbf{n}}$ the normal at contact, ϵ is the coefficient of restitution and $m_{\text{eff}} = (\frac{1}{m_1} + \frac{1}{m_2})^{-1}$ is the effective mass of the particles. The contact time t_{contact} is determined by the properties of the material. However in most cases experimental data is not readily available for a particular material. For such cases K_n is chosen such that physical quantities of interest (such as energy) are conserved during integration for the typical range of velocities observed in a simulation [15]. Typical DEM simulations use a spring stiffness and time-step that limits the maximum penetration depth to $\delta_{max} \leq 0.05r$ where r is the radius of the smallest particle [19, 24, 25].

Tangential Contact. A stick-slip columbic model [15, 19, 25] is used to calculate the tangential force magnitude between particles given by :

$$F_T = -\min \left[\mu \| \mathbf{F}_N \|, \frac{\min [\min [\| \mathbf{V}_{1T} \|, \| \mathbf{V}_{2T} \|], \mu \| \mathbf{V}_T \|] m_{\text{eff}}}{\Delta t} \right], \quad (2)$$

where \mathbf{V}_{1T} and \mathbf{V}_{2T} are the tangential velocities of each particle, $\mathbf{V}_T = (\mathbf{V}_R - (\mathbf{V}_R \cdot \bar{\mathbf{n}}) \bar{\mathbf{n}})$ is the relative tangential velocity and μ the coefficient of friction.

Angular motion. In addition to translation forces a particle also experiences a torque as a result of contact given by :

$$\boldsymbol{\Gamma} = (\mathbf{r} \times \mathbf{F}_N) \quad (3)$$

where \mathbf{r} is the vector from the center of mass to the contact point $\mathbf{PC}(x, y, z)$. A detailed description of the models and numerical techniques used in BLAZE-DEM can be found in [14, 15, 23]. In a DEM simulation the model parameters are chosen to either match experimental results or to reproduce a desired behavior. Tuning these parameters is a tedious task with the plethora of different models used in DEM simulations. For DEM to be useful in hopper simulations we need to be able to accurately capture the effect of geometrical changes in the hopper using the same model parameters. In this paper we use the experimentally determined properties.

3. Experimental Setup

In order to verify the suitability of the GPU based BLAZE-DEM code for hopper simulation, we performed experiments using lab-scale plexi-glass hoppers at three discharge angles ($\beta = 30^\circ, 60^\circ, 90^\circ$) as depicted in Figure 3(a). We printed 2000 regular dodecahedron and spherical particles as depicted in Figure 3(b) and packed them in alternating colors (Figure 3(a)) to observe the flow patterns. The hopper is filled by dropping particles down the center in order to obtain a random loose packing (three tests we performed for each discharge angle). The friction coefficients between particles and particles with the boundaries are evaluated by a dedicated started angle experiment similar to that of Abriak et al. [26]. Note that for spheres, the test consists of a clump of three spheres to prevent rolling. The average frictional values was found to be $\mu_{particle} = 0.35$ and $\mu_{wall} = 0.30$.

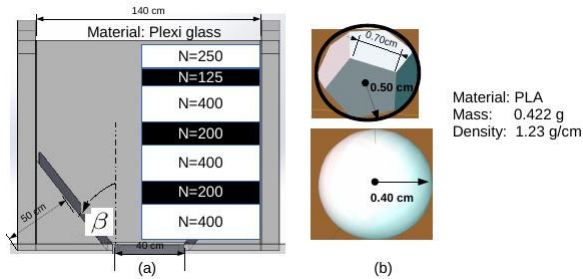


Figure 3: (a) Experimental setup indicating the number of particles N in each layer, discharge angle β and dimensions of the inlet and outlet. (b) particle specifications.

4. Comparisons of results

Figure 4(a)-(c) shows the flow rates with polyhedra for DEM and experiment while Figure 4(d)-(f) shows the flow rates with spheres for DEM and experiment. We see very good agreement with both spheres and polyhedra against experimental results. We notice that the fastest flow is for the case of $\beta = 30^\circ$ as it has the steepest inclination, with $\beta = 90^\circ$ not discharging completely as expected for both spheres and polyhedra. The model parameters used are : $\epsilon = 0.4$ $K_n = 3.2 \times 10^5 \text{ N.cm}^{-1}$ for a time-step of 1×10^{-5} .

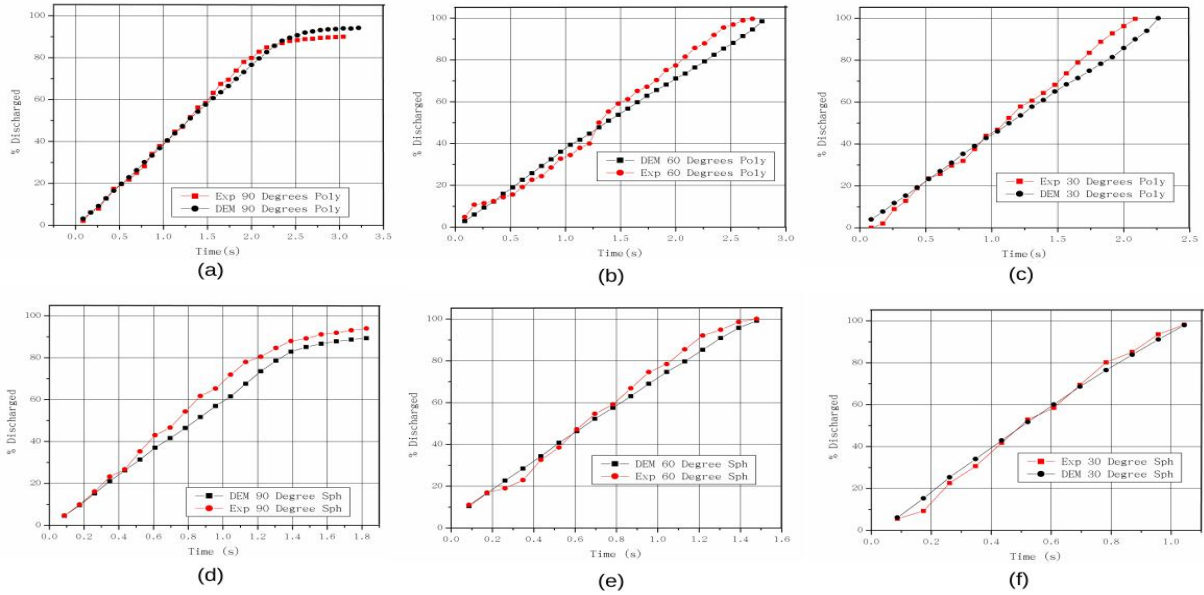


Figure 4: (a-c) Flow rates of polyhedra and (d-f) flow rates for spheres.

Figure 5 shows the flow patterns for the three hopper configurations with polyhedral particles. We notice that for 90 degrees we have funnel flow with the particles in the center discharging first and those in the sides last, while we have mass flow for both 60 and 30 degrees.

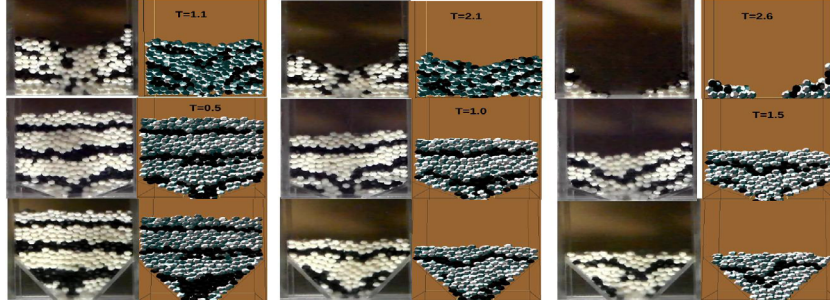


Figure 5: Flow patterns for polyhedra with experiment and DEM (time in seconds).

4.1. Effect of particle shape

To ascertain the effect of particle shape we used spheres that had the same mass and material properties of the polyhedra as depicted in Figure 3(a). Figure 6 shows the DEM predicted flow rates between spheres and polyhedra. We notice that the spheres flow faster, which can be attributed to polyhedra being able to rotate and pack more efficiently as depicted in Figure 6(b) and (c). We also notice that with polyhedra the flow-rate for the hopper angle of $\beta = 60^\circ$ is slower than that of $\beta = 90^\circ$, which is opposite to what we observe with spheres. While it is possible to increase friction (rolling and tangential) for spheres to obtain a better match, the trends between different geometries is clearly dependent on particle shape.

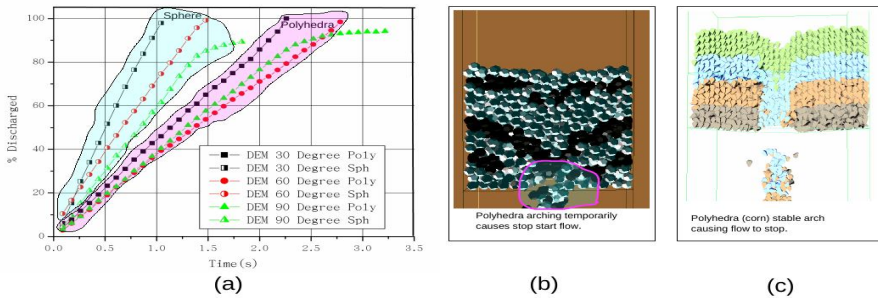


Figure 6: (a) Combined flow rates for polyhedra and spheres, (b) transient arch forming for polyhedra flow, (c) stable arch for polyhedral simulation of corn.

4.2. Large-scale simulations

The parallel computational efficiency of the BLAZE-DEM framework on the GPU architecture allows us to create simulations that are closer to reality by increasing the number of particles we can simulate in a shorter time frame as depicted in Table 1.

Table 1: Comparison to other codes (mono sized particles) *Kepler class GPU.

Author	Shape	Physics Fidelity	N particles	C Number
Harida et.al [20]	Clumped	Low	1.64×10^4	0.66×10^6
Longmore et.al [19]	Clumped	High	2.56×10^5	1.49×10^6
Radake et.al [27]	*Sphere	High	20×10^6	20×10^6
Nvidia SDK (2014) [28]	*Sphere	Low	2.5×10^5	125×10^6
BLAZE-DEM [23]	*Sphere	High	60×10^6	100×10^6

Note: No published GPU/CPU parallel polyhedra codes			Compute Time (N=5 × 10 ⁵)
BLOCKS [29]	Poly ^{cpu}	Highest	5 × 10 ³ days
iDEM [29]	Poly ^{cpu}	Low	5 × 10 ⁵ days
BLAZE-DEM [15]	Poly ^{gpu}	High	32 × 10 ⁶ min

To gauge the large-scale performance of our code we simulated a hopper with a length of 128 cm and filled height of ≈ 245 cm and variable depth (16 – 256) cm depending on the number of particles . We filled the hopper using a chute which is typical of reality, resulting in an uneven fill level as depicted in Figure 7. Figure 7 shows the hopper with particles colored by velocity. We notice that the left-side of the hopper which has the higher fill level starts to discharge at a faster rate than the right side until the height on both sides reach an equilibrium.

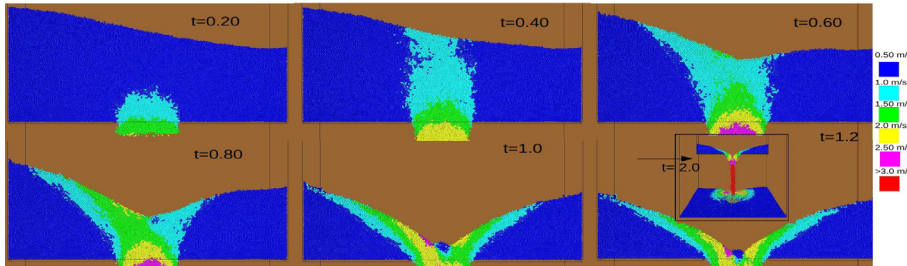
**Figure 7:** Translational velocity magnitude of flow for a large-scale simulation.

Figure 8 shows the rate of change of flow (% discharged / Δt) . We notice an erratic behavior up-to 0.90 seconds, after which it becomes stable as an equilibrium level is reached within the hopper. We also notice that the discharged particles fall into the same area as depicted at ($t=2.0$) in Figure 7 regardless of the packing within the hopper. This is of importance as the discharged particles typically fills trucks or container vessels, which remain static during the filling process, thus any change in the discharge stream will require them to be dynamic.

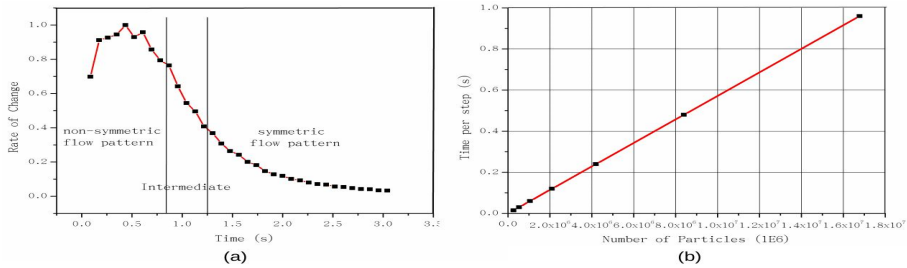


Figure 8: (a) Rate of change of flow, (b) computational time as a function of particle number.

5. Conclusion

In this paper we validated the BLAZE-DEM code against experiment for both polyhedra and spherical particles. We found an excellent agreement in both the flow-rate and pattern of the particles. We then made comparisons between spherical and polyhedral shaped particles and demonstrated that there is a difference in the predicted results. Finally we demonstrated the power of our GPU DEM implementation by performing a large scale simulation. Thus using a typical desktop computer an engineer can now obtain results on design changes and flow dynamics in a realistic time frame. Furthermore this increase in computing power can also be exploited to increase the fidelity of particle shape which we have demonstrated to have an effect of particle discharge.

REFERENCES

- [1] W. Beverloo, H. Leniger, J. Van de Velde, The flow of granular material through orifices, *Journal of Chemical Engineering Science* 15 (1961) 260–296.
- [2] V. Vidyapati, S. Subramaniam, Granular flow in silo discharge: Discrete element method simulations and model assessment, *Industrial and Engineering Chemistry Research* 52 (2013) 13171–13182.
- [3] P. Cleary, M. Sawley, DEM modelling of industrial granular flows: 3D case studies and the effect of particle shape on hopper discharge, *Applied Mathematical Modelling* 26 (2002) 89–111.
- [4] P. Cundall, Strack, A discrete numerical model for granular assemblies, *Geotechnique* 29 (1979) 47–65.
- [5] P. Cleary, The filling of dragline buckets, *Math. Eng. Ind.* 29 (1998) 1–24.

- [6] B. Mishra, R. Rajamani, Simulation of charge motion in ball mills. Part 1: experimental verifications, *Int. J. Mineral Process* 40 (1994) 171–186.
- [7] C. Radeke, B. Glasser, J. Khinast, Large-scale powder mixer simulations using massively parallel GPU architectures, *Chemical Engineering Science* 65 (2010) 6435–6442.
- [8] J. Latham, A. Munjiza, The modelling of particle systems with real shapes, *Philosophical Transactions of The Royal Society of London Series A: Mathematical Physical and Engineering Sciences* 362 (2004) 1953–1972.
- [9] H. Abou-Chakra, J. Baxter, U. Tuzun, Three-dimensional particle shape descriptors for computer simulation of non-spherical particulate assemblies, *Advanced Powder Technology* 15 (2004) 63–77.
- [10] D. Hohner, S. Wirtz, V. Emden, H.K. Scherer, Comparison of the multi-sphere and polyhedral approach to simulate non-spherical particles within the discrete element method, *Powder Technology* 208 (2011) 643–656.
- [11] D. Zhao, E. Nezami, Y. Hashash, J. Ghaboussi.J., Three-dimensional discrete element simulation for granular materials, *Computer-Aided Engineering Computations: International Journal for Engineering and Software* 23 (2006) 749–770.
- [12] D. Markauska, Investigation of adequacy of multi-sphere approximation of elliptical particles for DEM simulations, *Granular Matter* 12 (2010) 107–123.
- [13] S. Mack, P. Langston, C. Webb, York.T., Experimental validation of polyhedral discrete element model, *Powder Technology* 214 (2011) 431–442.
- [14] N. Govender, D. Wilke, S. Kok, R. Els, Development of a convex polyhedral discrete element simulation framework for NVIDIA Kepler based GPUs, *JCAM* 270 (2014) 63–77.
- [15] N. Govender, D. Wilke, S. Kok, Collision detection of convex polyhedra on the NVIDIA GPU architecture for the discrete element method, *Journal of Applied Mathematics and Computation* <http://dx.doi.org/10.1016/j.amc.2014.10.013>.
- [16] A. Munjiza, A combined finite-discrete element method in transient dynamics of fracturing solids., *Int. J. Eng. Computation* 12 (1995) 145–174.
- [17] P. Cundall, Formulation of a three-dimensional distinct element model - part i: a scheme to detect and represent contacts in a system composed of many polyhedral blocks, *Int. J. of Rock Mech* 25 (1988) 107–116.

- [18] J. Sanders, E. Kandrot, CUDA by example, Vol. 12, 2010.
- [19] J. Longmore, P. Marais, M. Kuttel, Towards realistic and interactive sand simulation: A GPU-based framework, Powder Technology 235 (2013) 983–1000.
- [20] T. Harada, GPU Gems 3: Real-time rigid body simulation on GPUs, Vol. 3, 2008.
- [21] J. H. Walther, F. Sbalzarini, Large-scale parallel discrete element simulations of granular flow, Engineering Computations 26 (2009) 688–697.
- [22] P. Cleary, M. Sawley, Three-dimensional modeling of industrial granular flows, Proceeding of CFD in the minerals and process industries, CSIRO, Melbourne, Australia, 1999.
- [23] N. Govender, R. Rajamani, D. Wilke, S. Kok, Discrete element simulation of mill charge in 3d using the blaze-dem gpu framework., Journal of minerals engineering <http://dx.doi.org/10.1016/j.mineng.2015.05.010>.
- [24] P. W. Cleary, Recent advances in DEM modelling of tumbling mills, Minerals Engineering 14 (2001) 1295–1319.
- [25] N. Bell, Y. Yu, Particle-based simulation of granular materials, Eurographics/ACM SIGGRAPH Symposium on Computer Animation 25 (2005) 29–31.
- [26] N. Abriak, Local friction effect of the global behaviour of granular media, Mathematical and Computational Modelling 28 (1998) 121–133.
- [27] G. Neubauer, C. A. Radek., GPU Based Particle Simulation Framework With Fluid Coupling Ability, NVIDIA GTC 2014, San Jose, USA, 2014.
- [28] NVIDIA, Cuda 6 (May 2014).
URL <http://www.nvidia.com/cuda>
- [29] S. Jaelee, PhD Thesis:developments in large scale discrete element with polyhedral particles simulations, University of Illinois at Urbana-Champaign,, www.uiuc.edu, 2014.

DEM PARTICLE CHARACTERIZATION BY ARTIFICIAL NEURAL NETWORKS AND MACROSCOPIC EXPERIMENTS

Luca BENVENUTI ¹, Christoph KLOSS ², Stefan PIRKER ¹

¹ Johannes Kepler University Linz, Department on Particulate Flow Modelling
Altenbergerstrasse 69, 4040, Linz, Austria
luca.benvenuti@jku.at - www.jku.at/pfm

³ DCS Computing GmbH
Altenbergerstr. 66a - Science Park, 4040 Linz, Austria
christoph.kloss@dcs-computing.com - www.dcs-computing.com

Key words: Discrete Element Method (*DEM*) Simulations, Parameter Identification, Artificial Neural Networks

Abstract. The macroscopic simulation results in Discrete Element Method (DEM) simulations are determined by particle-particle contact laws. These usually depend on semi-empirical parameters, difficult to obtain by direct microscopic measurements. Subsequently, macroscopic experiments are performed, and their results need to be linked to the microscopic DEM simulation parameters. Here, a methodology for the identification of DEM simulation parameters by means of macroscopic experiments and dedicated artificial neural networks is presented. We first trained a feed forward artificial neural network by backward propagation reinforcement through the macroscopic results of a series of DEM simulations, each with a set of particle based simulation parameters. Then, we utilized this artificial neural network to forecast the macroscopic ensemble behaviour in dependence of additional sets of particle based simulation parameters. We finally realized a comprehensive database, to connect particle based simulation parameters with a specific macroscopic ensemble output. The trained artificial neural network can predict the behaviour of additional sets of input parameters fast and precisely. Further, the numerical macroscopic behaviour obtained with the neural network is compared with the experimental macroscopic behaviour obtained with calibration experiments. We hence determined the DEM simulation parameters of a specific granular material.

1 Introduction

Particles in various forms - ranging from raw materials to food grains and pharmaceutical powders - play a major role in a variety of industries. Discrete Element Methods (*DEMs*) are widely used to simulate particle behaviour in these granular processes

(Cleary and Sawley [1]).

In their original formulation of *DEM*, Cundall and Strack [2] allowed two particles to slightly overlap upon contact, and consequently they proposed repulsive forces in relation to this overlap distance. Their fundamental modelling concept has since been widely accepted in the literature and their soft-sphere contact law has been developed further by numerous researchers (Vu-Quoc and Zhang [3] and Di Renzo and Di Maio [4]). With increasing computational resources, *DEM* simulation have become very popular giving rise to the development of commercial (e.g., *PFC3D*, used by Wensrich and Katterfeld [5]) and open-source software (e.g., *LIGGGHTS*, Kloss et al. [6], Aigner et al. [7]). Soft-sphere *DEM* simulations of thousands of particles have been proven to faithfully model particle bulk behaviour (Hohner et al. [8]).

In these macroscopic *DEM* simulations, the contact law kernel between a pair of particles determines the global bulk behaviour of the granular material (Ai et al. [9]). As a consequence, defining a correct contact law is of crucial importance for the predictive capability of *DEM* simulations. Since *DEM* contact laws are based on a set of semi-empirical parameters, correct contact law parameters must be defined for a given granular material or *DEM* simulations will fail (Combarros et al. [10]).

Identifying *DEM* contact law parameters is not a trivial task. Due to the huge number of particles in a granular material, it may be impractical to identify valid parameter sets by performing bilateral particle collision experiments. Furthermore, some contact law parameters such as the coefficient of rolling friction are purely empirical and cannot be determined by direct particle-to-particle measurements (Wensrich and Katterfeld [5]). Therefore, *DEM* contact law parameters are commonly determined by comparing the macroscopic outcome of large-scale *DEM* simulations with bulk experiments (Alenzi et al. [11]). We considered the following parameters: particle radius R (m), size distribution, Young's modulus E (Pa), Poisson's ratio ν (-), time step Δt (s), coefficient of sliding friction μ_s (-), coefficient of rolling friction μ_r (-), coefficient of restitution COR (-), particle density ρ_p (kg/m³), geometry factor $dCylDp$ (-). If *DEM* simulation results disagree with bulk measurements, the set of contact law parameters must be adjusted until reasonable agreement is achieved.

However, this purely forward methodology of parameter identification is limited by the multi-dimensionality of the parameter space and the associated computational costs of the required *DEM* test simulations. Moreover, one parameter set which is valid for one bulk behaviour (e.g., angle of repose) might fail for another (e.g., shear tester).

Clearly, there is a need for an efficient method for identifying *DEM* contact law parameters. In our study, we harnessed Artificial Neural Networks (*ANNs*) in order to reduce the number of *DEM* test simulations required. *ANNs* have proven to be a versatile tool in analysing complex, non-linear systems of multi-dimensional input streams (Vaferi et al. [12], and Haykin [13]). In our case, we fed an *ANN* with *DEM* contact law parameters as input and compared the output with the bulk behaviour predicted by a corresponding *DEM* simulation. The difference between *ANN* prediction and *DEM* prediction is used

to train our specific *ANN* with a backward-propagation algorithm (described further below). After a training phase comprising a limited number of *DEM* test simulations, the *ANN* can then be used as a stand-alone prediction tool for the bulk behaviour of a granular material in relation to *DEM* contact law parameters.

In this study, we applied this parameter identification method to two different granular bulk behaviours, namely the angle of repose (*AoR*) test and the Schulze shear cell (*SSC*) test. In both cases, we first trained a specific *ANN* using a number of *DEM* test simulations before we identified valid sets of *DEM* contact law parameters by comparing the stand-alone *ANN* predictions with corresponding bulk experiments. For both cases we obtained valid sets of contact law parameters, which we then compared to formulate a reliable contact law for a given granular material. We further show that the same *ANN* can be used to characterize different granular materials.

In the next section we define some prerequisites including *DEM* contact law definitions, a general description of the *ANN* functionality, and the proposed method of *DEM* contact law parameter identification. We then describe how it is applied to characterize the *DEM* contact law parameters of sinter fines.

2 DEM Parameter Identification

Fig. 1 illustrates the methodology used.

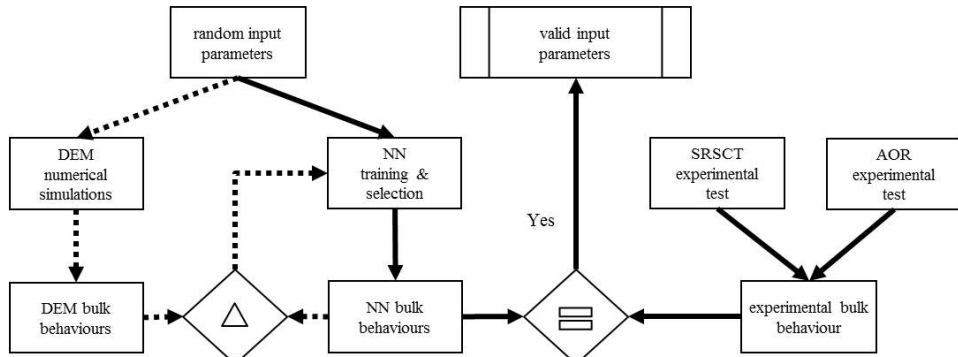


Figure 1: Method. In the training phase (dashed lines) *DEM* simulations are performed with random initial input parameters. The behaviours obtained are used to train the Artificial Neural Networks (*ANNs*) in a loop that continues until the difference between the outputs of each *ANN* and its simulations is below the limit (Δ) (see Section 2.2). In the parameters identification phase (solid lines) we identify valid input parameters by comparing ($=$) *ANNs* and experimental behaviours. Further explanations can be found in Section 2.

2.1 Discrete element method

We decided to utilize a single contact law for all the simulations performed, for details see Benvenuti et al. [18]. The *DEM* parameters for the Young's modulus (E) and the

Poisson's coefficient (ν) were taken from the literature, see [14] and [15]; however we reduced the former to increase the time step (Δt), following the recommendations of Ai et al. [9]. The time step was between 1.29% and 1.53% of the Rayleigh time, which also depends on the particle density (ρ_p). Furthermore, we locked the size distribution, which was obtained by experimental sieving, see Table 1. In the contact law we used, the tangential component of the contact force between two generic particles (F_t) is truncated to fulfil:

$$F_t \leq \mu_s F_n, \quad (1)$$

where F_n is the normal component and μ_s is the coefficient of sliding friction, one of the particle-based *DEM* parameter we investigated, another being the coefficient of rolling friction (μ_r). For coarse non-spherical particles, this is a critical parameter and describes inter-particle friction in medium to dense granular flow simulations. It is proportional to the torque counteracting the rotation of the particle. The μ_r parameter enters the equations according to the elasto-rolling resistance model presented by Wensrich and Katterfeld [5] and Ai et al. [9] based on the work of Jiang et al. [16]. The model is called *EPSD2* in *LIGGGHTS* and is appropriate for both one-way and cyclical rolling cases. The maximum magnitude of rolling resistance torque is (Eq. 2):

$$T_{r\ max} = \mu_r R_r |\tilde{F}_n|, \quad (2)$$

where R_r is the equivalent radius and F_n the normal force. The last two particle-based *DEM* parameters we investigated were ρ_p and the coefficient of restitution (*COR*) as defined by Ai. et al. [9]. These coefficients, *COR*, μ_s , μ_r , ρ_p and *dCylDp* (the cylinder dimension, proportional to the mean particle diameter), as indicated in Table 2, were constant in each simulation, but their combination differed between simulations. Further, *dCylDp* was used to evaluate the wall effect, but only 10% of the simulations had a *dCylDp* larger than 20 (additional information can be found in Benvenuti et al. [18]). The normal stress σ_n and its percentage during the incipient flow condition $\tau\%$ varied to replicate twelve shear-cell load conditions. The complete description of the shear-cell and the *AoR* simulations can be found in Benvenuti et al. [18]. A Matlab script allowed us to extract from the simulation output the numerical values representative of bulk behaviour (hereafter called *bulk values*) for each *DEM* simulation parameter combination, which consists of bulk density (ρ_b), coefficient of internal friction in the pre-shear phase (μ_{psh}), coefficient of internal friction in the shear phase (μ_{sh}), and angle of repose (*AoR*). The first bulk value (ρ_b) was provided directly. For correctly performed simulations, see Benvenuti et al. [18], we observed a stress path as in Fig. 2b. First, the σ_n was kept constant while the coefficient of internal friction (μ_{ie}) initially increased and then reached a plateau. The second bulk value (μ_{psh}) was calculated as the average of the μ_{ie} in this plateau. The σ_n was then automatically reduced, in our example to 80% of its initial value. Subsequently, a second plateau developed. We obtained the third value (μ_{sh}) as the average of μ_{ie} in this second plateau. The stress path accords with the experimental one, especially the

plateaux.

In the *AoR* tests the average of the repose angles provided us with the fourth bulk value, allowing us to define the numerical bulk behaviour.

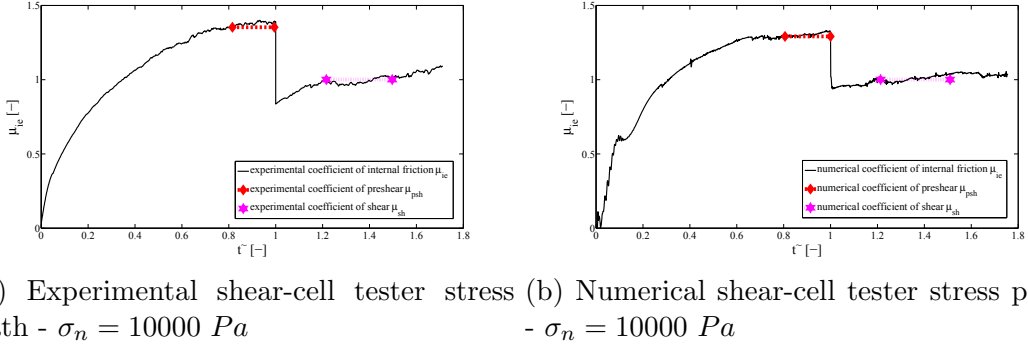


Figure 2: Experimental and numerical samples of the stress path for the Schulze ring shear cell tester. Time was normalized: $\tilde{t} = t/t_{change}$, where t_{change} is the point in time at which the normal stress (σ_n) was modified during the tests. Until $\tilde{t} = 1$, the σ_n was kept constant at 10,000 Pa. In Fig. 2a, a plateau was reached at $\tilde{t} = 0.91$. The coefficient of pre-shear (μ_{psh}) was calculated as the average of the coefficient of internal friction (μ_{ie}) in this first plateau. At $\tilde{t} = 1$, the σ_n was reduced to 80% of its initial value, and soon after a second plateau developed. We obtained the coefficient of shear (μ_{sh}) as the average of μ_{ie} in this second plateau. The stress paths agree well, especially the plateaus. They were clearly relevant because the values representative of the bulk behaviours were collected there.

Mean R (mm)	Std.dev. R (mm)	Young's modulus (MPa)	Poisson's ratio (-)	Δt (s)
0.732	0.41	10	0.40	10^{-6}

Table 1: DEM fixed input values

2.2 Artificial Neural Networks

We first defined the typology of Artificial Neural Networks (*ANNs*) we used and the input we fed them, see Benvenuti et al. [18]. Our *ANNs* have three different layers: the input layer has a number of neurons equal to the number of different inputs of the network. The hidden (or central) layer's number of neurons was to be investigated. The output layer contains one neuron for the output. The transfer functions between the first two layers are the tangential sigmoid, and those between the hidden and central layers are linear.

Thus, we were able to use the *DEM* parameter combinations and their corresponding

μ_s (-)	μ_r (-)	COR (-)	ρ_p (kg/m3)	$dCylDp$ (-)
0.4 / 0.6 / 0.8	0.4 / 0.6 / 0.8	0.5 / 0.7 / 0.9	2500 / 3000 / 3500	20 / 36 / 38 / 40

Table 2: DEM variable input values for training the Artificial Neural Networks

	μ_s (-)	μ_r (-)	COR (-)	ρ_p (kg/m3)
range	[0.1 … 1.0]	[0.1 … 1.0]	[0.5 … 0.9]	[2000 … 3500]
number of values	100	100	25	25

Table 3: DEM random input values. Within each range the indicated number of random values was chosen according to a standard uniform distribution.

bulk values to train the *ANNs*. Note that 15% of the simulations (*test simulations*) were randomly picked and excluded from the training processes. We started with all the *DEM* parameter combinations and their corresponding numerical μ_{psh} to create 36 *ANNs* that differed in their numbers of neurons in the hidden layer (between five to forty neurons). We then determined the coefficient of determination (R^2) between the *bulk – macro* behaviours in the output of the *ANN* and the 15% *test simulations*, which were not correlated with the remaining 85% used for the training. Thus, we could select for μ_{psh} the *ANN* with the maximum R^2 , again as suggested by Vaferi et al. [12], and we noted its number of neurons. We repeated the same *ANN* creation steps for μ_{sh} , ρ_b and *AoR*, obtaining one trained *ANN* for each bulk value.

Since μ_{psh} , μ_{sh} and ρ_b belonged to the shear-cell simulations, their *ANNs* were handled together: we had one cluster with three *ANNs* for the shear cell and one with only one *ANN* for the *AoR*. We could then proceed in identifying valid input parameters. Oberkampf et al. [17] suggested using a Design of Experiments (*DoE*) method to determine the parameter combinations to be simulated. They stated that this approach allows optimization of computation time with an acceptable loss of precision. The speed of the trained *ANNs* enabled us to follow a different approach to maximizing the precision of the characterization. We created random values in the range and numbers defined in Table 3 according to a standard uniform distribution. The total number of combinations of these random values was 6,250,000. These combinations were then fed to and processed by the selected *ANNs*, and thus three bulk values for the shear cell and one for the *AoR* were obtained.

2.3 Macroscopic Experiments and Parameter Identification

The experimental characterization was performed as described in Benvenuti et al. [18]. We obtained for each of the twelve load conditions of the *SSC* three bulk values (μ_{psh} , μ_{sh} and ρ_b). The fourth bulk value was the result of two angle of repose (*AoR*) tests that recreated the repose angle observed in a pile of the real material.

Subsequently, we compared the *ANN* and experimental bulk behaviours for the twelve

shear-cell load conditions. If in a DEM-parameter combination all the three bulk values differed by less than 5% from those of the corresponding experiments, i.e.:

$$\begin{cases} \text{if } |1 - \frac{\mu_{psh,num}}{\mu_{psh,exp}}| < 5\%, \\ \text{and if } |1 - \frac{\mu_{sh,num}}{\mu_{sh,exp}}| < 5\%, \\ \text{and if } |1 - \frac{\rho_p,num}{\rho_p,exp}| < 5\%, \end{cases} \quad (3)$$

the combination was marked. The marked combinations were processed by the *AoR ANN*, and then compared with the experiment. Were considered valid those that differed by less than 5% also in this comparison (Eq. 4):

$$\text{if } |1 - \frac{AoR_{num}}{AoR_{exp}}| < 5\%. \quad (4)$$

Further, to prove the validity of the system, we tested the marked combinations by modifying the experimental bulk values of the shear cell. We artificially decreased or increased the shear force, and thus μ_{psh} and μ_{sh} , by a product coefficient (P), e.g. $\mu_{psh,new} = \mu_{psh,old} \cdot P$.

3 Results and discussion

3.1 DEM Simulations

For sinter fine, 546 shear cell and 81 static *AoR* simulations were run with the parameter combinations described in Table 2. The computational time amounted to 1 hour with 32 AMD cores for a benchmark shear-cell simulation and to 9 hours for a benchmark *AoR* simulation, both with 50,000 particles. Simulations with larger *dCylDp* required more time (e.g., about 12 hours for the shear cell with 400,000 particles).

3.2 ANN model development

First, we determined the regression of the bulk behaviour parameters, for instance the μ_{psh} . The plot shows a consistent agreement between the *DEM* and the *ANN* values and an almost linear regression ($R^2 = 0.94$). We then investigated how the R^2 changed with the number of neurons for the μ_{psh} . In this case, we achieved a $R^2 = 0.96$ for an *ANN* with fifteen neurons. Increasing the number of neurons did not improve the R^2 ; it even started to oscillate with higher numbers of neurons. We subsequently obtained the optimal number of neurons for all *ANNS*. Further, we processed the random combinations (Table 2) with the *ANN*. The *ANN* evaluation was significantly faster than the *DEM* simulations. The individuation of the numerical bulk behaviours for all the *DEM* combinations did not take more than a few seconds on a single core.

3.3 Experiments and Parameter Identification

Experimental values identifying the bulk behavior, μ_{psh} , μ_{sh} and ρ_b , of sinter fine were acquired through *SSC* tests. Two *AoR* tests were performed that gave an average an-

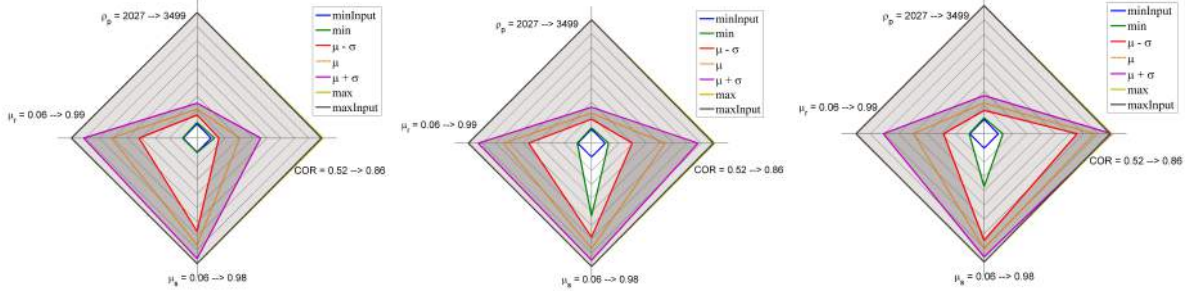
gle of 38.85° . We obtained the radius (R) mean and standard deviations, as shown in Table 1, from sieving experiments. The comparison between numerical and experimental behaviours led to a first series of marked combinations ($MC1$) for one load condition of the shear cell ($\sigma_n = 10,070$ Pa, $P=1.0$), as plotted in Fig. 3b, where the minimum and maximum values are shown, together with the mean. Note that the confidence interval is large, especially for the COR , which highlights its insignificant influence on the characterization. Both the ρ_p and the μ_s , however, show a narrow confidence interval, which demonstrates their influence and the ability of this procedure to find valid *DEM* parameters. These results agree with our examination of the ratio of the standard deviation to the range, see Table 4. Further, we observed that various *DEM* parameter combinations could reproduce the experimental behaviour, and thus evaluated their mutual dependencies. This is shown more clearly in a density plot (see Fig. 4b for $MC1$) of the particles' coefficient of restitution (COR) in relation to the coefficients of sliding friction (μ_s) and rolling friction (μ_r). Multiple combinations (250,407 or 4% of the total) of μ_s and μ_r reproduced the experimental behaviour with varying COR . This underlines once more their correlation, as already stated by Wensrich and Katterfeld [5]. To further demonstrate the validity of the procedure, we modified the product coefficient. First, we set it to $P = 0.8$, and we obtained another series of marked combinations ($MC2$). It can be seen in the parameter space plot in Fig. 3a that the confidence range is narrower than for $P = 1.0$, while in the density plot in Fig. 4a the area appears larger, although slightly less densely populated. Finally, for $P = 1.2$ and its marked combinations ($MC3$) the parameter space plot in Fig. 3c shows a largely different confidence range, while the density plot in Fig. 4c shows a smaller area. As expected, the procedure was highly sensitive to variations in the experimental data. Our approach could therefore be used for a wide range of bulk materials.

We then processed the random combinations with the *AoR ANN*. In Fig. 5a the parameter space plot for the same criteria as before can be seen. In accordance with theory (Wensrich and Katterfeld [5]), in a simulation dominated by rolling particles, the coefficient of rolling friction has the maximum influence.

Finally, we extracted from the $MC1$ values the *AoR ANN* behaviour and compared it with the experimental one. As can be seen in the parameter space plot in Fig. 5b, the confidence interval is very small, indicating that all the parameters but the COR played an important role, and demonstrating the reliability of these parameter combinations in representing the bulk behaviour. From the initial 6,250,000 combinations, only 3,884 were valid (0.0621 %), see Table 4.

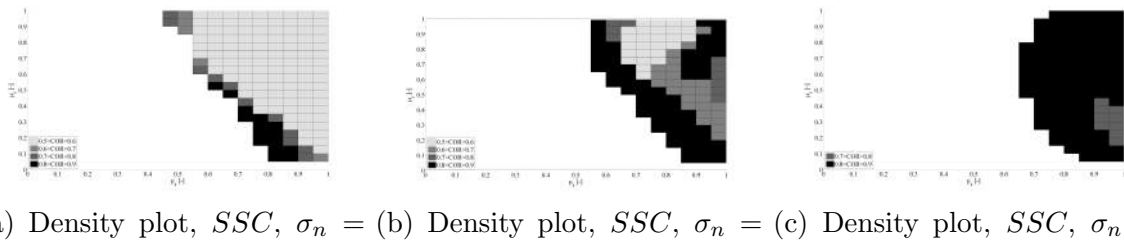
4 Conclusions

We have presented a two-step method for *DEM* simulation parameter identification. In the first step, an artificial neural network is trained using dedicated *DEM* simulations in order to predict bulk behaviours as function of a set of *DEM* simulation parameters. In the second step, this artificial neural network is then used to predict the bulk behaviour



(a) Parameter space plot, (b) Parameter space plot, (c) Parameter space plot,
 $SSC, \sigma_n = 10070 \text{ Pa}, P=0.8$ $SSC, \sigma_n = 10070 \text{ Pa}, P=1.0$ $SSC, \sigma_n = 10070 \text{ Pa}, P=1.2$

Figure 3: Parameter space plot of valid simulation parameters for three different bulk behaviours measured by a shear cell tester (SSC). Each axis of the parameter space plot represents one simulation parameter. The shaded area indicates valid parameter combinations, and dark shaded values indicate the confidence range. The marked combinations for $\sigma_n = 10070 \text{ Pa}$ are presented. Further explanations can be found in Section 3.3.



(a) Density plot, $SSC, \sigma_n = 10070 \text{ Pa}, P=0.8$ (b) Density plot, $SSC, \sigma_n = 10070 \text{ Pa}, P=1.0$ (c) Density plot, $SSC, \sigma_n = 10070 \text{ Pa}, P=1.2$

Figure 4: Density plot comparison of shear cell tester (SSC) results. The marked combinations for $\sigma_n = 10070 \text{ Pa}$ are presented. Density plot of the particles' coefficient of restitution (COR) as a function of the coefficient of sliding friction (μ_s) and the coefficient of rolling friction (μ_r); in the white area, no valid sets of simulation parameters can be found. In each cell the valid sets are grouped according to the 4 different COR ranges. Each cell is colored according to the group with the most members. The values plotted here were initially selected between the numerical values from the Artificial Neural Network with the original experimental results for the SSC , with a product coefficient $P = 1.0$ (Fig. 4b). Subsequently, they were chosen with a lower virtual shear stress ($P = 0.8$) (4a). The last image (Fig. 4c) represents the selection with a higher virtual shear stress ($P = 1.2$).

	type	SSC	AoR	SSC & AoR
μ_s (-)	mean	0.831	0.177	0.664
	std. dev. (SD)	0.097	0.095	0.029
	range (R)	0.9	0.9	0.9
	SD / R	0.108	0.106	0.032
μ_r (-)	mean	0.692	0.830	0.916
	std. dev. (SD)	0.215	0.193	0.042
	range (R)	0.9	0.9	0.9
	SD / R	0.239	0.214	0.046
COR (-)	mean	0.708	0.590	0.590
	std. dev. (SD)	0.104	0.073	0.065
	range (R)	0.4	0.4	0.4
	SD / R	0.259	0.183	0.161
ρ_p (kg/m ³)	mean	2245.7	3192.8	2283.9
	std. dev. (SD)	80.5	277.4	67.1
	range (R)	1500	1500	1500
	SD / R	0.054	0.185	0.045
valid combinations	number (%)	290203 4.64	816552 13.06	3884 0.06

Table 4: Valid DEM values. For each parameter we show the valid parameter statistics in the two tests and in their intersection. Finally, we show the number of valid parameter combinations over the total (6250000).

of a huge number of additional *DEM* parameter sets. We can then state that an artificial neural network can be trained by a limited number of dedicated *DEM* simulations. The trained artificial neural network is then able to predict granular bulk behaviour. Further, this prediction of granular bulk behaviour is much more efficient than computationally expensive *DEM* simulations. Thus, the macroscopic output associated with a huge number of parameter sets can be studied. If the predictions of the artificial neural network are compared to a bulk experiment, valid sets of *DEM* simulation parameters can be readily deduced for a specific granular material. More importantly, this *DEM* parameter identification method can be applied to arbitrary bulk experiments. Combining two artificial neural networks which predict two different bulk behaviours leads to winnowing the set of valid *DEM* simulation parameters. As part of future work, we will develop this method further by considering different fractions of granular materials, which will lead to size-dependent sets of *DEM* simulation parameters.

Acknowledgments

This study was funded by the Christian Doppler Forschungsgesellschaft, Siemens VAI Metals Technologies, and Voestalpine Stahl. The authors gratefully acknowledge their support.

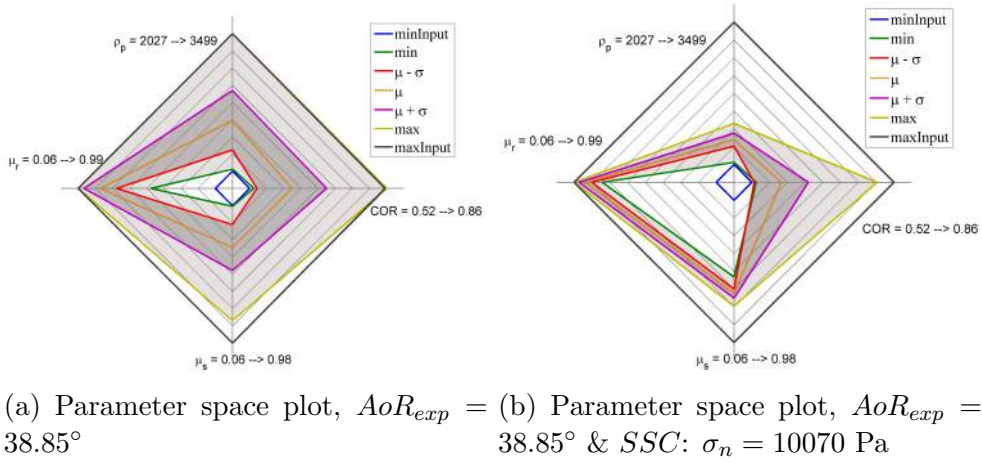


Figure 5: Parameter space plots of valid simulation parameters for the angle of repose tester (AoR) and the combination of AoR and shear cell tester (SSC). Each axis of the parameter space plot represents one simulation parameter. The shaded area and dark shaded values indicate valid parameters combinations and the confidence interval, respectively. Further explanations are given in Section 3.3.

REFERENCES

- [1] P. W. Cleary, M. L. Sawley, DEM modelling of industrial granular flows: 3D case studies and the effect of particle shape on hopper discharge, *Applied Mathematical Modelling* 26 (2) (2002) 89–111.
- [2] P. A. Cundall, O. D. L. Strack, A discrete numerical model for granular assemblies, *Geotechnique* 29 (Volume 29, Issue 1) (1979) 47–65(18).
- [3] L. Vu-Quoc, X. Zhang, An accurate and efficient tangential force-displacement model for elastic frictional contact in particle-flow simulations, *Mechanics of Materials* 31 (4) (1999) 235–269.
- [4] A. D. Renzo, F. P. D. Maio, Comparison of contactforce models for the simulation of collisions in DEM-based granular flow codes, *Chemical Engineering Science* 59 (3) (2004) 525–541.
- [5] C. M. Wensrich, A. Katterfeld, Rolling friction as a technique for modelling particle shape in DEM, *Powder Technology* 217 (0) (2012) 409–417.
- [6] C. Kloss, C. Goniva, A. Hager, S. Amberger, S. Pirker, Models, algorithms and validation for opensource DEM and CFDDEM, *Progress in Computational Fluid Dynamics, an International Journal* 12 (2) (2012) 140–152.

- [7] A. Aigner, S. Schneiderbauer, C. Kloss, S. Pirker, Determining the coefficient of friction by shear tester simulation, 3rd International Conference on Particle-Based Methods (2013) 335–342.
- [8] D. Hohner, S. Wirtz, V. Scherer, A numerical study on the influence of particle shape on hopper discharge within the polyhedral and multi-sphere discrete element method, Powder Technology 226 (0) (2012) 16–28.
- [9] J. Ai, J.-F. Chen, J. M. Rotter, J. Y. Ooi, Assessment of rolling resistance models in discrete element simulations, Powder Technology 206 (3) (2011) 269–282.
- [10] M. Combarros, H. J. Feise, H. Zetzener, A. Kwade, Segregation of particulate solids: Experiments and DEM simulations, Particuology 12 (0) (2014) 25–32.
- [11] A. Alenzi, M. Marinack, C. F. Higgs, J. J. McCarthy, DEM validation using an annular shear cell, Powder Technology 248 (0) (2013) 131–142.
- [12] B. Vaferi, F. Samimi, E. Pakgohar, D. Mowla, Artificial neural network approach for prediction of thermal behavior of nanofluids flowing through circular tubes, Powder Technology 267 (0) (2014) 1–10.
- [13] S. Haykin, Neural Networks and Learning Machines, no. v. 10, Prentice Hall, 2009, 2008034079.
- [14] N. Tsafnat, N. Amanat, A. S. Jones, Analysis of coke under compressive loading: A combined approach using microcomputed tomography, finite element analysis, and empirical models of porous structures, Fuel 90 (1) (2011) 384–388.
- [15] J. Kovacik, Correlation between young modulus and porosity in porous materials, Journal of Material Science 18 (1999) 1007–1010.
- [16] M. J. Jiang, H. S. Yu, D. Harris, A novel discrete model for granular material incorporating rolling resistance, Computers and Geotechnics 32 (5) (2005) 340–357.
- [17] W. L. Oberkampf, C. J. Roy, Verification and Validation in Scientific Computing, Cambridge University Press, 2010.
- [18] L. Benvenuti, C. Kloss, S. Pirker, Identification of dem simulation parameters by artificial neural networks and bulk experiments, manuscript submitted for publication.

OPTIMAL PARTICLE PARAMETERS FOR CLC AND CLR PROCESSES - PREDICTIONS BY INTRA-PARTICLE TRANSPORT MODELS AND EXPERIMENTAL VALIDATION

THOMAS FORGBER,¹ JULIAN R. TOLCHARD,² ABDELGHAFOUR ZAABOUT,²
PAUL INGE DAHL,² AND STEFAN RADL¹

¹ Institute of Process and Particle Engineering
Graz University of Technology, Graz, Austria
e-mail: radl@tugraz.at, thomas.forgber@tugraz.at, URL: <http://ippt.tugraz.at>

² SINTEF Materials and Chemistry
e-mail: Julian.R.Tolchard@sintef.no, Abdelghafour.Zaababout@sintef.no, PaulInge.Dahl@sintef.no
URL: <http://www.sintef.com/home/SINTEF-Materials-and-Chemistry>

Key words: Granular Materials, Heterogeneous Reactions, Chemical Looping Combustion, Chemical Looping Reforming.

Summary. *Validated models for predicting oxidation and reduction kinetics of multi-component porous particles in chemical looping combustion (CLC) and chemical looping reforming (CLR) processes are of key importance to identify the rate limiting step in these processes. Since particle properties (i.e., their composition, porosity, pore size, grain size, etc.) can be adjusted by modern synthesis techniques, there is an open question on the optimal set of these properties that would lead to the most economic process. We introduce a general open-source simulation environment, called ParScale that can be used to simulate models relevant for CLC and CLR processes, and hence can be used for their optimization. Most important, ParScale features a generalized one-dimensional spherical discretization which enables the user to predict an arbitrary number of reactions within non-isothermal porous particles consisting of multiple solid (reactive or inert) species. We perform an optimization study (constrained by typical process requirements like the maximum reaction time) for an isothermal first-order reaction, as well as for an n-th order reaction typical for hematite reduction. Finally, materials consisting of active nanoparticles embedded in a matrix of a different composition are synthesized and analyzed.*

1 INTRODUCTION

The modeling of heterogeneous reactions occurring at the inner surface of porous particles is an important tool for the design of CLC and CLR processes. These processes typically consist of two reactors, the first being a so-called air reactor in which a metal (or metal oxide, e.g., FeO, denoted here as the “carrier”) is oxidized. In a second reactor, the metal oxide is used to oxidize a fuel (e.g., methane, in case of CLC), or partially oxidize a fuel to produce hydrogen or syngas (in case of CLR) [1,2]. Despite the potential economic advantages and the great scientific interest in these processes, it is still unclear which particle configuration leads to a cost-optimal operation. Modeling of CLC and CLR processes can help to identify such

optimal conditions, and minimize costly and tedious experiments.

Particle-scale models for CLC and CLR describe intra-particle reaction-advection-diffusion phenomena, as summarized in the recent work of Noorman et al. [3]. Key phenomena that need to be modeled include (i) Maxwell-Stefan multi-component gas diffusion, (ii) gas-phase convective transport, and (iii) the heat release due to one or multiple heterogeneous reactions. While analytical solutions exist in some limiting cases [4], a non-uniform initial active solids distribution within the particle, time-depended boundary conditions, or the coupling to external flow models (e.g., CFD) require the adoption of a numerical solution strategy [5,6]. Unfortunately, there exists no open-source particle-scale modeling toolbox that performs such a numerical integration, and which can be easily coupled to existing DEM or CFD-DEM simulators. Also, grain models [7] that model changes of the inner pore structure of the particle due to non-catalytic reactions, e.g., the formation of a product layer, are typically not considered [3].

1.1 Goals and Outline

This contribution focusses on the above issues by first introducing the open-source simulation tool *ParScale* [8]. *ParScale* is designed as a library to be linked to existing Lagrangian-based particle flow simulators, and is already integrated with the DEM-based simulator *LIGGGHTS®*.

First, we will introduce a rigorous grain-scale model that accounts for the effect of a porous matrix layer on the grains, and the formation of a dense product layer that slows down non-catalytic heterogeneous reactions. Second, we present results of an optimization study that is based on an analytical solution for a first-order reduction of hematite, as well as on *ParScale* simulations for a more general n -th order reaction. Specifically, we ask the question: “What is the optimal hematite loading of an otherwise inert support particle, and how does the porosity and pore size of the support particle influence this optimum?”. Clearly, such an optimum must exist, since for a given pore size (of the support particle), a higher active solids loading (i.e., an increase in the solids volume fraction ε_s) leads to a smaller pore diameter d_s :

$$\frac{d_s}{d_{pore}} = \sqrt{1 - \frac{\varepsilon_s}{\phi_G \varepsilon_{support}}} \quad (1)$$

Here $\varepsilon_{support}$, d_{pore} , and ϕ_G is the porosity and the pore size of the support material, as well as the solids content of the grain layer, respectively (see Figure 1). In our model we assume that the grains of constant size and covered with a porous matrix layer with diameter d_M , are deposited at the walls of cylindrical pores. Thus, when increasing the active solids content, the available surface area of the grains, and hence the total reaction rate, increases. However, diffusion in the pores becomes slower due to (i) the lower overall porosity of the particle, and (ii) Knudsen effects (i.e., the overall diffusion coefficient D_{tot} and the diffusion parameter Ψ decrease with decreasing d_s , since the Knudsen diffusivity D_{Kn} decreases linearly with d_s):

$$D_{Kn} = \frac{d_s}{3} \sqrt{\frac{8 R_g T}{\pi M W_i}} \quad (2)$$

$$D_{tot}^{-1} = D_{mol}^{-1} + D_{Kn}^{-1} \quad (3)$$

$$\Psi = D_{tot} / D_{mol} \quad (4)$$

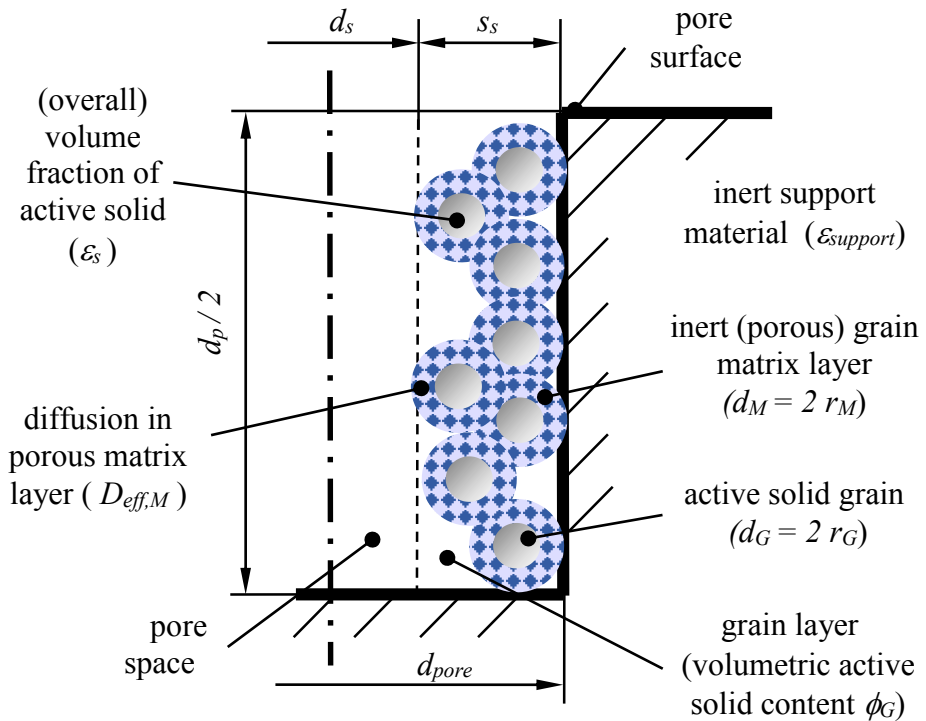


Figure 1. Model of a single pore including grain layer model.

2 POROUS PARTICLE MODEL

In order to introduce key dimensionless quantities, we now consider mole-based species transport equations and account for accumulation, diffusion and reaction of species i in a spherical porous particle. The (mole-based) volumetric source term in these transport equations due to a single chemical reaction, and in case only one gas-phase species and the active solid influence the reaction rate, is modelled as:

$$s_i = \nu_i k c_s^m c_i^n \quad (5)$$

Here ν_i is the stoichiometric constant of gas-phase species i , c is the concentration, and k is a volume-based reaction rate parameter (see next Chapter for details). m and n indicate the order of the reaction with respect to the active solid and gas-phase species, respectively. The resulting dimensionless transport equations for gas species i and the active solid (in which dimensionless quantities are indicated by an asterisk) are:

$$\partial_{t^*} (\epsilon c_i^*) = \frac{1}{\xi^2} \partial_\xi (\xi^2 \partial_\xi c_i^*) + \nu_i^* \Phi^2 c_i^{*n}, \quad (6)$$

$$\partial_{t^*} (c_s^*) = \nu_s^* \Phi^2 c_i^{*n} \frac{c_{i,0}}{c_{s,0}} \frac{|\nu_s|}{|\nu_i|}. \quad (7)$$

Here the reference quantities for the length, the time and the concentration are the particle radius $d_p/2$, the diffusion time $t_{diff} = d_p^2/4/D_{eff}$, and the reference (i.e., bulk) concentration $c_{i,0}$ of the gas-phase reactant, respectively. D_{eff} is the effective diffusion coefficient taking the particle porosity ϵ and tortuosity τ into account:

$$D_{\text{eff}} = D_{\text{tot}} \varepsilon / \tau. \quad (8)$$

The key dimensionless reaction parameter is the Thiele modulus

$$\Phi^2 = \frac{d_p^2 |\nu_i| k c_s^m c_{i,0}^{n_i-1}}{4 D_{\text{eff}}}, \quad (9)$$

and the dimensionless boundary condition for the above partial differential equation is

$$\partial_\xi c_i^* = Bi(1 - c_i^*)/2, \quad (10)$$

where $Bi = Sh D_{\text{mol}} / D_{\text{eff},i}$. Note that the above equations neglect multi-component diffusion effects, and the drift flux, since these effects are often small [3]. More details regarding individual models and the approximations made are detailed in the *ParScale* online documentation [8].

3 GRAIN MODEL

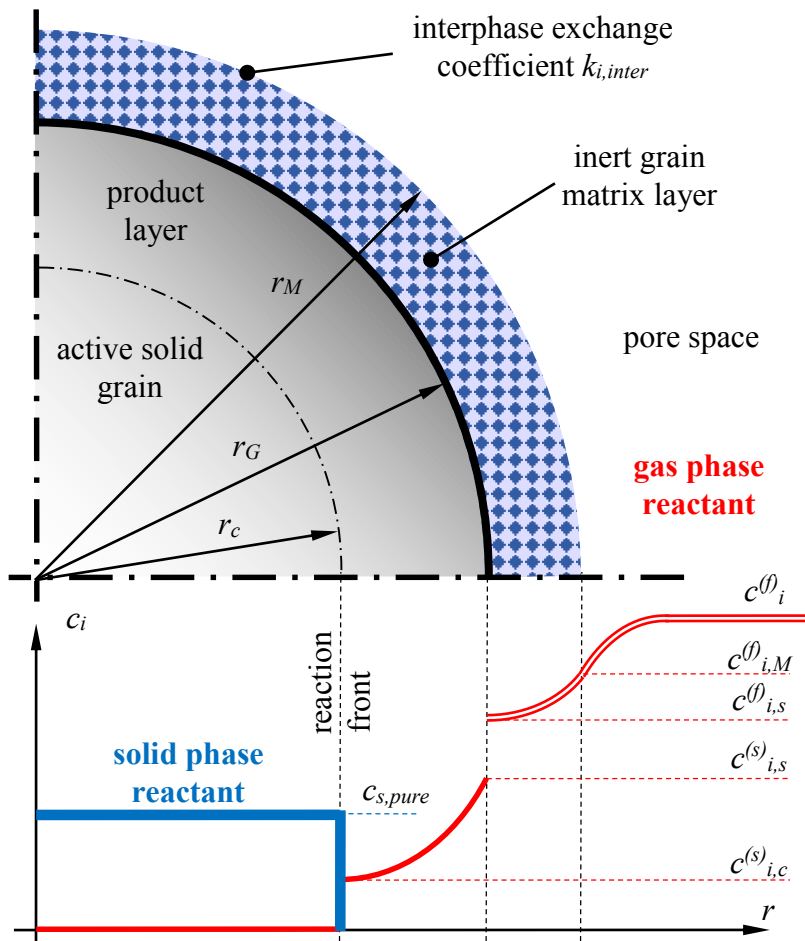


Figure 2. Grain-scale model including concentration profiles of the solid and the gas-phase reactant ($c_{s,pure}$ is the molar concentration of pure solid, which is different from the particle-average solid concentration $c_{s,0}$).

For a general heterogeneous reaction, the reaction rate parameter k in the above particle model is affected by (i) a surface area-specific reaction parameter k_s , (ii) the volume-specific

surface area of the active solid, and (iii) grain-scale effects (e.g., the formation of a product layer on, or in the spherical grains). In what follows, we show how k and k_s are related for a single non-catalytic reaction that is first-order (i.e., $n = 1$) with respect to the gas phase reactant. Specifically, we assume that the rate of reaction is affected by diffusion through an inert porous grain matrix layer, by dissociation/dissolution in a non-porous product layer (e.g., an active metal), as well as diffusion of the dissolved gas-phase reactant through the product layer to the reaction front (see Figure 2). All this is done in the context of a shrinking core type of model, assuming spherical monodisperse grains. Such a type of model and approach is typically adopted for grain-scale models, since it allows the derivation of an analytical expression for the volumetric reaction rate k [7]. Also, our idea of using a shrinking core type of model is justified by the formation of a rather sharp reaction front that forms between the educt and product layer in typical applications, i.e., in the $\text{Fe}_2\text{O}_3/\text{Fe}_3\text{O}_4/\text{FeO}$ system [9]. Due to the lack of more detailed diffusion and phase equilibrium data, we (i) model the phase equilibrium at the active solid grain / matrix layer interface using the constant H_i , and (ii) assume that the rate of diffusion is proportional to the gradient of the concentration of dissolved gas-phase reactant. Future work may incorporate more realistic approaches for modeling diffusion and phase equilibria in the active solid and the product layer (see, e.g., Ågren [9], or Kattner and Campbell [10]). Under the above assumptions, the gas consumption rate of a single grain \dot{N}_i (in [kmol/s]) is governed by transport (R_{inter} , R_M , R_G) and reaction resistances (R_{react}) in the grain:

$$\dot{N}_i = 4\pi c_i^{(f)} / \left[R_{\text{inter}} + R_M + H_i (R_G + R_{\text{react}}) \right], \quad (11)$$

$$R_{\text{inter}} = 1 / (r_M^2 k_{i,\text{inter}}), \quad (12)$$

$$R_M = \frac{1}{D_{\text{eff},M}} \left(\frac{1}{r_G} - \frac{1}{r_M} \right), \quad (13)$$

$$R_G = \frac{1}{D_G} \left(\frac{1}{r_c} - \frac{1}{r_G} \right), \text{ and} \quad (14)$$

$$R_{\text{react}} = 1 / (v_i k_s c_{s,pure} r_c^2). \quad (15)$$

Here $c_i^{(f)}$ is the concentration of the gas-phase reactant in the pore space and at the grain position. Since we use a one-dimensional discretization of the porous particles, $c_i^{(f)}$ is only a function of the radial distance in the porous support, and is obtained by solving the transport equations presented in the last chapter. We now introduce a dimensionless radial position of the reaction front ξ_c in the grain, as well as a fractional conversion X_G of the grain:

$$\xi_c = r_c / r_G \quad (16)$$

$$X_G = 1 - \xi_c^3 \quad (17)$$

The latter, i.e., X_G , can be calculated from the particle-scale transport equations, and hence can be used to close the grain-scale model equations. Finally, we define a correction factor f that only depends on the conversion X_G of the grain and a set of constant parameters:

$$\dot{N}_i = v_i 4\pi r_G^2 f k_s c_{s,pure} c_i^{(f)} \quad (18)$$

$$f^{-1} = f_{\text{inter}+M}^{-1} + f_G^{-1} + f_{\text{react}}^{-1} \quad (19)$$

$$f_{inter+M}^{-1} = \nu_i r_G^2 k_s c_{s,pure} \left(\frac{1}{r_M^2 k_{i,inter}} + \frac{1}{D_{eff,M}} \left(\frac{1}{r_G} - \frac{1}{r_M} \right) \right) \quad (20)$$

$$f_G^{-1} = H_i \nu_i r_G k_s c_{s,pure} \left[(1-X_c)^{-1/3} - 1 \right] / D_G \quad (21)$$

$$f_{react}^{-1} = H_i (1-X_c)^{-2/3} \quad (22)$$

Note, that these expressions reduce to the result presented by Melchiori and Canu [7] in (i) the absence of a matrix layer, (ii) infinitely fast interphase mass transfer (i.e., $k_{i,inter} = \infty$), and (iii) in case we set $H_i = 1$ (since Melchiori and Canu [7] did not model dissolution and diffusion of gas-phase reactants in a solid, there was no need to describe a phase equilibrium in this previous work). Also, we have set $m = 0$ and have used the (constant) concentration $c_{s,pure}$ of the pure solid to compute the reaction rate. By doing so, the grain model will account for the change of the reaction rate due to the conversion of the solid. We can now relate the grain-based and the volume-based reaction rate parameter:

$$k = (6/d_G) \varepsilon_s f k_s c_{s,pure} \quad (23)$$

Note, that for the general case of an n -th order reaction, no analytical solution for the correction factor f exists. Also, the dependency of f on the solids conversion leads to a non-linear particle model even in case $n = 1$. Hence, it is natural to consider a hypothetical situation in which $n = 1$, and no grain effects exist (i.e., $f = 1$). We adapt such a view in the next chapter to demonstrate our optimization strategy.

4 OPTIMAL PARAMETERS FOR FIRST-ORDER REACTIONS

4.1 Optimization strategy

In case we consider a reaction with $m = 0$, $n = 1$, and $f = 1$, analytical expressions for the temporal evolution of the concentration profiles $c_i(r)$, and $c_s(r)$ can be derived [4]. We hence have adopted such a parameter set, which has been also used to verify the correct implementation of the governing equations in *ParScale*. Specifically, we have used the oxidation of copper as presented by Noorman et al. [3] as the verification case. The setup and the results of this verification study which can be accessed online.

Furthermore, it is useful to define an instantaneous particle-averaged reaction rate $\bar{s} = \eta k c_{i,0}$, which depends on the concentration profiles (see, e.g., [4]). Here η is a (dimensionless) effectiveness factor that is a function of Φ and Bi . While the effect of Bi is typically weak, Φ (and hence η) is affected by the porosity ε and the pore diameter d_s . Both ε and d_s decrease with increasing solids loading ε_s as illustrated in Figure 1. η is time-invariant for the first stage of the reaction in which the solid-phase reactant is available over the full radial distance of the particle (clearly, the solid-phase reactant will deplete first at $r = d_p/2$, leading to an unreactive outer shell of the particle, ending the first stage of the reaction). It is now easy to observe that

$$\bar{s} \propto \eta \varepsilon_s k_s c_{s,pure} c_{i,0} / d_G \quad (24)$$

Hence, one can maximize the particle-averaged reaction rate by (i) maximizing the surface-area specific reaction rate k_s , (ii) maximizing the gas-phase concentration, (iii)

minimizing the grain diameter, and by (iv) maximizing the product of the effectiveness factor and the solids loading ε_s . In case we would like to take grain-scale effects into account, we must maximize f as well. Clearly, f is at a maximum in case of (i) a thin matrix layer (i.e., r_M is close to r_G), (ii) large diffusivities in the grain matrix and in the product layer, (iii) a large gas solubility in the product layer (i.e., low H_i), and (iv) a large interphase exchange coefficient $k_{i,inter}$. Since it is clear which factors lead to an optimal f , and to keep the analysis simple by avoiding the introduction of unknown parameters, grain-scale effects are not considered in what follows.

4.2 Base case parameters

We now aim on maximizing $\eta \varepsilon_s$ for a typical CLC/CLR by varying the solids loading. The system under consideration is characterized by the base case parameters shown in Table 1.

Table 1. Base case parameters used for the optimization.

Parameter	Value	Parameter	Value
$\varepsilon_{support}$	0.5	v_i	-4
τ	1.5	T	1098 [K]
d_p	100 [μm]	p	1 [bar]
d_{pore}	200 [nm]	Sh	2
ϕ_G	0.5	gas properties	CH ₄ in N ₂

4.3 Results

In Figure 3 (left panel) we plot the optimal solids loading normalized with the maximum possible solids loading (i.e., in case the pores are completely filled with solid reactant). A normalized reaction rate is shown on the horizontal axis in Figure 3. Therefore, we have defined a reference Thiele modulus Φ_{ref} based on a hypothetical maximum reaction rate k_{max} (that would be observed at the maximal possible solids loading), and the effective diffusion coefficient in the porous support at zero solids loading:

$$\Phi_{ref}^2 = d_p^2 |v_i| k_{max} / (4 D_{eff,support}). \quad (25)$$

Our results summarized in Figure 3 indicate that

- the optimal solids loading is close to the maximum solids loading for slowly reacting systems (i.e., small Φ_{ref}). For highly reactive systems, however, the maximum solids loading should be in the range of 40 to 50% of the maximum possible solids loading. This is due to the fact that the decrease of the effective diffusion coefficient upon an increase in the solid loading outweighs the gain in the reactivity already at low ε_s .
- the pore size of the support has only a small effect on the optimal relative active solid loading. The only limitation is hence that pores must be large enough to deposit the active solid inside the pores. Also, pores should be small enough to keep the layer of deposited grains as thin as possible.
- as expected, the importance of Knudsen diffusion (quantified by the parameter Ψ_{opt}) increases for smaller pore diameters. Clearly, Knudsen effects need to be considered for all pore sizes considered, since Ψ_{opt} is substantially smaller than unity.

- there is no effect of the porosity of the support on the optimal relative metal loading at constant pore size (data not shown). Thus, in order to maximize the solids loading, the porosity of the support matrix should be as high as possible.

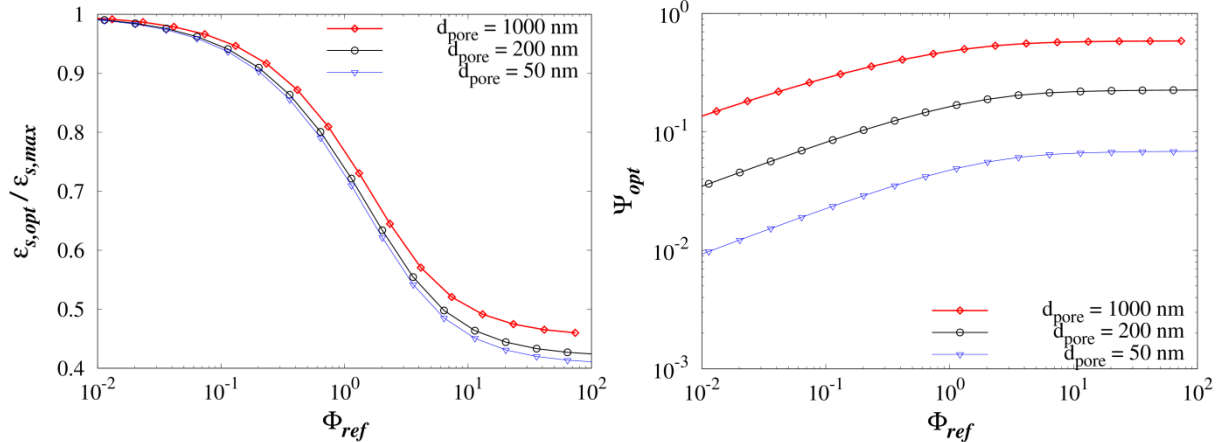


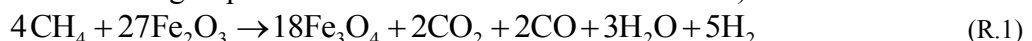
Figure 3. Optimal relative metal loading (left panel) and optimal dimensionless diffusivity (right panel) for various pore sizes.

5 OPTIMAL METAL OXIDE LOADING FOR THE REDUCTION OF HEMATITE

5.1 Reaction mechanism

We now consider the reduction of hematite (Fe_2O_3) using methane. Previous work on the $\text{Fe}_2\text{O}_3/\text{CH}_4$ system has been done by Monazan et al. [11], which proposed a reaction scheme consisting of two parallel reactions. Previous work did not take inter-particle transport limitations into account, since a fine-grained powder was used in the experiments, and the effect of support on the reaction outcome was not modeled. No detailed analysis regarding the catalytic effect of the metal was considered in previous work. Hence, we consider these previous results as the grain-scale reaction rates, which already account for the product layer formation. Consequently, we have not employed the grain model in what follows.

Following Monazan et al. [11], we adopt the following reactions (note, that hematite was modified with traces of Mg in previous work to accelerate the reaction)



A typical conversion rate expression for these reactions is (only valid at zero conversion; for higher conversions the rate decreases appreciably):

$$\partial_t X_i = w_i X_\infty y_{\text{CH}_4}^{n_i} k_i \exp[-E_{A,i} / T] \quad (26)$$

with the closures

$$w_1 = 1 - w_2 \quad (27)$$

$$w_2 = -0.828 + 0.0017 T + 0.1404 y_{\text{CH}_4} \quad (28)$$

$$X_\infty = 1.366 - 4.180 \cdot 10^5 / T^2 + 18.05 y_{\text{CH}_4}^3 \quad (29)$$

$$k_1 = 383.9; k_2 = 144.6; n_1 = 0.182; n_2 = 0.272 \quad (30)$$

$$E_{A,1} = 6040; E_{A,2} = 7798 \quad (31)$$

The conversion rate is connected to the molar reaction rate s_i via:

$$s_{\text{Fe}_2\text{O}_3,i} = \partial_t X_i \frac{(1-\varepsilon) \rho_{\text{Fe}_2\text{O}_3}}{MW_{\text{Fe}_2\text{O}_3}} \quad (32)$$

The results of Monazan et al. [11] indicate conversion rates (typical for 825°C and $y_{\text{CH}_4} = 0.10$) between 0.04 (for reaction R2) and 0.4 [min⁻¹] (for reaction R1). Thus, a typical reaction time scale is 2.5 and 25 minutes of the first and second reaction, respectively (i.e., R2 is substantially slower than R1). Assuming a particle porosity of $\varepsilon = 0.5$, pure Fe₂O₃ particles, a density of pure Fe₂O₃ of 5,240 [kg/m³], as well as a molecular weight of 160 [kg/kmol] (see Han et al., [5]), this translates into a typical iron oxide consumption rate $s_{\text{Fe}_2\text{O}_3}$ of ca. 0.11 [kmol/m³/s], and a corresponding reaction rate of $R_{\text{R1}} = 4.1 \cdot 10^{-3}$ [kmol/m³/s]. When neglecting the effect of y_{CH_4} on X_∞ , and the effect of w_I in the conversion rate expression, the following expression for the (linearized) reaction rate (exactly valid only for $y_{\text{CH}_4} = 0.10$ and at 825°C) can be extracted from literature:

$$r_i = 6.23 \cdot 10^{-3} y_{\text{CH}_4}^{0.182} \left[\frac{\text{kmol}}{\text{m}_{\text{tot}}^3 \text{s}} \right] \quad (33)$$

5.2 Concentration profiles

We consider the reduction of a hematite-impregnated porous support at different hematite loading levels ε_s (parameters are as shown in Table 1, with the exception of: $d_p = 1$ [mm], $Bi = \infty$, and $y_{\text{CH}_4} = 0.20$; the characteristic reaction time scale in the absence of pore diffusion effects was set to 60 [s] in order to model reaction R1). Since the reaction order is $n < 1$, *ParScale* was used to solve the governing equations for the gas- and solid-phase concentration profiles. Figure 4 highlights the effect of the relative solids loading level ε_s on these profiles. ε_s affects both (i) the volumetric reaction rate, as well as (ii) the effective rate of diffusion in the pores, and consequently Φ .

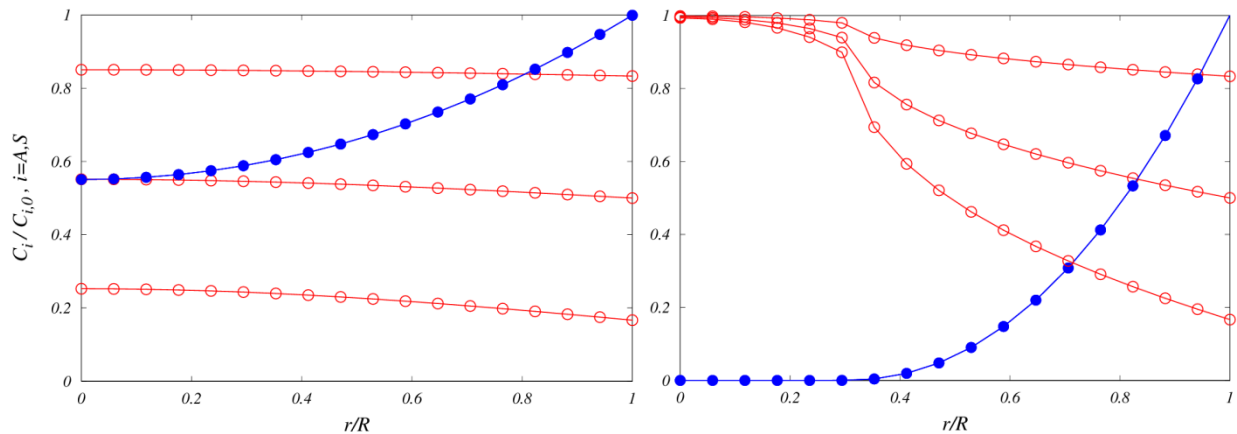


Figure 4. Normalized concentration profiles of gas (blue dots) and Fe₂O₃ (red circles, $t = 10, 30, 50$ [s] from top to bottom; left panel: $\varepsilon_s / \varepsilon_{s,\max} = 0.90$, $\Phi = 1.70$; right panel: $\varepsilon_s / \varepsilon_{s,\max} = 0.96$, $\Phi = 3.39$).

Interestingly, for high hematite loadings (see right panel in Figure 4) a rather sharp front in the hematite concentration profile develops at $r/R \sim 0.3$. Also, the results for the smaller Thiele modulus (see left panel in Figure 4) indicate a uniform solids concentration profile. In contrast, the concentration profile of the gas-phase reactant has a significant gradient. This is due to the insensitivity of the reaction rate on the methane concentration indicated by the small value of n .

5.3 Optimal solids loading

The variation in the solids loading both effects the particle-averaged reaction rate \bar{s} , as well as the final solids conversion after a pre-defined amount of time. We have decided to consider the latter in the following optimization analysis, since it is closer to the final application. Specifically, we have considered that the particles have a residence time of $t_{res} = 100$ [s] in the reduction reactor. The function to optimize is hence the total amount of consumed active solid per m³ of particle:

$$c_{s,t_{res}} = c_{s,0} X_s(t_{res}) \quad (34)$$

Note, that the initial (particle-averaged) solids concentration is related to ε_s :

$$c_{s,0} = \varepsilon_s \rho_s / MW_s \quad (35)$$

The results of the optimization study are summarized in Figure 5. Our data indicates that for the comparably slow reaction of CH₄ with hematite, the optimal solids loading is in the range of 85% to 95% of the maximal possible loading, depending on the pores size. This is in line with the findings summarized in Chapter 4 for a first-order reaction.

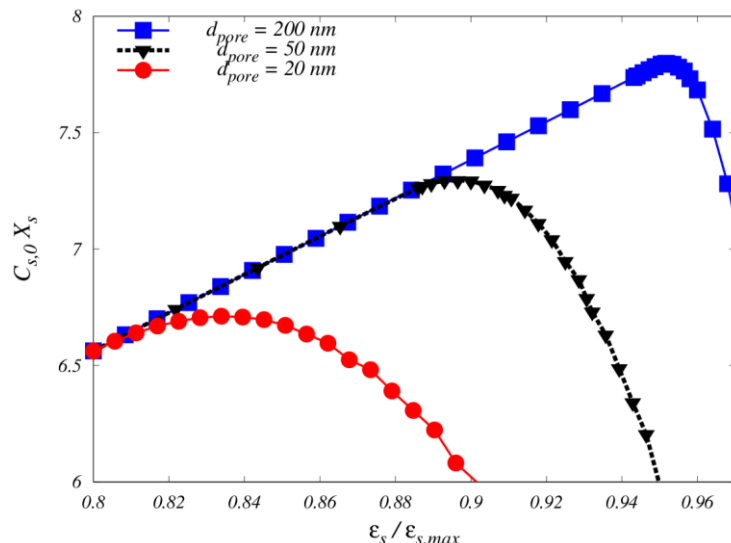


Figure 5. Normalized metal consumption as a function of the relative metal loading and pore size of the support.

6 EXPERIMENTAL VALIDATION

To work towards a validation of the presented models, as well as to investigate the thermochemical compatibility, commercially available Fe₂O₃ nanoparticles were embedded in a highly porous support matrix of SrAl₆O₁₉. The support matrix was synthesized through a

sol-gel route adapted from the method reported by Solunke et al. [12]. The active Fe_2O_3 nanoparticles and the highly porous support material are depicted in Figure 6. The Fe_2O_3 nanoparticles are not spherical as in the grain model, but are rather rod shaped with a width of 10-15 nm and a length in the range of 50-100 nm. Future work will attempt to quantify the effect of the grain shape on the conversion. Also, smaller and more spherical nanoparticles may be synthesized in future work, enabling us to fill even small pores in the support matrix. The BET specific surface area of the synthesized matrix material (with nanoparticles embedded) was measured to be $363 \text{ m}^2/\text{g}$, with a typical pore diameter in the lower mesoporous range ($\sim 5 \text{ nm}$). The matrix material is expected to coarsen, and the pores will widen during cycling at relevant operating temperatures (i.e., 600-900 °C).

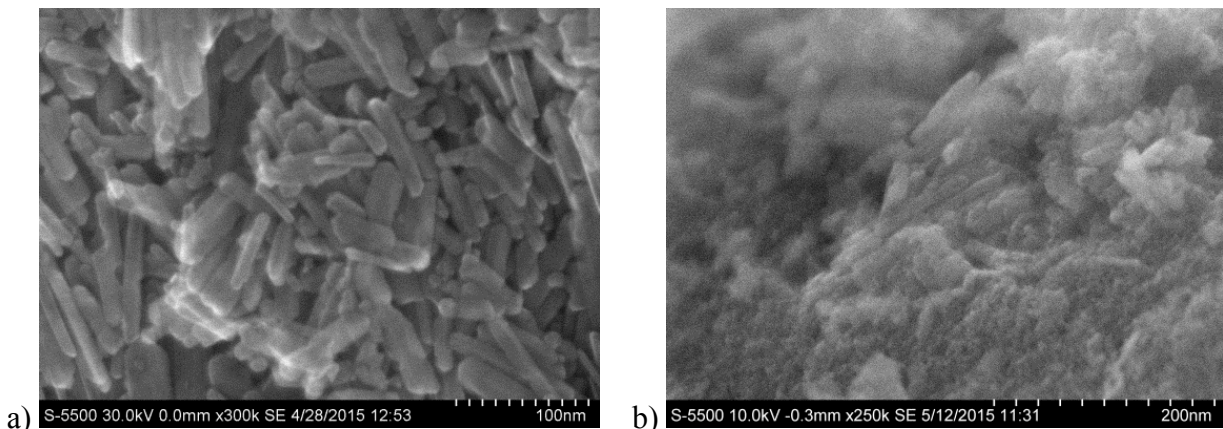


Figure 6 Scanning electron micrographs of a) Fe_2O_3 nanoparticles and b) the highly porous support matrix material (with Fe_2O_3 nanoparticles embedded).

7 CONCLUSIONS

We have presented a model for describing reaction-diffusion phenomena inside porous particles, including a novel grain-scale model. Our models account for transport limitations imposed by mass transfer to the surface of the porous support, pore diffusion, as well as diffusion and dissolution of reactive gases in the grains. The models are implemented in the open-source simulation tool *ParScale*, which is licensed under LGPL. This licensing model allows the linking of *ParScale* to any open-source and commercial particle-based flow solver.

We have demonstrated how an analytical solution of the governing equations, as well as numerical predictions of *ParScale* can be used to optimize the solids loading of the carrier particles. A key result is that the optimal loading level of active solid is close to the porosity of the support particle. Thus, the pores of the support particle should be filled by ca. 85% to 95% with the active solid, depending on the pore size of the support. In case the reactivity of the active solid is high (i.e., the reference Thiele modulus is large), only ca. 45% of the pore volume should be filled.

The current study was limited to a single heterogeneous reaction, and convective transport in the pores, as well as multi-component diffusion, was neglected. While the latter can be expected to have a negligible effect on our predictions, we expect that for reactions that result in a significant change in the gas-volume more work is needed. In these situations convective

transport in the pores might become important. Future work will show if this effect leads to a significant shift of the optimal solids loading.

ACKNOWLEDGEMENT

The authors acknowledge support by the European Commission through FP7 Grant agreement no. 604656 (“NanoSim”). *LIGGGHTS®* is a registered trademark of DCS Computing GmbH.

REFERENCES

- [1] Wei, G., He, F., Huang, Z., Zhao, K., Zheng, A., and Li, H., Chemical-Looping Reforming of Methane Using Iron Based Oxygen Carrier Modified with Low Content Nickel. *Chinese J. Chem.* (2014) **32**: 1271–1280.
- [2] Adanez, J., Abad, A., Garcia-Labiano, F., Gayán, P., and de Diego, L.F., Progress in Chemical-Looping Combustion and Reforming technologies. *Prog. Energy Combust. Sci.* (2012) **38**: 215–282.
- [3] Noorman, S., Gallucci, F., Van Sint Annaland, M., and Kuipers, J. a M., A theoretical investigation of CLC in packed beds. Part 1: Particle model. *Chem. Eng. J.* (2011) **167**: 297–307.
- [4] Wen, C.Y., Noncatalytic solid fluid reactions. *Ind. Eng. Chem. Res.* (1968) **60**: 34–54.
- [5] Han, L., Zhou, Z., and Bollas, G.M., Heterogeneous modeling of chemical-looping combustion. Part 1: Reactor model. *Chem. Eng. Sci.* (2013) **104**: 233–249.
- [6] Han, L., Zhou, Z., and Bollas, G.M., Heterogeneous modeling of chemical-looping combustion. Part 2: Particle model. *Chem. Eng. Sci.* (2014) **113**: 116–128.
- [7] Melchiori, T., and Canu, P., Improving the quantitative description of reacting porous solids: Critical analysis of the shrinking core model by comparison to the generalized grain model. *Ind. Eng. Chem. Res.* (2014) **53**: 8980–8995.
- [8] Radl, S., Forgber, T., Kloss, C., and Aigner, A., ParScale - A Compilation of Particle Scale Models. (2015). Url: <https://github.com/CFDEMproject/ParScale-PUBLIC>.
- [9] Agren, J., Oxidation and diffusion in oxides - a progress report, in: 10th NIST Diffus. Work., 2012. Url: http://www.nist.gov/mml/msed/thermodynamics_kinetics/upload/Agren-2012.pdf.
- [10] Kattner, U.R., and Campbell, C.E., Modelling of thermodynamics and diffusion in multicomponent systems. *Mater. Sci. Technol.* (2009) **25**: 443–459.
- [11] Monazam, E., and Breault, R., Thermogravimetric Analysis of Modified Hematite by Methane (CH₄) for Chemical-Looping Combustion: A Global Kinetics Mechanism. *Ind. Eng. Chem. Res.* (2013) **52**: 14808–14816.
- [12] Solunke, R.D., and Veser, G., Nanocomposite oxygen carriers for chemical-looping combustion of sulfur-contaminated synthesis gas. *Energy and Fuels.* (2009) **23**: 4787–4796.

PARSCALE - AN OPEN-SOURCE LIBRARY FOR THE SIMULATION OF INTRA-PARTICLE HEAT AND MASS TRANSPORT PROCESSES IN COUPLED SIMULATIONS

Stefan Radl¹, Thomas Forgber¹, Andreas Aigner² and Christoph Kloss²

¹ Institute of Process and Particle Engineering
Graz University of Technology, Graz, Austria
Email: radl@tugraz.at, thomas.forgber@tugraz.at
Web page: <http://ippt.tugraz.at>

² DCS Computing GmbH
Altenbergerstr. 66a Science Park
4040 Linz, Austria
Email: andreas.aigner@dcs-computing.com, christoph.kloss@dcs-computing.com
Web page: <http://www.dcs-computing.com>

Key words: Granular Materials, DEM, LIGGGHTS®, ParScale, Resolved Intra Particle Profiles, Heat and Mass Transfer, Sheared Bed

Abstract. We introduce the open-source library *ParScale* for the modeling of intra-particle transport processes in non-isothermal reactive fluid-particle flows. The underlying equations, the code architecture, as well as the coupling strategy to the widely-used DEM solver *LIGGGHTS®* is presented. A set of verification cases, embedded into an automated test harness, is presented that proofs the functionality of *ParScale*. To demonstrate the capabilities of *ParScale*, we perform simulations of a non-isothermal granular shear flow including heat transfer to the surrounding fluid. We present results for the conductive heat flux through the particle bed for a wide range of dimensionless cooling rates and particle volume fractions. Our data suggests that intra-particle temperature gradients need to be considered for an accurate prediction of the conductive flux in case of (i) a dense particle bed and (ii) for large cooling rates characterized by a critical Biot number of ca $Bi_{crit} \approx 0.1$.

1 Introduction

Over the past ten years the coupling of the Discrete Element Method (DEM) and Computational Fluid Dynamics (CFD) has been widely adopted by academia and industry to predict fluid-particle flows [1]. Recently, the trend towards CFD-DEM has been fueled by the introduction of open-source toolboxes [2]. These tools are able to model momentum and thermal energy transport of the particles and the fluid with high computational efficiency, hence provide a detailed understanding of granular flow behavior. However, these tools typically do not take intra-particle transport phenomena into account, and hence are unable to model intra-particle processes, e.g., heterogeneous reactions and diffusion inside a porous particle. Unfortunately, in these reactive particulate systems intra-particle processes often play a central role, and hence may dictate overall reactor performance. Thus, spatially-resolved particle properties (e.g., the local gas concentration in the pores of the particle) need to be resolved to account for all relevant phenomena in the system [3].

ParScale, a newly developed open-source library implemented in a C/C++ environment and publicly available through www.github.com [4], closes this gap. At the current development state, **ParScale** contains a plurality of models that aim on predicting heat and mass transfer, as well as homogeneous and heterogeneous reactions inside flowing porous particles. Also, it is possible to account for a single or multiple-reactions, i.e., a whole reaction network. Due to a modular class-based structure, and the integration into an automated test harness, easy extendibility and a high software quality is ensured. Our contribution outlines the governing equations for modeling various intra-particle phenomena in Section 2. In section 3 a number of verification cases is presented in order to demonstrate and verify the functionality of **ParScale**. Section 4 demonstrates the coupling to LIGGGHTS® and evaluates the need to account for intra-particle temperature gradients in non-isothermal granular shear flows cooled by a surrounding fluid.

2 Simulation method and parallel coupling strategy

The key purpose of **ParScale** is to predict intra-particle target properties (e.g., the temperature) as a function of time and space in a spherical particle and a fixed grid consisting of equidistant grid points. The governing equations for the relevant transport phenomena within each particle are outlined in the next section.

2.1 Transport within a particle

To illustrate a typical transport equation to be solved by **ParScale** within a single particle, the Fourier equation in spherical coordinates with $\lambda_{eff} = const.$ is considered:

$$\rho c_p \frac{\partial T}{\partial t} = \text{div}(\lambda_{eff} \text{grad } T) + s_T \quad (1)$$

where ρ is the density, c_p is the heat capacity, T represents the target property profile, t is the time, λ_{eff} is an effective conductivity (e.g., for heat), and s_T is a volume-specific

source term (e.g., for thermal energy). By introducing the thermal diffusivity

$$a = \frac{\lambda_{eff}}{\rho c_p} \quad (2)$$

and for constant thermal conductivity λ_{eff} , Eqn. (1) can be re-written as

$$\frac{\partial T}{\partial t} = a \cdot \left(\frac{\partial^2 T}{\partial r^2} + \frac{2}{r} \frac{\partial T}{\partial r} \right) + \frac{s_T}{\rho c_p} \quad (3)$$

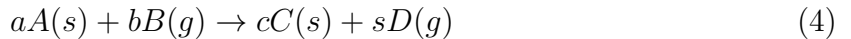
where r is the radial coordinate.

This partial differential equation (PDE) can be discretized in space, e.g., using a central-differencing scheme, in the spirit of the so-called method of lines. The resulting system of ordinary differential equations (ODEs) needs to be solved using a robust integration approach, since the source s_T might lead to a stiff behavior of the PDE. Specifically, we have chosen the flexible multi-step, variable-order solver CVODE, which uses a (modified) Newton-iteration approach to robustly integrate stiff systems of ODEs. CVODE contains a plurality of direct and iterative linear solvers for solving the resulting matrix-algebra problems, and is actively maintained by the Lawrence Livermore National Laboratory (LLNL, U.S.A) as part of the SUNDIALS package [5]. ParScale inherits the flexibility of CVODE, and hence can handle quickly changing environmental conditions, or fast, strongly exothermal reactions in porous particles.

For the second verification example (see Section 3.2), we will consider a single heterogeneous reaction in a porous particle. The corresponding transport equations are presented in the next section.

2.2 Chemistry model

The following equations model the mole-based reactive species balance equations in a particle with constant porosity ϵ . We have adopted the notation of Noorman et al. [6], and from which we have extracted typical system parameters for a relevant application. Here we focus on a single chemical reaction, which is considered to be irreversible and involves a solid species A, as well as a gas species B educt that forms a solid product C and a gaseous product D:



Relevant real-world examples following this scheme are (i) the reduction of iron oxides by H₂, (ii) the oxidation of ZnS and FeS with O₂ to metal oxides (i.e., ZnO, Fe₂O₃), or (iii) the combustion of coal with a high ash content. The mole balance equation for each species in the porous particle is written as:

$$\frac{\partial \epsilon c_i}{\partial t} = -\frac{1}{r^2} \frac{\partial}{\partial r} (r^2 N_i) + s_i \text{ with } i = B, D \quad (5)$$

Here ε is the phase fraction, c_i is the gas concentration (in $kMol$ per m^3 gas volume), N_i the (convective and diffusive) flux, and s_i is the chemical source term. A typical model for s_i is

$$s_i = \sum_{j=1}^{NR} \nu_{ij} \cdot \prod_k^{NG+NS} c_k^{n_{k,j}} \quad (6)$$

where NR is the number of reactions, NG is the number of gas components, ν_{ij} is the stoichiometric coefficient of species i in reaction j , NS is the number of solid species, and $n_{k,j}$ is the reaction exponent. The mole balance equations for the solid phase are similar, however, exclude the flux and are based on molar concentrations in $kMol$ per m^3 total volume:

$$\frac{\partial c_i}{\partial t} = s_i \text{ with } i = A, C \quad (7)$$

For spatial discretizing a second order central differencing scheme is used. For further information about the underlying equations, available models and discretization schemes the interested reader may refer to the online documentation in the public repository of **ParScale** [4]. The next section briefly outlines the run modes of **ParScale** including the coupling to the open-source DEM-based solver **LIGGGHTS®**.

2.3 Parallel coupling strategy

Besides a stand-alone mode the current development state of **ParScale** provides coupling capabilities to **LIGGGHTS®** and selected solvers of **CFDEMcoupling** in parallel. The key idea is that **ParScale** acts as a slave to the master (i.e., **LIGGGHTS®**), and can exchange its data containers between individual processes as requested by the master. In this paper we will only focus on the coupling to **LIGGGHTS®**. The coupling to **CFDEMcoupling** is handled via **LIGGGHTS®** data structures, and hence is in fact unproblematic. Figure 1 illustrates the underlying coupling algorithm.

At every timestep t_n **LIGGGHTS®** advances the particle position and velocity (and other integral particle quantities if desired) in the simulation domain. After this computation is finished, the coupling is realized by updating the particle surface temperature ($T_{surface}$) directly, or (alternatively) a heat transfer coefficient α together with the fluid temperature in the vicinity of the particle. In addition, a conductive heat flux due to particle-particle collisions (\dot{q}_{cond}) can be imposed as well. **ParScale** initializes from the last time step t_{n-1} , and calculates all internal property fields according to the imposed boundary conditions. Additional coupling options are available, e.g., **LIGGGHTS®** is able to push a particle-unique environment temperature (i.e., fluid temperature) to **ParScale**. This enables **ParScale** to react due to changes in the environment temperature, e.g., if the particle enters a region of a fixed temperature. Furthermore, the coupling provides the option to reset the value of the target property to a certain value. Due to the automatic sub-time

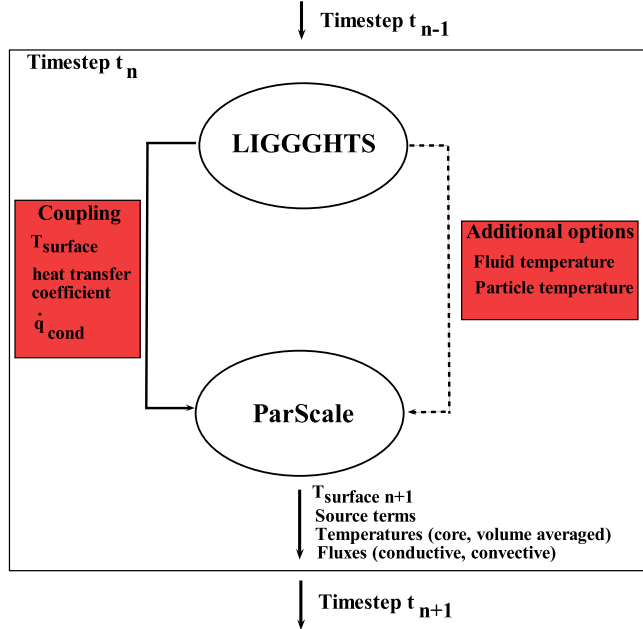


Figure 1: Coupling between LIGGGHTS® and ParScale for one timestep including required coupling parameters and additional coupling options.

stepping of CVODE, the internal ParScale timestep does not necessarily has to correspond to the DEM timestep from LIGGGHTS®. After ParScale completed its calculation of the surface temperatures of all particles, these temperatures are updated and taken into account by LIGGGHTS® at timestep t_{n+1} when computing conductive fluxes. Furthermore, source terms due to reactions, the core and the volume-averaged temperature and surface fluxes handed over to LIGGGHTS®.

Next, two verification cases, i.e., transient cooling of a sphere and a heterogeneous reaction, is presented.

3 Verification cases

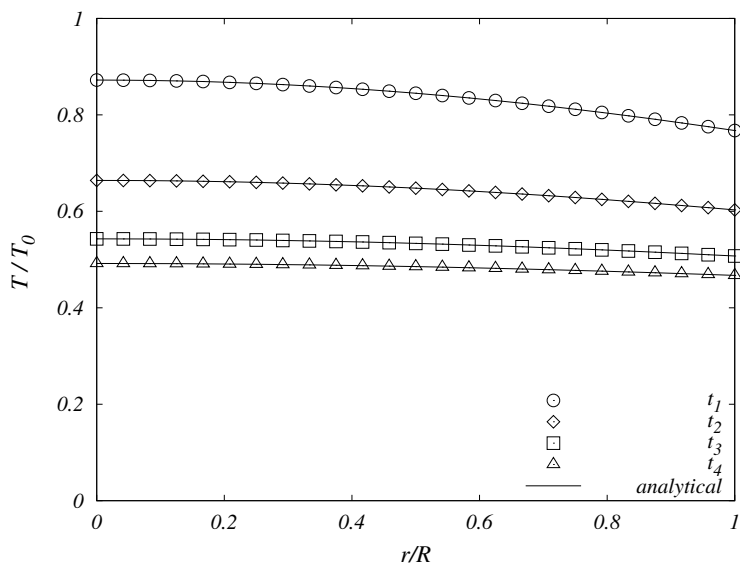
3.1 Cooled sphere

The first verification case considers a classical situation in which a spherical particle (initially having the uniform temperature T_0) is convectively cooled by an ambient fluid with temperature T_{enviro} . Table 1 summarizes the parameters of this case. Figure 2 illustrates the comparison between the numerical solution by ParScale and the analytical solution provided by [7] for a number of time coordinates.

As expected, excellent agreement (i.e., an average error of 10^{-6} , and a maximum error of 10^{-5}) between analytical and numerical solution can be found.

Table 1: Parameters for the verification case 'cooling of a sphere'.

c_p	300	[J m ⁻³ K]
ρ	1000	[kg m ⁻³]
λ_s	1	[W m ⁻¹ K ⁻¹]
α_p	100	[W m ⁻² K ⁻¹]
r_p	$5 \cdot 10^{-3}$	[m]
T_0	800	[K]
T_{enviro}	300	[K]
t_1, t_2, t_3, t_4	2,5,8,10	[sec]

Figure 2: Numerical (symbols) and analytical results (lines) for the temperature distribution in a convectively cooled sphere at $t_1 = 2$ s, $t_2 = 5$ s, $t_3 = 8$ s, and $t_4 = 10$ s.

3.2 Heterogeneous reaction

This verification case considers a single reaction, and follows the analytical solution provided by Wen [8] for a relative reaction speed (characterized by the Thiele Modulus) of ≈ 3.16 . All parameters are chosen following the copper oxidation case considered in Noorman et al. [6]. The three basic assumptions are (i) an isothermal particle, (ii) a reaction rate that is first-order with respect to the gas-phase species, (iii) and a reaction of: $2CO + O_2 \rightarrow 2CuO$. Figure 3 shows a comparison of the solid and fluid concentration inside the particle for two characteristic times.

Figure 3 (a) shows an excellent agreement for the early stage of the reaction. The small, but noticeable, differences in the later stage (see Figure 3 (b)) are due to the pseudo-steady state assumption that needs to be adopted when deriving the analytical solution provided

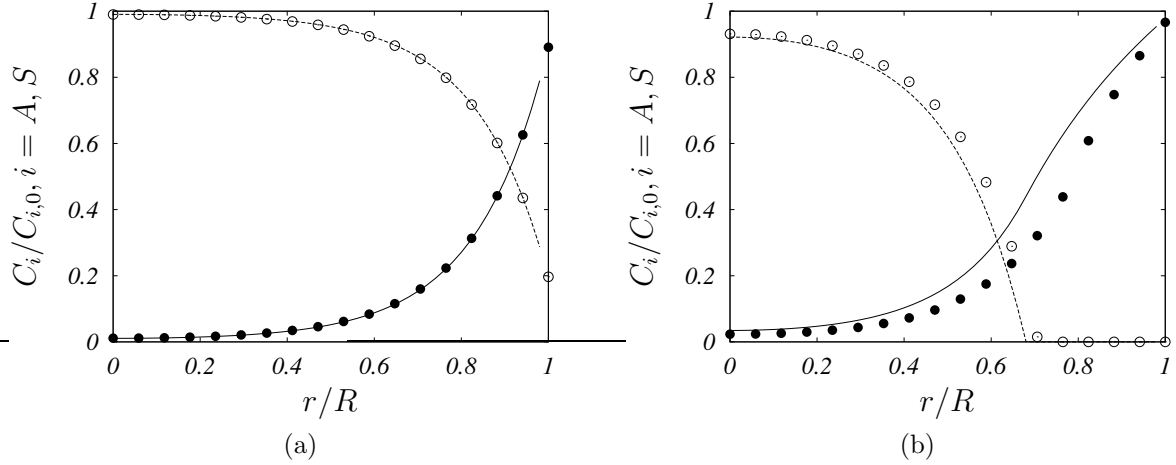


Figure 3: Solid and gas-phase concentration profiles inside a porous copper particle for the early stage (a) and the late stage (b) of a heterogeneous reaction (lines: analytical solution, symbols: predictions by **ParScale**).

by Wen [8]. Figure 4 shows the overall conversion, again indicating only minor differences that can be explained by the shortcomings of the analytical solution. The comparison of the analytical and numerical solution shows good agreement, and the mean difference is below 2 %. We note here that previous work [6] came to a similar conclusion.

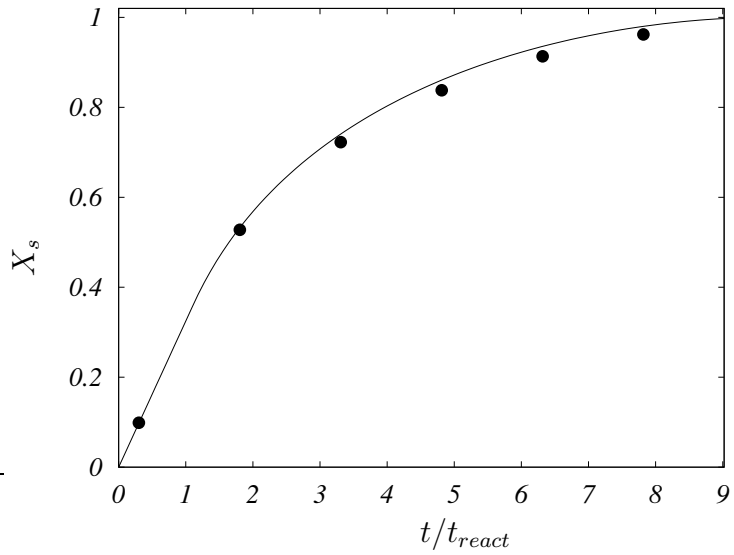


Figure 4: Conversion characteristics during a typical oxidation cycle of a porous copper particle (line: analytical solution, dots: prediction by **ParScale**).

4 Simple shear flow

We now investigate the influence of **ParScale** under well-controlled flow conditions. Therefore, particles are placed in a cubic periodic box ($H/d_p = 15$) at various particle volume fractions $\phi_p = (0.3 - 0.64)$. LeesEdwards boundary conditions are applied to drive a homogeneous shear flow, which is typically used in studies of granular rheology [9]. In the current contribution, the shear gradient is pointing in the y -direction, and we analyze all quantities of interest (e.g., the conductive flux) only in this direction. Along with the shear gradient, a temperature gradient is applied. We determine the Biot (Eqn. 8) and the Peclet (Eqn. 9) number as the two main non-dimensional influence parameters as already mentioned by [10]. With the usage of **ParScale** at low Biot numbers, we expect that our results agree with previous work [10]. However, for higher Biot numbers the transferred flux to the ambient fluid is much larger than that sustained by conduction inside the particle. Consequently, the influence on the heat transfer rate on the particles' shell temperature, and hence the conductive flux becomes important. Therefore, we expect that intra particle temperature profiles should be considered above some critical Biot number Bi_{crit} .

$$Bi_t = \frac{\alpha d_p}{\lambda_p} \quad (8)$$

where α is the heat transfer coefficient that characterized the rate of cooling by the ambient fluid.

$$Pe = \frac{(d_p/2)^2}{\lambda_p / \rho_c c_p} \cdot \dot{\gamma} \quad (9)$$

where $\dot{\gamma}$ is the shear rate. The conductive reference flux is expressed as [9]

$$\dot{q}_{cond,ref} = -\lambda_p (\partial_y T)_{middle}. \quad (10)$$

where $\dot{q}_{cond,ref}$ is the reference conductive heat flux and y_{middle} is the length of the region over which the temperature gradient is applied. Table 2 shows the main non-dimensional parameters of the sheared bed simulation. All other parameters, e.g., the particle stiffness, the coefficient of restitution and time step are in agreement with our earlier simulations [10].

Table 2: Dimensionless properties of the sheared bed particle case.

ϕ_p	0.3...0.64
Bi_t	$10^{-6}...10$
Pe	0.25

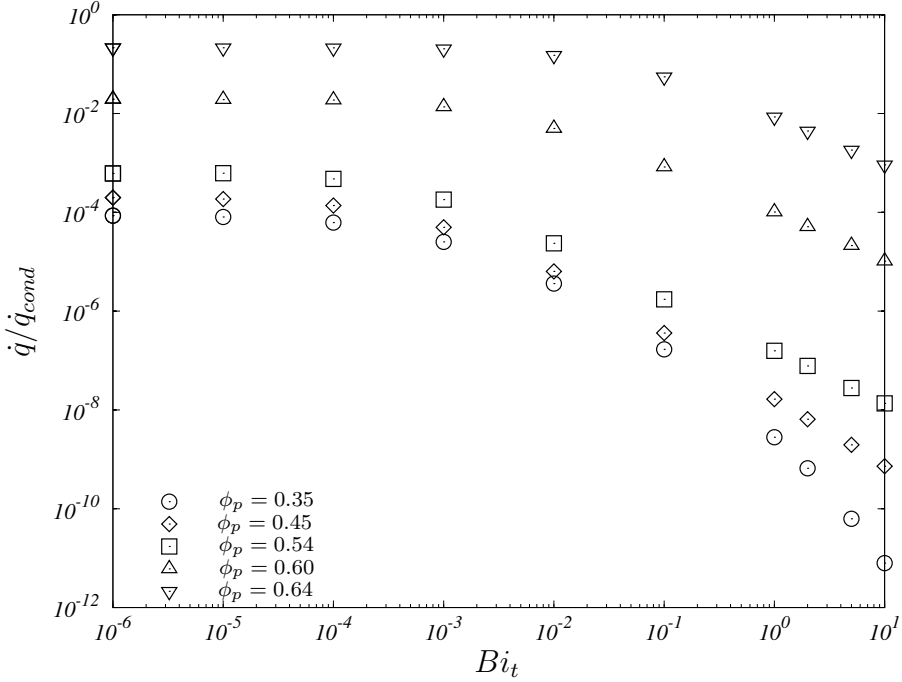


Figure 5: Effect of the Biot number on the conductive heat flux in the gradient direction for various particle volume fractions.

It can be seen in Figure 5 that the influence of the Biot number on the overall conductive flux needs to be considered above a certain value for the Biot number, which depends on ϕ_p . Even at low Biot number regimes (i.e., $Bi_t \approx 10^{-3}$) the conductive flux is underpredicted by up to 10 %. For the highest particle volume fractions considered, for which conductive fluxes are most relevant since they are comparable to the particle-convective flux, the critical Biot number is $Bi_{crit} \approx 10^{-2}$. Above this Biot number intra particle profiles should be taken into account for the moderately fast sheared particle bed that we considered. It is also shown that the influence of the Biot number on the conductive heat flux is becoming more important in case the particle volume fraction is decreasing. Thus, the slope of the curve indicating the relationship between Bi and q_{cond} is becoming larger with decreasing ϕ_p for the high Bi regime. However, in the rather dilute flow at which these extreme dependency is observed, the conductive flux is negligibly small compared to the particle-convective flux.

5 Conclusions

We presented a novel open-source simulation tool **ParScale** which is published under LGPL licence and can be linked to any particle-based solver. We outlined the coupling to the open-source DEM solver **LIGGGHTS®** and demonstrated the usage of **ParScale** with selected verification cases. A good agreement is found between numerical results produced

by **ParScale** and analytical solutions available in literature. We extended the analysis of the well-known sheared particle bed by taking intra-particle temperature gradients into account. A key result is that even at comparably low Biot numbers the intra-particle property profiles have a substantial influence on the conductive flux. The physical reason is that the particle surface temperature is lower than the particle-average temperature in case cooling by the ambient fluid is taken into account. This leads to smaller surface temperature differences in the event of a particle-particle collisions. Thus, the transferred heat flux to the environment should be considered when predicting the particle-particle conductive fluxes. This is especially true for high particle concentrations and fast cooling conditions, since the conductive flux for low particle concentrations is anyhow very low. The current study was limited to selected particle volume fractions and Peclet numbers. Future work will consider wider ranges of these parameters.

6 Acknowledgement

The authors acknowledge support by the European Commission through FP7 Grant agreement no. 604656 (NanoSim). T.F. and S.R. acknowledge support from "NAWI Graz" by providing access to dcluster.tugraz.at. LIGGGHTS® is a registered trademark of DCS Computing GmbH.

References

- [1] C. L. Wu, O. Ayeni, a. S. Berrouk, and K. Nandakumar. Parallel algorithms for CFD-DEM modeling of dense particulate flows. *Chemical Engineering Science*, 118:221–244, 2014.
- [2] C. Kloss, C. Goniva, A. Hager, S. Amberger, and S. Pirker. Models , algorithms and validation for opensource DEM and CFD-DEM. *Progress in Computational Fluid Dynamics*, 12:140–152, 2012.
- [3] A. G. Dixon, M. Ertan T., E. Hugh S., and M. Nijemeisland. 3D CFD simulations of steam reforming with resolved intraparticle reaction and gradients. *Chemical Engineering Science*, 62:4963–4966, 2007.
- [4] <https://github.com/CFDEMproject/ParScale-PUBLIC>, 2015.
- [5] S. D. Cohen, A. C. Hindmarsh, and P. F. Dubois. CVODE, A Stiff/Nonstiff ODE Solver in C. *Computers in Physics*, 10:138–148, 1996.
- [6] S. Noorman, F. Gallucci, M. V. S. Annaland, and J. a M Kuipers. A theoretical investigation of CLC in packed beds. Part 1: Particle model. *Chemical Engineering Journal*, 167:297–307, 2011.
- [7] J. Crank. *The Mathematics of Diffusion*. Clarendon Press, Oxford, 2nd edition, 1975.
- [8] C. Y. Wen. Noncatalytic Heterogeneous Solid Fluid Reaction Models. *Industrial and Engineering Chemistry Research*, 60:34–54, 1968.
- [9] S. Chialvo, J. Sun, and S. Sundaresan. Bridging the rheology of granular flows in three regimes. *Physical Review E.*, 85:021305–1 – 021305–8, 2012.
- [10] B. Mohan, C. Kloss, J. Khinast, and S. Radl. Regimes of Liquid Transport through Sheared Beds of Inertial Smooth Particles. *Powder Technology*, 264:377–395, 2014.

HYDRO-MECHANICAL CONTINUUM MODELLING OF AN EXPERIMENTAL SLOPE WITH A MATERIAL STABILITY CRITERION

EVANTHIA KAKOGIANNOU¹, MARCO LORA¹ AND LORENZO SANAVIA¹

¹Department of Civil, Architectural and Environmental Engineering (DICEA)
University of Padua (UNIPD)

Via F. Marzolo 9, 35131 Padua, Italy

evanthia.kakogiannou@unipd.it, marco.lora@dicea.unipd.it, lorenzo.sanavia@unipd.it
web page: <http://www.dicea.unipd.it>

Key words: Landslides, Infiltration process, Multiphysics problems, Variably saturated porous media, Second order work criterion.

Abstract. In the case of hydrologically driven slope instability, the behaviour of the variably saturated soil is closely related not only to the distribution of pore-water pressure, but also to the stress state during rainfall infiltration. This phenomenon involves both mechanical and hydrological processes. The aim of the scientific community focuses on the development of powerful models capable of a reliable prediction of the landslide initiation. Multiphysics numerical modelling approaches can account for these complex processes including increased saturation, fluid flow and inelastic solid deformation. To this end, a physics based framework is presented in this work for the continuum modelling of an experimental slope subjected to rainfall infiltration. The failure mechanism is assessed, also by the use of the second order work criterion. The rainfall induced deformation is quantified and the evolution of the pore water pressure is compared with the in situ measurements.

1 INTRODUCTION

Hydrologically-driven slope instability represents a major threat to human life and property. Due to the usual large extension of rainfall events this type of slope failure can be triggered over large areas and generally involves shallow soil deposit of different grading and origin [1]. Considering the destructiveness of these landslides, the understanding and the hydro-mechanical modelling of the mechanisms occurring inside the source areas are a fundamental issue for the mitigation of the posed risk to life and facilities.

The most common approach for the numerical modelling of rainfall induced slope failure in engineering practice is to uncouple the fluid flow and slope stability problems and treat them in a sequential fashion. In this sense, a seepage analysis (assuming a rigid solid skeleton) is performed first for the calculation of the water pressure distribution, which is then followed by a limit equilibrium analysis for the slope stability problem.

However, the behaviour of a soil slope under rainfall conditions is closely related not only to the distribution of pore-water pressure but also to the stress state during infiltration. More realistic solutions to the coupled governing equations for deformation and seepage should be obtained when the soil of the slope are considered as deformable and in variably saturated

conditions. For this reason, in this work, the modelling of rainfall induced landslides is considered as a coupled variably saturated hydro-mechanical problem. In order to examine this argument, a hydro-mechanical analysis of a large scale slope stability experimental test, subjected to rainfall infiltration, is presented in this paper; for the numerical simulation the geometrically linear finite element code Comes-Geo [2], [3] for non-isothermal elasto-plastic multiphase solid porous materials as developed by [4], [5], [6] is used.

Furthermore, a recently proposed criterion for instability, the second order work criterion, based on Hill's sufficient condition of stability [7] is implemented on the abovementioned code. It is based on studying the sign of the second order work at the material point level and it is used in this analysis for the detection of the onset of the failure.

In the following, the mathematical model for non-isothermal multiphase porous materials is summarised first. Then the definition of the second order work criterion is reviewed. Finally the results of the hydro-mechanical analysis are presented and discussed.

2 MATHEMATICAL MODEL

The mathematical model necessary to simulate the thermo-hydro-mechanical transient behaviour of fully and partially saturated porous media is developed in [4] following the works by [2] and [8] and using averaging theories by [9], [10]. For sake of brevity, only a summary of the underlying physical model is presented here. For the complete description of the model from its mathematical formulation to the numerical implementation, the reader can refer to the abovementioned works of the authors.

The geomaterial is considered as a variably saturated porous medium and is treated as a multiphase system composed of a solid skeleton (s) with open pores filled with liquid water (w) and gas (g). All constituents are assumed to be immiscible and chemically non-reacting, except for the gas which is assumed to behave as an ideal mixture of dry air (non-condensable gas, ga) and water vapour (condensable one, gw). In the model, heat conduction, vapour diffusion, heat convection, water flow due to pressure gradients or capillary effects and water phase change (evaporation and condensation) inside the pores are taken into account. All fluids are in contact with the solid phase and the solid is deformable resulting in coupling of the fluid, the solid and the thermal effects.

The final model consists of four balance equations: mass balance of the dry air, mass balance of the water species (both liquid and vapour, phase change is taken into account), enthalpy of the whole medium (latent heat of the phase change is considered) and the equilibrium equations of the multiphase medium. They are completed with an appropriate set of constitutive and state equations, as well as some thermo-dynamic relationships.

The governing equations of the model, are expressed in terms of the chosen state variables: gas pressure p^g , capillary pressure $p^c = p^g - p^w$ (p^w is the water pressure), temperature T and the displacement vector of the solid matrix \mathbf{u} .

2.1 Macroscopic Balance Equations

The macroscopic equations of the model are now summarized [3], [4]. These equations are obtained introducing the following assumptions in the model:

- at the micro-level the porous medium is assumed to be constituted of incompressible solid and water constituents, while gas is considered compressible

- the process is considered as quasi-static and is developed in the geometrically linear framework.

The equilibrium equations of the mixture in terms of generalized Cauchy effective stress $\sigma'(\mathbf{x}, t)$, assume the form:

$$\operatorname{div}(\sigma' - [p^g - S^w p^c] \mathbf{1}) + \rho \mathbf{g} = 0 \quad (1)$$

where $\rho(\mathbf{x}, t)$ is the density of the mixture, $\rho = [1-n] \rho^s + n S_w \rho^w + n S_g \rho^g$ with $n(\mathbf{x}, t)$ the porosity, $S_w(\mathbf{x}, t)$ and $S_g(\mathbf{x}, t)$ the liquid water and gas degree of saturation, respectively and $\mathbf{1}$ is the second order identity tensor.

The mass balance equation for the solid phase, the liquid water and the water vapour is:

$$\begin{aligned} & n \left[\rho^w - \rho^{gw} \right] \left[\frac{\partial S_w}{\partial t} \right] + \left[\rho^w S_w - \rho^{gw} [1 - S_w] \right] \operatorname{div} \left(\frac{\partial \mathbf{u}}{\partial t} \right) \\ & + [1 - S_w] n \frac{\partial \rho^{gw}}{\partial t} - \operatorname{div} \left(\rho^g \frac{M_a M_w}{M_g^2} \mathbf{D}_g^{gw} \operatorname{grad} \left(\frac{\partial p^{gw}}{\partial p^g} \right) \right) \\ & + \operatorname{div} \left(\rho^w \frac{\mathbf{k} k^{rw}}{\mu^w} \left[-\operatorname{grad}(p^g) + \operatorname{grad}(p^c) + \rho^w \mathbf{g} \right] \right) \\ & + \operatorname{div} \left(\rho^{gw} \frac{\mathbf{k} k^{rg}}{\mu^g} \left[-\operatorname{grad}(p^g) + \rho^w \mathbf{g} \right] \right) - \beta_{swg} \frac{\partial T}{\partial t} = 0 \end{aligned} \quad (2)$$

where $\rho^{gw}(\mathbf{x}, t)$ is the microscopic mass density of the water vapour, $\mathbf{k}(\mathbf{x}, t) = \mathbf{K}_w \mu^w / (\rho^w g)$ is the intrinsic permeability tensor of the porous matrix in saturated condition [m^2], with $\mathbf{K}_w(\mathbf{x}, t)$ the hydraulic conductivity tensor [m/s] and \mathbf{g} the gravity acceleration value. $k^{rw}(\mathbf{x}, t)$ is the water relative permeability parameter and $\mu^w(\mathbf{x}, t)$, the dynamic viscosity of liquid water, function of the temperature, $T(\mathbf{x}, t)$. Similarly, $k^{rg}(\mathbf{x}, t)$ is the gas relative permeability parameter and $\mu^g(\mathbf{x}, t)$ the dynamic viscosity of gas; $\beta_{swg}(\mathbf{x}, t)$ is the cubic thermal expansion coefficient; $\mathbf{D}_g^{gw}(\mathbf{x})$ is the effective diffusivity tensor of water vapour (the diffusing phase) in the gas phase (the phase in which diffusion takes place) contained in the pore space, function of the tortuosity factor, and M_a , M_w and $M_g(\mathbf{x}, t)$ the molar mass of dry air, liquid water and gas mixture, respectively. In order to account for the diffusive – dispersive flux of the vapour in the gas phase Fick's law is used, while advective flows are modelled with Darcy's law.

The mass balance equation for dry air is:

$$\begin{aligned}
 & n\rho^{g\alpha} \left[\frac{\partial S_w}{\partial t} \right] + \rho^{g\alpha} [1 - S_w] \operatorname{div} \left(\frac{\partial \mathbf{u}}{\partial t} \right) + nS_g \frac{\partial \rho^{g\alpha}}{\partial t} - \operatorname{div} \left(\rho^g \frac{M_\alpha M_w}{M_g^2} \mathbf{D}_g^{g\alpha} \operatorname{grad} \left(\frac{\partial p^{g\alpha}}{\partial p^g} \right) \right) \\
 & + \operatorname{div} \left(\rho^{g\alpha} \frac{\mathbf{k}k^{rw}}{\mu^g} [-\operatorname{grad}(p^g) + \rho^g \mathbf{g}] \right) - \beta_{swg} \rho^{g\alpha} [1 - n] [1 - S_w] \frac{\partial T}{\partial t} = 0
 \end{aligned} \tag{3}$$

where, similarly, $\rho^{ga}(\mathbf{x}, t)$ is the microscopic mass density of the dry air, $\mathbf{D}_g^{ga}(\mathbf{x})$ is the effective diffusivity tensor of dry air in the gas phase contained in the pore space. Equations (2), (3) include the mass balance equation for the solid phase:

$$\frac{\partial n}{\partial t} = [1 - n] \operatorname{div} \left(\frac{\partial \mathbf{u}}{\partial t} \right) - [1 - n] \beta_s \frac{\partial T}{\partial t} \tag{4}$$

The enthalpy balance equation of the mixture is:

$$\begin{aligned}
 & (\rho C_p)_{eff} \frac{\partial T}{\partial t} + \rho^w C_p^w \left(\frac{\mathbf{k}k^{rw}}{\mu^w} [-\operatorname{grad}(p^g) + \operatorname{grad}(p^c) + \rho^w \mathbf{g}] \right) \cdot \operatorname{grad}(T) \\
 & + \rho^g C_p^g \left(\frac{\mathbf{k}k^{rg}}{\mu^g} [-\operatorname{grad}(p^g) + \rho^g \mathbf{g}] \right) \cdot \operatorname{grad}(T) - \operatorname{div} (\chi_{eff} \operatorname{grad}(T)) = -m_{vap} \Delta H_{vap}
 \end{aligned} \tag{5}$$

where, $(\rho C_p)_{eff}$ is the effective thermal capacity of the porous medium, $\rho^w C_p^w$ and $\rho^g C_p^g$ are the specific heat of the water and gas mixture respectively, χ_{eff} the effective thermal conductivity of the porous medium and the right hand side term considers the contribution of the evaporation and condensation. This balance equation takes into account the heat transfer through conduction and convection as well as latent heat transfer and neglects the terms related to the mechanical work induced by density variations due to temperature changes of the phases and induced by volume fraction changes [2].

2.2 Constitutive relations

The mechanical behaviour of the soil skeleton is described within the elasto-plastic constitutive framework. For the simulations analyzed in this report, the Drucker-Prager yield surface with isotropic linear hardening behaviour and non-associated plastic flow [4] is used for simplicity:

$$F(p', \mathbf{s}', \xi) = 3\alpha_F p' + \|\mathbf{s}'\| - \beta_F \sqrt{\frac{2}{3}} [c_0 + h\xi] \tag{6}$$

in which $p' = \frac{1}{3} [\boldsymbol{\sigma}' : \mathbf{1}]$ is the mean effective Cauchy stress tensor, $\|\mathbf{s}'\|$ is the norm of the deviator effective Cauchy stress tensor $\boldsymbol{\sigma}'$, c_0 is the apparent cohesion, α_F and β_F are two material parameters related to the friction angle ϕ of the soil

$$\alpha_F = 2 \frac{\sqrt{2}}{3 - \sin \varphi} \quad \beta_F = 2 \frac{6 \cos \varphi}{3 - \sin \varphi} \quad (7)$$

and h and ξ the hardening/softening modulus and the equivalent plastic strain variable, respectively.

For the gaseous mixture which is assumed to be a perfect mixture of two ideal gases (dry air and water vapour) the ideal gas law is introduced. The equation of state of perfect gas (the Clapeyron equation) and Dalton's law are applied to dry air (ga), water vapour (gw) and moist air (g). In the partially saturated zones, the water vapour pressure $p^{gw}(\mathbf{x}, t)$ is obtained from the Kelvin-Laplace equation. The saturation $S_x(\mathbf{x}, t)$ and the relative permeability $k^{rx}(\mathbf{x}, t)$ are experimentally determined functions of the capillary pressure and the temperature.

4 FINITE ELEMENT FORMULATION

The governing equations of the problem are discretized in space by means of the finite element method. Their discretized form is obtained by means of the Bubnov-Galerkin method for the discretization in space. The time discretization is accomplished through a fully implicit finite difference scheme. Because of the non-linearity of the system of equations the solution is obtained with a Newton-Raphson type procedure. Details concerning the matrices and the residuum vector of the linearized equations system of the finite element model can be found in [4].

5 SECOND ORDER WORK MATERIAL INSTABILITY CRITERION

Although the notion of failure in soils (or more generally geomaterials) was long described as a perfect plastic limit, it has been observed in practice that failure can occur well before the Mohr-Coulomb criterion is met. This is due to the non-associated behaviour (the yield surface does not coincide with the plastic potential) of frictional materials, such as soils. According to [11], [12] in case of such materials, one can find an unstable domain strictly inside the plastic limit envelope. What is more, material instabilities can lead to diffuse modes of failure inside the plastic limit condition, which are characterized by the lack of localization patterns and for this reason cannot be detected neither by a plastic limit criterion nor by a localization criterion [13], [14]. A characteristic example of this kind of failure can be illustrated through an undrained test on loose sand. If a small additional force is applied at the stress peak value, a sudden failure occurs with no localisation pattern strictly inside the Mohr-Coulomb plastic limit condition.

Hill's sufficient condition of stability [7], which is based on the sign of second-order work, seems to be a pertinent stability criterion to detect these diffuse modes of failure [15], according to which a mechanical stress-strain state is considered as stable if, for any couple $(d\boldsymbol{\sigma}, d\boldsymbol{\varepsilon})$ linked by the rate-dependent constitutive relation (stiffness tensor: \boldsymbol{M}) the second order work W_2 is strictly positive:

$$\forall (d\boldsymbol{\sigma}, d\boldsymbol{\varepsilon}) \in \mathbb{R}^{2n} \setminus \{0\} \text{ with } d\boldsymbol{\varepsilon} = \boldsymbol{M} : d\boldsymbol{\sigma}, W_2 = d\boldsymbol{\sigma} : d\boldsymbol{\varepsilon} > 0 \quad (8)$$

where n is the dimension of the stress space. Otherwise, if the scalar product is zero or negative then the material point is found on a potentially unstable state.

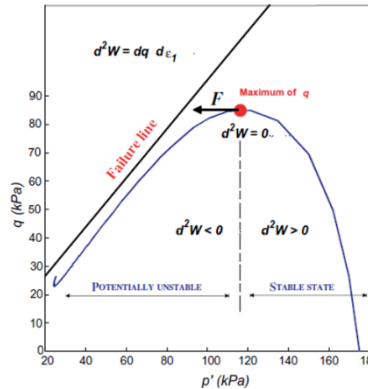


Figure 1: Typical triaxial behaviour of a loose sand [13].

As illustrated in Figure 1, the transition from the stable to the unstable regime can be detected by the sign of the second order work criterion.

6 NUMERICAL SIMULATION OF AN UNSATURATED SOIL SLOPE SUBJECTED TO RAINFALL INFILTRATION

6.1 Description of the experiment and the numerical modelisation

The experiment which was carried out in the University of Padua [16],[17],[18] reproduces a stability problem of a large-scale slope due to rain infiltration.

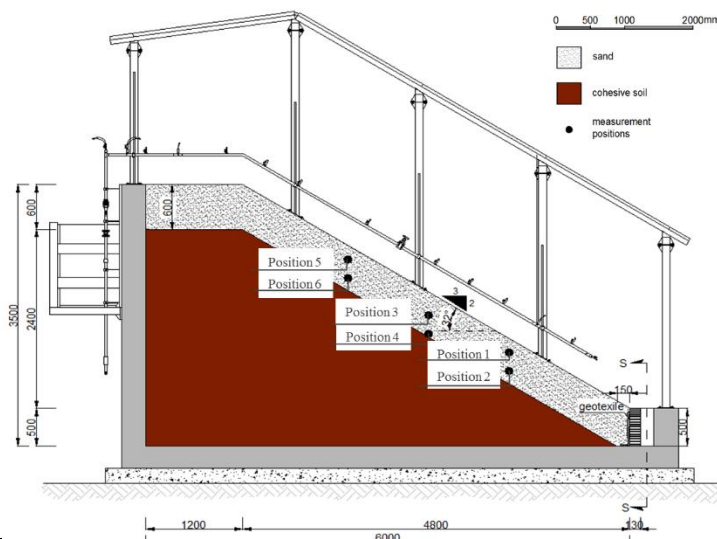


Figure 2: Geometry and stratigraphy of the slope (longitudinal section) and representation of the measurement positions [16], [17].

To this end, a steady rainfall intensity equal to 150mm/h is applied until the mobilization of the soil. The slope consists of two soil layers: a shallow permeable layer of loose sand

overlying a dense clayey soil substratum. The height varies linearly from 3.5m to 0.5m, such that a sloping angle of 32° can be assigned to the soil. The dimensions of the model and the stratigraphy are presented in Figure 2. The values of the mechanical and hydraulic properties of the each material layer, which were used in the computation, are presented on Table 1.

Table 1: Soil parameters used in the computation

Definition	Label	Loose Sand	Clay
Density	ρ^s [kg/m ³]	2718	2680
Friction angle	ϕ [°]	34.0	22.0
Cohesion	c [Pa]	1.0E+03	1.0E+04
Initial Young modulus	E [Pa]	2.5E+06	1.0E+07
Poisson's ratio	ν [-]	0.3	0.3
Angle of dilatancy	ψ [°]	0	4
Hardening modulus	h [Pa]	4.8E+03	0.0
Intrinsic Permeability	k [m ²]	2.091E-11	2.98E-13
Initial porosity	n [-]	0.569	0.384

The estimates of the retention functions for the loose sand layer were inferred by fitting the retention tests data as well as by an inverse modelling, applied to the measurements data which were obtained from the landslide test. The curves (the continuous and dashed black lines in Figure 3) were obtained in accordance to the Brooks and Corey [19] and van Genuchten [20] models.

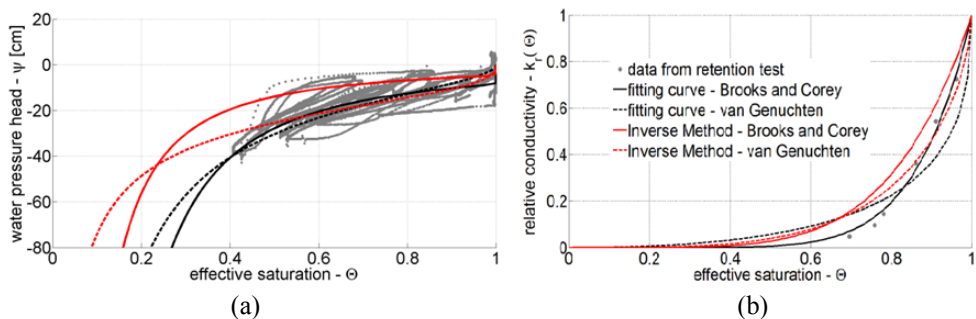


Figure 3: Retention curves of the loose sand layer: (a) the relation of the effective saturation with the pressure head; (b) the relation of the relative conductivity with the effective saturation [16], [17].

The Brooks and Corey [19] model appeared to approach better the field data especially in terms of water pressure head and therefore it was the expression that was implemented on the numerical code:

$$\Theta = \left(\frac{h}{h_b} \right)^{-\lambda} \quad \text{and} \quad K(\Theta) = K_s \cdot \Theta^{\frac{2}{\lambda} + l + 2} \quad \text{if } h < h_b \quad (9)$$

where $\Theta = \frac{\theta - \theta_r}{\theta_s - \theta_r}$ is the effective saturation, with θ_r and θ_s the residual and the saturated volumetric water content respectively; h is the water pressure head and h_b the bubbling pressure; $K(\Theta)$ and K_s are the hydraulic conductivity in partially saturated conditions, respectively; λ and l are shape parameters.

Regarding the clayey layer, the only measured hydraulic parameter was the hydraulic conductivity in saturated conditions. Other unknown parameters concerning the retention curves are assigned from the literature [21].

In Figure 4 the mesh which has been created, is presented along with the initial and boundary conditions applied to the slope. The finite element mesh is composed of 468 eight-noded quadratic quadrilateral elements. Vertical and horizontal displacements are constrained at the bottom and horizontal displacements at the lateral surfaces. Initially, the stress state is computed in equilibrium with the gravity load and the initial hydro-thermal conditions (Figure 4). The stress state and the state variables calculated by this first analysis form the initial conditions for the successive run. Subsequently, rainfall infiltration is simulated by means of an imposed boundary flux of 150mm/hr along the upper surface (the rain input has the real value as this that was applied during the experiment). When the toe of the slope saturates, an outflow is distributed along its vertical side, with a value equal to the one that was measured in situ at the moment of the failure, as a first approximation.

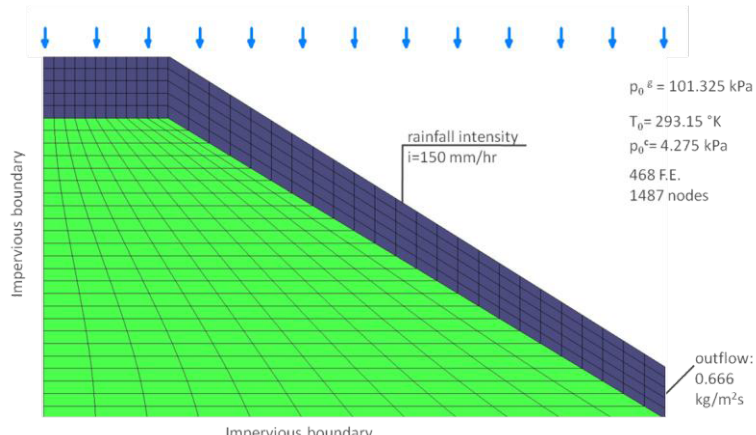


Figure 4: Description of the discretization of the slope, initial and boundary conditions.

6.2 Results and discussion

After 1.8 hr of the applied rainfall, the numerical solution became unstable and the numerical convergence was lost. This was also the actual time failure of the field experiment. Figure 5 illustrates the contours of degree of saturation nearly at the beginning of the simulation and after 1.8hr, when the convergence of the norm of displacements cannot be achieved any further. In more detail, in figure 5a can be observed the procedure of rainfall infiltration: a wetting front percolating vertically downwards, across the sand layer. The wetting front does not saturate the sand in this case as the infiltration capacity is not exceeded by the rainfall intensity. While in figure 5b it can be observed that there has been formed a

water table in the fill material (loose sand layer). Once the water front reached the interface between the two layers, a thin seepage layer was formed which started increasing upwards and more precisely from the toe towards the top due to the rainfall integration along the slope.

Only a small fraction was absorbed by the clay layer due to the large difference in the permeability values between the two layers: in fact the cohesive soil represents an unsaturated permeability barrier.

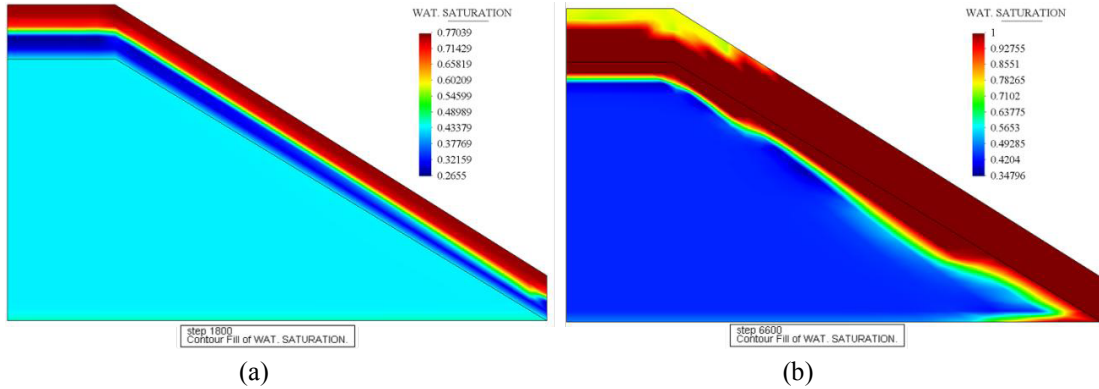


Figure 5: Evolution of the wetting front (a) and the water table (b), during the rainfall infiltration.

The hydraulic response of the model is also depicted in Figure 6, through the volumetric water content time evolution at two different positions of the slope; at position 5 (TDR5) near the top of the sand layer and at position 6 (TDR6) near the interface between the two layers. The comparison is shown between the in-situ measurements and the prediction of the model. A two step evolution is noted: the water content increases from 0.18 to approximately 0.45 and subsequently it increases up again to 0.578. The first rise involves the probes from the top to the bottom while the second one progresses from the bottom to the top. As it can be observed the computed volumetric contents are in a good agreement with the field measurements.

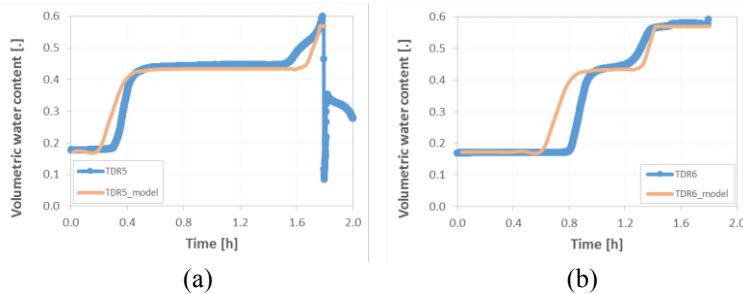


Figure 6: Comparison between computed and in-situ measured volumetric water content at the positions 5 and 6 (TDR5 and TDR6 respectively).

The maximum displacements are concentrated on the upper surface near the toe, as illustrated in Figure 7. The vectors of the incremental displacements indicate that the sand is under swelling conditions at the end of the analysis because of the water overpressure and the constrained displacements at the toe. The equivalent plastic strain is also concentrated at the toe and coincides with the contours of the second order work (Figure 7c, 7d). The fact that the

maximum displacements contours coincide with the contour of the equivalent plastic strains and the second order work contour, indicates that the onset of the failure is located at the toe.

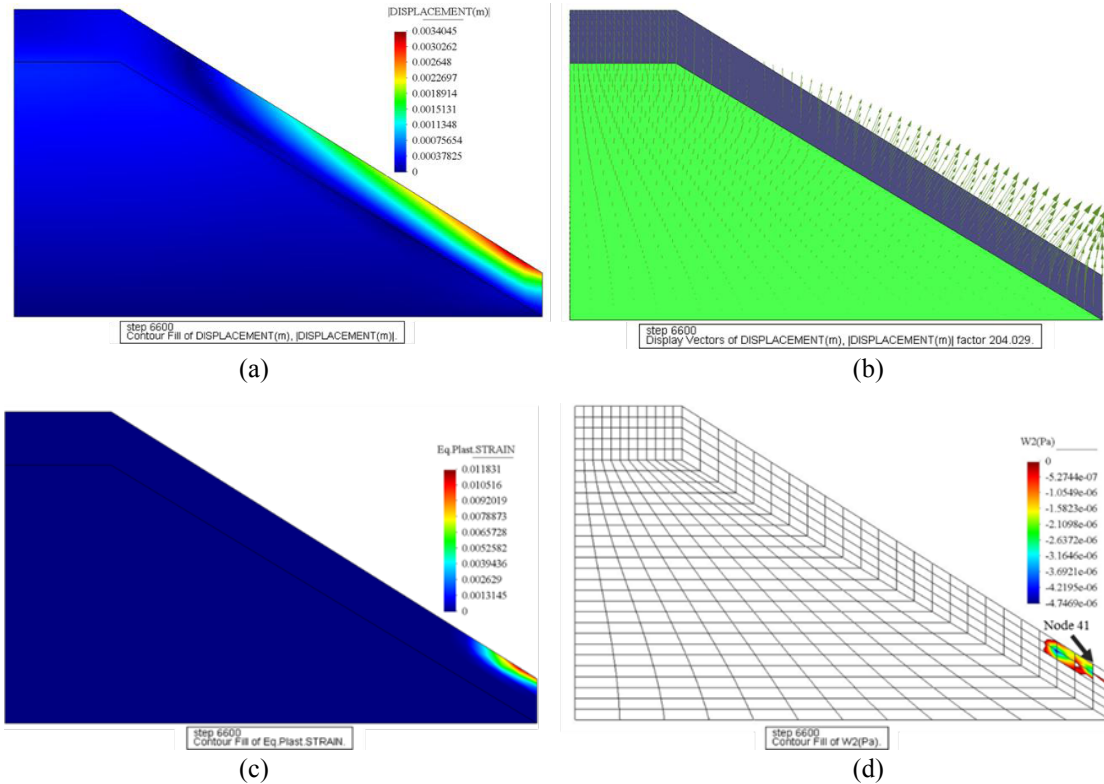


Figure 7: Displacement contours (a) and displacement vectors (b), equivalent plastic strain (c) and second order work contours (d), at the end of the analysis (after 1.8hr of rainfall input).

This is what is actually expected since it is the most sensitive point of the slope: there ends up all the seepage water within the layer and at the same time, it is being received the rainfall infiltration water as a flux input from the upper boundary surface. With increasing water content, the capillary forces acting between the soil particles decrease. This de-bonding effect of wetting is taken into account in the model through Schrefler's effective stress [22]

$\sigma' = \sigma + [p^g - S^w p^c] \mathbf{1}$ which decreases during rain infiltration and as a consequence the soil loses its strength. When the point of significant excess pore water development is reached, there will be little or no effective confining stress acting on the soil. Eventually, the soil state approaches a zone of instability in which the shear strength can decrease significantly. Figure 8a, 8b describes exactly this phenomenon of a probable liquefaction occurrence, as it was captured, indicatively, on node 41 at the toe of the slope. Nearly at 1.5 hr the capillary pressure becomes negative (relative water pressure) and it is at that moment that the mean pressure starts to decrease until the 1.6 hr that becomes zero. At the same time, the deviatoric stress increases considerably and slightly after (1.7 hr) drops abruptly. At the moment of the peak deviatoric stress the equivalent plastic strain begins to develop and it is obtained the first negative value of the second order work at the material point level, as illustrated in Figure 8c.

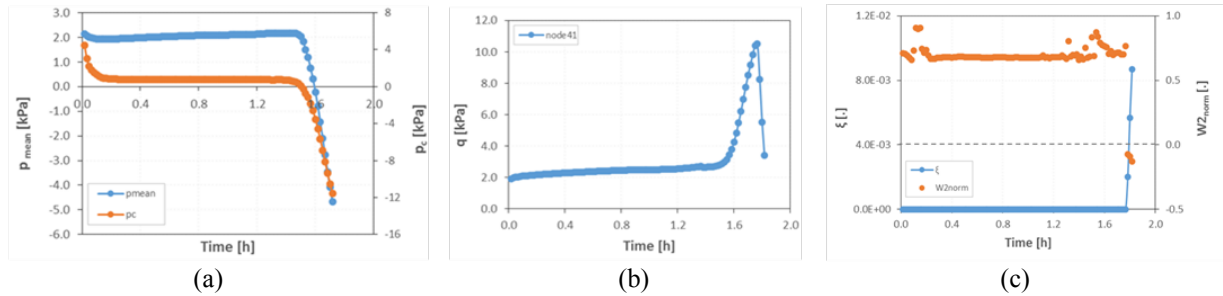


Figure 8: Evolution of: the capillary pressure and the mean stress (a); deviatoric stress (b); equivalent plastic strain and the second order work (c).

7 CONCLUSION

In this work, the modelling of rainfall-induced slope failure is considered as a coupled variably saturated hydro-mechanical problem. Therefore, a multiphase model for elasto-plastic porous media is used for the analysis of a large scale experimental test, in conjunction with a criterion based on the sign of the second-order work for the detection of instability. It is shown that multiphysics modelling of the initiation of flowslides can give results in a good agreement with the in-situ observations and can be a powerful tool for the better understanding of the triggering mechanisms that take place during the progressive failure. In particular, it is shown that the model can predict the field measurements of the volumetric water content and also provide us with the necessary mechanical results which indicate the liquefaction occurrence at the real time of the failure. The results taken from the second order work criterion at the material scale are in consistency with the mechanical response of the slope (results obtained from the equivalent plastic strain, mean and deviatoric stress) encouraging further research on this criterion.

ACKNOWLEDGEMENT

The authors would like to thank the 7th Framework Programme of the European Union (ITN MuMoLaDe project 289911) for the financial support.

REFERENCES

- [1] Cascini, L., Cuomo, S., Pastor, M., Sorbino, G. Modeling of Rainfall-Induced Shallow Landslides of the Flow-Type. *Journal of Geotechnical and Geoenvironmental Engineering*, vol. 136, no. 1, pp. 85-98, 2010.
- [2] Lewis, R. W., Schrefler, B. A. *The Finite Element Method in the Static and Dynamic Deformation and Consolidation of Porous Media*. Second. Chichester, UK: John Wiley & Sons, 1998.
- [3] Gawin, D., Schrefler, B. A. Thermo-hydro-mechanical analysis of partially saturated porous materials. *Engineering Computations*, vol. 13, no. 7, pp. 113-143, 1996.
- [4] Sanavia, L., Pesavento, F., Schrefler, B. A. Finite element analysis of non-isothermal multiphase geomaterials with application to strain localization simulation. *Computational Mechanics*, vol. 37, no. 4, pp. 331-348, May 2006.

- [5] Sanavia, L., François, B., Bortolotto, R., Luison, L., Laloui, L. Finite element modelling of thermo-elasto-plastic water saturated porous materials. *Journal of Theoretical and Applied Mechanics*, vol. 38, no. 1-2, pp. 7-24, 2008.
- [6] Sanavia, L. Numerical modelling of a slope stability test by means of porous media mechanics. *Engineering Computations*, vol. 26, no. 3, pp. 245 - 266, 2008.
- [7] Hill, R. A general theory of uniqueness and stability in elastic-plastic solids. *Journal of the Mechanics and Physics of Solids*, vol. 6, no. 3, pp. 239-249, 1958.
- [8] Schrefler, B. A. Mechanics and thermodynamics of saturated/unsaturated porous materials and quantitative solutions. *Applied Mechanics Reviews*, vol. 55, no. 4, pp. 351-388, 2002.
- [9] Hassanizadeh, M., Gray, W. G. General conservation equations for multi-phase systems: 1. Averaging procedure. *Advances in Water Resources*, vol. 2, no. C, pp. 131-144, 1979.
- [10] Hassanizadeh, M., Gray, W. G. General conservation equations for multi-phase systems: 3. Constitutive theory for porous media flow. *Advances in Water Resources*, vol. 3, no. 1, pp. 25-40, 1980.
- [11] Darve, F. Stability and uniqueness in geomaterials constitutive modelling. *Localisation and bifurcation theory for soils and rocks*. Chambon, Desrues, and Vardoulakis, Eds. Balkema, 1994, pp. 73–88.
- [12] Laouafa, F., Darve, F. Modelling of slope failure by a material instability mechanism. *Computers and Geotechnics*, vol. 29, no. 4, pp. 301-325, 2002.
- [13] Darve, F., Servant, G., F., Laouafa, F., Khoa, H. D. V. Failure in geomaterials: continuous and discrete analyses. *Computer methods in applied mechanics and engineering*, vol. 193, no. 27-29, pp. 3057-3085, 2004.
- [14] Nicot, F., Daouadji, A., Laouafa, F. Second-order work , kinetic energy and diffuse failure in granular materials. *Granular Matter*, vol. 13, no. 1, pp. 19-28, 2011.
- [15] Lignon, S., Laouafa, F., Prunier, F., Khoa, H. D. V., Darve, F. Hydro-mechanical modelling of landslides with a material instability criterion. *Géotechnique*, vol. 59, no. 6, pp. 513-524, 2009.
- [16] Lora, M. *Rainfall-triggered shallow landslides in a large-scale physical model*. Ph.D. Thesis, University of Padua, Padua (Italy), 2015.
- [17] Lora, M., Camporese M., Salandin, P. Rainfall-triggered shallow landslides: infiltration dynamics in a physical hillslope model. *Submitted to Hydrological Processes*.
- [18] Lora, M., Camporese M., Salandin, P. Design and Performance of a Nozzle Rainfall Simulator for Landslide Triggering Experiments. *Submitted to Cattena*.
- [19] Brooks, R. H., Corey, A. T. Hydraulic properties of porous media. *Hydrology Papers*, vol. 3, no. 3, p. 27, 1964.
- [20] Van Genuchten, M. T. A closed-form equation for predicting the hydraulic conductivity of unsaturated soils. *Soil Science Society of America Journal*, vol. 44, no. 5, pp. 892-898, 1980.
- [21] Carsel, R. F., Parrish, R. S. Developing joint probability distributions of soil water retention characteristics. *Water Resources*, vol. 24, pp. 755-769, 1988.
- [22] Schrefler, B. A. *The finite element method in soil consolidation (with applications to surface subsidence)*. Ph.D. Thesis, University College of Swansea, C/Ph/76/84, Swansea (UK), 1984.

MIXED FINITE ELEMENT FORMULATION FOR NON-ISOTHERMAL POROUS MEDIA IN DYNAMICS

T.D. Cao¹, Y. Wang¹, L. Sanavia² and B.A. Schrefler²

¹ Department of Mechanical Engineering, Technische Universität Darmstadt
Otto-Berndt-Strasse 2, 64287 Darmstadt, Germany
E-mail: cao@fdy.tu-darmstadt.de and wang@fdy.tu-darmstadt.de

² Dipartimento di Ingegneria Civile, Edile e Ambientale, Università degli Studi di Padova
via F. Marzolo 9, 35131 Padova, Italia
E-mail: lorenzo.sanavia@unipd.it and bernhard.schrefler@dicea.unipd.it

Key words: Hydro-Thermo-Mechanical processes; FEM; Mixed elements; Multiphase materials

Abstract. We present a mixed finite element formulation for the spatial discretization in dynamic analysis of non-isothermal variably saturated porous media using different order of approximating functions for solid displacements and fluid pressures/temperature. It is known in fact that there are limitations on the approximating functions N_u and N_p for displacements and pressures if the Babuska-Brezzi convergence conditions or their equivalent [1] are to be satisfied. Although this formulation complicates the numerical implementation compared to equal order of interpolation, it provides competitive advantages e.g. in speed of computation, accuracy and convergence.

1 INTRODUCTION

The numerical modelling of the dynamic response of non-isothermal multiphase geomaterials is of great interest in many fields, including Environmental Geomechanics, Structural Mechanics and Biomechanics. Based on the improved efficiency and stability of appropriate numerical methods, and the increased performance of the computational equipments, the efficient numerical treatment of coupled multi-field problems has become possible in the last decades. Effective numerical simulations require a mixed element (e.g. Taylor-Hood element [2]) with different order of approximating functions for solid displacements and fluid pressures/temperature. Consequently, numerical complexities arise in the solutions because the basis functions in the $u-p$ (solid-displacements and pressure) formulation are of different order (e.g. second order for displacements, first order for pressure, to obtain the same kind of approximation for effective stress and fluid pressures). In the use of mixed elements it has been reported by several authors [3, 4, 5, 6] that inaccuracies in pressure estimates can result from spurious spatial fluctuations of estimated

pore pressure between adjacent elements. This is especially likely to occur at permeable boundaries in the initial time-marching steps, or when short time steps are used to represent rapidly changing of fluid phases or transient applied loads. Moreover, Murad et al. [7] noted that, even with Taylor-Hood elements, potentially unstable results may occur when there are discontinuous initial conditions at the initiation of a time-marching solution.

This work presents, as a novel contribution, a mixed finite element formulation for fully coupled non-isothermal multiphase geomaterials in dynamics.

The multiphase model is developed following Lewis and Schrefler [8]. The u - p - T formulation is obtained by neglecting the relative fluids acceleration and their convective terms, which is valid for low frequency problems as in earthquake engineering [9]. In the model development, the dynamic seepage forcing terms in the mass balance equations and in the enthalpy balance equation and the compressibility of the grain at the microscopic level are neglected. The Taylor-Hood approach is applied to discretize the governing equations in space, while the generalized Newmark scheme is used for the time discretization. The final non-linear set of equations is solved by the Newton-Raphson method with a monolithic approach [8, 10]. The model has been implemented in the finite element code COMES-GEO, [8, 11, 12, 13, 14, 15, 16, 17, 18].

The implemented model is validated through the comparison with analytical or finite element quasi-static or dynamic solutions.

2 MACROSCOPIC BALANCE EQUATIONS

The full mathematical model necessary to simulate the thermo-hydro-mechanical behaviour of partially saturated porous media was developed within the Hybrid Mixture Theory by Lewis and Schrefler [8], using averaging theories according to Hassanizadeh and Gray [19, 20]. After neglecting the acceleration of the fluids in the governing equations of Lewis and Schrefler [8], a set of balance equations for the whole multiphase medium is obtained and presented in this paper.

Linear momentum balance equations of the mixture

$$\operatorname{div} \boldsymbol{\sigma} + \rho \mathbf{g} - \rho \mathbf{a}^s = \mathbf{0} \quad (1)$$

Dry air mass balance equation

$$\begin{aligned} & \operatorname{div} \left(\rho^{ga} \frac{k^{rg} \mathbf{k}^g}{\mu^g} [-\operatorname{grad} p^g + \rho^g \mathbf{g}] \right) + \operatorname{div} \left(\rho^g \frac{M_a M_w}{M_g^2} \mathbf{D}_g^{ga} \operatorname{grad} \left(\frac{p^{gw}}{p^g} \right) \right) \\ & + \rho^{ga} S_g \operatorname{div} \mathbf{v}^s + n S_g \dot{\rho}^{ga} - \rho^{ga} n \dot{S}_w - \rho^{ga} \beta_s [1 - n] S_g \dot{T} = 0 \end{aligned} \quad (2)$$

Water species (liquid and vapour) mass balance equation

$$\begin{aligned} & \operatorname{div} \left(\rho^w \frac{k^{rw} \mathbf{k}^w}{\mu^w} [-\operatorname{grad} (p^g - p^c) + \rho^w \mathbf{g}] \right) + \operatorname{div} \left(\rho^{gw} \frac{k^{rg} \mathbf{k}^g}{\mu^g} [-\operatorname{grad} p^{gw} + \rho^{gw} \mathbf{g}] \right) \\ & - \operatorname{div} \left(\rho^g \frac{M_a M_w}{M_g^2} \mathbf{D}_g^{gw} \operatorname{grad} \left(\frac{p^{gw}}{p^g} \right) \right) + [\rho^w S_w + \rho^{gw} S_g] \operatorname{div} \mathbf{v}^s + n [\rho^w - \rho^{gw}] \dot{S}_w \\ & - [\rho^w \beta_{sw} + \rho^{gw} \beta_s [1 - n] S_g] \dot{T} + n S_g \dot{\rho}^{gw} + \rho^w \frac{n S_w}{K_w} [p^g - p^c] = 0 \end{aligned} \quad (3)$$

Enthalpy balance equation for the multiphase medium

$$\begin{aligned}
& -\operatorname{div} \left(\rho^w \frac{k^{rw}\mathbf{k}}{\mu^w} [-\operatorname{grad}(p^g - p^c) + \rho^w \mathbf{g}] \right) \Delta H_{vap} - \operatorname{div} (\chi_{eff} \operatorname{grad} T) - \rho^w S_w \operatorname{div} \mathbf{v}^s \Delta H_{vap} \\
& + \left[C_p^w \rho^w \frac{k^{rw}\mathbf{k}}{\mu^w} [-\operatorname{grad}(p^g - p^c) + \rho^w \mathbf{g}] + C_p^g \rho^g \frac{k^{rg}\mathbf{k}}{\mu^g} [-\operatorname{grad} p^g + \rho^g \mathbf{g}] \right] \cdot \operatorname{grad} T \\
& + (\rho C_p)_{eff} \dot{T} - \rho^w \frac{n S_w}{K_w} [\dot{p}^g - \dot{p}^c] \Delta H_{vap} + \beta_{sw} \dot{T} \Delta H_{vap} - n [\rho^w - \rho^{gw}] \dot{S}_w \Delta H_{vap} = 0
\end{aligned} \tag{4}$$

The meaning of each variable of equations 1 to 4 is described in [8, 11, 15, 12].

3 CONSTITUTIVE RELATIONSHIPS

For the gaseous mixture of dry air and water vapour, the ideal gas law is introduced. The equation of state of perfect gas (Clapeyrons equation) and Dalton's law are applied to dry air (ga), water vapor (gw) and moist air (g). In the partially saturated zones, the equilibrium water vapor pressure $p^{gw}(\mathbf{x}, t)$ can be obtained from the Kelvin-Laplace equation, where the water vapor saturation pressure $p^{gws}(\mathbf{x}, t)$ depending only upon the temperature, can be calculated from the Clausius-Clapeyron equation or from an empirical correlation. The saturation degree $S_\pi(\mathbf{x}, t)$ and the relative permeability $k^{r\pi}(\mathbf{x}, t)$ are experimentally determined functions. The solid skeleton is assumed elastic, homogeneous and isotropic in the numerical simulations described in Section 5.

4 SPATIAL AND TIME DISCRETIZATION

The Petrov-Galerkin method with different interpolation functions for the primary variables and the test functions is applied for the spatial discretization. Isoparametric mixed element (see. Figure 1) is used and the shape functions for each phase are

$$\left\{ \begin{array}{l} p^g = \mathbf{N}_g \bar{\mathbf{p}}^g \\ p^c = \mathbf{N}_c \bar{\mathbf{p}}^c \\ T = \mathbf{N}_T \bar{\mathbf{T}} \\ \mathbf{u} = \mathbf{N}_u \bar{\mathbf{u}} \end{array} \right. \tag{5}$$

After spatial discretization, the following non-symmetric, non-linear and coupled system of equations is obtained

$$\left\{ \begin{array}{l} \mathbf{M}_{uu} \ddot{\mathbf{u}} + \int \mathbf{B}^T \boldsymbol{\sigma}' dV - \mathbf{K}_{ug} \bar{\mathbf{p}}^g + \mathbf{K}_{uc} \bar{\mathbf{p}}^c = \mathbf{f}_u \\ \mathbf{C}_{gg} \dot{\bar{\mathbf{p}}}^g + \mathbf{C}_{gc} \dot{\bar{\mathbf{p}}}^c - \mathbf{C}_{gT} \dot{\bar{\mathbf{T}}} + \mathbf{C}_{gu} \dot{\bar{\mathbf{u}}} + \mathbf{K}_{gg} \bar{\mathbf{p}}^g - \mathbf{K}_{gc} \bar{\mathbf{p}}^c - \mathbf{K}_{gT} \bar{\mathbf{T}} = \mathbf{f}_g \\ \mathbf{C}_{cg} \dot{\bar{\mathbf{p}}}^g + \mathbf{C}_{cc} \dot{\bar{\mathbf{p}}}^c + \mathbf{C}_{cT} \dot{\bar{\mathbf{T}}} + \mathbf{C}_{cu} \dot{\bar{\mathbf{u}}} - \mathbf{K}_{cg} \bar{\mathbf{p}}^g + \mathbf{K}_{cc} \bar{\mathbf{p}}^c + \mathbf{K}_{cT} \bar{\mathbf{T}} = \mathbf{f}_c \\ -\mathbf{C}_{Tg} \dot{\bar{\mathbf{p}}}^g - \mathbf{C}_{Tc} \dot{\bar{\mathbf{p}}}^c + \mathbf{C}_{TT} \dot{\bar{\mathbf{T}}} - \mathbf{C}_{Tu} \dot{\bar{\mathbf{u}}} - \mathbf{K}_{Tg} \bar{\mathbf{p}}^g + \mathbf{K}_{Tc} \bar{\mathbf{p}}^c + \mathbf{K}_{TT} \bar{\mathbf{T}} = \mathbf{f}_T \end{array} \right. \tag{6}$$

The generalized Newmark method is applied to discretize in time the non-linear system equations 6 and the dynamic response at step $n+1$ for the general non-linear system is obtained, in which the unknowns are $\mathbf{X}_{n+1} = [\Delta \ddot{\mathbf{u}}, \Delta \dot{\bar{\mathbf{p}}}^g, \Delta \dot{\bar{\mathbf{p}}}^c, \Delta \dot{\bar{\mathbf{T}}}]$. The non-linear

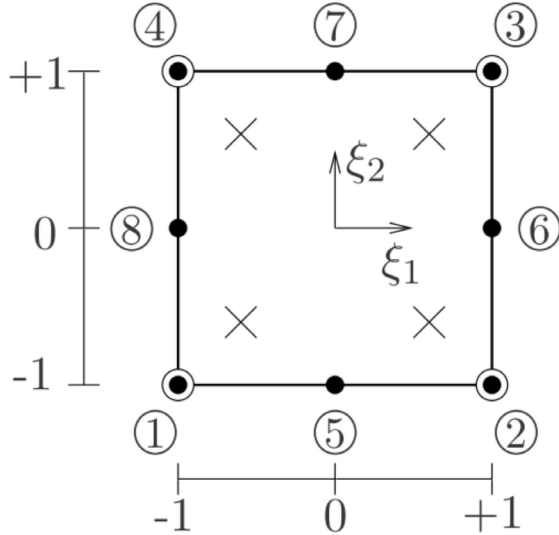


Figure 1: Isoparametric mixed element. According to the interpolation model (biquadratic for \mathbf{u} , bilinear for p^g , p^c and T), the process variables are related to different nodes: (●) solid skeleton displacements, (○) fluids pressure/temperature

system is solved by the Newton-Raphson method, written in concise form as

$$\mathbf{J}(\mathbf{X}^i)|_{n+1} [\mathbf{X}^{i+1} - \mathbf{X}^i]_{n+1} = -\mathbf{G}(\mathbf{X}^i)|_{n+1} \quad (7)$$

5 FINITE ELEMENT VALIDATION

5.1 Force vibration tests under harmonic load

In this example the response of an homogeneous and isotropic, water-saturated, poroelastic column defined in Figure 2 is analyzed under plane-strain confined compression conditions, following [21] and [22]. The domain is surrounded by impermeable, frictionless but rigid boundaries except for the loaded top side which is perfectly drained. Furthermore, 2x2 Gauss integration points were used for numerical computation. The value of the tolerance for the global iterative Newton-Rapson procedure is fixed to 10^{-4} and the maximum number of iteration inside a time step is fixed to 30. The geomechanical characteristics of the material are given in [21]. In particular, two scenarios are tested: an high permeability case, $k=10^{-2}$ m/s, and a lower permeability case, $k=10^{-5}$ m/s. The objective of this benchmark problem is to compare the dynamic finite element solution obtained with standard and mixed elements with an existing analytical solution obtained via Laplace transform [22] as reported in [21].

The vertical displacement history at the top of the column for the two cases is plotted in Figure 3, where a period equal to 0.1 second, which is the period of the harmonic load, is shown. Figure 3a displays the comparison with the analytical solution presented in [21]

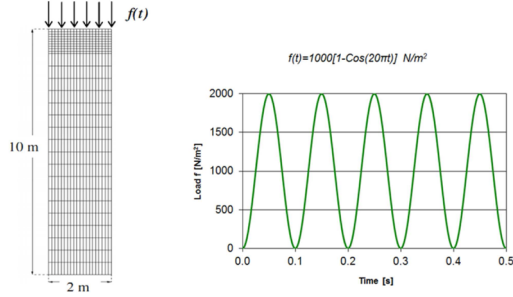


Figure 2: Description of the test model

in case of hydraulic permeability of $k=10^{-2}$ m/s and a good convergence is observed. With the lower permeability, the development of the vertical displacement of the top surface is lower than the case with higher permeability. Moreover, for permeability $k=10^{-5}$ m/s, Figure 3b shows a diversity in the accuracy of the solution when the mixed element formulation is used.

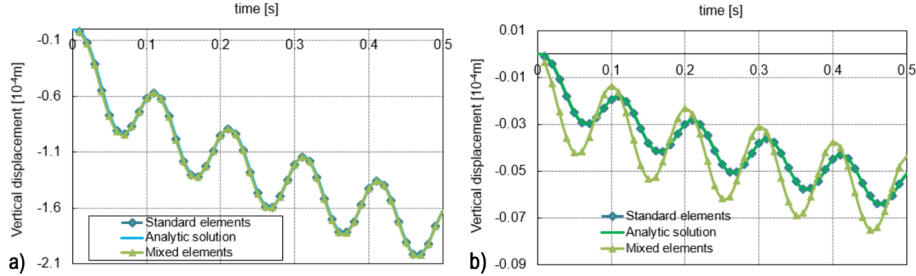


Figure 3: Top displacement history for a) $k=10^{-2}$ m/s, b) $k=10^{-5}$ m/s

5.2 Non-isothermal water saturated consolidation problem

The test problem concerning the fully saturated thermo-elastic consolidation defined in Figure 4 is now solved and its solution is compared with the solution of quasi-static and dynamic problems (with standard elements) done in previous work [23, 18]. The plane-strain medium is confined in a column of 7 m height and 2 m width and subjected to a surface loading 10 kPa and a surface temperature jump of 50 K above the initial temperature of 293.15 K.

The geomechanical characteristics of the Abousta material are given in [23, 13] with permeability: $k = 2.55 \cdot 10^{-7}$ m/s. The liquid water and the solid grain are assumed incompressible for the static analysis, whereas the compressibility of the liquid water is taken into account in the dynamic analysis.

The initial variables for whole node are the liquid water pressure in hydrostatic condition, the air pressure at atmospheric pressure and the temperature at 293.15 K. The

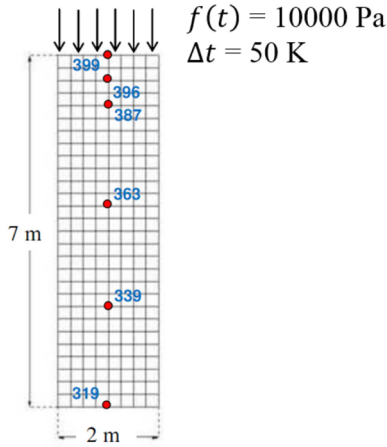


Figure 4: Description of the Aboustit test model

boundary conditions of this problems are as follows: the bottom and lateral surface are impervious to both water and air; the top boundary is drained. The normal and tangential displacements are constrained at bottom; at lateral surface, the normal displacement is constrained. 2x2 Gauss point integration scheme was used. During the computation, the value of the tolerance for the global iterative Newton-Rapson procedure is fixed to 10^{-4} and the maximum number of iteration inside a time step is fixed to 30.

Figure 5 presents the comparison between the quasi-static solution with standard elements, the dynamic solution with standard elements and the dynamic solution with mixed elements for the nodes 319 and 399 displayed in Figure 4. It is observed a difference in the solution with mixed elements for vertical displacements and capillary pressure, while the solution of temperature is not affected by the element type used for the computations.

6 CONCLUSIONS

A mixed finite element formulation for the dynamic analysis of hydro-thermo-mechanical behavior of water saturated and partially saturated porous media has been presented. The model has been implemented in the finite element code Comes-Geo [8, 11, 12, 13, 14, 15, 16, 17, 18] developed at the University of Padova, Department of Civil, Environmental and Architectural Engineering. The comparison between the finite element solution obtained with standard elements and mixed elements in dynamics has been presented, showing that the use of quadratic-linear Taylor-Hood elements for the monolithic treatment of dynamics results less accurate with respect the case of applied equal-order approximation when low permeability is considered. This aspect deserves further investigations.

Acknowledgments

The authors would like to thank the 7th Framework Programme of the European Union (ITN MuMoLaDe project 289911) for the financial support.

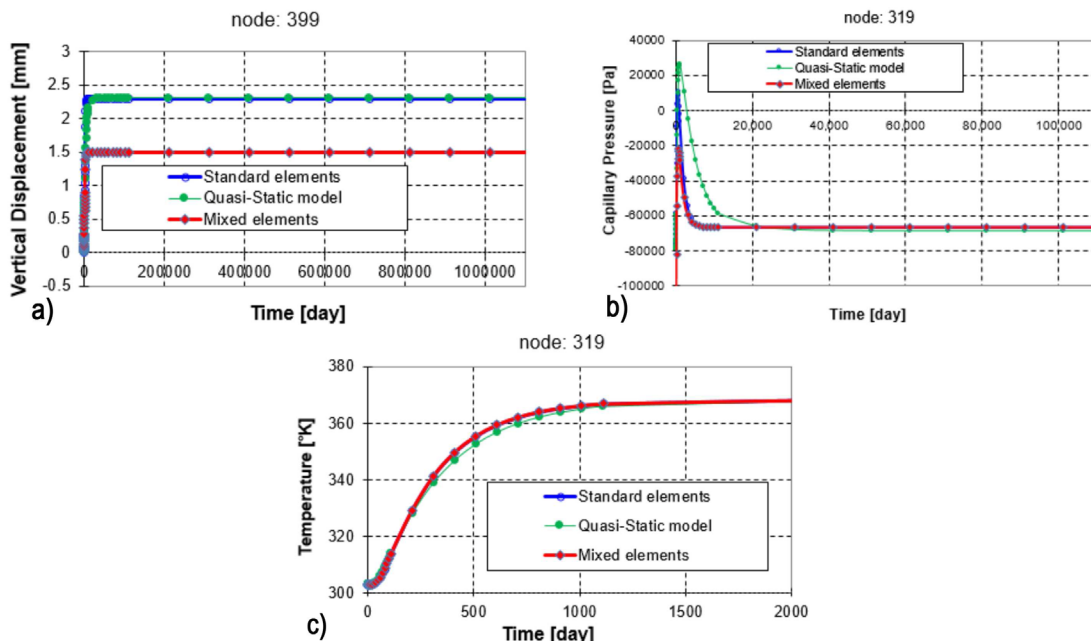


Figure 5: Time-history variables at node references; a) vertical displacement at top sample, b) capillary pressure at bottom sample and c) temperature at bottom sample

REFERENCES

- [1] Zienkiewicz, O.C., Qu, S., Taylor, R.L. and Nakazawa, S. The patch test for mixed formulations. *International Journal for Numerical Methods in Engineering* (1986) **23(10)**:1873–1883.
- [2] Falk, R.S. A fortin operator for two-dimensional taylor-hood elements. *ESAIM: Mathematical Modelling and Numerical Analysis* (2008) **42(14)**:411–424. doi:10.1051/m2an:2008008.
- [3] Ferronato, M., Gambolati, G. and Teatini, P. Ill-conditioning of finite element poroelasticity equations. *International Journal of Solids and Structures* (2001) **38(34-35)**:5995–6014.
- [4] Ehlers, W., Karajan, N., Markert, B. An extended biphasic model for charged hydrated tissues with application to the intervertebral disc. *Biomechanics and Modeling in Mechanobiology* (2009) **8(3)**:233–251. doi:10.1007/s10237-008-0129-y.
- [5] Görke, U.-J., Kaiser, S., Bucher, A. and Kreibig, R. A consistent mixed finite element formulation for hydro-mechanical processes in saturated porous media at large strains based on a generalized material description. *European Journal of Mechanics - A/Solids* (2012) **32(0)**:88–102. doi:<http://dx.doi.org/10.1016/j.euromechsol.2011.09.009>.

- [6] Huang, M., Yue, Z.Q., Tham, L.G. and Zienkiewicz, O.C. On the stable finite element procedures for dynamic problems of saturated porous media. *International Journal for Numerical Methods in Engineering* (2004) **61**(9):1421–1450.
- [7] Murad, M., Thomée, V. and Loula, A. Asymptotic behavior of semidiscrete finite-element approximations of biots consolidation problem. *European Journal of Mechanics - A/Solids* (1996) **33**(3):1065–1083.
- [8] Lewis, R.W. and Schrefler, B.A. *The Finite Element Method in the Static and Dynamic Deformation and Consolidation of Porous Media*, 2nd ed. John Wiley & Sons: New York, (1998).
- [9] Zienkiewicz, O.C., Chan, A.H., Pastor, M., Schrefler, B.A. and Shiomi, T. *Computational geomechanics with special reference to earthquake engineering*. Wiley, (1999).
- [10] Hauser, J.R. *Numerical methods for nonlinear engineering models*. Springer, (2009).
- [11] Gawin, D. and Schrefler, B.A. Thermo-hydro-mechanical analysis of partially saturated porous materials. *Engineering Computations* (1996) **13**: 113–143.
- [12] Sanavia, L., Pesavento, F. and Schrefler, B.A. Finite element analysis of non-isothermal multiphase geomaterials with application to strain localization simulation. *Computational Mechanics* (2006) **37**: 331–348.
- [13] Sanavia, L., Franois, B., Bortolotto, R., Luison, L. and Laloui, L. Finite element modelling of thermo-elasto-plastic water saturated porous materials. *Journal of Theoretical and Applied Mechanics* (2008) **38**:7–24.
- [14] Sanavia, L. Numerical modelling of a slope stability test by means of porous media mechanics. *Engineering Computations* (2009) **26**: 245-266.
- [15] Gawin, D. and Sanavia, L. A unified approach to numerical modelling of fully and partially saturated porous materials by considering air dissolved in water. *CMES: Computer Modeling in Engineering & Sciences* (2009) **53**: 255-302. DOI 10.3970/cmes.2009.053.255.
- [16] Gawin, D. and Sanavia, L. Simulation of cavitation in water saturated porous media considering effects of dissolved air. *Transport in Porous Media* (2010) **81**: 141-160. DOI 10.1007/s11242-009-9391-4.
- [17] Sanavia, L., Luison, L., Passarotto, M. and Laloui, L. Finite element modelling of thermo-elasto-plastic multiphase porous materials. In: *Bytes and Science, G. Zavarise and D.P. Boso (Eds.)*, Cimne, Barcelona, Spain (2012). ISBN: 978-84-940243-2-0. Pages: 99-118.

- [18] Sanavia, L., Cao, T.D., Passarotto, M., Schrefler, B.A. A model for non-isothermal variably saturated porous media in dynamics. In *Proceedings of the 11th World Congress of Computational Mechanics WCCM 2014*, 20-25 July 2014, Barcelona; 3473–3482.
- [19] Hassanzadeh, M. and Gray, W.G. General conservation equations for multi-phase system: 1. Averaging technique. *Advances in Water Resources* (1979) **2**:131-144.
- [20] Hassanzadeh, M. and Gray, W.G. General conservation equations for multi-phase system: 2. mass, momenta, energy and entropy equations. *Advances in Water Resources* (1979) **2**: 191-201.
- [21] Markert, B. Weak or strong on coupled problems in continuum mechanics. *Habilitation thesis*, Universitt Stuttgart, Germany, (2010).
- [22] de Boer, R., Ehlers, W. and Liu, Z. One-dimensional transient wave propagation in fluid-saturated incompressible porous media. *Archive of Applied Mechanics* (1993); **63**(1):59–72.
- [23] Aboustit, B.L., Advani, S.H., Lee J.K. Variational principles and finite element simulations for thermo-elastic consolidation. *International Journal for Numerical and Analytical Methods in Geomechanics* 1985; **9**(1):49-69.

MULTIPHASE ANALYSIS OF STRAIN LOCALIZATION WITH REGULARIZED MODELS

MARIA LAZARI, LORENZO SANAVIA AND BERNHARD A. SCHREFLER

Department of Civil, Architectural and Environmental Engineering (ICEA)
University of Padua (UNIPD)
Via F. Marzolo 9, 35131 Padova, Italy
e-mail: maria.lazari@unipd.it, lorenzo.sanavia@unipd.it, bernhard.schrefler@dicea.unipd.it,
web page: <http://www.dicea.unipd.it/>

Key words: Viscoplasticity, Non-local approach, Strain localization, Multiphase porous media.

Abstract. In this paper rate-dependent plasticity is employed to regularize, from the scope of mesh independency, the numerical solution in strain localization process of multiphase geomaterials. Towards this goal, an already existing model for multiphase porous media is enhanced with local and non-local elasto-viscoplasticity to obtain mesh insensitive results even in case of weakly rate-sensitive materials where artificial viscosities are needed for the regularization of the numerical solution. The numerical validation and analysis of the regularization properties of both viscoplastic models is illustrated by simulating numerical examples from the geomechanics field like a biaxial strain localization test and a slope stability problem.

1 INTRODUCTION

Computational investigation of natural slopes' stability with a coupled hydro-mechanical approach becomes more and more attractive due to an increasing number of slope movements caused by heavy rainfall events. Basic elements of interest in modelling the initiation of slope failure are the triggering mechanisms and the prediction of the location and the time of occurrence of the failure event. Another element that should be addressed is whether the numerical solution is objective with respect to the spatial discretization of the slope's geometry, especially when applying FEM based on Cauchy continuum to simulate the slope failure with a localized pattern. In such a case a particular care is required, to avoid the dependency of the shear band from the element size upon mesh refinement. It is worth noting that from experimental investigations it has become clear that the width of the shear band is directly connected to a micro-structural length. For instance Roscoe [1], based on direct experimental observations, proposed that the width of shear bands is about 10 times the averaged grain diameter. In addition, as it is addressed by many authors [2,3], strain softening or the use of a non-associated flow rule within the framework of elasto-plasticity theory, cause numerical instabilities and pathological mesh sensitivity.

To overcome these drawbacks, suitable constitutive models containing a characteristic internal length scale related to the observed shear band width can be found in the literature, e.g. rate-dependent constitutive models [4-7] and gradient plasticity models [8]. Alternatively, kinematics has to be enhanced, e.g. by adopting micropolar continuum [9].

The present contribution is dealing with the elimination of mesh sensitivity problems in strain localization simulation of multiphase geomaterials under the scope of realistic modeling of the shear zone thickness in geotechnical applications. Viscoplasticity and non-local theories are employed and implemented in an existing finite element code for multiphase porous media [10-13]. The non-local model is of integral-type and is used in conjunction with viscosity as an extension of an already available viscoplastic Drucker-Prager model with non-associated flow rule [14,27]. This coupling allows for eliminating mesh dependency in strain localization even in case of weakly rate-sensitive materials (i.e. dense sand) for which viscoplasticity is not sufficient to suit numerical requirement of mesh independency [15].

The present study is structured as follows: Section 2 includes the main assumptions and features of the mathematical model for porous media along with a synopsis of the particular characteristics of viscoplasticity and non-local theories. In Section 3 the numerical results coming out from the simulation of a plane strain compression test using local and non-local viscoplasticity are presented, followed by the numerical simulation of a slope failure in Section 4. The conclusions drawn from these investigations are given in Section 5.

2 MULTIPHASE MODEL – A GENERAL DESCRIPTION

In the present work we make use of a mathematic model for non-isothermal variably saturated porous media developed within the Hybrid Mixture Theory [16,17] following [18-21]. For the sake of brevity only a general description of the model with its basic assumptions will be presented hereafter and more details regarding its numerical implementation, for the interested reader, is referred to [10,13].

In the framework of realistic description of natural geomaterials it is necessary to proceed from an unsaturated soil based on a multiphase model. Therefore, the variably saturated porous medium is treated as a multiphase system consisting of a solid skeleton with open pores filled with liquid water and gas. The gas phase is modelled as an ideal gas composed of dry air (non-condensable gas) and water vapour (condensable gas), which are considered as two miscible species. Phase changes of water (evaporation and condensation) as well as heat transfer through conduction and convection are considered. Furthermore, the non-polar solid is deformable, resulting in a coupling of the fluid, the solid and the thermal fields. All fluid phases are in contact with the solid phase. In the partially saturated zones the liquid water is separated from its vapour by a concave meniscus (capillary water). Due to the curvature of this meniscus, the sorption equilibrium equation [18] gives the relationship, $p^c = p^g - p^w$ between the capillary pressure p^c , gas pressure p^g and liquid water pressure p^w .

The mathematical model consists of four kind of balance equations (mass of dry air, mass of water species, enthalpy of the whole medium and equilibrium equation of the multiphase medium), as well as appropriate constitutive equations for the fluids and solid phase. The balance equations were developed in the geometrically linear framework considering quasi-static loading conditions. The chosen macroscopic primary variables are: gas pressure, capillary pressure, temperature and displacements [13], corresponding to real measurable quantities directly linked to laboratory practice. This is an important aspect when selecting the appropriate constitutive equations.

The governing equations are discretized in space by means of the standard finite element method (Bubnov-Galerkin method) and in time by a fully implicit finite difference scheme

(backward difference) and are solved by means of Newton-Raphson type procedure. Further particulars and general references on the numerical treatment can be found in [10,13].

In the following, direct notation will be adopted. Boldface letters will denote vector or tensors and lightface italic letters will be used for scalar quantities.

2.1 Equilibrium equation

The equilibrium equation of the mixture in terms of generalized effective Cauchy's stress tensor $\sigma'(\mathbf{x}, t)$ assumes the form:

$$\operatorname{div}\left(\sigma' - \left[p^g - S_w p^c\right] \mathbf{1}\right) + \rho \mathbf{g} = 0 \quad (1)$$

where $\rho = [1-n]\rho^s + nS_w\rho^w + nS_g\rho^g$ is the mass density of the overall medium, $n(\mathbf{x}, t)$ is the porosity, $S_w(\mathbf{x}, t)$ and $S_g(\mathbf{x}, t)$ are respectively the water and gas degree of saturation, \mathbf{g} is the gravity acceleration vector and $\mathbf{1}$ is the second order identity tensor.

2.2 Mass balance equations

The mass conservation equation for the mixture of solid skeleton, liquid water and its vapour is:

$$\begin{aligned} & n \left[\rho^w - \rho^{gw} \right] \left[\frac{\partial S_w}{\partial t} \right] + \left[\rho^w S_w + \rho^{gw} [1 - S_w] \right] \operatorname{div} \left(\frac{\partial \mathbf{u}}{\partial t} \right) \\ & + [1 - S_w] n \frac{\partial \rho^{gw}}{\partial t} - \operatorname{div} \left(\rho^g \frac{M_a M_w}{M_g^2} \mathbf{D}_g^{gw} \operatorname{grad} \left(\frac{p^{gw}}{p^g} \right) \right) \\ & + \operatorname{div} \left(\rho^w \frac{\mathbf{k}^w k^{rw}}{\mu^w} \left[-\operatorname{grad}(p^g) + \operatorname{grad}(p^c) + \rho^w \mathbf{g} \right] \right) \\ & + \operatorname{div} \left(\rho^{gw} \frac{\mathbf{k}^g k^{rg}}{\mu^g} \left[-\operatorname{grad}(p^g) + \rho^g \mathbf{g} \right] \right) - \beta_{swg} \frac{\partial T}{\partial t} = 0 \end{aligned} \quad (2)$$

where $\mathbf{k}^\pi(\mathbf{x}, t) = k^\pi(\mathbf{x}, t)\mathbf{1}$ is the intrinsic permeability tensor of the porous matrix in π -fluid saturated condition [m^2], which is assumed to be isotropic, $k^\pi(\mathbf{x}, t)$ is the fluid relative permeability parameter and $\mu^\pi(\mathbf{x}, t)$ is the dynamic viscosity of the fluid [$\text{Pa}\cdot\text{s}$], with $\pi = w, g$. \mathbf{D}_g^{gw} is the effective diffusivity tensor of water vapour in the gas phase contained within the pore space, $\beta_{swg} = \beta_s(1-n) \cdot (S_g \rho^{gw} + \rho^w S_w)$ and M_a , M_w and $M_g(\mathbf{x}, t)$ are the molar mass of dry air, liquid water and gas mixture, respectively. Similarly, the mass balance equation for the dry air is:

$$\begin{aligned}
 & -n\rho^{ga} \left[\frac{\partial S_w}{\partial t} \right] + \rho^{ga} [1 - S_w] \operatorname{div} \left(\frac{\partial \mathbf{u}}{\partial t} \right) + n [1 - S_w] \frac{\partial \rho^{ga}}{\partial t} - \operatorname{div} \left(\rho^g \frac{M_a M_w}{M_g^2} \mathbf{D}_g^{ga} \operatorname{grad} \left(\frac{p^{ga}}{p^g} \right) \right) \\
 & + \operatorname{div} \left(\rho^{ga} \frac{\mathbf{k}^g k^{rg}}{\mu^g} \left[-\operatorname{grad}(p^g) + \rho^g \mathbf{g} \right] \right) - [1 - n] \beta_s \rho^{ga} [1 - S_w] \frac{\partial T}{\partial t} = 0
 \end{aligned} \tag{3}$$

2.3 Enthalpy balance equation

The enthalpy balance equation of the mixture has the following form:

$$\begin{aligned}
 & (\rho C_p)_{eff} \frac{\partial T}{\partial t} + \rho^w C_p^w \left[\frac{\mathbf{k}^w k^{rw}}{\mu^w} \left[-\operatorname{grad}(p^g) + \operatorname{grad}(p^c) + \rho^w \mathbf{g} \right] \right] \cdot \operatorname{grad} T \\
 & + \rho^g C_p^g \left[\frac{\mathbf{k}^g k^{rg}}{\mu^g} \left[-\operatorname{grad}(p^g) + \rho^g \mathbf{g} \right] \right] \cdot \operatorname{grad} T - \operatorname{div} (\chi_{eff} \operatorname{grad} T) = -\dot{m}_{vap} \Delta H_{vap}
 \end{aligned} \tag{4}$$

where, $\rho(C_p)_{eff}$ is the effective thermal capacity of the porous medium, $C_p^w(\mathbf{x}, t)$ and $C_p^g(\mathbf{x}, t)$ are the specific heat of the water and gas mixture respectively, and $\chi_{eff}(\mathbf{x}, t)$ is the effective thermal conductivity of the porous medium. The right hand side term of Eq. (4) considers the contribution of the evaporation and condensation.

2.4 Constitutive equations

For the gas phase which is assumed to be a perfect mixture of two ideal gases, the state equation of a perfect gas (Clapeyron's equation) and Dalton's law are applied to dry air (ga), water vapour (gw) and moist air (g). In the partially saturated zones, the water vapour pressure $p^{gw}(\mathbf{x}, t)$ is obtained from the Kelvin-Laplace equation. The saturation $S_\pi(\mathbf{x}, t)$ and the relative permeability $k^{rw}(\mathbf{x}, t)$ are experimentally determined functions of the capillary pressure p^c and the temperature T .

The behaviour of the soil skeleton is described within the framework of elasto-viscoplasticity theory for geometrically linear problems. The generalized effective stress state is limited by the Drucker-Prager yield surface with isotropic linear hardening and non-associated plastic flow:

$$f(p', \mathbf{s}', q) = 3\alpha_f p' + \|\mathbf{s}'\| - \beta_f \sqrt{\frac{2}{3}} \left[c_0 + H \xi^{vp} \right] \tag{5}$$

In Eq. (5) $p' = (1/3)\operatorname{tr}\sigma'$ is the mean effective Cauchy pressure, $\|\mathbf{s}'\|$ is the norm of the deviator effective Cauchy stress tensor σ' , c_0 is the apparent cohesion, α_f and β_f are two material parameters related to the friction angle ϕ of the soil defined by Eq. (6), H is the hardening/softening modulus and ξ^{vp} is the equivalent viscoplastic strain. The flow rule is of non-associated type, with the plastic potential function given by Eq. (5) but with the dilatancy angle ψ substituting the friction angle in Eq. (6).

$$\alpha_f = 2 \frac{\sqrt{2/3} \sin\varphi}{3 - \sin\varphi}, \quad \beta_f = 2 \frac{6 \cos\varphi}{3 - \sin\varphi} \quad (6)$$

The total strain rate in an elasto-viscoplastic material is additively decomposed into an elastic and a viscoplastic strain rate:

$$\dot{\boldsymbol{\epsilon}} = \dot{\boldsymbol{\epsilon}}^e + \dot{\boldsymbol{\epsilon}}^{vp} \quad (7)$$

where the superimposed dot denotes time derivative. Considering linear elasticity, the stress rate is related to the strain rate via the following constitutive relation:

$$\dot{\boldsymbol{\sigma}} = \mathbf{D}^e : (\dot{\boldsymbol{\epsilon}} - \dot{\boldsymbol{\epsilon}}^{vp}) \quad (8)$$

where \mathbf{D}^e is the fourth-order elastic tensor and double dots “:” denote the doubly contracted tensor product.

In the viscoplastic model proposed by Perzyna [22] (which from this point on will be referred as local to distinguish from non-local), the viscoplastic strain rate is directly linked to the yield function through the viscous nucleus:

$$\dot{\boldsymbol{\epsilon}}^{vp} = \gamma \left\langle \Phi \left(\frac{f}{f_0} \right)^N \right\rangle \frac{\partial g}{\partial \boldsymbol{\sigma}'} \quad (9)$$

with f being the yield function, f_0 introduced as a reference fixed value making the viscous nucleous dimensionless, γ is a fluidity parameter which depends on the viscosity η of the material ($\gamma=1/\eta$), N is a calibration parameter ($N \geq 1$) and g is the viscoplastic potential function. Associative flow is invoked by $g=f$.

In Eq. (9), “<··>” are the McCauley brackets, such that:

$$\left\langle \Phi(x) \right\rangle = \begin{cases} \Phi(x) & \text{if } \Phi(x) \geq 0 \\ 0 & \text{if } \Phi(x) < 0 \end{cases} \quad (10)$$

Non-local approach is introduced next because in case of weakly rate-sensitive materials (such as dense sand) artificial viscosities have to be chosen to obtain objective finite element results. To ensure a regularized numerical solution physically based, the local viscoplastic model of Perzyna is expanded with respect to the non-local approach following [25].

According to Jirásek [23] in non-local approach a certain variable, f , is substituted with its non-local counterpart, \hat{f} , obtained by weighted averaging over a spatial neighbourhood (distributing points located at ξ) of each point under consideration (located at x):

$$\hat{f}(x) = \int_V a(x, \xi) f(\xi) d\xi \quad (11)$$

Key points for the formulation and implementation of a non-local approach are the chosen weighting function for the averaging and as non-locality is introduced into the constitutive equations. The weighting function contains at least one parameter with the dimension of length, which incorporates information about the microstructure and controls the size of the localized plastic zone [24]. Herein, inspired by [25], the yield function is chosen to be the

non-local variable and a Gaussian weighting function with a bounded support is selected (Eq.12).

$$\alpha_0(\mathbf{x} - \boldsymbol{\xi}) = \begin{cases} \exp\left(-\frac{2 \cdot (\mathbf{x} - \boldsymbol{\xi})}{1}\right)^2 & \text{if } \|\mathbf{x} - \boldsymbol{\xi}\| \leq R \\ 0 & \text{if } \|\mathbf{x} - \boldsymbol{\xi}\| > R \end{cases} \quad (12)$$

Choosing yield function as the non-local variable, the viscous nucleus and consequently the viscoplastic flow rule are modified:

$$\dot{\epsilon}^{vp} = \gamma \Phi(\hat{f}) \frac{\partial g}{\partial \sigma'} \quad (13)$$

3 PLANE STRAIN COMPRESSION TEST

In this section, local and non-local viscoplasticity is applied to a biaxial strain compression test of an initially water saturated, globally undrained dense Hostun RF sand, where strain localization and cavitation (phase change of the liquid water to vapour) were experimentally observed. This numerical example was previously studied by Sanavia et al. [13], inspired by the experimental work of [26], assuming a rate-independent behaviour for the description of the mechanical behaviour of sand.

Herein, mesh sensitivity of the numerical results is examined by using two different finite element discretizations. The adopted meshes consist of 340 (10x34) and 1360 (20x68) elements respectively, for a rectangular sample of homogeneous soil of 34 cm height and 10 cm width. The finite element mesh consists of eight node quadrilateral isoparametric elements with reduced Gaussian (2x2) integration scheme. The bottom of the sample was assumed to be fixed and rough, whereas the boundaries are impervious and adiabatic. Quasi-static loading conditions are assumed and gravity acceleration is taken into account. Axial compression is applied to the specimen by imposing vertical velocity ($v=1.2$ mm/s) on the top. No weak elements are specified since the boundary value problem inherently generates a non-uniform stress field. The material parameters used in the computation are as in [13].

For brevity, indicative results are presented for the sake of comparison of the proposed methods. A more detailed presentation and analysis of the influencial parameters of the problem, such the loading velocity, the value of permeability and the interaction of the internal lengths (introduced by viscosity and non-locality) can be found in [27].

The numerical validation of both models in the Comes-geo [10,13] code is first presented. In Figure 1a are plotted the equivalent inelastic strains in the vertical section at the centre of the sample for both elastoplastic (solid line) and elasto-viscoplastic (square markers) constitutive models to verify that for rather small values of viscosity elastoplastic limit is approached [28]. The comparison of the results shows the coincedence between the elastoplastic and the considered viscoplastic solution for nil viscosity value. In addition, in Fig. 1b it is observed that for small values of the internal length l , the non-local solution approaches the local one. The difference between the non-local and the local elasto-viscoplastic solution tends to disappear for very small values of l , owing to the fact that in such a case only one integration point may be inside the interaction radius where the non-local

averaging is performed.

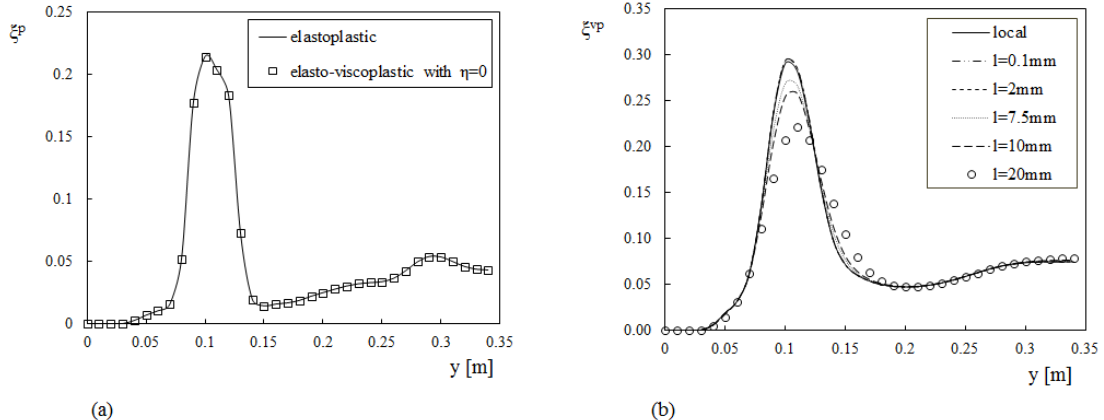


Figure 1: Numerical validation of (a) local and (b) non-local elasto-viscoplastic Perzyna model in Comes-geo code (10x34 mesh).

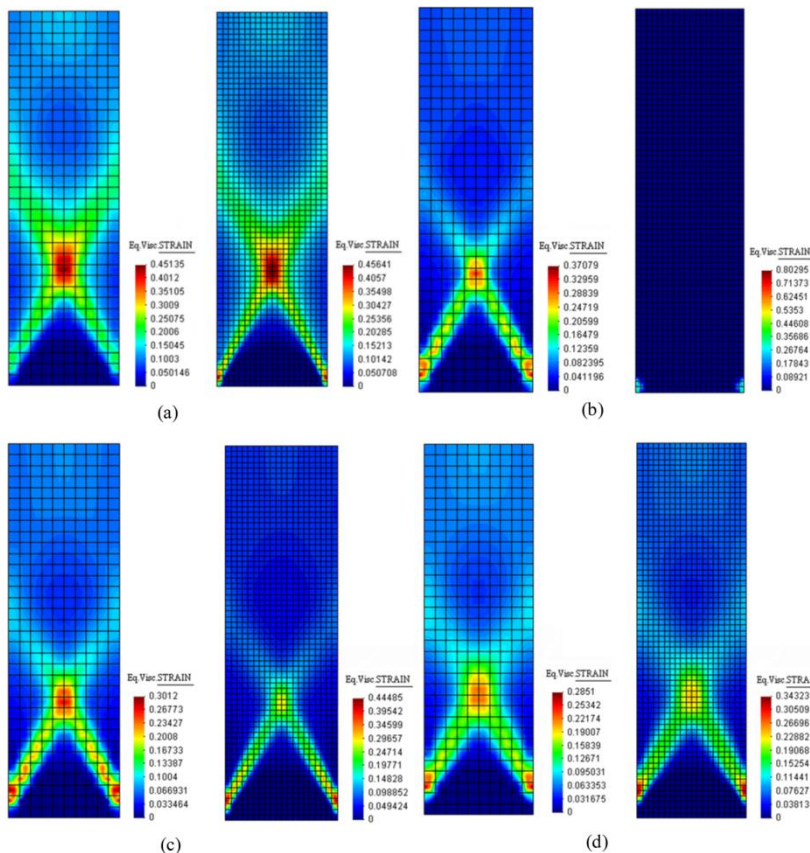


Figure 2: Numerical results for (a) local viscoplasticity with $\eta=30\text{s}$, (b) local viscoplasticity with $\eta=10\text{s}$, (c) non-local viscoplasticity with $\eta=10\text{s}$, $l=0.01\text{m}$ and (d) non-local viscoplasticity with $\eta=10\text{s}$, $l=0.02\text{m}$, for two meshes (10x34 and 20x68 respectively).

The effect of the local and non-local elasto-viscoplastic model of Perzyna in the regularization of the mesh dependency problem is illustrated in Fig. 2. The influence of the viscosity parameter, η , is clearly depicted for the local elasto-viscoplastic model. In the case of $\eta=30s$, a regularized solution is obtained for both meshes: the shear band width remains unaltered upon mesh refinement and the peak value of equivalent viscoplastic strain coincides for the two meshes. However, considering a less rate-sensitive material with $\eta=10s$ (and as approaching the elastoplastic limit), the regularizing effect of the local elasto-viscoplastic model is lost and the contour of the more refined mesh reveals strong mesh-sensitivity (Fig. 2b). In this case, the non-local elasto-viscoplastic model proves to be sufficient to regularize the finite element solution for the given material parameters and the shear band propagates for internal length value, $l=0.01m$ (Fig. 2c). Moreover, in the case of internal length value $l=0.02m$ (Fig. 2d), the width of the shear band increases accordingly to the l value for both meshes adopted.

In Fig. 3 the numerical solution for the liquid phase is presented in terms of capillary pressure and water saturation. The results are presented for the case of non-local elasto-viscoplastic plastic model, and mesh independency is apparent also for the fluid part. It is evident that pore water decreases up to the development of capillary pressure, accompanied by desaturation in the strain localization zones. It is noted that at the same time water pressure decreases below the vapour saturation pressure and the phase change of the liquid water to vapour occurs.

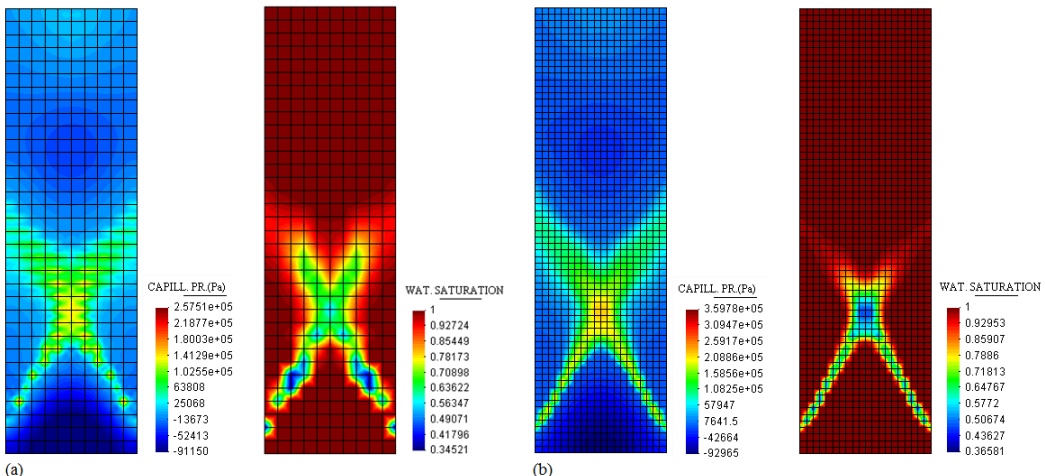


Figure 3: Non-local approach: Capillary pressure and water degree of saturation contours for (a) 10x34 mesh and (b) 20x68 mesh, in case of $l=7.5\text{mm}$ and $\eta=10\text{s}$.

4 SLOPE STABILITY TEST

A slope stability problem, inspired by Regueiro and Borja [29], is now presented to demonstrate the effectiveness of adopting the regularization techniques developed in this work. The dimensions and boundary conditions of the problem are shown in Fig. 4 whereas the soil parameters considered in the analysis are indicated in Table 1. The initial stress field is given by geostatic stress state; drained conditions are imposed. Next, a downward displacement with a constant rate of 10^{-3} m/s is applied on a portion of 4m on the top slope

surface (Fig. 4). Two meshes with 400 and 1600 eight node quadrilateral isoparametric elements are used to analyze the problem. The analyses are performed using: the elastoplastic model, the local elasto-viscoplastic model of Perzyna with viscosity $\eta=100\text{s}$ and the non-local elasto-viscoplastic model with an internal length of $l=0.8\text{ m}$. The results from these models are compared in Fig. 5 in terms of equivalent (visco)plastic strain and in Fig. 6 with the force-displacement plots.

Table 1: List of soil parameters for the slope stability problem.

E [MPa]	v	γ [kN/m ³]	c_0 [kPa]	φ [°]	ψ [°]	h [kPa]	n	k [m ²]
10	0.4	20	40	10	3	-10	0.3	1E-10

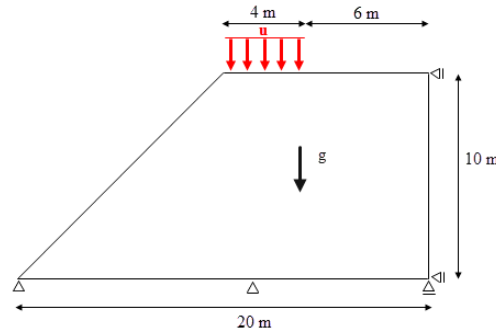


Figure 4: Slope stability problem. Geometry and boundary conditions.

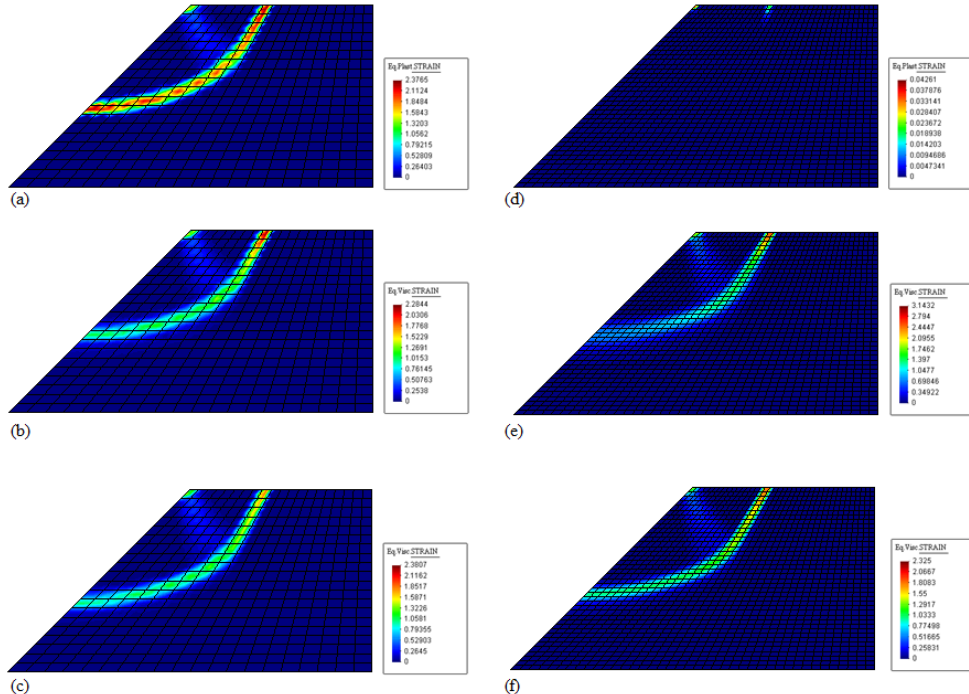


Figure 5: Equivalent (visco)plastic strain contours as calculated using the elastoplastic model (a,d), the local elasto-viscoplastic model (b,e) and the non-local elasto-viscoplastic model (c,f) for a mesh of 400 elements (a), (b) and (c) and for a mesh of 1600 elements (d), (e) and (f), respectively.

The failure initiates in the element just to the right of the applied force and propagates in a manner depended on the angle of friction. When the elastoplastic constitutive model is used to solve this initial boundary value problem, a classical mesh dependent numerical solution is observed with the model being unable to simulate the failure process of the slope when the mesh is refined (Fig. 5d). As is shown in Fig. 6b when the elasto-viscoplastic formulation of Perzyna is adopted, even if the number of elements is increased, the shear band formation and the force-displacement relationship are not affected by the element size. However, the peak value of the viscoplastic strain field depends on the element size of the mesh (Fig. 5e). Finally, the non-local elasto-viscoplastic model is able to predict a clearly defined shear band and the slope's strain-softening response (Fig. 6c) independently of the mesh adopted (Fig. 5f).

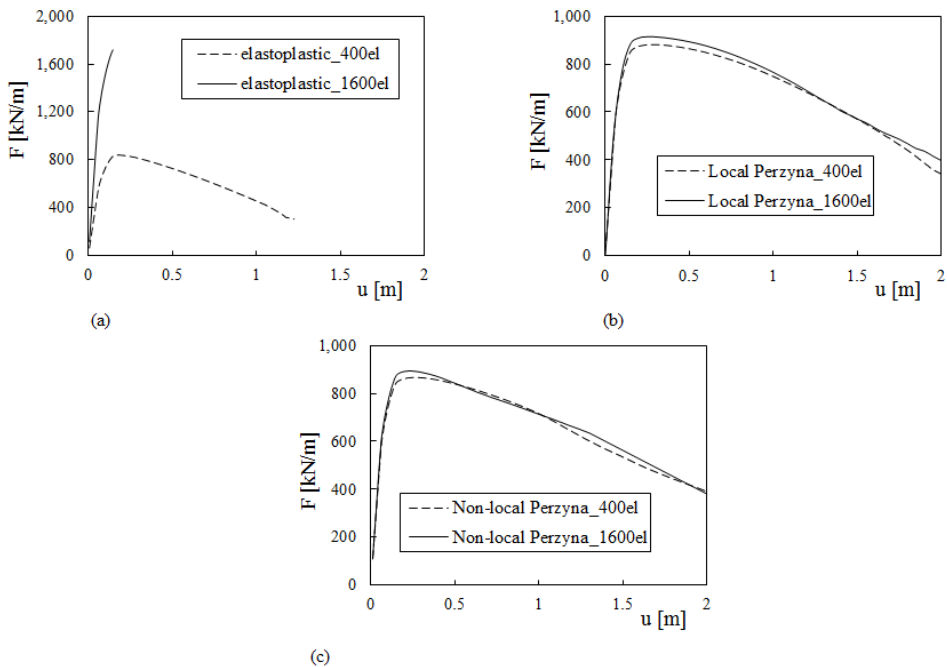


Figure 6: Force-displacement plots for (a) the elastoplastic model, (b) the local elasto-viscoplastic model and (c) the non-local elasto-viscoplastic model, for the two meshes.

5 CONCLUSIONS

In this work the mesh sensitivity problem in strain localization simulation of multiphase geomaterials is overcomed by means of viscoplasticity and nonlocal theory. These formulations are implemented in an existing finite element code for multiphase porous media. Both methods introduce a characteristic length scale (implicitly and explicitly) which prevents strains from localizing into infinitely narrow bands when the mesh is refined.

The validation of the implementation of the methods is presented and the effectiveness of the methods is studied, within the framework of an undrained biaxial test. The initiation and the propagation of the shear band are effectively described by means of FEM analysis, regardless of the mesh size adopted. The strain localization process realistically occurs within the shear band failure mode and its size is governed by the viscosity parameter and the

internal length variable, which can be directly estimated by experimental tests. The rate sensitivity of the material is investigated showing the holistic confrontation of the strain localization phenomenon by the combination of the two methods.

The efficiency of the models in terms of regularized performance is also illustrated using a numerical example of a slope failure problem. The numerical results indicate that only by using the applied regularization techniques the location and the propagation of the shear zone is reliably simulated in a mesh independent manner.

ACKNOWLEDGMENT

The authors would like to thank the 7th Framework Programme of the European Union (ITN MuMoLaDe project 289911) for the financial support of this work.

REFERENCES

- [1] Roscoe, K.H. The influence of strains in Soil Mechanics. *Géotechnique* (1970) **20**:129-170.
- [2] Nova, R. The role of non-normality in soil mechanics and some of its mathematical consequences. *Computers and Geotechnics* (2004) **31**:185–191.
- [3] Rudnicki, J.W and Rice, J.R. Conditions for the localization of deformation in pressure-sensitive dilatant materials. *Journal of the Mechanics and Physics of Solids* (1975) **23**:371-394.
- [4] Ehlers, W., Graf, T. and Ammann, M. Deformation and localization analysis of partially saturated soil. *Computer Methods in Applied Mechanics and Engineering* (2004) **193**:2885–2910.
- [5] Loret, B. and Prevost, J.H. Dynamic strain localization in fluid-saturated porous media. *Journal of Engineering Mechanics* (1991) **117**(4):907-922.
- [6] Schrefler, B.A., Zhang, H.W. and Sanavia, L. Fluid-structure interaction in the localization of saturated porous media. ZAMM Zeitschrift für Angewandte Mathematik und Mechanik, *Journal of Applied Mathematics and Mechanics. Z. Angew. Math. Mech.* (1999) **79**:481-484.
- [7] Schrefler, B.A, Zhang, H.W and Sanavia, L. Interaction between different internal length scales in fully and partially saturated porous media – The 1-D case, *International Journal for Numerical and Analytical Methods in Geomechanics* (2006) **30**:45-70.
- [8] Zhang, H.W and Schrefler, B.A. Gradient-dependent plasticity model and dynamic strain localization analysis of saturated and partially saturated porous media: one dimensional model. *European Journal of Mechanics A/Solids* (2000) **19**(3):503–524.
- [9] Ehlers, W. and Volk, W. On theoretical and numerical methods in the theory of porous media based on polar and non-polar elasto-plastic solid materials. *International Journal of Solids and Structures* (1998) **35**:4597-4617.
- [10] Gawin, D. and Schrefler, B.A. Thermo-hydro-mechanical analysis of partially saturated porous materials. *Engineering Computations* (1996) **13**(7):113-143.
- [11] Gawin, D. and Sanavia, L. A unified approach to numerical modelling of fully and partially saturated porous materials by considering air dissolved in water. *CMES-Comp. Model. Eng. Sci.* (2009) **53**:255-302.
- [12] Gawin, D. and Sanavia, L. Simulation of cavitation in water saturated porous media

- considering effects of dissolved air. *Transport Porous Media* (2010) **81**:141-160.
- [13] Sanavia, L., Pesavento, F. and Schrefler, B.A. Finite element analysis of non-isothermal multiphase geomaterials with application to strain localization simulation. *Computational Mechanics* (2006) **37**:331-348.
 - [14] Lazari, M., Sanavia, L. and Schrefler, B.A. Viscoplastic regularization of strain localization in fluid-saturated porous media. *Proceedings of WCCM XI-ECCM V*, Tomo IV: 3495-3503, Barcelona, (2014). ISBN: 978-84-942844-7-2
 - [15] di Prisco, C., Imposimato, S. and Aifantis, E.C. A visco-plastic constitutive model for granular soils modified according to non-local and gradient approaches. *International Journal for Numerical and Analytical Methods in Geomechanics* (2002), **26**:121-138.
 - [16] Lewis, R.W. and Schrefler, B.A. *The Finite Element Method in the Static and Dynamic Deformation and Consolidation of Porous Media*, Wiley and Sons: Chichester, (1998).
 - [17] Schrefler, B.A. Mechanics and thermodynamics of saturated/unsaturated porous materials and quantitative solutions. *Applied Mechanics Reviews* (2002) **55**(4):351-388.
 - [18] Gray, W.G. and Hassanizadeh, M. Unsaturated flow theory including interfacial phenomena. *Water Resources Research* (1991) **27**:1855-1863.
 - [19] Hassanizadeh, M and Gray, W.G. General conservation equations for multi-phase system: 1. Averaging technique. *Advances in Water Resources* (1979a) **2**:131-144.
 - [20] Hassanizadeh, M and Gray, W.G. General conservation Equations for multi-phase system: 2. Mass, momenta, energy and entropy equations. *Advances in Water Resources* (1979b) **2**:191-201.
 - [21] Hassanizadeh, M. and Gray, W.G. General conservation equations for multi-phase systems: 3. Constitutive theory for porous media flow. *Advances in Water Resources* (1980) **3**(1):25-40.
 - [22] Perzyna, P. Fundamental problems in viscoplasticity. *Advances in Applied Mechanics* (1966) **9**:243-377.
 - [23] Jirásek, M. Objective modeling of strain localization. *Revue Française de Genie Civil* (2002) **6**:1119-1132.
 - [24] Jirásek, M. and Rolshoven, S. Comparison of integral-type nonlocal plasticity models for strain-softening materials. *International Journal of Engineering Science* (2003) **41**:1553-1602.
 - [25] di Prisco, C. and Imposimato, S. Nonlocal numerical analyses of strain localization in dense sand. *Mathematical and Computer Modelling* (2003) **37**:497-506.
 - [26] Mokni, M. and Desrues, J. Strain localisation measurements in undrained plane-strain biaxial tests on hostun RF sand. *Mechanics of Cohesive-Frictional Materials* (1998) **4**:419-441.
 - [27] Lazari, M., Sanavia, L. and Schrefler, B.A. Local and non-local elasto-viscoplasticity in strain localization analysis of multiphase geomaterials. *International Journal for Numerical and Analytical Methods in Geomechanics* (2015), in print.
 - [28] Needleman, A. Material rate dependence and mesh sensitivity on localization problems. *Computer Methods in Applied Mechanics and Engineering* (1988) **67**:69-86.
 - [29] Regueiro, R.A. and Borja, R.I. Plane strain finite element analysis of pressure sensitive plasticity with strong discontinuity. *International Journal of Solids and Structures* (2001) **38**:3647-3672.

WHAT IS WRONG IN LOVE-WEBER STRESS FOR UNSATURATED GRANULAR MATERIALS?

C. CHALAK¹, B. CHAREYRE² AND F. DARVE³

¹ 1. Univ. Grenoble Alpes, 3SR, F-38000 Grenoble, France

2. CNRS, 3SR, F-38000 Grenoble, France

Domaine Universitaire BP53, 38041 Grenoble cedex 9, France
caroline.chalak@3sr-grenoble.fr and URL

² 1. Univ. Grenoble Alpes, 3SR, F-38000 Grenoble, France

2. CNRS, 3SR, F-38000 Grenoble, France

Domaine Universitaire BP53, 38041 Grenoble cedex 9, France
bruno.chareyre@3sr-grenoble.fr and URL

³ 1. Univ. Grenoble Alpes, 3SR, F-38000 Grenoble, France

2. CNRS, 3SR, F-38000 Grenoble, France

Domaine Universitaire BP53, 38041 Grenoble cedex 9, France
felix.darve@3sr-grenoble.fr and URL

Key words: Granular Materials, DEM, Unsaturated, Roughness

Abstract. This paper presents the micromechanical model for unsaturated soil in pendular regime, taking into account the roughness of the grains and the interfaces that separate the different phases present in the medium. It supplements the oral presentation with more technical content. Laplace equation is solved for two grains configuration to calculate the capillary force and all the geometric properties of the meniscus connecting the grains. Many configurations are solved and the look up table method is then used during the simulations. Results for grains moving at constant suction and constant volume are presented. It is also shown that the roughness has an important impact on the value of capillary force and it is evolution with the change of suction.

1 INTRODUCTION

Unsaturated soils has been an interest for many studies recently. Different approaches has been used to study the behavior of such materials.

One of these approaches is the thermodynamic approach([2],[5],[4],[10]). All these studies, highlighted the importance of the interfaces separating the different phases, and insisted that specific terms accounting for them must be included in the formulation of the effective stress.

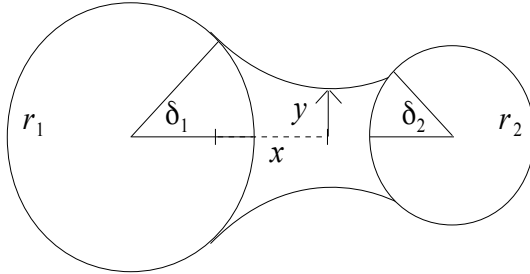


Figure 1: Illustration of a liquid bridge between 2 spherical grains.

On the other side, many recent work has been dedicated to studying unsaturated soils using the discrete element method DEM [1]. See for instance ([3], [7], [11]).

Bridging the theoretical frameworks mentioned previously, all these numerical tools need to define the interfacial areas accurately which has not been done yet.

This paper details in the first part the micromechanical model inspired by [11] and implemented in the open source code YADE and in which the interfaces that exist in the partially saturated medium are taken into account.

The model takes also into account the roughness of the grains. The influence of the roughness on the behavior of the unsaturated granular matter is discussed in the second part.

2 LAPLACE EQUATION

The geometry of the water bridges connecting the particles is determined by Laplace equation. Laplace equation relates the pressure jump p_c across the wetting-non wetting interface to its curvature through the surface tension:

$$p_c = \gamma C \quad (1)$$

Even if the form of the Laplace equation is simple, it is very difficult to solve. In the pendular regime, the capillary force is easy to compute and can be linked to the geometry of the grains and the suction in the medium. For higher saturations, the problem becomes much more complicated. This section details the resolution of Laplace in the pendular regime.

The pendular regime is over when the disconnected bridges start to overlap. The overlapping of the bridges is tested using the filling angles of the bridges on each particle.

For sake of more simplicity, the grains are assumed to be spherical in order to have an axisymmetric problem. In this case, the curvature and the Young-Laplace equation can be written as following:

$$C = \frac{1}{y(x)\sqrt{1+y'(x)^2}} + \frac{-y''(x)}{(1+y'(x)^2)^{\frac{3}{2}}} \quad (2)$$

$$\frac{p_c}{\gamma}(1+y'(x)^2)^{\frac{3}{2}} + \frac{(1+y'(x)^2)}{y(x)} - y''(x) = 0 \quad (3)$$

To generalize the study and describe the capillary phenomena for different particle sizes and different liquid types, all the variables are normalized. We introduce the factor R that is the radius of the smallest (r_2) at biggest (r_1) grains in one meniscus configuration:

$$x^* = \frac{x}{R} \quad (4)$$

$$y^* = \frac{y(x)}{R} \quad (5)$$

$$y'^* = \frac{\frac{dy(x)}{dx}}{\frac{R}{R}} = y'(x) \quad (6)$$

$$y''^* = \frac{dy'(x)}{dx} = \frac{y''(x)}{R} \quad (7)$$

$$p_c^* = \frac{p_c R}{\gamma} \quad (8)$$

$$F_{cap}^* = \frac{F_{cap}}{\gamma R} \quad (9)$$

$$V^* = \frac{V}{R^3} \quad (10)$$

$$A^* = \frac{A}{R^2} \quad (11)$$

F_{cap} refers to the capillary force, V to the volume of the meniscus and A to interfaces. The normalized Laplace equation becomes then :

$$\frac{y''^*}{(1+y'^2)^{\frac{3}{2}}} - \frac{1}{y^* \sqrt{1+y'^2}} = p_c^* \quad (12)$$

Based on the work of [8] , Laplace equation can be integrated into a first order differential equation:

Assuming $Q = 1 + y'^2$ the equation becomes:

$$\frac{dQ}{dy^*} - \frac{2Q}{y^*} = 2p_c^* Q^{\frac{3}{2}} \quad (13)$$

This is a Bernoulli type equation that gives the following solution:

$$Q = \frac{4y^{*2}}{(2K - p_c^* y^{*2})^2} \quad (14)$$

In perfect wetting condition, K is determined from the contact boundaries at the triple line connecting the bridge to the grains, or at the gorge ([6], [8]) for given spheres sizes, suction and distance separating the grains.

The calculations show that K is proportional to the capillary force.

$$K = y^* + \frac{y^{*2} p_c^*}{2} = F_{cap}^* * 2\pi = F_{cap} * 2\pi\gamma R \quad (15)$$

The final form of the integrated equation is then:

$$\frac{1}{2\pi} \left(\frac{y^*}{2\sqrt{1+y'^2}} - p_c^* y^{*2} \right) = F_{cap}^* \quad (16)$$

For the same spheres sizes, suction and distance configuration, we can also calculate the volume of the liquid bridge ([13])and the values of the interfaces separating the different phases in the system.

$$V^* = \int \pi y^{*3} dx^* - V_1^* - V_2^* \quad (17)$$

V_1^* and V_2^* are the volumes of the spherical caps covered by the filling angles δ_1 and δ_2

The wetting-non wetting interface is:

$$A_{wn}^* = \int 2\pi y^{*2} \sqrt{1 + y'^{*2}} dx^* \quad (18)$$

The other interfaces are calculated using the equation to calculate the interface of spherical cap using the values of the filling angles (δ_1 and δ_2).

The solid-wetting interface is:

$$A_{sw}^* = \frac{1}{R^2} (2\pi r_1^2 (1 - \cos(\delta_1)) + 2\pi * r_2^2 (1 - \cos(\delta_2))) \quad (19)$$

The solid-non wetting interface is:

$$A_{sn}^* = \frac{1}{R^2} (2\pi r_1^2 (1 + \cos(\delta_1)) + 2\pi * r_2^2 (1 + \cos(\delta_2))) \quad (20)$$

As for the rupture distance of the meniscus connecting the grains, it is determined automatically when there is no possible physical solution for Laplace equation.

3 Lookup table.

For different imposed R , p_c^* and D^* values (D refers to the distance between the particles), all these variables are calculated and saved in text data files, to be used in the simulations. The values of the imposed input values cover all the possible range of solution. R varies from 0.1 to 1 to allow simulating different particle size distribution in the packing, D^* cover the range of distance from the formation to the rupture of the bridge, and the suction varies from 0 to very high suction values. The look up table methods that consists in creating the data file that replaces the runtime computations makes the calculations much faster.

During the simulation at imposed suction, the grain size particles, their positions are known. The trio (R, p_c^*, D^*) can be deduced. The discrete set of solutions in the text files is triangulated using Delaunay triangulation, and the capillary force applied to the particles and the other variables are obtained by interpolation. This interpolation is called the P-Based interpolation and is used to simulate drained quasi-static simulations.

The values obtained from the interpolation in the text files are normalized, and need to be re-upscaled to the real particles size distribution present in the sample.

Another type of simulations is also possible in the capillary law code. The V-Based interpolation is then introduced. The input variables for the V-Based interpolation are (R, V^*, D^*) and the same procedure is repeated with different triangulation set.

Simulations are done on two grains connected by a water bridge and the variation of the force and the geometric properties of the meniscus are plotted as function of the distance separating the grains in the case of P-Based and V-Based interpolations in figure 2.

It is noticed that for the capillary force and interfaces, the results are the same for grains moving at constant suction or constant volume of water up to a critical value ($D^*=0.03$) before they start diverging.

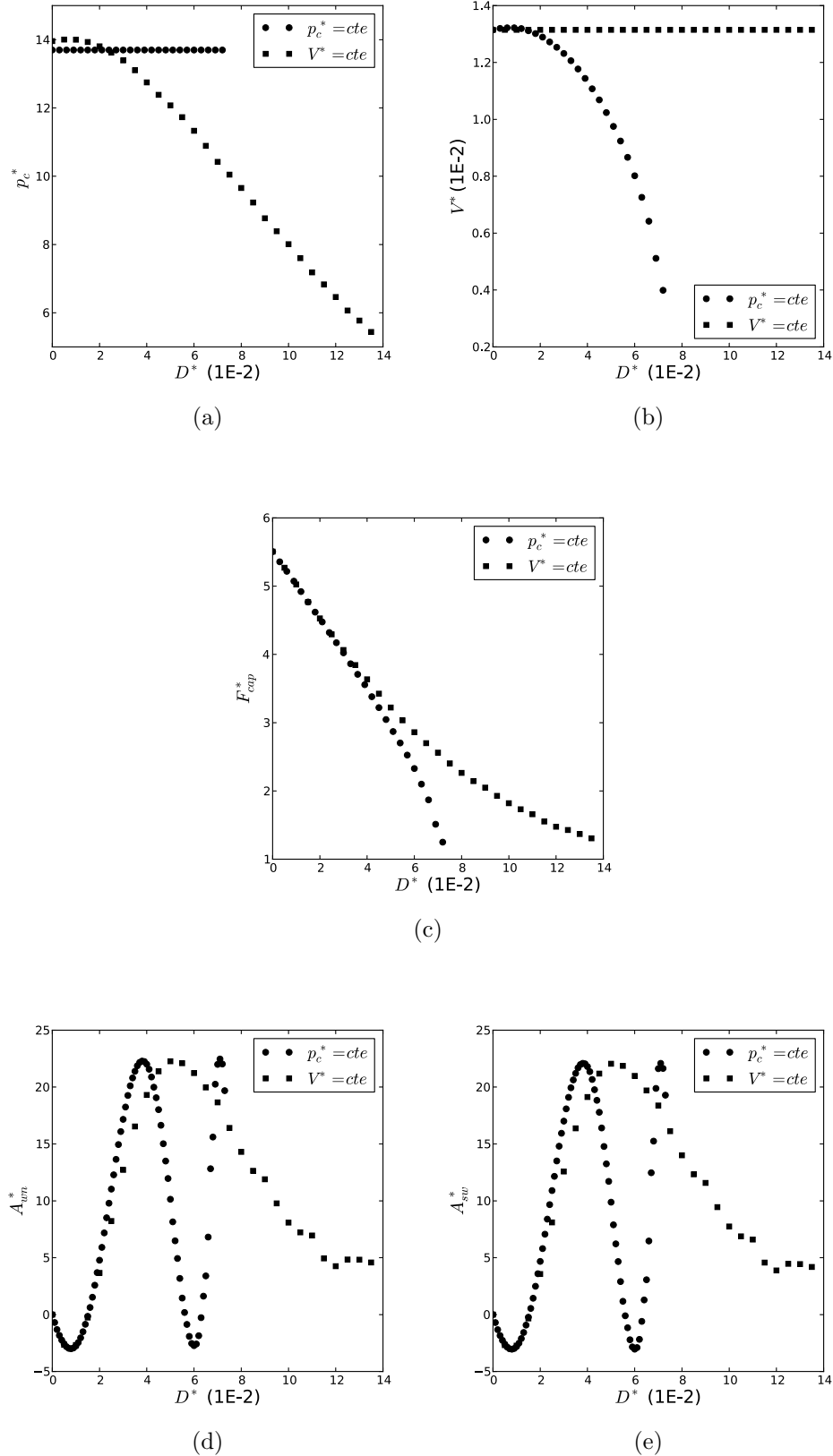


Figure 2: The variation as function of the distance of (a)-suction , (b)-volume of the bridge , (c)-capillary force, (d)-wetting-non wetting interface and (e)-solid-wetting interface for constant suction and volume.

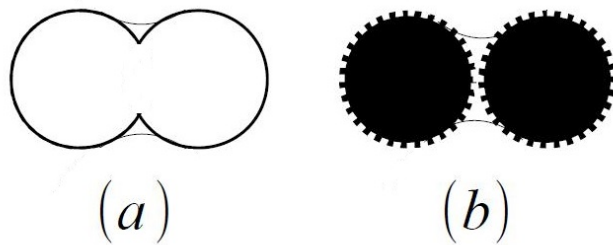


Figure 3: Illustration of 2 grains connected by a meniscus with (a) negative roughness and (b) positive roughness.

4 Roughness of the grains

Another aspect added to the capillary law in YADE is the roughness of the grains. The roughness aspect helps representing the real shape of the grains and the dependence of the capillary effect on that. The model is based on the work of [9]. The roughness is represented by considering that the meniscus is formed between spherical grains slightly smaller or bigger than the grains for the contact law. The roughness can be then either positive or negative. In the case of positive roughness, the grains are touching through asperities (figure 3(b)). When the roughness is negative, the sphere has some plane surfaces, and it's volume is smaller than the sphere used for the capillary law law(figure 3(a)). The model is not able to describe the behavior of quite angular grain shape.

The value κ of the roughness is taken into account for each grain as following:

$$r = r - r * \kappa \quad (21)$$

The way the roughness is taken into account in the DEM code is represented in figure 4.

In the case of packing, a mean value of the roughness κ_m and the value of the dispersion from the mean value in such a way to have a uniform distribution of the values of roughness are defined.

The impact of the roughness on the capillary force is shown in figure 5. It is noticed that for smooth grains in contact, the force is almost constant with the change of suction. For positive roughness, the capillary force decreases with increasing suctions. The negative roughness instead increases the value of the capillary force with increasing suction.

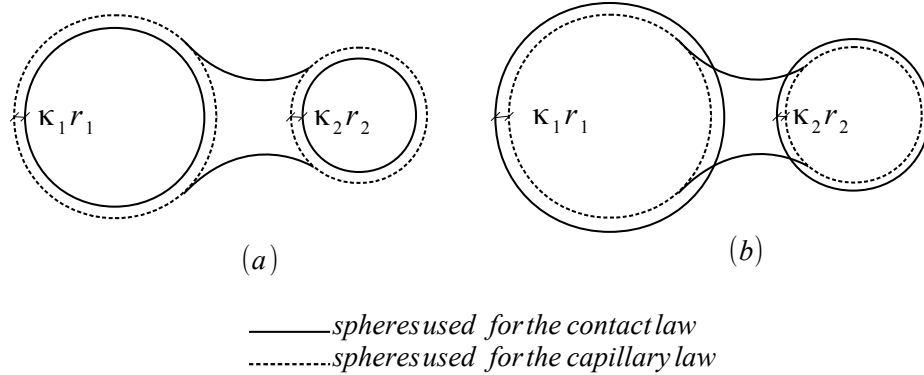


Figure 4: Illustration of a liquid bridge taking into account the roughness in the DEM capillary law for (a) negative roughness and (b) positive roughness.

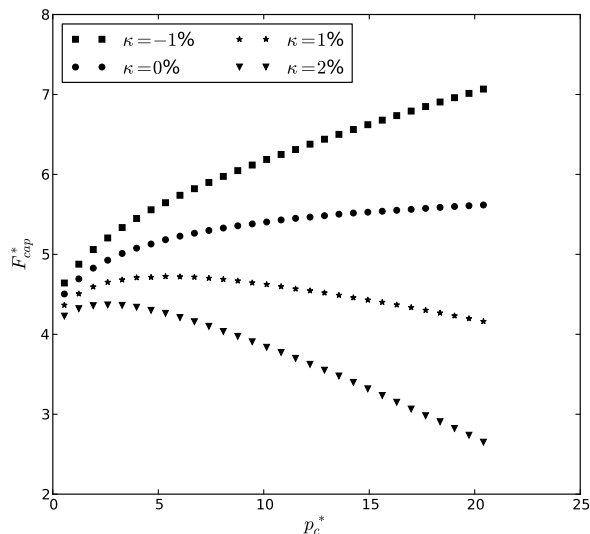


Figure 5: The influence of the roughness on the capillary force.

5 Conclusion

The numerical model presented hereabove offers a consistent framework for studying unsaturated materials. It provides accurate values of interfacial areas, a cornerstone

of thermodynamics and variational methods applied to such materials. This method was used to produce results which serve as a base in the companion oral presentation. Therein, the validity of Love-Weber stress tensor $\sigma_c = \frac{1}{V} \sum f \otimes l$ for defining the effective stress in three phase materials ([12]) is discussed.

REFERENCES

- [1] Cundall, P. A., and Strack, O. D. A discrete numerical model for granular assemblies. *Géotechnique* (1979) **29(1)**:47–65
- [2] Dangla, P. and Coussy, O. Approche énergétique du comportement des sols non saturés. *Mécanique des sols non saturés* (2002)
- [3] Gili, J. and Alonso, E. Microstructural deformation mechanisms of unsaturated granular soils. *Int. J. Numer. Anal. Met.* (2002) **26(5)**:433–468
- [4] Gray, W.G. and Schrefler, B.A. Thermodynamic approach to effective stress in partially saturated porous media. *Eur. J. Mech. A-Solid* (2001) **20(4)**:521–538
- [5] Hassanizadeh, S.M. and Gray, W.G. Mechanics and thermodynamics of multiphase flow in porous media including interphase boundaries. *Adv. Water Resour.* (1990) **13(4)**:169–186
- [6] Hotta, K., Takeda, K., Iino, K. The capillary binding force of a liquid bridge. *Powder Technol.* (1974) **10(4)**:231–242
- [7] Jiang, M., Leroueil, S. and Konrad, J. Insight into shear strength functions of unsaturated granulates by dem analyses. *Comput. Geotech.* (2004) **31(6)**:473–489
- [8] Lian, G., Thornton, C. and Adams M.J. A theoretical study of the liquid bridge forces between two rigid spherical bodies. *J. Colloid Interface Sci.* (1993) **161(1)**:138–147
- [9] Molenkamp, F. and Nazemi A.H. Interaction between two rough spheres, water bridge and water vapour. *Géotechnique* (2003) **53(2)**:255–264
- [10] Nikooee, E., Habibagahi, G., Hassanizadeh, S.M. and Ghahramani, A. Effective stress in unsaturated soils: A thermodynamic approach based on the interfacial energy and hydromechanical coupling. *Transport Porous Med.* (2013) **96(2)**:369–396
- [11] Scholtès, L., Hicher, P.Y., Nicot F., Chareyre B. and Darve, F. On the capillary stress tensor in wet granular materials. *Int. J. Numer. Anal. Met.* (2009) **33(10)**:1289–1313
- [12] Scholtès, L., Chareyre, B., Nicot, F., and Darve, F. Micromechanics of granular materials with capillary effects. *Int. J. Eng. Sci.* (2009) **47(1)**:64–75

- [13] Soulie, F., Cherblanc, F., El Youssoufi M.S. and Saix C. Influence of liquid bridges on the mechanical behaviour of polydisperse granular materials. *Int. J. Numer. Anal. Met.* (2006) **30(3)**:213–228

NUMERICAL SIMULATION OF SHAPED CHARGE JET PENETRATING A PLATE USING SMOOTHED PARTICLE HYDRODYNAMICS

ZHANG ZHIFAN, MING FUREN AND ZHANG AMAN

College of shipbuilding engineering
Harbin Engineering University, Harbin 150001, China
zhangzhifan@hrbeu.edu.cn, mingfuren2006@126.com, zhangaman@hrbeu.edu.cn

Key words: SPH Method; Shaped Charge Jet; Underwater Explosion; Damage Characteristics.

Abstract. The shaped charge jet has a stronger penetration effect onto the structure than normal charges. The SPH method with mesh-free and Lagrange properties has an advantage to solve extremely dynamic problems, such as large-deformation, moving interface and multiphase mixing and so on. Therefore, the SPH method is applied to simulate shaped charge detonation, jet formation and its penetration into a plate. And a SPH model of the shaped charge penetrating the plate is established. Firstly, the simulation of the shaped charge detonation is conducted to study the shock wave propagation and underwater explosion shock loading. Secondly, the formation of the metal jet is studied, and the jet velocity and the pressure are investigated in detail. Finally, the damage characteristics of the plate subjected to the metal jet and underwater explosion shock loading are discussed. The whole analysis and conclusions provide a reference for the structural design of shaped charge warheads.

1 INTRODUCTION

The shaped charge jet (SCJ) associated with underwater explosion can cause server damages to warships and submarines; it is one of the major threats and research focuses of navy platform technology. The three stages, namely detonation, formation of the metallic jet and its impact on the target plate, are included when a plate is penetrated by the metal jet. Although experimental research ^[1-5] is the most effective and direct countermeasure to investigate the formation of the jet and the SCJ penetration, it has disadvantages of less-safety and high-cost as well as unrepeatability. Therefore, numerical method is usually combined with experiments to study the performance of shaped charge. Modeling and simulation have been used to develop the shaped charge and test configuration by Baker ^[6]. Basic investigations were continued with theoretical studies supporting the findings in ^[7] by numerical simulations of the SCJ perforation ^[8]. Cheng ^[9] has employed some real explosion test data regarding the perforation size and penetration depth to verify the numerical simulation.

However, large deformation of liner, steel and explosion products may be caused during the jet penetrating the plate, and there will be computational difficulties (e.g. grid distortion) to be overcome while using the finite element method ^[10-12] as a result. The Smoothed Particle Hydrodynamics (SPH) method ^[13-20] has natural advantages in simulating the SCJ penetration and underwater explosion because its mesh-less nature is suitable for solving

problems of large deformation, and its Lagrangian nature makes it extremely easy to capture material interfaces. In addition, explosively-formed projectile (EFP), a new kind of shaped charge, has higher penetration ability. Therefore, the SPH method is adopted to simulate the shaped charge jet (SCJ) associated with underwater explosion, with the analysis of characteristics of shock wave propagation, the formation process of metal jet (EFP formation with hemispherical liner) and damage characteristics of the plate.

2 THEORETICAL BACKGROUND

2.1 SPH Equations of Motion

In SPH method, the approximation of function $f(x)$ and its derivative $\nabla \cdot f(x)$ can be discretized as^[21]

$$f(\mathbf{x}_i) \approx \sum_j \frac{m_j}{\rho_j} f(\mathbf{x}_j) W_{ij} \quad (1)$$

$$\nabla \cdot f(\mathbf{x}_i) \approx \sum_{j=1}^N \frac{m_j}{\rho_j} f(\mathbf{x}_j) \cdot \nabla_i W_{ij} \quad (2)$$

Thus, the conservation of mass, momentum and energy in SPH can be expressed as (regardless of body force)^[21, 22]:

$$\begin{bmatrix} \frac{d\rho_i}{dt} \\ \frac{d\mathbf{v}_i^a}{dt} \\ \frac{de_i}{dt} \end{bmatrix} = \begin{bmatrix} m_i \sum_{j=1}^N \mathbf{v}_{ij}^b \\ -\sum_{j=1}^N \frac{m_j}{\rho_j} \left(\frac{\sigma_i^{ab} + \sigma_j^{ab}}{\rho_i} + \Pi_{ij} \right) \\ \frac{1}{2} \sum_{j=1}^N \frac{m_j}{\rho_j} \left(\frac{\sigma_i^{ab} + \sigma_j^{ab}}{\rho_i} + \Pi_{ij} \right) \mathbf{v}_{ij}^b \end{bmatrix} \cdot \frac{\partial W_{ij}}{\partial \mathbf{x}_i^b} \quad (3)$$

where ρ , m , \mathbf{v} , e , t , \mathbf{x} , σ denote density, mass, velocity, energy, time, coordinates and stress respectively; a and b indicate the direction along axis; W_{ij} is the smoothed function of a pair of particles i and j , the cubic spline function is applied in present paper; Π_{ij} represents artificial viscosity^[21].

2.2 Constitutive model

In the process of strong impact such as underwater explosion, the viscosity of water and exploding gas is small and can be ignored. The pressure of detonation products and water can be obtained from Jones-Wilkins-Lee (JWL) EOS^[23] and Mie-Gruneisen equation of state^[24] respectively.

Jones-Wilkins-Lee (JWL) EOS^[23] for explosive gas is given by

$$P = A(1 - \frac{\omega\eta}{R_1})e^{-\frac{R_1}{\eta}} + B(1 - \frac{\omega\eta}{R_2})e^{-\frac{R_2}{\eta}} + \omega\eta\rho_0 e \quad (4)$$

where ρ_0 is initial density; D is detonation velocity; A , B , R_1 , R_2 and ω are experimental fitting coefficients; E_0 is detonation energy per unit mass. Parameters are shown in Tab. 1.

Table 1 Parameters in Jones-Wilkins-Lee (JWL) EOS for explosive gas [23]

ρ_0 (kg/m ³)	D (m/s)	A (Pa)	B (Pa)	R_1	R_2	ω	E_0 (J/kg)
1630	6930	3.74	3.75	4.15	0.90	0.35	6.0×10^6

Mie-Gruneisen equation of state [24] for water is expressed as

$$P = \begin{cases} \frac{\rho_0 C^2 \mu [1 + \left(1 - \frac{\gamma_0}{2}\right)\mu - \frac{a}{2}\mu^2]}{[1 - (S_1 - 1)\mu - S_2 \frac{\mu^2}{\mu + 1} - S_3 \frac{\mu^3}{(\mu + 1)^2}]^2} + (\gamma_0 + a\mu)e & \mu > 0 \\ \rho_0 C_0^2 \mu + (\gamma_0 + a\mu)e & \mu < 0 \end{cases} \quad (5)$$

where ρ_0 , C , η , a and E_0 denote initial density, sound velocity, density ratio before and after the perturbation, volume correction coefficient and initial energy respectively; S_1 , S_2 and S_3 are fitting coefficients. Parameters are shown in Tab. 2.

Table 2 Parameters in Mie-Gruneisen EOS for water [24]

ρ_0 (kg/m ³)	C (m/s)	γ_0	a	S_1	S_2	S_3	E_0 (J/kg)
998	1480	0.5	0	2.56	1.986	1.2268	357.1

However, the shear force of steel and copper with high shear strength should be taken into account. Steel and copper are used as the materials of the plate and the liner, respectively. The stress is composed of isotropic pressure P and deviatoric stress tensor S . For pressure P , Mie-Gruneisen EOS for solid mechanics [25] is introduced, given by

$$P = \left(1 - \frac{1}{2}\Gamma\eta\right) \cdot (\alpha\eta + \beta\eta^2 + \gamma\eta^3) + \Gamma\rho e \quad (6)$$

where Γ is Gruneisen parameter; if η is less than 0, $\beta = \gamma = 0$; $\alpha = \rho_0 C_s^2$, $\beta = \alpha[1 + 2(S_s - 1)]$ and $\gamma = \alpha[2(S_s - 1) + 3(S_s - 1)^2]$, in which ρ_0 , C_s , S_s and E_0 denote initial density, linear

participation coefficient of impact velocity and particles velocity, slope and initial energy. Parameters are shown in Tab. 3.

Table 3 Parameters in Mie-Gruneisen EOS for steel and copper [25]

Material	ρ_0 (kg/m ³)	Γ	C_s (m/s)	S_s	E_0 (J/kg)
steel	7890	1.587	3075	1.294	0
copper	8960	2.0	3940	1.489	0

As for deviatoric stress tensor S , it be drawn from the stress rate \dot{S} by integration, and yet \dot{S} can be gained from Jaumann stress rate [21]. The Johnson-cook [26] model and Von Mises yield criterion are applied to calculate yield strength and determine whether the stress should be renewed through the comparison between Mises Stress σ_{Mises} and yield strength Y . If Mises Stress is less than the yield strength, there is no need to modify the stress component. On the contrary, the deviatoric stress S should be modified [27]. The Johnson-cook [26] model is given as

$$Y = \left[\sigma_0 + B_0 \varepsilon_e^n \right] \left[1 + C \ln \left(\dot{\varepsilon}_e / \dot{\varepsilon}_0 \right) \right] \left[1 - (T^*)^M \right] \quad (7)$$

where σ_0 , C and M denote the static yield strength, strain rate strengthening coefficient and thermal softening coefficient; B and n are strain hardening exponents; ε_e is equivalent plastic strain, i.e. $\varepsilon_e = 2\sqrt{3I_2}/3$, in which I_2 is the second invariant of deviator stress tensor; $\dot{\varepsilon}_e$ and $\dot{\varepsilon}_0$ denote equivalent plastic strain rate and reference strain rate, repectively; T^ϕ is dimensionless temperature corresponding to T , i.e. $T^\phi = (T - T_r)/(T_m - T_r)$, in which T_r is room temperature, T_m is melting temperature and $T = T_r + (e - e_0)/(MC_v)$, in which e , e_0 and C_v denote specific internal energy, initial specific internal energy and specific heat. Some parameters are listed in Table 4.

Table 4 Parameters in Johnson-Cook constitutive model for steel and copper [26]

Material	σ (MPa)	B (MPa)	$\dot{\varepsilon}_0$ (s ⁻¹)	n	C	m	T_m (K)	T_r (K)	C_v (J/kgk)
steel	350	275	1	0.36	0.022	1.0	1811	288	452
copper	90	292	1	0.31	0.025	1.09	1356	288	383

2.3 Some numerical techniques

(a) Variable Smoothing length

The accuracy and robustness of the SPH processor depends on the quality (in particular the number) of the local neighboring particles. In expansive flow of material, the distance

between SPH particles increases. If this distance exceeds twice the smoothing length of the particles, then the two particles will no longer interact. This loss of interaction may be unphysical and is commonly described as “numerical fracture”. In an attempt to reduce the problem of numerical fracture, an option to include a variable smoothing length has been included; as particles separate and their density decreases, their smoothing length increases so that interaction with neighboring particles is maintained [28-30].

(b) Artificial viscosity

The Monaghan Artificial Viscosity [21, 28] has been used to spread shocks over a few particle diameters (smoothing lengths), stabilize the numerical scheme and prevent particle penetration. This form of artificial viscosity includes a term which is a function of the local velocity field, a linear term, and one which is a function of the local velocity field squared. Each of these terms has a multiplying coefficient that can be adjusted depending on the type of problem being solved.

(c) Treatment of multi-materials

We use a slight penalty force of Lennard-Jones model [21] to solve interface problem, and the molecular force is so slight that it just prevents particles' penetration. When particles on both sides of an interface tend to penetrate, in the case where $r_0 \geq r_{ij}$, there would be a molecular force $F_{ij} = f \cdot [(r_0 / r_{ij})^a - (r_0 / r_{ij})^b] \cdot x_{ij} / r_{ij}^2$ acting on two approaching particles; where r_0 is cutoff radius and it is generally close to the initial spacing of particles and r_{ij} is the distance between particles i and j . The direction of the F_{ij} is along the center line of the particles, preventing the particle from penetrating; f , a and b are set parameters. Consequently, we use the ratio of r_0 to r_{ij} to deal with the interface; this can guarantee good numerical stability without errors caused by the smoothing length.

3 NUMERICAL SIMULATION

3.1 Numerical model

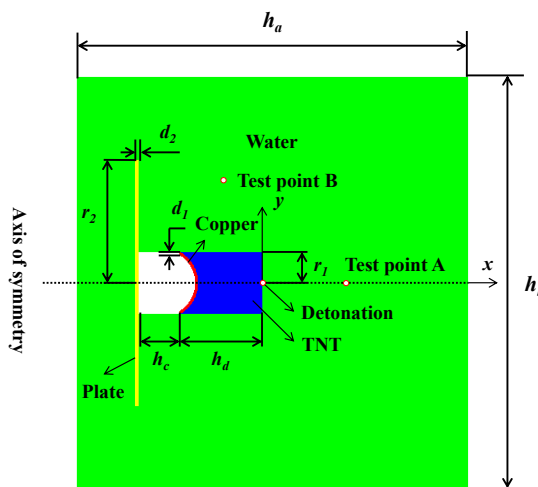


Figure 1 Distribution of particles

The model of shaped charge jet penetrating a plate subjected to underwater explosion can

be simplified as Figure 1. The relevant parameters are listed in Table 5. The material of the liner is copper. The column TNT is detonated from the center which is also the origin of coordinates. Test points A and B are located at (28, 0) and (-16, 43) respectively. The entire model is discretized with non-uniform particle spacing, 0.1m for the plate, copper and TNT and 0.2mm for water. There are 24000 steel particles, 3442 copper particles, 101676 TNT particles and 654500 water particles.

Table 5 Parameters in numerical model (mm)

h_a	h_b	h_c	d_1	d_2	r_1	r_2
190	200	20	1.0	2.0	15	60

3.2 Explosion process

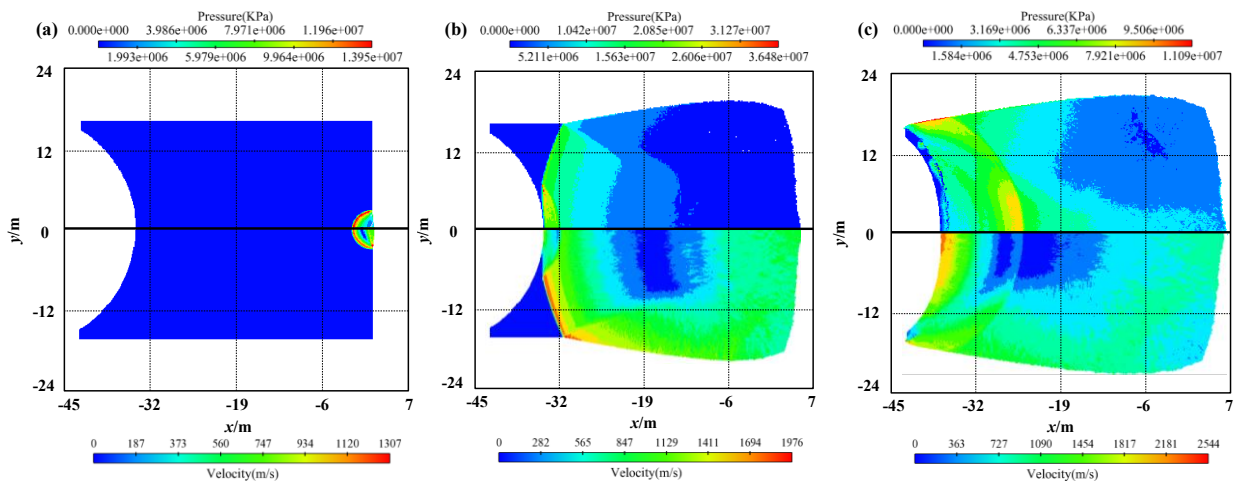


Figure 2 Pressure distribution (upper) and velocity distribution (lower) of TNT and copper in the explosion process; from (a) to (c) the times are: $t \approx 0.4 \mu\text{s}$, $4.8 \mu\text{s}$ and $6.4 \mu\text{s}$

Figure 2 illustrates the detonation process of the TNT. It can be seen that a spherical detonation wave is generated after the detonation, with the pressure up to about 14 GPa at 0.4 μs . As Figure 2(a) shows, the velocity on the wavefront reaches about 1307 m/s. After that, the detonation wave propagated with high speed and explosion products continued to expand. At 4.8 μs , the shock wave reached the liner and the pressure peak value soared to about 36 GPa as shown in Figure 2(b). The velocity rose slightly, peaking at about 1976 m/s on the boundary of explosion products. As can be seen from Figure 2(c), the detonation finishes at around 6.4 μs and the maximum pressure declined to about 11 GPa. It can also be observed from the pressure nephogram that there was a rarefaction wave reflected when the shock wave propagated to the liner whose other side is exposed to air. As a result, the pressure of explosion products gradually decreases. Figure 2(c) also shows that the maximum velocity went up to about 2544 m/s and it occurs around the symmetry axis. In addition, it is clear that the liner is accelerated under the tremendous pressure behind it as shown in Figures 2(b) and

2(c). Consequently, the numerical results agree with the basic laws of shock wave propagation.

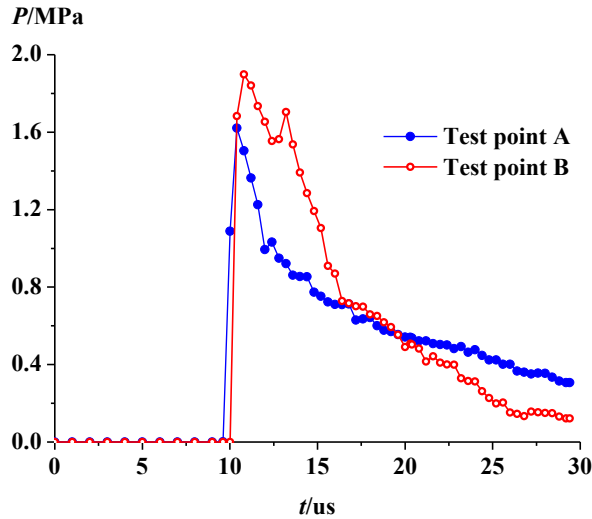


Figure 3 Pressure-time curve at tests point A and B

The time history curves of the shock wave pressure at test points A and B are shown in Fig. 3. Test points A and B are located in the axial and radial directions in the water area, which are marked in Fig. 2. It can be observed that the shock wave arrives at the test points at around 10 μ s, with the pressure shooting up to about 1.6 MPa and 1.9 MPa respectively. Obviously the radial pressure peak value at test point B is higher than that of the axial peak value at test point A. Subsequently, the pressure rapidly declined. There are two peaks of the curves, the first peak is caused by the direct wave of the explosion, and the second peak may just result from the second propagation. As the detonation waves propagating from the TNT to the water, the reflection waves will be generated and subsequently converged at the TNT center, which will lead to the generation of compressive waves back into water again. Comparing these two curves, we can also see that the tangent at point B is larger than that at point A after the pressure reaches the peak value, i.e. the radial pressure drops faster than the axial pressure. It is clear that the radial pressure becomes lower than the axial pressure after 18 μ s. Finally, the pressures at test points decrease to about 0.306 MPa and 0.121 MPa at about 30 μ s.

3.3 Formation of metal jet

After the detonation of TNT, the metal jet gradually is formed under the effect of the detonation wave. In this section, we will simulate the formation of the metal jet and discuss some variables (e.g. velocity, length and width of the metal jet) at special moments. Fig.4 and Tab. 6 illustrate the velocity distribution of the liner in the formation of metal jet and some variables, respectively.

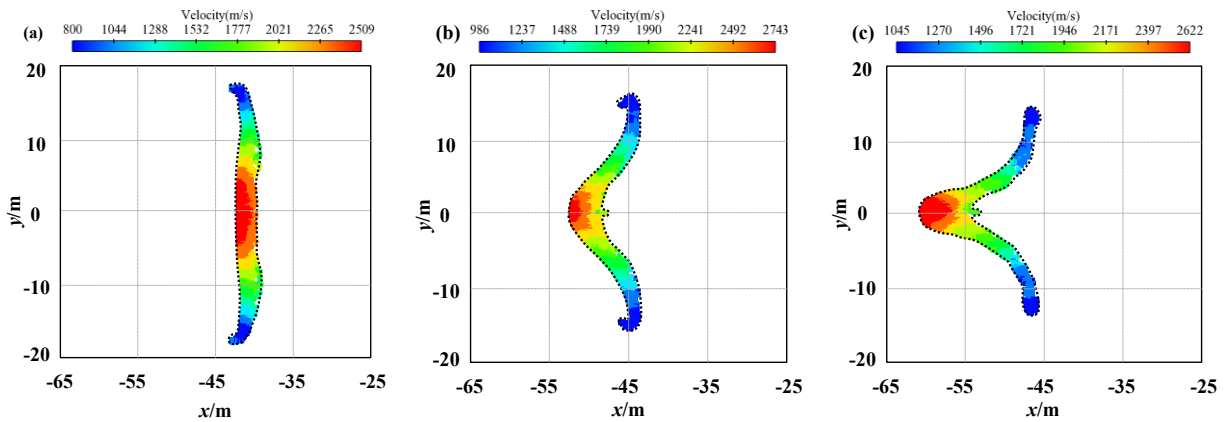


Figure 4 Velocity distribution of copper in the formation of metal jet; from (a) to (c) the times are: $t \approx 9.2 \mu\text{s}$, $12.8 \mu\text{s}$ and $16 \mu\text{s}$

Fig.4 shows the velocity distribution of liner in the formation of metal jet. Hemispherical liner is chosen as the liner. As can be seen from Fig. 4(a), under the effect of the detonation wave of the liner is squeezed and plastic large-deformation of the liner comes out, with the top of the liner rolling over. The detonation products at the end with the hollow cavity converge towards the centerline, i.e. axis of symmetry, at high velocity as high as 2509 m/s. With the deformation of the liner, the pressure turns the original outer surface into inner surface, with the original inner surface converted to the outer surface. Besides, we can see from Fig. 4(b) that due to the effect of axial tension and radial compression, the liner converges to the axis of symmetry, and the initial metal jet (EFP) with a high speed is formed. The velocity reaches its peak at $12.8 \mu\text{s}$ and it is as high as about 2743 m/s. Subsequently, the velocity declines gradually and it dropped to around 2622 m/s at $16 \mu\text{s}$. It can be observed that the inner surface has turned into the jet head and the metal jet is elongated to several times of its initial length as Fig. 4(c) shown.

Table 6 Jet velocity, length and width at special moments (mm)

Parameters of metal jet	Time (μs)		
	9.2	12.8	16.0
Velocity (m/s)	2509	2743	2622
Length (mm)	-	2.2	4.5
Width of jet head (mm)	-	3.6	3.8

Tab. 6 gives the information of parameters of metal jet, namely velocity, length and width, at special moments. At $9.2 \mu\text{s}$, the original inner surface of liner begins to be transformed into the outer surface. The velocity of jet head rises to its maximum at $12.8 \mu\text{s}$. At the same time, the initial metal jet is produced, with the length and width being 2.2 mm and 3.6 mm, respectively. At $16.0 \mu\text{s}$, the metal jet is poised to penetrate the plate. Besides, the length and

the width are larger than the initial ones.

3.4 Metal jet penetrating a plate

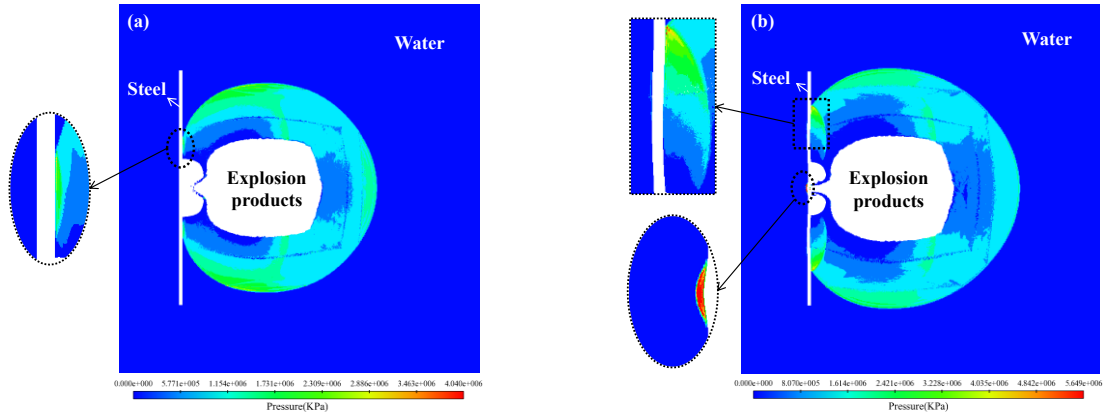


Figure 5 Pressure nephogram of water; from (a) to (b) the times are: $t \approx 14.0 \mu\text{s}$ and $16.8 \mu\text{s}$

Pressure nephogram of water is shown as Fig. 5. It is clear that the shock wave reaches the steel at $14.0 \mu\text{s}$ as shown in Fig. 5(a), and a reflected shock wave is generated in the water as a result, which is presented in the elliptical region. It can also be observed in Fig. 5(a) that the shock wave arrives at the steel earlier than the jet. Subsequently, the reflected shock wave propagates in the water and the directive wave leads to the deformation of the steel, which is shown in the rectangular region in Fig. 5(b). Besides, as the elliptical region in Fig. 5(b) shows, the shock wave generated at the jet head has passed through the steel and arrived at the water on the other side of the steel.

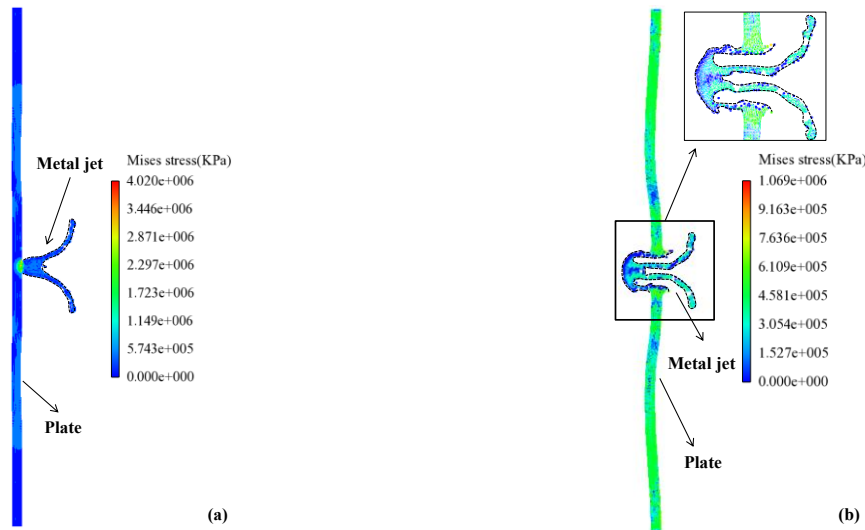


Figure 6 Mises stress distribution of steel and copper; from (a) to (b) the times are: $t \approx 16.4 \mu\text{s}$ and $21.2 \mu\text{s}$

Fig. 6 illustrates mises stress distribution of steel and copper in the process of metal jet penetrating the plate. According to Fig. 6(a), we can see that the jet begins to penetrate the plate, with the stress up to about 4 GPa. Besides, it is clear that there are not only a reflected

shock wave but also a shock wave generated in the steel as shown in Figs. 5(b) and 6(a). After that, the middle of the plate is completely penetrated by the metal jet and the plate subjected to the shock wave load produces deformation at 18.4 μ s. At the same time, the stress decreases to about 1.1 GPa at 21.2 μ s. In addition, it can be observed that the main failure mode is plastic large-deformation and tensile failure as shown in Fig. 6.

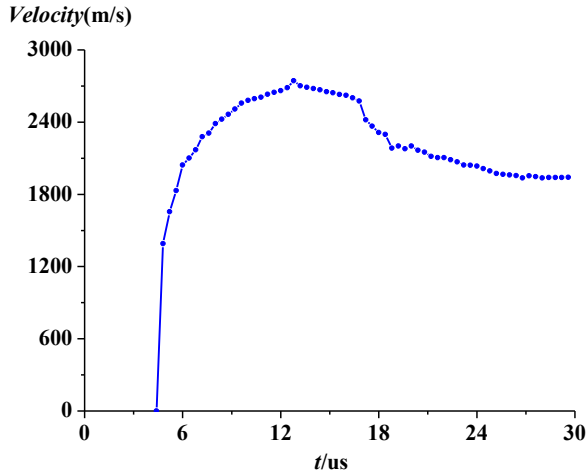


Figure 7 Velocity-time curve of the liner

Velocity-time curve of the liner is shown in Fig. 7. It can be seen that the figure rises dramatically after the detonation wave reaches the liner, peaking at 2743 m/s at 12.8 μ s. At this moment, the initial metal jet is formed. After that, the velocity begins to decrease and has slightly dropped to around 2602 m/s at 16.0 μ s. Subsequently, due to the impact effect of the jet on the plate, the velocity of the jet falls again but more steeply, reaching about 2297 m/s at 18.4 μ s. After the plate is completely penetrated by the metal jet, the velocity experiences a slight decline, with the velocity decreasing to about 2104 m/s at 22 μ s. Finally, the curve remained stable at 25.6 μ s and the velocity is as high as about 1941 m/s at 29.6 μ s.

4 CONCLUSIONS

An SPH method with mesh-free and Lagrange properties is applied to solve extremely dynamic problems of a plate penetrated by shaped charge jet (SCJ) associated with underwater explosion in this paper. The whole process of such a complex physical phenomenon as SCJ penetrating the plate is simulated, including three phases, namely the detonation, the formation of metal jet and the penetration. The following conclusions can be drawn through the analysis of shock wave propagation, jet velocity and damage characteristics of the plate: (a) the numerical results agree with the basic laws of shock wave propagation and the shock wave arrives at the plate prior to the metal jet; (b) the velocity of the jet increases first and then decrease, peaking at about 2743 m/s; (c) the crevasse of the plate is caused by the penetration of the metal jet and the deformation of the plate arises from underwater explosion shock wave as well.

ACKNOWLEDGE

The project is supported by The Scientific Research Foundation for Returned Overseas Chinese Scholars, Heilongjiang Postdoctoral Sustentation Fund (LBH-Q11136) and Harbin Science and Technology Innovation Fund.

REFERENCES

- [1] Kibe, S., Yamamoto, T. and Katayama, M. Development of conical shaped charge and remaining problems. *50th IAF Congress*, IAA-99-1AA.6.5.03, Amsterdam, 4-8 Oct. (1999).
- [2] Hu, G.L., Liu, R.Z. and Li, B. et al. Power Experiments on Compound Torpedo Warhead Assembly. *Journal of Nanjing University of Science and Technology* 29 (2005): 6-8. (in Chinese)
- [3] Hornemann, U. and Holzwarth, A. Shaped charge penetration in alumina targets. *Int. J. Impact Engng* (1997) **20**: 375-386.
- [4] Huang, Hongfa. Characterization of Powder Metal Jet and Penetration Calculation. *Procedia Engineering* (2013) **58**: 471-478.
- [5] Manfred, H. Disturbance of Shaped Charge Jets by Bulging Armour. *Propellants, Explosives, Pyrotechnics* (2001) **26**: 191–195.
- [6] Ernest, L.B., James, P. and Timothy, M. et al. Shaped Charge Jet Characterization and Initiation Test Configuration for IM Threat Testing. *Procedia Engineering* (2013) **58**: 58-67
- [7] Werner, A. and Ernst, R. Shaped Charge Jet Initiation Phenomena of Plastic Bonded High Explosives. *Proceedings of the 2012 Insensitive Munitions & Energetic Materials Technology Symposium (IMEMTS)*, Las Vegas, NV, USA, May 14-17. (2012)
- [8] Werner, A. and Ernst, R. High Explosive Initiation Behavior by Shaped Charge Jet Impacts. *Procedia Engineering* (2013) **58**: 184-193
- [9] Cheng, S.Q., Chen, G.J. and Zhao, H.G. Numerical Damage Analysis of Shaped Charge Warheads on Double-Deck Target Plates. *Chinese Journal of Ship Research* (2013) **8**: 53-57 (in Chinese)
- [10] Hans, U.M. Review: hydrocodes for structure response to underwater explosion. *Shock and Vibration* (1999) **6**:81-96.
- [11] Benson, D.J. Computational methods in Lagrangian and Eulerian hydrocodes. *Computer Method in Applied Mechanics and Engineering* (1992) **99**: 235-394.
- [12] Charles, E. and Anderson, Jr. An overview ofthe theory ofhydrocodes. *International Journal of Impact Engineering* (1987) **5**: 33-59.
- [13] Liu, M.B., Liu, G.R. and Lam, K.Y. Comparative study of the real and artificial detonation models in underwater explosions. *Electronic Modeling* (2003) **25**: 113-124.
- [14] Liu, M.B., Liu, G.R. and Lam, K.Y. A one dimensional meshfree particle formulation for simulation shock waves. *Shock Waves* (2003) **13**:201-211.
- [15] Liu, M.B., Liu, G.R. and Zong, Z. et al. Smoothed particle hydrodynamics for numerical simulation of underwater explosions. *Computational Mechanics* (2002) **30**:106-118.
- [16] Feng, D.L., Liu, M.B. and Li, H.Q. et al. Smoothed particle hydrodynamics modeling of linear shaped charge with jet formation and penetration effects. *Computers & Fluids* (2013) **86**: 77-85.

- [17] Yang, G., Han, X., Hu, D.A. Computer simulation of two-dimensional linear-shaped charge jet using smoothed particle hydrodynamics. *Engineering Computations: International Journal for Computer-Aided Engineering and Software* (2011) **28**: 58-75.
- [18] Qiang, H.F., Wang, K.P. and Gao, W.R. Numerical Simulation of Shaped Charge Jet Using Multi-Phase SPH Method. *Tianjin Univ.* (2008) **14**: 495-499.
- [19] Zhang, A.M., Yang, W.S. and Yao, X.L. Numerical simulation of underwater contact explosion. *Applied Ocean Research* (2012) **34**: 10-20.
- [20] Zhang, A.M., Yang, W.S. and Huang, C. et al., Numerical simulation of column charge underwater explosion based on SPH and BEM combination. *Computers & Fluids* (2013) **71**: 169-178.
- [21] Liu, G.R. and Liu, M.B. Smoothed Particle Hydrodynamics - A Meshfree Particle Method. *Singapore: World Scientific Publishing Co. Pte. Ltd* (2003).
- [22] Zhang, Z.F., Ming, F.R. and Zhang, A.M. Damage Characteristics of Coated Cylindrical Shells Subjected to Underwater Contact Explosion. *Shock and Vibration* (2014) **2014**.
- [23] Dobratz, B.M. LLNL Explosive Handbook: properties of chemical explosives and explosives and explosive simulants. *Report UCRL 52997*, Lawrence Livermore National Laboratory, Livermore, Calif, USA. (1981).
- [24] Steinberg, D.J. Spherical explosions and the equation of state of water. *Lawrence Livermore National Laboratory*. Livermore, CA, (1987)
- [25] Libersky, L.D., Petschek, A.G. and Carney, T.C. et al. High strain lagrangian hydrodynamics a three dimensional SPH code for dynamic material response. *Journal of Computational Physics* (1993) **109**: 67-75.
- [26] Johnson, G.R. and Cook, W.H. A constitutive model and data for metals subjected to large strains, high strain rates and high temperatures. In *Proc. 7th International Symposium on Ballistics*, USA, (1983).
- [27] Meyer, M.A. Dynamic behavior of materials. *JOHN WILEY & SONS INC*, USA. (1994).
- [28] Clegg, R.A., Hayhurst, C.J. Development of a Smooth Particle Hydrodynamics Option for Continuum Hydrocodes, Final Report, User Instructions. *DRA Contract No. WSF/798, Century Dynamics Report No. R066:01*, (1996).
- [29] Clegg, R.A., Sheridan, A.J. Hayhurst, C.J. et al. The Application of SPH Techniques in AUTODYN-2D to Kinetic Energy Penetrator Impacts on Multi-Layered Soil and Concrete Targets. *8th International Symposium on Interaction and Effects of Munitions with Structures*, USA, (1997).
- [30] Hayhurst, C.J., Clegg, R.A. Cylindrically Symmetric SPH Simulations of Hypervelocity Impacts on Thin Plates", *Int. J. Impact Engng* (1997) **20**: 337-348.

NUMERICAL STUDY OF FLUID-STRUCTURE INTERACTION WITH MACRO-SCALE PARTICLE METHODS

GUANGZHENG ZHOU

State Key Laboratory of Multiphase Complex Systems, Institute of Process Engineering,
Chinese Academy of Sciences, Beijing 100190, China
E-mail address: gzzhou@ipe.ac.cn

Key words: Fluid-structure interaction, Particle methods, Smoothed particle hydrodynamics,
Macro-scale pseudo-particle modelling, Gas-solid suspension, Outflow.

Abstract The problems of fluid-structure interaction (FSI) are often encountered in different industries as well as the nature. The macro-scale particle methods are advantageous in the FSI simulations, which include smoothed particle hydrodynamics (SPH), macro-scale pseudo-particle modelling (MaPPM), and so forth. Compared with the grid-based numerical techniques, particle methods could provide the flow and/or deformation details without complex tracking of interfaces. The progress of FSI simulation of multiphase flows with rigid particles is presented, and some major findings about heterogeneous structures are stressed. Meanwhile, weakly compressible outflow from elastic tube is investigated, and some preliminary results of flow details are presented. The possible development of macro-scale particle methods in the FSI simulation is prospected finally.

1 INTRODUCTION

The problems of fluid-structure interaction (FSI) are extensively encountered in many industrial applications as well as biological systems, such as multi-phase flows in fluidized beds, transports in flexible pipeline, and coupled membrane-fluid systems. In general, they are often too complex to be solved analytically, while numerical simulation could play an important role in this aspect. The well-known arbitrary Lagrangian-Eulerian method^[1] (ALE) formulates the fluid field on deforming grids, and takes into account the convection of these grid points. Nevertheless, the remeshing procedure in ALE is usually rather complicated and also computationally expensive, particularly for large deformation. On the other hand, the fluid domain of immersed boundary method^[2] (IBM) is based on uniform background grids, and the immersed set of boundary points interact with the fluid through the introduction of body forces. Actually, the distributed Lagrange multiplier based fictitious domain method^[3] (DLM\FDM) shares many similarities with IBM, but the force between the fluid and structure in DLM\FDM is distributed using an integral formulation. However, there still exists some difficulty in the accurate representation of structure with finite volume and/or complicated constitutive laws in the above two fixed grid methods as well as their variants.

In contrast, macro-scale particle methods offer notable advantages in FSI problems, including smoothed particle hydrodynamics^[4,5] (SPH), macro-scale pseudo-particle modelling^[6] (MaPPM), moving particle semi-implicit (MPS) method^[7], and so forth. In these approaches, the continuum is discretized into a collection of particles without background

meshes, and these particles move in Lagrangian manner according to the macro-scale interaction with their neighboring ones. Consequently, the large deformation of material interface or free surface is naturally handled without the vexing problem of mesh distortion. Actually, the classical SPH method originally developed for astrophysical contexts, has been extended to various fields due to the conceptual simplicity^[8,9], including turbulent flow, multiphase flows, non-Newtonian flows, and elastic dynamics.

In the FSI simulations with particle methods, complex tracking of interface is completely avoided. However, the structure/solid could be rigid or elastic, which corresponds to totally different treatment. As for the rigid solids usually in the form of a large number of particles, the interactions between particles are generally depicted by the discrete element method (DEM)^[10,11]. DEM follows the motion of every particle, while their interactions are based on certain contact model. On the other hand, for the interaction between elastic structure and fluid, both of them could be simulated by unified SPH descriptions with their own constitutive relations. However, the classical SPH generally suffers from the problem of so-called “tensile instability” in the simulations of elastic or brittle solid^[8]. When the SPH particles are under a tensile state, they tend to form small clumps, resulting in unphysical fractures eventually. The source of this instability has been analyzed in details by Swegle et al.^[12], and several techniques have been proposed to remedy this drawback, such as adding extra stress points^[13], corrective smoothed particle method^[14] (CSPM), and artificial stress method^[15,16]. In the artificial stress method, additional artificial stress was particularly incorporated into the momentum equation by mimicking atomic forces. The artificial stress exerted a small repulsive force for particles in the state of tensile stress, and thus effectively prevented them from clustering. Based on the analysis of the dispersion relation in elastic wave, the resulting algorithm of artificial stress was found to be effective and accurate for various benchmark problems in elastic dynamics^[16,17].

A good understanding of FSI phenomena is crucial to relevant industrial applications. As for the FSI problem of rigid solids, the direct numerical simulation (DNS) of classical multiphase suspensions is generally full of challenges due to its large computational cost. On the other hand, most simulations on FSI problems cope with the nearly incompressible fluid and hypoelastic structure^[17-19], and thus further study of FSI problems with weakly compressible flow would be quite significant. In this paper, the progress of FSI simulation of rigid particles is presented, which combines MaPPM (or SPH) with DEM. Also, weakly compressible outflow from elastic tube is investigated with unified SPH formulations, where a particular outflow boundary is applied, and the artificial stress is employed to remove the tensile instability in elastic solid. Besides, the outflow simulation is based on the previous researches on selective withdrawal from rigid microcavity^[20] and immiscible displacement in rigid cavity-fracture structures^[21].

2 NUMERICAL FORMULATIONS OF FSI PROBLEMS

2.1 SIMULATION OF FLUIDS

In nature, the macro-scale particle methods are based on interpolation theory. An arbitrary field variable $f(\mathbf{r})$ at location \mathbf{r} is evaluated as sum over a set of neighboring points (particles)

$$f(\mathbf{r}) = \sum_{j=1}^N \frac{m_j}{\rho_j} f(\mathbf{r}_j) W(\mathbf{r} - \mathbf{r}_j, h) \quad (1)$$

where m_j and ρ_j are the mass and density of particle j ; while $W(\mathbf{r} - \mathbf{r}_j, h)$ is the weighting function with h as its smoothing length. The weighting function should satisfy several requirements, including the normalization condition and the property of Dirac delta function. Among a number of weighting functions, the cubic spline is employed for both fluid and solid in the present work^[8].

Following Eq. 1, the local density of particle i is given by

$$\rho_i = \sum_j m_j W(|\mathbf{r}_i - \mathbf{r}_j|, h) \quad (2)$$

In regard to the SPH formulation of Navier-Stokes equation, there exist different forms of pressure component as well as viscous component. Based on the symmetric pressure which conserves linear and angular momentum exactly, the momentum equation of SPH particles could be written as^[22]

$$\frac{d\mathbf{v}_i}{dt} = -\sum_j m_j \left(\frac{P_i}{\rho_i^2} + \frac{P_j}{\rho_j^2} \right) \nabla_i W_{ij} + \sum_j \frac{m_j (\mu_i + \mu_j)(\mathbf{v}_i - \mathbf{v}_j)}{\rho_i \rho_j} \left(\frac{1}{r_{ij}} \frac{\partial W_{ij}}{\partial r_i} \right) + \mathbf{g} \quad (3)$$

where \mathbf{v} is the velocity, μ is the dynamic viscosity, and ∇_i denotes the gradient with respect to its coordinates.

Besides, the two-dimensional version of momentum equation in MaPPM^[6] is

$$\frac{d\mathbf{v}_i}{dt} = -c_f^2 \sum_j \frac{2}{\rho_i + \rho_j} \nabla_i W_{ij} + 4\mu \sum_j \frac{(\mathbf{v}_j - \mathbf{v}_i)W_{ij}}{0.25(\rho_i + \rho_j)(D_i + D_j)} + \mathbf{g} \quad (4)$$

$$D_i = \sum_j r_{ij}^2 W_{ij} \quad (5)$$

where c_f is numerical sound speed of fluid in the artificial state equation. The compressibility of fluid could be adjusted with suitable choice of numerical sound speed, and the incompressibility is approximately guaranteed through sufficiently large sound speed.

2.2 SIMULATION OF EALSTIC STRUCTURES

The stress tensor σ of momentum conservation could be decomposed into the isotropic pressure P and the deviatoric stress S . In regard to elastic solid with Hooks' law, the Jaumann rate is commonly adopted to satisfy the material frame indifference of large deformation. The evolution of deviatoric stress in elastic solid^[16,23] can be written as

$$\frac{dS^{\alpha\beta}}{dt} = 2G(\dot{\epsilon}^{\alpha\beta} - \frac{1}{3}\delta^{\alpha\beta}\dot{\epsilon}^{\alpha\beta}) + S^{\alpha\gamma}\Omega^{\beta\gamma} + \Omega^{\alpha\gamma}S^{\beta\gamma} \quad (6)$$

where G is the shear modulus, $\dot{\epsilon}$ is the strain rate, Ω is the rotation tensor, while superscripts α and β indicate the spatial coordinates.

Moreover, the momentum equation of solid can be depicted by the following form

$$\frac{d\mathbf{v}_i^\alpha}{dt} = -\sum_j m_j \left(\frac{\sigma_i^{\alpha\beta}}{\rho_i^2} + \frac{\sigma_j^{\alpha\beta}}{\rho_j^2} + \Pi_{ij} + R_{ij}^{\alpha\beta} f^q \right) \nabla_i W_{ij} + \mathbf{g} \quad (7)$$

where Π_{ij} and $R_{ij}^{\alpha\beta} f^q$ refer to the terms of artificial viscosity and artificial stress^[16], respectively.

Generally, the introduction of artificial viscosity could effectively enhance the stability of numerical algorithm. Among various types of artificial viscosity, a popular one^[24] is

$$\Pi_{ij} = \begin{cases} \frac{-\alpha_\Pi c_s \mu_{ij} + \beta_\Pi \mu_{ij}^2}{\bar{\rho}_{ij}}, & \mathbf{v}_{ij} \cdot \mathbf{r}_{ij} < 0; \\ 0, & \mathbf{v}_{ij} \cdot \mathbf{r}_{ij} > 0 \end{cases} \quad (8)$$

where c_s represents the numerical speed of sound in the solid, $\mu_{ij} = \frac{h \mathbf{v}_{ij} \cdot \mathbf{r}_{ij}}{\mathbf{r}_{ij}^2 + 0.01h^2}$, and

$\bar{\rho}_{ij} = \frac{\rho_i + \rho_j}{2}$. The linear term with α_Π produces shear and bulk viscosity, while the quadratic term with β_Π suppresses the unphysical penetration among particles.

In addition, the term of artificial stress has the expression^[16]

$$R_{ij}^{\alpha\beta} f^q = (R_i^{\alpha\beta} + R_j^{\alpha\beta}) \left(\frac{W(r_{ab})}{W(d)} \right)^q \quad (9)$$

where d is the initial interparticle distance, and q is a parameter. To obtain the artificial stress R , the original stress tensor is diagonalised for the signs of principal stresses, and the diagonal components of artificial stress in the rotated frame could be specified as follows

$$\bar{R}_i^{\alpha\alpha} = \begin{cases} -e \frac{\bar{\sigma}_i^{\alpha\alpha}}{\rho_i^2}, & \bar{\sigma}_i^{\alpha\alpha} > 0; \\ 0, & \bar{\sigma}_i^{\alpha\alpha} \leq 0 \end{cases} \quad (10)$$

where e is also a parameter. The artificial stress in the original coordinates is further calculated through rotating the coordinates back. Besides, the strain rate $\dot{\epsilon}$ and rotation tensor Ω in Eq. 6 are obtained with corresponding SPH formulations.

3 FSI SIMULATION OF MULTIPHASE FLOWS WITH RIGID PARTICLES

As for the gas-solid or liquid–solid multiphase flows in industrial systems, such as fluidized bed, the systems usually involve huge number of rigid particles. In the DNS simulation of such flows using SPH or MaPPM, the size of numerical particles should be much smaller than that of solid particles. Therefore, the computational cost is generally proportional to the involved particle number of the system. Potapov et al.^[25] carried out the investigation of liquid–solid flows combining SPH and DEM with soft-particle technique. In the shear-cell simulation, there were only 8 or 17 solid particles, corresponding to solid area fractions of 17% and 37%, respectively.

Furthermore, the simulation of gas-solid suspension with 1024 particles was implemented by coupling MaPPM and DEM with hard-sphere collisions^[26], based on the large-scale parallel

computing with CPU (central processing unit) clusters. The parallel was realized through message-passing interface (MPI) with the techniques of space-decomposition, shift-mode communication, and dynamic load balancing. The result revealed dynamic multi-scale structures characterized by heterogeneity with clustering solids. The solid particle velocity distribution was rather anisotropic, although it was nearly Maxwellian in each direction. The drag forces on the particles were also quite different, and locally structure-dependent to some extent. They were much larger in the dilute phase than those in the center of the dense phase, and become maximum on the phase interface. Besides, the distribution of drag force was somewhat close to the Gaussian function.

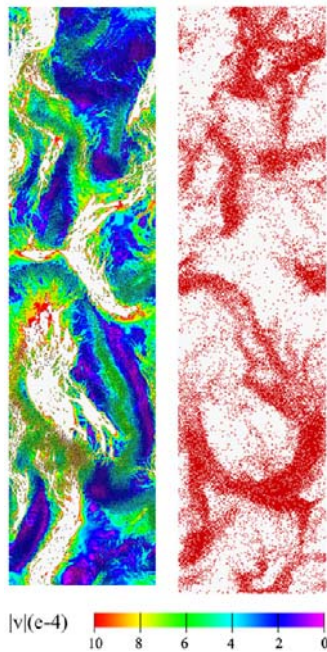


Figure 1: Heterogeneous structure with corresponding velocity field of a gas-solid suspension^[27]

With the newly developed general computing technique based on GPU (graphic processing unit), the large computational burden of DNS could be greatly alleviated. Actually, up to 30,000 fluidized solids were further simulated by MaPPM using GPU-based Mole-8.7 HPC (high performance computing) system^[27]. The GPU computing in a computer node was realised through CUDA (compute unified device architecture), while the data exchange between different nodes was implemented by MPI technique. Large speedup of nearly 19 folds for one GPU (NVIDIA GT200) over one typical CPU core was achieved. The result reproduced detailed destabilization process of initial uniform suspension and the following formation of solid clusters (Fig. 1). Moreover, the scale-dependence of some important parameters in the suspension with moderate solid/gas density ratio was also revealed. According to the statistical analysis on gas-rich dilute phase and particle-rich dense phase with relatively large solid/gas density ratio (beyond 1000), it was found that the drag coefficient was essentially dependent on the specific cluster configuration.

4 FSI SIMULATION OF OUTFLOW FROM ELASTIC TUBE

Deformation of elastic tube due to the flow of its inner fluids is quite common in both industrial systems and everyday life. To investigate the interaction between weakly compressible fluid and elastic structure, simulation of outflow from elastic tube is carried out with SPH method. As presented in Fig. 2, the particles are initially arranged in a densely packed array of hexagonal lattice inside the whole region. The outer hollow particles represent the elastic microtube, the inner solid bulk represents the fluid, and the solid particles on the rightmost side of the tube are the fixed ends. The flow inside the tube is induced by the control region, where all the particles automatically flow out with the following velocity

$$V_0 = \alpha \sqrt{\rho - \rho_{\text{cri}}} \quad (11)$$

where α is a flow coefficient depending on many factors, including the pressure difference between fluid and outer atmosphere, flow resistance inside the tube, and so forth. Besides, ρ_{cri} is the critical density of fluid, below which the flow would come to an end. When these particles leave the control region, they are immediately eliminated from the simulation. With the quick outflow of inner fluid, the density of fluid would decrease correspondingly, and thus the outflow velocity V_0 would become zero eventually.

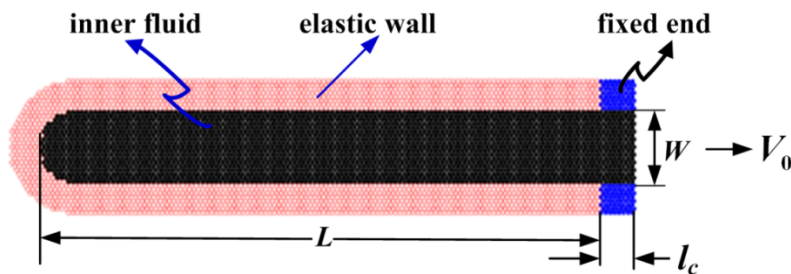


Figure 2: Sketch of elastic tube with initial particle distribution

In our simulation, the length and width of the microtube are $L=6.0\times 10^{-4}$ m and $W=1.0\times 10^{-3}$ m. The density of the fluid and solid are $\rho_f=0.92\times 10^3$ kg m⁻³ and $\rho_s=2.76\times 10^3$ kg m⁻³, respectively. The length of velocity control region is 4.0×10^{-5} m, the critical density of fluid ρ_{cri} (Eq. 11) is appointed as $0.85\rho_f$, and the flow coefficient α is 8.615×10^{-5} kg^{-0.5} m^{2.5} s⁻¹. The smoothing length h is 5.333×10^{-5} m, while the numbers of initial fluid particles and solid particles are 35,783 and 2498, respectively. Besides, according to the analysis on dispersion relation of elastic waves^[16], the parameters in the artificial stress (Eqs. 9 and 10) are $e=0.3$ and $q=4$. The simulation is switched on at the time $t=0$.

Fig. 3 displays some typical snapshots during the whole deformation process of elastic tube. With the continuous outflow of fluid in the control region, the inner fluid of the tube is induced to quickly flow out. Since the fluid is weakly compressible, its density gradually becomes smaller, which leads to the reduction of its pressure. The pressure reduction of fluid destroys the initial pressure balance between fluid and tube, resulting in the deformation of the elastic tube. As shown in Figs. 3a-c, with more and more fluid flows out of the tube, the deformation extent of tube increasingly becomes large. Meanwhile, the fluid density and

coreresponding pressure become smaller, and thus the outflow rate of fluid quickly reduces according to Eq. 11. Finally, the fluid flow completely stops due to the zero pressure difference between fluid and outer atmosphere. Fig. 3c is the steady state of this FSI system, where the deformation of tube reaches maximum and fluid density becomes minimum. Note that the deformation of tube in Fig. 3c is so large that the upper and lower sides of this tube nearly connect with each other in their central sections.

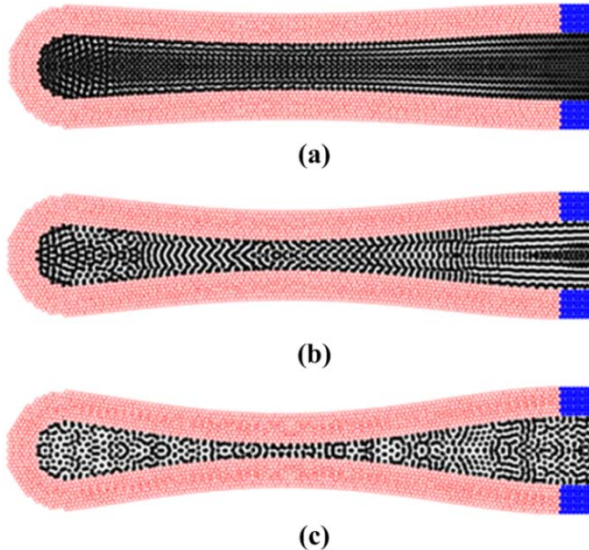


Figure 3: Deformation process of elastic tube due to the outflow of inner fluid:
0.2 s (a), 0.4 s (b), and 1.2 s (c)

4 CONCLUSIONS

As elucidated in the two FSI examples of rigid particles and elastic tube, the FSI simulations with macro-scale particle methods are suitable and also advantageous in providing flow and/or deformation details without complex tracking of interfaces in grid-based numerical techniques. Actually, SPH has been coupled with other particle methods to combine their respective advantages, such as element bending group for modeling flexible fibers^[28]. However, the computational cost of macro-scale particle methods is generally rather large (particularly for industrial systems), and thus the further development of efficient algorithm and computational decive would be quite significant in this regard. Besides, the outflow from elastic tube is only preliminarily investigated. Further extension to the liquid-liquid immiscible flows (such as water and oil) inside the large-scale complex ealstic and/or rigid structure network would be more meanfuling.

Acknowledgements

This work was supported by the National Key Basic Research Program of China under Grant No. 2015CB251402, the National Natural Science Foundation of China under Grant No. 21206167, 21225628, and 91334204, and the “Strategic Priority Research Program” of the

Chinese Academy of Sciences under Grant No. XDA07080203. The authors are grateful to Dr. Zhongcun Liu of China Petrochemical Corporation for some helpful discussions.

REFERENCES

- [1] Farhat, C., Geuzaine, P., and Brown, G. Application of a three-field nonlinear fluid-structure formulation to the prediction of the aeroelastic parameters of an F-16 fighter. *Comput. Fluids* (2003) **32**:3-29.
- [2] Mittal, R., and Iaccarino, G. Immersed boundary methods. *Annu. Rev. Fluid Mech.* (2005) **37**:239-261.
- [3] Yu, Z. A DLM/FD method for fluid/flexible-body interactions. *J. Comput. Phys.* (2005) **207**:1-27.
- [4] Lucy, L.B. A numerical approach to the testing of the fission hypothesis. *Astron. J.* (1977) **82**:1013-1024.
- [5] Gingold, R.A. and Monaghan, J.J. Smoothed particle hydrodynamics: Theory and application to non-spherical stars. *Mon. Not. R. Astron. Soc.* (1977) **181**:375-389.
- [6] Ge, W. and Li, J. Simulation of particle-fluid systems with macro-scale pseudo-particle modeling. *Powder Technol.* (2003) **137**:99-108.
- [7] Koshizuka, S. and Oka, Y. Moving-particle semi-implicit method for fragmentation of incompressible fluid. *Nucl. Sci. Eng.* (1996) **123**:421-434.
- [8] Liu, M. and Liu, G. Smoothed particle hydrodynamics (SPH): An overview and recent developments. *Arch. Comput. Method Eng.* (2010) **17**:25-76.
- [9] Zhou, G. and Ge, W. Progress of smoothed particle hydrodynamics in complex flows. *CIESC Journal* (2014) **65**:1145-1161(in Chinese).
- [10] Cundall, P.A. and Strack, O.D.L. A discrete numerical model for granular assemblies. *Geotechnique* (1979) **29**:47-65.
- [11] Zhu, H.P., Zhou, Z.Y., Yang, R.Y., and Yu, A.B. Discrete particle simulation of particulate systems: Theoretical developments. *Chem. Eng. Sci.* (2007) **62**:3378-3396.
- [12] Swegle, J.W., Hicks, D.L., and Attaway, S.W. Smoothed particle hydrodynamics stability analysis. *J. Comput. Phys.* (1995) **116**:123-134.
- [13] Dyka, C.T., Randles, P.W., and Ingel, R.P. Stress points for tension instability in SPH. *Int. J. Num. Meth. Engng* (1997) **40**:2325-2341.
- [14] Chen, J.K., Beraun, J.E., and Jih, C.J. An improvement for tensile instability in smoothed particle hydrodynamics. *Comput. Mech.* (1999) **23**:279-287.
- [15] Monaghan, J.J. SPH without a tensile instability. *J Comput Phys* (2000) **159**:290-311.
- [16] Gray, J.P., Monaghan, J.J., and Swift, R.P. SPH elastic dynamics. *Comput. Methods Appl. Mech. Eng.* (2001) **190**:6641-6662.
- [17] Antoci, C., Gallati, M., and Sibilla, S. Numerical simulation of fluid-structure interaction by SPH. *Comput. Struct.* (2007) **85**: 879-890.
- [18] Rafiee, A. and Thiagarajan, K.P. An SPH projection method for simulating fluid-hypoelastic structure interaction. *Comput. Methods Appl. Mech. Engrg.* (2009) **198**:2785-2795.
- [19] Liu, M., Shao, J., and Li H. Numerical simulation of hydro-elastic problems with smoothed particle hydrodynamics method. *J. Hyrodyn.* (2013) **25**:673-682.

- [20] Zhou, G., Ge, W., Li, B., Li, X., and Wang, P., Wang, J., and Li, J. SPH simulation of selective withdrawal from microcavity. *Microfluid. Nanofluid.* (2013) **15**:481-490.
- [21] Zhou, G., Chen, Z., Ge, W., and Li, J. SPH simulation of oil displacement in cavity-fracture structures. *Chem. Eng. Sci.* (2010) **65**:3363-3371.
- [22] Morris, J.P., Fox, P.J., and Zhu, Y. Modeling low Reynolds number incompressible flows using SPH. *J. Comput. Phys.* (1997) **136**:214-226.
- [23] Libersky, L.D., Petschek, A.G., Carney, T.C., Hipp, J.R., and Allahdadi, F.A. High strain Lagrangian hydrodynamics: A three-dimensional SPH code for dynamic material response. *J. Comput. Phys.* (1993) **109**:67-75.
- [24] Monaghan, J.J. Simulating free surface flows with SPH. *J. Comput. Phys.* (1994) **110**:399-406.
- [25] Potapov, A.V., Hunt, M.L., and Campbell, C.S. Liquid-solid flows using smoothed particle hydrodynamics and the discrete element method. *Powder Technol.* (2001) **116**:204-213.
- [26] Ma, J., Ge, W., Wang, X., Wang, J., and Li, J. High-resolution simulation of gas-solid suspension using macro-scale particle methods. *Chem. Eng. Sci.* (2006) **61**:7096-7106.
- [27] Xiong, Q., Li, B., Chen, F., Ma, J., Ge, W., and Li, J. Direct numerical simulation of sub-grid structures in gas-solid flow—GPU implementation of macro-scale pseudo-particle modeling. *Chem. Eng. Sci.* (2010) **65**:5356-5365.
- [28] Yang, X., Liu, M., and Peng S. Smoothed particle hydrodynamics and element bending group modeling of flexible fibers interacting with viscous fluids. *Phys. Rev. E* (2014) **90**:063011[11 pages].

APPLICATION OF KINETIC DAMPING IN DYNAMIC MATERIAL POINT METHOD FOR STATIC PROBLEMS

YUJIN SUN¹, ERXIANG SONG² AND JUN YANG³

¹Department of Civil Engineering, Tsinghua University
 Beijing 100084, China
 sunyj12@mails.tsinghua.edu.cn

²Department of Civil Engineering, Tsinghua University
 Beijing 100084, China
 songex@mail.tsinghua.edu.cn

³Department of Civil Engineering, Tsinghua University
 Beijing 100084, China
 junyang@mail.tsinghua.edu.cn

Key words: Dynamic Relaxation; Kinetic Damping; MPM; Large Deformation; Static Problem.

Abstract. Material point method (MPM) is widely used in geotechnical engineering, owing to its powerful capability of modelling large deformation problems. But the static equilibrium problems involving very large deformation and material non-linearity can be difficult to solve using the quasi-static MPM, because of numerical difficulties with convergence in iterative procedure. An alternative method is the dynamic relaxation (DR) method, which converts the static problem to a dynamic one by considering the virtual masses and artificial damping. This paper presents a method to solve static problems using dynamic MPM with DR technique. An energy ratio and a force ratio are defined to recognize the static equilibrium state from dynamic process first. Then the kinetic damping as an DR technique is introduced into the dynamic MPM for the first time. Finally, two numerical examples are presented to illustrate the convenience and efficiency of the kinetic damping in dynamic MPM for static problems.

1 INTRODUCTION

In managing static problems involving very large deformation such as cone penetration testing (CPT), the jacking of piles and passive earth pressure problems, the classical Finite Element Method (FEM) encounters numerical difficulties due to mesh distortion and inherent problems associated with modelling slipping, separation and breakage. In contrast, the MPM developed recently, has enormous advantages in handling the large deformation problems in geomechanics^[1-6].

Similar to finite element method, the quasi-static MPM^[7] discrete the governing partial differential equations of a static equilibrium problem into a system of simultaneous algebraic equations, which may be written as:

$$[K]\{u\} = \{F^{\text{ext}}\} \quad (1)$$

where $[K]$ is the stiffness matrix, $\{u\}$ is the nodal displacement vector and $\{F^{\text{ext}}\}$ is the

equivalent nodal external force vector.

Whenever consider the large deformation, the material properties and state variables e.g. stresses and strains are nonlinear, which makes Eqation (1) a complex system of equations and hard to solve. One alternative method is DR method, which can be much more computationally efficient than the static one.

DR method converts the static problem to a dynamic one by considering the virtual masses and artificial damping. The dynamic equations of motion, which are equivalent to Eqation (1), are as follows:

$$[M]\{a\} = \{F^{\text{ext}}\} - \{F^{\text{int}}\} - \{F^{\text{damp}}\} \quad (2)$$

where $[M]$ is the virtual mass matrix, $\{a\}$ is acceleration vector, $\{F^{\text{int}}\} = [K]\{u\}$ is nodal internal force vector and $\{F^{\text{damp}}\}$ is the artificial damping force vector. Eqation (2) can be easily solved by an explicit time integration method, which does not need to assemble the stiffness matrix. The steady state response of this dynamic system is the solution of Eqation (1), when the acceleration and velocity vectors are damped to zero ($\{F^{\text{damp}}\}$ is zero at steady static state). The selection of mass matrix $[M]$ affects the dynamic property of the system such as frequency and critic time step size^[8], while the damping force vector $\{F^{\text{damp}}\}$ affects the dissipation speed of kinetic energy of the system and the iteration number to get static equilibrium state.

The common used artificial damping is viscous damping. The viscous damping force $\{F^{\text{damp}}\} = 2\beta [M]\{v\}$ is proportional to the product of nodal velocitie vector $\{v\}$ and mass matrix $[M]$, where β is a damping factor. Zabala et al.^[9] adopted an adaptive viscous damping in modeling progressive failure of Aznalcollar dam. Andersen et al.^[4] proposed a similar damping scheme by decreasing the updated velocities. In order to achieve the most rapid convergence, the critical viscous damping factor of the system must be used. However, the critical damping factor might be difficult to estimate. Cundall^[10] working on unstable geo-mechanical problems, suggested using kinetic damping which proved to be robust and rapidly converging when dealing with large unbalanced local forces. There is no need for prior determination of any constant. The basic idea of kinetic damping is that as an oscillating particle passes through a minimum potential energy state (equilibrium state), its total kinetic energy reaches a local maximum. For a multi-degree of freedom system, upon detection of a local energy peak, all current nodal velocities are set to zero. The process is then restarted from the current configuration and continued through resetting velocities until the energy of all modes of vibration has been dissipated then the system attains its static equilibrium state.

This paper calculate static problems using dynamic MPM with kinetic damping, which is proved as a robust and powerful DR technique. An energy ratio and a force ratio are defined to recognize the static equilibrium state from dynamic process first. Then the kinetic damping as an DR technique is first introduced into the dynamic MPM. Finally, two numerical examples, elongation of an elastic bar and progresive failure of a slope, are presented to illustrate the convenience and efficiency of the kinetic damping in dynamic MPM for static problems.

2 METHODOLOGY

2.1 Static equilibrium state

When using a dynamic code to solve static problems, A detection of static equilibrium state is required. Such state is achieved if and only if both the maximum out-of-balance force and

the kinetic energy of the system vanish. The maximum out-of-balance force approaches zero, indicating that the system is reaching an equilibrium state. The kinetic energy of the system decays to zero representing a static state.

Let us define a dimensionless force ratio K_F of the maximum out-of-balance force divided by maximum external force for all the background grid nodes in the model as

$$K_F = \frac{\|\{F^{\text{ext}}\} - \{F^{\text{int}}\}\|_{\infty}}{\|\{F^{\text{ext}}\}\|_{\infty}} = \frac{\max_{n_g} |F_i^{\text{ext}} - F_i^{\text{int}}|}{\max_{n_g} |F_i^{\text{ext}}|} \quad (3)$$

where n_g is the number of the background grid nodes. And define a dimensionless energy ratio K_E of kinetic energy of all the material points divided by the work induced by the external forces as

$$K_E = \frac{E_k}{W^{\text{ext}}} \quad (4)$$

where n_p is the number of the material points, E_k is the kinetic energy of all the material points

$$E_k = \frac{1}{2} \sum_{p=1}^{n_p} m_p \mathbf{v}_p \cdot \mathbf{v}_p \quad (5)$$

and W^{ext} is the external work calculated by

$$W^{\text{ext}} = W_0^{\text{ext}} + \Delta W_0^{\text{ext}} = W_0^{\text{ext}} + \sum_{p=1}^{n_p} \mathbf{f}_p^{\text{ext}} \cdot \Delta \mathbf{u}_p \quad (6)$$

where $\mathbf{f}_p^{\text{ext}}$ and $\Delta \mathbf{u}$ are the external force and incremental displacement of material point p , respectively. W_0^{ext} is the external work at the beginning the current step.

The force ratio K_F and the energy ratio K_E are calculated in each computational cycle. If they are less than a pre-defined tolerance, the computation is terminated. The experience of the author shows that a tolerance of 0.01 is sufficient for both criteria. And this will be adopted in this paper.

2.2 Kinetic damping

When an oscillation particle passes through a static equilibrium position without damping, the kinetic energy curve reaches the maximum value. The kinetic damping is based on this theorem. In the computer program with kinetic damping, the kinetic energy is constantly monitored, and all velocities are set to zero when a peak in the energy is detected^[11-13]. In the past few decades, the kinetic damping often used in form-finding of pre-stressed nets and membranes. A typical kinetic energy trace is shown in Figure 1 for the case of form-finding of a cable net or membrane with inaccurate initial geometry^[14]. The early energy peaks (1) are associated with high frequency modes caused by large out-of-balance forces in boundary or mast-support regions. After these modes have been substantially damped out, subsequent peaks (2) are associated with the overall structural form and lowest frequency modes; the motion in these modes being generally normal to the changing surface. Near convergence, low energy peaks (3) occur rapidly, associated with slight in plane motion. The process is then ideally suited to continued modification of the form, involving local changes in boundary geometry and

surface topology.

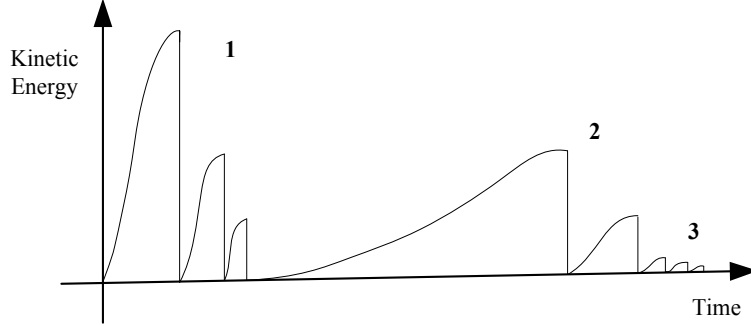


Figure 1: The dissipation of kinetic energy of system with kinetic damping ^[14]

The kinetic energy damping is an artificial damping, which is not a real effect, but offers a drastic reduction in the number of iterations required to find the static solution.

2.3 MPM implementation

The main steps of the material point method with kinetic damping for static problem is listed below. For more details, the reader can refer to ^[15-18].

- (1) Map the momenta, external forces and internal forces of material points to the regular background grid nodes.
- (2) Impose the essential boundary conditions on the background grid nodes.
- (3) Solve global equations of background grid nodes to update the nodal velocities.
- (4) Update the velocities of the material points using interpolation of the nodal accelerations.
- (5) Calculate the kinetic energy of the system and if a peak value is detected, then reset the velocity of all the material points zero, otherwise update the positions of the material points using interpolation of the updated nodal velocities.
- (6) Remap the velocities of the material points to the background grid nodes to calculate the incremental strain tensor and the incremental vorticity tensor of the material points. Then update the stress tensor by an objective constitutive model, as well as the density of the material points.
- (7) Calculate the force ratio and the energy ratio of the system using Equation (3) and Equation (4), respectively, to judge the static equilibrium state.
- (8) Reset the deformed grid and use the initial regular background grid in the next step.

In this paper, we adopt an incremental elastoplastic constitutive model with Jaumann stress rate.

$$\sigma_{ij}^{\nabla} = C_{ijkl}^{ep} \dot{\varepsilon}_{kl} \quad (7)$$

with Jaumann stress rate:

$$\sigma_{ij}^{\nabla} = \dot{\sigma}_{ij} - W_{jk} \sigma_{ki} - W_{ik} \sigma_{kj} \quad (8)$$

where, W_{ij} is vorticity tensor

$$W_{ij} = \frac{1}{2} \left(\frac{\partial v_i}{\partial x_j} - \frac{\partial v_j}{\partial x_i} \right) \quad (9)$$

strain tensor

$$\dot{\varepsilon}_{ij} = \frac{1}{2} \left(\frac{\partial v_i}{\partial x_j} + \frac{\partial v_j}{\partial x_i} \right) \quad (10)$$

3 EXAMPLES

Two numerical examples are shown to illustrate the efficiency of the kinetic damping in MPM: a simple problem of elongation of a linearly elastic bar^[19] in the case of small deformation and the progressive failure of a slope.

3.1 Example 1: elongation of elastic bar with dimensionless parameters

The problem of elongation of a linearly elastic bar with the length $L=10$ and the side length of the cross-section $a=1$ is considered, see Figure 2(a). It is assumed that the left end of the bar is fixed while the point force F is applied to its right end. In the numerical model, the bar is discretized into 20 material points which lie in 10 C₁ elements. In order to apply the external surface load, a material point carrying a body force with the magnitude being F is added on the right end of the bar, see Figure 2(b). In the dynamic analysis, the force is applied immediately at simulation time $t=0$ s. The calculations have been made with the following data: the force magnitude, $F=0.001$, the density $\rho=1$, the Young's modulus $E=1$ and the Poisson's ratio $\nu=0$, see Table 1. The time step size $\Delta t=0.01$. During the calculations, the displacements and the stresses of particle A, representing the material point in the middle of the bar and labeled in Figure 2(b), are traced.

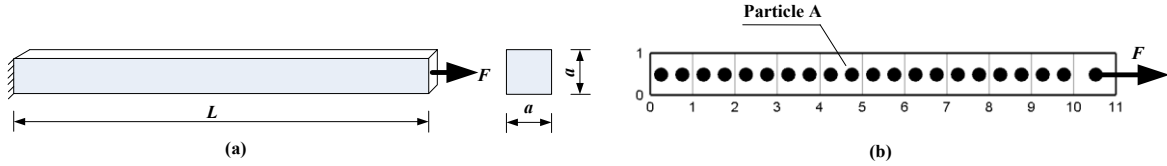


Figure 2: Model of the bar. (a) Schematic of the bar. (b) Numerical model of the bar.

Table 1: Parameters in example

Density	Young's modulus	Poisson's ratio	L	a	F
1	1	0	10	1	0.001

Figure 3 shows the kinetic energy dissipation of the bar with different damping in semilog coordinate system. For kinetic damping, the peak kinetic energy decays very fast with exponential rate. For viscous damping, the following values of the damping parameter β have been applied: 0.08, 0.1 and 0.12 respectively. We found that the best damping parameter value is 0.10 which is smaller than the “proper” damping factor $\beta=\omega_1 \approx 0.16$ with the first natural frequency of vibration:

$$\omega_1 = \frac{\pi}{2} \sqrt{\frac{E}{\rho l^2}} \quad (11)$$

For complex problem, it is difficult to estimate the best damping factor for viscous damping. But there is no need to determine any factors with kinetic damping.

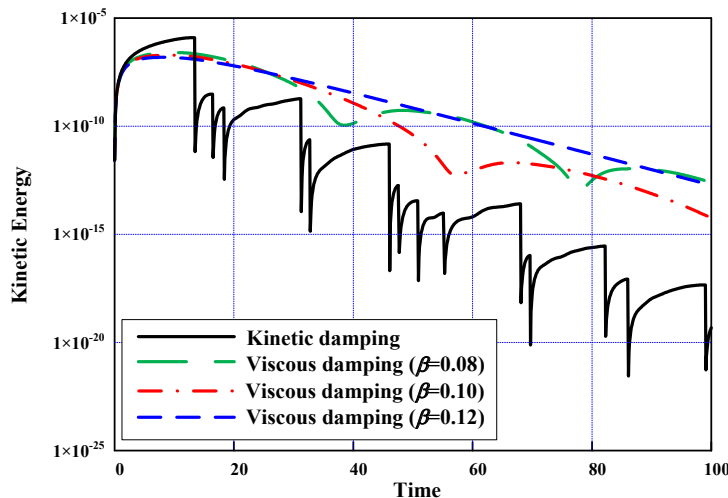


Figure 3: Kinetic energy dissipation of example 1 with different damping

The displacements and stresses of particle A with different damping are shown in Figure 4. For kinetic damping, the displacement and horizontal normal stress convergence very fast to the static solution, 4.75×10^{-3} and 10×10^{-4} respectively. But the solutions with viscous damping are slower although using different damping constants. The convergence time for the computation with different damping are shown in Table 2.

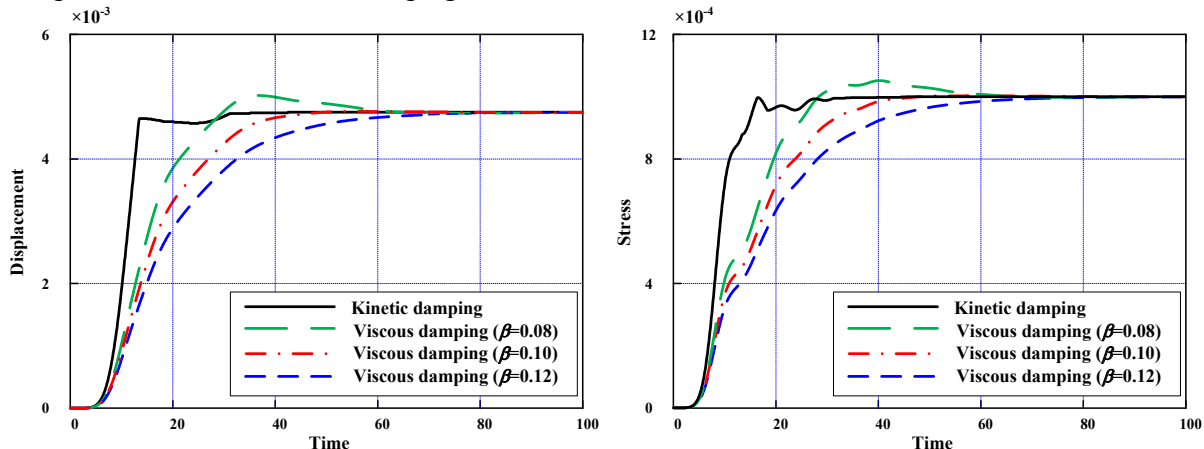


Figure 4: Displacements and stresses of particle A with different damping

Table 2: Convergence time for the computation of example 1 with different damping.

Damping type	Kinetic damping	Viscous damping		
		$\beta=0.10$	$\beta=0.10$	$\beta=0.10$
Convergence time	32.3	103.2	89.7	114.6

From Table 2, we can find that the convergence time are $t=32.3$ for kinetic damping, $t=89.7$ for viscous damping with best damping factor. The convergence time with viscous damping is nearly three time that with kinetic damping. So it is convenient and efficient to use the kinetic

damping to get the static solution in dynamic material point method.

3.2 Example 2: progressive failure of cohesiveless soil slope

The second example is a homogenous high cohesiveless soil slope in plane strain condition with the height $h = 40\text{m}$, the slope angle $\theta=30^\circ$, as shown in Figure 5. The bottom is fixed on the base rock. Symmetric boundary conditions are imposed at the left and right sides of the slope. The simulations are performed in 3D MPM code with thickness being 0.5m. The element is a cube with a side length $\Delta x = 1\text{m}$. Initially, there are 2×2 particles per element and the gravity is applied immediately.

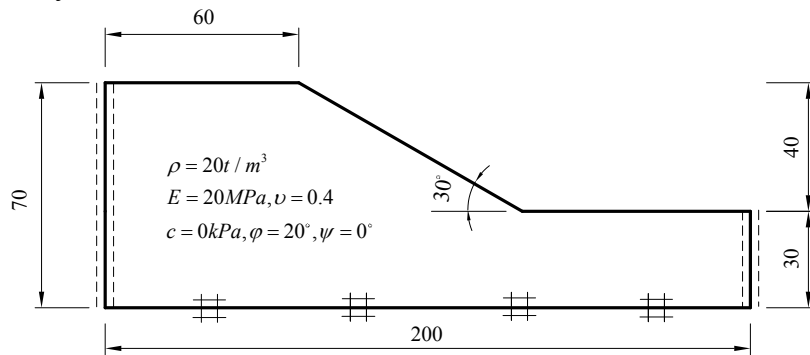


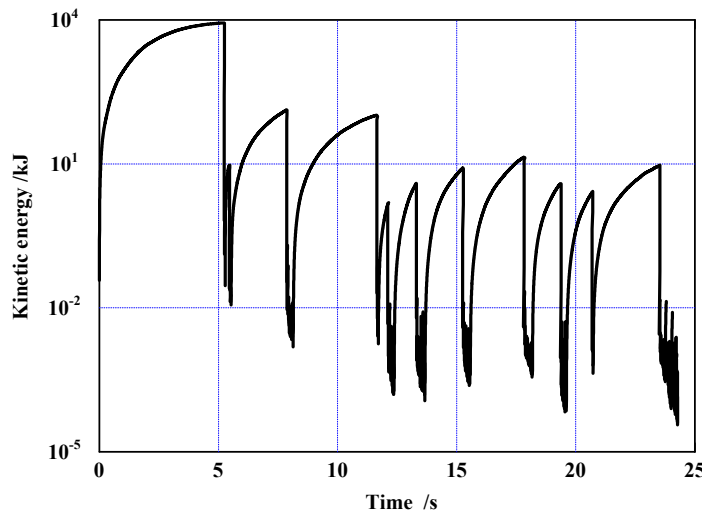
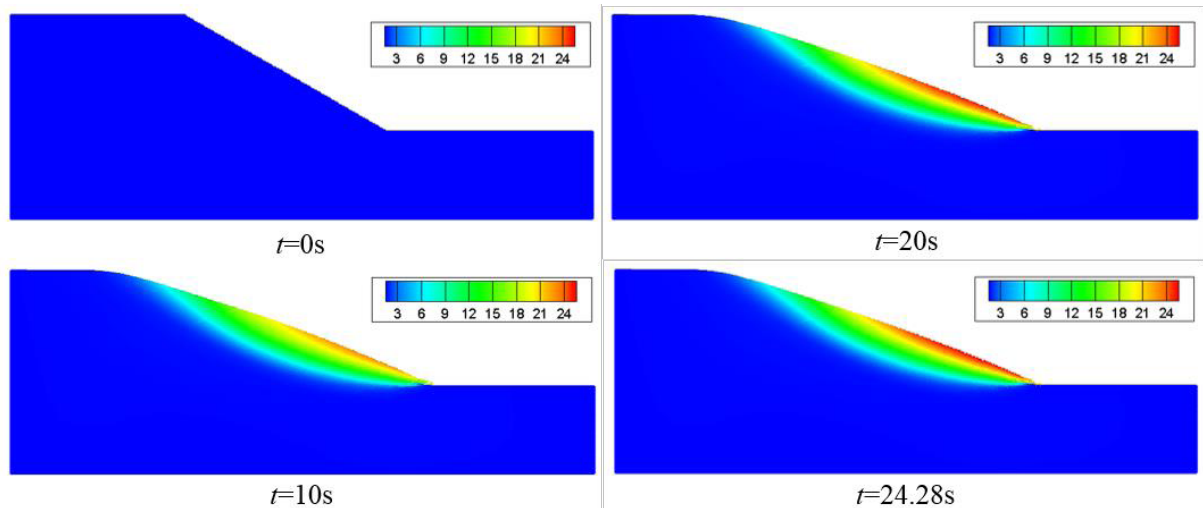
Figure 5: Schematic of the slope (unit: m)

The soil is modeled by Mohr-Coulomb linear elastic perfectly plastic model, whose Young's modulus $E=20\text{MPa}$, Poisson's ratio $\nu=0.4$, cohesion $c=0\text{kPa}$, friction angle $\varphi=20^\circ$, dilatancy angle $\psi=0^\circ$, and density $\rho=2\times 10^3\text{kg/m}^3$, see Table 3. The maximum longitudinal wave speed is 146 m/s. Taking the Courant number $\alpha_c=0.2$, the explicit time step size $\Delta t=1.366\times 10^{-3}\text{s}$.

Table 3: Material constants of soil in example 2.

Density	Young's modulus	Poisson's ratio	c	φ	ψ
$2\times 10^3\text{kg/m}^3$	20 MPa	0.4	0kPa	20°	0°

The kinetic energy peaks dissipation curve is shown in Figure 6 using semilog coordinate. The kinetic energy peaks is damped below 1% of the first kinetic energy peak after the first work of the kinetic damping. That is to say, the energy ratio $K_E<0.01$ after the first work of the kinetic damping. The simulation convergence at $t=24.28\text{s}$ with force ratio $K_F = 0.01$ and the energy ratio $K_E= 0.00$. The horizontal displacements of the soil during the simulation are shown in Figure 7.

**Figure 6:** Kinetic energy dissipation of slope**Figure 7:** Horizontal displacements of the soil (unit: m)

From Figure 7, we can find that the major motion of the soil has completed before $t=10s$, and local movement with small magnitude after that. Finally, the angle of repose is about 20° , which is equal to the friction angle φ of the soil.

4 CONCLUSIONS

The MPM provides a convenient framework for the dynamic simulation of very large deformation problems in geomechanics. But it is not efficient for the calculation of static problems. This paper introduces the kinetic damping into MPM to calculate static problems. The energy dissipation effect of the kinetic damping is very efficient and the implementation of the algorithm is convenient, which is more important to some extent.

ACKNOWLEDGEMENTS

The work reported in this paper is financially supported by the National Key Fundamental Research and Development Program of China (Project No. 2014CB047003).

REFERENCES

- [1] Coetzee C.J., Basson A.H. and Vermeer P.A. Discrete and continuum modelling of excavator bucket filling. *Journal of Terramechanics* (2007),44(2):177-186.
- [2] Beuth L., Benz T., Vermeer P.A. and Wieckowski Z. Large deformation analysis using a quasi-static Material Point Method. *Journal of Theoretical and Applied Mechanics* (2008), 38(1-2):45-60.
- [3] Shin W.K. Numerical simulation of landslides and debris flows using an enhanced material point method. University of Washington,(2009).
- [4] Andersen S. and Andersen L. Modelling of landslides with the material-point method. *Computational Geosciences* (2010), 14(1):137-147.
- [5] Jassim I., Stolle D. and Vermeer P. Two-phase dynamic analysis by material point method. *International Journal for Numerical and Analytical Methods in Geomechanics* (2013), 37(15):2502-2522.
- [6] Yerro A., Alonso E. and Pinyol N. The Material Point Method: A promising computational tool in Geotechnics. Proceeding of the 18th International Conference on Soil Mechanics and Geotechnical Engineering. Paris,(2013).
- [7] Beuth L. Formulation and application of a quasi-static material point method. University of Stuttgart,(2012).
- [8] Stolle D., Jassim I. and Vermeer P. Simulation of incompressible problems in geomechanics. Springer Berlin Heidelberg,(2009).
- [9] Zabala F. and Alonso E.E. Progressive failure of Aznalcóllar dam using the material point method. *Géotechnique* (2011),61(9):795-808.
- [10] Cundall P. Explicit finite-difference methods in geomechanics. Proceeding of the 2nd International Conference on Numerical Methods in Geomechanics. Blacksburg,VA,(1976), 132-150.
- [11] Lee K.S., Han S.E. and Park T. A simple explicit arc-length method using the dynamic relaxation method with kinetic damping. *Computers & Structures*(2011), 89(1-2): 216-233.
- [12] Han S.E. and Lee K.S. A study of the stabilizing process of unstable structures by dynamic relaxation method. *Computers & Structures* (2003),81(17):1677-1688.
- [13] Lewis W.J., Jones M.S. and Rushton K.R. Dynamic relaxation analysis of the non-linear static response of pretensioned cable roofs. *Computers & Structures* (1984),18(6):989-997.
- [14] Barnes M.R. Form-finding and analysis of prestressed nets and membranes. *Computers & Structures* (1988),30(3):685-695.
- [15] Sulsky D., Chen Z. and Schreyer H.L. A particle method for history-dependent materials. *Computer Methods in Applied Mechanics and Engineering* (1994),118(1):179-196.
- [16] Sulsky D., Zhou S. and Schreyer H.L. Application of a particle-in-cell method to solid mechanics. *Computer Physics Communications* (1995),87(1):236-252.
- [17] Zhang X., Sze K.Y. and Ma S. An explicit material point finite element method for hyper-velocity impact. *International Journal for Numerical Methods in Engineering* (2006), 66(4):689-706.

- [18] Chen Z., Hu W., Shen L., Xin X. and Brannon R. An evaluation of the MPM for simulating dynamic failure with damage diffusion. *Engineering Fracture Mechanics* (2002), 69(17): 1873-1890.
- [19] Wieckowski Z. Application of dynamic relaxation in material point method. Proceeding of the 19th International Conference on Computer Methods in Mechanics. Warsaw, Poland, (2011), 9-12.

IMPROVING ACCURACY IN PARTICLE METHODS USING NULL SPACES AND FILTERS

Chris Gritton¹, Martin Berzins², Robert M Kirby³

SCI Institute, University of Utah, Salt Lake City, USA

¹ cgritton@sci.utah.edu ² mb@sci.utah.edu ³ kirby@sci.utah.edu

Key words: Particle in Cell Method, Ringing Instability, Singular Value Decomposition, Material Point Method

Abstract. While particle-in-cell type methods, such as MPM, have been very successful in providing solutions to many challenging problems there are some important issues that remain to be resolved with regard to their analysis. One such challenge relates to the difference in dimensionality between the particles and the grid points to which they are mapped. There exists a non-trivial null space of the linear operator that maps particles values onto nodal values. In other words, there are non-zero particle values values that when mapped to the nodes are zero there. Given positive mapping weights such null space values are oscillatory in nature. The null space may be viewed as a more general form of the ringing instability identified by Brackbill for PIC methods. It will be shown that it is possible to remove these null-space values from the solution and so to improve the accuracy of PIC methods, using a matrix SVD approach. The expense of doing this is prohibitive for real problems and so a local method is developed for doing this.

1 Introduction to Particle in Cell Methods

Particle-in-cell, PIC, methods have been in use and development since the mid 1950's. The original PIC method was developed by F.H. Harlow as a hydrodynamics code [7] to handle fluid dynamics problems that involved large slips and distortions. The PIC method combines both Lagrangian and Eulerian components. The Lagrangian component involved particles that could be advected over the given domain and the Eulerian component involved a grid that would be used to perform calculations. While successful at achieving its original intent the original PIC was shown in the work done in the 1970s and 1980s [8, 3] to be subject to errors that are introduced into PIC calculations due to an aliasing affect caused by a mismatch in the degrees of freedom at the cell compared to the degrees of freedom at the particles. Brackbill [3] stated that, "Because the number of particles is finite, the number of Fourier modes is also finite. Thus, when there are n particles in each cell, there are n times as many Fourier modes as there are grid points."

When values are mapped from nodes to particles the lack of resolution at the nodes compared to resolution at the particles can cause an aliasing error. Again to quote Brackbill, "Aliases occur because all Fourier modes with wavelengths shorter than the grid spacing are indistinguishable at the grid points." [3].

The fluid implicit particle, FLIP, [4] method is a modification to the original PIC method that is applied to fluid dynamics problems. Like the PIC methods that have been used in plasma simulations, the FLIP method also has material properties that are carried with the Lagrangian particles. One major difference though from other PIC methods is that in most PIC methods velocities are calculated on the grid and then interpolated to the particles. In FLIP the change in velocity is calculated at the grid level and then interpolated to the particles where the particle velocity is then updated. By doing this there is a reduction in the numerical diffusion or viscosity due to interpolation. A derivative of the FLIP method is the material point method, MPM, [11] which extends the FLIP method to solid mechanics problems. Despite these and many other developments in particle methods [2, 1, 10, 12] the understanding of this phenomenon has not increased greatly. The intention here is to shed some light upon this issue.

2 The PIC Method Applied to Gas Dynamics

In considering the ringing instability Brackbill [3] started with simple gas dynamics linearized equations

$$\frac{\partial \rho_1}{\partial t} + u_0 \frac{\partial \rho_1}{\partial x} + \rho_0 \frac{\partial u_1}{\partial x} = 0 \quad (1)$$

$$\rho_0 \left[\frac{\partial u_1}{\partial t} + u_0 \frac{\partial u_1}{\partial x} \right] + \frac{\partial p_1}{\partial x} = 0, \quad (2)$$

where u_0 and ρ_0 are constants representing the constant flow and the initial uniform density, respectively, and u_1 and ρ_1 are the unknown velocity and density. Substituting $p_1 = c^2 \rho_1$ where c is the wave speed and rewriting these equations in terms of their material derivative,

$$\frac{D(\cdot)}{Dt} = \frac{\partial(\cdot)}{\partial t} + u_0 \frac{\partial(\cdot)}{\partial x}, \quad (3)$$

After setting $\rho_0 = 1$, we get the following set of coupled equations,

$$\frac{D\rho_1}{Dt} + \frac{\partial u_1}{\partial x} = 0, \quad (4)$$

$$\frac{Du_1}{Dt} + c^2 \frac{\partial \rho_1}{\partial x} = 0. \quad (5)$$

Applying the $\frac{D(\cdot)}{Dt}$ operator to equation 4 and the $\frac{\partial(\cdot)}{\partial x}$ operator to equation 5 gives, after some simple manipulation, the form of the wave equation on a grid moving with the

velocity u_0 as,

$$\frac{D^2\rho_1}{Dt^2} = c^2 \frac{\partial^2\rho_1}{\partial x^2}. \quad (6)$$

If our initial conditions are $\rho_1(x, 0) = f(x)$ and $\frac{\partial\rho_1(x, 0)}{\partial t} = 0$ and the boundary conditions are periodic then the solution [9] in the fixed frame is the modified d'Alembert's formula,

$$\rho_1(x, t) = \frac{1}{2}(f(x - (c - u_0)t) + f(x + (c - u_0)t)). \quad (7)$$

2.1 Mapping Matrix

In particle methods, it is necessary to map values from the particles to the nodes [11, 2]. For example, one mapping of values g_p , where $g_p = g(x_p)$ are the values at particles, to the nodes can be written as,

$$g_i = \frac{\sum_p g_p \phi_{ip}}{\sum_p \phi_{ip}}, \quad (8)$$

$$= \sum_p S_{ip} g_p. \quad (9)$$

where ϕ_{ip} is the linear basis function $\phi_i(x)$ with value 1 at node x_i and zero at other nodes evaluated at the particle point x_p . This mapping from particles to node can also be expressed in terms of a system-wide matrix

$$\mathbf{g}_i = \mathbf{S}_{ip} \mathbf{g}_p, \quad (10)$$

where \mathbf{g}_i contains the mapped values at the nodes and \mathbf{g}_p are the values at the particles.

2.2 PIC Method Description

One PIC type approach maps particle values to the nodes and then calculates the gradient by taking the gradient of the interpolating function. Using the piecewise linear basis functions, $\phi_i(x)$, the data values at the nodes the linear approximation to the function $g(x)$ can be defined as follows,

$$g_l(x) = \sum_i g_i \phi_i(x). \quad (11)$$

The gradient of the function $g(x)$ can be defined as,

$$\nabla g_l(x) = \sum_i g_i \nabla \phi_i(x). \quad (12)$$

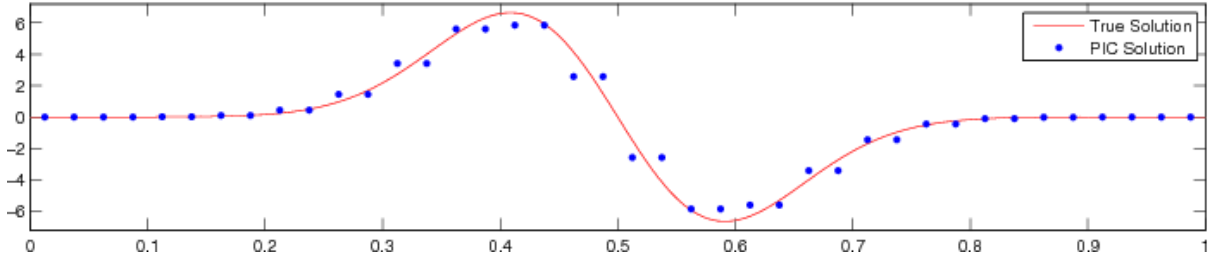


Figure 1: Computed versus true solution for $\frac{\partial g(x)}{\partial x}$

For a piecewise linear function, the gradient of $\phi_i(x)$ is defined as,

$$\nabla \phi_i(x) = \begin{cases} \frac{1}{h} & \text{if } x_{i-1} \leq x < x_i \\ \frac{-1}{h} & \text{if } x_i \leq x < x_{i+h}. \end{cases} \quad (13)$$

When using a piecewise linear basis function, the gradient is piecewise constant across each interval. Figure 1 shows the comparison between the computed gradients at the particles and the true solution given by $g(x) = e^{-60(x-0.5)^2}$ and so $\frac{\partial g(x)}{\partial x} = -120(x-0.5)e^{-60(x-0.5)^2}$. The pairing of point values is due to the piecewise constant derivative of the linear basis functions.

3 Null Space of the Mapping Matrix

The matrix \mathbf{S}_{ip} is rectangular and may have a nontrivial nullspace. For example, let \mathbf{c} be a vector in \mathbb{R}^n . If $\mathbf{S}_{ip}\mathbf{c} = \mathbf{0}$, then we say that \mathbf{c} is in the nullspace of \mathbf{S}_{ip} . We can determine the nullspace of \mathbf{S}_{ip} by making use of its singular value decomposition, SVD [5]. Taking the SVD of \mathbf{S}_{ip} gives the following decomposition,

$$\mathbf{S}_{ip} = \mathbf{U}\Sigma\mathbf{V}^T, \quad (14)$$

where \mathbf{U} has dimension m by m , Σ is m by n , and \mathbf{V} is n by n . The matrices \mathbf{U} and \mathbf{V} are unitary, meaning that the columns are orthonormal [13]. In other words, if \mathbf{u}_i and \mathbf{u}_j are columns of the matrix \mathbf{U} , then,

$$\mathbf{u}_i^T \mathbf{u}_j = \delta_{ij}, \quad (15)$$

where the superscript T is the transpose of the vector and δ_{ij} is the Kroenecker delta. The columns of \mathbf{U} and \mathbf{V} are orthogonal, linearly independent and span the spaces \mathbb{R}^m and \mathbb{R}^n respectively, [13]. Any vector $\mathbf{a} \in \mathbb{R}^m$ can be expressed as a linear combination of the columns of \mathbf{U} .

$$\mathbf{a} = c_1 \begin{bmatrix} u_1 \\ u_2 \\ \vdots \\ u_m \end{bmatrix} + \cdots + c_m \begin{bmatrix} u_1 \\ u_2 \\ \vdots \\ u_m \end{bmatrix} \quad (16)$$

where c_1, \dots, c_m are constants. The matrix Σ is an m by n matrix of the form

$$\Sigma = \begin{bmatrix} \sigma_1 & 0 & \dots & 0 & 0 & \dots & 0 \\ 0 & \sigma_2 & \dots & 0 & 0 & \dots & 0 \\ \vdots & \vdots & \ddots & \vdots & \vdots & \ddots & 0 \\ 0 & 0 & \dots & \sigma_r & 0 & \dots & 0 \\ 0 & 0 & \dots & 0 & 0 & \dots & 0 \\ \vdots & \vdots & \dots & \vdots & \vdots & \ddots & \vdots \\ 0 & 0 & \dots & 0 & 0 & \dots & 0 \end{bmatrix} \quad (17)$$

in which the columns 1 to r are zero apart from their diagonal elements which contain the nonzero singular values $\sigma_1, \dots, \sigma_r$ and the columns $r+1$ to n are zero, [5, 13]. Taking the matrix product of Σ and \mathbf{V}^T , gives,

$$\Sigma \mathbf{V}^T = (\mathbf{V} \Sigma^T)^T = \left[\begin{array}{c|c|c|c|c} & & & & \\ \sigma_1 \mathbf{v}_1 & \dots & \sigma_r \mathbf{v}_r & 0 * \mathbf{v}_{r+1} & \dots & 0 * \mathbf{v}_n \\ \hline & & & & & \end{array} \right]^T. \quad (18)$$

Consequently the column vectors \mathbf{v}_{r+1} to \mathbf{v}_n span the nullspace of Σ , which in turn means that they span the nullspace of \mathbf{S}_{ip} . From equation 16, any vector can be decomposed into its orthogonal components [13]. Since the columns of \mathbf{V} are orthogonal, they form a basis for \mathbb{R}^n , which means that any vector $b \in \mathbb{R}^n$ can be expressed as a linear combination of the columns of \mathbf{V} ,

$$\mathbf{b} = c_1 \begin{bmatrix} \mathbf{v}_1 \end{bmatrix} + \dots + c_r \begin{bmatrix} \mathbf{v}_r \end{bmatrix} + \underbrace{c_{r+1} \begin{bmatrix} \mathbf{v}_{r+1} \end{bmatrix} + \dots + c_m \begin{bmatrix} \mathbf{v}_n \end{bmatrix}}_{\text{null}(\mathbf{S}_{ip})}. \quad (19)$$

From this it can be seen that a portion of \mathbf{b} is in the nullspace of \mathbf{S}_{ip} . Using the inner product [13] allows the components of a vector that are in the null space to be found. Given a vector \mathbf{u}_p if we define the vector \mathbf{r}_i as,

$$\mathbf{r}_i = \mathbf{u}_p - (\mathbf{v}_i^T \mathbf{u}_p) \mathbf{v}_i, \quad (20)$$

then as $(\mathbf{v}_i^T \mathbf{r}_i) = 0$ it follows that \mathbf{r}_i , has no component in the direction of \mathbf{v}_i . The vector \mathbf{u}_p can now be expressed as linear combination of two vectors,

$$\mathbf{u}_p = (\mathbf{v}_i^T \mathbf{u}_p) \begin{bmatrix} \mathbf{v}_i \end{bmatrix} + \begin{bmatrix} \mathbf{r}_i \end{bmatrix}. \quad (21)$$

Repeating this process using the first r column vectors of V , and defining the vector \mathbf{r} by,

$$\mathbf{r} = \mathbf{u}_p - \sum_{i=1}^r (\mathbf{v}_i^T \mathbf{u}_p) \mathbf{v}_i, \quad (22)$$

gives a vector, \mathbf{r} , that is the sum of the components of \mathbf{u}_p that lie entirely in the nullspace of \mathbf{S}_{ip} . The filtered form of \mathbf{u}_p with no nullspace component is denoted here by \mathbf{u}_p^F and given by

$$\mathbf{u}_p^F = \sum_{i=1}^r (\mathbf{v}_i^T \mathbf{u}_p) \mathbf{v}_i. \quad (23)$$

This filtering operation can be described using a Matlab style of syntax in a function called *Filter()* that takes as its parameters an n dimensional vector \mathbf{u}_p and the matrix \mathbf{S}_{ip} , uses a function called *svd()*, which decomposes a matrix into \mathbf{U} , Σ , and \mathbf{V} and a function called *rank()*, which returns the number of singular values in a matrix. The function returns the filtered form of \mathbf{u}_p^F in \mathbf{u}_p

```
function Filter(up, Sip)
    U, S, V = svd(Sip)      \\ S = singular values
    k = rank(S)
    r = 0
    for i = 1 to k
        r = r + (up' * V(:,i))*V(:,i)
    end
    return r
```

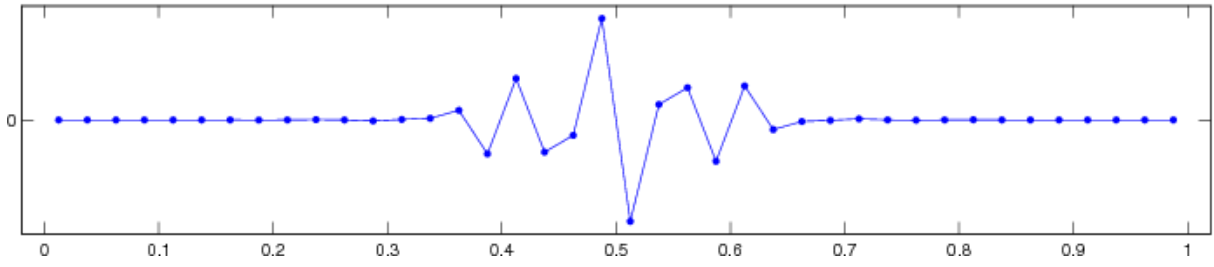
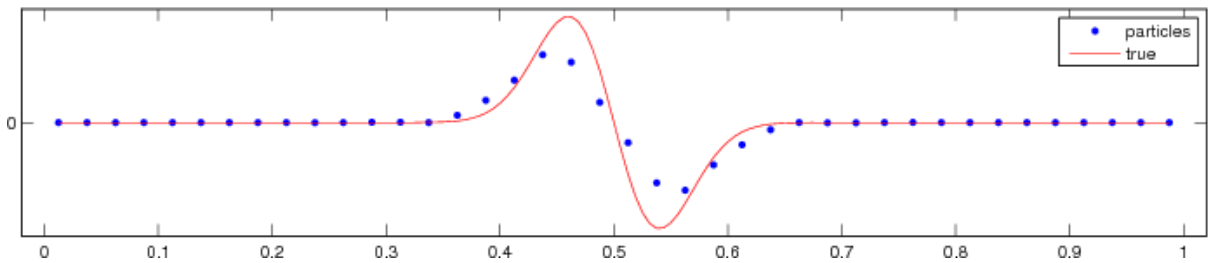
The central idea of this paper is to use a filter such as this to remove numerical noise associated with the null space.

3.1 Removing the Nullspace

Equation 11 maps particle values to the nodes. In matrix form, this is,

$$\mathbf{g}_i = \mathbf{S}_{ip} \mathbf{g}_p. \quad (24)$$

At this point, the nullspace component of \mathbf{g}_p has been removed by the nature of the mapping. It is at the next step in the computation, equation 12, that a nullspace component can be re-introduced. If we express the computed gradients at the particles, ∇g_p , in the vector form \mathbf{dg}_p then we can decompose the vector into a nullspace and a non-nullspace component in the same way as above. Figure 2 show what the nullspace components look like. Once the nullspace component is known, it can be removed from the computed gradient, to get a smoothed version of \mathbf{dg} . Figure 3 show \mathbf{dg} with the nullspace component removed.

**Figure 2:** Nullspace of computed $\frac{\partial g(x)}{\partial x}$ **Figure 3:** The results of $\frac{\partial g(x)}{\partial x}$ with the nullspace component removed

3.2 Nodalwise Noise Removal

Using singular value decomposition for the removal of nullspace noise works well for small one-dimensional problems, but it does not scale well when running a multidimensional simulation across multiple cores. A second issue is that the computational complexity of generating the matrix \mathbf{V} with a singular value decomposition is $O(m^2n + n^3)$ [5]. In order to have a method for removing the nullspace noise that scales well across hundreds of cores, we need a new approach that works locally across just a few nodes and not the entire set of nodes.

3.2.1 Local Method

This method takes a different approach than the SVD method to removing the nullspace components. The key idea in the local method is to use the already mentioned fact that any vector, $\mathbf{a} \in \mathbb{R}^n$, can be decomposed into a nullspace and non-nullspace component, so when the matrix \mathbf{S}_{ip} is applied to the vector \mathbf{a} , the nullspace portion of \mathbf{a} is removed. In our case, the gradient at the particles is computed by first mapping particle values to the nodes, using equation 9. and then computing the gradients at the particles by using the gradient of the the interpolating function that interpolates values from nodes to particles, equation 12. When this happens, a nullspace component is introduced by this gradient calculation. Taking advantage of the observation made earlier, if the newly computed

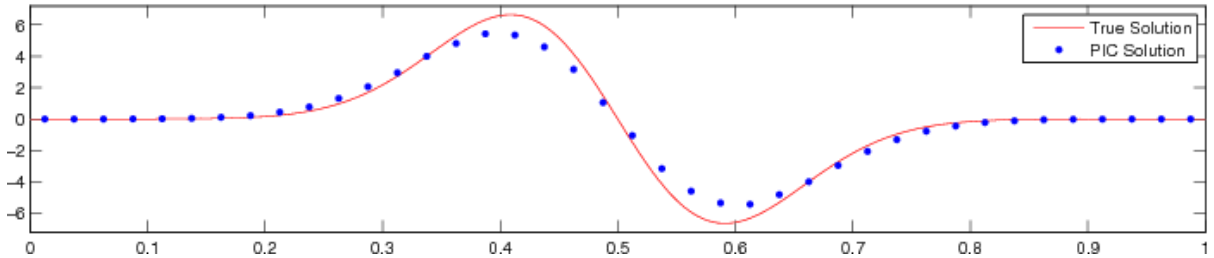


Figure 4: Comparison between the true solution and the computed solution using the local method as a filter for $\frac{\partial g}{\partial x}$

gradient values are mapped back to the nodes,

$$\nabla g_i = \frac{\sum_p \phi_{ip} \nabla g_p}{\sum_p \phi_{ip}}, \quad (25)$$

or in matrix form,

$$\nabla \mathbf{g}_i = \mathbf{S}_{ip} \nabla \mathbf{g}_p, \quad (26)$$

then its nullspace component is removed. With gradient values mapped to the nodes, all that needs to be done now is to interpolate the values back to the particles,

$$\nabla g_p = \sum_i \nabla g_i \phi_{ip}. \quad (27)$$

While there is no nullspace component at the nodes, there is nothing to prevent nullspace noise from being introduced at the particle via the interpolation process. Furthermore, there is no longer a need to explicitly calculate the nullspace in order to smooth out the particle gradients. Figure 4 show a comparison between the true gradient and the calculated solution at the particles.

3.3 PIC Formulations for Compressible Flow

The approach used here is to map only the particle values for ρ to the nodes nodes, to compute the gradient of ρ , and update the particle values of u . The updated particle values for u are then mapped to the nodes. The gradients of u are then calculated and are used to update the particle values of ρ . Finally, the particles are then moved.

This approach has at its heart a stable nodal method [6]. We use Formulation 2 as defined by [6] in its vector form (p36-37) and its filtered form as defined above using the Filter function.

Formulation 2	Formulation 2 Filtered
<ol style="list-style-type: none"> 1. $u_i^t = \sum_{p=1}^{np} S_{ip} u_p^t$ 2. $\rho_p^{t+1} = \rho_p^t + c \frac{dt}{h} (u_{i+1}^t - u_i^t)$ 3. $\rho_i^{t+1} = \sum_{p=1}^{np} S_{ip} \rho_p^{t+1}$ 4. $u_p^{t+1} = u_p^t + c \frac{dt}{h} (\rho_{i+1}^{t+1} - \rho_i^{t+1})$ 5. $x_p^{t+1} = x_p^t + vdt$ 	<ol style="list-style-type: none"> 1. $u_i^t = \sum_{p=1}^{np} S_{ip} u_p^t$ 2. $du = \text{Filter}((u_{i+1}^t - u_i^t), S_{ip})$ 3. $\rho_p^{t+1} = \rho_p^t + c \frac{dt}{h} (du)$ 4. $\rho_i^{t+1} = \sum_{p=1}^{np} S_{ip} \rho_p^{t+1}$ 5. $d\rho = \text{Filter}((\rho_{i+1}^{t+1} - \rho_i^{t+1}), S_{ip})$ 6. $u_p^{t+1} = u_p^t + c \frac{dt}{h} (d\rho)$ 7. $x_p^{t+1} = x_p^t + vdt$

Note that to avoid confusion in notation, the variable v is used instead the variable u_0 that is found in equations 1 and 2 to represent the particle velocity. The nullspace filter is applied to this model by applying the filter function to the updates to u and ρ . In this case we first need to construct the matrix S_{ip} . It is important to remember that this needs to be done after each iteration because the mapping is dependent on particle position. Two options are available when filtering. The first is to use the full SVD filter while the second is to use the local filter. It is now possible to look at how the nullspace noise can be filtered out during each computation cycle. As discussed above, nullspace noise can be injected any time a value goes from node to particle. When the interpolation is linear, the noise tends to be minimal, but in the cases when the piecewise constant gradient calculated using nodal values is mapped to a particle, then there tends to be more nullspace noise. There are two points in Formulation 2 when this occurs. The first is when the gradient of u_i is calculated, and the second is when the gradient at ρ_i is calculated.

3.4 Comparison of Filtered and Nonfiltered Formulations

Figures 5, 6, and 7 are snapshots from a simulation that was run comparing Formulation 2 without the nullspace filter and Formulation 2 with the nullspace filter. As can be seen by Figure 6 at time step 700, the method without the nullspace filter is showing the results of the numerical nullspace noise. On the other hand, it is shown in Figure 7 that the method with the nullspace filter is still stable at 1000 steps even though the original method is clearly unstable. One interesting feature of the two filters is that if the calculation is continued out too 5000 steps the solution obtained with the local filter remains stable but the SVD filtered solution does finally become unstable. The two solutions are shown in Figure 8 We have also experimented with the use of this filter with the Material Point Method. Numerical calculations show that the MPM method

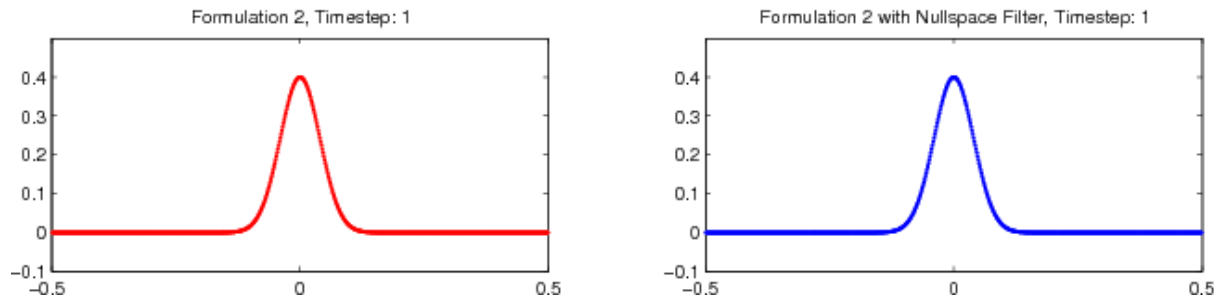


Figure 5: Initial time step

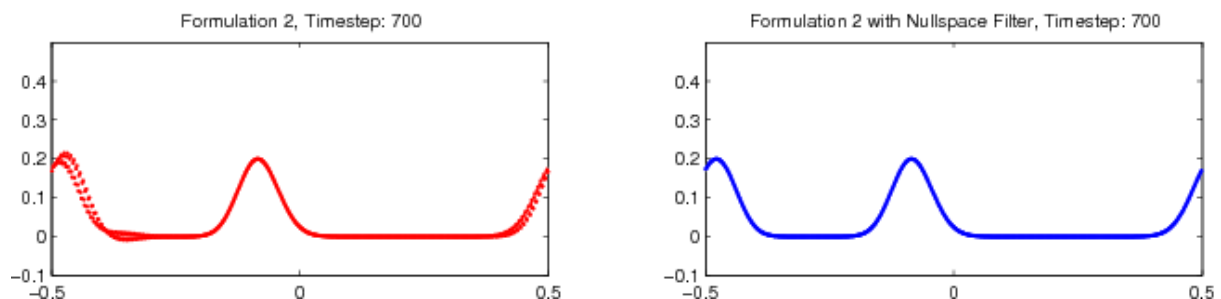


Figure 6: Time step 700

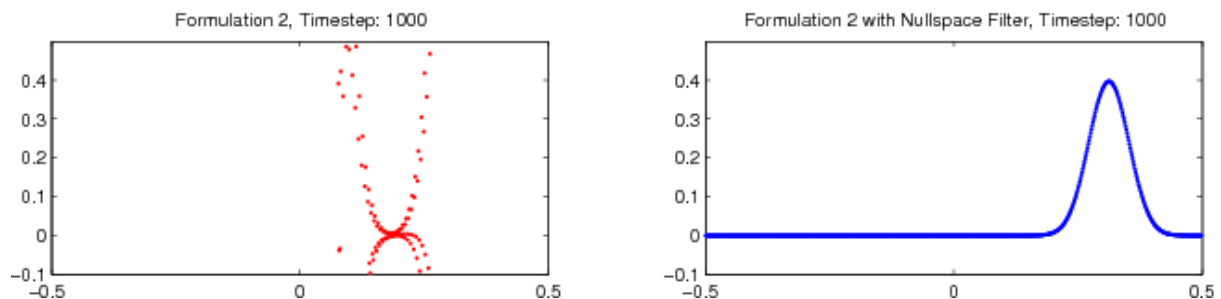


Figure 7: Time step 1000

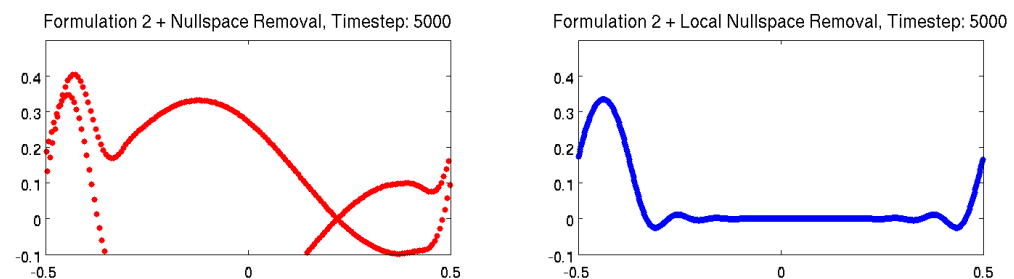


Figure 8: Time step 5000

has some important advantages over the PIC approach, [6]. In part these appear due to the different formula used by MPM in discretising the wave equation. Our observation is that it is the grid crossing error derived by [12] and discussed by [10] that may dominate the error in cases such as those considered above, but further work is required.

4 Conclusion

The removal of the nullspace error from the PIC method used has resulted in much improved stability. While the original method uses an expensive SVD decomposition, a local method that is much less expensive has also been proposed. This local method also seems to work well. These ideas have also been applied to the MPM method in work that will be reported elsewhere.

Acknowledgement: Research was primarily sponsored by the Army Research Laboratory and was accomplished under Cooperative Agreement Number W911NF-12-2-0023. The views and conclusions contained in this document are those of the authors and should not be interpreted as representing the official policies, either expressed or implied, of the Army Research Laboratory or the U.S. Government.

REFERENCES

- [1] S. Bardenhagen, *Energy conservation error in the material point method for solid mechanics*, Journal of Computational Physics, 180 (2002), pp. 383 – 403.
- [2] S. Bardenhagen and E. Kober, *The generalized interpolation material point method*, Computer Modeling in Engineering and Science, 5 (2004), pp. 477 – 495.
- [3] J. Brackbill, *The ringing instability in particle-in-cell calculations of low-speed flow*, Journal of Computational Physics, 75 (1988), pp. 469 – 492.
- [4] J. Brackbill, D. Kothe, and H. Ruppel, *Flip: A low-dissipation, particle-in-cell method for fluid flow*, Computer Physics Communications, 48 (1988), pp. 25 – 38.
- [5] G. H. Golub and C. F. V. Loan, *Matrix Computations*, The John Hopkins University Press, third ed., 1996.
- [6] C.E. Gritton, *Ringing Instabilities in Particle Methods*, M.S.Thesis in Computational Engineering and Science, August 2014, School of Computing, University of Utah.
- [7] F. H. Harlow *The particle-in-cell method for fluid dynamics*, Methods in Computational Physics, 3 (1964).
- [8] A. Langdon, *Effects of the spatial grid in simulation plasmas*, Journal of Computational Physics, 6 (1970), pp. 247 – 267.
- [9] J. D. Logan, *Applied Partial Differential Equations*, Springer-Verlag, New York, second ed., 2004.

- [10] M. Steffen, R. M. Kirby, and M. Berzins, *Analysis and reduction of quadrature errors in the material point method (mpm)*, International Journal for Numerical Methods in Engineering, 76 (2008), pp. 922–948.
- [11] D. Sulusky, Z. Chen, and H. Schreyer, *A particle method for history-dependent materials*, Computer Methods in Applied Mechanics and Engineering, 118 (1994), pp. 179 – 196.
- [12] L.T. Tran and J. Kim and M. Berzins, *Solving Time-Dependent PDEs using the Material Point Method, A Case Study from Gas Dynamics*, International Journal for Numerical Methods in Fluids”, 62,7,709–732”,2009.
- [13] L. N. TREFETHEN AND I. DAVID BAU, *Numerical Linear Algebra*, SIAM, 1997.

IMPLEMENTATION AND APPLICATION OF VECTOR FORM INTRINSIC FINITE ELEMENT IN PUSHOVER ANALYSIS FOR REINFORCED CONCRETE BUILDINGS

FU-PEI HSIAO¹, HERMANTO HO², REN-ZUO WANG¹ AND YU-CHEN OU²

¹National Center for Research on Earthquake Engineering (NCREE)
No.200, Sec. 3, HsinHai Rd., Da'an Dist., Taipei City 10668, Taiwan (R.O.C.)
e-mail: fphsiao@ncree.narl.org.tw, web page: <http://w3r2.ncree.narl.org.tw/index.aspx>

²National Taiwan University of Science and Technology (NTUST)
No.43, Sec. 4, Keelung Rd., Da'an Dist., Taipei City 10607, Taiwan (R.O.C.)
e-mail: yuchenou@mail.ntust.edu.tw, web page: <http://www-e.ntust.edu.tw/home.php>

Key words: Vector Form Intrinsic Finite Element, Reinforced Concrete, Pushover Analysis.

Abstract. This study aims to build numerical model of retrofitting analysis of Reinforced Concrete (RC) buildings with vector form intrinsic finite element (VFIFE). Fiber element method is introduced in the paper to acquire the moment-curvature relation of the section and to define the behaviour of RC material. This paper also uses equivalent truss to build the analysis model of brick wall. In the end, lab and in-situ test specimens are utilized to assess analysis method.

The VFIFE method using in this study is one of the particle-based methods. The VFIFE method is included with the point value description, path element and convected material frame as the important characteristics. Thus, the RC structure is represented by finite particles. Each particle is subjected to the external forces and internal forces. The particle satisfies the Newton's Law. A fictitious reversed rigid body motion is used to remove the rigid body motion from the deformations of the element.

Pushover analysis is large deformation analysis. The conventional finite element method base program such as ETABS can encounter numerical difficulties in converging to a correct solution during an analysis involving large element deformation, highly non-linear plasticity or contact between surfaces. This research applied the VFIFE to solve the problems that usually occur on finite element program while performing pushover analysis. The analysis results show that for complex structures, VFIFE still could perform the pushover analysis until all the elements were collapsed but ETABS could not continue the analysis after reach the performance point. Automatically, VFIFE can predict better result in ductility rather than ETABS.

As indicated in analysis results, better performance is identified in initial stiffness, yield strength, maximum strength, or steady strength of specimens when compared with lab test results. Biases are within the tolerance range. Additionally, when failure model of specimens is compared, similar performance with lab test result is found. Hence, analysis method proposed by this paper is able to effectively simulate seismic capacity and failure behaviour of RC buildings.

1 INTRODUCTION

Currently, Seismic design criteria tend to shift from the force based procedure to performance based procedure for design and evaluation purpose. The nonlinear static analysis, which is also called pushover analysis, is a transparent and efficient method for predicting seismic behavior of the structures. The accuracy of the pushover analysis depends on the well-defined properties of nonlinear hinges in structure elements. This method appears in all publications of ATC-40 Report [1], and ASCE 41 report [2], which is the latest in a series of document developed to assist engineers with the seismic assessment and rehabilitation of existing buildings [3, 4].

Software programs such as ETABS, SAP2000, and Perform3D are used to perform pushover analysis. Finite element method is adopted by the programs. Finite element method can encounter numerical difficulties in converging to a correct solution during an analysis involving large element deformation, highly non-linear plasticity or contact between surfaces.

The nonlinear analysis of a structure is an iterative procedure. It depends on the final displacement, as the effective damping depends on the hysteretic energy loss due to inelastic deformations, which in turn depends on the final displacement. This makes the analysis procedure iterative.

The vector form intrinsic finite element (VFIFE) method can overcome the large deformation from pushover analysis. The VFIFE is a vector mechanics-based mathematical calculation method for structures with large deformations. It is based on an intrinsic finite-element modeling approach, an explicit algorithm, and a corotational formulation of kinematics [5~7]. The primary objective of this method is to handle the motion and deformation of a system of multiple continuous bodies and their interactions. The VFIFE method considers that the motion of a structure can be represented by a finite particles.

2 VECTOR FORM INTRINSIC FINITE ELEMENT (VFIFE) METHOD

2.1 Fundamentals of the Vector Form Intrinsic Finite Element (VFIFE) Method

The VFIFE is a vector mechanics-based mathematical calculation method for structures with large deformations. It is based on an intrinsic finite-element modelling approach, an explicit algorithm, and a corotational formulation of kinematics [5~7]. The primary objective of this method is to handle the motion and deformation of a system of multiple continuous bodies and their interactions.

The main objective of the VFIFE method development is to estimate the structural responses under various types of loading conditions especially from the continuous states to the discontinuous states of the structures. It is expected that VFIFE method could consider the geometrical and mechanical properties of the structure during the motion accurately. Nevertheless, the VFIFE method modelling concept of the structure is represented by finite particles, so that the conventional nonlinear structural analysis methods (CNSAM) could not be applied. The VFIFE method establish a new analysis strategy based on the intrinsic theories of mechanics[5] and avoid the difficulties such as the iterative and perturbation procedures in solving partial differential equations commonly adopted in the CNSAM. The primary concept of VFIFE is that the structure is illustrated as a system composed of particles and forces components. The forces that acting on the particles include the internal forces and external

forces. There are general assumptions that used to explain the deformation of the structure:

1. The internal forces are calculated from the deformations of structural members such as truss, frame, or solid elements.
2. Each structural members has geometry and position changes simultaneously. The changes of the geometry and the position for the deformable structure are not separated.
3. Each particles might has their own motion trajectory.

According to these assumptions, the associated analytical operations will use:

- a. Point value description (PVD)
- b. Path element.
- c. Convected material frame (CMF).

Types of the particles and internal forces from the deformation of the frame element for each of above assumptions will be explained in the following sections.

2.2 Point value description (PVD)

The characteristic of the VFIFE analysis that use PVD concept could be seen from Figure 1. Numerical procedures that use VFIFE method can be solved by using the vector form concept and PVD. The deformations and motions of a structure are represented by the positions of the particles in spatial-temporal space and discrete times points that shown in Figure 1(a). The discrete time points is used by the PVD to describe the whole time trajectory of deformable body. The VFIFE method does not use a continuous time function such as $f(x, y, z, t)$, the response parameters such as displacement, and velocity are not continuous function of time and position in the whole time trajectory which is different from the conventional analysis methods. Therefore, it does not involve in solving the partial differential equations for structural members because the equations of motion of the particles at each different time point are built using Newton's law. The reference configuration of the structure at time t_a can be identified by connecting the representative particles ($i_a, j_a, 1_a, 2_a, \text{ and } 3_a$). The trajectory of any representative particles fulfil the definition of a path element at each set of time points (e.g. $i - i_1, i_1 - i_a, i_a - i_t, i_t - i_b, i_b - i_c, i_c - i_f$ in Figure 1(b)). The PVD and the function of time trajectory are shown in Fig. 1(b). The dotted line represents the particle trajectories from the positions at time t_0 to positions at time t_f .

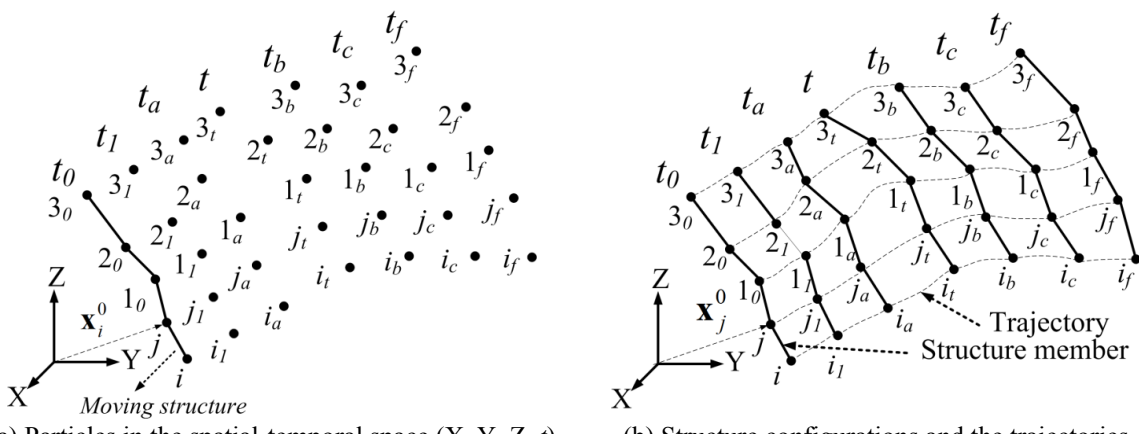


Figure 1: Motion of a structure in VFIFE method

2.3 Path element and types of the particle

The motion of a structure is needed in order to introduce the concept of path element that shown in Figure 2(a). The whole time trajectory of the particles i and j are the end particles of the structure members. The PVD is used to describe the whole time trajectory of particles i and j. For instance, a series of time points ($t_0 < t_1 < \dots < t_a < t < t_b < t_c \dots < t_f$) is being used to represent the entire time for the particle i. If the time interval is (t_a, t_b) , \mathbf{x}_i^a and \mathbf{x}_i^b are position vectors of the particle i at time t_a and t_b , and if the point values (t_a, \mathbf{x}_i^a) and (t_b, \mathbf{x}_i^b) are known. Afterwards the time trajectory of the particles in time interval (t_a, t_b) could be described by using a position function $\mathbf{x}_i(t)$.

$$\mathbf{x}_i = \mathbf{x}_i(t), \quad t_a \leq t \leq t_b \quad (1)$$

The position function $\mathbf{x}_i(t)$ is in vector form. Hence, it is defined as a position vector time function and abbreviated as position vector. The $\mathbf{x}_i(t)$ can be used to fulfil the equations of motion for the particles, or any physical conditions such as a fixed support of a structure. The motion of the frame element i-j in the time interval (t_a, t_b) as shown in Figure 2(a) could be described by using two position vectors $(\mathbf{x}_i(t), \mathbf{x}_j(t))$.

According to the physical conditions of the particles, three basic types of the particles are presented as follows:

1. Motion particle: The motion particle i has a mass, internal forces \mathbf{f}_i and external forces \mathbf{F}_i on the particle. This mass is a constant mass. The position vector $\mathbf{x}_i(t)$ of the motion particle must fulfil the Newton's Law as follows:

$$m_i \ddot{\mathbf{x}}_i = \mathbf{F}_i - \mathbf{f}_i \quad (2)$$

where m_i is the mass of the particle i. The initial conditions are:

$$\mathbf{x}(t_a) = \mathbf{x}_i^a, \mathbf{x}(t_b) = \mathbf{x}_i^b, \dot{\mathbf{x}}(t_a) = \dot{\mathbf{x}}_i^a, \dot{\mathbf{x}}(t_b) = \dot{\mathbf{x}}_i^b \quad (3)$$

The path element can be viewed as a position vector $\mathbf{x}_i(t)$ to describe the motion of the particle only in the time interval (t_a, t_b) .

2. Connected particle: The particle i in the frame element i-j is connected to the particle n in the frame element n-h. The position vectors of particles i and n fulfill the initial condition and the relationship of the two particles:

$$\mathbf{x}_i(t_a) = \mathbf{x}_i^a = \mathbf{x}_n(t_a) = \mathbf{x}_n^a, \quad \mathbf{x}_i(t) = \mathbf{x}_n(t), \quad t_a \leq t \leq t_b \quad (4)$$

3. Displacement particle: The position vector of the particle i in the time interval (t_a, t_b) is established by a function of time $g(t)$:

$$\mathbf{x}_i(t) = g(t) \quad (5)$$

And the initial condition have to fulfil:

$$\mathbf{x}_i(t_a) = g(t_a) = \mathbf{x}_i^a \quad (6)$$

In general, the displacement particle is for the displacement control. For instance, setting $g(t)$ as a constant value \mathbf{x}_i^0 , then the position vector is:

$$\mathbf{x}_i(t) = \mathbf{x}_i^0 \quad (7)$$

For each type of particle, the whole time trajectory in time interval (t_0, t_f) needs the use of f path elements. Each path element determines the motion of the particle in each time interval and the initial time and final time could be redefined if the physical condition of the particle is

changed suddenly.

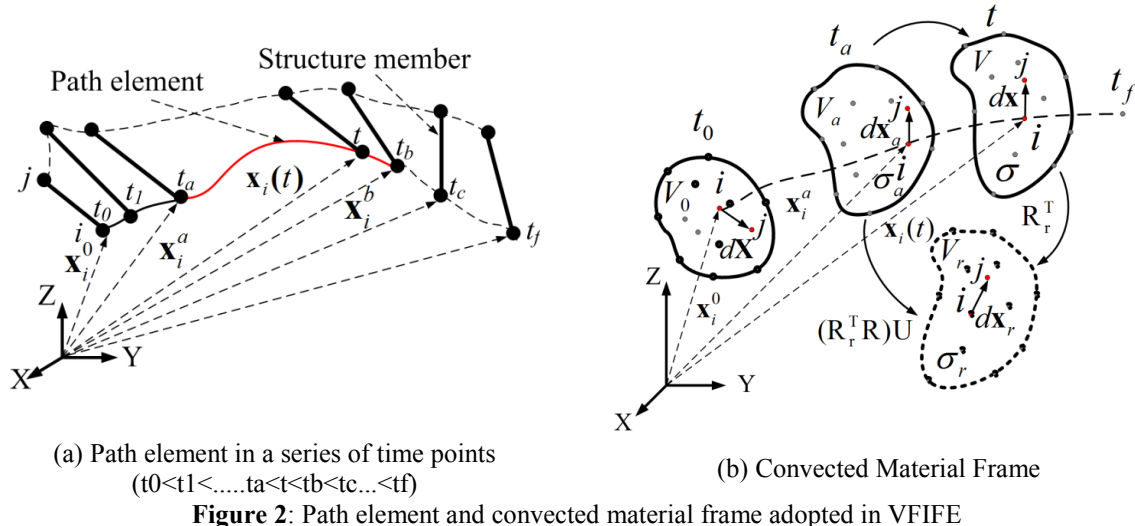


Figure 2: Path element and convected material frame adopted in VFIFE

2.4 Structural models

The structure model for a space frame in Figure 3(a) is represented in this section using many particles from Figure 3(b). Each particles is subjected to the internal forces or the external forces. The internal forces on particles could be calculated from the deformations of the frame elements.

Interaction forces between two end particles of the element are internal forces. The particles 1, 2, 3, and 4 from Figure 3(b) are specified as displacement particles. The particles $i, j, 5$ and 6 are specified as motion particles.

In the traditional Finite Element Method, the particle's position vector $\mathbf{x}(x, y, z, t)$ is a function of the current position (x, y, z) and at any time t from the initial states to the final states.

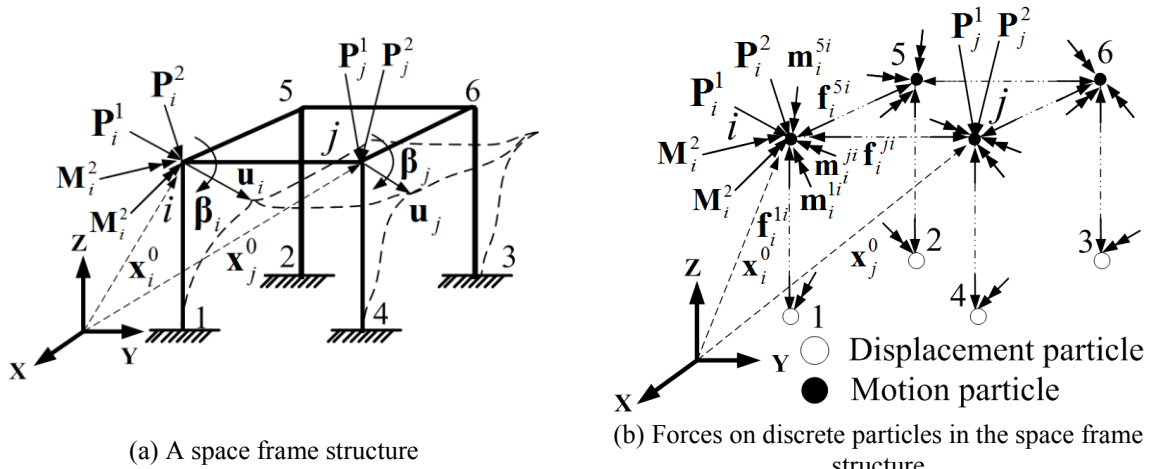


Figure 3: Analytical model of a space frame structure

In VFIFE, the particle's position vector $\mathbf{x}(t)$ of each particle is a time function at the interval of (t_a, t_b) only. In this case, the displacement particles are act as fixed ends. The displacements and rotations of the motion particle i in the global coordinates could be calculated from the

following equations:

$$\bar{m}_i \ddot{u}_i = F_i - f_i \quad (8)$$

$$\bar{I}_i \ddot{\beta}_i = M_i - m_i \quad (9)$$

where

$$F_i = \sum_{s=1}^2 F_i^s, \quad M_i = \sum_{k=1}^2 M_i^k \quad (10)$$

$$f_i = \sum_{n=1}^3 f_i^{ni}, \quad m_i = \sum_{n=1}^3 m_i^{ni} \quad (11)$$

$$\bar{m}_i = \sum_{n=1}^3 \bar{m}_i^{ni}, \quad \bar{I}_i = \sum_{n=1}^3 \bar{I}_i^{ni} \quad (12)$$

where s is the external force and k is the moment numbers. The n represents the particle number. The F_i and M_i are the total external forces and moments. The f_i and m_i are the total internal forces and moments. The Computation of these internal forces will be acquainted in the following sections. The u_i and β_i are the particle's displacement and rotation vectors. The \bar{m}_i and \bar{I}_i are the particles mass and the mass moment inertia. In Eq. (12), the mass \bar{m}_i^{ni} and the mass moment of inertia \bar{I}_i^{ni} of the end particles of the frame element can be computed from:

$$\bar{m}_i^{ni} = \begin{bmatrix} \bar{m}_i^{ni} & 0 & 0 \\ 0 & \bar{m}_i^{ni} & 0 \\ 0 & 0 & \bar{m}_i^{ni} \end{bmatrix}, \quad \bar{I}_i^{ni} = \Omega_a \hat{I}_i^{ni} \quad (13)$$

where

$$\bar{m}_i^{ni} = 1/2 \rho l^0 A^0, \quad l^0 = |\mathbf{x}_{ji}^0| \quad (14)$$

$$\mathbf{x}_{ji}^0 = \mathbf{x}_j^0 - \mathbf{x}_i^0 \quad (15)$$

$$\hat{I}_i^{ni} = \begin{bmatrix} \hat{I}_{i1}^{ni} & 0 & 0 \\ 0 & \hat{I}_{i2}^{ni} & 0 \\ 0 & 0 & \hat{I}_{i3}^{ni} \end{bmatrix}, \quad \hat{I}_{iq}^{ni} = \bar{m}_i^{ni} r_{iq}^{ni} = \bar{m}_i^{ni} \sqrt{I_{iq}^{ni} / A}, \quad q=1\sim 3 \quad (16)$$

The l^0 and A^0 are the length and cross-sectional area of the frame element at the initial state. The ρ and \bar{m}_i^{ni} are the mass density and mass of the two ends of the frame element.

The \bar{I}_i^{ni} and I_{iq}^{ni} are the i^{th} particle's mass moment of inertia and the moment of inertia of the cross-sectional area with respect to the q principal direction. The transformation matrix Ω_a and the principal directions will be explained in the following sections. The advantage of using path elements is to facilitate the computation of the material frame within the time interval (t_a, t_b) . For example, geometrical changes of an element could be assumed to fulfil the following:

(a) The initial values at time t_a are required for the analysis in each path element but the deformation history before the time t_a is not considered in VFIFE model. Moreover, the rates of stress such as the Jaumann and Green-Naghdi rates of Kirchhoff stress are not even considered because the deformations of the elements in VFIFE model are total deformations in each path element. Nevertheless, in the traditional Finite element method and the explicit Finite

element method, the deformation history and the current deformation of the frame must take into consideration in order to compute the incremental deformations of the structural member. It utilizes a position vector $\mathbf{x}(x, y, z, t)$ to describe the deformation of the member. Hence, it needs to consider the rates of stress.

(b) In each path elements, the element is prismatic in which the section and the material along the element length remain constant when the geometrical changes are neglected while calculating the internal forces. The stresses and strains are used. The stress and strain analysis of the frame element are a straight forward problems for the large displacement and small deformation. That is, over the entire analysis from the initial to the final states, the total geometrical change can still be very large. Moreover, the discontinuous changing of the physical properties at each time point is permitted.

3 TEASPA METHOD

This research utilizes VFIFE method that combine with TEASPA method [8] to perform pushover analysis of 3-D reinforced concrete structures compares with experimental results and also ETABS. It needs to add another parameters in order to perform pushover analysis with the most accurate result compares to the experiment result. Columns, Frame elements and a school building are taken as the source of database for this research.

The shear drift capacity of the shear damage column is estimated from the following empirical equation. This equation is based on the observation of 50 shear-critical column databases that is proposed by Elwood and Moehle [9].

$$\frac{A_s}{H} = \frac{3}{100} + 4\rho'' - \frac{1}{133}x \frac{v_m}{\sqrt{f'_c}} - \frac{1}{40}x \frac{P}{A_g f'_c} \geq \frac{1}{100} \quad (17)$$

where H is the length of the column; ρ'' is the transverse reinforcement ratio as A_{st}/bxs ; A_{st} is the transverse reinforcement area; b is the width of column section; s is the spacing of the transverse reinforcement; v is the maximum nominal shear stress in kgf/cm^2 as V/bd ; d is the depth from the extreme fiber of concrete to the center line of tension reinforcement; f'_c is the concrete compressive strength in kgf/cm^2 ; and A_g is the gross cross-sectional area of the column. The shear drift capacity is associated to the maximum shear stress, transverse steel ratio and also axial load. The shear drift ratio is getting lower if the axial load ratio is getting higher. As the nominal shear stress degrades, the shear drift ratio will increase, and the shear drift ratio is proportional to the amount of transverse reinforcement.

The axial drift capacity of shear damage column is estimated based on the shear friction model proposed by Elwood and Moehle which the axial drift capacity is the function of the axial load, the amount of transverse reinforcement, and the critical angle [10].

$$\frac{A_a}{H} = \frac{4}{100}x \frac{1+(\tan\theta)^2}{\tan\theta + Px \frac{s}{k' A_{st} f_{yt} d_c \tan\theta}} \quad (18)$$

where f_{yt} is the yield strength of the transverse reinforcement; d_c is the depth of the column

core from center line to center line of the ties.

The flexural shear strength is the required lateral load to reach the maximum flexural capacity M_n at column end. The flexural shear strength of a double curvature column can be calculated as follow:

$$V_b = \frac{2M_n}{H} \quad (19)$$

where M_n is the nominal moment strength of a reinforced concrete column.

The nonlinear moment hinge is placed at the both ends of the column to present the flexural failure mode or flexural-shear failure mode. The parameters of the nonlinear hinge of the column are calculated as follows:

$$a = \frac{A_s}{H} - \frac{A_y}{H} \quad (20)$$

$$b = \max\left(\frac{A_a}{H}; \frac{A_s}{H}\right) \quad (21)$$

$$\Delta_y = \frac{V_b}{k} = \frac{V_b H^3}{12 \alpha \alpha E I_g} \quad (22)$$

Moment SF = M_n ; Rotation SF = 1; α is the stiffness coefficient that consider the reduction of the element stiffness on second order analysis.

According to ACI 318-05[11], it is permitted to assume $\alpha = 0.35$. The nonlinear shear hinge is placed at the middle of the column to illustrate the shear failure mode. The parameter are calculated as follows:

$$c = \min\left(\frac{A_s}{H}; 0.04\right) \quad (23)$$

Force SF = V_n ; Displacement SF = H .

4 CASE STUDY

Each specimens was model using ETABS program and VFIFE program. The plastic hinges of elements of the model were calculated and defined by using modified TEASPA method. Finally the pushover curves were obtained by solving nonlinear problem by using the ETABS program and VFIFE program. Based on the experimental results, the beam was remained in elastic behavior. The failures were occurred in columns and brick walls so there are no plastic hinges on beam from our models in ETABS and VFIFE.

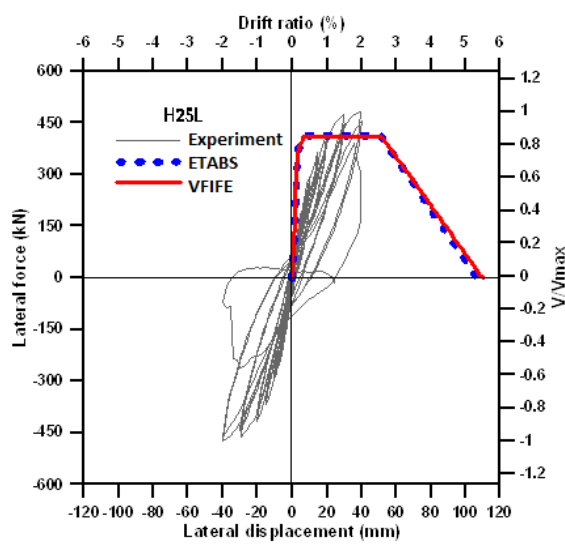


Figure 4: Base shear - Displacement comparison of H25-L

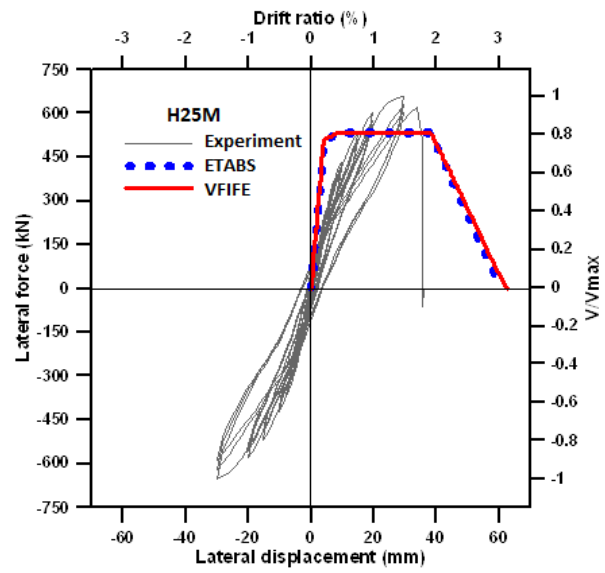


Figure 5: Base shear - Displacement comparison of H25-M

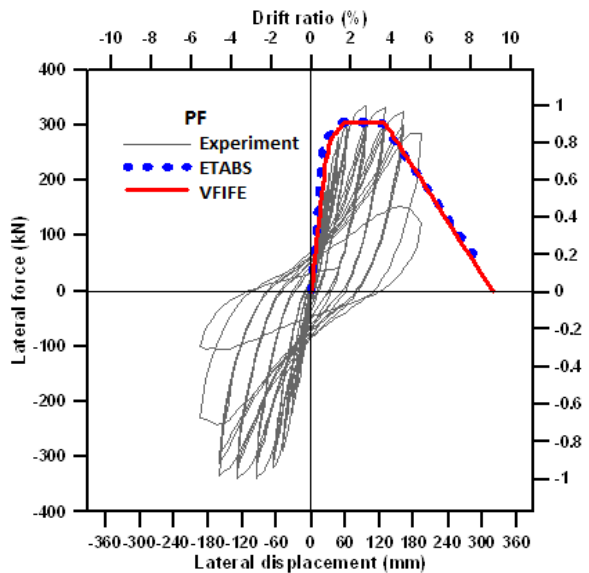


Figure 6: Base shear - Displacement comparison of PF

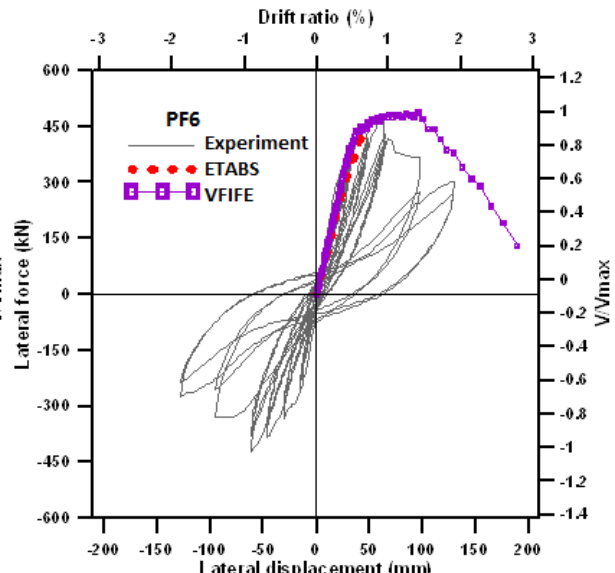


Figure 7: Base shear - Roof Displacement comparison of PF6

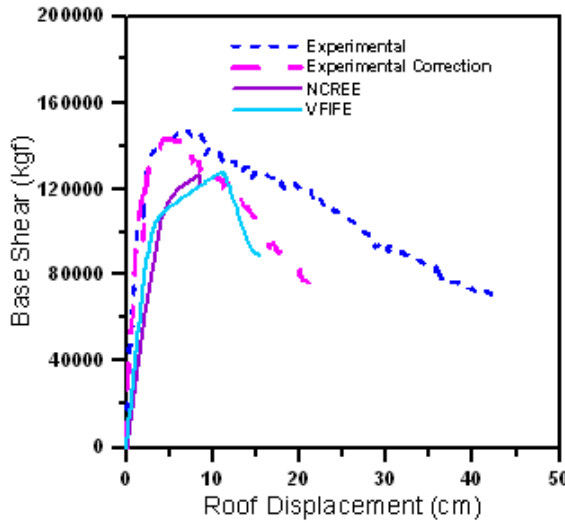


Figure 8: Base shear - Roof displacement comparison of Guanmiao

Figure 4 and Figure 5 are shown that the stiffness from ETABS and VFIFE of each column specimens has a higher stiffness compares to experimental result. It shows that the stiffness coefficient from TEASPA method is too large for the column specimen.

The ultimate strength from ETABS and VFIFE are lower than the experimental result. ETABS and VFIFE show much the same result for column specimens. For columns with high axial load have displacement almost half compares with small axial load columns but their strength are lower.

Figure 6 and Figure 7 illustrate that the initial stiffness for both specimen are approximately the same. The ultimate strength from VFIFE and ETABS are almost the same with the experimental result. The PF specimen shows the same ductility for both VFIFE and ETABS. However, The ductility from ETABS is different from VFIFE for specimen PF6. It shows that after reach the ultimate point, ETABS could not continue to obtain the displacement result. It indicates that ETABS is not suitable for a complex model for pushover analysis. VFIFE still could continue the pushover analysis until most of the elements were collapsed.

Figure 8 illustrates the comparison among the pushover curves obtained by the two analysis cases and the test. Obviously, the results of the analysis cases are conservative in comparison with the test. Figure 8 indicates that the stiffness of the pushover curve obtained from both VFIFE and ETABS are significantly smaller than the stiffness measured from the test. The imperfect condition of the test may account for the problem. The specimen was created from the real building; therefore, some non-structure elements not be taken in the analysis may contribute to increase the stiffness of the specimens.

It also indicates the same situation with the PF6 specimen for ETABS analysis. It will stop the pushover analysis after reach the performance point. It is happened because of pushover analysis is a large deformation analysis. Finite element method in this case ETABS can encounter numerical difficulties in converging to a correct solution during an analysis involving large element deformation, highly non-linear plasticity or contact between surfaces.

The nonlinear analysis of a structure is an iterative procedure. It depends on the final

displacement, as the effective damping depends on the hysteretic energy loss due to inelastic deformations, which in turn depends on the final displacement. This makes the analysis procedure iterative. Difficulty in the solution is faced near the ultimate load, as the stiffness matrix at this point becomes negative definite due to instability of the structure becoming a mechanism .Therefore, the result of a specimen that starts to collapse while performing pushover analysis with finite element software will shown inaccurate result.

5 CONCLUSIONS

Several main conclusions of this research are gathered as follows:

1. Analysis results for Column specimens using ETABS and VFIFE show approximately the same results in stiffness, ultimate base shear and also the ductility. For columns with high axial load have displacement almost half compares with small axial load columns but their strength are lower.
2. For PF specimen which is one story pure frame, ETABS and VFIFE also show more or less the same results in stiffness, ultimate base shear and also the ductility. For PF6 specimen also shows approximately the same in initial stiffness and ultimate base shear. However, the ductility between ETABS and VFIFE are not the same. After reach the ultimate value, ETABS can't continue to show the deformation but VFIFE could continue to do the pushover until most of elements failed . It indicates that ETABS is not capable for Pushover Analysis for complex structures.
3. The stiffness of the pushover curve obtained from both VFIFE and ETABS are significantly smaller than the stiffness and shear strength measured from the test for Guanmiao School Building specimen. The imperfect condition of the test may account for the problem. The specimen was created from the real building; therefore, some non-structure elements not be taken in the analysis may contribute to increase the stiffness of the specimens. The ductility from ETABS has the same problem with PF6 specimen if it compares with VFIFE.
4. From all the analysis results, They show tendency that the more complex the specimen, the softer the stiffness.

REFERENCES

- [1] ATC-40, *Seismic evaluation and retrofit of concrete buildings*, ATC-40 Report, Applied Technology Council, Redwood City, California, USA, (1996).
- [2] ASCE 41-06, *Seismic rehabilitation of existing buildings*, American Society of Civil Engineers, ASCE, (2006).
- [3] FEMA 273, *NEHRP guidelines for the seismic rehabilitation of buildings*, Federal Emergency Management Agency, Washington, D.C., (1997).
- [4] FEMA 356, *Prestandard and commentary for the seismic rehabilitation of buildings*, Federal Emergency Management Agency, Washington, D.C., (2000).

- [5] Ting, E. C., Shih, C. and Wang, Y. K., Fundamentals of a vector form intrinsic finite element: Part I. Basic procedure and a plane frame element, *Journal of Mechanics* (2004) **20**(2):113-122.
- [6] Ting, E. C., Shih, C. and Wang, Y. K., Fundamentals of a vector form intrinsic finite element: Part II. Plane solid elements, *Journal of Mechanics* (2004) **20**(2):123-132.
- [7] Shih, C., Wang, Y. K. and Ting, E. C., Fundamentals of a vector form intrinsic finite element: Part III. Convected material frame and examples, *Journal of Mechanics* (2004) **20**(2):133-143.
- [8] NCREE-09-023, *Technology handbook for seismic evaluation and retrofit of school buildings (Second edition)*, National Center on Research for Earthquake Engineering, Taipei Taiwan, (in Chinese), (2009).
- [9] Elwood, K. J., and Moehle, J. P., Drift Capacity of Reinforced Concrete Columns with Light Transverse Reinforcement, *Earthquake Spectra* (2005) **21**(1):71-89.
- [10] Elwood, K. J., and Moehle, J. P., Axial capacity model for shear damaged columns, *ACI Structural Journal* (2005) **102**(4):578-587.
- [11] ACI Committee 318, *Building code requirement for structural concrete (ACI 318-05) and commentary (318R-05)*, American Concrete Institute, Farmington Hills, Mich., (2005).

NUMERICAL SIMULATION ANALYSIS OF REINFORCED CONCRETE STRUCTURE USING VFIFE FIBER-ELEMENT

REN-ZUO. WANG¹, BING-CHANG LIN² AND CHAO-HSUM HUANG³

¹National Center for Research on Earthquake Engineering
200, Sec. 3, Xinhai Rd., Taipei City 10668, Taiwan, R.O.C.
e-mail: rzwang@ncree.narl.org.tw, web page: <http://www.ncree.org/>

²Department of Civil Engineering, Chung Yuan Christian University
200 Chung Pei Road, Chung Li District, Taoyuan City, Taiwan 32023, R.O.C.
e-mail: tbinchan@cycu.edu.tw, web page: <http://www.cycu.edu.tw/>

³ Department of Civil Engineering & Disaster Prevention Engineering, National Taipei University of Technology
1, Sec. 3, Zhongxiao E. Rd., Taipei 10608 Taiwan, R.O.C.
e-mail: steve@ntut.edu.tw, web page: <http://www-en.ntut.edu.tw/>

Key words: Vector form intrinsic finite element, fiber-element model.

Abstract. In this paper, a vector form intrinsic finite element (VFIFE or V-5) method is used to compute the nonlinear responses of reinforced concrete (RC) structure. In addition, the fiber-element model of VFIFE frame element is formulated. Material models of both concrete and steel on the cross section of the member are considered. The VFIFE method is a particle-based method. They have three key VFIFE processes such as the point value description, path element and convected material frame [1]. The RC structure is represented by finite particles. Each particle is subjected to the external forces and internal forces. The particle satisfies the Newton's Law. A fictitious reversed rigid body motion is used to remove the rigid body motion from the deformations of the element [2]. The internal forces of the element in deformation coordinates satisfy the equilibrium equations. Comparing the results of numerical simulations and experiments of the reinforced concrete members subjected to external loads, the proposed method demonstrate accuracy and efficiency.

1 INTRODUCTION

For nonlinear material structures, most of the existing nonlinear material models can be classified into two main categories: lumped and distributed plasticity models. The lumped model is an efficient way to represent inelasticity in frames. A typical finite element method considering the geometrical and material nonlinearities requires iterations at each incremental step to achieve the equilibrium. This method encourages flexural yielding and can ensure that plastic hinge rotation will occur at the member ends rather than along the column length. The second-order plastic hinge concept based on the use of stability interpolation functions has been proposed for frame structure analysis proposed a general criterion of localization and two plastic hinges at the end of the frame member. Some researches improved the lumped

plastic hinge method, such as for example the distributed plasticity model (also called plastic-zone model), which allows for the gradual spread of yielding within the member. In the distributed plasticity model, the frame element stiffness can be computed by using either the displacement or the force-based approach. This allows plastic hinges to form at any location in an element. In addition, the element cross-section can be a fiber section using different stress-strain models for different fibers within the cross-section. Without properly taking into account the internal forces due to pure deformations, most of these studies may not be able to simulate inelastic structural responses of moving structures subjected to extremely-large displacements or deformations.

Recently, the VFIFE method has been proposed by Ting, et al. [1] and Wang [2]. This method applies a unique approach to compute the effects of rigid motion, allowing the simulation of extremely large deformation of elastic motion structures. The key objective of this study is to construct a fiber-section of the frame element subjected to extremely large deformation having inelastic material properties. In this study, in order to model the reinforced concrete member, the fiber-element formulation has considered two material types such as steel and concrete is proposed. It can be used to compute nonlinear responses of reinforced concrete structure. Three numerical examples are presented to illustrate the capability and the accuracy of the proposed method.

2 FUNDAMENTALS OF VFIFE METHOD

In this study, the VFIFE method is extended in order to analyze reinforced concrete members containing multiple deformable bodies with the following characteristics: (1) interact with each other, (2) or are discontinuous, (3) undergo large deformations and arbitrary rigid body motions. The VFIFE method establish a new analysis strategy based on the intrinsic theories of mechanics and avoid the difficulties such as the iterative and perturbation procedures in solving partial differential equations commonly adopted in the conventional nonlinear structural analysis methods (CNSAM). The key VFIFE concept is that the structure is viewed as a system composed of particles and forces components. The forces on the particles include the internal forces and external forces. In order to describe the deformation of the structure, the following general assumptions are adopted: (1) the internal forces are computed from the deformations of the structural members such frame element, (2) each structural member has geometry and position changes simultaneously. In addition, the changes of the geometry and the position for the deformable structure are not separated, and (3) each particle may have a motion trajectory. Base on these assumptions, the associated analytical operations are using: (1) the point value description (PVD), (2) the path element, and (3) the convected material frame (CMF).

Figure 1 shows the characteristic of the VFIFE analysis using the PVD concept. The motions and deformations of a structure are described by the positions of the particles and discrete time points as shown in Fig. 1(a). The PVD uses many discrete time points to describe the entire time trajectory of the deformable body. VFIFE analysis is not required to solve the partial differential equations for structural members. This is because the equations of motion on particles at each time point are established using Newton's Law. The reference configuration of the structure at time t_a can be identified by connecting the representative

particles ($i_a, j_a, 1_a$). The trajectory of any representative particle satisfies the definition of a path element at each set of time points (e.g. $i-i_1, i_1-i_a, i_a-i_t, i_t-i_b, i_b-i_c, i_c-i_f$ in Fig. 1(b)). Details of the path element will be explained in the following sections. The PVD and the function of time trajectory are shown in Fig. 1(b). The dotted line represents the particle trajectories from the positions at time t_0 to positions at time t_f .

In order to introduce the concept of the path element, the motion of a structure member is considered as shown in Fig. 2(a). The PVD is used to describe the entire time trajectory of particles i and j . For example, a series of time points ($t_0 < t_1 < \dots < t_a < t < t_b < t_c < \dots < t_f$) is used to describe the entire time for the particle i . Figure 2(b) shows four configurations, original configuration V_0 at time t_0 , configuration V_a at time t_a , current configuration V at time t and the fictitious configuration V_r . The position vectors used to describe the motion of the deformable body are continuous functions of time. In the VFIFE method, the deformable body is represented by many particles using PVD to describe its motion as shown in Fig. 1. The entire time trajectory of the deformable body uses many path elements. For the purpose of discussion, choose the time interval (t_a, t_b) as one of the path elements in the entire time trajectory of the deformable body. The position, material properties, stress and the geometric features of the deformable body at time t_a is known as the configuration V_a . In Fig. 2(b), the relative position $d\mathbf{x}$ between particles i and j in the current configuration V is computed from $d\mathbf{x}_a$:

$$d\mathbf{x} = \mathbf{F} d\mathbf{x}_a = \mathbf{R} \mathbf{U} d\mathbf{x}_a \quad (1)$$

where \mathbf{F} is the deformation gradient. \mathbf{R} is a rigid body rotation matrix. \mathbf{U} is a matrix of the deformation. The fictitious configuration V_r can be computed as follows:

$$d\mathbf{x}_r = \mathbf{F}_r d\mathbf{x} = \mathbf{R}_r^T d\mathbf{x} \quad (2)$$

where \mathbf{F}_r is a virtual deformation gradient and \mathbf{R}_r is a reversed rigid body rotation matrix. In this study, \mathbf{F}_r is equal to a reversed rotation matrix \mathbf{R}_r . Substitute equations (1) into (2), the following can be obtained:

$$d\mathbf{x}_r = \mathbf{F}_r \mathbf{F} d\mathbf{x}_a = (\mathbf{R}_r^T \mathbf{R}) \mathbf{U} d\mathbf{x}_a \quad (3)$$

If the reversed rotation matrix \mathbf{R}_r is close to \mathbf{R} , the \mathbf{R}_r can be used to reduce the effects of the rigid body rotation on the deformation gradient \mathbf{F} of a deformable body. Then:

$$d\mathbf{x}_r = \mathbf{U} d\mathbf{x}_a \quad (4)$$

In this study, a procedure to obtain the best approximate rotation matrix \mathbf{R}_r is proposed for the VFIFE method. The internal forces of the structural members are computed from using the CMF, PVD and path element.

4 REINFORCED CONCRETE FIBER FRAME ELEMENT

The internal force formulation of reinforced concrete fiber frame element (RCFFE) is introduced. The internal virtual work in the deformation coordinates of the RCFE is:

$$\delta W = (\hat{\mathbf{d}}^*)^T \hat{\mathbf{f}}_c + (\hat{\mathbf{d}}^*)^T \hat{\mathbf{f}}_s \quad (5)$$

The deformations of the RCFE are based on Euler beam theory. The pure deformations $\Delta\hat{u}^d$ of the RCFE at any cross section can be computed by the pure concrete deformation $\Delta\hat{u}_c^d$ and

steel deformation $\Delta\hat{u}_s^d$ along the axis of the frame element in the deformation coordinates. In Fig. 3, Total deformation of RCFFE can be represented as:

$$\Delta\hat{u}^d = \Delta\hat{u}_c^d + \Delta\hat{u}_s^d \quad (6)$$

where

$$\Delta\hat{u}_c^d = \hat{u}_m^d - \hat{y} \frac{d\hat{v}^d}{d\hat{x}} \quad (7)$$

$$\Delta\hat{u}_s^d = \hat{u}_m^d - (h_c - h_{sj}) \frac{d\hat{v}^d}{d\hat{x}} \quad (8)$$

$$\hat{u}_m^d = a_1 + a_2 \hat{x} \quad (9)$$

$$\hat{v} = a_3 + a_4 \hat{x} + a_5 \hat{x}^2 + a_6 \hat{x}^3 \quad (10)$$

where h_c is a center line of the frame section. The compatibility conditions of the frame element are:

$$\hat{x} = 0, \quad \hat{u}_m^d = 0, \quad \hat{v}^d = 0, \quad \frac{d\hat{v}^d}{d\hat{x}} = \hat{\phi}_{iz} \quad (11)$$

$$\hat{x} = l_a, \quad \hat{u}_m^d = \Delta_e, \quad \hat{v}^d = 0, \quad \frac{d\hat{v}^d}{d\hat{x}} = \hat{\phi}_{iz} \quad (12)$$

The deformation functions are used to compute the internal forces of the frame element. In VFIFE method, the effects of rigid body motion must be removed from the deformation functions in each path element. Then, the internal forces in the fictitious configuration V_r can be evaluated from the traditional procedures. The pure deformation $\Delta\hat{u}^d$ satisfy Eqs. (11) to (12). The concrete deformation $\Delta\hat{u}_c^d$ and steel deformation $\Delta\hat{u}_s^d$ can be written as:

$$\Delta\hat{u}_c^d = s\Delta_e - \{(1-4s+3s^2)\hat{\phi}_{iz} + (-2s+3s^2)\hat{\phi}_{jz}\} \hat{y} \quad (13)$$

$$\Delta\hat{u}_s^d = s\Delta_e - \{(1-4s+3s^2)\hat{\phi}_{iz} + (-2s+3s^2)\hat{\phi}_{jz}\} (h_c - h_{sj}) \quad (14)$$

where $s = \hat{x}/l_a$ is a non-dimensional parameter. Because the deformation of the RCFFE is small deformation in each path element, the infinitesimal concrete strain $\hat{\varepsilon}_c$, steel strain $\hat{\varepsilon}_s$ and total axial strain $\hat{\varepsilon}_s$ are:

$$\hat{\varepsilon} = \hat{\varepsilon}_c + \hat{\varepsilon}_s \quad (15)$$

$$\hat{\varepsilon}_c = \varepsilon_{ac} + \Delta\hat{\varepsilon}_c, \quad \Delta\hat{\varepsilon}_c = \frac{1}{2} \left\{ \frac{\partial(\Delta\hat{u}_c^d)}{\partial\hat{x}} + \left[\frac{\partial(\Delta\hat{u}_c^d)}{\partial\hat{x}} \right]^T \right\} = \frac{d\hat{u}_c^d}{d\hat{x}} = \frac{1}{l_a} \frac{d(\Delta\hat{u}_c^d)}{ds} = \mathbf{B}_c \hat{\mathbf{d}}^* \quad (16)$$

$$\hat{\varepsilon}_s = \varepsilon_{as} + \Delta\hat{\varepsilon}_s, \quad \Delta\hat{\varepsilon}_s = \frac{1}{2} \left\{ \frac{\partial(\Delta\hat{u}_s^d)}{\partial\hat{x}} + \left[\frac{\partial(\Delta\hat{u}_s^d)}{\partial\hat{x}} \right]^T \right\} = \frac{d\hat{u}_s^d}{d\hat{x}} = \frac{1}{l_a} \frac{d(\Delta\hat{u}_s^d)}{ds} = \mathbf{B}_s \hat{\mathbf{d}}^* \quad (17)$$

Where

$$\hat{\mathbf{d}}^* = \begin{Bmatrix} \Delta_e \\ \hat{\phi}_{iz} \\ \hat{\phi}_{jz} \end{Bmatrix} \quad (18)$$

$$\mathbf{B}_s = \frac{1}{l_a} [1 \quad (4-6s)(h_c - h_{sj}) \quad (2-6s)(h_c - h_{sj})] \quad (19)$$

$$\mathbf{B}_c = \frac{1}{l_a} [1 \quad (4-6s)\hat{y} \quad (2-6s)\hat{y}] \quad (20)$$

where ε_{ac} and ε_{as} are the concrete and steel axial strain at time t_a . The $\Delta\hat{\varepsilon}_c$ and $\Delta\hat{\varepsilon}_s$ are the concrete and steel relative axial strains from time t_a to t . The l_a is the length of the frame element at time t_a . In Eqs. (19) and(20), the $\Delta\hat{\varepsilon}_c$ and $\Delta\hat{\varepsilon}_s$ can be written as

$$\Delta\hat{\varepsilon}_c = \frac{\Delta_e}{l_a} + K(s)\hat{y} \quad (21)$$

$$\Delta\hat{\varepsilon}_s = \frac{\Delta_e}{l_a} + K(s)(h_c - h_{sj}) \quad (22)$$

where $K(s)$ is the incremental curvature from time t_a to t . The concrete stress $\hat{\sigma}_c$, steel stress $\hat{\sigma}_s$ and total axial stress $\hat{\sigma}$ of the section can be computed from:

$$\hat{\sigma} = \hat{\sigma}_c + \hat{\sigma}_s \quad (23)$$

$$\hat{\sigma}_c = \sigma_{ac} + \Delta\hat{\sigma}_c, \Delta\hat{\sigma}_c = E_{ac}\Delta\hat{\varepsilon}_c \quad (24)$$

$$\hat{\sigma}_s = \sigma_{as} + \Delta\hat{\sigma}_s, \Delta\hat{\sigma}_s = E_{as}\Delta\hat{\varepsilon}_s \quad (25)$$

where σ_{ac} and σ_{as} are the concrete and steel axial stress at time t_a . The $\Delta\hat{\sigma}_c$ and $\Delta\hat{\sigma}_s$ are the concrete and steel relative axial stress from time t_a to t . In Eqs. (24) and (25), the E_{ac} and E_{as} represents the instantaneous constitutive relationships of the concrete and steel at time t_a . The virtual strain energy δU :

$$\delta U = \delta U_s + \delta U_c \quad (26)$$

$$\delta U_c = \int_{\hat{V}} \delta(\hat{\varepsilon}_c)^T \hat{\sigma}_c d\hat{V} \quad (27)$$

$$\delta U_s = \int_{\hat{V}} \delta(\hat{\varepsilon}_s)^T \hat{\sigma}_s d\hat{V} \quad (28)$$

In the deformation coordinates (\hat{x}, \hat{y}) , the internal virtual work δW equals to the virtual strain energy δU :

$$\delta U = \delta W \quad (29)$$

The three internal forces $\hat{\mathbf{f}}$ can be computed from:

$$\hat{\mathbf{f}} = \hat{\mathbf{f}}_a + \Delta\hat{\mathbf{f}} = \begin{Bmatrix} \hat{f}_{jx}^{ij} & \hat{m}_{iz}^{ji} & \hat{m}_{jz}^{ij} \end{Bmatrix} \quad (30)$$

$$\hat{\mathbf{f}}_a = \begin{Bmatrix} (\hat{f}_{jx}^{ij})_a & (\hat{m}_{iz}^{ji})_a & (\hat{m}_{jz}^{ij})_a \end{Bmatrix} \quad (31)$$

$$\Delta \hat{\mathbf{f}} = \left\{ \Delta \hat{f}_{jx}^{ij} \quad \Delta \hat{m}_{iz}^{ji} \quad \Delta \hat{m}_{jz}^{ij} \right\} \quad (32)$$

The remaining three internal forces can be obtained from the equilibrium equations:

$$\sum F_{\hat{x}} = 0 \quad \hat{f}_{ix}^{ji} = -\hat{f}_{jx}^{ij} \quad (33)$$

$$\sum M_{\hat{y}} = 0 \quad \hat{f}_{jy}^{ij} = -\frac{1}{l_a} (\hat{m}_{iz}^{ji} + \hat{m}_{jz}^{ij}) \quad (34)$$

$$\sum F_{\hat{y}} = 0 \quad \hat{f}_{iy}^{ji} = -\hat{f}_{jy}^{ij} \quad (35)$$

The internal forces ($\hat{\mathbf{f}}_i^{ji}$, $\hat{\mathbf{f}}_j^{ij}$) at the particle i and j in the deformation coordinates are (see Fig. 4):

$$\hat{\mathbf{f}}_i^{ji} = \left\{ \hat{f}_{ix}^{ji} \quad \hat{f}_{iy}^{ji} \right\}^T, \quad \hat{\mathbf{f}}_j^{ij} = \left\{ \hat{f}_{jx}^{ij} \quad \hat{f}_{jy}^{ij} \right\}^T \quad (36)$$

In order to compute the actual internal forces, the internal forces in fictitious configuration V_r must be rotated back to the current configuration V . In addition, since all the force directions at each particle are defined in the global coordinates, they need to be transformed into global coordinates. Thus, the internal forces in the global coordinates can be computed:

$$\mathbf{f}_i^{ji} = \mathbf{R}_r^T \boldsymbol{\Omega}_a^T \hat{\mathbf{f}}_i^{ji}, \quad \mathbf{f}_j^{ij} = \mathbf{R}_r^T \boldsymbol{\Omega}_a^T \hat{\mathbf{f}}_j^{ij} \quad (37)$$

fiber section method is used to analyse various material on cross section of member as shown in Fig. 5. These materials include the reinforced steel, steel, well-confined concrete and not well-confined concrete. The fiber section method can consider the effects of frame element axial force-bending moment interaction on nonlinear dynamic structural simulation for behavior of real reaction. In this paper, we focus on numerical analysis of reinforced concrete structures. The fiber-element model can be used fiber section model in each area using different stress-strain models. The stress-strain relation of confined concrete model is adopted for each fiber as shown in Fig. 6. Thus, the bending moment-curvature relation of complex section can be calculated. Wang and Restrepo [3] have suggested a formulation of Mander concrete model on rectangular section. Now, this formulation is written on VFIFE method in this paper. It can be expressed as:

$$\sigma_{cc} = \alpha_1 \alpha_2 f'_c \quad (38)$$

where

$$\alpha_1 = \left[1.4 \frac{f'_{l1}}{f'_{l2}} - 0.6 \left(\frac{f'_{l1}}{f'_{l2}} \right)^2 - 0.8 \right] \sqrt{\frac{f'_{l2}}{f'_c}} + 1 \quad (39)$$

$$\alpha_2 = 1.25 \left(1.8 \sqrt{1 + \frac{7.94 f'_{l2}}{f'_c}} - 1.6 \frac{f'_{l2}}{f'_c} - 1 \right) \quad (40)$$

$$f'_{l2} = \max \left[f'_{lx}, f'_{ly} \right] \quad (41)$$

$$f'_{l1} = \min \left[f'_{lx}, f'_{ly} \right] \quad (42)$$

Thus, $f'_{lx} = k_e f_{lx}$ and $f'_{ly} = k_e f_{ly}$ was the effective lateral confining stress for rectangular confined concrete in the spiral of x and y direction and k_e was effective confined coefficient. For the stress-strain model for confined concrete, the modified Mander confined model is

used to analyse numerical simulation analysis of reinforced concrete members. For steel material model, the stress-strain relation of steel by Mirza and MacGregor [4] is adopted.

5 NUMERICAL EXAMPLES

In this paper, three numerical examples are given. Comparison experimental and numerical results of reinforced concrete members are studied. Firstly, example has been studied by Yang [5]. Figures 7 and 8 are design details of the specimens for the C1 and C1W. Figures 9 and 10 show that the analytical results computed from the VFIFE method are close to experimental results. It has been demonstrated that the proposed method can be used to compute responses of the reinforced concrete members

6 CONCLUSIONS

In this paper, following the VFIFE approach, we developed a numerical procedure for the analysis of fiber-element model using different stress-strain models. The numerical procedure can be used to simulate the extremely large deformation of inelastic structures. One example has been presented. It has been demonstrated that the proposed method can be used to analyze the large static deformation responses of reinforced concrete members under loads or deformations.

7 ACKNOWLEDGMENT

This study is supported by the National Science Council of Republic of China under grant NSC102-2221-E-033 -036

REFERENCES

- [1] Ting, E.C. and Wang, C.Y. *Vector mechanics of solids*. China Engineering Consultants Inc, Taipei, Taiwan, (2008) (in chinese).
- [2] Wang, C.Y., Wang, R.Z., Chuang, C.C. Chuang and Wu, T.Y. Nonlinear analysis of reticulated space truss structures, *J. Mech*, (2006) **22**(3):199-212.
- [3] Wang, Y. C., and Restrepo, J. I., Investigation of concentrically loaded reinforced concrete columns confined with glass fiber-reinforced polymer jackets, *ACI Structural Journal*, (2001) **98**(3):377-385.
- [4] Mirza S. A., and MacGregor J. G., Variability of mechanical properties of reinforcing bars, *Journal of the Structural Division*, ASCE, (1979)**105**(5):921-937.
- [5] Yang, C.P. Experimental study of RC columns of Hsin-Tseng Junior high school, National Taiwan University of Science and Technology, Master. (in Chinese), (2005).

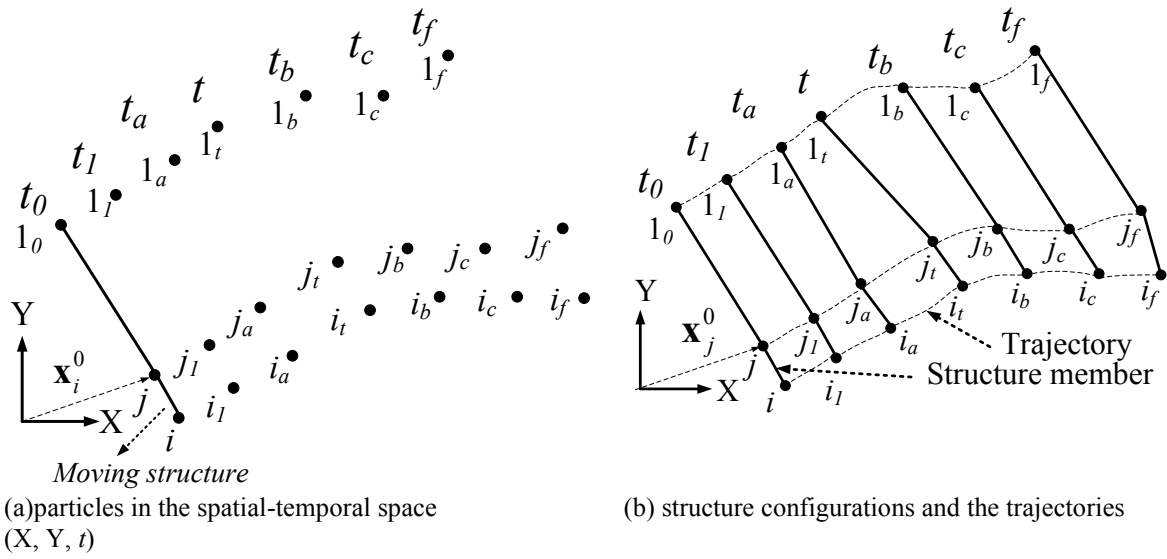


Figure 1: Motion of a structure in VFIFE method

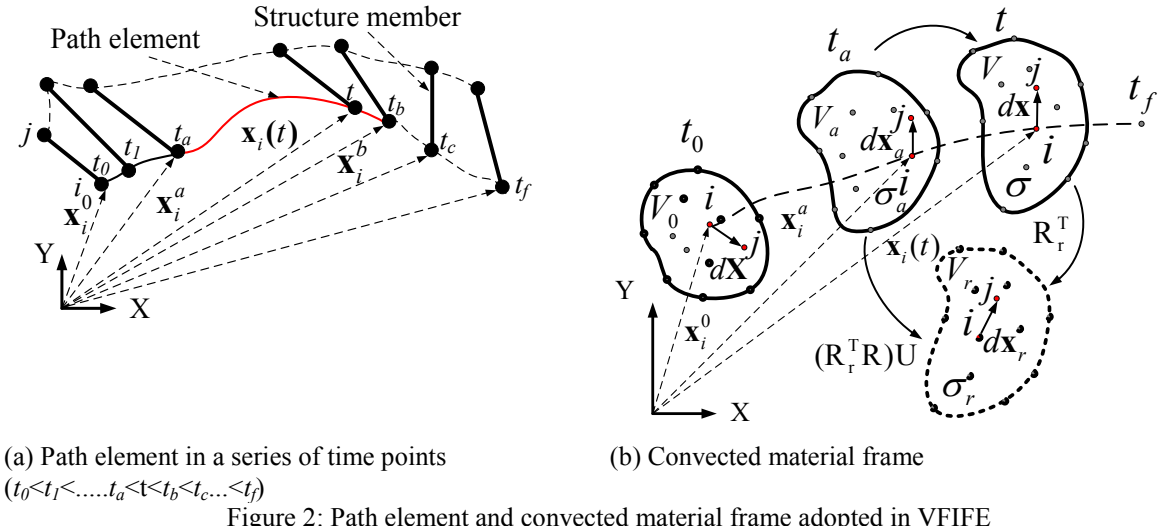
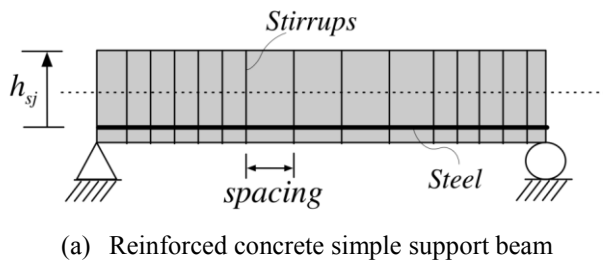
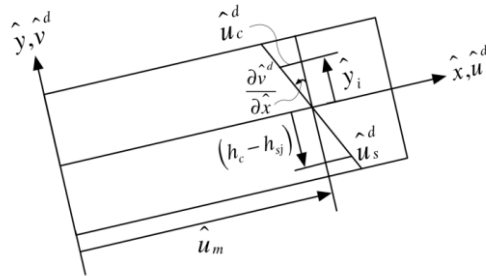


Figure 2: Path element and convected material frame adopted in VFIFE





(b) Frame element section.
Figure 3: Reinforced concrete section of the frame element.

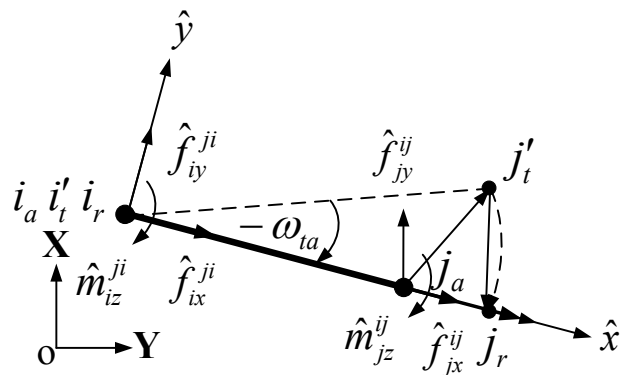


Figure 4: Internal forces in the deformation coordinates

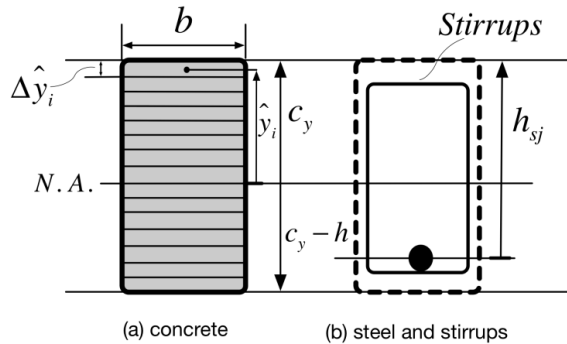


Figure 5: Fiber section of the RCCFE.

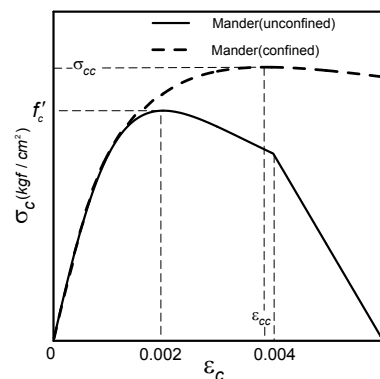


Figure 6: Mander concrete model

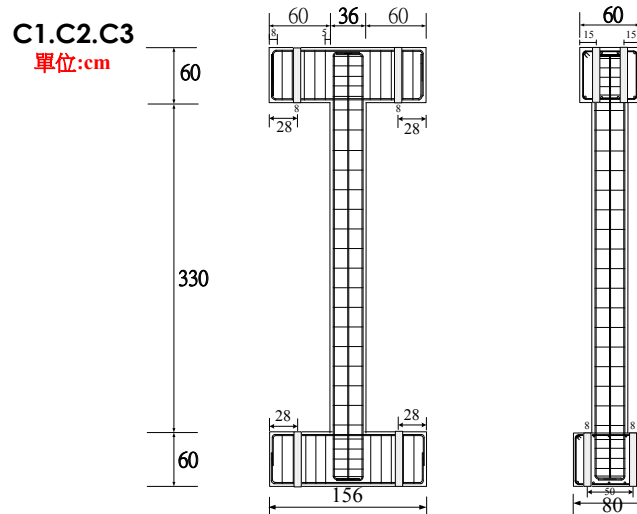


Figure 7: Design details of the specimens for the C1 by Yang [5]

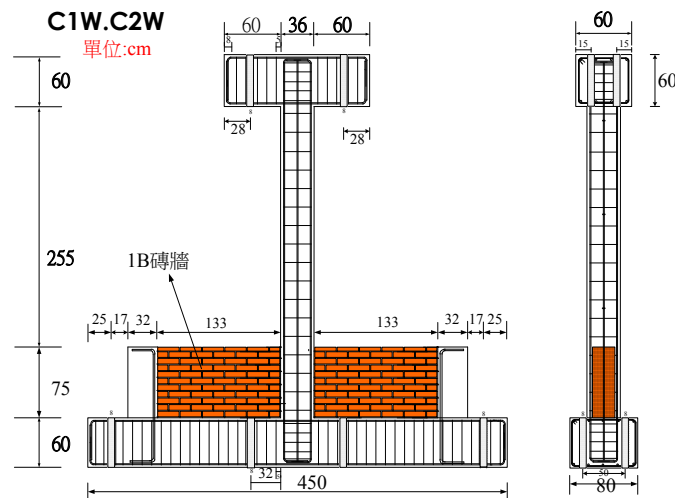


Figure 8: Design details of the specimens for the C1W by Yang [5]

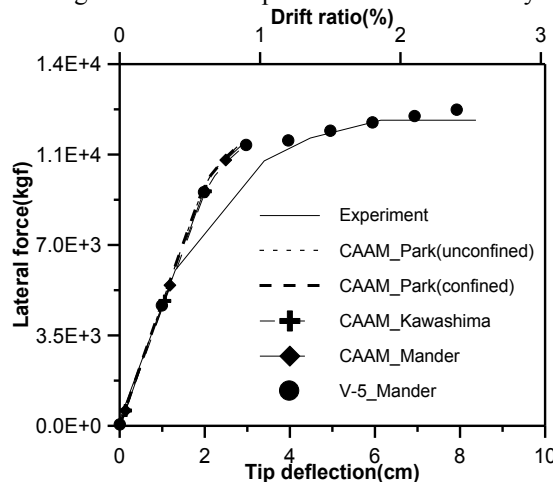


Figure 9: Comparison experimental and numerical results (C1)

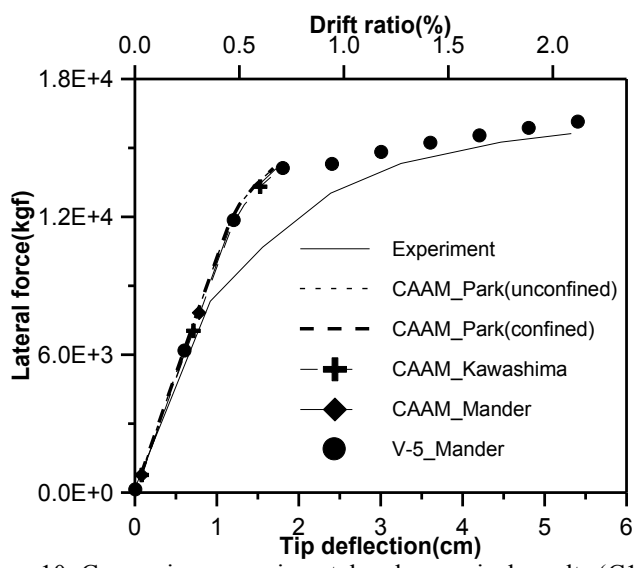


Figure 10: Comparison experimental and numerical results (C1W)

A DISCRETE ELEMENT ANALYSIS OF COHESIVE GRANULAR BULK SOLID MATERIALS

LIZ I. DEL CID¹ AND GRAHAM MUSTOE²

Colorado School of Mines
College of Computational Sciences and Engineering
Mechanical Engineering Department
1610 Illinois Street
Golden, Colorado 80401

¹lidelcid@mymail.mines.edu, ²gmustoe@mines.edu

Key words: Granular Materials, DEM, Contact Problems.

Abstract. In bulk handling applications, such as conveying and storage, understanding the effect cohesion has upon the flow-ability of particulate systems at the macroscopic scale is crucial in increasing the avenues of operation unit design improvements and handling scenarios of industrial operational units. This research provides a better understanding of the role cohesion has on the flow-ability of bulk solids materials through the development, implementation and application of a macroscopic elasto-plastic adhesive (MEPA) contact model within an open source HPC general purpose Discrete Element Method (DEM) computer code.

This investigation proposed a DEM history dependent particle-particle MEPA contact model that accounts for both elastic and plastic contact deformations and adhesive attractions. The research tasks are focused in three major areas: 1) DEM applications for the analysis of cohesive bulk solids, 2) modeling stress history dependency of cohesive strength, and 3) the prediction of flow properties in test applications that are comparable to experimental results. The MEPA model applied herein is a three branched non-linear contact model that simulates the virgin compaction loading, unloading/reloading and adhesion behavior of a particulate solid.

1 INTRODUCTION

For a given bulk handling application, adequately capturing the DEM simulated behavior of cohesive solids is crucial when evaluating its handle-ability. Characterization of bulk solids is required for the reliable design and operation of industrial processes related to the physical storage and handling units of granular materials. The movement of granular matter which exhibits “sticky” or cohesive phenomena gives rise to a wide variety of different flow behaviors. The changing contact networks and stress distributions produce large fluctuations of forces and reorganization of the contacts. The added influence of cohesive forces creates a challenge in predicting the macroscopic flow behavior of a material. Numerical simulation DEM studies conducted with the industry accepted cohesive models show discrepancies between the bulk responses observed in physical tests and those predicted in numerical simulations. The research conducted provides a method for evaluating cohesive strength

history conditions for the purpose of providing a tool that can be used within the engineering design of industrial storage and handling systems of frictional-adhesive particulate solids.

2 FLOW MODELING OF COHESIVE BULK SOLIDS WITH THE MACRO ELASTO-PLASTIC ADHESIVE (MEPA) MODEL

The MEPA cohesive model simulates the elastic and plastic regimes. It is capable of modeling material yielding through hysteresis and steady-state flow. This section describes the details of the contact duration with cohesive attraction for each particle contact.

2.1 The MEPA Cohesive Model

The flow behavior of bulk solids under large deformations and displacements is difficult to model with a particle-particle force law that is solely based upon micro-mechanical considerations. The proposed model uses a maximum force-based failure criterion. It determines the maximum displacement of the contact with a material stiffness described by the material's tensile strength, elastic modulus and Poisson's ratio. The novel aspect of this MEPA model is that material behavior is described by macro and micro-mechanics such as the material yield strength and physical properties. This model simulates the mechanical behavior of material physical data in a shear test rather than the micro and molecular mechanics laws. It simulates the results from the physical testing used to determine the parameters of the Mohr-Coulomb shear failure criterion and complements studies in cohesive, frictional bulk solids for micro and macro-models of different materials [1-7].

In the implementation of the MEPA model within the DEM algorithm non-uniform sized spherical particles are used throughout. The material roughness is mimicked with a rolling resistance model that applies additional torques and resistances [8]. In this work, the cohesive bond strength is viewed as a fundamental material parameter and used to numerically resolve macro-mechanical behaviors experimentally observed and described by the Mohr-Coulomb theory within flow property tests.

2.2 Particle Contact Constitutive Model

The relationship between the interaction force and the normal overlap of two rigid DEM particles is established to simplify the contact mechanics. The force-overlap diagram for this model is shown in Figure 1. The MEPA model takes into account plastic contact deformation and cohesive attraction. As two particles are pressed together the particle contact undergoes elastic and plastic deformations. As they continue to be pressed together the pull-off force increases with the increase of the plastic contact area.

The loading, unloading/re-loading and cohesive branches in the MEPA model are represented by four parameters: the virgin loading stiffness parameter k_1 , the unloading and reloading stiffness parameter k_2 , the cohesive stiffness parameter k_{adh} and the index parameter n , controlling the nonlinear force-displacement response of the system [4-6]. In the initial loading of the contact, the force increases with stiffness k_1 . A linear viscous damping dash-pot is used to dissipate energy during contact. Cohesion between the contacts is represented by cohesive stiffness k_{adh} , which allows for attractive forces controlled by a limiting force f_{min} . Note, when $n = 1$, the model becomes linear and is represented by the branched model of Figure 1a. If k_1 is set equal to k_2 , the model is reduced to the linear or Hertzian contact model

previously discussed. Each branch can be expressed by the following sets of bounding equations:

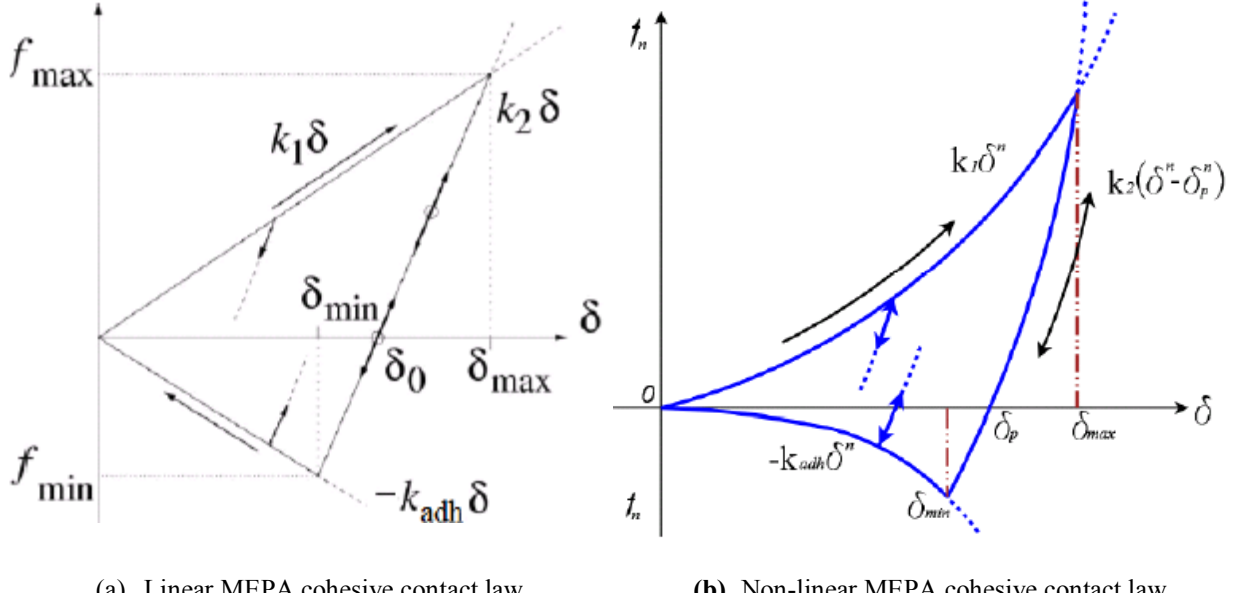


Figure 1: Different MEPA contact models from [9].

$$f_1(\delta) = k_1 \delta^n \quad (1)$$

$$f_2(\delta) = k_2 (\delta^n - \delta_p^n) \quad (2)$$

$$f_3(\delta) = -k_{adh} \delta^n \quad (3)$$

where $f_1(\delta)$ represents the virgin loading branch, $f_2(\delta)$ the re/unloading branch, and $f_3(\delta)$ the cohesive branch. The branched relationship as a whole can be expressed as:

$$f_{hys} = \begin{cases} f_1(\delta) & \text{if } f_2(\delta) \geq f_1(\delta) \\ f_2(\delta) & \text{if } f_1(\delta) > f_2(\delta) > f_3(\delta) \\ f_3(\delta) & \text{if } f_3(\delta) \geq f_2(\delta) \end{cases} \quad (4)$$

The normal force on particle i is described by:

$$\mathbf{f}_0^n = -\gamma_n \mathbf{v}_n + f_{hys} \mathbf{n} \quad (5)$$

with the normal direction unit vector $\hat{\mathbf{n}}$ directed from the center of particle j to particle i. The variable \mathbf{v}_n describes the normal relative velocity of the particle and γ_n the viscous dissipation coefficient. The tangential force includes dissipation due to Coulomb friction and tangential elasticity that allows for stick-slip behavior at the contact level [1, 6, 7]. The tangential force is related to the normal force via Coulomb's law in equation 6.

$$f^t \leq \mu_s f_{hys} \quad (6)$$

The overall solution of the non-linear DEM problem is obtained by incrementally solving Newton's equations of motion with the MEPA cohesive model.

In this study a value of $n = 3/2$ is used. This converts the MEPA cohesive model into a nonlinear hysteretic spring contact model. The maximum adhesion is determined by the stiffness parameters and the maximum normal overlap f_{max} . The tangential stiffness is calculated based on the contact stiffness k_t , which is set to the value of k_1 . The tangential force is calculated from the product of the tangential stiffness and the tangential displacement, subject to the frictional limit according to Coulomb's law. Following the branches of the MEPA cohesive model, during initial compressive loading, the contact force increases with increasing contact overlap. At the maximum contact overlap, f_{max} , the contact stiffness increases instantaneously to the value k_2 . Further loading and un-loading is defined by the force-displacement relation $f = f_2(\delta)$. Elastic unloading to a zero contact force leads to a non-zero contact overlap equal to the maximum plastic contact indentation, $\delta = \delta_p$, which is recorded and updated over the contact lifetime. When the contact overlap is further decreased as the particles separate, the contact force enters the tensile regime. The maximum tensile contact force $f = -k_{adh}\delta_{min}^n$ that the contact can experience corresponds to a contact displacement $\delta = \delta_{min}$. Further unloading in the tensile regime generates a tensile contact force that decreases in accordance with $f = -k_{adh}\delta$. In addition to the loading and unloading branches shown in Figure 1a and b, loading and unloading may also occur within the bounding branches. Any loading stage within the bounding branches loads or unloads elastically in accordance with $f = f_2(\delta)$. [8].

3 DEM SIMULATIONS OF THE MECHANICAL BEHAVIOR OF THE MATERIAL COPPER ORE

This section presents the DEM predictions using the MEPA cohesive model for copper ore and compares it to the experimental data of flow property test Report 11040-1 [9].

3.1 Experimental Behavior of Cohesive Granular Materials

The results of a flow property test for copper ore performed by Jenike & Johanson provided by OCC [10] was used as the mechanical testing material data in this study. The data presented in flow property test Report 11040-1 is used to evaluate the capability of the MEPA cohesive model to simulate the mechanical test data [9].

For this study, the results of Sample 1 are used at 5% and 8% moisture contents (mc). The particle size of copper ore tested is 6.35 mm in diameter with a bulk density of 1042.8-1752.4 kg/m³ for 5% mc and 1350.4-1797.3 kg/m³ for 8% mc. The weight density of an individual particle of copper ore Sample 1 is 2481.3 kg/m³. An image of the physical copper ore material with 8% mc can be seen in Figure 2.

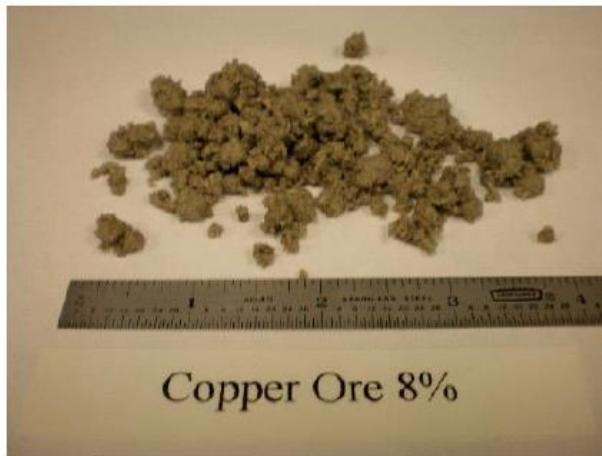


Figure 2: Copper ore material at 8% mc from [9].

3.2 The Testing Model Systems and Methods

In this study experimental data sets obtained with the ring cell shear tester series RST-01 developed by Dietmar Schulze [11, 12] are used to validate and calibrate the DEM simulations [11-14]. The yield locus can be plotted from the measured shear points as seen in Figure 3.

3.3 Numerical DEM Model Parameters

The virtual ring cell shear tester was filled with spherical particles with a truncated Gaussian distribution where the mean particle radius is 3.175 mm, and variation in particle radius is $\pm 10\%$ of the mean particle size. This size variation prevents ordered crystal-like packing. A random insertion method was adopted to provide a random packing of the material. Cohesion between particles is accounted for with the k_{adh} value set to a percentage of unloading/reloading stiffness value in the filling process to allow for the development of a similar packing to the physical cohesive material. Static and rolling frictional values are used to account for the roughness of copper ore and the non-spherical nature of the material. The values of material parameters used in the simulations of 5% mc and 8% mc of copper ore are listed in Table 1. The material properties are representative of copper ore. The material reloading and unloading stiffness, k_2 , is derived from the material properties such as Young's Modulus, Poisson's ratio and particle density. The loading stiffness, k_1 ; is equivalent to $\frac{1}{5}k_2$ as suggested in literature [5, 15]. The cohesive stiffness, k_{adh} , was determined iteratively for the moisture content specified. Finally, the frictional values selected are representative of an abrasive material as copper ore is highly abrasive. All the parameters were kept constant throughout the shearing process.

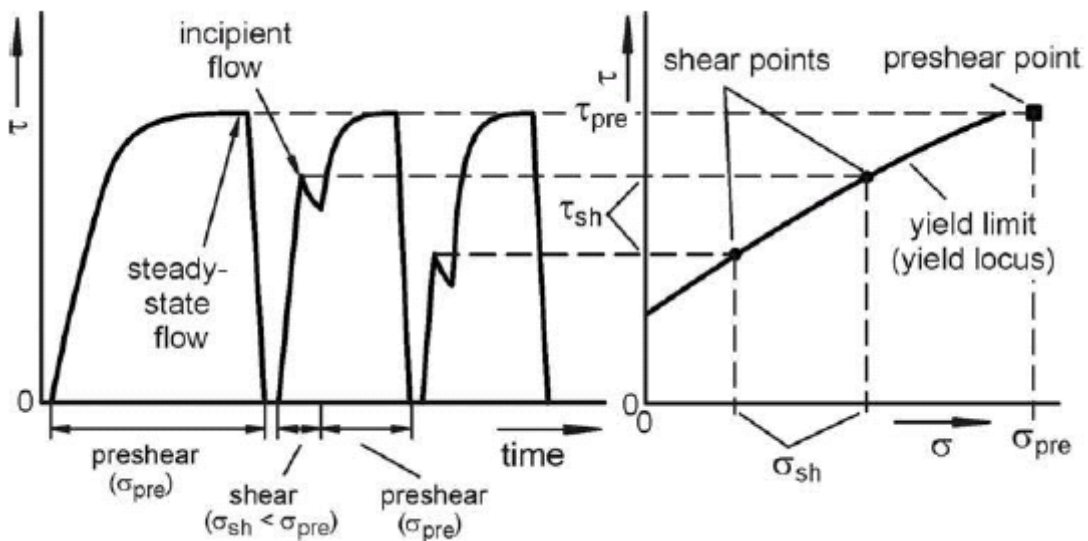


Figure 3: Conceptual shear test procedure of a ring shear tester from [13].

4 MEPA COHESIVE MODEL RESULTS AND DISCUSSIONS

MEPA Cohesive Model Results for Copper Ore Sample 1 with 5% and 8% mc. The yield locus determined through physical experiments for copper ore with a moisture content of 5% and 8% are shown in Figure 4 and Figure 6 respectively. The 6.35 mm diameter material is sheared with a Jenike Shear Tester and serves as the reference case. The ring shearing tests were performed with 6.35 mm diameter material and a cohesive stiffness of $k_{adh} = 3.56 \times 10^8$ Nm for the 5% mc and a cohesive stiffness, $k_{adh} = 5.93 \times 10^8$ Nm for 8% mc. Table 2 shows the determined internal angle of friction of the material as a comparable measurement between tests. The numerical simulation results represent material consolidated at 54.8 kPa for the 5% mc copper ore material conditions and a consolidation of 38.7 kPa for the 8% mc copper ore material conditions listed in Table 1. Figures 5 and 7 show the simulated yield locus for the 5% and 8% mc condition obtained from the shearing cell, respectively, in a comparable graph to the Jenike shear results. The static and rolling frictional values together with the selected cohesive stiffness can account for the variation in the expected result. Additional work should be performed to validate the parameters seen in Table 1 for the consolidation compaction phase in order to gain more confidence in their use. The variation in the shearing points is more evident in lower consolidation pressures.

Discrete Element Method Application of Copper Ore using the MEPA Cohesive Contact Model. To illustrate the application of the MEPA cohesive contact model, a transfer chute DEM simulation was performed with dry copper ore and 8% mc copper ore. The DEM material parameters used for copper ore followed those described in Table 1 with the cohesive stiffness, k_{adh} , set to zero for the dry material simulation. The simulations were performed to observe the mechanical behavior of the simulated copper ore. Figure 8 shows dry copper ore on a transfer belt. It is observed the material is free owing and displays no cohesive agglomerations. In Figure 9, 8% mc copper ore is simulated and compared with the physical material. In Figure 9a, the DEM simulated copper ore displays the mechanical behavior of cohesive materials. Clumps or agglomerations of particles ranging in size from 2.85 mm -

3.49 mm in radius form using the MEPA cohesive contact model and the material parameters described in Table 1. The effective cohesive behavior observed illustrates the capabilities of the MEPA cohesive model to simulate material strength described by physical tests. A more accurate representation is expected with further refinement of the material parameters and DEM particles shapes.

Table 1: Simulation parameters used in the ring shear testers for 5% and 8% mc of copper ore.

	5% mc Copper Ore	8% mc Copper Ore
Poisson's Ratio, ν	0.34	0.34
Young's Modulus, E (GPa)	119	119
Particle Radius, R (mm)	[2.85-3.49]	[2.85-3.49]
Particle Density, ρ (kg/m^3)	2481.3	2481.3
Loading Spring Stiffness, k_1 (N/m)	4.75×10^8	4.75×10^8
Unloading Spring Stiffness, k_2 (N/m)	2.37×10^9	2.37×10^9
Cohesive Stiffness, k_{adh} (N/m)	3.56×10^8	5.93×10^8
Particle Static Friction, μ_s	0.35	0.35
Particle Rolling Friction, μ_r	0.3	0.3
Wall Friction, μ_s	0.0	0.0
Base Friction, μ_s	0.7	0.7
Simulation Time step, Δt (sec)	1.0×10^{-7}	1.0×10^{-7}

Table 2: Internal frictional angle, φ , for 5% and 8% mc of Copper Ore.

Test	Internal Frictional Angle, φ (degrees) of 5% mc Copper Ore	Internal Frictional Angle, φ (degrees) of 8% mc Copper Ore
Jenike Shear	47.3	46.7
DEM Ring Shear	44.6	44.8

5 CONCLUSIONS

The work contained herein can be broken down into three substantial sections: development of the MEPA cohesive model methodology, modeling of material behavior and its application to simulate large cohesive granular bulk solid systems. The contributions of each of these concepts provide an improved understanding of cohesive flow behavior for the geo-mechanics and bulk material handling communities.

1. *Development of a macro-mechanical cohesive contact model.* The discrete element methodology developed as the MEPA cohesive model uses a maximum force-based failure approach. The model is a three-branch bounded system with stiffness values denoted by k-parameters that describe the following physical effects: compaction (plastic-like deformation), elastic unloading and re-loading of pre-compacted material and adhesive tensile strength of material modeled with cohesion-like behavior.
2. *Modeling material failure via the simulation of physical flow property tests.* To further test the MEPA cohesive model, the effect of moisture content within two copper ore samples was investigated. In application, the MEPA succeeded in illustrating material shearing failure with cohesion by simulating the mechanical behavior of physical data

as seen in Figure 5 and Figure 7. These graphs more closely modeled the observed mechanical behavior of the copper ore material.

3. *Application of the MEPA cohesive contact model in bulk transfer.* The mechanical behavior of copper ore in a transfer system was simulated with the MEPA cohesive contact model. The simulation properly displayed the cohesive agglomerations observed in a sample of the physical copper ore material.

The discrete element method approach to the MEPA cohesive contact model methodology has been successfully implemented and applied to the simulation of copper ore at two different cohesive levels. Initial studies of the available micro cohesive contact models in comparison to the qualitative simulation results obtained from the three-dimensional parallel implementation of the MEPA cohesive constant model illustrates the potential of this new methodology to accurately simulate mechanical behavior in granular bulk solids.

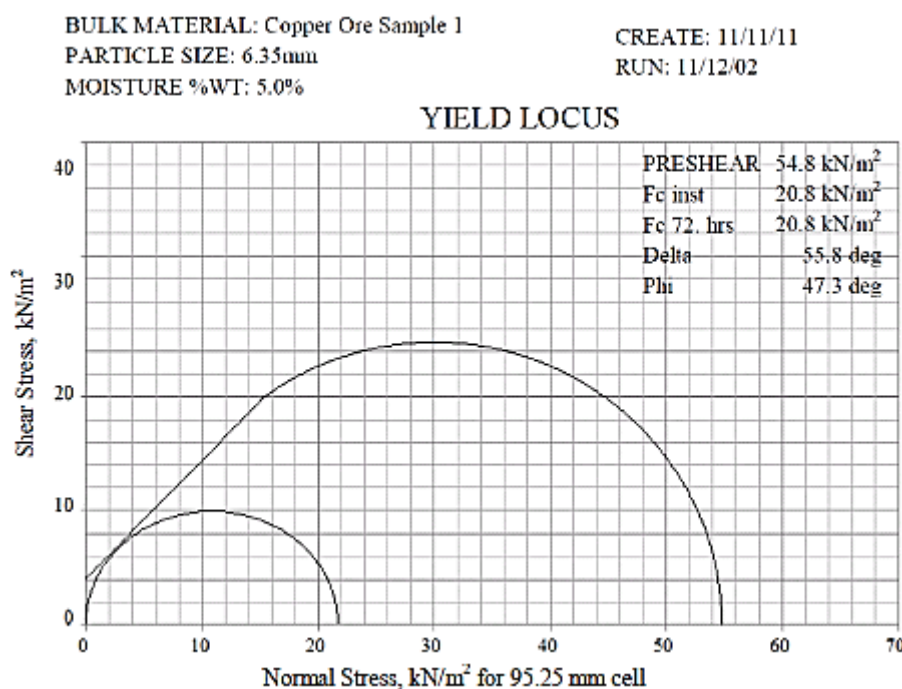


Figure 4: Physical testing results of the loading for Copper Ore Sample 1 at 5% mc [9].

BULK MATERIAL: Copper Ore Sample 1
PARTICLE SIZE: 6.35 mm

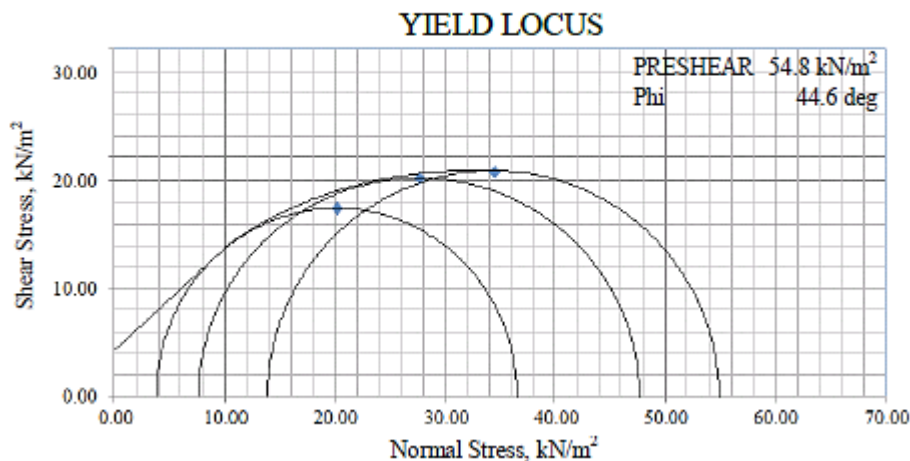


Figure 5: DEM testing results of the loading for Copper Ore Sample 1 at 5% mc with cohesive stiffness, $k_{adh} = 3:56 \times 10^8$ Nm.

BULK MATERIAL: Copper Ore Sample 1
PARTICLE SIZE: 6.35 mm
MOISTURE % WT: 8.0%

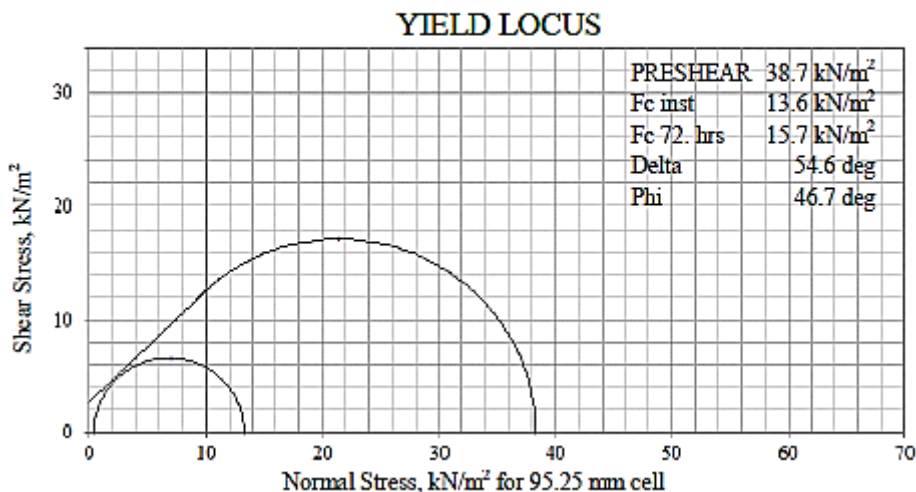


Figure 6: Physical testing results of the loading for Copper Ore Sample 1 at 8% mc [9].

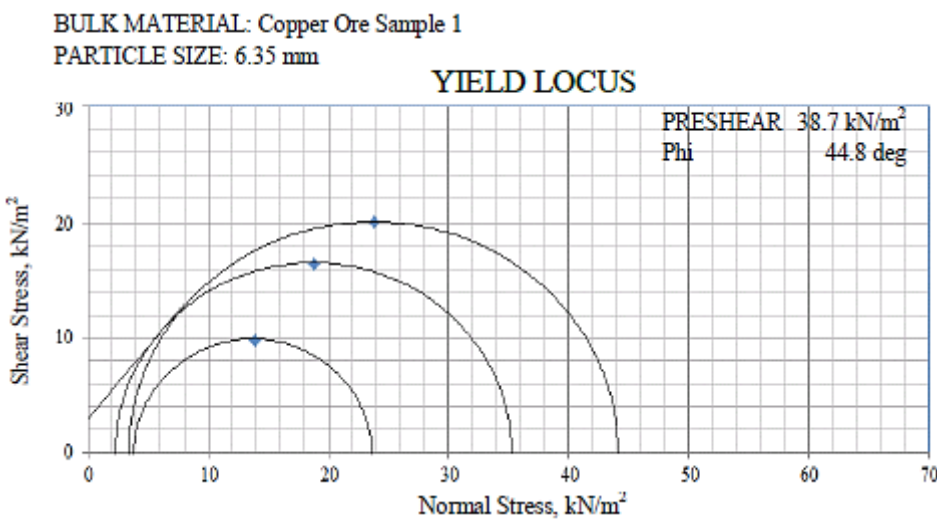


Figure 7: DEM testing results of the loading for Copper Ore Sample 1 at 8% mc with cohesive stiffness, $k_{\text{adh}} = 5.93 \times 10^8 \text{ Nm}$.

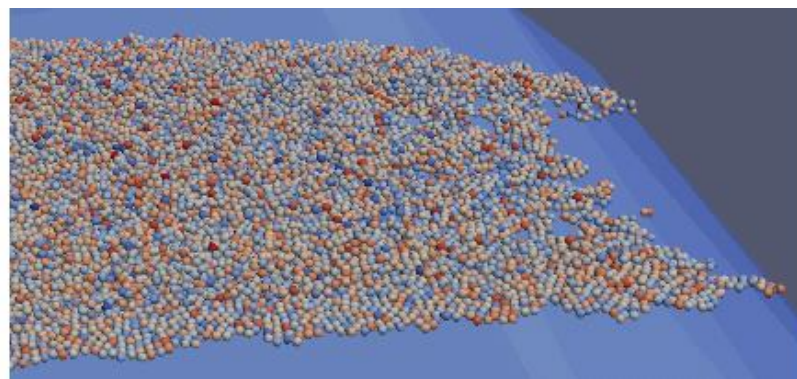
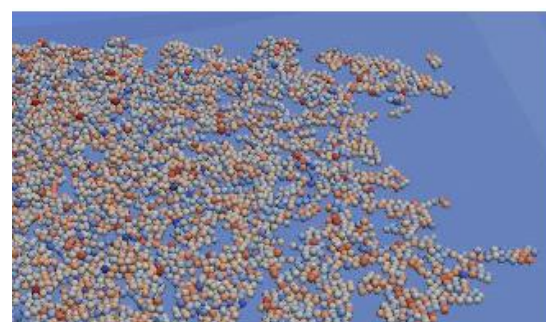


Figure 8: Virtual DEM material representation of dry copper ore on conveying belt.



(a) Physical copper ore material at 8% mc from [9].



(b) Virtual DEM copper ore material at 8% mc.

Figure 9: DEM simulated material representation of the 8% mc copper ore material.

REFERENCES

- [1] Thornton C. and S. J. Antony. Quasi-static shear deformation of a soft particle system. *Powder technology*, 109(1):179-191, 2000.
- [2] D'Addetta G. A., F. Kun, and E. Ramm. On the application of a discrete model to the fracture process of cohesive granular materials. *Granular matter*, 4(2):77-90, 2002.
- [3] Kruyt N. P. and L. Rothenburg. Statistics of the elastic behaviour of granular materials. *International Journal of Solids and Structures*, 38(28):4879-4899, 2001.
- [4] Luding S., M. Latzel, W. Volk, S. Diebels, and H. J. Herrmann. From discrete element simulations to a continuum model. *Computer methods in applied mechanics and engineering*, 191(1):21-28, 2001.
- [5] Tomas J. Assessment of mechanical properties of cohesive particulate solids. Part 1: particle contact constitutive model. *Particulate science and technology*, 19(2):95-110, 2001.
- [6] Luding S. Shear flow modeling of cohesive and frictional fine powder. *Powder Technology*, 158(1):45-50, 2005.
- [7] Luding S., R. Tykoniuk, and J. Tomas. Anisotropic material behavior in dense, cohesive-frictional powders. *Chemical engineering & technology*, 26(12):1229-1232, 2003.
- [20] Ai J., J. F. Chen, M. J. Rotter, and J. Y. Ooi. Assessment of rolling resistance models in discrete element simulations. *Powder Technology*, 206(3):269-282, 2011.
- [8] Thakur S., J. P. Morrissey, J. Sun, J. F. Chen, and J. Y. Ooi. Particle scale modelling of cohesive powders for bulk handling applications. In EDEM Conference, 2011.
- [9] Jenike & Johanson, Report 11040-1 : Copper Ore Flow Property Test Report for the Freeport McMoRan Concentrator Feasibility Project as Morenci, Arizona, Overland Conveyor Company Inc. Lakewood, CO 80228, 2011.
- [10] Overland Conveyor Company Inc. Lakewood CO 80228. Bulk Material Handling Solutions. <http://www.overlandconveyor.com/>, 2013.
- [11] Schulze D. Development and application of a novel ring shear tester. *Aufbereitungstechnik*, 35(10):524-535, 1994.
- [12] Schulze D. A new ring shear tester for owability and time consolidation measurements. In Proc. 1st International Particle Technology Forum, pages 11-16, 1994.
- [13] Schulze D. Flow properties of powders and bulk solids. Braunschweig/Wolfenbu ttel, Germany: University of Applied Sciences, 2006.
- [14] Standard ASTM. D6773-02: Standard shear test method for bulk solids using the Schulze ring shear tester, ASTM international.
- [15] Zhou Y. C., B. H. Xu, A. B. Yu, and P. Zulli. An experimental and numerical study of the angle of repose of coarse spheres. *Powder Technology*, 125(1):45-54, 2002.

MOLECULAR DYNAMICS MODELLING OF BOUNDARY MIGRATION IN BICRYSTALS UNDER NANOBURNISHING

ANDREY I. DMITRIEV^{*,†,‡}, ANTON YU. NIKONOV^{*,†}

^{*}Institute of Strength Physics and Materials Science (ISPMS), Russian Academy of Science
Akademichesky pr. 2/4, 634021 Tomsk, Russia
e-mail: dmitr@ispms.tsc.ru, web page: <http://www.ispms.ru/>

[†]National Research Tomsk State University (TSU)
Lenin pr. 36, 634050 Tomsk, Russia
web page: <http://www.tsu.ru>

[‡]National Research Tomsk Polytechnic University (TPU)
Lenin pr. 30, 634050 Tomsk, Russia
web page: <http://www.tpu.ru>

Key words: numerical modeling, molecular dynamics, nanostructuring burnishing, vortex-like displacements.

Abstract. The paper reports the molecular dynamics simulation results on the behavior of a copper crystallite in local frictional contact. The crystallite has a perfect defect-free structure and contains a high-angle grain boundary of type $\Sigma 5$. The influence of the initial structure on the specimen behavior under loading was analyzed. It is shown that nanoblocks are formed in the subsurface layer. The atomic mechanism of nanofragmentation was studied. A detailed analysis of atomic displacements in the blocks showed that the displacements are rotational. Calculations revealed that the misorientation angle of formed nanoblocks along different directions does not exceed 2 degrees.

1 INTRODUCTION

The state of the surface layer, its hardness, wear resistance, strength properties, quality, and other characteristics are crucial for a whole range of modern applications. They to a large extent determine the operating properties of various machine components. That is why much attention is given to the investigation of physical and mechanical properties of the surface and improvement of its properties by various treatment methods [1, 2]. Despite continuous improvement of experimental methods, the structural evolution features that accompany these improvements are still poorly explored. The difficulties are due to the simultaneous effect of a large number of different-scale secondary factors occurring in contact between the indenter and indented material. Today this problem is efficiently solved using various numerical simulation methods combined with experiment. The molecular dynamics method remains the main tool for the solution of atomic-scale problems which theoretically describes the simulated system behaviour. With the increasing performance of modern computing systems, the molecular dynamics method greatly contributes to the generation of new knowledge. It

has become possible to study the evolution of the atomic subsystem under dynamic loading with an explicit representation of the internal structure of a polycrystalline material.

The objective of this work is to study the generation and development of structural defects in a crystalline material with a grain boundary under localized surface plastic deformation. To achieve this, the numerical modelling of the nanostructuring burnishing process was undertaken with help of molecular dynamics method.

2 NUMERICAL MODEL

The object of investigation was a fragment of a copper polycrystalline that initially consisted of two grains divided by a planar defect such as a high-angle boundary of special type $\Sigma = 5$ (210)[001]. Two positions of the boundary along X0Z and Y0Z were simulated (Fig. 1). The copper polycrystalline was chosen because we have accumulated experience in simulating this metal both in the initial defect-free state and with internal interfaces of different types [3, 4]. Interatomic interaction was described using an interatomic potential calculated in the framework of the embedded atom method, which had earlier been verified in test problems on the calculation of elastic and energy characteristics [5, 6].

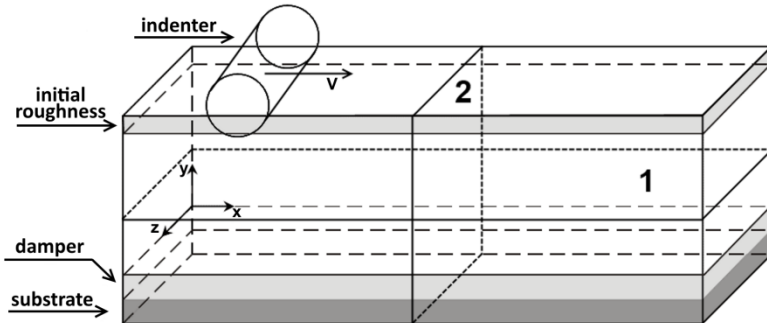


Figure 1: Schematic of the simulated specimen

Periodic boundary conditions were given along the Z axis, and the free surfaces were simulated along the X axis. The simulated specimen was thus a single elongated asperity on the surface (a fold on the surface). The microasperity had smaller-scale roughness on its surface, owing to which stresses arising in the crystallite under localized shear loading were not distributed uniformly but varied in different contact spot areas, which favored local stress redistribution and structural defect generation. The lower atomic layer imitated the substrate (Fig. 1). A special “damping” atomic layer was placed above the substrate for which a procedure of kinetic energy reduction was used. Using the layer that absorbs kinetic energy allowed us to simulate energy propagation deep into the material bulk along the Y axis. The simulated specimen measured $40.13 \times 24.95 \times 16.63$ nm along the coordinate axes. The total number of atoms exceeded 1 500 000. Motion equations were integrated with the time step $\Delta t = 0.001$ ps.

Localized shear loading was performed by simulating contact between the microasperity surface and a counterbody that was an absolutely rigid indenter. The action of the indenter was simulated by a force field and described by the formula $F(r) = -K(r-R)^2$, where K is the constant, r is the distance from the cylinder center to an atom, R is the cylinder radius, and

$F(r) = 0$ at $r > R$. The simulated material was loaded by an indenter of radius 8 nm. The motion of the indenter was simulated along the X axis at the constant speed $V = 10$ m/s, which is close to speed limits in surface finishing.

3 RESULTS OF SIMULATION

First we considered a specimen with a grain boundary of type Σ5 lying in the X0Z plane in the middle of the crystallite (position 1 in Fig. 1). The crystal lattice structure was analyzed using a common neighbor analysis [4, 7] which reveals the formation of structural defects. The simulation results showed that the motion of a microasperity on the counterbody surface causes the formation of numerous stacking faults in the grain bulk. The grain boundary inhibits the defect propagation to the neighboring grain. External shear loading makes the grain boundary to move along the direction perpendicular to the plane of the defect. This effect was studied and described by Dmitriev et al. [8]. Analysis of the structure at different points of time showed that the boundary motion is not simultaneous. Parts of the grain boundary which located in front and under the indenter are move only. This leads to a curvature of the plane of the defect and its output to the free surface. Fig. 2 shows the change in the structure of the simulated sample when the GB under the influence of external localized load rises up to the free surface. The figure marked only the atoms, which local topology of structural relations is differ from the initial FCC lattice. It can be seen that the defects are concentrated in the upper grain. Only after the grain boundary beyond the free surface (Figure 2d), structural defects are formed in the lower grain.

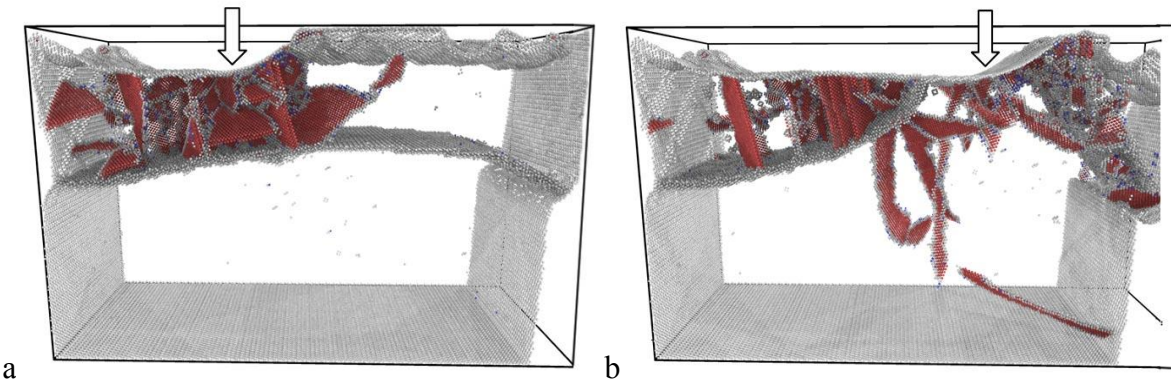


Figure 2: The structure of the modeled fragment at two consecutive time steps: a) 1.0 ns, b) 2.5 ns. Hereafter atoms with hcp local topology of atoms relation are marked by red; gray color depicts atoms located at the border and close to the GB. Blue spheres denote atoms with undetermined local topology.

Figure 3a illustrates the grain boundary position at different points of time. It is clearly seen that the boundary profile is distorted with the passage of the indenter. The only part of the boundary that moves to the free surface is in front of and beneath the indenter. The farther from the initial position of the indenter is a part of the boundary along the X axis, the longer is the period of its shear deformation and the larger is the distance to which it is shifted in the direction perpendicular to the applied load. According to the obtained results, a part of the grain boundary reaches the free surface at the time point $t = 2.5 \times 10^6 \Delta t$. After the passage of the indenter the position of this part of the boundary does not change with time.

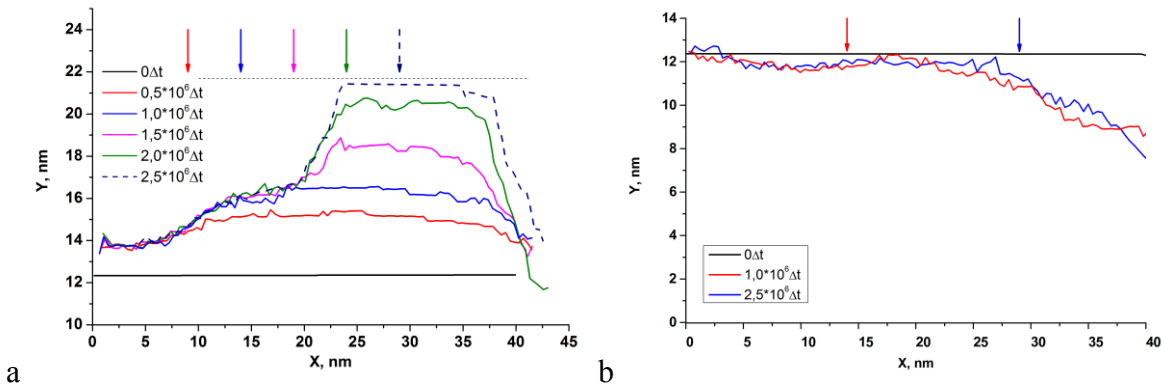


Figure 3: Grain boundary position at different points of time. Arrows indicate the position of indenter for the selected time step.

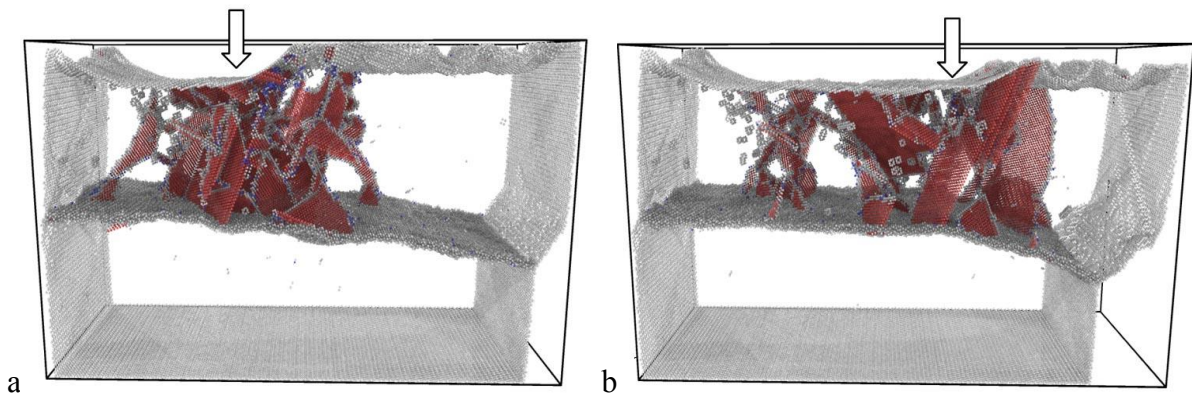


Figure 4: The structure of the modeled sample in which GB was mirrored relative to the plane of the defect as compared with the example shown in Fig. 2 at two consecutive time steps: a) 1.0 ns, b) 2.5 ns.

In order to verify the influence of the loading direction with respect to the boundary structure, we simulated a specimen with a grain boundary of special type $\Sigma 5$ whose structure was mirrored relative to the plane of the defect as compared to the above example. Two variants were studied: 1) sample with the same geometry and 2) the sample where the bottom grain was increased twice to avoid the influence of substrate. Figure 4 shows the structure of the sample (1) at the same time steps as in Figure 2. It can be seen that the plane of the defect in this case is less distorted. This is because the distance between the grain boundary and indenter increases due to motion of defect far from the free surface in a direction perpendicular to the applied loading. According to the initial distribution of structural defects depicted on the Fig. 4a some defects form in the grain, located below the GB. Closeness to free side surface leads to further annihilation of its (Fig. 4b). So, plural structural defects form only in the grain, which are directly exposed to the action of the indenter (Fig. 4c and 4d). The similar conclusion can be done for the sample (2) shown in Figure 5.

Figure 3b illustrates the grain boundary position for this case at an initial and final time point. Unlike the previous case, the resultant displacement of the boundary towards the substrate from the free surface changes insignificantly on the first stage. The boundary

displacement increases with distance from this region with respect to the initial position of the indenter. This is related to specific stress and strain redistribution during the formation of a system of defects in the loaded grain. Subsequent motion of the boundary to the surface of the lower grain is impeded by the fixed substrate.

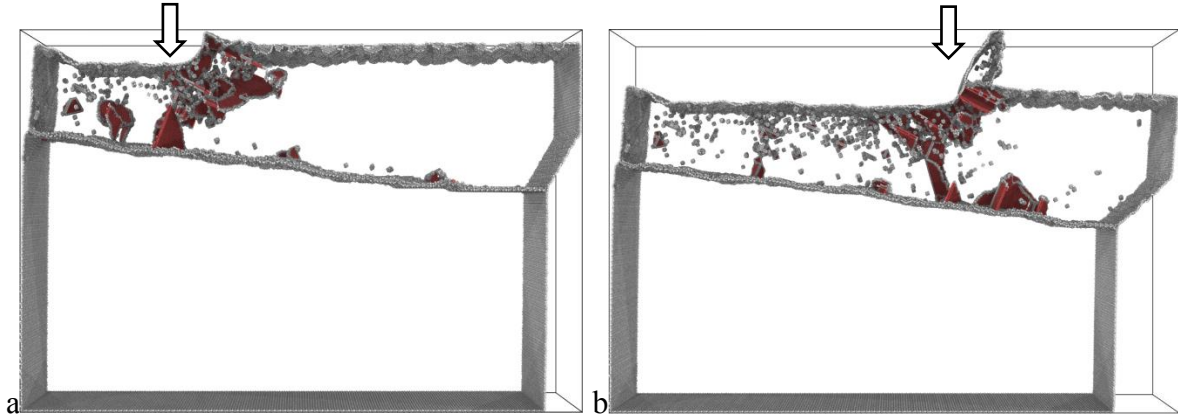


Figure 5: The structure of the modeled sample with increased bottom grain at two consecutive time steps:
a) 2.0 ns, b) 5.0 ns.

The simulation results showed that for the both considered specimen configurations numerous structural defects are generated in the grain bulk under local shear loading. These are mostly stacking faults. The formation of numerous defects in the surface layer can also be indicative of possible surface nanofragmentation and nanoblock structure formation. In order to identify possible mechanisms leading to the formation of the fragmented structure of the material in the volume of loaded grain atomic displacements at different time intervals for the central layer of the sample were analyzed. The thickness of the selected layer was equal to three atomic planes and its orientation was parallel to the X0Y plane. Atomic displacements in the middle layer of the bicrystal in the time interval 50 ps close to $t = 0.5$ ns are represented in Fig. 6. One can clearly see the structure of formed blocks in the upper grain deformed by the indenter.

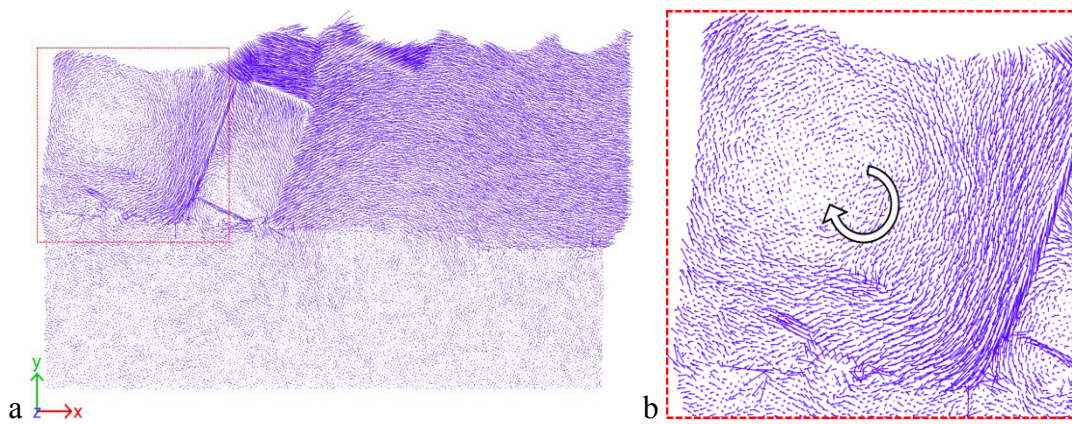


Figure 6: The map of displacements at the time interval (0.50 - 0.55) ns for the atoms of the central cutting of the modeled bicrystal with the thickness of 3 atomic layers. Hereafter the size of segments is increased up to 5 times for the better visualization. The arrow in zoomed fragment indicates the direction of rotation.

A detailed analysis of atomic displacements in the formed blocks showed that they can be rotational. Figure 6 gives a magnified image of a formed structural block. The block is seen to rotate as a whole about the axis parallel to the Z direction. Further calculations revealed that the angle of rotation along different directions for formed blocks is no more than 2 degrees.

Similar conclusions can be done by analyzing the displacements of atoms for selected central layer in the subsequent time intervals as depicted in Figure 7.

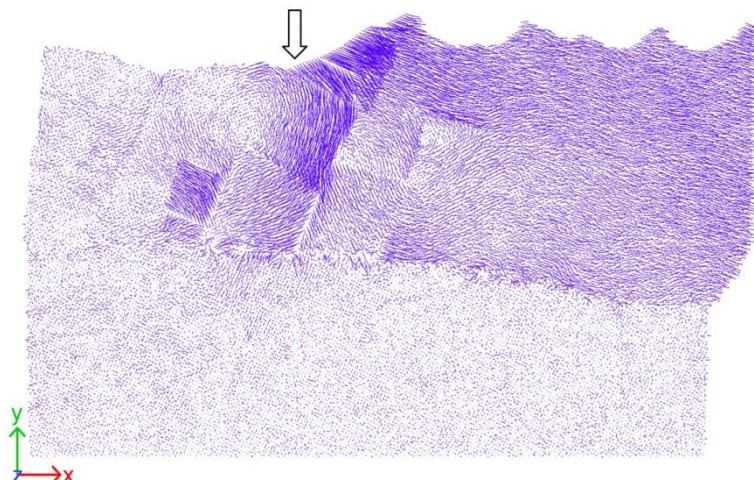


Figure 7: The map of displacements at the time interval (1.0 - 1.05) ns for the atoms of the central cutting layer of the modeled bicrystal with the thickness of 3 atomic layers. The size of segments is increased up to 5 times for the better visualization.

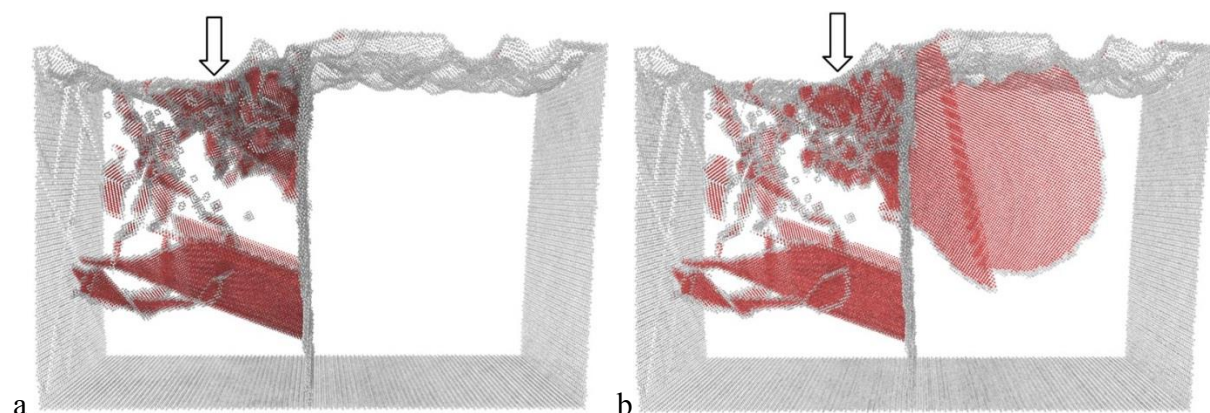


Figure 8: The structure of the modeled fragment with vertical orientation of the GB at different time steps: a) 0.8 ns, b) 0.9 ns. Red spheres indicate position of atoms with hcp local topology of atoms relation; gray spheres depict atoms located at the border and close to grain boundary.

On the next stage we simulated a specimen with a grain boundary oriented parallel to the YOZ plane (position 2 in Fig. 1). In this case, no grain boundary displacement along the X axis was observed under the action of the counterbody microasperity. The presence of the grain boundary, like in the previous case, inhibits the propagation of structural defects, but only until the indenter is at a sufficient distance from the boundary plane. When the indenter

approaches the grain boundary, stacking faults are also formed in the distant (relative to the loaded) grain. The structures of the modeled fragment for the respective time steps are shown in Figure 8.

5 CONCLUSION

The computer simulation performed on the scale of single atoms revealed plastic deformation mechanisms in a material with internal structure under local shear loading. According to the obtained results, plastic deformation can occur through the formation of a system of numerous intersecting planar defects such as stacking faults. This leads to the formation of individual material nanofragments divided by an interfacial layer. Atomic displacements in the formed fragments can be rotational. The resultant structure of the modified surface layer is a system of misoriented nanoblocks.

Simulation showed that the presence of a grain boundary in the crystallite inhibits defect propagation to the specimen bulk under shear loading and can induce recrystallization of individual grains only. Despite only two limiting cases of grain boundary orientation were considered, it can be suggested that the behavior of a crystallite with a defect oriented at an arbitrary angle to the free surface is a combination of processes occurring in the studied cases.

Additionally, the obtained results can be used to explain features of surface layer nanostructuring in final burnishing.

Acknowledgements:

The work was carried out at the financial support of the Russian Science Foundation Grant No. 14-19-00718. A.Y.N. also acknowledges RFBR grant no. 15-08-01511a.

REFERENCES

- [1] Papshev D. D. Finishing & hardening processing by surface plastic deformation. Moscow: Mechanical engineering, 1978.
- [2] Kuznetsov, V.P., Tarasov, S.Yu., Dmitriev, A.I. Nanostructuring burnishing and subsurface shear instability. *J. Mater. Proc. Techn.*, (2015) **217**:327-335.
- [3] Dmitriev, A.I., Kuznetsov, V.P., Nikonov, A.Yu., Smolin, I.Yu. Modeling of nanostructuring burnishing on different scales. *Phys. Mesomech.*, (2014) **17**:243–249.
- [4] Psakhie, S.G., Zolnikov, K.P., Dmitriev, A.I. et al., Local structural transformations in the fcc lattice in various contact interaction. Molecular dynamics study. *Phys. Mesomech.* (2012) **15(3-4)**:147-154.
- [5] Bondar, M.P., Psakhie, S.G., Dmitriev, A.I., Nikonov, A.Yu. On the conditions of strain localization and microstructure fragmentation under high-rate loading. *Phys. Mesomech.* (2013) **16(3)**, 191–199.
- [6] Suzuki, A. and Mishin, Y. Atomistic modeling of point defects and diffusion in copper grain boundaries. *Interface Sci* (2003) **11**:131–148.
- [7] Honeycutt, J.D. and Andemen, H.C. Molecular dynamics study of melting and freezing of small Lennard-Jones clusters. *J. Phys. Chem* (1987) **91**:4950-4963.
- [8] Dmitriev, A.I., Nikonov, A.Yu. Simulation of the behavior of a $\Sigma 5$ grain boundary under combined thermal and external shear loading. *Tech. Phys. Lett.*, (2013) **39(8)**:709-712.

ROLE OF VORTEX-LIKE MOTION IN CONTACT LOADING OF STRENGTHENING COATING. MOVABLE CELLULAR AUTOMATON MODELING

ALEXEY YU. SMOLIN¹, GALINA M. EREMINA² AND SERGEY G. PSAKHIE³

¹ Institute of Strength Physics and Materials Science
Siberian Branch of Russian Academy of Sciences
pr. Akademicheskiy 2/4, 634021, Tomsk, Russia
e-mail: asmolin@ispms.tsc.ru , web page: <http://www.ispms.ru>

² Tomsk State University
pr. Lenina 36, 634050, Tomsk, Russia
e-mail: rector@tsu.ru , web page: <http://www.tsu.ru>

³ Tomsk Institute of High Technology Physics,
Tomsk Polytechnic University
pr. Lenina 30, 634050, Tomsk, Russia
e-mail: rector@tsu.ru , web page: <http://www.tpu.ru>

⁴ Skolkovo Institute of Science and Technology (Skoltech)
Novaya St., 100, Karakorum Building, 4th floor, Skolkovo, 143025, Russia
e-mail: sp@ispms.tsc.ru , web page: <http://www.skoltech.ru>

Key words: Vortex, Velocity Field, Coating, Contact Loading, DEM.

Abstract. Movable cellular automata (MCA) is an efficient numerical method in particle mechanics, which assumes that any material is composed of elementary objects interacting among each other according to many-particle forces. In this paper MCA method is applied to modeling deformation of 3D coating-substrate system under its contact loading by rigid indenter. Main attention of the research is focused on the role of vortex-like structures in the velocity fields in deformation of the strengthening coating and substrate. The mechanical properties of model coating correspond to multifunctional bioactive nanostructured film (TiCCaPON) and the properties of substrate, to nanostructured titanium. Loading is performed by hard conical indenter. The peculiarities of velocity vortex formation and propagation, as well as its interaction with structural elements are studied. One of possible application of the study is non-destructive technique for detecting nanoscale defects in surface layer of a material using frequency analysis of the force resisting to sliding of a small counter-body on the material surface, known as tribospectroscopy. Possibilities of this technique are studied based on 3D modeling by MCA method for the above mentioned coating with nano-pores. It is shown that specific peaks at the friction force spectrum correspond to different geometrical characteristics of the nano-pores.

1 INTRODUCTION

Dynamic loading of solids results in generation and propagation of surface elastic waves (Rayleigh and Love types) that have elliptical polarization and manifest themselves as vortex structures in the velocity field [1]. In thin plates such vortex structures are typical for Lamb waves [2]. It is known that during deformation of a heterogeneous material containing internal interfaces or/and free surfaces a collective vortex motion near these boundaries is formed [3]. For example, molecular dynamics simulations [4] show that vortex structures in the velocity field are formed at grain boundaries under shear loading of polycrystals [5]. Therefore, one should expect that rotational motion in nanomaterials takes place at different scales from the atomic scale to the macroscopic one. Results of theoretical studies and experimental evidence indicate that in nanomaterials the contribution of rotational mode of deformation can significantly increase under the condition of dynamic loading [6]. Nevertheless such a fundamental factor as elastic vortex motion in material formed during dynamic loading still remains out of discussion. A distinctive feature of the elastic vortex motion is its dynamic nature. It provides not only strain compatibility, but also serves as a mechanism of transfer and redistribution of elastic energy in the bulk of material and determines many features of the deformation process.

The above mentioned confirms that revealing the role of vortex displacement in redistribution of elastic energy and, as a result, in the process of deformation and fracture of nanomaterials is a topical fundamental problem in mechanics of nanostructured materials and materials science.

Due to principal significance of free surface, internal interfaces and dynamic nature of the considered vortex phenomena the main method of studying them seems to be computer modelling based on particle methods [7]. Therefore, the aim of this paper is revealing the role of vortex displacements in the contact interaction of strengthening coating with hard counter-body by means of 3D modelling using movable cellular automata.

We modelled brick samples of a coating under contact loading by a conical counter-body which moved along the upper surface of the coating. The bottom surface of the coating was fixed. The vector field of particle velocities as well as force of interaction between the counter-body and the coating were analysed. To detect vortices in the vector field we plot streamlines of the velocities vectors at different times. Note, that these streamlines show just a tendency of the particle motion not their real trajectories. Nevertheless, such an approach allows detecting position and measuring “power” of the vortex structures in 3D vector field of velocities.

A practical application of this study might be identification of defects in surface layers of materials based on measuring and analysing friction force (so called tribospectroscopy method [8]). That is why we also considered the peculiarities of vortices generation and propagation in case of presence of nanoscale pores and inclusions in the coating.

2 DESCRIPTION OF THE MODEL

For modelling interaction of a small counter-body moving over the coating surface we used movable cellular automaton (MCA) method, which is a new efficient numerical method in particle mechanics. Within the frame of MCA, it is assumed that any material is composed of a certain amount of elementary objects (automata) which interact among each other and

can rotate and move from one place to another, thereby simulating a real deformation process [9]. The automaton motion is governed by the Newton-Euler equations. The forces acting on automata are calculated using deformation parameters, i.e. relative overlap, tangential displacement and rotation, and conventional elastic constants, i.e. shear and bulk moduli. A distinguishing feature of the method is calculating of forces acting on the automata within the framework of multi-particle interaction [10], which among other advantages provides for an isotropic behaviour of the simulated medium. Moreover, stress tensor components can be calculated for the automaton taking into account all the forces acting on it, which enables realization of various models of elastic and plastic behaviour developed in the frame of continuum mechanics.

A pair of elements might be considered as a virtual bistable cellular automaton (bonded and unbonded states), which permits simulation of fracture by the MCA. Switching-over of a pair of automata to an unbonded state would result in a changeover in the forces acting on the automata; in particular, they would not resist moving away from one another. Removing of automata from initial dense packing allows explicitly account of voids or pores in material. Changing sort (i.e. mechanical properties) of automata in initial packing allows account of various kind of inhomogeneity in the material.

In this paper the coating of multifunctional bioactive nanostructured film (TiCCaPON) on nanostructured titanium substrate [11] has been modelled (Figure 1,a). These materials are used in medicine for producing various kinds of implants. The thickness of the model coating is $H = 60$ nm. The model sample length $L = 350$ nm, width $M = 250$ nm, the size of the automata $d = 3$ nm. Diamond counter-body has a conical shape with a base diameter of 60 nm. We use cubic packing of automata, which is much more suitable for studying elastic deformation of the material due to less number of automata in the model and more uniform shape of the crack-like defects.

Motion of the counter-body is simulated by setting the constant velocity $V = 5$ m/s in the direction of axis Y for automata of the upper layer of the counter-body (Figure 1,a). The lower surface of the sample is fixed and its lateral surfaces are free. When the counter-body is moving the resistance force of its movement on the surface is registered and associated with the friction force F varying in time t . The Fourier transform is made for the registered friction force $F(t)$ and the corresponding spectra are analysed in order to study the influence of internal structure of the material and velocity field on the dynamics of friction force [12].

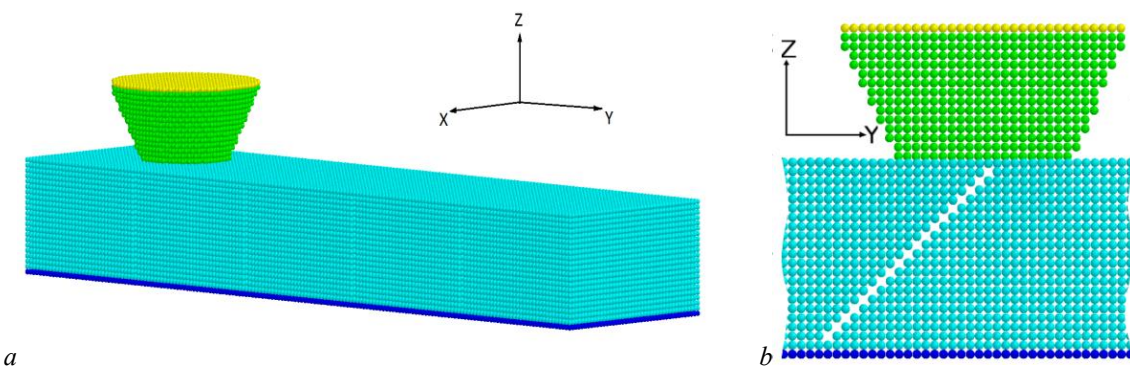


Figure 1: General view of the modelled system (a) and cross-section of the coating with a pore (b)

3 MODELLING RESULTS

Main attention of this research is focused on the role of vortex-like structures in the velocity fields in deformation of the strengthening coating and substrate. That is why first we studied the peculiarities of the velocity field in homogeneous coating under contact loading with hard conical counter-body moving along the free upper surface. Due to artificial roughness caused by discrete representation of the material and its surface, the movement of the counter-body along the surface with constant velocity results in periodic loading of the coating surface right in the contact patch. This cause generation of elastic waves in the coating, which propagate in the bulk and along the surface, and interact with another waves and structure elements of the material. As a result, the velocity field in the coating is drastically non-uniform and time dependent.

Analysis of numerical 2D vector field is very easy, one can see vortices in this case right from the picture of vectors shown as arrows or lines. Analysis of 3D fields is much more complicated problem. Evidently, one can try to look at 2D vector fields in a series of parallel sections of the 3D body. But, to see a vortex in this case you need to make sections by planes perpendicular to the direction of vorticity vector of the field (Figure 2,a). This means that first you need to compute the vorticity. But, the vorticity may have different orientations in different points; that is why this is not a right way. From the other hand, vorticity analysis is a typical task in hydrodynamics, and there are special tools in the computational fluid dynamics software for visualizing vortices. To analyse vorticity of the 3D vector field we used post-processor software VisIt [13]. To find vortices we plot streamlines of the velocity field at characteristic time steps (Figure 2,b). To make picture clearer we try different options and select the optimal ones. Of course, the resulting streamlines show just a tendency of the particle motion at the current time step, not real trajectories like in fluid dynamics. Nevertheless, this approach allows detecting position and “power” of vortex structures in 3D vector field of velocities and therefore is quite applicable for our task.

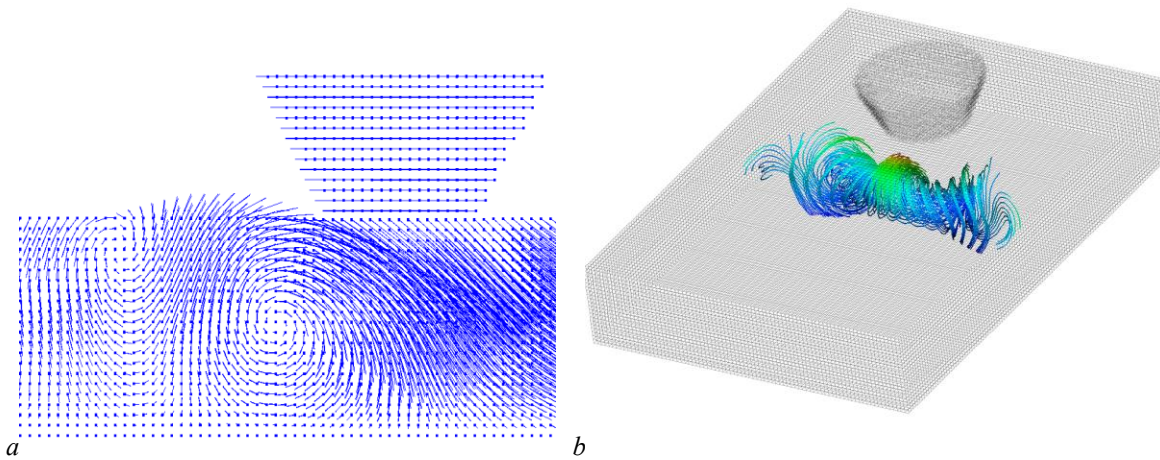


Figure 2: Vortex in the velocities of coating particles in front of the moving counter-body shown in cross-section of the sample (a, 2D picture) and in streamlines of the velocity field in 3D (b)

The peculiarities of velocity vortex formation in intact coating are as follows. Mainly, vortices occur in the corners of the coating, and are results of relaxation of elastic energy near free surface where it is allowed to move in several directions. But we tried to pay our attention to the vortices in the vicinity of counter-body. This vortex is formed periodically in time in front of the counter-body, and then it becomes wider, propagates ahead and rounds the counter-body. Lifetime of such vortex structure is about 0.015 ns, which corresponds to the time of sound propagation through the coating height. The vortex size is commensurable with half of the coating height.

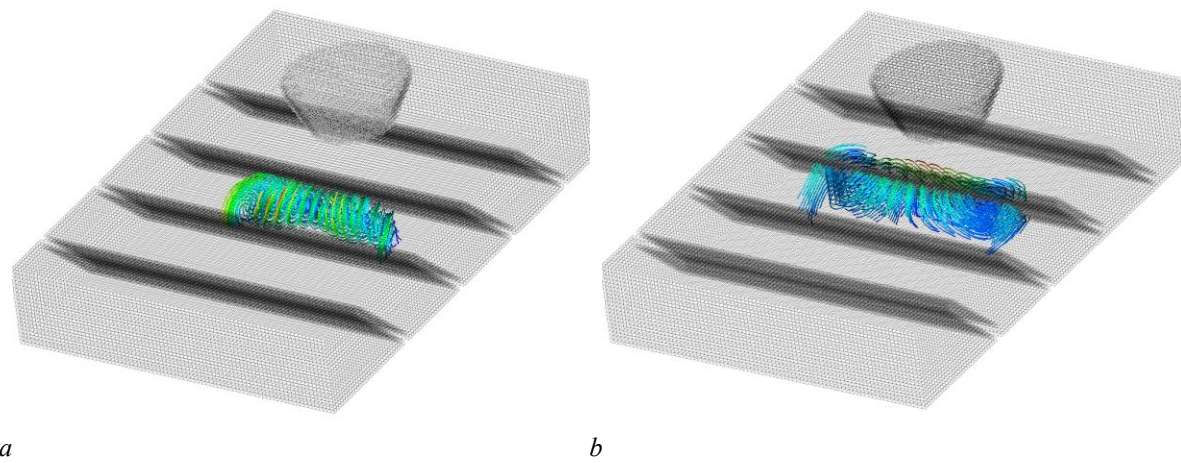


Figure 3: Streamlines showing the vortices in the particles velocities of coating with pores (a) and hard inclusions (b)

Then we considered coating containing damages. The damage of the coating was simulated by specifying the extended discontinuities, nano-pores. These nano-pores were located periodically at the predetermined distance from one another and inclined to the upper surface by 45° (Figure 1,b). In this case vortex-like motion takes place only in the material between the pores and due to their specific geometry the vortex axis cannot round about the counter-body (Figure 3,a). The size of the vortex is less than one in case of intact material. The vertex is generated approximately in the middle of height of the coating. Then it becomes larger, propagates towards the lower surface along the orientation of the pores, and finally is divided into two parts which start to propagate to the right and left lateral surfaces of the coating correspondingly and vanishes. Lifetime of the vortex is the same as for the case of intact material.

The third coating sample modelled in this study contained hard inclusions of the same geometry as the pores in the sample of second type. Elastic properties of the inclusions are two times greater than elastic properties of the coating. That means that sound velocity in the material of inclusions is approximately 1.4 times greater than that of the coating. Typical vortex in the sample with hard inclusions is shown in Figure 3,b. One can see that it is similar to the case of intact material, but a little bit smaller.

One possible application of the study is non-destructive technique for detecting nanoscale

defects in surface layer of a material using frequency analysis of the force resisting to sliding of a small counter-body on the material surface, known as tribospectroscopy [12]. When the counter-body is moving the resistance force of its movement on the surface is being recorded and correlated with the friction force F varying in time t . The Fourier transform is made for the registered friction force $F(t)$ and the corresponding spectra are analysed. Here, the possibilities of this technique are studied based on 3D modelling by MCA method for the above mentioned coating with nano-pores and inclusions.

The Fourier spectrum for the inclined nano-pores (Figure 1,b) are shown in Figure 4,a. They have peaks characterizing the distance between the damages calculated by the formula proposed in [14]:

$$f = V / (P - D) \quad (1)$$

where V is the velocity of the counter-body, P is the distance between pores, D is the diameter of contact area of conical counter-body with coating. For the specimen with the distance between the nano-pores equal to 96 nm this frequency is 0.128 GHz, and for the specimen with distance between pores 78 nm it is 0.277 GHz.

On the spectrum, one more peak at the frequency of 0.089 GHz occurs that is characterized by the following relation:

$$f = V / a \quad (2)$$

where a is the projection of the nano-pore to the testing surface.

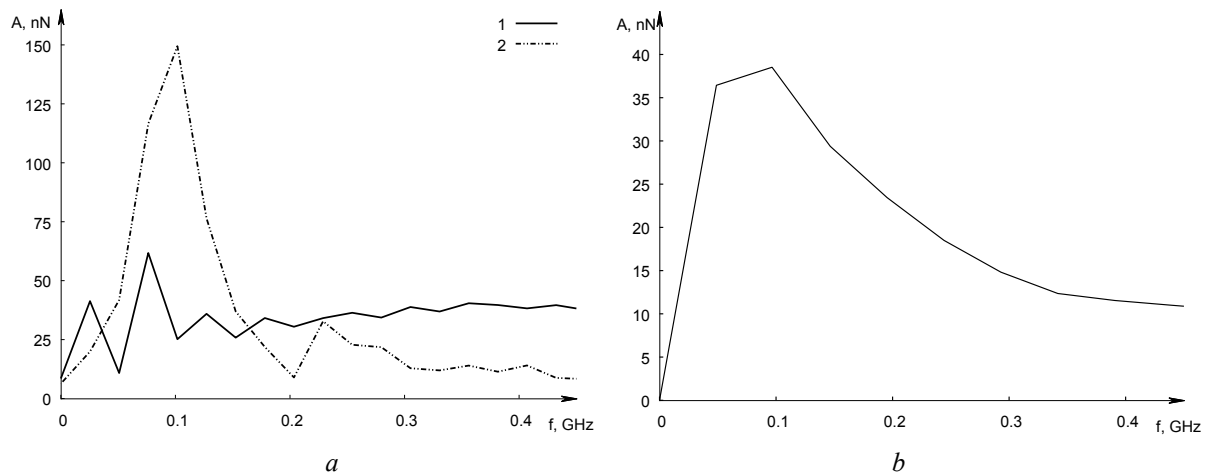


Figure 4: Fourier spectra of the force $F(t)$ acting on the counter-body moving along coating with inclined nano-pores (a) spaced at 1) 96 nm and 2) 78 nm from each other; and with hard inclusions spaced at 96 nm (b)

The spectrum for the coating with hard inclusions is shown in Figure 4,b. One can see that it has a peak corresponding to the size of inhomogeneity and the distance between them. But in general the curve is smoother and has no peak, corresponding to the projection of the inclusion to the testing surface defined by Equation 2. It may be explained by the specific features of the vortex behaviour in case of presence of the pores. Namely that in this case the vortex propagates between the pores.

4 CONCLUSIONS

- A numerical model for studying peculiarities of vortex-like motion in contact loading of strengthening coating by hard counter-body has been developed based on movable cellular automaton method.
- To study vortex structures in 3D numerical velocity field a series of streamline pictures of the vector field at different time steps is analysed as well as vectors in plane slices of different orientation.
- Modelling results show that a counter-body sliding on the coating surface generate periodically vortex structures in velocity field of the coating. Each of these vortices is located in front of the counter-body at distance of the radius of contact area. Lifetime of the vortex is about the time of sound propagation through the height of the coating. After this time the vortex vanishes, and then after certain time appears again.
- Presence of pores and hard inclusions can change the shape and size of the vortex.
- We assume that such vortices play significant role in friction force dynamics that may be very important for tribospectroscopy method of detecting damages in surface layers of material.

5 ACKNOWLEDGMENTS

The investigation has been carried out at financial support of the Project No. III.23.2.4 (S.G. Psakhie) of the Basic Scientific Research Program of State Academies of Sciences for 2013–2020, and the grant No. 14-19-00718 of the Russian Science Foundation (A.Yu. Smolin, G.M. Eremina).

REFERENCES

- [1] Landau, L.D. and Lifshitz, E.M. *Theory of elasticity*. Pergamon Press (1970).
- [2] Chertov, M.A., Smolin, A.Yu., Sapozhnikov, G.A. and Psakhie, S.G. The effect of surface waves on the interaction of incident particles with a solid surface *Tech. Phys. Lett.* (2004) **30**(12):1009-1012.
- [3] Psakhie, S.G., Zolnikov, K.P., Dmitriev, A.I. et al. Dynamic vortex defects in deformed material *Phys. Mesomech.* (2014) **17**(1):15-22.
- [4] Psakh'e, S.G. and Zol'nikov, K.P. Anomalously high rate of grain boundary displacement under fast shear loading *Tech. Phys. Lett.* (1997) **23**(7):555-556.
- [5] Psakh'e, S.G. and Zol'nikov, K.P. Possibility of a vortex mechanism of displacement of the grain boundaries under high-rate shear loading *Combust. Explos. Shock Waves* (1998) **34**(3):366-368.
- [6] Zhang, Z.F., He, G., Zhang, H., Eckert, J. Rotation mechanism of shear fracture induced by high plasticity in Ti-based nano-structured composites containing ductile dendrites *Scripta Materialia* (2005) **52**:945-949.
- [7] Oñate, E. and Rojek, J. Combination of discrete element and finite element methods for dynamic analysis of geomechanics problems *Comput. Methods Appl. Mech. Engrg.* (2004) **193**:3087-3128.
- [8] Popov, V.L., Starcevic, J. and Filippov, A.E. Reconstruction of potential from dynamic experiments *Phys. Rev. E* (2007) **75**(6):066104-1.

- [9] Psakhie, S.G., Shilko, E.V., Smolin, A.Yu., et al. Approach to simulation of deformation and fracture of hierarchically organized heterogeneous media, including contrast media *Phys. Mesomech* (2011) **14**(5-6):224-248.
- [10] Shilko, E.V., Psakhie, S.G., Schmauder, S., et al. Overcoming the limitations of distinct element method for multiscale modeling of materials with multimodal internal structure *Comput. Mater. Sci* (2015) **102**:267-285.
- [11] Levashov, E.A., Petzhik, M.I., Shtansky, D.V., et al. Nanostructured titanium alloys and multicomponent bioactive films: Mechanical behavior at indentation *Mater. Sci. Engrg. A* (2013) **570**:51-62.
- [12] Psakhie, S.G., Popov, V.L., Shilko, E.V., Smolin, A.Yu., Dmitriev, A.I. Spectral analysis of the behavior and properties of solid surface layers. Nanotribospectroscopy *Phys. Mesomech* (2009) **12**(5-6):221-234.
- [13] <https://wci.llnl.gov/simulation/computer-codes/visit>
- [14] Eremina, G.M., Smolin, A.Yu., Sergeev, V.V., Psakhie, S.G. Identification of nanosized defects using tribospectroscopy. Modeling by movable cellular automaton method *AIP Conf. Proc* (2014) **1623**:139-142.

COUPLING OF PARTICLE-BASED AND GRID-BASED METHODS WITHIN OBJECT-ORIENTED MULTI-PHYSICS CFD FRAMEWORK

RENE STEIJL¹, SIMONE COLONIA² AND GEORGE N. BARAKOS³

¹ CFD Laboratory, School of Engineering, University of Liverpool
Brownlow Hill, L69 3GH Liverpool, United Kingdom
r.steijl@liverpool.ac.uk, <https://www.liv.ac.uk/flight-science/cfd/multi-physics-code>

² CFD Laboratory, School of Engineering, University of Liverpool
Brownlow Hill, L69 3GH Liverpool, United Kingdom
s.colonia@liverpool.ac.uk, <https://www.liv.ac.uk/flight-science/cfd/rarefied-gas>

³ CFD Laboratory, School of Engineering, University of Liverpool
Brownlow Hill, L69 3GH Liverpool, United Kingdom
g.barakos@liverpool.ac.uk, <https://www.liv.ac.uk/engineering/staff/george-barakos>

Key words: Molecular Dynamics, Hypersonic Flows, Boltzmann-Kinetic Models

Abstract. A novel multi-physics approach involving mesh-based methods for kinetic-Boltzmann equations coupled with molecular dynamics (MD) simulations of thermal relaxation is introduced. The particle method, its parallel performance and the implementation in MFC are discussed, including the unification and re-use of the source code for different methods and models. The hypersonic partially rarefied flow of a diatomic gas around a sphere and a spaceplane configuration are considered as examples, providing details about the thermal non-equilibrium conditions to be modelled using MD simulations. The MD results show that existing empirical models may not provide sufficient accuracy for the gas flow in strong expansions and that the proposed method provides a mechanism for improving the accuracy.

1 INTRODUCTION

The multi-physics solver MFC[1, 2, 3], developed within the CFD Laboratory at the University of Liverpool was designed for hybrid simulations with a coupling of numerical methods for different mathematical models in different parts of the flow domain. A key feature of the framework is the object-oriented design, i.e. the framework constitutes a library of C++ classes on top of which a range of particle-based methods (Molecular-Dynamics, Vortex Particle method) as well as mesh-based methods for the Navier-Stokes

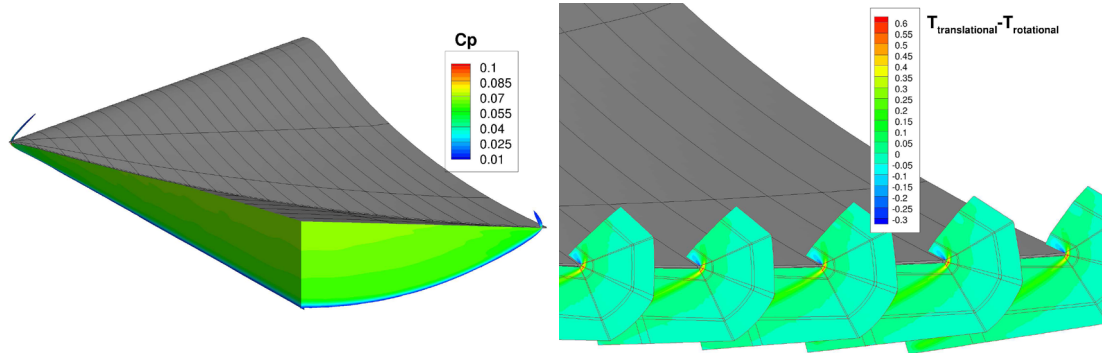


Figure 1: Hybrid kinetic-Boltzmann/Navier-Stokes simulation of Mach 8 flow around waverider

equations and the kinetic Boltzmann equations (Shakhov/Rykov-BGK[4, 5] and Ellipsoidal Statistical (ES) models[6]) were built. The design enables a large degree of re-use of source code for different methods as well as prototyping of novel coupling approaches. In previous works, the framework was demonstrated for coupled Navier-Stokes/Molecular Dynamics problems involving nano-scale flow of liquids[1, 2] as well as coupled Navier-Stokes/kinetic-Boltzmann simulations[3].

The Navier-Stokes equations form the baseline level mathematical model for the vast majority of Computational Fluid Dynamics (CFD) simulations, since the assumptions upon which the equations are based are satisfied in continuum-flow cases with weak thermodynamic non-equilibrium. MFC was developed for the simulation of complex flows with a multi-scale character and strong thermodynamic non-equilibrium, including rarefaction effects. An important application is the modelling of high-speed, hypersonic flows around aerospace vehicles such as shown in Figure 1. The flow at Mach 8 around a waverider hypersonic cruise vehicle develops a strong shock wave on the underside of the vehicle with high-pressure air captured in a region bounded by the vehicle surface and the shock wave. Around the blunt leading-edges of the vehicle, the air previously compressed and heated by the bow shock wave leaks away towards the upper surface, creating a local area of strong expansion. Accurate modelling of these effects requires more detailed models than Navier-Stokes. On the right-hand side of Figure 1, the flow in the vicinity of the vehicle leading edge was modelled using a kinetic Boltzmann model (diatomic ES model). In the shock wave as well as the strong expansion regions, strong thermodynamic effects occur with the rotational temperature of the diatomic molecules getting out of equilibrium with the translational temperature, as can be seen from the figure. Through a shock wave, the temperature associated with the translational motion, T_{trans} , increase more rapidly than the temperature corresponding to the rotational motion (T_{rot}), while in strong expansions, the opposite effect can be observed.

The present work focuses on the recent development of molecular dynamics modelling of diatomic gas flows in strong thermodynamic non-equilibrium and the coupling of the molecular-level modelling to mesh-based kinetic models. In particular, the development

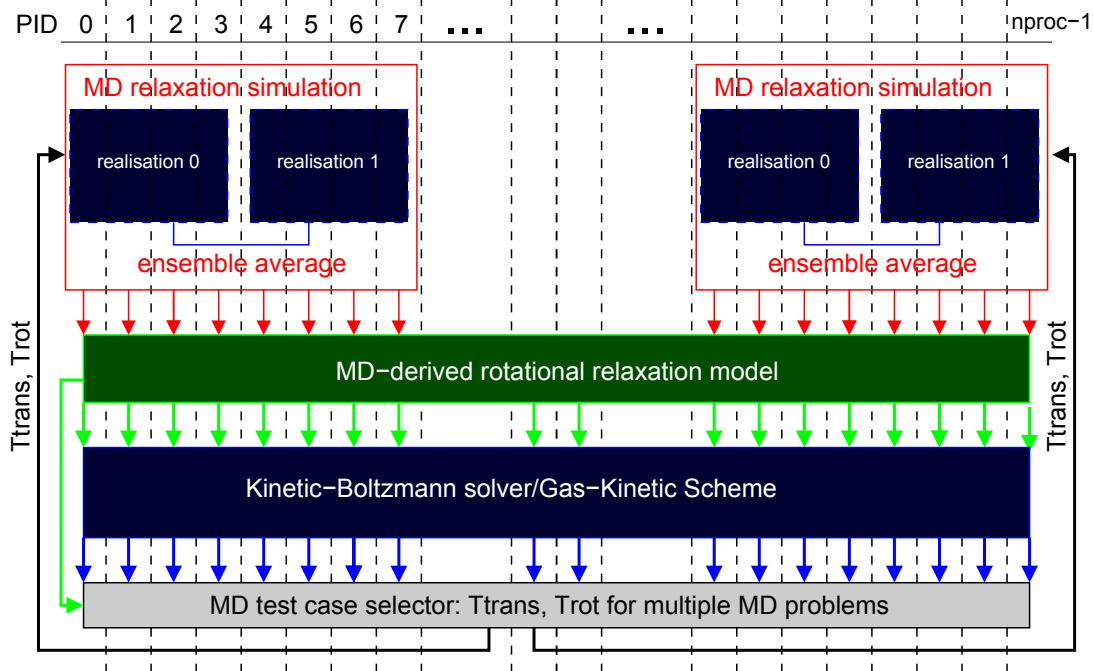


Figure 2: Multi-physics simulation of diatomic gas flow in thermodynamic non-equilibrium with a rotational-relaxation model based on multiple-sample MD simulations.

of a multi-physics simulation approach in which the rotational-relaxation model in the kinetic-Boltzmann solver takes detailed information from a series of molecular dynamics (MD) simulations. The rotational motion of diatomic molecules is assumed to be fully excited degrees of freedom, for which a classical MD model can be used, while, at present, it is assumed that the temperatures stay sufficiently low so that vibrational excitation present in high-temperature conditions plays a negligible role. Figure 2 sketches the principle of the multi-physics approach, where an 'MD-layer' is created in which all processes in a parallel simulation are involved in conducting multiple MD simulations representing a number of thermodynamic non-equilibrium situations. For each of these conditions, multiple realisations are created and ensemble-averaging is then used to feed the information into an empirical rotational-relaxation model, which is used in the flow simulation conducted using either of the following approaches: (i) a Gas Kinetic Scheme (GKS) based on the Rykov model recently developed by the authors[7] is used throughout the flow domain, (ii) a discrete-velocity method (DVM) for the Rykov or diatomic-ES model is used or (iii) a hybrid approach coupling the GKS and the DVM methods. In the following, the development of the multi-physics approach as well as results from MD modelling of rotational relaxation at conditions representative of hypersonic flows around aerospace vehicles are discussed along with the steps involved in the further development of the multi-physics approach in MFC.

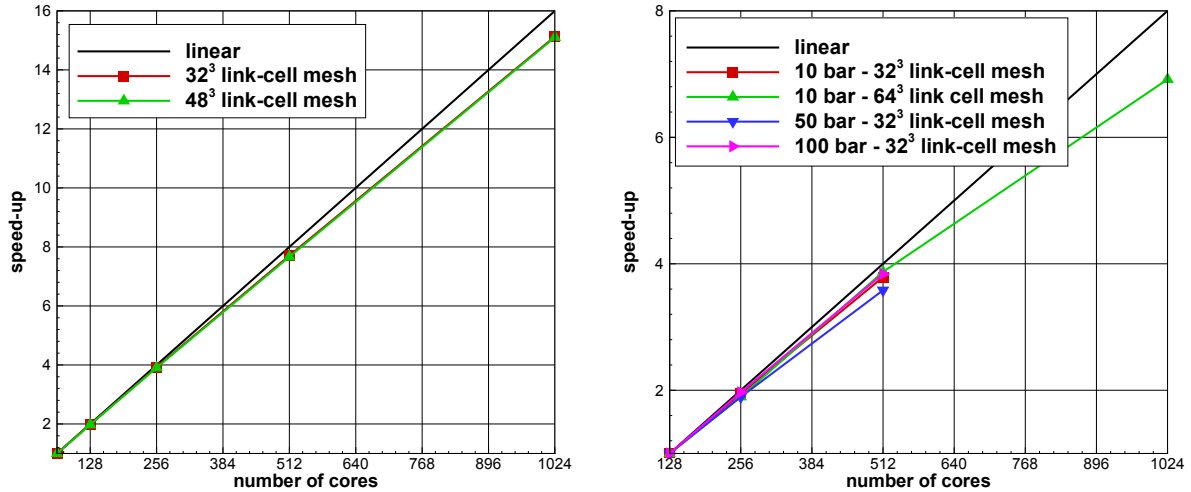


Figure 3: Multi-sample MD simulation. Parallel speed-up for liquid water (two different domain size) and for nitrogen gas at different pressures. Timings recorded on IBM BlueGene/Q machine.

2 MULTI-PHYSICS SIMULATION - MFC FRAMEWORK

The framework was designed starting from a generalisation of the domain-decomposition paradigm, i.e. the particle-based and mesh-based methods included in the framework were designed for large-scale parallel simulation with sub-domains divided across multiple processes. For hybrid simulations coupling different models and methods, data is exchanged using message passing between the different domains. Generic container and iterator classes were created, along with classes to define problem topology, message-passing based data transfer, etc. A high level of abstraction was used in the basic classes such that re-use of software, i.e. the C++ template classes in the framework’s library, can be used for both particle-based and mesh-based methods for a range of mathematical models.

3 MFC - MOLECULAR DYNAMICS SOLVER

The MD solver employs a linked-cell list algorithm to determine the interaction for each molecule with its neighbours within a predefined interaction range. The rectangular domain is split in multiple sub-domains for parallel computation. For non-linear molecules, a quaternion formulation is used to define the rotational motion of the molecule[8]. A predictor-corrector method is used for the time integration. The main class defining a cell in the linked-cell method is defined as,

```
// class T = particle class
// class U = link-cell container iterator
// class V = data storage class
// class W = data storage class for translation
template <class T, class U, class V, class W>
```

```
class MD_Quat_Cell {
    ...
};
```

The particle class T in the template class `MD_Quat_Cell` for a non-linear molecule (e.g. water) is defined as,

```
class WaterQuat {
    int sitesMol; // Number of 'sites' within molecule
    VecR mol_r, mol_rv, mol_ra, mol_ra1, mol_ra2, mol_ro, mol_rvo;
    Quat mol_q, mol_qv, mol_qa, mol_qa1, mol_qa2, mol_qo, mol_qvo;
    VecR *site_force; // forces acting on molecule 'sites'
    ...
};
```

In the parallel data exchange, molecule positions and orientations need to be exchanged between process to correctly define the particles in the 'halo' cells. Furthermore, molecules will migrate from cell to cell in the linked-cell method, which might also involve the migration to another process. For the non-linear molecules, e.g. defined through class `WaterQuat`, the following structures are defined,

```
typedef struct {
    int icell;
    int ic,jc,kc;
    double pos[NDim+NQuat]; // mol_r , mol_q
    double vel[NDim+NQuat]; // mol_rv, mol_qv
} MD_ParticleQuatData;

typedef struct {
    int icell;
    int ic,jc,kc;
    double pos[NDim+NQuat]; // mol_r , mol_q
    double vel[NDim+NQuat]; // mol_rv, mol_qv
    double acc[3*NDim+3*NQuat]; // mol_ra, mol_ra1, mol_ra2, mol_qa, mol_qa1, mol_qa2
} MD_ParticleQuatTrans;
```

where `NQuat`=4 and `NDim`=3. These datatypes are used as templates `V` and `W` in class `MD_Quat_Cell`, respectively.

For linear molecules, with only two rotational degrees of freedom rather than three, a simplified model[8] is used in the MD solver. In this model, the torque on a molecule is defined as,

$$\vec{n} = \sum_k \vec{r} \times \vec{f}_k = \vec{s} \times \sum_k d_k \vec{f}_k = \vec{s} \times \vec{g} \quad (1)$$

where the orientation is defined by \vec{s} , the unit vector along the molecular axis, and where d_k is the signed distance along the axis of each interaction site from the centre of mass. For the linear nitrogen molecule considered in the present work, the angular momentum is $I\vec{\omega}$, with I the moment of inertia about the two principal axes, giving the following equations for the rotational motion,

$$I \frac{d\vec{\omega}}{dt} = \vec{s} \times \vec{g} ; \quad \frac{d\vec{s}}{dt} = \vec{\omega} \times \vec{s} \quad (2)$$

$$I \frac{d^2\vec{s}}{dt^2} = \vec{g} - \left[(\vec{s} \cdot \vec{g}) + I \frac{d\vec{s}}{dt} \cdot \frac{d\vec{s}}{dt} \right] \vec{s} \quad (3)$$

Equation (3) along with the equations of motion for the translational motion are integrated using a predictor-corrector method. For the linear-molecule case, modified versions of the above C++ classes are used, while the main container, iterator and message-passing classes are identical.

3.1 Liquid water and nitrogen gas models

The MD solver in MΦC was first validated using a number of test cases for liquid water. For MD simulations of liquid water, the well-known TIP4P water model was used. The model molecule is based on four interaction sites located in a planar configuration. For the Lennard-Jones (LJ) part of the potential, the potential well depth is taken as $\epsilon/k_B = 78.2$. In the simulations, the problem is non-dimensionalised in LJ units. The interaction cutoff is $r_c = 7.5 \text{ \AA}$ or 2.38σ .

For MD simulations of nitrogen gas, a Lennard-Jones based model was used with two sites on each molecule coinciding with the atom locations. The potential well depth is taken as $\epsilon/k_B = 37.3$, while a reduced length $\sigma = 3.31 \text{ \AA}$ was used. For the linear molecule, the moment of inertia about the two axes with non-zero inertia is defined by a radius of gyration of 0.0547 \AA .

3.2 Parallel performance

The parallel speed-up was investigated for a number of different multi-sample MD simulations on the BlueGene/Q computer at the Hartree Centre in the UK. Figure 3 presents the parallel speed-up for the liquid water as well as the nitrogen gas test cases. For liquid water, a temperature of $298K$ and density of $1000kg/m^3$ were used. In LJ units, the employed time step was 0.0005. The cases with 32^3 and 48^3 cells in the cell-linked list correspond to 2.10 and 6.97 million molecules, respectively. The simulations used 4 realisations, with the number of cores per realisation increasing from 16 to 256, with a parallel efficiency of 94%. For the nitrogen cases, the 10, 50 and 100 bar cases correspond to 32768, 110592 and 262144 molecules for the cases with 32^3 cells in the cell-linked list. For 10 bar, a case with 64^3 cells was also considered. In LJ units, the employed time step was 0.000025. The nitrogen simulations used 64 realisations, so that the number of cores per realisation varied from 2 to 16 and a parallel efficiency of approximately 80% was observed. For the water simulations, the number of molecules each of the molecules interacts with is significantly higher than in any of the nitrogen gas cases. Therefore, within each of the cells of the cell-linked list formulation used, the liquid water simulations have a significantly larger number of molecules than the cells in the nitrogen gas

simulations. Furthermore, the molecules in the liquid phase are far more uniformly distributed in space as compared with especially the low-density gas simulations. For these reasons, the present parallel simulations based on the spatial domain-decomposition approach show a better parallel speed-up for the water simulations than for the nitrogen simulations. However, the obtained results indicate that for a suitable chosen set of samples, a good parallel speed-up can be achieved for MD simulations of nitrogen gas with multiple realisations.

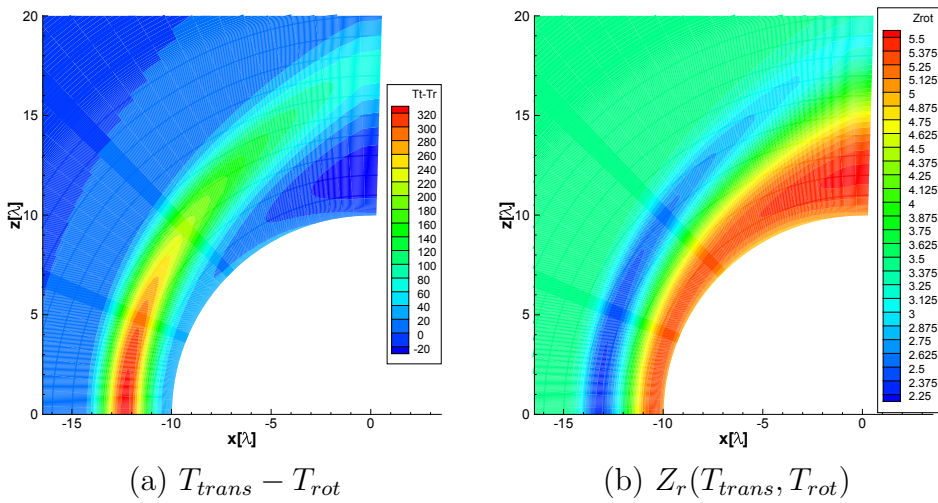


Figure 4: Rarefied Mach 5 flow over sphere simulated using the Rykov-based Gas Kinetic Scheme. Free-stream temperature $T_\infty = 116K$, wall temperature $290K$. sphere radius 10 mean-free path lengths at free-stream conditions (λ).

4 MFC - GRID-BASED KINETIC-BOLTZMANN SOLVERS

Using the container and iterator classes in MFC, cell-centred finite-volume methods were created for the simulation of kinetic-Boltzmann models using a Gas Kinetic Scheme (GKS) based on the Rykov model recently developed by the authors[7]. A discrete-velocity method (DVM) for the kinetic models as well as hybrid approaches coupling the GKS and the DVM methods have also been developed. In the present work, the focus is on diatomic gas flows modelled with the Rykov model, which is a kinetic-Boltzmann model in which the rotational degree of freedom of the molecules is taken into account using an additional particle distribution function compared to a monoatomic kinetic model. The two particle distribution functions in the Rykov model are governed by the following equations,

$$\begin{aligned} \frac{\partial F_0}{\partial t} + \mathbf{c} \frac{\partial F_0}{\partial \mathbf{x}} &= \frac{F_0^{eq} - F_0}{\tau} ; \quad \frac{\partial F_1}{\partial t} + \mathbf{c} \frac{\partial F_1}{\partial \mathbf{x}} = \frac{F_1^{eq} - F_1}{\tau} \\ F_0^{eq} &= \frac{1}{Z_r} F_0^r + \left(1 - \frac{1}{Z_r}\right) F_0^t ; \quad F_1^{eq} = \frac{1}{Z_r} F_1^r + \left(1 - \frac{1}{Z_r}\right) F_1^t \end{aligned} \quad (4)$$

with F_0^r , F_0^t , F_1^r , F_1^t modified equilibrium functions involving translational as well as rotational temperature. The total collision time τ is expressed as μ_t/p with the viscosity and pressure determined from the translational temperature. The Rykov model is based on the assumption that the fraction of collisions involving the excitation of the rotational degrees of freedom, Z_r , is a given constant or a function of the flow temperatures. In the present work, Z_r will be investigated in more detail using molecular dynamics in section 5.

Gas Kinetic Schemes (GKS) are a class of methods in which the numerical flux across through cell faces in a finite-volume method is derived from a local kinetic problem around the cell interfaces. In the present work, this flux includes both convective and and viscous contributions but is more expensive than Roe or AUSM fluxes with central discretisation of the viscous fluxes. The Rykov-based GKS was defined starting from Equation (4). The non-equilibrium particle distribution functions were defined using a Chapman-Enskog expansion, which limits the scheme to moderate levels of thermal non-equilibrium. Integrating in time for a one-dimensional flow in a control volume dx with a continuous particle velocity c_x and discretised space x_i and time t^n , with step sizes of Δx and Δt respectively, one obtains

$$F|_i^{n+1} = F|_i^n + \frac{1}{\Delta x} \int_{t^n}^{t^{n+1}} ([c_x F]|_{i-1/2} - [c_x F]|_{i+1/2}) dt + \frac{\Delta t}{2} \left(\frac{F|_i^{n+1} - F|_i^{n+1}}{\tau^{n+1}} + \frac{F|_i^n - F|_i^n}{\tau^n} \right)$$

where the trapezoidal rule has been employed for the collision term integral, S , and $[c_x F]|_{i\mp 1/2}$ are the fluxes of the distribution function across the cell interface. Then, taking the moments $\hat{\Psi} = (1, c_x, \mathbf{c}^2)^T$ of equation above, the update of the conservative variables can be found as

$$\mathbf{W}_i^{n+1} = \mathbf{W}_i^n + \frac{1}{\Delta x} \int_{t^n}^{t^{n+1}} \int_{-\infty}^{+\infty} \hat{\Psi} ([c_x F]|_{i-1/2} - [c_x F]|_{i+1/2}) d\mathbf{c} dt + \frac{\Delta t}{2} (S^{n+1} + S^n) \quad (5)$$

5 MD MODELLING OF ROTATIONAL RELAXATION IN NITROGEN

In a system of colliding particles, energy is transferred between the various internal modes. These collisions tend to drive the internal energy distributions towards their respective equilibrium state. In a diatomic gas, the time required for the different modes to relax towards the equilibrium state is different, i.e. the translational motion generally approaches its equilibrium faster than the rotational motion of the gas. For the rotational relaxation time we can then write $\tau_r = Z_r \tau$, where τ is the translational relaxation time and $Z_r > 1$ the rotational collision number. Theoretical works by Parker[9] and Lordi and Mates[10] considered pairs of molecules sampled from equilibrium conditions for the considered temperature to create empirical expressions for the rotational collision

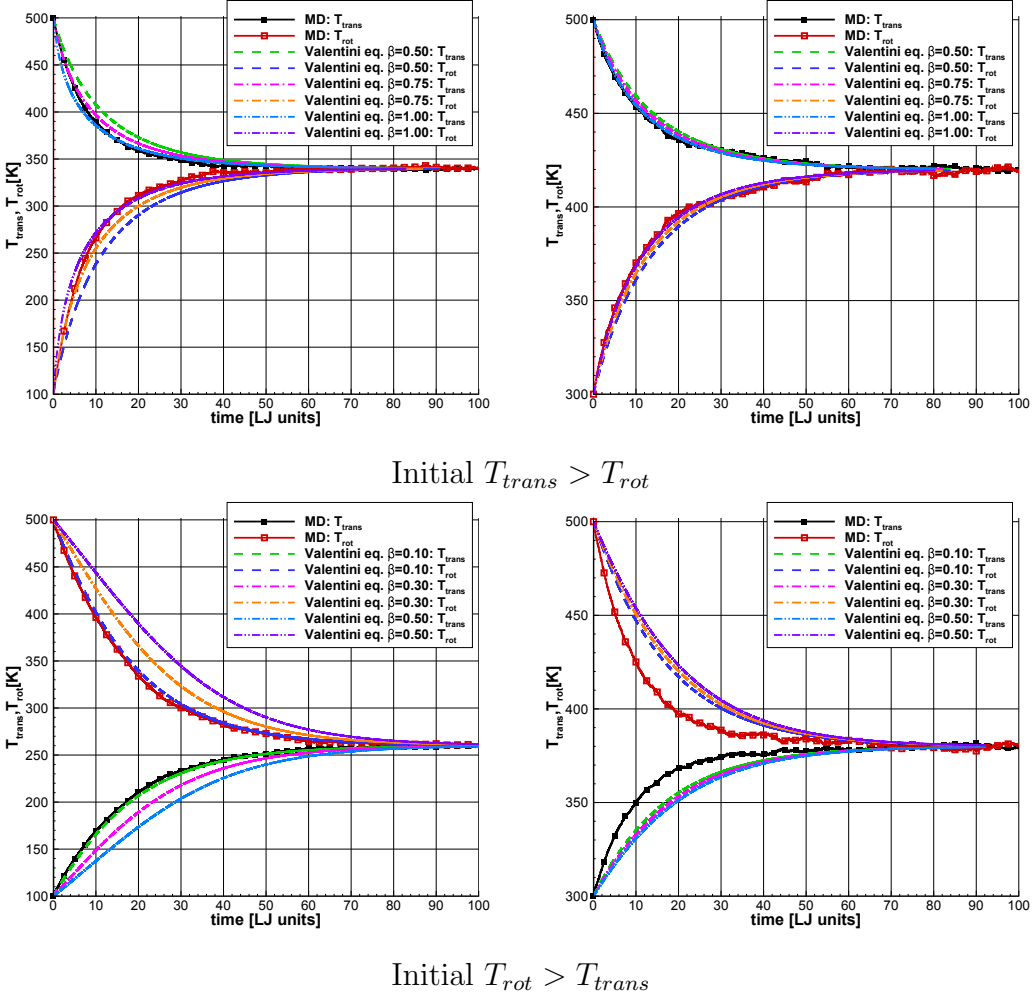


Figure 5: MD simulation of rotational relaxation in nitrogen. Non-equilibrium initial conditions with translational temperature exceeding the rotational temperature is representative of strong gas compression through shock wave. Non-equilibrium initial conditions with rotational temperature exceeding the translational temperature are representative of strong expansions.

number as function of temperature. Despite the fact that Parker's work involved a large number of simplifying assumptions such as a restriction to co-planar collisions to enable an analytical treatment, the overall dependence on the temperature is in agreement with the more rigorous numerical analysis of Lordi and Mates[10], who also considered general non-planar collisions. In the literature, empirical formulas derived from data fitting, either from numerical or experimental results, have been presented. Valentini and co-workers derived an expression for $Z_r(T_{trans}, T_{rot})$ derived from molecular dynamics simulations,

defined as,

$$Z_r = \left[a_1 \left(\frac{T_{trans}}{1K} \right)^{1/4} + a_2 \left(\frac{T_{trans}}{1K} \right)^{-1/4} - a_3 \left(\frac{T_{trans}}{1K} - 1000 \right) \right] \left[1 - \beta \left(1 - \frac{T_{rot}}{T_{trans}} \right) \right] \quad (6)$$

where $a_1 = 1.33868$, $a_2 = -6.19992$, $a_3 = -0.00107942$ and $0 < \beta \leq 1$. In their work, Valentini et al. performed a series of adiabatic and isothermal MD simulation starting from a non-equilibrium gas state, in which the translational and rotational motions were sampled from Maxwellians at different temperatures. The emphasis was on the situation in which the translational temperature exceeds the rotational temperature, i.e. representative of the situation downstream of a strong shock wave in a high-Mach number flow.

Figure 4 presents results for the Mach 5 flow around a sphere obtained with the Rykov GKS method. The shock can be seen to create a difference in translational and rotational temperatures of the order of $300K$ with the considered free-stream temperature of $116K$, while the expansion over the sphere leads to smaller differences. Figure 4(b) shows Z_r evaluated using Equation (6) with $\beta = 1$ as used in the simulation.

For the proposed multi-physics approach, the Z_r , which for Rykov GKS simulations appears in the equilibrium functions as well as the relaxation source term S , is to be evaluated using an equation of the type (6) which is then adjusted and extended with MD-derived data. As a first step, the rotational relaxation for non-equilibrium conditions observed in Figure 4(a) are analysed using the MD solver in MFC.

A cubic domain with dimensions $[154.9\sigma_{LJ}]^3$ was created with 32768 molecules. For the gas at $298K$ this would correspond to a pressure of 10 bar. For all simulations, the molecules were initialized on a regular lattice with random velocity vectors sampled from a Maxwellian distribution. First, an equilibration phase was conducted during $10\tau_{LJ}$ reduced time units. Then, an non-equilibrium situation was created by rescaling either the rotational motions or translational motions, to adjust the rotational or translational temperature, respectively. During this non-equilibrium phase of the simulation, no thermostat was applied and a sufficiently small time-step was used to prevent excessive numerical errors. A time step of $0.000025\tau_{LJ}$ was used in the simulations presented here.

The results from the MD simulations of nitrogen in rotational relaxation were analysed in detail by comparing the present results with those obtained using Valentini's expression, i.e. Equation (6). To compare the empirical expression for Z_r with the present MD results, the rotational relaxation in a gas at constant volume and total energy was simulated using the Jeans-Teller model for the relaxation term, a power-law model for the gas viscosity (based on the translational temperature T_t and $\omega = 0.74$) and expression for rotational relaxation time $Z_r\mu/p$, with the gas pressure evaluated from the constant density and the translational temperature. This problem was integrated in time using a 4th-order accurate Runge-Kutta method until the two temperatures were within a small predefined tolerance. In the following, the values for the constant a_1 , a_2 , a_3 were those reported[11], while the constant $0 < \beta \leq 1$. For the non-equilibrium MD simulations with $T_{trans} > T_{rot}$

a very good agreement with Valentini's fit was found for β was close to 1, as can be seen from Figure 5. For the opposite situation, i.e. $T_{rot} > T_{trans}$ (which was not considered by Valentini et al.), using Equation (6) with β similarly close to 1 was found to give a poor agreement. By reducing β to approximately 0.1 a better agreement with the present MD results can be seen for some of the cases considered, as shown in the plots in the bottom row of Figure 5. For some of the considered conditions, the empirical expression needs an adjustment to the constants a_1 , a_2 , a_3 to create a match.

For the multi-physics approach defined in Figure 2, the relaxation-model gets refined and adjusted during the course of the flow simulation. The MD test case selection step should involve criteria defining the validity of the used relaxation-model in terms of which thermodynamic non-equilibrium condition which can be reliably modelled with the relaxation model and for which conditions further MD simulations need to be initiated.

6 CONCLUSIONS

The development of a multi-physics solution method for hypersonic rarefied flows was described. For the implementation in the MFC framework, the re-use of C++ template classes available in the template-class library to unify the source for the particle-based and mesh-based solvers were described. The simulation of rotational relaxation in nitrogen gas, the Molecular Dynamics solver was analysed in detail and the obtained results were compared against available data in the literature. For gas conditions representative of strong expansion regions, it was found that available empirical models may be inadequate and that therefore the proposed multi-physics approach in which the MD simulations are integrated with the flow simulation may provide an important step forward, provided sufficient computer resources are available. Future work will analyse how best to integrate the MD-derived data into a rotational-relaxation model in the context of hybrid simulations based on kinetic Boltzmann models.

ACKNOWLEDGEMENT

The financial support by the University of Liverpool is gratefully acknowledged. We acknowledge PRACE for awarding us access to SuperMUC based in Germany at the Leibniz Rechenzentrum (LRZ) in Munich. Furthermore, we would like to acknowledge the Hartree Centre in the UK for access to the BlueGene/Q through the BlueJoule Access Programme.

REFERENCES

- [1] Steijl, R. and Barakos, G., Coupled Navier-Stokes–Molecular dynamics simulations using a multi-physics flow simulation framework, *International Journal for Numerical Methods in Fluids* (2010) **62**:1081–1106.
- [2] Steijl, R. and Barakos, G., Coupled Navier-Stokes/molecular dynamics simulations in nonperiodic domains on particle forcing, *International Journal for Numerical Meth-*

- ods in Fluids* (2012) **69**:1326–1349.
- [3] Steijl, R. and Barakos, G., Computational Fluid dynamics of Partially Rarefied Flows with Coupled Kinetic Boltzmann/Navier-Stokes Methods, ECCOMAS 2012, 10-14 September, Vienna, Austria 2012.
 - [4] Cercignani, C., *Theory and Application of the Boltzmann Equation* Scottish Academic Press, 1975.
 - [5] Rykov, V., A Model Kinetic Equation for a Gas with Rotational Degrees of Freedom, *Fluid Dynamics* (1975) **10(6)**:959–966.
 - [6] Andries, P., LeTallec, P., Perlat, J.-P., and Perthame, B., The Gaussian-BGK Model of Boltzmann Equation with Small Prandtl Number, *European Journal of Mechanics - B/Fluids* (2000) **19(6)**:813–830.
 - [7] Colonia, S., Steijl, R., and Barakos, G., Kinetic Models and Gas Kinetic Schemes for Hybrid Continuum/Kinetic-Boltzmann Methods, AIAA Aerospace Science and Technology 2015, January 5-9 2015, Kissimmee, Florida, USA.
 - [8] Rapaport, D.C.. *The Art of Molecular Dynamics Simulation*. Cambridge University Press, 2nd edition. (2004).
 - [9] Parker, J., Rotational and Vibrational Relaxation in Diatomic Gases, *Physics of Fluids* (1959) **2(4)**:449–462.
 - [10] Lordi, J. and Mates, R., Rotational Relaxation in Nonpolar Diatomic Gases, *Physics of Fluids* (1970) **9(4)**:291–308.
 - [11] Valentini, P., Zhang, C., and Schwartzentruber, T., Molecular Dynamics Simulation of Rotational Relaxation in Nitrogen: Implications for Rotational Collision Number Models, *Physics of Fluids* (2012) **(24)**:106101:1–23.

Hybrid Thermo-Mechanical Contact Algorithm for 3D SPH-FEM Multi-physics Simulations

Kirk A. Fraser^{1,2*}, Lyne St-Georges², Laszlo I. Kiss² and Yves Chiricota²

¹ Aluminium Research Centre-REGAL

² Université du Québec à Chicoutimi (UQAC)

555, boulevard de l'Université

Saguenay (Québec) G7H 2B1

* e-mail: kirk.fraser1@uqac.ca

Key words: Thermo-mechanical contact, smoothed particle hydrodynamics, computational plasticity, solid mechanics, friction stir welding, high speed machining, forging, extrusion

Abstract: Numerical simulation of complex industrial processes has become increasingly common in recent years. Depending on the nature of the industrial application, multiple types of physical phenomena may need to be considered as well as the interaction of multiple disjoint bodies. This paper is focused on industrial applications with large plastic deformation. Such processes are typically not well treated by finite element (FE) methods. For this reason, the smoothed particle hydrodynamics method (SPH) is used. In this work, we introduce a robust and straightforward thermo-mechanical contact algorithm for multi-physics SPH simulations in 3D.

1. INTRODUCTION

Multi-physics simulations more often than not include the interaction of multiple bodies. For example, in a ballistics impact analysis, the projectile is considered as a distinct body and the object to be impacted is another. The interaction between these two bodies is a large area of research. A contact algorithm is needed to prevent the elements of one body from penetrating into those in the other body. The type of contact algorithm to be used depends strongly on the simulation approach. For highly non-linear transient problems, typically an explicit time stepping tactic is used. In such a case penalty contact methods provide an efficient and robust means to transfer forces from one body to another. One of the earlier implementation was by Hughes et al. [1].

In the smoothed particle hydrodynamics (SPH) method, contact between bodies has been enforced by many different approaches. One of the simpler approaches is to allow the two bodies to interact directly through the SPH equations. This has certain qualities, however, the biggest drawback is that the elements at the interface of the two bodies will impart shear stresses that will cause a “no-slip” behavior. For industrial processes like friction stir welding (FSW) and high speed machining (HSM), the “no-slip” boundary condition cannot easily be implemented. A very high SPH element density is needed in the contact region to correctly resolve the shear stresses due to this type of boundary condition. For such industrial processes, a friction based contact model is often adopted with little to no loss of coherency.

Throughout SPH literature, very little has been presented in terms of a node to surface

penalty contact method with friction. Node to node contact models on the other hand have been reasonably well documented. Of the models that have been published, the Belytschko [2, 3] pinball method is rather popular and requires very little modification to be applied to SPH. Vignjevic and Campbell [4] discuss three penalty based contact models and compare the results of the impact of two blocks in 2D. They note that all the methods that they investigate suffer from an instability at the corners of the SPH body. Seo et al. [5, 6] present a rigorous treatment of SPH contact for axisymmetric problems. Wang et al. [7] provide a succinct treatment of a general contact algorithm with friction between a flexible SPH body and either a flexible or rigid body. They present their formulation in 2D and mention that only minor changes are needed to move to 3D. We have found on the other hand that a number of modifications are indeed needed in 3D.

Many commercial simulation codes such as LS-DYNA, Abacus, Hyperworks, etc. provide a means to couple SPH and finite element (FE) bodies mechanically. However, to our knowledge, a robust thermo-mechanical contact algorithm has not yet been presented nor implemented in any presently available multi-physics SPH codes.

In this paper, we outline the implementation of a thermo-mechanical penalty contact algorithm that can be used for SPH-SPH or SPH-FE simulations. The implementation that we will present supposes that the SPH body is flexible, while the FE body is reasonably approximated as rigid. Some minor changes would be needed to extend the algorithm to account for a deformable SPH body with either another deformable SPH body or FE body. The code is written using CUDA Fortran, this allows us to use a fine grained parallel implementation of the SPH code on the graphics processing unit (GPU). At the end of the paper, we present a validation case for the algorithm using a high speed machining example. The underlying physics show close parallels to other industrial processes such as friction stir welding, extrusion and forging and as such we expect the algorithm to be useful for these processes as well.

2. THE SPH METHOD

A brief overview of the SPH implementation used for this work is presented here. Most of the details are glazed over since the focus of the paper is the contact algorithm. The conservation of mass for a temporally changing compressible system is:

$$\frac{d\rho}{dt} + \nabla \cdot \rho \bar{v} = 0 \quad (1)$$

ρ is the material point density, \bar{v} is the velocity and t is time. We can write the discrete SPH equation for conservation of mass:

$$\frac{d\rho_i}{dt} = \sum_{j=1}^{N_i} m_j (v_i^\beta - v_j^\beta) \frac{\partial W_{ij}}{\partial x_i^\beta} \quad (2)$$

N_i is the number of neighbors of the i^{th} particle, m_j is the mass of the j^{th} particle and $\partial W_{ij}/\partial x_i^\beta$ is the gradient of the smoothing function (see Liu and Liu [8] for more details). Conservation of momentum for a continuum is given by:

$$\frac{d\bar{\nu}}{dt} = \frac{1}{\rho} \nabla \cdot \bar{\sigma} + \bar{g} + \frac{1}{m} \bar{F}_{contact} \quad (3)$$

$\bar{\sigma}$ is the Cauchy stress tensor (total stress), \bar{g} is the gravity vector and $\bar{F}_{contact}$ is the contact force vector that is found from the contact algorithm (to be explained latter). The SPH equation is then:

$$\frac{dv_i^\alpha}{dt} = \sum_{j=1}^{N_i} m_j \left(\frac{\sigma_i^{\alpha\beta}}{\rho_i^2} + \frac{\sigma_j^{\alpha\beta}}{\rho_j^2} \right) \frac{\partial W_{ij}}{\partial x_i^\beta} + g_i^\alpha + \frac{1}{m_i} F_{contact_i}^\alpha \quad (4)$$

This is known as the symmetric form of the momentum equation. For many industrial processes, including the effects of heat transfer is of key importance. We seek to provide a discrete SPH equation for the heat diffusion equation:

$$\frac{\partial T}{\partial t} = \frac{1}{\rho C_p} (k \nabla^2 T + \dot{q}) \quad (5)$$

T is the material point temperature, C_p is the specific heat capacity, k is the thermal conductivity and \dot{q} takes into account heat generation due to plastic deformation or friction work. We have found that Jubelgas's [9] SPH formulation for heat transfer works well and is used in this work:

$$\frac{dT_i}{dt} = \frac{1}{\rho_i C_{p_i}} \left[\sum_{j=1}^{N_i} \frac{m_j}{\rho_j} \frac{(4k_i k_j)}{(k_i + k_j)} \frac{(T_i - T_j)}{|x_{ij}|^2} x_{ij} \frac{\partial W_{ij}}{\partial x_i^\beta} + \dot{q} \right] \quad (6)$$

This form uses the harmonic mean for the thermal conductivity and has been shown to provide good results for materials with large variations of thermal conductivity. Strain rates, deviatoric stresses, the spin tensor and objective stress updates are calculated according to the common approach; further details can be found in any SPH publication that treats strength of materials [10-20]. We use a semi-implicit (modified Euler, similar to Cleary et al. [11]) integration scheme that is well suited for solid mechanics problems with SPH. The plasticity algorithm is a standard Johnson-Cook model with the radial-return approach. We also use a novel adaptive neighbor searching algorithm that is described by Fraser [14]. The smoothing function we use in this work is the hyperbolic spline recently developed by Yang et al. [21]. We have found this kernel to be a nice compromise between the good performance of Monaghan's cubic spline for disordered SPH elements and the improved behavior of Johnson's quadratic function for impact problems with strong compression.

3. THE THERMO-MECHANICAL CONTACT ALGORITHM

The remaining portion of the paper is now focused on finding the value of $F_{contact_i}^\alpha$ and the transfer of thermal energy. A contact example is shown on the left side of Figure 1. Here, a flexible body with an initial velocity is meshed with SPH elements (red part), a rigid surface (grey part) is meshed with finite elements. The general layout for the contact between the SPH and finite elements is shown in the right side of Figure 1. The i^h SPH element has a center at

\bar{x}_i . The j^{th} triangular element has vertices A , B and C with positions; \bar{x}_{A_j} , \bar{x}_{B_j} and \bar{x}_{C_j} respectively. The triangular element has a surface normal vector that is \hat{n}_{FEM_j} . The normal vector is found from:

$$\hat{n}_{FEM_j} = \frac{\bar{U}_j \times \bar{V}_j}{\|\bar{U}_j \times \bar{V}_j\|} \quad (7)$$

$\bar{U}_j = \bar{x}_{B_j} - \bar{x}_{A_j}$ and $\bar{V}_j = \bar{x}_{C_j} - \bar{x}_{A_j}$, the $\|\ \|$ signifies the magnitude of the vector and the $\hat{\ }$ represents a normalized unit vector.

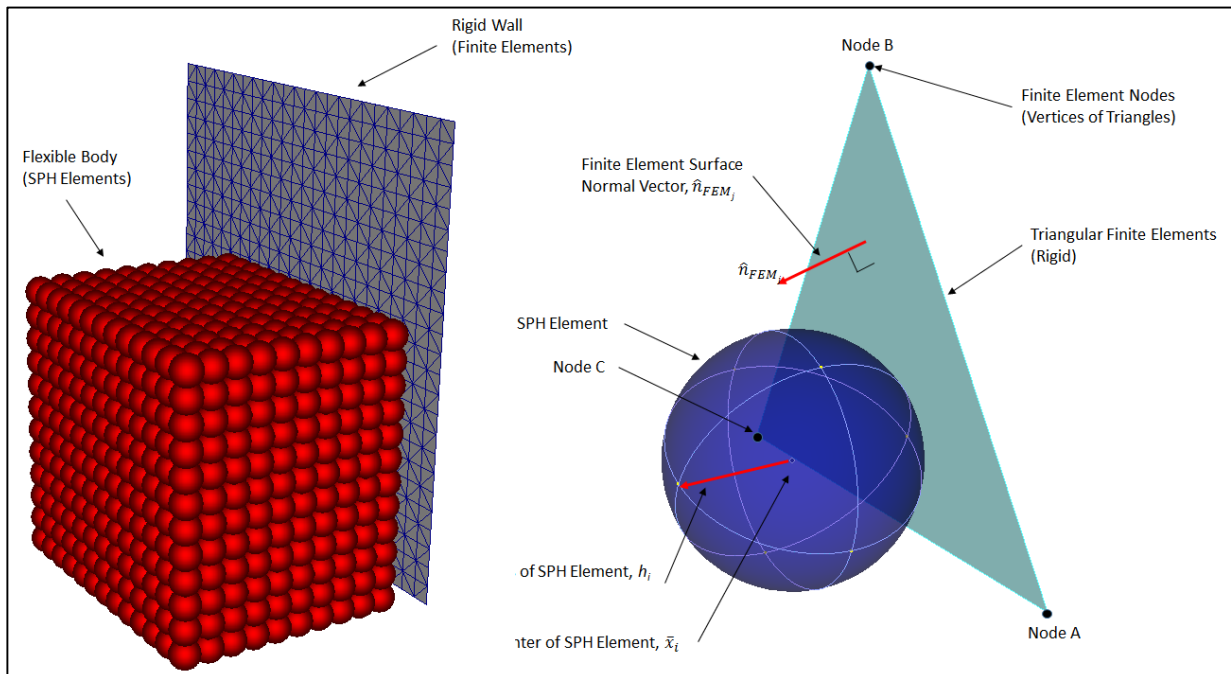


Figure 1 – Node to Surface Contact

In order to take advantage of the efficiency of the uniform grid neighbor search (also called bucket search, see Fraser [14] for details of our implementation), a sphere is embedded at the centroid of each of the triangular finite elements. The radius of the sphere is chosen so that all of the nodes of the element are enclosed within the sphere. In this manner, the neighbor search is performed not only over the SPH domain, but also over the embedded spheres in the finite elements. This allows us to form a list of potential contact pairs between the SPH body and the FE body.

3.1 CONTACT DETECTION

The next step is to determine which of the potential pairs are contact pairs. Our approach is similar to the algorithm described by Ericson [22]. We have made some slight modification in order account for the movement of the SPH and the FE body. This is done by taking into account

the relative velocity, $\bar{v}_{Rel} = \bar{v}_i - \bar{v}_j$, between an SPH element with velocity \bar{v}_i , and a finite element node with velocity \bar{v}_j , as shown in Figure 2.

We perform a check to ensure that the SPH and finite elements are approaching each other (impending contact). This is done by ensuring that the penetration rate, $\dot{\delta} = -(\hat{n}_{FEM_j} \cdot \bar{v}_{Rel})$, is greater than zero. If this is less than or equal to zero, the pair are moving away and are not considered to be contact candidates. Next, we test to see if the contact point, \bar{Q}_j lies within the bounds of the triangular element. This is done by performing what is called the “inside-outside” check:

$$\begin{aligned} & [(\bar{x}_{Bj} - \bar{x}_{Aj}) \times (\bar{Q}_j - \bar{x}_{Aj})] \cdot \hat{n}_{FEM_j} \geq 0 \text{ and} \\ & [(\bar{x}_{Cj} - \bar{x}_{Bj}) \times (\bar{Q}_j - \bar{x}_{Bj})] \cdot \hat{n}_{FEM_j} \geq 0 \text{ and} \\ & [(\bar{x}_{Aj} - \bar{x}_{Cj}) \times (\bar{Q}_j - \bar{x}_{Cj})] \cdot \hat{n}_{FEM_j} \geq 0 \end{aligned} \quad (8)$$

All of the above relations must hold for the contact point to be within the triangle. \bar{x}_{Aj} is the position vector for the A^{th} node on the triangular element. The right hand rule is respected for finding the normal of the element. The greater than or equal to ensures that a contact point on the edge of the triangle is considered to be within bounds.

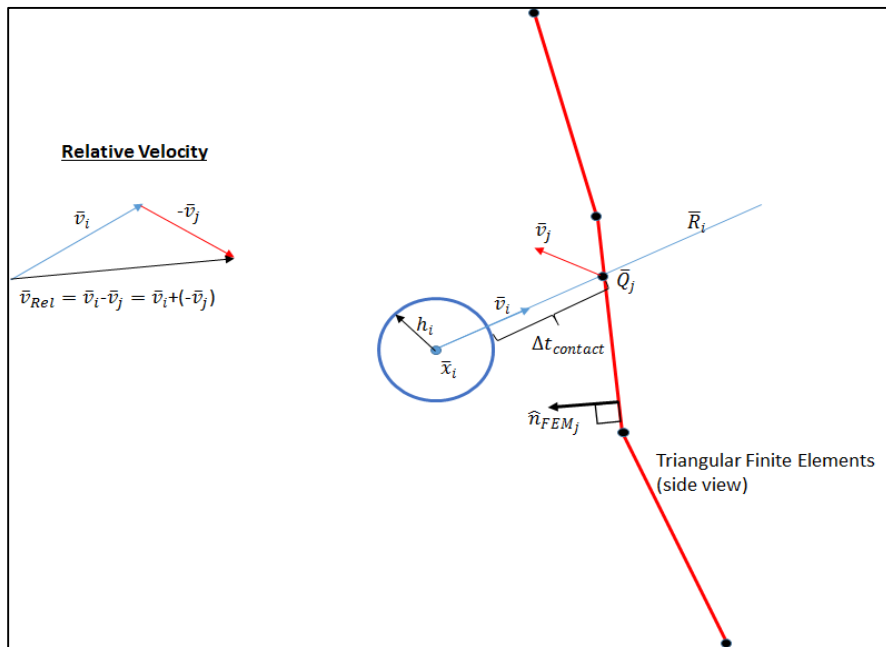


Figure 2 – Relative velocity diagram

Once a contact point that lies within the triangle is found, we calculate the penetration depth, δ , from

$$\delta = \frac{1}{2} \frac{h_i}{SFAC} - |\hat{n}_{FEM_j} \cdot (\bar{x}_i - \bar{x}_{Aj})| \quad (9)$$

Note that we can use either \bar{x}_{A_j} , \bar{x}_{B_j} or \bar{x}_{C_j} in the above equation without any change in the result. h_i is the smoothing length of the i^{th} SPH element and $SFAC$ is the factor on the smoothing length that is set to 1.2 in this work. The value of $0.5 \cdot h_i / SFAC$ can be seen as the actual radius of the SPH element. For example, if a uniform SPH grid is made with inter-particle spacing of 2mm, the actual radius of the SPH element would then be 1mm; whereas h_i would be 2.4mm. This ensures that no portion of the mass of the SPH body penetrates into the FE body.

3.2 PENALTY FORMULATION

The next step is to determine a force that will apply to the SPH element to remove the penetration. Although the bodies do not actually penetrate one within the other, the penalty contact approach does have a direct relationship to the actual compression in the bodies. This can be shown by considering two elastic bodies, body i and body j that have come into contact. The contact model can be represented by spring and damper in parallel as shown below the penetrating bodies in Figure 3. The reaction force is taken to be proportional to the penetration depth and the stiffness at the contact interface, k_{ij} , which will be related to the elastic moduli E of the two bodies and the interparticle spacing, d_p .

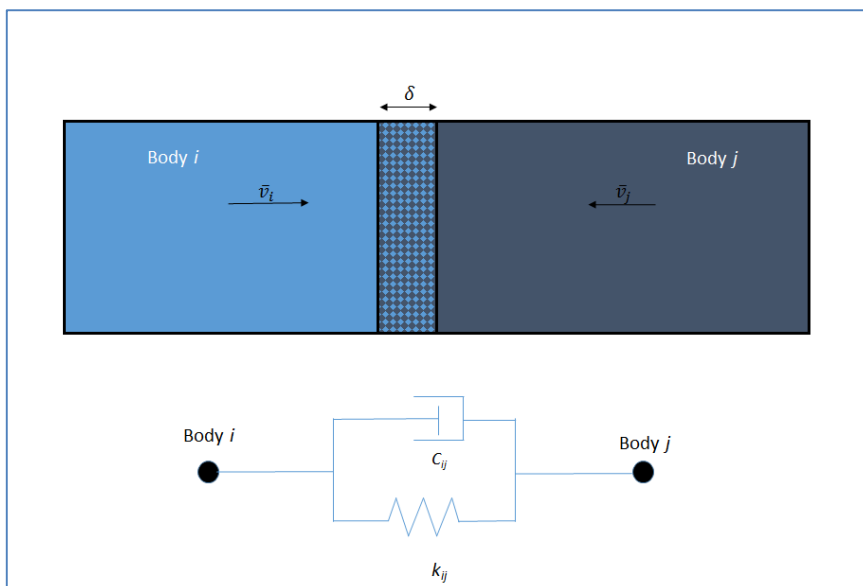


Figure 3 – Spring and damper contact model

The stiffness can be derived from Hooke's law: The amount that the bodies penetrate must be the same as the sum of the compression in each body. Furthermore, when an elastic body is compressed, it will want to return to its original shape, the force felt as the body tries to regain its original shape will be equal to and opposite the force required to compress the body.

$$k_{ij} = PFAC \left(\frac{E_i E_j d_p}{E_i + E_j} \right) \quad (10)$$

The penalty factor is needed to allow the stiffness to be easily adjusted for different simulations. $PFAC$ is typically set to 1.0, but can be set to lower values in the case of high velocity impact. Contact damping, C_{ij} , is included to damp out oscillations in the contact behavior along the element unit normal direction. The damping is proportional to the relative velocity of the contacting bodies. The value of the damping factor is found from:

$$C_{ij} = DFAC \left[(m_i + m_j) \sqrt{k_{ij} \left(\frac{m_i + m_j}{m_i m_j} \right)} \right] \quad (11)$$

Again, a factor is used to provide a damping that can be a fraction of the critical damping. If $DFAC$ is set to 1.0, critical damping is obtained. This damping approach here is similar to the method used in LS-DYNA [23]. The contact force vector, \bar{F}_{Normal} , along the normal direction is then:

$$\bar{F}_{Normal} = (k_{ij}\delta - C_{ij}\dot{\delta}) \hat{n}_{FEM_j} \quad (12)$$

3.3 FRICTION FORMULATION

We use a sliding friction model that is commonly referred to as Coulomb friction. In this model, a force is applied to the SPH element that is opposite to the relative motion of travel. Consider the situation where body i is moving with velocity \bar{v}_i and body j is moving with velocity \bar{v}_j , then the relative direction of travel will be along $\bar{v}_{Rel} = \bar{v}_i - \bar{v}_j$. The friction force, $\bar{F}_{Friction}$, is:

$$\bar{F}_{Friction} = \mu(\sigma_y, T) \bar{F}_{Normal} (-\hat{n}_T) \quad (13)$$

$\mu(\sigma_y, T)$ is the coefficient of friction that can be a function of the yield stress of the material and the temperature. \hat{n}_T is a normalized unit vector in the direction of relative motion. Although tangential damping can be added to the friction force, we do not include this in the current work. The tangential relative velocity is found by decomposing the relative velocity vector into its normal and tangential components:

$$\begin{aligned} \bar{v}_{Rel_T} &= \bar{v}_{Rel} - \bar{v}_{Norm} \\ \bar{v}_{Norm} &= \dot{\delta} \hat{n}_{FEM_j} \end{aligned} \quad (14)$$

Once we have the relative tangential velocity, we can easily find the unit normalized tangential vector from:

$$\hat{n}_T = \frac{\bar{v}_{Rel_T}}{\|\bar{v}_{Rel_T}\|} \quad (15)$$

3.4 CONTACT FORCE

The penetration resisting force (in the surface normal direction, \bar{F}_{Normal}) and the friction force ($\bar{F}_{Friction}$) have to be combined together to give the total contact interface force, $\bar{F}_{Contact}$:

$$\bar{F}_{Contact} = \bar{F}_{Normal} + \bar{F}_{Friction} \quad (16)$$

In the explicit SPH code, the forces are combined to impose an acceleration that is included when performing the time integration. The total acceleration due to contact is:

$$\frac{dv_i^\alpha}{dt} \Big|_{contact} = \frac{1}{m_i} F_{contact_i}^\alpha = \frac{1}{m_i} (F_{Normal_i}^\alpha + F_{Friction_i}^\alpha) \quad (17)$$

3.5 THERMAL CONTACT

A reasonable approximation of thermal contact can be attained by assuming no contact resistance (perfect thermal contact). To this end, the SPH heat diffusion equation can be used to include thermal contact. The key to including thermal contact is to provide separate neighbors lists for the mechanical part and the thermal part. In this work, we have used four different lists:

- | | |
|------------------|--|
| 1. NeibMech | - This is a list that contains the neighbors only within the deformable parts |
| 2. NeibTherm | - This is a list that contains the neighbors for the thermal problem |
| 3. NeibCont | - This is a list that contains the neighbors for the potential contact pairs |
| 4. NeibContTherm | - This is a list that contains the neighbors for the potential contact pairs to distribute the heat generated due to friction work |

A bit of extra work is needed to build the individual lists; however the overhead is not significant as long as the lists are built within the same subroutine. The crucial concept in this sense is that we only perform the bucket search once for each particle to form the four individual lists.

Imagine a two body collision problem with non-collinear approaching velocities (upon impact a certain amount of sliding will occur), where one body is at 500°C and the other body is at 20°C. Body #1 is made of aluminum and is very soft at 500°C. We expect the body to be subject to large deformation, as such, body #1 is modeled with SPH elements. We will assume that body #2 is rigid (steel) and can be modeled by creating a contact surface with zero thickness triangular plate elements. Upon impact we want to be able to treat the mechanical contact along with friction as well as the transfer of thermal energy from one body to the other. In this example, the lists will contain the following elements:

- | | |
|------------------|--|
| 1. NeibMech | - All SPH elements from body #1 (with self-interaction) |
| 2. NeibTherm | - All SPH elements from body #1 and 2 (both with self-interaction) |
| 3. NeibCont | - Body #1 with the spheres imbedded in the triangular FE mesh |
| 4. NeibContTherm | - Body #2 (no self-interaction) with body #1 (no self-interaction) |

By creating different neighbor lists, the conservation of mass and momentum equations are evaluated using NeibMech for body #1 only. The heat transfer equation (includes the thermal contact) will be evaluated using NeibTherm for body #1 and 2. The mechanical contact is evaluated by finding actual contact pairs within the NeibCont list. And finally, heat is divided between the two interfaces during friction heat generation using NeibContTherm. Again, it is important to remember that this thermal contact model is representative of perfect thermal contact. We could account for contact resistance, convection and radiation at the contact

interface using a source term in the SPH heat equation. The method will become clearer following the HSM example in the next section.

4. HIGH SPEED MACHINING EXAMPLE

The HSM example is set up according to the work of Villumsen and Fauerholdt [24] and Limido et al. [25]. In their work, they employ an adiabatic SPH approach. In our implementation we will investigate the chip formation including the effect of heat generation due to plastic deformation and friction work. Furthermore, heat will be allowed to transfer not only within the aluminum work piece (WP) but also to the cutting tool. The model setup is as explained in [24], all parameters are kept the same except the value of C in the Johnson-Cook model is zero in our work. We argue that the effect of strain rate should not be included in a velocity scaled model (they use a factor of 5 as do we here). Also, we have not put a limit on the effective plastic strain (Villumsen used a limit of 1.2). We found that doing so provides a significant underestimation of the cutting forces.

Figure 4 shows the AL 6082-T6 WP and the cutting tool (CT). Notice that the tool SPH elements do not belong to the NeibMech list. Both the SPH elements on the WP and the CT are included in the NeibTherm list. The zero thickness triangular finite elements that define the contact surface of the tool can also be seen. The WP and the CT interact mechanically through the NeibCont list (not shown in figure), the heat transfer back and forth between the WP and the CT occurs through the SPH heat transfer kernel using the NeibTherm list. In a friction heating model, the heat generated at the interface must be split according to the ratio of thermal material properties of the two bodies. This is done through the NeibContTherm list.

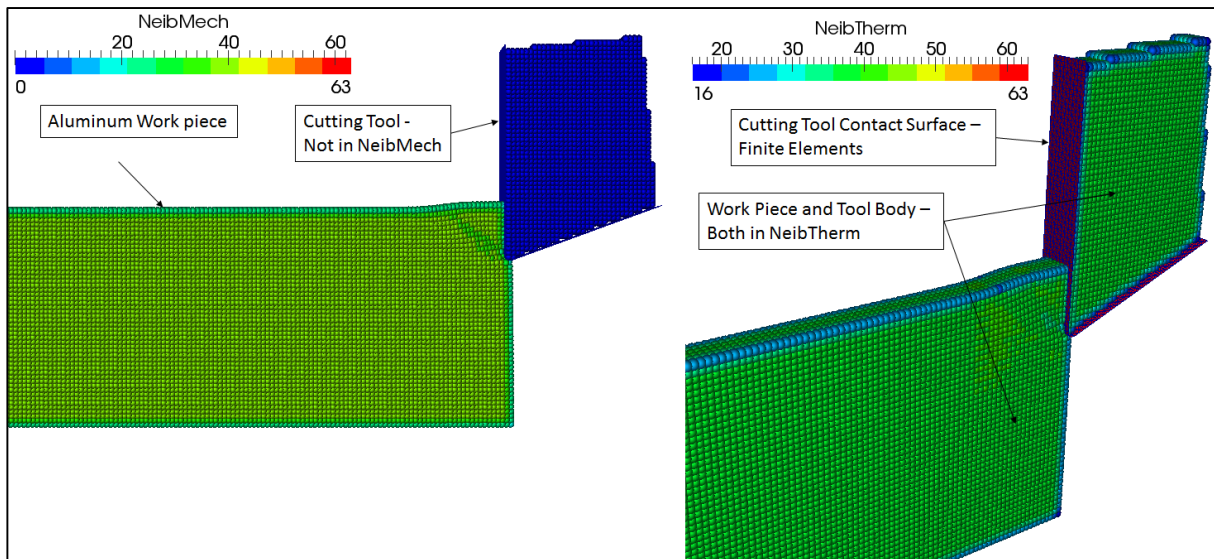


Figure 4 – Cutting Model

The results of the stress and temperature distribution when the tool has cut 1.75mm into the work piece can be seen in Figure 5. We note that the chip formation is very similar to that obtained in [24]. The high stress zone in the simulation model correlates very well with what we have seen in the literature. This stress distribution cannot be reproduced with a mesh based

method such as the finite element method. A number of authors have reported on the importance of including the temperature rise during the cutting process. Abukhshim et al. [26] report that the cutting temperature can range between 150°C to over 400°C depending on the cutting parameters. We have found a maximum interface temperature (averaged over the cutting simulation) of 376°C. This is well within the reported range from [26]. Other authors [27-29] have investigated the cutting temperature, they typically report temperatures in the range of 0.25 - 0.7 of the melting temperature of the metal. We expect the interface temperatures to be higher for AL 6082-T6 compared to AL 6061-T6 since it is a higher strength alloy.

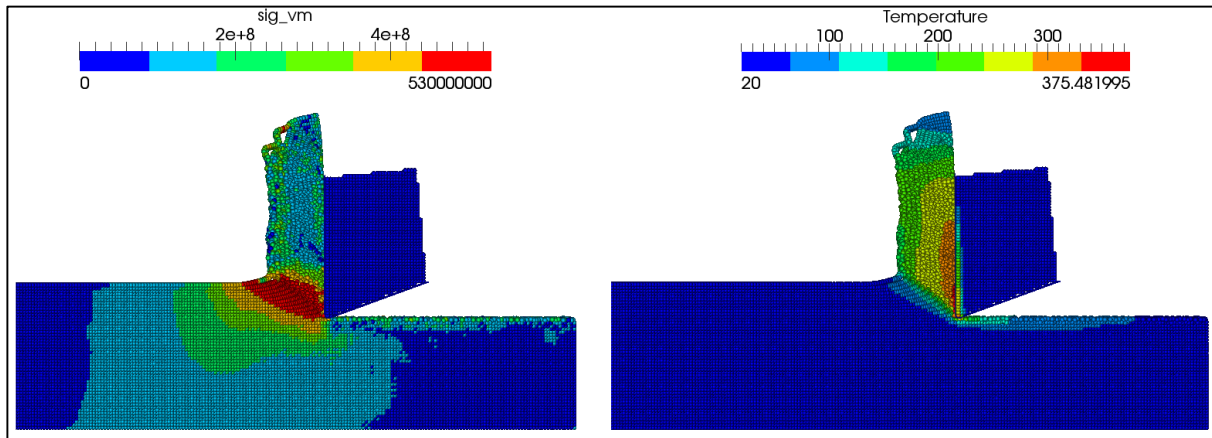


Figure 5 – Stress and temperature results (tool position: 1.75mm)

We are now in a position to show that the effect of temperature in a high speed cutting model is significant and should not be ignored. We have run the same model with heat transfer and heat generation (w HT) and without (wo HT). The decrease in normal cutting force is significant when the heat generation due to plastic deformation and friction work is included. The thickness of the chip increases slightly with heat transfer. This then leads to a slight increase in tangential force.



Figure 6 – Cutting force results (average cutting force)

Using a friction coefficient of 0.2 and no heat transfer provides an overestimate on the normal cutting forces by 12.5%. When we take into account heat generation effects, the normal cutting force drops and provides a slight underestimate by 3.9%. The tangential cutting forces are strongly influenced by the value of the coefficient of friction chosen. We have used 0.2 since this was the value used in [24]. However, the exact value for the tangential force can easily be obtained in the model by tuning the coefficient of friction. A comparison of the cutting forces is shown in Figure 6. The experimental cutting forces are taken from [24]. The mesh density used in our work is 125,000 SPH elements per cm^3 , this density provides high enough resolution to predict the cutting forces. However, this density is not fine enough to reproduce the shear band pattern. Villumsen used 512,000 elements/ cm^3 in order to show this phenomenon.

5. CONCLUSIONS

In this paper we have outlined a straightforward and robust approach to simulate 3D multi-physics problems with thermo-mechanical contact. The algorithm presented uses a penalty mechanical contact algorithm by using a node to surface approach. The deformable SPH body is checked for contact against a rigid zero thickness triangular plate element mesh. The thermal contact is carried out through the SPH heat diffusion kernel, which provides a thermal contact interface with no losses.

In the future, we plan to work towards extending the algorithm to include a thermal contact resistance. This could be done by introducing a heat loss term in the heat diffusion equation for the elements at the interface of the contacting bodies.

In this work, we have shown the accuracy of the proposed thermo-mechanical contact algorithm through a high speed machining example. The cutting forces found using our algorithm are very close to the forces obtained experimentally.

6. ACKNOWLEDGEMENTS

The authors would like to acknowledge the financial support of CQRDA, FQRNT and GRIPS. A part of the research presented in this paper was financed by the Fonds de recherche du Québec - Nature et technologies by the intermediary of the Aluminium Research Centre REGAL. Also, we are grateful to NVIDIA for providing the GPU used for the simulations and to PGI for providing the license for the CUDA Fortran Compiler.

REFERENCES

- [1] Hughes TJR, Taylor RL, Sackman JL, Curnier A, Kanoknukulchai W. A finite element method for a class of contact-impact problems. *Computer Methods in Applied Mechanics and Engineering*. 1976;8:249-76.
- [2] Belytschko T, Lin JI. A three-dimensional impact-penetration algorithm with erosion. *International Journal of Impact Engineering*. 1987;5:111-27.
- [3] Belytschko T, Yeh IS. The splitting pinball method for contact-impact problems. *Computer Methods in Applied Mechanics and Engineering*. 1993;105:375-93.
- [4] Vignjevic R, Campbell J. A penalty approach for contact in smoothed particle hydrodynamics. *International Journal of Impact Engineering*. 1999;23:945-56.
- [5] Seo S, Min O. Axisymmetric SPH simulation of elasto-plastic contact in the low velocity impact. *Computer Physics Communications*. 2006;175:583-603.
- [6] Seo S, Min O, Lee J. Application of an improved contact algorithm for penetration analysis in SPH.

- International Journal of Impact Engineering. 2008;35:578-88.
- [7] Wang J, Wu H, Gu C, Hua H. Simulating frictional contact in smoothed particle hydrodynamics. Science China - Technological Sciences. 2013;56:1779-89.
- [8] Liu GR, Liu MB. Smoothed particle hydrodynamics : a meshfree particle method. Hackensack, New Jersey: World Scientific; 2003.
- [9] Jubelgas M. Cosmological Hydrodynamics: Thermal Conduction and Cosmic Rays. München: Ludwig-Maximilians-Universität München; 2007.
- [10] Benz W, Asphaug E. Simulations of brittle solids using smooth particle hydrodynamics. Computer Physics Communications. 1995;87:253-65.
- [11] Cleary PW, Prakash M, Das R, Ha J. Modelling of metal forging using SPH. Applied Mathematical Modelling. 2012;36:3836-55.
- [12] Cleary PW, Prakash M, Ha J. Novel applications of smoothed particle hydrodynamics (SPH) in metal forming. Journal of Materials Processing Technology. 2006;177:41-8.
- [13] Das R, Cleary PW. Evaluation of Accuracy and Stability of the Classical SPH Method Under Uniaxial Compression. Journal of Scientific Computing. 2014;1-40.
- [14] Fraser K. Adaptive smoothed particle hydrodynamics neighbor search algorithm for large plastic deformation computational solid mechanics. 13th International LS-DYNA Users Conference. Dearborn Michigan: LSTC; 2014.
- [15] Gray JP, Monaghan JJ, Swift RP. SPH elastic dynamics. Computer Methods in Applied Mechanics and Engineering. 2000.
- [16] Libersky L, Petschek AG. Smoothed particle hydrodynamics with strength of materials. The Next Free Lagrange Conference. NY: Springer-Verlag; 1991.
- [17] Libersky LD, Petschek AG, Carney TC, Hipp JR, Allahdadi FA. High Strain Lagrangian Hydrodynamics: A Three-Dimensional SPH Code for Dynamic Material Response. Journal of Computational Physics. 1993;109:67-75.
- [18] Libersky LD, Randles PW, Carney TC, Dickinson DL. Recent improvements in SPH modeling of hypervelocity impact. International Journal of Impact Engineering. 1997;20:525-32.
- [19] Owen JM, Villumsen JV, Shapiro PR, Martel H. Adaptive Smoothed Particle Hydrodynamics. The Astrophysical Journal. 1998.
- [20] Randles PW, Libersky LD. Smoothed Particle Hydrodynamics: Some recent improvements and applications. Computer Methods in Applied Mechanics and Engineering. 1996;139:375-408.
- [21] Yang X, Liu M, Peng S. Smoothed particle hydrodynamics modeling of viscous liquid drop without tensile instability. Computers and Fluids. 2014;92:199-208.
- [22] Ericson C. Real Time Collision Detection San Fransisco California: Morgan Kauffmann; 2005.
- [23] LSTC. LS-DYNA Keywords User Manual Volume 1. 2012.
- [24] Villumsen MF, Fauerholdt TG. Simulation of metal cutting using smoothed particle hydrodynamics. 7th International LS-DYNA Conference. Bmberg2008.
- [25] Limido J, Espinosa C, Salaün M, Lacome JL. SPH method applied to high speed cutting modelling. International Journal of Mechanical Sciences. 2007;49:898-908.
- [26] Abukhshim NA, Mativenga PT, Sheikh MA. Heat generation and temperature prediction in metal cutting: A review and implications for high speed machining. International Journal of Machine Tools and Manufacture. 2006;46:782-800.
- [27] Masillamani DP, Chessa J. Determination of Optimal Cutting Conditions in Orthogonal Metal Cutting Using LS-DYNA with Design of Experiments Approach. 8th International LS-DYNA Conference. Detroit2006.
- [28] Zaghbani I, Songmene V. A force-temperature model including a constitutive law for Dry High Speed Milling of aluminium alloys. Journal of Materials Processing Technology. 2009;209:2532-44.
- [29] Davoodi B, Hosseinzadeh H. A new method for heat measurement during high speed machining. Measurement. 2012;45:2135-40.

NUMERICAL SIMULATION OF HEAT AND MASS TRANSFER UNDER THE CONDITIONS OF PHASE TRANSITIONS AND CHEMICAL REACTION DURING IGNITION OF CONDENSED SUBSTANCES BY SINGLE HOT PARTICLES

DMITRII O. GLUSHKOV, PAVEL A. STRIZHAK AND
OLGA. V. VYSOKOMORNAYA

National Research Tomsk Polytechnic University
Lenina Avenue, 30, 634050, Tomsk, Russia
E-mail pavelspa@tpu.ru

Key words: Heat and Mass Transfer, Ignition, Condensed Substance, Local Energy Source, Numerical Research.

Abstract. Physical and mathematical models of heat and mass transfer under the conditions of phase transitions and chemical reactions have been developed for the numerical analysis of condensed substances ignition by a single particle (size from 0.5 mm to 5 mm) heated up to high temperature (above 800 K). Liquid, solid and gel fuels were considered as condensed substances. Metal and non-metal particles were used as ignition sources. A heat and mass transfer mathematical model is presented as a system of nonlinear non-stationary differential equations in the private derivatives corresponding to the basic provisions of the general theory of heat transfer in chemical kinetics and free convection. An algorithm for solving differential equations with the corresponding initial and boundary conditions is based on the finite-difference method. The locally one-dimensional method was used to solve difference analogous of differential equations. One-dimensional difference equations were solved using an implicit four-point difference scheme. Nonlinear equations were solved by the iteration method. Mathematical model verification and the assessment of numerical research results reliability was executed by its comparison with experimental results. Also the verification of the law of conservation of energy in the solution area of the ignition problem was performed. Besides, testing of applied numerical methods and the developed silving algorithm on the example of a group of less complex challenges of thermal conduction and thermal convection was held. The minimum parameters of hot particles (temperature, size) and the ignition delay time of condensed substances were determined for local heat sources with different shapes. The influence of thermal conduction, convection and radiative heat transfer mechanisms in the “particle – condensed substance” system was established on the ignition characteristics.

1 INTRODUCTION

The ignition and combustion of various fuels are among the most common technological processes. Their effectiveness is of great importance for the implementation of these processes. Thus, in recent years a large number of theoretical and experimental studies have been devoted to the features and characteristics of heat and mass transfer during local energy supply to various combustible condensed substances (solid, liquid, gel) [1–3]. In particular,

focused light streams, rods heated to high temperatures, hot (with the temperature over 800 K) metal and non-metallic particles may act as local ignition sources. The different mechanisms of heat transfer play a decisive role when using these ignition sources.

It should be noted that among practical applications of the study of condensed substance ignition, there may be identified the technologies of energy efficient fuel initiation, as well as the technologies of fire danger prediction in industries, where the interaction between local heat sources and combustible substances may occur.

The aim of this work is to perform a comparative analysis of the features and characteristics of heat and mass transfer during the ignition of various condensed substances (solid, liquid, gel-like) by single metal and nonmetal particles heated up to high temperatures.

2 PROBLEM STATEMENT

As an example of a numerical model for studying heat and mass transfer during ignition, we consider a model developed for studying the features of these processes during the initiation of gel-like fuel ignition.

The investigation of heat and mass transfer with phase transitions and chemical reactions during the ignition of gel-like condensed substances (hydrazine + 38 % of liquefied oxygen + 5 % of high molecular organic acid salt) has been carried out on the example of the system “hot particle – condensed substance – inert gas” (Figure 1). An oxidizer was thickened by adding salt to render the composition gel state; the temperature of the condensed substance was close to cryogenic (about 90 K). We considered single metal (steel, aluminum) and nonmetal (ceramic, carbon) particles as the sources of limited energy capacity. We examined cylindrical disc shaped particles of small sizes (up to $5 \cdot 10^{-3}$ m) heated up to high (over 1000 K) temperatures.

We considered the following scheme of the investigated process. At the initial time, a hot particle (Figure 1) is deposited inertially on the surface of a cold condensed substance (Figure 1). The subsurface layer of the condensed substance warms up due to the heat generated by the source of limited energy capacity as a result of conductive heat transfer. The additional heat supply in the system (Figure 1) is taken into account during the crystallization of the preheated metal particle material to a temperature above the melting point. Two endothermic phase transitions (melting and evaporation) are implemented consistently in the system “fuel – oxidizer” during the heating of the gel-like condensed substance in the vicinity of the contact border with the hot particle. Fuel and oxidizer vapor enter the area filled with an inert gas due to diffusion-convective mass transfer. The gas-vapor mixture is formed in the vicinity of the energy source. The additional heating of the mixture is transferred from radiation-conductive heat transfer with the hot particle. The temperature growth of the gas-vapor mixture initiates the exothermic interaction between the combustible component (hydrazine) and oxidant (oxygen). One effective chemical reaction is considered to occur. Its speed increases exponentially by the Arrhenius dependence. Gas-phase ignition occurs when the limit (sufficient for ignition) temperatures and concentrations of mixture components are reached. Accepted ignition conditions are similar to the criteria of the gas-phase ignition of liquid condensed substances during local heating [1, 2], which are relevant to the concepts of the modern ignition theory [4]:

1. The energy released as a result of a chemical reaction of fuel oxidation, is more than heat transferred from the heated particle to fuel and the emerging gas mixture.

2. The temperature of the gas-vapor mixture in the localization zone of the leading oxidation reaction exceeds the temperature of the local source of limited energy capacity.

The following assumptions were taken for the model of the investigated process. These assumptions do not impose significant restrictions on the common problem statement:

1. It is not considered the mechanical introduction of the heat source into the subsurface layer of the gel-like condensed substance.

2. It is not considered the burning of the subsurface layer of the gel-like condensed substance.

3. Substances with known thermal and kinetic characteristics are formed during the evaporation of fuel and oxidant. As a rule, the “effective” values of the activation energy E and pre-exponential factor k_0 are determined from experimental studies. These parameters are used for calculating the rate of one “effective” reaction using a first order kinetic scheme.

4. The thermophysical characteristics of substances do not depend on the temperature.

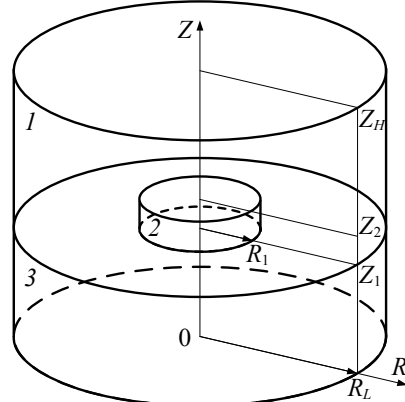


Figure 1: A diagram of the solution area of the ignition problem: 1 – inert gas (gas-vapor mixture), 2 – hot particle, 3 – gel-like condensed substance

Interrelated physical and chemical processes occur during the ignition of the gel-like condensed substance by the local source of limited energy capacity (Figure 1).

3 MATHEMATICAL MODEL AND SOLUTION METHODS

The processes were described by the system of nonlinear nonstationary differential equations of mathematical physics in dimensionless variables. In the mathematical model, we used the elements of numerical algorithms for solving the problems of heat and mass transfer during the ignition of liquid [1, 2] and solid [3] condensed substances by hot particles. This allowed us to obtain a good correlation between theoretical and experimental studies.

Poisson's equation for gas mixture ($R_1 < R < R_L$, $Z_1 < Z < Z_2$; $0 < R < R_L$, $Z_2 < Z < Z_H$):

$$\frac{\partial^2 \Psi}{\partial R^2} - \frac{1}{R} \frac{\partial \Psi}{\partial R} + \frac{\partial^2 \Psi}{\partial Z^2} = -R\Omega \quad (1)$$

The equation of motion for the gas-vapor mixture:

$$\frac{1}{Sh} \frac{\partial \Omega}{\partial \tau} + U \frac{\partial \Omega}{\partial R} + V \frac{\partial \Omega}{\partial Z} - U \frac{\Omega}{R} = \frac{1}{Re_1} \left[\frac{\partial^2 \Omega}{\partial R^2} + \frac{1}{R} \frac{\partial \Omega}{\partial R} + \frac{\partial^2 \Omega}{\partial Z^2} - \frac{\Omega}{R^2} \right] + \frac{\partial \Theta_1}{\partial R} \quad (2)$$

The energy equation for the gas-vapor mixture:

$$\frac{1}{Sh} \frac{\partial \Theta_1}{\partial \tau} + U \frac{\partial \Theta_1}{\partial R} + V \frac{\partial \Theta_1}{\partial Z} = \frac{1}{Re_1 Pr_1} \left[\frac{\partial^2 \Theta_1}{\partial R^2} + \frac{1}{R} \frac{\partial \Theta_1}{\partial R} + \frac{\partial^2 \Theta_1}{\partial Z^2} \right] + Sr_1 \quad (3)$$

The diffusion equation of fuel vapor in the gas-vapor mixture:

$$\frac{1}{Sh} \frac{\partial C_f}{\partial \tau} + U \frac{\partial C_f}{\partial R} + V \frac{\partial C_f}{\partial Z} = \frac{1}{Re_{12} Sc_{12}} \left[\frac{\partial^2 C_f}{\partial R^2} + \frac{1}{R} \frac{\partial C_f}{\partial R} + \frac{\partial^2 C_f}{\partial Z^2} \right] - Sr_2 \quad (4)$$

The diffusion equation of oxidant vapor in the gas-vapor mixture:

$$\frac{1}{Sh} \frac{\partial C_o}{\partial \tau} + U \frac{\partial C_o}{\partial R} + V \frac{\partial C_o}{\partial Z} = \frac{1}{Re_{13} Sc_{13}} \left[\frac{\partial^2 C_o}{\partial R^2} + \frac{1}{R} \frac{\partial C_o}{\partial R} + \frac{\partial^2 C_o}{\partial Z^2} \right] - Sr_2 \quad (5)$$

The balance equation for the gas-vapor mixture:

$$C_f + C_o + C_g = 1 \quad (6)$$

The energy equation for a hot particle ($0 < R < R_1$, $Z_1 < Z < Z_2$):

$$\frac{1}{Fo_2} \frac{\partial \Theta_2}{\partial \tau} = \frac{\partial^2 \Theta_2}{\partial R^2} + \frac{1}{R} \frac{\partial \Theta_2}{\partial R} + \frac{\partial^2 \Theta_2}{\partial Z^2} + Sr_3 \quad (7)$$

The energy equation for the gel-like condensed substance ($0 < R < R_L$, $0 < Z < Z_1$):

$$\frac{1}{Fo_3} \frac{\partial \Theta_3}{\partial \tau} = \frac{\partial^2 \Theta_3}{\partial R^2} + \frac{1}{R} \frac{\partial \Theta_3}{\partial R} + \frac{\partial^2 \Theta_3}{\partial Z^2} - Sr_4 \quad (8)$$

The numbers of similarity and dimensionless complexes:

$$Sh = \frac{V_m t_m}{z_H}, \quad Re = \frac{V_m z_H}{\nu}, \quad Pr = \frac{\nu C \rho}{\lambda}, \quad Sc = \frac{\nu}{D}, \quad Fo = \frac{\lambda t_m}{\rho C z_H^2}, \quad Sr_1 = \frac{Q_o W_o z_H}{C_1 \rho_1 \Delta T V_m}, \quad Sr_2 = \frac{z_H W_o}{\rho_{12} V_m},$$

$Sr_3 = \frac{Q_c W_c z_H}{z_p \Delta T \lambda_2}$ (for the metal particle taking into account material crystallization), $Sr_3 = 0$ (for

the nonmetal particle), $Sr_4 = \frac{Q_m W_m z_H}{z_p \Delta T \lambda_3}$.

Accepted symbols: τ – dimensionless time; R, Z – dimensionless coordinates of cylindrical system; R_L, Z_H – dimensionless equivalents of r_L, z_H ; z_p – the height of the particle ($z_p=z_2-z_1$), m; Ψ – dimensionless equivalent of the stream function; Ω – dimensionless equivalent of the vorticity vector; U, V – dimensionless velocity components of fuel vapor in the projection onto the axis R, Z ; Θ – dimensionless temperature; C_f – dimensionless concentration of fuel in the gas-vapor mixture; C_o – dimensionless concentration of an oxidant in the gas-vapor mixture; C_g – dimensionless concentration of an inert gas in the gas-vapor mixture; Sh – Strouhal number; Re – Reynolds number; Pr – Prandtl number; Sc – Schmidt number; Fo – Fourier number; v – kinematic viscosity coefficient, m^2/s ; ρ – density, kg/m^3 ; C – specific heat capacity, $J/(kg \cdot K)$; λ – thermal conductivity, $W/(m \cdot K)$; D – diffusion coefficient, m^2/s ; Q_m – thermal effect of gel-like condensed substance melting, J/kg ; W_m – mass rate of gel-like condensed substance melting, $kg/(m^2 \cdot s)$; Q_o – thermal effect of fuel vapor oxidation reaction, J/kg ; W_o – mass rate of fuel vapor oxidation, $kg/(m^3 \cdot s)$; Q_c – thermal effect of the crystallization of a metal particle material, J/kg ; W_c – mass rate of the crystallization of the metal particle material, $kg/(m^2 \cdot s)$; indexes: 1 – gas-vapor mixture; 2 – hot particle; 3 – gel-like condensed substance; 12 – fuel vapor; 13 – oxidizer vapor.

The following ratios were used in the transition to dimensionless variables:

$$\tau = \frac{t}{t_m}, R = \frac{r}{r_L}, Z = \frac{z}{z_H}, U = \frac{u}{V_m}, V = \frac{v}{V_m}, \Theta = \frac{T - T_0}{\Delta T}, \Psi = \frac{\psi}{\psi_m}, \Omega = \frac{\omega}{\omega_m},$$

$$V_m = \sqrt{g\gamma\Delta T z_H}, \psi_m = V_m z_H^2, \omega_m = \frac{V_m}{z_H}, \Delta T = T_m - T_0,$$

where t – time, s; t_m – time scale ($t_m=10^{-3}$ s); r, z – cylindrical system coordinates, m; r_L, z_H – dimensions of the solution area ($r_L=z_H=0.02$ m); u, v – velocity components of the gas-vapor mixture in projection onto the axis r, z , m/s; V_m – convection velocity scale, m/s; g – acceleration of gravity, m/s^2 ; γ – thermal expansion coefficient, K^{-1} ; T – temperature, K; T_0 – initial temperature of the condensed substance ($T_0=90$ K); T_m – temperature scale ($T_m=1000$ K); ψ – stream function, m^3/s ; ψ_m – stream function scale, m^3/s ; ω – vorticity, s^{-1} ; ω_m – vorticity scale, s^{-1} .

The stream function ψ and a vorticity vector ω :

$$u = \frac{1}{z} \frac{\partial \psi}{\partial z}, v = -\frac{1}{r} \frac{\partial \psi}{\partial r}, \omega = \text{rot}_z \vec{v} = \frac{\partial v}{\partial r} - \frac{\partial u}{\partial z}.$$

The temperature distribution in the solution area of the problem was specified as initial (at $\tau=0$) conditions (Figure 1):

$$\frac{1}{Fo_3} \frac{\partial \Theta_3}{\partial \tau} = \frac{\partial^2 \Theta_3}{\partial R^2} + \frac{1}{R} \frac{\partial \Theta_3}{\partial R} + \frac{\partial^2 \Theta_3}{\partial Z^2} - Sr_4 \quad (8)$$

$$\Theta_1 = \Theta_0, C_f = 0, C_o = 0, \Psi = 0, \Omega = 0 \text{ at } R_1 < R < R_L, Z_1 < Z < Z_2; 0 < R < R_L, Z_2 < Z < Z_H \quad (9)$$

$$\Theta_2 = \Theta_p \text{ at } 0 < R < R_1, Z_1 < Z < Z_2 \quad (10)$$

$$\Theta_3 = \Theta_0 \text{ at } 0 < R < R_L, 0 < Z < Z_1 \quad (11)$$

It was assumed that the thermal contact was ideal at the boundaries “particle – gas”, “particle – condensed substance”, “gas – condensed substance” taking into account the evaporation of fuel and oxidizer vapor from the condensed substance surface and radiant heat removal from the power source surface to surrounding gas environment. The conditions were specified that temperature gradients were equal to zero on the axis of symmetry and the external borders of the solution area.

$$R=0, R=R_L, 0 < Z < Z_1: \quad \frac{\partial \Theta_3}{\partial R} = 0; \quad (12)$$

$$R=0, Z_1 < Z < Z_2: \quad \frac{\partial \Theta_2}{\partial R} = 0; \quad (13)$$

$$R=R_1, Z_1 < Z < Z_2: \quad \frac{\partial \Theta_1}{\partial R} + \frac{q_r}{\lambda_1} \frac{z_H}{\Delta T} = \frac{\lambda_2}{\lambda_1} \frac{\partial \Theta_2}{\partial R}, \quad \Theta_1 = \Theta_2; \quad (14)$$

$$R=0, Z_2 < Z < Z_H;$$

$$R=R_L, Z_1 < Z < Z_H: \quad \frac{\partial \Theta_1}{\partial R} = 0, \quad \Theta_2 = \Theta_1; \quad (15)$$

$$Z=0, 0 < R < R_L: \quad \frac{\partial \Theta_3}{\partial Z} = 0; \quad (16)$$

$$Z=Z_1, 0 < R < R_1: \quad \frac{\partial \Theta_3}{\partial Z} + \frac{z_H}{\lambda_3 \Delta T} (\mathcal{Q}_{ef} W_{ef} + \mathcal{Q}_{eo} W_{eo}) = \frac{\lambda_2}{\lambda_3} \frac{\partial \Theta_2}{\partial Z}, \quad \Theta_3 = \Theta_2; \quad (17)$$

$$Z=Z_1, R_1 < R < R_L: \quad \frac{\partial \Theta_3}{\partial Z} + \frac{z_H}{\lambda_3 \Delta T} (\mathcal{Q}_{ef} W_{ef} + \mathcal{Q}_{eo} W_{eo}) = \frac{\lambda_1}{\lambda_3} \frac{\partial \Theta_1}{\partial Z}, \quad \Theta_3 = \Theta_1; \quad (18)$$

$$Z=Z_2, 0 < R < R_1: \quad \frac{\partial \Theta_1}{\partial Z} + \frac{q_r}{\lambda_1} \frac{z_H}{\Delta T} = \frac{\lambda_2}{\lambda_1} \frac{\partial \Theta_2}{\partial Z}, \quad \Theta_1 = \Theta_2; \quad (19)$$

$$Z=Z_H, 0 < R < R_L: \quad \frac{\partial \Theta_1}{\partial Z} = 0. \quad (20)$$

The average thermophysical characteristics of the gel-like condensed substance were calculated by formulas:

$$\lambda_3 = \varphi \lambda_{fs} + (1-\varphi) \lambda_{os},$$

$$C_3 = \varphi C_{fs} + (1-\varphi) C_{os},$$

$$\rho_3 = \varphi \rho_{fs} + (1-\varphi) \rho_{os},$$

where indexes fs – fuel component; os – oxidizer.

The mass rates of the evaporation of fuel and an oxidizer were calculated by the equations:

$$W_{\text{ef}} = \varphi \frac{\beta}{1 - k_{\beta} \beta} \frac{(P_e^n - P_e)}{\sqrt{2\pi R_t T_s / M_{12}}},$$

$$W_{\text{eo}} = (1 - \varphi) \frac{\beta}{1 - k_{\beta} \beta} \frac{(P_e^n - P_e)}{\sqrt{2\pi R_t T_s / M_{13}}},$$

where β – dimensionless coefficient of evaporation; k_{β} – dimensionless coefficient ($k_{\beta} \approx 0.4$); P^n – pressure of saturated fuel vapor (oxidizer), N/m²; P – pressure of fuel vapor (oxidizer) near the border of evaporation (calculated according to the Mendeleev–Clapeyron equation), N/m²; R_t – universal gas constant, J/(mol·K); T_s – temperature at the border of phase transition, K; M – molar mass of fuel vapor (oxidizer), kg/kmol.

The mass rate of metal particle material crystallization was calculated by the formula:

$$W_c = V_c \rho_2,$$

where V_c – linear crystallization rate, m/s.

The linear rate of metal particle material crystallization was determined from the following equation:

$$V_c = \frac{\delta(r, z, \tau + \Delta\tau) + \delta(r, z, \tau)}{\Delta\tau},$$

where $\delta(r, z, \tau + \Delta\tau)$ and $\delta(r, z, \tau)$ – the distance between the bottom particle edge and the front of crystallization in the $(\tau + \Delta\tau)$ -th and τ -th time steps, m; $\Delta\tau$ – time step, s.

The mass rate of gel-like condensed substance melting was calculated by the formula:

$$W_m = V_m \rho_3,$$

where V_m – linear melting rate, m/s (calculated similarly to V_c).

The mass rate of fuel vapor oxidation was determined by the Arrhenius equation:

$$W_o = \rho_i C_f C_o k_0 \exp\left(-\frac{E}{R_t T_l}\right),$$

where k_0 – preexponent of the oxidation reaction, s⁻¹; E – activation energy of the oxidation reaction, J/mol.

The density of heat flux discharged from the heated particle by radiant heat transfer was calculated by the formula:

$$q_r = \sigma \varepsilon T^4,$$

where σ – Stefan-Boltzmann constant, W/(m²·K⁴); ε – emissivity.

The following methods were used for developing the algorithm of the numerical solution of the system of nonlinear nonstationary differential equations with appropriate initial and boundary conditions: finite differences, alternating directions, locally one-dimensional, simple iterations, sweep in the case of an implicit four-point difference scheme.

Recent reports [1–3] described physical and mathematical problems of heat and mass transfer during the ignition of liquid and solid condensed substances by hot particles.

Mathematical modeling was performed with the following parameters [5, 6]: the initial temperature of the gel-like condensed substance and inert gas $\Theta_0=0$, local energy source $\Theta_p=1\div1.5$; hot particle sizes $R_p=Z_p=0.15$ (Figure 1, $R_p=R_1$, $Z_p=Z_2-Z_1$); the thickness of the condensed substance $Z_1=0.15$; the dimensions of the solution area $R_L=Z_H=1$. The thermal effect of gel-like condensed substance melting $Q_m=395\cdot10^3$ J/kg, melting temperature $\Theta_m=0.274$. The thermal effects of hydrazine evaporation $Q_{ef}=1390\cdot10^3$ J/kg and liquefied oxygen $Q_{eo}=2100\cdot10^3$ J/kg; dimensionless evaporation coefficient $\beta=0.1$; molar mass of fuel vapor $M_{12}=32.05$ kg/kmol and oxidizer $M_{13}=32$ kg/kmol; volume fraction of the fuel component $\varphi=0.57$; kinematic viscosity coefficient of the gas-vapor mixture $\nu=1.41\cdot10^{-5}$ m²/s; diffusion coefficient of mixture components $D=7.83\cdot10^{-6}$ m²/s; thermal expansion coefficient $\gamma=0.001$ K⁻¹. The thermal effects of the crystallization of the metallic particle material from steel $Q_c=205\cdot10^3$ J/kg and aluminum $Q_c=398\cdot10^3$ J/kg, crystallization temperature $\Theta_c=1.5$ and $\Theta_c=0.95$ respectively. The kinetic parameters of the oxidation reaction of the gas mixture $E=162\cdot10^3$ J/mol, $k_0=2.25\cdot10^9$ s⁻¹, $Q_o=14.644\cdot10^6$ J/kg. The emissivity of steel $\varepsilon=0.55$ and aluminium $\varepsilon=0.06$. The thermophysical characteristics [7, 8] of substances (Figure 1) are shown in Table 1.

Table 1: Thermophysical characteristics

Substance	λ , W/(m·K)	ρ , kg/m ³	C , J/(kg·K)
inert gas	0.026	1.161	1190
hydrazine	0.161	1010	1380
hydrazine vapor	0.072	2.498	3876
liquefied oxygen	0.065	1141	1680
liquefied oxygen vapor	0.027	2.511	2280
steel	49	7831	470
aluminum	98	2700	900
ceramics	20	3800	930
carbon	1.512	1700	1100

Studies [7, 8] described the thermophysical characteristics of liquid (kerosene) and solid metalized fuels.

3 RESULTS AND DISCUSSION

Figure 2 shows the temperature fields at the moment of ignition for three types of condensed substances at local energy supply from a single metal particle. The temperature fields were obtained for liquid and solid condensed substances using the mathematical models developed in studies [1–3]. Previously, it was established that there were three ignition modes typical for the gas-phase ignition of liquid condensed substances when the heat content of a source varied: above the particle (Figure 4a), near its lateral surface, in the immediate vicinity of the border of fuel evaporation. The localization zone of the leading exothermic reaction (Figure 4b) is located in the immediate vicinity of the border of contact with the hot particle near the symmetry axis in the case of the solid-phase ignition of the metalized condensed

substance. Unlike liquid and solid condensed substances, a leading oxidation reaction zone is formed in a small vicinity of the particle base and the boundaries of evaporation products injection (Figure 4c) in the case of the local heating of the gel-like condensed substance subsurface layer by the source of limited energy capacity. It can be seen that an inert gas warmed up substantially faster than fuel and oxidizer components coming from the evaporation surface. The oxidation rate increases when the temperature of the gas-vapor mixture increases due to intensive diffusion-convective heat and mass transfer. Heat release in the system (Figure 1) becomes irreversible, thus ignition occurs.

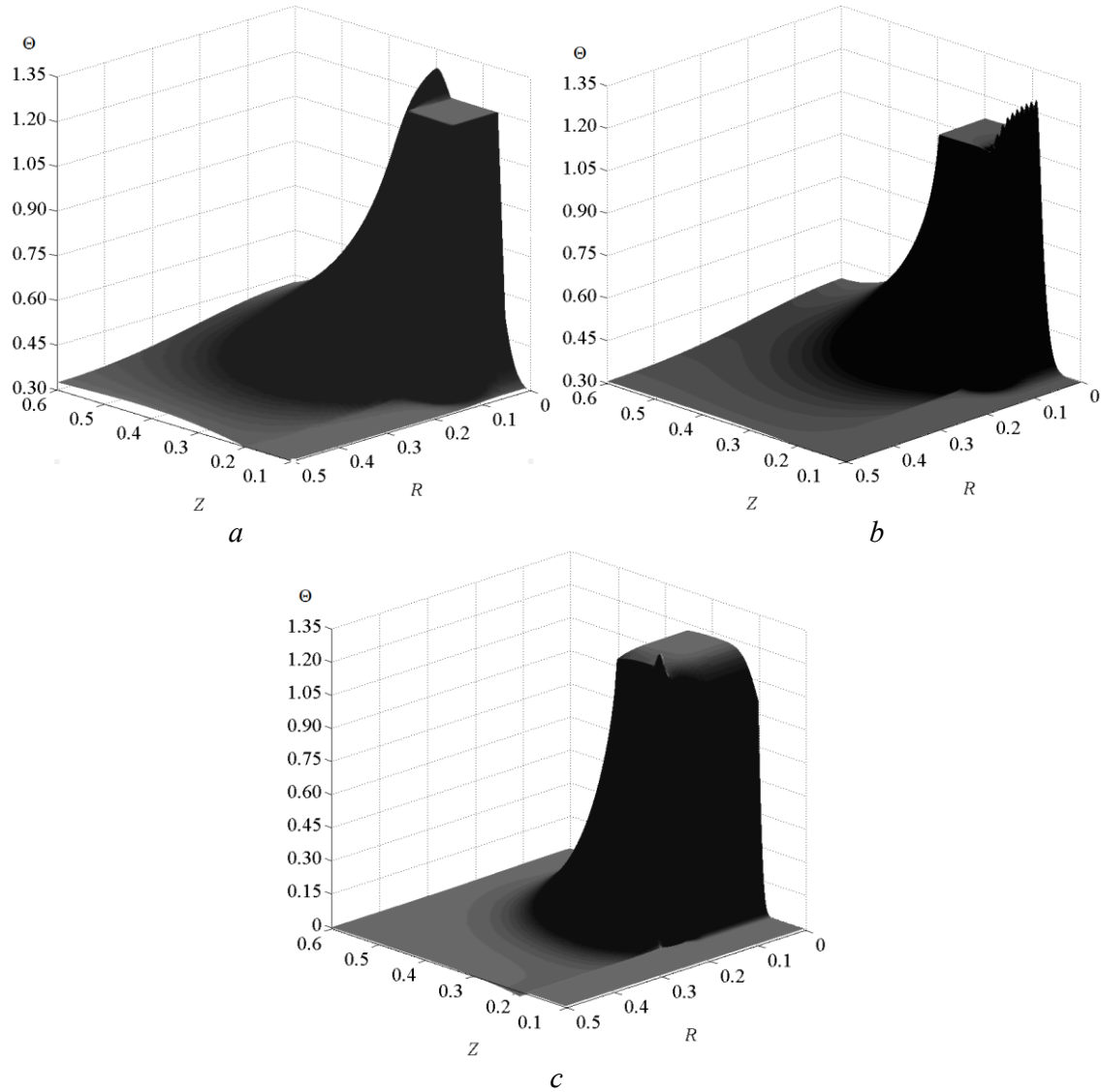


Figure 2: The dimensionless temperature fields at the moment of the ignition of the liquid condensed substance (a) at $R_p=Z_p=0.1$, $\Theta_p=1.2$, metalized solid condensed substance (b) at $R_p=Z_p=0.1$, $\Theta_p=1.2$, gel-like condensed substance (c) at $R_p=Z_p=0.15$, $\Theta_p=1.2$

Table 2 shows the dependencies of dimensionless ignition delay times for liquid, solid and gel-like fuels on the dimensionless initial temperature of the metal particle.

The ignition delay times of the gel-like condensed substance are substantially shorter compared to the similar characteristics of solid and liquid condensed substances. The minimum temperatures of particles ($\Theta_p \approx 1.1$ at $R_p = Z_p = 0.15$, when ignition occurs in the system (Figure 1)), exceed the threshold temperatures of the source ($\Theta_p \approx 1$) to initiate the combustion of solid and liquid condensed substances ceteris paribus. Thus, the minimum temperature $\Theta_p = 1.1$ and sizes $R_p = Z_p = 0.15$ of the disc-shaped local source may be assumed as the maximum values for the ignition of the gel-like condensed substance “hydrazine – liquified oxygen”. Established feature can be explained by a significant influence of endothermic phase transitions (melting and evaporation) on the intensity of heat and mass transfer and chemical reaction.

Table 2: Dimensionless ignition delay times τ_d of liquid, solid and gel-like condensed substances depending on the dimensionless initial temperature of a single hot metal particle Θ_p at $R_p = Z_p = 0.15$

Θ_p	1.000	1.100	1.125	1.150	1.175	1.200
Condensed substance						
Liquid condensed substance	1.431	1.047	0.923	0.802	0.716	0.604
Solid condensed substance	1.622	0.756	0.627	0.585	0.491	0.464
Gel-like condensed substance	no ignition	0.163	0.108	0.059	0.037	0.028

It should be noted that aluminum, ceramic and carbon particles heated up to high temperatures were used in the experiments as the ignition source. However, the results of numerical studies allowed us to conclude that steel particles had the shortest ignition delay times of condensed substances.

Numerical investigations established the features and differences between the ignition mechanisms of condensed substances during local heating. Thus, it was found that the leading oxidation reaction zone of the gas-vapor mixture is generated around the lateral droplet face in the small vicinity of the contact boundary with the gel-like condensed substance.

The solid condensed substance is characterized by the ignition zone localization near the contact border between fuel and the ignition source. The liquid condensed substance is characterized by three possible localizations: above the particle, near its lateral surface, and in the immediate vicinity of the fuel evaporation border.

Investigations have also revealed the differences between limiting characteristics of the heat source for three types of condensed substances. The temperature limit of the ignition source is $\Theta_p \approx 1$ for liquid and solid condensed substances. The temperature limit of the ignition source is $\Theta_p \approx 1$ for gel-like fuel.

These differences between the main characteristics and features of heat and mass transfer

during the ignition of liquid, solid and gel-like fuels by single hot metal particles, expand modern concepts of the ignition theory [4].

This work was financially supported by the Russian Science Foundation (Project No. 15-19-10003).

REFERENCES

- [1] Kuznetsov, G.V. and Strizhak, P.A. Effect of the Shape of a Particle Heated to a High Temperature on the Gas Phase Ignition of a Liquid Film. *Russ. J. Phys. Chem. B+* (2010) **2**:249–255.
- [2] Kuznetsov, G.V. and Strizhak, P.A. Analysis of Possible Reasons for Macroscopic Differences in the Characteristics of the Ignition of a Model Liquid Fuel by a Local Heat Source and a Massive Heated Body. *Russ. J. Phys. Chem. B+* (2012) **4**:498–510.
- [3] Glushkov, D.O., Kuznetsov, G.V. and Strizhak, P.A. Numerical Study of Ignition of a Metallized Condensed Substance by a Source Embedded into the Subsurface Layer. *Russ. J. Phys. Chem. B+* (2013) **3**:269–275.
- [4] Vilyunov, V.N. and Zarko, V. E. *Ignition of Solids*. Elsevier, Amsterdam, (1989).
- [5] Paushkin, Ya.M. and Chulkov, A.Z. *Rocket fuel*. Moscow, Mir, (1975) [in Russian].
- [6] Sarnet, S. *Chemistry of propellants*. Moscow, Mir, (1969) [in Russian].
- [7] Vargaftik, N.B., Filipov, L. P., Tarzimanov, A. A. and Totskii, E. E. *Handbook of Thermal Conductivity of Liquids and Gases*. CRC Press, Boca Raton, Fla, USA, (1994).
- [8] Vargaftik, N.B. *Tables of Thermophysical Properties of Liquids and Gases*. Hemisphere Publishing, New York, (1975).

RADIATION HEAT TRANSFER WITHIN THE DISCRETE ELEMENT METHOD - RELEVANCE, IMPLEMENTATION AND EXAMPLES -

S. WIRTZ^{1*}, J. WIESE¹, F. WISSING¹ AND V. SCHERER¹

¹*Lehrstuhl für Energieanlagen und Energieprozesstechnik (LEAT)
Ruhr-Universität Bochum

Universitätsstraße 150, D-44780 Bochum, Germany
email: wirtz@leat.rub.de, web page: <http://www.leat.rub.de>

Key words: DEM, Radiative Heat Transfer, Solid Fuel Combustion.

Abstract. Current developments in the energy sector increasingly demand the consideration of fuels with much larger particle sizes, either from alternative sources or due to a reduced pre-processing effort. In numerical simulations of such systems the particles can no longer be considered as non-colliding material points. Municipal waste incineration on grates or wood pellet combustion in domestic boilers are such examples, where the Discrete Element Method (DEM) can be applied to extend the Lagrange tracking of moving particles to a mechanically and thermally fully interacting flow of reacting granular material. In some situations where sufficiently large time scale differences between the processes in the gas phase and in the solid phase exist, distinctive interfaces can be identified between domains, thus allowing a different modelling in these regions. The treatment of the radiative heat transfer between such domains poses particular difficulties at the interfaces. Based on the two exemplary applications mentioned, details of the modelling approach are discussed and corresponding results presented.

1 INTRODUCTION

The theoretical description of fuel conversion processes and the numerical simulation of the equipment employed has gained considerable industrial application throughout the last two decades. Starting from the Eulerian gaseous fuel conversion in homogeneous multi-species turbulent flows, the further development led to the Lagrangian description of droplets or pulverized solid fuel particles. By tracking the material points representing these small particles, the movement and conversion within the flow field and the associated mass and heat transfer could be assessed. In many technically relevant applications collisions or any other direct interactions within the particulate phase could either be neglected or statistically represented.

The increasing exploitation of alternative fuel sources, especially biomass and agricultural residues, results in a growing significance of systems where much larger particles are directly converted. This largely avoids the otherwise required fuel preparation through energy intensive processes like cutting, crushing or grinding and thus supports the overall efficiency. With respect to the numerical simulation of such systems, the individual particles or objects must be

considered as thermally thick and also often require a spatial resolution of the temperature field within each object. In addition, their mechanical interaction may dominate the flow of the solid phase while the transport processes associated with the interstitial gas phase still control the mass and heat transfer. A straightforward combined CFD/DEM approach, fully resolving the evolution of all relevant processes over time, may be applied in these situations, but still requires extremely large computational resources if systems of technical scale are considered. The assumption of steady state conditions in a part of the domain considered allows to reduce this effort.

2 EXAMPLES OF TECHNICAL APPLICATIONS

The application of DEM combined with the simulation of heat transfer and/or chemical reaction is still in an early phase of development and the application to systems of industrial or technical scale is scarce. If carried out, these investigations are complicated with respect to physics and chemistry, computationally very expensive and time consuming [2, 5]. Early applications and explorative investigations were possible for situations where the specific conditions eased these requirements to some extent. A DEM code developed at the Department of Energy Plant Technology [1, 3, 4] describes the particle motion and thermochemical processes of the reacting granular phase. The commercial CFD software package ANSYS FLUENT (Version 14.5) is connected with this code and used to solve the governing equations of the continuous fluid phase surrounding the particles.

Two examples of largely different geometric scale, namely the conversion of bulky material on the grate of a municipal waste incinerator and the combustion of wood pellets in a domestic heater will be presented and compared with respect to the heat transfer models applied.

2.1 Municipal waste incinerator

Thermal treatment, gently circumscribing ultimate combustion, is an efficient, ecologically favorable and long established process for the energetic utilization of municipal waste. In these systems the untreated material is introduced through a waste feeder chute into the furnace (approx. 60 MW_{th}) forming a waste layer on a grate of about 10 m length and 60 cm initial height. Moving bars mechanically induce the transport of this layer through the furnace, while it is passed by primary air from below.

The gas mixture leaving the upper surface of the layer consists of partially oxidized pyrolysis products, carbon monoxide and air. This flow enters the combustion chamber atop of the grate, becomes mixed with additional secondary air injected from the roof and/or the sidewalls and finally is converted under turbulent conditions (fig. 1). The harsh conditions in these combustion chambers render reliable measurements of gas temperatures, species concentrations or radiative fluxes technically ambitious and costly; within the waste layer they are virtually impossible. Thus only numerical simulations are left for the purpose of “looking” into details of these systems for optimization.

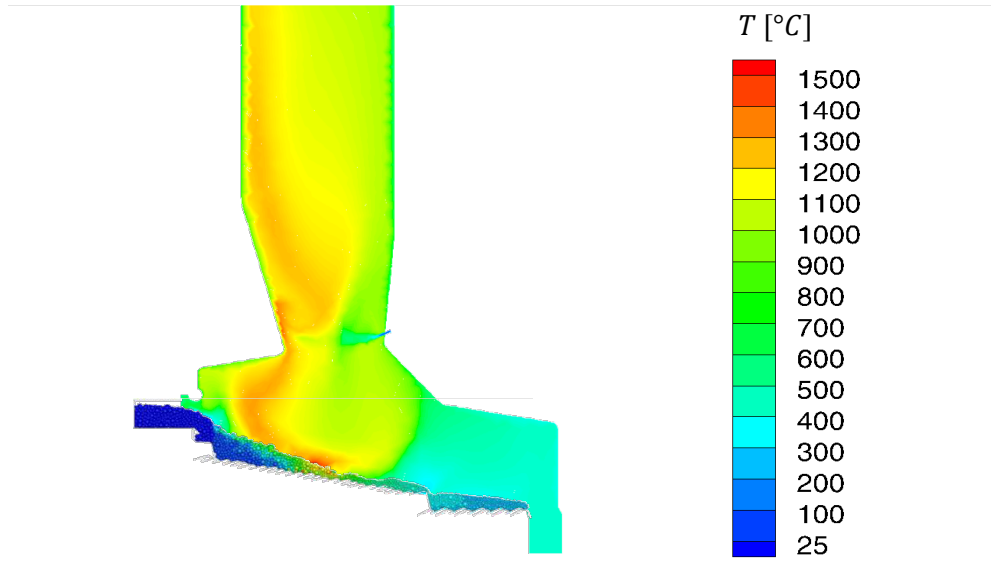


Figure 1: Temperature distribution in the boiler (gas phase) and in the bulk material (solid fuel) on the grate

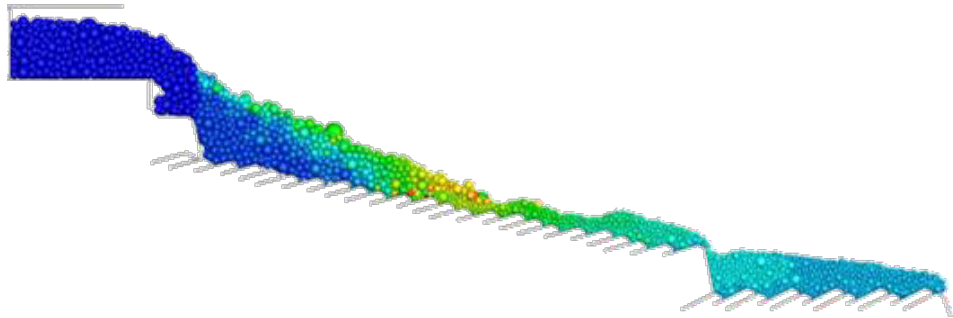


Figure 2: Close-up of the temperature distribution in the waste layer, scaled as in fig. 1.

As depicted in fig. 1 and fig. 2 the domain required for an overall simulation comprises of two distinctly different domains with respect to the prevailing physical and thermochemical conditions. While the fluid passes the combustion chamber in just a few seconds, the solid fuel (only a “strip”, 50 cm wide and containing approx. 7500 particles is modeled) needs about 80 minutes to travel along the grate. Thus the overall time scales are wide apart, suggesting a separation at the boundary between fuel layer surface and combustion chamber.

With respect to the appropriate models, the combustion chamber may be represented as a conventional reactive multi-species turbulent steady state flow field, occasionally blown out

small particles and their conversion may be readily described as transported and reacting material points using the commonly used particle tracking procedure.

The process on the grate with the waste-layer atop is dominated by the interaction of the mechanical transport and mixing of the bed, with the concurrent heat transfer, heterogeneous reaction in the bulk (drying, pyrolysis, char oxidation) and with the crossflowing primary air. Several grate designs based on different mechanical transport principles (forward acting, backward acting roller grates) coexist in the waste incineration technology. Depending on the specific grate design different combustion chamber layouts are favored (counter-current, co-current, center-flow firing). The example shown is a forward acting grate with counter-current firing [3].

Heating of the waste-layer, ignition of the combustible material contained therein and the resulting conversion rate, are to a large extent controlled by radiation from the combustion chamber above the layer. The intensity of the radiation incident on the layer surface tightly couples with the surface temperature of the particles in the top layer since radiation is transported “infinitely fast”. The height of the fuel layer is typically in the range of several decimeters, thus a considerable conversion of the gaseous components released within the bed appears to be a reasonable assumption; within the DEM model successive thermochemical equilibria are computed in the vertical direction. Since the major pressure loss occurs across the grate, an even distribution of the primary air passing through the fuel layer can be prescribed as the inlet boundary condition.

Typical municipal waste consists of a large variety of solid objects of widely varying size, shape, mechanical, physical and thermochemical properties. At this point any particle-based simulation method requires rigorous simplifications. This is not only due to the large number of objects involved but even more since the required data on the fuel, which (if known at all) is only available as long time averages. Combining detailed knowledge on the properties of individual fuel fractions (heat of reaction of different types of plastic material, wood, inert materials, water) and their respective content with known “typical” size distributions [7] allows to parametrize a “theoretical waste” which exhibits both, reasonable conversion behavior and transport properties resulting in realistic residence times on the grate. Therefore the actual geometric shape of the fuel objects may be reduced to cohesive spherical particles, interacting with each other and reducing size and cohesive forces during conversion. Since the large particles are thermally thick, their one-dimensional radial discretization allows to approximate their thermal inertance. Further details on the models and a comparison of results obtained with measurements in an actual incinerator may be found in [3].

The time scale associated with the final conversion of the products in the boiler is short if compared to the 80 minutes residence time. Therefore the movement, heating and reaction of the fuel objects need to be considered as unsteady processes, while the boiler atop always achieves steady state conditions within much shorter times. This provides the time scale difference required for a separation of the simulation into two distinct but coupled domains as described in chapter 2.4

2.2 Wood pellet furnace

The second example (fig. 3) discussed is a domestic heater (13 kW thermal) fired with wood pellets. This system differs in several aspects from the waste incinerator presented above. Obviously, the absolute scale of the system is much smaller, since the volume of the combustion chamber is only about 20 liter, installed atop a burner bowl of approximately 15 cm diameter which contains less than 1000 reacting particles during steady state and at nominal load. In contrast to the municipal waste, the wood pellets are geometrically and thermochemically well defined (cylindrical shape of 6 mm diameter and a length varying between 6 and 30 mm, known heating value, water content and measured temperature dependence of the gas release during pyrolysis). The initial geometry of the individual particles can be assumed to be preserved during drying (constant volume) and to be reduced in size during pyrolysis and char burnout (constant density), which roughly reflects the actual behavior during burnout. Since the primary air is introduced into the burner bowl from below and secondary air is injected radially through circular holes on the circumference at two different heights. The distribution of the air inflow through these ports is strongly controlled by the geometry of the air supply, thus the required boundary conditions can be determined in advance by a separate simulation of the distribution system.

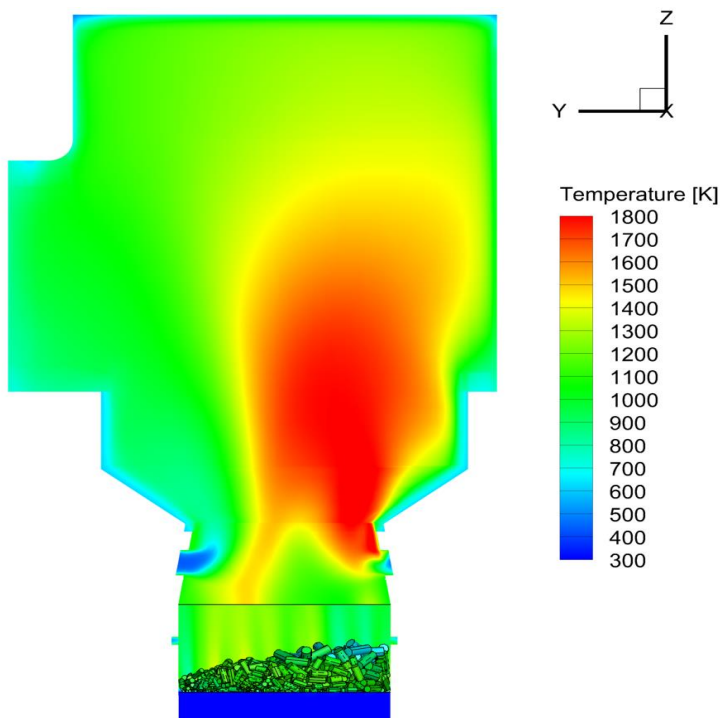


Figure 3: Temperature distribution in the fuel layer and the combustion chamber of a pellet fired domestic heater

As shown in fig. 4, the discrete fuel objects, the wood pellets, are discontinuously dropped onto the fuel layer through a chute. About 10 gram every 10 seconds are introduced to obtain an averaged fuel feed rate of 1.0 g/s. This results in an unsteady heating and conversion process within the burner bowl, every 10 seconds the onset of drying releases water vapor, subsequently volatiles and later on carbon monoxide (as the primary char conversion product) occur. Since the particles fall on a small area of the surface a distinctive movement of the particles in the bed is induced, being overlain by the particle size reduction resulting from char burnout. The average residence time of the pellets until full burnout is 375 seconds.

Similar as in the waste incinerator, the flow in the combustion chamber atop of the fuel bowl must be considered to be partially premixed, turbulent and three-dimensional, thus the reaction of the gaseous products is controlled by the spatially distributed release of the components from the reacting pellet bed and the mixing with the secondary air. Different descriptions (Eddy Dissipation/Eddy Dissipation Combustion) were compared, a detailed comparison may be found in [1].

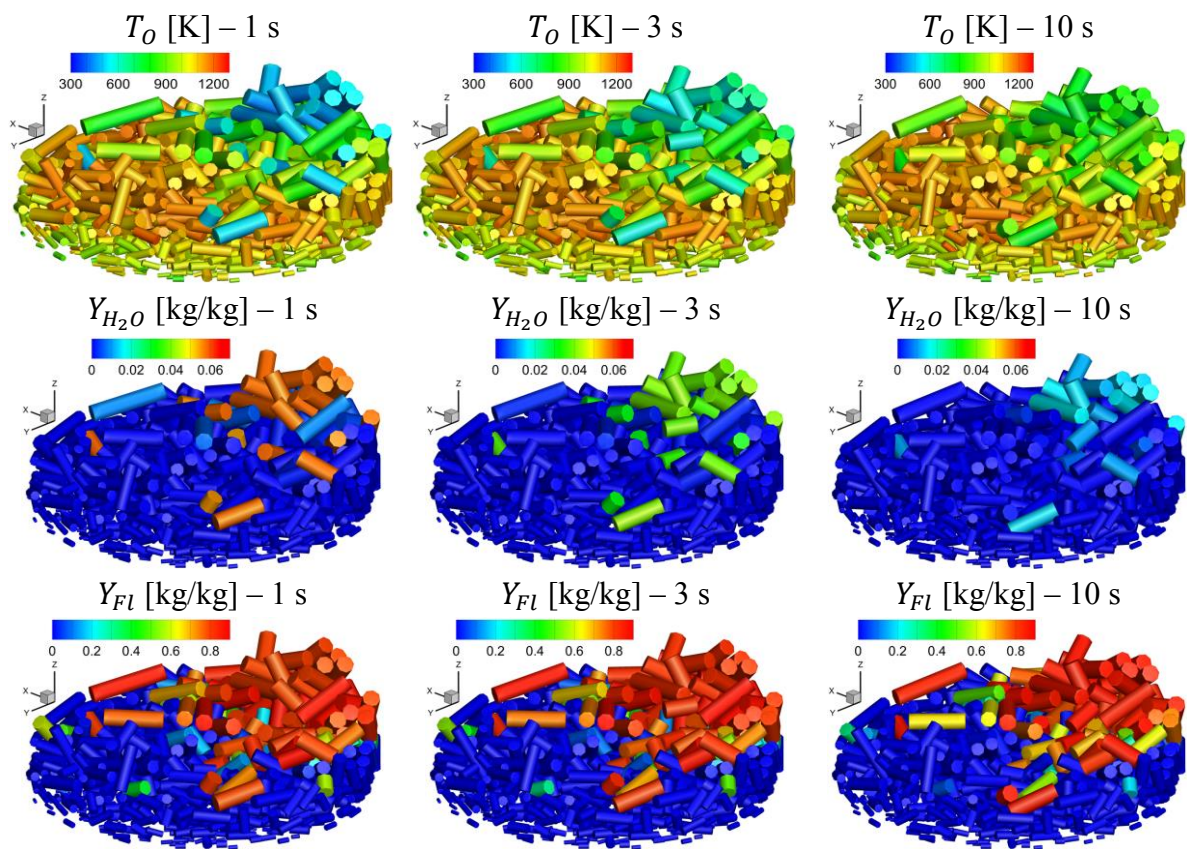


Figure 4: Surface temperature, water and volatile content of the pellets in the burner bowl

In contrast to the waste incineration, the pellet layer height is quite small and the residence time of the gaseous components released in the bed approaches the same magnitude as the time required for fuel conversion. Due to the essentially “laminar” conditions in the small gaps between the pellets and the constrained spatial mixing, a kinetic description (only one step global reaction of the hydrogen content) is required to allow for a partial conversion of pyrolysis products in the bed.

2.3 DEM-CFD coupling / radiative transfer

As previously shown, the surface of the waste layer and in the other case, the interface between the burner bowl and the combustion chamber atop, represent natural interfaces with a sufficient scale separation to allow for a separated but externally coupled (iteratively, via files and User Defined Functions) simulation of the overall system. Averaging the time resolved conversion on the grate or in the pellet bed over appropriate prescribed times (cycling time of the waste push rod and time between successive pellet additions) provides the inlet boundary conditions for a steady state simulation of the respective combustion chamber.

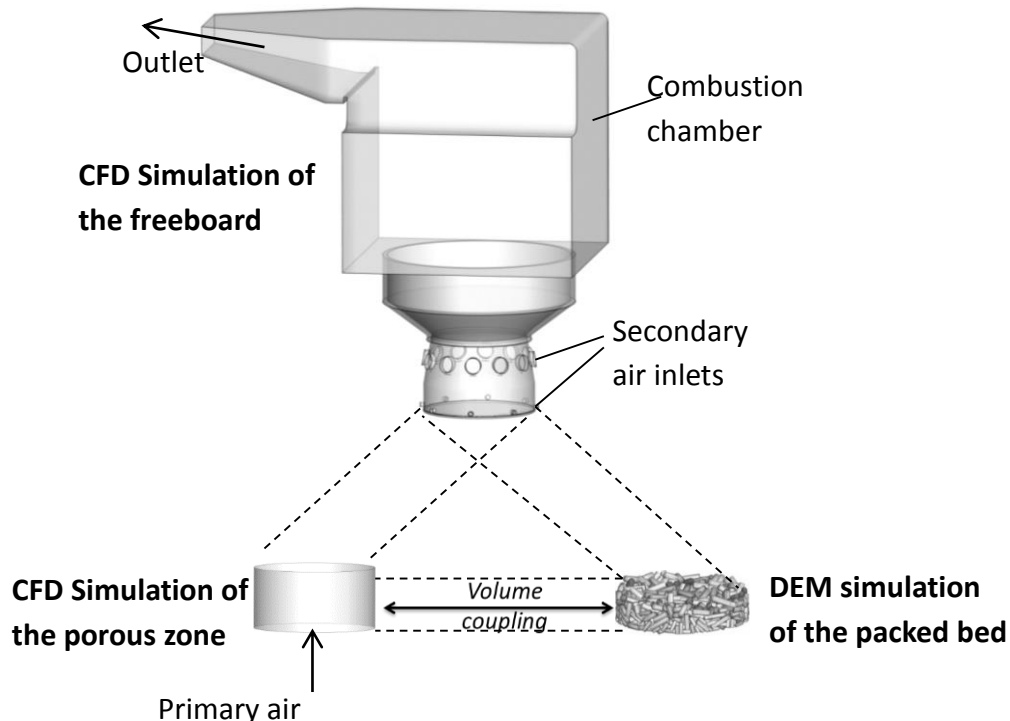


Figure 5: Data exchange concept for DEM/CFD coupling

Fig. 5 depicts this approach for the case of the pellet stove. While a two-dimensional, two-way interface is sufficient for the waste incinerator (steady state CFD in the combustion chamber and reacting, time resolved DEM on the grate), additional volume coupling is required for the process in the pellet burner bowl. Turbulent steady state simulation and time resolved “laminar” flow in the porous medium representing the pellet bed are not compatible enough to be treated in one single domain.

This results in three distinct computing tasks (CFD in the combustion chamber, CFD in fluid phase and reacting DEM for the solid particles in the burner bowl) which need to exchange data of mass and heat fluxes in tightly synchronized (and consistent) manner.

In this context the thermal radiation heat transfer requires specific attention since the overall system behavior and thus the rate of fuel conversion is distinctively influenced by the radiative fluxes. Any inconsistencies at this point add to the uncertainties already resulting from the many assumptions and simplifications contained in the other model components (e.g. fuel conversion, convective flow and diffusive mass transfer, thermochemical model).

From a general perspective the three-dimensional radiative transfer equation in an absorbing, emitting and scattering medium must be solved with respect to the boundary conditions imposed by multiple enclosing surfaces. The radiative intensity I in position \vec{r} arriving from (or being emitted in) direction \vec{s} can be obtained by integration of

$$\frac{dI(\vec{r}, \vec{s})}{ds} + \kappa(s) I(\vec{r}, \vec{s}) = a n^2 \frac{\sigma T^4}{\pi} + \frac{\sigma_s}{4\pi} \int_0^{4\pi} I(\vec{r}, \vec{s}') \phi(\vec{s}' \cdot \vec{t}) d\Omega \quad (1)$$

with the absorption coefficient a , the scattering coefficient σ_s , the optical thickness $\kappa(s)$, the refractive index n of the gray medium passed, a scattering phase function ϕ relating scattered to incident radiation and the Stefan-Boltzmann constant σ . In the commonly used CFD tools several approximations to the solution of this equation do exist. A comparison of the most popular models, the so called P-1, the Discrete Transfer Radiation Model (DTRM), the Discrete Ordinates Model (DO) and the Surface-to-Surface (S2S) model may be found in [6]. If the optical thickness of the participating medium is large, either due to a strong absorption or due to a “large” length scale, the P-1 model provides the most robust and efficient approach and is used in the waste incinerator simulations. In contrast, if the optical thickness is small and the radiative exchange is dominated by the direct exchange among the surfaces involved, like in the case of the pellet stove, the S2S model or the DO-model are reasonable choices.

Here the major difficulty arises from the fact that the thermal radiation acts instantaneously between the surfaces and gas volumes involved. If a reacting fuel object changes its surface temperature over time, the resulting change in heat flux from the combustion chamber atop occurs immediately and thermal equilibration must be obtained before the next time step. This would require to solve (to converge) at least the radiation transport problem in the combustion chamber domain for every step of the DEM simulation, which currently is not possible with reasonable effort.

An “ad hoc” approach to resolve this conflict between steady state and time dependent solutions uses the domain interfaces such that a common, time averaged “radiative background temperature” T_{rad} is associated with the interfacing surface to compute on the particle side the time resolved heat exchange with the individual particles and on the other side the radiative exchange with the combustion chamber as a whole, iteratively balancing the integral heat flux. Figure 6 depicts, in order to show the sensitivity, the effect of a reduction of this radiative temperature on the conversion and particle temperature on the grate. As can be seen, 20 % difference in the value of T_{rad} decides between stable operation and full extinction of the reaction. Unfortunately the measurement of radiative fluxes in devices of technical scale is difficult and expensive, thus no direct comparison is currently available.

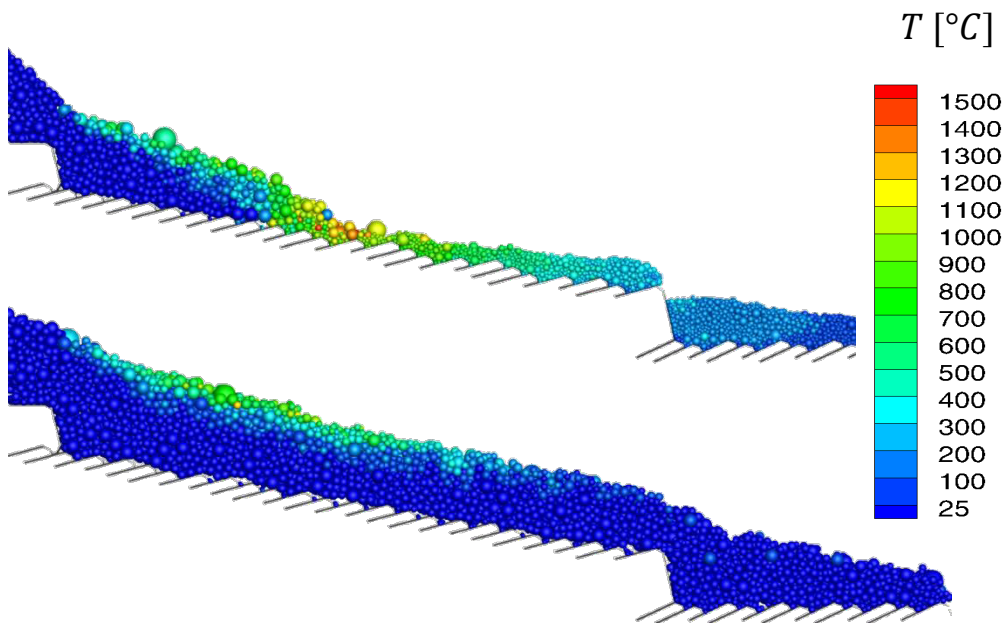


Figure 6: Particle temperatures and conversion on the grate of a municipal waste incinerator,
upper part: nominal operation,
lower part: radiation temperature at the interface reduced by 20%

3 CONCLUSIONS

Coupled CFD/DEM simulations are an emerging methodology for the numerical treatment of mechanically and thermally interacting and chemically reacting two phase flows with large reacting particles. Although, many details especially with respect to the generalisation of the modelling approaches require further investigation. First demonstrations and exemplary

applications could be realized with quantitatively reasonable results. Thermal radiation in these systems requires special attention since it immediately transfers energy and therefore has a strong influence on the conversion rates, this complicates scale separation of the problem in time and space.

ACKNOWLEDGEMENTS

The work presented was performed in part within the project “Modellentwicklung zur Beschreibung von Transport, Mischung und Abbrand von Hausmüll auf Roststsystemen (German Research Foundation, Sche: 322/10-1)” and the two projects “Simulationswerkzeuge für Pelletfeuerungen (EF 2005A)” and “Steigerung der Energieeffizienz in Steinkohlefeuerungen mit Sekundärbrennstoffeinsatz durch zusätzliche Nachverbrennung (EN3005B)“ from the program Ziel2.NRW financed by the Ministry for Economy, Energy, Industry, Economic Affairs and Handicrafts of the German State of North Rhine-Westphalia and the European Union through the European regional development fund EFRE.



EUROPÄISCHE UNION
Investition in unsere Zukunft
Europäischer Fonds
für regionale Entwicklung

Ziel2.NRW
Regionale Wettbewerbsfähigkeit und Beschäftigung

Ministerium für Wirtschaft, Energie,
Industrie, Mittelstand und Handwerk
des Landes Nordrhein-Westfalen



REFERENCES

- [1] Wiese, J.: *DEM/CFD-Simulation und experimentelle Untersuchungen von Holzpelletfeuerungen*, PhD-Thesis, Ruhr-Universität Bochum, 2015.
- [2] Krause, B., Liedmann, B., Wiese, J., S. Wirtz, S., Scherer,V.: *Coupled three dimensional DEM-CFD simulation of a lime shaft kiln - Calcination, particle movement and gas phase flow field*, Chemical Engineering Science (2015, accepted for publication).
- [3] Brosch, B.; Wirtz, S.; Scherer, V.: *Simulation of municipal solid waste incineration in grate firing systems with a particle based novel Discrete Element Method*, VGB Power Tech 1 (2014).
- [4] Komossa, H.; Wirtz, S.; Scherer, V.; Herz, F.; Specht, E.: *Transversal bed motion in rotating drums using spherical particles: Comparison of experiments with DEM simulations*, Powder Technology, Vol. 264, 96-104, (2014).
- [5] Rickelt, S., Sudbrock, F., Wirtz, S., V. Scherer, V.: *Coupled DEM/CFD simulation of heat transfer in a generic grate system agitated by bars*, Powder Technol. 249 (2013) 360–372. doi:10.1016/j.powtec.2013.08.043.
- [6] Lu, X., Wang, T.: *Investigation of radiation models in entrained-flow coal gasification simulation*, International Journal of Heat and Mass Transfer 67 (2013) 377-392.
- [7] Machado, S. L., Karimpour-Fard, M., Shariatmadari, N., Carvalho, M. F., do Nascimento, J. C. F.: *Evaluation of the geotechnical properties of MSW in two Brazilian landfills*, Waste Management 30 (2010) 2579-2591.
- [8] Siegel, R., J. Howell, J.: *Thermal Radiation Heat Transfer*, Taylor & Francis, 1980.

TWO-PHASE MODELING OF CONDUCTION MODE LASER WELDING USING SMOOTHED PARTICLE HYDRODYNAMICS

Haoyue Hu and Peter Eberhard

Institute of Engineering and Computational Mechanics, University of Stuttgart,
Pfaffenwaldring 9, 70569 Stuttgart, Germany
[haoyue.hu, peter.eberhard]@itm.uni-stuttgart.de
www.itm.uni-stuttgart.de

Key words: SPH, Conduction Mode Laser Welding, Heat Transfer, Phase Transition, Marangoni Convection, Melt Flow

Abstract. The process of conduction mode laser welding is simulated using the meshless Lagrangian method Smoothed Particle Hydrodynamics. The modeling of the solid phase is based on the governing equations in thermoelasticity. For the liquid phase, surface tension effects including the Marangoni force caused by a temperature-dependent surface tension gradient are taken into account to simulate the melt flow in the weld pool. A non-isothermal solid-liquid phase transition with the release or absorption of additional energy known as the latent heat of fusion is considered. The major heat transfer process through conduction is modeled, whereas heat convection and radiation are neglected. The energy input from the laser beam is approximated as a Gaussian heat source acting on the material surface. Numerical results obtained with the developed model are presented for laser spot welding and seam welding of aluminum. The change of process parameters like welding speed and laser power, and their effects on the weld pool dimensions can be investigated through simulations, and the overall welding quality may be assessed.

1 INTRODUCTION

Laser welding is widely applied in industry due to several advantages compared to conventional arc or gas welding: high welding speed, a small heat affected zone, ease of automation, and weight savings. Depending on the absorbed radiation intensity from the laser beam, laser welding may be classified into conduction mode welding and deep penetration welding. Conduction mode laser welding is a preferred manufacturing method to obtain visually appealing weld seams without further grinding or finishing. It is suitable for joining thin sheets and tubes, e.g. visible surfaces of device housings or stainless steel sinks. The process is characterized by high quality welds without defects like pores or spatter, and low mechanical and thermal distortions in the work piece. During the welding

process, a laser beam melts the parts to be welded along a common joint, while the maximum temperature stays below evaporation temperature. The energy is transferred to the work piece merely through heat conduction and thus, the weld depth is limited by the heat conductivity of the material. The molten materials coalesce and solidify to form a weld, whose width is greater than its depth.

To gain insight into the influence of process parameters on the melt flow and resulting weld, the conduction mode laser welding process is simulated using Smoothed Particle Hydrodynamics (SPH) [8, 15]. As a meshless Lagrangian method, it has the ability to accurately describe the free surface melt flow by fulfilling the continuity equation at the same time. The underlying heat transfer phenomena including the solid-liquid interface and the occurring phase transitions, melting and solidification, are modeled based on the works of Cleary and Monaghan [3, 20]. Temperature-dependent material properties are taken into account, as an example, the temperature-dependent surface tension gradient is considered in order to describe the Marangoni convection which dominates the weld pool [11, 24]. The energy input from the laser beam is approximated as a moving heat source acting on the material surface.

2 MODELING WITH SPH

In SPH [16, 18], the continuum is represented by a set of particles acting as discretization points. Material properties and field variables like velocity and acceleration are associated to each particle such that the overall state of the system is characterized properly. The particles interact with each other within a defined influence range h of a smoothing kernel function W . The evaluation of field variables f_i and their derivatives for particle a is approximated by sums over all neighboring particles b

$$f_i^a = \sum_b \frac{m_b}{\rho_b} f_i^b W(\mathbf{r}_a - \mathbf{r}_b, h) = \sum_b \frac{m_b}{\rho_b} f_i^b W_{ab}, \quad (1)$$

$$\frac{\partial f_i^a}{\partial x_j} = - \sum_b \frac{m_b}{\rho_b} f_i^b \frac{\partial W(\mathbf{r}_a - \mathbf{r}_b, h)}{\partial x_j} = - \sum_b \frac{m_b}{\rho_b} f_i^b \frac{\partial W_{ab}}{\partial x_j}, \quad (2)$$

where m is the mass, ρ the density, \mathbf{r} the position vector, and h the smoothing length. The Gaussian kernel function as introduced in [8] is applied here. As a general discretization method, all systems that are described by partial differential equations can be simplified to a set of ordinary differential equations. For time integration, the explicit second-order Leapfrog scheme [21] with time step control is used.

2.1 Solid phase

A coupled thermoelastic approach is developed for modeling the solid phase, in order to analyze both the temperature distribution and the stress and strain in the workpiece during the welding process.

Equation of motion

The balance equation of linear momentum is given as

$$\dot{v}_i = \frac{1}{\rho} \frac{\partial \sigma_{ij}}{\partial x_j} + g_i \quad (3)$$

with the gravity force per unit mass g_i acting as body force. Discretizing this equation into SPH form, the acceleration acting on a particle a due to interaction with its surrounding neighbor particles b is according to [18]

$$\dot{v}_i^a = \sum_b m_b \left(\frac{\sigma_{ij}^a}{\rho_a^2} + \frac{\sigma_{ij}^b}{\rho_b^2} + R_{ij}^{ab} \Phi_{ab}^n + \Pi_{ab} \delta_{ij} \right) \frac{\partial W_{ab}}{\partial x_j^a} + g_i . \quad (4)$$

For numerical reasons, an artificial stress term $R_{ij}^{ab} \Phi_{ab}^n$ introduced in [17] and an artificial viscosity term $\Pi_{ab} \delta_{ij}$ proposed in [19, 16] are added in Eq. (4) to reduce the tensile instability and to smooth spurious numerical oscillations, respectively.

The stress tensor consisting of elastic and thermal stresses due to linear thermal expansion is defined as

$$\sigma_{ij} = (-p - 3K\alpha(T - T_0))\delta_{ij} + S_{ij} , \quad (5)$$

where p is the pressure, K the bulk modulus, α the thermal expansion coefficient, T the absolute temperature in K, T_0 the reference temperature, and S_{ij} the deviatoric stress tensor. Both the pressure and the thermal expansion term only have influence on the hydrostatic part of the stress tensor.

The hydrostatic part of the stress tensor can be evaluated directly. The pressure is calculated using a state equation. Here, an isothermal approach is chosen

$$p = c_0^2(\rho - \rho_0) , \quad (6)$$

where $c_0 = \sqrt{K/\rho_0}$ is the speed of sound, ρ the current density, and ρ_0 the initial reference density.

The Updated Lagrangian method is used for updating the deviatoric part of the stress tensor, which evolves as follows according to [18]

$$\dot{S}_{ij} = 2\mu \left(\dot{\epsilon}_{ij} - \frac{1}{3}\delta_{ij}\dot{\epsilon}_{kk} \right) + S_{ik}\Omega_{jk} + \Omega_{ik}S_{kj} , \quad (7)$$

where $\dot{\epsilon}_{ij} = \frac{1}{2} \left(\frac{\partial v_i}{\partial x_j} + \frac{\partial v_j}{\partial x_i} \right)$ is the strain rate tensor, $\Omega_{ij} = \frac{1}{2} \left(\frac{\partial v_i}{\partial x_j} - \frac{\partial v_j}{\partial x_i} \right)$ the rotation rate tensor, and μ the shear modulus. Note that the Jaumann stress rate is employed to ensure the objectivity of the formulation [5].

Energy equation

The thermoelastic coupled heat equation may be derived using the internal energy equation [6]

$$\rho \dot{e} = \sigma_{ij} \dot{\epsilon}_{ij} - \frac{\partial q_i}{\partial x_i} + q_s \delta(\mathbf{r} - \mathbf{R}_s) , \quad (8)$$

where e is the specific internal energy, q_i the heat flux, q_s the source strength in the dimension power per unit volume, δ the Dirac delta function, and \mathbf{R}_s the position vector of the heat source. Inserting the formula for the internal energy density [6]

$$e = c(T - T_0) + \frac{3K}{\rho_0} \alpha T_0 \epsilon_{kk} + \frac{1}{2\rho_0} (\lambda + 2\mu) \epsilon_{kk}^2 + \frac{\mu}{\rho_0} ((\epsilon_{kk})^2 + \epsilon_{kk}^2) + \text{const.} \quad (9)$$

with the heat capacity c , the Lamé parameters λ and μ , the approximation $\rho = \rho_0$, and Fourier's law of heat conduction for a material with constant thermal conductivity k

$$q_i = -k \frac{\partial T}{\partial x_i} \quad (10)$$

into Eq. (8) yields the coupled heat equation in linear thermoelasticity

$$\rho c \dot{T} = -3K \alpha T \dot{\epsilon}_{kk} + k \Delta T + q_s \delta(\mathbf{r} - \mathbf{R}_s) . \quad (11)$$

Equation (11) is converted to its corresponding SPH form following [3] and [20] for the heat conduction and source term

$$c \dot{T}_a = \sum_b \frac{m_b}{\rho_a \rho_b} (-3K \alpha T_a (\mathbf{v}_b - \mathbf{v}_a) \cdot \nabla W_{ab} + 2k(T_a - T_b) F_{ab}) + \frac{1}{\rho_a} \sum_k Q_s \zeta_s W(\mathbf{r}_k - \mathbf{R}_s) , \quad (12)$$

where $F_{ab} = (\mathbf{r}_a - \mathbf{r}_b) \cdot \nabla W_{ab} / \|\mathbf{r}_a - \mathbf{r}_b\|^2$, Q_s is the power of the heat source, and ζ_s a normalizing factor for the heat source such that the rate of change of thermal energy is correctly considered [20].

2.2 Liquid phase

The molten material is modeled as an incompressible Newtonian fluid with constant dynamic viscosity η . The constitutive law is characterized following [9] by

$$\sigma_{ij} = -p \delta_{ij} + \eta \left(\frac{\partial v_i}{\partial x_j} + \frac{\partial v_j}{\partial x_i} \right) = -p \delta_{ij} + 2\eta \dot{\epsilon}_{ij} , \quad (13)$$

where the pressure is calculated through a quasi-incompressible state equation as given in [1]

$$p = \frac{\rho_0 c_0^2}{\gamma} \left(\left(\frac{\rho}{\rho_0} \right)^\gamma - 1 \right) \quad (14)$$

with a constant value $\gamma = 7$ and an artificial speed of sound c_0 .

Continuity equation

The conservation of mass is ensured by the continuity equation, see [9],

$$\dot{\rho} = -\rho \frac{\partial v_i}{\partial x_i} \quad (15)$$

which is discretized in SPH form as

$$\dot{\rho}_a = \sum_b m_b \frac{\rho_a}{\rho_b} (\mathbf{v}_a - \mathbf{v}_b) \cdot \nabla W_{ab} . \quad (16)$$

Momentum equation

The conservation of linear momentum is described by the Navier-Stokes equation as stated in [9]

$$\rho \dot{v}_i = -\frac{\partial p}{\partial x_i} + \eta \Delta v_i + \rho f_i + \rho g_i . \quad (17)$$

The discretization of the pressure term is treated analogously to the pressure term for solid particles in Eq. (4). The viscous forces are modeled by the term proposed in [22]. Additionally, the surface tension force f_i is applied to fluid particles in the melt flow. The computation of the surface tension force is based on the Continuum Surface Force (CSF) model described in [2]. For modeling the Marangoni convection in the melt flow caused by a temperature-dependent surface tension coefficient, we follow the approach from [25]. A linear dependence of the surface tension coefficient τ on temperature with the proportionality factor τ_T is assumed and the volumetric surface tension force is

$$\mathbf{f} = \frac{1}{\rho} (\tau \kappa \mathbf{n} + \tau_T \nabla_s T) , \quad (18)$$

where κ is the curvature, \mathbf{n} the normal vector pointing outwards, and $\nabla_s T$ the surface temperature gradient. As suggested in [25], $\nabla_s T$ is projected onto the tangential space and the spatial temperature gradient is calculated using the Corrective Smoothed Particle Method (CSPM) described in [12].

Internal energy equation

The internal energy equation is given in [9] as

$$\rho \dot{e} = \rho c \dot{T} = \frac{\partial v_i}{\partial x_j} \eta \dot{\epsilon}_{ij} + k \Delta T + q_s \delta(\mathbf{r} - \mathbf{R}_s) . \quad (19)$$

Compared to Eq. (11), the coupled term has vanished as a result of incompressibility. Instead, there is a positive viscous dissipation term which represents the energy dissipated as heat.

2.3 Solid-liquid phase transition and interaction

The solid-liquid phase transition is assumed to take place between a significant temperature range, which is the usual case for metal alloys. Therefore, two parameters are set for the phase transition temperature marking the lower solid and upper liquid limit, T_s and T_l . As different material parameters apply for the solid and liquid phase, the temperature dependency is partially considered by using different heat capacities c_s and c_l . During the phase transition from solid to liquid, heat is absorbed by the material. If the absorbed heat value exceeds the latent heat of fusion H_f , the transition has completed. The particle type is then changed from a solid to a fluid particle.

Using the enthalpy method for a non-isothermal phase transition as basis [10], the temperature of each particle is determined from the specific enthalpy h

$$T = \begin{cases} \frac{h}{c_s} & \text{solid: } T < T_s, h < c_s T_s, \\ \left(h + \frac{H_f}{T_l - T_s} T_s \right) \left(c_{in} + \frac{H_f}{T_l - T_s} \right)^{-1} & \text{mushy: } T_s \leq T \leq T_l, c_s T_s \leq h \leq c_{in} T_l + H_f, \\ \frac{1}{c_l} (h - H_f - c_{in}(T_l - T_s)) & \text{liquid: } T \geq T_l, h \geq c_l T_l + H_f + c_{in}(T_l - T_s). \end{cases} \quad (20)$$

For a continuous function at $T = T_l$, the intermediate heat capacity c_{in} has to fulfill the constraint

$$c_l T_l + H_f + c_{in}(T_l - T_s) = c_{in} T_l + H_f, \quad (21)$$

leading to $c_{in} = c_l T_l / T_s$.

The elastic interaction for solid particles given in Eq. (4) is also applied to the interaction between solid and fluid particles. The difference lies in the evaluation of the stress tensor of the fluid particle from Eq. (13). In contrast to other contact algorithms for fluid-structure interaction with SPH that introduce repulsive forces between two approaching particles similar to the penalty contact force scheme [14], or e.g. the CD-FSIT algorithm [13], this approach is purely based on the stress tensors for the solid and fluid particle. The interaction does not contain any additional artificial parameters and hence avoids the cumbersome process of parameter identification. Concerning the energy equation, both Eq. (8) and Eq. (19) are combined. The coupled thermoelastic term is only applied to the solid particle, whereas the viscous dissipation term is solely applied to the fluid particle.

2.4 Laser beam

According to the Beer-Lambert law [24], the laser beam intensity I decreases exponentially with respect to the depth z after penetrating the surface of the workpiece

$$I(z) = (1 - \Gamma) I_0 \exp(-Az), \quad (22)$$

where Γ is the reflection coefficient, and $A = 4\pi n \kappa / \lambda_0$ the absorption coefficient, with the refractivity n , the absorbance κ , and the wave length of the laser beam in vacuum λ_0 .

For metals, the depth of absorbing 95 % of the laser radiation is less than one micrometer [11, 24], therefore the laser beam may be regarded as a surface source.

The assumption of a Gaussian intensity distribution is most common when modeling a laser beam. Due to the use of the Gaussian kernel in the presented SPH simulations, the Gaussian intensity distribution is implicitly considered. The power intensity is defined as

$$I(x, y) = \frac{(1 - \Gamma)P_{\text{laser}}}{\exp(-0.5)\pi r_s^2} \exp\left(-\frac{x^2}{r_s^2} - \frac{y^2}{r_s^2}\right), \quad (23)$$

in which the radius of influence of the heat source r_s is set equal to the smoothing length. Hence, the strength of the heat source is identified as $Q_s = (1 - \Gamma)P_{\text{laser}}/\exp(-0.5)$ such that the intensity at the distance $r_s/\sqrt{2}$ is equal to the mean absorbed radiation intensity $(1 - \Gamma)P_{\text{laser}}/\pi r_s^2$.

3 SIMULATION RESULTS

For the simulations, the suggested model is implemented into the object-oriented software package Pasimodo [7, 23]. Two exemplary welding processes of aluminum are presented. First, a spot weld generated by a short-term laser heating process and subsequent solidification is modeled. The second example shows a seam welding process with a moving laser beam. As boundary condition, a few bottom layers of particles are fixed in all directions to prevent rigid body motion.

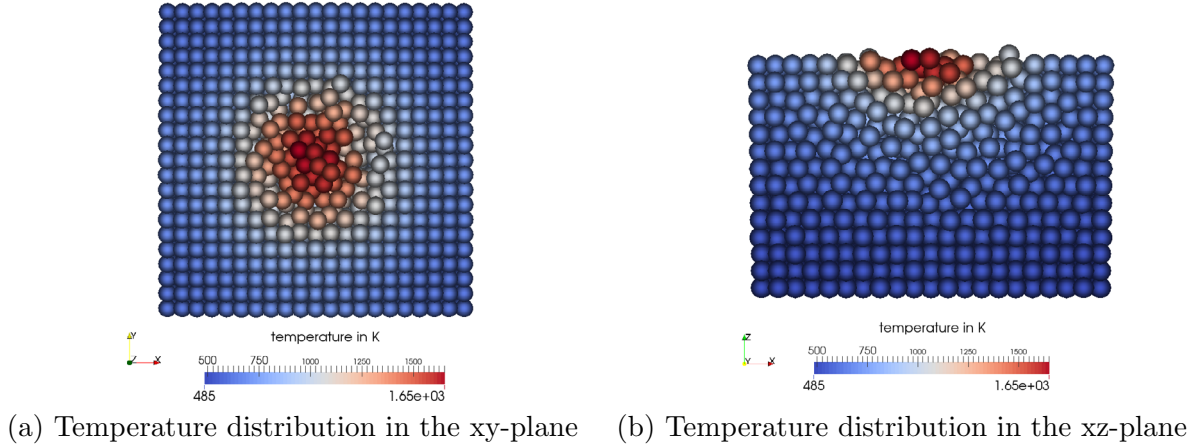
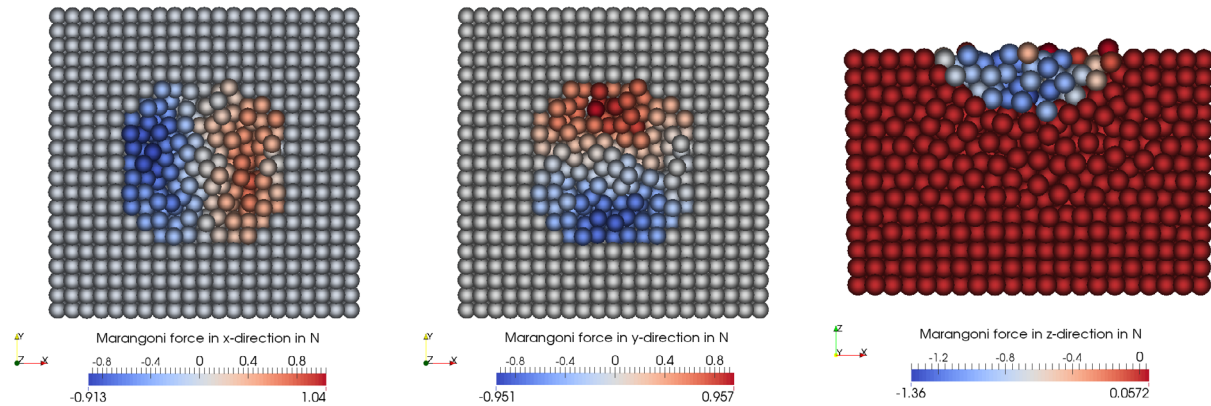
The explicit time integration scheme has to fulfill the Courant-Friedrichs-Lowy condition [4] for the maximum time step to achieve stable results. The limiting factor for the time step is the speed of sound of the material. To reduce the computation time, the speed of sound may be decreased, if the analysis of thermal effects is in the focus and the error in the coupling term of Eq. (11) may be neglected.

3.1 Static heat source

First, we simulate the process of laser spot welding where a static laser beam irradiates the workpiece for 15 ms. The initial temperature distribution is homogeneous at 293 K, no additional temperature boundary conditions are set. The temperature distribution after the heating process is shown in Figure 1. The effect of the Gaussian distribution of the laser radiation on the resulting temperature field is clearly visible.

The Marangoni force acting in the melt flow due to a temperature-dependent surface tension coefficient is plotted in Figure 2. The molten material flows in the negative direction of the temperature gradient and the Marangoni force in x and y-direction have their maxima near the solid-liquid interface. In z-direction, the force is negative with no distinct minimum value.

The resulting spot weld dimensions are visualized in Figure 3, which shows the workpiece after the solidification has completed. The particles in red were melted during the heating process and solidified to form the spot weld, whereas the particles in blue stayed


 Figure 1: Temperature distribution at $t = 15$ ms

 Figure 2: Marangoni force in x-, y-, and z-direction at $t = 15$ ms

solid during the welding process. The spot weld has a smaller depth than its radius, which is typical for conduction mode laser welding. The roughness of the surface after the weld solidified can be seen in the results.

3.2 Moving heat source

Next we investigate the process of seam welding where the laser beam is moved along a straight trajectory with a constant velocity of 1 m/min. At the beginning, the workpiece has the ambient temperature of 293 K. Through the moving laser beam, the material begins to melt and a weld pool with constant width and depth is formed. The shape of the weld pool and the position of the heat source after 50 ms can be seen in Figure 4(a). The effect of the surface tension force is noticeable at the border of the weld pool, since

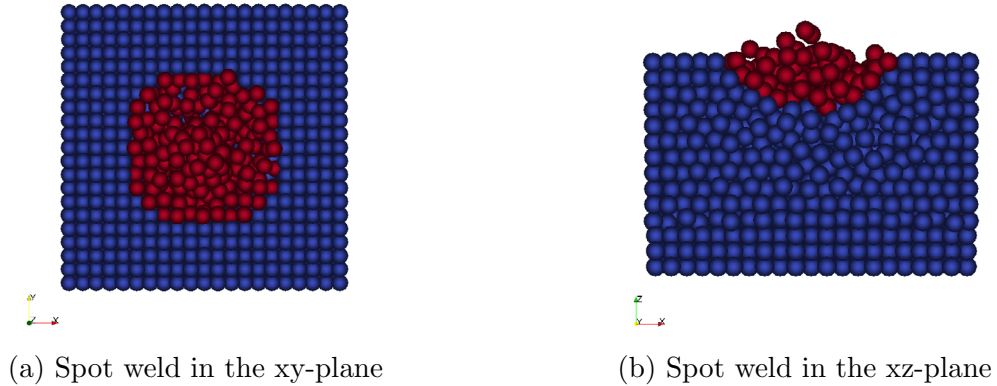


Figure 3: Resulting spot weld colored in red

all particles are held together and the border particles do not move in the negative z-direction due to gravity. Figure 4(b) shows the corresponding temperature distribution in the xy-plane.

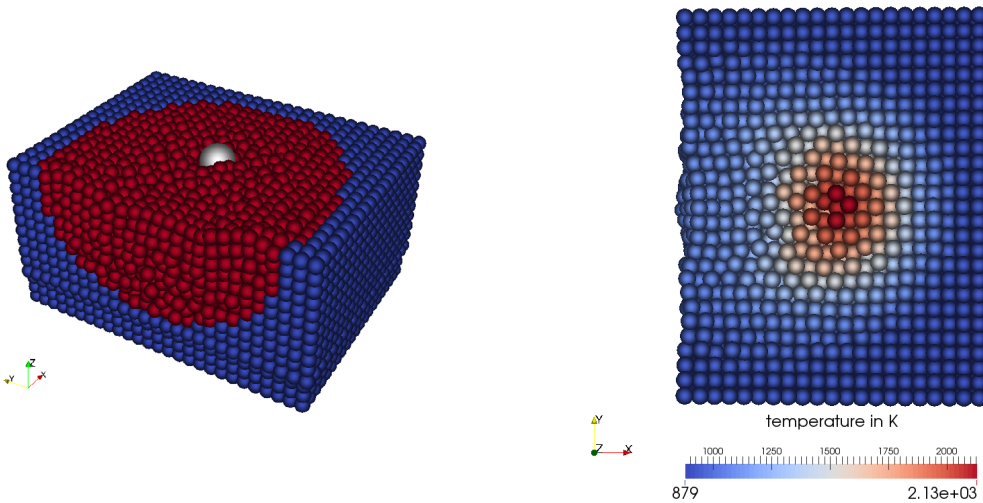


Figure 4: Weld pool and temperature distribution at $t = 50$ ms

The Marangoni force at $t = 50$ ms in the case of a moving laser beam where the temperature gradient is constantly changing with time, is visualized in Figure 5. In the vicinity of the laser beam, the particles are accelerated in radial direction with the maximum force acting at the distance r_s . The value of the force in positive x-direction is slightly larger than in the negative direction, which is a consequence of the moving heat source. The force in z-direction has its minimum at the center of the heat source.

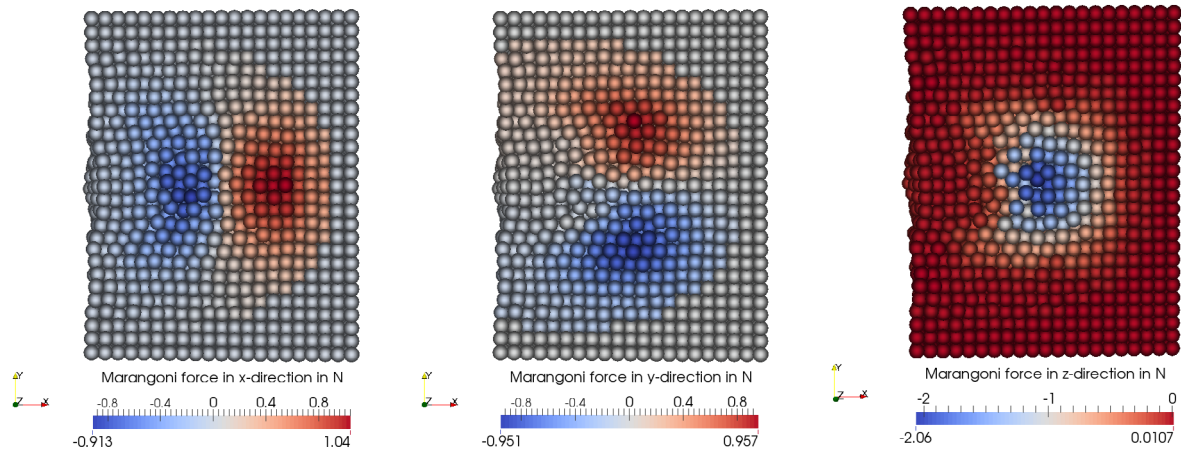


Figure 5: Marangoni force in x-, y-, and z-direction at $t = 50$ ms (view at xy-plane)

4 CONCLUSIONS

The process of conduction mode laser welding may be simulated with SPH and the obtained results are plausible. Compared to mesh-based methods, the advantage of using SPH lies in the relatively simple conversion from a solid to a fluid particle, the modeling of the free-surface melt flow, and the fluid-structure interaction. With welding simulations, the influence and sensitivity of each process parameter or material property on the weld pool dimensions and resulting weld can be investigated. Optimal process parameters like welding speed and laser power may be found for each welding application. The maximum temperature during the whole process can be monitored which might be useful for heat sensitive components that must not exceed a critical temperature value. For a quantitative validation, experiments under real operating conditions are planned to be carried out.

A multi-phase SPH formulation that is able to handle large density differences is in development. Then, the welding of different materials, e.g. steel and aluminum, could be simulated as well. Also, the modeling of laser deep penetration welding is in progress. For this physically much more complex welding technique, the liquid-vapor phase transition and the interaction of three different phases have to be modeled to achieve feasible results.

ACKNOWLEDGEMENT

The research leading to the presented results has received funding from the German Research Foundation (DFG) under the project EB 195/13-1 “Modeling of the capillary in laser beam penetration welding with the Smoothed Particle Hydrodynamics Method”. This support is highly appreciated. Helpful discussions with our project partners, especially Peter Berger of the Institut für Strahlwerkzeuge (IFSW), University of Stuttgart, are also gratefully acknowledged.

REFERENCES

- [1] Batchelor, G.K.: An Introduction to Fluid Dynamics. Cambridge University Press, Cambridge (1974).
- [2] Brackbill, J.U., Kothe, D.B., Zemach, C.: A Continuum Method for Modeling Surface Tension. *Journal of Computational Physics* **100**(2), 335–354 (1992).
- [3] Cleary, P.W., Monaghan, J.J.: Conduction Modelling Using Smoothed Particle Hydrodynamics. *Journal of Computational Physics* **148**, 227–264 (1999).
- [4] Courant, R., Friedrichs, K. and Lewy H.: On the Partial Difference Equations of Mathematical Physics. *IBM Journal of Research and Development* **11**(2), 215–234 (1967).
- [5] Doghri, I.: Mechanics of Deformable Solids. Springer, Berlin (2000).
- [6] Eringen, A.C.: Mechanics of Continua. Wiley, New York (1967).
- [7] Fleißner, F.: Parallel Object Oriented Simulation with Lagrangian Particle Methods. Doctoral Thesis, Institute of Engineering and Computational Mechanics, University of Stuttgart. Shaker, Aachen (2010).
- [8] Gingold, R.A., Monaghan, J.J.: Smoothed Particle Hydrodynamics: Theory and Application to Non-Spherical Stars. *Monthly Notices of the Royal Astronomic Society* **181**, 375–389 (1977).
- [9] Hauke, G.: An Introduction to Fluid Mechanics and Transport Phenomena. Springer Netherlands, Dordrecht (2008).
- [10] Hu, H., Argyropoulos, S.A.: Mathematical Modelling of Solidification and Melting: A Review. *Modelling and Simulation in Materials Science and Engineering* **4**, 371–396 (1996).
- [11] Hügel, H., Graf, T.: Laser in der Fertigung – Grundlagen der Strahlquellen, Systeme, Fertigungsverfahren. Springer Vieweg, Wiesbaden (2014).
- [12] Liu, G., Liu, M.: Smoothed Particle Hydrodynamics – A Meshfree Particle Method. World Scientific Publishing, Singapore (2003).
- [13] Liu, M., Shao, J., Li, H.: Numerical Simulation of Hydro-Elastic Problems with Smoothed Particle Hydrodynamics Method. *Journal of Hydrodynamics, Ser. B* **25**(5), 673–682 (2013).
- [14] Lobovský, L.; Groenenboom, P.H.L.: Smoothed Particle Hydrodynamics Modelling in Continuum Mechanics: Fluid-Structure Interaction. *Applied and Computational Mechanics* **3**(1), 101–110 (2009).

- [15] Lucy, L.B.: A Numerical Approach to the Testing of the Fission Hypothesis. *The Astronomical Journal* **82**(12), 1013–1024 (1977).
- [16] Monaghan, J.J.: Smoothed Particle Hydrodynamics. *Annual Reviews in Astronomy and Astrophysics* **30**, 543–574 (1992).
- [17] Monaghan, J.J.: SPH without a Tensile Instability. *Journal of Computational Physics* **159**, 290–311 (2000).
- [18] Monaghan, J.J.: Smoothed Particle Hydrodynamics. *Reports on Progress in Physics* **68**, 1703–1759 (2005).
- [19] Monaghan, J.J., Gingold, R.A.: Shock Simulation by the Particle Method SPH. *Journal of Computational Physics* **52**, 374–389 (1983).
- [20] Monaghan, J.J., Huppert, H., Worster, M.: Solidification Using Smoothed Particle Hydrodynamics. *Journal of Computational Physics* **205**, 684–705 (2005).
- [21] Monaghan, J.J., Kos, A., Issa, N.: Fluid Motion Generated by Impact. *Journal of Waterway* **129**(6), 250–259 (2003).
- [22] Morris, J.P., Fox, P.J., Zhu, Y.: Modeling Low Reynolds Number Incompressible Flows Using SPH. *Journal of Computational Physics* **136**, 214–226 (1997).
- [23] Pasimodo: http://www.itm.uni-stuttgart.de/research/pasimodo/pasimodo_en.php. Accessed May 26, 2015.
- [24] Steen, W.M., Mazumder, J.: *Laser Material Processing*. Springer, London (2010).
- [25] Tong, M., Browne, D.J.: An Incompressible Multi-Phase Smoothed Particle Hydrodynamics (SPH) Method for Modelling Thermocapillary Flow. *International Journal of Heat and Mass Transfer* **73**, 284–292 (2014).

ADAPTIVE REFINEMENT TECHNIQUE FOR DISCRETE STATIC MODELS OF FRACTURE

JAN ELIÁŠ

Brno University of Technology, Faculty of Civil Engineering
Veverí 331/95, Brno, 60200, Czech Republic
elias.j@fce.vutbr.cz, <http://www.fce.vutbr.cz/STM/elias.j/>

Key words: discrete model, random geometry, statics, adaptivity, discretization, concrete

Abstract. The discrete static models are advantageously used for fracture simulations in heterogeneous materials. These simulations are often extremely computationally demanding. The contribution aims to reduction of computational cost via adaptivity in construction of the discrete model geometry. The simulation starts with coarse discretization that provides correct elastic behavior; the discretization is adaptively refined during the simulation in regions that suffer high stresses.

1 INTRODUCTION

Discrete representation of materials is a natural alternative to continuous approaches. A collection of interconnected rigid cells organized into a net structure is often called discrete or lattice model. Lattice models are being used in several versions; we focus here only on static models with lattices of random geometry based on Voronoi tessellation, such as [1, 2, 3].

The fine discretization of the discrete model leads to extreme computational demands, but it is often necessary; especially when it is related to meso-scale structure of the simulated material. The contribution presents a technique to adaptively refine model discretization. Without this tool, it is necessary to densely discretize the whole domain and therefore to create computationally demanding model. Availability of adaptive refinement allows starting simulation with coarse discretization and refining it adaptively during simulation run.

Successful attempts to introduce this important feature already exist [4, 5]. They are based on adaptive replacement of some continuous model with the discrete one, but problematic interface between continuum and discrete model is involved and the discrete model has to have regular geometry (that produces directional bias).

Another approach is proposed here. The adaptive refinement is performed within the discrete lattice model only and allows using irregular geometry based on Voronoi

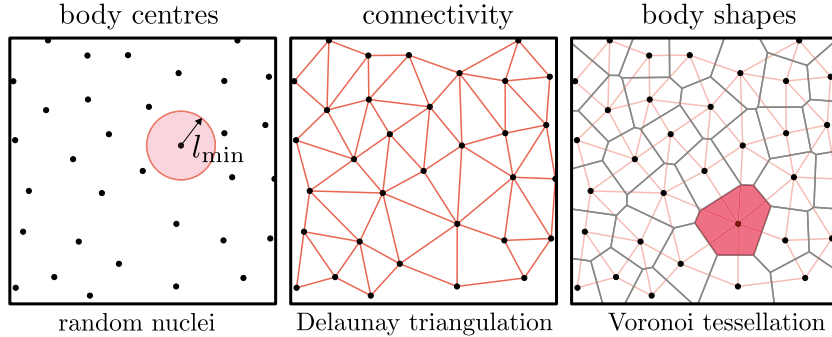


Figure 1: Model geometry obtained by Voronoi tessellation on randomly placed nuclei with restricted minimum distance l_{\min} , 2D sketch.

tessellation. The algorithm works as follows. Initially, the whole domain is coarsely discretized. Whenever any region of the coarse model exceeds some criterion based on the equivalent stress, the coarse discretization in its vicinity is replaced by the finer one and some transitional area connecting the coarse and fine discretization is inserted around. The rest of the domain discretization will remain the same. Finally, comparison of adaptively discretized and fully densely discretized models is presented.

2 RANDOM GEOMETRY OF THE MODEL

The model geometry is random to avoid directional bias that occur in any regular structure. Domain of the modeled element is filled by nuclei with randomly generated positions. These nuclei are added sequentially and accepted only when distances to previously placed nuclei are greater than chosen parameter l_{\min} , see Fig. 1. The parameter l_{\min} controls discretization density and therefore it should correspond to the size of heterogeneities in the material (e.g. aggregate diameter). Varying discretization density in the model can be achieved by spatial varying the parameter l_{\min} . Each of the nuclei will serve as center of one rigid body and three translational \mathbf{u} and three rotational $\boldsymbol{\theta}$ degrees of freedom (DOF) will be associated with it.

The domain is considered as saturated by nuclei when new nucleus is rejected for large number of subsequent trials. Delaunay triangulation that provides connectivity between the nuclei is performed. Dual diagram of Voronoi tessellation then provides geometry of the rigid bodies, see Fig. 1. Rigid bodies has common contact facets that are perpendicular to their connections; facet centroids are denoted \mathbf{c} , see Fig. 2.

3 LINEAR ELASTIC BEHAVIOR

The elastic behavior of the discrete system is *independent* on discretization density. This statement is fundamental assumption of the adaptive technique, but it is not obvious. The proof and numerical verification is delivered here.

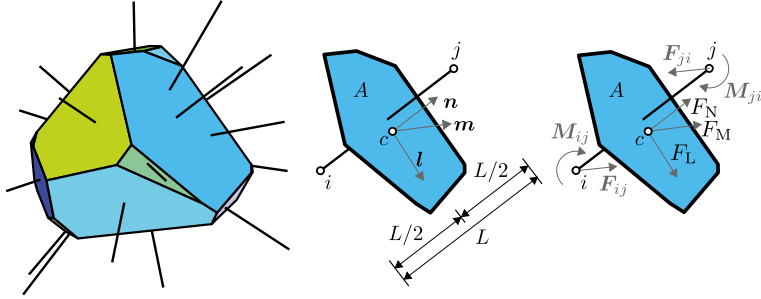


Figure 2: One discrete body of random geometry and one contact facet between nuclei i and j - normal and tangential directions and forces.

3.1 Scaling of elastic problem

This section is based on work [6], from which it adopts both notation and theory.

Let us analyze one contact between nuclei i and j of coordinates $\mathbf{x}_i = [x_{1i}, x_{2i}, x_{3i}]^T$ and \mathbf{x}_j with central point \mathbf{c} , elastic modulus E and length L , see Fig. 2. The translations of point i are denoted $\mathbf{u}_i = [u_{1i}, u_{2i}, u_{3i}]^T$ and rotations are $\boldsymbol{\theta}_i = [\theta_{1i}, \theta_{2i}, \theta_{3i}]^T$. Then from rigid body motion (assuming small rotations), position of any point \mathbf{x} inside the body associated with nucleus i can be expressed as

$$\mathbf{u}(\mathbf{x}) = \mathbf{u}_i + \boldsymbol{\theta}_i \times (\mathbf{x} - \mathbf{x}_i) = \mathbf{A}_i(\mathbf{x}) \begin{bmatrix} \mathbf{u}_i \\ \boldsymbol{\theta}_i \end{bmatrix} \quad (1)$$

with matrix $\mathbf{A}_i(\mathbf{x})$ being

$$\mathbf{A}_i(\mathbf{x}) = \begin{bmatrix} 1 & 0 & 0 & 0 & x_3 - x_{3i} & x_{2i} - x_2 \\ 0 & 1 & 0 & x_{3i} - x_3 & 0 & x_1 - x_{1i} \\ 0 & 0 & 1 & x_2 - x_{2i} & x_{1i} - x_1 & 0 \end{bmatrix} \quad (2)$$

Displacement jump Δ_{ij} between bodies i and j is measured by their separation at common facet centroid \mathbf{c} . Therefore, it can be expressed as

$$\Delta_{ij} = [\Delta_{1ij} \ \Delta_{2ij} \ \Delta_{3ij}]^T = \mathbf{A}_j(\mathbf{c}) \begin{bmatrix} \mathbf{u}_j \\ \boldsymbol{\theta}_j \end{bmatrix} - \mathbf{A}_i(\mathbf{c}) \begin{bmatrix} \mathbf{u}_i \\ \boldsymbol{\theta}_i \end{bmatrix} \quad (3)$$

Based on displacement jumps, contact forces are calculated. Three contact forces acting at point \mathbf{c} in normal direction, \mathbf{n} , and two tangential directions, \mathbf{m} and \mathbf{l} , are given by

$$\mathbf{F} = [F_N \ F_M \ F_L]^T = \left[\frac{\mathbf{n}^T \Delta_{ij} E A}{L} \ \frac{\mathbf{m}^T \Delta_{ij} \alpha E A}{L} \ \frac{\mathbf{l}^T \Delta_{ij} \alpha E A}{L} \right]^T \quad (4)$$

Model parameter α controls the macroscopic Poisson's ratio.

Forces and moments acting on nuclei i (\mathbf{F}_{ij} and \mathbf{M}_{ij}) and j (\mathbf{F}_{ji} and \mathbf{M}_{ji}) due to contact ij can be obtained from principle of virtual work

$$\begin{bmatrix} \mathbf{F}_{ij} \\ \mathbf{M}_{ij} \end{bmatrix}^T \begin{bmatrix} \delta\mathbf{u}_i \\ \delta\boldsymbol{\theta}_i \end{bmatrix} + \begin{bmatrix} \mathbf{F}_{ji} \\ \mathbf{M}_{ji} \end{bmatrix}^T \begin{bmatrix} \delta\mathbf{u}_j \\ \delta\boldsymbol{\theta}_j \end{bmatrix} = \begin{bmatrix} F_N \\ F_M \\ F_L \end{bmatrix}^T \begin{bmatrix} \mathbf{n}^T \delta\Delta_{ij} \\ \mathbf{m}^T \delta\Delta_{ij} \\ \mathbf{l}^T \delta\Delta_{ij} \end{bmatrix} \quad (5)$$

where δ denotes the virtual quantities. Substitution of equation (3) provides

$$\begin{bmatrix} \mathbf{F}_{ij} \\ \mathbf{M}_{ij} \end{bmatrix}^T = -F_N \mathbf{n}^T \mathbf{A}_i(c) - F_M \mathbf{m}^T \mathbf{A}_i(c) - F_L \mathbf{l}^T \mathbf{A}_i(c) \quad (6)$$

$$\begin{bmatrix} \mathbf{F}_{ji} \\ \mathbf{M}_{ji} \end{bmatrix}^T = F_N \mathbf{n}^T \mathbf{A}_j(c) + F_M \mathbf{m}^T \mathbf{A}_j(c) + F_L \mathbf{l}^T \mathbf{A}_j(c) \quad (7)$$

The equilibrium must be achieved in every nuclei when contribution from all contacts and external forces are summarized.

Now, what happen when the whole problem is scaled in all three dimensions by factor ξ . Then, coordinates, contact lengths and areas becomes $\bar{\mathbf{x}} = \xi \mathbf{x}$, $\bar{L} = \xi L$ and $\bar{A} = \xi^2 A$. The matrix $\bar{\mathbf{A}}$ has now form

$$\bar{\mathbf{A}}_i(\mathbf{x}) = \begin{bmatrix} 1 & 0 & 0 & 0 & \xi(x_3 - x_{3i}) & \xi(x_{2i} - x_2) \\ 0 & 1 & 0 & \xi(x_{3i} - x_3) & 0 & \xi(x_1 - x_{1i}) \\ 0 & 0 & 1 & \xi(x_2 - x_{2i}) & \xi(x_{1i} - x_1) & 0 \end{bmatrix} \quad (8)$$

To induce the same stress level in the scaled domain, the external force load must scale with the same factor ($\bar{\mathbf{F}}_e = \xi^2 \mathbf{F}_e$) as areas. We now search for displacements and rotations $\bar{\mathbf{u}}$ and $\bar{\boldsymbol{\theta}}$ that satisfy equilibrium in all nuclei.

Apparently, the unknown DOF are $\bar{\mathbf{u}} = \xi \mathbf{u}$ and $\bar{\boldsymbol{\theta}} = \boldsymbol{\theta}$, i.e. translations are linearly scaled and rotations remains unchanged. Plugging this solution into Eqs. (6) and (7), the nodal forces are scaled with ξ^2 while the moments with ξ^3 . The nodal equilibrium then yields

$$\bar{\mathbf{F}}_e + \sum_j \bar{\mathbf{F}}_{ij} = \xi^2 \left(\mathbf{F}_e + \sum_j \mathbf{F}_{ij} \right) = \mathbf{0} \quad (9)$$

$$\bar{\mathbf{M}}_e + \sum_j \bar{\mathbf{M}}_{ij} = \xi^3 \left(\mathbf{M}_e + \sum_j \mathbf{M}_{ij} \right) = \mathbf{0} \quad (10)$$

based on equilibrium achieved in the original unscaled problem.

Let us now estimate the macroscopic elastic modulus \tilde{E} and Poisson's ratio ν . These two variables relates the stresses and strains in the structure. Since both stresses (forces scaled with ξ^2 over areas scaled with ξ^2 as well) and strains (deformations scaled with ξ over length scaled with ξ as well) remain unchanged, also the elastic modulus and Poisson's ratio on discretization with $\bar{l}_{min} = \xi l_{min}$ are constant for arbitrary ξ .

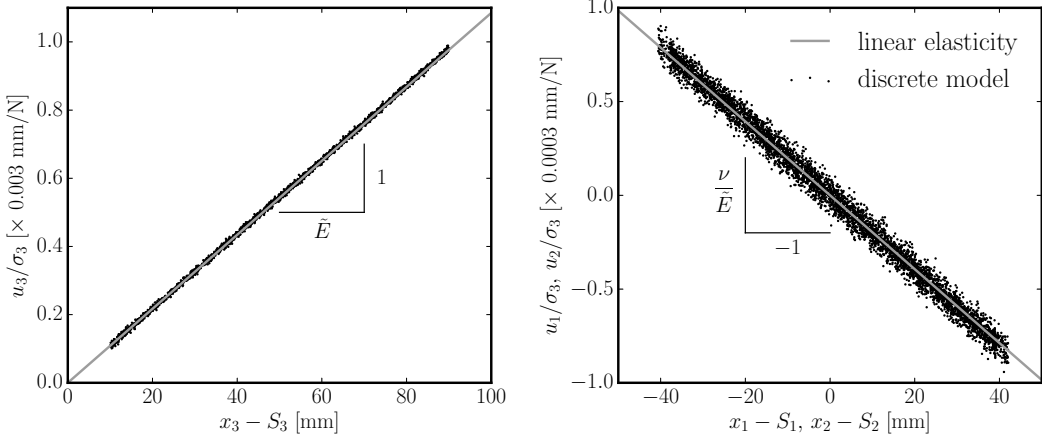


Figure 3: Estimation of macroscopic elastic constants via least square fitting of deformation field.

3.2 Numerical verification

The analytically derived conclusion is verified numerically here. Volume $100 \times 100 \times 100 \text{ mm}^3$ is compressed by low level stress σ_3 in z direction. Assuming ideally homogeneous material, constant stress over the whole domain with the only nonzero component σ_3 is obtained and the strain field is constant as well having three nonzero components

$$\begin{bmatrix} \varepsilon_1 & \varepsilon_2 & \varepsilon_3 \end{bmatrix}^T = \frac{\sigma_3}{\tilde{E}} \begin{bmatrix} -\nu & -\nu & 1 \end{bmatrix}^T \quad (11)$$

with \tilde{E} and ν being the macroscopic elastic modulus and Poisson's ratio. The deformation field can be obtained from strains

$$u_i = \varepsilon_i(x_i - S_i) \quad (12)$$

with $i \in \{1, 2, 3\}$ being the Cartesian coordinates and S_i coordinates of a point that preserves constant position during loading. The point S is typically known from the boundary conditions.

Combining Eqs. (11) and (12), the following equalities hold

$$\frac{u_1}{\sigma_3} = -\frac{\nu}{\tilde{E}}(x_1 - S_1) \quad \frac{u_2}{\sigma_3} = -\frac{\nu}{\tilde{E}}(x_2 - S_2) \quad \frac{u_3}{\sigma_3} = \frac{1}{\tilde{E}}(x_3 - S_3) \quad (13)$$

These equations offer simple way to determine macroscopic elastic modulus and Poisson's ratio. Simulating the compressed cube using the discrete model, one can simply obtain deformations u_i and locations x_i . Then, least square fitting can be performed to determine the unknown elastic constants. The fitting is shown in Fig. 3. Meso-scopic elastic modulus was $E = 48 \text{ GPa}$ and $\alpha = 0.29$.

Several discretization densities were tested and macroscopic elastic parameters were fitted. The results are shown in Fig. 4 where the mean value and the standard deviation of

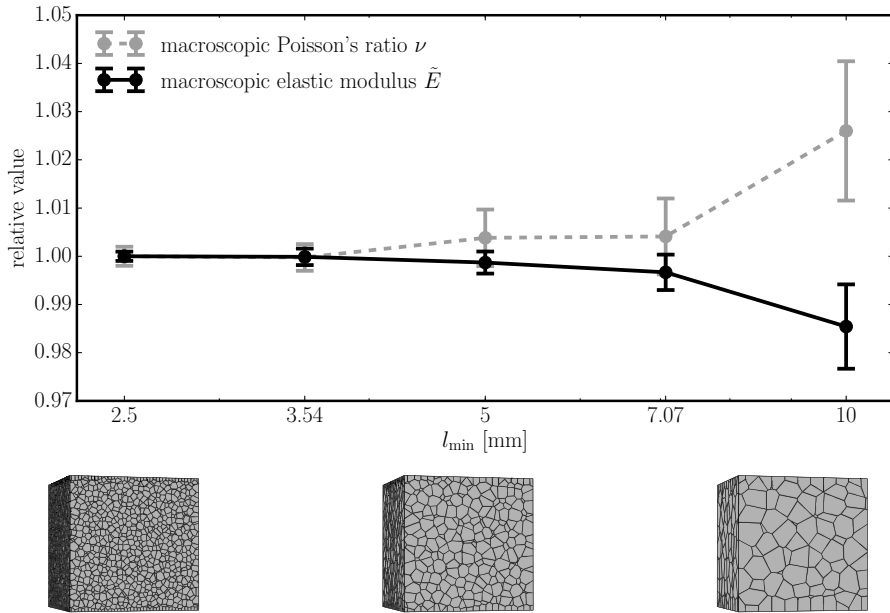


Figure 4: Elastic constants identified on discrete system with different discretization density l_{\min} .

relative quantity (with respect to the one obtained with smallest l_{\min}) from 20 realization are computed for every considered l_{\min} . One can see that

- the difference between values of both elastic modulus and Poisson's ratio are within $\pm 3\%$. Therefore, one can conclude that elastic behavior of the particle system is independent on discretization density.
- the standard deviation decreases with decreasing l_{\min} . This is because as the number of bodies in the model increases, the response becomes less sensitive to the random location of the nuclei.
- there is certain convergence pattern. This has to be attributed to the boundary effect. The rigid bodies at the boundary have slightly different shapes as they have one or more sides determined by the boundary planes. Therefore, they have slightly different elastic properties. With increasing density of the discretization, this boundary layer occupies lower portion of the volume and the effect diminishes.

Especially the last point is important. The elastic behavior is invariant with respect to l_{\min} but not with respect to body shapes, e.g. anisotropic elastic behavior can be expected for bodies elongated in one direction. The discretization has to be also fine enough to account for strain gradients in the model.

4 NON-LINEAR BEHAVIOR

The nonlinear constitutive model applied at facets is based on damage parameter D ranging from 0 (healthy material) to 1 (completely damage material). The details of the

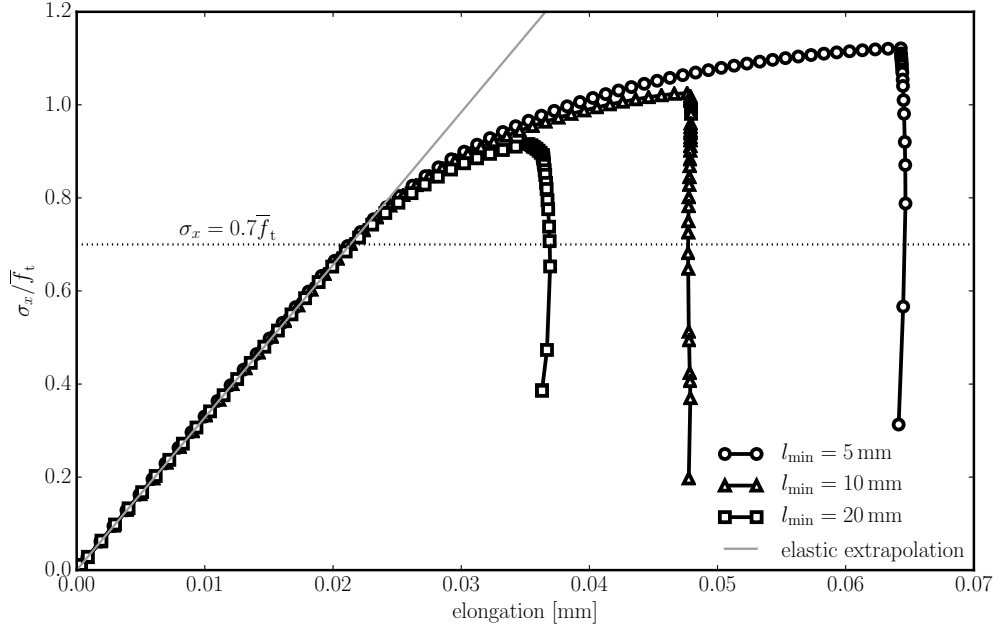


Figure 5: Response of discrete system loaded in tension.

nonlinear constitutive equations are not provided here since these are not crucial for the presented concept of adaptivity. The nonlinear behavior model is again adopted from works of Gainluca Cusatis [7, 8, 6, 9]. Fracture parameters of the model were taken from simulations [10] of large experimental series [11, 12, 13] on concrete. The meso-scopic tensile strengths in tension and shear were 2.66 MPa and 7.98 MPa, the meso-scopic fracture energies in tension and shear were 20 J m^{-2} and 320 J m^{-2} .

Contrary to the linear elastic behavior, the nonlinear behavior of the model is *dependent* on discretization density. This is, however, understood as beneficial. The model discretization should correspond to the material heterogeneity and therefore dependence on l_{\min} reflects changes in material behavior due different grain size.

Simple tension simulations were performed to investigate effect of discretization in nonlinear regime. The beam cross-section was $100 \times 100 \text{ mm}^2$ and length was 400 mm. The relative stress in the beam is calculated as the loading force divided by cross-section area (0.01 m^2) and meso-level tensile strength ($f_t = 2.66 \text{ MPa}$). Beam elongation against the relative beam stress is plotted in Fig. 5. The finer the discretization, the higher the strength. However, until approximately 70% of the relative stress, all the models remain elastic.

5 ADAPTIVE DISCRETIZATION REFINEMENT

Two types of nuclei are distinguished. Those that belong to fine discretization region of target density $l_{\min} = l_f$ and the others. Initially, the coarse discretization is performed using $l_{\min} = l_c$ and all nuclei belongs to the latter group. Non-linear behavior is allowed

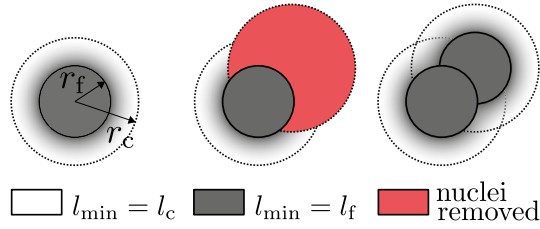


Figure 6: Adaptive refinement of discretization in steps.

only at facets connecting nuclei from the former group, any connection that involves nucleus from coarser discretization behaves linearly elastic.

The adaptive refinement of discretization is performed within sphere of radius r_c . All nuclei that belongs to this sphere but not to the fine discretization are removed. Then, new nuclei are added using the same procedure as described in Sec. 2. The parameter l_{\min} is set to l_f inside inner sphere of radius r_f and is linearly changing with distance from the sphere center r

$$l_{\min} = \begin{cases} l_f & \text{for } r < r_f \\ l_f + r \frac{l_c - l_f}{r_c - r_f} & \text{otherwise} \end{cases} \quad (14)$$

Described replacement of nuclei is schematically shown in Fig. 6. The linear transition from coarse to fine discretization is included to keep the shape of the bodies approximately the same in statistical sense. If the transitional regime is omitted, the sharp change in discretization density would produce significantly elongated body shapes, directional bias and anisotropy.

On the newly created nuclei, triangulation and tessellation is performed. New system stiffness matrix is assembled and calculation continues. The damaged connections are only between nuclei from fine discretization that were not affected by the discretization refinement and therefore all the state variables are automatically transferred to the new discrete system.

Last component of the adaptivity algorithm is the decision where and when the refinement should take place. The straightforward way would be to check all the connections from the coarse discretization and build the adaptivity criterion on the level of equivalent stress reached at the facets. This would however lead to refinement of the model in excessively many regions. Due to random discretization, some of the facet suffer high equivalent stress even under low far field stress. To identify the regions of high stress more robustly, application of some stress averaging is reasonable.

Therefore, refinement criteria is base on an average stress in rigid bodies. The fabric stress tensor can be utilized to evaluate average stress tensor components in body i

$$\sigma_{kl}^{(i)} = \frac{1}{V^{(i)}} \sum_j F_k^{(ij)} c_l^{(ij)} \quad (15)$$

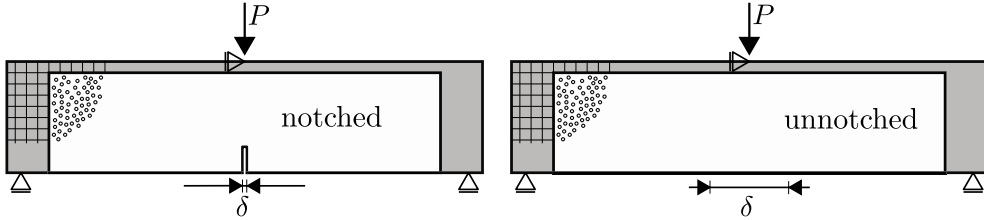


Figure 7: Beam subjected to three-point bending with notch (left) and without notch (right).

where j runs over all nuclei in contact with nucleus i ; k and l are Cartesian coordinates, \mathbf{F} is a vector of contact force and \mathbf{c} is centroid of contact facet.

The Mazar's equivalent stress [14] serves as measure of the stress level in the body

$$\sigma_{\text{eq}} = \sqrt{\sum_{p=1}^{\text{III}} \langle \sigma_p \rangle^2} \quad (16)$$

with $\sigma_{\text{I-III}}$ being the principal stresses and $\langle \cdot \rangle$ returning the positive part of the argument. After every solution step, stress tensors in all rigid bodies belonging to coarse discretization are evaluated (Eq. (15)). Then, principal stresses and equivalent stresses (Eq. (16)) are calculated. Whenever $\sigma_{\text{eq}}/f_t > \gamma$, the discretization os adapted and the nuclei associated with that rigid body serves as a center of the refinement sphere.

The adaptivity model brings additional 4 parameters: coarse discretization density l_c , radii l_c and l_f and relative stress limit γ . Based on uniaxial tension simulations, reasonable limit seems to be $\gamma = 0.7$.

6 EXAMPLE

Proposed adaptive algorithm is tested on simulation of three-point bending tests. The beams had 200 mm in depth, 800 mm in span and thickness was 100 mm. Two variants were considered: notched variant with relative notch depth 0.25 and unnotched variant. The geometry of the beam as well as area where the discrete model was applied is shown in Fig. 7.

The same material parameters as in Sec. 3.2 and 4 of the model were used. Fine discretization density was set to $l_f = 10$ mm, the coarse one was $l_c = 20$ mm, radii of adapted region were $r_f = 60$ mm and $l_f = 120$ mm, limit for refinement was kept $\gamma = 0.7$. The adaptive model response is compared with response of finely discretized model, that serves as a reference solution.

Figure 8 shows response of the reference and adaptive model for both notched (left) and unnotched (right) beams. The blue circles highlight steps where refinement was performed. In linear part and initial nonlinear part of the diagrams the adaptive and reference model coincide. However, the peak load is different. This is attributed to the randomness of the response, the models have different location of the nuclei and therefore

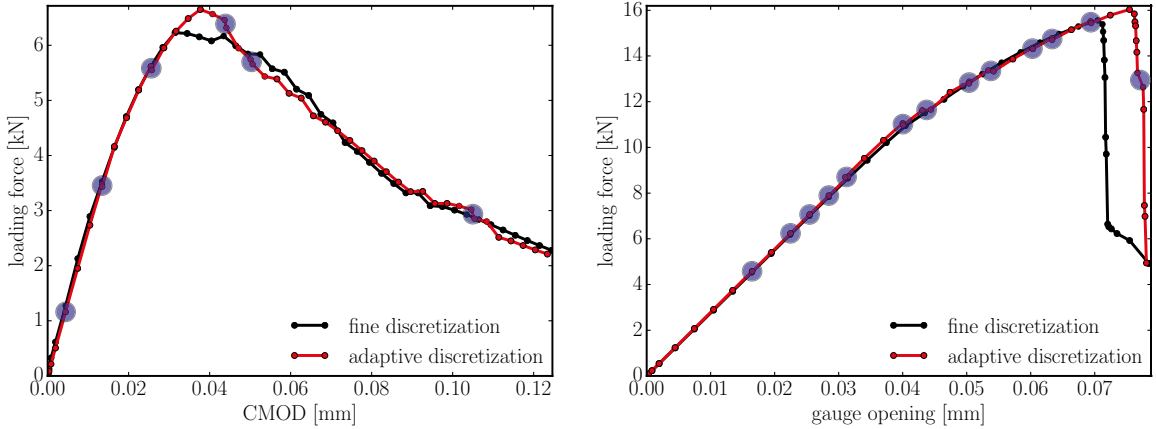


Figure 8: Comparison of responses of beams with notch (left) and without notch (right) with fine discretization and with adaptive discretization refinement.

also different response. Further simulations will be performed to show whether the mean value and also variance of the peak load from the adaptive model matches those from the reference model.

Finally, Fig. 6 shows crack patterns developed in both models. Three stages - initial, at the peak load and at the end of the simulation - are presented. Number of DOF at each stage is listed bellow the figures. Finely discretized model has about 50000 DOF during the whole simulation. Adaptive models starts at 9000 (approx. 1/8 as the l_{\min} is doubled) but number of DOF increases during refinements.

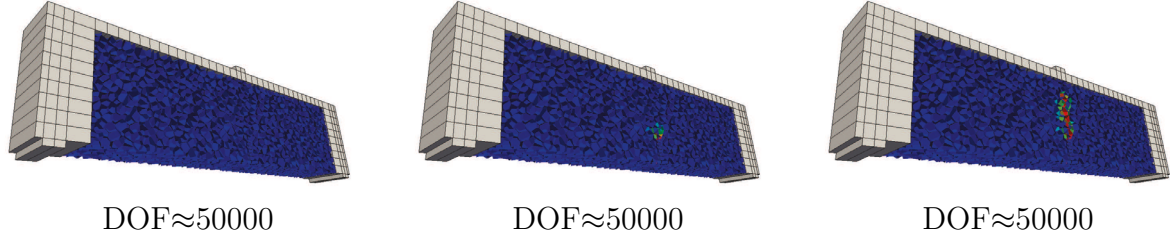
7 CONCLUSIONS

- The adaptive discretization refinement for discrete meso-scale models of fracture was presented. The adaptivity is performed in model of random geometry created via Voronoi tessellation.
- The developed approach was verified on simulations of beams subjected to three-point bending. Significant time savings were achieved.
- Presented concept of adaptivity can be successfully applied in problems where material non-linearity is localized into small portion of the modeled element, but the location of that region is not known in advance.

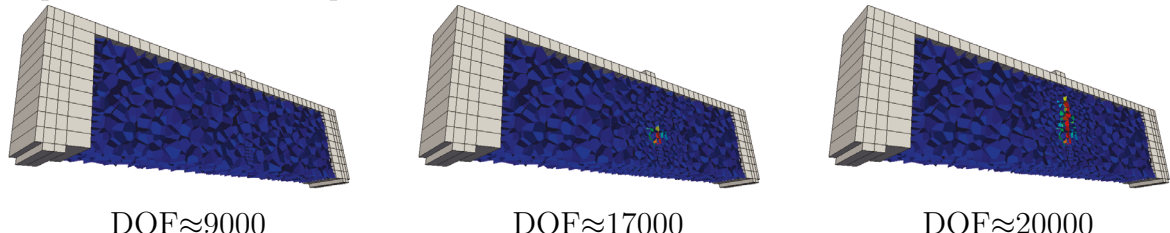
ACKNOWLEDGEMENT

The financial support provided by the Czech Science Foundation under project No. 15-19865Y is gratefully acknowledged.

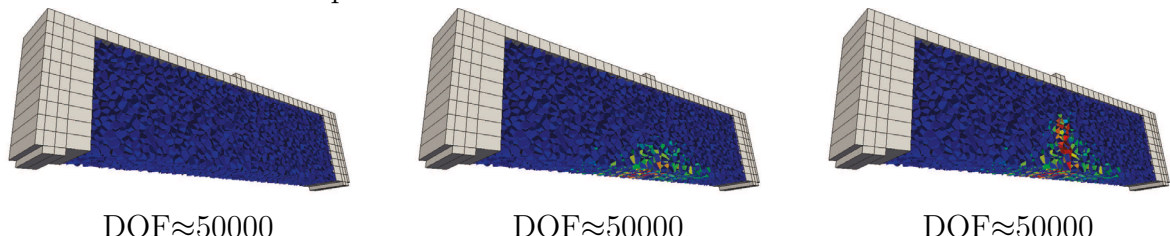
- notched beam - fine discretization



- opennotched beam - adaptive discretization



- unnotched beam - adaptive discretization



- unnotched beam - adaptive discretization

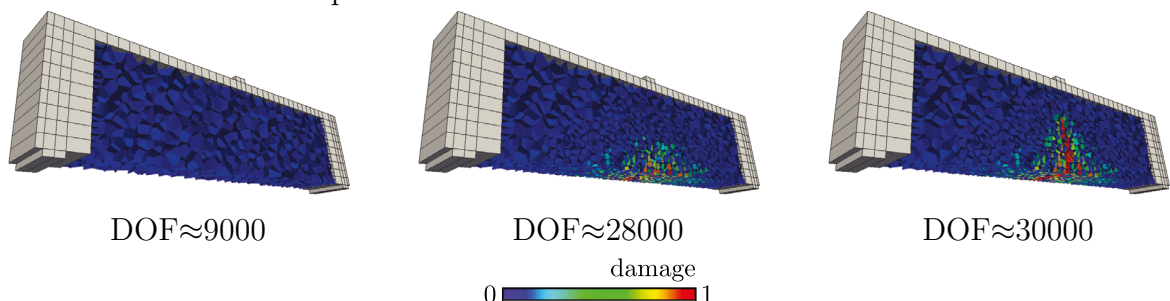


Figure 9: Damage patterns developed during simulations. Two stages are shown - in the solution step when the maximum load was reached and at the end of the simulation. Approximate number of DOF in the simulation stages is written below.

REFERENCES

- [1] J. E. Bolander and S. Saito. Fracture analyses using spring networks with random geometry. *Eng. Fract. Mech.*, 61:1569–591, 1998. ISSN 0013-7944. doi: 10.1016/S0013-7944(98)00069-1.
- [2] Y. H. Gedik, H. Nakamura, Y. Yamamoto, and M. Kunieda. Evaluation of three-dimensional effects in short deep beams using a rigid-body-spring-model. *Cement Concrete Comp.*, 33:978–991, 2011. ISSN 0958-9465.
- [3] Jan Eliáš and Jia-Liang Le. Modeling of mode-i fatigue crack growth in quasibrittle structures under cyclic compression. *Eng. Fract. Mech.*, 96:26–36, 2012. ISSN 0013-7944. doi: <http://dx.doi.org/10.1016/j.engfracmech.2012.06.019>.
- [4] J. Bolander, T. Shiraishi, and Y. Isogawa. An adaptive procedure for fracture simulation in extensive lattice networks. *Eng. Fract. Mech.*, 33:325–334, 1996. ISSN 0013-7944. doi: 10.1016/0013-7944(95)00200-6.
- [5] Annika Sorg and Manfred Bischoff. Adaptive discrete-continuous modeling of evolving discontinuities. *Eng. Computation.*, 31(7):1305–1320, 2014. doi: 10.1108/EC-03-2013-0072.
- [6] Gianluca Cusatis, Daniele Pelessone, and Andrea Mencarelli. Lattice discrete particle model (LDPM) for failure behavior of concrete. I: Theory. *Cement Concrete Comp.*, 33(9):881–890, 2011. ISSN 0958-9465.
- [7] Gianluca Cusatis, Zdeněk P. Bažant, and Luigi Cedolin. Confinement-shear lattice CSL model for fracture propagation in concrete. *Comput. Method. Appl. M.*, 195(52):7154–7171, 2006. ISSN 0045-7825.
- [8] Gianluca Cusatis and Luigi Cedolin. Two-scale study of concrete fracturing behavior. *Eng. Fract. Mech.*, 74(12):3–17, 2007. ISSN 0013-7944.
- [9] Gianluca Cusatis, Andrea Mencarelli, Daniele Pelessone, and James Baylot. Lattice discrete particle model (LDPM) for failure behavior of concrete. II: Calibration and validation. *Cement Concrete Comp.*, 33(9):891–905, 2011. ISSN 0958-9465. doi: <http://dx.doi.org/10.1016/j.cemconcomp.2011.02.010>.
- [10] Jan Eliáš, Miroslav Vořechovský, Jan Skoček, and Zdeněk P. Bažant. Stochastic discrete meso-scale simulations of concrete fracture: comparison to experimental data. *Eng. Fract. Mech.*, 135:1–16, 2015. ISSN 0013-7944. doi: 10.1016/j.engfracmech.2015.01.004.

- [11] Christian G. Hoover, Zdeněk P. Bažant, Jan Vorel, Roman Wendner, and Mija H. Hubler. Comprehensive concrete fracture tests: Description and results. *Eng. Fract. Mech.*, 114(0):92–103, 2013. ISSN 0013-7944. doi: <http://dx.doi.org/10.1016/j.engfracmech.2013.08.007>.
- [12] Christian G. Hoover and Zdeněk P. Bažant. Comprehensive concrete fracture tests: Size effects of types 1 & 2, crack length effect and post-peak. *Eng. Fract. Mech.*, 110:281–289, 2013. ISSN 0013-7944. doi: <http://dx.doi.org/10.1016/j.engfracmech.2013.08.008>.
- [13] Roman Wendner, Jan Vorel, Jovanca Smith, Christian G. Hoover, Zdeněk P. Bažant, and Gianluca Cusatis. Characterization of concrete failure behavior: a comprehensive experimental database for the calibration and validation of concrete models. *Mat. Struct.*, pages 1–24, 2014. ISSN 1359-5997. doi: 10.1617/s11527-014-0426-0.
- [14] Jacky Mazars. *Application de la mécanique de l’endommagement au comportement non linéaire et à la rupture du béton structure*. Ph.d. thesis, Université de Paris, 1984.

COMPARISON OF WEAR MODELS USING A LAGRANGIAN APPROACH

Florian Beck and Peter Eberhard

Institute of Engineering and Computational Mechanics, University of Stuttgart,
Pfaffenwaldring 9, 70569 Stuttgart, www.itm.uni-stuttgart.de,
[\[florian.beck, peter.eberhard\]@itm.uni-stuttgart.de](mailto:[florian.beck, peter.eberhard]@itm.uni-stuttgart.de)

Key words: Wear Models, Smoothed Particle Hydrodynamics, SPH, DEM, Abrasive Wear

Abstract. Abrasive wear of hydraulic machines is commonly simulated with grid based methods. In this work we present a mesh-free approach for modeling abrasive wear. The transport fluid is modeled with the Smoothed Particle Hydrodynamics method. The advantage of this method is the simple handling of free surfaces and complex interfaces, e.g., the interface between the fluid and the abrasive particles. The small solid particles and the boundary geometry of the machine are simulated with the Discrete Element Method. The amount of removed material on the boundary geometry is predicted with three wear models with different complexity. We simulate the impact of a free jet with particle loading on a simplified pelton bucket as working example. The resulting wear patterns of the three different wear models are analyzed and compared. In this work we take the parameters for the wear models from literature.

1 Introduction

The surface of hydraulic machines is damaged by different mechanisms. In this work we are taking damage due to abrasive wear into account. Small solid particles are transported by the working fluid and in case of a contact with the surface of the hydraulic machine they cause damage.

There are different approaches for simulating abrasive wear which were applied during the last years. We present a Lagrangian approach and three different wear models. The fluid is modeled with the Smoothed Particle Hydrodynamics (SPH) method, for the loading of the fluid the small solid particles are modeled with the Discrete Element Method (DEM) and we are using the DEM also for the boundary geometry of the machine. The removed material at the boundary is modeled with wear models.

The idea behind predicting abrasive wear with wear models is, that one estimates the amount of removed material due to an impact of a solid particle and stores and updates the value at each boundary discretization point. The wear models take different parameters

like velocity or impact angle into account for calculating the amount of removed material. There are several wear models available in literature which cover the different kind of mechanisms of abrasive wear, e.g., chip building. In this work we compare three of them and analyze the resulting shape of the wear patterns.

The impact of a free jet with loading on a simplified bucket of a pelton turbine is simulated, see Figure 1. The shape of the wear pattern of each scenario is compared. The attack angle of the free jet is changed to compare different scenarios.

This work is divided into three parts. First a short overview is given about the simulation methods which are used, i.e., SPH, DEM, and the wear models. Then, the simulation results are presented with the three wear models and finally we give a conclusion of our work.

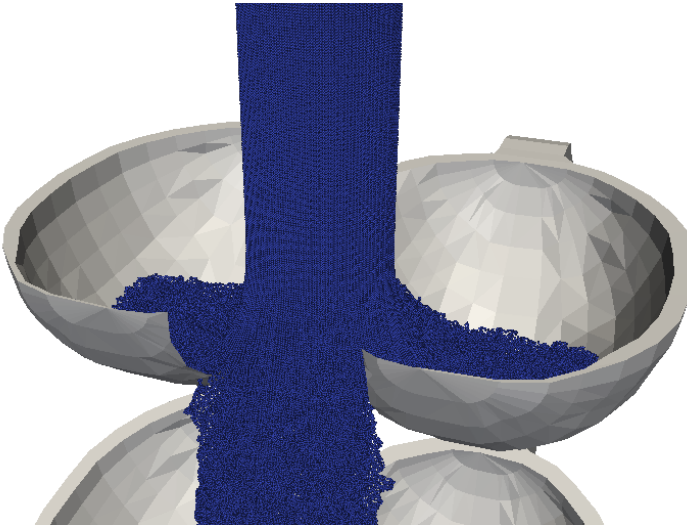


Figure 1: Impact of free jet with loading.

2 Theoretical Background

2.1 Smoothed particle hydrodynamics

The Navier-Stokes equations are used to describe the fluid in the simulations. In this work the SPH method is used for solving these equations. In doing so, the conservation of the mass of the fluid with the velocity \mathbf{v} is stated

$$\nabla \cdot \mathbf{v} = 0 \quad (1)$$

and the conservation of linear momentum is

$$\rho \left(\frac{\partial \mathbf{v}}{\partial t} + \mathbf{v} \cdot \nabla \mathbf{v} \right) = -\nabla p + \mu \nabla^2 \mathbf{v} + \mathbf{f}, \quad (2)$$

with the density ρ , the viscosity μ , the pressure p of the fluid and the body forces \mathbf{f} . The basic ideas of the SPH method for simulating fluids, which are described with the Navier-Stokes equation, are consisting of two steps. The first one is called kernel approximation and the second particle approximation [22]. In its beginning, the SPH method was introduced in [16] and [23]. During the last years the SPH method was applied in several studies with different field of applications, e.g., free surfaces [25, 24, 28], fluid-solid interaction [10, 19], or multi-phase flow [11, 17]. Mainly there are two different approaches used in these studies, i.e., the weakly compressible SPH method and the truly incompressible SPH method. The pressure field is solved in a different way. A review of the various applications in more detail can be found in [22].

2.2 Discrete element method

For the loading of the free jet the solid particles are simulated with the Discrete Element Method [12]. In the past years the method was used not only for simulating granular but also bulk material. In [14] the method is applied to an application where particles have not a permanent contact. When some particles are coupled with breakable inner-particles bonds it is possible to model failure of different materials like in [15]. The Newton-Euler equations [27]

$$m_i \mathbf{a}_i = \mathbf{f}_i, \quad (3)$$

$$\mathbf{I}_i \cdot \dot{\boldsymbol{\omega}}_i + \boldsymbol{\omega}_i \times \mathbf{I}_i \cdot \boldsymbol{\omega}_i = \mathbf{l}_i \quad (4)$$

are used to describe the motion of the particles. In (3), m_i is the mass, \mathbf{I}_i the inertia tensor and \mathbf{f}_i and \mathbf{l}_i are forces and torques, \mathbf{a}_i the acceleration, $\boldsymbol{\omega}_i$ the angular velocity of particle i . There are different possibilities for calculating the forces between two adjacent particles [29], e.g., a classical force law corresponding to a spring damper combination. In this work a Hertian force law [20], is used where the contact force is calculated to

$$F_{ij} = K_{ij} \delta_{ij}^{\frac{3}{2}} + d \dot{\delta}_{ij} \quad (5)$$

with

$$K_{ij} = \frac{4}{3\pi(h_i + h_j)} \left(\frac{R_i R_j}{R_i + R_j} \right)^{\frac{1}{2}},$$

$$h_j = \frac{1 - \nu_j^2}{\pi E_j}.$$

Here, R_j is the radius of a particle j , E_j Young's modulus of the granular material, ν_j the Poisson number, d a damping parameter and δ_{ij} the overlap of two particles.

For the coupling of the DEM and SPH particles an approach like in [26] is used. The SPH particles are smaller than the DEM particles and the contact force is calculated as a penalty force taking distance and the velocity difference into account.

2.3 Wear

Abrasive wear of the surface of hydraulic machines is caused by different mechanisms [30]. There are different approaches for modeling abrasive wear, whereby one possibility is to use a single particle wear model. In several studies corresponding models were introduced which take various mechanisms and material combinations into account. An overview and more details regarding different wear models can be found in [6, 5] and [7]. A common crucial point of the wear models is the determination of the model parameters.

In this work we have selected three different wear models. The models were originally applied to different but similar application scenarios, e.g., wear in oilfield control valves or rocket nozzles. In Figure 2 the resulting wear patterns for the simulation scenario of the impact of a free jet are shown. The resulting shape is very similar for the different wear models. The purple blade (a) is the Finnie model [3], the red blade (b) is the Bitter model [1] and the turquoise blade (c) is the Tabakoff model [8]. In this figures the blades are color coded with the amount of removed material but here at the moment only the shape of the pattern is interesting.

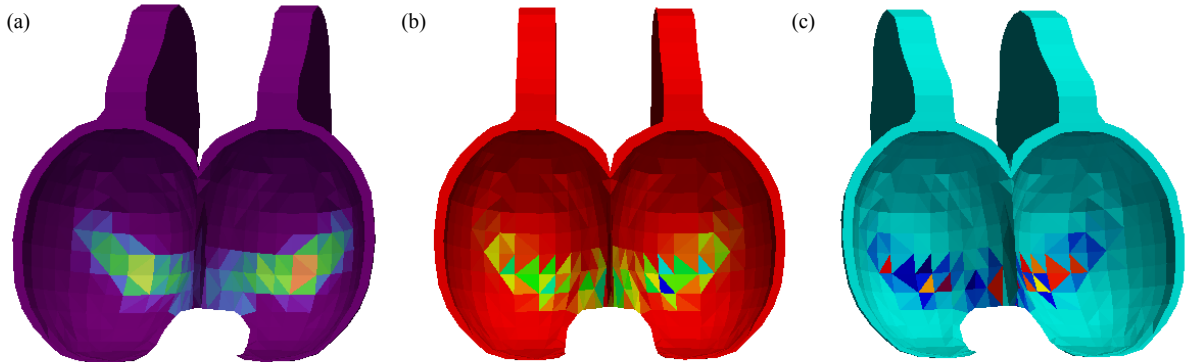


Figure 2: Comparison of the wear pattern for three different wear models.

The Finnie wear model was one of the first approaches to model the removed material of the surface of a hydraulic machine. The model was introduced in [3] and the removed material of the surface, mainly through cutting mechanism, is calculated to

$$W = \begin{cases} \frac{mU^2}{\psi pk} \left[\sin(2\alpha) - \frac{6}{k} \sin^2(\alpha) \right] & \text{for } \tan(\alpha) \leq \frac{k}{6}, \\ \frac{mU^2}{\psi pk} \left[\frac{6 \cos^2(\alpha)}{k} \right] & \text{else.} \end{cases} \quad (6)$$

Here, m is the mass of the particle, α is the attack angle, k is the ratio of the force components, ψ is the ratio of the depth of contact to the length of the swarf, U is the

absolute velocity of the solid particle and p is the flow stress of the hydraulic machine. The physical assumptions for this model are that the material is removed by an idealized particle with unit width, the particle is rigid and the rotation is small during the cutting process. It attempts to predict an amount of removed material which is proportional to the kinetic energy of the solid wear particle. In Figure 3 the removed material at the surface of hydraulic machine is shown at different points.

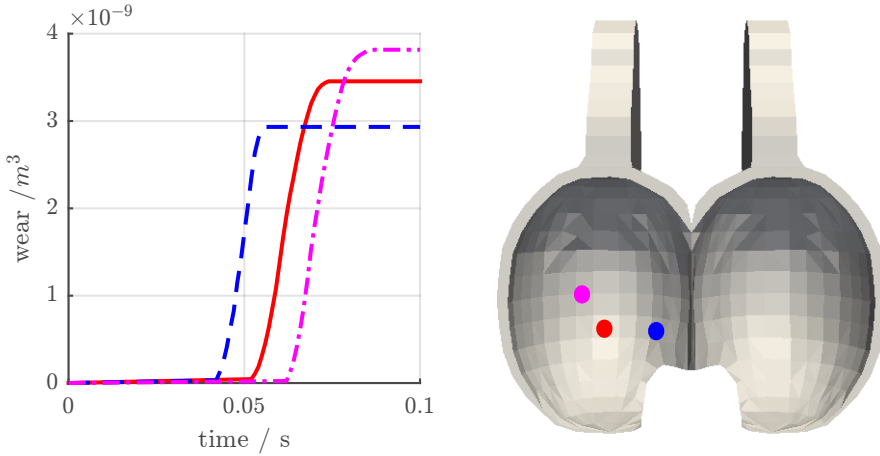


Figure 3: Abrasive wear predicted with the Finnie model at the marked points.

The second more complex model, here referred to as Bitter model, takes not only cutting mechanisms into account but also wear due to repeated deformation. The assumptions for this wear model are that these two types of wear occur simultaneously. Besides the removed material due to cutting wear, the surface of the hydraulic machine is plastically deformed because the elastic stress is exceeded due to frequent impacts of wear particles. It was introduced in [1, 2] and extended in [4]. The removed material is modeled to be

$$W = \left[\frac{100}{2\sqrt{29}} r_p^3 \left(\frac{U}{C_k} \right)^n \sin 2\alpha \sqrt{\sin \alpha} \right] + \left[\frac{M_p (U \sin \alpha - D_k)^2}{2E_f} \right] \quad (7)$$

with

$$C_k = \sqrt{\frac{3\sigma R_f^{0.6}}{\rho_p}}, \quad D_k = \frac{\pi^2}{2\sqrt{10}} (1.59Y)^{2.5} \left(\frac{R_f}{\rho_t} \right)^{0.5} \left[\frac{1 - q_p^2}{E_p} + \frac{1 - q_t^2}{E_t} \right]^2. \quad (8)$$

In these equations, r_p is the radius, M_p the mass, q_p the Poisson ratio, E_p Young's modulus, ρ_p the density and R_f the roundness factor of the particle, ρ_t the density, q_t the Poisson ratio, Y the yield stress and E_f is the Young's modulus of the boundary, σ the plastic flow stress, E_f the deformation erosion factor and n the velocity exponent.

The third model was introduced in [8], here referred to as Tabakoff model. This wear model takes the same wear mechanisms into account like the Bitter wear model, but it uses a statistical approach instead of an energy based approach for estimating the wear due to deformation. The removed material is calculated to be

$$W = \frac{M_p}{\rho_t} K_1 [1 + C_K(K_{12} \sin 2\beta_0)]^2 U^2 \cos^2 \alpha (1 - R_t^2) + K_3 (U \sin \alpha)^4, \quad (9)$$

with

$$R_t = 1 - 0.0016U \sin \alpha, \quad C_K = \begin{cases} 1 & \text{for } \alpha \leq 2, \\ 0 & \text{else.} \end{cases} \quad (10)$$

Here, K_1 , K_{12} and K_3 are empirical constants and β_0 the impact angle where the maximum material is removed. In the next section the simulation results are discussed.

3 RESULTS

The simulation scenario is the impact of a free jet with loading to a simplified pelton turbine blade. We have simulated three cases with different attack angles of the free jet. In Figure 4 the results predicted with the Finnie model are shown, in Figure 5 the results for the Bitter model and in Figure 6 for the Tabakoff model. In these figures the removed material is color coded, but only the shapes of the patterns are compared in this work. As expected the shape of the wear patterns is similar.

The three wear models take different wear mechanisms into account and as a result the amount of removed material is different. The absolute value of the amount of removed material is depending on the model parameters which are here taken from literature [1, 2, 3, 4, 6, 8]. Depending on the application scenario the corresponding wear model has to be chosen. If the main interests are the parts of the hydraulic machine where damage takes place, a relative simple model can be applied. For different kind of loadings which influence the amount of removed material, e.g., mixtures of fine and coarse sand, a more complex wear model which takes different wear mechanisms into account should be used.

4 CONCLUSIONS

The modeling of abrasive wear with three different models is presented. The impact of a free jet with loading under three different attack angles was simulated. The simulation results are satisfying for all three models, because the wear patterns predicted with the different models are similar. It is possible to take different wear mechanisms with the applied wear models into account which lead as expected to similar wear patterns, but the amount of removed material is different. The Lagrangian approach can be used to predict wear patterns caused by different mechanisms. Depending on upcoming questions due to abrasive wear a simple wear model or a more complex one should be chosen. If only the place of damaged parts is of interest or the mixture of the loading is unknown a

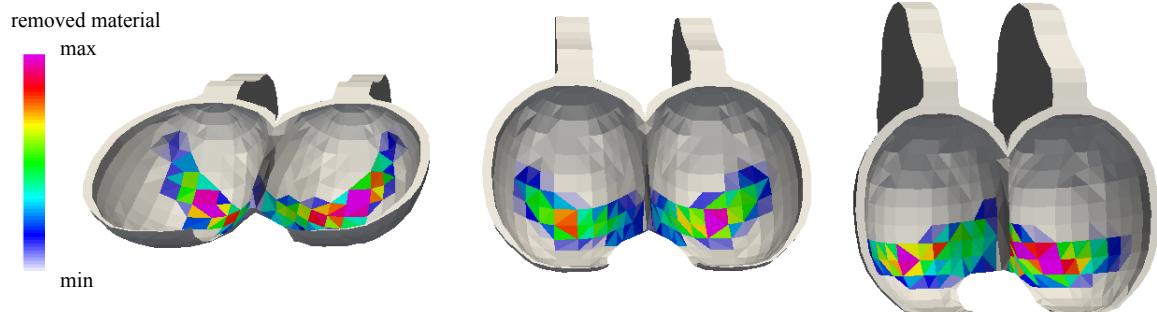


Figure 4: Wear pattern for different impact angles with the Finnie model.

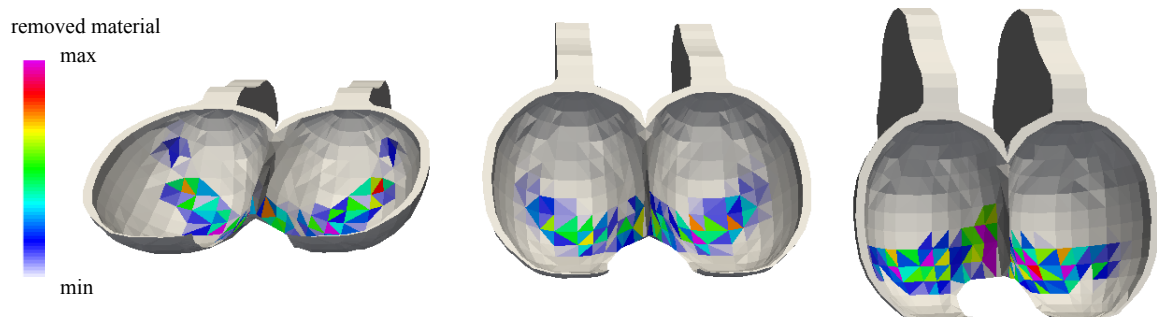


Figure 5: Wear pattern for different impact angles with the Bitter model.



Figure 6: Wear pattern for different impact angles with the Tabakoff model.

less complex wear model can be applied. A crucial point is the exact amount of removed material as the wear models have to be calibrated with experimental studies. In this work we have taken the model parameters from literature [1, 2, 3, 4, 6, 8] but not conducted own hardware experiments.

ACKNOWLEDGEMENT

The research leading to the presented results has received funding from the German Research Foundation (DFG) under the program SFB 716 ‘Dynamic simulation of systems with large particle numbers’, subproject A5 ‘Simulation of abrasive damage processes using hybrid smoothed particle hydrodynamics’. This support is highly appreciated.

REFERENCES

- [1] Bitter, J.: A Study of Erosion Phenomena: Part I. *Wear* 6(1), 5–21 (1963)
- [2] Bitter, J.: A Study of Erosion Phenomena: Part II. *Wear* 6(3), 169–190 (1963)
- [3] Finnie, I.: Some Observations on the Erosion of Ductile Metals. *Wear* 19, 81–90 (1972)
- [4] Forder, A., Thew, M., Harrison, D.: A Numerical Investigation of Solid Particle Erosion Experienced Within Oilfield Control Valves. *Wear* 216, 184–193 (1998)
- [5] Crowe, C.: *Multiphase Handbook*. Taylor and Francis, London (2006)
- [6] Lyczkowski, R.W., Bouillard, J.X.: State-of-the-Art Review of Erosion Modeling in Fluid/Solids Systems. *Progress in Energy and Combustion Science* 28(6), 543–602 (2002)
- [7] Meng, H., Ludema, K.: Wear Models and Predictive Equations: Their Form and Content. *Wear* 181–183, Part 2, 443–457 (1995)
- [8] Grant, G., Tabakoff, W.: Erosion Prediction in Turbomachinery Resulting from Environmental Solid Particles. *Journal of Aircraft* 12, (5), 471–478 (1975)
- [9] Aquaro, D., Fontani, E.: Erosion of Ductile and Brittle Materials. *Meccanica* 36(6), 651–661 (2001).
- [10] Campbell, J., Vignejevic, R., Libersky, L.: A Contact Algorithm for Smoothed Particle Hydrodynamics. *Computer Methods in Applied Mechanics and Engineering* 184, 49–65 (2000).
- [11] Colagrossi, A., Landrini, M.: Numerical Simulation of Interfacial Flows by Smoothed Particle Hydrodynamics. *Journal of Computational Physics* 191, 448–475 (2003).

- [12] Cundall, P.A., Strack, O.D.L.: A Discrete Numerical Model for Granular Assemblies. *Géotechnique* 29(1), 47–65 (1979).
- [13] El-Tobgy, M., El-Bestawi, M.: Finite Element Modeling of Erosive Wear. *International Journal of Machine Tools and Manufacture* 45, 1337–1346 (2005).
- [14] Ergenzinger, C., Seifried, R., Eberhard, P.: A Discrete Element Model to Describe Failure of Strong Rock in Uniaxial Compression. *Granular Matter* 13(4), 341–364 (2011).
- [15] Ergenzinger, C., Seifried, R., Eberhard, P.: A Discrete Element Approach to Model Breakable Railway Ballast. *Journal of Computational and Nonlinear Dynamics*, doi10.1115/1.4006731 (2012).
- [16] Gingold, R.A., Monaghan, J.J.: Smoothed Particle Hydrodynamics: Theory and Application to Non-Spherical Stars. *Monthly Notices of the Royal Astronomic Society* 181, 375–389 (1977).
- [17] Hu, X., Adams, N.: A Multi-Phase SPH Method for Macroscopic and Mesoscopic Flows. *Journal of Computational Physics* 213, 844–861 (2005).
- [18] Huang, Y.J., Nydal, O.: Coupling of Discrete Element Method and Smoothed Particle Hydrodynamics for Liquid-Solid Flows. *Theoretical & Applied Mechanics Letters* 2, doi10.1063/2.1201202 (2012).
- [19] Kulasegaram, S., Bonet, J., Lewis, R.W., Profit, M.: A Variational Formulation Based Contact Algorithm for Rigid Boundaries in Two-Dimensional SPH Applications. *Computational Mechanics* 33, 316–325 (2004).
- [20] Lankarani, H.M., Nikravesh, P.E.: A Contact Force Model with Hysteresis Damping for Impact Analysis of Multibody Systems. *Journal of Mechanical Design* 112, 369–376 (1990).
- [21] Lehnart, A., Fleissner, F., Eberhard, P.: Simulating Sloshing Liquids in Tank Vehicles. In: K. Berns, C. Schindler, K. Dreßler, B. Jörg, R. Kalmar, J. Hirth (eds.) *Proceedings of the 1st Commercial Vehicle Technology Symposium (CVT 2010)*, March 16–18, 2010, University of Kaiserslautern, Germany. Shaker Verlag, Aachen (2010).
- [22] Liu, M., Liu, G.: Smoothed Particle Hydrodynamics (SPH): an Overview and Recent Developments. *Archives of Computational Methods in Engineering* 17, 25–76 (2010).
- [23] Lucy, L.B.: A Numerical Approach to the Testing of the Fission Hypothesis. *The Astronomical Journal* 82(12), 1013–1024 (1977).

- [24] Monaghan, J., Kocharyan, A.: SPH Simulation of Multi-Flow. *Computer Physics Communication* 87, 225–235 (1995).
- [25] Monaghan, J.J.: Simulating Free Surface Flows with SPH. *Journal of Computational Physics* 110, 399–406 (1994).
- [26] Potapov, A.V., Hunt, M.L., Campbell, C.S.: Liquid Solid Flows Using Smoothed Particle Hydrodynamics and the Discrete Element Method. *Powder Technology* 116(2–3), 204–213 (2001).
- [27] Schiehlen, W., Eberhard, P.: Applied Dynamics. Springer, Heidelberg (2014).
- [28] Takeda, H., Miyama, S., Sekiya, M.: Numerical Simulation of Viscous Flow by Smoothed Particle Hydrodynamics. *Progress of Theoretical Physics* 92(5), 939–960 (1994).
- [29] Zhu, H., Zhou, Z., Yang, R., Yu, A.: Discrete Particle Simulation of Particulate Systems: Theoretical Developments. *Chemical Engineering Science* 62(13), 3378–3396 (2007).
- [30] Duan, C.G., Karel, V.Y.: Abrasive Erosion & Corrosion of Hydraulic Machinery. London, Imperial College Press, (2002).

MODELLING OF CONCRETE FRACTURE AT AGGREGATE LEVEL USING DEM BASED ON X-RAY μ CT IMAGES OF INTERNAL STRUCTURE

M. NITKA AND J. TEJCHMAN

Faculty of Civil and Environmental Engineering
Gdańsk University of Technology, Gdańsk, Poland
micnitka@pg.gda.pl, tejchmk@pg.gda.pl

Key words: DEM, Concrete, Interfacial Transitional Zones, X-ray computed tomography.

Abstract. The paper describes two-dimensional meso-scale numerical results of fracture in notched concrete beams under quasi-static three-point bending. Concrete was modelled as a random heterogeneous 4-phase material composed of aggregate particles, cement matrix, interfacial transitional zones (ITZs) and air voids. As a numerical approach, the discrete element method (DEM) was used. The concrete micro-structure in calculations was directly taken from real concrete specimens based on 3D x-ray micro-computed tomography images and 2D images by the scanning electron microscope (SEM). Attention was paid to the shape of a fracture zone between aggregate grains. In addition, the effect of properties of ITZs on fracture was studied.

1 INTRODUCTION

Fracture is a fundamental phenomenon in concrete material [1-3]. It is very complex since it consists of main cracks with various branches, secondary cracks and micro-cracks [1]. During fracture, micro-cracks first arise in a hardening region on the stress-strain curve which change gradually during material softening into dominant distinct macroscopic cracks up to damage. The fracture process strongly depends upon a heterogeneous structure of materials over many different length scales, changing e.g. in concrete from the few nanometres (hydrated cement) to the millimetres (aggregate particles). In order to properly describe fracture in detail, material micro-structure has to be taken into account since its effect on the global results is pronounced [3]. The understanding of a fracture process is of major importance to ensure the safety of the structure and to optimize the material behaviour.

At the meso-scale, concrete may be considered as a composite material wherein four important phases may be separated: cement matrix, aggregate, interfacial transition zones ITZs and macro-voids [2,4,5]. In particular, the presence of aggregate and ITZs is important since the volume fraction of aggregate can be as high as 70-75% in concrete and ITZs with the thickness of about 50 μ m are always the weakest regions in usual concretes [2], wherein cracking starts (because of their higher porosity). ITZs are a porous region of the cement paste around aggregate particles which is perturbed by their presence [6-8]. Their origin lies in the packing of the cement grains against the much larger aggregate which leads to a local increase in porosity (micro-voids) and a presence of small cement particles. A paste with the lower w/c

(higher packing density) or made from finer cement particles leads to ITZ of a smaller extent. This layer is highly heterogeneous and damaged and thus critical for the concrete behaviour. According to [8], two different types of failure exist for ITZs: the ITZ-aggregate separation (related to some delamination processes directly at the aggregate surface) and the ITZ-failure (related to cracking). The accurate understanding of the properties and behaviour of ITZ is one of the most important issues in the meso-scale analyses because damage is initiated in the weakest region and ITZ is just this weakest link in concrete.

The concrete behaviour at the meso-scale may be described with discrete models [2,9,10]. Within discrete methods, the most popular ones are: the classical particle discrete element method (DEM) [9-13], interface element models with constitutive laws based on non-linear fracture mechanics [14,15] and lattice methods [2,10,16-18]. In the models, the position and shape of inclusions was assumed to be random. The improved two-dimensional (2D) meso-scale fracture modelling results during uniaxial tension for 3-phase concrete based on x-ray computed tomography images was demonstrated by Ren et al. 2015 [19] using cohesive elements with a traction-separation law. The advantage of meso-scale modelling is the fact that it directly simulates micro-structure and can be used to comprehensively study local phenomena at the micro-level such as the mechanism of the initiation, growth and formation of localized zones and cracks which affect the macroscopic concrete behaviour (the concrete behaviour at the meso-scale fully determines the macroscopic non-linear behaviour). The mesoscopic results allow also for a better calibration of continuous and discontinuous constitutive continuum models and an optimization design of concrete with enhanced both strength and ductility [3,13]. Discrete models (if they are enough consistent) might progressively replace experimental tests to study the influence of concrete meso-structure (aggregates size, aggregate shape, aggregate roughness, aggregate/mortar volume, macro porosity, etc.) on the concrete behaviour. The disadvantages are: enormous computational cost and a difficult calibration procedure with respect to geometric and mechanical properties of ITZs.

The main objective of this study is to investigate a complicated fracture process 2D conditions in concrete elements under bending at aggregate level discrete model (based on DEM). The concrete heterogeneity was characterised by four phases, namely, aggregate grains, cement matrix, ITZs and air voids. The geometry of concrete micro-structure was directly taken from real concrete specimens using 2 high resolution and non-destructive techniques, i.e. 3D x-ray micro-computed tomography and 2D scanning electron microscope (SEM). Calculations were performed with the three-dimensional spherical discrete element model YADE, which was developed at University of Grenoble [20-21]. The model was successfully used for describing the behaviour of different engineering materials with a granular structure (mainly of granular materials by taking shear localization into account [22]). It demonstrated also its usefulness to fracture simulations in concrete [13]. The numerical outcomes were directly compared with the experimental results with respect to force-deflection curves and crack patterns.

The major contribution of the paper are calculation results on concrete fracture under bending by meso-scale model, wherein concrete was modelled as the 4-phase material with angularly-shaped aggregate particles. The calculated results were directly compared with the experimental images from an in-situ micro-scale x-ray micro-tomograph test. In the first step, 2D calculations were carried out only in order to check the capability of method. Attention

was laid on the crack shape propagating between aggregate particles and the effect of ITZs on the macroscopic concrete response with respect to the strength and crack formation.

2 EXPERIMENTAL RESULTS

The concrete was prepared from the ordinary Portland cement (CEM I 32.5 R), aggregate and water. The mean aggregate diameter was $d_{50}=2$ mm, maximum aggregate diameter $d_{max}=16$ mm and aggregate volume $V_{agg}=75\%$.

The tests were carried out on 2 free-supported rectangular notched concrete beams (height $H=80$ mm, depth $B=40$ mm and length $L=320$ mm) (Fig. 1). The notch of the height of $H/10=8$ mm and width of 3 mm was located in the beam mid-span. The average uniaxial compressive strength f_c measured on the concrete specimens $10\times10\times10$ cm³, Young's modulus E and Poisson's ratio ν measured on the concrete specimens 15×30 cm² were equal to: $f_c=51.81$ MPa, $E=36.1$ GPa and $\nu=0.22$ respectively. The measured tensile strength during bending on the concrete beams $4\times4\times16$ cm² was $f_t=3.7-4.3$ MPa. The quasi-static beam tests were performed with a controlled notch opening displacement rate (crack mouth opening displacement (CMOD)) of 0.002 mm/min using the loading machine Instron 5569. The CMOD gauge with the length of 5 mm was located in the notch at the beam bottom. Its accuracy was 0.0025 mm for the maximum permissible axial displacement of 2 mm. The test ended for CMOD=0.10-0.15 mm.

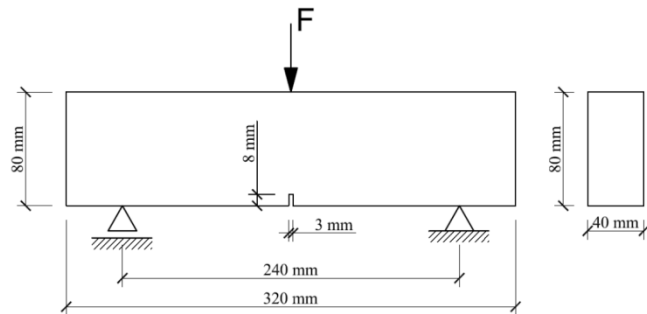


Figure 1: Concrete notched beam under quasi-static three-point bending: geometry and boundary conditions of beam (F -vertical force)

Figure 2 demonstrates the 3D images of the cracked cubical concrete specimens $80\times50\times40$ mm³ (height×width×depth) which were cut out from the beams in the notch region after each test. The specimen of Fig.2a was cut out from the beam '1' for CMOD≈0.15 mm (when the beam was totally cracked along its height) and the specimen of Fig.2b comes from the beam '2' for CMOD=0.10 mm.

The total volume of air voids was 5.02% (specimen '1') and 4.67% (specimen '2'). In order to examine the crack variation in performance with micro-structural heterogeneity, the results for 3 various vertical cross-sections of the concrete cuboids after the tests are presented in Fig.3 (for CMOD=0.15 mm - beam '1' and CMOD=0.10 mm - beam '2').

The main crack was strongly curved mainly due to presence of aggregate grains (Fig. 2). Its shape changed along the specimen depth in spite of the fact that 2D boundary value problem (plane stress) was considered. The crack mainly propagated through ITZs (which

were the weakest phase in concrete) and sometimes through macro-voids (Fig. 4a). It might very rarely propagate through a single weak aggregate particle (Fig.4b). The crack branching also occurred (Fig.4c). The effect of air macro-voids on the crack shape was small.

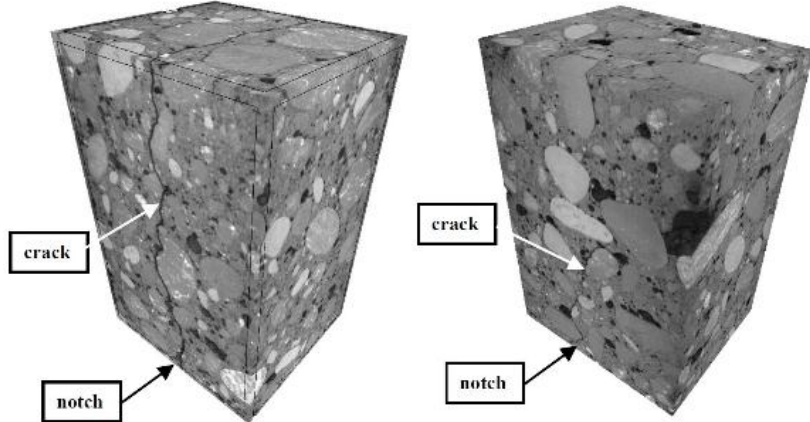


Figure 2: Images of cracked cuboidal specimens $50 \times 50 \times 40 \text{ mm}^3$ obtained by 3D micro-CT cut out from:
a) beam '1' and b) beam '2' (black spots – voids)

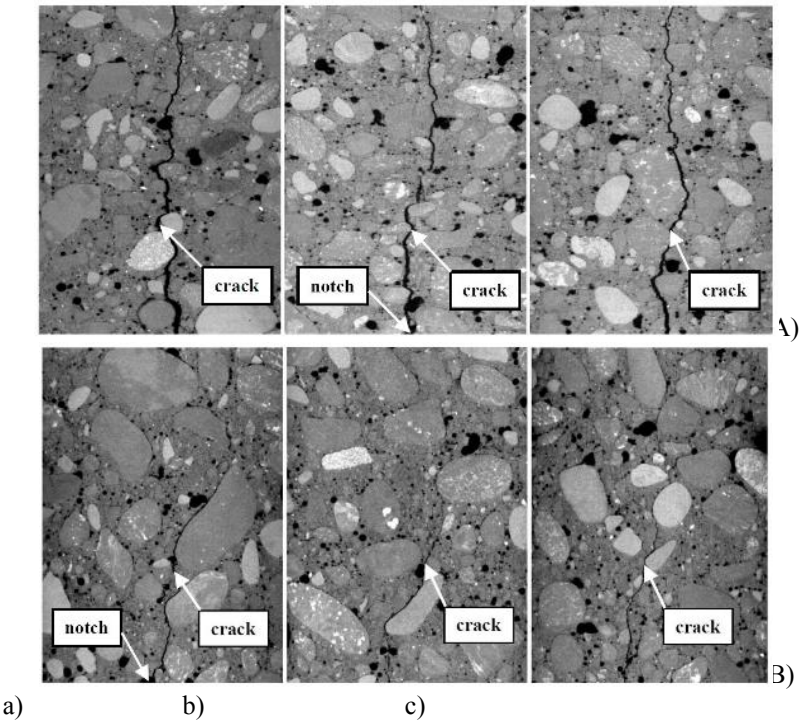


Figure 3: Crack shape in cuboidal concrete specimens $80 \times 50 \times 40 \text{ mm}^3$ of A) Fig.2a and B) Fig.2b after test based on 3D μ CT images in 3 different vertical cross-sections: a) at depth of 3 mm, b) at depth of 20 mm (mid-region) and c) at depth 37 mm from front beam surface (black spots denote voids)

The crack width changed non-linearly with the specimen height from $w_c=0.75 \text{ mm}$ (just above the notch) down to $w_c=0.22 \text{ mm}$ (top) (mid-cross-section of the specimen '1') and from

$w_c=0.32$ mm (just above the notch) down to $w_c=0.02$ mm (top) (mid-cross-section of the specimen '2'). The crack width above the notch varied with the specimen depth from $w_c=0.45$ mm (at the depth of 10 mm from the face side) up to $w_c=0.75$ mm (the mid-sectional cross-section) (specimen '1') and from $w_c=0.32$ mm (at the depth of 5 mm from the face side) down to $w_c=0.13$ mm (at the depth of 35 mm) (specimen '2'). The average crack width in the specimen '1' was $w_c=0.41$ mm wherein the crack propagated through the specimen. In the specimen '2', the average crack width and height were: $w_c=0.20$ mm and $h_c=50$ mm, respectively. The crack height in the specimen '2' changed along the specimen depth, from $h_c=45$ mm up to $h_c=56$ mm on the front specimen side. The width of the localized zone above the notch on the beam surface, measured by DIC, was $w_L=3.11\text{--}3.40$ mm [23].

In order to measure the width of ITZs, the scanning electron microscope (SEM) Hitachi TM3030 with the maximum magnification factor 30'000 was used. ITZs around aggregate particles were characterised by a very non-uniform porous structure and presence of separated small sand particles. ITZs appeared mainly aggregate particles but sometimes they were also visible around larger cement matrix particles. The width of ITZs changed between 30-50 μm (Fig. 5). The width was not dependent upon the aggregate diameter.

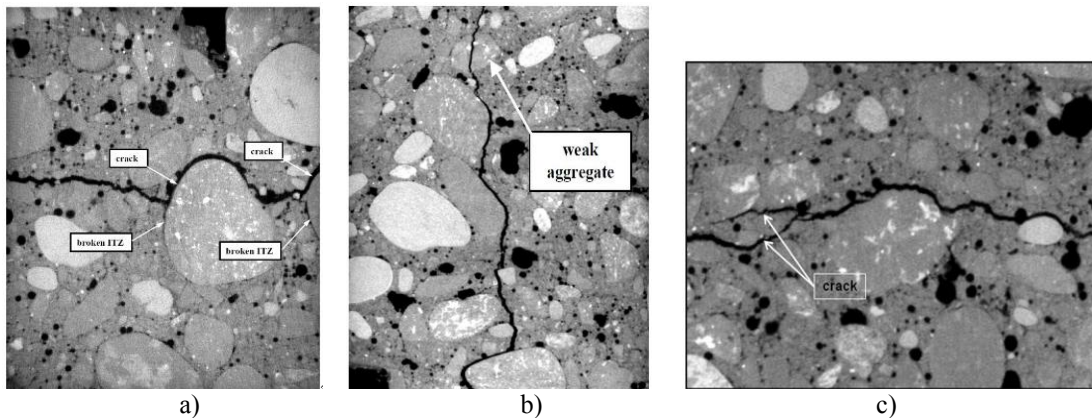


Figure 4: Crack propagation a) in ITZ b) through single aggregate and c) crack branching in experiments based on 3D μCT images (beam '1') (black spots denote voids)

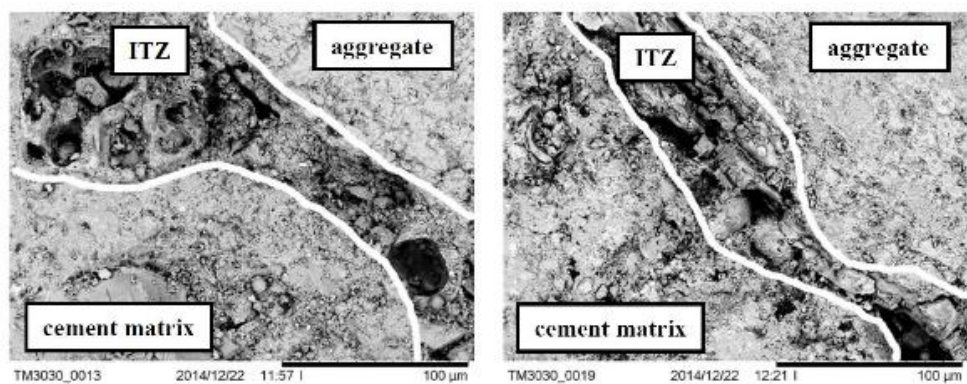


Figure 5: Scanning electron micrographs of ITZ around aggregate particles in concrete specimen '1' (magnification factor 1'000)

3 DISCRETE ELEMENT METHOD FOR CONCRETE

The 3D spherical discrete element model YADE takes advantage of the so-called soft-particle approach (i.e. the model allows for particle deformation which is modelled as an overlap of particles) [31-32]. A linear normal contact model under compression was used. Aggregate grains were modelled as clusters composed of spheres. The interaction force vector representing the action between two spherical discrete elements in contact was decomposed into a normal and tangential vector, respectively. The normal forces acting on spheres were modelled by an elastic law with cohesion. The normal and tangential forces were linked to the displacements through the normal stiffness K_n and the tangential stiffness K_s (Figs. a-6c) [21]

$$\vec{F}_n = K_n U \vec{N} \quad (1)$$

$$\vec{F}_s = \vec{F}_{s,prev} + K_s \Delta \vec{X}_s \quad (2)$$

where U is the overlap between spheres, \vec{N} denotes the normal vector at the contact point, $\Delta \vec{X}_s$ is the incremental tangential displacement and $\vec{F}_{s,prev}$ is the tangential force from the previous iteration.

The stiffness parameters were computed with the aid of the modulus of elasticity of the grain contact E_c and two neighbouring grain radii R_A and R_B (to determine the normal stiffness K_n) and with the aid of the modulus of elasticity E_c and Poisson's ratio ν_c of the grain contact and two neighbouring grain radii R_A and R_B (to determine the tangential stiffness K_s), respectively [21]. The contact forces \vec{F}_s and \vec{F}_n satisfied the cohesive-frictional Mohr-Coulomb equation (Fig. 6d)

$$\|\vec{F}_s\| - F_{max}^s - \|\vec{F}_n\| \tan \mu \leq 0 \quad (\text{before contact breakage}) \quad (3)$$

and

$$\|\vec{F}_s\| - \|\vec{F}_n\| \tan \mu \leq 0 \quad (\text{after contact breakage}) \quad (4)$$

where μ denotes the inter-particle friction angle and F_{max}^s is the cohesive force between spheres. The normal force might be negative down to the minimum value of F_{min}^n if there was no a geometrical contact between elements. If this minimum normal force between spheres F_{min}^n was reached, the contact was broken. Moreover, if any contacts between grains reappeared, cohesion between them was not taken into account. A crack was considered as open if cohesive forces between grains disappeared when a critical threshold was reached. The movement of fragments (mass-spring systems with cohesion) was similar to the rigid body movement [32].

A choice of a very simple linear elastic normal contact was intended to capture on average various contact possibilities in real concrete. One assumed that the cohesive force and tensile force were a function of the cohesive stress C (maximum shear stress at pressure equal to zero), tensile normal stress T and sphere radius R [21]

$$F_{max}^s = C \cdot R^2 \quad \text{and} \quad F_{min}^n = T \cdot R^2 \quad (5)$$

For two elements in contact, the smaller values of C , T and R were assumed. To dissipate excessive kinetic energy in a discrete system, a simple local non-viscous damping scheme was adopted [24] which assumed a change of forces by using the damping parameter α :

$$\vec{F}_{damped}^k = \vec{F}^k - \alpha \cdot \text{sgn}(\vec{v}^k) |\vec{F}^k|, \quad (6)$$

where \vec{F}^k and \vec{v}^k are the k^{th} components of the residual force and translational velocity, respectively. A positive damping parameter α is smaller than 1 ($\text{sgn}(\bullet)$ returns the sign of the

k^{th} component of velocity). The equation can be separately applied to each k^{th} component of a 3D vector x, y and z .

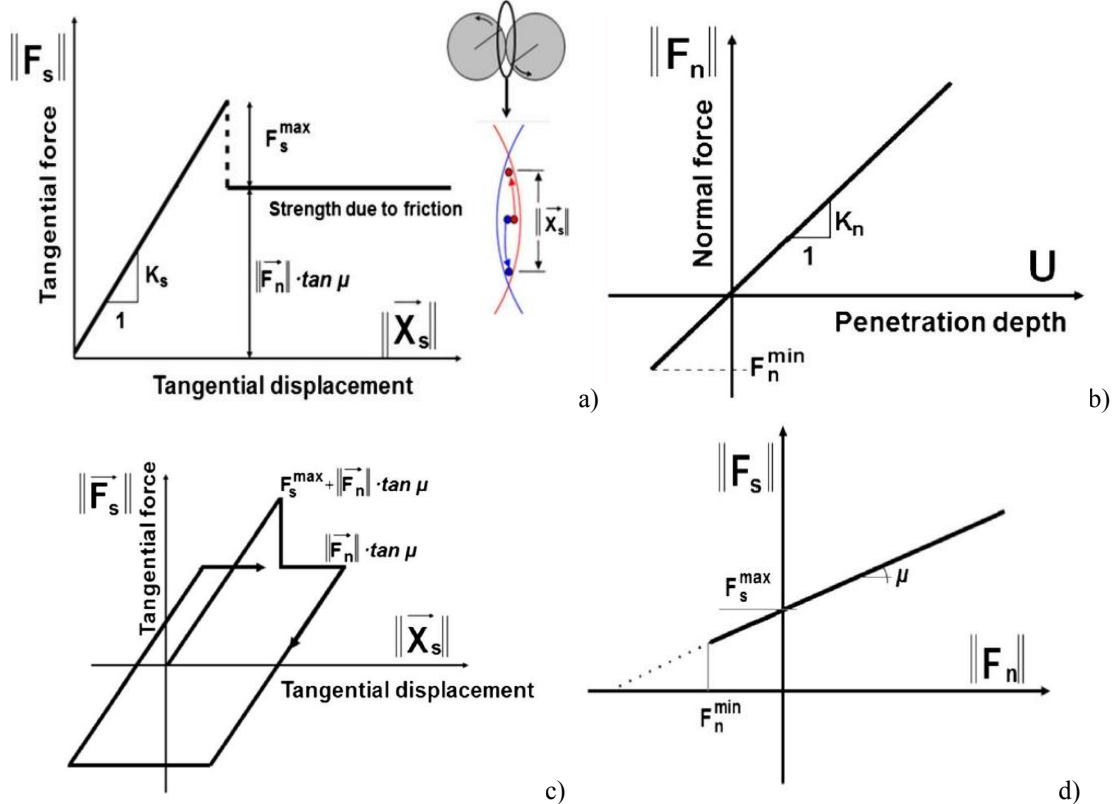


Figure 6: Mechanical response of DEM: a) tangential contact model, b) normal contact model, c) loading and unloading path in tangential contact model and d) modified Mohr-Coulomb model [20], [21]

The following 5 main local material parameters were needed for our discrete simulations: E , v , μ , C and T which may be successfully calibrated with real laboratory uniaxial tests on compression and tension of concrete specimens [13]. In addition, the particle radius R , particle mass density ρ and damping parameters α are required. Note that material softening was not directly assumed in the model.

In DEM computations of the concrete beam as a four-phase material, aggregates ($d=2\text{-}16$ mm) were modelled as grain clusters with the diameter of $d=0.5$ mm connected to each other as rigid bodies. One aggregate, depending upon its diameter, included 10-500 cylinders. All aggregate grains ($d>2$ mm) included ITZs. The aggregate volume was 75%. The cement matrix was modelled with the spheres with the diameter $d=0.25\text{-}2$ mm without ITZs. The cement matrix grains filled the concrete specimen in 95% [13]. The macro air voids ($d>0.8$ mm) were assumed as the empty spaces. The remaining beam region (outside the meso-region close to the notch) was simulated with the spheres of $d=2\text{-}8$ mm (Fig. 7a). In order to significantly shorten the computations, the beam included only one layer of grains [13] for 2D calculations. For the sake of simplicity, ITZs were solely simulated as the contacts between aggregate and cement matrix grains (thus they had a no physical width).

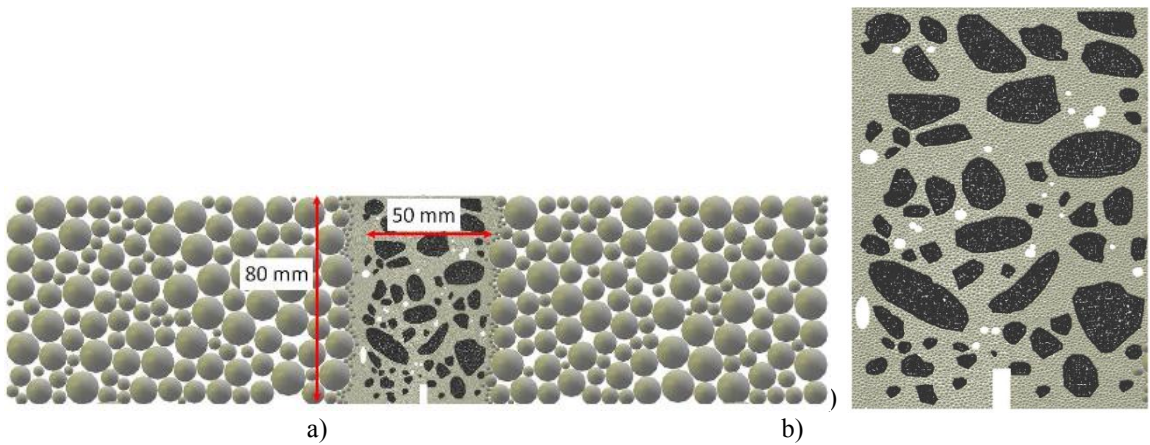


Figure 7: 2D DEM grain geometry for concrete beam '2': a) entire beam and b) meso-region close to notch of $50 \times 80 \text{ mm}^2$ based on tomography image of Fig.2 (mid-sectional cross-section)(white spots denotes voids)

Based on preliminary calculations of uniaxial compression and uniaxial tension tests [13] biaxial compression tests, the following parameters of cohesion and tensile strength were assigned to the cement matrix ($E_{c,cm}=29.2 \text{ GPa}$, $C_{cm}=140 \text{ MPa}$ and $T_{cm}=25 \text{ MPa}$) and ITZs ($E_{c,ITZ}=20.4 \text{ GPa}$, $C_{ITZ}=100 \text{ MPa}$ and $T_{ITZ}=17.5 \text{ MPa}$). Note that there were no contacts between aggregate grains. In the remaining region outside the meso-region with large grains was described by the constants: $E_{macro}=36.1 \text{ GPa}$, $C_{macro}=140 \text{ MPa}$ and $T_{macro}=25 \text{ MPa}$. The contact elastic stiffness of the cement matrix and beam macro-zone of Fig. 9a were taken directly from laboratory tests. The remaining material parameters were constant for all phases and regions: $\nu_c=0.2$ (Poisson's ratio of grain contact), $\mu=18^\circ$ (inter-particle friction angle), $\alpha_d=0.08$ (damping parameter) and $\rho=2.6 \text{ kG/m}^3$ (mass density). The inter-particle friction angle was assumed based on triaxial compression tests with granulates in the form of clumps [28]. The material constants C i T were adopted with the aid of the uniaxial compression test (2D concrete specimen $10 \times 10 \text{ cm}^2$) and bending test (2D concrete specimen $4 \times 16 \text{ cm}^2$) with concrete (Section 2) through a comparison between experiments and numerical outcomes [13]. With the assumed material properties and grain size distribution curve, the DEM calculations provided the uniaxial compressive strength of 49.5 MPa, the compressive elastic modulus of 36 GPa and the tensile strength during bending of 4.40 MPa (2D concrete specimen $4 \times 16 \text{ cm}^2$), i.e. similarly as in the experiments of Section 2 ($f_c=51.81 \text{ MPa}$, $f_t=4.04 \text{ MPa}$, $E=36.1 \text{ GPa}$ and $f_i=3.7-4.3 \text{ MPa}$).

The beam included in total about 25'000 grains (20'000 grains in the meso-region with $d_{min}=0.25 \text{ mm}$) (Fig. 7). Each concrete beam was constructed in a simple way by putting grain clusters in the position of aggregate in the beam meso-region. Next the cement matrix grains were randomly added to the meso-region with the inter-granular friction angle equal to $\mu=0^\circ$ in order to obtain a relatively dense specimen. The beam macro-region was filled up with the spheres of the beam of $d=2-8 \text{ mm}$ with $\mu=0^\circ$. The entire assembly was then allowed to settle to a state when the kinetic energy was negligible and then all contact forces between spheres were deleted. In the places where macro air voids existed, the grains were deleted. Before the beam was loaded, the final parameters C , T and μ were imposed. Afterwards the element assembly was subjected to deformation. The constant vertical velocity $v=2 \text{ mm/s}$ was applied

at the place of F . The imposed damping factor and the velocity of the prescribed displacement did not affect the results [13]. The calculated nominal inertial number I (which quantifies the significance of dynamic effects) was $<10^{-3}$ that usually corresponded to a quasi-static regime.

4 NUMERICAL RESULTS

Figures 10 demonstrate the force-CMOD curves obtained for the concrete beams '1' and '2' with the real aggregate and air voids distribution in three different cross-sections of Figs. 3A and 3B in the notch region using. The calculated maximum vertical force was $F=2.11-2.21$ kN for CMOD=0.014-0.015 mm (beam '1') and $F=2.22-2.70$ kN for CMOD=0.015-0.016 mm (beam '2') (Fig. 8). The peaks were similar like in experimental (except beam '2' mid-section where peak was higher 20%). The calculated residual forces were similar in the beam '1' and higher by 20-100% in the beam '2'. The calculated forces versus CMOD indicated clear fluctuations after the peak (smaller d_{min} or 3D calculations should solve this fluctuations).

The shape of the crack in DEM was also similar as in the experiments; the crack propagated mainly through ITZs and sometimes by macro air voids (Figs.9 and 10). The maximum calculated length and height of the crack above the notch (beam '2') were: $l_z=59.6-63.0$ mm and $h_z=51.3-53.1$ mm ($h_z/H\approx0.71-0.74$). However, some differences with respect to the propagation way appeared. In the mid-section of the beam '2' (Fig. 10B), the way of the calculated crack was different from the same beginning. Sometimes the calculated crack run around the different side of small aggregate particles. One also could observe clear crack branches in some points (e.g. in the beam '2', Figs.10B and 10C), similarly as in the experiments (Fig. 4c). Some single contacts also broke down away from the main crack.

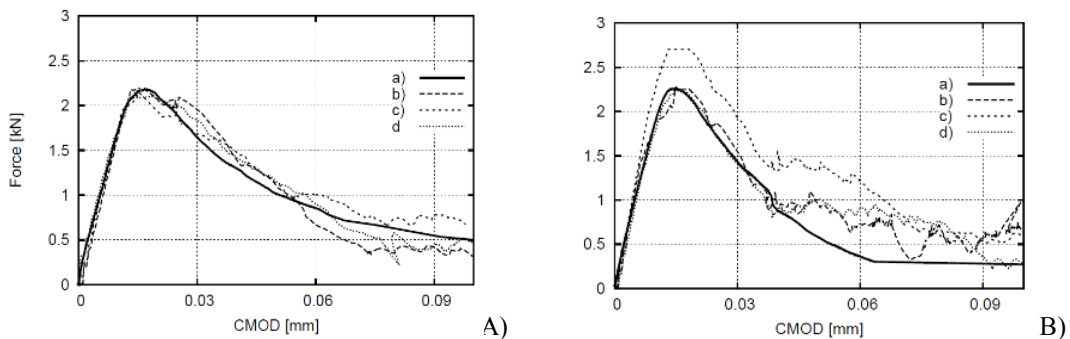


Figure 8: Evolution of vertical force against CMOD from numericla calculations: a) experimental curves of Fig.3, b-d) calculated curves for concrete micro - structure of Fig.6A and 6B (beam '1' (A) and beam '2' (B))

In Fig. 11a, the evolution of the broken contacts in DEM is shown. The total number of contact decreased from 35'380 (for CMOD=0.015 mm – the point of the maximum vertical force) down to 33'300 (CMOD=0.06-0.10 mm). A large number of interfacial micro-cracks initiated very quickly at an early stage of loading (their growth was stable). The largest non-uniform development of micro-cracks took place when $CMOD\approx0.019$ mm (slightly after the peak load). From $CMOD>0.06$ mm, the breakage was negligible. Some sudden drops in the broken contact number denoted the crack propagation in ITZs (the weakest phase); the mild

drops denoted the crack propagation in the cement matrix. Some secondary cracks beyond the main crack could also close. The width of the damage zone (corresponding to the broken contacts) was about 1.5-2 mm (Fig. 11b). The width of fully open cracks was about 0.15-0.29 mm (in experiments the crack width was slightly smaller 0.11-0.23 mm). The width of the localized zone above the notch (based on grain displacements) was $w_{Lz}=2.16-2.84$ mm (beams '1' and '2') for CMOD=0.014 mm (above the beam notch). Its largest width was $w_{Lz}=3.44$ mm (at the high of $h=30$ mm).

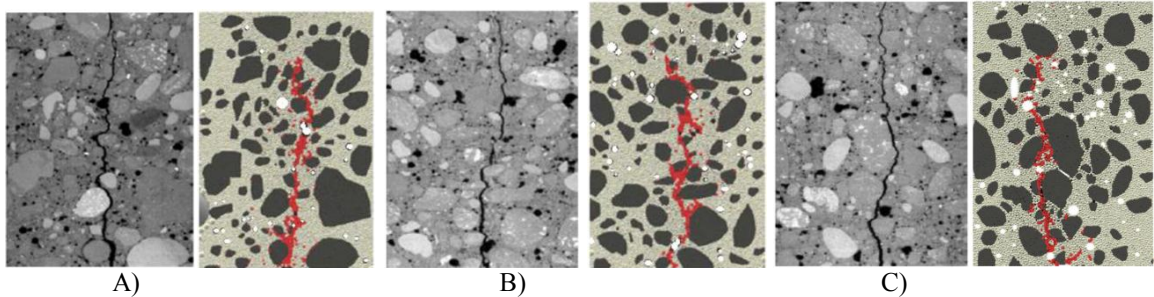


Figure 9: Fracture in concrete beam '1' above notch: left) experiments (images by micro-CT after test for CMOD=0.15 mm and right) breakage of contacts in DEM (CMOD=0.10 mm), A) at depth of 3 mm, B) at depth of 20 mm (mid-region) and C) at depth 37 mm from front beam surface of Fig.3A)

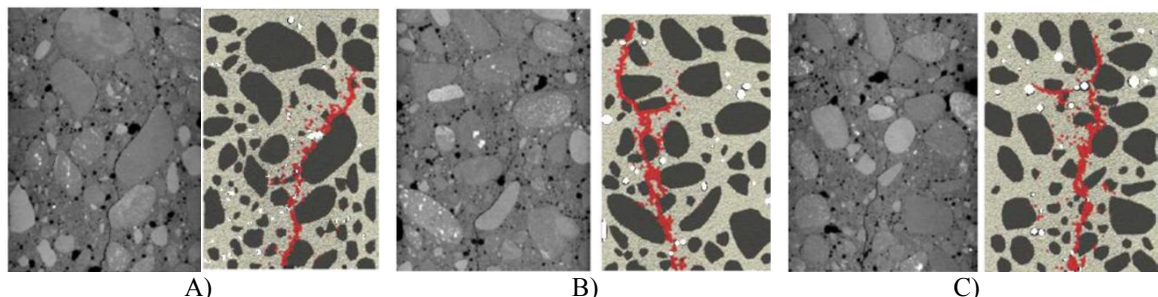


Figure 10: Fracture in concrete beam '2' above notch: left) experiments (images by micro-CT after test for CMOD=0.15 mm and right) breakage of contacts in DEM (CMOD=0.10 mm), A) at depth of 3 mm, B) at depth of 20 mm (mid-region) and C) at depth 37 mm from front beam surface of Fig.3B)

5 CONCLUSIONS

Discrete meso-scale model based on DEM were developed based on high-resolution x-ray micro-tomography images to simulate fracture processes in concrete beams under three-point bending. The calculation 2D results for four-phase concrete at aggregate level using a discrete element model showed satisfactory quantitative agreement with experimental observations.

The experimental crack above the notch was strongly curved and depended on concrete micro-structure. It mainly propagated through the weakest contact zones (ITZs) between the cement matrix and aggregates. The width of ITZs varied between 30 and 50 μm . Their porosity was strongly uniform. The crack might rarely propagate through a weak aggregate

particle. Some small crack branches were also visible. The crack shape was different with the beam depth.

It was found that the mechanical properties of ITZs had a pronounced influence on the material strength and macro-cracking that demonstrates the necessity of their experimental investigations, 3D modelling and small grain presence in DEM computations.

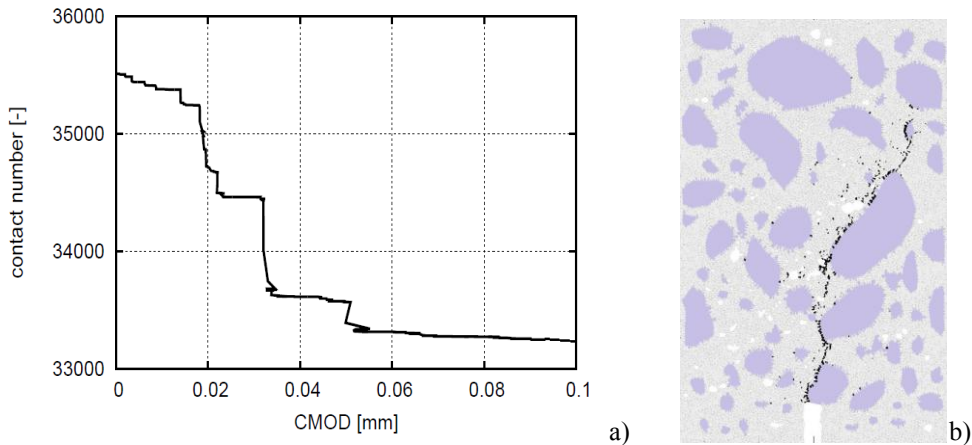


Figure 11: Broken contacts in concrete beam '2' at depth of 3 mm for DEM calculations a) evolution of contact number versus CMOD and b) broken contacts in notch region above for CMOD=0.1 mm (black lines)

Acknowledgements

The research work has been carried out within the project: “*Innovative ways and effective methods of safety improvement and durability of buildings and transport infrastructure in the sustainable development*” financed by the European Union (POIG.01.01.02-10-106/09-01) and the project “*Experimental and numerical analysis of coupled deterministic-statistical size effect in brittle materials*” financed by National Research Centre NCN (UMO-2013/09/B/ST8/03598).

REFERENCES

- [1] Bažant, Z. and Planas, J. *Fracture and size effect in concrete and other quasi-brittle materials*. CRC Press LLC (1997), Boca Raton.
- [2] Lilliu, G. and van Mier, J.G.M. 3D lattice type fracture model for concrete. *Engineering Fracture Mechanics* (2003) **70**:927-41.
- [3] Tejchman, J. and Bobiński, J. *Continuous and discontinuous modelling of fracture in concrete using FEM*. Springer, Berlin-Heidelberg (2013)(eds. W. Wu and R. I. Borja).
- [4] Skarżyński, Ł. and Tejchman, J. Calculations of fracture process zones on meso-scale in notched concrete beams subjected to three-point bending. *European Journal of Mechanics A/Solids* (2010) **29**:746-60.
- [5] Skarżyński, Ł. and Tejchman, J. Modelling the effect of composition on the tensile properties of concrete. *Understanding the tensile properties of concrete* (ed. J. Weerheim). Woodhead Publishing Limited (2013), 52-97.
- [6] Scrivener, K.L., Crumbie, A.K. and Laugesen, P. The interfacial transition zone (ITZ) between cement paste and aggregate in concrete. *Interface Science* (2004) **12**:411-21.

- [7] Mondal, P., Shah, S.P. and Marks, L.D. Nanomechanical properties of interfacial transition zone in concrete. *Nanotechnology in Construction* (2009) **3**:315-20.
- [8] Königsberger, M., Pichler, B. and Hellmich, Ch. Micromechanics of ITZ-aggregate interaction in concrete Part II: strength upscaling. *Journal of American Ceramic Society. Journal of American Ceramic Society* (2014) **97**:543-51.
- [9] Hentz, S., Daudeville, L. and Donze, F. Identification and validation of a Discrete Element Model for concrete. *Journal of Engineering Mechanics ASCE* (2004) **130**:709-19.
- [10] Kozicki, J. and Tejchman, J. Modelling of fracture processes in concrete using a novel lattice model. *Granular Matter* (2008) **10**:377-88.
- [11] Donze, F.V., Magnier, S.A., Daudeville, L. and Mariotti, C. Numerical study of compressive behaviour of concrete at high strain rates. *Journal for Engineering Mechanics* (1999) **122**:1154-63.
- [12] Dupray, F., Malecot, Y., Daudeville, L. and Buzaud, E.A. mesoscopic model for the behaviour of concrete under high confinement. *I. J. Numerical and Analytical Methods in Geomechanics* (2009) **33**:1407-23.
- [13] Nitka, M. and Tejchman, J. Modelling of concrete behaviour in uniaxial compression and tension with DEM. *Granular Matter* (2015) **17**:145-64.
- [14] Carol I, López CM, Roa O. Micromechanical analysis of quasi-brittle materials using fracture-based interface elements. *I. J. Num. Methods in Engineering* (2001) **52**:193-215.
- [15] Caballero, A., Carol, I. and López, C.M. New results in 3D meso-mechanical analysis of concrete specimens using interface elements, *Computational Modelling of Concrete Structures EURO-C* (eds.:G. Meschke, R. de Borst, H. Mang and N. Bićanić), Taylor and Francis Group (2006);43-52.
- [16] Jirásek, M., Bažant, Z.P. Particle model for quasi-brittle fracture and application to sea ice. *Journal of Engineering Mechanics* (1995);**121**:1016-25.
- [17] Schlangen, E. and Garboczi, E.J. Fracture simulations of concrete using lattice models: computational aspects. *Engineering Fracture Mechanics* (1997) **57**:319-32.
- [18] Bolander, J.E. and Sukumar, N. Irregular lattice model for quasi-static crack propagation. *Physcial Review B* (2005) **71**:094106.
- [19] Ren, W., Yang, Z., Sharma, R., Zhang, Ch. and Withers, P.J. Two-dimensional X-ray CT image based meso-scale fracture modelling of concrete. *Engineering Fracture Mechanics* (2015) **133**: 24-39.
- [20] Kozicki, J. and Donze F. A new open-source software developer for numerical simulations using discrete modeling methods. *Computer Methods in Applied Mechanics and Engineering* (2008) **197**:4429-43.
- [21] Šmilauer, V. and Chareyre, B. *Yade DEM Formulation*. Manual, (2011).
- [22] Kozicki, J., Tejchman, J. and Mühlhaus, H.B. Discrete simulations of a triaxial compression test for sand by DEM. *I. J. Numerical and Analytical Methods in Geomechanics* (2014) **38**:1923-52.
- [23] Skarżyński, Ł. and Tejchman, J. Experimental investigations of fracture process in plain and reinforced concrete beams under bending. *Strain* (2013) **49**:521-43.
- [24] Cundall, P.A. and Hart, R. Numerical modelling of discontinua. *Engineering Computations* (1992) **9**:101-13.

MODELING PLASTICITY BY NON-CONTINUOUS DEFORMATION

YARON BEN-SHMUEL¹ AND ELI ALTUS²

Faculty of Mechanical Engineering
Technion - Israel Institute of Technology
Haifa 32000, Israel

¹yaronbs@tx.technion.ac.il
²altus@tx.technion.ac.il

Key words: Plasticity, Non-continuous deformation, Particle interactions.

Abstract. Plasticity and failure theories are still subjects of intense research. Yet, no comprehensive theory has been achieved and the Molecular Dynamic method is far from providing a general model which contains only the essentials. This study is motivated by the observation that the continuum assumption in plasticity that neighbour material elements remain neighbours at all-time are physically impossible, since neighbour detachments, local slips and neighbour switching must operate, i.e., Non-Continuous Deformation (NCD). Material micro-structure is modelled by a set of point elements (particles) interacting with their neighbours. Each particle can detach from its neighbours and/or attach to a new neighbour during deformation. Simulations on two dimensional specimens subjected to uniaxial compression loading and unloading were conducted. Each specimen contained 100 particles with stochastic heterogeneity controlled by a “disorder” parameter λ . It was found that a. the macro response is typical to elasto-plastic behaviour; b. The number of detachments is linear with plastic energy; c. The number of attachments is linear with the residual strain, and d. Volume is preserved under plastic deformation. Rigid body displacement of local ensemble of elements was also observed. Higher disorder coefficient λ decreases the macro elastic modulus and increases the plastic energy.

1 INTRODUCTION AND MOTIVATION

Plastic deformation is strongly related to the microstructure. Well known phenomenon such as strain hardening and Bauschinger effect are mostly treated on the continuum basis. The lack of direct correlation between macro parameters and their micro processes makes it seem impossible that continuum theories can offer a physical interpretation for those complexities. Nevertheless, additional terms can reflect micro processes by second-order statistical quantities (point correlations) such as Reynolds stress tensor in Reynolds-averaged Navier-Stokes (RANS) equations ^[1]. Unfortunately this approach has not been materialized for solids.

Granular flow exhibits similar NCD mechanisms. Bazant ^[2] developed “Spot” model which assumes a specific local collective motion of particles which could be compared to experiments. Classical continuum mechanics was used by Kamrin et al.^[3,4] which showed limited capability. Both studies did not relate the model to plasticity in solids.

There are many studies on double well potential models which exhibit a strain jump in both directions of loading^[5,6]. However these models not sufficient to describe 2D deformation were material elements can be reorganised during deformation.

Prakash and W. Cleary^[7] used the Smooth Particle Hydrodynamics (SPH) method to simulate metal extrusion. Large plastic deformation is observed but macro continuum plastic model is incorporated ("radial return plasticity model").

Molecular Dynamics (MD) simulations can act as a bridge between the micro length and time scales and the macroscopic behaviour^[8]. Mordehai et al.^[9] studied the size effect of a single-crystal under compression using MD simulations compared with experimental results (Fig.1).

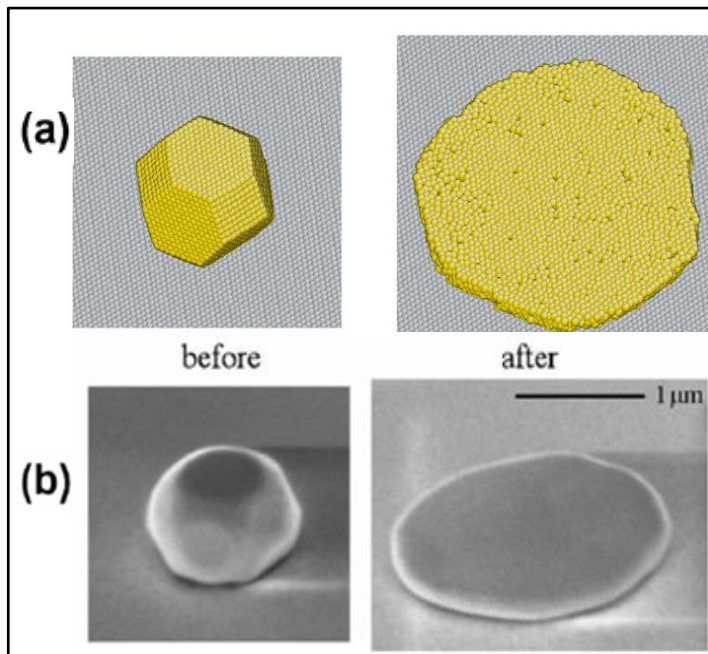


Figure 1: Atomistic ensemble under compression: (a) MD simulation of initially 4.9 nm size crystal (b) a small ~300 nm top diameter real crystal before and after deformation (Mordehai et al., 2011).

Since the total amount of atoms per unit area is conserved non-continuous deformation must be admitted. Nano "holes" are also observed. Thus, the NCD is materialized in two forms: attachments and detachments between neighbour atoms. These mechanisms are not included in the classical continuum plasticity theories.

Diffusion based models contains the physical mechanisms of attachments and detachments but their effect is commonly modelled directly on the macro (averaged) level.

2 MATERIAL MORPHOLOGY

Material is composed of a set of N "particles" located at \mathbf{x}^I , where $(^I)$ is the particle's index.

2.1 Initial configuration

In the undeformed state the internal and the external forces are zero and the "material" is

stress free. For the research to be based on fundamental cell distribution, the particle morphology is built on a net containing $n \times m$ cells with dimensions:

$$a_1 = n\alpha_1 ; \quad a_2 = m\alpha_2 \quad (1)$$

where a_1, a_2 are the height and width of a 2D morphology and n, m are the number of cells in the e_1 and e_2 direction, respectively.

A single particle is inserted in each cell (constraint a). Its location is controlled by a disorder parameter $0 \leq \lambda \leq 1$ (constraint b). When $\lambda=0$ all particles are located at the centre of each cell, i.e., fully ordered and deterministic case. When $\lambda=1$ each particle is randomly located anywhere within the boundaries of the cell. This type of microstructure is related to a Voronoi tessellation with the above two constraints.

Fig.2 demonstrates the initial state morphology as a function of λ . It includes the interaction between particles which will be discussed in later. Microstructure versatility is clearly observed.

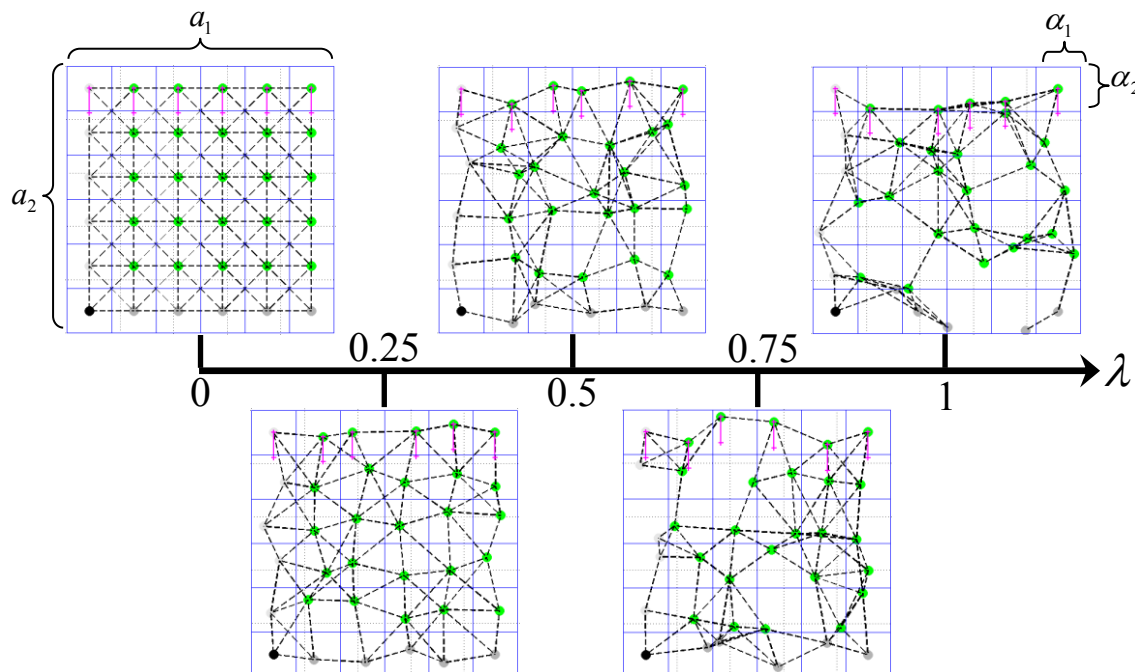


Figure 2: Typical initial configurations of the 2D microstructure for various values of λ .

2.2 Particle interactions

Each particle interacts (force) with its neighbours. The neighbouring particles are located within a circle R which controls the morphological connectivity,

$$R = C(\alpha_i \alpha_i)^{1/2} \quad (2)$$

The radius R is proportional to the diagonal of the cell ($C=1$). $C>1$ reflects higher connectivity. In this study $C=1.1$ is chosen to minimize severe discontinuities in the model and still

allow Attach-Detach (AD) mechanism.

Define d^{IJ} as the Euclidean distance between particles I, J ,

$$d^{IJ} = \|x^I - x^J\|_2 \quad (3)$$

if $d^{IJ} \leq R$ particles I, J are in interaction.

2.3 Incremental configuration evolution

There are two possibilities of changing the interaction status of every 2 particles during loading: from non-interacting to interacting ('attachment rule') and vice versa ('detachment rule'). The two rules are sufficient ingredients for our NCD model.

The characteristics of interaction between two neighbouring particles are very similar to the atomistic model, i.e., repulsive and attractive forces. The repulsive force is consistent with the "exclusion principle" and the attractive force act as a 'glue' which keeps the material points together. The specific constitutive relation is not important for our study, and therefore we consider a linear stress-strain law.

Define d_0^{IJ} as the zero force distance during deformation and the interaction force between particles I, J at some time t as,

$$f^{IJ} = H(d_0^{IJ}(S+1) - d^{IJ})k^{IJ}(d^{IJ}, d_0^{IJ}) \quad (4)$$

H is the Heaviside Function, S is a predefined parameter (strain) which remains constant through the simulation and k^{IJ} is a function describing the interaction relation between the two particles.

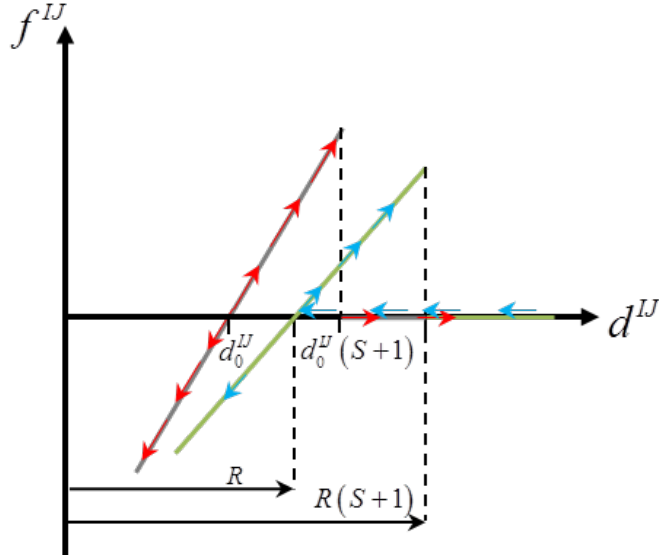


Figure 3: The micro constitutive relation schematically describing the AD mechanism of interaction between two particles.

Fig.3 shows schematically the basic features of f^{IJ} . $d^{IJ}=d_0^{IJ}$ at $t=0$. As d^{IJ} increases the force increases (red arrows) until $d^{IJ}=d_0^{IJ}(S+1)$ where particles are no longer in interaction (zero

force) i.e., detachment. Notice that a correction to f^J is needed to fulfil the 'exclusion principle' e.g., the force must go to $-\infty$ at some threshold. However, in our case the strains are small enough not to reach such an extreme state.

The 'attachment rule' is as follows: two far away particles with no interaction may come close ($d^{IJ} \leq R$), then the new interaction is based on a zero interaction distance $d_0^{IJ} \leq R$ (blue arrows).

Note that two interacting particles experiencing detachment (red arrows) are not necessarily the same two particles experiencing the attachment (blue arrows).

3 CONSTITUTIVE EQUATIONS

This chapter describes the collective behaviour of the N particles set in a matrix formulation and is the basis for future constitutive macro equations.

3.1 Mathematical background

The Hadamard product of two $m \times m$ matrices \mathbf{A} and \mathbf{B} is defined by

$$(\mathbf{A} \circ \mathbf{B})_{ij} = A_{ij} B_{ij} \quad \forall 1 \leq i, j \leq m , \quad (5)$$

which is element-wise multiplication [Horn, R., 1994].

The identity matrix \mathbf{J} under Hadamard product is $m \times m$ matrix with all entries equal to 1.

$$\mathbf{J}_{ij} = 1 \quad \forall 1 \leq i, j \leq m \quad (6)$$

\mathbf{A} has a Hadamard inverse, denoted by $\hat{\mathbf{A}}$, if and only if $A_{ij} \neq 0$ for all $1 \leq i, j \leq m$:

$$\hat{\mathbf{A}}_{ij} = (A_{ij})^{-1} . \quad (7)$$

The Hollow matrix \mathbf{J}' is defined as,

$$\mathbf{J}' \triangleq \mathbf{J} - \mathbf{I} \quad (8)$$

where \mathbf{I} is the common identity matrix.

The Euclidean Distance Matrix (EDM) $\mathbf{d}(t)$ contains the complete set of distances between every two particles. d_{ij} denotes the corresponding distance between particles I, J at time t ,

$$d_{ij} = d_{ji} = \|\mathbf{x}^I - \mathbf{x}^J\|_2 \geq 0 ; \begin{cases} 0, & i = j \\ > 0, & i \neq j \end{cases} \quad (9)$$

Notice that d_{ij} is an element (row i , column j) from a $N \times N$ matrix and d^J is a standalone scalar.

The Primary Euclidean Distance Matrix (PEDM) $\mathbf{d}_0(t)$ is the zero force distance between every pair. At $t=0$,

$$t = 0 : \quad \mathbf{d}_0 \equiv \mathbf{d} \quad (10)$$

Define \mathbf{R} and \mathbf{S} related to the 'attachment rule' and 'detachment rule', respectively:

$$\mathbf{R} \triangleq R\mathbf{J}' = \mathbf{R}^T \quad (11)$$

$$\mathbf{S} = \mathbf{SJ}' = S^T \quad (12)$$

The interaction indicator matrix $\mathbf{m}(t)$ for any pair is 1 if the corresponding particles are in interaction and 0 if the particles have no interaction. At $t=0$ \mathbf{m} depends solely on \mathbf{R} :

$$\mathbf{m}(t=0) = H(\mathbf{R} - \mathbf{d}_0(t=0)) = \mathbf{m}^T \quad (13)$$

H sorts out all pairs with distance $\text{abs}(\mathbf{d}) > R$. The value of $\mathbf{m}(t)$ will be discussed in the following.

3.2 Load increments

In each load (or time) increment a deformation change takes place, where the particles move to new locations $\mathbf{x}(t+dt)$. This is carried out in two stages: elastic continuous deformation and inelastic NCD in the form of "Attach-Detach" (AD) mechanism. In stage one structural morphology remain fixed and $\mathbf{x}(t+dt)$ is obtained from the elastic equilibrium equations and effects $\mathbf{d}(t+dt)$. Stage two contains pure attachment or detachment of interactions according to the new locations. $\mathbf{m}(t)$ and $\mathbf{d}_0(t)$ are updated with no additional deformation.

The 'detachment rule' formulation in the second stage is:

$$\mathbf{m}^- = H((\mathbf{S} - \boldsymbol{\varepsilon}(t+dt)) \circ \mathbf{m}(t)) \quad (14)$$

where \mathbf{m}^- is a matrix containing all the remaining interactions not exceeding \mathbf{S} and $\boldsymbol{\varepsilon}$ is the strain matrix given by,

$$\boldsymbol{\varepsilon}(t+dt) = (\mathbf{d}(t+dt) - \mathbf{d}_0(t)) \circ \hat{\mathbf{d}}'_0 ; \quad \mathbf{d}'_0 = (\mathbf{d}_0(t) + \mathbf{I}) \quad (15)$$

In (14) the Hadamard product with $\mathbf{m}(t)$ act as a filter to cancel out all those non feasible interactions.

The 'attachment rule' formulation in the second stage is: all the non-interacting particles which admit ($d_{ij} < R$) are in interaction with updated \mathbf{d}_0 . This is done by first subtracting $\mathbf{m}(t)$ from all possible interactions and then employ the rule on the remaining interactions,

$$\mathbf{m}^+ = H((\mathbf{R} - \mathbf{d}(t+dt)) \circ (\mathbf{J}' - \mathbf{m}(t))) \quad (16)$$

The updated interaction matrix is now given by the sum of (14) and (16),

$$\mathbf{m}(t+dt) = \mathbf{m}^- + \mathbf{m}^+ = H((\mathbf{S} - \boldsymbol{\varepsilon}(t+dt)) \circ \mathbf{m}(t)) + H((\mathbf{R} - \mathbf{d}(t+dt)) \circ (\mathbf{J}' - \mathbf{m}(t))) \quad (17)$$

Thus, the two stages are assumed independent and can be linearly superposed, which is the simplest approximation.

In the case where $\mathbf{m}^+ \neq 0$, new interactions are formed with zero strain which means there is no additional elastic (free) energy. This ensures positive dissipative energy of the plastic deformation. The \mathbf{d}_0 matrix is updated as,

$$\mathbf{d}_0(t+dt) = \mathbf{d}_0(t) + \mathbf{m}^+ \circ (\mathbf{d}(t+dt) - \mathbf{d}_0(t)) \quad (18)$$

Notice that when $\mathbf{m}^+ = 0$, \mathbf{d}_0 remains unchanged as expected.

3.3 Tangent stiffness matrix (local and global)

In this section we explore the relationship between AD mechanism and the stiffness matrix in order to build a basis for future macro non-continuous model.

Each interaction has a distinct local stiffness matrix \mathbf{k}^{IJ} [$2n \times 2n$], where n is the dimension of the problem (here $n=2$):

$$\mathbf{k}^{IJ} = \mathbf{k}_E^{IJ} + \mathbf{k}_G^{IJ} = \frac{c_0}{d_0^{IJ}} \mathbf{G}^{IJ} + \frac{f^{IJ}}{d^{IJ}} (\mathbf{A}^T \mathbf{A} - \mathbf{G}^{IJ}) \quad (19)$$

c_0 is the intensity of the interaction which is constant and the same for all interactions. The matrix \mathbf{G} ,

$$\mathbf{G}^{IJ} \triangleq (\mathbf{n}^{IJ} \mathbf{A})^T (\mathbf{n}^{IJ} \mathbf{A}) \quad (20)$$

where,

$$\mathbf{n}^{IJ} = \frac{1}{d^{IJ}} (\mathbf{x}^I - \mathbf{x}^J); \quad I \neq J \quad (21)$$

is the unit vector indicating the orientation of interaction at time t and \mathbf{A} is simply,

$$\mathbf{A} = \begin{bmatrix} -\mathbf{I}_{[n \times n]} & \mathbf{I}_{[n \times n]} \end{bmatrix} \quad (22)$$

(19) indicates that \mathbf{k}^{IJ} splits naturally into two parts which are called the material stiffness matrix and the geometric stiffness matrix, respectively, in the literature [10]. Notice that when $f^{IJ}=0$ (attachment), the geometric stiffness matrix vanishes. (19) also expresses the local stiffness matrix for $1 \leq I, J \leq N$. However only few interactions exist in the current configuration and a suitable entry from $\mathbf{m}(t)$ is needed:

$$\mathbf{k}^{IJ} = (m_{ij} \mathbf{I}) \left(\frac{c_0}{d_0^{IJ}} \mathbf{G}^{IJ} + \frac{f^{IJ}}{d^{IJ}} (\mathbf{A}^T \mathbf{A} - \mathbf{G}^{IJ}) \right) \quad (23)$$

This ensures that only existing interactions will contribute to the global tangent stiffness matrix \mathbf{K}_t . The AD mechanism is expressed through (23) via m_{ij} and d_0^{IJ} : attachment "equals" an increase in the global stiffness and vice versa for detachment.

The global stiffness matrix \mathbf{K}_t [$2N \times 2N$] (2 degrees of freedom per particle) is the sum of contributions from all interactions:

$$\mathbf{K}_t = \sum_{I=1}^N \sum_{J=1}^N (\mathbf{C}^T \mathbf{k} \mathbf{C})^{IJ} \quad (24)$$

where \mathbf{C}^{IJ} [$2n \times 2N$] is an indicator matrix which transforms the elements of \mathbf{k}^{IJ} into the global stiffness matrix in a systematic procedure described in many books [11]:

$$\mathbf{C}^{IJ} = \begin{cases} C_{1,2I-1} = C_{2,2I} = C_{3,2J-1} = C_{4,2J} = 1 \\ 0, \quad \text{all others} \end{cases} \quad (25)$$

4 SIMULATION AND RESULTS

4.1 Problem description and boundary conditions

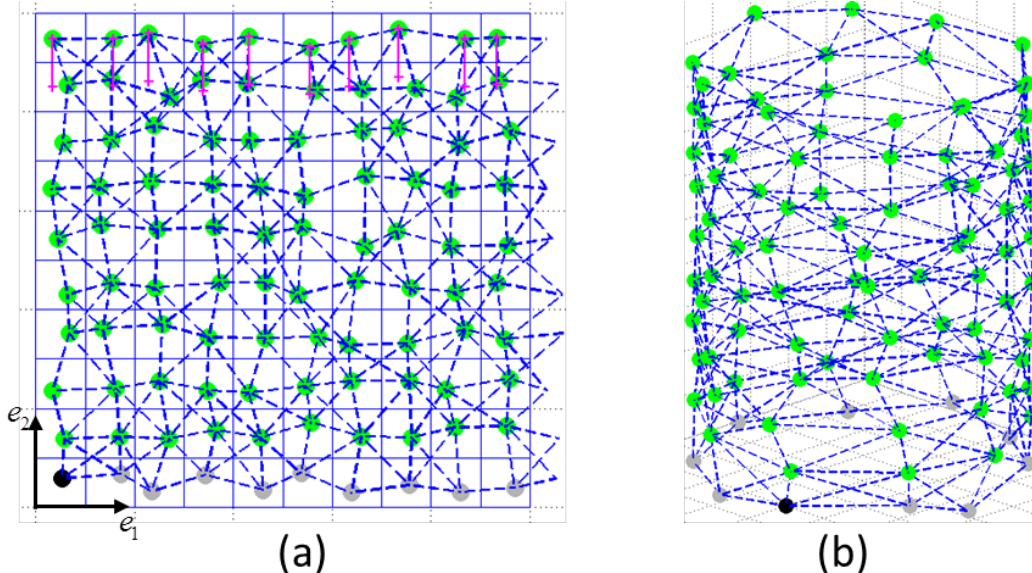


Figure 4: Typical initial configuration ($\lambda=0.2$) containing 100 particles: a) 2D microstructure subjected to compression load (pink arrows). Particle at the bottom left corner (black) is fixed to prevent rigid body motion, b) the same 2D microstructure projected on a cylinder, demonstrating PBC.

Consider typical morphology for $\lambda=0.2$ at ($t=0$) as shown in Fig.4. (10x10) particles are connected by "truss elements" having stiffness according to (4). External force is evenly distributed between all particles in the upper edge throughout the simulation (pink arrows in Fig.4a). Lower edge is controlled by the Boundary Conditions:

$$u_2 = 0, \sigma_{12} = 0 \quad (26)$$

In order to avoid "surface effects", we impose Periodic Boundary Conditions (PBC) as follows: the left and right edges are "stitched" together to form a cylinder-like structure as seen in Fig.4b. The proper "stitching space" is calculated by finding the equilibrium point at which the sum of the horizontal forces is zero.

The above simulates the macro conditions:

$$\sigma_{11}^M = 0, \sigma_{22}^M = \sigma_c \quad (27)$$

Under the ergodic assumption, prediction of the macro behaviour is done by calculating the ensemble average of at least 200 specimens for each λ . Thus, smooth macro stress-strain curve is obtained.

4.2 Results

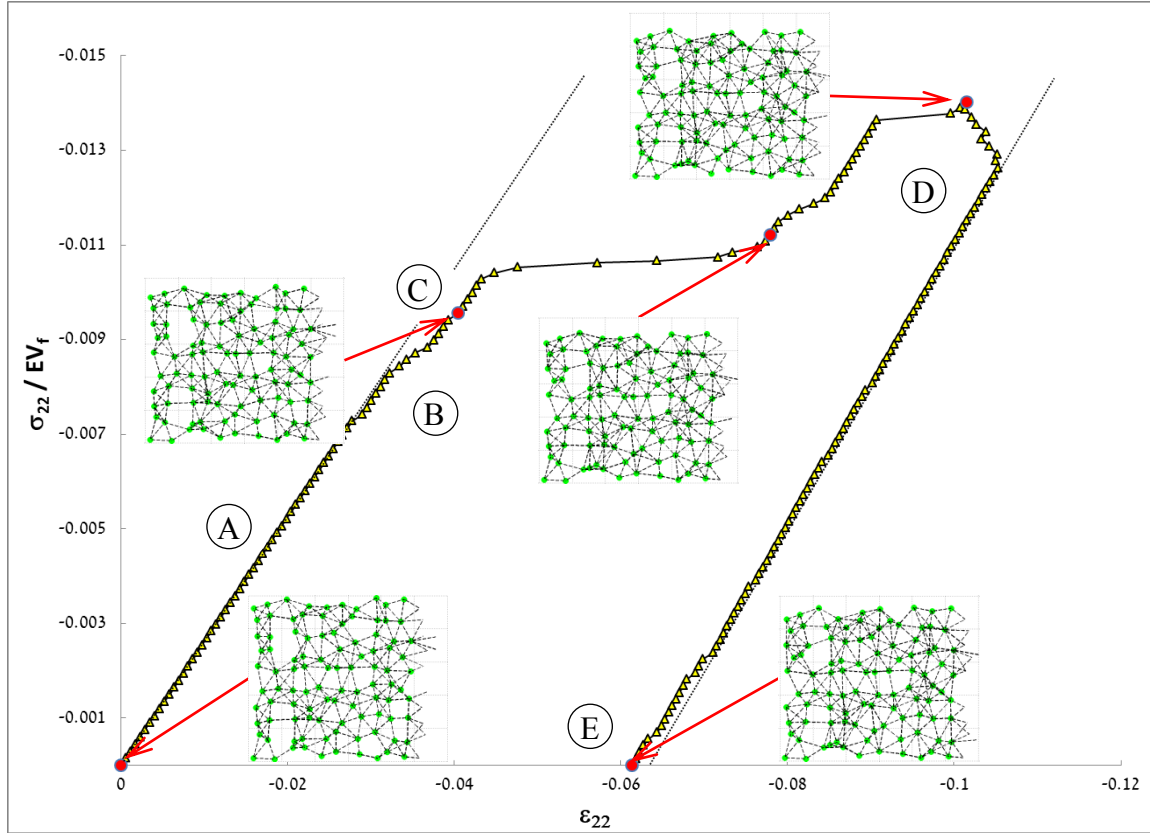


Figure 5: Typical true stress-strain curve ($\lambda=0.5$) of single specimen under uniaxial compression, $\sigma_c=-0.015$. σ_{22} is normalized by $V_f E$, where E is the elastic modulus of a single interaction and V_f is the ($\lambda=0$) volume fraction as seen in Fig.2.

A typical stress-strain curve of a single specimen is plotted in Fig.5 ($\lambda=0.5$). Selected configurations at several loading & unloading stages are shown. At the first part of the loading phase (A) the structure deforms linearly elastic. At a certain loading point the 'detachment' criteria (14) is reached resulting in decreasing stiffness of the structure i.e., yielding (B). The morphology changes and new interactions appear partially restoring the structure's stiffness (C) and the whole process is repeated. At the unloading phase (D-F) the structure deforms elastically with approximately the same modulus. At the end of the unloading phase (E) a slight stiffness decrease is observed due to local detachments. It was found that the Poisson ratio at (A) is $\nu=0.36$ and at (E) is $(0.066/0.061)\approx 1$. Noticing that (E) contains essentially the net plastic deformation, we see that the result complies with the macro volume preservation postulate under plastic deformation.

Fig.6 shows the ensemble average (macro) stress-strain curves for several values of λ . All specimens were subjected to the same load history i.e., compression loading and unloading. The stress-strain curves demonstrate typical elasto-plastic behaviour.

It can be seen that:

1. There is a correlation between morphology disorder (λ) and the structure's stiffness as well as residual plastic strain (ϵ_p). As λ increases the structure's stiffness decreases and the plastic deformation initiates at an earlier stage.
 2. From (23) and (24) we conclude that increasing number of interactions also means increasing the stiffness of the structure. In order to gain insight relations between λ , average number of interactions $\langle M \rangle$ and the elastic stiffness $\langle E_{22} \rangle$ we have calculated $\langle M \rangle$ and $\langle E_{22} \rangle$, both at the initial configuration, as a function of λ (see Fig.7). Notice the approximately linear dependence between $\langle M \rangle$ and λ .
 3. Increasing λ also leads to wider range of plasticity, suggesting that plastic energy strongly influenced by material morphology, more specifically to the level of ordering.
 4. Unloading is composed of three stages: (A), (B) and (C).
- In stage (A) an artificial behaviour is observed. It was found that this phenomenon diminishes when loading increments are sufficiently small. It is concluded that the source of this abnormality is numerical only. The slope in stage (B) is not affected by λ . Stage (C) reflects the detachment mechanism emphasized in the loading direction. This behaviour resembles the well-known "Bauschinger effect".
5. The AD mechanism depends on the loading direction and reflects non-isotropic behaviour.

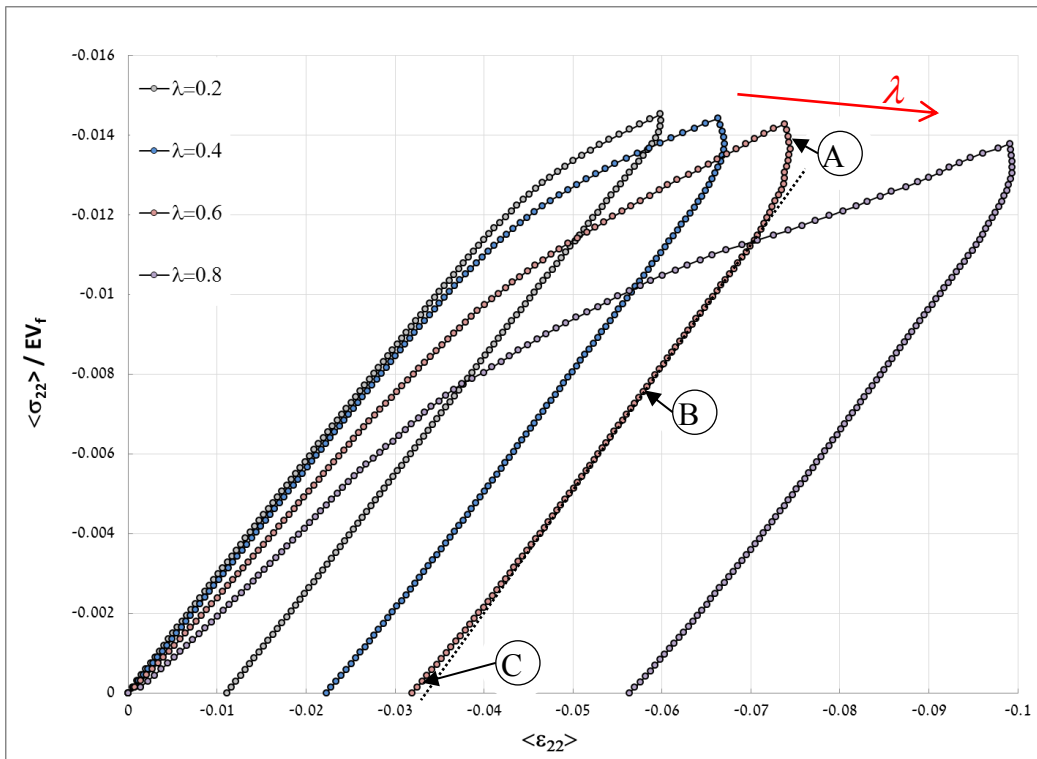


Figure 6: True stress-strain curves for several values of λ ranging from 0.2 to 0.8. Results obtained under uniaxial compression with $\sigma_c = -0.015$.

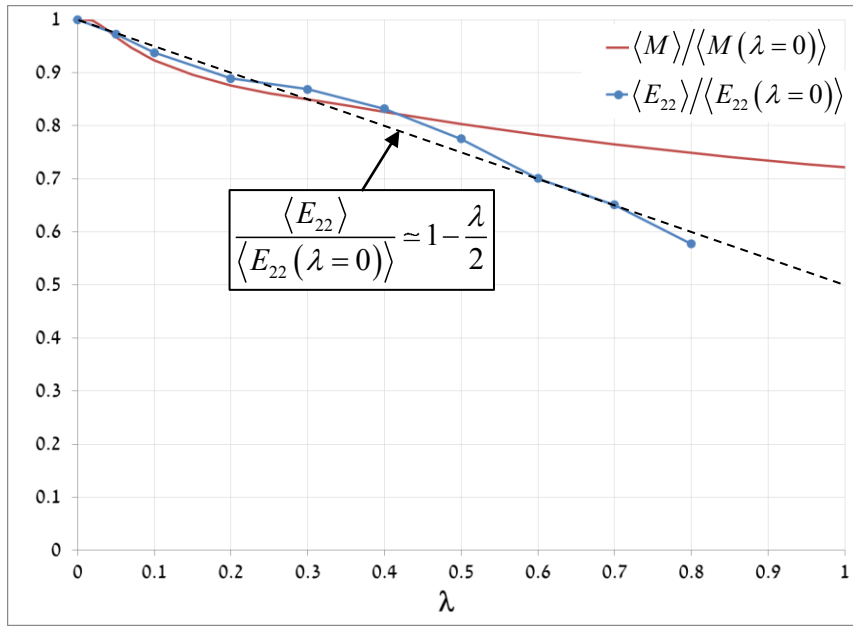


Figure 7: Trends of the elastic modulus $\langle E_{22} \rangle$ and number of interactions $\langle M \rangle$ as a function of the disorder parameter λ .

Fig 8 exhibits the two main correlations between the AD micro mechanisms and the plastic behaviour. Fig.8a shows that plastic energy is essentially linear with the accumulative number of *detachments*. The effect of λ decreases asymptotically for $\lambda \rightarrow 1$. Fig.8b shows typical linear correlations between residual (after unloading) plastic strain and accumulative number of *attachments*. The aim is to find these coefficients analytically in following studies.

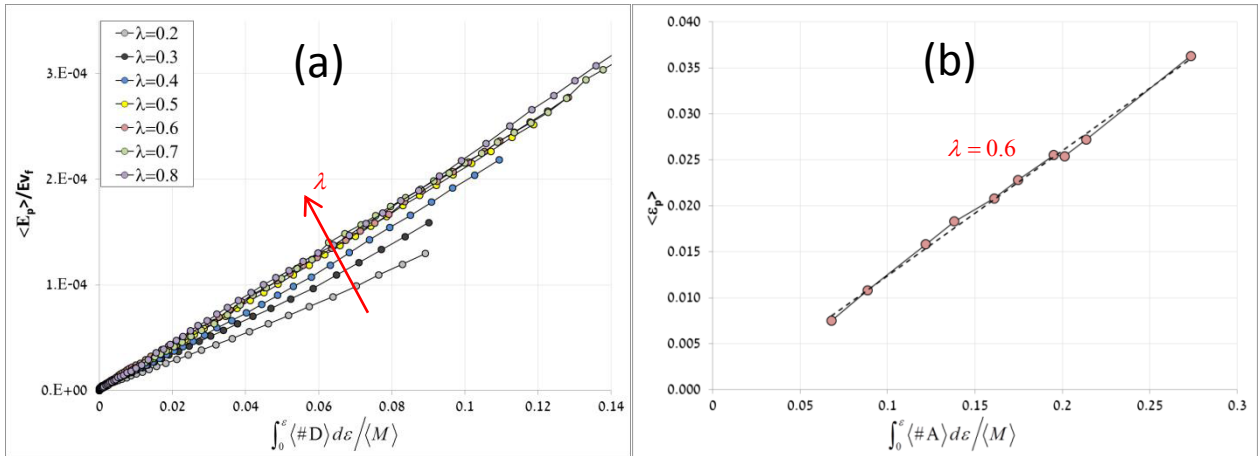


Figure 8: a) Plastic energy vs. accumulative average number of detachments for several values of λ . b) Residual plastic strain vs. accumulative average number of attachments, for $\lambda=0.6$.

5 CONCLUSIONS

- It is demonstrated that macro plastic deformation can be modelled as an accumulation of local (micro) non-continuous deformation based on particle detachments and attachments.
- A linear correlation is revealed between macro plastic energy and number of detachments, and between residual plastic strain and the number of attachments.
- The micro incremental procedure used in this study, i.e., elastic step followed by inelastic one is consistent with the macro strain decomposition i.e., $\varepsilon = \varepsilon_e + \varepsilon_p$ used in classical continuum plasticity. Both assume the deformation is the superposed sum of elastic and inelastic parts. This assumption is a 1st order approximation of the general elastic-plastic interaction.

REFERENCES

- [1] McDonough, J. M. [2004], Introductory Lectures on Turbulence. Physics, Mathematics and Modeling, Departments of Mechanical Engineering and Mathematics, University of Kentucky.
- [2] Bazant, M. Z. [2006], The spot model for random-packing dynamics. Mechanics of Materials, Vol. 38, pp. 717-731.
- [3] Kamrin, K., Rycroft, C. H. and Bazant, M. Z. [2007], The stochastic flow rule: a multi-scale model for granular plasticity. Modelling Simul. Mater. Sci. Eng. 15 S449–S464.
- [4] Kamrin, K. [2008], Stochastic and Deterministic Models for Dense Granular Flow. Ph.D. thesis, MIT.
- [5] Salman, O. U., Truskinovsky, L. [2012], On the critical nature of plastic flow: One and two dimensional models. International Journal of Eng. Sci., Vol. 59, pp. 219-254.
- [6] Benichou, I., Givli, S. [2013], Structures undergoing discrete phase transformation. Journal of the mechanics and physics of solids, Vol. 61, pp. 94-113.
- [7] Prakash, M., Cleary, P. W. [2015], Modelling highly deformable metal extrusion using SPH. Comp. Part. Mech., doi:10.1007/s40571-015-0032-0.
- [8] Allen, M. P. [2004], Introduction to Molecular Dynamics Simulation. NIC Series, Vol. 23, ISBN 3-00-012641-4, pp. 1-28.
- [9] Mordehai, D., Lee, S. W., Backes, B., Srolovitz, D. J., Nix, W. D., Rabkin, E. [2011], Size effect in compression of single-crystal gold microparticles. Acta Materialia 59, 5202–5215.
- [10] Argyris, J. H., Balmer, H., Doltsinis, J.St., Dunne, P. C., Haase, M., Kleiber, M., Malejannakis, G. A., lejnek, H. -P., Müller, M., Scharpf, D. W. [1979], Finite element method – the natural approach. Computer Methods in Applied Mechanics and Engineering, Vol. 17–18, pp. 1–106.
- [11] Bathe, K. -J. [1982], Finite element procedures in engineering analysis. Prentice-Hall, New Jersey.

VIRTUAL CONCRETE SPECIMENS: DISCRETE ELEMENT SIMULATIONS OF THE QUASISTATIC AND DYNAMIC MATERIAL BEHAVIOR AND FAILURE MECHANISMS OF CONCRETE AND MORTAR

DIRK S. REISCHL¹ AND MANFRED CURBACH²

¹ Faculty of Civil Engineering, Institute of Concrete Structures
Technische Universität Dresden
George-Bähr-Str. 1, 01069 Dresden, Germany
Dirk.Reischl@tu-dresden.de

² Faculty of Civil Engineering, Institute of Concrete Structures
Technische Universität Dresden
George-Bähr-Str. 1, 01069 Dresden, Germany
Manfred.Curbach@tu-dresden.de

Key words: Granular Materials, DEM, Contact Problems

Abstract. A quite minimalistic approach is described which allows to generate differently shaped ensembles of densely packed spherical particles. The distributions of the particle diameters approximate realistic sieving distributions of concrete aggregates. An ad hoc approach is used in order to add cohesive interaction forces to the model which allows first plausibility tests.

1 INTRODUCTION

Real experiments to investigate the damage behavior of concrete provide insight into the damage behavior of the specimens used and, after having carried out a sufficient number of experiments, into the damage behavior of the material itself. However, such experiments always imply destruction and non-reusability. The generation of representative, standardized specimens is a non-trivial task and the application of similar loading scenarios in the testing machine requires considerable skill and care.

Virtual specimens are destructible and indestructible at the same time. Each individual specimen may be used for numerous situations of loading, may they be uniaxial or multiaxial, monotonic or cyclic, possibly for situations that cannot be realized in the laboratory for reasons of principle or for practical reasons. Slight modifications of the size distribution of the virtual aggregates and even the generation of different virtual specimens consisting of an identical ensemble of aggregates (so-called clones) are possible and

allow to repeat the numerical experiments under slightly different initial conditions any number of times.

This article concentrates on a detailed description of the generation of virtual specimens. An ad hoc approach to paste the particle ensembles is used in order to perform some tests for plausibility. We start with a first 1D approach to wave propagation and spall fracture, which leads in a quite natural way to the Distinct/Discrete Element Method.

2 A 1D DISCRETE ELEMENT APPROACH

Spallation experiments are performed in order to investigate the material behavior in situations of high compressive loading or impact. For that purpose the specimen is hit at one end by a Hopkinson pressure bar or similar device. Then a wave propagates through the specimen which under certain circumstances causes the specimen to split into fragments. Fig. 1 shows a specimen of cylindrical shape that was exposed to high compressive loading and fragmented into three pieces.



Figure 1: Concrete specimen, destroyed by spall fraction. (Photography: Ulrich van Stipriaan)

As a first approach to simulate the spallation phenomenon, the specimen is considered to be consisting of a number of pairwise mutually overlapping segments (or slices or *discrete elements*). All segments are supposed to have the same longitudinal extension or segment length a , and – at the beginning, i. e. at equilibrium – any two segments have the same overlapping area $\lambda_0 a$, where the initial relative depth of penetration λ_0 is a small positive number (see Fig. 2). Then the initial length L_0 of the entire specimen (neither loaded in compression nor in tension) can be calculated by

$$L_0 = [N - \lambda_0(N - 1)] a , \quad (1)$$

or, since it is more convenient to give the specimen a certain initial length, the segment length a can be calculated by

$$a = \frac{L_0}{N - \lambda_0(N - 1)} . \quad (2)$$

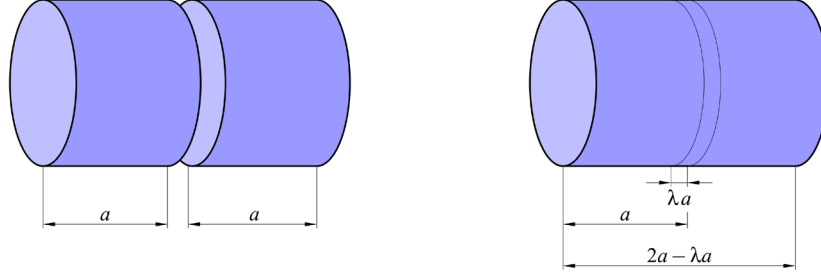


Figure 2: Geometrical relations for two non-overlapping and two overlapping segments.

The value of a depends on our choices for N and λ_0 . λ_0 itself depends on N and different material parameters, which can be seen after it was explained what mechanical properties the virtual specimen is supposed to have.

The specimen will have a certain density ϱ , which allows to calculate its mass by

$$m = \varrho L_0 A , \quad (3)$$

where A denotes the cross-sectional area of the rod. If the total mass is equally distributed to the respective segments, the segment mass m_S is obtained by:

$$m_S = \varrho \frac{L_0 A}{N} . \quad (4)$$

When (slowly) loaded in tension, the specimen should behave as if consisting of a perfectly linear-elastic, not at all ductile material with modulus of elasticity E and maximum tensile strength σ_{max} . That means, there is a maximum tensile force F_{max} the specimen can withstand. When this force is exceeded it breaks into its N different segments at the same time. At this moment, the specimen has a length

$$L_{max} = N a , \quad (5)$$

which means that all regions of contact are stretched to the maximum, and all relative depths of penetration become zero. Thus, for the maximum tensile strain ϵ_{max} we obtain:

$$\epsilon_{max} = \frac{L_{max} - L_0}{L_0} = \frac{\lambda_0(N - 1)a}{[N - \lambda_0(N - 1)]a} . \quad (6)$$

For σ_{max} , E , and ϵ_{max} holds the following the simple relation, according to Hooke's law,

$$\sigma_{max} = E \epsilon_{max} , \quad (7)$$

from which the following formula for λ_0 can be obtained:

$$\lambda_0 = \frac{N}{N-1} \frac{1}{1 + \frac{E}{\sigma_{max}}} . \quad (8)$$

The specimen, spatially discretized in longitudinal direction, can be understood as a chain of mass points, pairwise connected by springs (and dampers, since real wave propagation dissipates energy). It can be shown, that for the inner segments (i. e. for all $N - 2$ segments other than the leftmost and the rightmost segment) the following equations of motion are given by Newton's second law:

$$m_i \ddot{x}_i = \frac{x_{i-1} - 2x_i + x_{i+1}}{\lambda_0 a} F_{max} + \delta v_{i-1} - 2\delta v_i + \delta v_{i+1}, \quad (9)$$

where x_i and v_i denote the i -th segment's position and velocity, respectively, and δ is a universal dissipation coefficient (responsible for viscous damping). The formulae for the leftmost and the rightmost segment slightly differ from the formula above, you shouldn't care about this at this point.

Applying the well-known Stoermer-Verlet method for time integration, the problem can be posed in matrix notation as follows:

$$\mathbf{x}^{n+1} = \mathbf{x}^n + \Delta t \mathbf{v}^n - \frac{\Delta t^2}{2} \mathbf{M}^{-1} (\mathbf{Q} \mathbf{x}^n + \mathbf{q} + \mathbf{K}^T \mathbf{D} \mathbf{K} \mathbf{v}^n), \quad (10)$$

$$\mathbf{v}^{n+1} = \left(\mathbf{I} + \frac{\Delta t}{2} \mathbf{M}^{-1} \mathbf{K}^T \mathbf{D} \mathbf{K} \right)^{-1} \left(\mathbf{v}^n - \frac{\Delta t}{2} \mathbf{M}^{-1} [\mathbf{Q} (\mathbf{x}^n + \mathbf{x}^{n+1}) + 2\mathbf{q} + \mathbf{K}^T \mathbf{D} \mathbf{K} \mathbf{v}^n] \right). \quad (11)$$

Here \mathbf{x}^n and \mathbf{v}^n denote the vectors of segment positions and velocities at the n -th time step, Δt the step size for time integration, \mathbf{M} and \mathbf{D} are diagonal matrices containing segment masses and dissipation coefficients, respectively, \mathbf{I} stands for the $N \times N$ identity matrix, and

$$\mathbf{Q} = \frac{F_{max}}{\lambda_0 a} \begin{pmatrix} 1 & -1 & & & \\ -1 & 2 & -1 & & \\ & \ddots & \ddots & \ddots & \\ & & -1 & 2 & -1 \\ & & & -1 & 1 \end{pmatrix}, \quad \mathbf{q} = \frac{1 - \lambda_0}{\lambda_0} F_{max} \begin{pmatrix} 1 \\ 0 \\ \vdots \\ 0 \\ -1 \end{pmatrix}. \quad (12)$$

The matrix \mathbf{K} , finally, is an $(N - 1) \times N$ matrix responsible for dissipative interaction,

$$\mathbf{K} = \begin{pmatrix} 1 & -1 & & & \\ & 1 & -1 & & \\ & & \ddots & \ddots & \\ & & & 1 & -1 \end{pmatrix}. \quad (13)$$

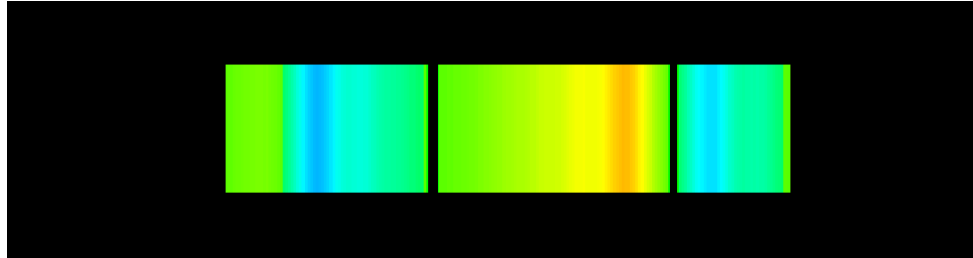


Figure 3: Virtual specimen after about 7 ms of simulation time.

Table 1: Parameters used in the 1D simulation of spall fracture

Parameter	Symbol	Value	Unit
Length	L_0	200	mm
Diameter	d	50	mm
Density	ϱ	0.0024	g/mm ³
Modulus of elasticity	E	37000	N/mm ²
Maximum tensile stress	σ_{max}	4.1	N/mm ²
Dissipation coefficient	δ	10	g/ms
Number of elements	N	200	—
Time step size	Δt	0.00025	ms

The model described can be implemented, for instance, in the MATLAB scripting language. Fig. 3 shows the simulation result for the model parameters given in Tab. 1. Within the first 0.355 ms the leftmost segment (or element or particle) was continuously accelerated to a velocity of 3 mm/ms which is equivalent to a momentum difference of 0.87 g mm/ms. The figure shows the virtual specimen after about 7 ms have been elapsed. The specimen spalled into three fragments. Colors indicate compressive (blue) and tensile (orange/yellow) strain at the respective positions of the specimen.

This 1D approach, of course, is much too simple to yield realistic simulation results. For instance no lateral strain is included in the model. Moreover, the fracture surfaces are not at all plane, but show a complicated, fractal structure. One would expect to obtain better simulation results by means of a 3D approach which takes into consideration concrete's heterogeneous nature. Fig. 4 shows the prototype of a cylindrical virtual specimen for usage in simulations of wave propagation and spall fracture, which raises the question how such specimen can be generated.

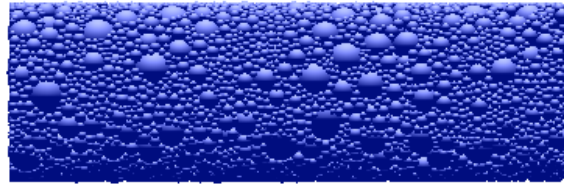


Figure 4: Virtual specimen for numerical simulations of spall fracture.

3 PARTICLE GENERATION AND INTERACTION

3.1 Particle Generation

Concrete aggregates are modelled as spherical particles of different diameter. The size distribution should approximate realistic sieving distributions for concrete. In this context several problems occur. First, realistic sieving distributions are obtained using a finite number of sieves (actually only a few), which makes the sieving result depending on the size distribution of the aggregates sieved. On the other hand, the well-known interpolations such as the Fuller parabola do not allow to construct suitable random generators.

3.2 Particle Interaction

The approach used for particle interaction is based on contact models for 2D polygon/polygon interaction as given by [1], [2], [3] and [4], for respective simulation results see also [5], [6] and [7]. In these models the magnitude of the repulsive contact force depends on the intersection area of two overlapping particles. This allows a permanent intersection at equilibrium if external forces are applied to the contact partners (Soft Contact approach). In case of 3D simulations the overlap area has to be replaced by the contact volume of the intersection of two spherical particles. Fig. 5 shows how the relative contact volume V_{rel}^C (i.e. the contact volume relative to the volume of the smaller particle) depends on the relative depth of penetration (i.e. the depth of penetration relative to the diameter of the smaller particle). The solid curve describes the special case of a particle contacting another particle of twice its diameter. The dashed lines show the extremal cases of two interacting particles of same diameter and a particle interacting with a "infinitely" larger particle (which represents the contact of a particle with a plane, a wall or a loading plate).

Besides the contact volume, the interaction of two particles with position and velocity vectors $\mathbf{x}_i, \mathbf{v}_i$ and $\mathbf{x}_k, \mathbf{v}_k$, respectively, depends on the distance vector

$$\mathbf{n} = \frac{\mathbf{x}_i - \mathbf{x}_k}{\|\mathbf{x}_i - \mathbf{x}_k\|} \quad (14)$$

and the relative velocity

$$\mathbf{v}_{rel} = \mathbf{v}_i - \mathbf{v}_k . \quad (15)$$

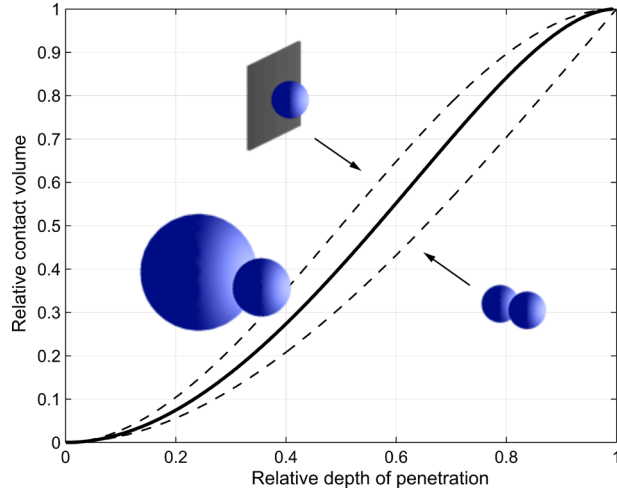


Figure 5: Relative contact volume in dependence of the relative depth of penetration.

The contact force resulting from particle interaction is composed by a normal and a tangential part:

$$\mathbf{F}^C = \mathbf{F}_\perp^C + \mathbf{F}_\parallel^C. \quad (16)$$

Using the projection \mathbf{v}_\parallel of \mathbf{v}_{rel} into the contact plane, which is described by the normal vector \mathbf{n} ,

$$\mathbf{v}_\parallel = \mathbf{v}_{\text{rel}} - (\mathbf{v}_{\text{rel}} \cdot \mathbf{n}) \mathbf{n}, \quad (17)$$

the components of \mathbf{F}^C can be expressed by:

$$\mathbf{F}_\perp^C = f_\perp^C(V^C, \mathbf{v}_{\text{rel}}) \mathbf{n}, \quad (18)$$

$$\mathbf{F}_\parallel^C = f_\parallel^C(\mathbf{v}_{\text{rel}}) \frac{\mathbf{v}_\parallel}{\|\mathbf{v}_\parallel\|}. \quad (19)$$

Adding the terms for viscous damping yields:

$$f_\perp^C(V^C, \mathbf{v}_{\text{rel}}) = \frac{k}{d} (V_{\text{rel}}^C - \kappa) V_{\text{min}} - \gamma_\perp m_{\text{eff}} v_\perp, \quad (20)$$

$$f_\parallel^C(\mathbf{v}_{\text{rel}}) = -\gamma_\parallel m_{\text{eff}} v_\parallel. \quad (21)$$

In the formulae above denote:

- V_{min} the volume of the smaller particle,
- V_{rel}^C the relative contact volume, i.e. the ratio of the contact volume and the volume of the smaller particle,
- κ a parameter to manipulate the contact law (see below),

- k a parameter that allows to scale the contact force,
- d the characteristic length, $1/d = 1/d_i + 1/d_k$, where d_i , d_k are the respective diameters of the particles,
- m_{eff} the effective mass, $1/m_{eff} = 1/m_i + 1/m_k$, where m_i , m_k are the respective particle masses,
- v_\perp and v_\parallel the normal and tangential components of the particles' relative velocity,
- γ_\perp and γ_\parallel parameters that allow to control normal and tangential dissipative interaction.

There exist different approaches for modelling static friction (see, for instance, [1], [4] and [8]). Numerical investigations on the respective effects on the simulation results are on the way.

For each particle, the equation of motion is now schematically given by:

$$m_i \ddot{\mathbf{x}}_i = \sum_{k \neq i} (\mathbf{F}^C(\mathbf{x}_i, \mathbf{x}_k) - \gamma m_{eff} (\mathbf{v}_i - \mathbf{v}_k)) . \quad (22)$$

Thus the method requires the solution of an initial value problem for a system of ordinary differential equations of second order, which can be obtained by any suitable numerical integration scheme.

4 IMPLEMENTATION

The simulation code, written in C, is based on the code fragments given by [9]. A good part of the code is dedicated to runtime efficiency. The well-known Linked Cells strategy with some refinements described in [10] is used to reduce the computational effort. However, the great differences in particle size require some modifications since the cell width is dictated by the largest particle diameter. The simulation therefore uses two different meshes of linked cells, a coarser mesh for the larger particles and a finer one for the smaller particles, an idea that can be refined to a Hierarchical Linked Cells mechanism.

5 VIRTUAL SPECIMENS

5.1 Packing of virtual aggregates

The generation of virtual concrete specimens starts with the successive generation of layers of virtual aggregates above a virtual shattering unit. Under the influence of gravitation and repulsive as well as dissipative interaction forces (particle/particle and particle/wall) densely packed particle ensembles of different size and geometry can be obtained. Fig. 6 shows three specimens with the same cross-sectional area, consisting of exactly the same ensemble of particles.

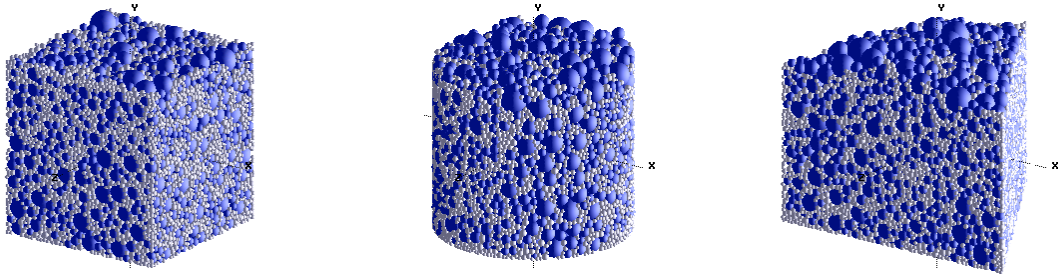


Figure 6: Cubic, cylindrical and prismatic specimens with the same cross-sectional area, generated by use of identical virtual aggregates. The simulation result is in good accordance with Cavalieri's principle.

5.2 Generation of virtual specimens

In order to obtain virtual specimens that keep shape when the respective shuttering unit is removed, cohesive interaction between adjacent particles has to be added to the model. One possibility to achieve this goal is to add a network of immaterial bars to the model (see, for instance, [4]).

Here the following ad hoc approach is chosen, which makes the repulsive and the cohesive interaction forces depending only on the amount of particle intersection: A certain, small value is subtracted from the relative contact volume, which formally allows negative values for the contact volume. This has to be done sufficiently slow in order to avoid premature crack evolution inside of the virtual specimens (see Fig. 7).

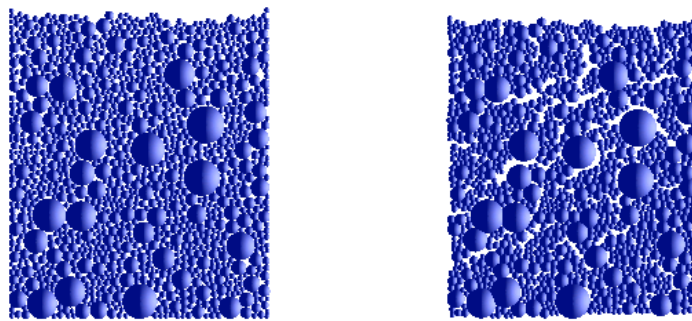


Figure 7: A 2D virtual specimen shortly before and immediately after cohesive interaction has been activated in an abrupt manner.

The virtual specimens obtained by this procedure keep shape and act together like a rigid body when being let loose or been thrown (Fig. 8).

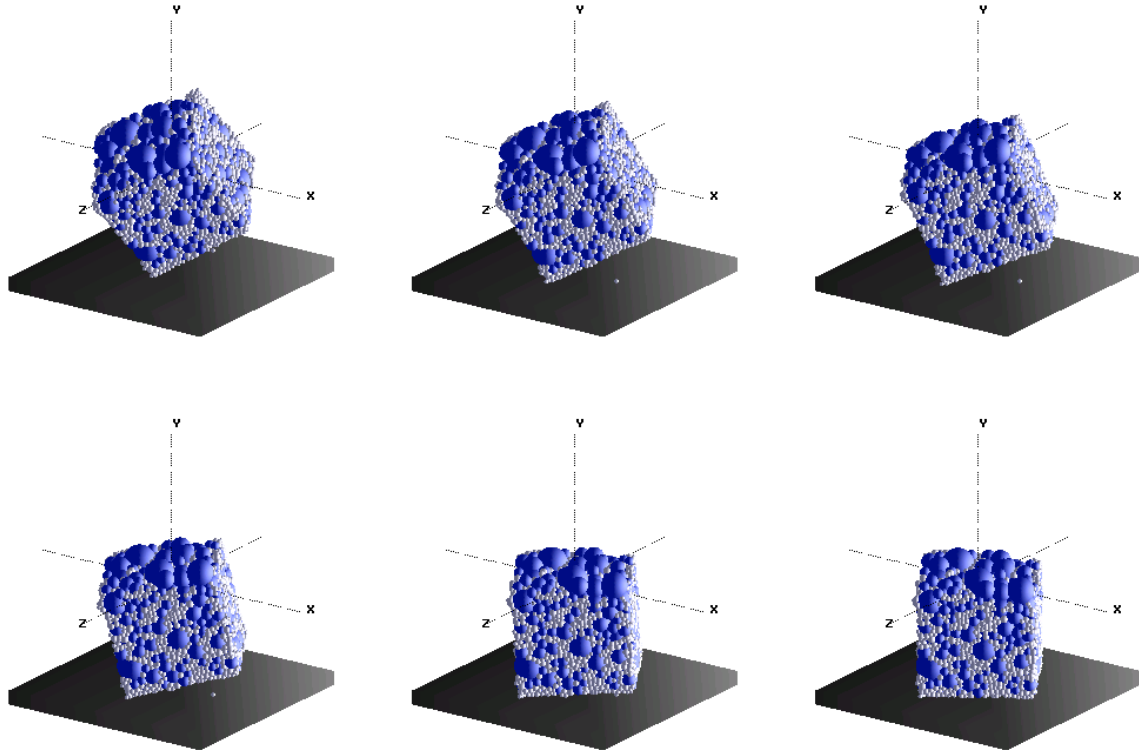


Figure 8: Even without static friction included, this specimen keeps shape when being dropped and hitting a loading plate.

Up to a certain amount of loading, the virtual specimens show elastic material behavior when loaded in compression or tension, while crack evolution and propagation can be observed when the applied forces are furthermore increased (Fig. 9).

6 CONCLUSIONS

The model described allows to generate densely packed ensembles of spherical particles with size distributions that approximate realistic sieving distributions for concrete aggregates. The approach can neither compete with sophisticated models of granular flow, nor with models that are tailored to special cases of loading. On the other hand, it contains no artificial supplements such as bars or other, and allows to detect crack evolution directly. Further efforts have to be made in order to obtain better simulation results, in particular the addition of a suitable model of static friction.

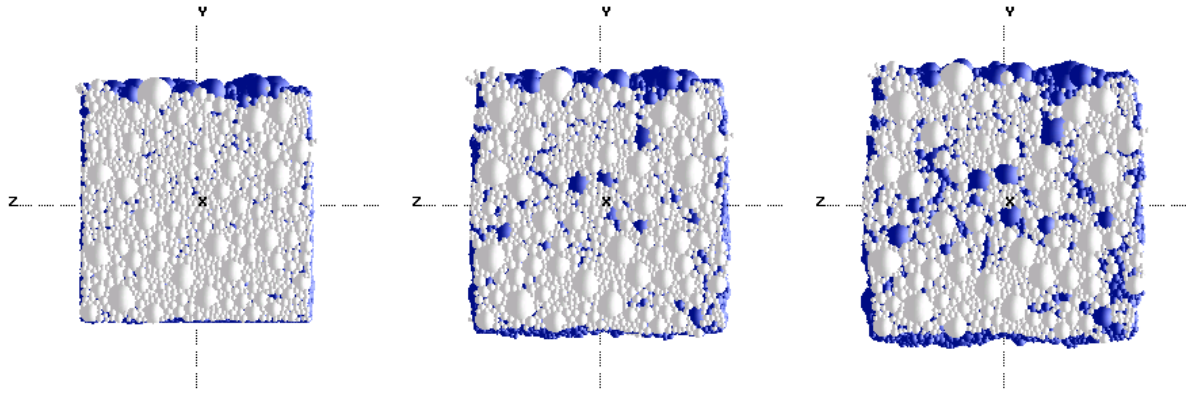


Figure 9: Crack evolution of a virtual specimen loaded in compression. Particles in the area of load application are drawn white in order to visualize the crack pattern.

7 ACKNOWLEDGEMENTS

This work was supported by the Deutsche Forschungsgemeinschaft (DFG). We thank Evans Amponsah, Strahinja Djukanovic and Trung Luu for their support in performing parameter studies and for the visualization of some of the simulation results. Fig. 1 shows a real-world specimen destroyed by spallation, obtained by experimental setup of Tino Kühn, Institute of Concrete Structures.

REFERENCES

- [1] Kohring, G.A., Melin, S., Puhl, H., Tillemans, H.J. and Vermöhlen, W.: Computer simulations of critical, non-stationary granular flow through a hopper. *Computer Methods in Applied Mechanics and Engineering* (1995) **124**:273–281.
- [2] Feng, Y.T. and Owen, D.R.J.: A 2D polygon/polygon contact model: Algorithmic aspects. *Engineering Computations* (2015) **21**:265–277.
- [3] D'Addetta, G.A., Kun, F. and Ramm, E.: On the application of a discrete model to the fracture process of cohesive granular materials. *Granular Matter* (2002) **4**:77–90.
- [4] D'Addetta, G.A.: *Discrete Models for Cohesive Frictional Materials*. Ph.D. Thesis, Universität Stuttgart (2004).
- [5] Beckmann, B., Schicktanz, K., Reischl, D., and Curbach, M.: DEM simulation of concrete fracture and crack evolution. *Structural Concrete* (2012) **13**:213–220.
- [6] Beckmann, B., Schicktanz, K. and Curbach, M.: DEM Simulation of Concrete Fracture Phenomena. *ICMM3 – 3rd International Conference on Material Modelling*. Warsaw, Poland (2013) no. 36.

- [7] Beckmann, B., Schicktanz, K. and Curbach, M.: Discrete Element Simulation of Concrete Fracture and Crack Evolution. *SSCS 2012 – International Conference on Numerical Modelling Strategies for Sustainable Concrete Structures*. Aix-en-Provence, France (2012) no. 301.
- [8] Tran, V.T., Donzé, F.-V. and Marin, P.: A discrete element model of concrete under high triaxial loading. *Cement & Concrete Composites* (2011) **33**:936–948.
- [9] Griebel, M., Knapek, S., Zumbusch, G. and Caglar, A.: *Numerische Simulation in der Moleküldynamik*. Springer (2004).
- [10] Munjiza, A.A.: *The Combined Finite-Discrete Element Method*. Wiley (2004).

ADAPTIVE METHODS FOR THE SIMULATION OF MULTISCALE FLUID DYNAMIC PHENOMENA USING VORTEX PARTICLE METHODS WITH APPLICATIONS TO CIVIL STRUCTURES

DARIO MILANI¹, GUIDO MORGENTHAL²

¹ Bauhaus-Universität
99423, Germany

dario.milani@uni-weimar.de, <http://www.uni-weimar.de/Bauing/MSK/19-en.html>

² Bauhaus-Universität
99423, Germany

guido.morgenthal@uni-weimar.de, <http://www.uni-weimar.de/Bauing/MSK/19-en.html>

Key words: Adaptive Methods, Remeshing, Substepping, Vortex Particle Methods

Abstract. Wind effects on long-span bridges and slender buildings constitute a major criterion during the design phase. These effects are very important in certain cases, because they can lead to strong dynamic excitations of the structure and in some cases also to its failure. The shape optimization often requires the usage of devices such as guide-vanes to enhance a passive flow control in order to reduce those excitations. Despite of their reduced dimensions, they often have a large influence on the entire flow field around the structure. It is then necessary to resolve the small scale fluid features that they generate. Vortex Particle Methods are successfully employed to study these phenomena. These methods consider a discrete number of mutual interacting vorticity-carrying particles to represent the continuous fluid domain. The boundary conditions are imposed by the Boundary Element Method approach which gives the advantage of a grid free Lagrangian formulation of the incompressible Navier-Stokes equations and a natural representation of the vortex creation process which is inherent in bluff body flows. This paper presents an adaptive scheme, the aim of which is the resolution of the small scale flow features in some regions by controlling the spatial and the temporal discretization of the problem of interest.

1 INTRODUCTION

A major criterion for designing civil structures is the estimation of the wind-induced response. Light flexible civil structures as long span suspended bridges are mainly bluff bodies. The wind caused forces lead in some cases towards strong excitation of the

structure and its failure. In these and many other cases it is very important to accurately resolve the flow field in order to evaluate the forces it provokes on the structure. The designer may choose to employ small-scale structures the aim of which is controlling the aerodynamic behaviour i.e. guide vanes in bridge design. In order to take into account their effect, the small scale features of the flow generated by these structured need to be accurately resolved. For these reasons it is required to resolve the multiscale phenomena on bluff bodies. The inherent unsteady flow field generated by bluff bodies is successfully resolved by Vortex Particle Methods (VPM). Furthermore the computational cost required to resolve the multiscale problem increases as the characteristic lengths difference. Adaptive methods needs to be employed in order to locally control the temporal and spacial discretization in order to resolve the smaller scales within certain regions e.g. around the guide vanes. In this paper a brief theory review of the general formulation of the Vortex Particle Methods (VPM) is firstly presented. Afterwards a description of the proposed adaptation schemes is detailed and an application of interest is presented.

2 THEORY REVIEW

A brief theory review is presented within the current section. The analytical expression of the Fluid Dynamic problem is derived, leading towards the formulation required for the Vortex Particle Methods (VPM). The equations are then discretized in order to enhance the numerical solution.

2.1 Analytical formulation

The aerodynamic problem satisfies in this framework the hypotheses of incompressibility of the fluid, zero summation of the external forces. When referring to an inertial frame the Navier-Stokes equations [1] are:

$$\frac{\partial \mathbf{u}}{\partial t} + (\mathbf{u} \nabla) \mathbf{u} = -\frac{1}{\rho} \nabla p + \nu \nabla^2 \mathbf{u}, \quad (1)$$

$$\nabla \cdot \mathbf{u} = 0, \quad (2)$$

where ρ is the fluid density, \mathbf{u} is the velocity vector, p is the pressure and ν is the kinematic viscosity. Vortex Particle Methods are successful techniques for modelling and simulating unsteady flow fields as in [7]-[9], require the vector vorticity $\boldsymbol{\omega}$ defined as:

$$\boldsymbol{\omega} = \nabla \times \mathbf{u}, \quad (3)$$

which appears by taking the curl of the Navier Stokes equations:

$$\frac{\partial \boldsymbol{\omega}}{\partial t} = \nabla \times (\mathbf{u} \times \boldsymbol{\omega}) + \nu \nabla^2 \boldsymbol{\omega}, \quad (4)$$

$$\nabla \cdot \boldsymbol{\omega} = 0. \quad (5)$$

It is straightforward to observe that (5) is always satisfied while (4) can be furthermore simplified when the flow can be assumed as evolving in two dimensions:

$$\frac{\partial \omega}{\partial t} + (\mathbf{u} \cdot \nabla) \omega = \nu \nabla^2 \omega, \quad (6)$$

where the vorticity is a scalar field. When the fluid is also inviscid (6) reduces to:

$$\frac{\partial \omega}{\partial t} + (\mathbf{u} \cdot \nabla) \omega = 0, \quad (7)$$

or:

$$\frac{D\omega}{Dt} = 0, \quad (8)$$

which make use of the compact notation:

$$\frac{D}{Dt} = \frac{\partial}{\partial t} + (\mathbf{u} \cdot \nabla). \quad (9)$$

The solution of the problem as expressed in (8) needs the velocity field to be computed and the boundary conditions to be applied. The boundary conditions are inherently applied using boundary elements. The velocity can be uniquely decomposed velocity into two different terms:

$$\mathbf{u} = \nabla \times \Psi + \mathbf{u}_\infty, \quad (10)$$

where \mathbf{u}_∞ , is a constant describing the velocity at infinity and $\nabla \times \Psi$ is the streamfunction. The curl of (10) leads to:

$$\nabla^2 \Psi = -\omega, \quad (11)$$

which is the Poisson equation associated to this problem. It is then possible to compute the streamline function Ψ through the usage of the Green's functions in two dimensions. By taking the curl of the computed Ψ the general expression of \mathbf{u} is straightforward:

$$\mathbf{u}(\mathbf{x}) = \mathbf{u}_\infty - \frac{1}{2\pi} \int \int_D \frac{\omega(\mathbf{x}_0) \times (\mathbf{x}_0 - \mathbf{x})}{|\mathbf{x}_0 - \mathbf{x}|^2} dD_0. \quad (12)$$

With (12) it is possible to compute velocity field when the vorticity field is known.

2.2 Numerical discretization

The vorticity ω is constant along its streamline as (8) shows. The strategy adopted by the VPM consists then into the discretization of continuous vorticity and velocity fields into particles as in [5]. The vorticity carrying particles evolve in a Lagrangian manner thus without the need for a grid. The discretization of the vorticity into N_p particles leads to the expression of the vorticity field as:

$$\omega(\mathbf{x}, t) = \sum_{p=1}^{N_p} \delta(\mathbf{x} - \mathbf{x}_p(t)) \Gamma_p, \quad (13)$$

where Γ_p is the particle's integral vorticity over it's surrounding area D_p :

$$\Gamma_p = \int_{D_p} \omega dD_p, \quad (14)$$

δ is the Dirac function, and $\mathbf{x}_p(t)$ is the particle location at a certain time t . By combining (12) and (13) the vorticity field can be expressed as:

$$\mathbf{u}(\mathbf{x}_i, t) = \mathbf{U}_\infty - \sum_{p=1}^{N_f} \kappa \Gamma_p, \quad (15)$$

$$\kappa = \frac{\mathbf{e}_y \times (\mathbf{x}_i - \mathbf{x}_p)}{2\pi |\mathbf{x}_i - \mathbf{x}_p|^2}, \quad (16)$$

where e_y is the unit vector in the y direction perpendicular to the plane and κ is the velocity kernel. The velocity at any point is computed by summation of the contributions coming from the entire set of particles used to discrete the fluid domain. Afterwards \mathbf{x}_p is computed by convecting the particles according to their velocities as:

$$\mathbf{x}_k^{n+1} = \mathbf{x}_k^n + \Delta t \mathbf{u}_k^n + O\left(\frac{1}{2}\Delta t^2 \mathbf{a}_k^n\right). \quad (17)$$

The computational cost CC required to solve the problems is dominated at each timestep by the (N_p^2) operations needed to resolve the mutual interaction among the N_p particles used to discrete the domain. This is necessary in order to compute each particle velocity as expressed in (15) at each timestep n . For a complete simulation the cost become:

$$CC = O(N_p^2 * N_t), \quad (18)$$

where N_t is the number of timesteps. If a body is immersed in the fluid domain, then its geometry also needs to be discretized. This discretization process is obtained by creating a polygon of N_i panels of lengths ds_i . At each panel central point the boundary conditions are enforced. This process leads towards a discretized representation of the the circulation on the surface γ_i defined over the panels. This circulation is then integrated over each panel length and released onto the domain as circulation-carrying particles $\Gamma_i = \int_{ds_i} \gamma_i$. This procedure, namely Boundary Element Method, constitutes a major discussion within the advancement proposed in this paper. It has to be noticed that the computational cost needed to enforce the boundary conditions is smaller compared with (N_p^2) i.e. it is not taken into account.

3 ADVANCEMENT ON ADAPTIVITY

Equation (17) shows the importance of the choice of Δt namely temporal discretization, to predict the next position x_k^{n+1} prediction, while comparing (12) against (15) it is

possible to notice the importance of the spacial discretization to represent the whole flow field. Furthermore the Boundary Element Method implies that the particles are released from the surface at a certain timestep. The mechanism of particle releasing plays as well an important role when the performances are evaluated. The importance of these three aspects is at first individually pointed out as the improvements proposed.

3.1 Spacial adaptation

A spatial resolution improvement could be achieved by increasing N_p , but the computational cost would increase as N_p^2 , as (18) shows. The strategy proposed allows to resolve the required features without increasing the total number of particles thus maintaining the computational cost. This will be achieved by modifying the particle map on the fluid domain using a grid. The VPMs are originally girdless methods because of the inherent Lagrangian formulation of the convection process as (8) exhibits. Recent advancements have been published which introduce a grid in order to accelerate the computation. An example are the Fast Multipole Methods [3] and the P3M algorithm [6]. The present method can be efficiently coupled with methods such as the [6] algorithm as a further extension. It is important to clarify that we refer to a mesh as to a collection of points on the fluid domain onto which the particles are projected thus constituting an updated set of particles. Within Fig. (1) the mesh is divided into two regions namely zones. On its right side the grid nodes spacing (δx) is equal to the one defined on the original uniform grid (Δx). We refer to this condition as 0 mesh *level*. On the left side of the grid it is possible to observe that $\delta x = 1/2\Delta x$. In this last case the mesh *level* is equal to one. The expression that links the local mesh *level* = n and the local grid node spacing ($\delta x, \delta y$) is:

$$(\delta x)_k = \frac{(\Delta x)_k}{2^n}, \quad n \in \mathbb{N} \quad (19)$$

$$(\delta y)_k = \frac{(\Delta y)_k}{2^n}, \quad n \in \mathbb{N} \quad (20)$$

where the new local mesh node spacing in a certain location k is $(\delta x)_k$ and $(\delta y)_k$. The *level* $n \in \mathbb{N}$ ensures the conformity of the adapted grid as it is shown in Fig. (1). The parameter n tunes the ratio of the initial x and y mesh node spacing to the adapted ones. According to (19) and (20), the particle spacing is reduced when n increases, and the particle density would be more important. It is then possible to compute a value of n which corresponds to the local need of spatial resolution within the same fluid domain to take into account the presence of the immersed bodies. The proposed expression for n is:

$$n_k(ds_j) = n_{panel}(ds_j) + a\|\mathbf{r}_{j,k}\| + b, \quad (21)$$

which is a linear expression in $\|\mathbf{r}_{j,k}\|$ whereas the coefficients a and b will be chosen to find an optimal balance between the accuracy requirements and the computational cost. The refinement factor computed for the particle k is $n_k(ds_j)$ where $\|\mathbf{r}_{i,j}\|$ is the distance to the

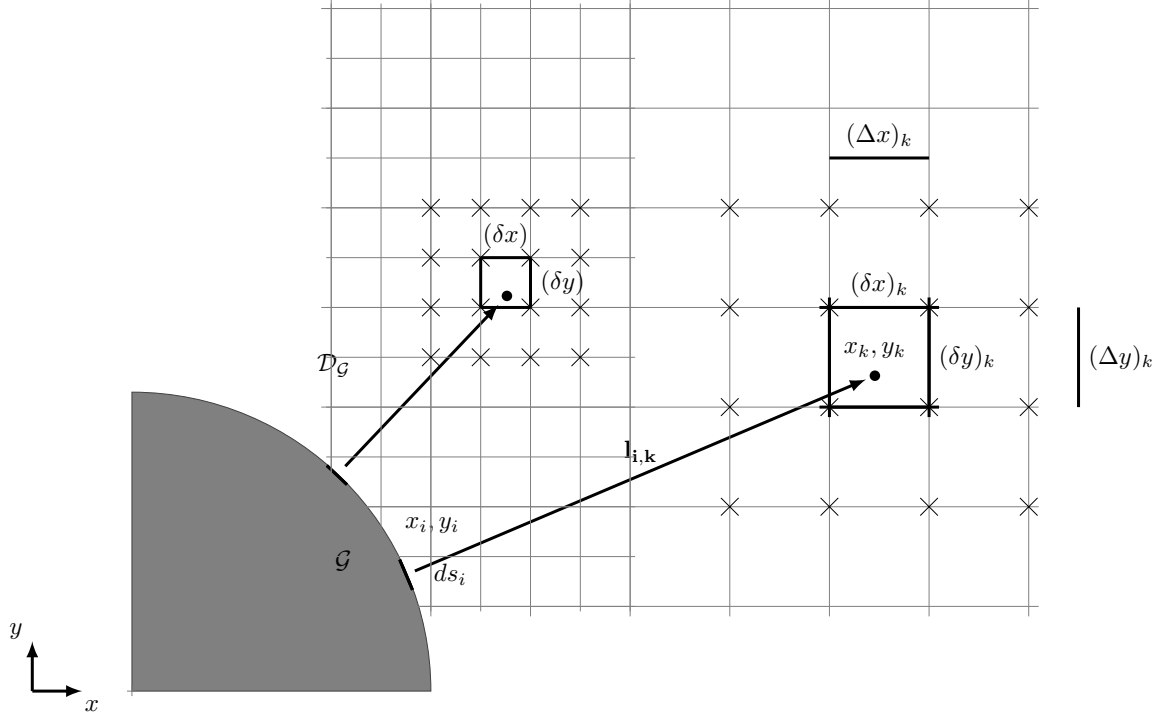


Figure 1: Remeshing strategy based on the distance to the closest surface panel i of length ds_i . The particle k located on the fluid domain at distance $l_{i,k}$ to the closest panel has been projected on the surrounding mesh nodes. Another particle is located on the left side of the grid which is closer to the surface, thus has been projected on the surrounding refined mesh nodes.

closest panel j whose length is ds_j . It is possible to notice in Fig. (5) that the parameter a defines the distance to the surface at which n decreases. The parameter b sets an offset that can be chosen to increase the value of n for each particle. Finally $n_{panel}(ds_j)$ induces the parameter n_k to increase in those regions which are close to the small scale structures, such as the guide vanes. These structures are generally discretized with the finest set of panels in order to apply the boundary conditions, but also the surrounding regions need to be refined in order to accurately consider their influence over the entire problem. The refinement factor on the grid will then increase in order to generate the finest spatial resolution around those structures as:

$$n_{panel}(ds_i) = \log_2\left(\frac{\sqrt{(\Delta x)^2 + (\Delta y)^2}}{ds_i}\right), \quad (22)$$

which can be reduced when dealing with homogeneous initial mesh ($\Delta x = \Delta y$) to:

$$n_{panel}(ds_i) = \log_2\left(\frac{\Delta x}{ds_i}\right) \quad (23)$$

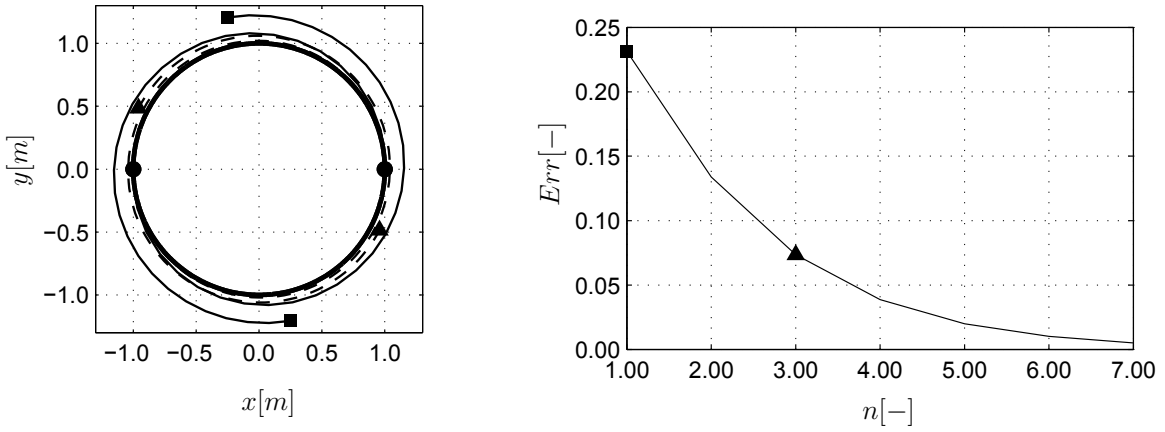
Equation (22) implies that an higher refinement factor is computed close to the smaller length panels. The real refinement factor applied should be an integer in order to assure the conformity of the adapted grid points. This is easily achieved by applying a rounding operator:

$$n_k = \max_i (n_k(ds_j)), \quad (24)$$

where the expression for $n_k(ds_j)$ was given in (21).

3.2 Temporal adaptation

Equation (17) shows how the temporal discretization affects the accuracy. Furthermore the example summarised in Figure (2) shows the impact of Δt on the resolution of a two interacting particles problem in which they are both assigned with a circulation of $\Gamma = 1 [m^2/s]$. Their initial distance is $1 [m]$ and they are free to convect. The circular pattern defines the analytical solution. After a period over T reach their initial position (thick line) while the discretized problem solved with (17) and (15) leads the particles distance to increase within the iteration process. The timestep adopted for the different



(a) Particle-Particle interaction path.

(b) Particle-Particle interaction error Err .

Figure 2: The round markers represent the initial position of the particles. The thick line represent the analytical solution of the problem requiring the particles to rotate and to reach their initial position over a period. The square and the triangle represent the final positions in (a) and the relative error in (b) when the substepping has been applied with different levels.

simulations is computed as:

$$\delta t = \frac{\delta t_0}{2^{level}}, \quad (25)$$

and the error Err is computed as:

$$Err = \frac{d - d_0}{d_0}, \quad (26)$$

where d_0 and d are respectively the initial and the final distance of the two particles and $\delta t_0 = T/60$. The analytical solution is characterised by $d = d_0$ that leads to $Err = 0$. It is then possible to increase the accuracy by reducing δt . The multi body problem represented by N_p particles is more difficult to solve and it does not have the analytical solution. However the considerations proposed for the two particles problem can be extended towards a complex case. The proposed strategy, proposes to classify the particles in different regions. Each one of those regions is assigned with a refinement factor n that determines the fractional duration of the local timestep duration to the global one. The particles belonging to regions in which n is large will convect with high accuracy because they velocities as in Fig. (3). Moreover the particles are introduced into the domain

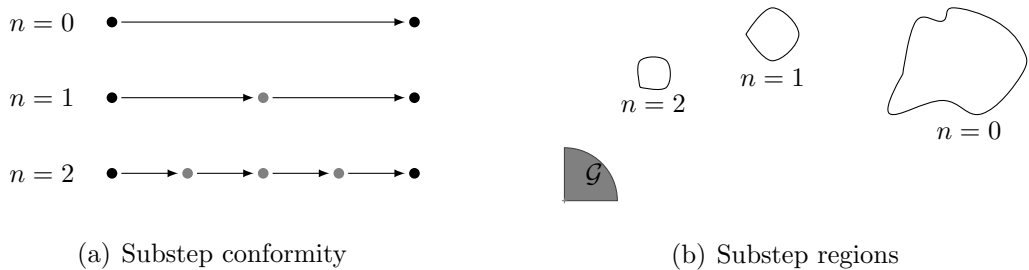


Figure 3: (a) The particles used to discretized the fluid domain are categorised in three regions based on their distance to the small structure \mathcal{G} . Each of these regions is assigned with a level n thus the local substep duration.(b).

through the external boundaries or they can be created on the surface of the immersed body thus released into the domain. For this second case a study has been performed in order to find the best way to couple the substepping strategy with the process of particle releasing. The first implementation of this strategy included the releasing of the particle at each timestep and substep. This procedure was improving the performance of the method although it was introducing numerical errors. A new procedure is presented within this paper in order to increase the impact of the strategy on the global performances. With that purpose the vorticity computed on the discretized surface is updated and released every timestep, as Fig. (4) shows, while only the iteration process occurs during the substeps. The computational cost is reduced because of the bound vorticity evaluations occurs once every timestep in spite of B times every timestep, where B is the number of timestep used to discretized the finest region, and a smaller amount of particles is released onto the fluid domain during a timestep. The accuracy increases because the boundary condition should be applied when the particles are coherently convected by the global timestep δt .

3.3 Full adaptivity

The substepping and the remeshing may be separately applied to the problem of interest. However it is important to notice that the spacial and the temporal discretization

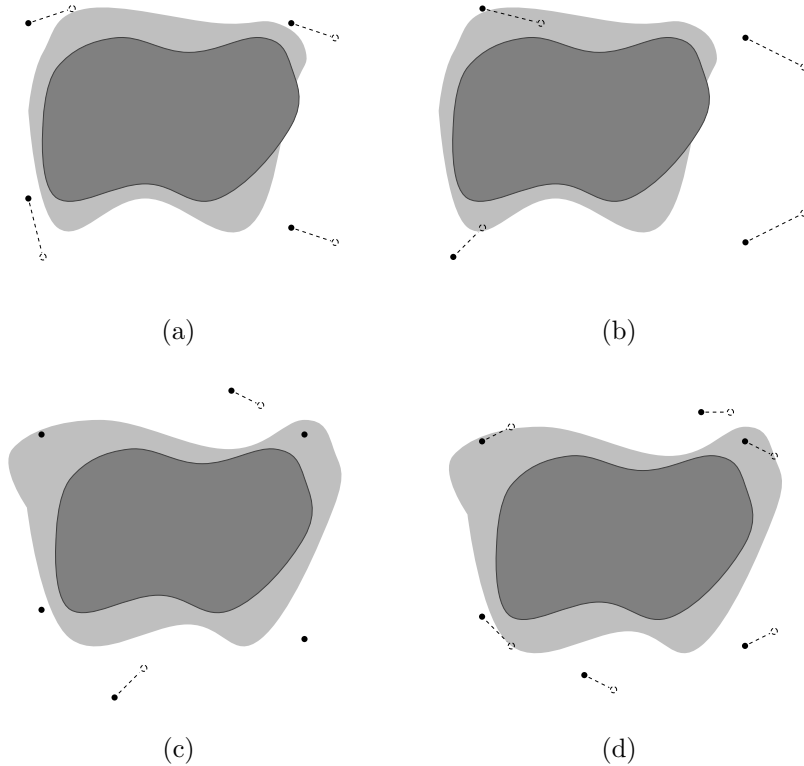


Figure 4: Releasing particle strategy from an immersed body; First substep $b = 1$ within a generic timestep s (a), particle convection process occurring from substep $b = 2$ until substep $b = B - 1$ (b), final convection substep $b = B$ within the timestep s with bound vorticity releasing into particles and computation of the new bound vorticity (c), convection of the new set of particles during the following timestep $s + 1$ (d).

are linked in all the numerical schemes present in literature e.g the Courant number [4] in finite difference schemes. Within this framework some numerical dissipation is introduced by the kernel in equation 16 because instabilities arise when the particle are close. When the remeshing and substepping strategy are applied together, the particle distance is controlled thus deleting the artificial dissipation.

With this purpose it is possible to compute a refinement factor n associated with the region of interest and to use simultaneously for the temporal and spacial discretization as prescribed. The next section will be devoted to apply these methods to a case of interest.

4 Reference object

The author chooses the Alcónetar Bridge as the reference object to exhibit the performances of these strategies. This bridge was built in 2006 in Spain in order to carry the route A-66 across the Tagus River. In spite of the low and regular speed of the air ($8m/s$), critical vibration episodes occurred. The introduction of the guide vanes allowed for a

passive control of the aerodynamic behaviour i.e. reducing the Vortex Induced Vibrations as in [8]. The two rectangular tandem arrangement that constitutes the shape of the bridge is shown in Fig. 5.

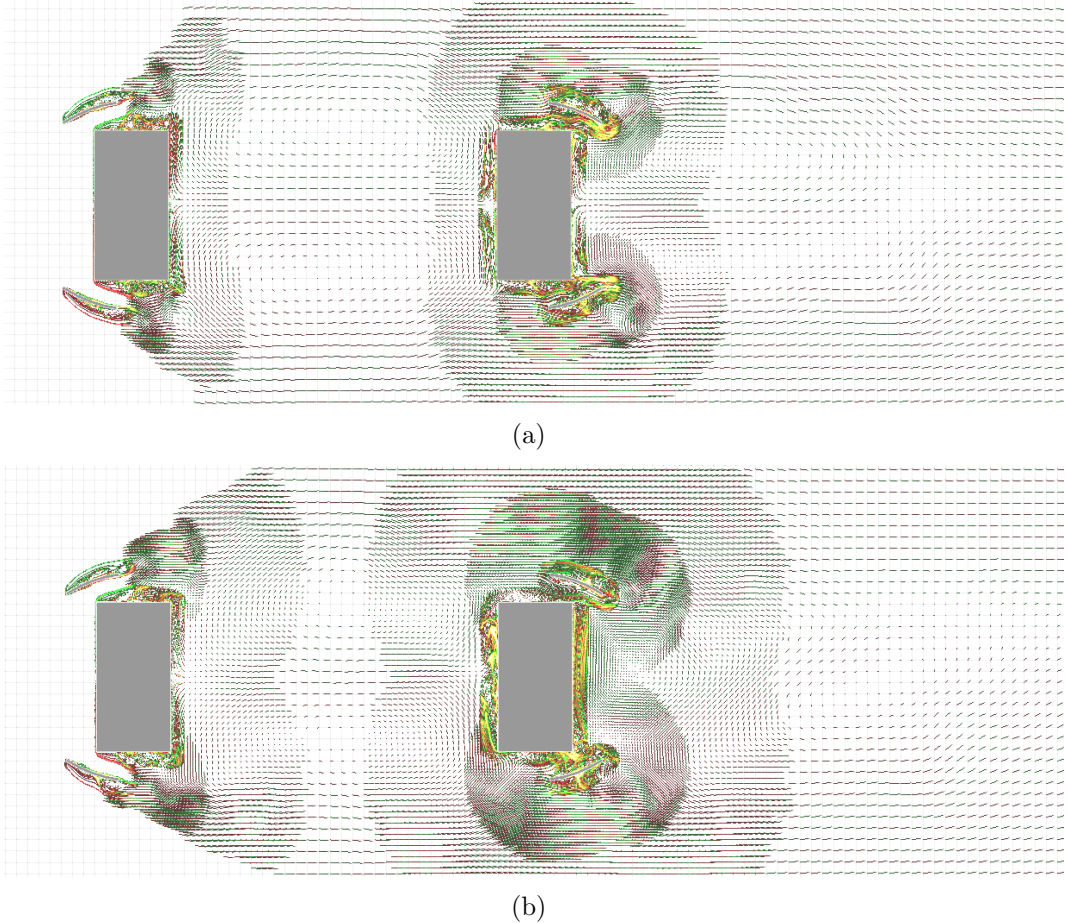


Figure 5: Projected particles for remeshing. In (a) the parameter a_1 is equal to 1, while in (b) $a = 0.6$ in order to extend the high refinement region.

The guide vanes are used to reduce the Vortex Induced Vibrations (VIV). The herein proposed mesh adaptations schemes are applied in order to prove that it is possible to enhance a good accuracy by efficiently resolving the small scale flow featured around the guide vanes while saving computational effort.

4.1 Numerical results

The Vortex Particle Method solver used for implementation is VXflow [6]. The comparison has been performed in terms of Strouhal number:

$$St = \frac{f_s D}{U_\infty}, \quad (27)$$

where f_s is the vortex shedding frequency, D is the depth of the cross section and U_∞ is the wind speed. The aim of this comparison is to show that it is possible to largely reduce the computational cost (CC) with a moderate error (Err). The comparison is presented in Table 4.1. It is possible to confirm from previous studies, as in [8], that the Strouhal number value of this problem is around 2. The value that has been computed here stands in a very good accordance with the previous results: $St = 2.0439$ and it is taken as reference.

It is possible to define an averaged particles number \bar{N}_{ps} for each simulation s :

$$\bar{N}_{ps} = \frac{\sum_{N_{ts}} N_{ps}(t)}{N_{ts}}, \quad (28)$$

where $N_{ps}(t)$ is the number of particles for each timestep t and N_{ts} is the number of timesteps. The computational cost Cc_s already expressed in (18) is defined here with respect to a reference simulation *free*:

$$CC_s = \frac{(N_{ps}^2 N_{ts})}{(N_{pFree}^2 N_{tFree})}, \quad (29)$$

and the error Err is defined as:

$$Err_s(\%) = \frac{St_s - St_{Free}}{St_{Free}} * 100. \quad (30)$$

Table 1: Alcónatar bridge

	N_{ps}	St_s	Cc_s	$Err_s(\%)$
Free	$3.7 * 10^5$	0.20439	1.00	0%
Remesh1	$8.1 * 10^4$	0.21855	0.05	5.81%
Remesh2	$1.1 * 10^5$	0.20752	0.09	1.52%
Remesh3*	$1.5 * 10^5$	0.20801	0.12	1.98%
Full adapt2	$2 * 2.1 * 10^5$	0.20308	0.33	-0.64%
Full adapt3*	$2 * 1.0 * 10^5$	0.20680	0.18	-0.71%

The results show that there is a satisfactory agreement with the literature St number and the simulations. In Remesh1 Remesh2 and Remesh3 (Table 4.1) the refinement factor near the body surface increases. The accuracy increases coherently from Remesh1 to Remesh2. The accuracy lack in Remesh3 suggests that the particles distance in the close surface proximity is too small. In that case the substepping is needed in order to discard the artificial dissipation introduced by (16). Then the substepping is applied to this case in Full adapt3* improving the accuracy as expected. Another important remark

concerns the difference between the two particles releasing procedures which has already been explained. In Full adapt2 the particles are released at each timestep while in Full adapt3* they are released only once each timestep. The lack of accuracy within Full adapt3* is largely justified by the computational cost reduction due to the herein devised releasing process.

5 CONCLUSIONS

The computation of the Strouhal number is crucial in this framework as it allows to describe the behaviour of the bluff body problem. An accurate Strouhal number prediction means, for such a problem, that the small flow features are resolved using the herein proposed adaptive scheme. It is possible to conclude that the proposed strategy allows for the resolution of the small scales while maintaining an affordable computational cost.

REFERENCES

- [1] A. Chorin, J. Marsden, *A mathematical introduction to fluid mechanics* volume 4. Springer, 1993.
- [2] G. H. Cottet, P. D. Koumoutsakos, *Vortex methods: theory and practice*, 2001.
- [3] Y. J. Liu, N. Nishimura *The fast multipole boundary element method for potential problems: a tutorial* Engineering Analysis with Boundary Elements 30.5 (2006): 371-381.
- [4] R. Courant, K. Friedrichs, H. Lewy, *On the Partial Difference Equations of Mathematical Physics*, IBM J. 11, 215-234, 1967.
- [5] J.H. Walther, A. Larsen, *Discrete vortex method for application to bluff body aerodynamics*, J. Wind Engineering and Industrial Aerodynamics, 67-68, 183-193, 1997.
- [6] G. Morgenthal, *Aerodynamic Analysis of Structures Using High Resolution Vortex Particle Methods*, Ph.D. thesis, University of Cambridge, 2002.
- [7] G. Morgenthal, A.S. Corriols, B. Bendig, *A GPU-accelerated Pseudo-3D Vortex Method for Aerodynamic Analysis*, Journal of Wind Engineering and Industrial Aerodynamics, 125 (2014), pp. 69-80, 2014.
- [8] A.S. Corriols, G. Morgenthal, *Vortex-Induced Vibrations on Cross Sections in Tandem Arrangement*, Structural Engineering International (IABSE) 2013.
- [9] J.M. Prendergast, *Simulation of unsteady 2-D wind by a vortex method*, PhD thesis, University of Cambridge, Department of Engineering, 2007.

APPLICATION OF THE LATTICE BOLTZMANN METHOD IN ACOUSTICS

ERIK M. SALOMONS¹, WALTER J.A. LOHMAN¹, AND HAN ZHOU¹

¹ TNO Netherlands Organization of Applied Scientific Research
Van Mourik Broekmanweg 6, 2628 XE Delft, The Netherlands
e-mail: erik.salomons@tno.nl

Key words: Lattice Boltzmann method, fluid flow, acoustics, porous materials.

Abstract. In this paper, practical aspects of the lattice Boltzmann method for fluid flow are explored and application to sound propagation is investigated. This work was performed within the framework of the European ITEA project MACH, which aims at optimizing scientific calculations on various parallel platforms. For fluid flow, our attention was drawn to the lattice Boltzmann method because of its advantages over other methods: the method is suitable for parallel computation, and it can be applied easily to systems with complex boundaries, such as porous media. We first developed simple 2D and 3D lattice Boltzmann codes for fluid flow in a lid-driven cavity. We explored possibilities to run it on the GPU of a personal computer, and we investigated GPU speedup factors. Next we developed a lattice Boltzmann code for simulation of sound waves. Various acoustic phenomena were investigated with this code, such as geometrical spreading of sound waves generated by a point source, reflection of sound waves by a rigid surface, and diffraction of sound waves by a noise barrier. Reflection of sound waves by a porous medium was also explored, and a comparison was made with theoretical solutions. Finally, the possibility to simulate sound propagation in an atmosphere with wind and temperature gradients was considered.

1 INTRODUCTION

Traditional methods for simulating fluid flow are based on the equations for conservation of mass and momentum in a fluid, i.e. the continuity equation and the Navier Stokes equations, respectively (see Refs. [1][2], for example). The conservation equations are differential equations based on the continuum model of a fluid. The equations can be solved by various numerical techniques.

The lattice Boltzmann method (LB method, or LBM) is an alternative approach for calculating fluid flow. An introduction to the LB method, and references to the literature, can be found in Ref. [3]. The LB method originates from lattice gas automata (LGA) for simulating fluid flow, which were developed in the 1980s. While the LGA method works with discrete particles on a regular lattice, the LB method works with a particle distribution function. The LB method is based on the Boltzmann equation from kinetic gas theory, which describes how distributions of particles in a gas propagate and collide [1]. Collisions may be modeled by the Bhatnagar-Gross-Krook (BGK) collision operator. The LB method with the BGK operator is often referred to as the LBGK method. From the LBGK equations, the Navier Stokes and continuity equations can be derived, under certain limiting conditions that depend on the actual formulation. Common limiting conditions are weak compressibility and

low Mach number (see Ref. [4] and references cited therein).

Sound propagation in the atmosphere is basically a special case of fluid flow. A sound wave is a small perturbation of the pressure and fluid velocity, which travels with the speed of sound. Consequently, fluid flow models may be applied for simulating sound propagation. An early application of the LB method to sound propagation is described in Ref. [5]. An extensive study of application of the LB method in acoustics was recently performed by Viggan [6][7].

In the present paper, application of the LB method in outdoor acoustics is described. A few practical cases are considered, including the cases of sound propagation near a (porous) ground surface and sound propagation over a noise barrier. A preliminary conclusion is that the LB method may be more powerful in dealing with complex geometries than other numerical methods in outdoor acoustics are [8][9][10][11].

This work was performed within the framework of the European ITEA project MACH, which aims at optimizing scientific calculations on various parallel platforms [12]. Computational fluid dynamics is one of the fields of application considered in MACH. We decided to explore the LB method because of its advantages over other fluid-flow simulation methods: the LB method is suitable for parallel computation, and it can be applied easily to systems with complex boundaries, such as porous media. Previous work on speeding up LB models by means of parallel computation, including computation on GPUs and supercomputers, is described in Refs. [13][14]. The focus in MACH is on (semi) automatic generation of computer code suitable for running on various platforms for parallel computation.

2 LATTICE BOLTZMANN METHOD FOR FLUID FLOW

2.1 Method

With the LB method a fluid is represented by means of a particle distribution function on a regular lattice [3]. The value of the distribution function at a lattice node represents the density of fluid particles at the node. Different particle velocities are distinguished, corresponding to the movement of particles to different neighboring lattice nodes during a time step. Consequently, the particle distribution function varies not only with position in the lattice but is also a function of the discrete set of particle velocities.

The LB particle distribution function is denoted as $f_i(\mathbf{x}, t)$, where index $i = 0, 1, 2, \dots$ distinguishes the different velocities to neighboring lattice nodes, \mathbf{x} denotes position on the lattice, and t represents time. Here we consider the formulation of the LB method based on the BGK (Bhatnagar-Gross-Krook) approximation. The evolution of the fluid is represented by the following equation:

$$f_i(\mathbf{x} + \mathbf{e}_i \Delta t, t + \Delta t) = f_i(\mathbf{x}, t) - \frac{1}{\tau} (f_i(\mathbf{x}, t) - f_i^{\text{eq}}(\mathbf{x}, t)), \quad (1)$$

where \mathbf{e}_i are the velocity vectors to neighboring nodes, Δt is the time step, τ is the relaxation time, and f_i^{eq} is the local equilibrium distribution function. We choose length and time units such that lattice spacing Δx and time step Δt are unity, so the particle speed $c = \Delta x / \Delta t$ is also

unity. The first part of the equation, $f_i(\mathbf{x} + \mathbf{e}_i \Delta t, t + \Delta t) = f_i(\mathbf{x}, t)$, represents streaming of particles between neighboring nodes. The last term represents collisions between particles. Collisions of the fluid particles correspond to a relaxation towards local equilibrium.

Figure 1 illustrates the widely used D2Q9 lattice for the LB method in 2D. There are nine velocity vectors \mathbf{e}_i to neighboring lattice nodes: $\mathbf{e}_0 = (0,0)$, $\mathbf{e}_1 = (1,0)$, $\mathbf{e}_2 = (0,1)$, ..., $\mathbf{e}_8 = (1,-1)$. Here we have used an xy coordinate system with a horizontal x axis and a vertical y axis. The first vector \mathbf{e}_0 corresponds to zero velocity, so particles with $i=0$ do not move to a neighboring node.

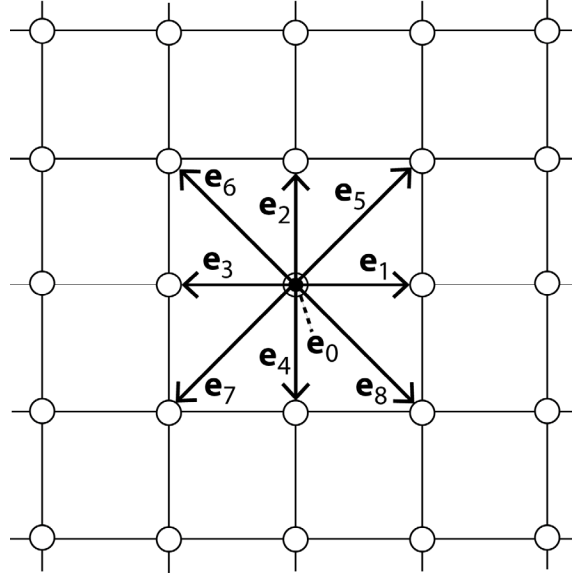


Figure 1: Rectangular 2D lattice illustrating the 2DQ9 scheme for the LB method.

The macroscopic fluid density ρ and the fluid velocity \mathbf{u} follow from the distribution function: $\rho = \sum_i f_i$ and $\mathbf{u} = \frac{1}{\rho} \sum_i f_i \mathbf{e}_i$. The fluid density is related to the pressure p through the ideal gas law $p = c_s^2 \rho$, where c_s is the sound speed in lattice units $\Delta x / \Delta t$, which is $1/\sqrt{3}$ for the D2Q9 and D3Q19 lattices. The density is included in the LB model as an independent variable in a regime close to fluid incompressibility [4]. The relaxation time τ is related to the kinematic shear viscosity ν of the fluid: $\nu = c_s^2 (\tau - \frac{1}{2})$. The viscosity is positive for $\tau > \frac{1}{2}$. As τ approaches $\frac{1}{2}$ numerical difficulties may occur. A safe choice is $\tau = 1$, which gives $\nu = \frac{1}{6}$. In the BGK approximation, the equilibrium distribution function is given by

$$f_i^{\text{eq}} = w_i \rho \left(1 + \frac{\mathbf{e}_i \cdot \mathbf{u}}{c_s^2} + \frac{(\mathbf{e}_i \cdot \mathbf{u})^2}{2c_s^4} - \frac{\mathbf{u}^2}{2c_s^2} \right), \quad (2)$$

which is a truncated expansion of the Maxwell velocity distribution. The factors w_i are weight factors for the different velocity directions. For the D2Q9 scheme, the weights w_i are

$$\left(\frac{4}{9}, \frac{1}{9}, \frac{1}{9}, \frac{1}{9}, \frac{1}{9}, \frac{1}{36}, \frac{1}{36}, \frac{1}{36}, \frac{1}{36}\right) \text{ for } i = 0, 1, \dots, 8.$$

The core of a LB code is a loop over four elements:

- collisions
- streaming
- boundary conditions
- macroscopic quantities.

The first three elements yield updates of the distribution function, due to collisions, streaming, and boundary conditions, respectively. The fourth element is the calculation of density ρ and velocity components u and v of fluid velocity $\mathbf{u} = (u, v)$, which are used in the collision calculation.

Different types of boundary conditions exist. At a stationary boundary (zero velocity at a wall) one may apply bounceback conditions, which means that a distribution function component f_i directed into the fluid is obtained from the component in the opposite (outward) direction. First-order and second-order bounceback formulations have been developed [3]. For a boundary with an imposed velocity or pressure, boundary conditions were presented in Ref. [15].

2.2 Lid-driven cavity

Figure 2 shows results of a D2Q9 LB calculation for the case of a lid-driven cavity in 2D. The fluid is enclosed in a square box with solid walls, while at the top of the box a constant horizontal velocity u_0 is imposed as a boundary condition. The calculation was performed for a 1000x1000 grid, with $u_0 = 0.06$ and $\nu = 0.06$. The Reynolds number $Re = u_0 L / \nu$ is equal to 1000 in this case, with grid size $L=1000$. The graphs show the (steady state) fluid flow after $16 \cdot 10^4$ time steps.

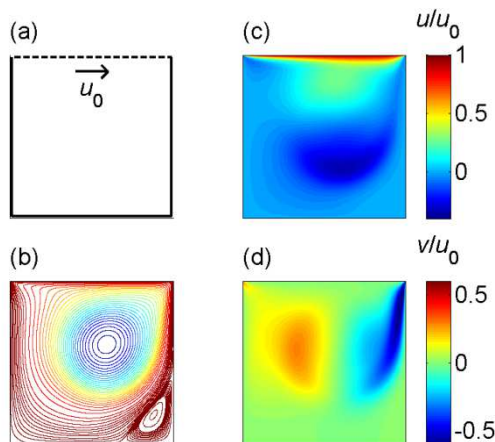


Figure 2: Results of a LB calculation for a lid-driven cavity, with the geometry (a), streamlines (b), and normalized velocity components u/u_0 (c) and v/u_0 (d).

2.3 Calculation times and GPU speedup

As mentioned in Section 1, this work was performed within the framework of the European project MACH, which aims at speeding up various types of scientific calculations. In this section we present a few calculation times for the LB model for a lid-driven cavity (see previous section). Calculations were performed with non-optimized codes on a PC with a 2.4 GHz CPU (Intel Xeon E5620, 6GB RAM) and an NVIDIA GPU (GeForce GTX 680, 4GB, 1536 CUDA cores).

For a 2DQ9 100x100 grid with $Re=1000$ ($u_0 = 0.6$, $\nu = 0.06$) we achieved a steady state within 4000 time steps, which took about 20 seconds with a Matlab code and 8 seconds with a code converted to C/C++ (running on a single CPU core). These times correspond to 2 and 5 MLUPS, respectively (MLUPS = mega lattice site updates per second). With a CUDA code [16] running on the GPU we found 2 seconds.

For a 2DQ9 1000x1000 grid with $Re=1000$ ($u_0 = 0.06$, $\nu = 0.06$) we needed $16 \cdot 10^4$ time steps to achieve a steady state, and with a Matlab code this took 32h (running on a single CPU core), corresponding to 1.4 MLUPS. With a modified Matlab code that employs the GPU, making use of the Matlab parallel processing toolbox, the time was 12h, corresponding to 3.7 MLUPS. The total number of $16 \cdot 10^4$ time steps is nearly two orders of magnitude larger than the 4000 times steps for the 100x100 grid, due to the fact that the equilibration time scales with the square of the linear grid size [17].

For a 3DQ19 100x100x100 grid with $Re=1000$ ($u_0 = 0.6$, $\nu = 0.06$) we achieved a steady state within 4000 time steps, which took about 6000 seconds with a Matlab code (running on a single CPU core), corresponding to 0.7 MLUPS. With Matlab running on the GPU we found about 1800 seconds, corresponding to 2.2 MLUPS.

It should be noted that the above results were obtained with codes that were not yet optimized with respect to calculation speed and memory performance. Currently we are working on the development of optimized codes in CUDA, both along the lines described in Ref. [13] (dedicated optimization) and by the generic optimization tools that will be developed in the project MACH. We expect to reach an enhancement of the calculation speed by at least one order of magnitude.

3 APPLICATION IN ACOUSTICS

3.1 Sound waves generated by a point source

The LB method can be used for simulating propagation of sound waves. We used the 2DQ9 LB model to model circular sound waves generated by a point source. Circular waves in 2D correspond to cylindrical waves in 3D. Figure 3 shows the sound field at time step 1600, generated by a point source at position (1000,1000) in a 2000x2000 grid with $\nu = 0.06$.

The fluid density at the source position was imposed at the end of each time step, according to the harmonic function $\rho = 1 + 0.01\sin(\omega t)$, where t is the time, $\omega = 2\pi/T$ is the angular frequency, and $T = 40$ is the harmonic period. The density oscillates around the equilibrium density of unity. The off-equilibrium density $\rho' \equiv \rho - 1$, or acoustic density, is given by (the real part) of the following function of time t and distance r to the source:

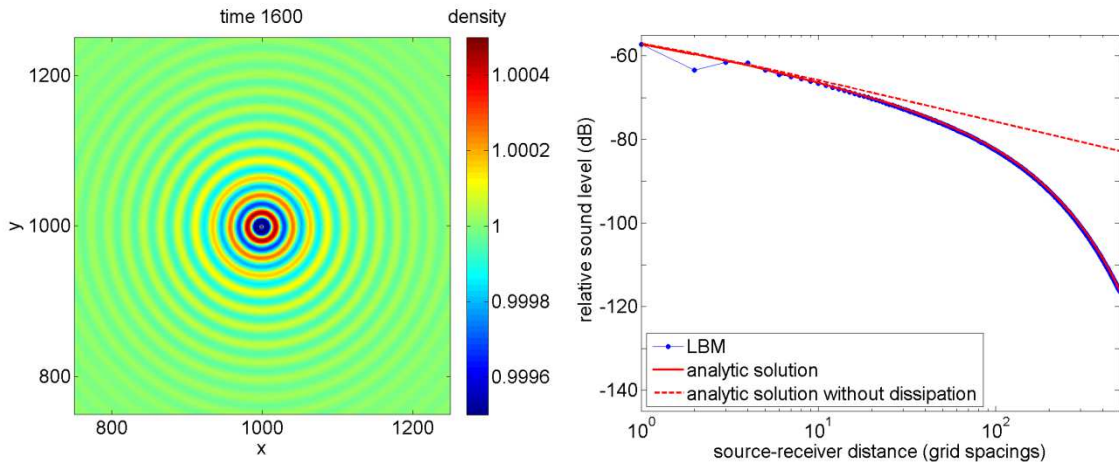


Figure 3: Results of a LB calculation for a sound wave, showing the sound field at time 1600 (left) and the relative sound level as a function of source-receiver distance (right).

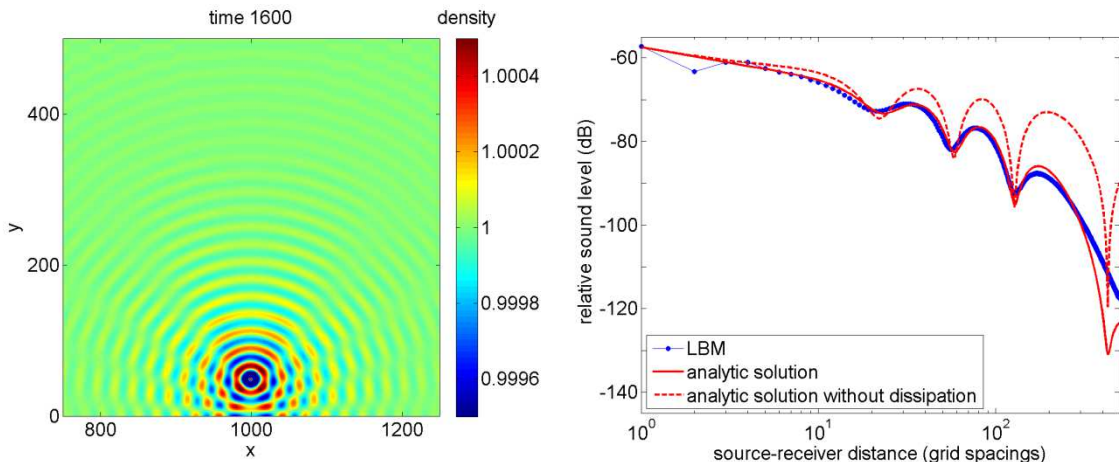


Figure 4: As Figure 3, for a point source and receivers at height $y = 50$.

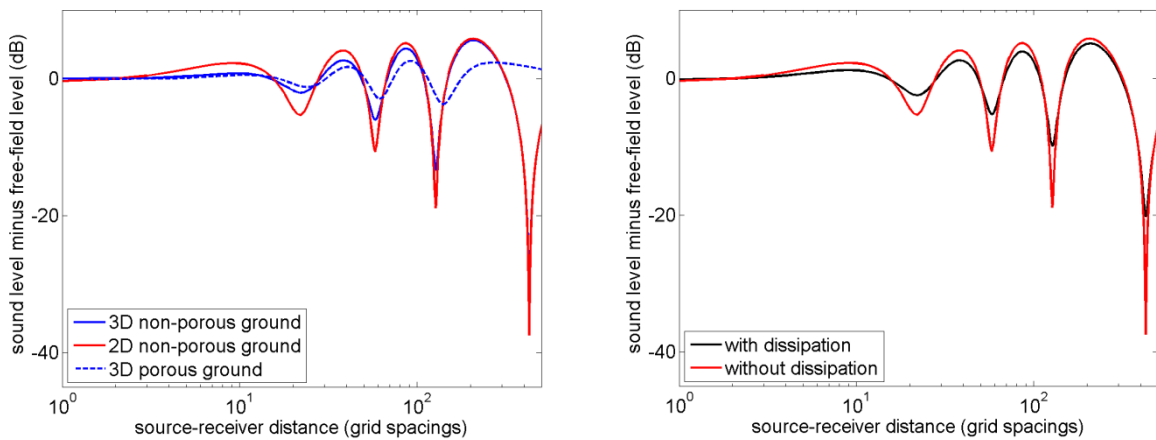


Figure 5: Analytical solutions for the sound level minus the free-field level, for the system of Figure 4 with a grid spacing of 0.1 m. The left graph shows 2D and 3D solution for non-porous and porous ground (without dissipation), and the right graph shows solutions with and without dissipation (2D, non-porous ground).

$$\rho' = AH_0^{(2)}(kr) \exp(i\omega t), \quad (3)$$

where A is a constant, $H_0^{(2)}$ is the Hankel function of order zero and second kind, and k is the wavenumber. This expression is a stationary solution of the lossy wave equation, taking into account effects of viscosity [6][18]. The wave number is given by $k = \omega/c_s - i\alpha_s$, where we have $\alpha_s = (\omega/\sqrt{2}c_s)\sqrt{[\sqrt{1+(\omega\tau_s)^2}-1]/[1+(\omega\tau_s)^2]}$ and $\tau_s = c_s^{-2}(\frac{4}{3}\nu + \nu')$, with kinematic shear and bulk viscosities ν and $\nu' = \frac{2}{3}\nu$. The wavelength is equal to $T \cdot c_s$, which is 23 lattice units in this case, in agreement with the wave pattern shown in Figure 3. The amplitude of the wave decreases with distance r from the source by two effects, geometrical spreading and dissipation. Geometrical spreading is represented by the factor $r^{-1/2}$, which is the asymptotic behavior of the Hankel function for real wavenumber k . Dissipation due to viscosity is represented by the imaginary part α_s of the wave number. Figure 3 shows how the relative sound level, defined as $20 \lg \rho'_{\text{rms}}$, with ρ'_{rms} the rms-value of ρ' , decreases with distance r . The LBM results agree with the analytic solution beyond a distance of three grid spacings (blue dots and the red solid line coincide here). Also shown is the analytic solution without dissipation ($\alpha_s = 0$), which decays with 10 dB per distance decade ($20 \lg 10^{-1/2} = -10$ dB). The figure demonstrates that dissipation dominates the attenuation at large distance, where the attenuation reaches a value of about 0.06 dB per grid spacing in this case.

The dissipation is a problem for direct application of the LB method in acoustics. The dissipation of sound waves in air is small, typically 0.1 dB/km at frequency 50 Hz and 1 dB/km at 250 Hz. If we choose a grid spacing of 0.1 m, for example, the above attenuation in the LB system is 0.6 dB/m, so much larger than real attenuations at audio frequencies. The attenuation in the LB system can be varied a bit through the choice of the value of $\nu = c_s^2(\tau - \frac{1}{2})$, but as indicated before numerical difficulties may occur for τ near $\frac{1}{2}$, so the possible variation is limited. A better approach may be to keep the frequency in the LB model low, thereby maximizing the region where geometrical attenuation dominates, and to convert the results to a real system by adding air absorption afterwards and applying the acoustical principle of scaling to convert to higher frequencies.

3.2 Effect of a non-porous ground surface

We have simulated the sound field of a point source near a non-porous ground surface. The system is similar to the previous system, except now we used a 2000x500 grid and the source was located at position (1000,50), so the source is 50 grid spacings above the ground surface. Figure 4 shows the results. The effect of interference between direct and reflected sound waves is visible as spatial oscillations of the sound level. The sound level was sampled at receivers at positions (1001-1500,50).

The analytic solutions in Figure 4 were calculated by (coherent) summation of the direct field and the field reflected by the ground surface. The LBM results agree well with the analytic solution (with dissipation). The analytic solutions are also represented in Figure 5,

now expressed as the excess level ΔL , defined as the sound level minus the free-field level. The dissipation effects largely cancel with this level difference. The LB units may be converted to physical units by assuming a grid spacing of 0.1 m, for example. This means that source and receivers are 5 m above the ground surface, and the frequency is 148 Hz.

Also included in Figure 5 is a 3D solution, calculated with $\exp(-ikr)/r$ instead of $H_0^{(2)}(kr)$. The difference in ΔL between the 2D solution and the 3D solution is small. The figure shows further that the dissipation effects largely cancel in the quantity ΔL . It is common practice in acoustics to work with excess level ΔL . The actual free field may be added to obtain the overall field.

The solution for a porous ground in Figure 5 deviates considerably from the other solutions, and is considered in the next section.

3.3 Effect of a porous ground surface

Next we have used the LB method for simulating the reflection of sound waves by a porous medium. We used a grid with 2000x700 nodes, with numerical parameters as before. The region between $y = 0$ and $y = 200$ was filled with a porous medium, and source and receivers were located at $y = 250$. The porous medium was generated by randomly selecting 30 percent of the nodes as solid nodes, where LB bounceback conditions apply. Figure 6 shows the results. The interference pattern is less pronounced than with the non-porous ground, since the reflection from the porous ground is weaker.

The analytic solution in Figure 6 was calculated with a theoretical model for sound reflection from a porous ground (see Ref. [8]), where we assumed again a grid spacing of 0.1 m to convert LB units to physical units. The total sound field is the sum of the direct field and the field reflected by the ground surface. The acoustic impedance of a porous ground is a function of the flow resistivity, the porosity, and a structure factor [19] (see also [8][9]). In this case, the porosity is 0.7, for the structure factor we used a value of 3, and the flow resistivity was estimated at 10 kPa s m^{-2} from a LB simulation illustrated in Figure 7. For this simulation we used a 100x100 grid with porous medium between $y = 25$ and $y = 75$, and an upward inflow condition at $y = 0$. The flow resistivity was estimated from the definition as the ratio of the pressure gradient and the velocity.

We also performed a calculation with the LB method for the same system as for Figure 6 with zero porosity, i.e. with a non-porous ground surface. The result should agree with the result shown in Figure 4, which was the case in good approximation. Small differences were attributed to small differences in the two LB implementations.

Figure 8 compares the results for porous and non-porous ground in terms of excess level ΔL . Both the LBM results and the analytic solutions show that the interference minima and maxima are more pronounced for the non-porous ground than for the porous ground. The differences between the LBM results and the analytic solutions should be investigated further. The approximations in both the LB method and the analytic solutions may play a role.

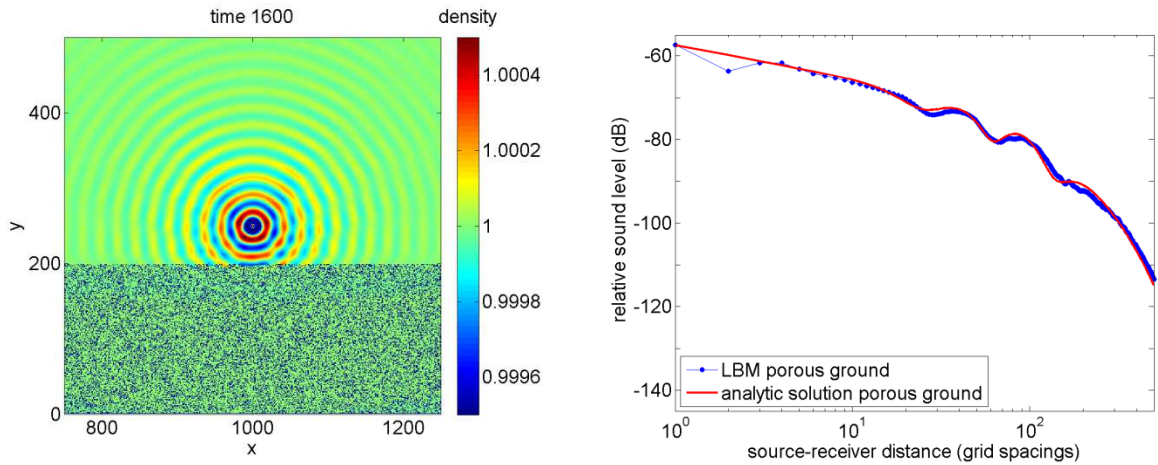


Figure 6: Results of a LB calculation for a point source and receivers at $y = 250$ and a porous medium below $y = 200$, showing the sound field at time 1600 (left) and the relative sound level as a function of distance (right).

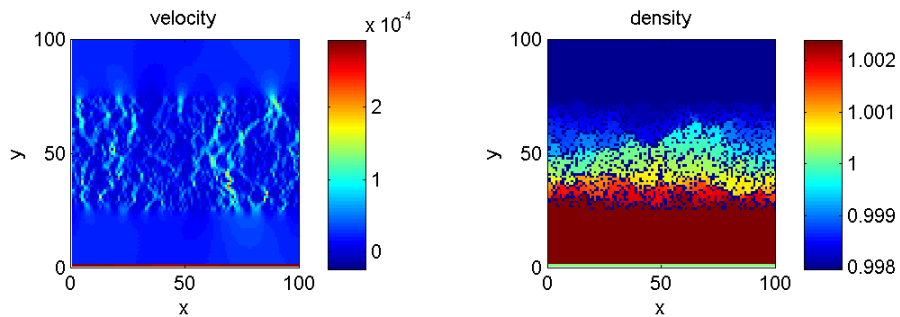


Figure 7: Stationary vertical velocity field (left) and density field (right) in a 100×100 LB system with a porous medium between $y=25$ and $y=75$ and an upward inflow condition at $y=0$, used for estimating the flow resistivity.

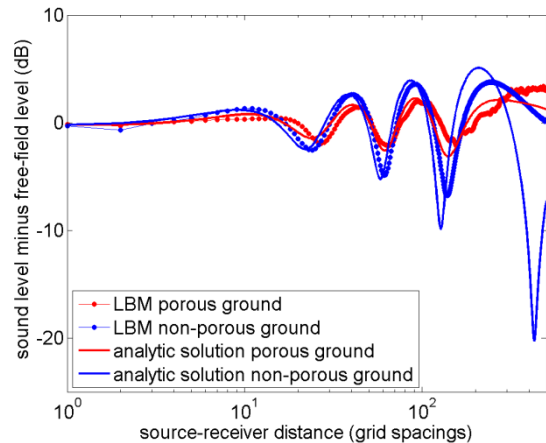


Figure 8: LB results and analytic solutions for porous and non-porous ground, expressed as the excess level ΔL as a function of distance.

3.4 Effect of a noise barrier

Finally we have used the LB method for simulating the effect of a noise barrier on a non-porous ground surface. We used a grid with 2000x1000 nodes, with numerical parameters as before. The source was located at position (1000,50). The noise barrier was located at position $x = 1100$, with a height of 100 grid spacings. Receivers were located at positions $x = 1001$ to $x = 1500$, at a height of $y = 50$. Figure 9 shows the results. The effect of the noise barrier is a decrease of the sound level by about 30 dB.

In Figure 10 the results are shown in terms of the excess level ΔL . Also included is an analytic solution for receivers behind the barrier, which deviates a bit from the LBM results. This solution is based on a theory of diffraction of spherical sound waves by wedge-shaped objects [20][21]. Dissipation was not included in the solution.

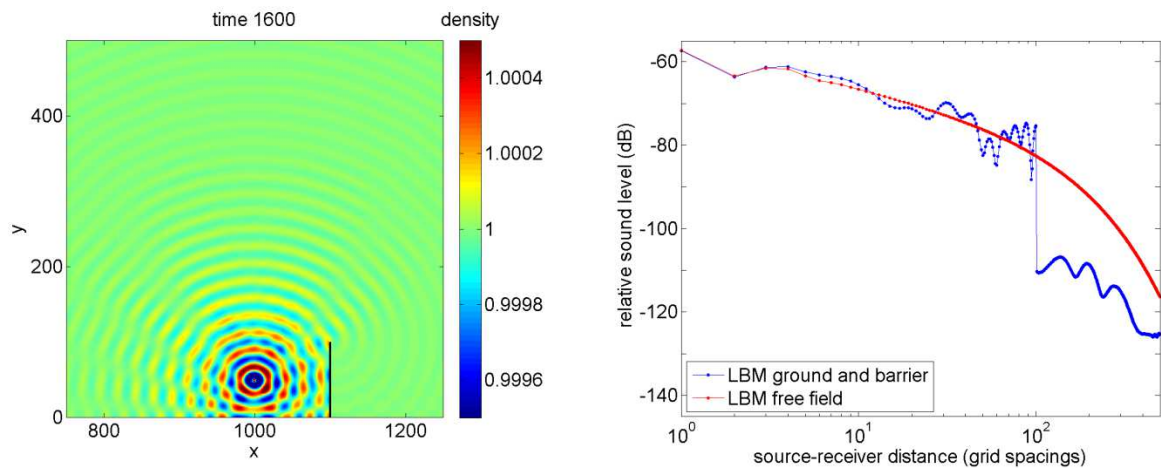


Figure 9: Results of a LB calculation for a non-porous ground surface with a noise barrier at $x = 1100$ (black line), showing the sound field at time 1600 (left) and the relative sound level as a function of distance (right).

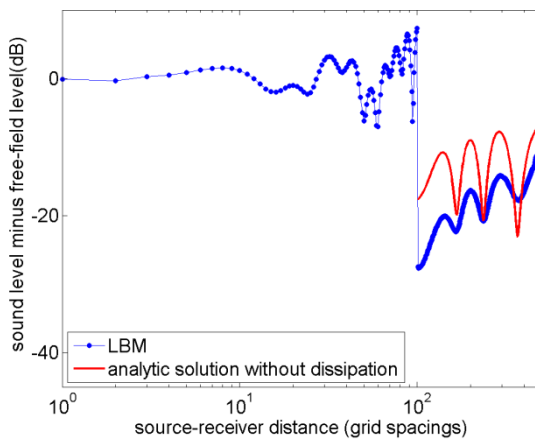


Figure 10: LBM result from Figure 9 and analytic solution, expressed as the excess level ΔL as a function of distance.

3.5 Refraction by wind and temperature gradients

The LB method can in principle deal with wind flow and sound propagation in a single simulation. This is an important advantage of the LB method over other sound propagation models. Wind effects on outdoor sound propagation are large, in particular in situations with noise barriers. The LB method may be extended to include temperature gradients [22], which also affect sound propagation.

4 CONCLUSIONS

In this paper we have explored application of the LB method in acoustics. LBM results were compared with analytic solutions for relatively simple cases, including cases with reflection by porous and non-porous ground surfaces and a case with screening and diffraction by a noise barrier. Reasonable agreement was obtained. The power of the LB method is that it can be applied to cases with complex boundary conditions, as illustrated here for the case with a porous ground surface. Another advantage of the LB method is that it can handle in principle wind flow and sound propagation in a single simulation.

A problem is the large dissipation of sound waves in an LBM simulation. Part of the dissipation effects are eliminated by considering the excess sound level, i.e. the level in excess of the free-field level. One may also keep dissipation effects small by choosing the sound frequency low and scale the results to higher frequencies. This will be explored in future work.

REFERENCES

- [1] Reichl, L.E., *A Modern Course in Statistical Physics*, (Edward Arnold, London, 1980), pp.468-475, 523-528.
- [2] Hughes, W.F., and Brighton, J.A., *Fluid Dynamics*, Schaum's outline series, (McGraw-Hill, New York, 1967), pp. 1-47.
- [3] Sukop, M.C., and Thorne Jr., D.T., *Lattice Boltzmann Modeling, An Introduction for Geoscientists and Engineers*, (Springer, Berlin, 2007).
- [4] Latt, J., Chopard, B., Malaspinas, O., Deville, M., and Michler, A., "Straight velocity boundaries in the lattice Boltzmann method", *Phys. Rev. E* (2008) **77** 056703.
- [5] Buick, J.M., Greated, C.A., and Campbell, D.M., "Lattice BGK simulations of sound waves", *Europhys. Lett.* (1998) **43**:235-240.
- [6] Viggen, E.M., "The lattice Boltzmann method with applications in acoustics", thesis NTNU 2009, Norway.
- [7] Viggen, E.M., "The lattice Boltzmann method: Fundamentals and acoustics", PhD thesis NTNU 2014, Norway.
- [8] Salomons, E.M., *Computational atmospheric acoustics* (Kluwer, Dordrecht, 2001).
- [9] Salomons, E.M., Blumrich, R., and Heimann, D., "Eulerian time-domain model for sound propagation over a finite-impedance ground surface. Comparison with frequency-domain models", *Acta Acustica united with Acustica* (2002) **88**: 483-492.
- [10] Van Renterghem, T., and Botteldooren, D., "Prediction-step staggered-in-time fdtd: An efficient numerical scheme to solve the linearised equations of fluid dynamics in outdoor

- sound propagation”, *Appl. Acoust.* (2007) **68**: 201-216.
- [11] Hornikx, M., Waxler, R., and Forssén, J., “The extended Fourier pseudospectral time-domain method for atmospheric sound propagation”, *J. Acoust. Soc. Am.* (2010) **128**: 297-319.
- [12] The MACH project is a European ITEA project. The project website is <http://www.mach-project.org>.
- [13] Tölke, J., and Krafczyk, M., “TeraFLOP computing on a desktop PC with GPUs for 3D CFD”, *International Journal of Computational Fluid Dynamics* (2008) **22**: 443 — 456.
- [14] Feichtinger, C., “Design and performance evaluation of a software framework for multiphysics simulations on heterogeneous computers”, PhD thesis (2012), Erlangen-Nürnberg University.
- [15] Zou, Q., and He, X., “On pressure and velocity boundary conditions for the lattice Boltzmann BGK model”, *Phys. Fluids* (1997), **9**: 1591-1598.
- [16] For more information on CUDA, see <http://www.nvidia.com>
- [17] Latt, J., “Choice of units in lattice Boltzmann simulations”, April 2008, see <http://wiki.palabos.org/howtos:main/>.
- [18] Kinsler, L., Frey, A., Coppens, A., and Sanders, J., *Fundamentals of Acoustics* (John Wiley & Sons, New York, 2000).
- [19] Zwicker, C., and Kosten, C.W., *Sound absorbing Materials* (Elsevier, New York, 1949).
- [20] Salomons, E.M., “Sound propagation in complex outdoor situations with a non-refracting atmosphere: model based on analytical solutions for diffraction and reflection”, *Acta Acustica united with Acustica* (1997) **83**: 436-454.
- [21] Hadden, J.W., and Pierce, A.D., “Sound diffraction around screens and wedges for arbitrary point source locations”, *J. Acoust. Soc. Am.* (1981) **69**: 1266-1276.
- [22] Guo, Z., Shi, B., and Zheng, C., “A coupled lattice BGK model for the Boussinesq equations”, *Int. J. Numer. Meth. Fluids* (2002) **39**: 325-342.

BRIDGES WASH OUT SIMULATION DURING TSUNAMI BY A STABILIZED ISPH METHOD

YOSHIYA MIYAGAWA¹, MITSUTERU ASAI² AND NUR'AIN BINTI IDRIS³

¹ Department of Civil Engineering, Graduate School of Engineering, Kyushu University
Motoka744, Nishi-ku, Fukuoka 819-0395, JAPAN
e-mail: y Miyagawa@doc.kyushu-u.ac.jp,
web page: http://www.doc.kyushu-u.ac.jp/kouriki/index_jp.htm

² Dr. Eng., Associate Prof., Department of Civil Engineering, Graduate School of Engineering,
Kyushu University
Motoka744, Nishi-ku, Fukuoka 819-0395, JAPAN
e-mail: asai@doc.kyushu-u.ac.jp,
web page: http://www.doc.kyushu-u.ac.jp/kouriki/index_jp.htm

³ Department of Civil Engineering, Graduate School of Engineering, Kyushu University
Motoka744, Nishi-ku, Fukuoka 819-0395, JAPAN
Email:nurain@doc.kyushu-u.ac.jp

Key words: Tsunami, stabilized ISPH method, simulation, bridge wash out.

Abstract. In 2011, the huge tsunami caused by the great east Japan earthquake devastated many infrastructures in pacific coast of north eastern Japan. Particularly, collapse of bridges caused a traffic disorder and these collapse behaviors led to delay of recovery after the disaster. In this study, the bridge wash away accident is selected as a target issue, and it is represented in order to investigate the criteria and its mechanism by a numerical simulation. For this purpose, Incompressible Smoothed Particle Hydrodynamics (ISPH) Method, which is one of the pure mesh free methods, is utilized for the rigid body motion simulation. In this study, rigid body motion is introduced for the fluid-rigid interaction behavior during bridge wash away simulation. In the numerical analysis, the upper bridge structure is washed out by receiving an impact fluid force. The validation tests in two scales showed good agreement with experimental test and the real accident on the great east Japan earthquake tsunami.

1 INTRODUCTION

On March 11, 2011, the huge tsunami caused by the great east Japan earthquake devastated many infrastructures in pacific coast of north eastern Japan. Particularly, the damage of outflow of bridge girders caused a traffic disorder and these collapse behaviours led to delay of recovery after the disaster. After 2011 tsunami, disaster prevention and mitigation techniques are actively developing in coastal infrastructures and establishing prediction method for tsunami disaster is one of the severe issues toward the next millennium tsunami.

In this study, the bridge wash out accident is selected as a target issue, and we try to represent these accidents by using a numerical analysis. For this purpose, one of the mesh free methods;

Smoothed Particle Hydrodynamics (SPH) Method is utilized for Tsunami flow. The SPH technique was originally proposed by Lucy [1] and further developed by Gingold and Monaghan [2] for treating astrophysical problems. The main advantage of SPH and the other particle simulation is the absence of a computational grid or mesh since it is spatially discretized into Lagrangian moving particles. This allows the possibility of easily modeling flows with a complex geometry or flows where large deformations or the appearance of a free surface occurs. Recently, this method is widely used in field of fluid and solid dynamics. A stabilized ISPH [3], which is one of the modified versions of the SPH and can evaluate much smoother pressure distribution, has been developed by our research group. Then a fluid-sorid interaction algorithm including rigid body motion is developed in this study.

2 FLUID-RIGID INTERACTION FORMULATION

In this section, a stabilized ISPH, which includes a modified source term in the pressure Poisson equation, for incompressible flow is summarized firstly. Then the treatment of moving rigid body is introduced by reviewing the related work in distinct element method (DEM).

2.1 GOVERNING EQUATION

The governing equations are the continuum equation and the Navier-Stokes equation. These equations for the flow are represented as

$$\frac{D\rho}{Dt} + \rho \nabla \cdot \mathbf{u} = 0 \quad (1)$$

$$\frac{D\mathbf{u}}{Dt} = -\frac{1}{\rho} \nabla p + \nu \nabla^2 \mathbf{u} + \frac{1}{\rho} \nabla \cdot \boldsymbol{\tau} + \mathbf{F} = \mathbf{0} \quad (2)$$

here, ρ and ν are density and kinematic viscosity of fluid, \mathbf{u} and p are the velocity and pressure vectors of fluid respectively. \mathbf{F} is external force, and t indicates time. The turbulence stress $\boldsymbol{\tau}$ is necessary to represent the effects of turbulence with coarse spatial grids. In the most general incompressible flow approach, the density is assumed by a constant value with its initial value.

2.2 MODIFICATION IN SOURCE TERM OF PRESSURE POISSON EQUATION

The main concept in an incompressible SPH method is to solve a discretized pressure Poisson equation at every time step to get the pressure value. In a sense of physical observation, physical density should keep its initial value for incompressible flow. However, during numerical simulation, the ‘particle’ density may change slightly from the initial value because the particle density is strongly dependent on particle locations in the SPH method. If the particle distribution can keep almost uniformity, the difference between ‘physical’ and ‘particle’ density may be vanishingly small. In other words, accurate SPH results in incompressible flow need to keep the uniform particle distribution. For this purpose, the different source term in pressure Poisson equation can be derived using the ‘particle’ density. The SPH interpolations are introduced into the original mass conservation law before the perfect compressibility condition is applied.

$$\langle \nabla \cdot \mathbf{u}_i^{n+1} \rangle = -\frac{1}{\rho^0} \frac{\langle \rho_i^{n+1} \rangle - \langle \rho_i^* \rangle}{\Delta t} \quad (3)$$

Then, the pressure Poisson equation reformulated as:

$$\langle \nabla^2 p_i^{n+1} \rangle = \frac{\rho^0}{\Delta t} \langle \nabla \cdot \mathbf{u}_i^* \rangle + \alpha \frac{\rho^0 - \langle \rho_i^* \rangle}{\Delta t^2} \quad (4)$$

where, α is relaxation coefficient, \mathbf{u}^* is temporal velocity and triangle bracket $\langle \rangle$ means SPH approximation. Note that this relaxation coefficient is strongly dependent on the time increment and the particle resolution. Then, the reasonable value can be estimated by the simple hydrostatic pressure test using the same settings on its time increment and the resolution.

2.3 TREATMENT OF MOVING RIGID BODY

In this study, the general momentum conservation law of the rigid body is solved numerically with the external forces including hydrodynamic as a fluid-rigid interaction formulation. Fig.1 show the rigid motion algorithm. The rigid body is discretized to particles at the beginning. Next, we postulate that the external force is calculated from the gravity \mathbf{g} , hydrodynamic force at the rigid surface \mathbf{F}_f and contact force between rigid body and fixed boundary \mathbf{F}_e , and these value are calculated by following equations.

$$\mathbf{F}_f = \sum_i^{\text{on the surface}} \mathbf{P}_i \Delta S_i \mathbf{n}_i \quad (5)$$

$$\mathbf{F}_e = k \delta^{3/2} \quad (6)$$

$$\delta = r - l \quad (7)$$

$$k = \frac{4\sqrt{r}}{3} \frac{E_i E_j}{(1 - \nu_i^2) E_j + (1 - \nu_j^2) E_i} \quad (8)$$

where, \mathbf{P}_i is the pressure of surface rigid particle, and ΔS_i is the area of surface rigid particle. And the contact force is modeled by the elastic contact theory by Hertz. In the above equation, l is the distance between rigid particle and the fixed boundary. In above equation, ν_i , E_i , E_j is Poisson ratio, elastic modulus of the particle coming into contact, elastic modulus of the contacted particle. Once the hydrodynamic and external forces are obtained, the moment is easily calculated by using the distance between the target particle and center of gravity of rigid body.

$$\mathbf{M}_f = \sum_i^{\text{on the surface}} (\mathbf{r}_i - \mathbf{r}_c) \times \mathbf{P}_i \Delta S_i \mathbf{n}_i \quad (9)$$

$$\mathbf{M}_e = \sum_i^{\text{on the surface}} (\mathbf{r}_i - \mathbf{r}_c) \times \mathbf{F}_e \quad (10)$$

The translational velocity \mathbf{T} and rotational velocity $\boldsymbol{\omega}$ of a solid object are calculated as:

$$\mathbf{T}^{n+1} = \mathbf{T}^n + \Delta t \left(\mathbf{g} + \frac{\mathbf{F}_f}{m} + \frac{\mathbf{F}_e}{m} \right) \quad (11)$$

$$\boldsymbol{\omega}^{n+1} = \boldsymbol{\omega}^n + \mathbf{I} \Delta t (\mathbf{M}_f + \mathbf{M}_e) \quad (12)$$

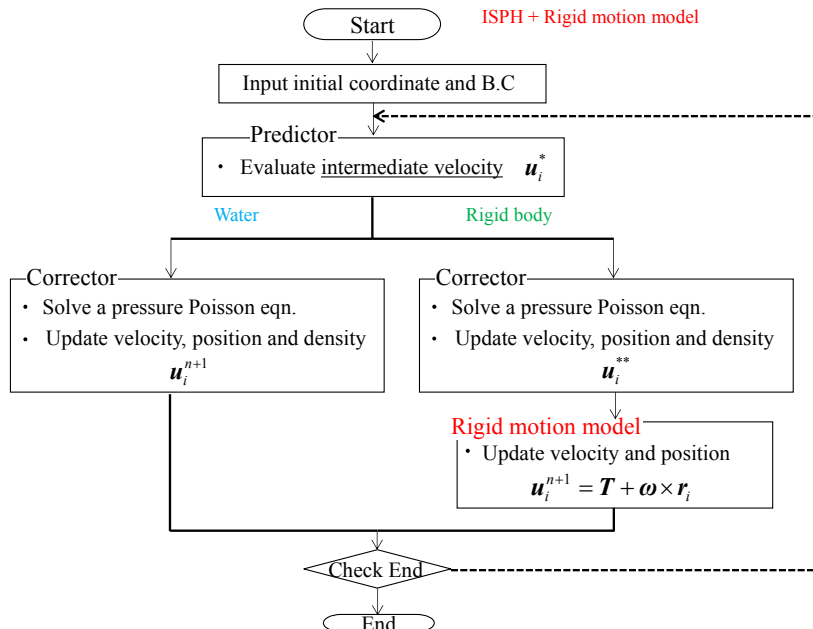


Figure 1. Rigid motion algorithm

Finally, the velocity of each particle in the solid body is updated by the following equation.

The position of the rigid particle is updated based on the velocity.

$$\mathbf{u}_i^{n+1} = \mathbf{T}_i^{n+1} + \boldsymbol{\omega}_i^{n+1}(\mathbf{r}_i - \mathbf{r}_j) \quad (13)$$

Fig. 1 summarizes the whole flowchart for the fluid-rigid coupling by the stabilized ISPH method.

3 VALIDATION TEST

In the following section, two type of validation tests have been introduced. One is comparison between analysis and experimental test in a small scale and the other is real scale validation by comparing with disaster report.

3.1 SMALL SCALE VALIDATION TEST

The analysis model and the detail of the girder model are shown in Fig.2 and Fig.3. In this experiment and analysis, water which collected on the left-hand flow and collide with the girder model by opening the gate and girder wash out. The experimental test is carried out three times and the location of girder model is recorded by using motion capture system. In this system, the self-light is attached on the four corners of bridge girder model, its position is measured by using multi cameras. The bridge pier is fixed and the density of the bridge girder which is on the pier is 1161kg/m^3 . The particle distance $d_0 = 0.25\text{cm}$, time increment $\Delta t = 0.0005\text{s}$ and the total number of particles is about 8millions.

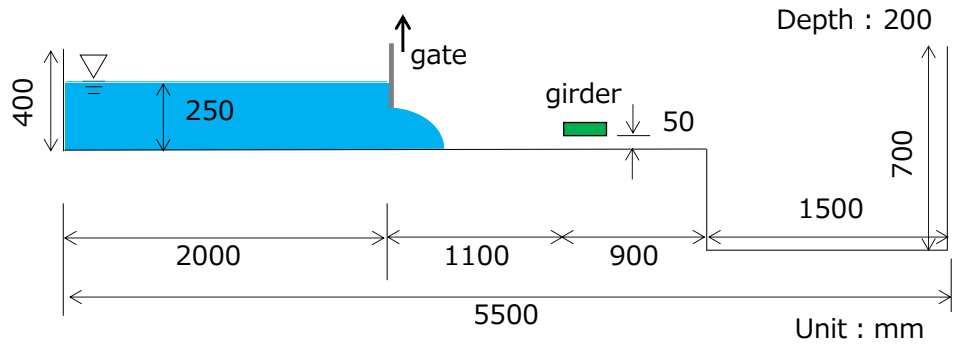


Figure 2. Analysis model

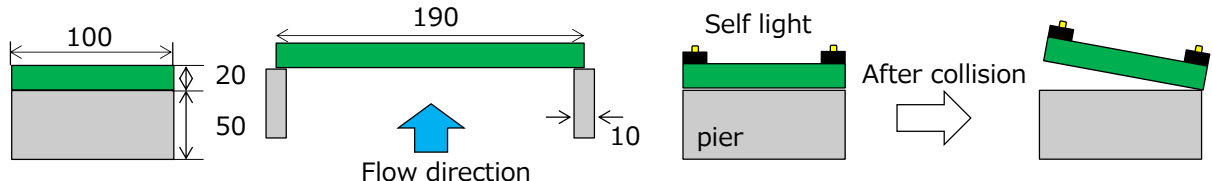


Figure 3. Detail of the bridge model and motion capture system

Fig.4 shows the comparison of rotational angle between the experimental test and the analysis. From this graph, there are some difference between the experimental result and the analysis, however, analysis result behaviors which rotate from positive angle to negative angle shows a good agreement. From this result, our proposed method can evaluate the rigid motion during flow in a small scale.

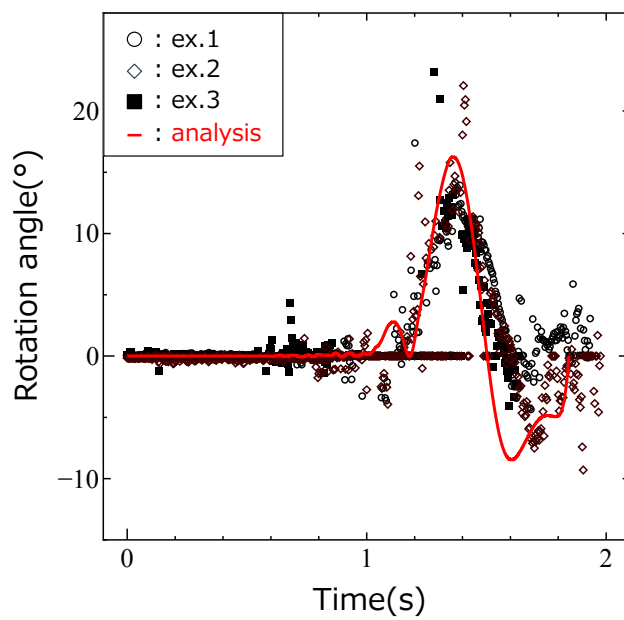


Figure 4. Comparison of rotational angle between the experiment and analysis

3.2 REAL SCALE VALIDATION TEST

One of the segments of a bridge girder, which was pushed away in the Tsunami, is selected as a target structure, and its numerical model is generated in 3D from the CAD data. The wave is modeled for a gentle stream and the initial water level is set to be 15m referring to the report that water levels in many disaster cities reached over 10m in the Tsunami (Fig.5). The initial velocity of the wave is set 10m/s referring to shallow water long-wave equation. In addition, 10m/s is continuously given at the position of 30m from the left corner of the water storage. The particle distance $d_0 = 6\text{cm}$, time increment $\Delta t = 0.001\text{s}$ and total number of particles is about 55millions. The density of particles of the girder model is 2450kg/m^3 .

The real scale wash out simulation is shown in Fig.6. According to the disaster report[4], this girder turned over in the Tsunami and the girder motion with rotate can be seen, however, the bridge girder don't overturn in the analysis. Now, the initial water level and the initial velocity is set constantly. It is necessary to reconsider inflow condition by using tsunami run up simulation in order to simulate in realistic.

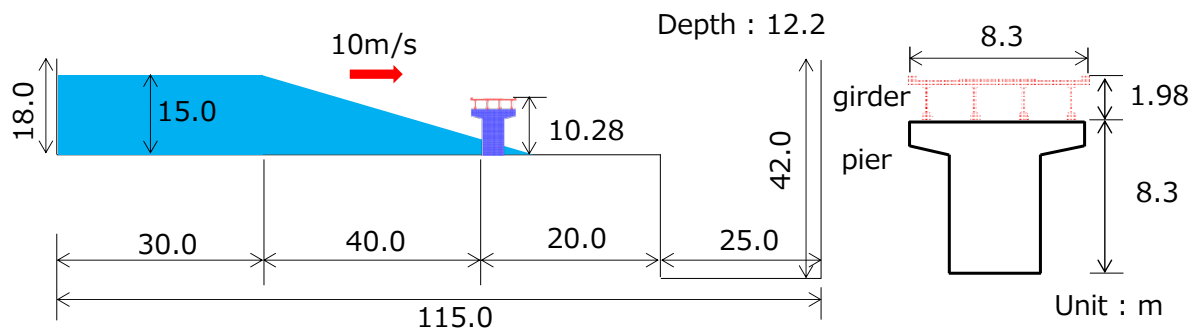


Figure 5. Analysis model and the shape of girder model

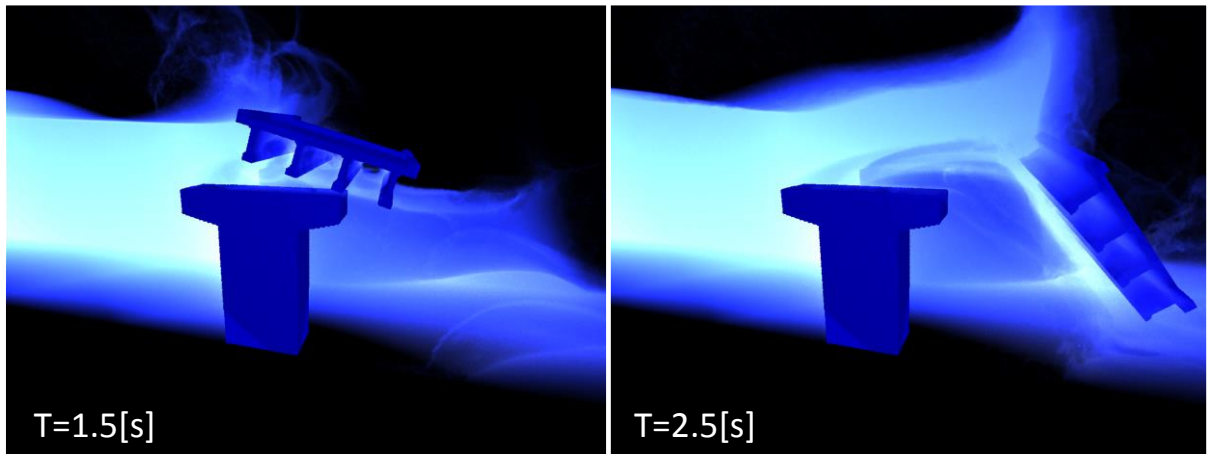


Figure 6. Analysis result (Real scale analysis)

4 CONCLUSIONS

In this study, fluid-rigid interaction formulation is conducted by introducing rigid motion algorithm into ISPH. In the small scale analysis, the validation of our fluid-rigid interaction technique is conducted by comparison with experimental test. From this result, the transition of rotational angle shows a similar tendency and a good agreement quantitatively. Then, real scale validation test is instituted by modeling the bridge which washed out in the Tsunami. There are some difference of rigid motion in report and analysis, however, analysis result behaviors shows largely rotation like the disaster report on March 11, 2011. In the future work, tsunami inflow condition must be reconsidered to predict the bridge wash out accident with accuracy.

ACKNOWLEDGEMENTS

This work was supported by JSPS Grant-in-Aid for Scientific Research(B) 26282106 and Grant-in-Aid for Exploratory Research15K12484.

REFERENCES

- [1] Lucy L.B: Numerical approach to the testing of the fusion process, *Astron J.*; 88: 1013–1024.
- [2] Gingold R.A., Monaghan J.J: Smoothed particle hydrodynamics: theory and application to non-spherical stars, *Mon Not R Astron Soc*, 181: 375–89.
- [3] M. Asai, AM. Aly, Y. Sonoda and Y. Sakai : A stabilized incompressible SPH method by relaxing the density invariance condition, *Int.l J. for Applied Mathematics*, Volume 2012, Article ID 139583, 2012.
- [4] Japan Society of Civil Engineers : Evaluation of Tsunami Force Acting on Bridge Structures, 2013

SNOW PROPERTY MODELING AND ITS APPLICATION TO PARTICULATE ICE-SNOW FLOW COMPUTING IN SNOWBLOWER

YOSUKE YAMAMOTO¹, JUN ISHIMOTO² AND NAOYA OCHIAI³

¹ Honda R&D Co., Ltd.

3-15-1 Senzui, Asaka-shi, Saitama 351-0024, Japan
e-mail: yosuke.yamamoto@h.rd.honda.co.jp

² Institute of Fluid Science, Tohoku University
2-1-1 Katahira, Aoba-ku, Sendai 980-8577, Japan
e-mail: ishimoto@fmail.ifs.tohoku.ac.jp

³ Institute of Fluid Science, Tohoku University
2-1-1 Katahira, Aoba-ku, Sendai 980-8577, Japan
e-mail: ochiai@alba.ifs.tohoku.ac.jp

Key words: Snow, Snowblower, Snow removal, Simulation, DEM, Lenard-Jones potential model.

Abstract. Snow properties are influenced by climate or region. For the efficient development of a snowblower, stable and quantitative performance evaluation method is required. We tried to reproduce the snow removal work using the Discrete Element Method (DEM) in this study. In addition to the conventional DEM, we developed potential model for reproducing the compaction of snow and air drag model to consider the properties of actual snow. And we have improved the snow property model for fallen snow simulation. As a result of present computational method, it was clarified that the detailed snow behavior in relation to snowblower can be successfully reproduced by simulation using the DEM. The obtained computational results were compared with the experimental results, and found that both results exhibit reasonable agreements. Therefore, we have succeeded in the computational reproduction of quantitative snow behavior in a snowblower using new snow property model.

1 INTRODUCTION

In Japan, about half of country is occupied by heavy snowfall area. Snowblowers are essential for people who live in such area and a high efficient snowblower is extensively required because quick snow removal closely related to decrease in the fuel consumption and operator's workload.

Performance of a snowblower is mostly investigated by manipulation with an actual machine in heavy snowfall area. However, it is difficult to maintain stable experimental condition because snow properties are influenced by climate or regional effect. For the efficient development of a snowblower, stable and quantitative performance evaluation method is required.

Without considering the phase change of snow, snow removal is treated as a mixing

phenomenon containing gas phase and solid phase. Moreover, large computational domain is required in order to reproduce snow throwing far away from the snowblower. Using grid method, such as VOF method which is used to calculate multiphase flow, requires a fine mesh over a large region to track the behavior of scattering snow, and computational time becomes enormous. Meanwhile, using particle method, it is possible to track the interface behavior in multiphase flow with comparative ease and calculate the scattering behavior of snow in large region because there is no need to calculate gas phase.

In this study, we have developed a simulation method using the DEM (Discrete Element Method) to reproduce snow removal characteristics. The DEM is widely used as an effective method in granular flow, powder mechanics, rock mechanics and simple snow behavior in a snowblower. [1, 2, 3] However, it is difficult for the DEM in application to reproduce unique behavior of snow because of the following reasons.

- (1) Microscopically, snow contains multiple elements, such as ice, water and air. Its physical properties change depending on the weight ratio and geometrical configuration of such elements. Namely, it is difficult to consider actual snow structure in the simulation.
- (2) Surrounding air flow cannot be computed by the DEM. It is necessary to consider the fluid dynamic influence on snow lumps creation in various sizes.
- (3) In spite of the fallen snow can maintain the initial shape even under gravitational field, the conventional DEM cannot be taken into account the initial shape of particles.

We constructed the advanced numerical model for the DEM to elucidate the snow compaction behavior using Lenard-Jones potential model [4] which is conventionally used in molecular dynamics. This newly presented computational method can applicable to reproduce the detailed snow structure, and effective air drag only acting on lumped snow surface formed by particle aggregation as a function of snow particle velocity. Furthermore, to reproduce the static behaviour of the fallen snow to maintain the initial shape, we have extended the numerical model to consider the constraint of tangential degrees of freedom and rotational degrees of freedom of snow particles.

2 SNOWBLOWER

The appearance of a snowblower is shown in Fig.1(left). This machine is called a two-stage type, which moves snow by two mechanisms: an auger feeds snow to a blower which rotates at high speed and blows snow out of the machine. Discharge direction and height of snow can be changed by operating a chuter. Fig.1(right) shows an actual field situation of snow removal.

As the performance of the snowblower, removal rate and throwing distance are required. Removal rate means how much snow we can remove per unit time. The enhancement of removal rate is important in order to reduce working hours in snowfall area. Throwing distance means how long we can throw snow from the snowblower. To perform snow removal smoothly, it is necessary to throw snow far enough in all directions other than the machine backward where the operator stands. Moreover, the adhesion of snow strongly

influences the performance of the snowblower. Snow adheres to the inside of the machine and it often causes the snowblower to clog with snow while working. In this study, the effect of adhesion is not considered.

The snowblower handles various types of snow depending on the weather and regions. Roughly, snow is classified into 4 types as follows: new snow, compact snow, hoar and granular snow. Furthermore, Compact snow and hoar can be subdivided, snow can be also classified into 12 types by adding items whether wet or dry. The performance of the snowblower changes depending on snow type, but it is required to work efficiently in various snow condition.

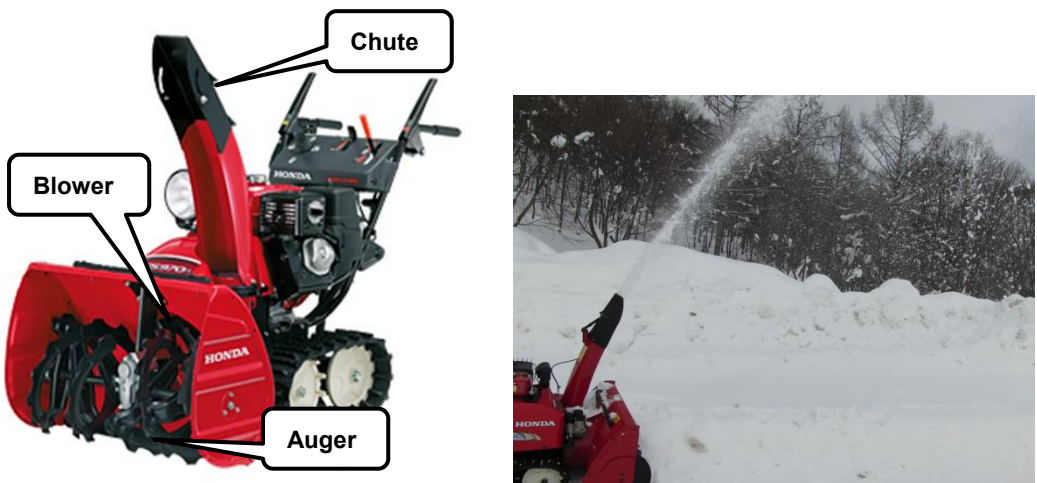


Figure 1: Appearance of snowblower(left) and snow removal(right)

3 COMPUTATIONAL METHOD

3.1 Discrete Element Method

In this study, we use the DEM, which is applied to the motion of discontinuum, such as granular flow, powder mechanism, rock mechanism, and snow. [2, 3] SPH(Smoothed Particle Hydrodynamics method) and MPS(Moving Particle Simulation) are also particle based methods, which are used to analyze continuum.

In the DEM, target materials(snow) are expressed as particles. Their connections are expressed using springs and dampers as shown in Fig.2. When particles approach and contact each other, the force of springs and dampers acts on them. Due to the joint, the force does not act on particles while moving away from each other. For tangential direction of contact surface, a friction slider is added to this model.

Particles have equations of motion for translational and rotational degrees of freedom, are introduced as follows:

$$m \frac{d^2u}{dt^2} + \eta \frac{du}{dt} + Ku = 0 \quad (1)$$

$$I \frac{d^2\psi}{dt^2} + \eta \frac{d\psi}{dt} + K \left(\frac{D}{2}\right)^2 \psi = 0 \quad (2)$$

where m is the mass of single particle, I is the moment of inertia, t is the time, u is the displacement between two particles, Ψ is the angle of rotation, K is the elastic coefficient, η is the viscosity coefficient, D is the diameter of the particle. The location and velocity of particles at the next step are determined explicitly by calculating the force acting on particles.

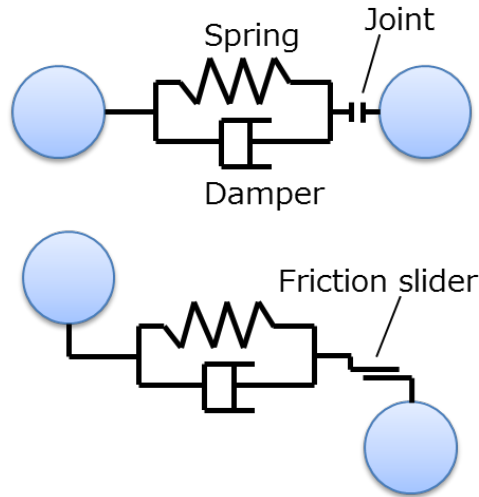


Figure 2: Contact model of Discrete Element Method

3.2 Model for snow compaction

Microscopically, snow is comprised of multiple elements, such as ice, water and air. Its properties change depending on the weight ratio and geometrical configuration of such elements. However, complex settings and enormous time are needed for calculating snow behavior while considering the microscopic structure of actual snow, which includes various conditions or interactions such as ice particle shape, water content, sintering and surface tension.

In this study, we constructed snow compaction behavior using Lenard-Jones potential model [4] which is used in molecular dynamics as shown in Eq. (3).

$$U(r) = \begin{cases} 4\epsilon \left[\left(\frac{\sigma}{r} \right)^{12} - \left(\frac{\sigma}{r} \right)^6 \right] & (0 < r \leq r_{eff}) \\ 0 & (r > r_{eff}) \end{cases} \quad (3)$$

U means the potential energy, r is the distance between two particles. ϵ and σ are Lenard-Jones potential parameters for each interaction. The potential force is obtained by differentiating the potential energy by the distance between two particles, an example of a force-distance curve is shown in Fig.3. A positive value means repulsion, a minus value means attraction. This force acts on separated particles as attraction, but large repulsion occurs in the range of $< 1.1\sigma$. In this study, the effect of repulsion is ignored in order to reproduce the compaction of snow. Moreover, the influence range of the potential force is limited. Essentially, the compaction of snow is generated by sintering or surface tension

among ice particles, there is no interaction between separated particles. However, the unlimited potential force acts on a separated particle over another particle, and that causes excessive shrink among non-contact particles. Therefore, we apply attraction to only adjacent particles regarded as in contact by limiting the influence range of the potential.

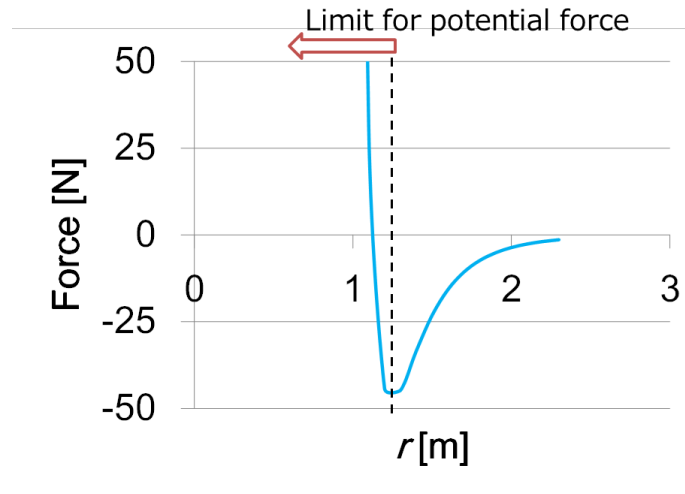


Figure 3: Force caused by Lenard-Jones potential model

3.3 Air drag for lump of snow

In this study, we consider only the solid phase, surrounding air flow is not taken into account. We assumed the air drag is defined as a function of snow particles velocity. Single snow particle and a lump of snow will be mixed while calculation progresses, but their influence of air drag is difference. Since inertia is proportional to mass, and air drag is proportional to projected area of a lump of snow, the ratio of surface area to volume must be considered. We assumed air drag only acting on surface particles of a lump, which are extracted by calculating the gradient of the particle number density.

Fig.4 shows a schema of the method for extracting surface particles of a two-dimensional lump. At first, we calculate normal vector of a lump by the following steps.

- 1) Calculate difference of the number of the particles inside a dashed line between positive and negative domain for each X and Y direction.
- 2) Count the number of the particles arranged in lattice shape at their diameter intervals.
- 3) Normalize the values obtained by 1) using the number of 2).

The value used for normalization means the number of the particles inside a lump, it decreases to 50% at surface of a lump. Therefore, we regard a particle whose normal vector is less than 0.5 as a surface particle, we assumed air drag that is proportional to the square of the velocity in the same direction as its normal vector.

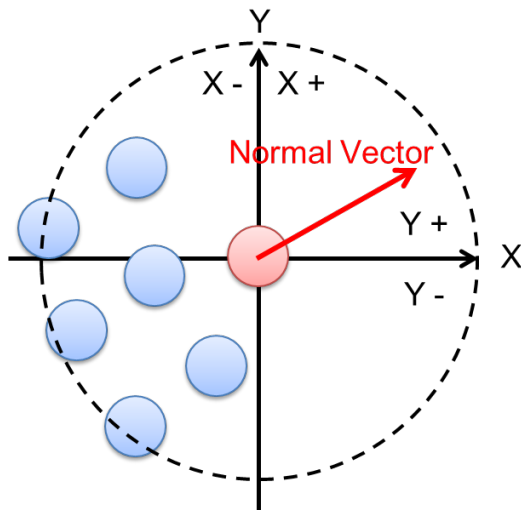


Figure 4: Schema of extracting surface particles of lump

3.4 Constraint of degrees of freedom of motion

In this study, we assumed that the snow is composed by particles. A lump of particles as block shape on the ground cannot be kept initial shape under the gravitational field because a particle shape is spherical and easy to roll down. However, actual fallen snow can be kept initial shape. It is because the ice shape in actual snow is different from spherical shape and difficult to roll down. Furthermore in snow modeling, we assumed that the tangential motion is constrained by surface tension of water or sintering.

Therefore, we constrain tangential and rotational degrees of freedom for snow behavior. Constraint of rotational motion means that Eq. (2) is ignored. Constraint of tangential motion means that friction slider between elements in Fig. 2 is ignored.

4 RESULTS AND DISCUSSION

4.1 Confirming effect of snow property model

We confirmed the effect of snow property model using the DEM computing in simple conditions. We assumed the numerical conditions of that the density of snow is 50 kg/m^3 , single particle diameter is 5 mm and other parameters of snow property model are shown in Table 1. Here, Case 1 does not include snow property, Case 2 include snow property.

At first, in order to confirm the effect of snow property model in a state of fallen snow, we arranged the lumped particles formed by a cubic shape of $100 \text{ mm} \times 100 \text{ mm} \times 100 \text{ mm}$ as the initial shape, and calculated under the gravitational field. The computational results after 1.0 sec in each condition is shown in Fig.5. Case1 is the same condition as the conventional DEM, the shape collapses conically. In Case2, the particles can be kept the initial shape. Snow behaviors in each condition are different and simulation result using the snow property model developed in this study is close to actual snow behavior.

Second, we carried out simulation of snow particles column behavior colliding the wall. The column particles are emitted in the initial numerical condition of $80 \text{ mm} \times 80 \text{ mm}$ square-

shaped, and inlet velocity at 10 m/s. The results are shown in Fig.6. In Case2, snow particles aggregate and will form the lump groups by colliding wall in comparison with Case1. It is found that the snow property model is reasonably computed in the dynamic state such as collision.

Table 1: Parameters of snow property model

	Case 1	Case 2
	without snow property model	with snow property model
ε [J] (Depth of potential well)	0	0.0001
σ [m] (Distance at which potential is zero)	0	0.005

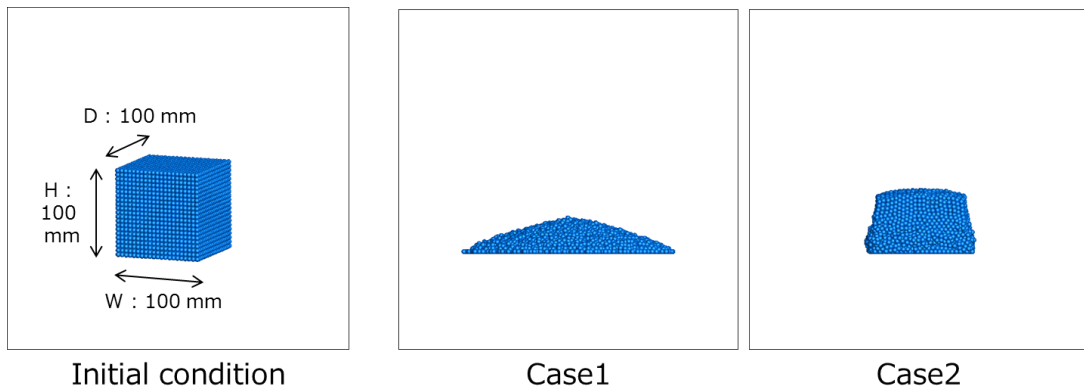


Figure 5: Simulation of particles keeping initial shape

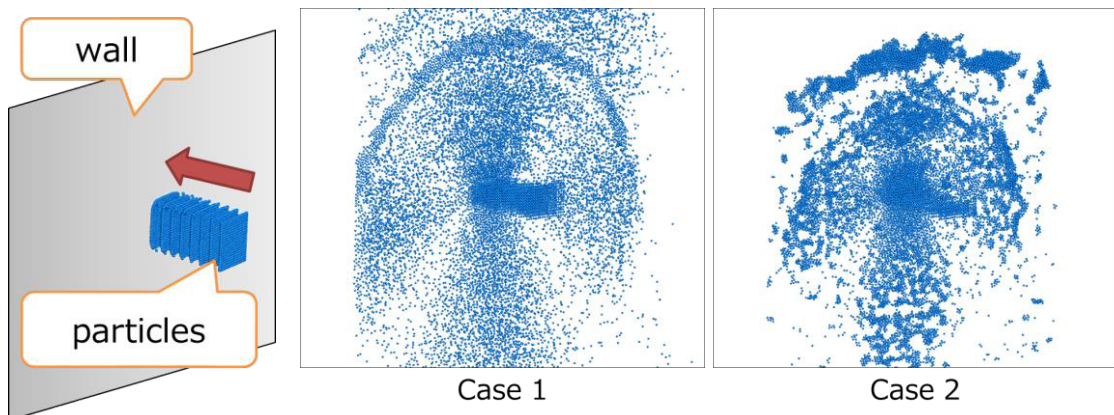


Figure 6: Simulation of particle aggregation colliding with wall

4.2 Snow behavior in application to snowblower

We made experimental apparatus which is half scale of an actual snowblower as shown in Fig.7, and the experimental results were compared with present simulation results. The apparatus is made modeling a chuter and blower of an actual snowblower. The experiment was carried out in the low temperature chamber kept at -25 °C. We conducted the experiment with new snow generated by the artificial snowfall machine. (Density 50 - 100 kg/m³) We

injected snow to the blower rotation with 1200 rpm, and conducted a comparative study for snow velocity at chuter inlet and outlet section by both experiment and simulation. In the experiment, we estimated the snow velocity by imaging snow behavior using a high-speed camera.

Experimental and numerical(Case 2) results are shown in Fig.8. It is found that the lumps of snow are discharged with bending motion along the chuter in both experiment and simulation. Furthermore found that the snow particle aggregation and discharge behavior from the chuter are successfully reproduced by present numerical method. Fig.9 shows comparison of snow velocity at inlet and outlet section. Particle diameter of 5.0 mm, and about 1,800 particles are used for simulation. Numerical condition is shown in Table 1. In Case 1, snow velocity is 9.5 m/s at chuter inlet, 7.5 m/s at outlet. In Case 2, snow velocity is 8.5 m/s at chuter inlet, 4.5 m/s at outlet. The numerical results in Case 2 is closer to the experimental result than Case 1. Therefore, it is found that our snow modeling reasonably reproduce the actual snow behavior in the snow blower.

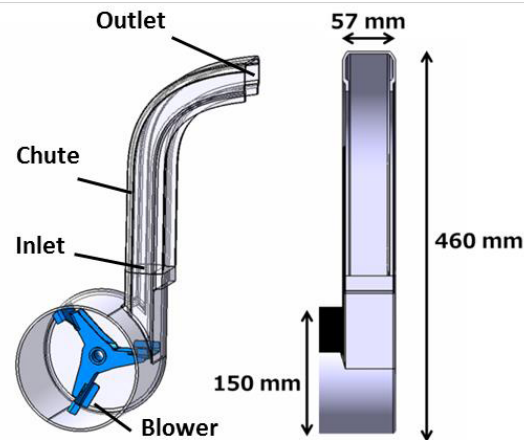


Figure 7: Appearance of experimental apparatus

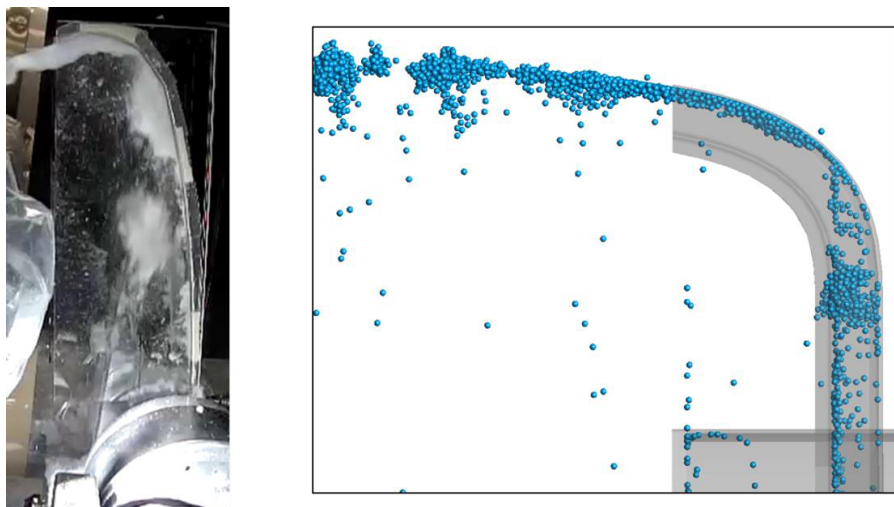


Figure 8: Experimental result(left) and numerical result(right)

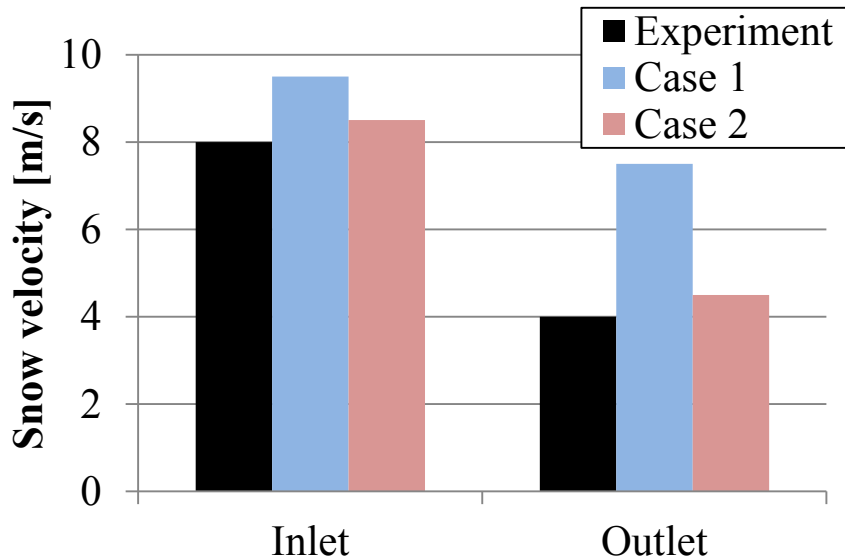


Figure 9: Comparison between experimental and numerical results

5 CONCLUSIONS

Detailed snow behavior in application to the snowblower was reproduced by new snow modeling with the DEM. In order to clarify the unique behavior of snow such as the effect of compaction, air drag and fallen snow, we have developed the new snow property model compare to the conventional DEM as follows.

- Reproducing the snow compaction using Lenard-Jones potential model.
- Implementing air drag on snow lumps creation in various sizes by extracting snow surface particles.
- Maintaining the particle aggregation to form the initial shape by considering with the constraint of degrees of freedom of motion.

Experimental and numerical results are compared and qualitatively good correspondence can be obtained by considering snow property model. In the future, we will numerically reproduce a phenomenon which estimates the actual snow removal performance of the snowblower.

REFERENCES

- [1] The Society of Powder Technology, JAPAN ed., Introduction of powder simulation (in Japanese), Sangyo-toshio (1998) 29-82.
- [2] Abe, M., Ariga, N., Furukawa, S., Journal of Snow Engineering 20(5), 2004-11-01 (2004) 67-68.
- [3] Abe, M., Saito, F., Nishijima, K., Journal of Snow Engineering 23(4), 2007-07-01 (2007) 55-56.
- [4] Kotake, S., Molecular dynamics for thermal fluids (in Japanese), Maruzen Company, Limited (1998) 133-134.

A DISCRETE APPROACH TO DESCRIBE THE ELASTIC-PLASTIC BEHAVIOUR OF SNOW

Bernhard Peters¹, Mark Michael¹ and Francois Nicot²

¹ Université du Luxembourg

Faculté des Sciences, de la Technologie et de la Communication
6, rue Coudenhove-Kalergi, L-1359 Luxembourg, Luxembourg

e-mail: bernhard.peters@uni.lu, web page: <http://www.uni.lu>, www.xdem.de

² IRSTEA Grenoble

Unité de Recherche Erosion Torrentielle Neige et Avalanches Domaine Universitaire

BP 76 F38402 - Saint Martin d'Hres Cedex - France

e-mail: francois.nicot@irstea.fr, web page: <http://www.irstea.fr>

Key words: Extended Discrete Element Method (XDEM), snow, brittle/ductile deformation

Abstract. Snow is composed of small ice particles and, therefore, behaves as a granular material with a variety of sizes and shapes. Understanding the mechanical behaviour of snow is important in areas such as natural hazards e.g. snow avalanches, or traction characteristics of tires with a snow covered road. Therefore, the objective of the current contribution is to present an advanced discrete approach to predict the elastic-plastic behaviour of snow. For this purpose, snow is described by a finite number of discrete ice grains similar to the Discrete-Element Method (DEM) with ice bonds as a link between individual grains and including a creep law for ice. Bonds may rupture under excessive load or may be formed during a contact between ice grains. Hence, the integral behaviour of snow is represented by the combined properties of impact and bonds depending on strain rate, density and temperature.

The collision model is based on the linear hysteretic model developed by Walton and Braun [], which accounts for the effect of plasticity. For this behaviour the impact between grains is distinguished into a loading and detaching phase represented by a loading and unloading stiffness constant. Additionally, friction behaviour into the tangential direction at the point of impact and dissipation i.e. coefficient of restitution is taken into account.

A bond between two ice grains is represented by a cylinder that is allowed to undergo tension, shear, torsion about its axis and bending. These translational and rotational displacements of a bonding cylinder lead to appropriate strains that yield corresponding stresses with a constitutive model including Youngs modulus E and the Poisson ratio ν . The stresses acting on a bond are converted to forces and moments that determine in conjunction with Newtons 2nd law the kinematics of the ice grains and the overall mechanical behaviour of the ensemble.

This approach was employed to predict the mechanical behaviour of snow under compression for different strain rates, and thus, covering the length scales of individual ice grains to the global dimensions of the specimen. Thus, both brittle and ductile behaviour of snow were represented and good agreement between experimental data and predictions was obtained.

1 INTRODUCTION

Snow regarded as a material exhibits a complex mechanical i.e. static and dynamic behaviour that has been subject to intensive research both experimentally and numerically. According to Bartelt and Lening [1], Brun et al. [2] and Jordan [3] modelling as a complementary effort to experiments is required to gain a deeper insight into the physical behaviour of snow. Therefore, models for snow have to address the following important characteristics of snow:

- micro-structure
- multi-component porous media
- strength, large deformations and fracture
- temperature

The above-mentioned aspects for snow modelling were largely covered by a continuous approach e.g. finite element method, whereas a discrete method has rarely been applied. First efforts to describe snow by FEM go back to Smith [4] and Lang and Sommerfeld [5].

Meanwhile, modelling of snow has progressed significantly to more sophisticated approaches as described by Creseri et al. [6]. They included an elastic-viscous-plastic law and a constitutive model that accounts for the sintering of snow and were able predict the ductile regime of snow accurately. Constitutive modelling was also employed by von Moos [7] to describe the ductile behaviour of snow for which the elastic and viscous material laws cummulated in a complex Burgers law. The latter was already applied by Shapiro et al. [8] who supported the Burgers model as a very versatile model description, however at the expense of a large number of parameters, that have to be determined mainly through validation by experiments. Similarly, Schweizer [9] described snow as a material with linear viscous property and investigated into skier induced load on layers of snow. Stoffel and Bartelt [10] and Stoffel [11] and Bartelt et al. [12] applied an elastic-viscous law within a 2-dimensional finite element code and predicted creep of snow and its mechanical load on snow defence structures. The interacion between snow and a plate aiming at a wheel-snow contact were predicted by Haehnel and Shoop [13] by a capped Drucker-Prager model. In addition to an elastic-plastic material law Gaume et al. [14] included a strain-softening correlation due to shear and thus, studied the impact of weak

layers and snow heterogeneity on the release angle for avalanches. The capabilities of elastic-viscous approaches were further developed by Nicot [15, 16] who introduced statistical micro-scale characteristics for snow by directional bonds that were allowed breaking and thus, accounting for fracture.

While the above-mentioned investigations relied on a macroscopic description of snow, the microscopic properties of snow moved into the focus of researchers. The micro-structure of snow was first considered by Schneebeli [17] who applied X-ray microtomography to re-construct the 3-dimensional micro-structure of a snow sample. X-ray microtomography was also used by Hagenmuller [18] to build the micro-structure and a linear elastic material law in conjunction with a fracture criterion represented the snow behaviour. A similar approach was employed by Theile et al. [19] in his finite element approach, however, extended by Glens law for secondary creep to describe the anisotropy of snow.

These modelling efforts based largely on an elastic-viscous description of snow in conjunction with finite elements contributed to a more comprehensive understanding of snow, however, large deformations as frequently encountered with snow are still difficult to address due to the continuous formulation of the finite element method. In addition, snow considered as ice grains suggests a discrete numerical technique to describe the behaviour of snow. Thus, Johnson and Hopkins [20] developed the so-called μ -model with the discrete element method as a first discrete approach. Bonds acted as joints between discrete elements that were allowed breaking and re-building i.e. refreezing. Michael [21] and Michael et al. [22, 23] applied also the discrete element method for snow modelling and was able to describe both the brittle and ductile behaviour of snow including the transition between the two regimes. Hagenmuller [24] developed a rather simple linear elastic model including a fracture criteria to describe a snow pack under deformation. However, no validation studies were carried out that could prove the quality of their approach. The material point method (MPM) was applied by Stomakhin et al. [25] as a representative of a hybrid approach to describe the behaviour of snow which was represented by an empirical correlation. A background grid is employed to account for changes in the topology, while snow particles were tracked by the Lagrangian method. However, their modeling efforts were motivated by nice appearances for movies rather than scientific investigations.

2 NUMERICAL APPROACH

Due to the discrete nature of ice grains, the Extended Discrete Element Method (XDEM), derived from the classical Discrete Element Method (DEM), was employed. It is an advanced approach on a micro-scale to describe the mechanical behaviour of snow. Hence, snow is built from individual ice grains that interact via forces and moments during a contact between two or several grains. The afore-mentioned forces and moments result from various interactions between grains:

- impact between grains

- bond between grains
- deformation of a bond
- fracture/generation of a bond

Besides grain collision, bonds between grains account for the the complex mechanical behaviour of snow. This behaviour is described by advanced physical models that represent the following inter-granular properties:

- elastic-plastic grain collision
- inter-granular friction
- bond growth due to creep of ice
- elastic viscous-plastic deformation of bonds
- fracture of bonds

The above-mentioned properties are formulated as to be dependent on temperature, pressure and loading rates. A validation of these advanced predictive capabilities of snow behaviour was carried out by a comparison between predicted results and sintering measurements of [26] and on creep models of ice developed by [27]. For a more detailed description, the reader is referred to Michael [22].

3 RESULTS

According to Kinisota [28], Narita [29] and Fukue [30], the mechanical behaviour of snow may be separated into two distinct regimes referred to as brittle and ductile. Between the brittle and ductile regimes exists a third regime that is characterised by a transitional behaviour and therefore, is called transitional regime. The most influential variable identified to distinguish into the different regimes is the strain rate $\dot{\varepsilon}$. Based on the experimental data of Kinisota [28] and Fukue [30] the transitional regime occurs at a strain rate of $\sim 5 \cdot 10^{-4} \text{ 1/s}$ and thus, acts as a separation parameter between the brittle and ductile regimes. Hence, snow deforms as a ductile material at strain rates below the critical strain rate of $\sim 5 \cdot 10^{-4} \text{ 1/s}$ and behaves as a brittle material above the critical strain rate.

In order to predict the above-mentioned behaviour, cylindrical snow samples were generated and compressed under unconfined conditions. The strain rates chosen were according to the two regimes namely ductile and brittle presented in the following sections. The predicted stress-strain relationship was compared to measurements and good agreement was achieved.

3.1 Brittle Deformation

As above-mentioned, the brittle deformation behaviour was predicted for cylindrical snow samples with a density $\rho = 408 \text{ kg/m}^3$ and strain rates of $4 \cdot \dot{\varepsilon} = 10^{-3} \text{ 1/s}$ and $4 \cdot \dot{\varepsilon} = 10^{-2} \text{ 1/s}$ under unconfined conditions which refers unambiguously to the brittle regime. The integral axial stress dependent on the strain was obtained as a result and is depicted in fig. 1.

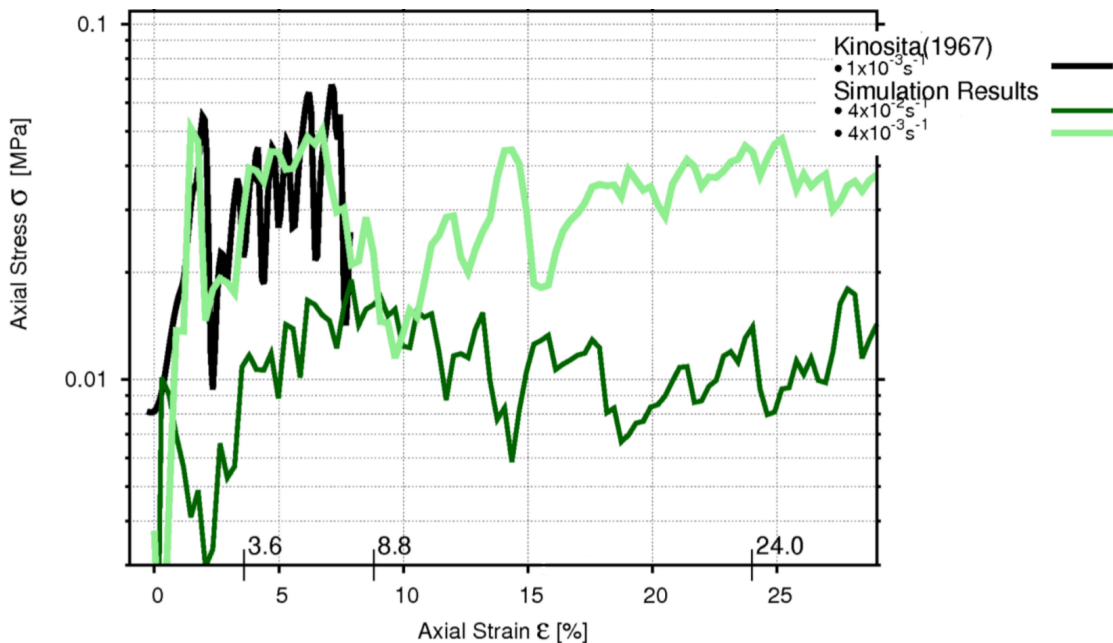


Figure 1: Axial stress versus strain during an unconfined compression test of a cylindrical snow sample ($\rho = 408 \text{ kg/m}^3$) in the brittle regime at strain rates of $\dot{\varepsilon} = 4 \cdot 10^{-3} \text{ 1/s}$ and $\dot{\varepsilon} = 4 \cdot 10^{-2} \text{ 1/s}$.

The predicted results were compared to measurements of Kinosita [28], who carried out experiments at a temperature of $T = -2\text{C}$ and a strain rate of $\dot{\varepsilon} = 10^{-3} \text{ 1/s}$. In particular, the predicted results of fig. 1 at a strain rate of $\dot{\varepsilon} = 4 \cdot 10^{-3} \text{ 1/s}$ agree well with the experimental data of Kinosita [28]. Both lines depict a similar saw tooth-like behaviour that is a characteristic property of the brittle deformation regime: A certain critical stress is reached during a period of almost linear increase of the stress versus strain representing a saw tooth. Fracture within the snow sample occurs at peak stress values and thus, releases abruptly the stress to lower values. The abrupt release of stress is accompanied by a significant plastic deformation of the sample as shown in fig. 2 for the lower line of fig. 1.

Fig. 2 shows that fracture occurs at the bottom part of the snow sample where also plastic deformation takes place. After rupture has taken place in the snow sample at a critical stress level, stress increases almost linearly with strain again repeating the next

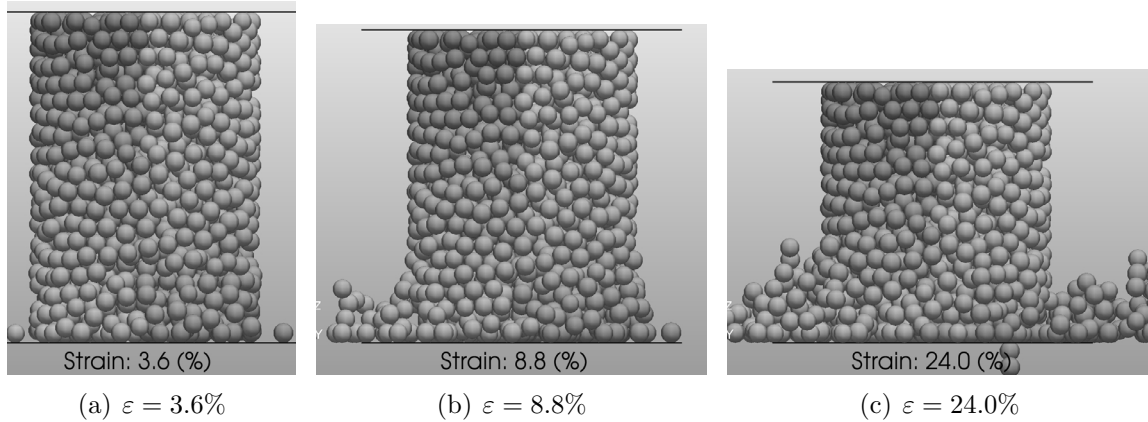


Figure 2: Brittle behaviour of a cylindrical snow sample ($\rho = 408 \text{ kg/m}^3$) during a strain rate of $4 \cdot 10^{-2} \text{ 1/s}$.

saw tooth until fracture occurs at almost the same peak stress level. The maximum peak stress is referred to as the yield stress of a sample in the brittle deformation regime.

3.2 Ductile Deformation

Similar to the previous section, ductile deformation of a snow sample was predicted for a strain rates of $\dot{\varepsilon} = 4 \cdot 10^{-6} \text{ 1/s}$, however different bonding properties which include the number of bonding neighbours N_b and the ratio of bond to grain radius r_b/r_g . Furthermore, predicted results were compared to experimental data of Scapozza and Bartelt [31], Von Moos [32] and Chadel et al. [33] at respective strain rates and temperatures and are depicted in fig. 3.

The stress-strain curves in fig. 3 initially increase almost linearly with a high gradient and flatten out by approaching the yield stress σ_y . During a further increase of strain, only insignificant variation in stress occurs, so that the sample remains at an almost constant stress level. The latter depends strongly on the bonding properties namely bonding neighbours N_b and the ratio of bond to grain radius r_b/r_g and is confirmed by experiments of Fukue [30]. He identified also the influence of the micro-structure as the main influence on the sample stiffness, that increases with longer sintering periods under the same density and is well captured with the predictions in fig. 3.

After the yield stress is reached, measurements show also a significant change in gradient, however, follow the characteristics of work-hardening behaviour was observed by Fukue [30], Scapozza and Bartelt and [31], Von Moos [32]. This behaviour is not represented by the predicted results indicating that creep of bonds subjected to stress is over-predicted.

The deformation behaviour is also shown in fig. 4 for different states referring to a strain of $\varepsilon = 4.4\%$, $\varepsilon = 16.0\%$ and $\varepsilon = 20.0\%$.

Contrary to the previous section on brittle deformation, the bonds experience almost

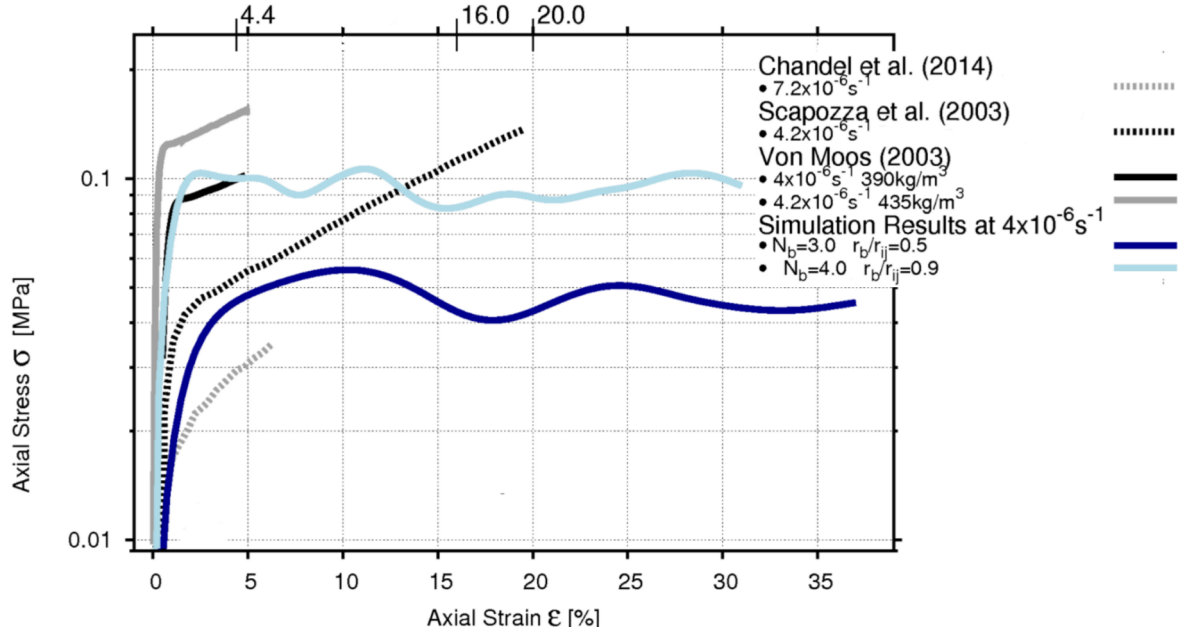


Figure 3: Axial stress versus strain during an unconfined compression test of a cylindrical snow sample ($\rho = 408 \text{ kg/m}^3$) in the ductile regime at strain rate of $\dot{\epsilon} = 4 \cdot 10^{-6} \text{ 1/s}$.

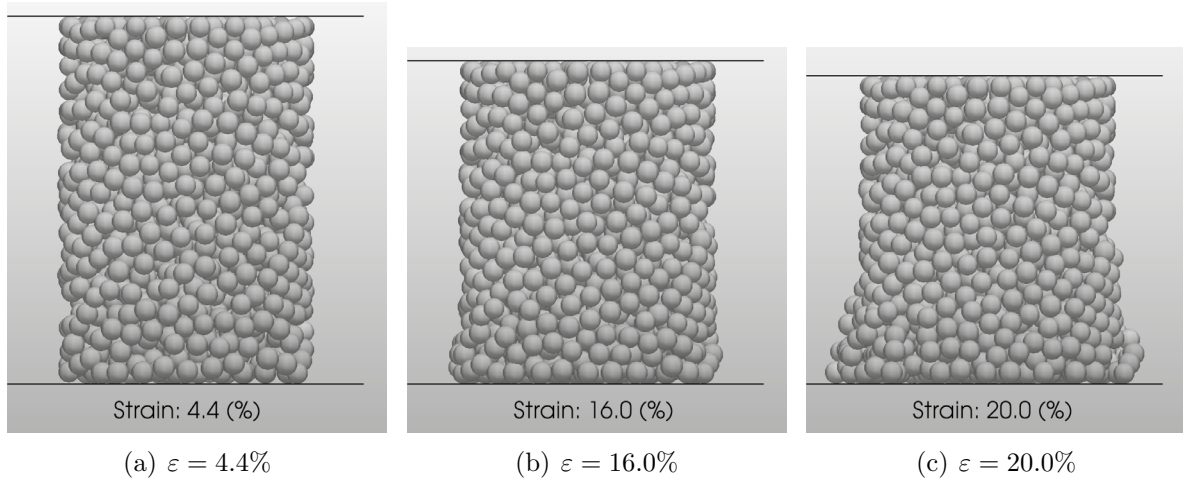


Figure 4: Ductile behaviour of a cylindrical snow sample ($\rho = 408 \text{ kg/m}^3$) during a strain rate of $4 \cdot 10^{-6} \text{ 1/s}$.

no fracture, so that the initial bonding structure of the sample remains intact. Thus, the bonds sustain the stress applied and only undergo deformation and displacement. Fig. 4a depicts the sample at the verge of yielding, for which only compaction of the sample without any significant change in shape took place. However, with an increased

strain of $\varepsilon = 20.0\%$, the sample deforms radially at the bottom area. This behaviour is accompanied by an inhomogeneous stress distribution, whereby higher stress values are found at the bottom of the sample. In addition, bonds experience tension due to radial deformation, however, in general are able to sustain the stress applied without failure.

4 CONCLUSIONS

Within this study a discrete approach derived from the classical Discrete Element Method (DEM) was employed to describe the behaviour of snow in both the brittle and ductile deformation regime. The numerical approach includes elastic-plastic grain collision, inter-granular friction, bond growth due to creep of ice, elastic viscous-plastic deformation of bonds and fracture of bonds. The predicted results were obtained from unconfined compression tests of cylindrical snow samples with a density of $\rho = 408 \text{ kg/m}^3$. In order to predict brittle and ductile deformation strain rates of $4 \cdot \dot{\varepsilon} = 10^{-3} \text{ 1/s}$, $4 \cdot \dot{\varepsilon} = 10^{-2} \text{ 1/s}$ and $\dot{\varepsilon} = 4 \cdot 10^{-6} \text{ 1/s}$ were applied. These values fall well into the brittle and ductile deformation regime that are separated by a transitional regime at a strain rate of $\sim 5 \cdot 10^{-4} \text{ 1/s}$.

Predicted results were compared to experimental data of Kinoshita [28] Scapozza and Bartelt [31], Von Moos [32] and Chandel et al. [33] that allowed correlating respective stress-strain curves. Under conditions applied good agreement between measurements and predictions was achieved. However, predicted results in the ductile regime after work hardening had occurred deviated from the measured data, and thus directing to an area for improved model development. Furthermore, results suggest that sintering age e.g. the history a snow sample has experienced is among the parameters having the most significant impact on the mechanical behaviour of a snow sample.

REFERENCES

- [1] P. Bartelt and M. Lehning. A physical SNOWPACK model for the Swiss avalanche warning: Part I: numerical model. *Cold Regions Science and Technology*, 35(3):123–145, 2002.
- [2] E. Brun, E. Martin, V. Simon, C. Gendre, and C. Coleou. An energy and mass model of snow cover suitable for operational avalanche forecasting. *J. of Glaciol.*, 35(121):333342, 1989.
- [3] Jordan. A one-dimensional temperature model for a snow cover. technical documentation for sntherm. Technical report, CRREL:9116, 1991.
- [4] F. W. Smith. Elastic stresses in layered snow packs. *Journal of Glaciology*, 11(63):407–414, 1972.
- [5] T. Lang and R. Sommerfeld. The modeling and measurements of the deformation of a sloping snow pack. *Journal of Glaciology*, 19(81):153–163, 1977.

- [6] S Cresseri, F. Genna, and C. Jommi. Numerical integration of an elasticviscoplastic constitutive model for dry metamorphosed snow. *International Journal for Numerical and Analytical Methods in Geomechanics*, 34(12):1271–1296, 2010.
- [7] M. von Moos. *Untersuchungen über das visko-elastische verhalten von Schnee auf der Grundlage von triaxialen Kriechversuchen*. PhD thesis, ETH Zürich, 2001.
- [8] L. H. Shapiro, J. B. Johnson, M. Sturm, and G. L. Blaisdell. Snow Mechanics - Review of the State of Knowledge and Applications. Technical report, US-Army CRREL, 1997.
- [9] J. Schweizer. The influence of the layered character of snow cover on the triggering of slab avalanches. *Annals of Glaciology*, 18:193–198, 1993.
- [10] M. Stoffel and P. Bartelt. Modelling snow slab release using a temperature-dependent viscoelastic finite element model with weak layers. *Survey in Geophysics*, 24:417–430, 2003.
- [11] M. Stoffel. *Numerical Modelling of Snow using Finite Elements*. PhD thesis, Swiss Federal Institute of Technology Zurich, 2005.
- [12] P. Bartelt, M. Christen, and M. Wittwer. Progam hafeleli - two dimensional numerical simulation of the creeping deformatino and temperature distribution in a phase changing snow pack. In *Snow Engineering: Recent Advances and Developments*, 2000.
- [13] R. B. Haehnel and S. A. Shoop. A macroscale model for low density snow subjected to rapid loading. *Cold Regions Science and Technology*, 40(3):193–211, 2004.
- [14] J. Gaume, G. Chambon, M. Naaim, and N. Eckert. Influence of the weak layers heterogeneity on slab avalanches releases using a finite element method. In Bonelli S., Dascalu C., and Nicot F., editors, *Advances in Bifurcation and Degradation in Geomaterials*, volume 11 of *Springer Series in Geomachanics and Geoengineering*, pages 261–266, 2011.
- [15] F. Nicot. Constitutive modelling of snow as a cohesive-granular material. *Granular Matter*, 6:47–60, 2004.
- [16] F. Nicot. From constitutive modelling of a snow cover to the design of flexible protective structures Part 1 – Mechanical modelling. *International Journal of Solids and Structures*, 41:3317–3337, 2004.
- [17] M Schneebeli. Numerical simulation of elastic stress in the microstructure of snow. *Annals Of Glaciology*, 38(1):339–342, 2004.

- [18] P. Hagenmuller. Experiments and simulation of the brittle failure of snow. Master's thesis, WSL Institute for Snow and Avalanche Research SLF, 2011.
- [19] T. Theile, H. Loewe, T. C. Theile, and M. Schneebeli. Simulating creep of snow based on microstructure and the anisotropic deformation of ice. *Acta Materialia*, 2011.
- [20] J. B. Johnson and M. A. Hopkins. Identifying microstructural deformation mechanics in snow using discrete-element modeling. *Journal of Glaciology*, 51, 2005.
- [21] M. Michael. *A discrete approach to describe the kinetics between snow and a tire tread*. PhD thesis, University of Luxembourg, 2014.
- [22] M. Michael, B. Peters, and F. Nicot. Advanced micromechanical description of snow behaviour part i mechanical and numerical modelling. *International Journal of Solids and Structures*, submitted.
- [23] M. Michael, B. Peters, and F. Nicot. Advanced micromechanical description of snow behaviour part ii model validation. *International Journal of Solids and Structures*, submitted.
- [24] P. Hagenmuller, G. Chambon, and M. Naaim. Microstructure-based modeling of snow mechanics: a discrete element approach. *The Cryosphere Discuss*, 9:1425–1460, 2015.
- [25] A. Stomakhin, C. Schroeder, L. Chai, J. Teran, and A. Selle. A material point method for snow simulation. In *Proceedings of Siggraph 2013*, 2013.
- [26] D. Szabo and M. Schneebeli. Subsecond sintering of ice. *Applied Physics letters*, 90, 2007.
- [27] P. Barnes, D. Tabor, and J. Walker. The Friction and Creep of Polycrystalline Ice. In Barnes, editor, *Proceedings of the Royal Society of London*, volume 324 of *A*, 1971.
- [28] Seiiti Kinoshita. Compression of Snow at Constant Speed. *Physics of Snow and Ice*, 1(2):911–927, 1967.
- [29] Hideki Narita. An experimental study on tensile fracture of snow. *Contributions from the Institute of Low Temperature Science*, A32:1–37, 1984.
- [30] Masaharu Fukue. *Mechanical performance of snow under loading*. PhD thesis, Department of Civil Engineering and Applied Mechanics, McGill, 1977.
- [31] C Scapozza and P Bartelt. Triaxial tests on snow at low strain rate. Part II. Constitutivebehaviour. *Journal Of Glaciology*, 49(164):91–101, 2003.
- [32] Markus von Moos. *Untersuchungen "uber das visko-elastische verhalten von Schnee auf der Grundlage von triaxialen Kriechversuchen*. PhD thesis, ETH Zürich, 2001.

- [33] Chaman Chandel, Praveen K. Srivastava, and P. Mahajan. Micromechanical analysis of deformation of snow using x-ray tomography. *Cold Regions Science and Technology*, (0):–, 2014.

A NOVEL SYSTEMATIC METHOD TO ESTIMATE THE CONTACT PARAMETERS OF PARTICLES IN DISCRETE ELEMENT SIMULATIONS OF SOIL

ROY LICHTENHELD¹

¹ German Aerospace Center (DLR) - Institute of System Dynamics and Control
Münchener Straße 20, 82234 Weßling, Germany
Roy.Lichtenheldt@dlr.de, www.dlr.de/sr

Key words: Granular Material, DEM, Parameter Estimation, Contact Parameters, Planetary Exploration, Soil, Regolith

Abstract. Recent advances in simulation of granular matter and computation hardware let the discrete element method (DEM) evolve into the field of dynamic simulation of soils, enabling to simulate physical effects of soil deformation at particle interaction-scale. However, DEM is still lacking a generally accepted method to determine material-specific but application-independent particle contact parameters. In this article a novel, systematic method to directly determine the contact parameters of the particles is proposed. These parameters are divided into two groups: 1) independent parameters whose values are measurable, real soil properties and 2) dependent parameters whose values are set according to sufficient, modeling-intrinsic requirements. With the proposed parameter estimation strategy, the number of parameters which actually need to be chosen by look-up tables has been decreased to one single parameter. Additionally, the look-up table is only computed once and reused for every new type of soil. Thus the method is time efficient and does not repeatedly need preliminary calibration simulations and the time required to develop a mature and valid model is drastically reduced. In the article the parameter setting method is validated for a quartz sand, used to simulate the impact-driven penetration of the HP³-Mole and its corresponding experimental measurements.

1 INTRODUCTION

Due to recent developments in computational hardware Discrete Element Method (DEM) is now a widely used method for the simulation of granular matter. The DEM is applied in a wide range of applications and even evolved into extraterrestrial terramechanics in planetary exploration [1]. However, for the dynamics of sandy soils the DEM is still lacking a widely accepted application-independent parameter estimation method. Most approaches in literature are relying on a priori parameter calibration using trial & error or optimization techniques in order to fit the simulation results to the measurements. Other

strategies [2, 3] are based on experience but lack the adaption to geometric properties of the simulation domain and the particular load situation. Often both strategies are combined in order to lower the number of parameters to be calibrated. Nevertheless such calibration is time consuming and needs to be renewed for every application. Thus, in this article a novel, systematic method to directly determine the contact parameters of the particles for the application in soil dynamics is proposed and implemented in the DLR-SR particle framework DEMETRIA (**D**iscrete **E**lement **M**ethod **E**nabled **T**erramechanics **I**nteraction **F**ramework) [1] based on the particle-simulator Pasimodo [4].

By classifying the parameters as 1) independent parameters whose values are measurable, real soil properties and 2) dependent parameters whose values are set according to sufficient, modeling-intrinsic requirements, most parameters are identified using analytical dependencies or directly measured values. Only a single parameter needs to be identified using look-up tables. The method as well as these look-up tables are application independent and thus there is no need for preliminary calibration simulations. In order to exemplify the approach the contact model developed by LICHTENHELD ET AL. [5] is used to simulate the HP³-Mole's locomotion into quartz sand.

2 CONTACT MODEL

In this section a short overview on the used inter-particle contact model, developed by LICHTENHELD ET AL. [6, 5, 1] is given. Thereby, the contact models will be explained for every load direction of the particles individually. An overview of the translational contact model is given in Figure 1.

2.1 Normal Contact

In normal direction the HERTZIAN contact law is used. Therefore, the implementation in [4] is adapted in order to incorporate mass-scaled damping factors. This scaling enables the same fraction of critical damping for all particle sizes. The resultant force in case of overlap evaluates to

$$\vec{F}_N^{nm} = \left(\frac{2E}{3(1-\nu^2)} \sqrt{r_C^{nm} |\vec{\delta}^{nm}|^3} \right) \vec{n}_c^n + k_{N\min}^{nm} \dot{\vec{\delta}}^{nm} \quad (1)$$

with YOUNG's Modulus E , POISSON's Ratio ν , r_C^{nm} the mean particle radius of particles m and n and $\vec{\delta}^{nm}$ the overlap. \vec{n}_c^n and $k_{N\min}^{nm}$ are the contact normal for each particle and the damping coefficient respectively.

2.2 Tangential Contact

In tangential direction, stick-slip friction is modeled by utilizing a regularized COULOMB friction model. Regularization is done by using a KELVIN element. Thus, the total tangential force yields

$$\vec{F}_{cT}^{nm} = c_T^{nm} \cdot \vec{\delta}_T^{nm} \cdot \text{sign}\left(\vec{\delta}_T^{nm} \cdot \dot{\vec{\delta}}_T^{nm}\right) + k_T^{nm} \cdot \dot{\vec{\delta}}_T^{nm} \quad (2)$$

$$\vec{F}_T^{nm} = \begin{cases} \vec{F}_{cT}^{nm} & \forall |\vec{F}_{cT}^{nm}| \leq |\vec{F}_N^{nm}| \cdot \tan(\phi_h) \wedge |\dot{\vec{\delta}}_T^{nm}| \leq v_{T\min}^{nm} \\ \vec{F}_N^{nm} \cdot \tan(\phi_g) \cdot (\dot{\vec{\delta}}_T^{nm})_0 & \forall |\vec{F}_{cT}^{nm}| > |\vec{F}_N^{nm}| \cdot \tan(\phi_h) \vee |\dot{\vec{\delta}}_T^{nm}| > v_{T\min}^{nm} \end{cases} \quad (3)$$

whereby \vec{F}_{cT}^{nm} is the force of the KELVIN element, and c_T^{nm} , k_T^{nm} and $\vec{\delta}_T^{nm}$ are the tangential stiffness, damping coefficient and displacement respectively. If the tangential velocity $\dot{\vec{\delta}}_T^{nm}$ is lower than the stick velocity limit $v_{T\min}^{nm}$, and the MOHR-COULOMB yield criterion is not yet met, the KELVIN element models the sticking condition limited by the sticking friction angle ϕ_h . Once either the yield force is met or the velocity exceeds $v_{T\min}^{nm}$, only slipping friction, characterized by the friction angle ϕ_g , is acting.

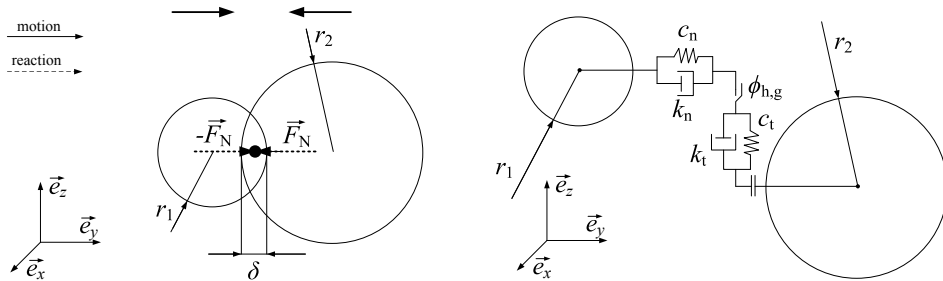


Figure 1: Soft particle contact generating overlap (left) and contact model for normal and tangential direction (right), [5]

2.3 Rotational Contact

As the soil's shear strength is highly dependent on the grains shape, the shape's influence on the rotational behaviour needs to be covered. For this article the rotation geometry approach of LICHTENHELD ET AL. [5] is used in order to cover the tilting motion and rotational behaviour of angular grains. This approach models the tilting torques of additional rotation geometries fixed to the spheres local coordinate system. Figure 2 illustrates the approach (left) and shows the opportunity to cover anisotropic effects of the grains shape by individual rotation geometries for every rotation axis (right). The generation of equivalent 3D-shapes as well as further information are given in [5]. The resulting torque exerted by both, tangential and normal forces acting on the moment arms

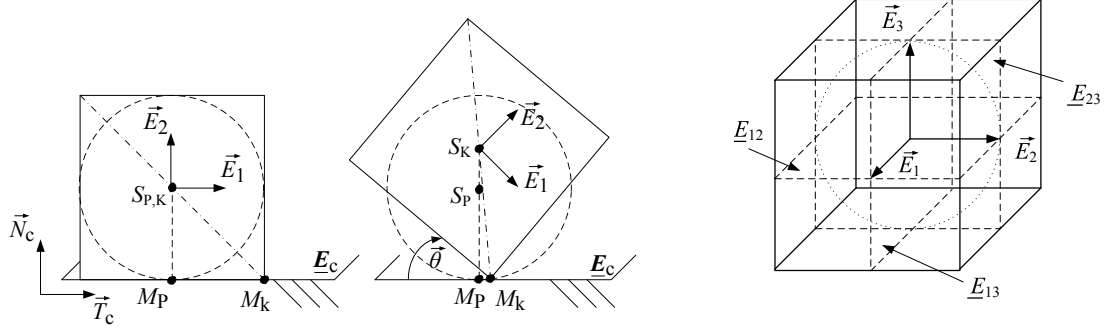


Figure 2: Nonlinear torque law applied to a spherical particle using additional rotation geometries (left) [5] and anisotropic rolling behaviour due to rotation geometries in 3D (right) [5]

$l_T^{jk}(\theta_i(t), \gamma_i)$ and $l_N^{jk}(\theta_i(t), \gamma_i)$ is calculated and summed for the rotation planes \underline{E}_R^{jk} as

$$\begin{aligned} \vec{M}_{RG} = \sum_{i,j,k=1}^3 & \left(- \left[l_T^{jk}(\theta_i(t), \gamma_i) \cdot \vec{N}_c^{jk} \right] \times \vec{F}_R^{jk} - \right. \\ & \left. \left[l_N^{jk}(\theta_i(t), \gamma_i) \cdot \vec{T}_c^{jk} \right] \times \vec{F}_R^{jk} \right) \cdot \varepsilon_{ijk}^2 \end{aligned} \quad (4)$$

$i, j, k \in \{1, 2, 3\}_{\mathbb{N}}$

wherein \vec{F}_R^{jk} is the resultant force on the particle in the rotation plane. Thereby, the moment arms are dependent on the rotation angle $\theta_i(t)$ of the rotation geometry with respect to the contact situation and the aspect ratio angle γ_i . \vec{N}_c^{jk} and \vec{T}_c^{jk} are the normal and tangential vector, of the rotation plane with respect to the contact. ε_{ijk} denotes the LEVI-CIVITA symbol. No additional damping torques are applied.

3 PARAMETER ESTIMATION METHOD

In order to have a systematic grouping of the parameters to be identified, they are stored in the parameter matrix $\underline{\Lambda}_P$:

$$\underline{\Lambda}_P := \begin{pmatrix} E, \nu & k_N & r & 0 & \rho \\ c_T & k_T & 0 & \phi & 0 \\ 0 & 0 & r & \gamma_{i,j,k} & J \end{pmatrix} \quad (5)$$

Therein the rows denote the membership to a certain contact model, whereas the columns separate elastic, dissipative, scale, grain shape dependent and inertia related parameters. In the following section the identification of these parameters will be explained in further detail. In addition to the given system, the parameters are classified as dependent and independent parameters. Thereby, the dependent parameters do not directly affect the

shear strength of the granular material. Independent parameters are directly influencing the shear strength of the simulated soil. The identification process in this article is given for the contact model presented in [5] and for the case of non-cohesive regoliths, as the soils on the planetary bodies of interest are showing negligible influences of cohesion [7].

3.1 Determinition of the dependent Parameters

The dependent parameters to be identified are: particle-size and size distribution, normal and tangential stiffness/damping related parameters, as well as the particle inertia tensor and mass. Since the shear strength sensitivity is low, their values can be chosen according to computational efficiency aspects only: Sufficiently high but as low as possible. This choice is done by analytical equations based on other contact-, simulation domain- and load-parameters (e.g. particles YOUNGs Moduli or particle size by tool-particle resolution).

Particle Size & Size Distribution

Due to computational constraints, particles cannot be modeled at the real grains size. Scaling is carried out in [8, 9, 10, 3, 11] a.o., but there is neither a widely accepted nor a systematic scaling method available. In order to describe the scale of the particles



Figure 3: Tool resolution for a planetary rover wheel (left), [6] and the HP³-Mole (right), [1]

with respect to the soil manipulating tool, LICHTENHELDT ET AL. [6] introduced the resolution Γ . The resolution describes the number of particles, that are manipulated by the minimal characteristic length L_{\min} of the tool at once. Thus, it is derived using the ratio of L_{\min} to the maximum particle diameter $2 \cdot r_{\max}$:

$$\Gamma := \frac{L_{\min}}{2r_{\max}} \quad (6)$$

Utilizing the resolution it can be shown that for most applications a resolution of $\Gamma \geq 10$ is sufficient, e.g. the Bevameter test or the HP³-Mole. For wheels of planetary rovers values of $\Gamma \geq 2.5$ are found to be sufficient. This value is in good agreement with the values based on experience shown in literature, e.g. NAKASHIMA [8] shows a range of $\Gamma \in [1.25, 5]$. The particle size distribution is not directly investigated in this article and

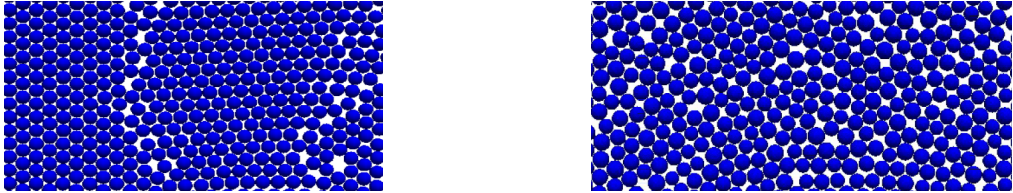


Figure 4: Comparison of two particle packages with respect to crystalline structuring: uniform particle size (left) and slight size distribution(right)

is set such, that the formation of crystalline structures like face centered cubic packages (Fig. 4, left) can be avoided in order to omit artificially high shear strength. When the size distribution is chosen in the range of

$$r_{\min} = \sigma_r \cdot r; \quad \sigma_r \in [0,6; 0,9] \quad (7)$$

crystalline structures are avoided efficiently (Fig. 4 right), by still maintaining a preferably low number of particles. Further investigation on the size distribution is given e.g. in [3, 12].

Young's Modulus

In order to cover realistic behaviour of the particles the equivalent stiffness of the normal contact needs to be sufficiently high to allow for realistic results. Nevertheless, by choosing higher values the integrator time step size needs to be decreased. The authors of [13, 3] a.o. have shown that the stiffness can be decreased with respect to the grain stiffness, however the available approaches only cover the weight of the soil itself but do not incorporate the external loads applied by tools or the soil displacement. In order

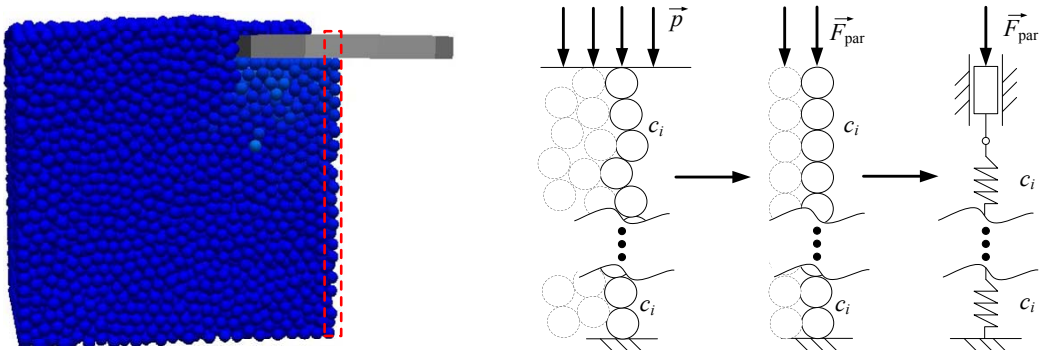


Figure 5: Simplifying the real situation towards the equivalent particle stack for stiffness identification, compare [6]

to cover the aforementioned effects, the real situation is simplified as shown in Figure 5 by improving the basic approach of LICHTENHELDT ET AL. [6]. By assuming the ideal particle stack and neglecting frictional interaction, a worst-case in terms of overlap is obtained. In this article the approach is exemplified for a cylindrical Bevameter plate. By

assuming the equivalent external load \vec{F}_L on the particle stack:

$$\vec{F}_L = \int_0^r \int_0^{2\pi} \vec{p} \cdot r \cdot d\varphi dr; \quad |\vec{p}(r)| = \text{const}; dA = r \cdot d\varphi dr \quad (8)$$

using the particles radius r and the assumed maximum pressure \vec{p} which is known from the material characterization. Using the equivalent external load and by covering the soils own weight, the YOUNGS Modulus can be estimated using the approximation for the equivalent particle stiffness given by ERGENZINGER [14] in conjunction with the extension of the basic approach given by LICHTENHELD [6]

$$E \geq \frac{2c_i}{\pi r} = z_h \frac{|3\vec{p} + z_h \cdot \rho_p \cdot \vec{g}|}{3|\vec{u}| \cdot r} \quad (9)$$

whereby the final sinkage z_h is known from material characterization, ρ_p is the particles density and \vec{u} the relative overlap of the particles with respect to r . This approximation gives an applicable lower boundary for the stiffness. An alternative approximation to give an upper boundary can be given directly by using HERTZian theory to determine E from the equivalent stiffness:

$$E \geq \pi z_h \frac{|3\vec{p} + z_h \cdot \rho_p \cdot \vec{g}|}{4r|\vec{u}|^{3/2}} \cdot (1 - \nu^2) \quad (10)$$

Normal Damping

Damping in normal direction of the contact is determined as a fraction of the critical damping:

$$k_{\text{krit}}^{nm} = \frac{4}{3} \cdot \sqrt{\frac{2\rho E \pi (r_{\min}^{nm})^4}{1 - \nu^2}} \sqrt{|\vec{u}|} \quad (11)$$

Using the approach in [15] the damping fraction can be chosen based on the coefficient of restitution ε_r :

$$k^{nm} = \frac{|\ln(\varepsilon_r)|}{\sqrt{\ln(\varepsilon_r)^2 + \pi^2}} \cdot k_{\text{krit}}^{nm} \quad (12)$$

It can be shown that a range between 10..30% of k_{krit}^{nm} and thus $\varepsilon_r \in [0.62, 0.85]$ is sufficient for most systems.

Tangential Regularization

In literature the regularization stiffness is usually chosen as a fraction of the normal stiffness by experience. As the time step size and the computational effort show a low sensitivity on the tangential stiffness, it is chosen rather too high than too low. The identification of c_t is carried out analogously to the determination of E , using the particle stack. Therefore, a pair of particles is considered, whereby one particle loaded by external

loads and the other is only influenced by gravity. In order to prohibit unrealistically high tangential deformations while in sticking state, the tangential spring stiffness can be chosen as

$$\left| \frac{\pi}{2} E \cdot r^2 \vec{u} \right| \mu \leq |\vec{u}_t r \cdot c_t| \quad (13)$$

$$c_t \geq \pi E \cdot r^2 \frac{|\vec{u}| \mu}{2 |\vec{u}_t|} \quad (14)$$

whereby \vec{u}_t is the relative tangential displacement of the particles. By choosing $\vec{u}_t = 0.0025$ it is always secured, that the particles only separate in slipping state considering pure shear loading. Tangential damping is chosen as 10% of critical damping in order to sufficiently damp oscillations but also to prohibit instant state changes at high initial particle shear rates $\dot{\delta}_{T0}^{nm}$.

3.2 Determination of the independent Parameters

In the contact model described in [5] the independent parameters are: grain shape aspect ratio, inter-particle friction, tool-particle friction and particle density. In order to avoid complex measurements of unknown parameters, e.g. inter-particle friction, look-up tables of outputs from DEM-simulated standard soil tests (triaxial test, Bevameter tests) at variation of the unknown parameters are prepared. The corresponding result of the identical but physical test applied to the real soil is then mapped onto the computed look-up table. The best match is found by minimizing the difference of real and computed test output graphs with help of optimization strategies. The identified optimum defines the set of unknown parameters.

Tool-particle friction is directly determined by measurements using a non-grousered Bevameter shear plate and particle density is set to the real material's grain density. The determination of the particles inertia is explained in [5].

Rotation Geometry

As the grains shape has a major influence on the shear strength of granular material it needs to be identified based on measurements. Thereby, the rotational behaviour can be described sufficiently detailed to model the macroscopic deformation behaviour of real soils.

The particles equivalent 3D rotation shape is determined by analysis of the grain shape. Therefore, microscopic pictures of the grains are taken and the aspect ratio is determined by image processing of the characteristic lengths of the grains. As shown in Figure 6 the most common aspect ratios are used for all the particles. Based on the high number of analyzed grains in a soil sample, the equivalent 3D shape can be chosen and built according to LICHTENHELD ET AL. [5]. For future applications different aspect ratios for mixed soils will be taken into account. Using only one shape for non-mixed soils like quartz sands was found to be sufficient.

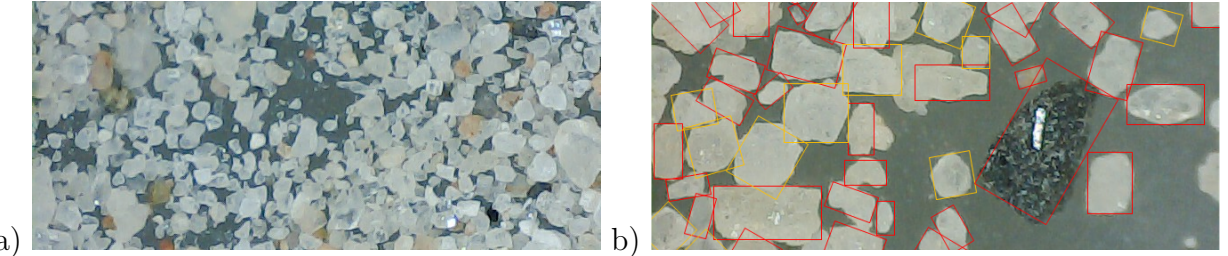


Figure 6: Microscopic pictures of quartz sands: a) 20-times magnification, b) 80-times magnification including identification of the aspect ratios

Inter-particle Friction

Another major influence on the shear strength of granular materials, both real and simulated, is inter-particle friction. In order to cover the initial shear strength before yielding, the sticking friction of the particles is the major friction parameter. The slipping friction coefficient is then determined based on the identified sticking friction coefficient. As there is no analytical way to relate the inter-particle sticking friction and grain shape to the shear strength yet, the sticking friction coefficient is determined based on a lookup table. As the Bevameter is widely used for characterization of soils in planetary exploration, it is the material test of choice to create the lookup table. However it should be noted that almost every available material test, i.e. triaxial or direct shear test a.o., may be used instead.

The lookup table is performed once and can be reused for future identification of new soils. Therefore, the material test is simulated for friction angles $\phi_h \in [5, 65]^\circ$ for the applicable aspect ratio angles γ . All other parameters are also set according to the previous sections. To characterize a soil for use with the DEM model, the bevameter test is performed and the pressure-sinkage relation is compared to the lookup table at discrete sinkages z_j . Thereby, an optimization strategy is used to determine the minimum summed error between simulation and measurement at z_j and thus to identify ϕ'_h :

$$\begin{aligned} \phi'_h \in \arg \min_{\phi_h \in [5, 65]} & \left[\sum_{j=1}^i (p_s(z_j, \gamma, \phi_h) - \bar{p}(z_j)) \right] \Leftrightarrow \phi'_h \in [5, 65] \\ & \wedge \sum_{j=1}^i (p_s(z_j, \gamma, \phi'_h) - \bar{p}(z_j)) \leq \sum_{j=1}^i (p_s(z_j, \gamma, \phi_h) - \bar{p}(z_j)) \quad (15) \\ & \forall \phi'_h \in [5, 65]; \quad i, j \in \mathbb{N} \end{aligned}$$

In order to determine friction angles, not covered by the simulations of the lookup table, linear interpolation was found to be applicable to find intermediate values. After identification, validation has to be carried out for the real application in order to prove applicability of the parameters for the actual load situation. In the following section the applicability will be proven using the method for the simulation of the HP³-Mole.

3.3 Results & Verification

The proposed method has been successfully applied to accurately model the penetration of InSight's [16] HP³-Mole [17] by LICHTENHELDT in [1, 18]. Figure 7 shows the soil part of the three-stage validation process. Therefore, the DEM soil model including the parameter estimation approach, the mechanism model and the full system co-simulation model were validated in individual steps. As shown in Figure 7 on the left, the penetrom-

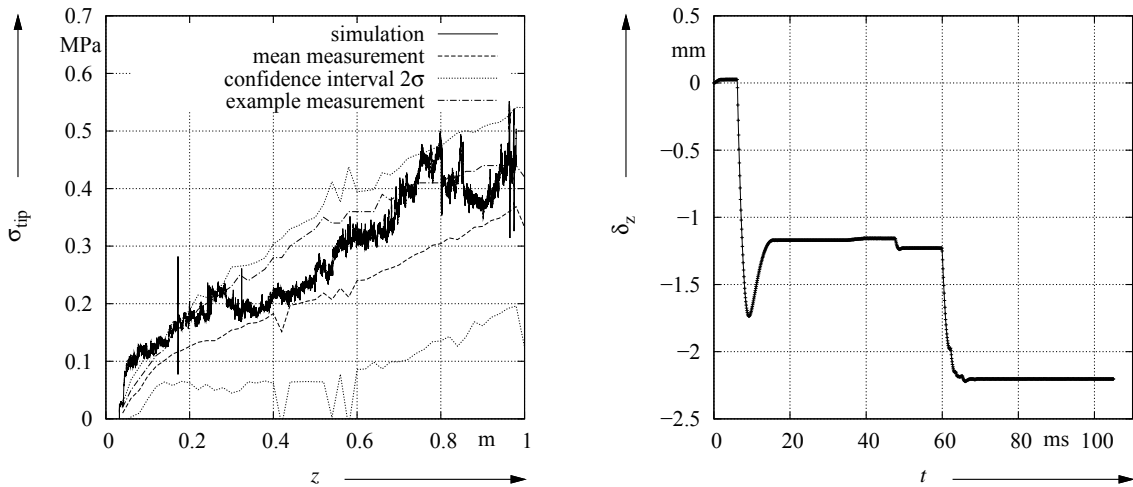


Figure 7: Comparison of the penetrometer measurement and respective DEM simulation (left) and penetration depth for one stroke cycle of the Mole co-simulation (right), [1]

eter measurement can be reproduced and the simulation results are well situated within the measurements confidence interval in the range of 0.1 m to 1 m depth. Regarding the full co-simulation process [1], Figure 7 shows the displacement of the Mole over one stroke cycle. Thereby, the reached per stroke penetration depth is 2.2 mm, which leads to a deviation of 15.8% to the depth of 1.9 mm in the measurement.

Additionally, the models and approaches have been verified using the DLR-RMC Bevameter test in measurement and simulation as well as for qualitative verification using planetary rover wheels. Additional verification and validation is currently carried out in order to further proof the applicability of the models and presented parameter estimation method.

4 CONCLUSION

In order to omit long parameter calibration processes, a novel systematic approach to determine the DEM contact parameters was presented. This approach classifies the parameters as either dependent or independent parameters based on their influence on the shear strength. Using this method most parameters can be chosen based on sufficient constraints. The parameters directly influencing the shear stiffness are either measured

directly or estimated using pre computed look up tables. Therein these tables need only to be computed once and can be reused for every new soil type. Thus, the need of calibration using material test or application simulations are totally omitted.

The method was implemented into the DEM framework DEMETRIA at DLR-SR in order to determine the parameters without a priori simulations. The applicability of the method is shown for InSight's HP³-Mole and further verification was carried out using the Bevameter test. Further work will focus on additional validation using planetary rover wheel tests, as well as on deeper investigation of the relation of inter-particle friction on the shear strength in order to omit the necessity of look up tables. Additionally, further research on the particle size distribution using the available scaling based on the tool resolution is needed.

REFERENCES

- [1] R. Lichtenheldt, B. Schäfer, and O. Krömer. Hammering beneath the Surface of Mars modeling and simulation of the impact-driven locomotion of the HP3-Mole by coupling enhanced multi-body dynamics and discrete element method. In *Shaping the future by engineering: 58th Ilmenau Scientific Colloquium IWK, URN (Paper): urn:nbn:de:gbv:ilm1-2014iwk-155:2 Technische Universität Ilmenau, 2014*, 2014.
- [2] T. Tsuji, Y. Nakagawa, N. Matsumoto, Y. Kadono, T. Takayama, and T. Tanaka. 3-d dem simulation of cohesive soil-pushing behavior. *Journal of Terramechanics*, 49, 2012.
- [3] M. Obermayr. *Prediction of Load Data for Construction Equipment using the Discrete Element Method*. PhD thesis, Universität Stuttgart, 2013.
- [4] F. Fleissner. Dokumentation, template-files und beispiele zum programmepaket "pasimodo". Technical report, Inpartik & Universität Stuttgart, 2012.
- [5] R. Lichtenheldt and B. Schäfer. Planetary rover locomotion on soft granular soils - efficient adaption of the rolling behaviour of nonspherical grains for discrete element simulations. In *3rd International Conference on Particle-Based Methods, S. 807-818, ISBN 978-84-941531-8-1, Stuttgart*, 2013.
- [6] R. Lichtenheldt and B. Schäfer. Locomotion on soft granular soils: A discrete element based approach for simulations in planetary exploration. In *12th Symposium on Advanced Space Technologies in Robotics and Automation, ESA, Netherlands*, 2013.
- [7] K.E. Herkenhoff, M.P. Golombek, E.A. Guinness, J.B. Johnson, A. Kusack, R.J. Richter, L. and. Sullivan, and S. Gorevan. *THE MARTIAN SURFACE - Composition, Mineralogy, and Physical Properties*. Cambridge University Press, 2008.

- [8] H. Nakashima, A. Oida, M. Momozu, Y. Kawase, and H. Kanamori. Parametric analysis of lugged wheel performance for a lunar microrover by means of dem. *Journal of Terramechanics*, 44, 2007.
- [9] W. Li, Y. Huang, Y. Cui, S. Dong, and J. Wang. Trafficability analysis of lunar mare terrain by means of the discrete element method for wheeled rover locomotion. *Journal of Terramechanics*, 47, 2010.
- [10] M. Obermayr, C. Vrettos, and P. Eberhard. A discrete element model for cohesive soil. *III International Conference on Particle-based Methods - Fundamentals and Applications PARTICLES 2013, Stuttgart*, 2013.
- [11] C. Ergenizer, R. Seifried, and P. Eberhard. A discrete element model predicting the strength of ballast stones. *Computers and Structures*, 108109:313, 2012.
- [12] H. Nakashima and T. Kobayashi. Effects of gravity on rigid rover wheel sinkage and motion resistance assessed using two-dimensional discrete element method. *Journal of Terramechanics*, 53:37–45, 2014.
- [13] J.-P. Plassiard, N. Belheine, and F.-V. Donze. A spherical discrete element model: calibration procedure and incremental response. *Granular Matter*, 2009.
- [14] C. Ergenizer, R. Seifried, and P. Eberhard. A discrete element model to describe failure of strong rock in uniaxial compression. *Granular Matter*, 2011.
- [15] K. Iwashita and M. Oda. *Mechanics of Granular Materials: An Introduction*. Balkema, Rotterdam, Netherlands, S. 356, 1999.
- [16] W.B. et al. Barnerdt. Insight: A discovery mission to explore the interior of mars. In *44th Lunar and Planetary Science Conference, Texas, USA*, 2013.
- [17] T. Spohn, M. Grott, S. Smrekar, C. Krause, and T.L. Hudson. Measuring the martian heat flow using the heat flow and physical properties package (hp3). In *45th Lunar and Planetary Science Conference*, 2014.
- [18] R. Lichtenheldt. Hammering beneath the Surface of Mars - Analyse des Schlagzyklus und der äußeren Form des HP3-Mole mit Hilfe der Diskrete Elemente Methode. In *IFTOMM D-A-CH, Dortmund*, 2015.

A THEORETICAL INVESTIGATION OF A MECHANICAL RESPONSE OF FLUID-SATURATED POROUS MATERIALS BASED ON A COUPLED DISCRETE-CONTINUUM APPROACH

**ANDREY V. DIMAKI^{1,2*}, EVGENY V. SHILKO^{1,2}, SERGEI V. ASTAFUROV¹ AND
SERGEI G. PSAKHIE¹**

¹ Institute of Strength Physics and Materials Science SB RAS
Akademicheskii av. 2/4, 634055, Tomsk, Russia
E-mail: dav@ispms.tsc.ru, URL: <http://www.ispms.ru>

² Tomsk State University,
Lenina av. 36, 643050, Tomsk, Russia
URL: <http://www.tsu.ru>

Key words: Porous media, Liquid, Discrete elements, Finite Difference

Summary. We propose a numerical model of liquid-saturated porous material, based on a coupled approach combining a discrete elements method and finite difference method. An ensemble of discrete elements simulates processes of deformation of a porous solid and filtration of single-phase liquid in an interconnected network of "micropores". Mass transfer of a fluid between the "micropores" and "macropores" (the latter are considered as the areas between spatially separated and non-interacting discrete elements) is calculated on a finer grid superimposed on an ensemble of movable discrete elements. The developed model was applied to study a mechanical response of brittle samples with water-saturated pore volume. It has been shown that the strength of liquid-saturated samples is determined not only by strength properties of "dry" material and a pore pressure, but largely by sample geometry, deformation rate and characteristics of porosity of a material. We suggest a generalizing dependence of the uniaxial compressive strength of water-saturated permeable brittle material on the specific diameter of filtration channels, which is the ratio of the characteristic diameter of the filtration channels to the square root of the strain rate. Values of parameters of mentioned dependence are strongly connected with the character of the relation between pore volume and pressure of a liquid.

1 INTRODUCTION

Porous media, saturated with a fluid, represent a wide class of natural objects, like a geological media, including coal seams, oil vessels etc, a biological media, such as a bone tissue, and artificial ones of a different purpose, including filtering materials, endoprostheses etc [1-3]. At that, the study of the response of such media to mechanical loading, including their deformation and fracture, remains the problem of high importance. In the paper we propose the method of theoretical study of fluid-saturated porous media, namely the method of hybrid cellular automaton, and the results of its application to study strength properties of brittle porous specimens, filled with a liquid.

2 DESCRIPTION OF THE DEVELOPED MODEL

The method of hybrid cellular automaton is based on the decomposition of a considered problem into two ones: 1) a description of a mechanical behavior of a solid skeleton and 2) a simulation of a mass transfer of a liquid within a filtration volume (a system of interconnected channels, pores, cracks etc). For the solution of the first sub-problem we apply the method of movable cellular automaton (MCA) that represents an implementation of discrete element method [4]. Also the problem of mass transfer of a fluid in a filtration volume is solved within a MCA layer. We suppose, following the ideas of Biot [5-6], that stress-strain state of a discrete element is directly interconnected with a change of a volume of pores and pore pressure of a fluid in the "micropores". A calculation of a mass transfer of a fluid between pores inside a solid skeleton and external macroscopic voids is performed on a finer finite-difference net, "frozen" into a laboratory coordinate system. The finite-difference net is also used to calculate volumes of macropores by means of integration over nodes belonging to a macropore.

For simulation of a mechanical response of fractured porous brittle materials we have implemented the model of rock plasticity with non-associated flow law and yield criterion of von Mises (the Nikolaevsky model) [7-8]. This model adequately describes a response of a wide class of brittle materials (geological materials, ceramics etc) at different scales with taking into account of influence of lower-scale structure. The Nikolaevsky model postulates a linear relationship between volume and shear deformation rates of plastic deformation with coefficient Λ named the coefficient of dilatancy. We adopted the Nikolaevsky model to the MCA method with use of so called Wilkins algorithm [9]. In the framework of this algorithm a solution of elastic-plastic problem is reduced to a solution of an elastic problem in increments and following correction of potential forces between particles (discrete elements) in accordance with the requirements of Nikolaevsky model, applied to values of local pressure and stress deviator [9].

In the framework of the proposed approach a solution of an elastic problem represents a calculation of normal and tangential forces acting from discrete element i as a result of interaction with a discrete element j . The corresponding equations are formulated based on a generalized Hooke's law in hypoelastic form [10]:

$$\begin{cases} \Delta\sigma_{i(j)} = \Delta F_{i(j)}^{centr} / S_{ij} = 2G_i \Delta\varepsilon_{i(j)} + \left(1 - \frac{2G_i}{K_i}\right) \Delta\bar{\sigma}_i^{mean}, \\ \Delta\tau_{i(j)} = \Delta F_{i(j)}^{tang} / S_{ij} = 2G_i \Delta\gamma_{i(j)}, \end{cases} \quad (1)$$

where symbol Δ indicates an increment of corresponding parameter during a time step Δt of numerical scheme; $\sigma_{i(j)}$ and $\tau_{i(j)}$ – are specific values of pair-wise central $F_{i(j)}^{centr}$ and tangential $F_{i(j)}^{tang}$ components of reaction force of i -th discrete element to j -th neighbour; S_{ij} – a contact square; G_i and K_i – shear and bulk moduli, correspondingly; $\Delta\varepsilon_{i(j)}$ and $\Delta\gamma_{i(j)}$ – increments of normal and shear strain of element i in pair $i-j$; $\bar{\sigma}_i^{mean}$ – average volume stress in element i [10, 11].

A stress state of a porous solid skeleton, containing a system of interconnected pores, channels and cracks, is rather complicated and depends both on a specific porosity and

geometry of pores and cracks and their spatial distribution [12]. In the absence of a pronounced orientation of cracks in a solid skeleton, the fluid pressure in a pore volume contributes only into a hydrostatic pressure in a solid skeleton (namely, into a hydrostatic tension). In this approximation the influence of a fluid in “micropores” can be taken into consideration by means of including of fluid pore pressure into a relation for a central force:

$$\Delta\sigma_{i(j)} = \Delta F_{i(j)}^{centr} / S_{ij} = 2G_i \left(\Delta\varepsilon_{i(j)} - \frac{\Delta P_i^{fluid}}{K_i} \right) + \left(1 - \frac{2G_i}{K_i} \right) \Delta\bar{\sigma}_i^{mean}, \quad (2)$$

where P_i^{fluid} – contribution of a fluid pore pressure (in “micropores”) into a mean stress in a volume of discrete element i . Note that the equation (2) is equal to the Hooke’s law in a model of linear poroelasticity.

The value of P_i^{fluid} is linearly related with average pore pressure P_i^{pore} of a fluid in micropores of discrete element i :

$$P_i^{fluid} = a_i P_i^{pore}, \quad (3)$$

where $a_i = 1 - K_i / K_{s,i}$. Here $K_{s,i}$ is a bulk modulus of non-porous grains of a solid skeleton of discrete element i . After solution of the elastic problem for an element i At current time step, an achievement of the yield criterion (namely the von Mises criterion) is checked, with explicit taking into account of pore pressure of a fluid:

$$\Phi_i = \beta_i (\bar{\sigma}_i^{mean} + b_i P_i^{pore}) + \bar{\sigma}_i^{eq} / \sqrt{3} \geq Y_i, \quad (4)$$

where Y_i is a shear yield stress of a material of element i , β_i is a coefficient of internal friction, $\bar{\sigma}_i^{eq}$ – von Mises stress, averaged over a volume of a discrete element i , b_i – dimensionless coefficient. A value of the coefficient b_i is determined by geometry of pores, channels and cracks in a solid skeleton. When a configuration of a pore volume allows an uniform distribution of a hydrostatic pressure in a local volume of a solid skeleton, the value of b_i is suggested to be equal to 1 [13,14]. At that, new cracks are assumed to appear from existing micropores/cracks. In the opposite case, when microscopic structure of a solid skeleton provides a more complicated interconnection between a pore pressure and fracture generation, the value of b_i is usually less than unity and depends on a porosity and pore pressure. The lower boundary of b_i is usually equal to initial porosity ϕ_0 of non-deformed material [13].

When the yield condition (4) is satisfied, the reduction of components of stress tensor in a volume of discrete element i to a yield surface is performed. In accordance with [11], the mentioned reduction can be performed by means of the following correction of specific normal and tangential forces of interaction between i -th element and j -th neighbor:

$$\begin{cases} \sigma'_{i(j)} = (\sigma_{i(j)} - \bar{\sigma}_i^{mean}) M_i + (\bar{\sigma}_i^{mean} - N_i) \\ \tau'_{i(j)} = \tau_{i(j)} M_i \end{cases}, \quad (5)$$

where $(\sigma'_{i(j)}, \tau'_{i(j)})$ – are reduced values of specific reaction forces; $M_i = 1 - (\sqrt{3}/\bar{\sigma}_i^{int})(3G_i(\Phi_i - Y_i)/(K_i \Lambda_i \beta_i + 3G_i))$ – coefficient of reduction of stress deviator;

$N_i = K_i \Lambda_i (\Phi_i - Y_i) / (K_i \Lambda_i \beta_i + G_i)$ – correction to a local mean stress, calculated after solving an elastic problem; Λ_i – dilation coefficient of material of element i .

A volume of a solid skeleton and, correspondingly, a pore volume changes under the influence of internal and external stresses. At that, a specific volume of pores ϕ (or so called “microscopic” porosity) can be defined as follows:

$$\phi = \frac{V_{pore}^{elast} + V_{pore}^{plast}}{V_{elem}}, \quad (6)$$

where V_{pore}^{elast} is a part of pore volume, which develops due to elastic deformations of material; and V_{pore}^{plast} is a part of pore volume, that appears as a result of “quasi-plastic” deformation of a material, namely as a result of opening of microscopic pores, cracks and other defects because of dilation of a material.

“Elastic” change of pore volume is determined by the relation of bulk moduli of porous solid skeleton K and of non-porous monolithic grains that constitute the solid skeleton K_s :

$$V_{pore}^{elast} = V_{elem}^{init} \left[\phi_0 + 3\sigma_{mean} \left(\frac{1}{K} - \frac{1}{K_s} \right) + 3\phi_0 \frac{aP_{pore}}{K} \right], \quad (7)$$

In turn, “inelastic” change of pore volume due to dilation of a material is given by the following relation:

$$V_{pore}^{plast} = V_{elem}^{init} \Omega_{plast}, \quad (8)$$

where Ω_i^{elast} and Ω_i^{plast} represent elastic and inelastic parts of volume deformation of a discrete element, that are formally determined as follows:

$$\begin{cases} \Omega_i^{elast} = 3(\bar{\sigma}_i^{mean} + P_i^{fluid})/K_i \\ \Omega_i^{plast} = (\varepsilon_i^{xx} + \varepsilon_i^{yy} + \varepsilon_i^{zz}) - \Omega_i^{elast} \end{cases}, \quad (9)$$

Here $\varepsilon_i^{\alpha\alpha}$ are diagonal components of strain tensor in a volume of a discrete element i [10,11].

In the paper we use the modified fracture criterion of Drucker-Prager that takes into account the contribution of a local pore pressure of a fluid in the following way:

$$\sigma_{DP} = 0.5(\lambda+1)\sigma_{eq} + 1.5(\lambda-1)(\sigma^{mean} + bP_{pore}) = \sigma_c, \quad (10)$$

where $\lambda = \sigma_c/\sigma_t$ is the relation of compression (σ_c) and tensile (σ_t) strengths of a link between a pair of discrete elements, the coefficient b is the same as in equation (4).

In the framework of the developed model of fluid transfer we use the following assumptions: 1) a fluid may occupy a pore volume completely or partially; 2) a fluid is compressible; 3) adsorption of a fluid on internal walls of pores, capillary effects and the effect of adsorption reduction of strength (Rehbinder effect) are not taken into account; and 4) a variation of sizes of micropores is not taken into account. In the framework of the latter

assumption the pore volume is completely described by the following two parameters: the value of open “microscopic” porosity ϕ and characteristic diameter of filtration channel d_{ch} . Note that the value of d_{ch} is defined by a size of smallest channels that determine the filtration rate of a fluid through a solid porous skeleton. An adequate choice of the value of d_{ch} allows correct description of a mass transfer of a fluid, despite simplicity of the assumptions given above.

A state of a compressible fluid (both in microscopic pores and macroscopic voids) can be described by the following equation [15]:

$$\rho(P) = \rho_0 \left(1 + (P - P_0) / K_f \right), \quad (11)$$

where ρ and P are the current values of density and pressure of a fluid, ρ_0 and P_0 are the values of density and pressure under atmospheric conditions, K_f – bulk modulus of a fluid. When the fluid occupies a pore volume only partially, we assume the fluid pressure is equal to the atmospheric pressure P_0 . Neglecting the influence of gravity, the equation of filtration transfer of a fluid can be written in the following form [16]:

$$\phi \frac{\partial \rho}{\partial t} = K_f \nabla \left[\frac{k}{\eta} \nabla \rho \right], \quad (12)$$

where η – fluid viscosity, k – coefficient of permeability of a solid skeleton that can be estimated as follows [16]:

$$k = \phi d_{ch}^2, \quad (13)$$

Note that, in the framework of the used assumptions, there is no mass transfer between elements with fluid pressure $\rho \leq \rho_0$.

In order to simulate a mass transfer between a solid skeleton and a macroscopic pores, we find nodes of finite-difference net, that belong to a boundary “solid skeleton – macropore”. Number of these nodes for each discrete element determines a length of a border between an element and a macropore (or several macropores). Having this length (or lengths for each macropore in contact), the calculation of mass transfer between a discrete element and a macropore(s) is performed basing on the equation (12). In order to describe a redistribution of a fluid in a volume of a micropores in a discrete element or in a macroscopic pore we use the approximation of equal pressure. Following this assumption, in every closed volume at each time step a density of a fluid and a pressure are distributed uniformly. This simplification remains adequate for relatively slow processes under consideration.

3 STUDY OF THE STRENGTH OF WATER-SATURATED BRITTLE SPECIMENS UNDER UNIAXIAL COMPRESSION

The developed model has been applied for the theoretical study of uniaxial compression of porous water-saturated specimens mounted between immovable matrix and piston, moving downwards with constant velocity V_y . (fig. 1a). The problem has been solved in a two-dimensional formulation in plain-strain approximation. A specimen had the uniform structure without any initial defects or inclusions. The value of the coefficient b was varied from $b = \phi = 0.1$ to $b = 1$.

The results of simulation demonstrate the significant influence of water pore pressure on the strength of specimens. Besides that, the strength of the specimens is influenced by the compression rate, permeability of the material and the geometry of the specimen.

Under the uniaxial compression, the water pressure in pores is determined by the competition of the following processes: 1) deformation of solid skeleton, accompanied with decreasing of pore volume; and 2) outflow of a fluid into outer space. While the first process leads to an increase of pore pressure, the second one leads to the decrease of the same. The balance of the mentioned processes is determined, in particular, by the value of permeability of a material that, in turn, depends on a characteristic size of a filtration channel d_{ch} . A typical dependence of strength of a specimen on a value of d_{ch} is shown in fig. 1b. This dependence has three characteristic regions. In the region I (at relatively low permeability) an outflow of a liquid from a specimen doesn't compensate a growth of pore pressure due to deformation of pores. In the result, a pore pressure in a specimen increases during the compression that results in the decrease of effective strength a specimen (see equation (4)). At relatively high values of permeability (region III) the outflow rate is high enough to provide a stable internal pressure of a liquid about the atmospheric pressure. In this case the influence of a pore pressure on the strength of a specimen is virtually absent, and strength of specimens tends to the strength of "dry" specimen. In the transition region II the outflow rate of a liquid is comparable with the rate of increase of pore pressure.

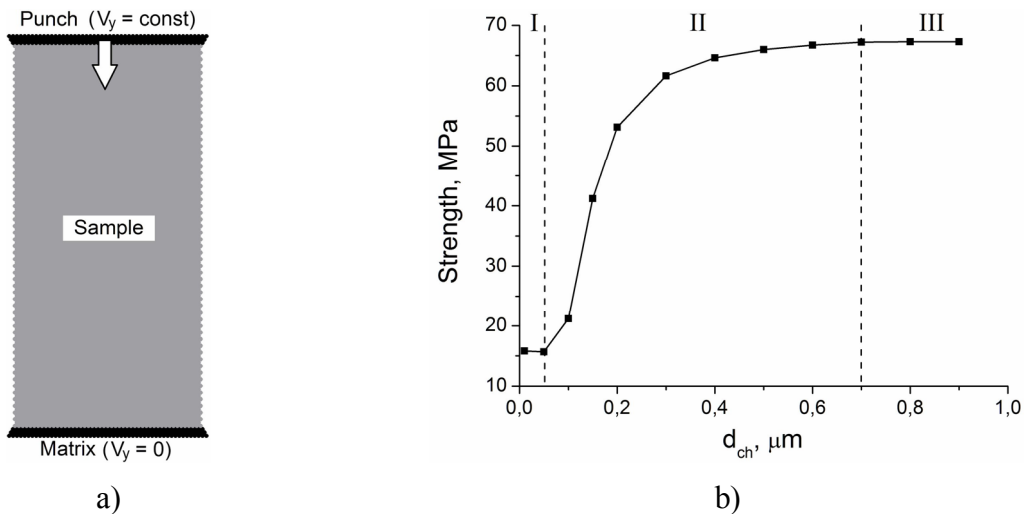


Figure 1. Scheme of the simulated specimen (a); typical dependence of compressive strength on characteristic size of a filtration channel of a brittle water-saturated porous specimen under uni-axial compression with constant velocity $V_y = 0,01$ m/sec and initial atmospheric pressure of a fluid (b).

In order to obtain a generalized dependence of strength of fluid-saturated specimens on material parameters and parameters of loading we have performed the series of numerical calculations with variation of characteristic size of filtration channel d_{ch} , deformation rate $\dot{\epsilon}_y$, coefficient b and width of a specimen W . At that, we have considered two limiting hypotheses about the character of influence of pore pressure on a strength of a material.

1. Micropores are distributed nearly uniformly and size of a micropore is much smaller than characteristic size of a fracture. In this case for relatively small values of porosity it is possible to suggest that damages generation is not connected with spatial location of micropores and more determined by higher-scale defects (in comparison with micropores). At that, an influence of pore pressure to a strength of solid skeleton is determined by the value of porosity, so that we assume $b = \phi$.

2. Micropores are distributed non-uniformly and damages originate by means of interconnection of several micropores by a crack. In this case, an influence of pore fluid is directly determined by the value of pore pressure: $b = 1$.

The dependencies of strength of a specimen on characteristic size of filtration channel under variation of deformation rate are shown in fig. 2. One can see that the value of the coefficient b produces a significant influence on the strength of fluid-saturated specimens. In the approximation of uniform distribution of micropores in solid skeleton ($b = \phi = 0.1$, fig. 2a) an influence of pore pressure on the strength is relatively weak (maximal decrease of strength doesn't exceed 25%). In the framework of the second approximation ($b = 1$, fig. 2b) a strength of water-saturated specimens may decrease by several times at low values of permeability. At that, a slope of dependencies of a strength on characteristic diameter of filtration channel decreases with the increase of b that is the result of stronger influence of a liquid, remaining in a pore volume, on the strength of specimens.

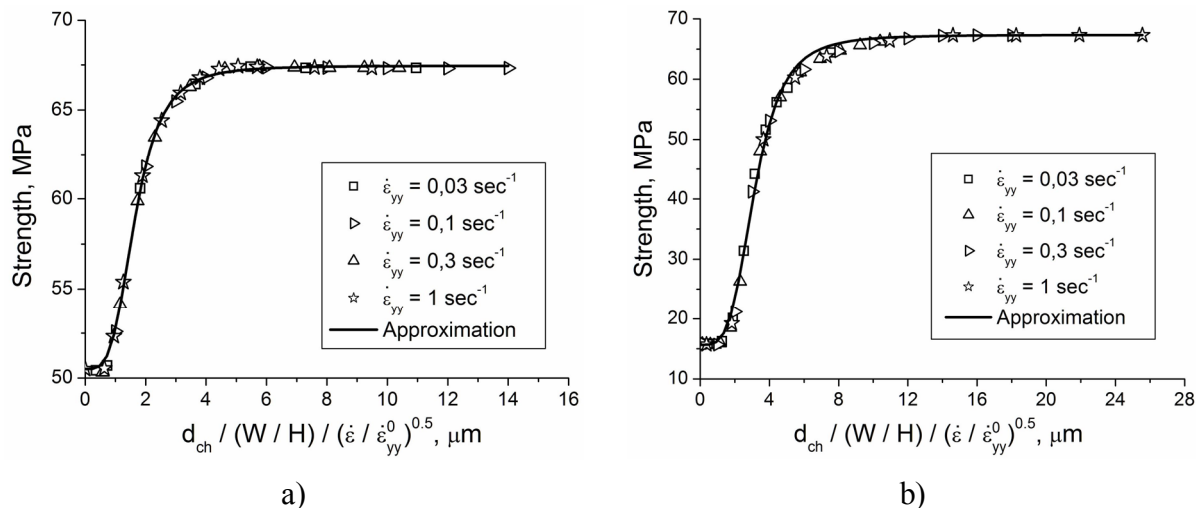


Figure 2. Generalized dependence of the strength of water-saturated specimens on characteristic diameter of filtration channel under various deformation rates: a) in the approximation of uniformly distributed micropores ($b = \phi = 0.1$); b) in the approximation of relatively big micropores that determine cracks nucleation ($b = 1$). Initial fluid pressure in solid skeleton is $P_{init} = P_0$. Relation of the width to the height of specimen is $W / H = 0.5$.

Basing on the analysis of the obtained dependencies of strength of specimens on characteristic diameter of filtration channel d_{ch} under various deformation rates, we have proposed a generalized curve of strength dependent on reduced diameter of filtration channel:

$$d_{ch} / \left((W/H) \sqrt{\dot{\epsilon}_{yy}/\dot{\epsilon}_{yy}^0} \right), \quad (14)$$

where $\dot{\epsilon}_{yy} = V_y / H$ is deformation rate, $\dot{\epsilon}_{yy}^0$ is a normalizing parameter, having a dimension of deformation rate. Curves, shown in fig 2, have been plotted in reduced coordinates (14).

It is well-known that processes, which flow is determined by a competition of several factors or phenomena (for instance, growth of biological populations etc), are often described by logistic function [17]. Basing on the mentioned above assumption on the determining role of competition of pore pressure growth and fluid outflow, we have suggested the logistic function for approximation of the obtained dependencies of compression strength on reduced diameter of filtration channel:

$$\sigma_c(d_{ch}, \dot{\epsilon}_{yy}) = \sigma_c^0 + \frac{\sigma_c^0 - \sigma_c^{\min}}{1 + \left(d_0 (W/H) \sqrt{\dot{\epsilon}_{yy}/\dot{\epsilon}_{yy}^0} \right)^p}, \quad (15)$$

where σ_c^0 is a compression strength of “dry” specimen (without a liquid in pores), σ_c^{\min} is a strength of water-saturated specimen with water “locked” in micropores (i.e. without a filtration transfer of a liquid in a solid skeleton), d_0 is a parameter of the approximation dependence, having the dimension of length, $\dot{\epsilon}_{yy}$ is the deformation rate of the specimen. The parameters of the dependence (19) are determined by elastic moduli of a solid skeleton and a liquid, by viscosity of a liquid, porosity etc. As one can see, the dependence (15) allows accurately approximate the results of numerical calculations (fig. 2). The value of σ_c^{\min} may be estimated based on the relations (7, 10) in the following way:

$$\sigma_c^{\min} = \sigma_c^0 \left[1 + 1.5(\lambda - 1) \frac{bK_f}{\phi_0} \left(\frac{1}{K_s} - \frac{1}{K_s} \right) \right], \quad (16)$$

As follows from (16), the strength of fluid-saturated specimens depends both on physical-mechanical properties of a solid skeleton and of a liquid, as well as on the value and character of spatial distribution of porosity (the latter determines a contribution of pore pressure into stress state and fracture of a solid skeleton). For the model parameters of the solid skeleton and liquid, used in the presented work, the estimation (16) of σ_c^{\min} is $\sigma_c^{\min} = 52.23 \text{ MPa}$ for $b = 0.1$, and $\sigma_c^{\min} = 15.83 \text{ MPa}$ for $b = 1$, that is in the good agreement with the results of simulation for $d_{ch} \rightarrow 0$ (fig. 2). The slight difference between the numerical results and estimation (16) is conditioned by the absence of taking into account of inhomogeneity of stress field near the matrix and the punch.

In general, the complicated character of the interrelations between the parameters of mechanical response of solid skeleton, physical-mechanical properties of a liquid and dynamics of its mass transfer etc., determines the nonlinear dependence of the strength of fluid-saturated specimens on the mentioned values and demonstrates the necessity of application of numerical methods for a study of a mechanical response of fluid-saturated media.

Authors acknowledge the financial support from the Program of Basic scientific research of the State academies of sciences for 2013-2020 (Russia).

REFERENCES

- [1] Taylor, D. Fracture and repair of bone: a multiscale problem. *J. Mater. Sci.* (2007) **42**:8911-8918.
- [2] Pan, Z. and Connell, L.D. A theoretical model for gas adsorption-induced coal swelling. *Int. J. Coal Geol.* (2007) **69**:243-252.
- [3] Zavsek, S., Dimaki, A.V., Dmitriev, A.I., Shilko, E.V., Pezdic, J. and Psakhie, S.G. Hybrid Cellular Automata Metod. Application to Research on Mechanical Response of Contrast Media. *Phys. Mesomech.* (2013) **1**:42-51.
- [4] Jing L., Stephansson O. *Fundamentals of discrete element method for rock engineering: theory and applications*. London: Elsevier. (2007).
- [5] Biot, M.A. General theory of three-dimensional consolidation. *J. Appl. Phys.* (1941) **12**:155-164.
- [6] Biot, M.A. The elastic coefficients of the theory of consolidation. *J. Appl. Mech.* (1957) **24**:594-601.
- [7] Garagash, I.A. and Nikolaevskiy, V.N. Non-associated laws of plastic flow and localization of deformation. *Adv. Mech.* (1989) **12**:131-183.
- [8] Stefanov, Yu.P. Deformation localization and fracture in geomaterials. Numerical simulation. *Phys. Mesomech.* (2002) **5-6**:67-77.
- [9] Wilkins, M.L. *Computer simulation of dynamic phenomena*. Heidelberg: Springer-Verlag. (1999).
- [10] Psakhie, S.G., Shilko, E.V., Smolin, A.Yu., Astafurov, S.V. and Ovcharenko, V.E. Development of a formalism of movable cellular automaton method for numerical modeling of fracture of heterogeneous elastic-plastic materials. *Fract. Struct. Integrity.* (2013) **24**:59-91.
- [11] Psakhie, S.G., Shilko, E.V., Grigoriev, A.S., Astafurov, S.V., Dimaki, A.V. and Smolin, A.Yu. A mathematical model of particle-particle interaction for discrete element based modeling of deformation and fracture of heterogeneous elastic-plastic materials. *Engng. Fract. Mech.* (2014) **130**:96-115.
- [12] Kushch, V.I., Shmegeera, S.V., Sevostianov, I. SIF statistics in micro cracked solid: effect of crack density, orientation and clustering. *Int. J. Engng. Sci.* (2009) **47**:192–208.
- [13] Paterson, M.S., Wong, T.F. *Experimental Rock Deformation. The Brittle Field*. Berlin-Heidelberg: Springer-Verlag. (2005).
- [14] Yamaji, A. *An Introduction to Tectonophysics: Theoretical Aspects of Structural Geology*. Tokyo: TERRAPUB. (2007).
- [15] Basniev, K.S., Dmitriev, N.M., Chilingar, G.V., Gorfunke, M. *Mechanics of Fluid Flow*. John Wiley & Sons, Inc., Hoboken. (2012).
- [16] Loytsyanskii, L.G. *Mechanics of Liquids and Gases*. Pergamon-Press. (1966).
- [17] Zwietering, M.H., Jongenburger, I., Rombouts, F.M., Van'T Riet, K. Modeling of the Bacterial Growth Curve. *Appl. Environ. Microbiol.* (1990) **56**:1875–1881.

CLARIFICATION OF SOIL SCOUR AND SEEPAGE FLOW BY USING A PARTICLE METHOD

TOMOTAKA NOGAMI ¹, MITSUTERU ASAI ² AND ALY ABDELRAHEEM ³

¹ Department of Civil Engineering, Graduate School of Engineering, Kyushu University
Motoka744, Nishi-ku, Fukuoka 819-0395, JAPAN
e-mail: t_nogami@doc.kyushu-u.ac.jp,
web page: http://www.doc.kyushu-u.ac.jp/kouriki/index_jp.htm

² Ph.D., Associate Prof., Department of Civil Engineering, Graduate School of Engineering,
Kyushu University
Motoka744, Nishi-ku, Fukuoka 819-0395, JAPAN
e-mail: asai@doc.kyushu-u.ac.jp,
web page: http://www.doc.kyushu-u.ac.jp/kouriki/index_jp.htm

³ Ph.D., Department of Civil Engineering, Graduate School of Engineering, Kyushu University
Motoka744, Nishi-ku, Fukuoka 819-0395, JAPAN
Email:abdelraheem@doc.kyushu-u.ac.jp

Key words: stabilized ISPH method, scouring, seepage flow, breakwater, simulation, governing equation.

Abstract. In 2011, Tohoku-Kanto earthquake tsunami caused serious damage to the port structures such as a breakwater and seawalls. Damage mechanisms of these structures have been studied in the past, and there are some causes. In this study, Soil scour and seepage flow are focused on. A particle simulation tool based on a stabilized ISPH method [1] has been extended to solve the different soil damage mechanisms; soil sour and seepage flow problem at the same time.

1 INTRODUCTION

In 2011, huge tsunami given by the Tohoku-Kanto earthquake tsunami caused serious damage to the port structures such as a breakwater and seawalls. Damage mechanisms of breakwater have been studied in the past, and there are mainly three causes; I. Horizontal force due to the water level difference between the front and rear breakwater, II. Soil scour and erosion behind the seawall during overflow and III. Piping destruction associated with the decline of the bearing capacity by seepage flow. Fluid-Structure-Soil coupling simulation is desired for a systematic comprehension of the seawall collapse mechanism, and it may help to develop next disaster prevention method. In this study, II. Soil scour and III. seepage flow are focused on. A particle simulation tool based on a stabilized ISPH has been extended to solve the different soil damage mechanisms; soil sour and seepage flow problem at the same time. In seepage flow analysis, surface flow and seepage flow are described by the same governing equations. In scour analysis, soil scour is judged based on quicksand quantity formula.

2 SEEPAGE FLOW ANALYSIS

In this chapter, as a first step, surface flow and seepage flow are described by the same governing equations, and an SPH formulation has been developed. After that, efficiency and adequacy of the proposed simulation technique has been validated through an application to two tests.

2.1 GOVERNING EQUATION

Fluid flowing outside the soil is generally modeled as Newtonian fluid, and described Navier-Stokes equation as

$$\frac{D\mathbf{v}}{Dt} = \frac{I}{\rho^w} (-\nabla P + \rho^w \mathbf{g}) + (\nu_w + \nu_T) \nabla^2 \mathbf{v} \quad (1)$$

In addition to the above equation, the mass conservation law was also used as governing equation.

$$\frac{D\rho}{Dt} + \rho \nabla \cdot \mathbf{v} = 0 \quad (2)$$

Here, \mathbf{v} , P , \mathbf{g} is water's velocity, pressure, gravitational acceleration. ν_w is the kinematic viscosity coefficient of water and ρ^w is specific density. ν_T is the kinematic eddy viscosity coefficient of water, and in this study, ν_T is modeled as the Smagorinsky eddy viscosity model and can be written as following equation

$$\nu_T = (C_S \Delta)^2 S \quad (3)$$

On the other hand, the soil is generally described Darcy's law as

$$\frac{\mu}{K} \mathbf{v} = -\nabla P + \rho^w \mathbf{g} \quad (4)$$

Here, K is a specific permeability coefficient in soil mound and μ is viscosity. In a field of the hydrology, the Darcy's law has been used as an equation of motion widely. However, it is reported that Darcy's law is not established in a flow field with a low Reynolds number, and then the non-Darcy flow rule is adapted as a model of seepage flow in this study.

Here, the traditional Extended Darcy's law suggested by Forchheimer is given by

$$\frac{\mu}{K} \mathbf{v} + \frac{\rho^w C}{\sqrt{K}} \mathbf{v} |\mathbf{v}| = -\nabla P + \rho^w \mathbf{g} \quad (5)$$

The above equation is not enough to simulate collapse behavior of seawall and breakwater structure, and it is necessary to unify the governing equations both for the free surface flow and seepage flow. Akbari equation [3],[4](Akbari, H.,2014/2013) is introduced as an unified governing equation as follows

$$\frac{C_r(\varepsilon)}{\varepsilon} \frac{D\mathbf{v}_D}{Dt} = -\frac{I}{\rho^0} \nabla P + \nu_E(\varepsilon) \nabla^2 \mathbf{v}_D - a(\varepsilon) \mathbf{v}_D - b(\varepsilon) \mathbf{v}_D |\mathbf{v}_D| + \mathbf{g} \quad (6)$$

Here, \mathbf{v}_D is Darcian velocity or average velocity, and it has a relationship with the regular velocity \mathbf{v} as $\mathbf{v}_D = \varepsilon \mathbf{v}$. Meanwhile, ε is porosity in the ground. Various coefficients in the Akbari's equation are given as a function of the porosity and their expressions of relations are as follows.

$$C_r(\varepsilon) = 1 + 0.34 \frac{1-\varepsilon}{\varepsilon} : \text{inertia coefficient} \quad (7)$$

$$\nu_E(\varepsilon) = \frac{\nu_w + \nu_T}{\varepsilon} : \text{effective viscosity coefficient} \quad (8)$$

$$a(\varepsilon) = \alpha_c \frac{\nu_w(1-\varepsilon)^2}{\varepsilon^3 D_{50}^2} : \text{linear coefficient} \quad (9)$$

$$b(\varepsilon) = \beta_c \frac{(1-\varepsilon)}{\varepsilon^3 D_{50}} : \text{nonlinear coefficient} \quad (10)$$

D_{50} is expressed the average particle size of ground materials and the value of α_c, β_c set $\alpha_c = 1000, \beta_c = 1.1$.

2.2 FORMULATION WITH ISPH METHOD

In this paper, smoothed particle hydrodynamics (SPH) method was adopted to solve the Akbari's unified equation for free surface and seepage flow. The basic concept in SPH method is that any function ϕ attached to particle "i" at a position r_i is written as a summation of contributions from neighbor particles.

$$\phi(r_i) \approx \langle \phi_i \rangle = \sum_j \frac{m_j}{\rho_j} \phi_j W(r_{ij}, h) \quad (11)$$

Note that, the triangle bracket $\langle \phi_i \rangle$ means SPH approximation of a function ϕ . The divergence of a vector function and the gradient can be assumed by using the above defined SPH approximation as follows

$$\nabla \cdot \bar{\phi}(r_i) \approx \langle \nabla \cdot \bar{\phi}_i \rangle = \frac{1}{\rho_i} \sum_j m_j (\bar{\phi}_j - \bar{\phi}) \cdot \nabla W(r_{ij}, h) \quad (12)$$

$$\nabla \phi(r_i) \approx \langle \nabla \phi_i \rangle = \rho_i \sum_j m_j \left(\frac{\phi_j}{\rho_j^2} + \frac{\phi_i}{\rho_i^2} \right) \nabla W(r_{ij}, h) \quad (13)$$

The Laplacian of the function adopts the following

$$\langle \nabla^2 \phi_i \rangle = \sum_j m_j \left(\frac{\rho_i + \rho_j}{\rho_i \rho_j} \frac{\mathbf{r}_{ij} \cdot \nabla W(r_{ij}, h)}{\mathbf{r}_{ij}^2 + \eta^2} \right) (\phi_i - \phi_j) \quad (14)$$

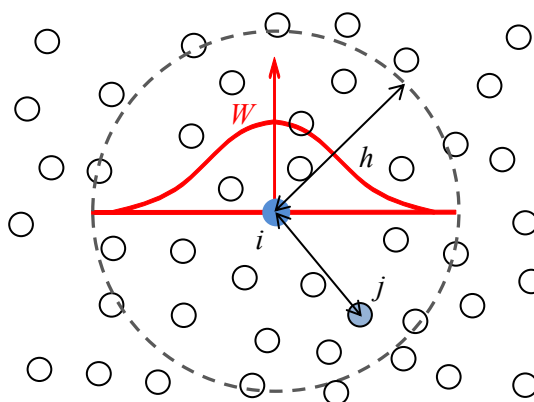


Figure 1. Particle placement and influence radius in the SPH method

The main concept in an incompressible SPH method (M. Asai et al.,2012) for Navier-Stokes equation is to separate the governing equations of the incompressible fluid by using projection method. In this method, the pressure is calculated implicitly and the velocity fields are updated explicitly. In this study, the same idea of ISPH for the Navier-Stoke equation is applied to solve the unified equation as follows,

$$\frac{D\bar{\rho}}{Dt} + \bar{\rho} \nabla \cdot \frac{\mathbf{v}_D}{\varepsilon} = 0 \quad (15)$$

$$\frac{C_r(\varepsilon)}{\varepsilon} \frac{D\mathbf{v}_D}{Dt} = -\frac{l}{\bar{\rho}} \nabla P + \frac{\mathbf{g}}{\varepsilon} + v_E(\varepsilon) \nabla^2 \mathbf{v}_D - a(\varepsilon) \mathbf{v}_D - b(\varepsilon) |\mathbf{v}_D| \mathbf{v}_D \quad (16)$$

Here, the density can be assumed as a constant value because of the incompressible assumption. Equation (15) can change as follows

$$\nabla \cdot \mathbf{v}_D = 0 \quad (17)$$

In the incompressible SPH method and treatment, the final pressure Poisson equation is given by

$$\langle \nabla^2 P_i^{n+1} \rangle = \frac{C_r(\varepsilon_i)}{\varepsilon_i} \frac{\rho_i^0}{\Delta t} \langle \nabla \cdot \mathbf{v}_{Di}^* \rangle \quad (18)$$

During numerical simulation, the ‘particle’ density may change slightly from the initial value because the particle density is strongly dependent on particle locations in the SPH method. If the particle distribution can keep almost uniformity, the difference between ‘physical’ and ‘particle’ density may be vanishingly small. In other words, accurate SPH results in incompressible flow need to keep the uniform particle distribution. For this purpose, the different source term in the pressure Poisson equation can be derived using the ‘particle’ density. In stabilized ISPH method, the pressure Poisson equation (18) reformulated as:

$$\langle \nabla^2 P_i^{n+1} \rangle \approx \frac{C_r(\varepsilon_i)}{\varepsilon_i} \left(\frac{\rho_i^0}{\Delta t} \langle \nabla \cdot \mathbf{v}_{Di}^* \rangle + \alpha \varepsilon_i \frac{\rho_i^0 - \langle \rho_i^n \rangle}{\Delta t^2} \right) \quad (19)$$

where α is relaxation coefficient, \mathbf{u}_i^* is temporal velocity and triangle bracket $\langle \rangle$ means SPH approximation. Note that this relaxation coefficient is dependent on the time increment and the particle resolution. Then, the reasonable value can be estimated by the simple hydrostatic pressure test using the same settings on its time increment and the resolution. In this study, $\alpha=0.01$.

2.3 VERIFICATION TEST

As a verification test of Fluid-Seepage flow interaction analysis, a simple free falling behavior of water throgh porous media was adopted. Fig.2. presents the schematic diagram for the analysis model. With three cases having different specific porosity, verification of this research formulation is carried out. The particle distance = 1cm, time increment = 0.001s and the total number of particles is 60798. Fig.3 shows analysis result when water mass arrived at the bottom of soil layer and contour shows pressure.

Analysis result shows that when porosity is high, the speed which water mass arrive at the air layer is fast. The velocity is also changed by the volume of porosity and soil layer is filled with water mass of the ratio of ε_0 . In this verification test, the effect of porosity is expressed correctly.

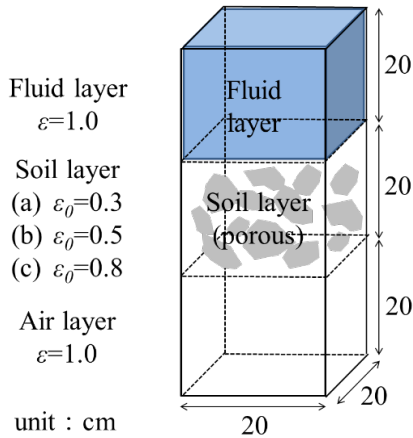


Figure 2. Analysis model

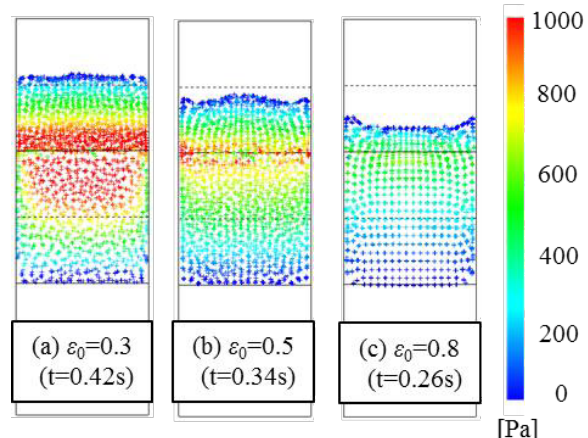


Figure 3. Analysis result

2.4 VALIDATION TEST

In validation, the experimental test related to seepage problem in breakwater structure is simulated. This experiment was conducted by Kasama et al. [5](2013). The penetration collapse of the breakwater in case given water level difference was observed.

The water level difference Δh is selected as 40mm, 80mm, 120mm, 145mm, and only in case of 145mm the mound collapsed. Experimental outline and analysis model is shown in Fig.4 and Fig.5. In Fig.4, blue points are water pressure gauge and Fig.6 shows their number. In this analysis, the particle distance $d_0 = 1\text{cm}$, time increment $\Delta t = 0.001\text{s}$ and the total numbers of particles are about 8 hundred thousand. Piezo water head shown below was used for a comparison between experimental and analysis.

$$Piezo = \frac{P}{\rho g} + \Delta z \quad (20)$$

In analysis, Δh is selected 145mm as the biggest water level. The analysis result of comparison of piezo water head in case of 145mm is shown in Fig.7. From this comparison, the value of the analysis is slightly different, however, analysis result behaviors shows a good agreement with the hydraulic experiment test. Finally, the seepage failure can be estimated by using our simulated hydraulic gradient by referring to its limitation as shown in Fig.8. In the figure, red color region shows the possible domain for seepage flow.

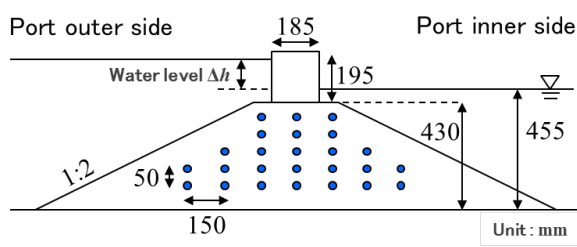


Figure 4. Experimental outline

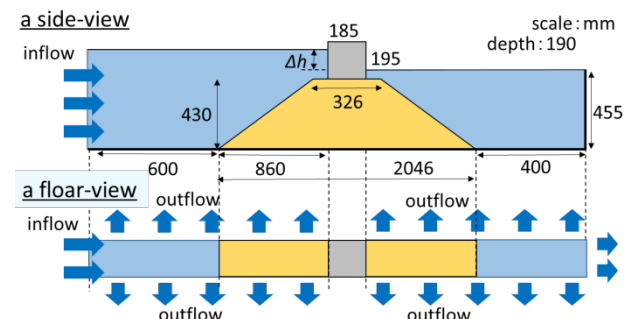


Figure 5. Analysis model

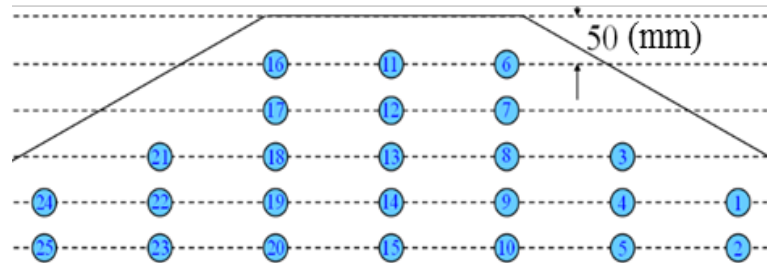


Figure 6. Water pressure gauge number

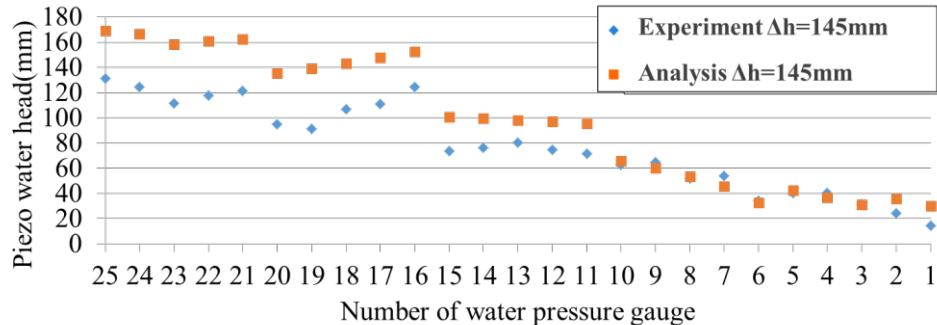


Figure 7. Analysis result (Piezo water head)

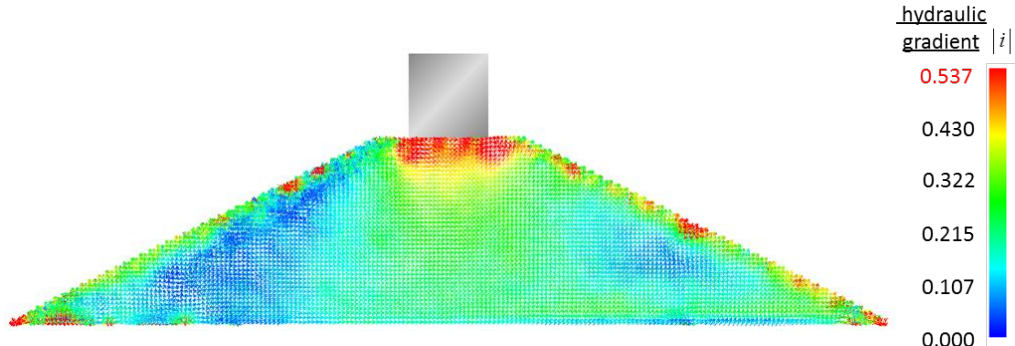


Figure 8. Analysis result (hydraulic gradient)

3 SCOURING ANALYSIS

3.1 SCOURING JUDGING FORMULA

Soil scour depends on velocity of fluid of flow and particle size of the sand. In this study, soil scour is judged by an experimental criteria based on quicksand quantity formula [6](H, Gotoh., 2004). The velocity Soil scour depends on velocity of fluid of flow and particle size of the sand. The velocity of threshold of sediment movement is shown below.

$$u_{bc} = \sqrt{\frac{2A_3(\mu_f \cos \theta - \sin \theta) \left(\rho_{sp}/\rho_l - 1 \right) gd}{\varepsilon(C_D + \mu_f C_L) A_2}} \quad (21)$$

Here, A_3 is three-dimensional shape coefficient of the soil particle, μ_f is coefficient of static friction, ρ_{sp} is density of soil particle, C_D is drag coefficient, C_L is lift coefficient, ε

is screening coefficient, A_2 is two-dimensional shape coefficient of the soil particle.

3.2 VERIFICATION TEST

It is necessary to reproduce scouring phenomenon of the fall type to enable simulation of scouring phenomenon with overflow caused by the tsunami. A vertical jet flow problem was adopted as the verification and validation test for soil scouring simulation. Fig.9. presents experimental outline, and analysis model is shown in Fig.10. Water with constant jetting speed u_0 ($=74\text{cm/s}$) inflows from exhaust nozzle of width B in downward. The distance from exhaust nozzle to soil surface is set as $h/B=5$ with reference to the experiment [7](N, Akashi.,1980).

with comparison between experiment and analysis, verification of this research formulation is carried out. The particle distance = 1cm, time increment = 0.001s and the total number of particles is 113766. In addition, the parameter of the velocity of threshold of sediment movement that was explained in a foregoing chapter set a value of Tab.1 as same as the experiment.

Tab 1. Parameter of velocity of threshold of sediment movement

static friction coefficient	1.0
Size of soil particle[cm]	0.084
Density of soil particle[g/cm³]	1.6
Screening coefficient	0.4
Drag coefficient	0.4
Lift coefficient	0.4

The scouring shape in analysis is shown in Fig. 11. Soil movement can be confirmed by the collision of soil and water from inflow boundary. To occur the share velocity over velocity of threshold of sediment movement on the soil surface let soil phenomenon progress and this can be consider as phenomenon according to formality. The comparison between experiment and analysis is shown in Fig.12. Fig.12 is comparison of the right half scouring shape from the center of exhaust nozzle after 15s from the starting of jet. From this comparison, the value of the analysis is slightly different, but analysis result behaviors can represent the tendency of this experimental response qualitatively. The current scouring criteria is given only by shear speed. It may need to discuss again because the vertical velocity in the center generates the first initiation of sourring behavior in this example.

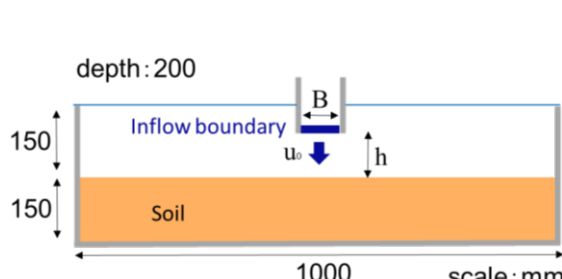


Figure 9. Experimental outline

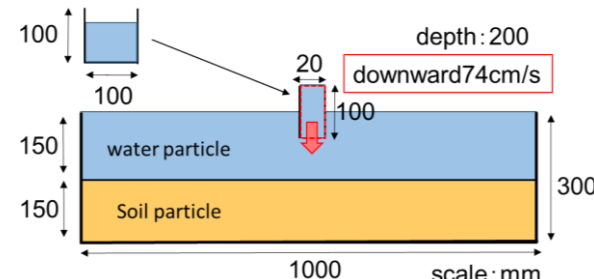


Figure 10. Analysis mode

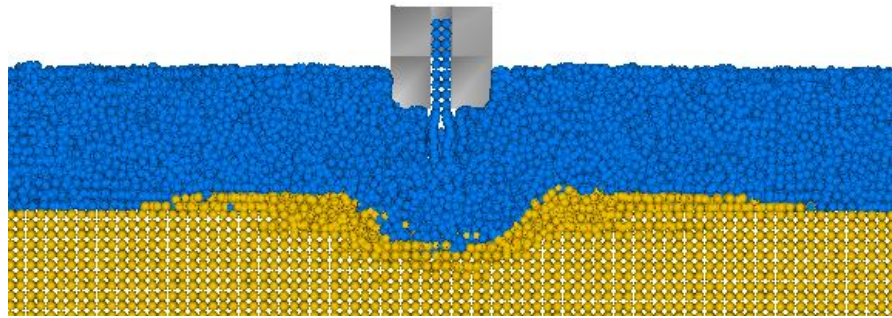


Figure 11. Analysis result (scouring shape)

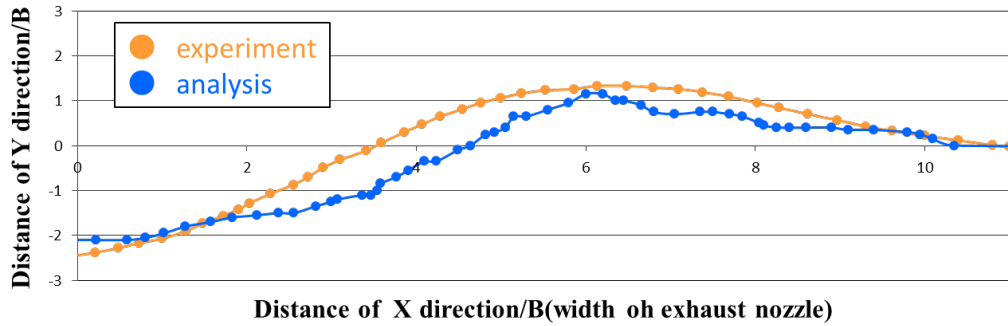


Figure 12. Comparison of scouring shape

3.2 SCOURING TEST OF BREAKWATER

The same algorithm can be applied to simulate the soil scouring behild the breakwater during the overflow. Fig. 13 shows one of the snapshot of this simulation. In the future, validation of this simply test will be conducted compared with its experimental test.

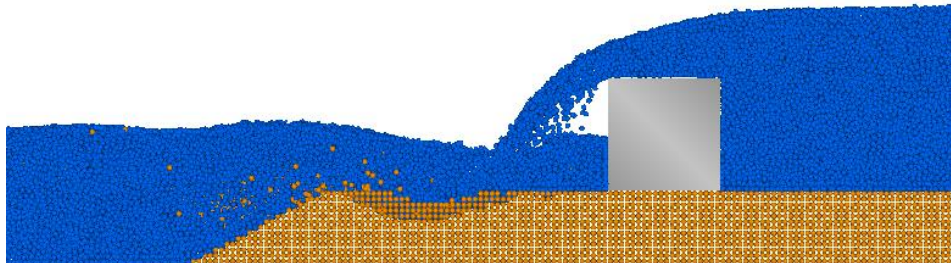


Figure 13. Simply scouring model

4 CONCLUSIONS

In this study, a particle simulation tool based on the SPH has been developed to solve both of the seepage failure problem and the soil scour problem. In seepage flow analysis, a unified government equation which can model both of free surface flow and seepage flow is applied to a particle simulation. From the verification and validation test, the effect of porosity and reasonable surface flow and seepage flow behavior has been given. In scouring analysis, scouring phenomenon was reproduced by using the scouring judging formula. In verification test, analysis result behaviors shows a good agreement with the experiment test. In the future

works, validation test for soil scouring will be conducted again with reasonable example, and finally this analysis method would be expanded to soil scour and seepage flow coupling simulator.

ACKNOWLEDGEMENTS

This work was supported by JSPS Grant-in-Aid for Scientific Research(B) 26282106.

REFERENCES

- [1] M. Asai, AM. Aly, Y. Sonoda and Y. Sakai : A stabilized incompressible SPH method by relaxing the density invariance condition, *Int. J. for Applied Mathematics*, Volume 2012, Article ID 139583, 2012.
- [2] Abdelraheem Mahmoud Aly Abd Allah : An Improved Incompressible Smoothed Particle Hydrodynamics to Simulate Fluid-Soil-Structure Interactions, Kyushu University, 2012.
- [3] Akbari, H. : Modified moving particle method for modeling wave interaction with multi layered porous structures. *Coast. Eng.* 89, 1-19, 2014
- [4] Akbari, H. and Namin, M.M. : Moving particle method for modeling wave interaction with porous structures, *Coast. Eng.*, Vol.74, 59-73, 2013.
- [5] Kasama K., Zen K. and Kasugai Y.: Model experiment for the instability of caisson-type composite breakwater under tsunami condition, Proceedings of Coastal Engineering, JSCE, 2013, November.
- [6] H. Gotoh : Computational mechanics of sediment transport. Morikita Shuppan Co.,Ltd.,2004
- [7] N. Akashi and T. Saito : Studies on the scour from submerged impinged jet . Journal of Japan Society of Civil Engineers, 298, 53-62, 1980

COMPARISONS OF SHEAR STRENGTH OF PARTICULATE MATERIALS DETERMINED BY THE DIRECT SHEAR TEST AND DEM SIMULATIONS

XUETAO WANG¹, CHRISTOPH NIKLASCH¹ AND PETER-MICHAEL MAYER¹

¹Tunnels Engineering, Zentrale Technik, Ed. Züblin

Albstadtweg 3, 70567 Stuttgart, Germany

xuetao.wang@zueblin.de, christoph.niklasch@zueblin.de, peter-michael.mayer@zueblin.de

Web page: <http://www.zueblin.de/>

Key words: Particulate Materials, shear strength, direct shear test, DEM

Abstract. This paper presents the two direct shear tests used to measure shear strength of particulate materials with large particles. These tests have been numerically simulated using discrete element method. Due to different packing methods in numerical modelling, three different simulations were performed which varying the material parameters of particles (i.e. friction and rolling friction of particles and between particles and walls). Numerical results are compared with laboratory tests results. The reasons for discrepancies of results between numerical and laboratory tests are analyzed in this paper. Moreover a reasonable method to minimize the effects of these differences is presented.

1 INTRODUCTION

Shear strength are very important properties of granular materials in geotechnical design and analysis. They can be defined by standardized laboratory tests such as the triaxial test and the direct shear test. Though using the triaxial test can yield more reliable values of shear strength, the direct shear test is mostly performed to determine shear strength of granular materials, especially in the design of storage and processing equipment that handle bulk materials because its simplicity and repeatability. Furthermore, in this study, the bulk material is an assembly of man-made ceramic balls with two diameters ranges, e.g. 14 - 17 mm and 29 – 35 mm. For measuring the shear strength of such particulate materials with such large particles, the direct shear test is more suitable than the triaxial test. Therefore in our study the direct shear test is used to measure shear strength of particulate materials with large particles.

Meanwhile the numerical studies are performed by using discrete element methods instead of finite element methods. In recent years, the discrete element method (DEM) ([1]) has been used extensively to investigate the behaviour of granular materials. With rapid development of computer techniques, 3D simulations become common and simulation time have significantly shortened. This paper presents the DEM simulations of the direct shear tests in 3D with spheres and the comparisons between the numerical simulations and laboratory tests to verify the predictive capability of DEM method.

2 DIRECT SHEAR TEST IN LABORATORY

2.1 Direct shear tests set-up

In this study, the particles used in the tests are ceramic balls with two types of diameter, e.g. 11 - 14mm and 29 - 35 mm, and the roundness (d_{\max}/d_{\min}) of ceramic balls is between 1 and 1.25. Ceramic balls have very high compression strength and the main component is SiO₂. For obtaining valid results, there are some requirements for the apparatus dimensions of direct shear tests to measure the shear strength of particulate materials with such large particles, e.g. the shear cell diameter D should be at least 20 times the maximum particle size and not less than 40 times the mean particle size, and the height H should be between 0.3D and 0.4D. The diameter of the shear cell should be at least 1.30 m in order to suit the tested particles with diameters between 29 mm and 35 mm, however in reality such large shear cell is uncommon. In the current study a metal box of square cross section with 1 m width is used in the shear tests, though it does not satisfy the requirement in Eurocode 1 ([2]) for the particles with diameters between 29 mm and 35 mm, it is the closest apparatus which is available for the study.

The schematic diagram of the direct shear test set-up is shown in Figure 1. It can be seen that the shear box is divided into two parts. The upper part of the box is moved horizontally at a constant velocity (1 mm/min), while the lower part is remained stationary. Due to the large dimension of particles, there was a 1 cm gap between the upper part and the lower part to reduce the effect of the boundaries of shear box on shear forces, especial initial shear force. The 10 cm thickness of shear box walls can minimize the loss of particles during shearing. H_{p,t} in Figure 1 represents the height of tested particulate material, and F represents the shear force applied to move the upper part of shear box.

There were two shear tests performed. One was performed on the assemblies of ceramic balls with diameters between 29 mm and 35 mm, another one was performed on the assemblies of ceramic balls with diameters between 14 mm and 17 mm. The total shear displacements for both shear tests were about 60mm. The shear processes were divided into three phases, which in every phase the shearing displacement was about 20 mm and the normal forces applied on the top cover were about 220 kN, 440 kN, and 660 kN correspondingly in the three phases. It means that three shear phases were performed on the same test sample. This arrangement of shear process was made due to consideration of consuming time, costs and the amount of tested particles for such shear tests with large dimension shear boxes.

During shearing the relative lateral displacement, normal force on the top cover, and applied shear force were monitored automatically. The relative vertical displacement was also measured by setting two sensors in the top cover.

It is already known that the methods of particle packing have a significant influence on the bulk behavior of the assembly ([3]). Many related researches have been presented ([4,5,6]), hence the current study did not focus on the packing influence. In the shear tests, the compacted filling method was used to achieve a dense packing. The shear box was filled in three layers and each layer was manually compacted by applying vertical pressure. Table 1 shows the set-up details of particles in the shear tests.

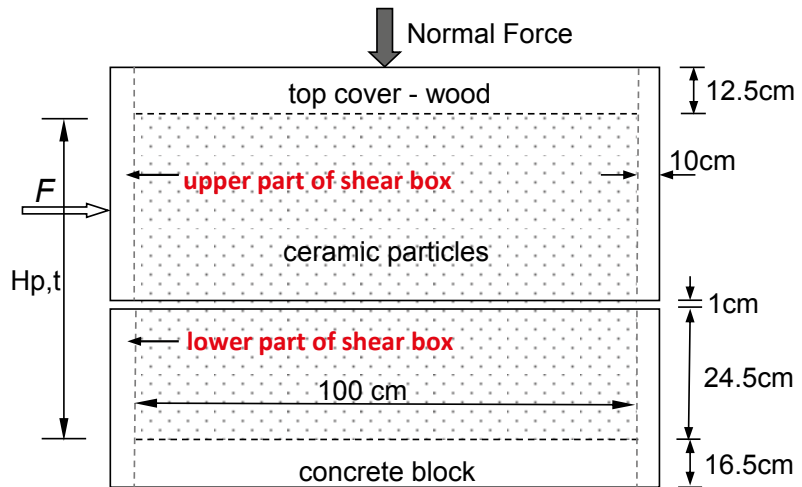


Figure 1: Schematic diagram of the direct shear test set-up

Table 1: Set-up details of particles in the shear tests

Diameters of ceramic balls [mm]	14 -17	29 – 35
Material density of ceramic balls [kg/m^3]	2400	2400
Total weight [kg]	937.85	973.5
Height of sample $H_{p,t}$ [m]	0.615	0.62
Density [kg/m^3]	1530	1570
Initial void ratio	0.5738	0.5285

2.2 Test results

Figure 2 and Figure 3 show the results of forces versus horizontal relative displacement between the two parts of the shear box obtained from these two shear tests.

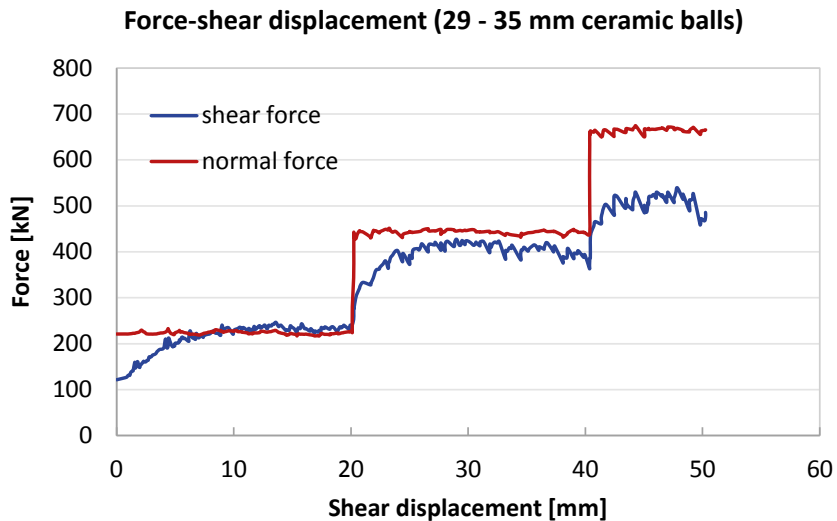


Figure 2: Force-Displacement for ceramic balls with 29 - 35 mm diameters

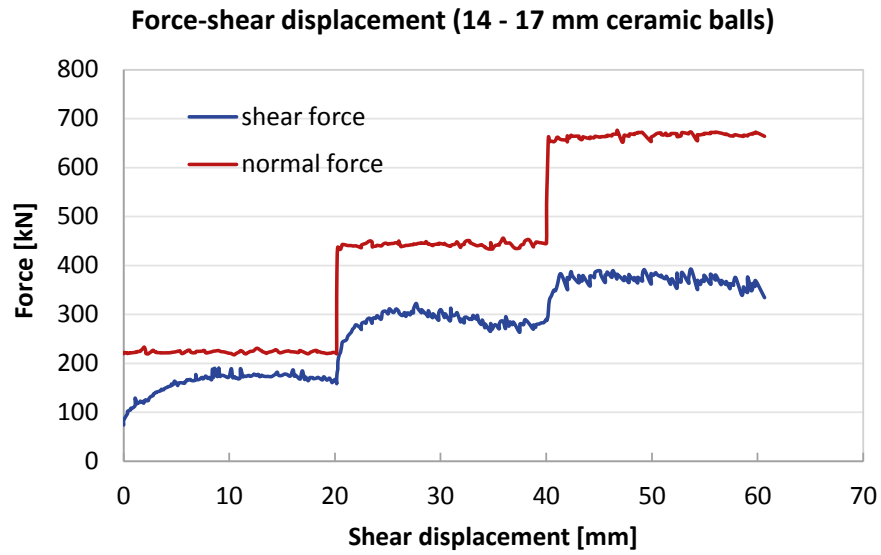
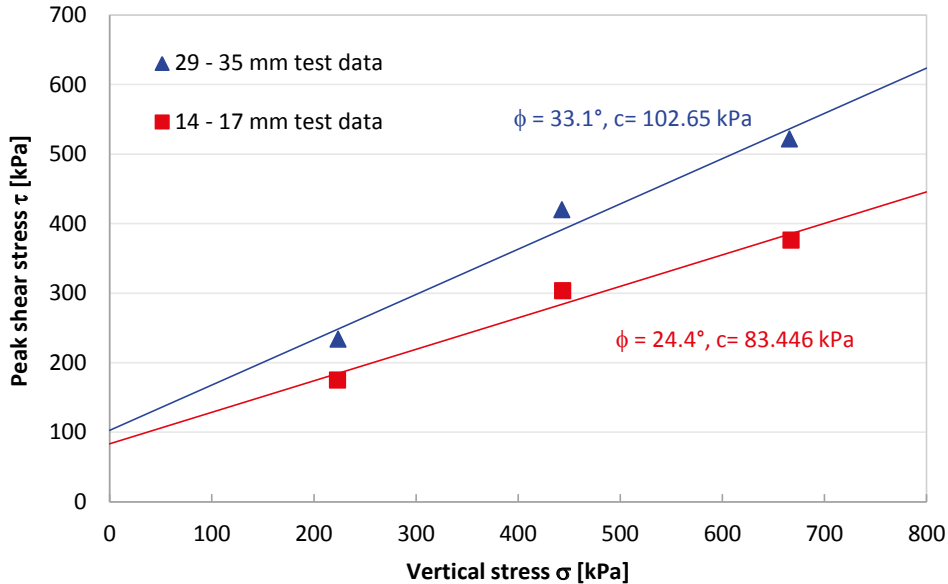


Figure 3: Force-Displacement for ceramic balls with 14 -17 mm diameters

Based on Figure 2 and Figure 3, the vertical stress and shear stress can be calculated using the traditional method by dividing the applied normal force and horizontal forces respectively with the tested particulate material's cross-section area, e.g. the area of cross-section of the shear box in this study was 1 m^2 . Thus the results of stresses can be summarized in Table 2. Figure 4 presents the strength envelopes from the tests results based on the Mohr-Coulomb failure criterion in soil mechanics.

Table 2. Summary of laboratory tests results

Ceramic balls	Stress [kPa]	Phase 1	Phase 2	Phase 3
14 – 17 mm	Normal stress σ	223.2	443.7	667.3
	Peak shear stress τ	174.9	303.4	376.1
	Stress ratio τ/σ	0.7836	0.6838	0.5636
29 – 35 mm	Normal stress σ	223.6	442.8	665.7
	Peak shear stress τ	233.7	420	521.9
	Stress ratio τ/σ	1.0452	0.9485	0.7840

**Figure 4:** Strength envelopes from test results

2.3 Discussions

Comparing the strength envelopes of ceramic with 14 - 17 mm and with 29 - 35 mm (as Figure 4 shown), it is noticed that the friction angle of particulate materials with 29 - 35 mm ceramic balls is larger than that of particulate materials with 14 - 17 mm ceramic balls, though they are made of same chemical compositions. This difference in friction angle is due to the shear specimen scale effects. Many researches about the effects of specimen scale show that friction angles increased with decreasing the shear box size ([7,8,9,10]). The results from the tests show the consistence with these researches e.g. the shear box size is considered as being decreased for assemblies of ceramic 29 - 35 mm balls comparing with the assemblies of ceramic 14 - 17 mm balls.

Furthermore, it is noted that there were obvious cohesions for both ceramic balls according to the strength envelopes based on tests results, though as particulate materials, theoretically they should be cohesionless. In this study the particulate materials with ceramic balls have quite larger cohesion than expected, while it can be explained. In soil mechanics, the normal stress on the shear failure plane is zero. However, the shear failure plane in this particulate material is not a smooth plane as shown in Figure 5. It is similar to move an object along planes with different shape. It is clear that it is more difficult to move an object along a wavy plane than along a smooth plane. That means that larger forces are needed to move an object along a wavy plane. In the tests, it means that larger shear forces will be needed to show that the particles climb over the contacting particles during the shearing. It is believed to be the main reason of the apparent cohesion shown in laboratory direct shear tests.

Moreover, if we compare the cohesions from both direct shear tests, apparently the cohesion of particulate material with smaller ceramic balls (14 - 17 mm) is smaller than the cohesion of particulate material with larger ceramic balls (29 - 35 mm). It is because the shear

plane in the particulate material with 14 - 17 mm balls is slightly smoother than the shear plane in the particulate material with 29 - 35 mm balls. It can be expected that the cohesion would vanish eventually if the particles in the particulate material are small enough.

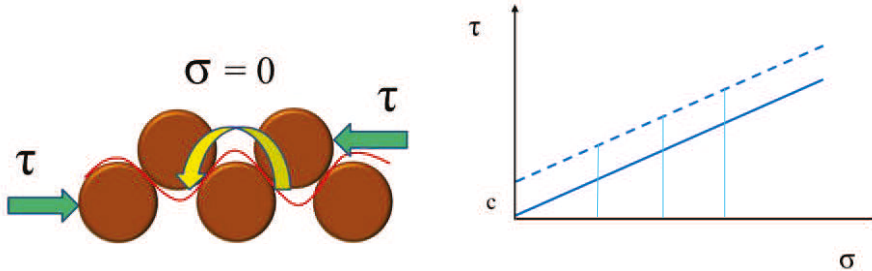


Figure 5: Shear plane in particulate material

At the end, it should be pointed out that only one shear test has been performed on each sample of particulate materials with ceramic balls, beside these two shear tests are slight different with the standard shear test. Therefore more repetitive shear tests are necessary.

3 DEM (DISCRETE ELEMENT METHOD) SIMULATIONS

3.1 Numerical program

The Discrete Element Method was introduced by Cundall and Strack ([1]). In the frame of the DEM, all particles in the computational domain are tracked in a Lagrangian way, explicitly solving each particle's trajectory. It is based on the use of an explicit numerical scheme in which the interaction of particles is monitored contact by contact and the motion of the particles modelled particle by particle.

In this study, an Open Source Discrete Element Method Particle Simulation Software – LIGGGHTS ([11]) is used. LIGGGHTS stands for LAMMPS Improved for General Granular and Granular Heat Transfer Simulations and is based on LAMMPS (Large-scale Atomic/Molecular Massively Parallel Simulator), a successful open source Molecular Dynamics code by Sandia National Laboratories for massively parallel computing on distributed memory machines. LAMMPS is a classical molecular dynamics simulator and is a very good platform for DEM simulations. LAMMPS offers a GRANULAR package to perform these kinds of simulations. LIGGGHTS aims to improve this capability with the goal to apply it to industrial applications. LAMMPS offers implementation for both linear (Hooke) and non-linear (Hertz) granular potentials. It also provides efficient algorithms for detecting and calculating the pair-wise interaction forces, while LIGGGHTS brings these features for granular simulations to a new level, implementing the following features on top of what is possible with LAMMPS:

- A re-write of the granular pair- and wall contact laws, including a macroscopic cohesion model
- Wall import of CAD, including stress analysis
- A moving mesh feature
- A 6 degree of freedom solver for bodies represented by a surface mesh

3.2 Numerical models

As described in section 2, the shear box is modeled as shown in Figure 6. The height of shear box in numerical simulations (H_s) is about 1 m and larger than the height of particle samples in the shear tests. It is because that the packing method used in numerical simulations was different with the packing method used in shear tests. In numerical simulations, all the particles were randomly placed into the shear box at one time, then particles were dropped into the shear box under gravity; if the model of shear box was not high enough, some of particles would be dropped out of the shear box, therefore the numerical model of shear box was higher than the shear box in tests.

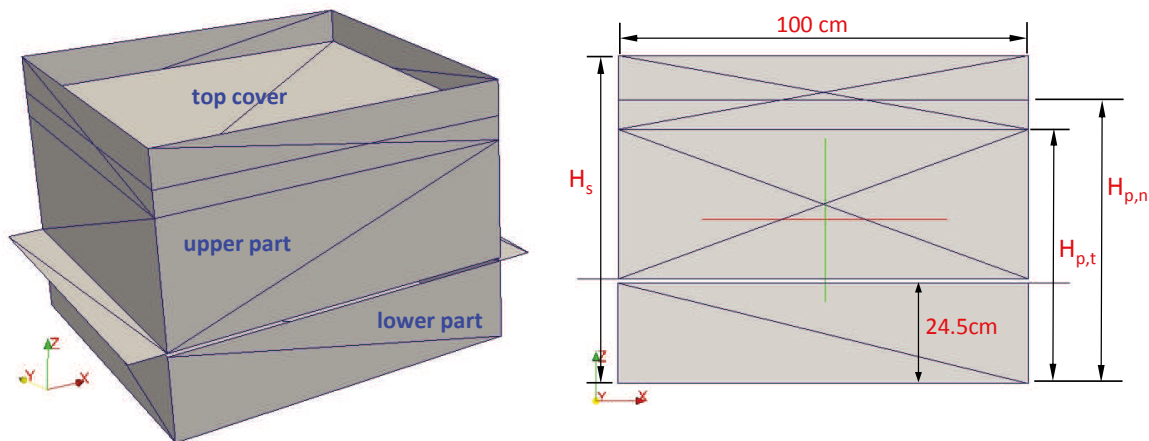


Figure 6: Numerical model of shear box

In the numerical simulations, the ceramic balls were simulated as spherical particles which were generated randomly. The total mass of these spherical particles and the range of diameters were same as in the tests, total 937.38 kg spheres with diameters between 14 mm and 17 mm, total 974.74 kg spheres with diameters between 29 mm and 35 mm. Table 3 shows the numerical parameters for the particles used in the numerical simulations.

Table 3. Numerical parameters for the particles used in the numerical simulations

Young's modulus of particles E_p [GPa]	10
Young's modulus of shear box E_w [GPa]	200
Poisson's ratio (particles and shear box)	0.3
Coefficient of friction of particles* μ_{pp}	0.5
Coefficient of friction between particles and shear box μ_{pw}	0.3
Coefficient of friction of shear box μ_w	0.3
Coefficient of restitution of particles*	0.8
Coefficient of restitution between particles and shear box	0.4
Coefficient of restitution of shear box	0.3
Coefficient of rolling friction of particles* c_{pp}	0.22
Coefficient of rolling friction between particles and shear box c_{pw}	0.22

Note: The parameters marked with * were determined by laboratory tests performed on ceramic balls. Others were defined empirically.

It should be noted that the particles in the numerical model were spheres, while the ceramic balls used in the tests were not. Previous experimental and numerical studies have shown that the particle shape strongly affects the quasi-static mechanical behavior of granular materials ([12,13,14,15,16,17]). It has been known that rolling at the contacts between the particles can be resisted due to the irregularities or asperities of particles' surfaces. Hence it is important to take into account the effects of rolling resistance (or rolling friction) due to particle shape. Rolling friction means a mechanical property which produces a resisting moment to the rolling at each contact. The numerical program LIGGGHTS has provided three rolling friction models ([18]). In this study, the constant directional torque (CDT) model ([19]) was used, e.g. a material parameter – coefficient of rolling friction was introduced. Previous researches ([20,21,22]) have presented the effects and applications of rolling friction in DEM simulations. And it is believed that the use of spherical particles introduced with the rolling friction as a shape parameter is suitable and adequate for our study.

In the numerical simulations it is known that the frictions of particles and between particles and wall play a very important role. Based on the theory of discrete element method, we know that the friction at contacts used in DEM is assumed to be fully mobilized ([2]). While, as mentioned previously, the particles in laboratory were packed three layers, thus it should be considered that friction of particles and between particles and shear box may not be fully mobilized. Therefore, in this numerical study, three simulations were performed for different selection of values for frictions and rolling resistance (as shown in Table 4). In simulation 1, it was assumed the frictions and rolling resistances of particles and between particles and shear box were fully activated, e.g. μ_{pp} (coefficient of friction of particles) = 0.5, μ_{pw} (coefficient of friction between particles and shear box) = 0.3, c_{pp} (coefficient of rolling friction of particles) = c_{pw} (coefficient of rolling friction between particles and shear box) = 0.22. In the simulation 2, the particles were packed with partially activated rolling friction, but fully mobilized friction, e.g. during packing $c_{pp} = 0.01$, while in the shearing phase $c_{pp} = c_{pw} = 0.22$. In the simulation 3, the particles were packed with partially activated friction, but fully activated rolling friction, e.g. during packing $\mu_{pp} = \mu_{pw} = 0.1$, while during shearing they are same with in the simulation 1. Table 5 presents the summary of initial conditions in the three simulations.

Table 4. Summary of selection of values for frictions in the three simulations

	During packing				During shearing			
	μ_{pp}	μ_{pw}	c_{pp}	c_{pw}	μ_{pp}	μ_{pw}	c_{pp}	c_{pw}
Simulation 1	0.5	0.3	0.22	0.22	0.5	0.3	0.22	0.22
Simulation 2	0.5	0.3	0.01	0.01	0.5	0.3	0.22	0.22
Simulation 3	0.1	0.1	0.22	0.22	0.5	0.3	0.22	0.22

Table 5. Summary of initial conditions of the three simulations

	Ceramic balls	Simulation 1	Simulation 2	Simulation 3
14 – 17 mm	Initial void ratio	0.8383	0.7097	0.7148
	Height after packing [m]	0.718	0.668	0.67
	Weight of particles [kg]	937.382	937.7115	937.7115
29 – 35 mm	Initial void ratio	0.7063	0.6695	0.6945
	Height after packing [m]	0.693	0.682	0.68
	Weight of particles [kg]	974.74	963.1172	963.1172

In the numerical simulations it has been found that the heights of particle samples (Table 5) were slightly higher than in the shear tests (Table 1), while the masses of particles were same as in the shear tests. It was believed that this is due to two discrepancies between the laboratory tests and numerical simulations, which they are packing method and particles shape. As described in 2.1, the sample of particles filled in the shear box was manually compacted by applying vertical pressure, but in numerical simulations the current DEM programs have difficulty to perform this kind of compacted packing method, furthermore the ceramic balls as non-spherical particles were modelled as spheres. As a result of these two differences between numerical simulations and the laboratory test, the heights of samples ($H_{p,n}$) in numerical simulations were larger than in laboratory tests. These discrepancies between numerical simulations and laboratory tests indicate that it is very difficult to replicate the exact details of the laboratory tests in the numerical simulations. It has been described by previous researchers ([4,23]).

3.3 Numerical results

The results of numerical simulations are presented in Table 6. Figure 7 and Figure 8 show the numerical results of force-displacement. Meantime, the corresponding results of force-displacement measured in the tests (see dash curves in Figure 7 and Figure 8) are presented for comparison. Figure 9 and Figure 10 presents the strength envelopes from the numerical results based on the Mohr-Coulomb failure criterion.

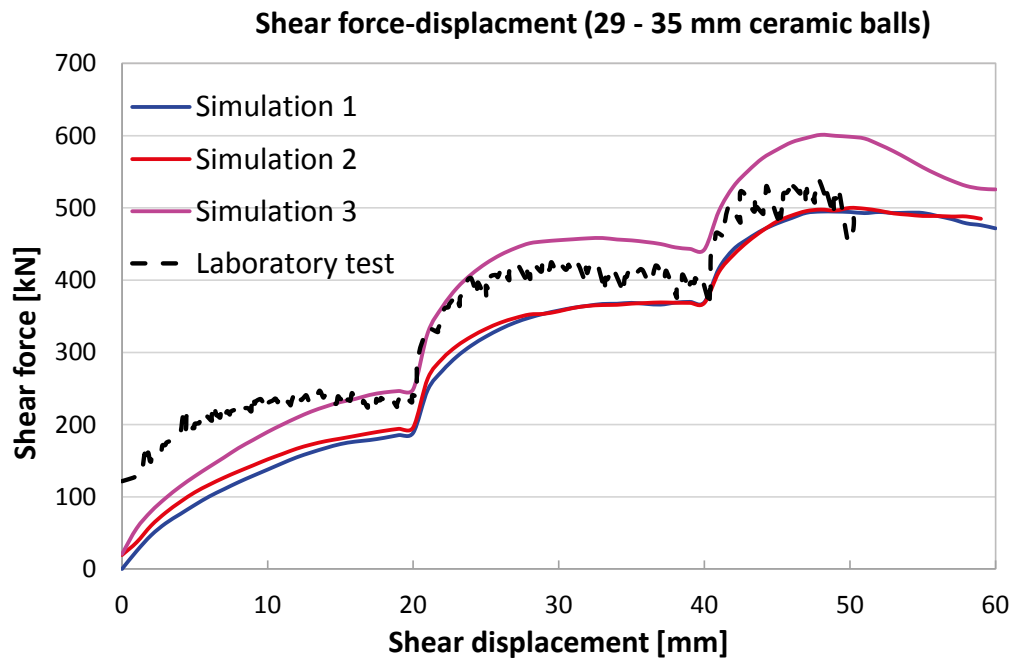


Figure 7. Numerical results of force-displacement for 29 – 35 mm spheres

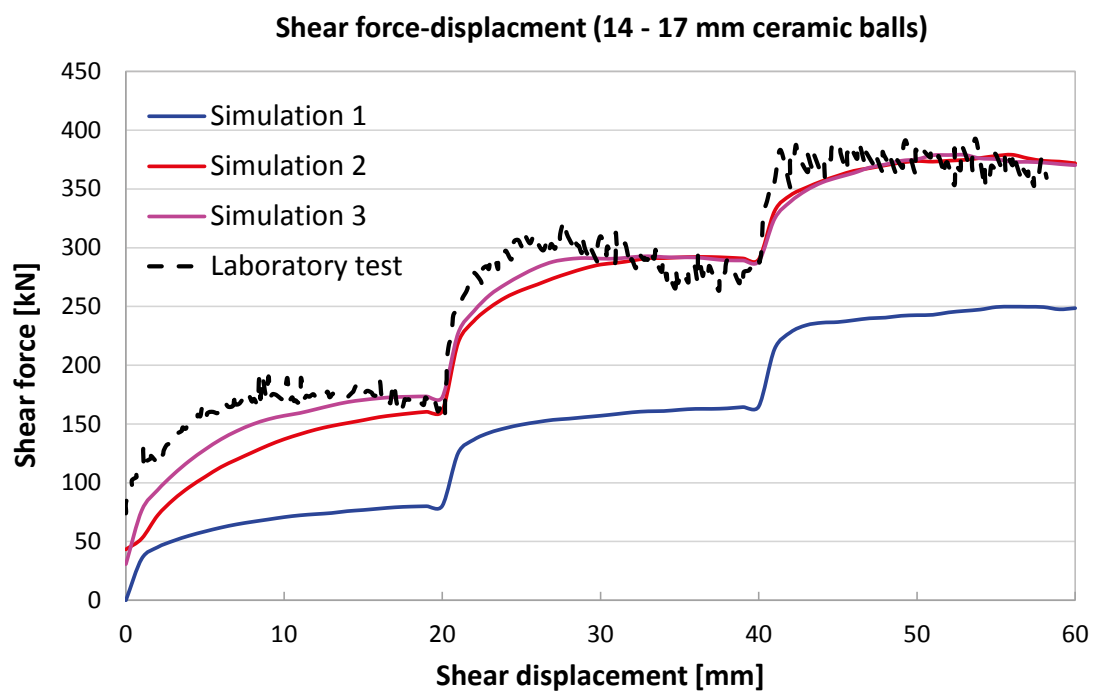
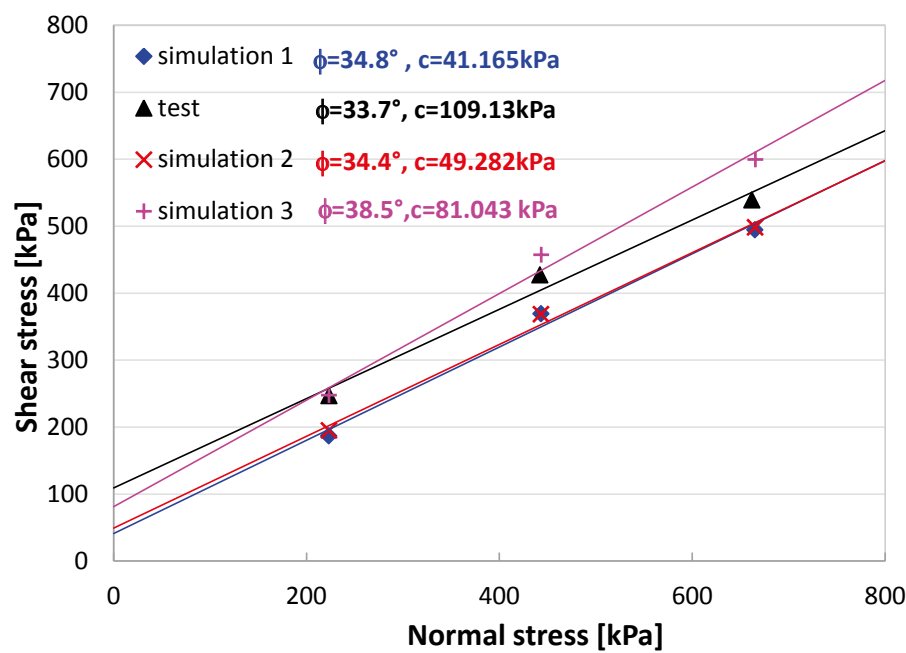


Figure 8. Numerical results of force-displacement for 14 – 17 mm spheres

Table 6. Summary of numerical simulations results

		Stress	Phase 1	Phase 2	Phase 3
14 - 17 mm	Simulation 1	σ [kPa]	222.8553	442.8733	665.4004
		τ [kPa]	80.2361	164.6970	249.6725
		τ/σ	0.3600	0.3719	0.3752
14 - 17 mm	Simulation 2	σ [kPa]	223.3016	443.4027	665.7724
		τ [kPa]	160.785	291.9608	377.4685
		τ/σ	0.7200	0.6585	0.5670
14 - 17 mm	Simulation 3	σ [kPa]	223.4282	443.5256	665.8775
		τ [kPa]	173.2159	292.1763	378.8720
		τ/σ	0.7753	0.6588	0.5690
29 - 35 mm	Simulation 1	σ [kPa]	223.4764	443.4103	665.4126
		τ [kPa]	186.9160	369.2163	494.5710
		τ/σ	0.8364	0.8327	0.7433
29 - 35 mm	Simulation 2	σ [kPa]	223.5604	443.4889	665.5502
		τ [kPa]	194.9730	358.4814	498.1005
		τ/σ	0.8721	0.8309	0.7484
29 - 35 mm	Simulation 3	σ [kPa]	223.6203	443.8192	665.8133
		τ [kPa]	247.594	457.1260	499.6693
		τ/σ	1.1072	1.0300	0.9007

**Figure 9.** Strength envelopes from numerical simulations for 29 - 35 mm ceramic balls

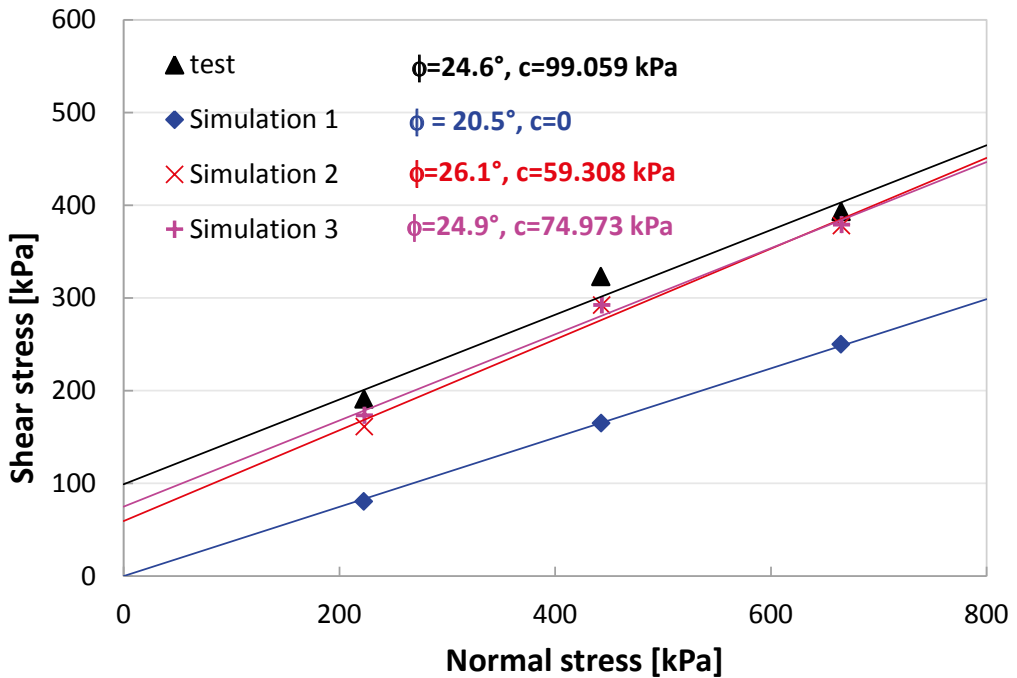


Figure 10. Strength envelopes from numerical simulations for 14 - 17 mm ceramic balls

3.4 Discussion

First, the numerical results of friction angle for 29 - 35 mm and 14 - 17 mm ceramic balls calculated from the numerical simulations (Figure 9 and Figure 10) have proved the effect of shear box scale on friction angle, that friction angle is decrease with the increasing of size scale of shear box.

And for ceramic balls with diameters between 29 - 35 mm, as Figure 9 shown, it can be seen that the numerical results of friction angle calculated from Simulation 1 and Simulation 2 show accordance with the laboratory tests, though the numerical results of cohesion obtained from these two simulations are only about half of the cohesion obtained from the laboratory tests. While the numerical results calculated from Simulation 3 show that the friction angle is about 10% larger than that from laboratory tests, but the cohesion is much close to the cohesion obtained from laboratory tests compared to the other two simulations.

As for ceramic balls with diameters between 14 - 17 mm, from Figure 10 it can be seen that the numerical results of friction angle calculated from Simulation 2 and 3 match well with the friction angle obtained from laboratory tests, and the difference of the cohesion calculated from these simulations and laboratory test are about 40% (Simulation 2) and 24% (Simulation 3). However the results of Simulation 1 shows no cohesion and the friction angle is about 17% smaller than the friction angle obtained from laboratory tests.

A reasonable explanation of the apparent difference of cohesion obtained between numerical simulations and laboratory tests is due to the discrepancies between numerical simulations and the laboratory tests as described in 3.2. It is known that the particles movement in particulate materials under shearing is complicated; it has always been hot topic

for DEM simulations. Nevertheless despite of the difficulty of modelling exact details of laboratory tests, the results of this study shows a possible method to minimize the effect of discrepancies between numerical simulations and laboratory tests, e.g. adjusting the material parameters of particles (for example, friction and rolling friction of particles and between particles and walls) during packing. Furthermore in order to better understand these differences between numerical simulations and laboratory tests, further laboratory tests are required.

4 CONCLUSIONS

- To study the shear strength of particulate materials with large particles, which are used in design of storage, two direct shear tests have been performed in the laboratory.
- These tests have been numerically simulated using discrete element method. Due to the different packing methods in numerical simulations, three different simulations were performed where the material parameters of particles (friction and rolling friction of particles and between particles and walls) were adjusted during packing. Though the agreement between the laboratory tests and numerical simulations was not completely satisfactory, the results of friction angle obtained from numerical simulations matched the laboratory tests well.
- It is noticeable that the numerical results from all three simulations for 29 - 35 mm ceramic balls have shown certain cohesion though all were less than the cohesion obtained from laboratory tests, and as for 14 - 17 mm ceramic balls, the cohesion obtained from numerical simulation 1 (which the material parameters of particles were not adjusted during packing) was zero. It is believed that it is due to the general challenge in DEM simulations, e.g. the difficulty of modeling the exact details of laboratory tests. As described in previous sections, the models of particles and sample packing method in numerical simulations were not exactly the same in laboratory tests. In view of these differences, this paper presents a possible method to minimize the effects of these differences, which adjusts the material parameters of particles during packing.
- Further laboratory tests are necessary for the further research.

ACKNOWLEDGMENT

The project has been supported by the German Federal Ministry for Economic Affairs and Energy.

REFERENCES

- [1] Cundall, P.A. and Strack, O.D.L. A discrete numerical model for granular assemblies. *Geotechnique* (1979) **29**(4765):47-65.
- [2] Eurocode 1 – Actions on structures – Part 4: Silos and tanks, BS EN 1991-4:2006
- [3] Lambe, T.W. and Whitman, R.V. *Soild mechanics*, SI Version. Wiley, NY (1979)
- [4] Härtl, J. and Ooi, J. Y. Experiments and simulations of direct shear tests: porosity, contact friction and bulk friction. *Granular Matter* (2008) **10**:263-271

- [5] Bilgili, E. et al: Stress inhomogeneity in powder specimens tested in the Jenike shear cell: *Myth or Fact. Part. Part. Syst. Charact.* (2004) **21**(4):293-302.
- [6] Lorenz, A., Tuozzolo, C. and Louge, M.Y. Measurements of impact properties of small, nearly spherical particles. *Exp. Mech* (1997). **37**(3):292-298.
- [7] Cerato, A.B. and Lutenegger, A.J. Specimen size and scale effects of direct shear box Tests on Sands. *Geotechnical Testing Journal*, Vol. 29, No.6
- [8] Moayed, R.Z. and Alizadeh , A. Effects of shear box size on the strength for different type of silty sands in direct shear tests. *Unsaturated Soils: Theory and Practice* (2011)
- [9] Palmeria, E.M. and Milligan, G.W.E. Scale effects in direct shear tests on sand. *Proc. 12th Int. Conf. Soil Mech. Found. Engng* (1989), Rio de Janeiro, Brazil 1, 739-742.
- [10] Vucetic, M. and Lacasse, S. Specimen size effect in simple shear test. *J. Geotech. Engng Div.* (1982) ASCE 108, No. 12, 1567-1585.
- [11] Kloss, C., Goniva, C., Hager, A., Amberger, S. and Pirker, S. Models, algorithms and validation for opensource DEM and CFD-DEM, *Progress in Computational Fluid Dynamcis, An Int. J.* (2012) – Vol. 12, No.2/3 pp. 140 – 152.
- [12] Matuttis, D.M., Luding, S. and Hermann, H.J. Discrete element simulations of dense packing and heaps made of spherical and non-spherical particles. *Powder Technol.* (2002) **109**, 278-292.
- [13] Rothenberg, L. and Bathurst, R.J. Micromechanical features of granular assemblies with planer elliptical particles. *Géotechnique* (1992) **42**(1), 79-95.
- [14] Guises, R., Xiang, J., Lathham, J.P. and Munjiza, A. Granular packing: numerical simulation and the characterization of the effect of particle shape. *Granul. Matter* (2009) **11**:281-292.
- [15] Lu, M. and McDowell, G.R. The importance of modeling ballast particle shape in the discrete element method. *Granul. Matter* (2007) **9**:6980.
- [16] Matsushima, T. and Chang, C.S. Qualitative evaluation of the effect of irregularly shaped particles in sheared granular assemblies. *Granul. Matter* (2011)
- [17] Iwashita, K. and Oda, M. Rolling resistance at contacts in simulation of shear band development by DEM. *Powder Technol.* (2000) **109**:192-205.
- [18] LIGGGHTS Documentation, Version 3.X
- [19] Ai, J., Chen, J.F., Rotter, J.M. and Ooi, J.Y. Assessment of rolling resistance models in discrete element simulations, *Powder Technology* (2011) **206**(3):269-282.
- [20] Fukumoto, Y., Sakaguchi, H. and Murakami, A. The role of rolling friction in granular packing. *Granular Matter* (2013) Volume 15, Issue 2, pp 175-182
- [21] Huang, J., Vicente da Silva, M. and Krabbenhoft, K. Three-dimensional granular contact dynamics with rolling resistance. *Computers and Geotechnics* (2013) **49**:289-298
- [22] Zhou, Y.C., Xu, B.H., Yu, A.B. and Zulli, P. An experimental and numerical study of the angle of repose of coarse spheres. *Powder Technology* (2002) **125**:45-54
- [23] O' Sullivan, C. and Cui, L. Three –dimensional discrete element simulations of direct shear tests. In *2nd International PFC Symposium*, A.A. Balkema Publishers, Kyoto (2004)

DISCRETE ELEMENT MODELLING OF GRAIN SIZE SEGREGATION IN BI-DISPERSE GRANULAR FLOWS DOWN CHUTE

LU JING¹, FIONA C.Y. KWOK² AND ANDY Y.F. LEUNG³

¹Department of Civil Engineering, The University of Hong Kong
Pokfulam Road, Hong Kong
E-mail: jing1989@hku.hk

² Department of Civil Engineering, The University of Hong Kong
Pokfulam Road, Hong Kong
E-mail: fiona.kwok@hku.hk

³ Department of Civil and Environmental Engineering, The Hong Kong Polytechnic University
Hong Kong
E-mail: andy.yf.leung@polyu.edu.hk

Key words: Granular Flow, Segregation, DEM.

Abstract. Three-dimensional DEM simulations of size segregation in granular flows down chute are presented. Different cubic bi-disperse samples are generated by pluviation, on the rough base formed by randomly placed particles. Periodic boundaries are applied to the flow direction and the two sides. Parametric studies involving slope angle, width, volume fraction, and the coefficient of friction are systematically performed. In all presented cases, the steady, fully developed (SFD) state is achieved, where the kinetic energy and fractional volume distribution remain constant. From the macroscopic view, segregations are completed prior to the SFD state with slightly different extents and a thick layer of coarse grains appears on the top of the flow. The profiles of volume fraction are calculated and presented by shear layers. In addition, the trajectories of individual particles are tracked and analysed, showing clearly the contact conditions and shear history experienced by individual particles. It is found that the connectivity of small particles is generally at a lower level than that of the large ones, indicating a high probability of small particles dropping into voids under gravity. On the other hand, the large particles experience a significant increase of connectivity as they migrate through the layer of small particles.

1 INTRODUCTION

Grain segregation due to the variation of particle size, shape, density or other properties is commonly found in industrial processes and in nature. Grain size segregation is the most effective one among all types of segregation [1], which can be vital in mineral processing procedures but it has an adverse effect on pharmaceutical manufacture and powder production where uniform mixing is desired [2]. Examples of size segregation in nature include the reverse grading of geo-materials found in avalanches and debris flows [3]. It may exacerbate the destructiveness of such natural hazards, as it produces higher debris erosive powers, longer run-

out distances and potentially higher impact forces [4–7].

Size segregation occurs in many different scenarios and different mechanisms have been proposed in experimental and numerical studies. For instance, the three main mechanisms identified in vibration-induced segregation are convection, inertia and buoyancy [8–15]. For shear-induced segregation under gravity, e.g. in a rotating drum or tumbler, percolation-based hypothesis states that small particles fall preferentially under gravity through the shear flow as a sieve [16–22]. Other driving factors include porosity gradients and velocity gradients [23]. Another common situation for gravity-driven segregation is the chute flow on a slope, or a heap [18]. Apart from the kinetic sieving mechanism in the direction normal to the base, secondary circulation in lateral directions [2] and recirculation near the bouldery front of the chute flow [4,24] are also reported in both small- and large-scale experiments. The recirculation and lateral transport of coarse grains may explain the formation of levees in the run-out of debris flows and avalanches [3,24,25]. In granular flows down a rough inclined plane, fingering instability, as a consequence of the frontal accumulation of coarse grains, has been reported [26–28]. Stratification is another phenomenon related to size segregation, which can be observed on the surface of a pile in the occurrence of avalanches [16,29–31]. Moreover, some researchers have studied the influence of interstitial water and other viscous fluids, and revealed that the viscous and buoyancy effects hinder the separation of different sizes [2,27,32].

The focus of the current work is on the size segregation in dense granular chute flows. Generally, it is explained by kinetic sieving and squeeze expulsion (after [33]). The basic idea of the two mechanisms is that small grains preferentially fall through the local voids underneath, which are randomly opened by the shearing flow. The imbalance in contact force and the mass conservation normal to the base lead the larger grains to drift towards the top of the flow. Over decades, experimental studies have been carried out and have provided evidences for these hypotheses [2,24,33–35]. The major measurements in experiments are the profiles of solid fraction and velocity from the side view, and the deposit granulometry. However, at present the measurements of phase fractions and velocities in the bulk of dynamic flows still remain a challenge, which hinders the collection of evidences to support the proposed mechanisms.

Recently, discrete element (particle) modelling (DEM or DPM) of bi-disperse granular flows has been reported, which allows a more detailed description of particle velocities, volume fractions and contact forces. The results from this sort of modelling are also interpreted in the macroscopic perspectives, e.g. the rheology of the flow [36,37], the profile of phase fractions [37–40], the kinetic energy [41] and the centre of mass for each species [5,42]. While most of the published numerical simulations were performed in two dimensions [36,41,42], three-dimensional modelling may be able to provide more information in the lateral direction as segregation is not a pure gravity-driven process [37,39]. On the other hand, the inter-particle interactions, grain packing patterns and the flow rheology are inherently different in a three-dimension configuration.

In this paper, three-dimensional DEM simulations of grain size segregation are performed to study the micro-mechanical behaviour of segregation process. It is important to be able to identify how the segregation develops and to understand the effect of slope angle, width, volume fraction, and coefficient of friction on the degree of segregation. Sample creation and the approach to modelling a steady, fully developed flow are introduced in Section 2. A new function is defined to measure the degree of segregation in the shear-dilated flows. In Section 3 and 4, simulation results are interpreted in both macroscopic and microscopic perspectives.

The parametric studies, the fraction profile of large grains by different layers and the trajectories of individual particles are presented in sequence.

2 DEM SIMULATIONS

The DEM simulations presented here are performed using the open-source LIGGGHTS code [43], adopting the Hertz model for inter-particle contacts. Young's modulus E , Poisson ratio ν , the coefficient of friction μ and the coefficient of restitution e are the major parameters specified in material properties. Bi-disperse cubic samples in periodic cells are created to study infinitely long and wide chute flows [44,45]. One typical sample is shown in Figure 1, where a layer of large particles and small particles are poured into the boundary box in sequence under gravity, hence the distribution of geostatic stress as indicated by colours (the transition from red to blue represents the highest to the lowest stress). The rough base (brown in colour) is constructed by fixing spheres, which are identical to a slice of randomly distributed small particles in the bulk, on the bottom of the box. Periodic boundaries are imposed to the flow directions and the two sides, while the top of the box is unbounded, allowing a free surface of the flow. To achieve flows down an inclined plane, the sample is tilted in xy plane to the target slope angle θ . The local coordinates shown in Figure 1 indicate that the x direction is the flow direction along the slope, while the y direction is normal to the inclined plane.

In all generated flows in this study, the steady, fully developed (SFD) state is achieved, where the kinetic energy and fractional volume distribution remain constant. Segregations are completed before the SFD state with slightly different extents and a thick layer of coarse grains appears on the top of the flow. In order to measure the degree of segregation being completed in the final steady state, a function of time is defined by considering the evolution of the centres of mass for the two types of particles. The degree of segregation $\alpha(t)$ is given by

$$\alpha(t) = 0.5 \times \left(1 - \frac{c_{1,t} - c_{2,t}}{c_{1,0} - c_{2,0}} \right) \quad (1)$$

where t is time, and c_1, c_2 are the y -coordinates of the centres of mass for small particles and large particles, respectively. The suffixes 0 and t denotes the initial state and the time t under consideration, respectively. The definition of $\alpha(t)$ considers the relative changes of c_1 and c_2 , as the sample may be dilated under shear and both c_1 and c_2 may increase due to the dilation. The initial condition is $\alpha_0 = \alpha(0) = 0$. If at some moment $c_1 = c_2$, then $\alpha = 0.5$, meaning that the two groups of particles are uniformly mixed. The final state is denoted as $\alpha_\infty = \alpha(\infty)$, and $\alpha_\infty = 1$ if totally complete segregation occurs. However, this will not happen either in reality or in the numerical simulations, because the diffusive mixing found in bi-disperse granular flows would prevent the fully-completed segregation [35].

After defining the degree of segregation, parametric studies on sample size, slope angle, the volume fraction of small particles, and the coefficient of friction are systematically performed. The length L and the height H of the sample have been studied in [42], following which $L = H = 40d_1$ is chosen in the current work. Here, d_1 is the diameter of small particles. In addition, it has been found in this study that sample size effects can be ignored with a sample measuring $W = 40d_1$ in width. On the other hand, since the influence of Young's modulus and Poisson ratio are not the focus of the current study, and the influence of the coefficient of restitution

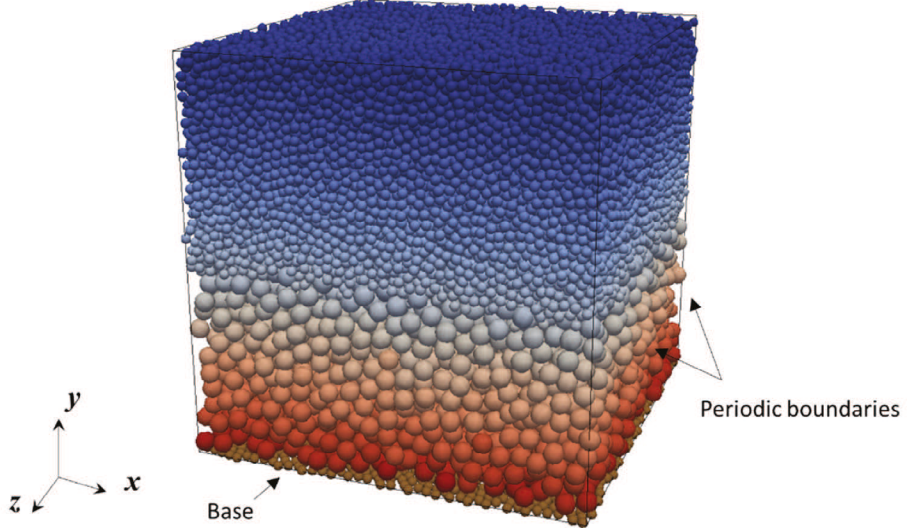


Figure 1: A bi-disperse sample with a rough base and periodic boundaries

is not significant in dense granular flows [44], these three parameters are fixed in the presented cases, i.e. $E = 5\text{ MPa}$, $\nu = 0.45$ and $e = 0.4$. The diameters of small and large particles adopted in all simulations are $d_1 = 0.005\text{m}$ and $d_2 = 0.01\text{m}$, respectively.

The modelled cases are divided into three groups for different slope angles θ , friction coefficients μ and volume fractions of small particles ϕ_1 (Table 1). ϕ_1 is calculated from the height ratio of the two layers, i.e. h_1/h_2 . The numbers of the two types of particles (n_1 and n_2) are also listed.

Table 1: Simulations performed

Group	θ (°)	μ	h_1/h_2	ϕ_1	n_1	n_2
I	21.5–30	0.4	1	0.53	20361	2273
II	25	0.1–0.5	1	0.53	20361	2273
III	25	0.1–0.5	0.5–3	0.27–0.69	10431–27037	3508–1484

3 RESULTS: MACROSCOPIC PERSPECTIVE

3.1 Degree of segregation

For the cases in Group I, the degrees of segregation with increasing slope angle are shown against time in Figure 2. It is observed that after a short period of delay, segregation starts at 16–20 seconds. By checking the snapshots of the simulations, the delay is attributed to the rearrangement of particles and the dilation of the sample as a whole. The segregation is completed faster with a higher slope angle, because the x -component of gravity is higher and it accelerates the flow. In all cases, the segregation process gets slower at a later stage and approaches to a steady state where α remains constant. The final degrees of segregation (α_∞)

are nearly converged at around 200s.

For Group II, keeping the same slope angle (25°), the degrees of segregation are plotted against time for different coefficients of friction, as shown in Figure 3. Similar results can be found for other slope angles. It is observed that a hinge point appears at around 58s, before which the case with lower μ evolves slightly faster, while after that the case with higher μ climbs higher. The hypothesis is that for the low friction case, the rearrangement of particles occurs faster in the first stage, and the small particles can percolate through the opened voids more easily as there are more sliding occurring. Meanwhile, the reason behind the correlation of μ and α_∞ is yet under investigation.

After analysing the simulation results of Group III, it is found that α_∞ does not change with different volume fractions of small particles (ϕ_1). The results are plotted in Figure 4, in comparison with the data from previous 2D simulations [42]. The y -axis $(c_\infty - c_0)/H$ is the normalised migration distance of the centre of mass of large particles. The slope of the solid and dashed lines then represents the final degree of segregation, following the definition in [42], which is equivalent to Equation (1) if the dilation of sample in the SFD stage is neglected. The solid line is reproduced using extrapolated values in [42] for comparison, since there is no distribution width for the two sizes in the current study. The blue dashed line is the fitting line of the 3D simulation results from all $\mu = 0.5$ cases, i.e. all the red hollow circles (the red solid circle is recognised as an outlier). It is found that in 3D simulations the final degree of segregation α_∞ (0.927) is lower than that in 2D (0.982). It indicates that in 2D segregation is completed more easily. It is attributed to the fact that in a two-dimensional configuration, the local voids fractions are higher and the movements in the other direction are constrained, promoting the upward migrations. Although the results for different volume fractions and slope angles converge to a single straight line, α_∞ increases with increasing μ for all different values of ϕ_1 (all symbols in black in Fig.4), which agrees with the findings in Figure 3.

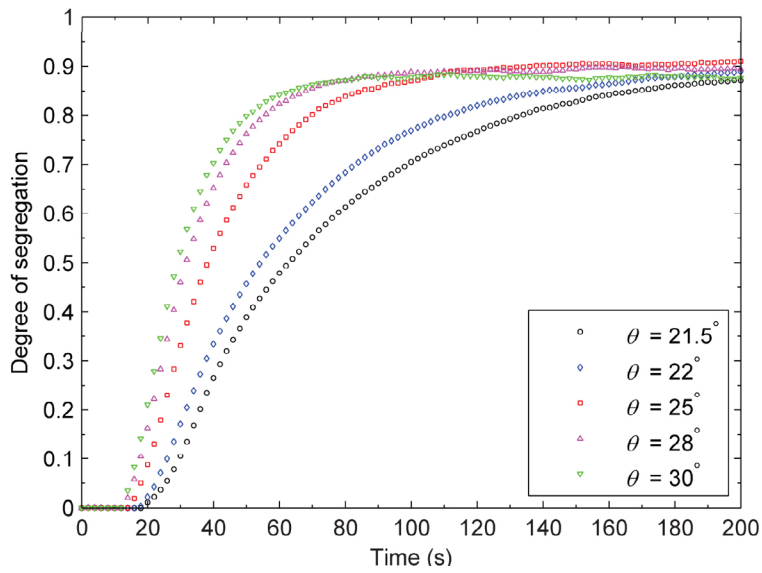


Figure 2: Degree of segregation with different slope angles ($\mu = 0.4$)

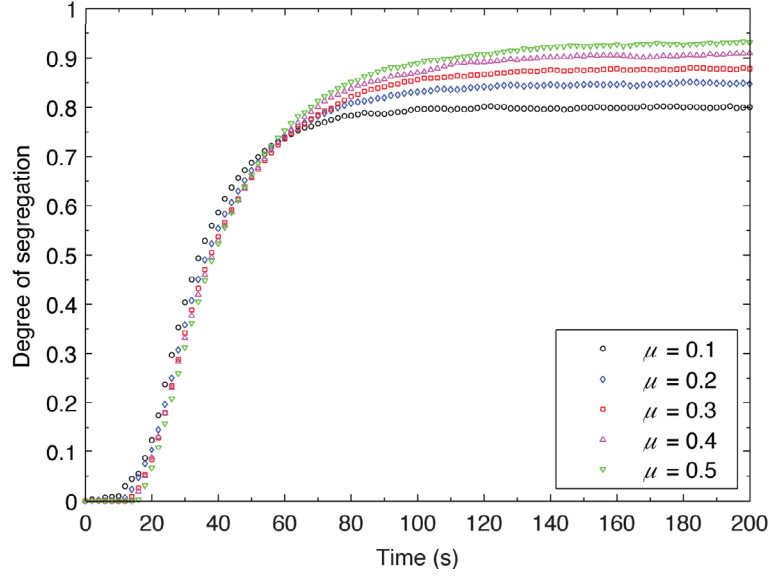


Figure 3: Degree of segregation with different coefficients of friction ($\theta = 25^\circ$)

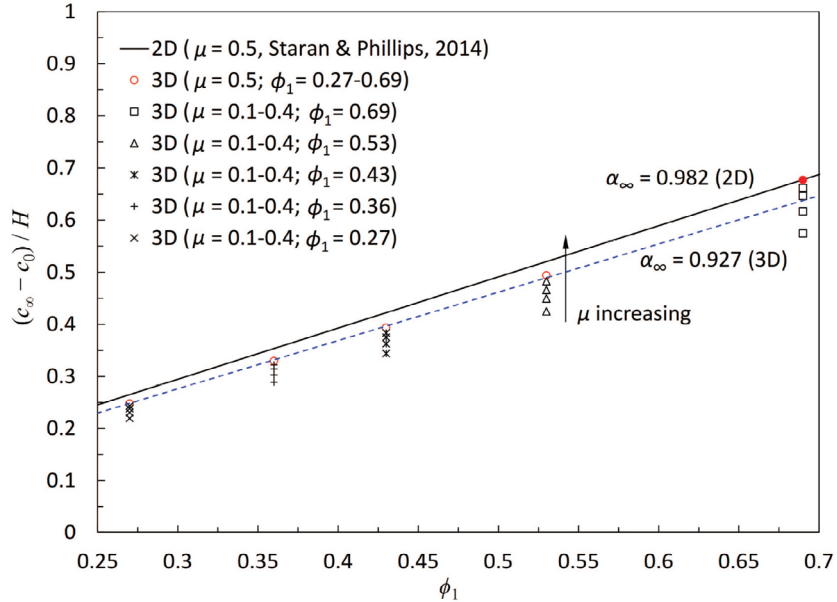


Figure 4: Final degree of segregation for various cases, compared to 2D simulations

3.2 Profile of volume fractions

Granular flows under shear exhibit layered behaviours because of the velocity gradients between different layers [46]. In bi-disperse flows, the evolution of the volume fractions of different species during mixing and segregation is also of interest. Here, the volume fractions

of large particles are averaged over different horizontal shear layers along the height of the sample. The case with $\mu = 0.4$, $\theta = 25^\circ$ and $\phi_1 = 0.53$ is presented in the followed sections as an example. The profiles of volume fractions for different time steps are shown in Figure 5. Basically, three main stages can be identified, i.e. the initial stage ($t = 0$ s) where large particles only appear in the lower half of the sample, the mixing/segregation stage ($t < 100$ s) and the steady stage ($t > 100$ s) where the profiles get converged. The profile at $t = 40$ s is nearly vertical in the bulk, indicating that the two groups are fully mixed (i.e. $\alpha = 0.5$ as in Fig.3). The S-shape profile in the SFD state is consistent with the findings in [35].

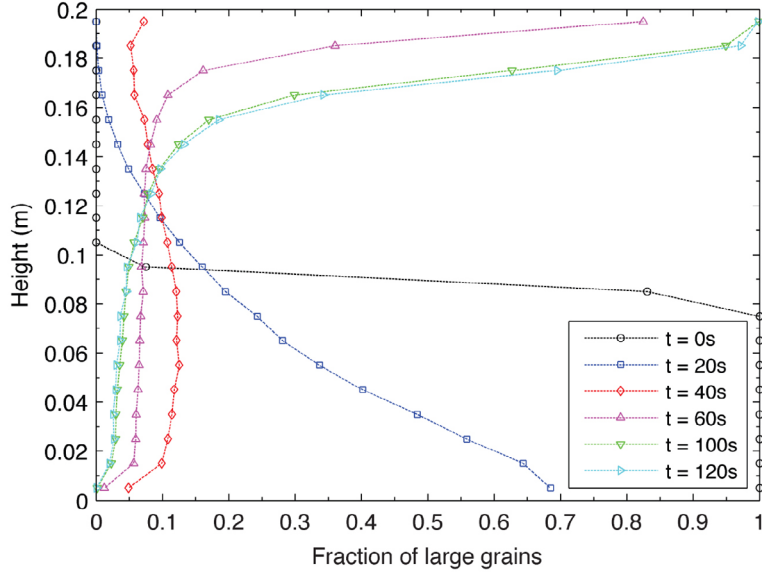


Figure 5: Profiles of volume fraction of large grains at different time

4 RESULTS: MICROSCOPIC PERSPECTIVE

For a randomly picked small particle that is initially in the top layer of the flow, the contact history and trajectory in y -direction are tracked and analysed (Figure 6). The red line shows that after being lifted by the overall dilation of the sample before 20s, the particle is continuously dropping (despite the random fluctuation) throughout the whole simulation and finally reaches the base. On the other hand, the connectivity (i.e. the number of contacts acting on the particle) remains low (or at a normal level) during the whole process, with an average value about 3. It indicates that the small particle is subjected to less contacts and has a higher chance to find voids opened by the shearing flow. These findings provides microscopic evidence for the proposed kinetic sieving mechanism, which states that the small particles can preferentially percolate through the voids [33].

A similar analysis is done for a typical large particle that is initially located at the base. The evolution of its elevation in Figure 7 shows that the upward migration is initiated at $t = 20$ s, and it then migrates rapidly to the top of the flow. Fluctuations are observed when it stays in the top layer in the SFD state. Correspondingly, a clear trend of connectivity is identified (Fig.7). When

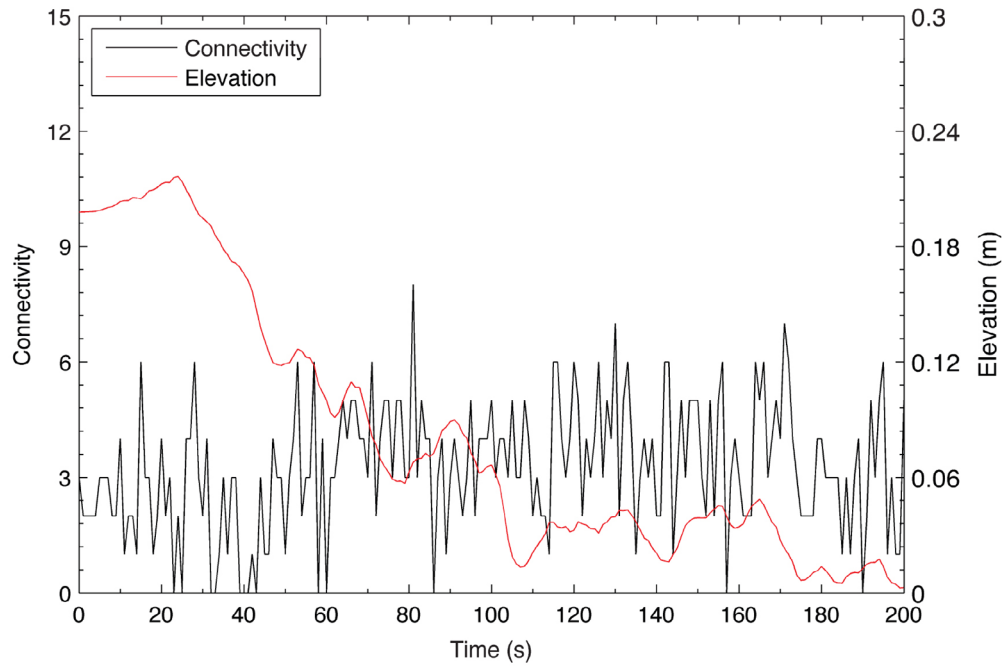


Figure 6: Trajectory and connectivity history of a single small grain

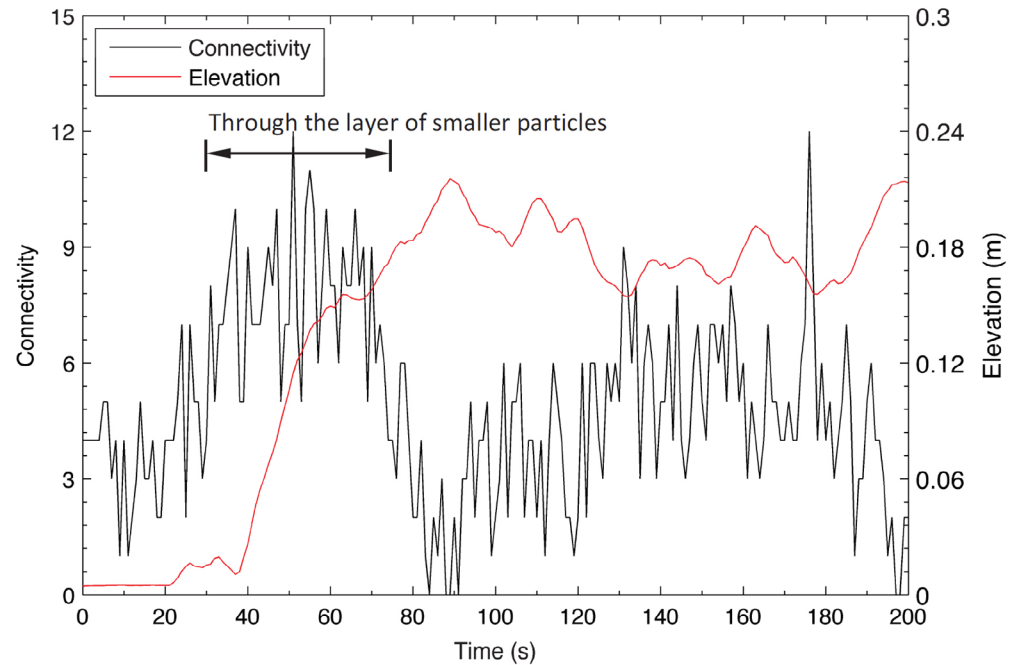


Figure 7: Trajectory and connectivity history of a single large grain

the particle is moving upward, the connectivity becomes significantly higher (8 on average, with peaks at nearly 12), implying that the large grain is mainly surrounded by the small ones. The connectivity returns to a lower level in the SFD state, as the particle stays with other large particles. The high connectivity of the large particle moving through the layer of small particles, in conjunction with the rapid upward movement, offers a microscopic interpretation of the squeeze expulsion mechanism [33].

5 CONCLUDING REMARKS

In this paper, three-dimensional DEM simulations of size segregation are presented. Parametric studies have been performed aiming to provide guidance for similar modelling on setting sample size, slope angle and the coefficient of friction. The effects of these parameters on the segregation process are analysed. It is found that higher slope angle leads to faster segregation, while higher friction coefficient results in higher degree of segregation. The results presented with a newly defined degree of segregation, α_∞ , are generally in good agreement with the previous 2D studies, as it is converged to a certain value for several different conditions. This comparison also reveals that the degree of segregation is higher in the 2D configuration, as the void fractions are higher and the movements in the other direction are constrained. In the macroscopic perspective, the profiles of volume fraction are presented. On the other hand, one of the major contribution of the current study is to provide microscopic evidences for the reviewed mechanisms (i.e., kinetic sieving and squeeze expulsion), since discrete element modelling produces more detailed information on the behaviour and contact conditions of individual particles. The trajectory of each particle is tracked and analysed, showing clearly the contact conditions experienced by each single particle. It is found that the connectivity of small particles are at a lower level than that of the large ones, indicating a higher probability of small particles dropping into voids under gravity. The large particles experience a significant increase of connectivity when they are migrating through the layer of small particles.

6 ACKNOWLEDGMENT

The work was supported by Research Grants Council of Hong Kong (under RGC/GRF 17203614), and the Research Institute for Sustainable Urban Development at The Hong Kong Polytechnic University. The computation was performed using the HKU Information Technology Services research computing facilities that are supported in part by the Hong Kong UGC Special Equipment Grant (SEG HKU09).

REFERENCES

- [1] Andreotti, B., Forterre, Y., Pouliquen, O., *Granular Media: Between Fluid and Solid*, Cambridge University Press, 2013.
- [2] Vallance, J.W., Savage, S.B., in: Rosato PAD, Blackmore PDL (Eds.), *IUTAM Symp. Segreg. Granul. Flows*, Springer Netherlands, 2000, pp. 31–51.
- [3] Kokelaar, B.P., Graham, R.L., Gray, J.M.N.T., Vallance, J.W., Fine-grained linings of leveed channels facilitate runout of granular flows. *Earth Planet. Sci. Lett.* 2014, 385, 172–180.
- [4] Iverson, R.M., The physics of debris flows. *Rev. Geophys.* 1997, 35, 245–296.

- [5] Zhou, G.G.D., Ng, C.W.W., Numerical investigation of reverse segregation in debris flows by DEM. *Granul. Matter* 2010, 12, 507–516.
- [6] Phillips, J., Hogg, A., Kerswell, R., Thomas, N., Enhanced mobility of granular mixtures of fine and coarse particles. *Earth Planet. Sci. Lett.* 2006, 246, 466–480.
- [7] Takahashi, T., *Debris flow: mechanics, prediction and countermeasures*, Taylor & Francis, London ; New York 2007.
- [8] Duran, J., Rajchenbach, J., Clément, E., Arching effect model for particle size segregation. *Phys. Rev. Lett.* 1993, 70, 2431.
- [9] Braun, J., Segregation of granular media by diffusion and convection. *Phys. Rev. E* 2001.
- [10] Huerta, D.A., Ruiz-Suárez, J.C., Vibration-Induced Granular Segregation: A Phenomenon Driven by Three Mechanisms. *Phys. Rev. Lett.* 2004, 92, 114301.
- [11] Zuriguel, I., Boudet, J.F., Amarouchene, Y., Kellay, H., Role of Fluctuation-Induced Interactions in the Axial Segregation of Granular Materials. *Phys. Rev. Lett.* 2005, 95.
- [12] Saez, A., Vivanco, F., Melo, F., Size segregation, convection, and arching effect. *Phys. Rev. E* 2005, 72.
- [13] Rapaport, D.C., Simulated three-component granular segregation in a rotating drum. *Phys. Rev. E* 2007, 76, 041302.
- [14] Liao, C.-C., Hsiau, S.-S., Tsai, T.-H., Tai, C.-H., Segregation to mixing in wet granular matter under vibration. *Chem. Eng. Sci.* 2010, 65, 1109–1116.
- [15] Windows-Yule, C.R.K., Weinhart, T., Parker, D.J., Thornton, A.R., Effects of Packing Density on the Segregative Behaviors of Granular Systems. *Phys. Rev. Lett.* 2014, 112.
- [16] Kleinhans, M.G., Sorting in grain flows at the lee side of dunes. *Earth-Sci. Rev.* 2004, 65, 75–102.
- [17] Zik, O., Levine, D., Lipson, S.G., Shtrikman, S., Stavans, J., Rotationally induced segregation of granular materials. *Phys. Rev. Lett.* 1994, 73, 644.
- [18] Ottino, J.M., Khakhar, D.V., Mixing and Segregation of Granular Materials. *Annu. Rev. Fluid Mech.* 2000, 32, 55.
- [19] Shinbrot, T., Muzzio, F.J., Nonequilibrium Patterns in Granular Mixing and Segregation. *Phys. Today* 2000, 53, 25.
- [20] Jain, N., Ottino, J.M., Lueptow, R.M., Regimes of segregation and mixing in combined size and density granular systems: an experimental study. *Granul. Matter* 2005, 7, 69–81.
- [21] Golick, L.A., Daniels, K.E., Mixing and segregation rates in sheared granular materials. *Phys. Rev. E* 2009, 80, 042301.
- [22] May, L.B.H., Golick, L.A., Phillips, K.C., Shearer, M., Daniels, K.E., Shear-driven size segregation of granular materials: Modeling and experiment. *Phys. Rev. E* 2010, 81, 051301.
- [23] Hill, K.M., Fan, Y., Isolating Segregation Mechanisms in a Split-Bottom Cell. *Phys. Rev. Lett.* 2008, 101, 088001.
- [24] Johnson, C.G., Kokelaar, B.P., Iverson, R.M., Logan, M., et al., Grain-size segregation and levee formation in geophysical mass flows. *J. Geophys. Res.* 2012, 117.
- [25] Félix, G., Thomas, N., Relation between dry granular flow regimes and morphology of deposits: formation of levées in pyroclastic deposits. *Earth Planet. Sci. Lett.* 2004, 221, 197–213.
- [26] Pouliquen, O., Delour, J., Savage, S.B., Fingering in granular flows. *Nature* 1997, 386, 816–817.

- [27] Pouliquen, O., Vallance, J.W., Segregation induced instabilities of granular fronts. *Chaos Interdiscip. J. Nonlinear Sci.* 1999, 9, 621–630.
- [28] Woodhouse, M.J., Thornton, A.R., Johnson, C.G., Kokelaar, B.P., Gray, J.M.N.T., Segregation-induced fingering instabilities in granular free-surface flows. *J. Fluid Mech.* 2012, 709, 543–580.
- [29] Makse, H.A., Havlin, S., King, P.R., Stanley, H.E., Spontaneous stratification in granular mixtures. *Nature* 1997, 386, 379–382.
- [30] Samadani, A., Kudrolli, A., Segregation Transitions in Wet Granular Matter. *Phys. Rev. Lett.* 2000, 85, 5102–5105.
- [31] Fan, Y., Boukerkour, Y., Blanc, T., Umbanhowar, P.B., et al., Stratification, segregation, and mixing of granular materials in quasi-two-dimensional bounded heaps. *Phys. Rev. E* 2012, 86.
- [32] Thornton, A.R., Gray, J.M.N.T., Hogg, A.J., A three-phase mixture theory for particle size segregation in shallow granular free-surface flows. *J. Fluid Mech.* 2006, 550, 1–25.
- [33] Savage, S.B., Lun, C.K.K., Particle size segregation in inclined chute flow of dry cohesionless granular solids. *J. Fluid Mech.* 1988, 189, 311–335.
- [34] Zanuttigh, B., Ghilardi, P., Segregation process of water-granular mixtures released down a steep chute. *J. Hydrol.* 2010, 391, 175–187.
- [35] Gray, J.M.N.T., Chugunov, V.A., Particle-size segregation and diffusive remixing in shallow granular avalanches. *J. Fluid Mech.* 2006, 569, 365.
- [36] Rognon, P.G., Roux, J.-N., Naaïm, M., Chevoir, F., Dense flows of bidisperse assemblies of disks down an inclined plane. *Phys. Fluids* 2007, 19, 058101.
- [37] Tripathi, A., Khakhar, D.V., Rheology of binary granular mixtures in the dense flow regime. *Phys. Fluids* 2011, 23, 113302.
- [38] Khakhar, D.V., McCarthy, J.J., Ottino, J.M., Mixing and segregation of granular materials in chute flows. *Chaos Interdiscip. J. Nonlinear Sci.* 1999, 9, 594–610.
- [39] Thornton, A., Weinhart, T., Luding, S., Bokhove, O., Modeling of particle size segregation: calibration using the discrete particle method. *Int. J. Mod. Phys. C* 2012, 23, 1240014.
- [40] Fan, Y., Schlick, C.P., Umbanhowar, P.B., Ottino, J.M., Lueptow, R.M., Modeling size segregation of granular materials: the roles of segregation, advection and diffusion. *J. Fluid Mech.* 2014, 741, 252–279.
- [41] Linares-Guerrero, E., Goujon, C., Zenit, R., Increased mobility of bidisperse granular avalanches. *J. Fluid Mech.* 2007, 593.
- [42] Staron, L., Phillips, J.C., Segregation time-scale in bi-disperse granular flows. *Phys. Fluids 1994-Present* 2014, 26, 033302.
- [43] Kloss, C., Goniva, C., Hager, A., Amberger, S., Pirker, S., Models, algorithms and validation for opensource DEM and CFD-DEM. *Prog. Comput. Fluid Dyn. Int. J.* 2012, 12, 140–152.
- [44] Silbert, L.E., Ertaş, D., Grest, G.S., Halsey, T.C., et al., Granular flow down an inclined plane: Bagnold scaling and rheology. *Phys. Rev. E* 2001, 64, 051302.
- [45] Delannay, R., Louge, M., Richard, P., Taberlet, N., Valance, A., Towards a theoretical picture of dense granular flows down inclines. *Nat. Mater.* 2007, 6, 99–108.
- [46] Forterre, Y., Pouliquen, O., Flows of Dense Granular Media. *Annu. Rev. Fluid Mech.* 2008, 40, 1–24.

DISCRETE MODELING OF GEOTEXTILE-WRAPPED SOIL UNDER SIMPLE SHEAR

H. CHENG¹ AND H. YAMAMOTO¹

¹Graduate School for International Development and Cooperation
Hiroshima University
1-5-1, Kagamiyama, Higashi-hiroshima, Japan
d132535@hiroshima-u.ac.jp
<http://www.hiroshima-u.ac.jp/idec>

Key words: DEM, Soilbag reinforcement, Woven geotextile, Stress path, Fabric anisotropy.

Abstract. Geosynthetic Reinforced Soil (GRS) is widely used in infrastructure projects such as retaining wall and road/railway subgrade for technical and economical reasons. Despite of the worldwide usage, the basic mechanism of such reinforcement remains obscure, owing to its discontinuous and heterogeneous nature. Instead of being layered by planar geosynthetic sheets, soil can be wrapped entirely in geosynthetic containers as soilbags, which improves bearing capacity and contains the dilatancy of soil. To gain insights into soilbag reinforcement mechanisms and facilitate the development of soilbag's constitutive relation, the authors numerically investigated the micromechanical behavior of the GRS inside a woven geotextile soilbag under simple shear, by using the Discrete Element Method (DEM). Global and local stress states and fabric anisotropies in the GRS were investigated. With sustained shear, the global stress path first approaches the critical state line of the GRS and then turns to soilbag's compression line. Meanwhile, local loading-unloading stress paths are experienced, which may account for high damping of soilbags in cyclic shear. The reducing fabric anisotropies of normal and tangential force chains suggest greater confinement from the lateral sides of the geotextile container during simple shear. With new findings in the stress states and the fabric anisotropies of the wrapped GRS, the confinement mechanism of soilbag is better understood.

1 INTRODUCTION

Our knowledge of geotechnical engineering has been examined and advanced by the increasing need for countermeasures against ground disasters such as earthquake, slope failure and landslide. On the other hand, the raising awareness of sustainable development demands geotechnical engineers of cost-effective and environmental-friendly solutions to geotechnical problems. In recent decades, Geosynthetic Reinforced Soil (GRS) has manifested itself as one of the most effective earth/subgrade reinforcement methods ([1], [2]) that deal with both concerns, e.g. geotextile sheets for soil nailing in retaining wall. Instead of being layered by planar geosynthetic sheets, soil can be wrapped entirely in geosynthetic containers as soilbags [3], [4], which brings astonishing rise in bearing capacity, taking advantage of the straining geosynthetic fabrics that inhibit the dilatancy of soil. Regardless of different ways of including geosynthetics in the ground, the GRS is fabricated more heterogeneous than natural soils. Adding to this the discontinuity and anisotropy at the soil-to-geosynthetic interface, it is

difficult to conduct a comprehensive evaluation on the performance and the mechanisms of the GRS from the onset of external load until the global/local failure of geosynthetic reinforcement in conventional continuum approach. On the other hand, the design of the GRS as road/railway subgrade or foundation reinforcement are mostly based on laboratory testing and empirical assumptions, thus presenting a great need of developing efficient numerical tools to model the GRS in various forms and types.

Several attempts on the finite modeling of the soilbag-wrapped GRS were made using truss elements for modeling the tensile behavior of geosynthetic fabric. The performance of soilbag reinforcement was examined at different scales, ranging from the soilbag-assembly level [5] to the soil-to-bag interface level where slip, surface separation and reclosure were dealt with explicitly by using master/slave surface concept [6], [7]. Discontinuity and large deformation at the interface can be effectively tackled by implement this concept in the finite element scheme, but they could be more straightforwardly handled using discrete approaches like the Discrete Element Method (DEM).

In present study, woven geotextile was considered as the wrapping material of soilbag. It has peculiar mechanical behaviors owing to ease relative motion between yarns, fabric abrasion and impregnation (e.g. resin matrix) [8]. The structural mechanics of this woven system can be well represented by orthogonal bars with nodes linked by diagonal and rotational springs. A simplified version was initiated by Thoeni et al. [9] using the DEM [10], considering only the stretching springs with a stochastically distorted law which accounts for the initial distortion of hexagonal wire mesh. Their approaches generally suit any woven system. In this work, the 3D woven structure of a DEM woven geotextile container was constructed in a similar manner. The filling material was prepared using a polydisperse packing with a scaled particle size distribution (PSD) of Toyoura sand. The macroscopic response of the geotextile and the sand were calibrated against laboratory results separately. Following the previous work [11] which validated the DEM soilbag in compression loading condition, this work aims to clarify the reinforcement mechanism of soilbag enclosure under simple shear, with the knowledge of fabric and stress state evolution attained from the micromechanical behavior of the GRS inside soilbag. This numerical study is conducted using an open-source frame work YADE [10].

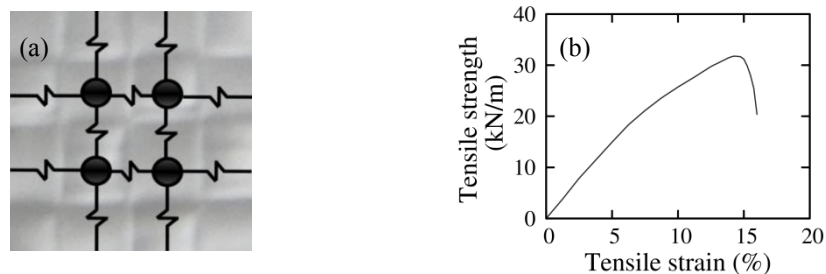


Figure 1: Characteristics of PP geotextile: (a) Woven fabric structure and (b) Tensile behavior according to [12]

2 CHARACTERISTICS OF WOVEN GEOTEXTILE BAG

The woven geotextile has a fabric structure that consists of polypropylene (PP) yarns overlapping one and another orthogonally, as shown in Fig. 1(a). This regular interlocked fabric ensures the stability of the woven system and reduces the dilatancy of the GRS

(affected by the aperture size ratio) [13]. In the previous shear tests [14], the PP (0.39mm in thickness) geotextile (see Fig. 1) was used as the wrapping material. Prior to shear, a woven geotextile soilbag was thoroughly compacted until 80 mm height was reached approximately, as illustrated in Fig. 2(a). Because curved lateral faces appeared after the initial compaction and the geotextile container was cuboid-shaped initially (400 mm in length and width, and 100 mm in height), the soilbag's cross sections perpendicular to long/short axis after the compaction are assumed as illustrated in Fig. 2(b). From these cross sections, the 3D mesh of the woven geotextile soilbag is derived as shown in Fig. 2(c).

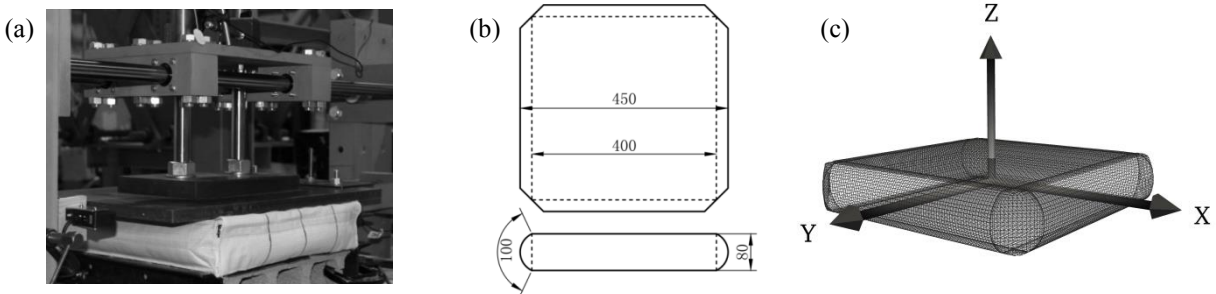


Figure 2: (a) Representative laboratory soilbag under shear and assumed (b) cross sections, (c) 3D mesh

3 DISCRETE MODELING OF SOILBAG

Discrete element modeling of soilbag needs to deal with not only discontinuity in particles, but anisotropy and heterogeneous caused by the geotextile enclosure as well. These problems can be solved radically by discretizing the GRS as an assembly of polydisperse particles that are capable of transferring loads and getting mobilized by sliding and rolling/twisting. In present work, the nodes where the woven fabric's warp and weft meet were idealized as imaginary spheres in an orthogonal grid, connected with each other by remote springs [9]. These geotextile nodes and springs were configured on the soilbag mesh as shown in Fig 2(c). The macro response of the sand and the woven PP geotextile fabric are separately calibrated. With the sand's representative volume (RV) properly prepared, a packing satisfying soilbag's boundary was generated, having a specified initial void ratio $e_0 = 0.68$.

3.1 Determination of local parameters

The materials considered in the DEM are usually calibrated against their macroscopic responses in laboratory. Results from triaxial/biaxial testing on soil specimen under different confining pressure are commonly compared with those replicated by the DEM models. In this work, the simplified Hertz-Mindlin non slip contact model [15] with the Moment Transfer Law (MTL) [16] was adopted for describing the local behaviors between spherical particles. Modeling tensile behavior of geotextile requires the tensile constitutive relations extracted from tensile tests and the interface frictional angle calibrated in pullout or shear tests. The tensile behavior of the PP geotextile was examined in laboratory (see Fig. 1(b)) and then represented by nonlinear remote springs in the DEM. Both the constitutive laws have been implemented in YADE by Modenese [17] and Thoeni [9] respectively.

The Toyoura sand inside the soilbag weighs 24 kg as in the previous tests [14]. The sand is uniformly graded ($D_{60}/D_{10} = 1.3$) with the average diameter $r_{\text{mean}} = 0.2$ mm and the specific

gravity $G_s = 2.65 \text{ g/cm}^3$. However, in the simulations, the DEM sand specimen was represented by a packing made of 1,000 particles with a scaled PSD with $r_{\text{mean}} = 3 \text{ mm}$ and $G_s = 2.65 \text{ g/cm}^3$, prepared in the periodic boundary condition (PBC). The same initial void ratio ($e_0 = 0.68$) as in the real sand specimen [18] was attained in the DEM packing before used for calibrating the parameters of the simplified Hertz-Mindlin contact model. Fig. 3 compares the response of the DEM packing and the Toyoura sand specimen (50mm in diameter and 100 mm in height) in drained triaxial compression conditions. Local behaviors of the DEM packing were controlled using the soil parameters listed in Table 1. Note that if the 3D geometry illustrated in Fig. 2(c) holds perfectly in laboratory, the volume of one soilbag after initial compaction would be 0.015 m^3 , i.e. an initial void ratio of 0.68 approximately after the initial compaction. Therefore it is reasonable to use the same PBC packing ($e_0 = 0.68$) as the representative volume to generate the GRS packing inside the soilbag.

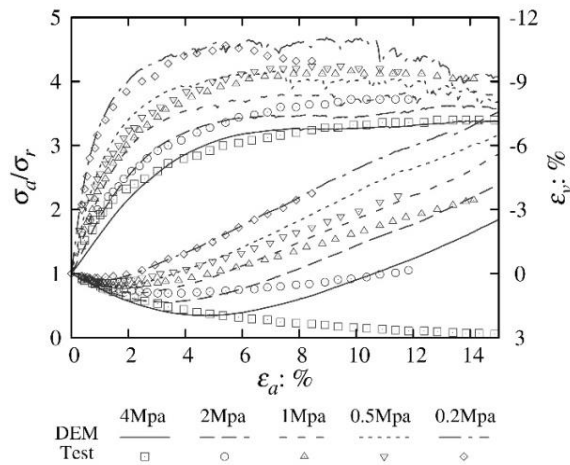


Figure 3: Response of dense Toyoura sand ($e_0 = 0.68$) in drained triaxial tests and simulations

Table 1: Local parameters for Hertz-Mindlin contacts

	Young's modulus (GPa)	Poisson ratio	Rolling/ twisting stiffness	Density (kg/m ³)	Frictional angle (°)
Soil/Soil	4/4	0.33	0.13	2650	29
Soil/Geotextile	4/8	0.33	0.13	444	21
Geotextile/Plate	8/200	0.33	0.13	7850	90

The current modeling purpose is to investigate dry woven fabric's interactions with soil. Therefore, the woven fabric was modeled in such a scale where the fabric's structural mechanics can be described. This is done by linking with remote springs the orthogonal placed physical nodes where the warp and the weft meet, as shown in Fig 1(a). Because the fabric is constantly strained with great tensile force during tests, sliding between warp and weft was excluded in the current modeling scheme. Though the authors are aware of the irregularities in yarn properties and fabric organization, the stochastically shift of force-displacement curve as formulated in [9] was not considered. Instead, the tensile behavior was solely governed by the constitutive relation shown in Fig. 1(b). The interface behavior was calibrated by shearing a sand box on a fixed geotextile sheet, considering a variety of normal

load. A series of DEM simulations were run under the same conditions. The best agreement against the test data was obtained when 21° was used as the interface frictional angle for the soil-geotextile contact. Detailed explanation on the calibration process can be found in [11].

3.2 Soilbag-wrapped GRS packing generation

With the 3D boundary of soilbag assumed in Fig 2(c), it is easy to fill the volume with a properly generated sphere packing by the radius expansion method. The primary concern is to prepare a soilbag-wrapped GRS packing which fits well into the soilbag boundary, and in the meantime preserves the same fabric structure as in the tests. Because void ratio is the most conventional and handy indicator to describe the structure of an isotropic specimen and also of great significance in classical soil models, the authors seek a packing generation process that eventually makes the packing attain at a preferred void ratio and sufficiently conform to the 3D boundary, without inducing large internal force.

For this purpose, the PBC packing in section 3.1 was used as the RV to generate the GRS packing. The assembled cuboid-shaped packing using 100 RV duplicates (10 along both x - and y -axis) has intrinsic fabric consistency, owing to the compatible contacts along the boundaries of the neighboring RV copies. Because the response of the RV packing was rigorously calibrated against a series of triaxial tests (though not precisely for volumetric strain at high confining stress), the cuboid packing is capable of quantitatively reproducing the macro response and providing insights into the fabric characteristics of the wrapped GRS.

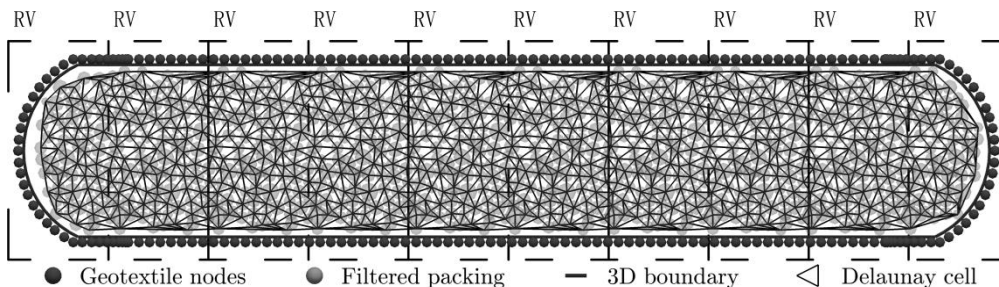


Figure 4: Filtered soilbag packing by assumed 3D boundary (x - y plane cross section)

The cuboid GRS packing was filtered to satisfy the 3D soilbag boundary (the thick black envelope in Fig. 4). The key components representing the soilbag on the cross section plane before the radius expansion is shown in Fig. 4. To make the filtered packing sufficiently conform to the boundary, each soil sphere was allowed to grow with a small multiplier ($E_r = 1.0001$) simultaneously whenever the unbalanced force was sufficiently dissipated (less than 10^{-3}). At this stage, the geotextile nodes (black spheres in Fig. 4) were fixed in space. While searching for the equilibrium state, the system was given a 0.9 damping coefficient so that the induced numerical viscosity could prevent the packing from deviating too much from the original fabric configuration. The expansion finished when the packing's Delaunay cells (2D triangles of Fig. 4 in 2D but tetrahedron in 3D) ceased to grow and the mean relative overlap ratio dropped down to 2.0×10^{-8} (same value as in the initial RV packing). At last the packing consists of 68,883 spheres with $e_0 = 0.675$ was gained as the GRS packing inside the bag. It should be noted that in the PBC the void ratio is computed using the periodic cell volume. Analogously, the void ratio of soilbag is based on the total volume of the Delaunay cells.

4 RESULTS AND DISCUSSIONS

4.1 Validation of the soilbag model

The macro responses obtained from the unconfined compression and the simple shear (SS) tests were used to validate the proposed DEM soilbag model [11]. Due to page limitation, this paper only focuses on the SS cases. Shearing (with vertical dead load $P = 1.33, 1.87, 2.41Q$ at a $0.02\%/\text{s}$ shear strain rate. To minimize the interface sliding, abrasive paper (grit 40) was firmly attached to the bottom of the loading plate and the top of the test platform. In the simulation, the geotextile-plate contacts were given a 90° frictional angle to eradicate the interfacial sliding. To lower computational cost, only one soilbag was modeled in the simulations and the initial compaction was left out. The compaction's effect on e_0 has been taken into account as stated in section 3.1. The strain rate was set constant at $10\%/\text{sec}$ in the simulations. At this rate, the unbalanced force was kept at a negligible level (lower than 10^{-3}). Though not shown here, consistent macro response was gained by using $1\%/\text{sec}$ and $0.1\%/\text{sec}$ strain rates.

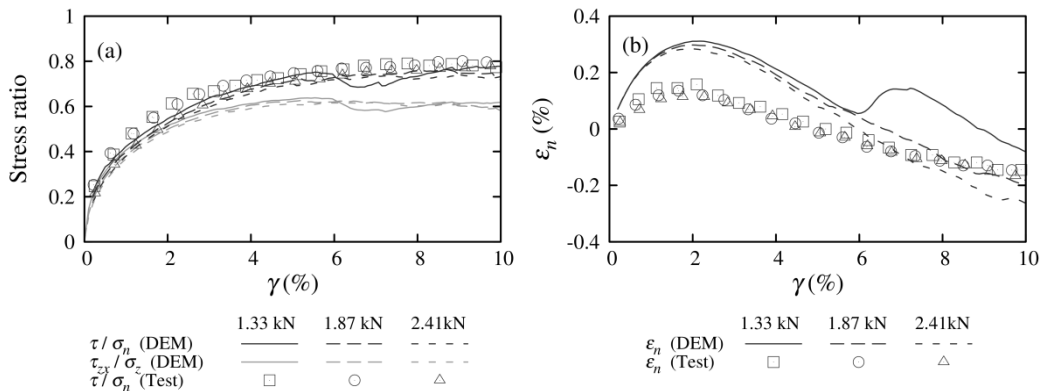


Figure 5: Response of soilbag under simple shear (a) tangential-normal stress ratio, (b) normal strain

Good agreement was gained between the responses from the tests and the simulations with the parameters given in Table 1. Fig. 5 gives the evolutions of two shear-to-tangential stress ratios on the loading plate $\tau/\sigma_n = Q/P$ and the x - y plane of the wrapped GRS τ_{zx}/σ_z , computed from the average stress tensor σ over the GRS domain using equation (1). In the simulation, the maximum of normal strain ϵ_n was reproduced higher than in the tests. This is possibly due to the lack of the initial compaction in the simulations. As stated in [19], cyclic loading (initial compaction) rearranges the strong force chain being increasingly anisotropic, which in return leads to the hardening of granular material. The response of τ/σ_n accurately matches with the test data. τ_{zx}/σ_z was found falling progressively behind τ/σ_n , owing to increasing σ_z in the GRS (see Fig. 6) due to the confinement effect from the soilbag enclosure. A closer look at the components of the average stress tensor σ in Fig. 6 further clarifies the contribution of soilbag confinement. It can be seen that when the wrapped GRS approached its shear strength the lateral stress σ_x and σ_y almost doubled. However it should be noted that because σ_z grows steadily with sustained shear, there should be neither maximum nor softening in the τ_{zx} response. It seems that upon reaching the critical condition, the stress state of the soilbag-

wrapped GRS can be approximated as an isotropic pressure coupled with a pair of shear stresses in the shear (x - z) plain.

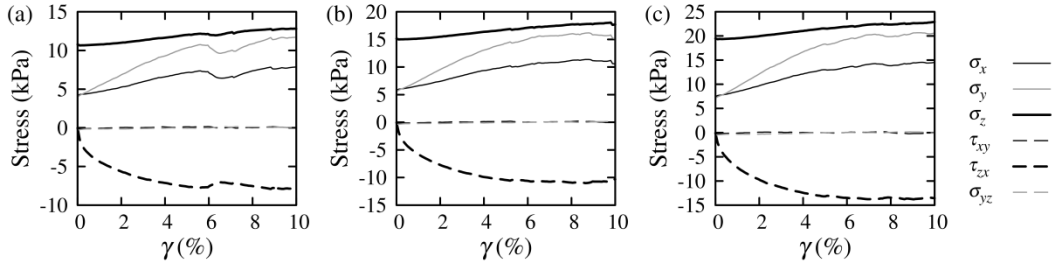


Figure 6: Average stress components over soil domain under simple shear with $P =$ (a) 1.33 (b) 1.87 (c) 2.41 kN

4.2 Stress states in soilbag

The particle-based stress tensor can be computed using equation (1) where σ is the bulk stress tensor, \mathbf{d}^c and \mathbf{f}^c are the branch vector and the contact force vector. V is the volume of a Voronoi cell containing one particle. Averaging over the stress tensors in a preferred domain, one can easily acquire the corresponding global/local macro stress tensor and thus the mean stress p and deviatoric stress q . As the soilbag packing is derived from the original RV packing in PBC cells, it is reasonable to base the local p , q values on these RV duplicates. The stress components in Fig. 5 and 6 are computed in such an averaging manner.

$$\sigma = \frac{1}{V} \sum_{N_c} \mathbf{d}^c \otimes \mathbf{f}^c \quad (1)$$

Stress tensors were averaged in five volumes #1 ~ #5 aligning along x axis. Each consists of four neighboring RVs as shown in Fig. 7. #0 represents the overall Delaunay volume of the soilbag from which the void ratio e is computed.

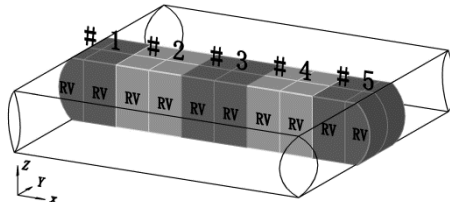


Figure 7: Illustration of five selected volumes for probing local stress path

The stress paths of the PP soilbag under SS are plotted in Fig. 8. Due to the page limitation, only four cases ($P = 2.41, 12.05, 24.1$ and 36.15 kN) are reported in here. In each case, the global stress path initially deviated from the compression path, approaching the critical state line (CSL). Because greater confinement comes with higher vertical load (as will be detailed in section 4.3), the GRS's CSL slope reduces as the vertical dead load increases. In all cases, interesting loading-unloading local stress paths were found in the middle part (#2 ~ #4) of the GRS. After passing the Phase Transformation Stage (PTS) which coincides with the transition of ε_n from compressive to dilative, further shear deformation resulted in persistent drop in both p and q levels along the CSL. With the soil in the middle flowing with almost constant

volume, the soil neighboring the lateral boundaries (#1, #5) was constantly compressed with stress states along the compression line. At global scale, stress states in the GRS evolved towards a uniform state after the PTS. Soilbag's high damping ratio [5] could be attributed to the hysteresis effect induced by the partial loading-unloading stress paths during each monotonic stage of cyclic shear. These absorbing local loading paths could be attributed to the redistribution of internal forces induced by SS loading. The transfer of concentrated forces into the domain in the vicinity of lateral boundary is visualized in the force chain of Fig. 9 ($P = 12.05$ kN). The chain's radii and color represent the magnitudes of normal and the tangential force vector respectively. Upon the soilbag reaching its shear strength, the tension distribution exhibited the opposite pattern as in the unconfined compression condition: tensile force on the lateral faces was higher than on the top and bottom surface of the geotextile bag.

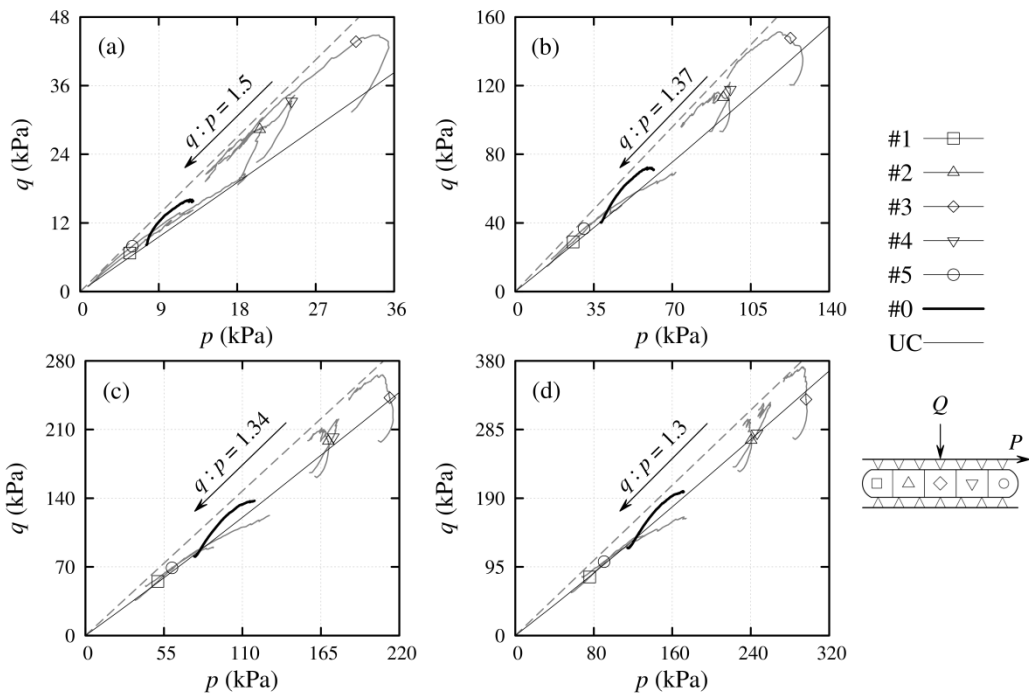


Figure 8: Global and local stress paths under SS with vertical load: (a) 2.41, (b) 12.05, (c) 24.1 and (d) 36.15 kN

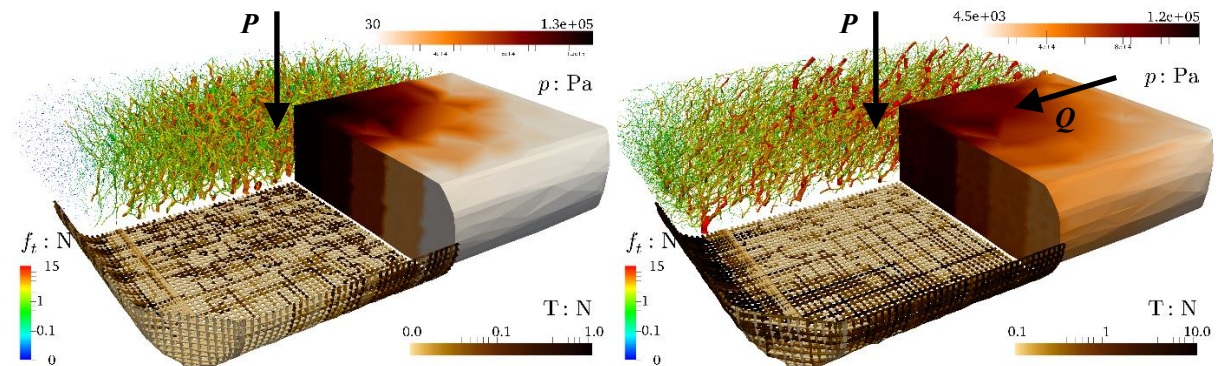


Figure 9: Force chain, p distribution in GRS and T distribution on geotextile at (a) initial state and (b) final state.

4.3 On fabric anisotropies of soilbag

Using the measurement of fabric configuration [20] the authors seek the characteristics of the fabric anisotropies in the soilbag-wrapped GRS. Getting this knowledge may help understand the soilbag confinement mechanism from a microscopic perspective. With the information on particles' spatial configuration and internal force chain, equation (2) ~ (4) give the corresponding fabric tensors namely φ^c , χ^n , and χ^t .

$$\varphi^c = \frac{1}{N_c} \sum_{N_c} \mathbf{n}^c \otimes \mathbf{n}^c \quad (2)$$

$$\chi^n = \frac{1}{N_c} \sum_{N_c} \frac{f_n^c \mathbf{n}^c \otimes \mathbf{n}^c}{1 + \mathbf{a}^c : (\mathbf{n}^c \otimes \mathbf{n}^c)} \quad (3)$$

$$\chi^t = \frac{1}{N_c} \sum_{N_c} \frac{f_t^c \mathbf{t}^c \otimes \mathbf{n}^c}{1 + \mathbf{a}^c : (\mathbf{n}^c \otimes \mathbf{n}^c)} \quad (4)$$

where \mathbf{n}^c , \mathbf{t}^c = the unit vectors normal and tangential to the contact plane, N_c = the total number of the possible contacts which include: (a) soil-to-soil, (b) soil-to-geotextile, (c) soil-to-plate (only definable after geotextile failure); f_n^c and f_t^c are the length of inter-particle contact force along normal and tangential direction. $\mathbf{a}^c = 15\text{dev}\varphi_c/2$ is the fabric anisotropy tensor due to geometrical change. Analogously using the averaged contact normal force $f^0 = \text{tr}\chi^n$, the other two mechanical induced anisotropy tensors can be defined as $\mathbf{a}^n = 15\text{dev}\chi^n/(2f^0)$, $\mathbf{a}^t = 15\text{dev}\chi^t/(3f^0)$. The second invariants of these tensors can be used to measure the magnitudes of anisotropies using equation (5).

$$a_* = \text{sign}(S_r) \sqrt{\frac{3}{2} \mathbf{a}^* : \mathbf{a}^*} \quad (5)$$

where * stand for c , n , t accordingly, S_r calculates the inclination between a specific anisotropy tensor with the stress deviator $\text{dev}\sigma$. The following sections will discuss the relation of these fabric anisotropies with the confinement effect and the shear strength.

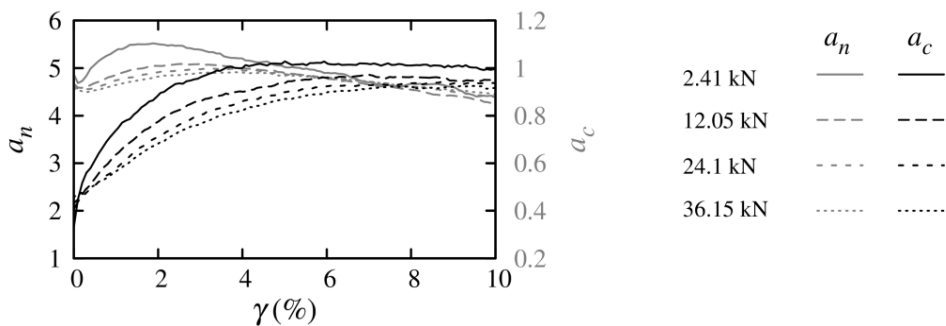


Figure 10: Evolution of fabric anisotropies a_n and a_c of soilbag during SS under different vertical dead loads

Fig. 10 shows the evolution of the fabric anisotropies a_n and a_c with shear strain γ under SS. For all the considered SS cases, a_n dropped gradually with sustained γ after passing the PTS, indicating increasing normal and tangential force chains built along the lateral directions. Macroscopically, this resulted in rising lateral stress σ_x and σ_y . Under SS, the fabric anisotropy

due to the geometrical configuration of the wrapped GRS has a similar tendency to that of soil specimen in triaxial compression DEM simulations. In both cases, a_c becomes stagnant when the soil reaches its shear strength. It is obvious that the critical value of a_c in granular material is closely related to the material's shear strength and frictional constant. For soilbag-wrapped GRS, the critical a_c should be determined from both the geotextile's tensile stiffness and the soil property. Fig. 10 also gives a group of fabric anisotropy responses under a variety of vertical dead loads. In addition to a_c 's variation with respect to shear, the critical a_c was found reducing with higher levels of normal load, indicating a_c as a state parameter related to the stress state of the wrapped GRS. Similar pattern exists among the response of the mechanical fabric anisotropy a_n under different vertical loads. However, as the vertical load increases, the curve of a_n in Fig. 10 is shifted downward. Though not shown in here, similar trend for a_t was obtained as well. It can be concluded that the confinement on the soilbag-wrapped GRS does not only develop under compression, but during shear as well. The greater the compression prior to shear, the greater attainable confinement presents in soilbag during shear. It is worth noticing that with higher vertical load, the slope of the CSL of the GRS decreases gradually. Because deviatoric stress in the GRS becomes comparatively lower than in soil specimen under the same loading condition, less distortion is anticipated in the GRS. As a result, the dilatancy of soil is better contained by using soilbag earth reinforcement method.

5 CONCLUSIONS

In present study, the polypropylene soilbag is modeled using the discrete element method under simple shear condition. The parameters for contact laws were calibrated against the response of triaxial, width-wide tensile and shearing box tests. With a properly assumed 3D geometry, the soilbag model was rigorously prepared by using the representative volumes generated in the periodic boundary condition which was also used for calibrating the contact model. The filtered packing's radii were expanded to conform to the soilbag boundary. The proposed model has been validated by a group of simple shear tests. Some interesting findings of the geosynthetic reinforced soil wrapped by soilbag are stated as follows.

- Global stress path during simple shear firstly approaches the critical state line then heads away towards soilbag's compression line. Interesting loading-reloading paths were observed in the middle part of the soilbag, which could result in partial hysteresis behavior, explaining high damping inside soilbag.
- Confinement is the soilbag reinforcement's primary mechanism which is measurable by using the mechanically induced fabric anisotropies. After passing the phase transformation stage, the confinement effect was found increasing with sustained shear.
- It can be concluded that soilbag's confinement does not only take place during loading at normal direction (unconfined and triaxial compression), shear loading facilitates the development of the confinement effect as well, resulting in the reduced slope of the critical state line of the geosynthetic reinforced soil and better control on the dilatancy of soil.

The current work is a part of an ongoing research project, aiming at the scientific design of soilbag earth reinforcement as sustainable solutions to geotechnical problems. The validated model will be examined in a variety of loads mostly encountered in infrastructure foundations and subgrades. Future work will cover a comparative study on the behavior and mechanism of the geosynthetic reinforced soil in the form of soilbag and in other types and forms.

REFERENCES

- [1] Cai Z. and Bathurst R. J. Seismic response analysis of geosynthetic reinforced soil segmental retaining walls by finite element method. *Comput. Geotech.* (1995) **17**: 523–546.
- [2] Indraratna, B. and Nimbalkar, S. Stress-strain degradation response of railway ballast stabilized with geosynthetics. *J. Geotech. Geoenviron. Eng.* (2013) **139**: 684–700.
- [3] Tatsuoka, F., Aqil, U., Lohani, T. N., Mohri, Y. and Matsushima, K. Evaluating the strength and deformation characteristics of a soil bag pile from full-scale laboratory tests. *Geosynth. Int.* (2006) **13**: 246–264.
- [4] Matsuoka, H. and Liu, S. New earth reinforcement method by soilbags (Donow). *Soils Found.* (2003) **43**: 173–188.
- [5] Muramatsu, D., Bin, Y. and Zhang, F. Numerical simulation of vibration damping effect of soilbag. *Jpn. Geotech. J.* (2009) **4**: 71–80. (in Japanese)
- [6] Ansari, Y., Merifield, R., Yamamoto, H. and Sheng, D. Numerical analysis of soilbags under compression and cyclic shear. *Comput. Geotech.* (2011) **38**: 659–668.
- [7] Tantono S. F. and Bauer E. Numerical simulation of a soilbag under vertical compression. In the 12th international conference of International Association for Computer Methods and Advances in Geomechanics (IACMAG) (2008). Goa, India.
- [8] Ben Boubaker, B., Haussy, B. and Ganghoffer, J. F. Discrete models of woven structures. Macroscopic approach. *Compos. Part B Eng.* (2007) **38**: 498–505.
- [9] Thoeni, K., Lambert, C., Giacomini, A. and Sloan, S. W. Discrete modelling of hexagonal wire meshes with a stochastically distorted contact model. *Comput. Geotech.* (2013) **49**: 158–169.
- [10] Šmilauer, V., Catalano, E., Chareyre, B., Duriez, J., Gladky, A., Kozicki, J. Modenese, C. Scholtès, L. Sibille, L. Stránský, J. and Thoeni, K. Yade Documentation (V. Šmilauer, ed.). The Yade Project, 1st ed. (2010)
- [11] Cheng, H. and Yamamoto, H. Modeling microscopic behavior of geotextile-wrapped soil by discrete element method. In *15ARCSMGE* (2015). Fukuoka, Japan. (in print)
- [12] D35 Committee. *Test Method for Tensile Properties of Geotextiles by the Wide-Width Strip Method*. (2011).
- [13] Haeri, S. M., Noorzad, R. and Oskoorouchi, A. M. Effect of geotextile reinforcement on the mechanical behavior of sand. *Geotext. Geomembr.* (2000) **18**: 385–402.
- [14] Cheng, H. and Yamamoto, H., Jin, S. and Okano, S. Soil reinforcement using soilbags – a preliminary study on its static and dynamic properties. In *Geotechnics for Sustainable Development* (2013). 569–578. Hanoi, Vietnam.
- [15] Thornton, C., Cummins, S. J. and Cleary, P. W. An investigation of the comparative behaviour of alternative contact force models during elastic collisions. *Powder Technol.* (2011) **210**: 189–197.
- [16] Iwashita, K. and Oda, M. Rolling resistance at contacts in simulation of shear band development by DEM. *J. Eng. Mech.* (1998) **124**: 285–292.
- [17] Modenese, C. Numerical study of the mechanical properties of lunar soil by the discrete element method. (University of Oxford, 2013).

- [18] Sun, D. A., Huang, W. X., Sheng, D. C. and Yamamoto, H. An elastoplastic model for granular materials exhibiting particle crushing. *Key Eng. Mater.* (2007) **340-341**: 1273–1278.
- [19] O'sullivan, C., Cui, L. and O'neill, S. C. Discrete element analysis of the response of granular materials during cyclic loading. *Soils Found.* (2008) **48**: 511–530.
- [20] Zhao, J. and Guo, N. Unique critical state characteristics in granular media considering fabric anisotropy. *Géotechnique* (2013) **63**: 695–704.

EFFECT OF WALL ROUGHNESS ON INTERFACE BEHAVIOR OF DEM-SIMULATED GRANULAR MATERIAL

KHADIJA A. EL CHEIKH^{1,2}, SÉBASTIEN RÉMOND², CHAFIKA DJELAL¹,
PATRICK PIZETTE² AND YANNICK VANHOVE¹

¹Université d'Artois, LGCgE
1230 Rue de l'Université, F- 62408, Béthune, France
chafika.dantec@univ-artois.fr, <http://www.iutbethune.org/>
yannick.vanhove@univ-artois.fr, <http://www.iutbethune.org/>

²Mines Douai, LGCgE
764 Boulevard Lahure, F- 59508 Douai, France
sebastien.remond@mines-douai.fr, <http://www2.mines-douai.fr/>
patrick.pizette@mines-douai.fr, <http://www2.mines-douai.fr/>

Key words: Granular Materials, DEM, Interface, Roughness, Shear strip, Friction.

Summary: This paper deals with the behavior of packed spherical particles sheared on rough surfaces. The discrete element method (DEM) is used to model the granular material. Likewise, the roughness is modeled by spherical boundary conditions. From the simulations the effect of surface roughness on the shear strength and the granular material behavior near the interface is reported for various shearing conditions. The results of the numerical simulations showed that, for a particles roughness diameter larger than the average particles diameter of the granular material, the medium is uniformly sheared and the shear strength reaches a constant value. For smaller diameter of the particles roughness, the interface shear strength and the shear strip thickness increased with the diameter of the particles roughness.

1 INTRODUCTION

There are many examples illustrating the importance of predicting shear strength and granular behaviour at the interface between granular material and rough surface. When fresh concrete is being placed into the forms or during concrete pumping, a lubrication layer [1], called “boundary layer” is formed at the interface as illustrated in Figure 1.

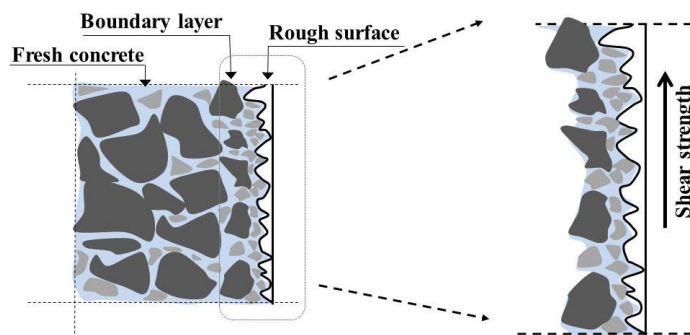


Figure 1: Schematic representation of the interface concrete – rough surface.

The understanding of the mechanisms leading to the formation of the boundary layer is important for the ability to ensure a good concrete placement in forms. As well, the concrete flow in the pipe is closely linked to the friction between the concrete and the wall [2]. Previous experimental work has been conducted on fresh concrete by using a plane tribometer, the results showed that many parameters related to the properties of the granular material and the surface characteristics play a crucial role in determining the shear strength at the interface [1]. Moreover, several studies in geotechnical engineering using different testing devices showed that the behaviour of the granular materials such as soils near the interface is closely related to soil deformations experienced by structures [3,4]. These two examples (interface concrete-wall and interface soil-structure) show that the interface behaviour plays an important role. This is why, understanding and characterizing the mechanisms at the interface, which is impossible by experiments due to difficulty in collecting microscopic information, is becoming increasingly important.

The Discrete Element Method (DEM) is a useful tool to model at grain scale the interface granular material – rough wall. To simulate such as interface, the main challenge is to be able to simplify its complexity and focus on determining the effect of roughness on the granular behaviour. At micro scale, the real surface roughness is represented by asperities. The shapes of asperities are irregular. In order to ease the roughness modeling, most of the previous studies have been conducted on regular roughness made of grains similar to the flowing grains. The results showed that the surface roughness has an effect on the behaviour of the granular material near the interface [5,6]. In this paper, an irregular roughness is modelled by monodispersed spherical particles spread arbitrarily on a horizontal plan. Regarding the real granular material which is composed of particles with different sizes and shapes, it is simplified by slightly polydispersed spheres, while the effects of particles rolling result from their shapes are taken into account by introducing a rolling resistance coefficient.

Until now, the influence of the roughness on the development of shear banding occurring near the interface and the shear strength is still not fully known. This paper presents a study on the effect of irregular roughness on interface behavior of DEM-simulated granular materials. The paper is organised as follows. The numerical model and the contact laws used are described in Sec.2. The simulation method is developed and described in Sec.3. The analysis of the data is given in Sec.4. In Sec. 5, the results of discrete particles simulations are discussed, while conclusions and perspectives are formulated in Sec.6.

2 NUMERICAL MODEL

Using DEM simulations, the understanding of the macroscopic behavior can be obtained from microscopic information. The Discrete Element Method (DEM) introduced by Cundall and Strack [7] is used here. In the DEM, the motion of each individual particle and its interactions with neighbouring particles and other objects over time are described. All the simulations presented here have been performed with an in-house DEM code (DemGCE) developed at Mines Douai [8,9,10,11]. The contact laws used in this study and presented below have been developed and tested in the silo configuration in previous works [11]. The semi-implicit Euler method is used for solving the differential equations of motion for each particle. In the smooth-DEM method, penetration between two particles in contact is allowed, and it is used as the basis of the force contact calculation. For instance, two adjoining particles

1 and 2 experience at contact point a relative overlap δ_n (1) which results in a contact force F_{12} (2) :

$$\overrightarrow{\delta_n} = (|X_1 - X_2| - R_1 - R_2) \overrightarrow{n_{12}} \quad (1)$$

with the normal vector between both particles, n_{12} , being parallel to the line connecting their centers and pointing from 2 to 1. Here, X_1 and X_2 are the particles positions, while R_1 and R_2 are their radii.

$$\overrightarrow{F_{12}} = F_n \vec{n} + F_t \vec{t} \quad (2)$$

The force between particles 1 and 2 acting at the contact point is decomposed into a normal (F_n) and tangential (F_t) components. The vectors n and t are respectively the unit vectors of the local reference system in the normal and tangential directions.

The normal contact force (3) shares between a nonlinear elastic force (Hertz model) and a dissipative force (Pöschel and Schwager model) [12,13]. The parameters of the elastic part are the Young's modulus E , Poisson's ratio v and the overlap δ_n while for the dissipative part, the model involves a damping coefficient A and the overlap δ_n .

$$\overrightarrow{F_{n,2 \rightarrow 1}} = -\frac{4\sqrt{R^*}}{3} \left(\frac{1-v_1^2}{E_1} + \frac{1-v_2^2}{E_2} \right)^{-1} \left(\delta_n^{\frac{3}{2}} + \frac{A_1 + A_2}{2} \delta_n \sqrt{\delta_n} \right) \cdot \vec{n} \quad (3)$$

where R^* is the effective radius $R^* = (R_1 \times R_2) / (R_1 + R_2)$.

The tangential contact force (4) is described by the Mindlin model (micro-slip) [14] (4) and limited by Coulomb criterion (entire slip) (8) which is characterized by the incremental linear force-displacement relationship in the elastic range.

$$\overrightarrow{F_{t,2 \rightarrow 1}(t)} = \overrightarrow{F_{t,2 \rightarrow 1}(t - \Delta t)} + \Delta \overrightarrow{F_t} \quad (4)$$

$$\Delta \overrightarrow{F_t} = K_t \overrightarrow{V_{12}(t)} \Delta t \quad (5)$$

The tangential stiffness K_t is given by equation (6), V_{12} is the relative velocity ($V_1 - V_2$) in the tangential direction and Δt is the time-step.

$$K_t = 8 G_{12} \sqrt{\delta_n R^*} \quad (6)$$

G_{12} represents the shear modulus (7).

$$G_{12} = \frac{1}{2} \left(\frac{E_1}{(2-v_1)(1+v_1)} \right) \left(\frac{E_2}{(2-v_2)(1+v_2)} \right) \quad (7)$$

Thereby the tangential contact force is represented by (8)

$$\overrightarrow{F_t} = \min (|\overrightarrow{F_{t,2 \rightarrow 1}(t)}|; |\mu \overrightarrow{F_{n,2 \rightarrow 1}}|) \quad (8)$$

The energy loss during the rolling is taken into account in our model by the rolling resistance torque defined in (9). Where $\mu_{rolling}$ is the rolling coefficient.

$$\vec{M}_{12} = -R^* \mu_{rolling} |F_{12,n}| \frac{\vec{\omega}_{12}}{|\vec{\omega}_{12}|} \quad (9)$$

$$\vec{\omega}_{12} = \vec{\omega}_1 - \vec{\omega}_2 \quad (10)$$

The relative angular velocity, ω_{12} , is calculated from the difference between the angular velocities of both particles.

The parameters used for the simulations are mentioned in Table 1. A parametric analysis was performed to elucidate the influence of the rolling and friction coefficients. The values of Young's modulus and time step were chosen to reduce the computational expense of simulation, while the values of the other parameters were fixed according to the most used values in the literature for glass beads which were used for an experimental approach and introduced in an earlier paper [15].

Table 1: Material and simulations parameters.

Parameter symbol (units)	Value
Young's modulus E (Pa)	1.0 E+8
Poisson's ratio ν (-)	0.29
Rolling coefficient $\mu_{rolling}$ (-)	0.002
Damping coefficient A (s^{-1})	4.5 E-5
Friction coefficient μ (-)	0.15
Time-step Δt (s)	1.0 E-6

3 SIMULATION METHOD

The discrete element simulations of dry spherical particles have been carried out in the plane shear geometry without gravity. Previous numerical investigations on this simple geometry were conducted for several purposes, e.g: Da Cruz et al [16] studied the third body flow inside a contact and the particle detachments have been modelled by Fillot et al [17].

In this study, to perform a simulation, two stages are requested: preparation of a confined packing and shearing stage. As a first stage, random sequential addition (RSA) algorithm [18] is used. 10000 spherical particles are randomly distributed without any overlap in a box with periodic boundary conditions in x and y directions [Figure 2-a]. The particles are slightly polydisperse in order to prevent crystallization, their size distribution lies within $\pm 10\%$ of the mean diameter d which is equal to 1.0 cm. The particles density ρ is 2.5 g/cm³. The box dimensions are 15d ; 20d ; 30d respectively in x, y and z directions. In order to prepare a confined packing, after the initial particles positions are determined, with no gravity, the rough walls move vertically at controlled velocity V_c (11).

$$V_c = signe(stress_t - P) * c \quad (11)$$

where $stress_t$ represents the confining pressure exerted by the particles on each rough wall at

instant t , P is the required confining pressure and c is a constant but influenced by the rigidity of the boundary condition.

During walls movement, the packing height changes [Figure 2-b]. The initial volume fraction was around 0.35 and the volume fraction of the confined packing reaches 0.62 [Figure 1-c].

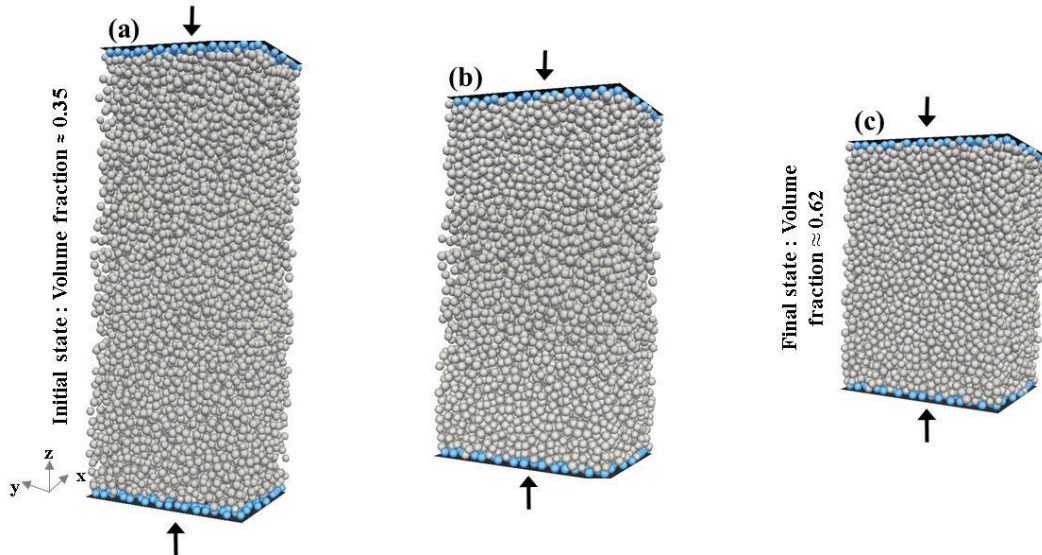


Figure 2: Preparation of confined packing.

The simulation was run until the confining pressure reaches the required confining pressure “ P ”. Figure 3-a depicts an example of the evolution of the confining pressure during the first stage for a desired value of 50 kPa. In the shearing stage [Figure 3-b], the confined packing is sheared between the two rough walls without gravity, y is the shear direction. As shown in figure 3-b the walls are moving horizontally in opposite direction at a velocity V_0 . During this stage, the confining pressure on each wall is controlled. Then, the normal velocity of the moving walls is given by (11).

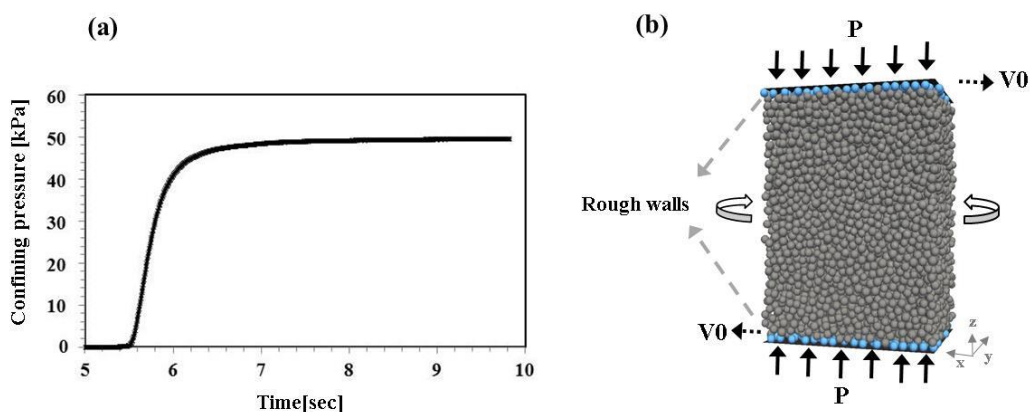


Figure 3: (a) Evolution of the confining pressure during the preparation of a confined packing and (b) Plane shear simulation.

The moving walls are roughened by coating their surface with a layer of monodispersed spheres (the spheres all have the same diameter). Wall roughness is thus defined as the diameter of the spheres. Indeed, actual surfaces are covered with hills and valleys of various sizes and shapes. To model an irregular roughness, the 2D RSA algorithm was used to distribute randomly the spheres on the wall. The spheres used for the roughness have diameters $0.5d$; $0.75d$; $1d$; $1.25d$; $1.5d$ and $2d$ respectively, where d is the mean diameter of the particles in the granular material.

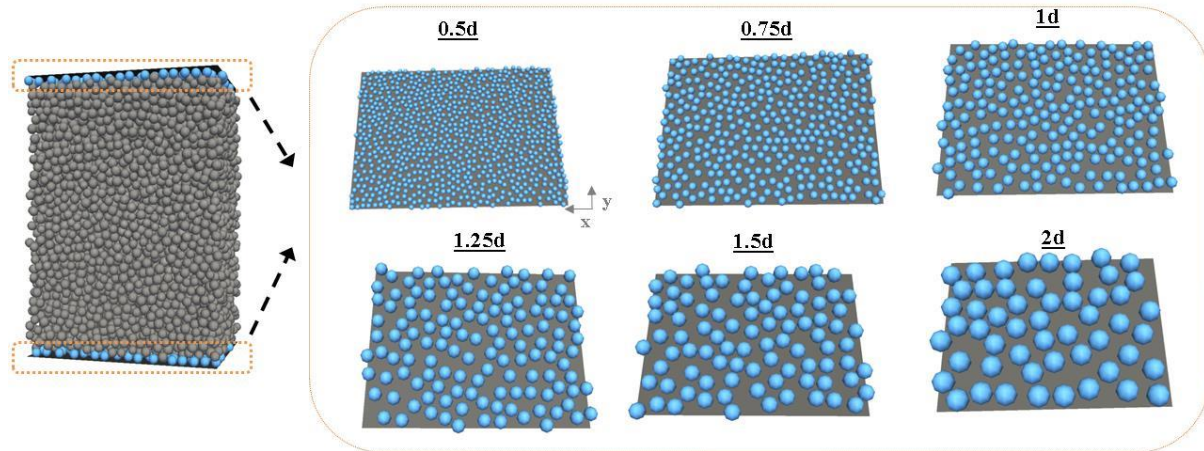


Figure 4: Roughness surfaces modeled by a packing of spherical boundary conditions.

Table 2 summarises the performed simulations.

Table 2: Summary of simulations.

Wall roughness	$0.5d \rightarrow 2d$
Confining pressure P (kPa)	50 ; 100 ; 200
Velocity V_0 (d/s)	10

The values mentioned in Table 2 are chosen for an inertial number I (12) smaller than 10^{-2} . Indeed, the results of discrete simulations conducted on regular roughness showed that the profile of mean velocity depends on I [19]. For small I (<0.1), the velocity profile is linear (absence of localization of the shear near the interface). However, the results obtained by Da Cruz et al [20] showed that localization may occur for very small I , small polydispersity, less rigid grains and with gravity which breaks homogeneity of the stress tensor.

$$I = \dot{\gamma} d \sqrt{\frac{\rho}{P}} \quad (12)$$

where $\dot{\gamma}$ is the shear rate (s^{-1}), d is the mean diameter of the particles in the granular material (m), ρ is the particles density (kg/m^3) and P is the confining pressure (Pa).

4 STEADY SHEAR STATE

During the rough walls movement, the particles of the granular material exert a force on each rough wall. The component of this force in the shear direction is called shear strength.

The Figure 5 shows an example of the shear strength evolution on the upper and the lower rough wall. The shear strength reaches a maximum “peak” and then decreases to a plateau. The peak corresponds to the necessary strength to interlock the irregularities of two surfaces in contact until motion occurs (static friction). The steady shear state is characterized by a kinetic regime (kinetic friction) where the fluctuations of the shear strength around the average are less than 10%. In this paper the term “shear stress” refers to the ratio of the average shear strength exerted on the two walls calculated in the plateau (steady shear state) to the rough wall surfaces. In each simulation, same upper and lower absolute value of the shear stress is obtained.

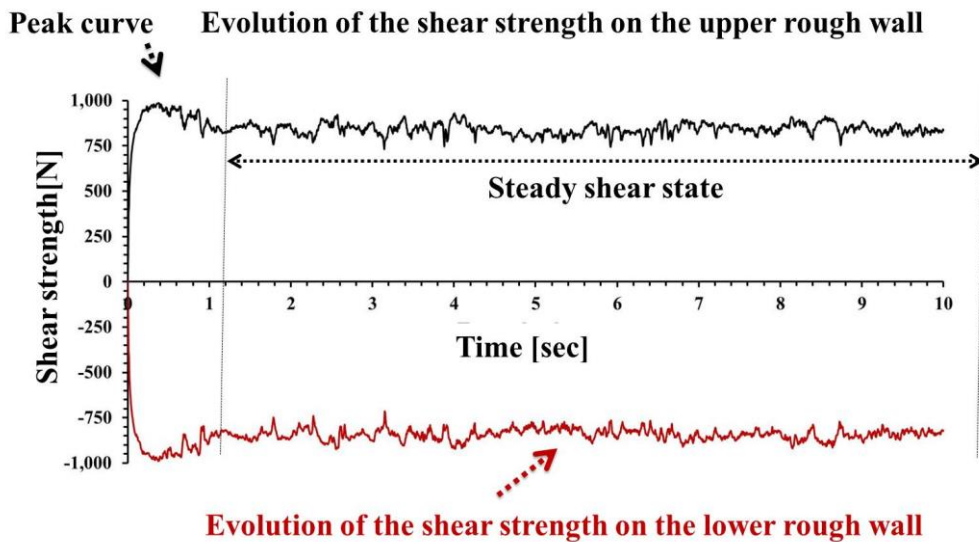


Figure 5: Evolution of the shear strength on the upper and the lower rough walls (roughness $2d$; $P = 100$ kPa and $V_0 = 10$ d/s).

As well, in the steady shear state, the velocity profile averaged in time has been plotted. This profile presents the variation of the particles velocities in the shear direction as a function of the simulated system height. For each momentary velocity profile (pr), the system is sliced into n horizontal layer with a thickness equal to mean particles diameter d [Figure 6-a]. The mean velocity $V_{m,j}$ in the layer j is then calculated : it is the sum of the ratio between particles velocities in the layer j , of all profiles (pr) and the particles number in the layer j .

$$V_{m,j} = \sum_{pr=1}^{pr=n_{pr}} \sum_{i=1}^{i=n_j(pr)} \frac{V_{ij}(pr)}{n_j(pr)} \quad (13)$$

$V_{i,j}(pr)$ is the momentary velocity in the shear direction of particle (i) in the layer (j) for profile (pr). And $n_j(pr)$ is the particles number in layer (j) for profile (pr).

Thus, the profile of mean velocity is described as the set of points which represent the mean velocities calculated in layer j ($j = 1 \rightarrow n$) [Figure 6-b].

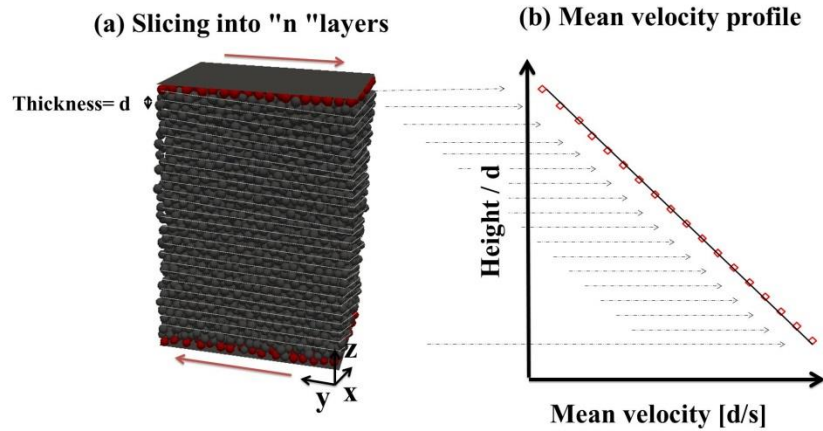


Figure 6: (a) slicing of the granular medium into n layers and (b) mean velocity profile.

5 RESULTS AND DISCUSSION

The Figure 7-a shows the influence of the roughness on the shear stress and mean velocity profile. In contrast of results obtained on regular roughness, the simulations of irregular roughness showed that for very small I ($< 10^{-2}$), the roughness has a significant effect on the shear stress and the mean velocity profile.

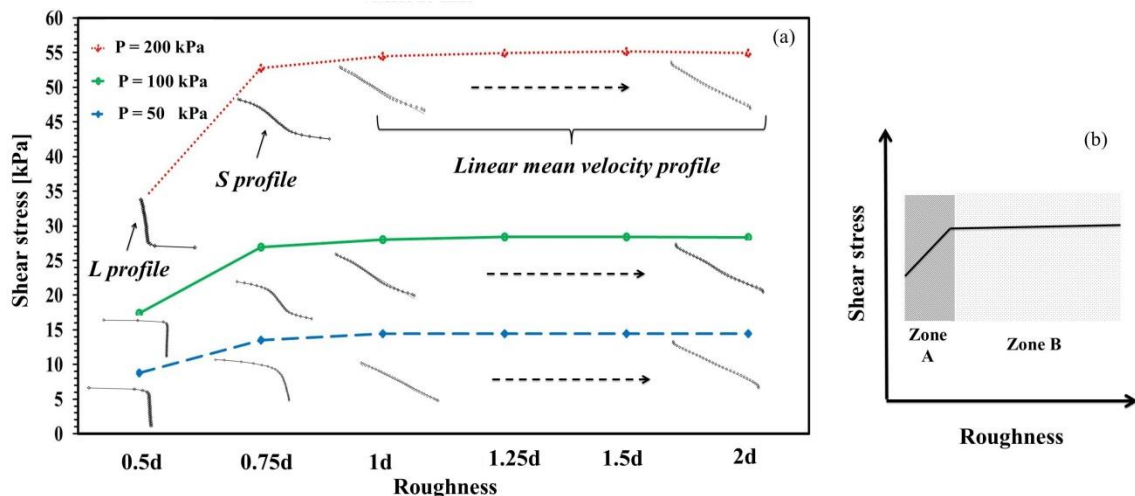


Figure 7: Shear stress as a function of roughness: mean velocity profile (dotted lines); $V_0 = 10$ d/s (Shear time = 10 seconds).

For each confining pressure P , the curve can be divided into two zones A and B [Figure 7-b]. The vertical line between both zones corresponds to a roughness diameter around $0.75d$. In zone A, it is revealed that for increasing roughness particles diameter, the shear stress increases. In addition, it can be observed that for a roughness of $0.5d$ the velocity profile has a

localization shear in one zone near the rough surface. In such cases, sliding occurs and the mean velocity profile has “L” shape. With increase in confining pressure and diameter of particles roughness, sliding decreases and the shape of the mean velocity profile passes from “L” to “S”. Whereas, in zone B, with the increase of the roughness particles diameter ($\geq 1d$), the shear stress remains constant and the velocity profile becomes linear. The transition from zone A to zone B shows that there is a critical diameter; in our case it is between $0.75d$ and $1d$, for which the roughness does not affect neither the shear stress, nor the velocity profile. Such findings may be explained as following: with the wall movement and for bigger roughness diameter, the asperities created between the roughness particles enhance the hanging of the granular material particles near the wall. Thus, shear can develop in the granular body and along the interface between granular material and rough wall (absence of shear localization). While for smaller roughness diameter ($< 1d$), the asperities of the rough wall are not large enough to allow shear development in the granular body.

5 CONSLUSIONS

The plane shear of spherical particles between two rough walls has been modeled with an in-house Discrete Element Method code (DemGCE) developed at Mines Douai. To generate a friction, both rough walls were moved in opposite directions, while the confining pressure is controlled. All simulations were performed with no gravity. In each simulation, the shear stress in the kinetic regime has been measured and the mean velocity profile has been plotted. Then, the effect on the wall roughness on each parameter has been studied.

In contrast with previous studies, the results showed that for small I (< 0.1), the roughness is an essential parameter which affects the shear stress and the mean velocity profile. Shear localization was observed for particles roughness diameter less than the mean particles diameter of the granular material. In this case, the shear stress increases with increasing roughness particles diameter. On the contrary, for bigger roughness particles diameter, the roughness has no effect on the shear stress nor mean velocity profile. The main outcome of this study was that the behavior of granular material near the interface depends essentially on the roughness asperities.

The effect of roughness on the granular behavior has been studied. A proper investigation on the understanding of the interlocking mechanisms near the interface should be carried out. Such a study leads to determine the critical depth of interlocking particles in the asperities from which the roughness does not affect the results.

REFERENCES

- [1] Djelal, C., Vanhove, Y. and Magnin, A. Tribological behaviour of self compacting concrete. *Cement and Concrete Research* (2004) **34**:821-828.
- [2] Ngo, T. T., Kadria, E. H., Bennacera, R. and Cussighb, F. Use of tribometer to estimate interface friction and concrete boundary layer composition during the fluid concrete pumping. *Construction and Building Materials* (2010) **24**:1253-1261.
- [3] Wang, J., Gutierrez, M. S. and Dove, J. E. Numerical studies of shear banding in interface shear tests using a new strain calculation method. *Int. J. Numer. Anal. Meth. Geomech* (2007) **31**:1349-1366.
- [4] Ebrahimian, B., Noorzad, A. and Alsaleh, M. I. Modeling shear localization along

- granular–structure interfaces using elasto-plastic Cosserat continuum. *International Journal of Solids and Structures* (2012) **49**:257-278.
- [5] Koval, G., Chevoir, F., Roux, J. N., Sulmen, J. and Corfdir, A. Interface roughness effect on slow cyclic annular shear of granular materials. *Granular matter* (2011) **13**: 525-540.
- [6] Da Cruz, F., Friction and jamming in granular flows, PhD thesis, Ecole Nationale des Ponts et Chaussées (2003).
- [7] Cundall, P. A. and Strack, O. D. L. *Géotechnique*, (1979) **29** : 47-65.
- [8] Rémond, S. DEM simulation of small particles clogging in the packing of large beads. *Physica A : Statistical Mechanics and its Applications* (2010) **389**:4485-4496.
- [9] Rémond, S. and Pizette, P. A DEM hard-core soft-shell model for the simulation of concrete flow. *Cement and Concrete Research* (2014) **58**:169-178.
- [10] Kimbonguila Manounou A. and Rémond, S. Discrete element modeling of the microstructure of fine particle agglomerates in sheared dilute suspension. *Physica A* (2014) **412**: 66-83.
- [11] Pizette, P. and Rémond, S. Experimental and numerical study of the effect of rolling friction for sandpile formation. WCCM XI conference, 20 – 24 July 2014, Barcelona, Spain.
- [12] Pöschel, T. and Schwager, T. Computational Granular Dynamics. *Springer* (2005).
- [13] Hertz, H. Über die Berührung fester elastische Körper. *J. Reine und angewandte Mathematik* (1882) **92**:156-171.
- [14] Mindlin, R. D. and Deresiewicz, H. Elastic spheres in contact under varying oblique forces. *Journal of Applied Mechanic*(1953) **20**:327-344.
- [15] El cheikh, K., Djelal, C., Vanhove, Y., Pizette, P. and Rémond, S. Etude de l'interface béton/paroi : Modélisation à l'échelle des grains. Acte de la conference Matériaux et Tribologie, Laboratoire de Physique et Mécanique Textiles, ENSISA, France-Mulhouse, 26-28 Mai 2014.
- [16] Da Cruz, F., Chevoir, F., Roux, J.N. and Iordanoff, I. Macroscopic friction of dry granular materials. *Transient Processes in Tribology, Proceedings of the 30th Leeds-Lyon Symposium on Tribiology (Tribology and Interface Engineering)*, Vol. **43** (2004).
- [17] Fillot, N., Iordanoff, I. and Berthier, Y. Kinetics of particle detachment : contribution of granular model. *Transient Processes in Tribology, Proceedings of the 30th Leeds-Lyon Symposium on Tribiology (Tribology and Interface Engineering)*, Vol. **43** (2004).
- [18] Sherwood, J. D. Packing of spheroids in three-dimensional space by random sequential addition. *J. Phys. A* (1997) **30**:839-843.
- [19] G. D. R. Midi. On dense granular flows. *The Europeon Physical Journal E* (2004) **14**:341-365.
- [20] Da Cruz, F., Emam, S., Prochnow M., Roux, J. N. and Chevoir, F. Rheophysics of dense granular materials : Discrete simulation of plane shear flows. *Physical Review E* (2008) **72** : 021309.

INVESTIGATIONS OF VORTEX STRUCTURES IN GRANULAR MATERIALS UNDER EARTH PRESSURE CONDITIONS BY DEM

MICHAŁ NITKA AND JACEK TEJCHMAN

Faculty of Civil and Environmental Engineering
Gdańsk University of Technology, Gdańsk, Poland
micnitka@pg.gda.pl, tejchmk@pg.gda.pl

Key words: DEM, Earth Pressure, Granular Materials, Shear Zone, Vortex.

Abstract. The evolution of shear zones in initially medium dense cohesionless sand for quasi-static earth pressure problems of a retaining wall was analysed with a 3D discrete element method DEM using spheres with contact moments. The passive sand failure for a very rough retaining wall undergoing horizontal translation was discussed. Attention was paid to vortex and anti-vortex structures appearing in granular shear zones. Three different methods were introduced to find granular vortices.

1 INTRODUCTION

The granular vortex structures (swirling motion of several grains around its central point) are frequently observed in experiments on dense granular materials - they are a direct manifestation of grain rearrangement and therefore they can be thought of as a basic mechanism of irreversible deformation [1-3]. They become apparent when the motion associated with uniform (affine) strain is subtracted from the actual granular deformation. They are reminiscent of turbulence in fluid dynamics (Radjai and Roux) [4], however the amount of the grain rotation is several ranges of magnitude smaller ($\sim 0.01^\circ$ - 0.1°) than the fluid vortex rotation and granular flow is too slow to induce inertial force characteristic for turbulences in fluid. They were studied by means of the discrete element method (DEM) by many researchers. The vortices are regarded as playing a strong role in heat convection in dry granular flows [5] and in reducing the amount of frictional dissipation in fault gouges [6]. According to Peters and Walizer [7] vortices represent an independent flow field following its own governing equations and satisfying its own (null) boundary conditions. The dominant mechanism responsible for vortex formation was the buckling of force chains [8], [9]. The collapse of main force chains leads to the formation of larger voids and their build-up to the formation of smaller voids [9].

In general, it is difficult to say at this stage of research whether vortex structures have any significant impact on the granular matter and how they could be taken into account in calculations. The reason is that the mechanisms ruling the creation and reduction of vortices are not fully recognized yet. The vortex structures were mainly observed in shear zones (they appear prior to shear banding) which are fundamental phenomena observed in granular soils under drained and undrained conditions [10-14]. Since the micromechanical behaviour and fabric properties of granular materials are inherently discontinuous, heterogeneous and non-linear, the application of the discrete element method DEM, which represents the material as an assemblage of independent grains interacting with one another, has immediate physical

appeal. DEM became more and more popular nowadays for modelling granular materials due to an increasing speed of computers, a connection to the finite element method [15], its usefulness in multi-scale approaches [16] and a realistic reproduction of micro-scale phenomena such as: vortices, periodic volume changes, micro-bands, force chains. Their disadvantages are: high computational cost, inability to model grain shape accurately and difficulty to validate it experimentally.

The objective of this paper is to present the comprehensive 2D studies by DEM of vortex and anti-vortex-structures in sand behind a rigid wall during its quasi-static passive translation by taking shear localization into account. We developed 3 different methods to identify swirling patterns of particle motions in the form of vortex- and anti-vortex-structures-structures from a displacement field in two dimensions. In order to accelerate the computation time, some simplifications were assumed: large cylindrical elements with contact moments, linear sphere distribution, linear normal contact model and no particle breakage. A three-dimensional discrete model YADE developed at University of Grenoble was applied [17,18]. The discrete calculations were solely carried out with initially dense sand. The paper consists of two main parts. In the first part, discrete elements results of a passive earth pressure were summarized to show the capability of DEM to realistically simulate shear localization in sand. In the second part, the formation of vortex structures was discussed. The evolution of these structures was compared with the evolution of force chains, contact forces, sphere contacts, local void ratio, grain rotations and grain displacements.

2 DISCRETE MODEL

In order to simulate the behaviour of real sand, a three-dimensional spherical discrete model YADE was developed at University of Grenoble [17,18] by taking advantage of the so-called soft-particle approach (i.e. the model allows for particle deformation which is modelled as an overlap of particles). A linear elastic normal contact model was used only. A choice of a very simple linear elastic normal contact was intended to capture on average various contacts possible in real sands. The normal and tangential forces were linked to the displacements through the normal stiffness K_n and tangential stiffness K_s (Fig.1A). The unloading was assumed to be purely elastic (Fig.1C). The frictional sliding starts at the contact point when the contact forces \vec{F}_s and \vec{F}_n satisfy the limit Coulomb condition (Fig.1Aa). No forces were transmitted when grains were separated. The elastic contact constants were specified from the experimental data of a triaxial compression sand test and could be related to the modulus of elasticity of grain material E and its Poisson ratio ν [19,20].

In order to increase the rolling resistance of pure spheres to better describe the grain kinematics encountered in real irregularly shaped grains (e.g. sand), contact moments were introduced [21-23]. The normal force was assumed to contribute to the rolling resistance. The contact moment increments were calculated by means of the rolling stiffness K_r multiplied by the angular rotational increment vectors $\Delta\vec{\omega}$ (Fig.1B). To dissipate excessive kinetic energy in the discrete system, a simple local non-viscous damping scheme was adopted [24], by assuming a change of forces and moment reduced due to the damping effect specified by the parameter α . Note that the effect of damping is insignificant in quasi-static calculations [20].

Although a non-linear contact law is more realistic, a linear contact law provides similar results with the significantly reduced computation time [20] and therefore was used in the

present simulations. The five main local material parameters are necessary in our discrete simulations: E_c (modulus of elasticity of the grain contact), ν_c (Poisson's ratio of the grain contact), μ (inter-particle friction angle), β (rolling stiffness coefficient) and η (limit rolling coefficient). In addition, a particle radius R , particle mass density ρ and numerical damping parameter α are required.

The discrete material parameters of DEM ($E_c, \nu_c, \mu, \beta, \eta$ and α) were calibrated using the corresponding homogeneous axisymmetric triaxial laboratory test results on Karlsruhe sand with the different initial void ratio and lateral pressure by Wu [25]. The index properties of Karlsruhe sand are: mean grain diameter $d_{50}=0.50$ mm, grain size between 0.08 mm and 1.8 mm, uniformity coefficient $U_c=2$, maximum specific weight $\gamma_d^{max}=17.4$ kN/m³, minimum void ratio $e_{min}=0.53$, minimum specific weight $\gamma_d^{min}=14.6$ kN/m³ and maximum void ratio $e_{max}=0.84$. The sand grains are classified as sub-rounded/sub-angular. The procedure for determining the discrete material parameters was described by Kozicki et al. [19,20].

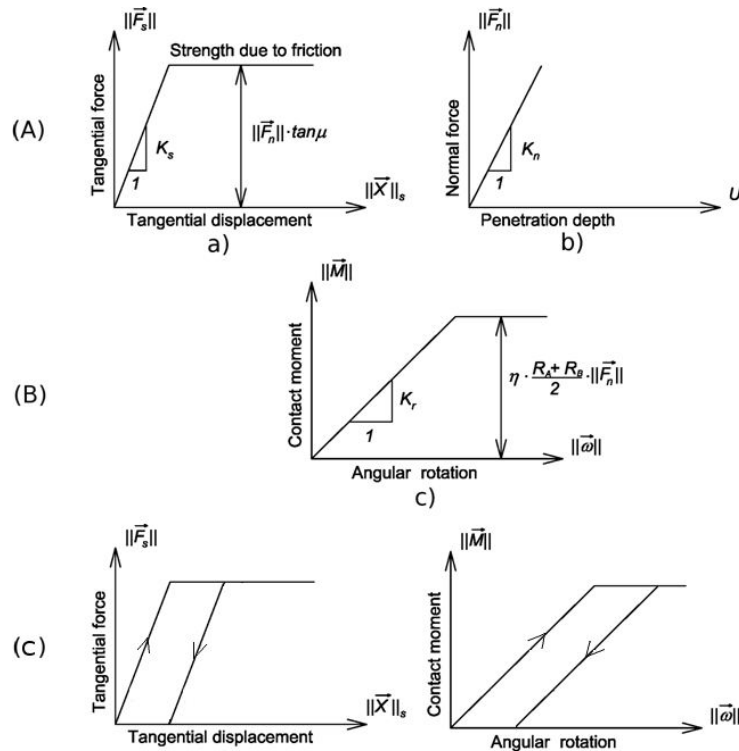


Figure 1: Mechanical response of linear contact model without (A) and with contact moments (A+B): a) tangential contact model, b) normal contact model and c) rolling contact model and C) loading and unloading path (tangential and rolling contact) wherein \vec{F}_s - tangential force vector between elements, \vec{F}_n - normal force vector between element, \vec{M} - contact moment vector, K_s - tangential stiffness, K_n - normal stiffness, K_r - rolling stiffness, U - penetration depth, \vec{x}_s - tangential displacement vector, $\vec{\omega}$ - angular rotation vector, μ - inter-particle friction angle, η - limit rolling coefficient [17], [18].

3 DISCRETE MODELLING RESULTS OF PASSIVE EARTH PRESSURE MODEL TESTS

The DEM calculations were performed for a sand body of 0.40 m length and 0.20 m height in order to compare with experiments with Karlsruhe sand ($d_{50}=0.5$ mm) [26,27]. The vertical retaining wall and the bottom of the granular specimen were assumed to be stiff and very rough, i.e. there was no relative displacement along vertical and bottom surface [9,27]. Since the experiments were idealized as a 2D boundary value problem [26] and the effect of the specimen depth in out of plane direction turned out to be almost negligible during direct shearing in DEM calculations [28], in order to significantly accelerate simulations, the computations were performed mainly with the specimen depth equal to the grain size (i.e. one layer of spheres was simulated only).

The spheres with $d_{50}=1.0$ mm, characterized by a linear grain size distribution, were assumed (grain size range 0.5-1.5 mm, 62'600 spheres). The initial void ratio of sand, obtained by generating random spheres above a box and then allowing them to fall down by gravity, was $e_o=0.62$. The loading speed was slow enough to ensure that the tests were conducted under quasi-static conditions. The calculated inertial number (which quantifies the significance of dynamic effects) in the analyses was below 10^{-3} , what corresponds to a quasi-static regime [29]. The calculations were carried out using parameters based on triaxial compression: $E_c=0.3$ GPa, $v_c=0.3$, $\mu=18^\circ$, $\beta=0.7$, $\eta=0.4$, $\rho=2.55$ g/cm³ and $a=0.08$. The CPU computation time was about 30 days using PC 3 GHz.

Figure 2A shows the evolution of the resultant normalized horizontal earth pressure force (earth pressure coefficient) $K_p=2E_h/(\gamma h^2 d_{50})$ versus the normalized horizontal wall displacement u/h ($h=0.2$ m, E_h – the horizontal force acting on the wall) from plane DEM simulation. The normalized horizontal earth pressure force evolves typically for initially dense granulates in biaxial compression, triaxial compression and shearing. The specimen exhibits on average the initial strain hardening up to the peak ($u/h=0.04$), followed by some softening before the common asymptote is reached. The force strongly fluctuates after the peak that can be attributed to the build-up and collapse of force chains - the main carrier of stresses transferred within the granular assembly [9]. The earth pressure coefficient is $K_p^{max}=3$. It can be thus anticipated that for $d_{50}=0.5$ mm (real sand), K_p^{max} should be about 25-27. The value of $K_p^{max}=30$ for $d_{50}=1$ mm is a little bit-smaller than $K_p^{max}=31$ obtained by FEM ($d_{50}=0.5$ mm) [27] and closer to the engineering earth pressure coefficients [30].

The distribution of single sphere rotations ω during wall translation is presented in Fig.2B (red denotes the sphere rotation $\omega>+30^\circ$ and blue $\omega<-30^\circ$, dark grey is related to the sphere rotation in the range $5^\circ \leq \omega \leq 30^\circ$ and light grey to the range $-30^\circ \leq \omega \leq -5^\circ$, positive sign means clockwise rotation). All grains rotating within the range $-5^\circ \leq \omega \leq 5^\circ$ are medium grey. Accepting such colour convention makes shear zones clearly observable (only particles within shear zones significantly rotate). There exists a clear grain separation regarding clockwise (red) and anti-clockwise (blue) rotation; the vast majority of ‘red grains’ is located within the dominant shear zone, while the vast majority of ‘blue grains’ is placed within the secondary radial shear zone (however there exists also a small amount of blue grains within the ‘red shear zone’ and vice versa). There is a qualitative agreement between DEM simulations and real experiments [27,31,32].

In order to determine the thickness of the shear zone, the assumption was made in this paper that the edges of a shear band are defined by an arbitrarily chosen amount of grain rotation, namely by the condition $|\omega|>5^\circ$. The shear zone thickness measured along the main curved shear zone at the mid-region at the residual state is: $t_s \approx 20$ mm ($20 \times d_{50}$) for $d_{50}=1.0$ mm. The mean inclination of the main curved shear zone to the horizontal is about 40° in the case of DEM results, and is close to the experimental values of 35° - 40° [27]. The maximum calculated single sphere rotation ω is about 75° at $u/h=0.15$ (Fig.2B). The inclination of the radial shear zone to the vertical is 50° . Except of the main shear zones, there exist also other faintly visible localized zones. The detailed DEM outcomes may be found in [16].

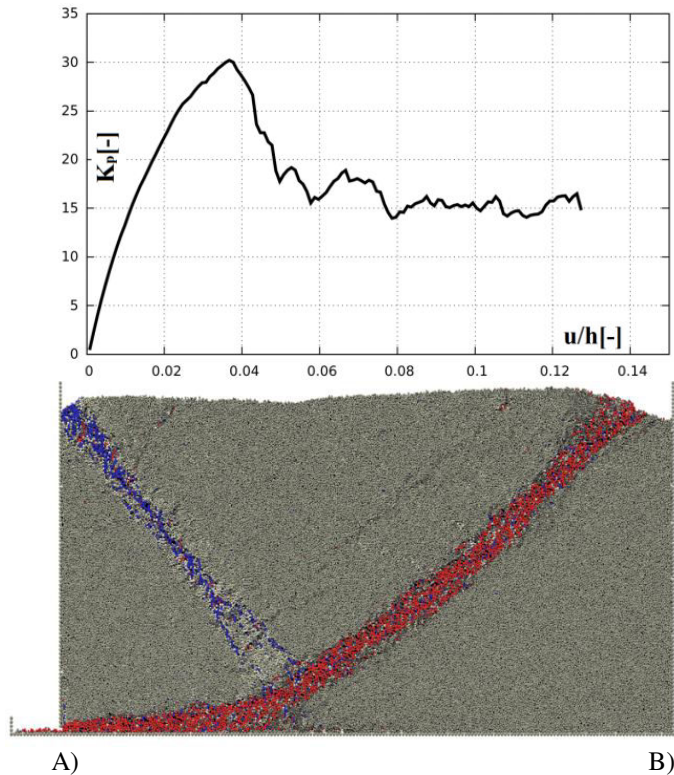


Figure 2: DEM results (passive case, translating wall): A) evolution of resultant normalized horizontal earth pressure force $2E_h/(\gamma h^2 d_{50})$ versus normalized horizontal wall displacement u/h and B) deformed granular body $0.2 \times 0.4 \text{ m}^2$ with distribution of rotation for initially medium dense sand ($\gamma=25.5 \text{ kN/m}^3$, $h=0.2 \text{ m}$, $e_o=0.62$, $d_{50}=1.0 \text{ mm}$, red colour denotes clockwise rotation $\omega > +30^\circ$, blue colour denotes anticlockwise rotation $\omega < -30^\circ$)

4 DETECTION OF VORTEX STRUCTURES

The vortex structures are equivalent with the fluctuation of the grain displacements which are usually calculated from the difference $\vec{V}_i - \vec{V}_{avg}$ between the displacement vector of each sphere and the average background translation corresponding to the homogeneous (affine) strain in the specimen. The vector \vec{V}_i represents the increment of sphere displacements and \vec{V}_{avg} is the average sphere displacement in the granular specimen.

The difference $\vec{V}_i - \vec{V}_{avg}$ was assumed to be equal to 10'000 iteration increments (that corresponded to the normalized wall horizontal displacement increment $u/h=0.002$). The

structures of vortices had the tendency to occur and to disappear in the course of deformation. The vortices along the radial shear zone were not calculated because of an insufficient magnitude of displacements within this zone (Fig.3). Looking at the curved shear zone, several clockwise rotating vortices ($k=13$) occurred along the shear zone (in agreement with the zone shear direction) having the diameter of about the shear zone width t_s ($t_s=20 \times d_{50}$). The distance between the vortices was variable – some of them were close to each other (at the distance of t_s) or far from each other (at the distance of about $4 \times t_s$).

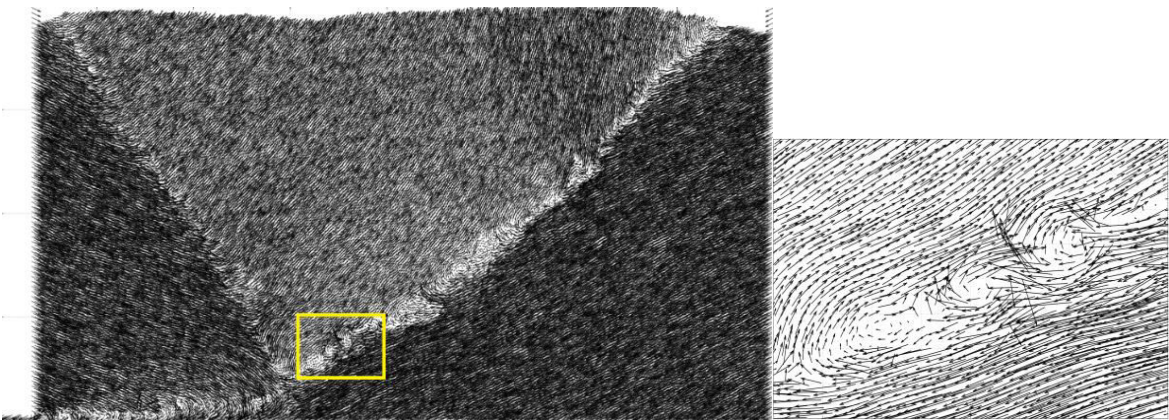


Figure 3: DEM results of displacement fluctuations of single spheres in granular specimen for $u/h=0.084$ (well visible vortex formation in curved shear zone in marked region) (vectors are multiplied by 50)

In order to detect vortex-structures, 3 different methods were used: 1) based on the mean pure rigid body rotation (called method '1'), 2) based on tangential displacement fluctuation vectors of spheres (called method '2'), 3) based on orientation angles of displacement fluctuation vectors of spheres (called method '3').

4.1 Method "1"

It was assumed that a vortex was connected with the rigid body rotation (spin) which was calculated by the usual formula (Fig.4): $R = 0.5(\frac{\Delta u_x}{\Delta y} - \frac{\Delta u_y}{\Delta x}) = 0.5(R_{x,y} - R_{y,x})$ with $R_{x,y} = \frac{u_{x1}-u_{x0}}{a_c} + \frac{u_{x3}-u_{x0}}{-a_c}$ and $R_{y,x} = \frac{u_{y2}-u_{y0}}{a_c} + \frac{u_{y4}-u_{y0}}{-a_c}$. The component Δu_x denotes the mean displacement increment in the direction 'X' (parallel to the shear zone), Δu_y denotes the mean displacement increment in the direction 'Y' (perpendicular to the shear zone) between two neighbouring square cells and u_{xi} and u_{yi} , the displacements in these cells and a_c - the square cell side size. The average background translation vanishes in this method. The field of the rigid body rotation (equivalent to the vortex-structures) was solely calculated for the curved shear zone inclined under the angle α to the horizontal (Fig.4). In general it may be calculated for each shear zone on condition that the inclination angle of the shear zone α is known in advance. The calculation algorithm was the following:

1. The displacement field of all single spheres was changed into a regular orthogonal lattice to calculate the mean displacement of spheres in the square cells $A_c=a_c \times a_c$ at the distance of d_{50} . The cell dimension was assumed to be smaller than the shear zone thickness t_s in order to capture the entire vortex whose diameter usually was $\leq t_s$.

2. In order to eliminate the rigid body rotation due to pure shear (e.g. $R_{x,y} \neq 0$ and $R_{y,x}=0$ or $R_{x,y}=0$ and $R_{y,x} \neq 0$ in Eq.10), the limitation was imposed on the shear components $R_{x,y}$ and $R_{y,x}$ in the following form: $R_{x,y}/R_{y,x} \leq m$.

The field of the rigid body motion limited to the curved shear zone is shown in Fig.5 with the cell area of $A_c=0.33t_s \times 0.33t_s$ and $m=3$. There were detected 7 vortices whose location was similar as in Fig.3. However their number was smaller than in Fig.3. The small vortices were not detected or they were connected to each other.

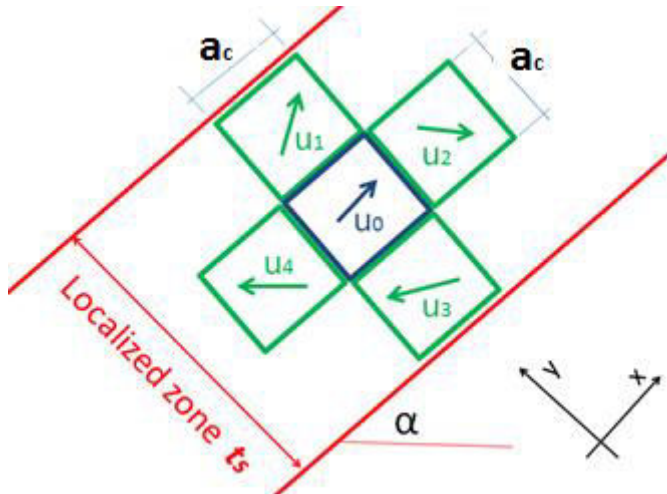


Figure 4: Schema for calculations of rigid body rotation in localized shear zone (u_i – mean displacement vector in cell area $a_c \times a_c$ (α – inclination angle of shear zone to horizontal, t_s - width of shear zone)

4.2 Method “2”

The vortices were calculated based directly on the displacement fluctuations of single spheres. The mean displacement fluctuation vector of sphere displacements in the square cell $A_c=a_c \times a_c$ (green spheres in Fig.6) in the neighbourhood of each central sphere (blue sphere in Fig.6) was decomposed into 2 vectors: the normal n and tangential t with respect to its movement direction. If the neighbouring spheres had a tangential displacement fluctuation component only, the blue sphere was assumed to be the vortex mid-point. The movement normal component moved solely the spheres closer or further from each other.

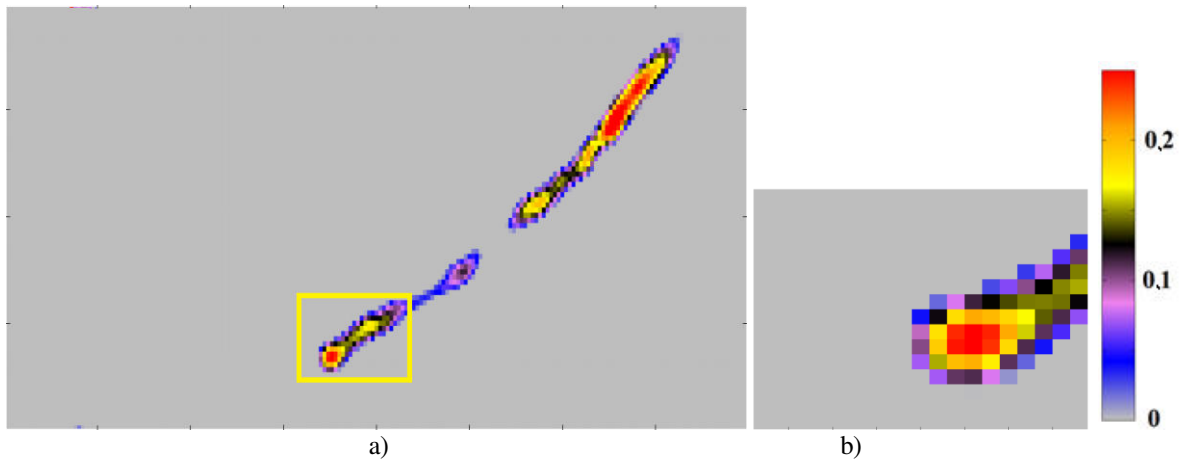


Figure 5: Map of spin A (Eqs.10-11) in curved shear zone using method '1' ($u/h=0.084$): a) entire specimen and b) zoom on marked region (red colour correspond to high rigid body rotation)

The vortex strength was determined as the sum of the tangential displacement fluctuation vectors of surrounding spheres for each single sphere. The anti-vortex strength was described as the sum of the absolute value of the tangential vectors of surrounding spheres. In order to avoid pure shear, the sum of the tangential displacement vectors was assumed to be higher than the sum of the normal displacement vectors: $\sum u_t / \sum u_n > m$. The average background translation was calculated for the entire granular specimen ($a_c = t_s$, $m = 2$). There were 13 clockwise vortices (as in Fig.3) and 2 anti-clock-wise vortices in the curved shear zone (Fig.7). The vortex size varied between 10-26 mm (the mean value was 18 mm $\approx t_s$).

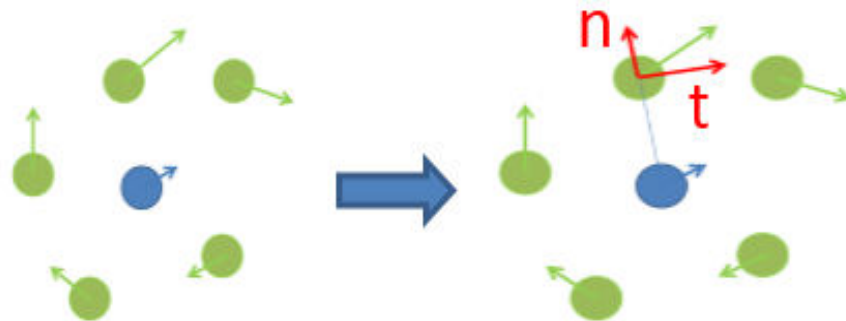


Figure 6: Decomposition of displacement vector v of green spheres surrounding main blue sphere into normal n and tangential t vector to its movement

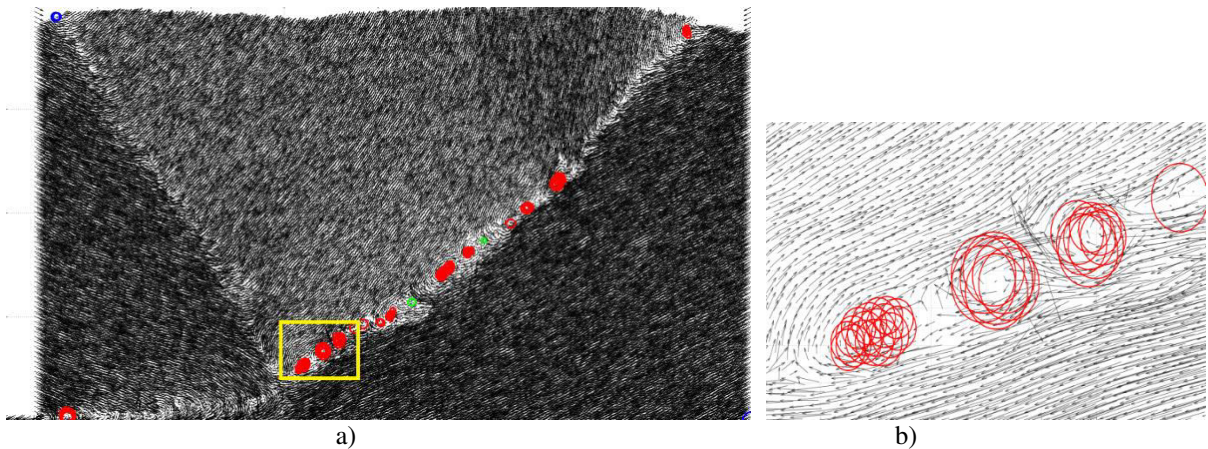


Figure 7: Displacement fluctuation vector field with marked vortices from DEM using method '2' ($u/h=0.084$):
a) entire specimen and b) zoom on marked region (red circles correspond to clock-wise vortices, blue circles to anti-clock-wise and green circle to anti-vortices)(vectors are multiplied by 50)

4.3 Method "3"

A special method used in the physics was applied, based on the orientation angles of the displacement fluctuation vectors of neighbouring single spheres was used [33]. Initially the displacement fluctuation field of irregularly distributed spheres was changed into a regular orthogonal lattice by calculating the mean displacement fluctuations of spheres inside the square cell $5d_{50} \times 5d_{50}$ at the points spaced by the d_{50} -distance in the both directions on the 2D grid. In order to find the centre of a vortex, a group of 4 angles (spins) was chosen which were the corners of the square $d_{50} \times d_{50}$ on the 2D grid. Each corner was the result of the average displacement fluctuation from the square $A_c = 5d_{50} \times 5d_{50}$. The set of 4 spins was chosen to determine whether they rotated by $\pm 2\pi$ as the eye went from one spin to the next in a clockwise or an anti-clockwise direction around the square (Fig.8). The vortex was detected in the lattice when the spins of the normalized displacement fluctuation vectors rotated by at least 2π , i.e.

$$-2.01\pi < \sum \alpha_i = \alpha_1 + \alpha_2 + \alpha_3 + \alpha_4 < -1.99\pi \quad (1)$$

as the eye moved clockwise around the closed path (Fig.8a) or 2π , i.e.

$$1.99\pi < \sum \alpha_i = \alpha_1 + \alpha_2 + \alpha_3 + \alpha_4 < 2.01\pi \quad (2)$$

in the anti-clockwise direction (Fig.8n). Note that the vector length was ignored. In turn, the anti-vortex (equivalent with shear, Fig.8d) might occur if $\sum \alpha_i = -2\pi$ as the eye moved in an anti-clockwise direction or $\sum \alpha_i = 2\pi$ as the eye moved in a clockwise direction (it could also be left- and right-handed). In order to describe the vortex type, two checks were always carried out; one in the clockwise and one in the anti-clockwise direction. Usually, only one check satisfied the conditions in Eqs.1 and 2. However, very rarely this condition was twice satisfied due to the assumed range equal to 0.02π . In order to eliminate the frequency noise (caused by the fact that spins rapidly and chaotically changed their directions as the eye moved to the next one), the maximum allowed angle which varied between the neighbouring corners was taken as $\leq 160^\circ$ (Fig.8a). If any angle between two neighbours was larger than 160° , the check in the cell was aborted. One may also use the approach with a higher number of vectors around the selected point 'p' - e.g. with 8 vectors (Figs.8c and 8d) that allows for determining more vortices.

The results are shown in Fig.9 (for 4-vector approach). This method allows for capturing for very small vortices. In the curved shear zone 22 vortex-structures were found for the average background translation calculated for entire granular specimen (Fig.9) against 13 in Fig.3. Some vortices were close to each other and create a large structure composed of 2-4 vortices.

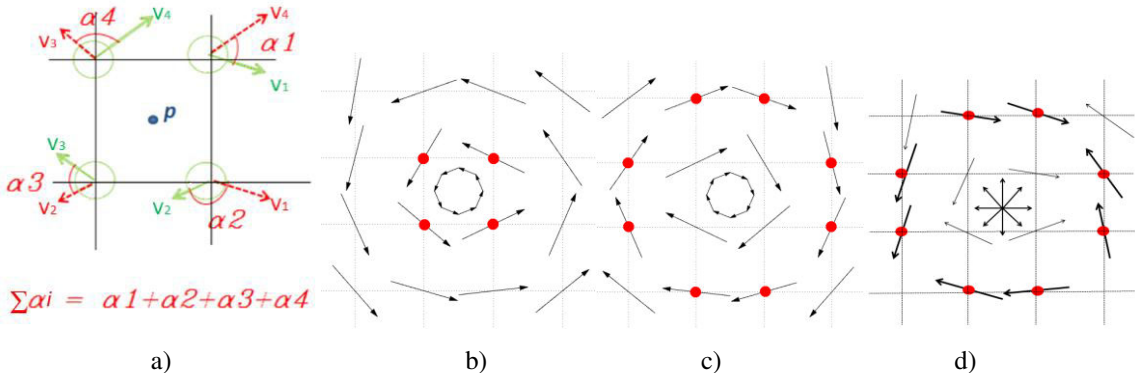


Figure 8: The displacement fluctuation vectors of single spheres using method '3' (p - sphere in mid-point):
a) orientation angles α_i , b) 4-vector approach to determine left-handed vortex, c) 8-vector approach to determine right-handed vortex and d) 8-vector approach to determine right-handed anti-vortex
(distance between spins is d_{50})

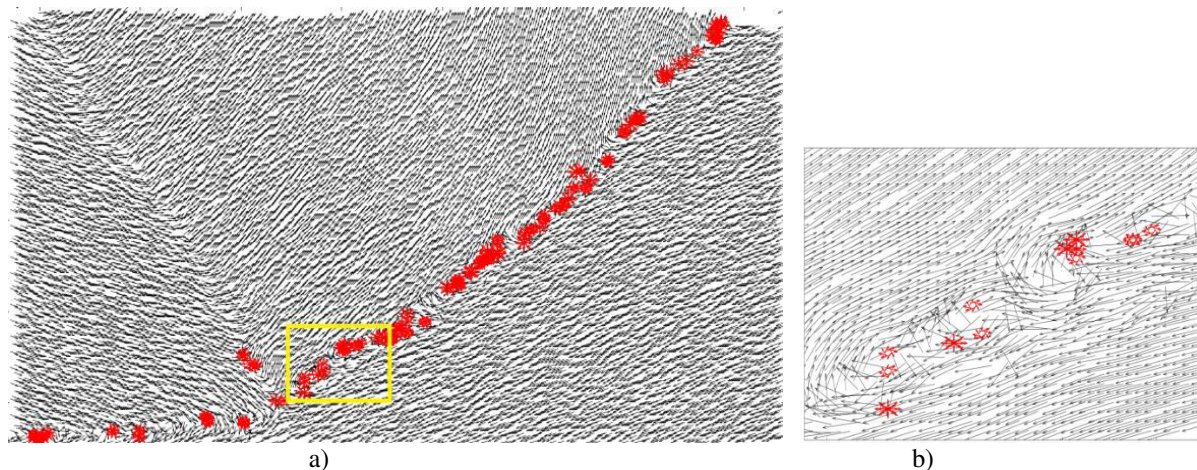


Figure 9: Displacement fluctuation vector field with marked vortices from DEM using method '3' ($u/h=0.084$): a) entire specimen and b) zoom on marked region (circles correspond to vortices and stars correspond to anti-vortices, black arrows correspond to mean displacement fluctuation field)

5 CONCLUSIONS

The following conclusions can be drawn from our DEM analyses of a pattern of shear zones during a passive earth pressure problem:

- DEM, which directly takes micro-structures of granular bodies into account, realistically predicts the experimental results of a pattern of shear zones in the interior of initially medium dense sand behind a retaining wall. Grain rotations are noticeable only in shear zones.

- In shear zones, vortex structures systematically occur which are a direct manifestation of grain rearrangement. The number of the detected vortices was the highest in the method “3” which did not take into account the length of the displacement vector.

Acknowledgment

The authors would like to acknowledge the support by the grant 2011/03/B/ST8/05865 “*Experimental and theoretical investigations of micro-structural phenomena inside of shear localization in granular materials*” financed by Polish National Research Centre.

REFERENCES

- [1] Utter B, Behringer RP. Self-diffusion in dense granular shear flows. *Phys. Rev. E.* (2004); 69(3), 031308-1–031308-12.
- [2] Abedi S, Rechenmacher AL, Orlando AD. Vortex formation and dissolution in sheared sands. *Granular Matter* (2012); 14: 695–705.
- [3] Richefeu V, Combe G, Viggiani G. An experimental assessment of displacement fluctuations in a 2D granular material subjected to shear. *Geotechnique Letters* (2012); 2: 113–118.
- [4] Radjai F, Roux S. Turbulent-like fluctuation in quasi-static flow of granular media. *Phys. Rev. Lett.* (2002); 89, 064302.
- [5] Rognon P, Einav I. Thermal transients and convective particle motion in dense granular materials. *Phys. Rev. Lett.* (2010), 105(21), 218301.
- [6] Williams JR, Rege N. Coherent vortex structures in deforming granular materials. *Mechanics of Cohesive-frictional Materials* (1997); 2: 223-236.
- [7] Peters JF, Walizer LE. Patterned nonaffine motion in granular media. *Journal of Engineering Mechanics* (2013); 139, 10: 1479-1490.
- [8] Tordesillas, A., Pucilowski, S., Lin, Q, Peters, J.F., Behringer, R. P. Granular vortices: identification, characterization and conditions for the localization of deformation. *Journal of Mechanics and Physics of Solids*, (2015).
- [9] Nitka, M., J. Tejchman, J., Kozicki, J. and Leśniewska, D. DEM analysis of micro-structural events within granular shear zones under passive earth pressure conditions. *Granular Matter*, (2015), doi: 10.1007/s10035-015-0558-0.
- [10] Desrues J, Viggiani C. Strain localization in sand: over- view of the experiments in Grenoble using stereophotogrammetry. *J. Numer. Anal. Methods Geomech.* (2004); 28(4):279–321.
- [11] Gudehus G., Nübel K. Evolution of shear bands in sand. *Geotechnique* (2004); 113 54(3):187–201.
- [12] Tejchman J. *FE modeling of shear localization in granular bodies with micro-polar hypoplasticity*. Springer Series in Geomechanics and Geoengineering (eds. Wu and Borja), Springer Verlag, Berlin-Heidelberg, (2008).
- [13] Tejchman, J., Gorski J. Computations of size effects in granular bodies within micro-polar hypoplasticity during plane strain compression. *Int. J. Solids Struct.* (2008); 45(6):1546–1569.
- [14] Gudehus G. *Physical Soil Mechanics*, Springer, (2011).

- [15] Rojek J. Discrete element modelling of rock cutting. *Computer Methods in Materials Science* (2007); 7, 2: 224–230.
- [16] Nitka M, Combe G, Dascalu C, Desrues J. Two-scale modeling of granular materials: a DEM-FEM approach. *Granular Matter* (2011), 13, 277-281.
- [17] Kozicki J, Donze FV. A new open-source software developed for numerical simulations using discrete modelling methods. *Computer Methods in Applied Mechanics and Engineering* (2008); 197, 4429-4443.
- [18] Šmilauer V, Chareyre B. *Yade DEM Formulation*. Manual, (2011).
- [19] Kozicki J, Tejchman J, Mróz Z. Effect of grain roughness on strength, volume changes, elastic and dissipated energies during quasi-static homogeneous triaxial compression using DEM. *Granular Matter* (2012), 14(4):457-468.
- [20] Kozicki J, Tejchman J., Mühlhaus HB. Discrete simulations of a triaxial compression test for sand by DEM. *Int. J. Num. Anal. Methods in Geomech.* (2014); 38, 1923-1952.
- [21] Iwashita K, Oda M. 1998. Rolling resistance at contacts in simulation of shear band development by DEM. *ASCE J Eng Mech*, 124(3), 285–92.
- [22] Jiang MJ, Yu H-S, Harris D. 2005. A novel discrete model for granular material incorporating rolling resistance. *Computers and Geotechnics* 32, 340-357.
- [23] Mohamed A, Gutierrez M. Comprehensive study of the effects of rolling resistance on the stress-strain and strain localization behaviour of granular materials. *Granular Matter* 12 (2010) 5, 527-541.
- [24] Cundall PA, Hart R. Numerical modeling of discontinua. *J. Eng. Comp.* (1992); 9: 101–113.
- [25] Wu W. Hypoplastizität als mathematisches Modell zum mechanischen Verhalten granularer Stoffe. *Heft 129, Institute for Soil- and Rock-Mechanics, University of Karlsruhe*, (1992).
- [26] Gudehus G and Schwing E. Standsicherheit historischer Stützwände. *Internal Report of the Institute of Soil and Rock Mechanics*, (1986), University Karlsruhe.
- [27] Tejchman J. FE modeling of shear localization in granular bodies with micro-polar hypoplasticity. *Springer Series in Geomechanics and Geoengineering* (eds. Wu and Borja), Springer Verlag, Berlin-Heidelberg (2008).
- [28] Kozicki J, Niedostatkiewicz M, Tejchman J, Mühlhaus H.-B. Discrete modelling results of a direct shear test for granular materials versus FE results. *Granular Matter* (2013), 15, 5: 607-627.
- [29] Roux, J.N., Chevoir, F. Discrete numerical simulation and the mechanical behaviour of granular materials. *Bulletin des Laboratoires des Ponts et Chaussees* 254 (2005), 109-138.
- [30] Gudehus, G. *Erddruckermittlung. Grundbautaschenbuch*, Teil 1, Ernst und Sohn. 1996.
- [31] Lucia J.B.A. Passive earth pressure and failure in sand. *Research Report*, University of Cambridge (1966).
- [32] Niedostatkiewicz M, Leśniewska D, Tejchman J. Experimental analysis of shear zone patterns in sand for earth pressure problems using Particle Image Velocimetry. *Strain*, 47, (2011) ,s2, 218-231.
- [33] Gould H, Tobochnik J, Christian W. Introduction to Computer Simulation Methods: Application to Physical Systems (3rd edition), chapter 15, page 655.

MICROMECHANICAL ANALYSIS OF THE SURFACE EROSION OF A COHESIVE SOIL BY MEANS OF A COUPLED LBM-DEM MODEL

PABLO CUÉLLAR¹, PIERRE PHILIPPE¹, STÉPHANE BONELLI¹, NADIA BENAHMED¹, FLORIAN BRUNIER-COULIN¹, JEFF NGOMA², JEAN-YVES DELENNE³ AND FARHANG RADJAI^{4,5}

¹ IRSTEA, French Research Institute of Science and Technology for Environment and Agriculture
3275 route de Cézanne, 13100 Aix-en-Provence, France
pablo.cuellar@irstea.fr, pierre.philippe@irstea.fr, stephane.bonelli@irstea.fr,
nadia.benahmed@irstea.fr, florian.brunier@irstea.fr, <http://www.irstea.fr/>

² Institut Jean Lamour, CNRS - Université de Lorraine, Parc de Saurupt
CS 50840, 54011 Nancy, France
jeff.ngoma@univ-lorraine.fr, <http://ijl.univ-lorraine.fr/>

³ UMR IATE, INRA – CIRAD - Montpellier Supagro - Université Montpellier 2
2 place Pierre Viala, 34060 Montpellier, France
delenne@supagro.inra.fr, <http://umr-iate.cirad.fr/>

⁴ Laboratoire de Mécanique et Génie Civil, CNRS - Université Montpellier 2
Place Eugène Bataillon, 34095 Montpellier, France
Franck.Radjai@univ-montp2.fr, <http://www.lmgc.univ-montp2.fr/>

⁵ UMI 3466 CNRS – MIT, Department of Civil and Environmental Engineering, MIT, 77
Massachusetts Avenue, Cambridge CA 02139, USA
fradjai@mit.edu, <http://www.cee.mit.edu/>

Key words: Surface erosion, cohesion, DEM, LBM.

Abstract. The elementary mechanisms driving the ubiquitous surface erosion of cohesive geomaterials can be analysed from a micromechanical perspective combining well-known numerical techniques. Here, a coupled model combining the Discrete Element and Lattice Boltzmann methods (DEM-LBM) provides an insight into the solid-fluid interaction during the transient erosion caused by a vertical fluid jet impinging on the surface of a granular assembly. The brittle cementation providing cohesion between the solid grains is described here by means of a simple bond model with a single-parameter yield surface. The initial topology of the surface erosion tends to mimic the profile of fluid velocity directly above the soil surface. We find that both the rate of erosion and the magnitude of eroded mass depend directly on the micromechanical strength of the single solid bonds.

1 INTRODUCTION

The geomechanical assessment of the surface erodibility of soils is usually performed empirically, often by means of standard experimental tests such as the Jet Erosion Test (JET, see e.g. [1]) and the Hole Erosion Test (HET, see e.g. [2] and [3]). The soils analysed by

means of these tests are generally cohesive geomaterials, while the water flowing on their surface behaves as eroding agent.

The erodibility is commonly quantified in terms of the average hydrodynamic shear stress at the soil surface with respect to a threshold, the critical shear stress, for the initiation of erosion. However, in practice the eroding process is much more complex and involves local transient flows such as turbulent jets with intermittent spikes of local hydrodynamic stress. On the other hand, the derivation of a reliable empirical expression for the critical stress has been hindered by the large variety of sediment properties that are relevant for the inter-particle forces of cohesive soils and their complex relationships [4]. All this has led to a general lack of consensus over the robustness of the different testing procedures as well as on the analysis methods, in particular on the assumptions for the assessment of the critical shear stress [5].

From the theoretical side, the starting point of most numerical approaches employed so far to study the erosion of geomaterials is merely macromechanical with both water and soil described as continuous media. Different techniques have therefore been proposed in order to track the transient evolution of their interface, where mass exchange between phases (i.e. the actual erosion) takes place [6]. On the one hand, the purely Eulerian approaches permit the use of a fixed mesh but they do not allow for a precise definition of hydro-mechanical variables at the interface. In a similar vein, hybrid Eulerian-Lagrangian methods may show a good precision at the interface but they often lead to severe and time-consuming remeshing issues [6].

The aim of the present work is to introduce an alternative approach based on discrete-element simulations of a cohesive granular bed impacted by a fluid jet modelled by the Lattice Boltzmann method. This is a micro-mechanical approach, which allows for the investigation of different factors driving the elementary mechanisms of erosion, such as the detachment of particle aggregates at the soil surface (surface erosion) or the dislodgement of lumps of material below the free surface (mass erosion) [7].

We introduce below our numerical approach and its application to a JET test on a granular bed with increasing cohesion between grains. A simple model of inter-particle cohesion will be considered, and its consequences for the bed's erodibility will be discussed.

2 NUMERICAL METHOD

There are various coupled methods developed so far for the numerical simulation of fluid-solid interactions at the particle-scale. The approach adopted here combines the computational efficiency of the Lattice Boltzmann Method (LBM) for the simulation of fluids with the relative simplicity of the Discrete Element Method (DEM) for the simulation of solid particles. This approach has already been applied to several geomechanical problems (see e.g. [8-10]).

2.1 Solid phase. A DEM approach

The granular soil is described here by means of a smooth discrete element approach based on the Molecular Dynamics method [11]. We use a two-dimensional assembly of circular particles whose trajectories are computed by simple integration of Newton's equations of motion. The smooth inter-particle contact and friction laws are supplemented by cohesive interactions (see e.g. [12-14]). Here, we consider a simple cohesive law depicted in Figure 1

for contact interactions [12].

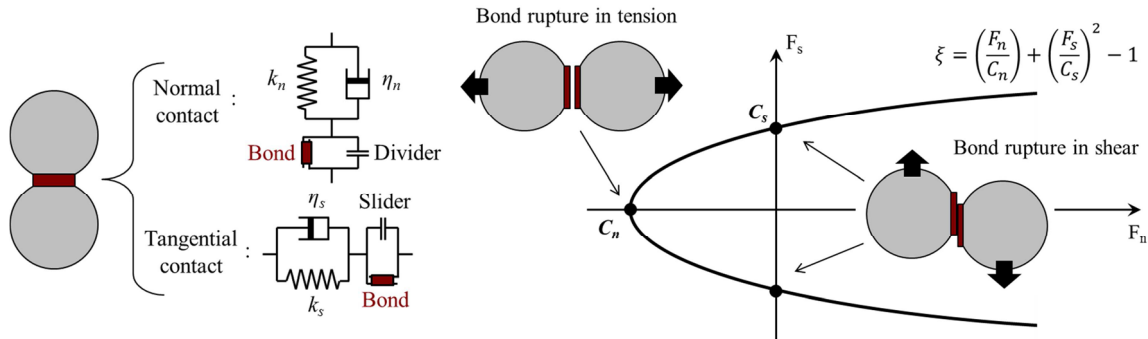


Figure 1: Left: Rheological model of solid contacts, after [14]; Right: Yield surface of cohesive bonds in the space of interaction forces

The interaction between two particles is thus formulated in terms of an interaction force F and an interaction moment M applied at the contact point. The interaction force is decomposed into its normal and shear components, F_n and F_s respectively, corresponding to the normal and tangential directions at the contact. The normal force F_n is described in terms of the local interpenetration δ_n by means of a classical Kelvin-Voigt viscoelastic relationship defined by the normal stiffness and damping coefficients, k_n and η_n . On the other hand, the shear force arising at a frictional (non-cohesive) contact is defined here by a viscous-regularized Coulomb law [15, 16] characterized by a static friction coefficient μ and a viscous coefficient of shear regularization k_s . In this way, the shear force is computed as a function of the sliding velocity $\dot{\delta}_s$, which in practice never really vanishes. Due to the small time steps considered here (in the order of 10^{-6} s), the quasi-static equilibrium of particles under the action of static friction forces is reached through residual micro-slips. The force moment acting on each particle's centre is defined from the shear force with the particle's radius as lever arm, and a rolling friction component that governs the rolling motion of the particles (relative rotation without sliding). The latter is analogous to the sliding friction in which the relative velocity of rotation replaces the sliding velocity, and the rolling friction coefficient μ_ω and the coefficient of regularization k_ω replace the sliding friction coefficient and its regularization factor [13, 15].

The ingredients presented so far describe the purely frictional contacts. In order to introduce cohesion allowing for tensile normal forces between the solid particles, a simple elastoplastic model with parabolic yield surface in the space of contact forces has been employed (Figure 1). In this way, a solid bond is defined for all particles initially at contact, featuring a linear elastic rheology characterized by the normal and shear bond stiffnesses $k_{n,b}$ and $k_{s,b}$. When a contact force reaches the yield surface, the bond is broken and the contact becomes purely frictional. For convenience, the normal and shear yield thresholds C_n and C_s are assumed to depend only on a single parameter $C = C_n = 2 \cdot C_s$, which represents the strength or degree of cementation of the solid bond. The relative strength of the bonds in the polydisperse assembly can be characterized by a dimensionless number defined as the ratio of bond cohesion to the particle's own buoyant weight. This cohesive Bond number would then be expressed as:

$$B = \frac{C}{\Delta\rho g V} \quad (1)$$

where $\Delta\rho$ is the submerged apparent density of the solid grains, g is the gravitational acceleration and V is the volume of the particle. In general it can be noted that $B \geq 0$ and that solid bonds with $B < 1$ are unstable and short-lived since any slight rearrangement of the assembly under its own weight has the potential to cause bond rupture. Our numerical tests show that the granular bed remains completely bonded under gravity for $B \geq 3$ for all particles in the sample.

2.2 Fluid phase. The LBM method

The transient flow of the fluid phase is described here by means of a classical D2Q9 scheme of the lattice Boltzmann method, which is an explicit finite difference scheme of the continuous Boltzmann equation [18, 19]. The LBM is based on a Cartesian lattice grid in the space and a discrete set of probability density functions and velocities of fluid particles at each grid point. The fluid dynamics are then computed in just two basic steps for the collision and advection of the fluid particles following a set of rules that ensure the conservation of mass, momentum and energy (i.e. the incompressible Navier-Stokes behaviour). However this only holds for low Mach numbers, i.e. when fluid velocity is much lower than the lattice speed. We used the generalized formulation of d'Humières with a multiple relaxation time (MRT) in order to overcome the well-known shortcomings of the classical Bhatnagar-Gross-Krook scheme (single relaxation time) [20, 21]. Hence, the fluid phase is fully defined by specifying the lattice grid size Δx and lattice speed c_s , the components s_α of the diagonal relaxation matrix S (inverse of the different relaxation times) and the fluid material parameters of density ρ_f and kinematic viscosity ν [10].

2.3 Solid-fluid coupling

The coupling between the fluid and solid phases and the computation of hydrodynamic forces on the particles are performed by means of the simple method for momentum exchange proposed by Bouzidi et al [22], which relies on a generalized bounce-back and linear interpolation strategy for arbitrary geometries in the LBM. The sub-cycling time integration technique proposed by Feng et al [23] was used to exploit the fact that the time step required for the fluid computation is generally much larger than that for particle dynamics. The number of DEM subcycles for each LBM step was nevertheless restricted to 2 in order to preserve the accuracy of the computed hydrodynamic forces on the solid particles. In order to account for fluid flow across a densely packed assembly of particles in two dimensions, a “hydraulic” radius slightly smaller than the particle radius was used [24, 25].

3 ANALYSIS OF JET EROSION

Figure 2 illustrates the general configuration of a jet erosion test and its relevant dimensions. The dimensions of the system were chosen to mimic our on-going physical tests [26] for a later comparison. We have an initial jet-bed distance $H = 70$ mm, a nozzle diameter of $d_0 = 5$ mm and average grain size $D_{mean} = 3$ mm. A size polydispersity ($D_{max}/D_{min} = 1.5$) was introduced in order to avoid crystalline configurations of the two-dimensional granular

sample.

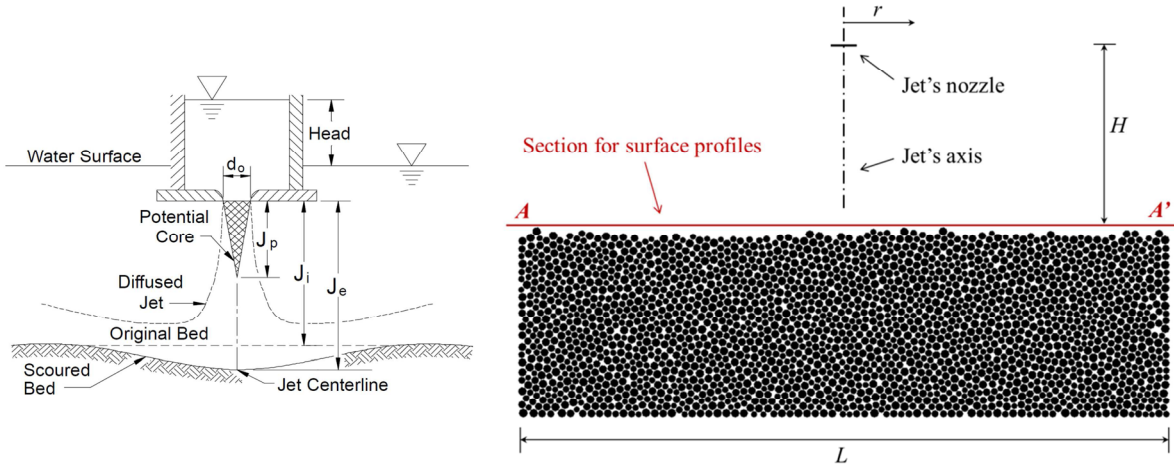


Figure 2: Left: Conceptual sketch of jet erosion test (source: [1]); Right: Spatial disposition of granular assembly, jet's nozzle and control section for fluid variables

The geometrical, material and rheological parameters of the system employed for these simulations are summarized in Table 1.

Table 1: Geometrical, material and model parameters adopted for the simulations

Solid phase	Fluid phase
Particle mean size, D_{mean}	3×10^{-3} m
Polydispersity, D_{max} / D_{min}	1.5
Length of granular sample, L	2.63×10^{-1} m
Height of granular sample, H_s	8×10^{-2} m
Particle density, ρ_s	2230 kg/m^3
Normal contact stiffness, k_n	$1.1 \times 10^5 \text{ N/m}$
Shear contact stiffness, k_s	$1.1 \times 10^5 \text{ N/m}$
Rolling stiffness, k_ω	$0.1 k_n$
Friction coefficients, $\mu = 3 \cdot \mu_\omega$	0.3
Normal bond stiffness, $k_{n,b}$	$0.5 k_n$
Shear bond stiffness, $k_{s,b}$	$0.2 k_n$
Bond strength, $C = C_n = 2 C_s$	[0-2.5] N
Jet's distance to surface, H	7×10^{-2} m
Jet's nozzle size, d_0	5×10^{-3} m
Kinematic fluid viscosity, ν	$5 \times 10^{-5} \text{ m}^2/\text{s}$
Fluid density, ρ_f	847 kg/m^3
Lattice grid size, Δx	2.3×10^{-4} m
Lattice speed, c_s	10 m/s
Hydraulic radius factor, R_h	0.8
Inlet fluid velocity, u_j	[0.8-1.5] m/s

The fluid flow may be described as an inertial laminar flow ($Re_{JET} \sim 80$ to 160), i.e. a flow in the transition from a laminar to a turbulent regime.

3.1 Jet analysis

The transversal profile of fluid velocity right above the soil surface shows a typical shape

with a stagnation point under the jet's axis and the two local maxima at some distance from it ($r/H \sim 0.25$). These features are nevertheless strongly conditioned by the actual shape and roughness of the bed surface.

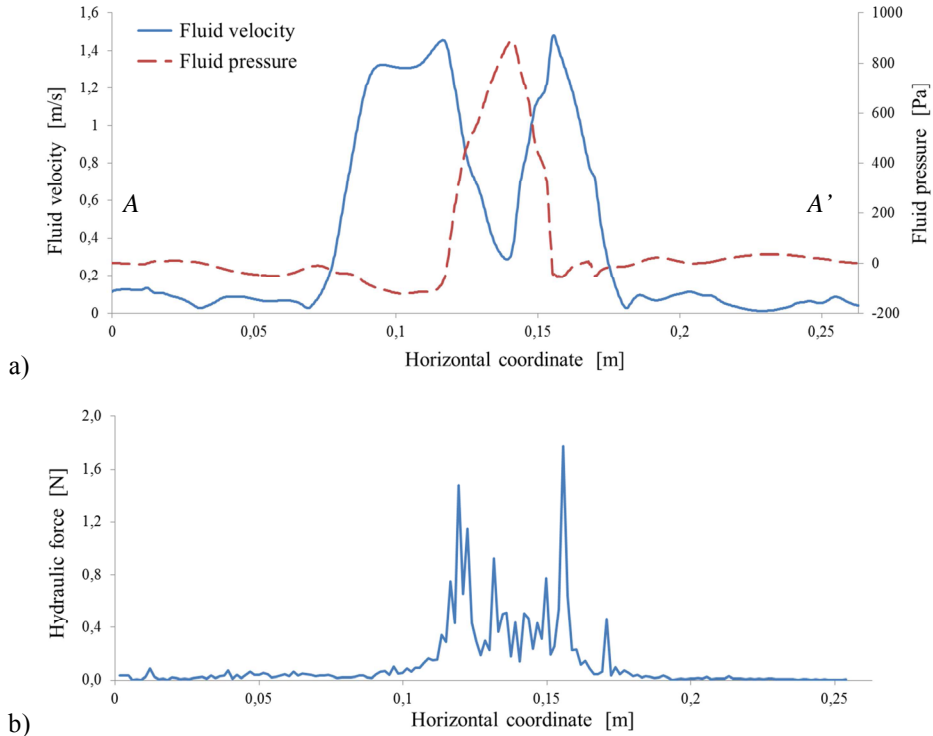


Figure 3: a) Transversal profiles of fluid velocity and pressure at control section A-A'; b) Integrated resultant of hydraulic forces acting on the solid particles at the soil's surface

The viscous drag forces acting on the soil surface are proportional to the fluid velocity and thus show a similar pattern of stagnation under the jet's axis and local maxima at $r/H \sim 0.25$ (Figure 3b).

3.2 Erosion process

The erosion process begins when the hydraulic shear stress at the soil surface exceeds a critical shear stress. For our configuration, this limit was reached for jet velocities equal to or greater than 0.6 m/s, in good agreement with our on-going experimental results [26]. As expected, the mobilization of solid particles then follows a pattern that is similar to the profiles of fluid velocity and hydraulic drag forces. Figure 4a shows the eroded profile of a cohesionless sample for a jet velocity of 0.8 m/s after 1.6 seconds of jet flow. At higher jet velocities and in the absence of cohesion, the picture becomes less clear due to the increased scouring depth, the ejection of solid particles and frequent avalanches of the scour pit walls.

In the presence of cohesive forces between particles, the erosion kinetics becomes slower but the initial topology of erosion does not change. Figure 4b shows the state of the granular sample for a cohesive strength of $C = 2.0$ N and a jet velocity of 1.5 m/s after roughly 0.5 seconds of jet flow. We observe a characteristic stagnation zone at the jet's axis and the

contiguous local maxima of scour depth. It is also observed that the grains are now detached either as single particles or in multi-grain clusters preserving a number of internal bonds.

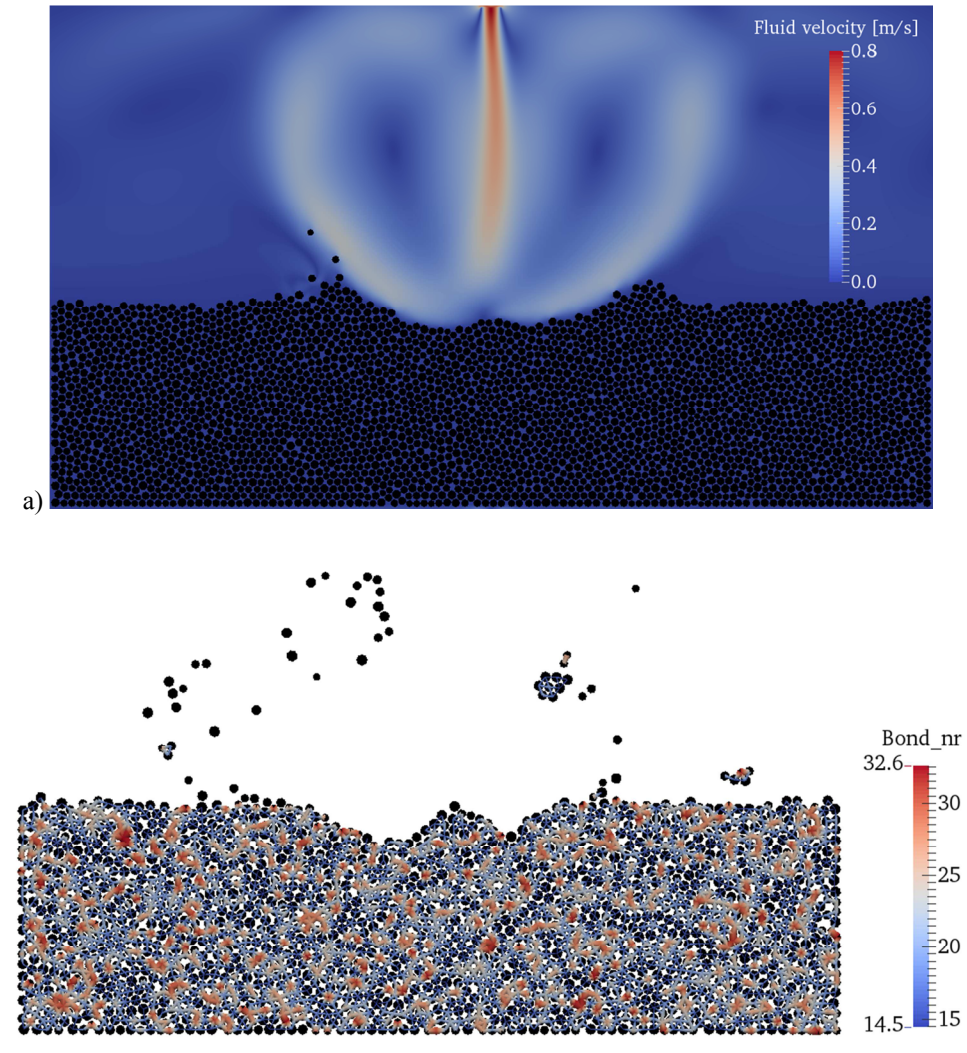


Figure 4: Initial topology of surface erosion; a) Cohesionless sample (bond strength $C = 0$ N), jet velocity $u_j = 0.8$ m/s; b) Cohesive sample ($C = 2$ N), jet velocity $u_j = 1.5$ m/s

In order to quantify and evaluate the erosion kinetics in a consistent manner for both the cohesive and cohesionless samples, it is necessary to specify an erosion criterion allowing us to distinguish between eroded and non-eroded particles. The cumulative particle displacement can be misleading for this purpose since it integrates the persistent residual micro-displacements of the particles, which can add up to significant magnitudes. Therefore it seems more appropriate to differentiate the particles as a function of an instantaneous quantity such as the kinetic energy:

$$K_i = \frac{1}{2}mv_i^2 + \frac{1}{2}I\omega_i^2 \quad (2)$$

where m , I , v_i and ω_i are the particle's mass, moment of inertia, translational velocity and angular velocity, respectively. In this way, if a particle attains at any moment a kinetic energy above a given threshold, it is classified as eroded. In this study, a threshold of 2×10^{-5} Joules allowed us to discriminate well the particles at the debonding front separating the cohesive assembly from the detached and re-settled particles (see Figure 5a), and thus was adopted as erosion criterion.

Figure 5b shows the time evolution of the relative eroded mass (i.e. the proportion of eroded particles compared to the total mass of the granular assembly) for different strengths of the cohesive bonds and a jet velocity of 1.5 m/s.

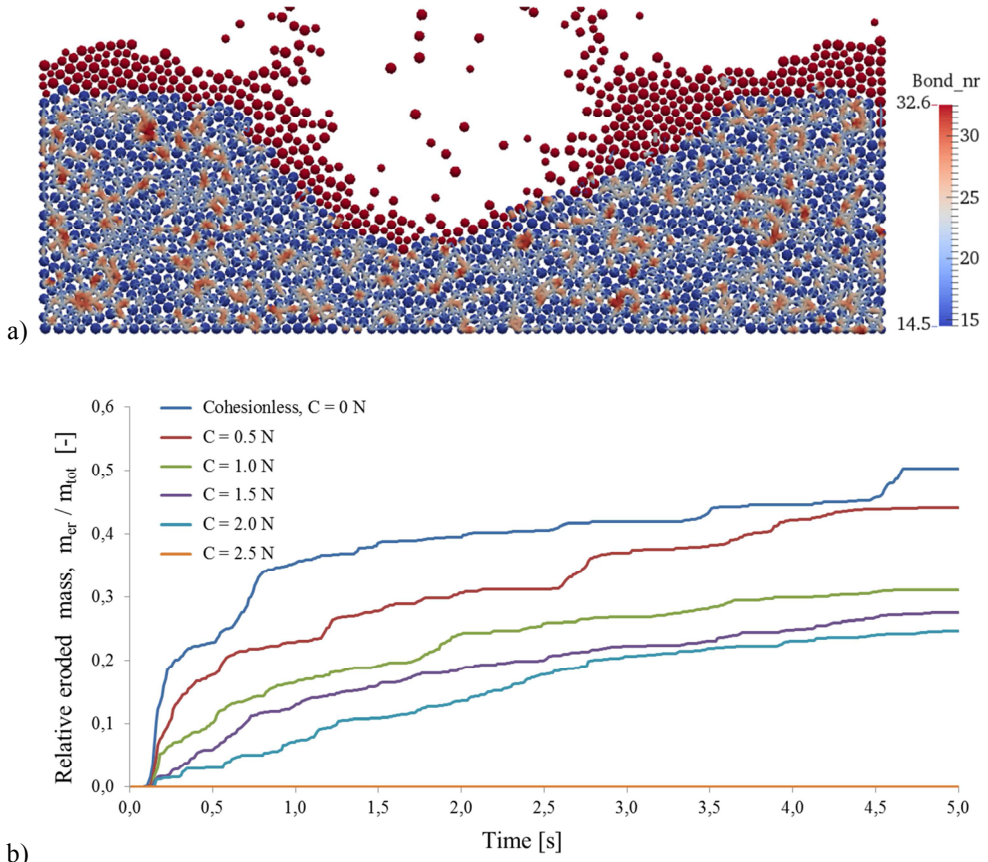


Figure 5: a) Eroded state of soil surface for $C = 2 \text{ N}$ after $t = 5 \text{ s}$, with particle discrimination in terms of kinetic energy (red: eroded particles; blue: intact particles); b) Erosion kinetics in dependence of the bond strength

The purely frictional sample ($C = 0 \text{ N}$) shows a sharp increase of eroded mass when the fluid jet reaches the soil surface and after 5 seconds half of the assembly has already been eroded. This proportion is significantly reduced by the introduction of cohesion, while the complete absence of erosion is achieved when the bond strength is $C = 2,5 \text{ N}$. Therefore, the critical cementation degree for the beginning of erosion in the presented conditions should feature a micromechanical bond strength somewhere between 2 and 2.5 N.

4 CONCLUSIONS

We used a coupled DEM-LBM model to investigate the micromechanics of surface erosion of cohesive geomaterials under the action of a fluid jet flow. We showed that for a given jet flow, there is a critical value of inter-particle cohesion for which surface erosion occurs. We presently work on the influence of more complex cohesion laws and the relation between the micromechanical and macroscopic yield thresholds.

REFERENCES

- [1] Hanson, G.J. and Cook, K.R. Apparatus, test procedures and analytical methods to measure soil erodibility in situ. *Engineering in Agriculture, ASAE*, 20(4): 455-462 (2004).
- [2] Wan, C.F. and Fell, R. Investigation of Rate of Erosion of Soils in Embankment Dams. *J. Geotech. Geoenviron. Eng.*, 130(4), 373–380 (2004).
- [3] Bonelli, S.; Brivois, O.; Borghi, R. and Benahmed, N. On the modelling of piping erosion. *Comptes Rendus de Mécanique*, 8-9(334): 555-559 (2006).
- [4] Xu, Y.; Jiang, H.; Chu, F. and Liu, C. Fractal model for surface erosion of cohesive sediments, *Fractals* **22**(3), (2014).
- [5] Cossette, D.; Mazurek, K.A. and Rennie, C.D. Critical shear stress from varied method of analysis of a submerged circular turbulent impinging jet test for determining erosion resistance of cohesive soils, *Proc. 6th Conf on Scour and Erosion ICSE6*, Paris (2012).
- [6] Mercier, F.; Golay, F.; Bonelli, S.; Anselmet, F.; Borghi, R. and Philippe, P. 2D axisymmetrical numerical modelling of the erosion of a cohesive soil by a submerged turbulent impinging jet, *European Journal of Mechanics - B/Fluids*, Vol. 45, pp. 36–50 (2014)
- [7] Winterwerp, J. C. and Van Kesteren, W. G. M. *Introduction to the physics of cohesive sediment in the marine environment*, Developments in Sedimentology Series no. 56. Elsevier (2004).
- [8] Mutabaruka, P.; Delenne, J.-Y.; Soga, K. and Radjai, F. Initiation of immersed granular avalanches, *Phys. Rev. E*. 89 (2014).
- [9] Sibille, L.; Lominé, F.; Poullain, P.; Sail, Y. and Marot, D. Internal erosion in granular media: direct numerical simulations and energy interpretation, *Hydrol. Process.* 29(9), pp 2149–2163, Wiley & Sons (2015).
- [10] Ngoma, J. *Etude numérique et expérimentale de la déstabilisation des milieux granulaires immergés par fluidisation*, PhD thesis, Université d'Aix-Marseille (2015).
- [11] Cundall, P.A. and Strack, O.D.L. A discrete numerical model for granular assemblies, *Géotechnique*, Vol. 29, pp. 47-65 (1979)
- [12] Delenne, J.-Y.; El Youssoufi, M.S.; Cherblanc, F. and Bénet, J.-C. Mechanical behaviour and failure of cohesive granular materials, *Int. J. Numer. Anal. Meth. Geomech.*, Vol. 28, pp. 1577–1594 (2004).
- [13] Richefeu, V. *Approche par éléments discrets 3D du comportement de matériaux granulaires cohésifs faiblement contraints*. PhD thesis. Université Montpellier II (2005).
- [14] Jiang, M.; Zhang, W.; Sun, Y. and Utili, S. An investigation on loose cemented granular materials via DEM analyses, *Granular Matter* **15**:65–84, (2013)
- [15] Richefeu, V.; El Youssoufi, M.S.; Peyroux, R. and Radjaï, F. A model of capillary

- cohesion for numerical simulations of 3D polydisperse granular media, *Int. J. Numer. Anal. Meth. Geomech.*, Vol. 32, pp. 1365–1383 (2008).
- [16] Schaefer, J.; Dippel, S. and Wolf, D. Force schemes in simulations of granular materials, *Journal de Physique I*, 6 (1), pp.5-20, EDP Sciences (1996).
- [17] McNamara, S. Molecular dynamics method, in *Discrete-element modeling of granular materials*, Eds. Radjaï, F. and Dubois, F., Wiley-Iste, (2011)
- [18] Succi, S. *The Lattice-Boltzmann Equation for fluid dynamics and beyond*. Oxford university press, Oxford (2001).
- [19] Lallemand, P. and Luo, L.-S. Lattice Boltzmann method for moving boundaries, *Journal of Computational Physics*, Vol. 184, pp. 406–421, (2003).
- [20] Lallemand, P. and Luo, L.-S. Theory of the Lattice Boltzmann Method: Dispersion, Dissipation, Isotropy, Galilean Invariance, and Stability, *ICASE Report No. 2000-17*, NASA/CR-2000-210103 (2000).
- [21] Yu, D.; Mei, R.; Luo, L.-S. and Shyy, W. Viscous flow computations with the method of lattice Boltzmann equation, *Progress in Aerospace Sciences*, **39**: 329–367, (2003).
- [22] Bouzidi, M.; Firdauss, M. and Lallemand, P. Momentum transfer of a Boltzmann-lattice fluid with boundaries, *Phys. Fluids*, Vol. 13, No. 11, (2001).
- [23] Feng, Y.T.; Han, K. and Owen, D.R.J. Coupled lattice Boltzmann method and discrete element modelling of particle transport in turbulent fluid flows: Computational issues, *Int. J. Numer. Meth. Engng* **72**:1111–1134, (2007).
- [24] Boutt, D.F.; Cook, B.K. and Williams, J. R. A coupled fluid–solid model for problems in geomechanics: Application to sand production, *Int. J. Numer. Anal. Meth. Geomech.* **35**:997–1018 (2011).
- [25] Cui, X.; Li, J.; Chan, A. and Chapman, D. A 2D DEM–LBM study on soil behaviour due to locally injected fluid, *Particuology* **10**: 242– 252, (2012).
- [26] Brunier-Coulin, F.; Cuellar, P. and Philippe, P. Local mechanisms of cohesive soil erosion, submitted to *13th Int. Conf. on Cohesive Sediment Transport Processes*, INTERCOH2015, Leuven, Belgium, 7-11 September 2015.

NUMERICAL SIMULATION OF FREE SURFACE SEEPAGE IN SATURATED SOIL USING SMOOTHED PARTICLE HYDRODYNAMICS

Chong Peng^{1,2}, Wei Wu¹, Haisui Yu² AND Chun Wang³

¹ Institute of Geotechnical Engineering, University of Natural Resources and Life Sciences
Feistmantelstrasse 4, 1180, Vienna, Austria

² Nottingham Centre for Geomechanics, University of Nottingham
University Park, NG7 2RD, Nottingham, UK

³ School of Architecture, Ocean and Civil Engineering
Shanghai Jiao Tong University, 200240, Shanghai, China

Key words: Seepage, Soil-water coupling, Delta-SPH, Drag force

Abstract. In this paper we present numerical simulations of free surface seepage in saturated soil using Smoothed Particle Hydrodynamics. The modeling of the water seepage is based on mixture theory. Soil skeleton and water are depicted by different kinds of particles. The water particles move according to momentum equations while the soil particles are fixed in position. The interactions between these two phases, consisting of drag force and buoyancy force, are added to the governing equations of the water phase. A non-linear drag force model is adopted. Numerical results are compared with that from literature. It is demonstrated that seepage surface and pressure field can be obtained with satisfactory accuracy with the present model.

1 INTRODUCTION

Strong soil water coupling is common in natural environment and engineering practices. For example, landslide and debris flow are natural hazards mainly caused by the motion of soil-water mixture. Other examples are bed erosion, dam break, water jet excavation, etc. In these phenomena coupling models usually used in soil mechanics, i.e., Biot consolidation theory, are no longer appropriate, because there is high relative velocity between soil and water, and the flow is mainly in turbulent regime. Moreover, numerical simulation of these problems is challenging, because free surface flow of fluid phase and large deformation of soil phase are difficult to model in the FEM method.

Smoothed particle hydrodynamics is a meshless method widely used in astrophysics and computational fluid dynamics. With an update Lagrangian scheme, it models large

deformation and material boundary conveniently. Owing to this property, it is a promising tool in the problems involving strong soil water coupling. In this paper we present the simulation of free surface seepage in saturated soil, which is a essential and preliminary step of the complete simulation of coupling problems. First we present our free seepage model based on SPH and then numerical examples are performed to validate it.

2 SEEPAGE MODEL

2.1 Governing equations

Mixture theory [1, 2] is a model category involves all phases presenting in soil mixture, i.e., soil, water and gas. It describes the conservation laws of each constituent while taking the inter-constituent interaction into consideration. In this work we consider soil as undeformable so the governing equations consisting only of mass and momentum conservation for water:

$$\frac{\partial(\tilde{\rho}_f\phi_f)}{\partial t} = -\nabla \cdot (\tilde{\rho}_f\phi_f \mathbf{v}_f) \quad (1)$$

$$\frac{\partial(\tilde{\rho}_f\phi_f \mathbf{v}_f)}{\partial t} + \nabla \cdot (\tilde{\rho}_f\phi_f \mathbf{v}_f \otimes \mathbf{v}_f) = \nabla \cdot \boldsymbol{\sigma}_f + \tilde{\rho}_f\phi_f \mathbf{g} - \mathbf{f}_s \quad (2)$$

where $\tilde{\rho}_f$ is the intrinsic density of water; ϕ_f is the volume fraction of water; \mathbf{v}_f is the Darcy velocity, also called unit discharge; \mathbf{g} is the gravity and \mathbf{f}_s is the force between fluid phase and soil phase. The stress tensor of fluid has the form $\boldsymbol{\sigma} = -p\mathbf{I} + \phi_f\boldsymbol{\tau}_f$, where p is the pressure, \mathbf{I} an identity tensor and $\boldsymbol{\tau}_f$ the shear stress tensor. The interaction force \mathbf{f}_s consists of drag force \mathbf{D} and buoyancy force $-\phi_s\nabla p$. For simplicity, time and spatial derivatives of volume fraction are neglected. Substituting interaction force \mathbf{f}_s in Eq. (2), omitting the subscript f and rewriting the equations in material derivatives, we have

$$\frac{d\rho}{dt} = -\rho \nabla \cdot \mathbf{v} \quad (3)$$

$$\frac{d\mathbf{v}}{dt} = -\frac{\nabla p}{\rho} + \frac{\boldsymbol{\tau}}{\rho} - \frac{\mathbf{D}}{\phi\rho} + \mathbf{g} \quad (4)$$

where ρ is the intrinsic density of water and the over-bar is omitted. We can see that by neglecting the time and spatial derivatives of ϕ Eq. (1) and (2) are greatly simplified. The form of equation (4) is similar to the momentum equation used by Lasere et al [3] and Shao [4]. But if fully coupled simulation with deformable soil is performed, the Eq. (2) should be used.

2.2 Constitutive relations

There are two ways to calculate pressure in SPH: one is to treat water as a weakly-compressible fluid (WCSPH), the other is incompressible SPH (ISPH) [4]. It is reported

that the ISPH results in better pressure results. However, in the ISPH, the Poisson equation has to be solved, so the computation is more complex and time consuming. Recent researches show that, if density diffusion term, like δ -SPH, is applied in the WCSPH, good results of pressure can be obtained [5]. Therefore, we use weakly-compressible formulation. The pressure of water is calculated from an equation of state

$$p = B \left[\left(\frac{\rho}{\rho_0} \right)^\gamma - 1 \right] \quad (5)$$

where ρ_0 denotes the reference density of water, i.e., $\rho_0 = 1000 \text{ kg/m}^3$; B is a pressure coefficient related to the configuration of the problem; γ is taken as $\gamma = 7$ for water.

The shear stress τ is calculated from the velocity gradient

$$\tau = \mu(\nabla \mathbf{v} + (\nabla \mathbf{v})^T) \quad (6)$$

where μ is the dynamic viscosity of water and $\nabla \mathbf{v}$ is the velocity gradient.

2.3 Drag force

The most used drag force model is the Darcy's law which is linear, valid in laminar flow. Based on experiment data, non-linear models have been proposed and proven to be more realistic. A quadratic form of non-linear drag force [3] is adopted in this work, which has the following form

$$\mathbf{D} = \frac{\mu \phi}{k} \mathbf{v} + \frac{1.75 \phi \rho}{\sqrt{150 k n^{3/2}}} \| \mathbf{v} \| \mathbf{v} \quad (7)$$

where k is the intrinsic permeability related only to the property of the soil material

$$k = \frac{\phi^3 D_{50}^2}{150(1-\phi)^2} \quad (8)$$

where D_{50} is used as an equivalent diameter of soil. One advantage of the adopted form of drag force is that in free flow area, where $\phi = 1$, the drag force drops to zero automatically. Therefore, the Eq. (4) can be applied to whole computational domain. There is no need to divide flow domain into free flow area and seepage area.

3 SPH FORMULATIONS

Conventional numerical methods based on mesh, such as FEM and FVM, have difficulty in solving Eq. (3) and (4) in seepage problems due to the presence of free surface. Additional numerical techniques, like level set method, have to be applied [3]. SPH is widely used to model free surface flow. Therefore it is applied here to solve the system of equations. In SPH the material is represented by particles carrying physical variables moving with material velocity. By using an update Lagrangian scheme, we track the

position change of the particle system and the carried variables, hence the problem is numerically solved.

3.1 Fundamentals

In SPH, a field function can be approximated by the following integral interpolation

$$f(\mathbf{x}) = \int_{\Omega} f(\mathbf{x}') W(r, h) d\Omega \quad (9)$$

where Ω is the integral domain; W is the weighting function, usually called kernel function in SPH literature; r denotes the Euclidean distance between \mathbf{x} and \mathbf{x}' , i.e., $r = \|\mathbf{x} - \mathbf{x}'\|$. Finally, h is called smoothing length determining the size of the kernel. The Wendland C^6 function is used as kernel function in this work

$$W(r, h) = \alpha_d (1 - \frac{1}{2}q)^8 (1 + 4q + \frac{25}{4}q^2 + 4q^3) \quad (10)$$

where $q = r/h$. α_d is a coefficient chosen to fulfill the normalization condition. The chosen kernel function is compactly supported. It is obvious that $W = 0$ when $q \geq 2$.

By particle summation, Eq. (9) can be written in the following form

$$f(\mathbf{x}_i) = \sum_{j=1}^n f(\mathbf{x}_j) W_{ij} m_j / \rho_j \quad (11)$$

where n is the number of particles in the support domain of kernel W_{ij} centered at particle \mathbf{x}_i . Following a similar way, the gradient of $f(\mathbf{x})$ can be calculated as

$$\nabla f(\mathbf{x}) = \sum_{j=1}^n f(\mathbf{x}_j) \nabla_i W_{ij} m_j / \rho_j \quad (12)$$

3.2 Discretization of governing equations

We use subscript a and b to denote fluid particles and i and j for soil particles in the subsequent content. The mass conservation equation is discretized as

$$\frac{d\rho_a}{dt} = \sum_b m_b (\mathbf{v}_a - \mathbf{v}_b) \cdot \nabla_a W_{ab} + \delta h c_0 \sum_b \frac{m_b}{\rho_b} \boldsymbol{\psi}_{ab} \cdot \nabla_a W_{ab} \quad (13)$$

In the right side of Eq. (13), the second term is the density diffusion named δ term. It is the key point to obtain a smooth pressure results in our simulation. In Eq. (13), c_0 is the reference speed of sound, δ is a constant determining the diffusion effect, and $\boldsymbol{\psi}_{ab}$ is

$$\boldsymbol{\psi}_{ab} = 2(\rho_a - \rho_b) \frac{\mathbf{r}_{ab}}{\|\mathbf{r}_{ab}\|^2} \quad (14)$$

where $\mathbf{r}_{ab} = \mathbf{x}_a - \mathbf{x}_b$ is the vector from \mathbf{x}_b to \mathbf{x}_a .

The discretized momentum equation is

$$\frac{d\mathbf{v}_a}{dt} = - \sum_b m_b \left(\frac{p_a}{\rho_a^2} + \frac{p_b}{\rho_b^2} \right) \nabla_a W_{ab} + \sum_b \frac{2m_b \mu r_{ab} \cdot \nabla_a W_{ab}}{\rho_a \rho_b (\| \mathbf{r}_{ab} \|^2 + 0.01h^2)} \mathbf{v}_{ab} - \sum_j \frac{m_j}{\phi_a \rho_a \rho_j} (K_{aj}^A \mathbf{v}_{aj} + K_{aj}^B \| \mathbf{v}_{aj} \| \mathbf{v}_{aj}) W_{aj} \quad (15)$$

where \mathbf{v}_{aj} is the relative velocity between fluid particle a and soil particle j ; ρ_j is the partial density of soil particle j . the coefficients K_{aj}^A and K_{aj}^B are

$$K_{aj}^A = \frac{\mu \phi_a}{k_a}, \quad K_{aj}^B = \frac{1.75 \phi_a \rho_a}{\sqrt{k_a} \phi_a^{3/2}} \quad (16)$$

representing respectively linear and non-linear effect. In Eq. (15) the discretization of the gradient of shear stresses follows the treatment in [4]. The volume fraction of fluid particle is interpolated over the neighboring soil particles

$$\phi_a = \sum_j \frac{m_j}{\rho_j} (1 - \phi_j) W_{aj} / \sum_j \frac{m_j}{\rho_j} W_{aj} \quad (17)$$

where ϕ_j is the volume fraction of soil at particle j .

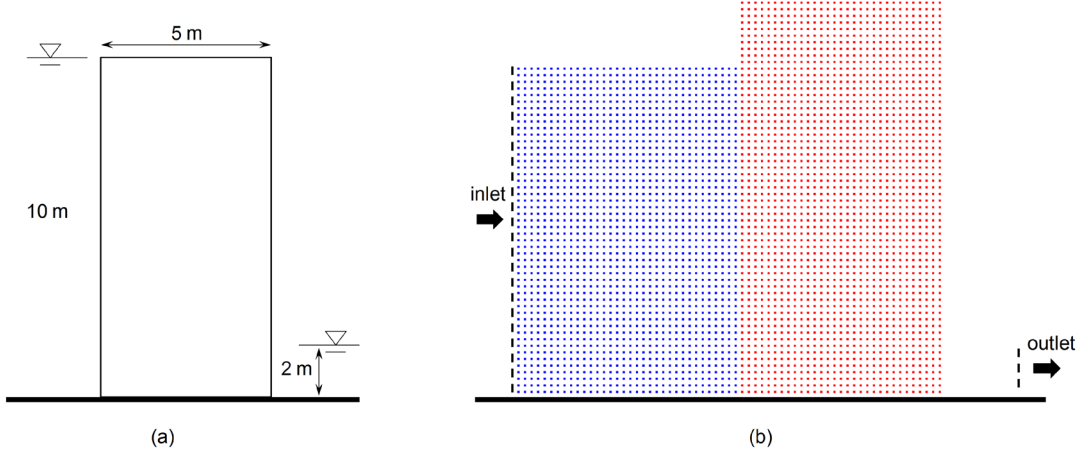


Figure 1: Simulation setup: (a) Geometry of the rectangular dam; (b) Boundary conditions and initial particle configuration used in the simulation. The blue particles denote water and red particles denote soil.

4 NUMERICAL EXAMPLES

The free surface seepage in a rectangular dam with tail water is investigated. The geometry and boundary condition is shown in Figure 1(a). The dam is 10 m in height

and 5 m in width. The upstream water level is 10 m and downstream tail water is 2 m deep. Figure 1(b) shows the configuration of simulation. The dam and water are discretized by soil particles and water particles respectively. The inlet boundary condition is set 7 m away from the dam, while outlet boundary condition is 3 m away. The impermeable bottom boundary is modeled by dummy particles fixed in position. Initially there is no particle downstream. The soil particles are fixed in position, thus they are only used in the calculation of fluid volume fraction and drag force.

The following material parameters are used in the simulation: soil partial density 1350 kg/m³; soil intrinsic density $\tilde{\rho}_s = 2700$ kg/m³; $D_{50} = 10$ mm; dynamic viscosity $\mu = 1 \times 10^{-3}$ Pa·s. The chosen material constants results in relatively large permeability. However, the permeability only affects the seepage velocity, not the shape and position of the seepage surface.

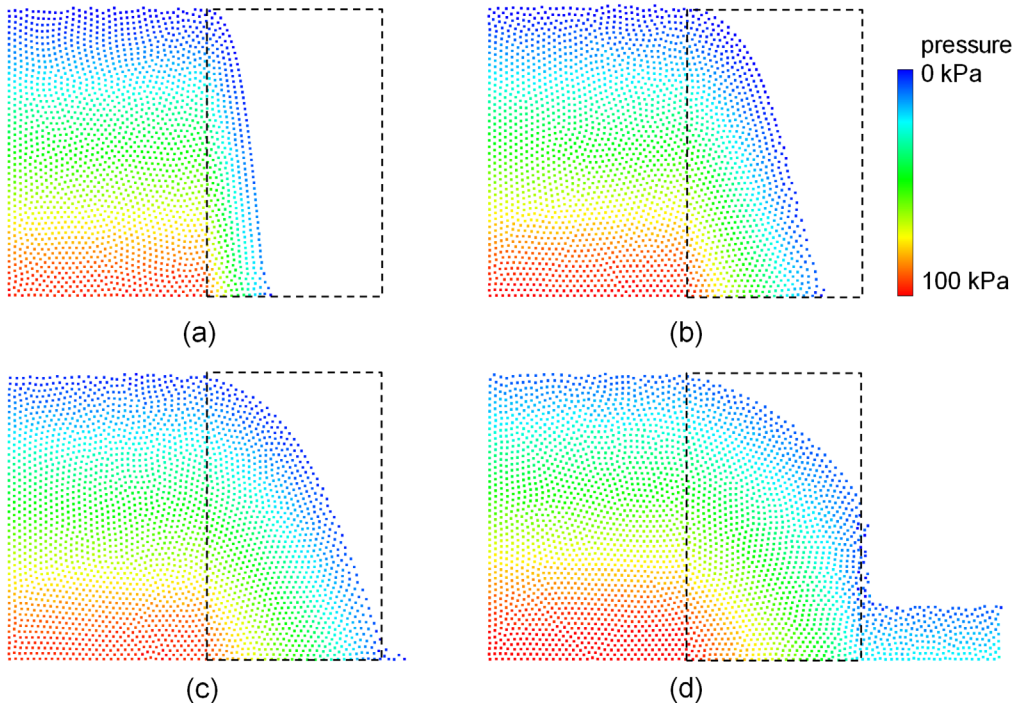


Figure 2: Seepage in the rectangular dam. The colored legend applies to all four figures.

Figure 2 shows the seepage process in the rectangular dam. The free surface is captured clearly and reasonably. No additional surface detection is needed. The obtained pressure field is smooth and accurate. The results are comparable to results obtained using more complicated and time consuming Imcompressible SPH [4]. The accuracy of pressure is significant, because when solving water-soil coupling problem, the pressure field affects the motion of the mixture a lot.

In Figure 3 we compare the free surface obtained using the present model to that

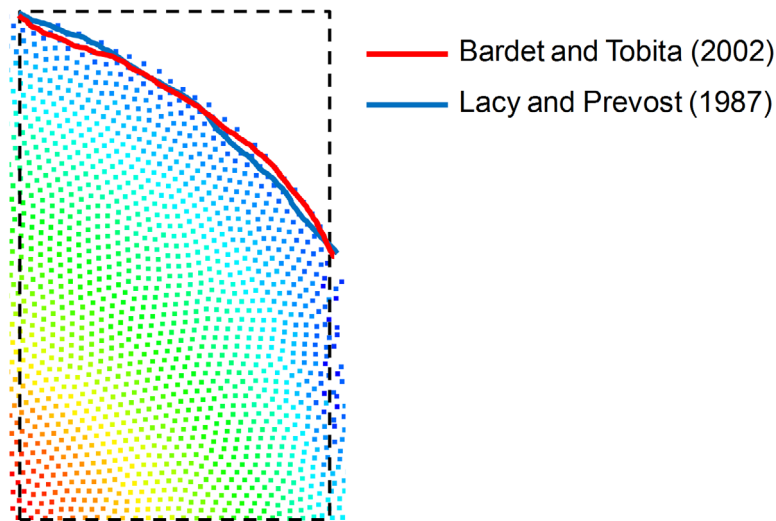


Figure 3: Comparasion of the free surface.

in literature [6, 7]. Good agreement is observed. Iteration or level set are required in obtaining the seepage surface in grid based methods. However, here no special treatment is needed, SPH computes the surface in a natural way. It is demonstrate that with the proposed SPH model, free surface seepage as well as pressure field, are modeled conveniently and with good quality.

5 CONCLUSIONS

In this paper we present a model to simulate free surface seepage in saturated soil using Smoothed Particle Hydrodynamics. The mixture theory is used to derive the governing equation of the seepage. Density diffusion, i.e., δ -SPH is applied to assure the accuracy of the pressure. Numerical examples are performed. It is shown that the present model is able to model free surface seepage conveniently and accurately.

In soils with very low permeability, the present method suffers long computational time because SPH is an explicit method. It is not suitable for seepage in clay. However, based on the mixture theory, the present model has the potential to be extended to solve problems involving strong water-soil coupling, if the mass and momentum conservation of soil phase is considered and soil constitutive models are provided.

REFERENCES

- [1] Drew, D.A. Mathematical modeling of two-phase flow. *Ann. Rev. Fluid Mech.* (1983) **15**:261–291.
- [2] Pitman, E.B. and Le, L. A two-fluid model for avalanche and debris flows. *Phil.*

- Trans. R. Soc. A* (2005) **363**:1573-1601.
- [3] Larese, A., Rossi, R. and Idelsohn S.R. A coupled PFEM-Eulerian approach for the solution of porous FSI problems. *Computational Mechanics* (2012) **50**:805-819.
 - [4] Shao, S.D. Incompressible SPH flow model for wave interactions with porous media. *Coastal Engineering* (2010) **57**:304-316.
 - [5] Molteni, D. and Colagrossi, A. A simple procedure to improve the pressure evaluation in hydrodynamics context using the SPH. *Computer Physics Communications* (2009) **180**:861-872.
 - [6] Bardet, J.P. and Tobita, T. A practical method for solving free-surface seepage problems. *Computers and Geotechnics* (2002) **29**:451-475.
 - [7] Lacy, S.J. and Prevost, J.H. Flow through porous media: a procedure for locating the free surface. *International Journal for Numerical and Analytical Methods in Geomechanics* (1987) **11**:585-601.

PS-MRT LATTICE BOLTZMANN MODEL FOR DIRECT SIMULATION OF GRANULAR SOILS AND SEEPAGE FLOW

Y. FUKUMOTO ¹, S. OHTSUKA ² AND A. MURAKAMI ³

¹Nagaoka University of Technology
1603-1, Kami-tomioka, Nagaoka-shi, Niigata 940-2188, Japan
yfukumoto@vos.nagaokaut.ac.jp

² Nagaoka University of Technology
1603-1, Kami-tomioka, Nagaoka-shi, Niigata 940-2188, Japan
ohtsuka@vos.nagaokaut.ac.jp

³ Kyoto University
Kitashirakawa Oiwake-cho, Sakyo-ku, Kyoto 606-8502, Japan
akiram@kais.kyoto-u.ac.jp

Key words: Multi-phase Flow, Seepage Failure, DEM, LBM.

Abstract. We proposed a direct numerical simulation model of granular soils and seepage flow by combining the discrete element method and the lattice Boltzmann method. The MRT model was introduced in order to obtain stable solutions of fluid flow under high Reynolds number condition. The PS model, which retains a local operation at each fluid node and keep from intensive increasing the computational costs for the calculation of collision term, was also introduced as a solid-fluid coupled model. We show the effectiveness of the PS-MRT lattice Boltzmann model through several validation tests.

1 INTRODUCTION

The solid particle-fluid multiphase flow and its multi-physics phenomena can be found in a lot of scientific fields: fluidization in chemical engineering, transport of blood cell in bio-engineering, sedimentation and erosion in environmental sciences, sand production in resource engineering and so on. These physical phenomena are not well understood because of the wide variety and the complexity of the particle-fluid or the particle-particle interactions. The particle-fluid systems are often experimentally observed by using an X-ray tomography [1] [2] and a high speed camera [3], but observation capacity and available information at particle-resolution by using such apparatuses are still limited.

In addition to experimental approaches, the development of numerical simulation can help our understanding of such complex particle-fluid systems. Because of the importance of capturing properly the interactions between particle and fluid, micro-scale numerical method which can deal with the fluid flow at less particle scale is needed. In contrast, macro-scale methods have less computationally load and are suitable for an industrial application, but require a local averaging which loses the essential details of the fluid flow. The former type of the direct methods is intently improved and new findings are obtained mainly in research fields such as chemical engineering, bio-engineering and soft matter physics.

In geo-mechanics, a particle-fluid system also exists in the form of solid particles and pore liquids or gases, which are characteristic of non-Brownian and highly concentrated suspensions. A deep understanding of such a system is a key to predict and control the various phenomena, such as sand boiling, weathering of rocks, internal erosion and liquefaction of foundation. However, compared to other research fields, there are still a few 3-D applications of a direct particle-fluid solution in geotechnical engineering or civil engineering, despite the importance of consideration of the particle-fluid interaction. The 3-D condition is especially important for the soil structure because an additional special treatment to handle the zero permeability is required for a 2-D congested granular system.

In this study, we proposed an effective direct simulation method in three dimensions for both soils and seepage flow by using the DEM (Discrete Element Method) and the LBM (Lattice Boltzmann Method). Firstly, in order to stabilize the flow analysis and to improve the accuracy of the non-slip boundary condition, the MRT (Multiple Relaxation Time) model [4] was introduced into the LBGK equation, which is also called the SRT (Single Relaxation Time) model and is standard solution of the non-compressible fluids. Secondly, PS (Partially Saturated) model [5] was chosen as a solution of the moving boundary, which can maintain the inherent parallel nature of the lattice Boltzmann equation. These two LB models and the DEM were combined, and the validation of the PS-MRT LB model was performed through several types of simulations.

2 MRT LB MODEL FOR SEEPAGE FLOW

The lattice Boltzmann method is one of the CFD methods and an alternative to the N-S equation. In the LBM, the velocity moments of the virtual fluid particles, \mathbf{f} , having finite directions are placed at each node, and the behaviors of them are governed by a propagation phase and a collision phase from node to node. When the velocity moments have Q directions, \mathbf{f} is defined as $\{f_\alpha | \alpha=0,1,\dots,Q-1\}$, where α is the number of the discrete velocities depending on the choice of the model for the velocity moment. With the consideration of the precision and the numerical efficiency, the D3Q19 model for the three dimensions is used in this study. The solution of the LBM is governed by the following lattice Boltzmann equation.

$$\mathbf{f}(\mathbf{x} + \mathbf{c}\delta_t, t + \delta_t) - \mathbf{f}(\mathbf{x}, t) = \boldsymbol{\Omega}(\mathbf{x}, t) + \mathbf{G}\delta_t. \quad (1)$$

The value for \mathbf{x} is the position of the node which is being calculated, t is the time, δ_t is the discrete time and δ_x is the grid space. \mathbf{c} is the grid velocity, which is calculated by δ_x/δ_t . One of the right term for $\boldsymbol{\Omega}$ indicates the collision operator and \mathbf{G} indicates the forcing term. For the SRT (single relaxation time) LB model [6], which is a standard solution of the LBM, $\boldsymbol{\Omega}$ is given as

$$\boldsymbol{\Omega}(\mathbf{x}, t) = -\tau^{-1} \mathbf{I} (\mathbf{f}(\mathbf{x}, t) - \mathbf{f}^{eq}(\mathbf{x}, t)), \quad (2)$$

where τ is the relaxation time coefficient, \mathbf{I} is the identity matrix and \mathbf{f}^{eq} is the equilibrium distribution function in the velocity space. The kinetic viscosity of the fluid ν is calculated by $c^2\delta_t(\tau-0.5)/3$.

Here, it is well known that the SRT model often results in numerical instability when

fluids have relatively low viscosities. Especially, serious instability problems occur in three dimensional flows in the case where physics may not be adequately resolved due to computational constraints. In order to obtain the numerical stability, we introduce the MRT (multiple relaxation time) model [4] as an alternative to the SRT model. In the MRT model, by choosing different time scales to represent changes in the various physical processes due to collisions, the stability of the LBM can be significantly improved. The collision operator for the MRT model is as follows.

$$\Omega(\mathbf{x}, t) = -\mathbf{M}^{-1} \hat{\mathbf{S}} (\mathbf{m}(\mathbf{x}, t) - \mathbf{m}^{eq}(\mathbf{x}, t)), \quad (3)$$

where \mathbf{M} is a $Q \times Q$ matrix which linearly transform the velocity space, \mathbf{f} , to the moment space, \mathbf{m} : $\mathbf{f} = \mathbf{M}^{-1} \mathbf{m}$, $\mathbf{m} = \mathbf{M} \mathbf{f}$. $\hat{\mathbf{S}}$ is the diagonal matrix where $\hat{\mathbf{S}} = \text{diag}(0, s_1, s_2, , s_4, 0, s_4, 0, s_4, s_9, s_2, s_9, s_2, s_9, s_9, s_9, s_9, s_{16}, s_{16}, s_{16})$. \mathbf{m}^{eq} is the equilibrium distribution function in the moment space. It should be noted here that the value for s_9 is equal to τ , and other diagonal components of $\hat{\mathbf{S}}$ is arbitrarily-assigned.

3 PS-MRT LB MODEL FOR PARTICLE-FLUID COUPLING

In order to perform the coupled particle-fluid simulations in the framework of the LBM, the PS (partially saturated) model allowing momentum transfer inside the solid phase, whose concept is originally suggested by Noble and Torczynski [5], is used. This model enables to deal with moving solid-liquid boundary and to calculate the hydrodynamic force acting on the solid obstacle. Compared to other coupled model [7] [8] [9], this method has advantages of being able to retain a local operation at each node and of keeping from intensive increasing the computational costs for the calculation of collision term. In this approach, the collision operator in the SRT model as shown in Equation (1) is reformulated to account for the solid fraction at a node, B , and the additional term, Λ .

$$\Omega(\mathbf{x}, t) = -(\mathbf{I} - \hat{\mathbf{B}})(\mathbf{f}(\mathbf{x}, t) - \mathbf{f}^{eq}(\mathbf{x}, t)) + \hat{\mathbf{B}}\Lambda(\mathbf{x}, t), \quad (4)$$

where $\hat{\mathbf{B}}$ is the diagonal matrix whose diagonal components are B and Λ is the additional term considering the velocities of the nodes inside the solid phase. Then, the value for Λ_α , which is the α -th component of Λ , is given as follows.

$$\Lambda_\alpha = f_{-\alpha}(\mathbf{x}, t) + f_{-\alpha}^{eq}(\rho, \mathbf{u}) + f_\alpha^{eq}(\rho, \mathbf{u}_p) - f_\alpha(\mathbf{x}, t), \quad (5)$$

where \mathbf{u}_p is the velocity of the solid including both translation and rotation motion of the corresponding particle. The notation $-\alpha$ is the opposite direction of α . According to above equations, when $|\mathbf{u}_p| = 0$ and $B = 1$, the bounce-back rule, i.e., the non-slip condition at solid-fluid boundary is obtained.

When the PS model is introduced into the MRT model, the collision operator is given as the following equation.

$$\Omega(\mathbf{x}, t) = -(\mathbf{I} - \hat{\mathbf{B}})\mathbf{M}^{-1} \hat{\mathbf{S}} (\mathbf{m}(\mathbf{x}, t) - \mathbf{m}^{eq}(\mathbf{x}, t)) + \hat{\mathbf{B}}\Lambda(\mathbf{x}, t). \quad (6)$$

We call this equation PS-MRT LB model in this study. Equation (6) also retains a local

operation at each node in the same as Equation (4). For this reason, it is easy to parallelize the LB solution in the frame of PS-MRT LB model.

4 COLLISION LAW AND MOTION OF SOIL PARTICLE

The handling of the collision law and the motion of the soil particle are presented in this subsection. The collision law for a contact force \mathbf{F}^{con} and a contact torque \mathbf{T}^{con} is governed by the DEM, where the contact logic is followed by the Voigt model. The normal repulsive force is assumed to be proportional to the overlap distance, and a dissipative component is set to be proportional to the relative normal velocity between particles. For the calculation of the tangential force, in addition to the same way as the normal force, the Coulomb law of friction is also considered. The value for \mathbf{F}^{con} and \mathbf{T}^{con} are given by summing up the change of momentum inside the solid phase

All of the calculations in the following subsections are performed on the graphic processing unit (NVIDIA GeForce GTX TITAN). Parallelized algorithm for the DEM suggested by Nishiura and Sakaguchi [10] is incorporated into the coupled particle-fluid code. Detailed parallelization methods relative to the coupling scheme on a many core architecture is not discussed in this literature.

5 DRAG FORCE ON SOIL PARTCLE

At the first step in the validation of the PS-MRT LB model, we simulate the obstacle flow, as shown in Figure 1, and obtain the correlation between drag force coefficient C_D and Reynolds number Re . Fluid flows are generated in positive direction of y -coordinate by imposing a constant velocity boundary condition on one side of zx plane, while the other side of zx plane is free outflow boundary. Grid space δ_x is 1.0×10^{-5} m and the system size is $150\delta_x \times 300\delta_x \times 150\delta_x$. Diameter of the sphere d is $30\delta_x$. The density of the fluid ρ_f is 1000 kg/m^3 and the kinetic viscosity of the fluid ν is $1.0 \times 10^{-6} \text{ m}^2/\text{s}$.

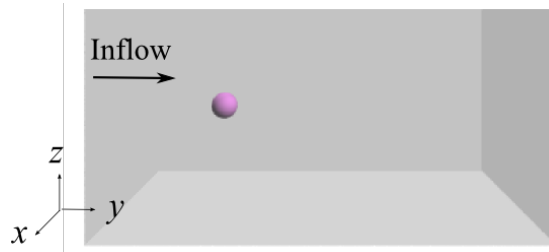


Figure 1: Model setup for the drag force acting on the sphere

As a result of the analysis, the relationships between C_D and Re for the PS-SRT model and the PS-MRT model are plotted in Figure 2. From this figure, it is shown that drag force coefficient C_D obtained from the numerical simulation is corresponding with the empirical equation: $C_D = 24/Re + 6/(1+Re^{0.5}) + 0.4$. Compared with two models, stability solution can be obtained in the range of $Re < 150$ in both cases, and remarkable differences between two models are not observed.

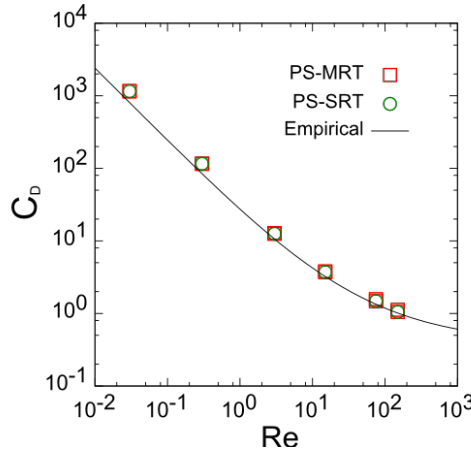


Figure 2: Drag force coefficient C_D vs. Reynolds number Re

6 SEEPAGE FLOW IN GRANULAR SOILS

At the next step in the validation of the PS-MRT LB model, we obtain the correlation between friction factor in porous media ψ and Reynolds number Re . Figure 3 shows the model setup for the seepage flow in granular soils, which are prepared by the packing analysis by using the DEM. The number of soil particles consisting of the porous media is about 1,000 and the diameter of the soil particle d is $16\delta_x$. Fluid flows are generated in positive direction of y -coordinate by imposing a constant velocity boundary condition on one side of zx plane, while the other side of zx plane is free outflow boundary, in the same manner as the analysis of the previous subsection. Grid space δ_x is 1.0×10^{-5} m and the system size is $128\delta_x \times 196\delta_x \times 128\delta_x$. The area occupied with the soil particles is $128\delta_x \times 128\delta_x \times 128\delta_x$. The density of the fluid ρ_f is 1000 kg/m^3 and the kinetic viscosity of the fluid ν is $1.0 \times 10^{-6} \text{ m}^2/\text{s}$.

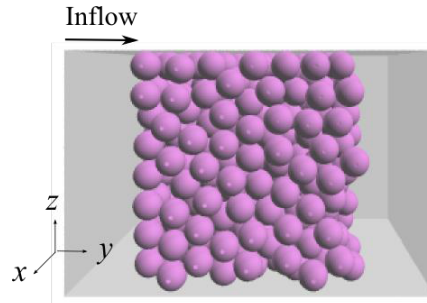


Figure 3: Model setup for the seepage flow in granular soils

Figure 4 shows the relationships between ψ and Re with the empirical equations: $\psi = 150/Re$ ($Re < 10$, Blake-Kozeny eq.), $\psi = 150/Re + 1.75$ ($10 < Re < 10^3$, Ergun eq.). From the figure, the PS-MRT LB model can simulate the flow in the porous media in the range of $Re < 30$. By contrast, the PS-SRT LB model cannot obtain stability solution more than $Re = 2$.

Thus, the PS-MRT LB model has an advantage to stably simulate in the flow inside the complex boundary.

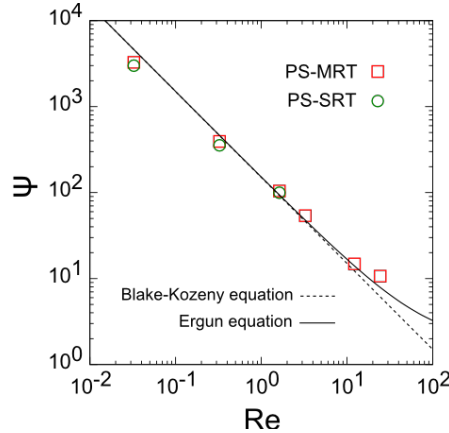


Figure 4: Model setup for the drag force acting on the sphere

7 PARTICLE SETTLING

The last simulation, as shown in Figure 5, illustrates the ability of the PS-MRT LB model to handle large systems of $O(10^4)$. The number of the soil particles is 12,000 and the particle diameter d is $4\delta_x$. Grid space δ_x is 4.0×10^{-5} m and the system size is $160\delta_x \times 160\delta_x \times 250\delta_x$. The density of the fluid ρ_f is 1000 kg/m^3 , the density ratio of the solid to the fluid is 2.5, and the kinetic viscosity of the fluid ν is $1.0 \times 10^{-5} \text{ m}^2/\text{s}$. The Stokes settling velocity is 2.1×10^{-3} m/s and Reynolds number Re is about 0.3.

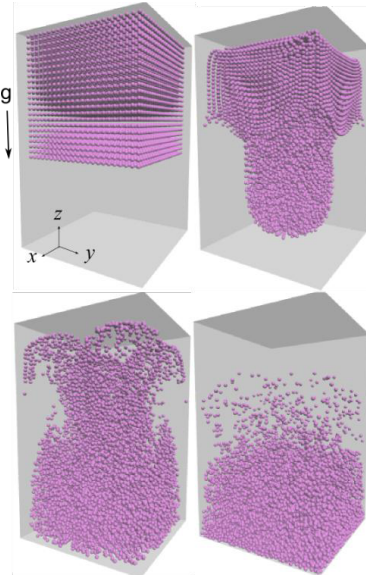


Figure 5: Snapshots of the simulation of particle settling

Figure 5 shows some snapshots during the settling simulation for different elapsed time. The core of the soil particles first swiftly settles followed by the rest of the particles. On the other hand, particles near the vertical walls fall very slowly because the strong interaction occurs between particles and walls. This type of particle settling can be observed in the previous research [11], in which a fictitious domain approach is employed for the coupling method. Therefore, the PS-MRT LB model also can obtain qualitative numerical results in such a large particle-fluid system.

8 CONCLUSIONS

In geo-mechanics, a particle-fluid system exists in the form of solid particles and pore liquids or gases, which are characteristic of non-Brownian and highly concentrated suspensions. For such complex particle-fluid systems, the PS-MRT LB model can be one of the effective way to directly solve both the soil particles and the seepage flow at pore scale. If some parallelization schemes are installed into the simulation code, we can apply the direct numerical model to not only the two-dimensional but also the three-dimensional phenomena.

REFERENCES

- [1] Sukop, M.C., Huang, H., Lin, C.L., Deo, M.D., Oh, K. and Miller, J.D., 2008. Distribution of multiphase fluids in porous media: Comparison between lattice Boltzmann modeling and micro-x-ray tomography. *Physical Review E*, **77**(2), 026710.
- [2] Moreno-Atanasio, R., Williams, R. A. and Jia, X., 2010. Combining X-ray microtomography with computer simulation for analysis of granular and porous materials. *Particuology*, **8**(2), 81-99.
- [3] Li, X., Hunt, M. L. and Colonius, T., 2012. A contact model for normal immersed collisions between a particle and a wall. *Journal of Fluid Mechanics*, **691**, 123-145.
- [4] D'Humieres, D., 2002. Multiple relaxation time lattice Boltzmann models in three dimensions. *Philosophical Transactions of the Royal Society of London. Series A: Mathematical, Physical and Engineering Sciences*, **360**(1792), 437-451.
- [5] Noble, D. R. and Torczynski, J. R., 1998. A lattice-Boltzmann method for partially saturated computational cells. *International Journal of Modern Physics C*, **9**(08), 1189-1201.
- [6] Qian, Y.H., D'Humi'eres, D. and Lallemand, P., 1992. Lattice BGK Models for Navier-Stokes Equation. *Europhysics Letters*, **17**, 479.
- [7] Ladd, A. J., 1994a. Numerical simulations of particulate suspensions via a discretized Boltzmann equation. Part 1. Theoretical foundation. *Journal of Fluid Mechanics*, **271**, 285-309.
- [8] Ladd, A. J., 1994b. Numerical simulations of particulate suspensions via a discretized Boltzmann equation. Part 2. Numerical results. *Journal of Fluid Mechanics*, **271**, 311-339.
- [9] Feng, Z.G. and Michaelides, E. E., 2004. The immersed boundary-lattice Boltzmann method for solving fluid-particles interaction problems. *Journal of Computational Physics*, **195**(2), 602-628.

- [10] Nishiura, D. and Sakaguchi, H., 2011. Parallel-vector algorithms for particle simulations on shared-memory multiprocessors. *Journal of Computational Physics*, **230**(5), 1923-1938.
- [11] Gallier, S., Lemaire, E., Lobry, L. and Peters, F., 2014. A fictitious domain approach for the simulation of dense suspensions. *Journal of Computational Physics*, **256**, 367-387.

REAL GRAIN SHAPE ANALYSIS: CHARACTERIZATION AND GENERATION OF REPRESENTATIVE VIRTUAL GRAINS. APPLICATION TO RAILWAY BALLAST.

N. OUHBI², C. VOIVRET², G. PERRIN³ AND J-N. ROUX¹

¹ Laboratoire Navier (UMR CNRS 8205)
CNRS, Ecole des Ponts et Chaussées, IFSTTAR
Champs-sur-Marne, France
e-mail: {jean-noel.roux}@ifsttar.fr

²Innovation and Research Department, SNCF, Paris, France
Immeuble Lumière
40 Avenue des Terroirs de France, F-75611 PARIS CEDEX 12
e-mail: {noura.ouhbi, charles.voivret}@sncf.fr

³CEA/DAM/DIF
F-91297, Arpajon, France

Keywords: Ballast, particle shape, Characterization, DEM, polyhedra, POD, generation.

Abstract. Grain shape significantly influences the mechanical properties of granular media. In order to explore this effect and to simulate realistic material morphology, we designed a method which well characterizes real grains shape. Starting from a representation of the particle surfaces as a points cloud, this paper presents a method to generate a set of virtual grains that are morphologically representative of real ballast grains. The model relies on a statistical modelling of the ballast grain morphology based on a dimensionality reduction approach (Proper Orthogonal Decomposition) leading to an optimal and nearly exhaustive shape characterization by extracting a hierarchy of shape functions that fully describe the grain sample. We will show the efficiency of the both characterizing and generating methods and describe their advantages, as well as a future outlook

1 INTRODUCTION

Granular materials are widely used in different applications ranging from food industry to civil engineering. Therefore, a better understanding of the overall behaviour of these materials is pivotal to improve and control their performance. Numerous studies have been carried out and enriched over the last years, about the impact of particle size, shape and mineralogy on the mechanical behaviour of the granular media. As for shape properties, several experimental analyses as well as numerical studies using Discrete Element Methods (DEM) [1] have shown the significant influence of particle shape on the evolution of granular assemblies [2-6, 11-13, 16, 17, 24, 26]. Understanding this influence is then a topic of interest in this study.

For DEM simulations, representing particle shape is a real challenge. Most discrete element codes represent particles as discs (2D) or spheres (3D), because of implementation simplicity and computational efficiency. However, it has been proved that these simple geometries fail to reproduce realistic material behaviour for an individual grain, as well as for a granular assembly [7, 14, 20]. Other attempts have then been made to take into account complexity that falls roughly in two classes: 1) parametric model based on given geometric construction rules and 2) fitted model based on real grain shapes. Both approaches can be fulfilled with simple primitive (sphere, ellipsoid, plane, clumps...) or with more versatile geometric shape as polyhedron [8, 10]. Over the last decades, SNCF (French railway company) has chosen the second approach to simulate the behaviour of the ballast with DEM based on polyhedron shaped particles. Railway ballast is a granular layer formed by irregular rock grains of a centimetric size extracted from hard stone quarries by crushing ((BS EN 13450, 2003) [1]). Currently, virtual grains used in simulations are sets of nearly 1000 sampled grains that have been 3D digitalized and meshed.

In order to properly study the impact of the ballast shape on the mechanical behaviour with DEM, a generator of virtual grains is needed, apt to produce large sets of virtual grains that are representative of a limited set of real grain, and that also allows to reach an accurate characterization of the grain shape. In this paper, we propose a method to achieve these goals. In Section 2, the proposed approach of real ballast grain shape modelling as well as its validation are presented and analysed. Some illustrations are presented in Section 3.

2 REAL BALLAST GRAINS MODELLING

2.1 Global view

In the literature, generation methods were presented, such as Fourier-Shape-Descriptors [19, 22], and spherical-based random fields [9, 18, 29]. These approaches have given good results in terms of similarity of generated grains and real ones, but introduce shape functions that are imposed.

We present in this paper an innovative approach based on a dimensionality reduction method leading to an optimal and nearly exhaustive shape characterization of real grains.

By means of Proper Orthogonal Decomposition (POD) [15], we identify the optimal hierarchy of shape functions that describe the grain set. The main advantage of this approach is to reduce the number of needed shape functions to represent the grain shape with a quantitative controlled approximation (error based), such that we reduce the parametric space to the optimal one.

2.2 Pre-processing: Sample preparation

A database of 121 different ballast grains is provided by SNCF. Ballast materials in France are selected based on the European railway ballast specification. The grains are represented by point clouds obtained experimentally by 3D digitization (3D scan) of the particle surfaces, and form irregular polyhedrons of 4000 faces, and about 2000 vertices. Fig.1 shows some of these grains.

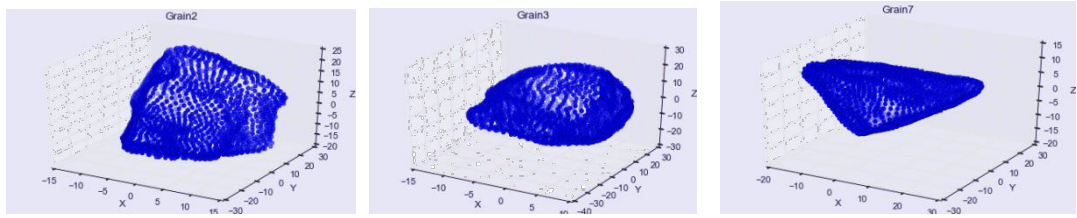


Figure 1 : Example of real ballast grains represented by dense point clouds - SNCF

The pre-processing is based on the following steps:

- ✓ Projection of the experimental points cloud on an imposed basis (B1) with constant angular step and N directions. Since the experimental point cloud are composed of many points (up to millions for finer digitalization) with random direction in a spherical frame, this step aims at reducing the number of point and having the same direction for each grain.
- ✓ Computation for all grains of volume, surface, inertia tensor, and mean radius.
- ✓ Centering grains and rotating vertices until the principal directions of the inertia tensor are parallel to the global coordinate axes, and interpolating (Fig.2)

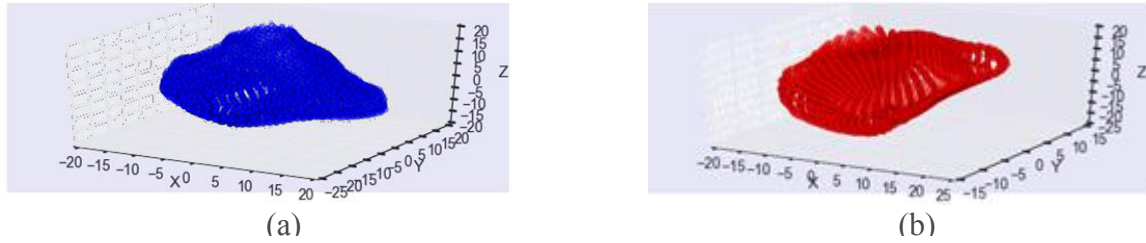


Figure 2: A grain of ballast: (a) Raw data (b) After projection and rotation

- ✓ Projection on a new basis (B2) with uniform density of number of direction by solid angle. Indeed, the previous basis, with constant angular step, lead to a high density of direction near the pole that can bias the statistic. This new basis with 500 directions is generated with a repulsion point iterative procedure. (Fig. 3)
- ✓ By concatenating all grains together, our set of experimental grain is then represented by a 500×121 matrix. Each column represents grain vertices distances along the 500 of the basis B2 (Fig.4). This matrix will be the input data of POD procedure.

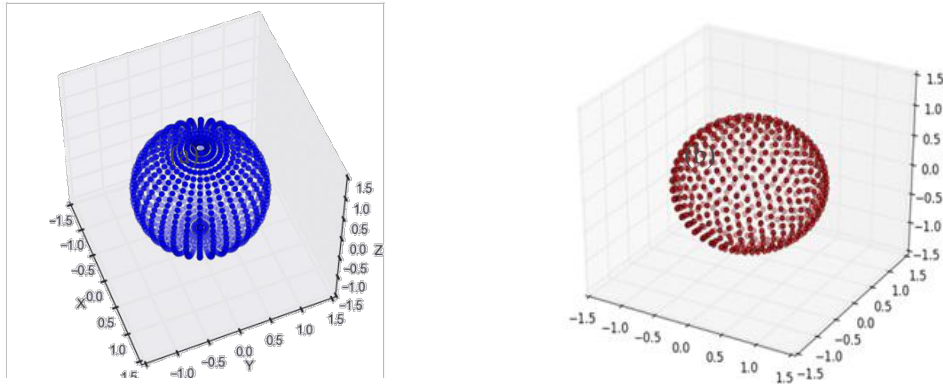


Figure 3: Basis with 500 direction: (a) basis B1 (b) basis B2

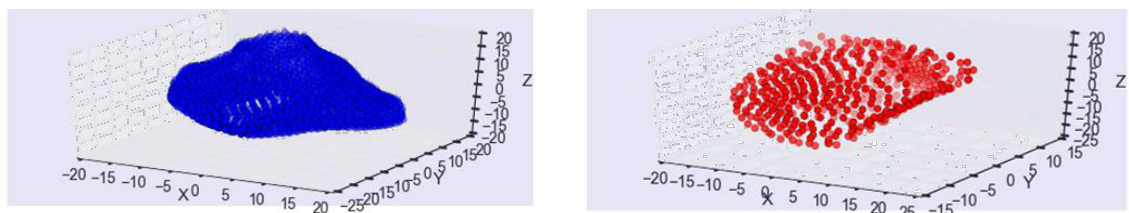


Figure 4: Interpolation on the generated basis with 500 directions and real grain

2.3 Grain characterization

A model reduction method, namely the Proper Orthogonal Decomposition or Principal Component Analysis (PCA) [27] is used. Starting from the data matrix of the Section 2.2, this multivariate statistical method aims at obtaining a compact representation of the data. It identifies an optimal and useful set of basic functions that allows to achieve a satisfactory approximation of the system.

This method serves two purposes, namely order reduction by projecting high-dimensional data into a lower-dimensional space and feature extraction by revealing relevant, but unexpected, structure hidden in the data. The first purpose allows to quantify the controlled approximation (error based), while choosing the dimension of the projection reduced space. The second purpose allows to characterize the shape features by associating them to POD outputs, i.e. basis functions (eigenmodes) and coefficients. Eigenmodes, or principal components, are the eigenvectors of the covariance matrix corresponding to original data, whereas coefficients are projection coordinates on the reduced space of projection. These two elements, in addition to eigenvalues of the covariance matrix are the three key elements of the method. For further explications of the method, see [15].

While applying POD on the data, a corresponding error ϵ is expressed in terms of the projection errors that are controlled in the construction of POD bases. In other words, it is defined as the deviation of the transformed data to the new space from the original data, normalized by the raw data and induced by the truncation of the POD basis. While POD error gives an indication of the magnitude of the “missing” information, the

energy of the system $e(k) = 1 - \varepsilon(k)$ represents the quantity of information captured by the k first POD basis vectors. (Fig. 5) shows the quantities of error/energy as a function of the dimension of the reduced space.

For zero error we have to keep all 121 modes. We see that with only 12 modes we represent 90% of the information and 99% of the information is represented with roughly 50 modes. With this precision, we have half-reduce our data.

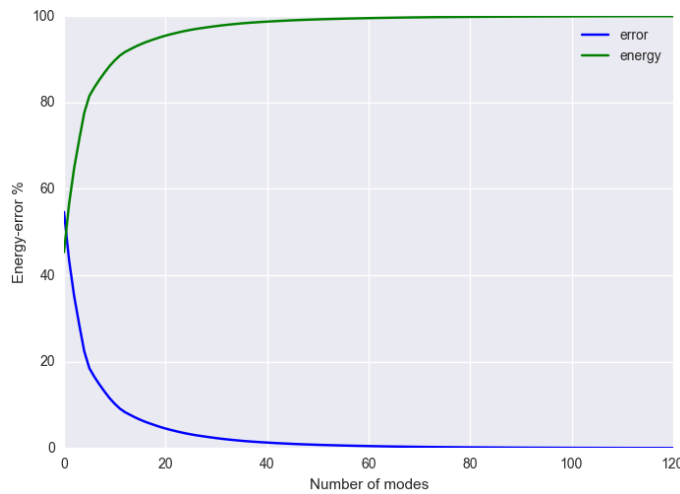


Figure 5: Error and energy quantification

As the accuracy of the grain approximation depends on the number of modes, it is important to check if the properties of grains (average radius, surface, volume) are sensitive to the number of modes. In (Fig.6), we compare those properties distributions for different error thresholds.

In order to quantify more precisely the comparisons, we perform Kolmogorov-Smirnov (KS) tests between original data surfaces/volumes/mean radius and reconstructed grains characteristics. The results are presented in Table 1.

Table 1: Values of Kolmogorov-Smirnov tests between original and reconstructed data S, V, Rm distributions

Error on shape	KS Surfaces	KS Volumes	KS Rayons moyens
0.1%	0.999	0.997	0.947
1%	0.999	0.997	0.879
5%	0.999	0.997	0.785
10%	0.997	0.984	0.465
15%	0.984	0.879	0.223

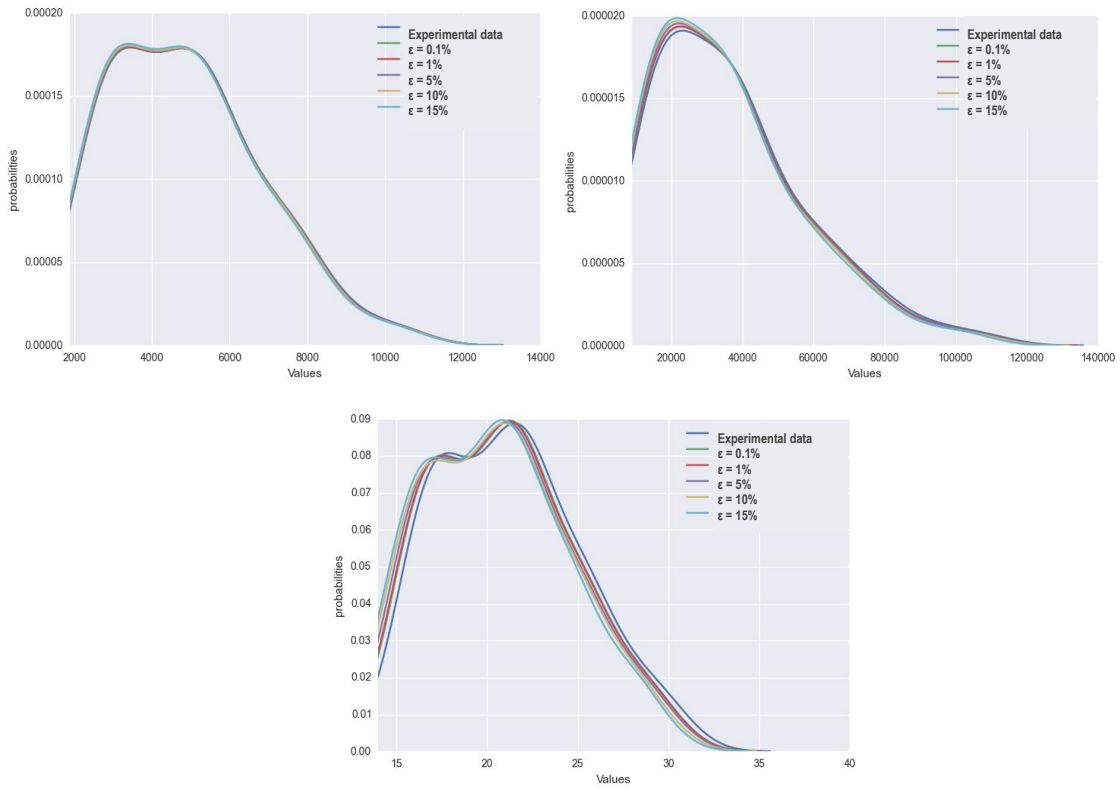


Figure 6: Reconstruction of the real grains for different error thresholds – Comparison of (a) Surfaces distributions (b) Volumes distributions (c) Mean radius distributions

We see that even with significant error (more than 10%) we have a very good shape approximation but with a much more reduced space.

Furthermore, by statistically identifying POD coefficients distributions, we can generate as many equivalent data as wanted. For a perfectly exhaustive shape characterization, we decide to keep all of the eigenmodes and therefore an error of 0% is made. The statistical analysis will concern the coefficients that are uncorrelated. (Fig. 7) shows statistical distributions of the first 8 coefficients as an example.

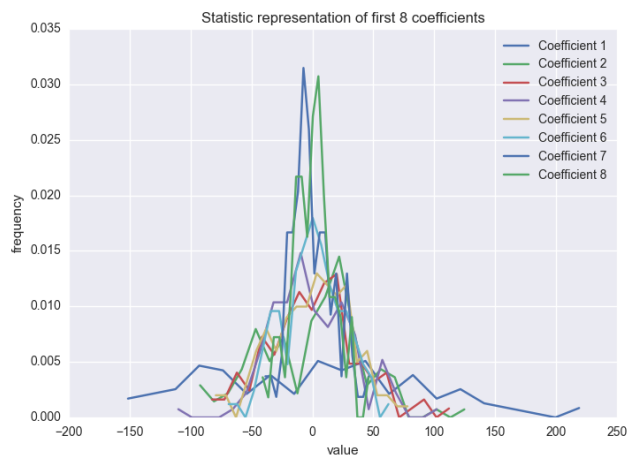


Figure 7: Statistic representation of the first 8 coefficients

The challenge is then to build a model of each distribution. While it is possible to search the best matching distribution or to fit the CDF, we presently prefer to keep the exact CDFs corresponding to discrete data, without transforming it to continuous fitted functions (Fig. 8).

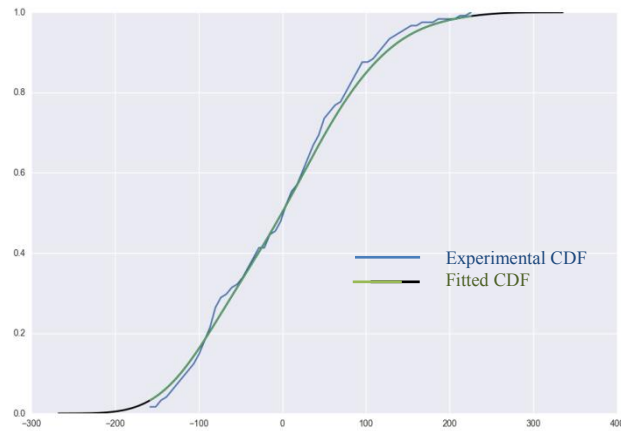


Figure 8: First coefficient CDF

2.4 Generation

Even though the coefficients are uncorrelated (not shown), these coefficients can be dependent in a more complex way. Therefore, the generation process has to take into account the dependence. Since the coefficients are of different marginal distributions, this cannot be done by only using a multivariate distribution, which suffers from the restriction that the marginal should be of the same type. One efficient way to do this is copula functions [28].

That is, copula functions allow one to model the dependence structure independently of the marginal distributions. Any multivariate distribution function can serve as a copula. That offers a good modelling flexibility.

For our generation process, we use the Gaussian copula, since two parameters (Mean and correlation matrices) are enough to describe it. The algorithm is explained in details in [21, 22, 25].

2.5 Validation

To validate our approach, we generate different sets of 300, 500, 800, 1000, 2000 and 10000 virtual grains. Surfaces, volumes and mean radius distributions are then computed and compared to those of the original data. (Fig. 9) shows the results, and Kolmogorov-Smirnov tests results are presented in Table 2.

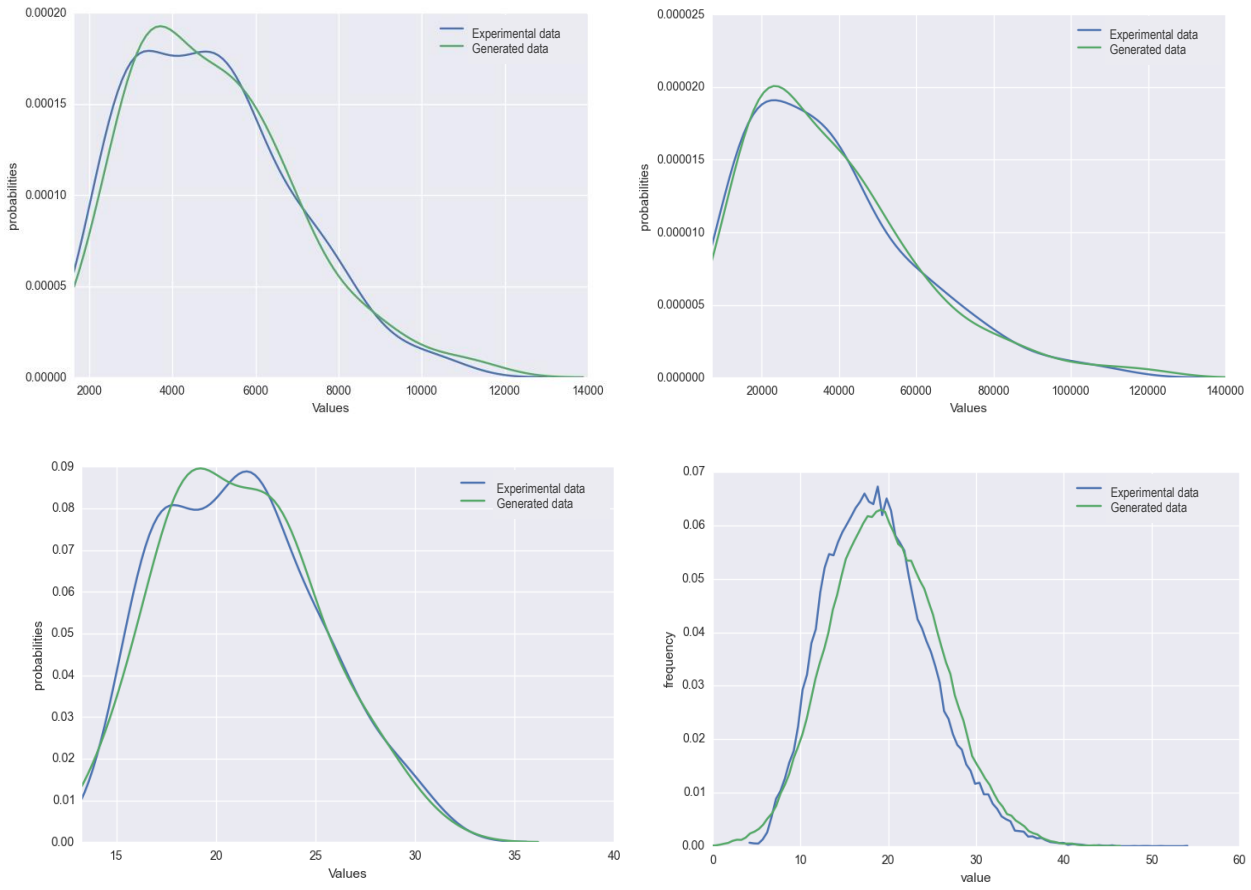


Figure 9: Sample validation – 10000 grains generated

Table 2: Values of Kolmogorov-Smirnov tests between original generated data S, V, Rm distributions

Number of generated grains	KS Surfaces	KS Volumes	KS Rayons moyens
300	0.949	0.949	0.811
500	0.993	0.993	0.831
800	0.994	0.994	0.883
1000	0.998	0.939	0.705
2000	0.976	0.896	0.870
10000	0.939	0.968	0.613

By analysing Fig. 9, we see that for surfaces, volumes and average radii, the peaks are the points that match the least. That can be explained by the fact that the real particle dataset (121 grains) is relatively small, and insufficient for estimating accurately statistics of the grains shape, and hence capturing all shape features. That was proved by Liu et al. [18] who analysed the impact of data set size on the accuracy of results using spherical harmonics approach, and by Grigoriu et al. [9] who also proved the insufficiency of a dataset of 128

aggregates to exactly represent the concrete grains shape. They showed that a “small data set was unable to accurately estimate statistics of aggregate geometry beyond second-moment properties and marginal distribution”.

However, the high values of KS tests obtained and the representations show that we get satisfactory results, even with a small data set. That confirms the accuracy of the approach and shows that enriching our data set will certainly allow to get an even better and exhaustive characterization of ballast shape, and offer an interesting transition between real and virtual grains in order to incorporate them in DEM simulations.

3 ILLUSTRATION

As shown previously, POD procedure allows to very well approximating the grains shape through eigenmodes and coefficients. One interesting question would be how to link eigenmodes and coefficients to shapes features.

One of the advantages of this method is ordering the dominating features by decreasing order (first modes have the biggest contributions to energy of the system, and the largest values of variance). We then expect the first mode to hold an important part of shape features (with 45% of the energy of the system).

To observe the evolution of grains shape through modes, we represent the same grain reconstructed with the first 1 (energy = 45%) to 20 modes (95%) in Fig. 11. We can see the progressive emergence of shape details as we add new modes. As the quantity of information increases (error decreasing), we minimize the sum of the squared differences of the distances between the point on the real grain and the same one represented with a finite number of basic functions.

The first four modes are shown in Fig. 12. We see that the first mode, contributing most to the energy of the system, has a complete shape of a grain while the rest of the modes constitute the other details of shape.

Finally, we represent reconstructed grains with only the first mode in Fig. 13. For all 121 grains, we have a “round” shape.

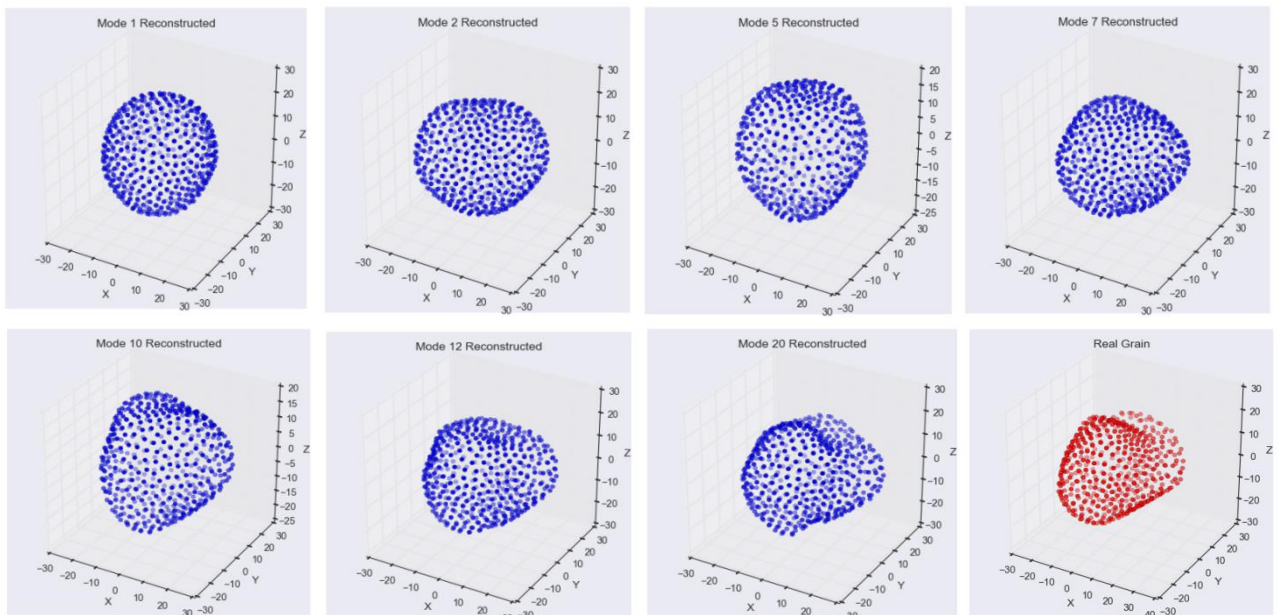


Figure 11: Grain shape evolution through modes 1 to 20 and real grain

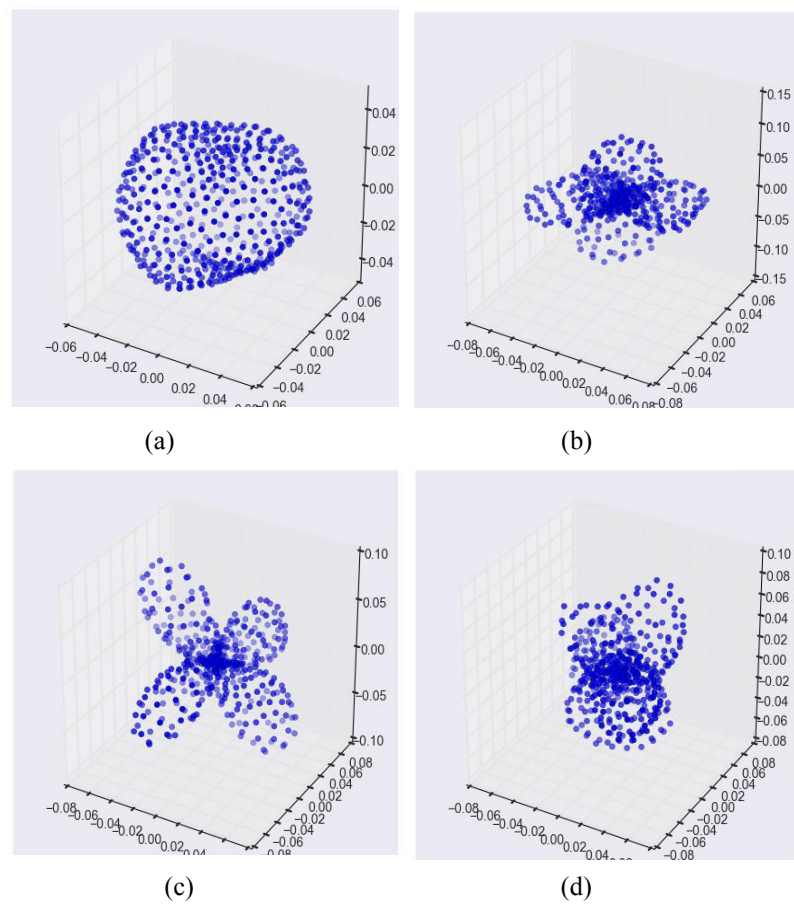


Figure 12: (a) Mode 1 (b) Mode 2 (c) Mode 3 (d) Mode 4

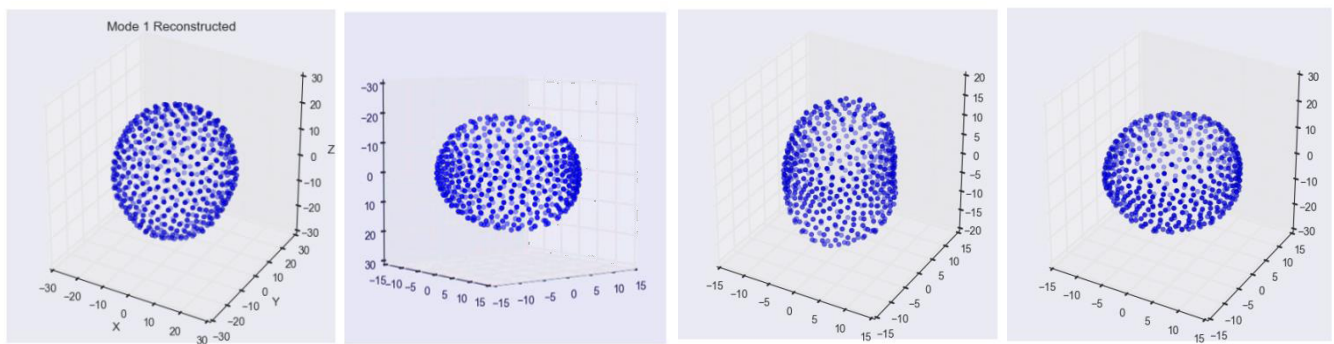


Figure 13: Different grains reconstructed from mode 1

3 CONCLUSION AND PROSPECTS

An innovative approach, based on dimensionality reduction by means of POD, leading to an optimal and nearly exhaustive shape characterization of real ballast grains has been presented. A method to generate sets that are representative of real grains has also been introduced, and validated by comparing some properties of the grains, such as surfaces and volumes. The method proved to give satisfactory results, and will give even better results for a data set of a larger size, as it will more accurately capture shape features. By observing the grain shape evolution through POD eigenmodes, studying more the link between the latters and shape features can be an interesting future outlook.

ACKNOWLEDGEMENTS

This work was supported by SNCF, the French railway company, Innovation and Research Department.

REFERENCES

- [1] AFNOR. Granulat pour ballast de voies ferrées. Technical report, 2003.
- [2] Azéma, E., Descantes, Y., Roquet, N., Roux, J. N., & Chevoir, F. (2012). Discrete simulation of dense flows of polyhedral grains down a rough inclined plane. *Physical Review E*, 86(3), 031303, 1–15.
- [3] Azéma, E. (2007). Etude numérique des matériaux granulaires à grains polyédriques: rhéologie quasi-statique, dynamique vibratoire, application au procédé de bourrage du ballast (Doctoral dissertation, Montpellier 2).
- [4] Azéma, E., & Radjaï, F. (2010). Stress-strain behavior and geometrical properties of packings of elongated particles. *Physical Review E*, 81(5), 051304.
- [5] Azéma, E., Radjai, F., & Dubois, F. (2013). Packings of irregular polyhedral particles: Strength, structure, and effects of angularity. *Physical Review E*, 87(6), 062203.
- [6] Azéma, E., Radjai, F., Peyroux, R., & Saussine, G. (2007). Transmission des forces dans un milieu composé de grains non sphériques. *arXiv preprint arXiv:0706.4007*.
- [7] Dong, K., Wang, C., & Yu, A. (2015). A novel method based on orientation discretization for discrete element modelling of non-spherical particles. *Chemical Engineering Science*.
- [8] Eliáš, J. (2013). DEM simulation of railway ballast using polyhedral elemental shapes. In particle-based methods III: fundamentals and applications, Proceedings of the 3rd International Conference on Particle-based Methods, Fundamentals and Applications, Held in Stuttgart, Germany (pp. 247-256).
- [9] Grigoriu, M., Garboczi, E., & Kafali, C. (2006). Spherical harmonic-based random fields for aggregates used in concrete. *Powder Technology*, 166(3), 123-138.
- [10] Höhner, D., Wirtz, S., Kruggel-Emden, H., & Scherer, V. (2011). Comparison of the multi-sphere and polyhedral approach to simulate non-spherical particles within the discrete element method: Influence on temporal force evolution for multiple contacts. *Powder Technology*, 208(3), 643-656.
- [11] Höhner, D., Wirtz, S., & Scherer, V. (2012). A numerical study on the influence of particle shape on hopper discharge within the polyhedral and multi-sphere discrete element method. *Powder Technology*, 226, 16-28.

- [12] Höhner, D., Wirtz, S., & Scherer, V. (2015). A study on the influence of particle shape on the mechanical interactions of granular media in a hopper using the Discrete Element Method. *Powder Technology*, 278, 286-305.
- [13] Quezada, J. C., Breul, P., Saussine, G., & Radjai, F. (2014). Penetration test in coarse granular material using Contact Dynamics Method. *Computers and Geotechnics*, 55, 248-253.
- [14] Latham, J. P., & Munjiza, A. (2004). The modelling of particle systems with real shapes. *PHILOSOPHICAL TRANSACTIONS-ROYAL SOCIETY OF LONDON SERIES A MATHEMATICAL PHYSICAL AND ENGINEERING SCIENCES*, 362, 1953-1972.
- [15] Liang, Y. C., Lee, H. P., Lim, S. P., Lin, W. Z., Lee, K. H., & Wu, C. G. (2002). Proper Orthogonal Decomposition and Its Applications—Part I: Theory. *Journal of Sound and Vibration*, 252(3), 527–544.
- [16] Lim, W. L. (2004). Mechanics of railway ballast behaviour (Doctoral dissertation, University of Nottingham).
- [17] Lim, W. L., & McDowell, G. R. (2005). Discrete element modelling of railway ballast. *Granular Matter*, 7(1), 19-29.
- [18] Liu, X., Garboczi, E. J., Grigoriu, M., Lu, Y., & Erdogan, S. T. (2011). Spherical harmonic-based random fields based on real particle 3D data: improved numerical algorithm and quantitative comparison to real particles. *Powder Technology*, 207(1), 78-86.
- [19] Liu, Z., Zhao, J., & Mollon, G. (2014). The influence of particle shape for granular media: A fourier-shape-descriptor-based micromechanical study. *Digital Humanitarians: How Big Data Is Changing the Face of Humanitarian Response*, 237.
- [20] Lu, G., Third, J. R., & Müller, C. R. (2014). Discrete element models for non-spherical particle systems: From theoretical developments to applications. *Chemical Engineering Science*.
- [21] Aas, K. (2004). Modelling the dependence structure of financial assets: A survey of four copulas.
- [22] Mollon, G., & Zhao, J. (2013). Generating realistic 3D sand particles using Fourier descriptors. *Granular Matter*, 15(1), 95-108.
- [23] Salinas-Gutiérrez, R., Hernández-Aguirre, A., Rivera-Meraz, M. J., & Villa-Diharce, E. R. (2011). Using Gaussian Copulas in Supervised Probabilistic Classification. In *Soft Computing for Intelligent Control and Mobile Robotics* (pp. 355-372). Springer Berlin Heidelberg
- [24] Saussine, G. (2004). Contribution à la modélisation de granulats tridimensionnels: application au ballast (Doctoral dissertation, Université Montpellier II-Sciences et Techniques du Languedoc).
- [25] Schmidt, T. (2007). Coping with copulas. *Copulas-From theory to application in finance*, 3-34.
- [26] Saint-Cyr, B., Szarf, K., Voivret, C., Azéma, E., Richefeu, V., Delenne, J. Y., ... & Radjai, F. (2012). Particle shape dependence in 2D granular media. *EPL (Europhysics Letters)*, 98(4), 44008.
- [27] Shlens, J. (2014). A tutorial on principal component analysis. *arXiv preprint arXiv:1404.1100*

- [28] Sklar, A. (1959). Fonctions de répartition à n dimensions et leurs marges. Publications de l’Institut de Statistique de l’Université de Paris 8, 229–231
- [29] Zhou, B., & Wang, J. (2015). Random generation of natural sand assembly using micro x-ray tomography and spherical harmonics. Geotechnique Letters, 5(January–March), 6–11.

TRANSIENT REGIME TO FLUIDIZED CHIMNEY WITHIN A GRANULAR BED BY MEANS OF A 2D DEM/LBM MODELING

JEFF NGOMA^{1,2}, PIERRE PHILIPPE¹, STEPHANE BONELLI¹, PABLO CUÉLLAR¹,
JEAN-YVES DELENNE³ AND FRANCK RADJAI^{4,5}

¹ OHAX, IRSTEA (French Research Institute of Science and Technology for Environment and Agriculture), 3275 route de Cézanne CS40061, 13182 Aix-en-Provence, France
jeff.ngoma@irstea.fr, pierre.philippe@irstea.fr, stephane.bonelli@irstea.fr, <http://irstea.fr/>

² Institut Jean Lamour, CNRS - Université de Lorraine, Parc de Saurupt
CS 50840, 54011 Nancy, France
jeff.ngoma@univ-lorraine.fr, <http://ijl.univ-lorraine.fr/>

³ UMR IATE, INRA – CIRAD - Montpellier Supagro - Université Montpellier 2
2 place Pierre Viala, 34060 Montpellier, France
delenne@supagro.inra.fr, <http://umr-iate.cirad.fr/>

⁴ Laboratoire de Mécanique et Génie Civil, CNRS - Université Montpellier 2
Place Eugène Bataillon, 34095 Montpellier, France
Franck.Radjai@univ-montp2.fr, <http://www.lmgc.univ-montp2.fr/>

⁵ UMI 3466 CNRS – MIT, Department of Civil and Environmental Engineering, MIT, 77
Massachusetts Avenue, Cambridge CA 02139, USA
fradjai@mit.edu, <http://www.cee.mit.edu/>

Key words: Granular Materials, DEM, LBM, Fluidization.

Abstract. Beyond a given threshold, an upward fluid flow at constant flowrate, injected through a small size section, is able to generate a fluidization along a vertical chimney over the entire height of a granular assembly. Fluidization is first initiated in the immediate vicinity of the injection hole and then the fluidized zone grows gradually until reaching the upper surface of the granular packing. In this work, we present numerical results on the kinetics of chimney fluidization in an immersed granular bed produced with two-dimensional simulations coupling the Discrete Element and Lattice Boltzmann Methods (DEM-LBM). A parametric study is carried out with 11 different sets of physical parameters and analyzed based on spatio-temporal diagrams. Then a dimensional analysis allows finding general scaling laws for both threshold and growth rate of the fluidized zone by use of two dimensionless numbers, namely Reynolds and Archimedes numbers, while quite simple empirical relationships can also be proposed.

1 INTRODUCTION

A fluidized state within a granular bed is reached when the upward force exerted by the flow can balance the buoyant weight of the particles. Fluidization is used extensively in industry for drying, mixing and agglomeration processes with many applications as gasification of biomass, ion exchange processes or high efficiency carbon capture. Some among these industrial processes rely more specifically on a localized state of fluidization as is the case for spouted beds [1] and tapered beds [2] which are generated by means of an upward gas flow injected most often at the neck of a conical container. Contrariwise, channelization, i.e. occurrence of such preferential channels of fluidization, is to be absolutely avoided for other types of fluidized bed applications. In sedimentology, some geologic formations of fluid escape structures by localized fluidization through vertical pipe have been specifically examined [3]. A somehow similar situation is encountered in the context of dike safety, when a seepage flow through the foundation of an embankment is susceptible to generate such a local fluidization, commonly called “sandboil”, and possibly initiate a piping process by backward erosion, which is one of the four basic mechanisms identified for soil particles removal by internal erosion [4].

Here the focus is put more restrictively on the development and growth of a local fluidized state within an immersed granular assembly induced at the bottom of the grain bed by an upward fluid flow passing through a small injection hole. Several previous works have studied specifically this configuration and analysed the formation of a vertical chimney of fluidized soil on the basis of either experiments [5, 6] or numerical simulations coupling Discrete Element Method (DEM) with Lattice Boltzmann Method (LBM) [7]. It should be noted, however, that most efforts have been so far dedicated to the steady state rather than to the transitory development of such fluidized chimney [6]. This transient regime of localized fluidization is therefore specifically under the scope of the present study. For this purpose, a numerical model based on a 2D DEM/LBM coupled approach has been implemented to carry out a systematic analysis of the temporal evolution of the fluidized zone, expanding progressively from the injection hole to the top of the granular layer. As will be detailed below, a critical fluid velocity U_c as well as the growth rate of the fluidized cavity above this threshold can be precisely defined. Using the relevant dimensionless numbers of the problem, a general collapse of the data can be obtained, which permits the proposal of empirical scaling laws both for the critical velocity and for the fluidization growth rate.

The following sections first introduce the numerical approach developed in the present study and then focus specifically on the transient regime to fluidized chimney within an immersed granular bed subject to a localized fluid injection at its base.

2 NUMERICAL METHODS

Many numerical methods are developed to simulate fluid-particles interactions at the micro-scale. The crucial point is the approach taken to couple the particles' dynamics and the interstitial fluid flow. Here we have chosen to tackle this issue by a simultaneous use of the Discrete Element Method (DEM) and of the Lattice Boltzmann Method (LBM). This choice has the advantage to combine the comparative simplicity of DEM with LBM, one of the most efficient computational methods for fluid dynamics. Both methods as well as the coupling strategy are briefly described below.

2.1 DEM modeling of the solid phase

In this study, the Discrete Element Method (DEM) is implemented through the Molecular Dynamics modeling, a numerical method originally developed by Cundall and Strack [8] for rock mechanics applications and which quickly became very popular in many other fields of application dealing with interacting solid particles [9]. The Molecular Dynamics method considers the solid material as discrete particles that interact with each other in areas of mutual contact. The particles are assumed to be rigid with possibly a small overlap at the contact while the interactions are modelled by appropriate and physically based laws depending on this overlap. Then, the particles' motion can be directly described by Newton's equations. More details can be found in [10, 11].

2.2 LBM modeling of the fluid phase

A classical D2Q9 scheme is used here for LBM describing the fluid flow within the grains, allowing for an explicit finite differences calculation of Boltzmann equation on a Cartesian lattice grid (2D) and using a discrete set of velocity vectors at each grid node (Q9) [12]. The calculation is related to a probability density function, discretized on the lattice, and computed in two successive steps: collision and advection, both assuming specific rules to ensure mass, momentum and energy conservation provided that Mach number is very low or, equivalently, that fluid velocity remains significantly smaller than the lattice speed. With this condition, the fluid flow follows the incompressible Navier-Stokes equations. Note also that, instead of the classical single relaxation time scheme originally proposed by Bhatnagar, Gross, and Krook [12], a multiple relaxation time (MRT) is advantageously implemented here, following the generalized formulation by d'Humières [13, 14]. Further details on this method can also be found in [10, 11].

2.3 Solid-fluid coupling

In our modelling, the simple technique proposed by Bouzidi et al. [15] for momentum exchange is implemented to calculate the hydrodynamic forces on each discrete particle and couple this way the fluid and solid phases. This computation is based on a generalized bounce-back condition with a linearly interpolated geometry of the particles boundary inside the fluid lattice. A key parameter for the fluid-solid coupling is the space resolution, i.e. the lattice grid size compared to the minimum particle diameter. It is commonly accepted that a satisfactory result can be obtained with at least 10 grid points per grain diameter, which is the resolution used in the present study for an affordable computational cost. Moreover, as the calculation time is much larger for LBM than DEM, we have used the sub-cycling time integration technique proposed by Feng et al [16] with a number of DEM sub-cycles which is restricted to 2 for each LBM loop, a good compromise to maintain the accuracy of the computed hydrodynamic forces on the solid particles. In order to overcome the fact that a real 2D assembly of discs in contact is an occluded space with a zero permeability value, the LBM calculations are here carried out with a constant reduction of the particles' radius by a factor of 0.8, which provides a realistic permeability value [17] and roughly accounts for lubrication forces [18].

3 TRANSIENT REGIME TO FLUIDIZED CHIMNEY

3.1 Configuration and parameters

Based on the coupled DEM-LBM technique described above, a two-dimensional numerical modeling was carried out to simulate an assembly of grains subjected to a localized fluid injection at its base. Grain sizes have a mean value d and are uniformly distributed from $0.8d$ to $1.2d$. Two different samples have been used with initial height H_0 equal respectively to approximately 86 mm and 54 mm while the overall domain dimensions are $L = 222$ mm in length and $H = 160$ mm in height. The bottom boundary is a solid wall except for a filtering orifice of width $D = 14$ mm at its center which allows the fluid to be injected upwards at a constant velocity U but remains impassable for the grains. A velocity inlet condition is thus implemented at the injection hole while a periodic condition is set at the top and bottom boundaries of the domain. A no-slip condition is implemented on all other boundaries, considered as solid walls. A sketch of the configuration is shown in Figure 1.

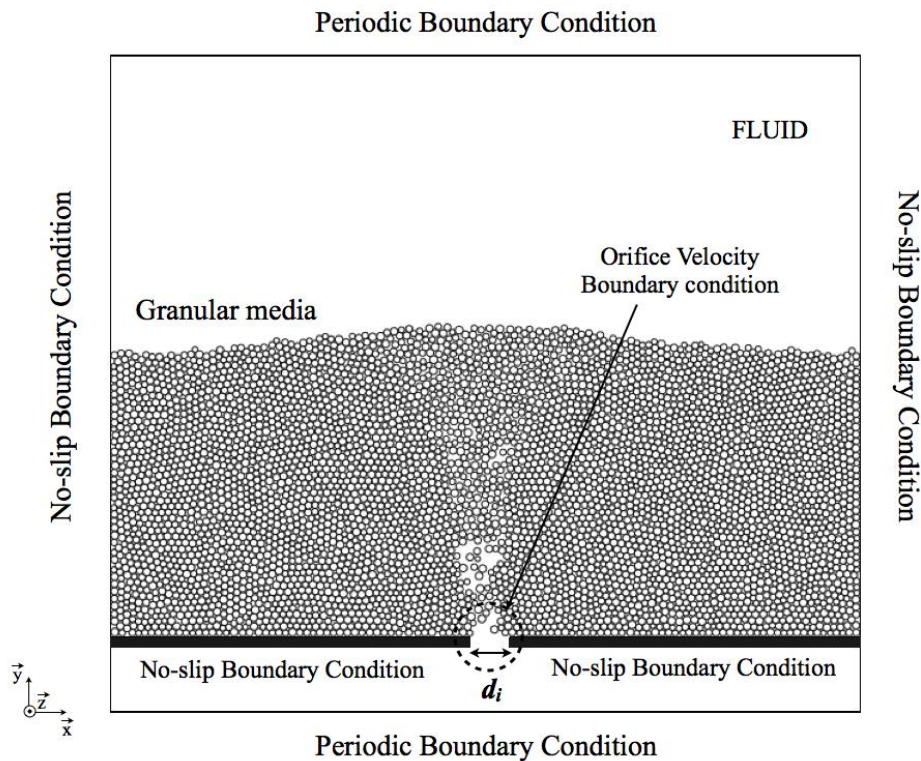


Figure 1: Configuration and boundary conditions of the numerical study.

To reach a fluidized state, the drag forces induced by the interstitial flow must overcome the inter-granular forces within the particles' sample. In the studied conditions of purely frictional interactions between grains, the internal granular stress is solely related to the buoyant weight of the system. Consequently, the physical parameters of the problem are: the diameter of the grains d , the kinematic viscosity of the fluid ν_f , the density of the fluid ρ_f and

of the grains ρ_g , and finally the gravity g . The control parameter used here is the injected fluid velocity U while the geometry of the system is fixed by the initial height H_0 , the width of the domain L and the diameter of the injection hole D . In what follows, L and D remain unchanged and, since D is much smaller than L ($D/L \approx 0.06$), it can be reasonably considered that L plays a minor role.

A parametric study has been carried out using 11 different parameter sets (see Table 1) enabling some of the physical parameters to be significantly varied, namely v_f , ρ_g , g and d . Two different values of the initial height H_0 has also been used while the injection diameter D was kept constant ($D = 14\text{mm}$).

Table 1: Sets of parameters

Set number	$v_f (\text{m}^2 \cdot \text{s}^{-1})$	$\rho_g (\text{kg} \cdot \text{m}^{-3})$	$g (\text{m} \cdot \text{s}^{-2})$	$d (\text{mm})$
1	$5 \cdot 10^{-5}$	2500	9.81	2
2	$1 \cdot 10^{-5}$	2500	9.81	2
3	$5 \cdot 10^{-5}$	2500	1	2
4	$1 \cdot 10^{-5}$	1500	9.81	2
5	$5 \cdot 10^{-5}$	1500	9.81	2
6	$5 \cdot 10^{-5}$	2500	1	2
7	$5 \cdot 10^{-6}$	2500	9.81	2
8	$5 \cdot 10^{-6}$	1500	9.81	2
9	$2 \cdot 10^{-6}$	2500	9.81	2
10	$2 \cdot 10^{-6}$	1500	9.81	2
11	$5 \cdot 10^{-5}$	2500	9.81	4

For all parameter sets, the analysis of the transitory evolution to final fluidized chimney is performed using space-time diagrams constructed at the injection from the different sequences obtained for each successive fluid velocity U imposed at the injection hole (Figure 2). From these diagrams, it is then possible to determine quite accurately the time T_0 needed for the fluidized zone to expand upwards to a height equal to H_0 .

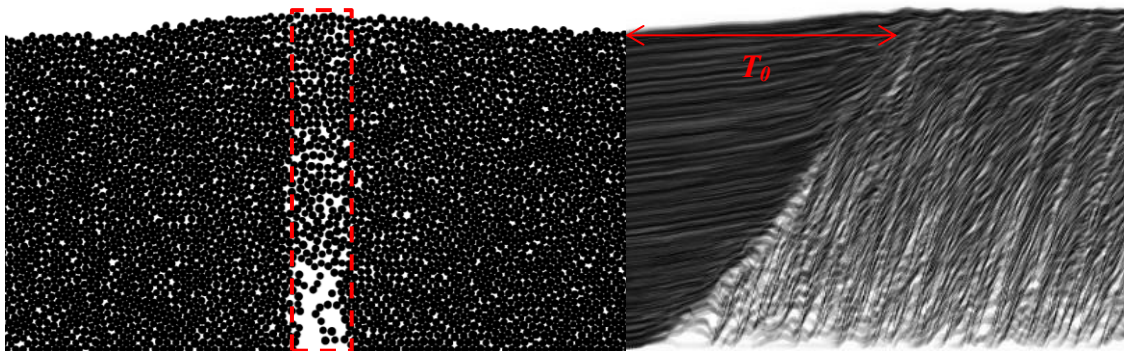


Figure 2: Typical space-time diagram used to determine the duration T_0 of the transient regime and calculated in the rectangular area (in dotted line) located above the injection hole.

3.2 Chimney expansion time and growth rate

Plotting the chimney expansion time T_0 as a function of the injection velocity U , a divergence is observed when U tends to a threshold value U_c which can be accurately determined by use of the following power law adjustment of the curve:

$$T_0(U) = \tau_0(U/U_c - 1)^{-\alpha} \quad (1)$$

where τ_0 is a constant equal to $T_0(U = 2U_c)$ and α is the opposite of the exponent.

The value of α can be satisfactorily chosen within the range $0.5 < \alpha < 0.7$ with a small but still significant impact on the threshold velocity U_c . Of probably greater interest is $V_0 = H_0/T_0$, the characteristic growth rate which quantifies the velocity at which the fluidized zone expands upwards. Here again, as shown in Figure 3, a power law can be used with the opposite exponent α :

$$V_0(U) = \Lambda_0(U/U_c - 1)^\alpha \quad (2)$$

where Λ_0 is a constant equal to $V_0(U = 2U_c)$.

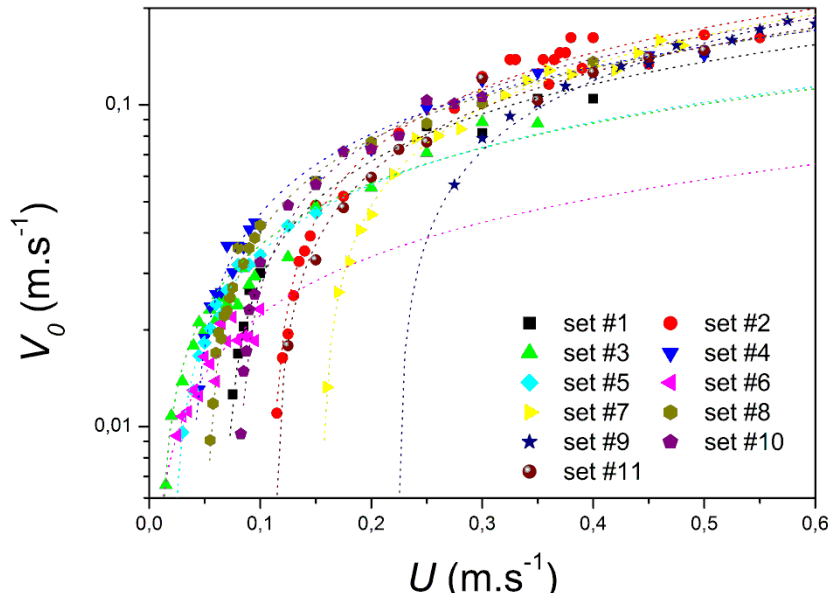


Figure 3: Characteristic growth rate V_0 of the fluidized zone versus fluid injection velocity U for $H_0 = 86$ mm.
The lines are power law functions given by Equation (2) with $\alpha = 0.6$.

It can be noted that in the present study α has been arbitrarily fixed equal to 0.6 and, depending on the parameters in Table 1, the values obtained for U_c vary on several orders of magnitude as can be noticed in Figure 3.

3.3 Scaling laws

Accounting for buoyancy, the only relevant physical quantities are the fluid kinematic viscosity ν_f , the fluid injection velocity U , the grain diameter d , and the resultant buoyant

gravity $g^* = g(\rho_g / \rho_f - 1)$. From these magnitudes, two dimensionless numbers can be formed, namely the Reynolds number $Re = Ud / \nu_f$ and the Archimedes number $Ar = g^* d^3 / \nu_f^2$. And thus, the critical Reynolds number $Re_c = U_c d / \nu_f$ should consequently be simply dependent on Ar . As shown in Figure 4, such a relationship is indeed reasonably well obtained for all values corresponding to the 11 different sets of parameters and a very simple empirical power law relation can be proposed:

$$Re_c \propto Ar^{3/4} \quad (3)$$

Therefore, the dependencies on the geometrical parameters H_0 and D are completely taken into account by the proportionality factor in Equation (3).

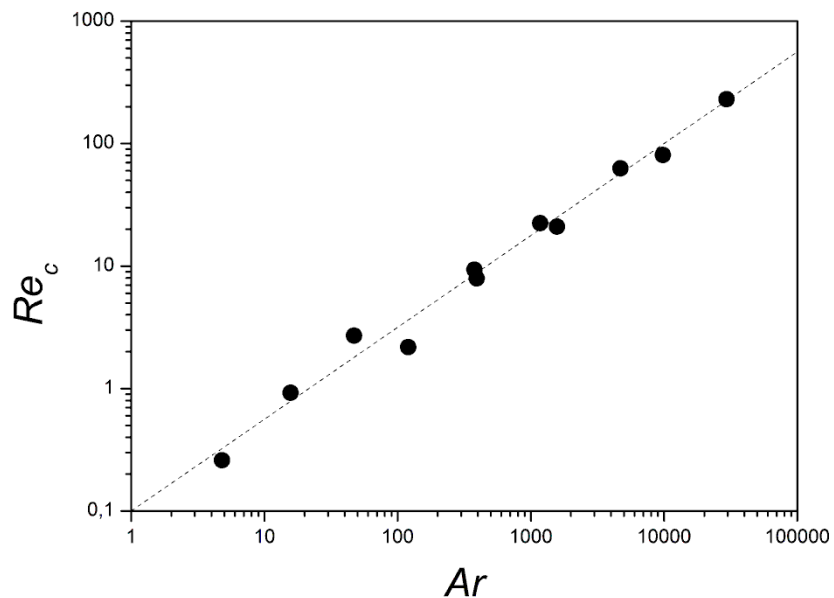


Figure 4: The critical Reynolds number Re_c plotted as a function of Archimedes number Ar for $H_0 = 86$ mm.
The line corresponds to Equation (3) with a proportionality factor equal to 0.1.

Such a dimensional analysis can be extended beyond the critical value for chimney fluidization to account more broadly for the transient behavior obtained once this threshold is exceeded, i.e. for $U > U_c$. For this purpose, we now use the general expression of the Reynolds number, $Re = Ud / \nu_f$, while the characteristic growth rate V_0 is also made dimensionless by introducing a new Reynolds numbers Re_0 defined as follows:

$$Re_0 = V_0 d / \nu_f \quad (4)$$

Finally, to get rid of the additional dependencies due to the geometry of the system (mainly through the initial height H_0), Re and Re_0 are both divided by the critical Reynolds number Re_c . This way, as shown in Figure 5, a global collapse of all the data is obtained, confirming the previous analysis. Moreover, following Equation (2), a general empirical scaling law can now be proposed in the form:

$$Re_0 / Re_c \propto (Re / Re_c - 1)^{3/5} \quad (3)$$

Note that the proportionality factors obtained for the two values of H_0 used in this study are indeed rather close although slightly different, equal to 0.75 and 0.95 respectively for $H_0 = 86$ mm and $H_0 = 54$ mm.

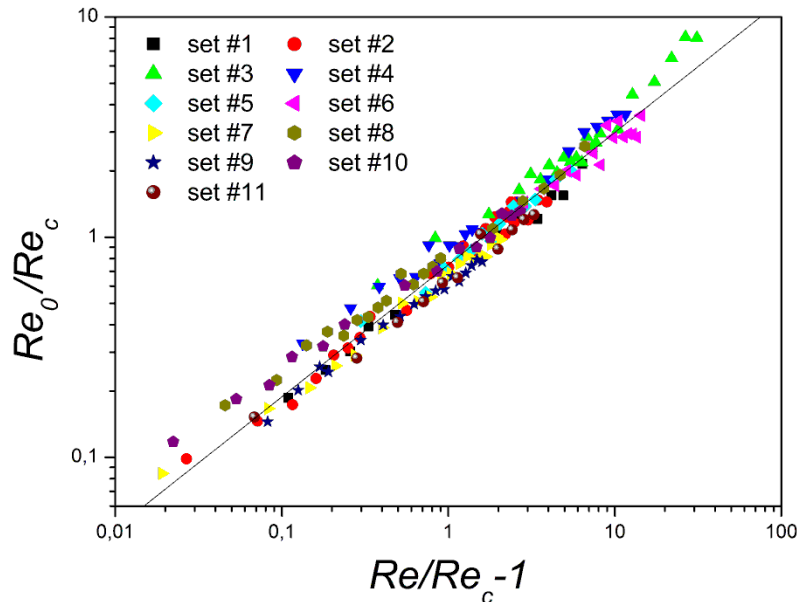


Figure 5: The ratio Re_0/Re_c plotted versus $Re/Re_c - 1$ for $H_0 = 86$ mm. The line stands for Equation (5) with a proportionality factor being equal to 0.75.

4 CONCLUSION

A 2D coupled DEM-LBM model has been implemented to produce a realistic representation of fluid-grains interactions and dynamics. This model has been successfully applied to study the particular phenomenon of development of a fluidized chimney within an immersed granular bed from a small fluid injection hole at the base of a grain assembly. Focusing specifically on the transient regime leading to a steady chimney, a parametric analysis has been undertaken with 11 different sets of the main physical parameters involved in the problem. The first outcome of this study shows that the critical fluid velocity U_c needed for such a chimney fluidization can be clearly interpreted in terms of dimensionless numbers. The corresponding critical Reynolds $Re_c = U_c d / \nu_f$ is indeed simply a function of the Archimedes number $Ar = g(\rho_g / \rho_f - 1) d^3 / \nu_f^2$ which is fairly compatible with an empirical power law relation: $Re_c \propto Ar^{3/4}$.

In addition, the characteristic growth rate V_0 , i.e. the upward expansion rate of the fluidized zone, can also be predicted from our dimensional analysis provided that additional Reynolds numbers are formed using the different velocities of the system: U , U_c and V_0 . This way, it is possible to obtain a general collapse of all data from the different parameter sets, allowing the proposal of a very simple empirical law: $Re_0 / Re_c \propto (Re/Re_c - 1)^{3/5}$.

REFERENCES

- [1] Mathur, K. and Epstein, N. *Spouted Beds*. Academic Press, New-York, USA (1974).
- [2] Peng, Y. and Fang, L.T. Hydrodynamic characteristics of fluidization in liquid-solid tapered beds. *Chemical Engineering Science* (1997) **52**(14):2277-2290.
- [3] Nichols, R.J., Sparks, R.S.J. and Wilson, C.J.N. Experimental studies of the fluidization of layered sediments ant the formation of fluid escape structures. *Sedimentology* (1994) **41**(2):233-253.
- [4] Bonelli, S. (Editor). *Erosion in Geomechanics Applied to Dams and Levees*. Wiley-ISTE (2013).
- [5] Zoueshtiagh, F. and Merlen, A. Effect of a vertically flowing water jet underneath a granular bed. *Physical Review E* (2007) **75**(5):053613.
- [6] Philippe, P. and Badiane, M. Localized fluidization in a granular medium. *Physical Review E* (2013) **87**(4):042206.
- [7] Cui, X., Li, H., Chan, A. and Chapman, D. A. A 2D DEM-LBM study on soil behaviour due to locally injected fluid. *Particuology* (2012) **10**:242-252.
- [8] Cundall, P.A. and Strack, O.D.L. A discrete numerical model for granular assemblies. *Géotechnique* (1979) **29**:47-65.
- [9] Radjai, F. and Dubois, F. (Editors). *Discrete-element Modeling of Granular Materials*. Wiley-ISTE (2011).
- [10] Ngoma, J., Philippe, P., Bonelli, S., Delenne J.-Y. and Radjai, F. Interaction between two localized fluidization cavities in granular media: Experiments and numerical simulation. In *Geomechanics From Micro to Macro*, Soga, K., Kumar, K., Biscontin, G. and Kuo, M. (Editors), CRC Press/Balkema, Taylor & Francis Group, London, UK (2015).
- [11] Ngoma, J. *Etude numérique et expérimentale de la déstabilisation des milieux granulaires immersés par fluidisation* (2015), PhD thesis, Aix-Marseille University, France.
- [12] Sukop, M. C. and Thorne, D. T. *Lattice Boltzmann Modeling. An Introduction for Geoscientists and Engineers*. Springer, Berlin (2005).
- [13] d'Humières, D., Ginzburg, I., Krafczyk, M., Lallemand, P. and Luo, L.-S. Multiple-relaxation-time lattice Boltzmann models in three dimensions. *Philosophical Transactions of the Royal Society London A* (2002) **360**:437-451.
- [14] Yu, D., Mei, R., Luo, L.-S. and Shyy, W. Viscous flow computations with the method of lattice Boltzmann equation. *Progress in Aerospace Sciences* (2003) **39**:329–367.
- [15] Bouzidi, M., Firdauss, M. and Lallemand, P. Momentum transfer of a Boltzmann-lattice fluid with boundaries. *Physics of Fluids* (2001) **13**(11):3452.
- [16] Feng, Y.T., Han, K. and Owen, D.R.J. Coupled lattice Boltzmann method and discrete element modelling of particle transport in turbulent fluid flows: Computational issues. *International Journal for Numerical Methods Engineering* (2007) **72**:1111–1134.
- [17] Boutt, D.F., Cook, B.K. and Williams, J. R. A coupled fluid–solid model for problems in geomechanics: Application to sand production. *International Journal for Numerical and Analytical Methods in Geomechanics* (2011) **35**:997–1018.
- [18] Mutabaruka, P., Delenne, J.-Y., Soga, K. and Radjai, F. Initiation of immersed granular avalanches. *Physical Review E* (2014) **89**(5):052203.

DEM SIMULATIONS OF PARTICLE DYNAMICS IN A SPHERONIZATION PROCESS TO DESCRIBE THE PELLETIZATION MECHANISMS

D. WEIS¹, D. THAETE², M. THOMMES², S. ANTONYUK¹

¹ Chair of Particle Process Engineering, University of Kaiserslautern
Gottlieb-Daimler-Straße 44, 67663 Kaiserslautern, Germany
dominik.weis@mv.uni-kl.de, mvt.mv.uni-kl.de

² Chair of Solids Process Engineering, Technical University Dortmund
Emil-Figge-Street 68, 44227 Dortmund, Germany
dennis.thaete@bci.tu-dortmund.de, fsv.bci.tu-dortmund.de

Key words: Pharmaceutical Pellets, Spheronization, DEM, PIV

Abstract. Spheronization is an important process to produce pharmaceutical pellets with a narrow particle size distribution and a homogeneous outer particle surface. Thereby, cylindrical extrudates are rounded by different pelletization mechanisms [1]. These mechanisms are highly dependent on the particle dynamics in the spheronizer. Discrete Element Method simulations of the particle motions in a spheronizer were performed to study the particle dynamics. The elastic-plastic contact model used in the simulations was calibrated by experiments with spheronized pellets. The influence of different process conditions and particle properties on the particle kinematics and interactions was analyzed. Also a comparison of the simulation results with PIV measurements was performed.

1 INTRODUCTION

Pharmaceutical pellets are spherical granules with a narrow particle size distribution and a reproducible outer particle surface. Extrusion and spheronization is a common technique to produce such pellets. A spheronizer consists of a static cylindrical wall and a rotating disk with a structured surface (friction plate) as shown in Figure 1. Cylindrical extrudates are placed on the friction plate and are rounded during the spheronization process by different formation mechanisms [1].

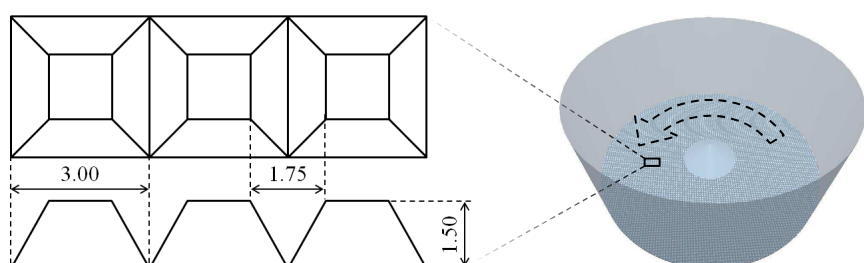


Figure 1: Schematic representation of the spheronizer (right) and the friction plate viewed from top (left top) and side (left bottom), (dimensions in mm) [2]

Describing the spheronization process is complex because these formation mechanisms take place simultaneously and are highly dependent on the particle dynamic, which is influenced by process conditions and particle properties. Therefore simulations can be helpful to predict the formation mechanisms. With Discrete Element Method (DEM) simulations the particle dynamics can be analyzed. Bouffard et al. have simulated the particle dynamics in the spheronizer using DEM to describe the segregation during spheronization of a bimodal particle system [3]. Koester et al. have performed DEM simulations of the movement of γ -Al₂O₃ particles in a spheronizer and have compared the results with PIV measurements [4].

The focus of the performed study was on the collision rate and collision forces of the particles, besides the particle motion. Various factors which influence the particle kinematic and collision characteristics were examined. In addition to process conditions like the rotational speed of the friction plate and the mass of particles in the spheronizer (loading) some properties of the particles like diameter, stiffness, coefficient of restitution and coefficient of static friction were varied. Also the obtained simulation results were compared with PIV measurements of the spheronization process of MCC pellets in [5].

To consider the particle-particle and particle-wall interactions in the DEM simulations, an elastic-plastic contact model was used because of the dominantly plastic behavior of the investigated pellets. The parameters of the contact model were calibrated by comparison with the performed single particle tests with spheronized pellets.

2 MATERIALS AND METHODS

2.1 Experimental Setup

The material parameters for the contact model of the DEM were determined by different uniaxial compression tests of pellets performed with the Texture Analyzer (TA.XTplus, Stable Micro Systems, UK). The pellets consist of 20 % (w) microcrystalline cellulose (MCC 102G SANAQ, Pharmatrans Sanaq, Switzerland) and 80 % (w) of α -lactose monohydrate (Granulac 200, Meggle, Germany) and are spheronized in a lab scale spheronizer (Schlueter RM300, Schlueter, Germany) [5]. Afterwards they are loaded up to a defined force or strain, while the force and the displacement are continuously recorded (see Figure 2). From these force displacement curves, different material parameters like compression strength, breakage force, stiffness and equivalent coefficient of restitution could be derived. Table 1 shows the results for pellets extruded with a water dosage rate of 15.5 g/min which have a diameter of $d_p = 1 - 3$ mm.

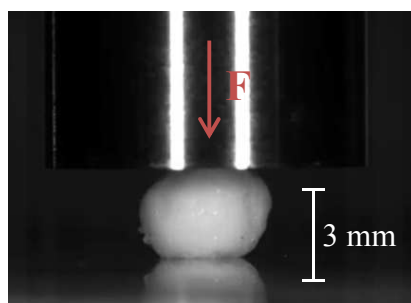


Figure 2: Uniaxial compression test of MCC pellets

Table 1: Results of uniaxial compression tests

Parameter	arithmetic mean \pm standard deviation
compression strength / MPa	0.11 ± 0.04
breakage force / N	0.28 ± 0.07
equivalent coefficient of restitution / -	0.31 ± 0.01
stiffness / N mm ⁻¹	0.87 ± 0.34

2.2 Simulation Method

The Discrete Element Method (DEM) was introduced in 1979 by Cundall and Strack [6] and is used mainly for simulating particulate systems. In the DEM solid discrete particles which can interact via contact forces F_c are modelled. These particles are assumed to be spherical and indestructible. For each particle the equations of motion (1) and (2) are solved.

$$m_p \frac{dv_p}{dt} = F_g + \sum_i^k F_{c,i} \quad (1)$$

The translational acceleration of a particle p with a mass m_p is calculated from the gravitational force F_g and the contact forces F_c . The contact force is divided into a normal component $F_{c,n}$ and a tangential component $F_{c,t}$ relative to the direction of the interaction. With the moments M_p acting on a particle, that are induced by the tangential components of the contact force, the rotational acceleration can be calculated.

$$J_p \frac{d\omega_p}{dt} = \sum_i^k M_{p,i} \quad (2)$$

The contact forces F_c needs to be modelled using an appropriate contact model. The performed compression tests showed that the pellets used have a dominantly plastic material behavior, which can be good predicted by the model of Walton and Braun [7], [8]:

$$F_{c,n} = - \begin{cases} K_1 \cdot \delta_n & \text{if } K_1 \cdot \delta_n < K_2 \cdot (\delta_n - \delta_0) \\ K_2 \cdot (\delta_n - \delta_0) & \text{if } \delta_n > \delta_0 \\ 0 & \text{if } \delta_n \leq \delta_0 \end{cases} \quad (3)$$

As can be seen in Figure 3 (left), the slope of the curve in the unloading case K_2 is greater than the slope in the loading case K_1 . This allows modeling the large plastic deformations δ_0 obtained by the uniaxial compression tests (Figure 3 right).

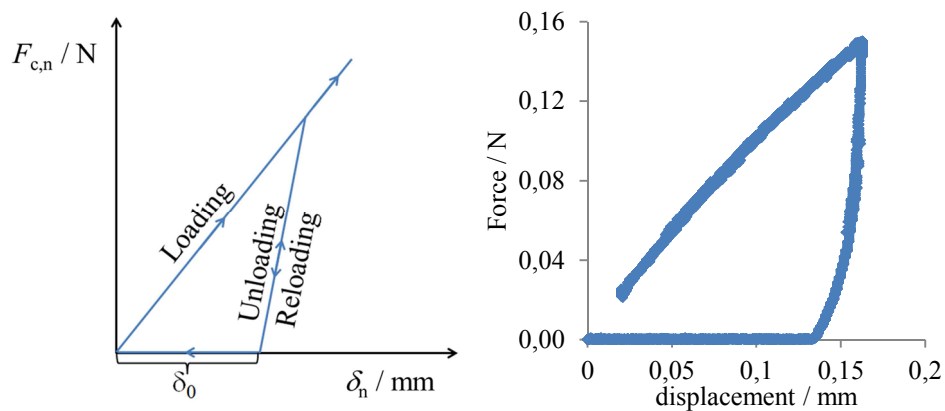


Figure 3: Force-displacement curve of the model of Walton and Braun (left) and experimental results (right)

The model considers the energy loss due to inelastic impact with a constant restitution coefficient e . Based on the restitution coefficient the stiffness of the unloading case can be calculated from the stiffness of the loading case [9]:

$$e = \sqrt{\frac{K_1}{K_2}} \quad (4)$$

Due to the nearly linear force-displacement curves, obtained by the uniaxial compression tests (Figure 3 right) the energy dissipation can be modelled only by the ratio between the stiffness of the loading and unloading case. Additionally, a viscous term is included to prevent possible un-damped low amplitude oscillations [8], [9]. For the numerical simulations the DEM software EDEM (DEM Solutions, UK) was used.

3 RESULTS AND DISCUSSION

The use of a cylindrical coordinate system instead of a Cartesian coordinate system is expedient, because the particle motion in the spheronizer is rotationally symmetric. Thus the spatial distribution of various time-averaged parameters can be displayed by discretizing the poloidal cut (rz-plane). In the evaluation of the collision characteristics, a distinction is made between interparticle collisions, collisions with the friction plate, and collisions with the spheronizer wall. All time-averaged distributions are calculated for the steady state, which was reached after a time of about $t = 0.8$ s.

3.1 Particle dynamics in the spheronizer

In this section the simulation results of a spheronizer loaded with $m = 600$ g of particles with a radius of $r_p = 2$ mm at a rotational speed of the friction plate of $n = 1000$ rpm are presented. The geometry used in the simulation corresponds to the physical dimensions of the spheronizer used for the experiments having a cross hatched friction plate (see Figure 1) with a diameter of $d = 300$ mm.

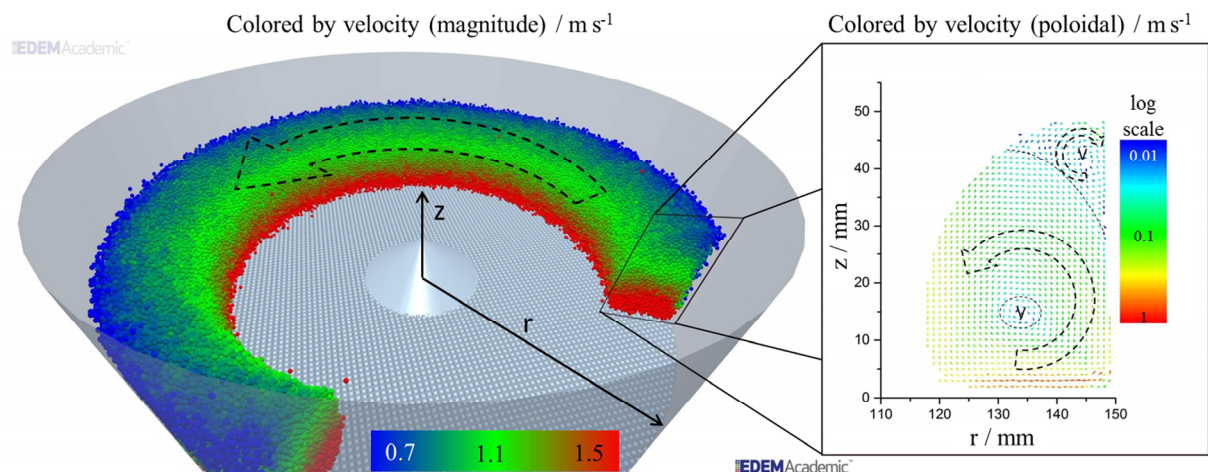


Figure 4: Particle velocities in the spheronizer at $n = 1000$ rpm and $m = 600$ g

The evaluation of the particle velocities exhibits rotational movements in poloidal direction superimposing the toroidal particle motion as shown in Figure 4. Koester et al. [4] describe five different zones of the particle movements in the poloidal cut. They found two zones V in which the mixing is limited due to the small poloidal velocities. The simulations performed in our work agree with these results. In addition they exhibit a counter-rotating movement in the upper zone V compared with the primary rotational movement (see Figure 4).

Figure 5 shows the time-averaged poloidal velocity field colored by toroidal velocities. As can be seen, the pellets have the greatest toroidal velocities immediately above the friction plate in the outer region. With increasing distance from the friction plate, the average toroidal velocities decrease. The lowest toroidal velocities occur in the upper region of the particle torus near the wall. The comparison of Figure 4 and Figure 5 shows that the velocities of the toroidal movement are significantly greater than that in the poloidal direction. The spatial distribution of the particle residence probability in the poloidal cut can be seen in Figure 6. Local maxima of the particle residence probability occur at regular intervals from the wall. From simulations with different particle sizes a correlation between the intervals of the maxima and the particle size was found. The first maximum is located at a distance which approximately corresponds to the particle radius r_p . The further maxima with decreasing intensity roughly occur at distances of odd multiples of the particle radius. Furthermore, Figure 6 shows a decrease in the particle residence probability near the friction plate with a local maximum at a distance of approximately r_p that is significantly smaller than the radial maxima. Moreover there is a significant increase in the intensity where it intersects the outer radial maximum.

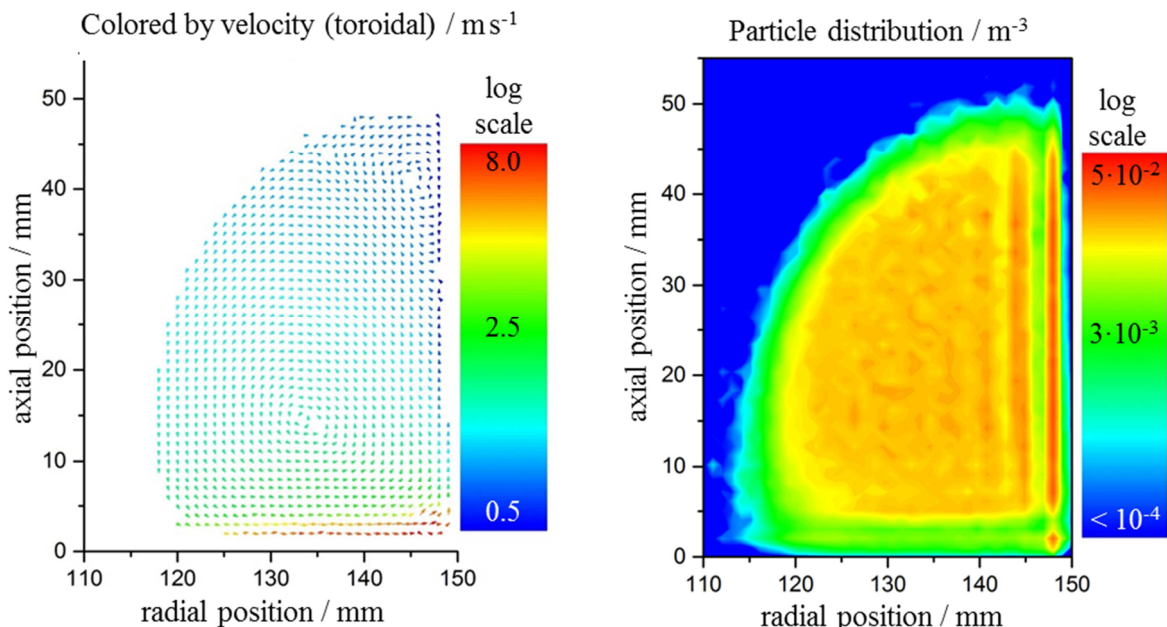


Figure 5: Time-averaged poloidal velocity field colored by toroidal velocities

Figure 6: Particle residence probability in poloidal cut

In addition to the spatial distribution of the particle residence probability in the spheronizer and the velocity fields, the interparticle collisions and the collisions with the friction plate and the wall are analyzed. The obtained interparticle collision rate is defined as the number of collisions per particle and second within a defined volume of the spheronizer:

$$\dot{N}_{c,p} = \frac{2 \cdot N_{c,p}}{(z_i - z_{i-1}) \cdot \pi \cdot (r_i^2 - r_{i-1}^2) \cdot \Delta t \cdot N_{p,ges}} \quad (5)$$

The particle geometry collision rate is defined as the number of collision per particle and second within a defined area of the wall or the friction plate:

$$\dot{N}_{c,f} = \frac{N_{c,f}}{\pi \cdot (r_i^2 - r_{i-1}^2) \cdot \Delta t \cdot N_{p,ges}} \quad (6)$$

$$\dot{N}_{c,w} = \frac{N_{c,w}}{(z_i - z_{i-1}) \cdot r_a \cdot \Delta t \cdot N_{p,ges}} \quad (7)$$

The axial coordinate z_i as well as the radial coordinate r_i are discretized in 1 mm elements. Figure 7 shows the spatial distribution of the average interparticle collision rate. It can be seen that the greatest values are reached in a lower region near the wall. The collision rate of the particle-friction plate and particle-wall interactions is shown in Figure 8. Overall, the rate of the collisions with the friction plate is an order of magnitude greater than that with the wall. It is remarkable that there is a significant increase of the values in the outer region of the friction plate and the lower region of the wall. Furthermore, the average collision forces are evaluated. The distribution of the interparticle collision forces is shown in Figure 9. It is apparent that the average collision forces are increasing with decreasing distance to the wall and the friction plate. The greatest interparticle collision forces occur immediately above the friction plate. Looking at the average forces of the particle-wall collisions in Figure 10, it can be seen that there is a maximum at a distance to the friction plate of about one particle diameter. Moreover Figure 10 shows that the decrease of the average collision forces with the distance to the friction plate can be described by a power law. The average collision forces of the particle friction plate interactions exhibit a small but characteristic maximum in the outer region. Due to a structured surface of the friction plate the mean collision rate curve shows a high fluctuation.

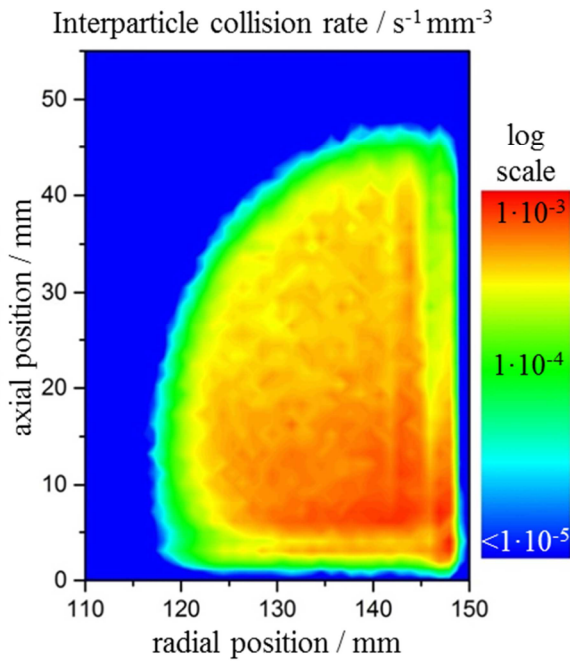


Figure 7: Rate of the interparticle collisions in poloidal cut

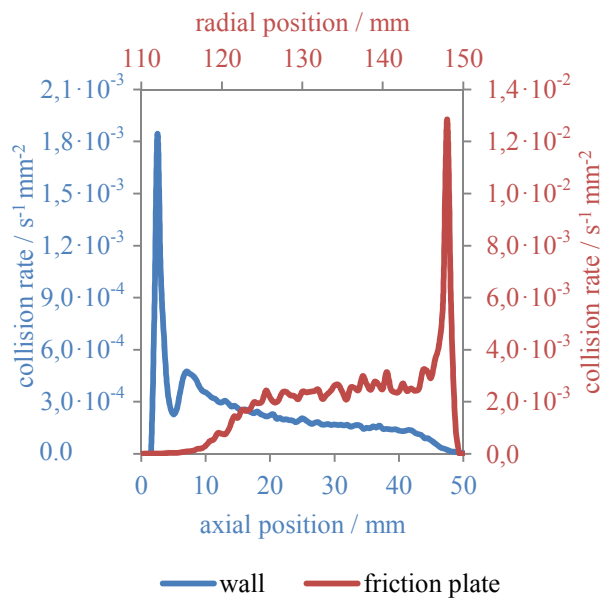


Figure 8: Rate of the collisions with the friction plate and the spheronizer wall

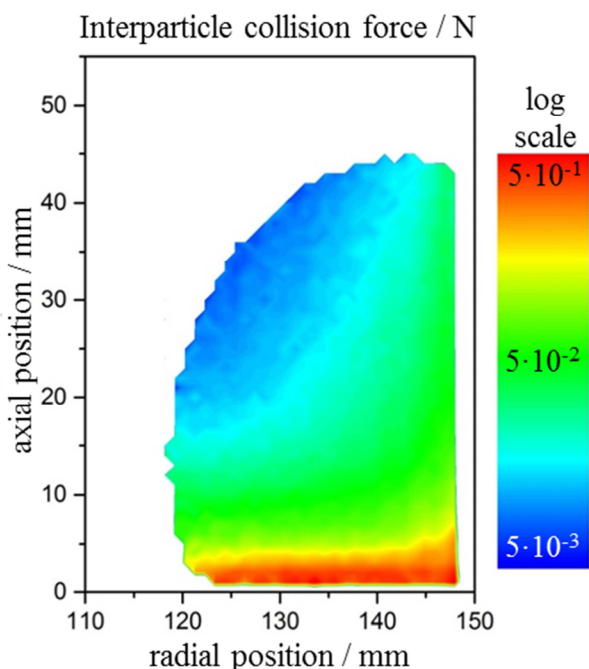


Figure 9: Average force of the interparticle collisions in poloidal cut

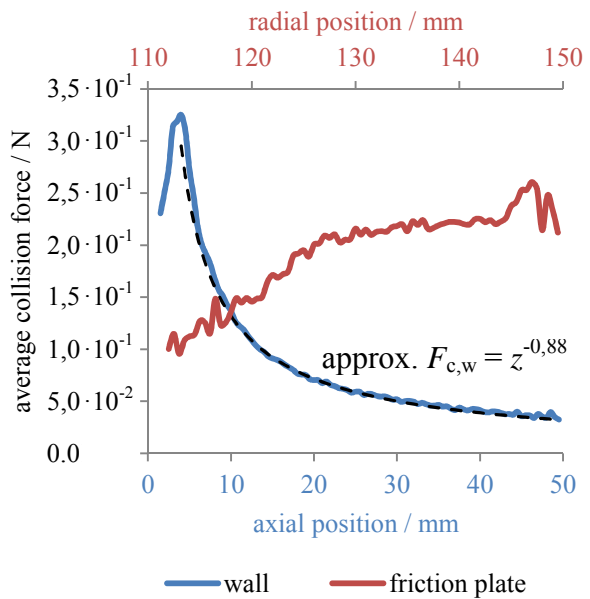


Figure 10: Average force of the collisions with the friction plate and the spheronizer wall

3.2 Influence of various factors on the particle dynamics and the collision characteristics

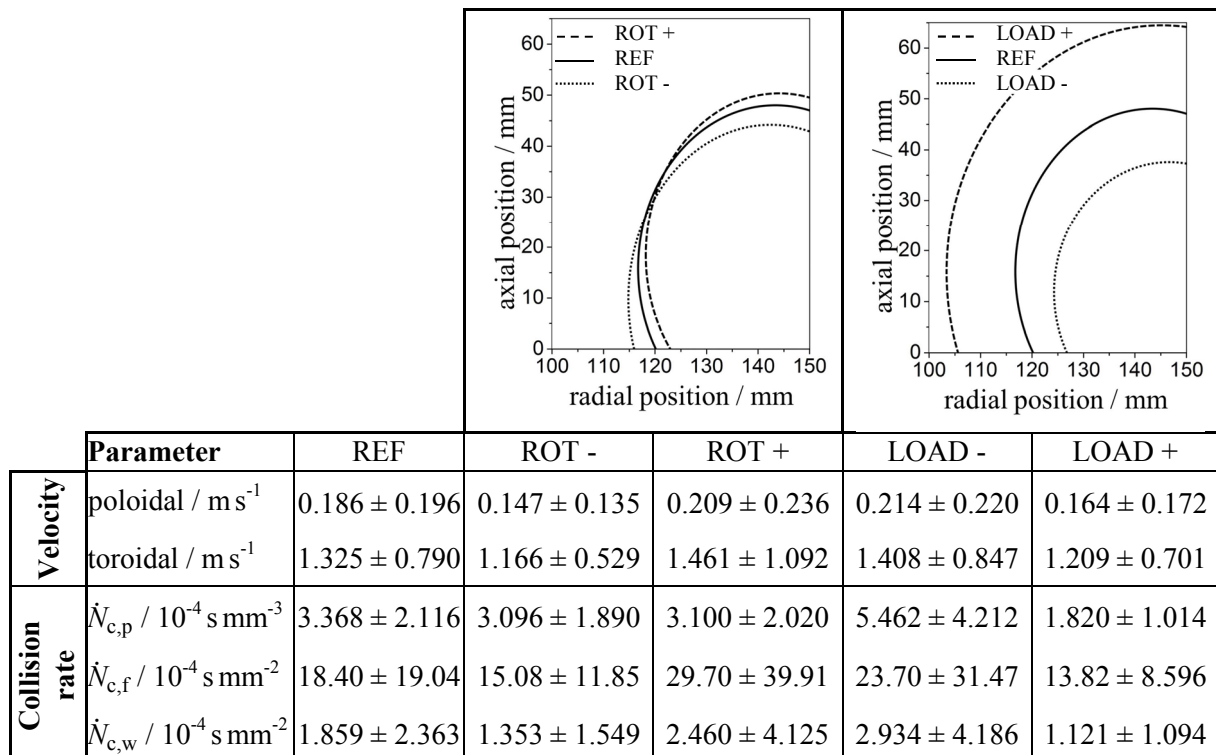
The influence of different factors affecting the particle dynamics and collision characteristics was investigated. For that purpose from the process conditions, the rotational speed of the friction plate (ROT) and the loading of the spheronizer (LOAD) were varied. From the material properties, the influences of the particle size (PS), coefficient of restitution (CoR), stiffness (ST), and coefficient of static friction (CoF) were investigated. The values of the parameters for the reference case (REF) are given in Table 2. Also, the values for the variation of each parameter are shown.

Table 2: Parameters varied in the simulations

Parameter	ROT / rpm	LOAD / g	PS / mm	CoR / -	ST / N mm ⁻¹	CoF / -
Reference	1000	600	2.0	0.25	0.8	1.0
+	1500	1200	2.4	0.50	1.6	1.5
-	500	300	0.8	0.10	0.4	0.5

In Table 3 the influence of the process conditions on the shape of the torus can be seen. Moreover, the distribution of the particle velocities in poloidal and toroidal direction, the collision rates, and the collision forces are characterized by arithmetic mean \pm standard deviation.

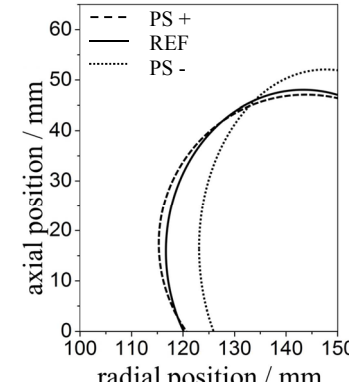
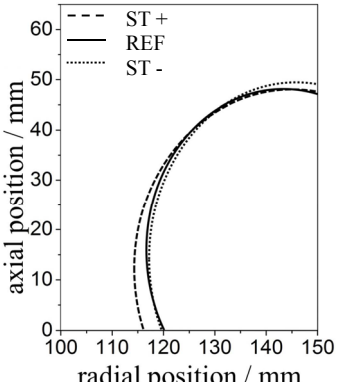
Table 3: Influence of different process conditions on the particle dynamics and collision characteristics



Collision force	$F_{c,p}$ / N	0.052 ± 0.082	0.037 ± 0.047	0.065 ± 0.116	0.059 ± 0.087	0.049 ± 0.081
	$F_{c,f}$ / N	0.217 ± 0.171	0.135 ± 0.100	0.333 ± 0.264	0.200 ± 0.168	0.215 ± 0.163
	$F_{c,w}$ / N	0.138 ± 0.149	0.089 ± 0.081	0.237 ± 0.149	0.131 ± 0.137	0.129 ± 0.133

The shape of the particle torus at different rotational speeds of the friction plate is shown in Table 3. It can be seen that the axial expansion of the torus near the wall is greater and the radial expansion of the torus near the plate is smaller for higher rotational speeds. Furthermore, the poloidal and toroidal velocities increase with the rotational speed. The average collision forces increase with the rotational speed as do the particle-friction plate and particle-wall collision rates. Especially the maxima of the collision rates of the particles with the spheronizer geometry, which can be seen in Figure 8, are increasing. In contrast, the inter-particle collision rate decreases slightly regardless whether the rotational speed is increased or decreased. Different loads of the spheronizer barely affect the shape of the torus. Only the volume of the torus varies. Table 3 shows that the particle velocities and collision rates increase with decreasing loading of the spheronizer. The influence of the loading on the average collision forces is less significant. In addition to the process conditions, Table 4 shows the influence of two particle properties on the particle dynamics and collision characteristics.

Table 4: Influence of different particle properties on the particle dynamics and collision characteristics

							
Parameter	REF	PS -	PS +	ST -	ST +		
Velocity	$\text{poloidal} / \text{m s}^{-1}$ 0.186 ± 0.196	0.151 ± 0.153	0.209 ± 0.215	0.184 ± 0.185	0.189 ± 0.204		
	$\text{toroidal} / \text{m s}^{-1}$ 1.325 ± 0.790	1.556 ± 0.801	1.319 ± 0.825	1.404 ± 0.847	1.256 ± 0.732		
Collision rate	$\dot{N}_{c,p} / 10^{-4} \text{s mm}^{-3}$ 3.368 ± 2.116	8.446 ± 5.022	2.834 ± 1.824	2.976 ± 2.106	3.594 ± 2.374		
	$\dot{N}_{c,f} / 10^{-4} \text{s mm}^{-2}$ 18.40 ± 19.04	10.09 ± 8.502	23.66 ± 25.20	29.81 ± 26.63	11.22 ± 11.47		
	$\dot{N}_{c,w} / 10^{-4} \text{s mm}^{-2}$ 1.859 ± 2.363	1.052 ± 0.981	2.258 ± 3.043	1.946 ± 2.797	1.812 ± 1.977		
Collision force	$F_{c,p}$ / N 0.052 ± 0.082	0.006 ± 0.011	0.084 ± 0.126	0.043 ± 0.063	0.064 ± 0.107		
	$F_{c,f}$ / N 0.217 ± 0.171	0.055 ± 0.039	0.284 ± 0.227	0.149 ± 0.110	0.304 ± 0.257		
	$F_{c,w}$ / N 0.138 ± 0.149	0.023 ± 0.025	0.205 ± 0.217	0.110 ± 0.116	0.166 ± 0.176		

For a smaller particle size, the torus is getting slimmer and higher. The average poloidal velocity decreases, while the average toroidal velocity increases with decreasing particle size. The average interparticle collision rate decreases with increasing particle size. In contrast, the collision rates of the particles with the spheronizer geometry increase with the particle size. Finally, the influence of the stiffness is analyzed. A smaller stiffness leads to a greater axial expansion of the torus while a larger stiffness causes a wider torus. While the poloidal velocity is barely affected by the stiffness the toroidal velocity increases with the stiffness. The interparticle collision rate increases with the stiffness. In contrast, the collision rates of the particles with the spheronizer geometry increase with decreasing stiffness.

3.3 Comparison of simulation results with PIV measurements

In this section the results of the performed DEM simulation are compared with PIV measurements by Koester et al. [5]. To obtain comparable results, some aspects need to be considered in the evaluation of the simulation data: Firstly, only the particles in an area which is also covered by the high-speed camera [5] should be taken into account (Figure 11). In the upper region of the wall ($z > 6$ mm) only the outer particles can be considered due to the close packing of the particles. Above the friction plate ($z < 6$ mm) the camera also captures particles with a greater distance to the wall Δr because of the low particle density (Figure 6). As it can be seen in Figure 11 different distances to the wall were used since it is difficult to assess which is most aptly. Secondly, the camera only captures the axial and circumferential positions of the particles, therefore the radial component of the velocities must not be taken into account. Velocity distributions evaluated in this way are compared with the results of the PIV measurements.

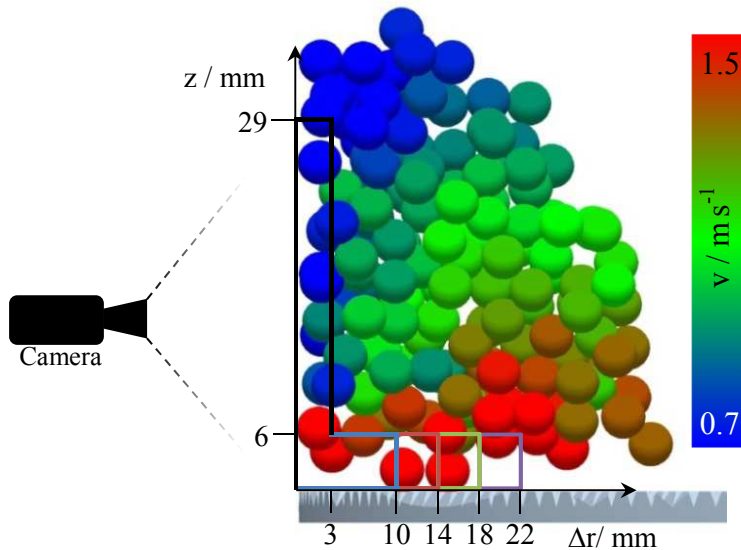


Figure 11: Evaluation of the velocities obtained by DEM for the comparison with the PIV results

In the experiment and simulation the spheronizer consists of a cross hatched friction plate with a diameter of $d = 300$ mm (Figure 1). Also the process conditions like rotational speed of the friction plate of $n = 750$ rpm and loading of $m = 900$ g were the same in the experiment

and simulations. Only the properties of the pellets used for the PIV measurements are not known exactly and may differ from the properties of the pellets tested in this work. Figure 12 shows the particle velocity distribution from the simulation for different areas (Figure 11). Figure 13 shows the averaged particle velocity distribution obtained by Koester et al. [5] in PIV measurements with MCC pellets. Except one modal value at high velocities in the simulation results, the distributions are similar. In the experiments as well as in the simulation there are two modal values at low velocities. These peaks are shifted slightly toward higher values in the simulation results. This difference can be attributed to uncertainties in the particle properties.

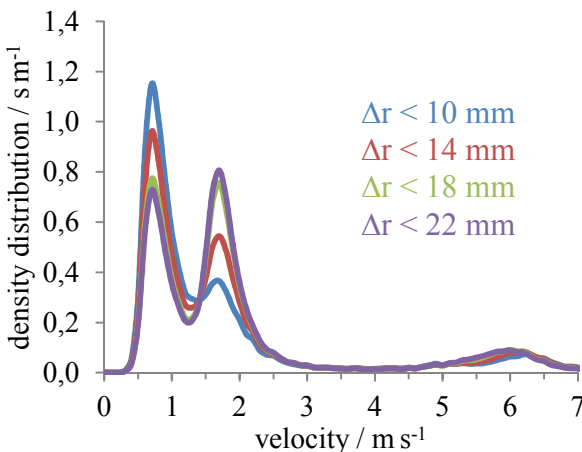


Figure 12: Particle velocity distribution obtained by DEM simulation in different areas

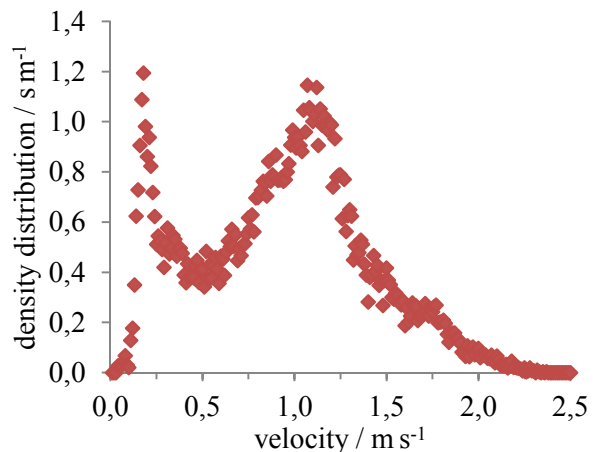


Figure 13: Averaged particle velocity distribution obtained by PIV measurements by Koester [5]

In addition to the PIV measurements with MCC pellets Koester et al. also performed PIV measurements with $\gamma\text{-Al}_2\text{O}_3$ particles [4]. They found a trimodal distribution of the particle velocities. Although pellets of different materials and different process conditions were used, their results are qualitatively similar to the results of the simulation of the present study with three modes each. All in all the comparisons indicate that the DEM simulations can reflect the PIV measurements. To validate this assumption, a consistent set of experiments and simulations needs to be performed with MCC pellets: The particle dynamics in the spheronization process must be measured via PIV and the material properties of the spheronized pellets must be measured immediately. The measured material properties can then be used for the contact model in the DEM simulation of the spheronization process.

4 SUMMARY AND CONCLUSIONS

In this work, the particle dynamics of a spheronization process with MCC pellets was investigated via DEM simulations. The elastic-plastic contact model used in the simulations was calibrated via experiments with spheronized pellets. The average particle movements in the stationary case was displayed as a vector field by spatial discretization of the poloidal cut and time averaging of the particle velocities. The average residence probability of the pellets in the poloidal cut was calculated. Therein local maxima at different radial positions and a decrease near the friction plate were shown. In this area of low residence probability above the friction plate a maximum at a distance of approximately r_p is located. This maximum is

significantly smaller than the radial maxima but exhibits a huge increase where it intersects the outer radial maximum. In addition to the particle residence probability and movements, the collision characteristics were investigated. A maximum in the interparticle and particle-wall collision rates in the lower outer region of the spheronizer was shown. The average collision force also increases with increasing radial and decreasing axial position. Moreover, the influence of different process conditions and material properties was investigated. The influence on the shape of the torus of particles was shown qualitatively. Also the influence on the distribution of the particle velocities, collision rates, and collision forces were determined. The simulation results were compared with results from PIV measurements. Except one modal value at high velocities in the simulation results, the results from PIV measurements with MCC pellets in [5] are similar with 2 modes each at velocities $v < 2.5$ m/s. Even the results from PIV measurements with $\gamma\text{-Al}_2\text{O}_3$ pellets with different properties in [4] are qualitatively similar because the trimodal distributions also exhibit a modal value at high velocities. To ensure the simulation results can represent the experimental results, further PIV measurements and simulations need to be performed with the same MCC pellets. For these simulations the contact model must be calibrated with the spheronized pellets used in the PIV experiments.

5 ACKNOWLEDGEMENTS

The authors gratefully acknowledge the financial support by the German Research Foundation (project number AN 782/2-1)

REFERENCES

- [1] Koester, M. and Thommes, M. New Insights into the Pelletization Mechanism by Extrusion/Spheronization. *AAPS PharmSciTech* (2010) **11**(4):1549-1551
- [2] Schmidt, C. and Kleinebudde, P. Comparison between a twin-screw extruder and a rotary ring die press. Part II: influence of process variables. *European Journal of Pharmaceutics and Biopharmaceutics* (1998) **45**:173–179
- [3] Bouffarda, J., Bertranda, F., Chaoukia, J. and Dumontb, H. Discrete element investigation of flow patterns and segregation in a spheronizer. *Computers and Chemical Engineering* (2013) **49**:170–182.
- [4] Koester, M., García, R.E. and Thommes, M. Spheronization process particle kinematics determined by discrete element simulations and particle image velocimetry measurements. *International Journal of Pharmaceutics* (2014) **477**:81–87.
- [5] Koester, M. and Thommes, M. Analysis of particle kinematics in spheronization via particle image velocimetry. *European Journal of Pharmaceutics and Biopharmaceutics* (2013) **83**:307–314.
- [6] Cundall, P.A. and Strack, O.D. Discrete numerical-model for granular assemblies. *Geotechnique* (1979) **29**:47–65.
- [7] Walton, O.R. and Braun, R.L. Stress Calculations for Assemblies of Inelastic Spheres in Uniform Shear. *Acta Mechanica* (1986) **63**:73–86.
- [8] DEM Solutions, *EDEM 2.6 Theory Reference Guide* (2014)
- [9] Walton, O. (*Linearized*) Elastic-Plastic contact model. Company report, DEM Solutions, (2006).

APPLICATION OF THE LATTICE-BOLTZMANN METHOD FOR MODELING ALL-VANADIUM REDOX FLOW BATTERIES

Dario Maggiolo¹, Francesco Picano¹ Andrea Marion¹ and Massimo Guarneri¹

¹ Department of Industrial Engineering, University of Padova
dario.maggiolo@unipd.it, www.unipd.it

Key words: Redox Flow Battery, Lattice-Boltzmann Method, Porous Media, Mixing

Abstract. All-Vanadium Redox Flow Batteries (VRFBs) represent a promising technology as a way to store energy because of their high energy efficiency, long cycle life, independently tunable power/energy size, and lack of contamination from cross-mixing of electrolytes. However, in order to improve VRFBs performance, some conceptual and technological issues are still open. In particular, a properly designed geometry of flow channels and porous medium, which guarantees a uniform distribution of the reacting species all along the electrode, is still under investigation. The ideal configuration aims to minimize the drag maximising the mixing. This will guarantee an increase of the performance and of the overall efficiency. In the present work a Lattice Boltzmann tri-dimensional multi-relaxation-time model (LBM) has been used to better understand the dependence of mass and momentum transports on the porosity and carbon fiber preferential orientation. The LBM has been coupled with a Lagrangian particle tracking algorithm in order to investigate the dispersion mechanisms induced by the porous medium on the species flowing in a typical VRFB. Results show that the drag measured by the permeability K is considerably reduced when the medium fibers are preferentially oriented along the streamwise direction, as expected. The fiber orientation also affects the species mixing that needs to be enhanced to optimize the VRFB performance. Surprisingly, the medium with fibers preferentially oriented along the streamwise direction, among all the considered medium, shows also the highest transversal dispersion rate characterized by super-diffusive behavior. In light of these results, this anisotropic medium appears to be optimal to enhance VRFBs performances by reducing the drag and enhancing the mixing.

1 INTRODUCTION

During the last years, VRFBs have been perceived as one of the most promising technologies to improve electrochemical energy storage. In comparison with other batteries, VRFBs are characterized by higher energy efficiency, longer cycle life and more flexible

power/energy sizing [1]. Even though the VRFB technology is well-known since the late 1980's, it is only during recent years that the scientific community has focused on improving VRFBs performance [1, 3]. A cell of a VRFB cell is composed by two porous media electrodes of carbon fibers. The inner surfaces of the porous media act as active site where electrochemical reduction and oxidation reactions of the Vanadium electrolytes occur. The reduction reaction at one electrode extracts electrons and ions from one electrolyte, while the oxidation at the other electrode recombines them into the other electrolyte. Ions may migrate from anode to cathode through a ion exchange membrane which separates the two half-cells. Both half-cells are fed by external storage tanks which pump freshen electrolyte solutions in the porous media electrode to keep on the reactions. The peak performance of VRFB is limited by a too slow electrolyte transport in the electrodes [1].

The fluid dynamic optimization of the porous medium which acts both as electrochemical active surface and as a mixing layer of chemical species in VRFBs is one of the main technological issues to be dealt [2].

Actually, the slow diffusion process of Vanadium species in water often represents a bottleneck for the peak performance of VRFBs. Specifically, the mass diffusion coefficients of the Vanadium species in water, $D \sim 10^{-10} m^2 s^{-1}$, are about 10000 smaller than the water kinematic viscosity, $\nu = \mu/\rho \sim 10^{-6} m^2 s^{-1}$ indicating that the mass diffusion is 10000 times slower than the momentum transport. The fibers constituting the porous medium enhance the effective mass transport perturbing the flow trajectories at micro-scales. A proper designed geometry of the porous medium may enhance this effective mass transport and minimize the drag improving and optimizing the VRFB performances. This is the topic of the present study.

While the influence of porous medium porosity on the flow drag has been largely studied [4], the impact of its microscopic design on mixing/transport mechanisms and drag is still not well assessed [4, 5].

In order to clarify this issue, several simulations varying the preferential orientation of fibers at different porosity and Reynolds number have been carried out by means of a Lattice-Boltzmann-based model coupled with a Lagrangian particle tracking algorithm. The aim of the present paper is to clarify how the nematic properties of the porous medium affects the mass and momentum transport mechanisms in order to design optimal porous media with low drag and high effective mass diffusion. The minimization of drag reduces the required pump power, while the maximization of the mixing improves the uniformity of reacting species all along the porous medium, resulting in enhanced performances of VRFBs. We will show that porous media constituted by fibers preferentially oriented along the flow direction exhibit smaller drag and higher effective diffusion.

2 NUMERICAL METHOD

In recent years the Lattice-Boltzmann Method (LBM) proved to be a good solution in solving Navier-Stokes Equations, allowing easy implementation and algorithm parallelization, especially in presence of complex geometries [6]. In the present work a

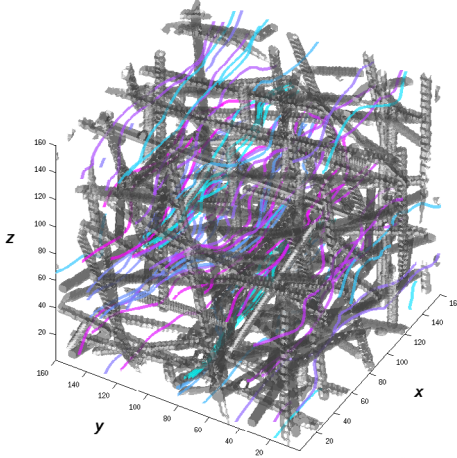


Figure 1: Tri-periodic cubic domain with particle trajectories for the isotropic case with porosity $\varepsilon = 0.9$. The domain size is 160^3 and the flow is driven by a pressure gradient along x .

three-dimensional multi-relaxation time Lattice-Boltzmann model has been developed to simulate the fluid flow inside a fiber-composed porous medium. The model has been successfully validated against theoretical solutions of the Volume Averaged Navier-Stokes Equations [7]. The multi-relaxation-time lattice Boltzmann equation reads as follows:

$$f_i(\mathbf{x} + \mathbf{c}_i, t + 1) - f_i(\mathbf{x}, t) = -\mathbf{M}^{-1}\mathbf{S}(m_i(\mathbf{x}, t) - m_i^e(\mathbf{x}, t)) , \quad (1)$$

where $f_i(\mathbf{x}, t)$, is the distribution function \mathbf{x} at the time t along the i -th lattice direction, $m_i(\mathbf{x}, t)$ and $m_i^e(\mathbf{x}, t)$ are the moment and the equilibrium moment obtained by the Gram-Schmidt orthogonalization procedure; \mathbf{c} is the discrete speed vector, S is the collisional matrix and M the transformation matrix [8].

The typical porosity used in VRFB, $\varepsilon = 0.7 \div 0.9$, is considered in a triperiodic box, see Fig.(1). The flow is driven along the x direction by a mean pressure gradient DP/Dx which imposes the Reynolds number $Re = Ud_f\rho/\mu = 0.1 \div 1.0$ with U the bulk velocity, d_f the fiber diameter, ρ the fluid density and μ the dynamic viscosity. The side of the periodic box is discretized by 160 computational cells, while the fiber diameter d_f corresponds to 6 cells. Three different porous medium orientations have been considered: an isotropic medium, a medium preferentially oriented along the streamwise direction and a medium preferentially oriented along the transverse direction. The medium is considered preferentially oriented along the streamwise or transverse direction when all the angles formed by the axes of the fibers and the x axis are lower or higher than $\pi/4$, respectively.

Since the diffusion coefficients of the Vanadium species in water are very small and the main aim is to characterize the effective diffusion induced by the porous medium micro-structure, the mass transport properties are evaluated following non-Brownian tracer

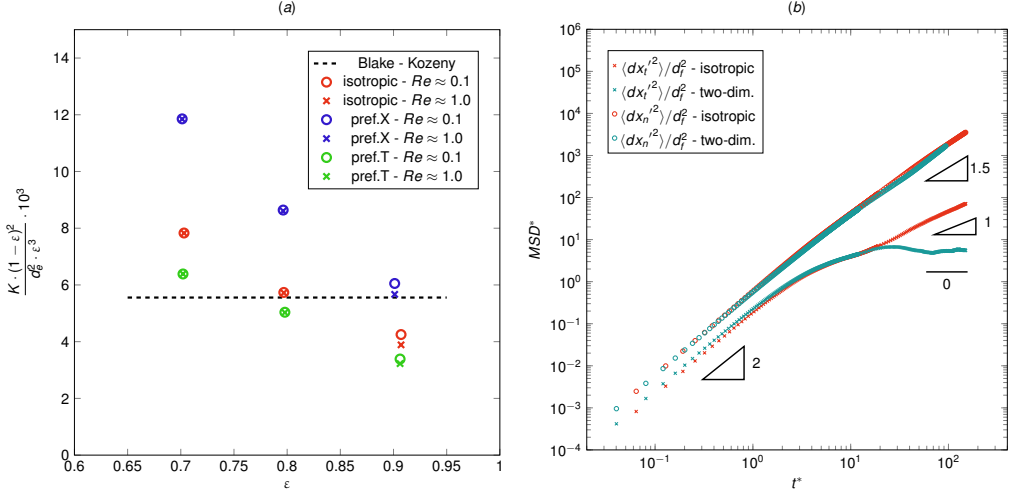


Figure 2: (a) Non-dimensional permeability with varying the porosity, the fiber orientation and the Reynolds number. The Blake-Kozeny equation is depicted by a black-dashed line. (b) Non-dimensional Mean Square Displacement plotted against the characteristic observation time for the isotropic case (red line) and the two-dimensional case (turquoise line).

particles injected in the fluid. The LBM stationary flow field has been used as input of the Lagrangian Particle tracking algorithm, see Fig.(1), and Lagrangian statistics of ten thousand particles have been analyzed in order to extract the effective diffusion coefficients in the porous media. Particles are randomly injected in the fluid phase and their trajectories are stored in time. All the observables shown in the following analysis have been normalized using the bulk velocity U and the fiber diameter d_f .

3 RESULTS

In the theoretical framework of flows in porous media, the Darcy's law is often used to describe the ability of the fluid to flow through the medium. It considers the bulk velocity U , which is the mean of the fluid velocity in the whole volume, and relates it to the pressure gradient by means of the permeability K [4]:

$$K = \varepsilon U \mu \cdot \left(-\frac{DP}{Dx} \right)^{-1}. \quad (2)$$

Fig.(2) shows the values of non-dimensional permeability K with varying the porosity and the porous medium orientation (left panel). The values of K of the isotropic medium are consistent with experimental values available in literature [4] and can be approximated using the Blake-Kozeny equation: $K/d_e^2 = \varepsilon^3 / [180(1 - \varepsilon^2)]$. It is strictly valid for packed beds of spheres, but can be used for cylindrical-shaped fibers using the characteristic length $d_e = 3/2 \cdot d_f$, see [4]. A decreasing behavior with increasing the porosity ε has been reported also in experimental investigations, see e.g. [4]. The values of permeability of the medium preferentially oriented along the transverse direction are

similar to the isotropic ones and well captured by Blake-Kozeny equation. On the contrary, the medium preferentially oriented along the streamwise direction presents much higher values of permeability, which correspond to lower flow drag inside the porous medium. Moreover, Fig.(2) clearly shows that the influence of finite Reynolds number on permeability is negligible in the present investigation range.

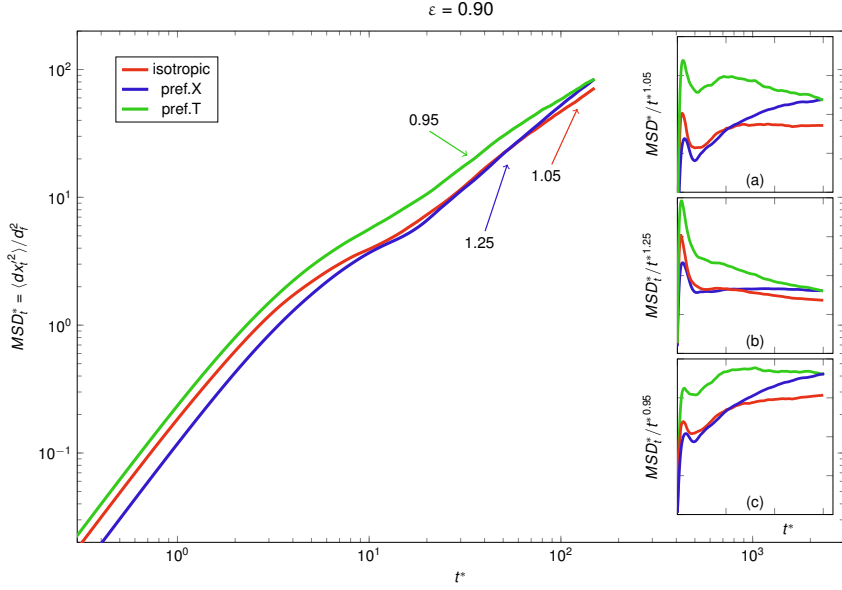


Figure 3: Non-dimensional Mean Square Displacement for three different orientation and $\varepsilon = 0.9$. Insets (a), (b) and (c): Non-dimensional mean square displacement normalized by $t^{1.05}$, $t^{1.25}$ and $t^{0.95}$, respectively.

The right panel of Fig.(2) instead shows the values of the non-dimensional mean square displacement MSD^* along the streamwise and transverse directions with increasing the observation time t^* . Two cases are shown: the isotropic medium and a medium fully oriented along one transversal direction y . This last case corresponds to a 2D porous medium in the (x, z) plane formed by circular solid being completely homogenous in the other direction. The non-dimensional values MSD^* and t^* are defined as follows:

$$MSD_{n,t}^* \equiv \frac{\langle dx'_{n,t}^2 \rangle}{d_f^2} \quad (3)$$

$$t^* \equiv t \cdot \frac{U}{df} \quad (4)$$

where $dx'_{n,t} = x_{n,t} - \langle x_{n,t} \rangle$ is the fluctuation of the displacement $x_{n,t}$ along the streamwise (subscript n) or transverse (subscript t) direction and $\langle \rangle$ indicates the averaging ensemble operator. The MSD^* is initially proportional to t^{*2} for all the considered cases, denoted by a slope 2 in the log-log plot of Fig.(2). This is an expected behavior until the particle

motion is still correlated. After a characteristic time $t^* \approx 10$, the behavior of the MSD^* along the streamwise direction changes as $MSD^* \propto t^{*\alpha}$ with $\alpha = 1.5$ for both cases. This exponent corresponds to a super-diffusive behavior and has been reported also in the recent paper of [5]. The super-diffusion process denotes an incredibly fast anomalous diffusion which has been found in biological and peculiar physical systems. While no significant differences are found in the dispersion along the streamwise direction between the two cases, the behavior dramatically changes in the transversal direction where the isotropic case exhibits an unitary exponent denoting a standard diffusion, while the 2D case shows a constant MSD^* , i.e. $\alpha = 0$. This behavior is not strange since the particle trajectories live in a 2D steady case where chaotic mixing cannot be observed. In other words, it indicates that the particles follows periodic trajectories of an incompressible (nearly) Stokes flow. The 3D isotropic porous medium instead acts as a random noise that perturbs the particle trajectories making them linearly diverging in time as a usual Brownian diffusion process.

For all the considered cases within a range $Re = 0.1 \div 1.0$, the diffusion behavior of particles in the porous medium does not depend on the Reynolds number (not shown here) indicating negligible inertial effects. In contrast, the preferential orientation of the porous medium affects the transport in the transverse direction.

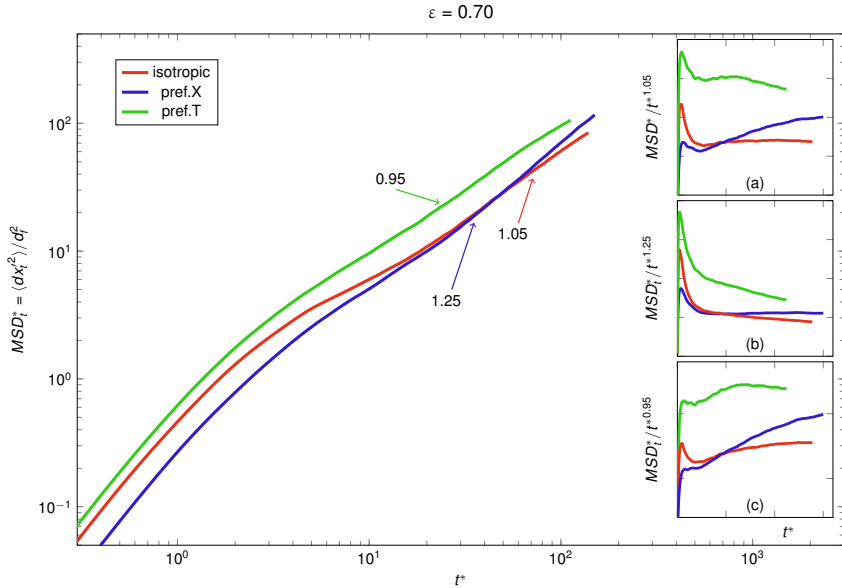


Figure 4: Non-dimensional Mean Square Displacement for three different orientation and $\varepsilon = 0.7$. Insets (a), (b) and (c): Compensated Mean Square Displacements obtained dividing MSD^* by $t^{1.05}$, $t^{1.25}$ and $t^{0.95}$, respectively.

The influence of the medium orientation on particle dispersion is shown in Figs. (3) and (4) for $\varepsilon = 0.9$ and $\varepsilon = 0.7$, respectively. The isotropic medium and the medium preferentially oriented along the transverse directions show a normal diffusion with small

differences. Note that the medium preferentially oriented along the transversal directions is now fully tridimensional cases. The mean square displacement is well represented by a standard diffusion equation, typical of Brownian processes:

$$MSD^* = 4D \cdot t^{*\alpha} \quad (5)$$

with $\alpha = 1 \pm 0.05$, see the (a) and (c) insets of Figg. (3) and (4). The diffusion coefficient D is similar in cases at same porosity. Surprisingly, when the medium is preferentially oriented along the streamwise direction, we observe an exponent $\alpha = 1.25$, that denotes once again a superdiffusive behavior ($\alpha > 1$). It is clear that for sufficiently long observation times t^* the dispersion of particle trajectories becomes significantly higher than for the other cases.

An explanation of this anomalous diffusion could be found considering the anisotropic geometry of the porous medium, in which the fibers are preferentially oriented with small angles with respect to the x axis. We believe that particles can occasionally follow the fiber surface along their axes for long distances, pushed by the pressure-gradient force. This highly correlated motion leads to high transverse displacement enhancing the diffusion process. The process could be modeled as a Levy-flight process where particles intermittently show long displacement when their trajectory is constrained for long time by almost aligned fibers.

The influence of the porosity ε on particle diffusion can be highlighted by comparing Figs. (3) and (4). While the α exponent remains the same, the diffusion coefficients are slightly higher by decreasing the porosity. Anyway the influence on particles dispersion of the diffusion coefficients (with $\alpha = 1$) is subleading compared to effect of a super-diffusive behavior with $\alpha > 1$ for long enough observation times t^* .

Table 1: Diffusion coefficients D , equivalent mass diffusion coefficients D_{eff} , effective viscosities ν_{eff} and Schmidt numbers Sc with $\varepsilon = 0.9$

case	α	D	ℓ^*	D_{eff}	ν_{eff}	Sc_{eff}
isotropic	1.05	0.09	10	0.12	0.37	3.03
isotropic	1.05	0.09	100	0.15	0.37	2.43
isotropic	1.05	0.09	1000	0.19	0.37	1.95
pref.X	1.25	0.04	10	0.14	0.29	2.03
pref.X	1.25	0.04	100	0.36	0.29	0.81
pref.X	1.25	0.04	1000	0.91	0.29	0.32
pref.T	0.95	0.18	10	0.14	0.47	3.28
pref.T	0.95	0.18	100	0.11	0.47	4.18
pref.T	0.95	0.18	1000	0.09	0.47	5.33

Table 2: Diffusion coefficients D , equivalent mass diffusion coefficients D_{eff} , effective viscosities ν_{eff} and Schmidt numbers Sc with $\varepsilon = 0.7$

case	α	D	ℓ^*	D_{eff}	ν_{eff}	Sc_{eff}
isotropic	1.05	0.12	10	0.15	3.38	21.82
isotropic	1.05	0.12	100	0.19	3.38	17.52
isotropic	1.05	0.12	1000	0.24	3.38	14.07
pref.X	1.25	0.06	10	0.19	2.27	12.12
pref.X	1.25	0.06	100	0.47	2.27	4.83
pref.X	1.25	0.06	1000	1.18	2.27	1.92
pref.T	0.95	0.30	10	0.24	4.18	17.57
pref.T	0.95	0.30	100	0.19	4.18	22.39
pref.T	0.95	0.30	1000	0.15	4.18	28.54

When dealing with diffusion of species inside porous media, it is useful to predict the mass transport via convection-diffusion-reaction Eulerian equations for the homogenized volume. When a standard diffusion process ($\alpha = 1$) takes place, the only parameter needed is the effective mass diffusion coefficient D_{eff} . Unfortunately, when $\alpha > 1$ the corresponding Eulerian transport equation is constituted by nontrivial fractional derivatives [9]. In order to overcome this issue, it is convenient for applications to transform the super-diffusive process in a equivalent standard diffusion process in order to solve a standard convection-diffusion-reaction equation for the Eulerian homogenized mass transport. However it is necessary to fix a typical displacement length $\ell^* \equiv \ell/d_f$ that characterizes the diffusion process of the system. The equivalent system is then obtained matching the real $MSD^* = \ell^{*2}$ with the equivalent normal diffusion process characterized by D_{eff} . The effective mass diffusivity can thus be derived by imposing the following equality:

$$\ell^{*2} = 4D \cdot t^{*\alpha} = 4D_{eff} \cdot t^* , \quad (6)$$

from which it follows:

$$D_{eff}(\ell^*) = 4^{\frac{1-\alpha}{\alpha}} \cdot D^{\frac{1}{\alpha}} \cdot \ell^{*2\frac{\alpha-1}{\alpha}} . \quad (7)$$

The Tabs. (1) and (2) report the values of D and D_{eff} for the cases $\varepsilon = 0.9$ and $\varepsilon = 0.7$, respectively, and for different characteristic displacement ℓ^* . The dispersion prediction by means of the equivalent mass diffusion coefficient D_{eff} with varying the characteristic length ℓ^* is well depicted in Fig.(5), right panel.

The medium preferentially oriented along the streamwise direction presents the higher equivalent mass diffusion coefficients, confirming the fast dispersion properties of the super-diffusive process. The effective diffusivity is higher for the lower porosity (i.e. $\varepsilon = 0.7$). However, even though the effective diffusivity is higher, also the drag exerted by the

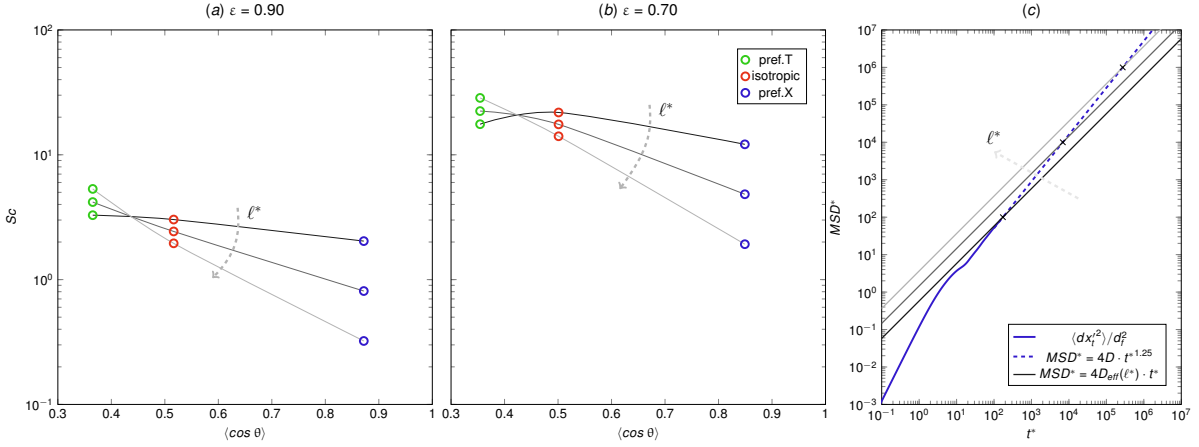


Figure 5: (a) Schmidt number plotted against the mean value of the cosine of the angle θ formed by the fibers axes and the x axis, for $\varepsilon = 0.9$, with varying the fixed characteristic lenght ℓ^* . (b) Schmidt number plotted against the mean value of the cosine of the angle θ , for $\varepsilon = 0.7$, with varying the fixed characteristic lenght ℓ^* . (c) Mean Square Displacement prediction with the normal effective coefficient D_{eff} with varying the characateristic lenght ℓ^* .

fluid is higher, being higher the surface of fibers opposing the flow, see Fig.(2). In order to take into account the both mechanisms, an effective viscosity ν_{eff} has been derived as the ratio between pressure-gradient force and viscous forces:

$$\nu_{eff} = \left(\frac{DP}{Dx} \frac{1}{\rho} \right) \frac{d_f^2}{U}. \quad (8)$$

Following this approach, the effective Schmidt number Sc_{eff} can be obtained by combining Eq.(7) and Eq.(8):

$$Sc_{eff} = \frac{\nu_{eff}}{D_{eff}}. \quad (9)$$

The effective Schmidt number values are reported for all cases in Tabs. (1) and (2) and the influence of the porous medium orientation on Sc_{eff} is depicted in Fig.(5), in the left and central panel. The lower the Schimdt number, the lower the ratio between the effective viscosity and the effective diffusion. In other words, low Schmidt numbers indicate low drag and high diffusivity, which in turn increases the VRFB performances. Thus, the medium preferentially oriented along the streamwise direction and with high porosity value (i.e. $\varepsilon = 0.9$), is the best configuration for VRFBs, allowing high diffusion and low pressure losses. Fig.(5) also shows that the benefits of using an oriented medium along the streamwise direction are more significant with increasing the characteristic displacement ℓ^* . Therefore, the orientation of the medium can significantly increase the performances of VRFBs, specially when the porous medium is thick which corresponds to high typical transversal length.

4 CONCLUSION

A Lattice-Boltzmann-Method in combination with a Lagrangian Particle Tracking algorithm has been used to investigate the effects of the microscopic properties of porous media on the mass and momentum transport, i.e. mixing and drag properties. These features are crucial to optimize and increase the performance of Vanadium-Redox-Flow-Battery. The present study shows that the nematic properties of the medium, i.e. the orientation properties, crucially affect the mass dispersion process. In particular a super-diffusive behavior is observed for all the considered porous media when the mass dispersion is evaluated along the streamwise direction. On the contrary a normal diffusive behavior is observed in the transversal direction when the constituting medium fibers are either isotropically oriented or preferentially oriented along the transversal directions. Surprisingly if the constituting fibers are preferentially oriented along the streamwise direction the transversal dispersion process is super-diffusive. This greatly enhances the transversal mixing. An effective model has been proposed to characterize this behavior in standard convection-diffusion Eulerian equation determining an effective diffusion coefficient which, however, depends also on the characteristic transversal scale of the system. Finally we have shown that the porous medium with preferentially oriented fibers along the flow direction shows also the smallest drag, as expected. Hence this kind of medium appears to be the optimal solution to enhance the mixing and minimizing the pressure drop in VRFB cells.

ACKNOWLEDGEMENTS : This work was supported as part of the MAESTRA project (From Materials for Membrane-Electrode Assemblies to Electric Energy Conversion and Storage Devices, 2014 - 2016) funded by the University of Padova.

REFERENCES

- [1] P. Alotto, M. Guarneri and F. Moro. Redox flow batteries for the storage of renewable energy: A review. *Renewable and Sustainable Energy Reviews* (2014) **29**:325-335.
- [2] A. Tang, J. Bao and M. Skyllas-Kazacos. Studies on pressure losses and flow rate optimization in vanadium redox flow batteries. *Journal of Power Sources* (2014) **248**:154-162.
- [3] A. Z. Weber, M. M. Mench, J. P. Meyers, P. N. Ross, J. T. Gostick, Q. Liu. Redox flow batteries: a review. *Journal of Applied Electrochemistry* (2011) **41**(10):1137-1164.
- [4] S. Whitaker. The Forchheimer Equation: A Theoretical Development. *Transport in Porous Media* (1996) **25**:26-61.
- [5] P. K. Kang, P. de Anna, J. P. Nunes, B. Bijeljic, M. J. Blunt and R. Juanes. Pore-scale intermittent velocity structure underpinning anomalous transport through 3-D porous media. *Geophysical Research Letters* (2014) **41**:6184-6190.

- [6] S. Succi. *The Lattice Boltzmann Equation: for Fluid Dynamics and Beyond*. Oxford University Press (2001).
- [7] D. Maggiolo, A. Marion, and M. Guarnieri. Lattice Boltzmann Modeling of Water Cumulation at the Gas Channel-Gas Diffusion Layer Interface in Polymer Electrolyte Membrane Fuel Cells. *Journal of Fuel Cell Science and Technology* (2014) 11(6):061008.
- [8] D. d'Humieres, I. Ginzburg, M. Krafczyk, P. Lallemand and L. S. Luo. Multiple-relaxation-time lattice Boltzmann models in three dimensions. *Philosophical Transaction of the Royal Society of London A* (2002) **360**:437-451.
- [9] D. Brockmann. *Superdiffusion in Scale-Free Inhomogeneous Environments*. Dissertation at Georg-August-University Gottingen (2003).

INVESTIGATION OF GREEN WATER IN FPSO BY A PARTICLE-BASED NUMERICAL OFFSHORE TANK

CEZAR AUGUSTO BELLEZI^{1 3 *}, DAVI TEODORO FERNANDES^{1 3}, LIANG-YEE CHENG^{2 3}, MÁRCIO MICHIHARU TSUKAMOTO^{2 3}, KAZUO NISHIMOTO^{1 3}

¹Department of Naval and Ocean Engineering
Escola Politécnica of University of São Paulo
Av. Prof. Mello Moraes, 2231, São Paulo – SP, Brasil
e-mail: polinaval@usp.br, web page : <http://www.pnv.poli.usp.br>

²Department of Construction Engineering
Escola Politécnica of University of São Paulo
Av. Prof. Almeida Prado, 83, São Paulo – SP, Brasil
web page: <http://www.pcc.usp.br>

³Numerical Offshore Tank (TPN)
Av. Prof. Mello Moraes, 2231, São Paulo – SP, Brasil
web page: <http://www.tpn.usp.br>

*cbellezi@tpn.usp.br

Key words: Green water, hydrodynamic impact, MPS method, large scale simulation

Abstract. The green water is a highly non linear hydrodynamic phenomenon that occurs when the wave height exceeds the freeboard of the floating structures in harsh environments, and may compromise the operation and security of the on deck equipment. In the present study, in order to assess the effects of the green water phenomenon in FPSO and FLNG systems, the Moving Particle Semi-implicit (MPS) method, which is a fully lagrangian particle-method for incompressible flow, is adopted to model the complex fluid structure interaction problem. This article is focused on the recent developments of the MPS based simulation system of Numerical Offshore Tank (TPN-USP) and its application to the real scale offshore engineering problem. Results of large scale simulations using distributed memory architecture for models from 30 million to 100 million particles are presented.

1 INTRODUCTION

The importance of offshore oil and gas exploitation in deepwater and ultra deepwater increased significantly along the past decade. The deepwater oil production grows from less than 2% of the worldwide oil production in 2000 to more than 10% ten years later. The oil exploration in deepwater and ultra deepwater is performed by floating offshore structures. In severe weather conditions, dangerous hydrodynamic impact phenomena related to large incoming waves may occur and may compromise the operation and safety of the floating structures.

One of the hydrodynamic impact phenomena related to the violent waves impact is the green water. The green water occurs when the sea surface height surpasses the freeboard of

the floating structures due to the relative motion between the structure and the sea surface, resulting in water boarding on deck. In case of floating production, storage and offloading (FPSO) platforms, the water that invades the deck may damage the equipment of the production plant. The green water is a highly nonlinear hydrodynamic impact phenomenon very challenging to numerical modeling. The complexity of the phenomenon is related to strong fluid-structure interaction with violent impulsive loads on structures with a variety of geometries and large free surface deformation and fragmentation due to wave breaking and splashing.

In order to study the complex green water phenomenon on FPSO, Moving Particle Semi-Implicit (MPS) method is adopted in the present study. The MPS method was developed by Koshizuka et al. [1] and Koshizuka & Oka [2] to model the incompressible flow based on a fully lagrangian scheme in which the computational domain is entirely modeled as particles. The method models very well problems involving large free surface deformations, fragmentation and merging, as well as complex shaped, moving and deformable structures.

The MPS method was applied to the green water investigation by Shibata & Koshizuka [3] and Shibata et al. [4] and Shibata et al. [5]. The validation of green water phenomenon for the MPS-based system developed at TPN-USP is presented by Bellezi et al. [6] based on the comparison between the numerical results with the experimental data obtained by Lee et al. [7]. Bellezi et al. [8] study the effect of the bow shaped in the green water phenomenon for fixed model under head seas.

The main disadvantage of the particle method is its large demand to computational resources, which limits the size and the resolution of the models. To overcome this challenge, particle based simulation systems using domain decomposition and distributed memory techniques were developed [9] [10].

The focus of the present paper is to show the evolvements of a particle-based modeling of the numerical offshore tank for the investigation of the green water, from the low resolution fixed reduced scale models to the simulation of large real scale floating models up to 100 million particles. The results presented in this work are divided in three parts: The first part shows the effects of the model resolution through the comparison of the results of a low resolution model with 1.6 million particle and a higher resolution model with 12 million particles. The second part shows the simulation of the 100 million particle model based on the Lee et al. [7] experiments and the performance of the distributed memory computation is brief analyzed. Finally, in the third part, a practical engineering application for a real scale model platform is carried out considering a large FLNG platform at critical weather conditions at Santos Basin.

2 NUMERICAL METHOD

The Moving Particle Semi-Implicit (MPS) method, also called Moving Particle Simulation, is a fully lagrangian particle-based CFD method for the incompressible free surface flow.

2.1 Governing equations

The governing equations solved by the MPS method are the continuity equation (eq. 1) and the Navier Stokes equation (eq. 2).

$$\frac{D\rho}{Dt} = -\rho(\nabla \cdot \vec{u}) = 0 \quad (1)$$

$$\frac{D\vec{u}}{Dt} = -\frac{1}{\rho}\nabla P + \vartheta\nabla^2\vec{u} + \frac{\vec{f}}{\rho} + \vec{g} \quad (2)$$

where ρ is the fluid density, ϑ is the fluid kinematic viscosity, P the pressure, \vec{g} the gravity acceleration, \vec{f} any other given field force and \vec{u} the velocity of a given particle.

The viscous term of the Navier Stokes equation is neglected in the studies carried out herein because the phenomena involving violent wave impact are often related to gravitational forces and high Reynold numbers.

2.2 Numerical model

The formulation of the MPS method is based on a weight function $\omega(r)$ given by.

$$\omega(r) = \begin{cases} \frac{r_e}{r} - 1 & \text{for } (0 \leq r < r_e) \\ 0 & \text{for } (r_e \leq r) \end{cases}, \quad (3)$$

where, r_e is a neighborhood radius and $r = |\vec{r}_i - \vec{r}_j|$ is the distance between two given particles i and j .

An important parameter is the particle number density (pnd). It is given by:

$$[pnd]_i = \sum_{j \neq i} \omega(|\vec{r}_j - \vec{r}_i|). \quad (4)$$

The algebraic operators of the MPS method are derived based on the weighted contribution of the neighbor particles. The gradient operator for a given Φ scalar quantity is presented by the eq. 5. The laplacian operator for a Φ scalar quantity is given by the eq. 6.

$$[\nabla\Phi]_i = \frac{d}{pnd^0} \sum_{j \neq i} \left[\frac{(\Phi_j - \Phi_i)}{|\vec{r}_j - \vec{r}_i|^2} (\vec{r}_j - \vec{r}_i) \omega(|\vec{r}_j - \vec{r}_i|) \right] \quad (5)$$

$$[\nabla^2\Phi]_i = \frac{2d}{pnd^0\delta} \sum_{j \neq i} [(\Phi_j - \Phi_i) \omega(|\vec{r}_j - \vec{r}_i|)], \quad (6)$$

where pnd^0 is the particle number density of regarding to initial particle configuration of a particle with fulfilled neighborhood, d is the dimension of the problem (2 for two dimensional modeling and 3 for three dimensional problems). The parameter δ is calculated based on the initial particle configuration and is given by

$$\delta = \frac{\int_V \omega(r) r^2 dv}{\int_V \omega(r) dv} \quad (7)$$

2.3 Algorithm

The algorithm of the MPS method is presented in Figure 1.

The algorithm is divided into two main steps. The first step is the explicit calculation to estimate velocity, position and particle number density of all fluid particles based on Eq. (2), except the pressure gradient term. In the second step, a linear system of Poisson equations of

pressure (eq. 8) is solved to satisfy the mass conservation.

$$[\nabla^2 P^{n+1}]_i = -k \frac{\rho}{\Delta t^2} \frac{[pnd^*]_i - pnd^0}{pnd^0} , \quad (8)$$

where pnd^* is the particle number density calculated in the explicit step. The pnd^0 is the initial particle number density and Δt is the time step. k is the pressure smooth coefficient.

From the pressures obtained implicitly, the pressure gradient is calculated and the velocity and the position of the fluid particles are corrected.

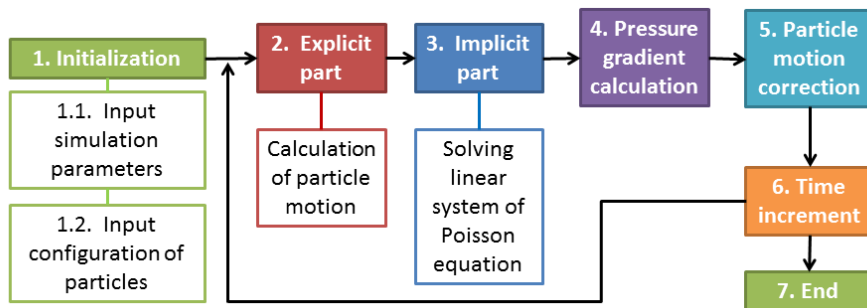


Figure 1: MPS method algorithm

2.4 Free surface boundary condition

The free surface boundary condition proposed by Lee et al. [11] is adopted in this study.

$$[pnd^*]_i = \beta \cdot pnd^0 \quad (9)$$

$$[N^*]_i = \gamma \cdot N^0 \quad (10)$$

where N is the number of particles inside the neighborhood radius for a given particle and N^0 the reference number of particles in the neighborhood, considering a particle whose neighborhood is completely fulfilled in the initial configuration. Based on Lee et al. [11] results, the coefficients are $\beta = 0.97$ and $\gamma = 0.85$.

2.5 Free solid modeling

In the MPS method the entire domain is modeled as particles, including the solid surface. The solid surface is modeled with three rows of particles. The row of solid particles in contact with the fluid are modeled as wall particles. The other two rows consist of dummy particles. The dummy particles are used to assure the correct calculation of the particle number density of the wall particles.

For the numerical offshore tank modeling, three types of solid are considered: fixed solid, solid with forced motion and a free floating solid. The velocity of the fixed and the forced motion solids are imposed as Dirichlet boundary conditions. On the other hand, the motion of the free floating solid are calculated based on forces and moments obtained from the integration of the pressure on the solid surface. The center of gravity, the mass and the moment of inertia of each free floating solid are input parameters.

This implementation of the free floating solid is based on Sueyoshi et al. [12] and Sueyoshi

et al. [13] work. Test and validation of the free floating solid implementation used in the present work are presented by Tsukamoto et al. [14] and Tsukamoto et al. [15].

3 FPSO NUMERICAL SIMULATION

In the present study the development of the particle-based numerical offshore tank for the investigation of green water phenomena are illustrated in three parts. The first is the validation through the comparison between the experimental data of Lee et al. [7] and the numerical results for a low resolution model of Bellezi et al. [6] with 1.6 million particles, and the numerical result of a higher resolution model, with 12 million particles, obtained by using the distributed memory framework for parallel processing developed by Fernandes [9]. The objective of this first stage is to show how the increase of the model resolution, which was limited in the previous works by hardware restrictions, could improve the results.

The second part consists of the simulation of a floating model with 100 million particles and the analysis is focused on the processing performance of the distributed memory version of MPS-TPN simulation system. Finally, the third part shows a practical engineering application using a very high resolution model to investigate the green water phenomenon in head seas on a FLNG system under Santos Basin extreme wave conditions.

3.1 Numerical towing tank

In the present work, the green water occurrences were investigated using a model inside a numerical towing tank as shown in Figure 2.

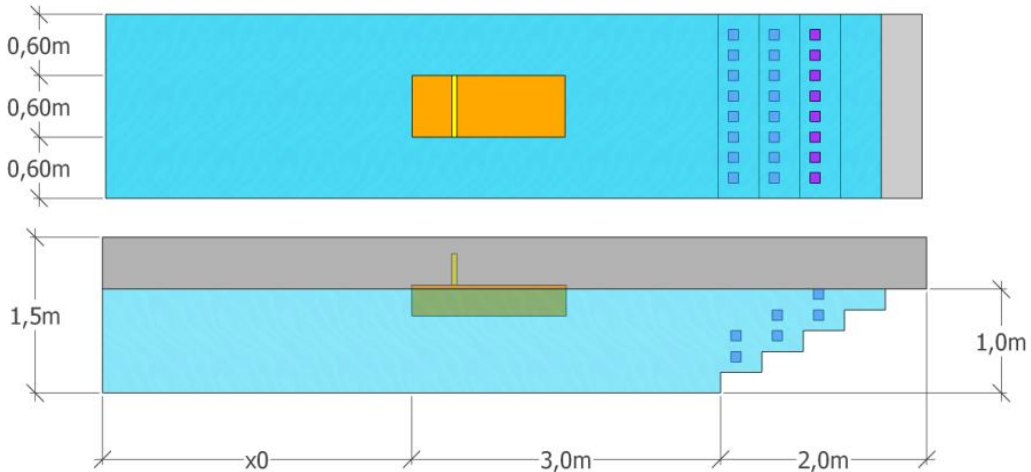


Figure 2: Main dimensions of the numerical tank

The waves were generated by a piston type wavemaker positioned in the left end of the tank. The piston type wavemaker was modeled as a forced solid wall with sinusoidal horizontal translation motion. A stair shaped beach and small fixed boxes were placed at the right end of the tank to absorb the waves and the disturbances due the body wave diffraction. The lateral walls of the tank were modeled as fixed ones. The distance between the model side and the tank lateral wall are equal to the beam of the model.

The waves conditions used in the sections 3.2 and 3.3 are based on those used by Lee et al.

[7] and presented in Table 1. After the wave calibration, the distance between the model and wavemaker (x_0) was obtained. The determination of this distance is necessary due the numerical damping that reduces the wave amplitude along the tank. More details about the wave calibration are presented in Bellezi et al. [6].

Table 1: Wave parameters

Wave Condition	Amplitude	Wave length	Wavemaker period	Wavemaker amplitude	Distance between wavemaker and model (x_0)
1	4.500 cm	225 cm	1.28 s	0.04 m	2.2 m
2	5.625 cm	225 cm	1.28 s	0.05 m	2.2 m
3	6.750 cm	225 cm	1.28 s	0.06 m	2.2 m
4	6.000 cm	300 cm	1.39 s	0.05 m	2.2 m
5	7.500 cm	300 cm	1.39 s	0.06 m	2.0 m
6	9.000 cm	300 cm	1.39 s	0.08 m	2.7 m
7	7.500 cm	375 cm	1.55 s	0.07 m	3.1 m
8	9.375 cm	375 cm	1.55 s	0.08 m	2.7 m
9	11.250 cm	375 cm	1.55 s	0.10 m	3.0 m

3.2 Validation and convergence analysis by fixed model

This section is focused on the validation of the particle based method for the simulation of green water phenomenon. The numerical results are compared to the experimental ones obtained by Lee et al. [7], which used a reduced scale fixed model in head seas condition. The model geometry and the position of the pressure probes are presented in Figure 3.

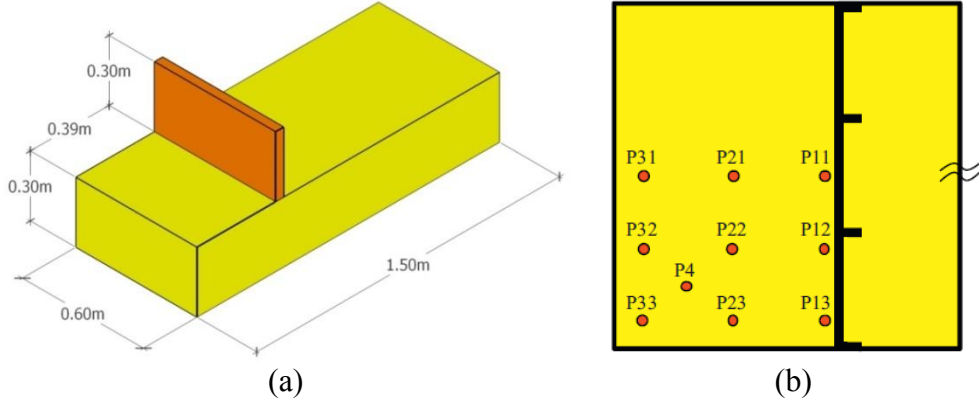


Figure 3: Model main dimensions (a) and position of pressure probes on deck (b)

In Bellezi et al. [6] the resulted obtained by a low resolution model, with 1.6 million particle, were compared to the experimental measurements. In the present work, taking the advantage of a new version of the simulation system for distributed memory architecture, a higher resolution model, of which the distance between particles is half of those used in the previous work, is used. The numerical parameters for the simulations using the low and higher resolution models are given in Table 2.

The Figure 4 shows the pressure histories at the P11 pressure probe. Figure 4-a shows the unfiltered pressure time series, and Figure 4-b shows filtered data by local mean value.

Table 2: Numerical parameters of the simulations

	Coarse resolution model	High resolution model
Distance between particles [m]	0.02	0.01
Time step [s]	0.001	0.0005
Number of particles	≈1,600,000	≈12,000,000
Simulation time [s]	20	20
Subdomains	1	10
Pressure smooth coefficient	0.075	0.05

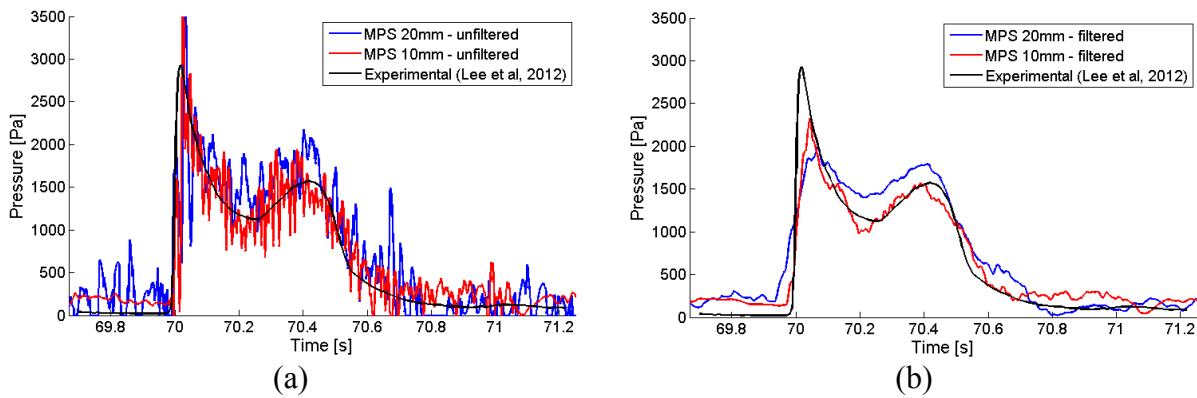


Figure 4: Pressure at P11 pressure probe for wave 9 –unfiltered (a) and filtered (b) numerical results

The P11 pressure probe is located in the center of the deck in front of the vertical bulkhead of the model. It registers the highest pressures of all the pressure probes located at the deck. The pressures histories shown in Figure 4 present two peaks pattern typical of wave impact load: The first peak is result of the merging of the water that come from the bow and from both sides during the ingress phase; The second peak is associated to the collapse of water column that occurs in the drainage phase of the green water phenomenon. Despite the oscillations of the computed pressure in P11, as the magnitude of the oscillations is lower than the magnitude of the peak pressure, in general the behavior of the numerical simulation matches the behavior of the experimental data. .

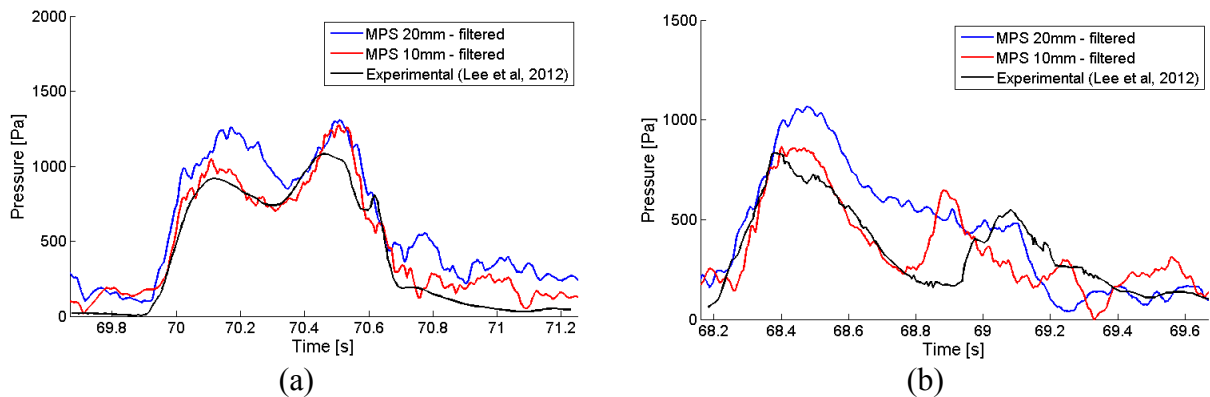


Figure 5: Filtered pressure at P21 (a) and P31 (b)

On the other hand, for the pressure probes in regions where lower pressures are registered,

such as P21 and P31, the pressure oscillation magnitude gets closer to those of the pressure peaks. P21 and P31 have a lower embarking water level in relation to P11. The filtered results for the P21 and P31 region are presented at the Figure 5.

The result presented at Figure 4-b shows relatively small differences between the filtered results at P11 using the coarse or the finer resolution and both the results fit well with the experimental curve. However, for the pressure computed at P21 and P31, as shown in Figure 5, the behavior of the curve for the finer resolution is better than the coarse one. At P21 (Figure 5-a), the two peaks observed for the coarse resolution have almost the same value. On the other hand, the first peak is significantly lower than the second peak for the finer resolution, which agrees well to the measurement. For P33, which involves even lower hydrodynamic pressures than P21, the coarse model is unable to show the occurrence of the two peaks, while the higher resolution model reproduced well the experimental result.

The simulation results showed that the coarse model predicts satisfactorily the hydrodynamic impact at the most critical point, where the highest impact pressure occurs. However, for other regions where the level of embarking water is relatively low, the pressure oscillation magnitude is close to the magnitude of the pressure peaks and the higher resolution model is required for accurate assessment of the hydrodynamic loads.

3.3 Analysis of distributed memory parallel processing performance using a very high resolution free floating model

In this section simulations of the dynamic behavior of a free floating model with 100 million particles in total, including the towing tank, were carried out using the distributed memory architecture [9]. The reduced scale model used in the previous section was adopted. Wave condition 9 shown in Table 1 was considered in this section. The numerical parameters used in the simulation are presented in Table 3.

Table 3: Simulation numerical parameters

Distance between particles [m]	0.005
Time step [s]	0.00025
Number of particles	≈100,000,000
Simulation time [s]	10
Pressure smooth coefficient	0.045

The properties of the floating model are presented at Table 4.

Table 4: Properties of the floating model

Mass [kg]	229.5
Vertical center of gravity [m] (from kell)	0.196
Pitch moment of inertia [kg.m²]	30.83

The performance of the parallel processing by the distributed memory architecture were analyzed through a high resolution model with 100 million particles partitioned in 5 to 40 subdomains. Each subdomain was allocated to a node of computer cluster composed by 20 core AMD Shanghai of 2.66 GHz processors with 128GB of shared memory. When 40 subdomains are used, the 10 second simulation required around 250 hours of processing time.

Figure 6 provides some snapshots of the simulation of the low resolution model with 1.6 million particles, whose distance between particles is 0.02 meters, and the snapshots obtained

using a very high resolution model with 100 million particles, whose distance between particles is 0.005 meters.

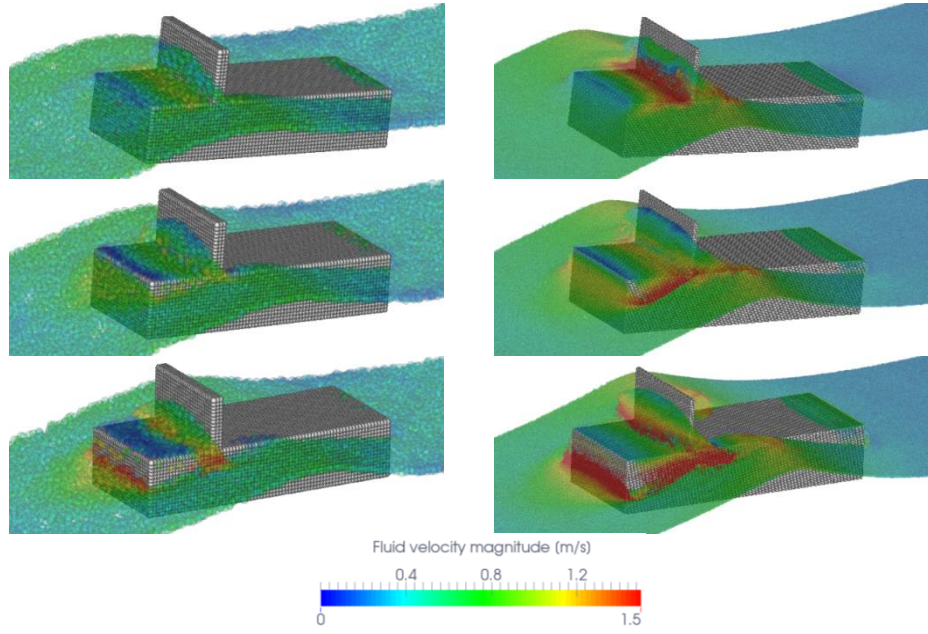


Figure 6: Snapshots of particle-based simulation of the floating models: Low resolution model with 1.6 million particles (left) and very high resolution model with 100 million particles (right)

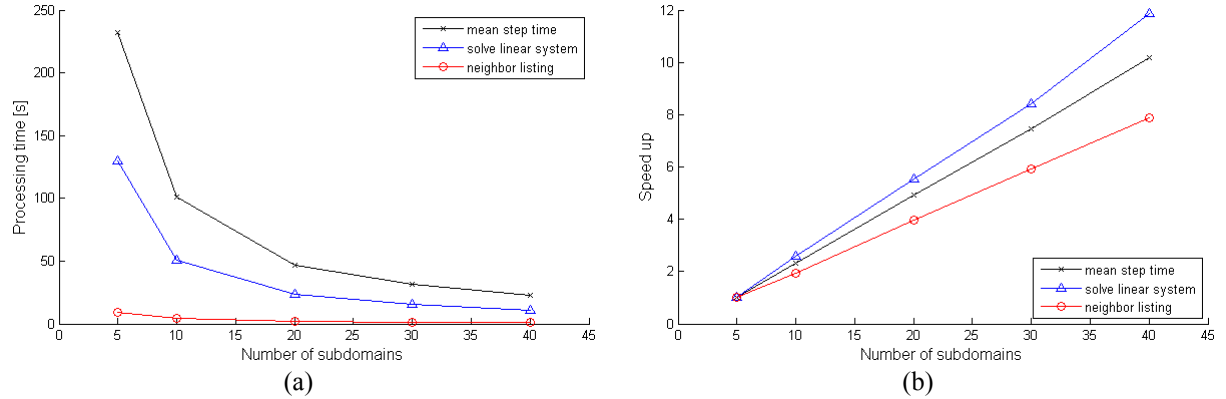


Figure 7: Processing time (a) and speedup (b) in relation to the number of subdomains

Figure 7-a shows the effect of the increasing in the number of subdomains on the processing time. The processing time of the two most time consuming parts of the algorithm, the solution of the linear system and the neighborhood particle search, are also shown. Figure 7-a shows the speedup in relation to the time consumed for the 5 subdomain model. From the results, when 40 subdomains are used, the processing time required is nearly 10 times lower, showing relatively good speed up in this case.

3.4 Real scale model simulations

This section briefly presents results of the application of the particle-based numerical offshore tank to a practical engineering problem. It consists of a study on the green water occurrence of a FLNG system for the oil and gas exploitation in Santo Basin, Brazil.

The mooring system of the FLNG consists in a turret positioned at the bow, so the floating structure could align itself with the most severe weather condition direction. Thus, the FLNG system will operate aligned in head seas for the most severe weather condition, and the particle-based simulations were carried out for head seas of the maximum wave height for the century wave of the worst weather condition of the Santos Basin. The simulations were also carried out for the average, the maximum and the minimum operational draught of the system.

The particle model used in this analysis, including the numerical offshore tank, has around 30 million particles, and it is enough to describe the geometry of the vessel topside. The wave condition has approximately 20 seconds of period and the simulation of 200 seconds requires around 36 hours using 10 subdomains. Figure 8 presents some snapshots of the particle-based simulations. In the left column the sequence of the images shows the FLNG motion in wave for the maximum draught and in the right column for the minimum operational draught.

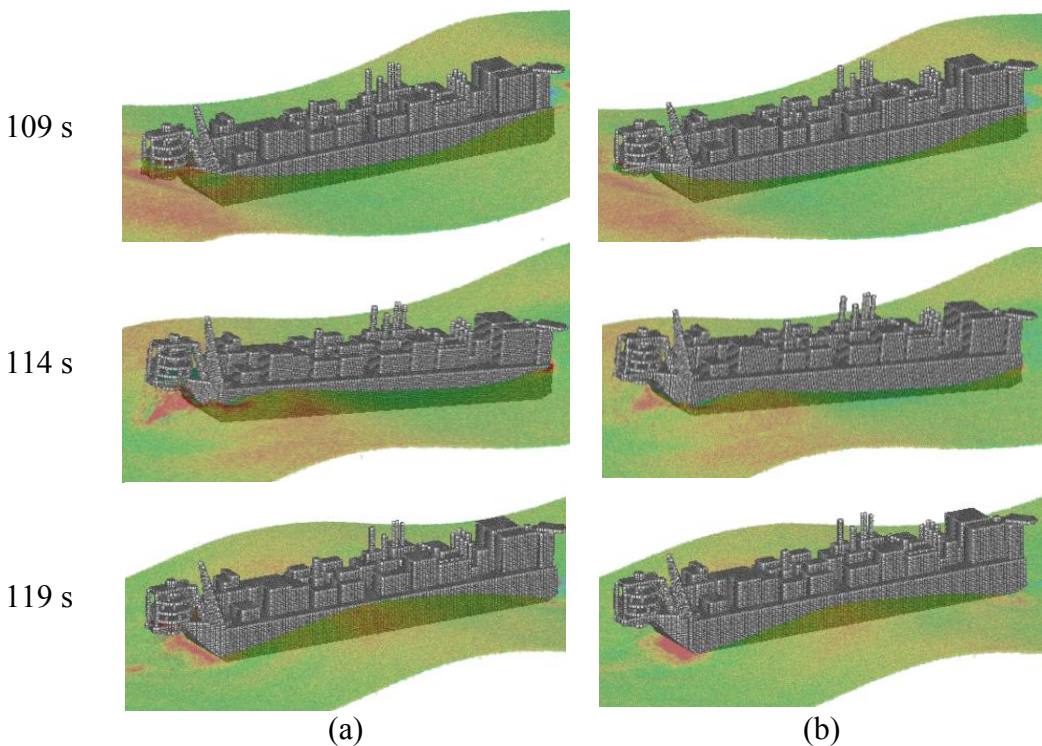


Figure 8: Snapshots of the particle-based simulations for the FLNG model for the maximum draught condition (a) and the minimum draught condition (b)

The maximum water levels at the bow, at the stern and at the middle section of the hull were evaluated in order to verify the occurrence of the green water phenomena. The water levels were measured in relation to the keel of the hull, in a local coordinate system. The Figure 9 shows the water level for the maximum and the minimum operational draught.

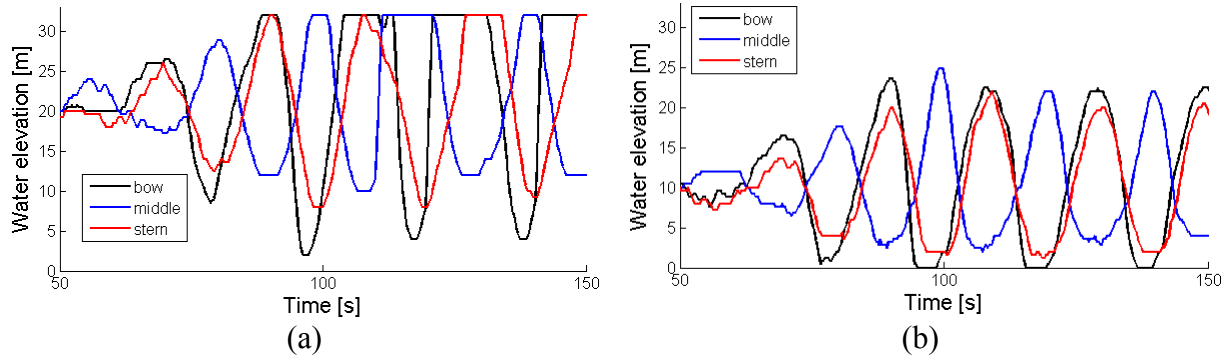


Figure 9: Maximum water level on the hull side for critical wave condition: Maximum draught (a) and minimum draught (b)

The FLNG system depth is approximately 33 meters. In Figure 9, when the water levels reach 33 meters, it indicates the presence of water on deck level and the occurrence of green water. The Figure 9 shows that the green water occurs only for the maximum draught condition. This behavior could also be observed at the snapshots of Figure 8, where the wave crest is very close to the deck level for the maximum operational draught condition.

4 CONCLUDING REMARKS

This paper presents the recent developments of a particle-based numerical offshore tank for the study of the green water phenomenon through three section: The first section shows the validation and convergence study based on a fixed FPSO model. The results show that the use of higher resolution models is more critical when accuracy is required for the regions where the level of embarking water is relatively low. The second section shows the importance of the simulation using floating models that take into account the relative motion between the floating body and the wave surface. A very high resolution floating model with 100 million particles was used to evaluate the performance of the distributed memory parallel processing. Finally, the third section shows an application of the numerical offshore tank. The recent achievements on the simulation of real scale high resolution models, with up to 100 million particles using the distributed memory architecture, provided speedup and scalability required for the application to practical engineering problems involving fluid-structure interaction problems with complex geometry and free surface.

ACKNOWLEDGEMENTS

The authors thank PETROBRAS for the financial support during the development of the particle-based numerical simulation system in Numerical Offshore Tank (TPN-USP) and to INPEX for the financial support on the study of the green water phenomena.

REFERENCES

- [1] S. Koshizuka, H. Tamako., and Y. Oka, "A Particle Method for Incompressible Viscous Flow with Fluid Fragmentation," *Journal of Computational Fluid Dynamics*, pp. 29-46, 1995.
- [2] S. Koshizuka and Y. Oka, "Moving particles semi-implicit method for fragmentation of

- incompressible fluid," *Nuclear Science and Engineering*, vol. 123, pp. 421-434, 1996.
- [3] Kazuya Shibata and Seiichi Koshizuka, "Numerical Analysis of Shipping Water Impact on a Deck Using a Particle Method," *Ocean Engineering*, vol. 34, pp. 585–593, 2007.
- [4] Kazuya Shibata, Seiichi Koshizuka, and Katsuji Tanizawa, "Three-dimensional Numerical Analysis of Shipping Water Onto a Moving Ship Using a Particle Method," *Journal of Marine Science and Technology*, pp. 214-227, 2009.
- [5] Kazuya Shibata, Seiichi Koshizuka, Mikio Sakai, and Katsuji Tanizawa, "Lagrangian Simulations of Ship-Wave Interactions in Rough Seas," *Ocean Engineering*, 2012.
- [6] Cezar Augusto Bellezi, Liang-Yee Cheng, and Kazuo Nishimoto, "Particle Based Numerical Analisys of Green Water on FPSO Deck," in *32nd International Conference on Ocean, Offshore and Arctic Engineering - OMAE 2013*, Nantes, France, 2013a.
- [7] Hyun-Ho Lee, Ho-Jeong Lim, and Shin Hyung Rhee, "Experimental Investigation of Green Water on Deck for a CFD Validation Database," *Ocean Engineering*, vol. 42, pp. p. 47-60, 2012.
- [8] Cezar Augusto Bellezi, Liang-Yee Cheng, and Kazuo Nishimoto, "A numerical study of the effects of bow shape on green water phenomenon," in *23rd International Conference on Ocean and Polar Engineering - ISOPE 2013*, Anchorage, 2013b.
- [9] D. T. Fernandes, Implementação de Framework Computacional de Paralelização Híbrida do Moving Particles Semi-Implicit Method para Modelagem de Fluídos Incompressíveis, Ph.D. thesis, Polytechnic School of Engineering of University of São Paulo, São Paulo, Brazil, 2013.
- [10] Yuxin Zhang, Xuyang Wang, Zhenyuan Tang, and Decheng Wan, Numerical Simulation of Green Water Incidents Based on Parallel MPS Method, 2013.
- [11] B.-H. Lee, J.-C. Park, and M.H. Kim, "Two-dimensional vessel-motion/liquid-sloshing interactions and impact loadings by using a particle method," in *Proceedings of the ASME 2010 29th International Conference on Ocean, Offshore and Arctic Engineering - OMAE2010*, Shanghai, China, June 2010.
- [12] M. Sueyoshi and S. Naito, "Aplication of MPS for Violent Free Surface Problems on Marine Engineering," Tokyo, Graduate school of Engineering 2002a.
- [13] M. Sueyoshi and S. Naito, "A Numerical Study of Very Large Motion of Floating Body by Particle Method," in *Asia and Pacific Maritime Congress*, Kobe, Japan, 2002b.
- [14] Márcio Michiharu Tsukamoto, Liang-Yee Cheng, and Kazuo Nishimoto, "Numerical study of the motions in shallow water waves of floating bodies elastically linked to the bottom," in *28th International Conference on Ocean, Offshore and Arctic Engineering - OMAE 2009*, Honolulu, USA, 2009.
- [15] Márcio Michiharu Tsukamoto, Liang-Yee Cheng, and Kazuo Nishimoto, "Numerical study of the effectiveness of a moving sloshing supression device," in *29th International Conference on Ocean, Offshore and Arctic Engineering - OMAE 2010*, Shanghai, China, 2010.

MODELLING CENTRIFUGAL MEMBRANE DEPLOYMENT OF SOLAR SAILS WITH THE DISCRETE ELEMENT METHOD

Zixuan Xu¹, Daxu Zhang^{2*}, Wujun Chen³, and Fujun Peng⁴

¹ School of Naval Architecture, Ocean & Civil Engineering,
Shanghai Jiao Tong University, Shanghai 200240, China
Email: xuzixuanatsjtu@hotmail.com

² School of Naval Architecture, Ocean & Civil Engineering,
Shanghai Jiao Tong University, Shanghai 200240, China
Corresponding author (daxu.zhang@sjtu.edu.cn)

³ Space Structures Research Centre,
Shanghai Jiao Tong University, Shanghai 200240, China
Email: cwj@sjtu.edu.cn

⁴ Shanghai Key Laboratory of Spacecraft Mechanism,
Aerospace System Engineering Shanghai, Shanghai, 201108, China

Key words: Solar Sail, Membrane Deployment, DEM.

Abstract: *Spin-stabilized solar sails have been extensively studied in recent years. In this paper, a DEM-based approach is proposed for dynamic analysis of the centrifugal deployment of solar sails. In order to validate the proposed approach, the deployment of a small-scale solar sail similar to “IKAROS” is studied. The membrane is discretised into a number of particles, with no physical contact between them. Non-contact interaction is introduced to model in-plane stiffness of the membrane. In order to improve the accuracy, additional forces are applied to the mass particles to model buckling strength, crease stiffness, air drag and damping. The predicted results of the membrane deployment are compared with the experimental data and numerical results in the literature.*

1 INTRODUCTION

Solar sails are a form of spacecraft propulsion using the radiation pressure (also called solar pressure) from stars to push large ultra-thin membranes to high speeds [1]. Japan Aerospace Exploration Agency (JAXA) successfully launched and deployed a solar sail “IKAROS” in 2010. Later, a deployment experiment of a small-scale solar sail similar to “IKAROS” is conducted in a vacuum chamber and corresponding dynamic response was analysed by using a spring-mass model [2].

The dynamic response of solar sail is typically predicted by the finite element methods [4] and spring-mass system models [2]. This paper introduces a DEM-based approach to analyse the dynamic deployment of a solar sail membrane structure. It provides a new alternative approach to effectively analyse the dynamic deployment of solar sails or other membrane structures.

2 MODELLING METHOD

2.1 DEM basics

Mass particles are the elementary units in Discrete Element Method (DEM) , which are indeformable [5]. The interaction forces between the particles are evaluated based on the overlap between them.

The equation of motion is described as follows:

$$m_i \frac{d^2}{dt^2} \mathbf{r}_i = \mathbf{f}_i, I_i \frac{d}{dt} \boldsymbol{\omega}_i = \mathbf{t}_i \quad (1)$$

where:

m_i and I_i denote the mass and moment of inertia of particle i , repectively;

\mathbf{r}_i and $\boldsymbol{\omega}_i$ denote the position and angular velocity of it, repectively;

$\mathbf{f}_i = \sum_c \mathbf{f}_i^c + m_i \mathbf{g}$ denotes all the forces acting on it;

$\mathbf{t}_i = \sum_c (\mathbf{l}_i^c \times \mathbf{f}_i^c + \mathbf{q}_i^c)$ denotes all the torques acting on it.

As shown in Figure 1, two spherical particles i and j , with radius a_i and a_j , respectively, interact with each other when they are in contact ($\delta > 0$). However, it is possible to establish an non-contact interaction when $\delta < 0$.

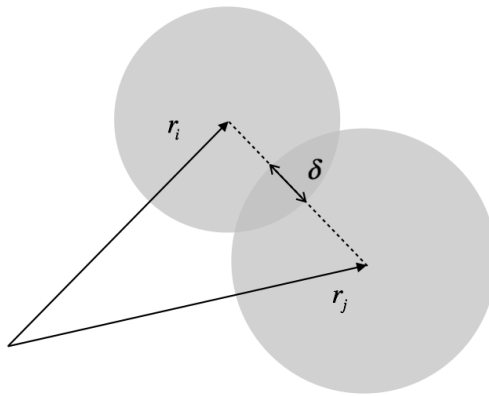


Figure 1: Two particles contact with overlap δ

The overlap δ can be described as follows:

$$\delta = (a_i + a_j) - (\mathbf{r}_i - \mathbf{r}_j) \cdot \mathbf{n} \quad (2)$$

where $\mathbf{n} = (\mathbf{r}_i - \mathbf{r}_j)/|\mathbf{r}_i - \mathbf{r}_j|$ denotes the unit vector pointing from j to i .

The force on particle i , from particle j , at contact C, can be decomposed into a normal and a tangential part as $\mathbf{f}_i^c = f^n \mathbf{n} + f^t \mathbf{t}$.

In linear normal contact model, f^n can be described as follows:

$$f^n = k\delta + c\dot{\delta} \quad (3)$$

where c denotes damping coefficient.

In the current work, there is no moment or torque between particles, and therefore the rotational equation of motion in Equation 1 is not taken into account. Neither the tangential force f^t is considered.

The basic method of DEM is the integration of Newton's equations of motion for all degrees of freedoms. Interaction forces are updated based on the positions and velocities of particles in each time-step.

2.2 Mass and stiffness

A membrane can be discretized into a number of mass particles, with non-contact interactions between them [3]. As shown in Figure 2, a triangular membrane element is discretized into 3 particles in the three corners, with interactions between them.

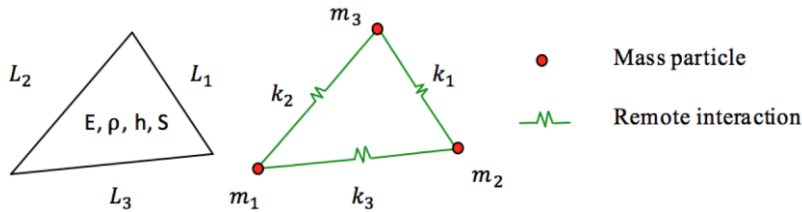


Figure 2: Triangular element

The mass of the three particles can be calculated as follows:

$$m = \frac{\rho h S}{3} \quad (i = 1, 2, 3) \quad (4)$$

In order to obtain the stiffness of the interactions, assume the strain energy of the element coincide with an actual membrane when the element is in one-axis stress states parallel to three sides [6]. Thus, we can obtain the stiffness:

$$\begin{bmatrix} k_1 \\ k_2 \\ k_3 \end{bmatrix} = B_{ij}^{-1} \begin{bmatrix} 1 \\ 1 \\ 1 \end{bmatrix}, B_{ij} = \frac{p_{ij}^2 L_j^2}{E h S}, p_{ij} = 1 - \frac{4(1 + \nu)S^2}{L_i^2 L_j^2} (1 - \delta_{ij}) \quad (5)$$

where:

E, ρ, ν denote Young's modulus, density and Poisson's ratio, respectively;

L_i denotes length of the sides of the triangle;

m_i denotes mass of the particles;

k_i denotes stiffness of the interactions;

δ_{ij} denotes Kronecker delta.

2.3 Buckling

In order to take buckling effects of the membrane into consideration, assume that the restoring force of the interactions keeps the same when the distance between two corresponding particles is less than a specific value l_{cr} , as shown in Figure 3. l_{cr} can be calculated as follows:

$$l_{cr} = L_i - \alpha \frac{\pi^2 h^2}{12L_i} \quad (6)$$

where α is a parameter that needs to be calibrated.

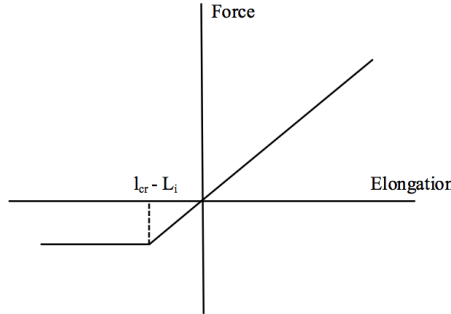


Figure 3: Contact force

2.4 Stiffness of crease and contact

Due to the fact that the crease of the folded membrane can generate restoring forces, the stiffness of the crease should be considered. It can be done by adding some extra restoring forces to the masses near the crease. Consider two adjacent elements ABC and ABD that contain a crease, as shown in Figure 4, restoring forces F_C and F_D induced by the crease should be added to the particles. Additionally, forces F_A and F_B need to be added as well, in order to cancel rigid-body motion of the elements.

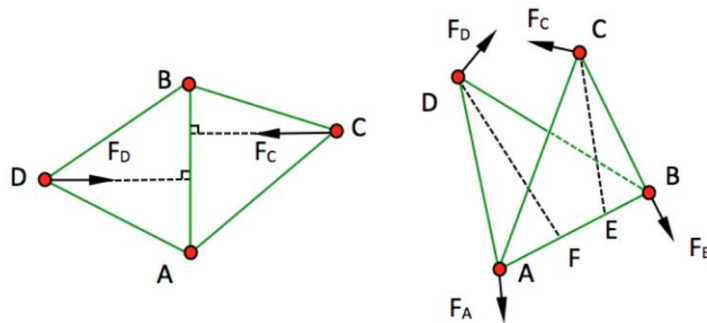


Figure 4: Restoring forces around crease

Forces F_C and F_D can be calculated as follows:

$$F_C = \beta \bar{\gamma} \frac{EJl_{AB}(\theta - \theta_0)}{l_{CE}^2}, F_D = \beta \bar{\gamma} \frac{EJl_{AB}(\theta - \theta_0)}{l_{DF}^2}, \bar{\gamma} = \begin{cases} 1 & \text{when } \theta \geq 0 \\ \gamma & \text{when } \theta < 0 \end{cases} \quad (7)$$

Forces F_A and F_B can be calculated as follows:

$$\mathbf{F}_A = -\frac{l_{BE}}{l_{AB}} \mathbf{F}_C - \frac{l_{BF}}{l_{AB}} \mathbf{F}_D, \mathbf{F}_B = -\frac{l_{AE}}{l_{AB}} \mathbf{F}_C - \frac{l_{AF}}{l_{AB}} \mathbf{F}_D \quad (8)$$

where:

θ and θ_0 denote angle and natural angle, respectively;

γ denotes a penalty factor to take account of self contacts around the crease lines;

$J = h^3/12$ denotes geometrical moment of area per unit width.

Note that, the forces calculated in Equation 7 are actually sensitive to mesh density. Therefore, for different mesh density chosen from the reference [2], the stiffness parameter β needs to be calibrated.

2.5 Damping

In order to take account of structural damping, velocity-proportional damping forces are added to the interactions. The damping coefficient c is described as follows:

$$c = 2\zeta\sqrt{k_i m} \quad (9)$$

where:

ζ denotes damping ratio;

$m = (m_j + m_k)/2$ denotes average mass.

2.6 Air Drag

The deployment experiment is conducted in a vacuum chamber, but there is still some air left. Therefore, air drag is taken into consideration. Air drag forces acting on an triangular element can be described as:

$$F_a = \rho S_n V^2 / 6 \quad (10)$$

where:

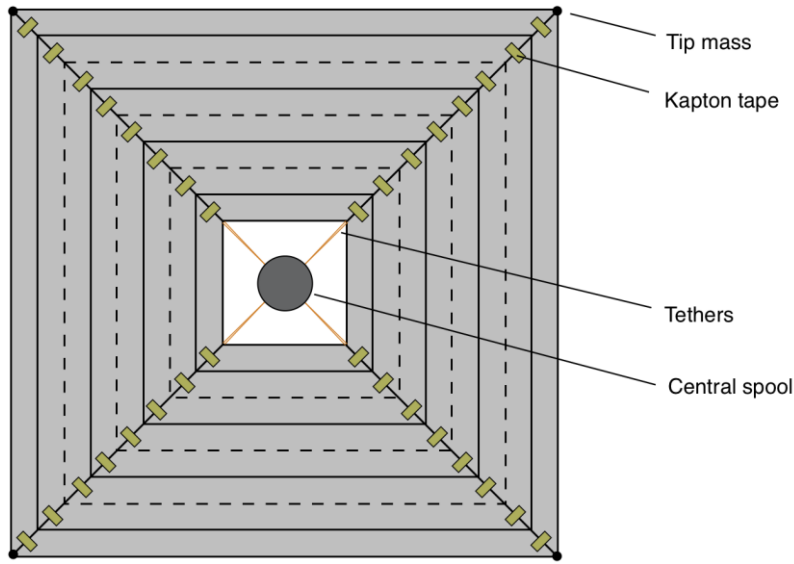
V denotes velocity of the mass;

S_n denotes the area projected to the direction of the velocity.

3 DEPLOYMENT MODELLING

3.1 Model introduction

The small-scale solar sail in the experiment is a square membrane, with side length of 10 m and thickness of 7.5 μm . The membrane is connected to the central spool by using tethers, and it has the same material with a real solar sail. The whole membrane consists of four trapezoidal petals, and each petal can be folded up into a strip. Kapton tapes are used to connect the four petals. Four tip masses are fixed on the four corners to generate enough centrifugal forces. Figure 5 shows the sketch of the model. In the figure, solid line represents mountain folding, and dashed line represents valley folding. The folding and deployment method can be found in the reference.

**Figure 5:** Model sketch

3.2 Model parameters

Table 1 shows the dimensions and material properties of the DEM model.

Table 1: Model parameters

Number of folding lines	7
Outer width	455 mm
Inner width	103 mm
Thickness	7.5 μ m
Radius of central spool	25 mm
Crease interval	22 mm
Young's modulus (membrane)	3.2 GPa
Poisson's ratio (membrane)	0.34
Density (membrane)	1420 kg/m ³
Tip mass	0.36 g
Rotation speed	6 π rad/s

3.3 Numerical model

The YADE Open DEM platform [7] was selected to simulate the centrifugal deployment of solar sails. Figure 6 shows the geometrical model of the solar sail. The mass of each triangular element is equally distributed to three masses. Tip masses are added to the corresponding corner masses. The non-contact interaction force is calculated by the equations aforementioned. Considering the fact that buckling strength of the crease is relatively high, the parameter α is set to be relatively large. Ignore physical contacts between the particles.

The central spool is modeled as facet cylinder. Tethers are also discretized into a number of mass particles. Two adjacent tethers are modeled as one. Tethers cannot bear compressive forces, therefore the parameter α is set to zero. The contact between tether masses and the

central spool is modelled. Buckling effects, stiffness of creases, structural damping and air drag are taken into account, by adding corresponding forces to the masses.

After creating the model of a fully deployed solar sail, the folded model was obtained by moving the positions of the particles. Then, centrifugal forces were added to the masses. In order to model the constraints of the four guide bars, the corresponding particles were attached to the bars. Because the experiment is conducted on the ground, gravity is taken into account. When the system reached a state of equilibrium, the constraints of guide bars were removed and the attached particles were released. During the rotation, the membrane deployed due to centrifugal forces. The time-step Δt was set to be 5×10^{-6} . Simulation results including deployment rate and phase difference are obtained.

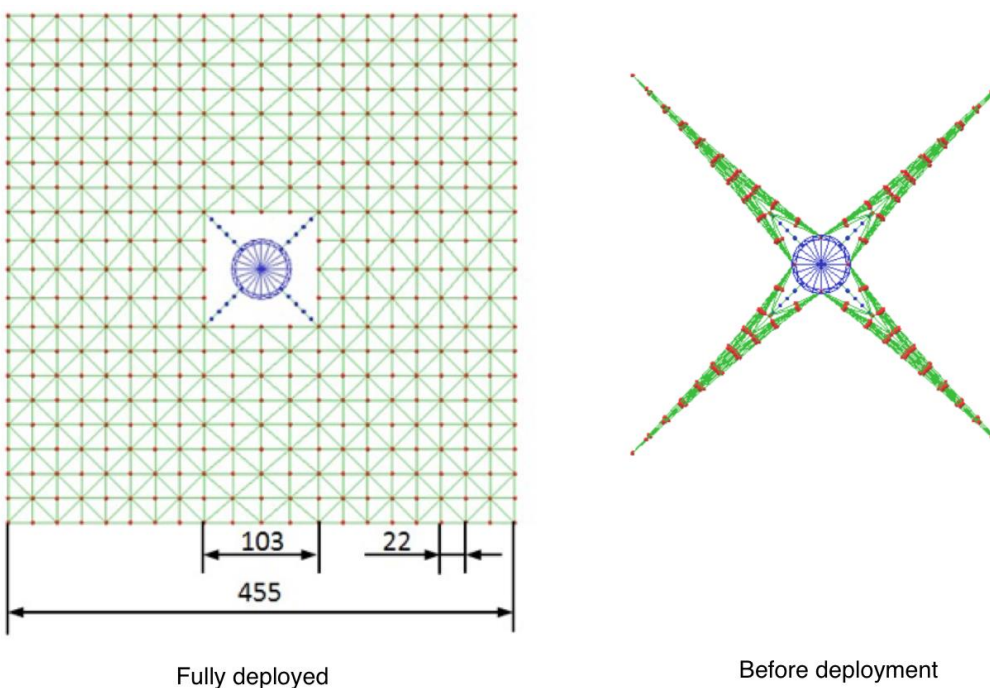


Figure 6: Geometry of the DEM model

3.4 Numerical results

Three cases are studied, with different simulation parameters. Several results are obtained to study the dynamic response of the membrane, including membrane shapes during deployment, deployment rate, and phase difference. The simulation parameters are shown in Table 2.

Table 2: Simulation parameters

Natural angle of crease θ_0	0
Buckling parameter α	100
Buckling parameter α_C (crease)	100, 1000
Stiffness of crease parameter β	0, 3, 30
Contact penalty factor γ	100

Damping ratio	0.02
---------------	------

Figure 7 shows the membrane shapes during deployment. Figure 8 and 9 plot the deployment rate and the phase difference comparisons. The results coincide with those obtained by the reference [2]. As shown in the figures, as the increase of α_c and β , the amplitude and period of the phase differences decrease.

However, the decrease is not as significant as the results shown in the reference, this is probably because the mesh density is different, and this may affect the interaction mechanism of the restoring forces of creases. It is possible to calibrate these parameters to tune the simulation results to the experiment data.

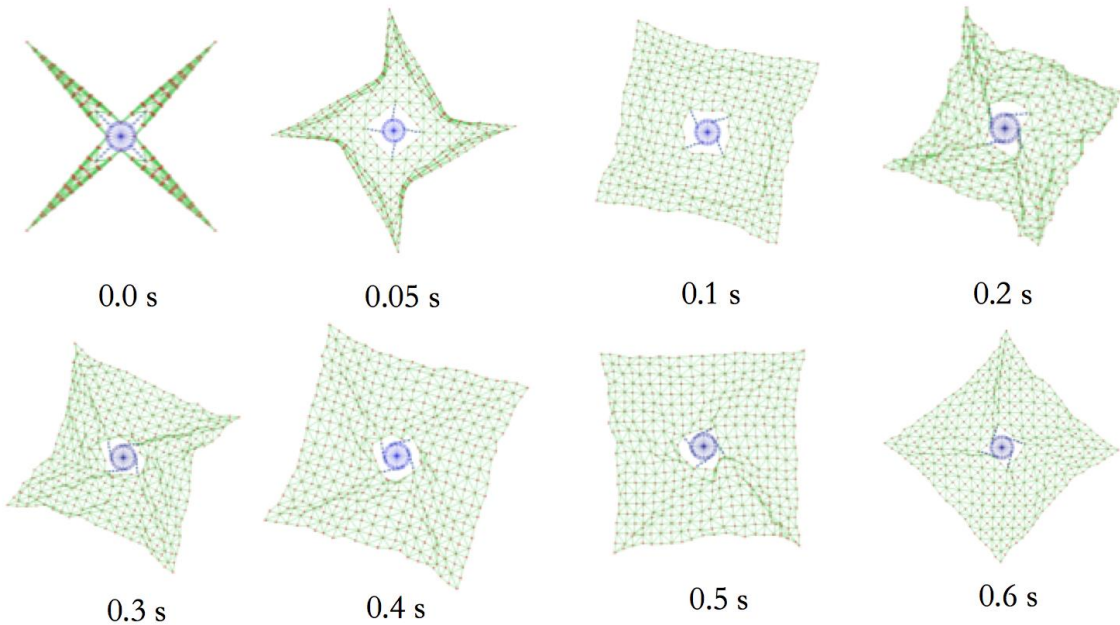


Figure 7: Membrane shapes during deployment ($\alpha = 1000, \beta = 30$)

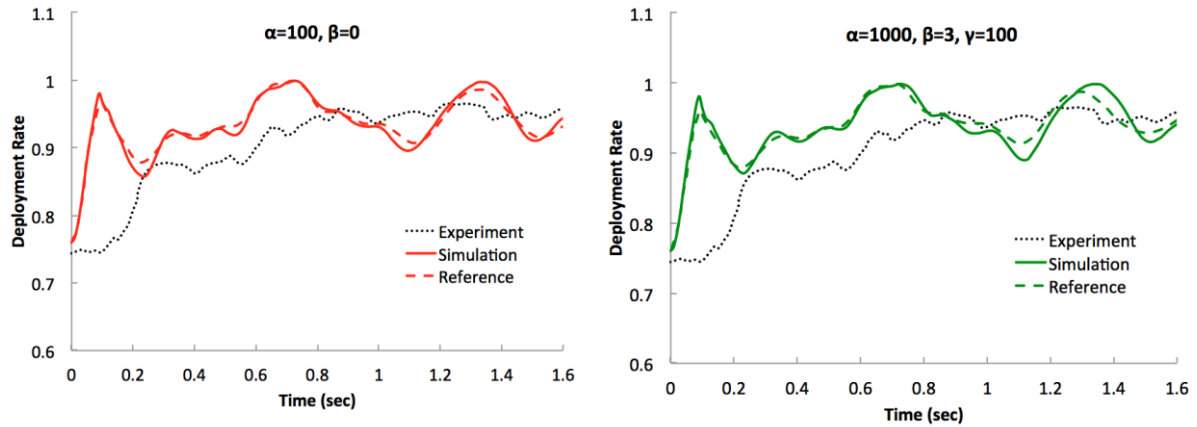


Figure 8: Results comparisons (part I)

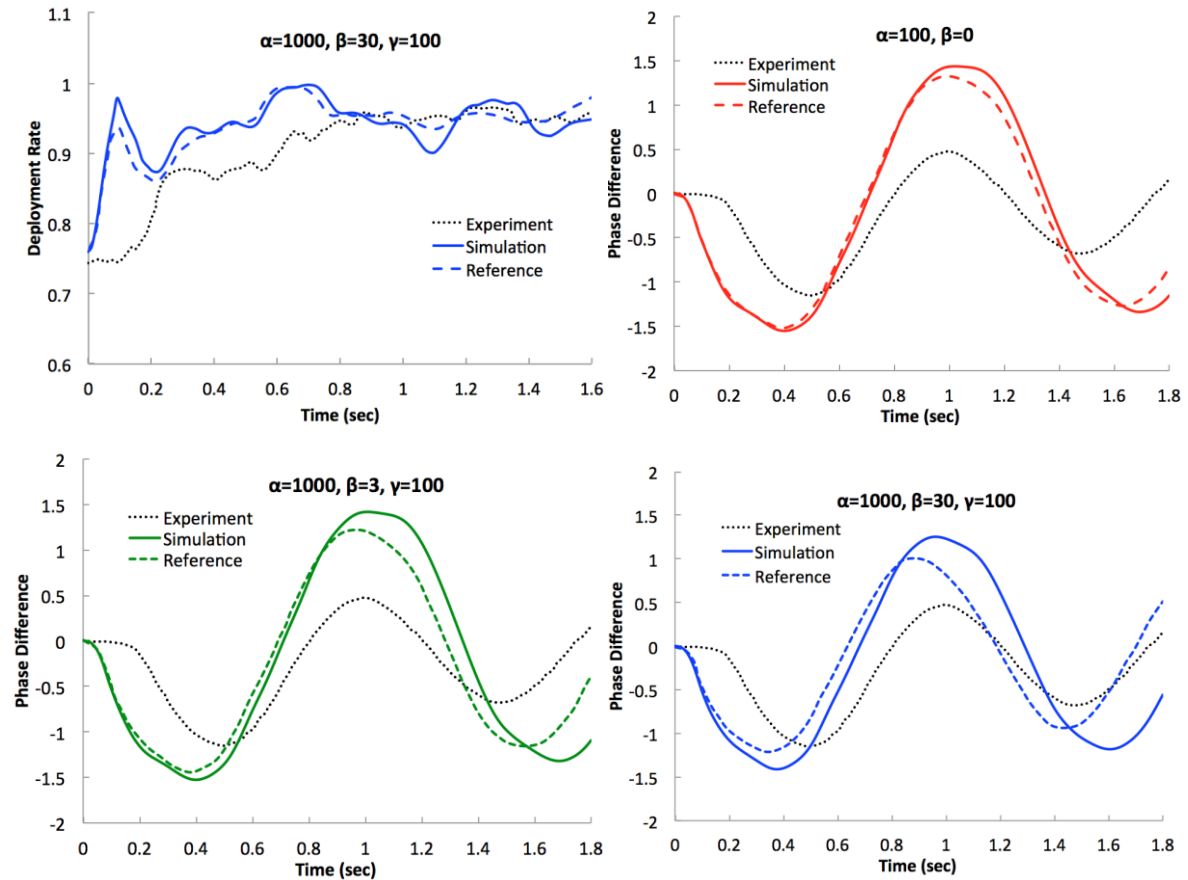


Figure 9: Results comparisons (part II)

4 CONCLUSIONS

In this paper, a DEM-based approach has been used to analyse the dynamic deployment behaviour of a small scale solar sail. The current prediction was compared with test data and the results obtained by using the spring-mass approach. A good correlation has been achieved. Studies on the deployment of a large scale solar sail by using the DEM method are underway. The current study provides a new alternative to analyse the membrane deployment of a solar sail and the mechanical behaviour of other membrane structures.

ACKNOWLEDGEMENT

Part of the research was financially supported by Science and Technology Commission of Shanghai Municipality under Grant No 12ZR1414800.

REFERENCES

- [1] Solar sail (31 January 2015). Retrieved from <http://en.wikipedia.org/wiki/Solar_sail>
- [2] Okuzumi, N., et al, Small-scale Experiments and Simulations of Centrifugal Membrane Deployment of Solar Sail Craft 'IKAROS', 52nd AIAA/ ASME/ASCE/AHS/ASC Structures, Structural Dynamics and Materials Conference, AIAA2011-1888, 2011.
- [3] Thoeni K, Lambert C, Giacomini A, Sloan SW. Discrete modelling of hexagonal wire meshes with a stochastically distorted contact model. *Comput Geotech* 2013;49:158–69.
- [4] Miyazaki, Yasuyuki, et al., "Conserving Finite Element Dynamics of Gossamer Structures and Its Application to Spinning Solar Sail IKAROS," 52nd Structures, Structural Dynamics and Materials Conference, 4–7 April 2011, Denver, Colorado.
- [5] Luding S, Introduction to discrete element methods: basics of contact force models and how to perform the micro-marco transition to continuum theory. *Eur. J. Environ. Civ. Eng.* 12(7–8), 785– 826 (2008)
- [6] Miyazaki, Y. and Iwai, Y., "Dynamics of Membrane Deployed by Centrifugal Force", Space Engineering Conference, Tokyo, Japan, 2005, pp.59-64 (in Japanese).
- [7] V. Šmilauer, E. Catalano, B. Chareyre, S. Dorofeenko, J. Duriez, A. Gladky, J. Kozicki, C. Modenese, L. Scholtès, L. Sibille, J. Stránský, K. Thoeni (2010), Yade Documentation. The Yade Project. (<http://yade-dem.org/doc/>)

THEORETICAL INVESTIGATION OF THE DYNAMICS OF FRICTION STIR WELDING PROCESS BY MOVABLE CELLULAR AUTOMATON METHOD

SERGEY V. ASTAFUROV^{1,2}, EVGENY V. SHILKO^{1,2}, EVGENY A. KOLUBAEV^{1,3},
ANDREY I. DMITRIEV^{1,2}, ANTON YU. NIKONOV^{1,2}, SERGEY G. PSAKHIE^{1,3}

¹ Institute of Strength Physics and Materials Science SB RAS (ISPMs SB RAS)
2/4, Akademicheskii ave., 634055 Tomsk, Russia
e-mail: svastafurov@gmail.com, web page: <http://www.ispm.su>

² National Research Tomsk State University (TSU)
36, Lenin ave., 634050, Tomsk, Russia
web page: <http://www.tsu.ru>

³ National Research Tomsk Polytechnic University (TPU)
30, Lenin ave., 634050, Tomsk, Russia
web page: <http://www.tpu.ru>

Key words: Friction Stir Welding, Movable Cellular Automaton Method, Welded Joint, Porosity, Technological Process Parameters.

Summary. The paper is devoted to development of a new approach to study of friction stir welding (FSW) process on the mesoscopic scale. This approach is based on computer-aided simulation by movable cellular automaton (MCA) method. In the framework of developed formalism of MCA method the dynamics of the friction stir welding process of duralumin plates was investigated. It was shown that ratio of rotation velocity to velocity of translation motion of rotating tool greatly influences the quality of welded joint. Optimal choice of the ratio of these parameters could significantly decrease volume content of pores and microcracks in the welded joint.

1 INTRODUCTION

Friction stir welding (FSW) is a relatively new method of obtaining non-detachable joints of materials [1,2]. Recent year studies have shown that FSW is an effective way to obtain high quality joints for structures of various dimensions and shapes, including sheets, 3D profile structures, and pipes. Possessing the broad technological capabilities for obtaining permanent joints of details or units, it can be used as an alternative to riveted joints, electric arc welding, electron beam and laser welding as well as for welding the dissimilar materials. Thus, FSW becomes a perspective technology that has a great potential in various industries, including aerospace area.

The FSW technology is based on the friction of the rotating cylindrical or specially shaped tool between two connected or overlapped faces (ends) of metal plates [1-3]. The rotating tool

is introduced into the joint of two metal plates to a depth approximately equal to their thickness. As a result of sliding friction (while rotating of the tool) a frictional heating the metal takes place. This leads to plastic deformation, flow and mixing of the material and, consequently, to formation of welded joint. The main problem when using FSW technology for producing of welded joints is the determination of an optimal regime (optimal parameters) of the rotating tool movement (in particular, the ratio of the angular and translational velocities of the tool). These parameters are determined by a wide range of factors, among which are the physical and mechanical properties of welded materials, the thickness of the connected plates, etc. Note, that incorrect determination of welding parameters is likely to cause of a large amount defects at different scales (pores, microcracks, etc.) in a weld seam and, consequently, to decrease of the quality of the joint [1-3].

Experimental determination of the parameters of FSW process is quite difficult task, because it requires obtaining and analysis of large amounts of data. In this regard, it is promising to use computer-aided simulation of process of formation of the welded joint. Since FSW processes are inseparably linked with the intensive formation of discontinuities, the generation of structural defects of different levels, the mass transfer, etc. the most preferable one is to use methods of discrete description of the simulated technology. In this paper, the dynamics of the FSW process of duralumin plates was investigated on the base of computer-aided simulation by the movable cellular automaton (MCA) method [4-7].

2 FORMALISM OF MOVABLE CELLULAR AUTOMATON METHOD

MCA method is the representative of the class discrete elements methods (DEM) and refers to subclass of simply deformable discrete elements [8,9]. In the framework of DEM simulated object on the considered scale is represented by ensemble of interacted elements of defined size and shape. In the process of loading a form of discrete elements may vary. The main feature of the method of simply deformable discrete elements is approximation of a uniform distribution of strains and stresses in the bulk of the discrete elements (in our case of the movable cellular automata). This approach imposes the requirement of proximity of initial linear discrete element size in different directions (in 2D case examples are the elements of round, square or hexagonal shape). In the framework of the described approach description of the evolution of the ensemble of interacting movable cellular automata is based on the numerical solution of the equations of Newton-Euler for centers of mass of the elements:

$$\begin{cases} m_i \frac{d^2 \vec{R}_i}{dt^2} = \sum_{j=1}^{N_i} (\vec{F}_n^{ij} + \vec{F}_\tau^{ij}) \\ \hat{J}_i \frac{d^2 \vec{\theta}_i}{dt^2} = \sum_{j=1}^{N_i} \vec{M}_{ij} \end{cases}. \quad (1)$$

Here \vec{R}_i and $\vec{\theta}_i$ are radius-vector and rotation angle of the automaton i , m_i and \hat{J}_i are the mass and moment of inertia of the automaton, \vec{F}_n^{ij} and \vec{F}_τ^{ij} are the forces of central and tangential interaction between automaton i and its neighbor j , \vec{M}_{ij} is the momentum of force, N_i is the number of interacting neighbors.

The form of the equations for the interautomata interaction forces is borrowed from the embedded atom method [10,11] and contains a pair-wise and volume-dependent components:

$$m_i \frac{d^2 \vec{R}_i}{dt^2} = \vec{F}_i = \left(\sum_{j=1}^{N_i} \vec{F}_{pair}^{ij} + \vec{F}_\Omega^i \right). \quad (2)$$

Here \vec{F}_i is a total force, acting on automaton i from the surrounding elements, \vec{F}_{pair}^{ij} and \vec{F}_Ω^i are its pair-wise (determined by the relative displacement of automata in pairs $i-j$) and volume-dependent (determined by the joint influence of the surroundings of the automaton i) components.

When modeling the FSW process at the mesoscopic scale (10 mm - 10 mm) it is adequate to consider of simulated metal as an isotropic medium. For locally isotropic materials volume-dependent component \vec{F}_Ω^i in relation (2) can be expressed in terms of the pressure P_i in the volume the automaton:

$$\vec{F}_i^\Omega = -A_i \sum_{j=1}^{N_i} P_j S_{ij} \vec{n}_{ij}. \quad (3)$$

Here S_{ij} is the area of interaction of elements i and j (area of plane face), A_i is the material parameter for the element i (in general case each distinct element simulates a material volume with unique phase or chemical composition and is characterized by a unique value of material parameter A), \vec{n}_{ij} is a unit-vector. In this case, the expression for the central and the tangential forces of interaction of automaton i with the adjacent the automaton j in (1) have the following general form:

$$\begin{cases} F_n^{ij} = F_{pair,n}^{ij}(h_{ij}) - A_i P_i S_{ij}, \\ F_\tau^{ij} = F_{pair,\tau}^{ij}(l_{ij}) \end{cases}, \quad (4)$$

where $F_{pair,n}^{ij}$ and $F_{pair,\tau}^{ij}$ are the central and tangential components of pair-wise potential interaction force \vec{F}_{pair}^{ij} . These components depend on the values of element i contributions to pair overlap h_{ij} and relative shear displacement l_{ij} respectively.

The specific form of dependencies $F_{pair,n}^{ij}(h_{ij})$ and $F_{pair,\tau}^{ij}(l_{ij})$ is directly connected with the type and parameters of the equation of state of the simulated material. Within the framework of the used approximation of locally isotropic material elastic interaction of movable cellular automata is described by linear Hooke's law for isotropic materials. The corresponding expressions for the forces of the central and the tangential linear-elastic interaction of movable cellular automata i and j are as follows [4-7]:

$$\begin{cases} \sigma_{ij}^{cur} = \sigma_{ji}^{cur} = \sigma_{ij}^{pre} + \Delta\sigma_{ij} = \sigma_{ij}^{pre} + 2G_i \Delta\varepsilon_{i(j)} + \left(1 - \frac{2G_i}{K_i}\right) \Delta\bar{\sigma}_{mean}^i, \\ \Delta h_{ij} = \Delta\varepsilon_{i(j)} \frac{d_i}{2} + \Delta\varepsilon_{j(i)} \frac{d_j}{2} \end{cases}, \quad (5)$$

$$\begin{cases} \tau_{ij}^{cur} = \tau_{ij}^{pre} + \Delta\tau_{ij} = \tau_{ij}^{pre} + 2G_i\Delta\gamma_{i(j)} = \tau_{ji}^{cur} = \tau_{ji}^{pre} + \Delta\tau_{ji} = \tau_{ji}^{pre} + 2G_j\Delta\gamma_{j(i)} \\ \Delta l_{shear}^{ij} = \Delta\gamma_{i(j)} \frac{d_i}{2} + \Delta\gamma_{j(i)} \frac{d_j}{2} \end{cases}. \quad (6)$$

Here, relations for calculating the central and tangential interaction forces are written in increments (in hypoelastic form); the upper indexes “cur” and “pre” denote values of specific respond forces at the current and previous time steps of integrating the motion equation (1); Δ is the increment of corresponding parameter during one time step Δt , $\varepsilon_{i(j)}$ and $\varepsilon_{j(i)}$ are the central strains of automata i and j in pair $i-j$; $\gamma_{i(j)}$ and $\gamma_{j(i)}$ are the shear strains of automata i and j in the pair; G_i and K_i are the shear and bulk moduli of material filling the element i ; $\bar{\sigma}_{mean}^i = -P_i$ is the average stress in the bulk of automaton i ; $\sigma_{ij} = F_n^{ij}/S_{ij}$ and $\tau_{ij} = F_t^{ij}/S_{ij}$ are the relative values of central (F_n^{ij}) and tangential (F_t^{ij}) interaction forces.

Average stresses $\bar{\sigma}_{mean}^i$ in (5) are calculated in terms of the diagonal components of the average stress tensor in the volume of automata $\bar{\sigma}_{\alpha\beta}^i$. Components $\bar{\sigma}_{\alpha\beta}^i$ are calculated using forces of interaction of automaton i with surroundings [4-7]:

$$\bar{\sigma}_{\alpha\beta}^i = \frac{1}{\Omega_i} \sum_{j=1}^{N_i} S_{ij} q_{ij} (\vec{n}_{ij})_\alpha [\sigma_{ij} (\vec{n}_{ij})_\beta + \tau_{ij} (\vec{t}_{ij})_\beta], \quad (7)$$

where $\alpha, \beta = x, y, z$ (XYZ is the laboratory coordinate system), Ω_i is the automaton volume, $(\vec{n}_{ij})_\alpha$ and $(\vec{t}_{ij})_\alpha$ are the projection of the normal and tangential unit vectors in a pair on the axis of α of the laboratory coordinate system.

For the description of inelastic deformation of movable cellular automata theory of plastic flow with von Mises yield surface criterion is used [4-6]. Implementation of this theory carried out using the algorithm radial return algorithm of Wilkins [12]. In the framework of radial return algorithm the calculation of forces interautomaton interaction σ_{ij} и τ_{ij} at each time step of numerical integration of the equations of motion (1) is carried out in two stages. At the first step the current values of the interaction forces are calculated in the elastic approach (using equations (5) - (6)). At the end of this stage, the current value of the second invariant $\bar{\sigma}_{eq}^i$ of the average stress deviator $\bar{D}_{\alpha\beta}^i = \bar{\sigma}_{\alpha\beta}^i - 1/3 \bar{\sigma}_{kk}^i \delta_{\alpha\beta}$ ($\bar{\sigma}_{\alpha\beta}^i$ are calculated in accordance with (7), using the current values of σ_{ij} and τ_{ij}) is compared with a threshold value σ_{pl}^i , which is corresponds to a point on the limit surface. In the case of fulfillment of inequality $\bar{\sigma}_{eq}^i > \sigma_{pl}^i$ the calculated at elastic stage values of specific forces σ_{ij} and τ_{ij} are corrected:

$$\begin{cases} \sigma'_{ij} = (\sigma_{ij} - \bar{\sigma}_{mean}^i) M_i + \bar{\sigma}_{mean}^i \\ \tau'_{ij} = \tau_{ij} M_i \end{cases}, \quad (8)$$

where $M_i = \sigma_{pl}^i / \bar{\sigma}_{eq}^i$. Note that relation (8) provides reduction of average stresses $\bar{\sigma}_{\alpha\beta}^i$ in the

volume of movable cellular automaton to the desired point of the yield surface [4-6].

The rheological properties of the material of the movable cellular automaton i are determined by the defined curve $\bar{\sigma}_{eq}^i = \Phi(\bar{\epsilon}_{eq}^i)$, where $\bar{\epsilon}_{eq}^i$ is the second invariant of the average strain deviator in the volume of the automaton [4-6]. This formulation corresponds to the approximation that plasticity is independent on the strain rate and is correct for the interval of loading parameters used in numerical modeling of FSW.

The major advantage of the formalism of DEM is the possibility of a discrete element to change its surrounding. This allows to explicitly consider the processes of fracture and restoration of the chemical bonds between the fragments of material that are modeled by individual elements.

The fracture in the DEM is simulated by switching the state of the pair of interacting discrete elements from the chemically bound (linked) state to unlinked one. In unlinked pairs of discrete elements contact interaction is possible only, including force of resistance to compression and force of dry/viscous friction. Switching from a linked state to unlinked one is criterial. When modeling FSW process by MCA method the two-parameter fracture criterion of Drucker-Prager was used in the following form:

$$\sigma_{eq}^{ij} 0.5(a+1) + \sigma_{mean}^{ij} 1.5(a-1) = \sigma_c, \quad (9)$$

where σ_{eq}^{ij} and σ_{mean}^{ij} are invariants of stress tensor $\sigma_{\alpha'\beta'}^{ij}$ [4-6]; σ_c is compressive strength of pair $i-j$, $a = \sigma_c / \sigma_t$ is the ratio of compressive strength to tensile one.

Viscous character of fracture of plastic materials is taken into account by the introduction of the kinetics of bond breaking for pairs of automata, for which the condition $\sigma_{eq}^{ij} 0.5(a+1) + \sigma_{mean}^{ij} 1.5(a-1) > \sigma_c$ is satisfied. In this kinetic model is assumed that debonding in the pair of automata occurs gradually and is characterized by a decrease in linked portion of the interaction surface. The share of linked surface portion k_{link}^{ij} ($0 \leq k_{link}^{ij} \leq 1$) defines the current value of the surface area of interaction $S_{ij} = S_{ij}^0 k_{link}^{ij}$ (S_{ij}^0 is the surface area of the completely linked pair), which is used to calculate forces of interautomaton interaction and average stress tensor. Dynamics of changes of k_{link}^{ij} value is defined by the kinetic equation $dk_{link}^{ij} / d\epsilon_{eq}^{ij} = -f(\epsilon_{eq}^{ij}) < 0$. In the paper a function $f(\epsilon_{eq}^{ij}) = 1/\epsilon_{max}$ was used, where ϵ_{max} is input parameter of the model.

Simulation of formation or recovery chemical bond in unlinked (contact) pairs of movable cellular automata also is based on the use of criteria and the kinetic equation bond formation. In the paper the condition of achieving of the threshold (minimum) value of the compressive force in the pair was used as a criterion of bonding:

$$(-\sigma_{ij}) \geq \sigma_{link}^{\min}, \quad (10)$$

where σ_{link}^{\min} is input parameter of the model. If the condition (10) is satisfied, then the dynamics of the bonding is defined by the individual kinetic equation for k_{link}^{ij} . The work of plastic deformation ΔW_{ij} in the pair i and j at time step of numerical integration scheme is used as a parameter that determines the rate of the pair bonding:

$$\Delta k_{link}^{ij} = \frac{\Delta W_{ij}}{W_\sigma}, \quad (11)$$

where W_σ is the normalizing value, determined by the input parameters of the model and the current value of σ_{ij} :

$$W_\sigma = \frac{(-\sigma_{ij}) - \sigma_{link}^{\min}}{\sigma_{link}^{\max} - \sigma_{link}^{\min}} (W_{\sigma_{link}^{\min}} - W_{\sigma_{link}^{\max}}) + W_{\sigma_{link}^{\min}}. \quad (12)$$

Here $W_{\sigma_{link}^{\min}}$ is the total value of work of plastic deformation needed for complete bonding of the pair under the value of normal compression $(-\sigma_{ij}) = \sigma_{link}^{\min}$; $W_{\sigma_{link}^{\max}}$ is the total value of work of plastic deformation needed for complete bonding of the pair under the value of normal compression $(-\sigma_{ij}) = \sigma_{link}^{\max}$ (as a rule, $W_{\sigma_{link}^{\max}} < W_{\sigma_{link}^{\min}}$). Parameters σ_{link}^{\min} , σ_{link}^{\max} , $W_{\sigma_{link}^{\min}}$ and $W_{\sigma_{link}^{\max}}$ are the input parameters of the model ($\sigma_{link}^{\min} \leq \sigma_{link}^{\max}$ and $W_{\sigma_{link}^{\max}} \leq W_{\sigma_{link}^{\min}}$). Work of plastic deformation in pair $i-j$ per one time step is defined as the sum of works in automata i and j : $\Delta W_{ij} = \Delta W_i + \Delta W_j$ [4-6].

Relations (1)-(12) make it possible to carry out an adequate numerical simulation of complex processes of elastoplastic deformation, fracture and bonding of fragments of metals during FSW process at the mesoscopic and macroscopic scales.

3 PROBLEM STATEMENT

To study the dynamics of the FSW process a 2D computer model in the framework of MCA method. The motion of a rigid non-destructive rotating disk (the working body or tool) along the interface of two metal plates (Me1 and Me2 in Fig. 1a) was considered. Plate dimensions were 10×25 mm (Fig. 1a). As working body was used disk of diameter 3 mm. In the initial position the tool was set at a distance of 8 mm from the left side of the modeled system (Fig. 1a). This choice of the initial position of the tool is determined by the need to minimize the influence of the lateral surfaces (in particular, the reflection of the elastic waves) on the dynamics of the FSW process. The elastic characteristics and the diagram of uniaxial loading of material were used as the input parameters of movable cellular automata. They determine the response function of the movable cellular automata. The response function of cellular automata simulating welded plates, characterized by elastic-plastic loading diagram with a linear hardening (Fig. 1d), was obtained by fitting of the diagram of uniaxial tension macroscopic samples of duralumin alloy.

Three-step loading scheme was used in the paper. In the first stage the initial stress state of the system was set through its hydrostatic compression with forces F_x and F_y (Fig. 1a). The necessity of this step is caused by the fact that in the work is modeled relatively small fragment of real system. In real FSW process movement of the tool lead to a spreading of a large amount of elastic waves in the plane of joined plates and, as a result, to appearing of significant elastic strains. Within the framework of the model these stresses were simulated by setting of the initial pressure, the value of which does not exceed the 20% of the yield stress of duralumin alloy.

In the second stage lateral, top and bottom surfaces of the modeled system were fixed (Fig. 1b) and the system was kept until the establishment of the force equilibrium.

In the third step simulation of the FSW process was carried out by movement of the tool with translational velocity V_{trans} along the line of the plates joint (Fig. 1c) and its rotation around the disc center with the angular velocity ω (an instantaneous linear speed to the disk surface was $V_{rot}=\omega R$, where R is the radius of the disk).

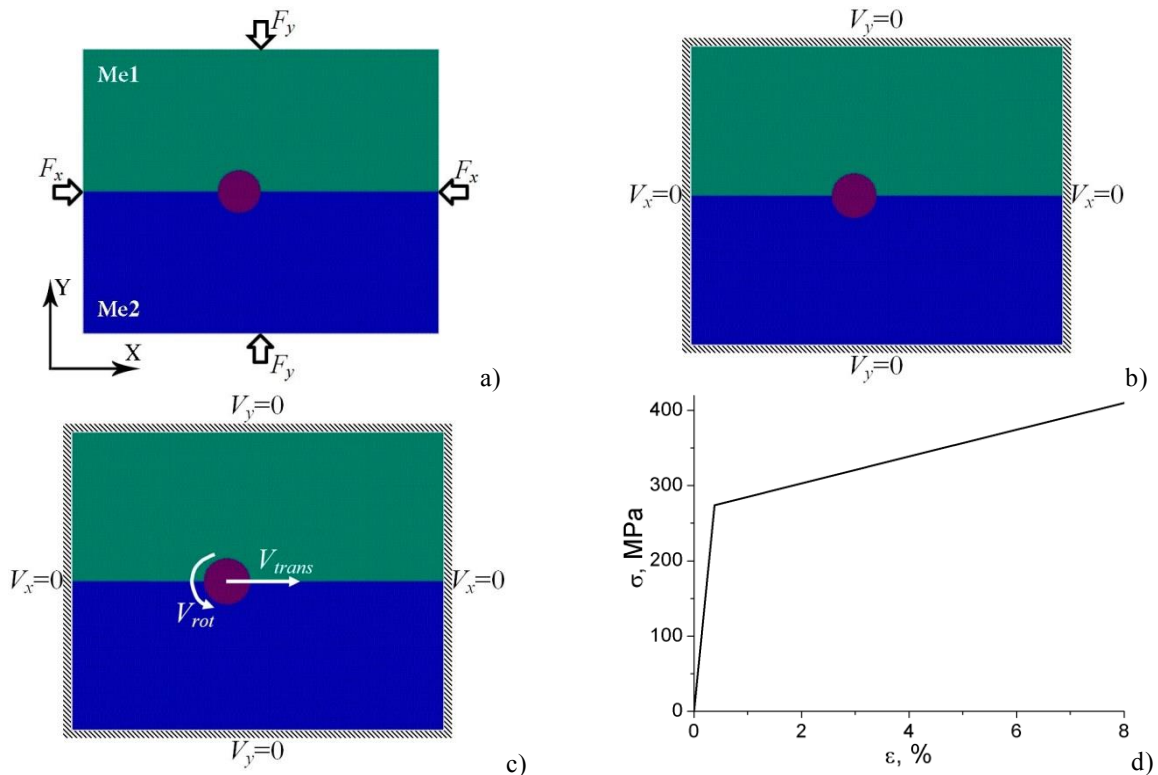


Figure 1: Loading scheme (a-c) and response function of duralumin plates (d).

4 RESULTS OF COMPUTER-AIDED SIMULATON

The dynamic of the FSW process was analyzed in the paper. In particular, the results of computer simulations show that at the beginning of the motion of the rotating tool occurs adhesion of duralumin alloy to the surface of working body, followed by separation of the

substance in the vicinity of the contact welded plates and tool and active mixing of detached fragments (Fig. 2b). The subsequent movement of the tool is accompanied by further mixing of materials of the plates and transfer of the mixed substance from the frontal area (in Fig. 2 region on the right of the rotating tool) to the backcourt (Fig. 2c). This process is accompanied by formation of a welded joint (Fig. 2d). It is seen in Fig. 2 d that the trace from the passing of the tool consists of at least two parts. Directly behind the tool is observed an area in which take place processes of mixing of the substance and which are characterized by relatively high porosity. At a distance of about 1/6 of the tool radius, starting the area in which the mixing processes are completed. This zone is characterized by a relatively uniform distribution of the materials Me1 and Me2. It should be noted that the resulting welded joint is characterized by a small asymmetry relative to the line of the plates conjugation. Thus the width of the seam in the area below the conjugation line is approximately 7% higher than in the upper region (Fig. 2d). This result is in good agreement the experimental data [3].

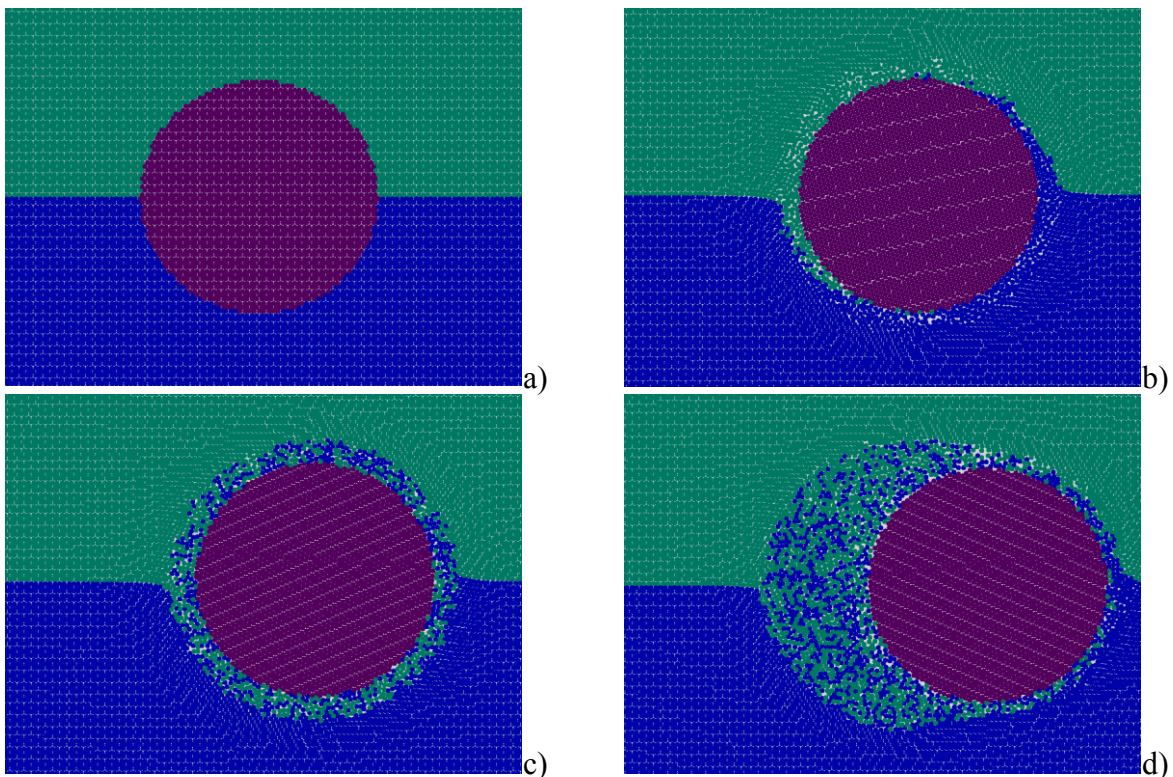


Figure 2: The structure of the material in the region of the rotating tool at various time points, $V_{trans}=0,2$ mps and $V_{rot}=7,6$ mps ($\omega=800$ Hz): a) – $t=0$ s; b) – $t=0,0004$ s; c) – $t=0,015$ s; d) – $t=0,07$ s.

Analysis of the results of computer simulation showed that the quality of the welded joint is determined, in particular, by its friability (porosity), uniform volume distribution of welding materials, etc., is largely determined by the regime of movement of the tool (the ratio of the instantaneous speed of rotation of the tool surface V_{rot} to translational velocity V_{trans}). Figure 3 shows the structures of the resulting welded joints for three different regimes of the

rotating tool movement. The figure shows that the decrease in V_{rot}/V_{trans} value (realized by increasing of the translational speed of the tool movement V_{trans}) leads to a decrease in the quality of welded joint. Thus, when $V_{rot}/V_{trans}=38$ ($V_{rot}=7,6$ mps, $V_{trans}=0,2$ mps, Fig. 3a), resulting welded joint is characterized by sufficiently low porosity (4.2 vol%, Table 1), a small amount of planar defects (microcracks) and relatively uniform volume distribution of Me1 and Me2 materials in the upper and lower parts of the joint (Fig. 4a).

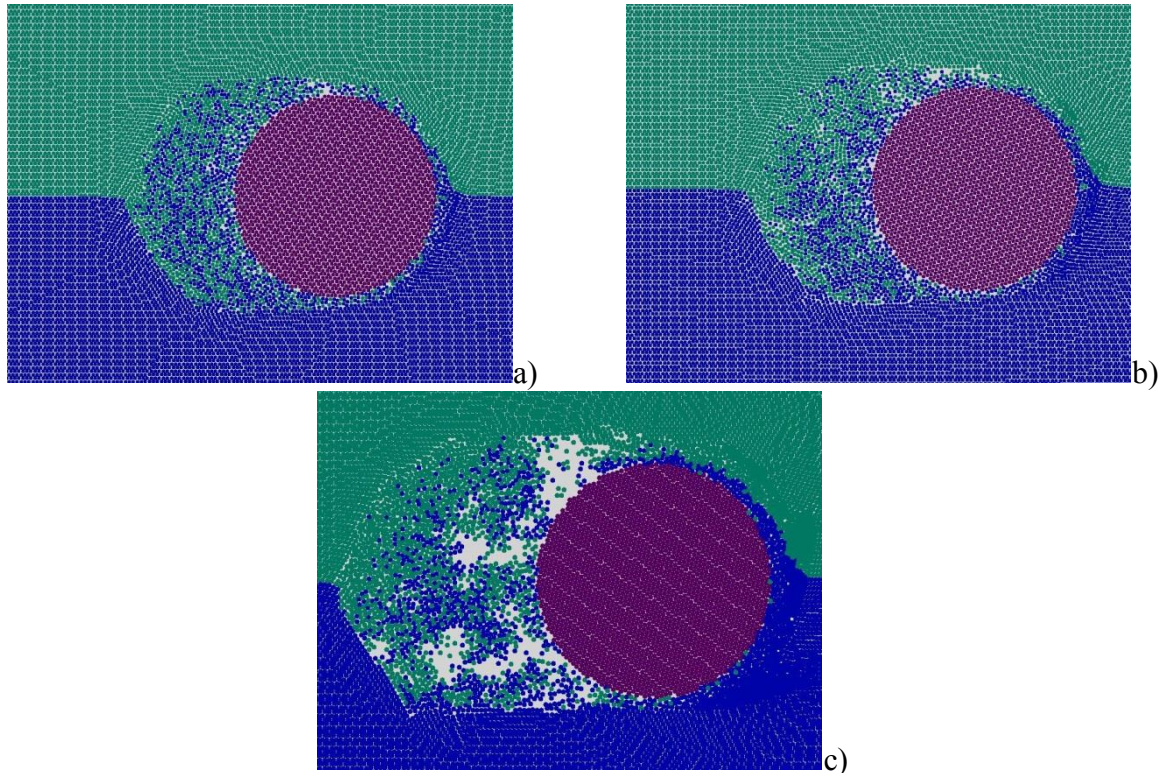


Figure 3: The structures of the resulting welded joint: a) - $V_{rot}=7,6$ mps ($\omega=800$ Hz) and $V_{trans}=0,2$ mps; b) - $V_{rot}=7,6$ mps ($\omega=800$ Hz) and $V_{trans}=0,4$ mps; c) - $V_{rot}=7,6$ mps ($\omega=800$ Hz) and $V_{trans}=0,8$ mps.

Table 1: The porosity in the welded joint depending on the regime of the tool movement.

No. of regime	V_{rot}/V_{trans}	Porosity, vol. %
1	38 ($V_{rot}=7,6$ mps; $V_{trans}=0,2$ mps)	4,2
2	19 ($V_{rot}=7,6$ mps; $V_{trans}=0,4$ mps)	6,5
3	9,5 ($V_{rot}=7,6$ mps; $V_{trans}=0,8$ mps)	23,4

Twofold decrease of the V_{rot}/V_{trans} value ($V_{rot}=7,6$ mps, $V_{trans}=0,4$ mps, Fig. 3b) leads to increase in porosity of the joint (more than 1.5-fold, Table 1) and to a rather uneven distribution of Me1 and Me2 materials in the upper and lower parts of the joint (Fig. 4b). In this case the seam itself (especially the lower part) contains sufficiently large number of relatively extended microcracks. The consequence of further reducing of the ratio V_{rot}/V_{trans} ($V_{rot}=7,6$ mps, $V_{trans}=0,8$ mps, Fig. 3c) is the loss of continuity of the joint. It could be seen

from Figure 3c that the seam can contain macropores and macro-cracks, even at a large distance from the rotating tool and the frontal area (in front of the working body) is characterized by a significant seal (jam) of the material. The value of porosity in the backcourt reaches about 23.4 % (Table 1).

Thus, the synchronization of speeds of rotation and translational motion of rotating tool is one of the essential conditions for obtaining welded joint with a low content of pores and microcracks and uniform volumetric distribution of the welded materials.

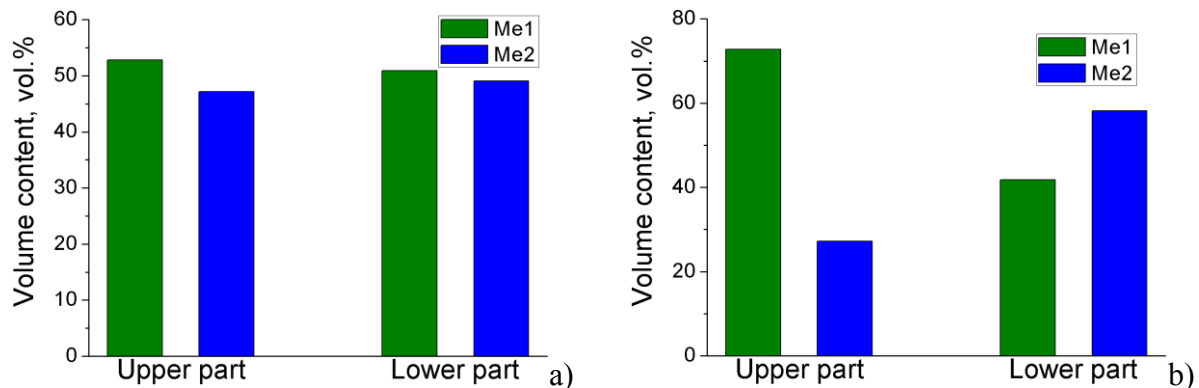


Figure 4: The distribution of the volume fractions of materials Me1 and Me2 in the upper and lower parts of the welded joint: a) - $V_{rot}=7,6$ mps ($\omega=800$ Hz) and $V_{trans}=0,2$ mps; b) - $V_{rot}=7,6$ mps ($\omega=800$ Hz) and $V_{trans}=0,4$ mps.

5 CONCLUSIONS

Thus, in the paper adaptation of movable cellular automata method for studying the dynamics of the process of friction stir welding with an explicit account of the processes of fracture and formation of new chemical bonds was performed. Using the developed approach the dynamics of the process of friction stir welding of plates of duralumin alloy was investigated. It was shown that synchronization of speeds of rotation and translational motion of rotating tool is one of the essential conditions for obtaining welded joint with a low content of pores and microcracks and uniform volumetric distribution of the welded materials.

This work was supported by the Russian Science Foundation (Grant 14-19-00718). E.A. Kolubaev and S.G. Psakhie acknowledge financial support from the RF Ministry of Education and Science (project ID RFMEFI57814X0045) on “Improving the technology of friction stir welding by ultrasonic treatment to form permanent connections of hardened aluminum alloy for aerospace and transport industry”

REFERENCES

- [1] Frolov, V.A., Ivanyukhin, A.N., Sabantsev, A.N. et. al Friction stir welding – pluses and minuses. *Welding International.* (2010) **24(5)**:358-365.
- [2] Sergeeva, E.V. Friction stir welding in aerospace industry (review). *The Paton Welding Journal.* (2013) **5**:56-60.
- [3] Kolubaev, E.A. Investigation of the microstructure of joints of aluminum alloys produced by friction stir welding. *Russian Physics Journal.* (2015) **57(10)**:1321-1327.

- [4] Psakhie, S., Shilko, E., Smolin, A. et al. Development of a formalism of movable cellular automaton method for numerical modeling of fracture of heterogeneous elastic-plastic materials. *Fract. Struct. Integrity* (2013) **24**:59-91.
- [5] Psakhie, S.G., Shilko, E.V., Grigoriev, A.S. et al. A mathematical model of particle-particle interaction for discrete element based modeling of deformation and fracture of heterogeneous elastic-plastic materials. *Eng. Fract. Mech.* (2014) **130**:96-115.
- [6] Shilko, E.V., Psakhie, S.G., Schmauder, S. et. al. Overcoming the limitations of distinct element method for multiscale modeling of materials with multimodal internal structure. *Comp. Mat. Sci.* (2015) **102**:267-285.
- [7] Psakhie, S., Ovcharenko, V., Baohai, Yu. et al. Influence of features of interphase boundaries on mechanical properties and fracture pattern in metal-ceramic composites. *J. Mater. Sci. Technol.* (2013) **29(11)**:1025-1034.
- [8] Mustoe, G.G.W. A generalized formulation of the discrete element method. *Eng. Comp.* (1992) **9**:181-190.
- [9] Bićanić, N. *Discrete element methods*. In: E. Stein, R. Borst, T.J.R. Hughes (Eds.), *Encyclopedia of computational mechanics*. Wiley, Chichester, Vol.1 (2004).
- [10] Daw, M.S., Baskes, M.I. Embedded atom method: Derivation and application to impurities, surfaces, and other defects in metals. *Phys. Rev.* (1984) **B29(12)**:6443-6453.
- [11] Rose, J.H., Smith, J.R., Guinea, F., Ferrante, J. Universal features of the equation of state of metals. *Phys. Rev.* (1984) **B29(6)**:2963-2969.
- [12] Wilkins, M.L. *Computer simulation of dynamic phenomena*, Springer-Verlag, (1999).

EFFECT OF BOUNDARY CONDITION APPLYING TYPE ON HEAT TRANSFER MODELING VIA DOUBLE SPECIES LATTICE BOLTZMANN METHOD

M. MOHAMMADI-AMIN^{1*}, M. BUSTANCHY²

¹ Aerospace Research Institute
Tehran 1465774111, Iran
mmohammadi@ari.ac.ir

² University of Tehran
Kish International Campus
Kish Island, Iran

Key words: Natural Convection, Thermal Lattice Boltzmann, Nusselt Number.

Abstract. The principle objective of the present study is to solve the velocity and temperature fields using two different distribution functions double species thermal lattice Boltzmann method (TLBM). The study is carried out for a wide range of Rayleigh numbers, velocity and temperature distributions as well as Nusselt numbers were obtained for the Rayleigh numbers ranging from 10^3 to 10^6 with the Prandtl number around 0.718 for air. In this simulation, the Boussinesq approximation applied to the buoyancy force term. Also we evaluate the order of derivatives' effect on the accuracy of macroscopic values. So, we applied this method for all of boundary condition types same as no slip, constant temperature and adiabatic walls in two different TLBM model and macroscopic states. We showed that boundary condition applying type has not any difference and based on computer code, we can use both of them with minimum term of derivatives. Results are presented in form of streamline and isothermal plots as well as the variation of average Nusselt number at the walls and domain and compared with commercial CFD softwares and other established methods referenced through literature. A good agreement is obtained between the current solution and the previous works and it shows that we can use double species TLBM with minimum terms of derivatives on a macroscopic and TLBM parameters in boundary conditions discretization. Results are in a good independency from the grids and size of mesh. Finally it is showed that we can solve the first rows and corners (the nodes on the body) of grid with macroscopic terms then continue for other lattices with TLBM to improve accuracy and save the time.

1 INTRODUCTION

For more than a decade, lattice Boltzmann method (LBM) has been demonstrated to be a very effective numerical tool for a broad variety of complex fluid flow phenomena that are problematic for conventional methods [1, 2]. Compared with traditional computational fluid dynamics, LBM algorithms are much easier to be implemented especially in complex geometries and multi component flows [1]. LBM is an ideal mesoscopic approach to solve nonlinear macroscopic conservation equations due to its simplicity and parallelization. For incompressible isothermal flows, the LBM is found to be at least as stable, accurate and computationally efficient, as traditional computational methods and has achieved excellent success in different application areas such as multiphase flow and complex fluid phenomena [3]. Natural convection in a porous enclosure with vertical partitioned walls at different temperatures is frequently encountered in many practical applications, such as insulation for buildings, industrial cold-storage installations, electronic cooling and heat exchangers [4].

Peng (2003), evaluated a 3-D incompressible thermal lattice Boltzmann model (TLBM) and its application to simulate natural convection in a cubic cavity by using two different particle velocity models of D3Q15 and D3Q19 in thermal models and compared results by Navier-Stokes solver [3]. Changqing et.al (2007) simulated a transient natural convection in square cavity with incompressible TLBM. They were shown that as Rayleigh number increase, the flow field gets more intensively [5]. Anilkumar and Jilani (2008) evaluated a natural convection heat transfer enhancement in a closed cavity with partition utilizing Nano-fluids. Their study was carried out numerically for a range of Rayleigh number (Ra), partition heights and aspect ratio in two dimensional for flow and temperature distributions [2]. Azwadi and Tanahashi (2008) presented relations for development of 2-D and 3-D double-population TLBM and investigated natural convection flows in a cubic cavity and 2-D porous plate Couette flow. They found a new lattice of four-velocity (2-D) and eight-velocity (3-D) models for internal energy density distribution function and developed this method for analyzing problems where the viscous and compressive heating effects were negligible [6]. The objective of this work is to investigate the effect of boundary condition applying type, macroscopic state and distribution functions, on heat transfer modeling via a lattice model.

2 GOVERNING EQUATIONS

In kinetic theory, the evolution of the single-particle density distribution function [$f(t, \vec{x}, \vec{c})$] which represents the probability density of a particle with unit mass moving with velocity \vec{c} at point \vec{x} at time t , is governed by the Boltzmann equation [7]:

$$\frac{\partial f}{\partial t} + \vec{c} \cdot \nabla f = \frac{\partial_e f}{\partial t} \quad (1)$$

where the term on the right hand side represents the collision operator. An approximation of this complicated operator is the so-called BGK or the single-relaxation time model [7].

The Boltzmann equation with the Bhatnagar-Gross-Krook (BGK), or single-relaxation-time approximation [6] with external force is given by

$$\frac{\partial f}{\partial t} + \vec{c} \cdot \nabla f = -\frac{1}{\tau_f} (f - f^{eq}) + F_f \quad (2)$$

where F_f is the external force and f^{eq} is the local Maxwell-Boltzmann equilibrium distribution function given by

$$f^{eq} = \rho \left(\frac{1}{2\pi RT} \right)^{\frac{D}{2}} \exp \left\{ -\frac{(c-u)^2}{2RT} \right\} \quad (3)$$

where R is the ideal gas constant, D is the dimension of the space, and ρ, \vec{u} , and T are the macroscopic density, velocity, and temperature respectively. The macroscopic variables ρ, \vec{u} , and T can be evaluated as the moment to the distribution function as follow

$$\rho = \int f d\vec{c} \quad (4)$$

$$\rho \vec{u} = \int \vec{c} f d\vec{c} \quad (5)$$

$$\frac{D\rho RT}{2} = \int \frac{1}{2} f (\vec{c} - \vec{u})^2 d\vec{c} \quad (6)$$

The pressure is determined by equation of state $P = \rho/3$ and the sound speed is $c_s = \sqrt{1/3}$. By applying Chapman-Enskog expansion [8], the above equations can lead to macroscopic continuity, momentum and energy equation. However the Prandtl number (Pr) obtained is fixed to a constant value [9]. This is caused by the use of single relaxation time in the collision process. The relaxation time of energy carried by the particles to its equilibrium is different to that of momentum. Therefore we need to use a different two relaxation times to characterize the momentum and energy transport. This is equivalent in introducing a new distribution function to define energy. To obtain the new distribution function modeling energy transport, the internal energy density distribution function is introduced as [6]

$$g = \frac{(c-u)^2}{DR} f \quad (7)$$

Substituting Eq. (7) into Eq. (2) results in

$$\frac{\partial g}{\partial t} + \vec{c} \frac{\partial g}{\partial x} = -\frac{1}{\tau_g} (g - g^{eq}) + F_g + f_q \quad (8)$$

where

$$g^{eq} = \frac{(c-u)^2}{DR} f^{eq} \quad (9)$$

$$F_g = \frac{(c-u)^2}{DR} F_f \quad (10)$$

Eq. (7) represents the internal energy carried by the particles and therefore Eq. (8) can be called as the evolution equation of internal energy density distribution function [6]. The macroscopic variables can thus be redefined in term of distribution function f and g as

$$\rho = \int f d\vec{c} \quad (11)$$

$$\rho \vec{u} = \int \vec{c} f d\vec{c} \quad (12)$$

$$\rho T = \int g d\vec{c} \quad (13)$$

where a new relaxation time τ_c is introduced for simplifying the collision term, and the local equilibrium distribution function is defined by Eq. (8). We have recently shown that in the limit of incompressibility ($Ma \ll 1.0$) and for the cases when the compression work and viscous heat dissipation are negligibly small, Eq. (8) can be simplified to [7]

$$\frac{\partial g}{\partial t} + \vec{c} \cdot \nabla g = -\frac{1}{\tau_g} (g - g^{eq}) \quad (14)$$

The kinetic viscosity (ϑ) is related to the relaxation time through the same equation of

$$\vartheta = \frac{2\tau_f - 1}{6} \quad (15)$$

and the thermal diffusivity (α) is given by [7]

$$\alpha = \tau_g RT \quad (16)$$

The macroscopic quantities such as density, velocity and temperature are then obtained through moment integrations of distribution function. We have also shown that the macroscopic conservation equations of mass, momentum, and energy can be recovered from the Boltzmann BGK equations (2) and (14) through the Chapman-Enskog expansion [7].

3 DISCRETIZATION METHOD

In order to apply the lattice Boltzmann scheme into the digital computer, we need to discretize the evolution equation of the continuous lattice Boltzmann BGK equation for the momentum and energy. Expanding both of the equilibrium distribution function up to u^2 results in

$$f^{eq} = \rho \left(\frac{1}{2\pi RT} \right)^{\frac{1}{2}} \exp \left\{ -\frac{c^2}{2RT} \right\} \left[1 + \frac{\vec{c} \cdot \vec{u}}{RT} + \frac{(\vec{c} \cdot \vec{u})^2}{2(RT)^2} - \frac{u^2}{2RT} \right] \quad (17)$$

$$g^{eq} = \rho T \left(\frac{1}{2\pi RT} \right)^{\frac{1}{2}} \exp \left\{ -\frac{c^2}{2RT} \right\} \left[1 + \frac{\vec{c} \cdot \vec{u}}{RT} \right] \quad (18)$$

The equations are discretized by energy method, reported in literature. The D2Q9 lattice for 2-D density and internal energy distribution function is shown in Fig.1 [6].

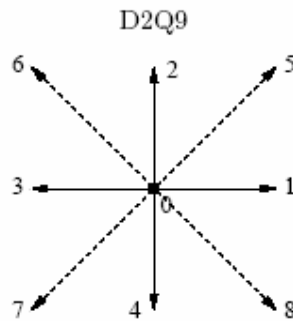


Figure 1: D2Q9 Lattice structure with nine velocities for 2-D distribution function

Eq. (18) is obtained by assuming that at low Mach number flow (incompressible flow), the higher order of $O(u^2)$ and viscous heat dissipation can be neglected [6]. For the two dimensional case, the resultant discrete velocity and thermal equations are given by [7]

$$\frac{\partial f_i}{\partial t} + \vec{c}_i \cdot \nabla f_i = -\frac{1}{\tau_f} (f_i - f_i^{eq}) \quad (19)$$

$$\frac{\partial g_i}{\partial t} + \vec{c}_i \cdot \nabla g_i = -\frac{1}{\tau_g} (g_i - g_i^{eq}) \quad (20)$$

where $f_i = f(t, \vec{x}, \vec{c}_i)$, $g_i = g(t, \vec{x}, \vec{c}_i)$ and the discrete velocities are given by [10]

$$\vec{c}_i = \begin{cases} (0,0) & i = 0 \\ c \left(\cos \left[\frac{\pi(i-1)}{2} \right], \sin \left[\frac{\pi(i-1)}{2} \right] \right) & i = 1, 2, 3, 4 \\ \sqrt{2}c \left(\cos \left[\frac{\pi(2i-9)}{4} \right], \sin \left[\frac{\pi(2i-9)}{4} \right] \right) & i = 5, 6, 7, 8 \end{cases} \quad (21)$$

with $c = \sqrt{3RT}$. The corresponding discrete equilibrium distribution function, f_i^{eq} , can be obtained from Eq. (3) by performing a Taylor expansion up to \vec{u}^2 as follows

$$f_i^{eq} = w_i \rho \left[1 + \frac{\vec{c} \cdot \vec{u}}{c_s^2} + \frac{(\vec{c} \cdot \vec{u})^2}{2c_s^4} - \frac{u^2}{2c_s^2} \right] \quad (22)$$

where $c_s = \sqrt{RT}$ is the sound speed and $w_0 = \frac{4}{9}$, $w_i = \frac{1}{9}$ for $i = 1 - 4$ and $w_i = \frac{1}{36}$ for $i = 5 - 8$. Apparently, a comparison between Eq. (17), Eq. (18) and Eq. (22) lead to

$$g_i^{eq} = T f_i^{eq} \quad (23)$$

and by neglecting the term $O(u^2)$

$$g_i^{eq} = w_i T \left[1 + \frac{\vec{c} \cdot \vec{u}}{c_s^2} \right] \quad (24)$$

The macroscopic variables are now defined by [7]

$$\rho = \sum_{i=0}^8 f_i \quad (25)$$

$$\rho \vec{u} = \sum_{i=0}^8 f_i \vec{c}_i \quad (26)$$

$$T = \sum_{i=0}^8 g_i \quad (27)$$

As a result, the discrete velocity Boltzmann BGK Eq. (19) and (20) recover the continuity equation, momentum conservation equation and the following temperature equation [7]

$$\partial T / \partial t + \vec{u} \cdot \nabla T = \nabla \cdot (\alpha \nabla T) \quad (28)$$

where the thermal diffusivity is $\alpha = \tau_g RT$.

4 SPECIFICATION OF THE PROBLEM

In this study, we solve the velocity and temperature fields using two different distribution functions TLBM for two natural convection heat transfer problems, constant temperature on the walls and adiabatic walls.

The study is carried out numerically for a range of Rayleigh numbers. The governing Eq. (1) to Eq. (8) were discretized and simplified resulting in a system of algebraic equations.

In first case, we evaluate the different models for application of boundary conditions in natural convection phenomena in square cavity.

The thermal conditions applied on the bottom wall is $T_h = 1.0$, top wall is $T_c = 0.0$ and partitioned wall is $T_p = 0.0$. The other faces being adiabatic, $\frac{\partial T}{\partial n} = 0$, where $\frac{\partial T}{\partial n}$ is the appropriate normal derivative. The temperature difference between the left and right walls introduces a temperature gradient in a fluid, and the consequent density difference induces a fluid motion, that is, convection. In the simulation, the Boussinesq approximation is applied to the buoyancy force term.

$$\rho \vec{G} = \rho \beta g_0(T - T_m) \vec{j} \quad (29)$$

where Boussinesq approximation is given by

$$\beta = -\frac{1}{\rho} \left(\frac{\partial \rho}{\partial T} \right)_P \quad (30)$$

and β is the thermal expansion coefficient, g_0 is the acceleration due to gravity, T_m is the average temperature and j is the vertical direction opposite to that gravity [6].

The dynamical similarity depends on two dimensionless parameters: the Prandtl number, Pr and the Rayleigh number, Ra defined as,

$$Pr = \frac{\vartheta}{\alpha} \quad (31)$$

$$Ra_L = \frac{\beta g_0 (T_h - T_c) L^3}{\vartheta \alpha} \quad (32)$$

The Nusselt number (Nu) is one of the most important dimensionless numbers in describing the convective transport. The Nu are averaged and evaluated along the length of cavity which may be expressed as

$$\overline{Nu} = \frac{\bar{h}L}{k_f} = f(Re_L, Pr) \quad (33)$$

Also about applying of boundary conditions on walls in macroscopic state:

$$\frac{\partial T}{\partial x} = 0 \begin{cases} T(i, j) = T(i + 1, j) \\ T(i, j) = \frac{1}{3}[4T(i + 1, j) - T(i + 2, j)] \end{cases} \quad (34)$$

and when we want to apply them on distribution functions (Appendix I):

$$\frac{\partial T}{\partial x} = 0 \begin{cases} g(i, j, k) = T(i + 1, j, k) & k = 0, 1, 2, \dots, 9 \\ g(i, j, k) = \frac{1}{3}[4g(i + 1, j, k) - g(i + 2, j, k)] & k = 0, 1, 2, \dots, 9 \end{cases} \quad (35)$$

where in all simulations $\text{Pr} = 0.718$, grid sizes are 50×50 , 100×100 , 150×150 for $\text{AR}=1$, 100×50 , 200×100 , 300×150 for $\text{AR}=2$ and the fluid in a partitioned cavity is air for $\text{Ra} = 10^3 - 10^6$.

Wall boundary conditions are used at the all walls of the partitioned cavity, and the non-equilibrium bounce back boundary conditions for velocity. The means of this term is $u = 0.0$ in x direction and $v = 0$ in y direction for all partitioned cavity walls. The bounce-back rule of the non-equilibrium distribution function proposed by Zou and He [14] is used for implementing the boundary condition.

For viscous flows bounce back boundary condition is employed which is equivalent to no slip condition. This boundary condition is employed on wall nodes. Here in the algorithm for performing the bounce-back step for D2Q9 Lattice structure:

$$\begin{aligned} f_0 &= f_0 \\ f_1 &= f_3, f_2 = f_4 \\ f_5 &= f_7, f_6 = f_8 \end{aligned}$$

The thermal conditions applied on the bottom wall is $T_h = 1.0$, top wall is $T_c = 0.0$ and partitioned wall is $T_p = 0.0$. The other faces being adiabatic, $\frac{\partial T}{\partial n} = 0$, where $\frac{\partial T}{\partial n}$ is the appropriate normal derivative. H is a height of cavity, W is a length of cavity, h is a height of partition in the cavity, C is a partition position and $\frac{W}{H}$ means by aspect ratio of the cavity.

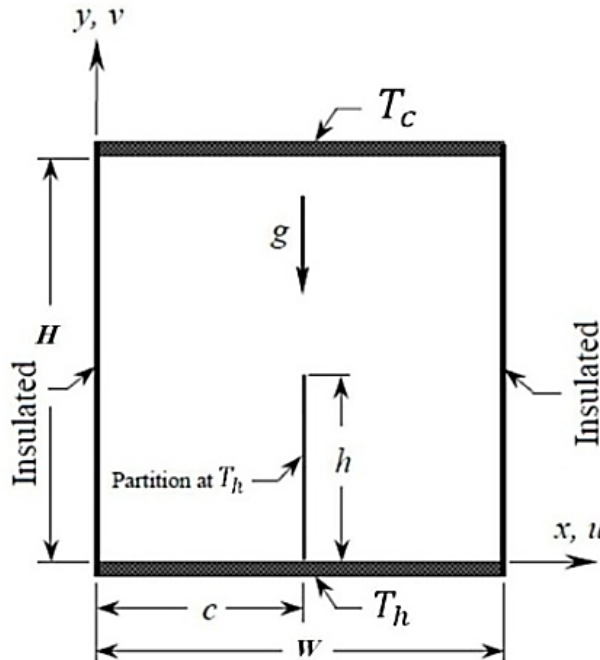


Figure 2: Schematic for the physical model function

5 RESULTS AND DISCUSSION

The considered problem is natural convection in a 2D square cavity and enclosure with two horizontal side walls maintained at different temperatures. The temperature difference between the walls introduces a temperature gradient in the fluid, and the consequent density difference induces fluid motion. The remaining walls are adiabatic. The problem definition and the boundary conditions are displayed in Fig. 2.

The non-dimensional heat transfer rate at the isothermal walls is a very important parameter in many engineering applications, such as electronic cooling, transportation, the environment and national security [2]. Numerical simulations of the natural convection in a partition cavity with $AR = 2$ at Rayleigh numbers from 10^3 to 10^6 are carried out using the two dimensional particle velocity model of D2Q9.

5.1 Isotherms and Streamlines

The streamlines and isothermal contours in the cavity with $AR = 2$ for $C = \frac{W}{5}$ and $\frac{h}{H} = 0.5$ are shown in Figs. 3 and 4 for different Rayleigh numbers from 2×10^4 to 10^6 and 100x50 uniform mesh cells. In this figures, the effects of Rayleigh numbers in the flow patterns and isothermals are investigated.

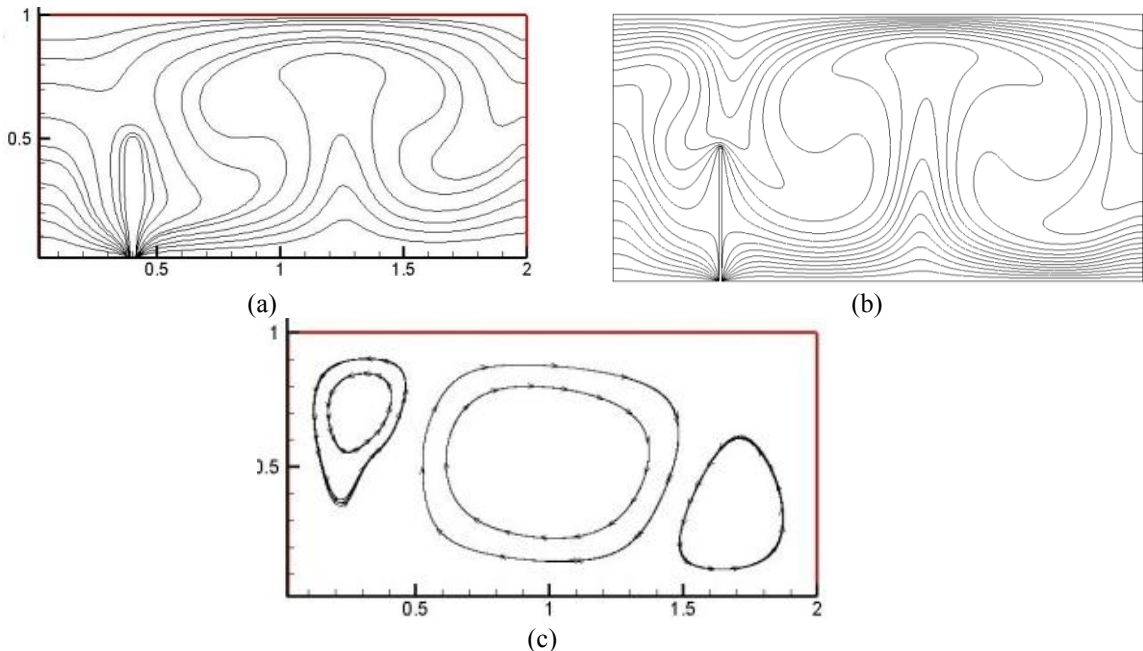


Figure 3: Isotherms with TLBM (a), Isotherms with CFX (b) and Streamlines with TLBM (c) for $Ra = 2 \times 10^4$, $AR = 2$, $C = \frac{W}{5}$, $\frac{h}{H} = 0.5$ and 100x50 uniform mesh cells

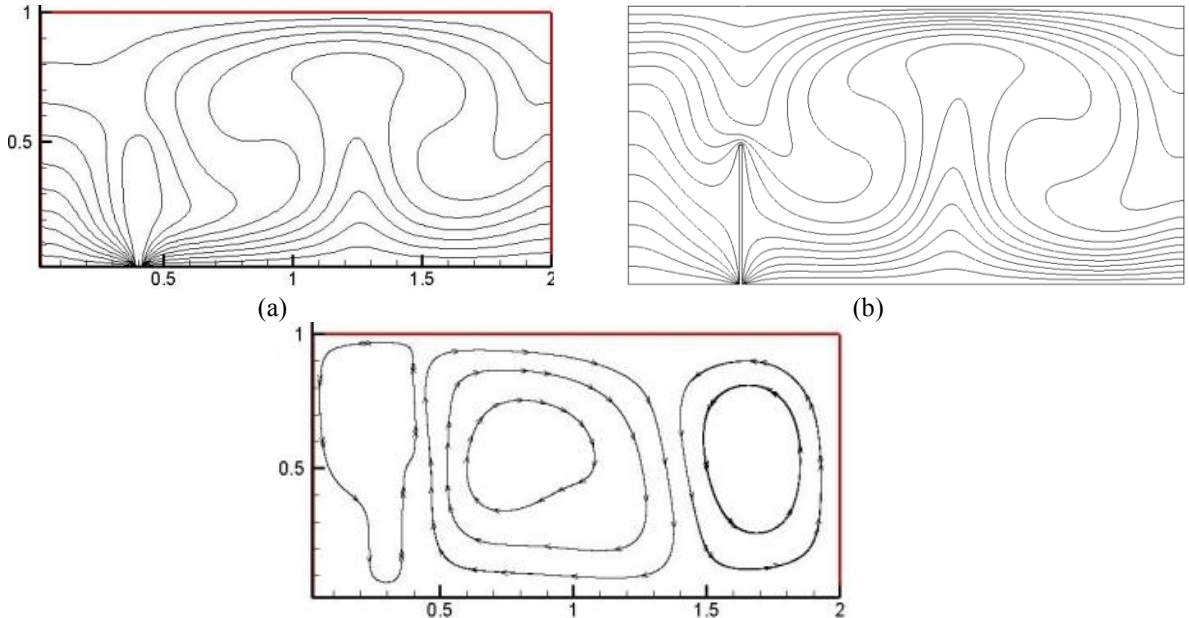


Figure 4: Isotherms with TLBM (a), Isotherms with CFX (b) and Streamlines with TLBM (c) for $Ra = 10^6$, $AR = 2, C = \frac{w}{5}, \frac{h}{H} = 0.5$ and 100x50 uniform mesh cells

Table 1 shows the macroscopic values on the partitioned cavity at $Ra = 2 \times 10^4$, $AR = 2, C = \frac{w}{5}, \frac{h}{H} = 0.5$ and 100x50 uniform mesh cells using D2Q9 lattice structure when we apply boundary conditions on thermal distribution function (method No.1) and macroscopic temperature directly (method No.2).

Table 1: Properties of some nodes for $Ra = 2 \times 10^4$, $AR = 2, C = \frac{w}{5}, \frac{h}{H} = 0.5$ and 100x50 uniform mesh

x	y	u	v	ρ	T (method 1)	T (method 2)
0.056	0.0522	0.0012	0.0007	1.0361	0.8104	0.8406
0.344	0.0488	0.0013	0.0004	1.0352	0.6084	0.6084
0.081	0.9350	0.0009	0.0006	0.9833	0.0045	0.0045
0.441	0.3190	0.0005	0.0008	1.0034	0.0331	0.0331
0.715	0.6030	0.0121	0.0270	0.9915	0.3864	0.3864
1.206	0.3770	0.0011	0.0001	1.0017	0.0936	0.0936
1.777	0.4820	0.0088	0.0513	0.9963	0.3138	0.3138

The streamlines in Figs. 3 and 4 show as Ra increases, the flow rate toward partitioned enclosure increases. The agreement of numerical results of isotherms and streamlines between TLBM and international previous literature is very good [2, 10].

For small Ra cases, the fluid motion driven by the buoyancy force is very slow, leading to rather weak natural convection in the enclosure. On the other hand, when Ra number increase, the buoyancy force accelerates the fluid flow and natural convection is significantly enhanced. This behavior is clearly similar to the related flow pattern in all ranges of Ra and buoyancy parameter. The above discussed behaviors are also found in the previous experimental and numerical studies [2, 6].

5.2 Grid-Independency of the Results

In order to see the influence of the grid size on the \overline{Nu} at the isothermal walls, the numerical simulations for $Ra = 2 \times 10^4$ using D2Q9 are carried out on three different grid sizes for all models in the following section, 50x50, 100x100 and 150x150 for portioned cavity with $AR = 1$, $c = \frac{W}{2}, \frac{h}{H} = 0.5$ and 100x50, 200x100 and 300x150 for portioned cavity with $AR = 2$, $c = \frac{W}{2}, \frac{h}{H} = 0.5$. Tables 2 and 3 show the values of Average Nusselt number (\overline{Nu}) are independent from the number of mesh cells.

Table 2: Ave. Nusselt number values for partitioned cavity with $Ra = 2 \times 10^4$, $AR = 2$, $C = \frac{W}{2}, \frac{h}{H} = 0.5$.

Grid	50x50	100x100	150x150
\overline{Nu}	1.091	1.085	1.087

Table 3: Ave. Nusselt number values for partitioned cavity with $Ra = 2 \times 10^4$, $AR = 2$, $C = \frac{W}{2}, \frac{h}{H} = 0.5$.

Grid	100x50	200x100	300x150
\overline{Nu}	1.005	1.006	1.005

5.3 Comparison of Average Nusselt Number

The Nu obtained in this work, the previous experimental data [11] and the previous numerical results are compared [2, 12, 13] are compared in Table 4. It is seen that the numerical results obtained by the present TLBM agree well with those reported in the previous studies for different Ra numbers mentioned here.

Table 4: Comparison of the average Nusselt number at the isothermal walls between TLBM and previous works partitioned cavity with $AR = 1$, $C = \frac{W}{2}, \frac{h}{H} = 0.5$ and 50x50 uniform mesh cells

	Present study	Anilkumar [2]	Barakos [11]	Devahl Davis [12]	Fusegi [13]
($Ra = 10^3$) \overline{Nu}	1.091	1.152	1.114	1.118	1.105
($Ra = 10^5$) \overline{Nu}	4.204	4.636	4.51	4.519	4.646
($Ra = 10^6$) \overline{Nu}	8.526	9.241	8.806	8.799	9.012

Table 5: Average Nusselt number at the isothermal walls for partitioned cavity with $AR = 2$, $C = \frac{W}{2}, \frac{h}{H} = 0.5$ and 100x50 uniform mesh cells

	Present study
($Ra = 10^3$) \overline{Nu}	1.0004
($Ra = 10^5$) \overline{Nu}	2.0040
($Ra = 10^6$) \overline{Nu}	2.8240

From the results presented above, we can say that as the Ra number increase, the \overline{Nu} at the isothermal walls of partitioned cavity increase. It is shown that the \overline{Nu} at the isothermal walls is increased as the aspect ratio decreased. The numerical results agree well with other results reported in the previous studies [2].

6 CONCLUSIONS

A two dimensional incompressible TLBM using D2Q9 lattice structure was proposed in this work. The study was carried out numerically for a range of Rayleigh numbers, partition heights and aspect ratio of the cavity. The numerical results of this model for simulation of 2D natural convection heat transfer of air in a partitioned cavity with different aspect ratio compared well with those from previous works. We have shown that based on computer codes and mixed program (i.e. TLBM with another methods), we can use both of types of applying the boundary conditions with minimum term of derivatives that reported in similar works. Also the results showed that as the Ra number increase, \overline{Nu} at the isothermal walls of cavity increased and \overline{Nu} at the isothermal walls is increased as the aspect ratio decreased.

APPENDIX I

$$\frac{\partial T}{\partial x} = 0 \quad \left\{ \begin{array}{lll} g(i,j,0) = g(i+1,j,0) & or & g(i,j,0) = \frac{1}{3}[4g(i+1,j,0) - g(i+2,j,0)] \\ g(i,j,1) = g(i+1,j,1) & or & g(i,j,1) = \frac{1}{3}[4g(i+1,j,1) - g(i+2,j,1)] \\ g(i,j,2) = g(i+1,j,2) & or & g(i,j,2) = \frac{1}{3}[4g(i+1,j,2) - g(i+2,j,2)] \\ g(i,j,3) = g(i+1,j,3) & or & g(i,j,3) = \frac{1}{3}[4g(i+1,j,3) - g(i+2,j,3)] \\ g(i,j,4) = g(i+1,j,4) & or & g(i,j,4) = \frac{1}{3}[4g(i+1,j,4) - g(i+2,j,4)] \\ g(i,j,5) = g(i+1,j,5) & or & g(i,j,5) = \frac{1}{3}[4g(i+1,j,5) - g(i+2,j,5)] \\ g(i,j,6) = g(i+1,j,6) & or & g(i,j,6) = \frac{1}{3}[4g(i+1,j,6) - g(i+2,j,6)] \\ g(i,j,7) = g(i+1,j,7) & or & g(i,j,7) = \frac{1}{3}[4g(i+1,j,7) - g(i+2,j,7)] \\ g(i,j,8) = g(i+1,j,8) & or & g(i,j,8) = \frac{1}{3}[4g(i+1,j,8) - g(i+2,j,8)] \end{array} \right.$$

REFERENCES

- [1] C. S. Nor Azwadi and A.R.M. Rosdzimin, Simulation of natural convection heat transfer in an enclosure using lattice Boltzmann method, Jurnal Mekanikal, 2008, No. 27, 42 - 50.
- [2] S. H. Anilkumar and G. Jilani, Natural convection heat transfer enhancement in a closed cavity with partition utilizing Nano fluids, Proceedings of the World Congress on Engineering 2008 Vol II, WCE 2008, July 2 - 4, 2008, London, U.K.

- [3] Y. Peng, C. Shu and Y.T. Chew, A 3D incompressible thermal lattice Boltzmann model and its application to simulate natural convection in a Cubic Cavity, Journal of Computational Physics 193 (2003) 260–274.
- [4] Z. Guo and T.S. Zhao, Lattice Boltzmann simulation of natural convection with temperature-dependent viscosity in a porous cavity, Progress in Computational Fluid Dynamics, Vol. 5, Nos. 1/2, 2005.
- [5] T. changing, H Yaling, W. Yong and L. Yingwen, Simulation of transient natural convection in square cavity with incompressible thermal lattice-Boltzmann method, JOURNAL OF XI'AN JIAATONG UNIVERSITY, vol.41 No.1, Jan 2007.
- [6] C. S. Nor Azwadi and T. Tanahashi, Development of 2-D and 3-D double-population thermal lattice Boltzmann models, MATEMATIKA, 2008, Volume 24, Number 1, 53-66.
- [7] Y. Shi, T.S. Zhao and Z.L. Guo, Finite difference-based lattice Boltzmann simulation of natural convection heat transfer in a horizontal concentric annulus, Computers & Fluids 35 (2006) 1–15.
- [8] S. Harris, Holt, Rinehart and Winston, An introduction to the theory of the Boltzmann equation, Holt, Rinehart and Winston, New York, 1971.
- [9] C. Cercignani, The Boltzmann equations and its application, in Applied Mathematical Sciences, Springer-Verlag, New York, 1988.
- [10] Y. H. Zhang, X. Jun, R. W. Barber and D. R. Emerson, A thermal lattice Boltzmann Model for Low speed rarefied gas flow, Council for the Central Laboratory of the Research Councils, DL-TR-2006-002.
- [11] G. Barakos and E. Mitsoulis, Natural convection flow in a square cavity revisited: laminar and turbulent models with wall functions, Int. J. Numer. Methods Fluids, vol.18, 1994, pp.695-719.
- [12]. G. De. Vahl Davis, Natural convection of air in a square cavity: a bench mark numerical solution, Int. J. Numer. Methods Fluids, vol.3, 1983, pp.249-264.
- [13] T. Fusegi, J.M. Hyuna, K. Kuwahara and B. Farouk, A numerical study of 3D natural convection in a differentially heated cubical enclosure, Int.J.HMT, vol.34, 1991, pp.1543-1557.

EFFECTS OF THE MPM DISCRETISATIONS ON SOIL-STRUCTURE PROBLEMS

S. FATEMIZADEH¹, F. HAMAD² AND C. MOORMANN³

¹University of Stuttgart
Institute of Geotechnical Engineering (IGS)
Pfaffenwaldring 35, 70569 Stuttgart, Germany
e-mail: farzad.fatemizadeh@igs.uni-stuttgart.de, URL: <http://www.uni-stuttgart.de/igs/>

² University of Stuttgart
Institute of Geotechnical Engineering (IGS)
Pfaffenwaldring 35, 70569 Stuttgart, Germany
e-mail: fursan.hamad@igs.uni-stuttgart.de, URL: <http://www.uni-stuttgart.de/igs/>

³ University of Stuttgart
Institute of Geotechnical Engineering (IGS)
Pfaffenwaldring 35, 70569 Stuttgart, Germany
e-mail: christian.moormann@igs.uni-stuttgart.de, URL: <http://www.uni-stuttgart.de/igs/>

Key words: Large deformation, MPM discretisations, Strip footing.

Abstract. Material point method (MPM) is a mesh based particle method which is suitable to simulate applications with large deformations. MPM adopts two discretisations, one is the space discretisation where the equation of motion is solved, and the other is the material discretisation where the continuum is replaced by material points or particles. Particles are allowed to move through the background computational mesh, which allows MPM to simulate large displacements and deformations of the material [9].

The effect of the spatial discretisation on the simulation results have been studied by others e.g. [1] considering a specific application like bending of a cantilevered beam. More generally, the sensitivity of the MPM solution to the two discretisations specially when dealing with bench mark problems in the field of geotechnical engineering has not been considered so far, although the method is applied widely in this area e.g. [2,13].

In this paper, the well-known problem in the field of geotechnical engineering is analyzed using MPM. In the case of available reference solutions the results are then evaluated. The effects of the two MPM discretisations on the quality of the final results have been investigated where some concluding remarks are presented.

1 INTRODUCTION

Since the formulation of Finite Element Method (FEM) is introduced, it has been used in different fields of engineering especially geotechnical engineering. This method has been shown its capabilities to simulate different phenomena. Considering applications include large deformations or displacements, FEM is not able to predict the behaviour of the continuum and suffers from the mesh distortion. During the simulation the mesh becomes so distorted which

causes numerical difficulties. In the field of geotechnical engineering, large deformations of the soil become evident in many applications e.g. sliding of slopes, failure of strip footing, pile driving, etc. which require other numerical schemes for simulating and studying them.

Available numerical methods for simulating large deformations can be categorized into three major groups. In the first group, the methods use the advantages of the both Lagrangian and Eulerian descriptions of motion while avoiding their drawbacks. The Arbitrary Lagrangian Eulerian (ALE) method [3] and the Coupled Eulerian Lagrangian (CEL) method [4] are categorized in this group. Second group includes the mesh free methods like the Element Free Galerkin (EFG) method [5] and the Smooth Particle Hydrodynamic (SPH) method [6]. The last group contains the mesh based particle methods. The Particle in Cell (PIC) method [7], Fluid Implicit Particle (FLIP) method [8] and the Material Point Method (MPM) [9,10] are recognized in this group.

MPM discretises the continuum using the material points or particles and discretises the space using an Eulerian background fixed mesh on which the equations of motion are solved. This mesh should cover the whole space where the material may go during the simulation process. Material points are the integration points which can move during the simulation. Using this property, MPM is able to analyze large deformations where particles carry all the permanent information (e.g. stresses, strain, etc.) during the simulation process and no permanent data are stored on the mesh.

Solution procedure of MPM for one time step consists of three phases. First is the initialization phase where all the data are mapped from particles to the nodes of the background mesh. Then is the Lagrangian phase in which the equations of motion are solved on the mesh. At the end is the convective phase in which information are mapped back from the mesh to the material points and updates the data of the particles. The background mesh goes back to its original position (as shown in Figure 1).

Sulsky et al. [9] applied the PIC method from fluid to solid mechanics and called it the material point method [10]. Bardenhagen et al. [11] introduced a frictional contact algorithm to the method based on the Coulomb friction law. Bardenhagen and Kober [12] presented the Generalized Interpolation Material Point Method (GIMP) to avoid the grid crossing error presented in the framework of original MPM. As MPM showed its capability to simulate the dynamics of large deformation, the method is adopted to investigate many applications in the field of geotechnical engineering [2,13].

The two discretisations in MPM (space discretization and the material discretization) play important role in the quality of the final results. The effects of the interpolation order of discretisation for a cantilevered beam is studied by Anderson and Anderson [1]. They showed that the best results for the small strain problems can be obtained using the quadratic shape functions whereas the cubic splines show better results for the large strain cases. The size of the mesh as well as the number of particles per element can also affect the simulation results.

In this paper the effects of the two discretisations on the strip footing problem are studied. For the sake of completeness, a short description on the governing equations of MPM are discussed then the enhanced volumetric strain method to overcome the volumetric locking that happens in low order elements are briefly explained [2,15]. Next the strip footing problem is analyzed using different combinations of the meshes. At the end of this paper, some conclusion remarks are presented.

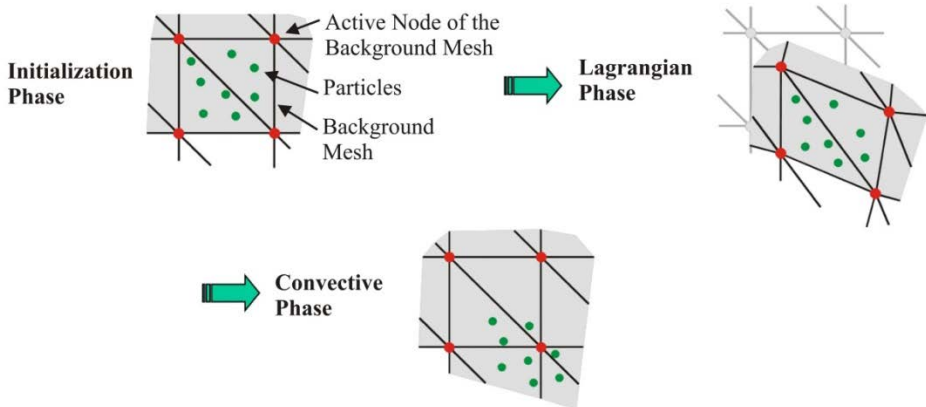


Figure 1: MPM discretisations and the solution procedure for one time step

2 GOVERNING EQUATIONS

The starting point is the Cauchy form of the conservation of linear momentum

$$\rho \ddot{\mathbf{u}} = \nabla \cdot \boldsymbol{\sigma} + \rho \mathbf{g} \quad \text{and} \quad \mathbf{t} = \boldsymbol{\sigma} \cdot \mathbf{n} \quad (1)$$

where ρ is the material density, \mathbf{u} is the displacement, a superposed dot declares differentiation with respect to time, $\boldsymbol{\sigma}$ is the Cauchy stress tensor and \mathbf{g} is the gravitational acceleration vector. The surface traction acting on the external boundary is denoted by \mathbf{t} and \mathbf{n} is the outward unit normal of the boundary. Applying the virtual work principle on a domain of volume V surrounded by boundary S yields

$$\int_V w \mathbf{u}^T \rho \ddot{\mathbf{u}} dV = - \int_V w \boldsymbol{\epsilon}^T \boldsymbol{\sigma} dV + \int_V w \mathbf{u}^T \rho \mathbf{g} dV + \int_S w \mathbf{u}^T \mathbf{t} dS \quad (2)$$

where w denotes a virtual quantity, $\boldsymbol{\epsilon}$ is the strain tensor and the superscript T specifies the transpose.

For space discretization, the displacement field \mathbf{u} is approximated in terms of the shape functions \mathbf{N} and nodal displacements \mathbf{a} . Then displacement and strain can be written as

$$\mathbf{u} = \mathbf{N} \mathbf{a} \quad (3)$$

$$\boldsymbol{\epsilon} = \mathbf{B} \mathbf{a} \quad \mathbf{B} = \mathbf{L} \mathbf{N} \quad (4)$$

where \mathbf{B} is the strain displacement matrix, \mathbf{L} is a linear differential operator. Substituting Eq. (3) and Eq. (4) into Eq. (2) gives [9,10]

$$\mathbf{M} \ddot{\mathbf{a}} = \mathbf{F}^{ext} - \mathbf{F}^{int} \quad (5)$$

in which

$$\mathbf{M} = \int_V \rho \mathbf{N}^T \mathbf{N} dV \quad (6)$$

$$\mathbf{F}^{ext} = \int_V \rho \mathbf{N}^T \mathbf{g} dV + \int_S \mathbf{N}^T \mathbf{t} dS \quad (7)$$

$$\mathbf{F}^{int} = \int_V \mathbf{B}^T \boldsymbol{\sigma} dV. \quad (8)$$

Eq. (5) is identical in the context of FEM and MPM.

To increase the computational efficiency, the consistent mass matrix Eq. (6) is lumped. The drawback of using a lumped mass matrix is a slight dissipation in the kinetic energy [14].

The particle discretization is achieved via approximating the continuous density field using the Dirac delta function (δ), such that

$$\rho(\mathbf{x}) = \sum_{P=1}^{n_p} m_p \delta(\mathbf{x} - \mathbf{x}^p) \quad (9)$$

where \mathbf{x} is an arbitrary position vector, \mathbf{x}^p is the position vector at particle p . By considering this approximation into account, Eq. (6), Eq. (7) and Eq. (8) can be rewritten as

$$\begin{aligned} \mathbf{M}_L &= \begin{bmatrix} m_1 & \cdots & 0 \\ \vdots & \ddots & \vdots \\ 0 & \cdots & m_n \end{bmatrix} \\ m_i &= \sum_{p=1}^{n_p} m_p N_i^p \end{aligned} \quad (10)$$

$$\mathbf{F}^{int} = \sum_{P=1}^{n_p} \mathbf{B}_P^T \boldsymbol{\sigma}_P V_P \quad (11)$$

$$\mathbf{F}^{ext} = \sum_{P=1}^{n_p} N_i^P m_P \mathbf{g} + \sum_{P=1}^{n_p} N_i^P \mathbf{t}_P \quad (12)$$

where V_P is the volume associated to particle P and \mathbf{t}_P is the force vector from the surface traction mapped to the boundary particle P .

Most of the MPM applications are based on the explicit time integration scheme. This method is conditionally stable and the time step size should be smaller than the critical time (Δt_{cr}) step value dictated by the CFL condition

$$\Delta t_{cr} = h_{min}/c_d \quad (13)$$

where h_{min} is the minimum representative distance in an element and c_d is the compression wave speed.

Explicit time integration of discretised momentum equation is performed via applying Euler forward integration scheme such that

$$\ddot{\mathbf{a}}^t = [\mathbf{M}_L^t]^{-1} \mathbf{F}^t, \quad \dot{\mathbf{a}}_p^{t+\Delta t} = \dot{\mathbf{a}}_p^t + \Delta t N_p \ddot{\mathbf{a}}^t \quad (14)$$

where Δt is the time increment, $\dot{\mathbf{a}}_p^{t+\Delta t}$ and $\dot{\mathbf{a}}_p^t$ are the particle velocities at time t and $t + \Delta t$ respectively and $\ddot{\mathbf{a}}^t$ is the nodal accelerations at time t .

The nodal velocities $\dot{\mathbf{a}}^{t+\Delta t}$ at time $t + \Delta t$ are then calculated from the updated particles velocities, solving the following equation [9]

$$\mathbf{M}_L^t \dot{\mathbf{a}}^{t+\Delta t} \approx \sum_{p=1}^{np} m_p \mathbf{N}_p^T \dot{\mathbf{a}}_p^{t+\Delta t} \quad (15)$$

Vector of nodal displacements is calculated using Euler backward integration method. Then the position of particles (\mathbf{x}_p) are updated

$$\begin{aligned} \Delta \mathbf{a}^{t+\Delta t} &= \Delta t \dot{\mathbf{a}}^{t+\Delta t} \\ \mathbf{x}_p^{t+\Delta t} &= \mathbf{x}_p^t + \mathbf{N}_p \Delta \mathbf{a}^{t+\Delta t} \end{aligned} \quad (16)$$

3 ENHANCED VOLUMETRIC STRAIN METHOD

In order to overcome the locking phenomena appears in low order elements being used here, the method suggested by Detournay & Dzik [15] and applied in MPM by Jassim et al. [2] is adopted. This method is based on the nodal volumetric strain averaging. First the strain is decomposed into the volumetric and deviatoric parts, then nodal volumetric strains are computed based on the average volumetric strain of the elements

$$\bar{\dot{\varepsilon}}_{vi} = \frac{\sum_{e=1}^{n_{elem}} \dot{\varepsilon}_{ve} \Omega_e}{\sum_{e=1}^{n_{elem}} \Omega_e} \quad (17)$$

where $\bar{\dot{\varepsilon}}_{vi}$ is the volumetric strain rate on node i , $\dot{\varepsilon}_{ve}$ is the volumetric strain rate of the element e , Ω_e is the volume of e and n_{elem} is the number of elements attached to node i . The smooth volumetric strain of the element is the average of the nodal values obtained from equation (17) in the form

$$\bar{\dot{\varepsilon}}_{ve} = \frac{1}{n_{en}} \sum_{i=1}^{n_{en}} \bar{\dot{\varepsilon}}_{vi} \quad (18)$$

where n_{en} is the number of nodes in an element and $\bar{\dot{\varepsilon}}_{ve}$ is the enhanced volumetric strain of element e . Then the final strain rate tensor of an element is defined as

$$\bar{\dot{\varepsilon}}_{ij} = \dot{\varepsilon}_{ij} - \frac{1}{3} (\dot{\varepsilon}_v - \bar{\dot{\varepsilon}}_v) \delta_{ij} \quad (19)$$

where δ_{ij} is the Kronecker delta. In MPM, equation (19) is applied for all individual material points.

4 NUMERICAL EXAMPLE

In this section the problem of a vertically loaded strip footing for undrained conditions [2] is solved here by developing a 2D MPM programm. The geometry, mesh and boundary conditions are shown in Figure 2. Due to the symmetry only one half of the space is simulated. The analytical solution for this problem is given by Hill [16]

$$q/c = \pi + 2 \quad (20)$$

in which q is the footing pressure and c is the cohesion of the soil.

The soil is assumed to behave according to the Tresca material model with the elastic modulus $E = 200 \text{ MN/m}^2$, Poisson ratio $\nu = 0.495$, density $\rho = 1800 \text{ kg/m}^3$ and

$c = 100 \text{ kN/m}^2$. The footing pressure is increased gradually in stepwise with an increment of 2 kN/m^2 .

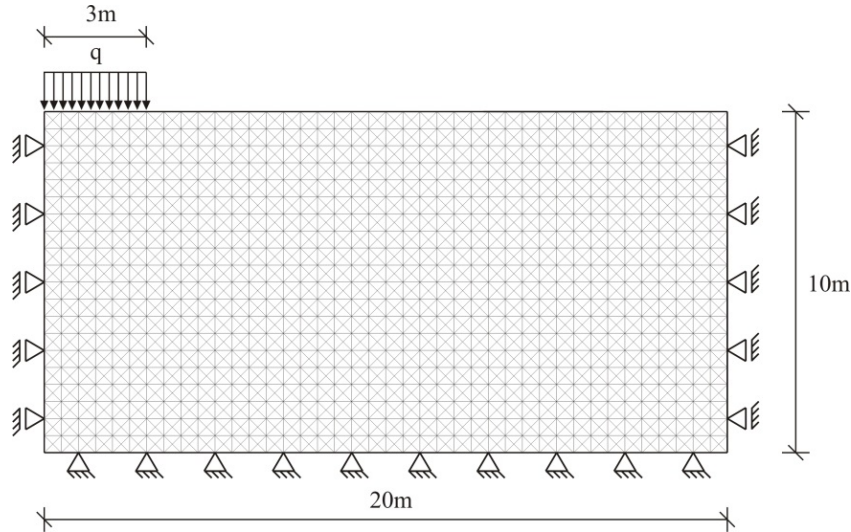


Figure 2: Geometry and boundary conditions of the strip footing problem

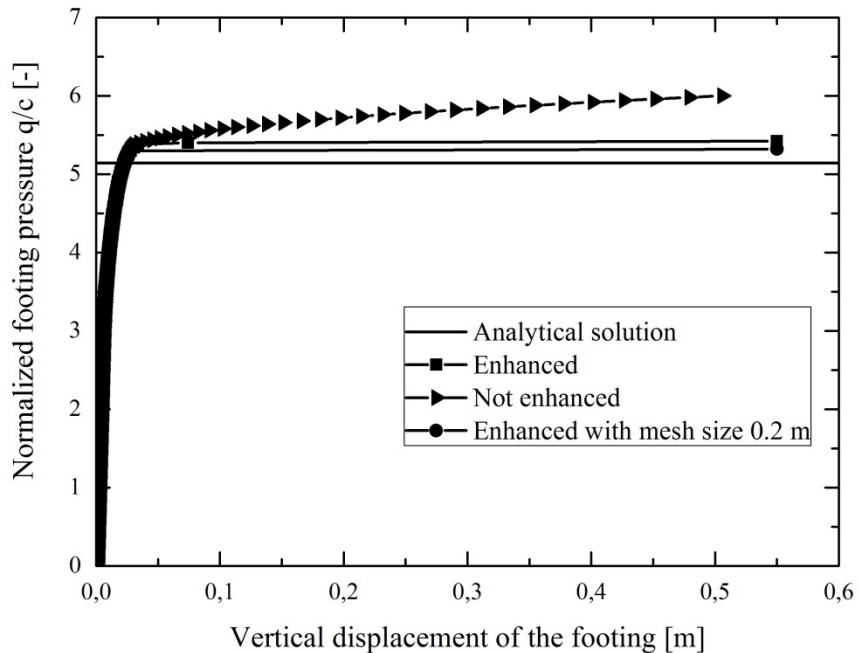


Figure 3: load displacement curve of the strip footing problem

4.1 Effectivity of the enhanced volumetric strain method

To show the effectivity of the enhanced volumetric strain method to mitigate the volumetric locking, the strip footing problem is solved using one particle per element. Small strain deformation is assumed, so the positions of the particles are not updated during the simulation. This problem is solved to evaluate the effect of enhanced volumetric strain

method. Equilibrium conditions are checked in each loading step and after fulfilling the equilibrium conditions the load is increased. The results are shown in Figure 3 together with the analytical solution. From this figure, it can be seen that the enhanced volumetric strain method is able to relax the elements from locking and the curve is nearer to the analytical solution. The gap between the enhanced solution and the analytical solution is attributed to the mesh refinement. By using finer mesh this gap becomes smaller. The same problem is solved using a finer mesh with cell size 0.2 m instead 0.5 m. The results are shown in Figure 3. It is obvious that the finer mesh reduces the distance between the analytical solution and the numerical one.

The effect of applying the load on particles (as performed previously) or on the nodes, furthermore, the effect of updating the location of the particles is analyzed using the mesh of cell size 0.5 m as shown in Figure 4. Applying the load on particles or as in classical FEM on nodes does not affect the results here as we do not update the locations of the particles, but by updating the particle locations this effect can be seen and the curve deviates from the classical FEM and becomes more separated from the analytical solution.

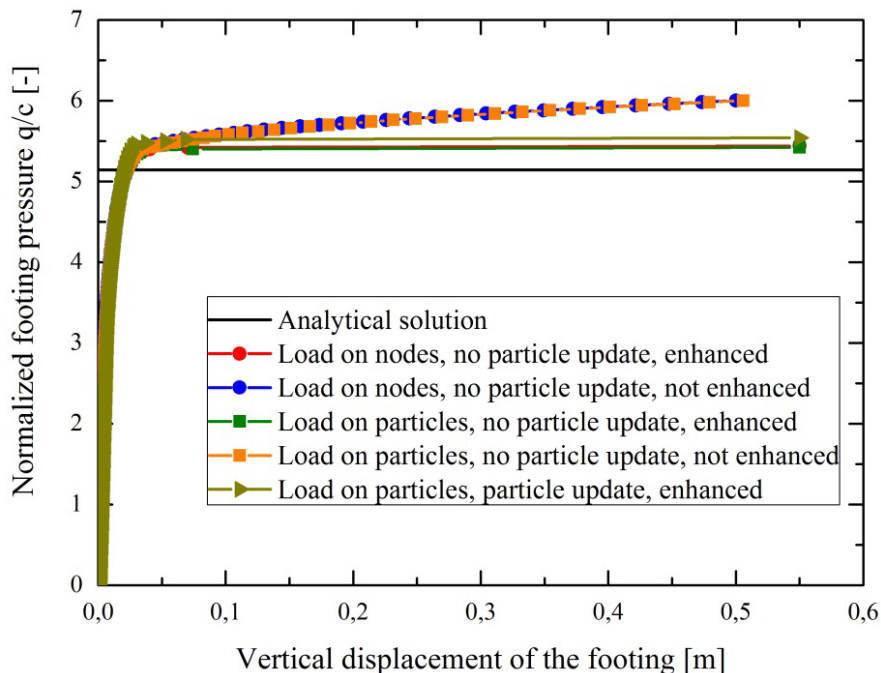


Figure 4: load displacement curve to investigate the effect of applying loads on nodes or particles and updating particle positions

4.2 The effect of the element size

The regular discretization, shown in Figure 2, with 0.5 m cell size has been compared to coarser mesh (1 m) and an unstructured mesh, see Figure 5. Four particles are placed initially inside each element. After applying the self-weight of the soil, the pressure of the footing is increased in stepwise with a value of 2 kN/m². After fulfilling the equilibrium conditions, [2], the loading procedure is continued.

Figure 6 shows the vertical displacement of a particle located immediately below the

footing on the left. In this figure the results from the three meshes together with the analytical solution are shown. Results of the cell size 0.5 m and the unstructured mesh are closer to the analytical solution than the coarse mesh. Figure 7 shows the total displacement of the particles using the mesh shown in Figure 2. Figure 8 takes a closer look at the particles displacement below the footing and shows their total displacement. As can be seen from this figure the particles under the footing start to travel to the other elements. As mentioned before, using this property MPM can simulate large deformations, but at the same time the grid crossing error appears which affect the final results.

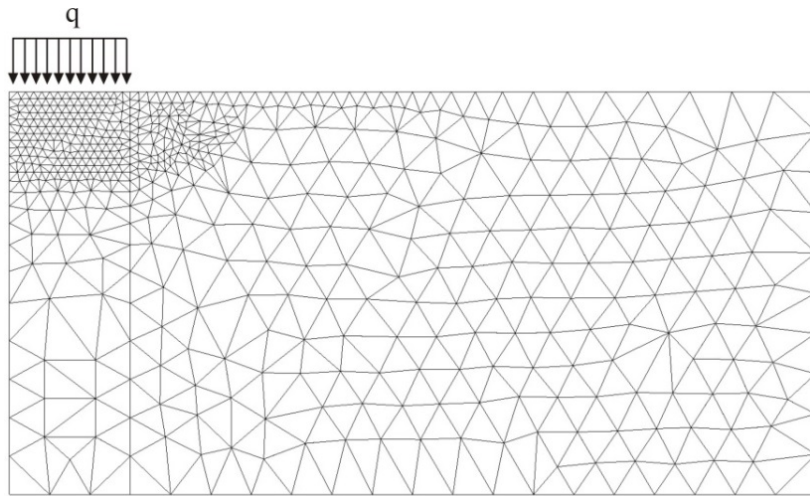


Figure 5: three-noded unstructured mesh

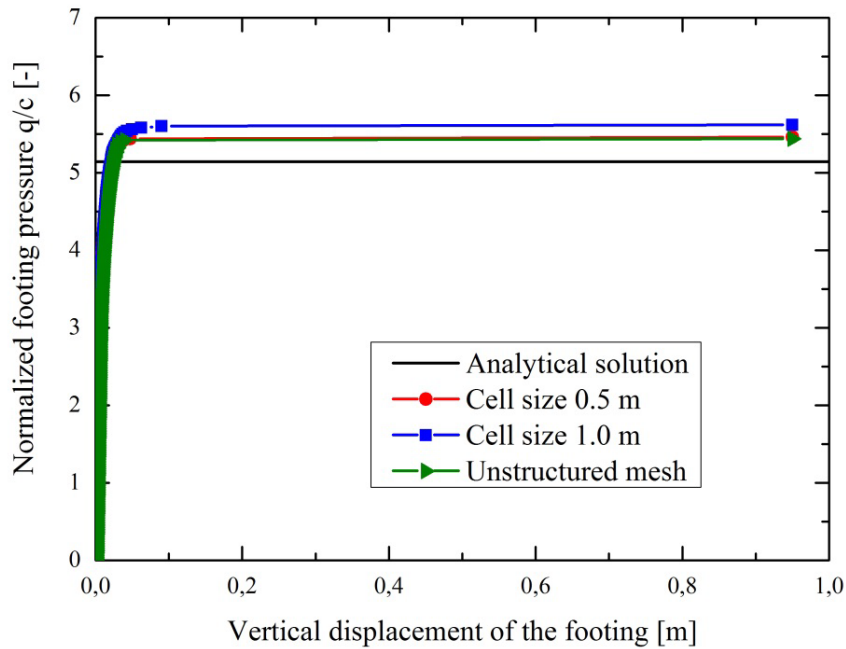


Figure 6: load displacement curve for the three different meshes

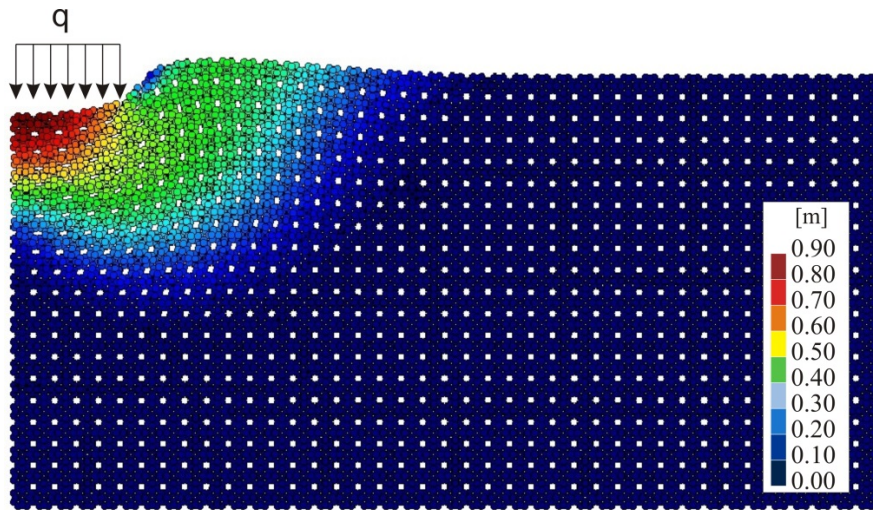


Figure 7: total displacement of the particles using 0.5 m mesh size

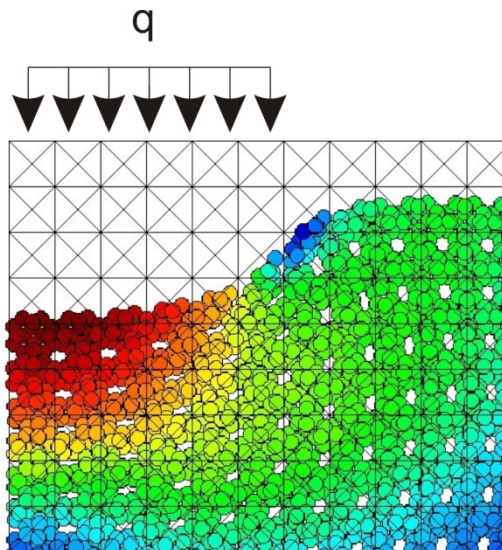


Figure 8: total displacement of the particles using 0.5 m mesh size

4.3 The effect of the number of particles

In this part of the paper, the effect of the initial number of particles per element on the final results of the footing problem is analyzed. A mesh with the cell size of 1.0 m is used with one, four and ten particles per element. The simulations are performed by applying the traction on the boundary particles and allowing the particles to follow the deformation. Figure 9 shows the vertical displacement of a particle located immediately below the footing on the left. As can be seen from Figure 9, no difference can be noticed between the ultimate bearing capacities. Figure 10 but focuses on the displacements between zero and 15 cm of Figure 9. For the same load, the model with initially 10 particles per element shows the smallest deformation. Next is the model with initially four particles per element and then the one with initially one particle per element. It can be concluded that the model with initially ten particles

per element shows more accurate results for the intermediate loading (before failure) than the two other models and the one with initially four particles per element is more accurate than the model with initially one particle per element.

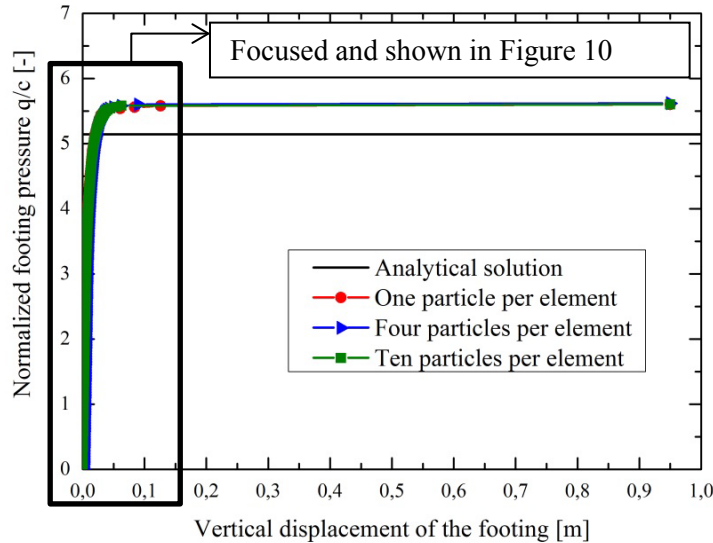


Figure 9: load displacement curve for the three different meshes

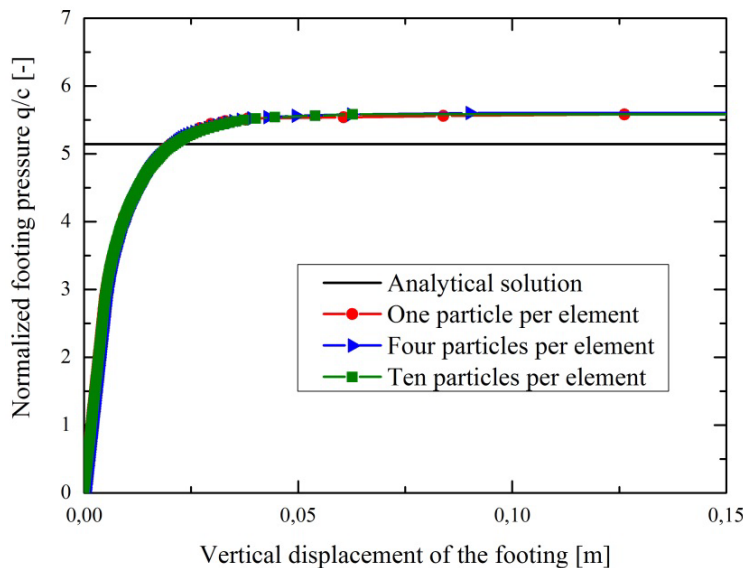


Figure 10: load displacement curve for the three different meshes zoomed on deformations between zero and 0.15 m

5 SUMMARY AND CONCLUSION

In this study the effect of different discretisations on the simulation results of a strip footing problem is investigated. After a short description of MPM working procedure and governing equations, the problem of strip footing with large deformation is analyzed using different meshes and different number of particles per element. Grid crossing of particles

which happen in the context of MPM influence the quality of the results. In the other side this particles moving to other elements enables MPM to simulate large deformations of the material. As shown in this study refining the mesh and increasing the initial number of particles per element helps to reduce this error.

REFERENCES

- [1] Anderson, S. Anderson, L. Analysis of spatial interpolation in the material-point method *Computers and structures* (2010) **88**:506-518.
- [2] Jassim, I.K. Hamad, F.M. and Vermeer, P.A. Dynamic material point method with applications in geomechanics. *Proc. 2nd Int. Symp. on Computational Geomechanics* (2011) Croatia.
- [3] Hirt, C.W. Amsden, A.A. and Cook, J.L. An arbitrary Lagrangian-Eulerian computing method for all flow speeds. *J. Comput. Phys.* (1974) **14**(3):227-253.
- [4] Noh, W.F. CEL: A time-dependent, two-space-dimensional, coupled Eulerian-Lagrangian code. *Methods in Computational Physics* (1964) **3**:117-179.
- [5] Belytschko, T. Lu, Y.Y. and Gu, L. Element-free Galerkin methods. *Int. J. Numer. Meth. Eng.* (1994) **37**(2):229–256.
- [6] Monaghan, J. J. An introduction to SPH. *Comput. Phys. Commun.* (1988) **48**(1):89–96.
- [7] Harlow, F.H. The particle-in-cell computing method for fluid dynamics. *Methods in Computational Physics* (1964) **3**:319–343.
- [8] Brackbill, J.U. and Ruppel, H.M FLIP: A low dissipation particle-in-cell calculations of fluid flows in two dimensions. *J. Comput. Phys.* (1986) **65**(2):314–343.
- [9] Sulsky, D. Zhou, S.J. and Schreyer, H.L. Application of a particle-in-cell method to solid mechanics. *Comput. Phys. Commun.* (1995) **87**:236–252.
- [10] Sulsky, D. and Schreyer, H.L. Axisymmetric form of the material point method with applications to upsetting and Taylor impact problems. *J. Comput. Method. Appl. M.* (1996) **139**:409–429.
- [11] Bardenhagen, S.G. Brackbill, J.U. and Sulsky, D. The material-point method for granular materials. *Comput. Method. Appl. M.* (2000) **187**:529-541.
- [12] Bardenhagen, S.G. and Kober, E.M. The generalized interpolation material point method. *Computer modelling in engineering and sciences* (2004) **5**(6):477-496.
- [13] Coetzee, C.J. Vermeer, P.A. and Basson, A.H. The modeling of anchors using the material point method. *Int. J. Numer. Anal. Met.* (2005) **29**:879-895.
- [14] Burgess, D. Sulsky, D. & Brackbill, J.U. Mass matrix formulation of the FLIP particle-in-cell method. *J Comput Phys* (1992) **103** 1-15.
- [15] Detournay, C. & Dzik, E. Nodal mixed discretization for tetrahedral elements, *4th International FLAC Symposium on Numerical Modeling in Geomechanics* (2006) Inc. Paper No. 02-07.
- [16] Hill, R. *The mathematical theory of plasticity*. Clarendon press, Oxford (1950).

SIMULATIONS OF DENSE SNOW AVALANCHES WITH GENERALIZED INTERPOLATION MATERIAL POINT METHOD: PRELIMINARY OUTCOMES

**WOJCIECH T. SOLOWSKI¹, DJEBAR BAROUDI², MOJTABA GHOBAKHLOU¹
AND LEENA K. KORKIALA-TANTTU¹**

¹ Department of Civil and Environmental Engineering
School of Engineering, Aalto University,
P.O. Box 12100, FI-00076 Aalto, Finland

wojciech.solowski@aalto.com, mojtaba.ghobakhlou@aalto.fi, leena.korkiala-tanttu@aalto.fi
<http://civil.aalto.fi/en/research/geoengineering/soil/>

² Department of Civil and Structural Engineering
School of Engineering, Aalto University,
P.O. Box 12100, FI-00076 Aalto, Finland
dje.baroudi@gmail.com

Key words: Granular Materials, Material Point Method, Avalanches.

Abstract. The paper presents material point method simulations of a dense snow avalanche replicating the avalanches observed at the Vallée de la Sionne test site. It has been observed that the dense snow avalanches behaviour is somewhere between the behaviour of very weak solid and very viscous liquid [1]. That is confirmed by difficulties in replicating such avalanches behaviour and the impact pressure with theories typical for fluid flows [2]. This paper results are based on numerical method used mainly for solids, though one allowing for extreme deformations [3-5]. The avalanche is modelled with a Mohr-Coulomb model, a simple constitutive model commonly used for modelling soils. The constitutive model has great many deficiencies and does not allow for modelling of all the complex behaviour of snow, however, the initial results presented are promising and show some agreement with the observed data. It is hoped that the presented approach can be refined and will lead to more accurate predictions of dense snow avalanches behaviour in the future.

1 INTRODUCTION

The snow avalanches may pose a threat to communities and infrastructure. Therefore, the prediction of avalanches outreach as well as impact pressures when an obstacle is hit are important problems. To investigate these issues, number of field tests sites monitor speed of avalanches and forces created by them upon hitting an artificial obstacle. These measurements are used, among others, to validate small-scale laboratory tests. However, such in-situ measurements are difficult and may be flawed for several reasons.

A wide range of flow regimes have been observed in avalanches. These span from dry powder-like avalanches, which generally move quicker to wet snow avalanches which have low velocity. The pressure recorded for quick avalanches include large number of impulses and

significant variability. Such avalanches can also be modelled with methods belonging to fluid dynamics with significant success.

However, it is particularly difficult to model wet snow avalanches as they behave in the regime transitory between solid and fluid. The paper aim is to model an abstracted wet snow avalanche hitting an instrumented pylon with Generalized Interpolation Material Point Method (GIMP), introduced by Bardenhagen & Kober [4].



Figure 1. Instrumented pylon on a slope in the Vallée de la Sionne, Swiss Alps. Photos courtesy of Dr Emmanuel Thibert (National Research Institute of Science and Technology for Environment and Agriculture IRSTEA) and Dr Betty Sovilla (WSL Institute for Snow and Avalanche Research SLF).

2 TEST SITE IN THE VALLÉE DE LA SIONNE, SWITZERLAND AND THE AVALANCHE DATA

The test site in the Vallée de la Sionne, Swiss Alps (for detailed description see [6]) monitors occurring real-scale avalanches. The avalanches, both of natural origin and man-induced hit a heavily instrumented pylon (see Fig. 1). The pylon, 20m high, 60 cm wide and 1.5 m long measures avalanche pressures with high-frequency piezo load cells located at 0.5m, 1.5m, 2.5m, 3.5m, 4.5 and 5.5m above the ground. The optical sensors located on the sides of the pylon measure avalanche speed. There are also flow depth sensors on the pylon.

The observed avalanches falls into several categories. They can be, for example, dilute / dense (depending on snow density), or dry / wet (depending on the amount of moisture in snow). Further qualification of avalanches may be done with respect to their Froude number, see [2].

The piezo pressure sensors mounted on the pylon have either 10 or 25cm diameter. It appears that size of these sensors does not affect the average pressure measured; however, it seems that the peak magnitudes of stress decrease with sensor dimension [2].

This paper shows some initial outcomes of simulating of a wet-dense, relatively quick avalanche with Generalized Interpolation Material Point Method (GIMP).

3 GENERALIZED INTERPOLATION MATERIAL POINT METHOD (GIMP)

The Material Point Method has been developed by Sulsky et al. [3,7] as an evolution of the Particle in Cell method. This paper uses a Generalized Interpolation Material Point Method (GIMP [4]) which is an improved version of the classical Material Point Method.

The Material Point Method as well as GIMP falls into the category of meshless methods, even though it uses a background (usually static) grid, on which the equations are resolved in each step. GIMP is usually formulated as a fully explicit method (though implicit formulation is possible). In explicit formulation, simulation is resolved over time, which is divided into sufficiently small time-steps. The maximum time-step size is influenced by the grid size as well as particle velocity (Courant number).

In the Material Point Method the grid is cast over the simulation domain. Subsequently, all the materials within the simulation domain are discretised into particles (material points). The material points carry all the material information, as well as have position, mass and velocity. GIMP improves the classical Material Point Method as it additionally assumes that the material is smeared over finite particle domain which increases accuracy and reduces numerical issues in solution.

During calculations, in the beginning of every time step the mass and the momentum of the material points are transferred to the grid nodes using grid shape function and particle characteristic function. GIMP introduces these functions in more general way than the Material Point Method and creates particle domains instead of just having the material concentrated in points in space, as it is the case in the older formulation.

Subsequently, the nodal internal forces are computed (for which we also get the stresses from particles), as well as accelerations. These are transferred back and used for updating particles positions and velocities. From velocity gradients the deformation gradients and finite strains are computed. These are used for updating stresses and particle volumes. Afterwards, next time-step may be resolved. The more complete description of the GIMP can be found in [4] whereas validation of the method for some engineering problems is in [9].

4 NUMERICAL MODEL FOR THE AVALANCHE

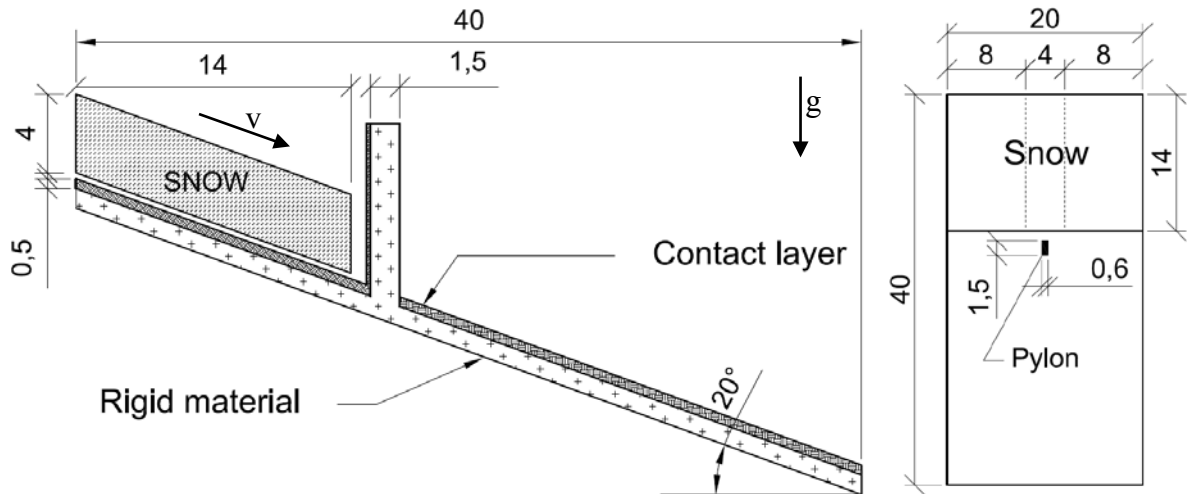
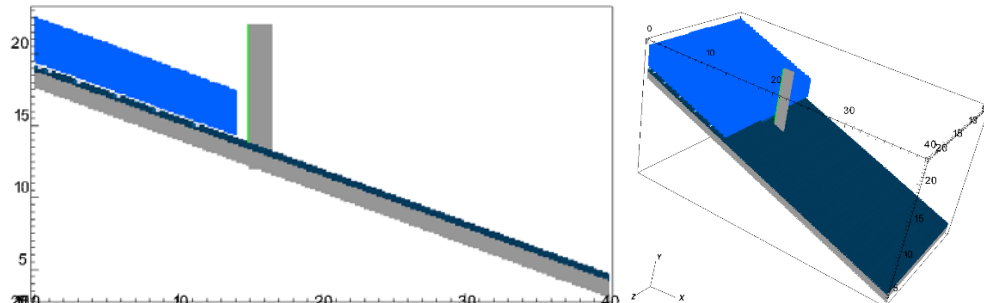
Numerical simulation of natural avalanches is difficult. That is because of a great number of uncertainties which are present in natural avalanches, as well as due to numerical difficulties due to discontinuities and very large displacements. Few numerical methods can be applied for even qualitative modelling of an avalanche hitting an obstacle. This paper uses GIMP, as coded in open source Uintah 1.6.0 software (<http://www.uintah.utah.edu/> [8]). The Uintah software has been enhanced with a Mohr-Coulomb model (for more details see [9-11]).

Table 1: Mohr-Coulomb parameters for snow

cohesion	friction angle	dilation angle	shear modulus	bulk modulus	density
[kPa]	[deg]	[deg]	[kPa]	[kPa]	[kg/m ³]
0.5	25	0	1,800	1,300	400

Table 2: Parameters for the contact layers

Material	cohesion [kPa]	friction angle [deg]	dilation angle [deg]	shear modulus [kPa]	bulk modulus [kPa]	density [kg / m ³]	friction coefficient
slope surface	0.5	25	0	1,800	1,300	400	0.3
pylon surface	-	-	-	75,000	160,000	2,650	0.2


Figure 2. Schematic for the initial state of simulation: cross section through the pylon (left) and view from the top (right). All dimensions in meters.

Figure 3. Side and 3D view of the initial state of the simulation. Different materials are shown with different colours.

4.1 Initial state

The scheme giving the initial state of the simulation is shown in Figure 2 and the initial actual simulation is given in Figure 3. The total size of the problem modelled is 40 m x 20 m. The slope angle is 20 degrees.

Only the 15m long, 20m wide part of avalanche is modelled. The thickness was taken as constant and equal to either 3 or 4m. The snow in the avalanche, as well as on the ground, is

modelled as a Mohr-Coulomb material (see Table 1 for the model parameters, which were taken in line with suggestions in [1] and [12] and may be representative for the wet snow).

To reduce the computation time, the snow has been modelled with 2 different densities of material points. The two 8 m wide sides of the avalanche are approximated with just a single material point per grid cell, whereas the central 4m of snow is modelled with $2 \times 2 \times 2 = 8$ particles per grid cell (which is also the density of material points in grid cell used for all other materials). The simulation begins with avalanche moving with the velocity of 10 m/s.

4.2 Contact

One of the most challenging parts of the calculations was to simulate the contact between the materials. In the model, the snow is interacting only with the contact layers on the rigid surface and on the pylon. These contact layers are attached to a rigid skeleton supporting it. The contact between snow block and contact surfaces is a frictional contact (as coded in Uintah, [13]). However, snow does not interact with rigid material at all. The material parameters for the contact layers are given in Table 2.

The contact layer simulating the slope surface is 0.5 m thick. That layer has been modelled with $2 \times 2 \times 2 = 8$ particles per grid cell. The friction coefficient between the snow and that surface is taken as 0.3. However, in GIMP, the interaction between particles starts when the particle domains share common node. As such, to ensure smoother contact, the block of snow is moved away from the contact surface by 0.3 m.

The friction coefficient between the pylon contact layer and snow is set to 0.2. The pylon contact layer is single particle thick (thus mesh dependent) and positioned such that the grid boundary overlap with the boundary between the pylon and the contact layer. That ensures that the particles in the contact layer can move (and thus have some readable stress). That is essential, as the readouts from these particles on the pylon is taken as approximation of the contact pressure. Such approximation has been necessary as no direct way of getting contact forces exist in the standard Uintah 1.6.0 software.

4.3 Grid densities

It is well known that in problems which involves material separation (that is losing contact between the material points), the simulation results may significantly depend on the grid density. Most often, material separation is unwelcome, as it breaks the assumed continuous material and should be avoided. However, in the simulation of the avalanche, the impact on the pylon forces the separation of the particles. Therefore, the impact of the grid density on the simulation results had been carefully investigated. The simulations have been performed with a wide range of grid densities. They range from 2 grid cells per meter in each direction ($2 \times 2 \times 2$) to $4 \times 5 \times 5$ cells per meter (4 cells per meter in the x direction). The problem dimensions have been kept (almost) constant during all the simulations. The number of particles in each grid cell was unchanged in all the simulation and is independent from the grid density.

5 SIMULATION RESULTS

Number of simulations have been done using different grid densities and two initial depths of the avalanche (3 & 4 meters). The results have been assessed qualitatively, that is whether the typical features of avalanche hitting an object are recovered. Additionally, the approximate

values of contact stresses on the pylon were obtained and compared to the recorded results from the pylon sensors.

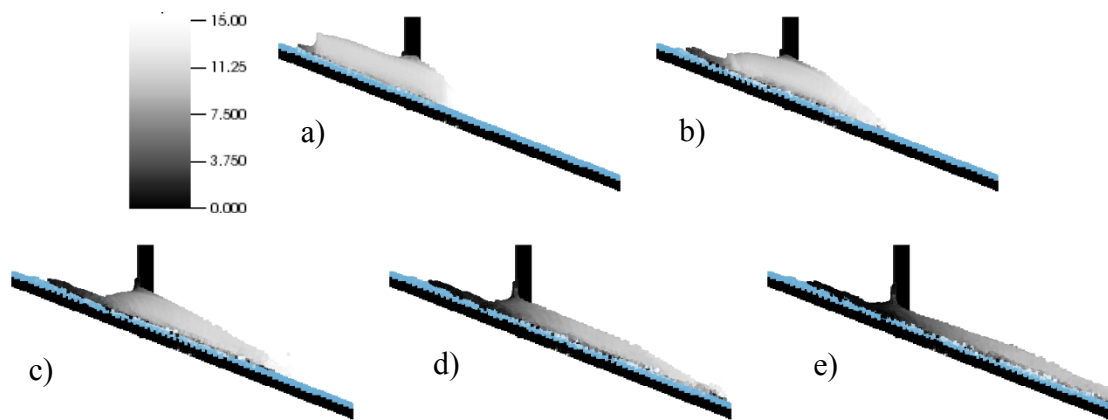


Figure 4. Velocity of the avalanche at simulation time 0.5, 1.0, 1.5, 2.0 and 2.5s. Side view. Grid density 3x4x4 (horizontal x height x depth) cells per meter.

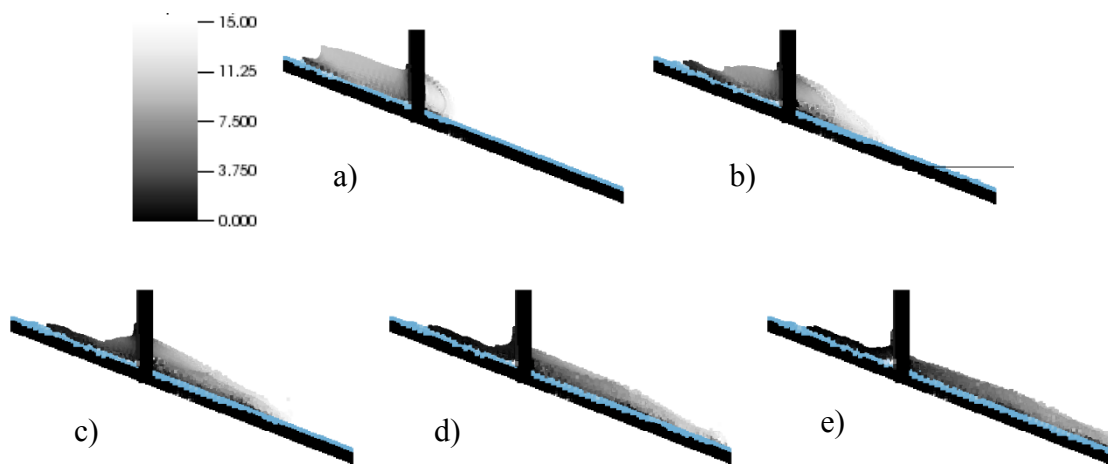


Figure 5. Velocity of the avalanche at simulation time 0.5, 1.0, 1.5, 2.0 and 2.5s. Intersection through the pylon. Grid density 3x4x4 (horizontal x height x depth) cells per meter.

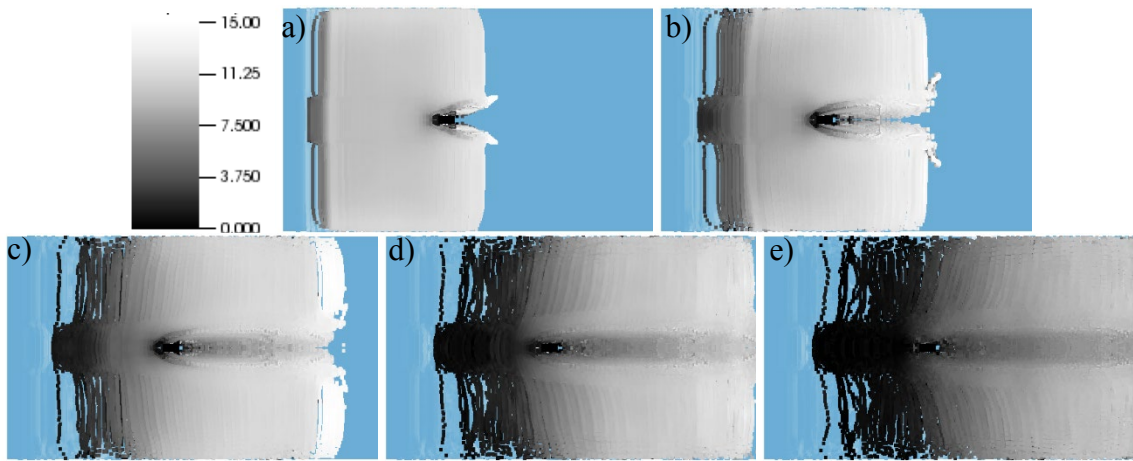


Figure 6. Velocity of the avalanche at simulation time 0.5, 1.0, 1.5, 2.0 and 2.5s. View from the top. Note some particles are stuck on the ground after the simulation (black lines). Grid density 3x4x4 (horizontal x height x depth) cells per meter.

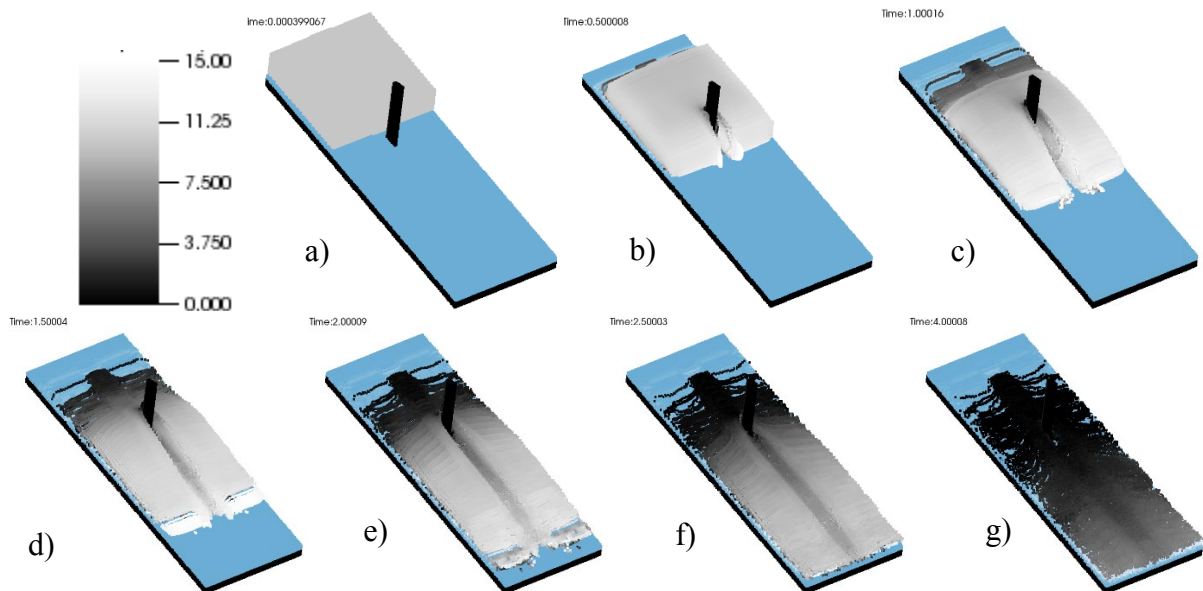


Figure 7. Velocity of the avalanche at simulation time 0.5, 1.0, 1.5, 2.0, 2.5 and 4.0s. Note some particles are stuck on the ground after the simulation (black lines). Grid density 3x4x4 (length x height x depth) cells per meter.

5.1 Qualitative agreement of the results

Before seeking good quantitative agreement between simulation and observed avalanche behavior, it is important to investigate whether the simulated avalanche exhibit number of behavior observed in real avalanches. The GIMP simulations perform rather well here. The wedge (dead zone) is created in front of the pylon, see Figures 5 and 6 a)-c) (all the data visualized with VisIt [14]). Also, some snow stays behind the pylon, Figure. 5 d), e) (note that this situation does not last till the end of simulation which is due to limitations of constitutive

model used). The velocity profiles around the pylon look realistic, see Figure 5 b) – d). Finally, the avalanche initially divided by the pylon is becoming unity after covering some ground as evidenced in Figures 6 c)-e) and 7 c)-g).

5.2 Quantitative agreement of the results

It is interesting to see how the available contact pressures compare to these obtained in the simulation. Unfortunately, such a direct comparison has not been possible at this stage. Currently, only the values of x-direction components of stress at particles at similar height to the sensors, but not the contact pressures per se could be obtained from the calculated results. Presumably, at least initially, stresses in single layer of particles resting on rigid material should not be very different to the actual contact pressures. That has been partially confirmed by setting elastic parameters of Pylon contact material: the bulk modulus to 100 MPa and the shear modulus to 150 MPa which correspond to Poisson ratio of 0. For that case, the stresses were very similar to these obtained with elastic values given in Table 2. Therefore, the interaction between the particles in the contact zone is probably not a major source of error (at least for the stresses in particles close to the middle of the pylon). On the other hand, when the stress is reduced, the particle will bounce back due to elastic forces. In such case particle inertia will significantly affect the stresses. As such, only the readout of stresses in the initial time (before the stress is reduced) could be close to the actual contact forces. However, the particles stress will be affected by the grid cell size anyway, as the stresses are resolved over whole grid cell, as well as the particle domain size.

In the simulation the axis of symmetry of the pylon corresponds to the grid boundary. That smooths the snow flow around the pylon and reduce the stresses. However, it also means that the particles from which the stress is read are moved somewhat to the side and do not correspond to the actual sensor position.

The avalanche modelled, with the code number of 6236 had wet-dense core with a powder layer [2]. That spatial non-uniformity has not been modelled – the material parameters of the snow may reflect a uniform wet-dense avalanche instead. Also, the 6236 avalanche has been recorded for approximately 40s, whereas the avalanche modelled impacted the pylon approximately during 1.5 second period.

To characterize the avalanche 6236 more accurately (recoupling data from [2]), it was recorded as having varied height, rising from a meter to approximately 4 m. The measured velocity ranged from below 5 m/s (initial part of the avalanche) to approximately 7-10 m/s when it reached its peak height, which was approximately 4 m. The stresses were significantly oscillating. At the peak time, with the avalanche having the highest speed, the contact pressures were between approximately 100 and 300 kPa at the 0.5 m sensor. Higher up, the stresses reduced to approximately 100 kPa (oscillating approximately between 50 and 150 kPa) and at 3.5 m they were mainly between 50 and 100 kPa with peaks reaching above 100 kPa. At 4.5 m, which was almost certainly above the wet-dense avalanche, the readouts were above 25 kPa and below 50 kPa.

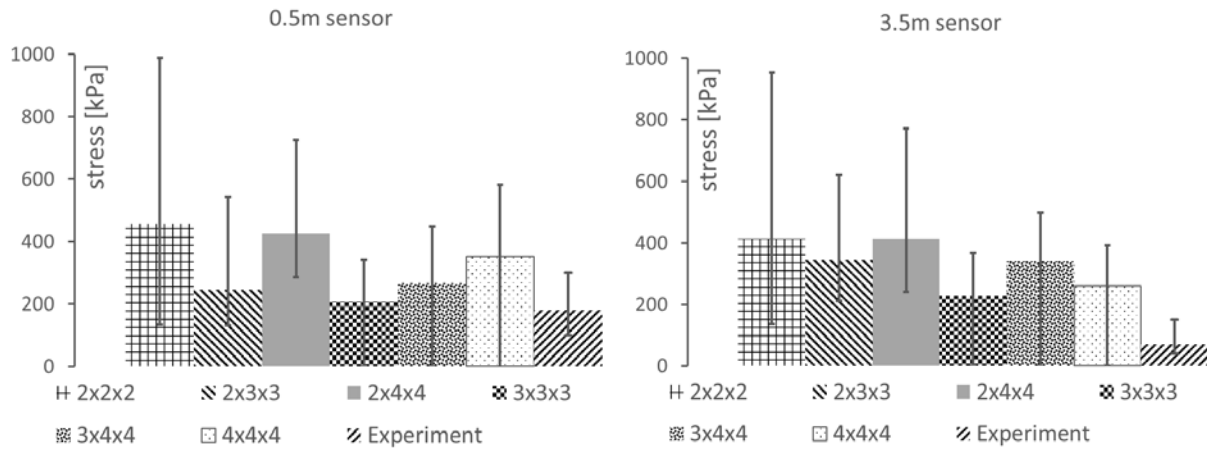


Figure 8. Grid density influence on the average stress on the pylon. The bar show averaged stress over the first 0.4 sec after the impact of the avalanche. The stresses shown are at points approximately at 0.5m and 3.5m. Error bar indicate maximum and minimum stress recorded. Grid cell densities varies between 2 cells per meter in each direction ($2 \times 2 \times 2$) to 4 cells per meter in each direction ($4 \times 4 \times 4$). Values for the pylon contact pressures (indicated as experiment) are based on [2] and approximate.

For this comparison, a simulation of initially 4m high avalanche were taken which resulted at acceptable heights of avalanche at the pylon. The results of simulations are given in Figure 8. It can be clearly seen that the modelled maximum and average stresses are too high. That may be partially due to generally too high speed of the avalanche at the pylon. In the simulation, the avalanche velocity was mainly between 10 and 15 m/s range, which is higher than the recorded values. Additionally, the assumption of the uniform snow density corresponding to the wet snow was incorrect. As the recorded velocity of the avalanche increases with the avalanche height, the lower recorded pressures are likely due to differences in the snow density.

The grid density does not appear to affect results too significantly. Of course, the results for the coarsest grid $2 \times 2 \times 2$, in which the pylon is modelled by just 2 particles (and is hit by just two particles of avalanche) are crude, as indicated by the difference by the maximum and minimum value (Fig. 8). However, for the finer meshes (with cell size of the hitting plane being $1/3$ m and $1/4$ m, denoted by the last number being 3 or 4 respectively) the differences between the results appear to be more acceptable. Still, the differences in stresses in simulations are probably mainly due to numerical reasons, whereas in the natural avalanches, they are due to natural factors.

Nonetheless, as GIMP is used in the shown simulations beyond its intended use range as the avalanche separates upon hitting a pylon and rejoins later, the differences between grids seem to be acceptable. Nonetheless, more control over separation of the material would be desirable as some difficult to account for mesh dependency is theoretically unavoidable with GIMP.

6 CONCLUSIONS

The paper presented initial results of simulation of a snow avalanche hitting an obstacle. The simulation recovered well the behavior of real avalanche qualitatively. In particular, the qualitative behavior of avalanche and leftover snow at the pylon has been well recovered.

Additionally, the final joining of the avalanche after hitting the pylon is also observable – something that would be difficult to achieve with most continuous numerical methods. The avalanche speed profile around the pylon is also qualitatively agreeing with experimental data.

The paper also compared the stresses on the pylon with the experimental data. The agreement should be improved further. The differences in the results may be due to number of issues. First, it appears that the speed of simulated avalanche should be decreased. Additionally, we do not know what material parameters are correct for given avalanche. The simulations shown are initial and not adjusted in order to improve the fit of the results. Finally, the avalanche has been modelled as uniform, whereas the avalanche we compared the results to is indicated as most likely non-uniform.

There are number of numerical shortcomings in the simulation. In particular, contact law and retrieval of contact pressures could be tweaked. Furthermore, Mohr-Coulomb is a very simple material model which is not very well validated for snow. As such, perhaps using a constitutive model uniquely suited for snow may improve the results. Finally, using a version of material point method enhanced such that for accurate modelling of separation and joining of particles would be possible (instead of relying on the hard coded mechanics of GIMP) would be welcome.

REFERENCES

- [1] Baroudi D., Sovilla B. and Thibert E. Effects of flow regime and sensor geometry on snow avalanche impact-pressure measurements. *Journal of Glaciology* (2011), **57** (202): 277-288.
- [2] Sovilla B., Schaeer M., Kern M. and Bartelt P. Impact pressures and flow regimes in dense snow avalanches observed at the Vallée de la Sionne test site. *Journal of geophysical research* (2008) 113, F01010
- [3] Sulsky, D., Zhou S.-J. and Schreyer H.L. Application of a particle-in-cell method to solid mechanics, *Comput. Phys. Comm.* (1995) **87**:236-252.
- [4] Bardenhagen, S.G. and Kober, E.M. The Generalized Interpolation Material Point Method. Computer Modeling in Engineering & Sciences (2004) **5**:477-495.
- [5] Sadeghirad, A., Brannon, R.M. and Burghard J. A convected particle domain interpolation technique to extend applicability of the material point method for problems involving massive deformations, *Int. J. Num. Meth. Engrn.* (2011), **86**(12):1435-1456.
- [6] Ammann, W.J. A new Swiss test-site for avalanche experiments in the Vallée de la Sionne/Valais. *Cold Reg. Sci. Technol.* (1999), **30**(1-3):3-11.
- [7] Sulsky, D., Chen, Z., Schreyer, H.L. A particle method for history-dependent materials. *Computer Methods in Applied Mechanics and Engineering* (1994), **118**:176-196.
- [8] Guilkey, J., Harman, T., Luitjens, J. et al. Uintah code (Version 1.6.0) 2014, [Computer program] (Available from <http://www.uintah.utah.edu>).
- [9] Sołowski, W.T. and Sloan S.W. Evaluation of material point method for use in geotechnics. *Int. J. Numer. Anal. Meth. Geomech.* (2015), **39**:685–701.
- [10] Clausen, J., Damkilde, L. and Andersen L. Efficient return algorithms for associated plasticity with multiple yield planes. *International Journal of Numerical Methods in Engineering* (2006), **66**:1036–1059.
- [11] Clausen, J., Damkilde, L. and Andersen L. An efficient return algorithm for non-associated

- plasticity. *Computers and Structures* (2007), **85**:1795–1807.
- [12] Vera, C. and Bartelt, P. Modelling Wet Snow Avalanche Flow with a Temperature Dependent Coulomb Friction Function plasticity. International Snow Science Workshop Grenoble – Chamonix Mont-Blanc – 2013. (2013), 691-696.
- [13] Bardenhagen, S.G., Guilkey, J.E., Roessig, K.M., Brackbill J.U., Witzel W.M. and Foster J.C. An improved contact algorithm for the material point method and application to stress propagation in granular material. *Computer Methods in the Engineering Sciences* (2001), **2**(4):509–522.
- [14] Childs, H., Brugger, E., Whitlock, B., Meredith, J., Ahern, S., Bonnell, K., Miller, M., Weber, G. H., Harrison, C., Pugmire, D., Fogal, T., Garth, C., Sanderson, A., Bethel, E. W., Durant, M., Camp, D., Favre, J. M., Rübel, O. and Navrátil P. Book chapter: “VisIt: An End-User Tool For Visualizing and Analyzing Very Large Data,” in High Performance Visualization: Enabling Extreme-Scale Scientific Insight, edited by E. Wes Bethel, H. Childs, C. Hansen, Chapman and Hall/CRC, October, 2012.

SOLUTION OF THE STATIONARY STOKES AND NAVIER-STOKES EQUATIONS USING THE MODIFIED FINITE PARTICLE METHOD IN THE FRAMEWORK OF A LEAST SQUARES RESIDUAL METHOD

D. Asprone¹, F. Auricchio^{2,3}, A. Montanino^{2,3}, A. Reali²

¹DiSt, Università degli Studi di Napoli “Federico II” - Napoli (ITALY)

²DICAr, Università degli Studi di Pavia - Pavia (ITALY)

³CeSNA, Istituto Universitario di Studi Superiori (IUSS) - Pavia (ITALY)

Key words: Meshless methods, incompressible flows, least squares residual method

Abstract. The present work is concerned with the solution of stationary Stokes and Navier-Stokes flows using the Modified Finite Particle Method for spatial derivative approximations and the Least Square Residual Method for the solution of the linear system deriving from the collocation procedure. The combination of such approaches permits to easily handle the numerical difficulty of the *inf-sup* conditions, without distinguishing between the discretizations of velocity and pressure fields.

The obtained results, both in the cases of linear and non-linear flows, show the robustness of the proposed algorithm

1 Introduction

The numerical simulation of incompressible fluid flows represents a challenge for many numerical methods due to the *inf-sup* condition [1], which imposes limitations in the discretization of velocity and pressure fields, and therefore in numerical methods some attention is needed in field discretization.

Among the existing numerical methods an important role has been played in recent years by meshless methods, which present many potentiality with respect to traditional mesh-based or grid-based methods. The main characteristic of meshless methods is, in fact, that nodes are not “rigidly” connected to each other, and therefore they can easily model large deformation and fluid-dynamics problems.

In the context of meshless methods the Radial Basis Functions (RBF) have been widely investigated from a theoretical point of view [2, 3] and applied to function approximation problems [4] and partial differential problems [5], in particular wave propagation [6] and fluid dynamics [7].

RBF collocation has also been used in combination with a Least Square Residual Method (LSRM), an algorithm for the solution of linear systems based on error minimiza-

tion. Such an algorithm is used when the number of equations overcomes the number of unknowns. In the field of collocation methods for the solution of partial differential problems, such a methodology is needed when the number of collocation points is higher than the number of nodal unknowns. In [8] it is shown that the combination of a collocation method with LSRM corresponds to the weak formulation with numerical quadrature. In [9] the use of LSRM is extended to linear incompressible elasticity, and it is shown that the different equations have to be properly weighted in order to balance the different components of the error. An important characteristic of the combination between Radial Basis Functions and Least Square Residual Method is that in this way pressure does not undergo any spurious oscillation, even approximating velocity and pressure fields using the same discrete differential operators.

In the present paper we combine the Least Square Residual Method with the Modified Finite Particle Method (MFPM), a meshless method for spatial derivative approximation first introduced in [10] and applied to 1D elasticity static and dynamic problems, to 2D elliptic problems [11], to 2D elasticity and plasticity [12]. In [13] a novel formulation is introduced and applied to 2D dynamics and to 3D statics.

The present paper is organized as follows: in Section 2 we present a version of the Modified Finite Particle Method where collocation points are decoupled from points where variables are evaluated; then in Section 3 we recall the governing equations for incompressible fluid flows and present a solution procedure using the Least Square Residual Method. In Section 4 we solve the problem of a flow in a quarter of annulus under internal body loads; in Section 5 we recall the stationary Navier-Stokes equations and introduce a numerical procedure for handling the non-linearity, and then, in Section 6, we solve the famous benchmark of the lid-driven cavity problem. Finally, in Section 7, we draw some conclusions.

2 Modified Finite Particle Method

The Modified Finite Particle Method is a numerical procedure for function and derivative approximation introduced in [10]. Here we introduce a novel formulation, where equations are collocated in a set of points (collocation points) and variables are evaluated in a different set of points (control points).

The node distributions considered in the MFPM are referred to as $\mathbf{x} = [x \ y]^T$ and $\boldsymbol{\xi} = [\xi \ \eta]$; the first one is the set of collocation points, placed on the physical domain; the second one is the set of control points, that is, the points where variables are computed. In general, the node distribution $\boldsymbol{\xi}$ has no physical evidence, and therefore nodes can be placed in any convenient way, i.e., on a Cartesian equispaced grid. We remark that this choice does not affect the characteristic of the MFPM of being a meshless method, since collocation nodes can assume any position within the physical domain.

In a first stage, in order to show the numerical approximation procedure of a function $u = u(\mathbf{x})$ and its derivatives, we assume to know the nodal values of u in the control points $\boldsymbol{\xi}$. The first step of the numerical method is the evaluation of the Taylor series

expansion of the function $u(\mathbf{x})$ in a control point $\boldsymbol{\xi}_j$. The Taylor series is centered in a collocation point \mathbf{x}_i and is expanded until second order

$$\begin{aligned} u(\boldsymbol{\xi}_j) = & u(\mathbf{x}_i) + D_x u(\mathbf{x}_i)(\xi_j - x_i) + D_y u(\mathbf{x}_i)(\eta_j - y_i) + \frac{1}{2} D_{xx}^2 u(\mathbf{x}_i)(\xi_j - x_i)^2 \\ & + \frac{1}{2} D_{yy}^2 u(\mathbf{x}_i)(\eta_j - y_i)^2 + D_{xy}^2 u(\mathbf{x}_i)(\xi_j - x_i)(\eta_j - y_i) \end{aligned} \quad (1)$$

Equation (1) contains 6 unknown terms (function and derivative values in the collocation point \mathbf{x}_i) and hence 6 equations are needed to compute their value. Therefore Equation (1) is evaluated in N_i control nodes surrounding \mathbf{x}_i , that constitute a subset referred as X_i . We then introduce 6 *projection functions* $W_\alpha^i = W_\alpha(\boldsymbol{\xi} - \mathbf{x}_i)$ and multiply the evaluations of Equation (1) in the nodes of X_i by the evaluations of W_α^i in the same points, and sum all terms, obtaining

$$\begin{aligned} & u_i \sum_j W_\alpha^{ij} + D_x u_i \sum_j (\xi_j - x_i) W_\alpha^{ij} + D_y u_i \sum_j (\eta_j - y_i) W_\alpha^{ij} + \\ & + \frac{1}{2} D_{xx}^2 u_i \sum_j (\xi_j - x_i)^2 W_\alpha^{ij} + \frac{1}{2} D_{yy}^2 u_i \sum_j (\eta_j - y_i)^2 W_\alpha^{ij} + \\ & + D_{xy}^2 u_i \sum_j (\xi_j - x_i)(\eta_j - y_i) W_\alpha^{ij} = \sum_j u(\boldsymbol{\xi}_j) W_\alpha^{ij} \quad \alpha = 1, \dots, 6 \end{aligned} \quad (2)$$

where $W_\alpha^{ij} = W_\alpha(\boldsymbol{\xi}_j - \mathbf{x}_i)$. Equation (2) can be rearranged in matrix form as

$$\mathbf{A}^i \begin{pmatrix} u(\mathbf{x}_i) \\ D_x u(\mathbf{x}_i) \\ D_y u(\mathbf{x}_i) \\ D_{xx}^2 u(\mathbf{x}_i) \\ D_{yy}^2 u(\mathbf{x}_i) \\ D_{xy}^2 u(\mathbf{x}_i) \end{pmatrix} = \begin{pmatrix} \sum_j u(\boldsymbol{\xi}_j) W_1^{ij} \\ \sum_j u(\boldsymbol{\xi}_j) W_2^{ij} \\ \sum_j u(\boldsymbol{\xi}_j) W_3^{ij} \\ \sum_j u(\boldsymbol{\xi}_j) W_4^{ij} \\ \sum_j u(\boldsymbol{\xi}_j) W_5^{ij} \\ \sum_j u(\boldsymbol{\xi}_j) W_6^{ij} \end{pmatrix} \quad (3)$$

Equation (3) is then rewritten in the form

$$\mathbf{A}^i \mathbf{D}(u_i) = \mathbf{C}^i \mathbf{u} \quad (4)$$

where

$$\mathbf{C}^i = [\mathbf{W}^{i1} \mid \mathbf{W}^{i2} \mid \dots \mid \mathbf{W}^{iN_i}] \quad (5)$$

and

$$\mathbf{W}^{ij} = [W_1^{ij} \mid W_2^{ij} \mid \dots \mid W_6^{ij}]^T \quad (6)$$

The vector \mathbf{u} collects the known nodal values in the node set $\boldsymbol{\xi}$. Then, by inverting (4), we obtain

$$\mathbf{D}(u_i) = \mathbf{E}^i \mathbf{C}^i \mathbf{u} \quad (7)$$

where $\mathbf{E}^i = (\mathbf{A}^i)^{-1}$, and finally

$$\mathbf{D}(u_i) = \mathbb{D}^i \mathbf{u} \quad (8)$$

with

$$\mathbb{D}^i = \mathbf{E}^i \mathbf{C}^i \quad (9)$$

The $6 \times N_i$ operator \mathbb{D}^i , applied to \mathbf{u} , gives back a 6×1 vector collecting all the approximations of functions and derivatives of $u(\mathbf{x})$ in the collocation point \mathbf{x}_i . We are interested in building 6 linear operators (\mathbb{I} , \mathbf{D}_x , \mathbf{D}_y , \mathbf{D}_{xx} , \mathbf{D}_{yy} , \mathbf{D}_{xy}) that, applied to the vector \mathbf{u} , return the evaluation of function and derivatives in all collocation points \mathbf{x} . These operators are simply built collecting, for each i , the correct row of \mathbb{D}^i , where the correct row is identified through Equation (3).

For example, in order to build the linear operator \mathbf{D}_x (the discrete counterpart of $\partial/\partial x$), we simply consider, for each i , the 2-nd row of \mathbb{D}^i . The final form of \mathbf{D}_x is then

$$\mathbf{D}_x = \begin{bmatrix} \mathbb{D}_2^1 \\ \mathbb{D}_2^2 \\ \dots \\ \mathbb{D}_2^N \end{bmatrix} \quad (10)$$

where \mathbb{D}_α^i is the α -th row of \mathbb{D}^i .

3 Governing equations for incompressible flows

The governing equations of incompressible fluid flows are the well known Navier-Stokes equations

$$\begin{cases} \rho \frac{\partial \mathbf{u}}{\partial t} + \mathbf{u} \cdot \nabla \mathbf{u} = -\nabla p + \mu \Delta \mathbf{u} + \mathbf{b} \\ \nabla \cdot \mathbf{u} = 0 \end{cases} \quad (11)$$

where the first equation is the dynamic equilibrium equation and the second equation is the incompressibility constraint. The variable ρ is the fluid density, \mathbf{u} is the velocity field, p is the pressure field, μ is the dynamic viscosity, \mathbf{b} is the vector of internal loads.

Navier-Stokes equations are non-linear equations, due to the presence of the convective term $\mathbf{u} \cdot \nabla \mathbf{u}$. Nevertheless, when inertial forces are negligible with respect to viscous forces, Navier-Stokes Equations can be simplified in the form

$$\begin{cases} \rho \frac{\partial \mathbf{u}}{\partial t} = -\nabla p + \mu \Delta \mathbf{u} + \mathbf{b} \\ \nabla \cdot \mathbf{u} = 0 \end{cases} \quad (12)$$

known as Stokes equations. Systems (11) and (12) have to be completed with suitable boundary conditions, that can be imposed on velocity or on the outward stress.

In the present work we restrict to stationary flows, that is, $\partial \mathbf{u} / \partial t = 0$. Moreover, the work is divided in two parts: in the first part we concentrate on Stokes Equations, in

order to study how the Modified Finite Particle Method, in combination with the Least Square Residual Method, deals with the inf-sup condition; in the second part we focus on the solution of the complete Navier-Stokes equations, and show a numerical procedure to handle the non linear term.

3.1 Solution of the Stokes equations

In the spirit of collocation methods the steady Stokes equations are discretized using the Modified Finite Particle Method. The discrete linear system of equations is

$$\begin{bmatrix} \mu\Delta & 0 & -\mathbf{D}_x \\ 0 & \mu\Delta & -\mathbf{D}_y \\ \mathbf{D}_x & \mathbf{D}_y & 0 \end{bmatrix} \begin{pmatrix} \hat{\mathbf{u}} \\ \hat{\mathbf{v}} \\ \hat{\mathbf{p}} \end{pmatrix} = \begin{pmatrix} \hat{\mathbf{f}}_x \\ \hat{\mathbf{f}}_y \\ \mathbf{0} \end{pmatrix} \quad (13)$$

where $\Delta = \mathbf{D}_{xx} + \mathbf{D}_{yy}$ is the discrete Laplace operator, $\hat{\mathbf{u}}$, $\hat{\mathbf{v}}$, and $\hat{\mathbf{p}}$ are the nodal unknowns associated to the velocity components u and v and to the pressure p , and $\hat{\mathbf{f}}_x$ and $\hat{\mathbf{f}}_y$ are the components of the internal loads at collocation points.

The required boundary conditions are imposed as linear algebraic equations on boundary collocation points. No boundary conditions are required on the incompressibility constraint, since incompressibility is imposed both on the interior and on the boundary of the domain [14]. We remark that this is not common in collocation methods, especially with collocated grids, where particular boundary condition for the incompressibility constraint are imposed [15, 16].

When collocation and control points coincide, the values of the control unknowns can be simply retrieved by inverting system (13). Unfortunately this algorithm is not valid with Stokes equations, due to the non-compliance of the discrete system (13) with the discrete inf-sup condition.

In order to overcome such a difficulty, we recur to a Least Square Residual Method, that is, we use a number of collocation points higher than the number of control nodes, and therefore System (13) is a rectangular, overdetermined system of equations, which can be solved through an error minimization. The global squared error, defined as

$$E = \|e\|^2 = \sum_i (K_{ij}d_j - f_i)^2 = (\mathbf{K}\mathbf{d} - \mathbf{f})^T(\mathbf{K}\mathbf{d} - \mathbf{f}) \quad (14)$$

can be rewritten as the sum of four contributions: (i) the error E_{eq} associated to equilibrium equations; (ii) the error E_{inc} associated to the discretized incompressibility constraints; (iii) the error E_{dir} associated to Dirichlet boundary conditions; (iv) the error E_{neum} associated to Neumann boundary conditions. The total error is therefore written as

$$E = E_{eq} + E_{inc} + E_{dir} + E_{neum} \quad (15)$$

As suggested in [9] the components of such an error have to be properly weighted, since they contribute differently to the global error. For this reason we introduce a different

definition of the error, referred as E_w , with expression

$$E_w = E_{eq} + \alpha_{inc}E_{inc} + \alpha_{dir}E_{dir} + \alpha_{neum}E_{neum} \quad (16)$$

where α_{inc} , α_{dir} , α_{neum} are weights associated to discrete incompressibility conditions, Dirichlet boundary conditions, and Neumann boundary conditions respectively.

Equation (16) can be rewritten as

$$E_w = \|\mathbf{K}_{eq}\mathbf{d} - f_{eq}\|^2 + \alpha_{inc}\|\mathbf{K}_{inc}\mathbf{d}\|^2 + \alpha_{dir}\|\mathbf{K}_{dir}\mathbf{d} - \bar{\mathbf{u}}\|^2 + \alpha_{neum}\|\mathbf{K}_{neum}\mathbf{d} - \bar{\mathbf{t}}\|^2 \quad (17)$$

where \mathbf{K}_{eq} , \mathbf{K}_{inc} , \mathbf{K}_{dir} , and \mathbf{K}_{neum} are the rows of the stiffness matrix \mathbf{K} associated to the equilibrium equations, incompressibility constraints, Dirichlet boundary conditions and Neumann boundary conditions. The vector $\bar{\mathbf{u}}$ is the known nodal velocity at Dirichlet boundary, $\bar{\mathbf{t}}$ is the known nodal outward stress at Neumann boundary.

The error (17) can be finally rewritten in compact form as

$$E_w = (\mathbf{K}\mathbf{d} - \mathbf{f})^T \mathbb{A}(\mathbf{K}\mathbf{d} - \mathbf{f}) \quad (18)$$

where \mathbb{A} is a diagonal matrix collecting the weights α associated to the different equations of system (13). Finally we minimize the error E_w with respect to the nodal unknowns \mathbf{d} , obtaining the linear system

$$\mathbf{K}^T \mathbb{A} \mathbf{K} \mathbf{d} = \mathbf{K}^T \mathbb{A} \mathbf{f} \quad (19)$$

that is a linear, symmetric system of equations, and can be solved using dedicated algorithms for symmetric matrix inversion. Nodal unknowns are therefore computed inverting System (19).

3.2 Choice of the weights

The choice of the weights to be assigned to the equations of system (13) is an important topic for the application of LSRM, since a wrong definition of weights may prevent the convergence of the numerical method.

The rigorous analysis conducted by [9] which takes in account the particular choice of the shape functions (in this case, Radial Basis Functions are used) leads to the choice of the following weights

$$\alpha_{inc} = (\mu N_s)^2 \quad \alpha_{dir} = (\mu N_s)^2 \quad \alpha_{neum} = 1 \quad (20)$$

In the present work, we prefer a different approach in order to define the set of weights to adopt: in fact we base our analysis on the consideration that different equations have different scales, in particular:

1. The equation of equilibrium has the dimensions of $\mu \partial u / \partial x^2$
2. The equation of incompressibility has the dimensions of $\partial u / \partial x$

3. The Dirichlet boundary conditions have the dimensions of u
4. The Neumann boundary conditions have the dimensions of $\mu \partial u / \partial x$

The second derivatives scale with $1/h^2$, where h is the distance between the control nodes; the first derivatives scale with $1/h$. The distance between particles is related to the total number of control nodes N_s , in particular we can assume $h \simeq 1/\sqrt{N_s}$. With these considerations, we can write the correct scaling of each equation in the form:

1. Equilibrium: $o(\mu/h^2) = o(\mu N_s)$
2. Incompressibility constraint: $o(1/h) = o(\sqrt{N_s})$
3. Dirichlet boundary conditions: $o(1)$
4. Neumann boundary conditions: $o(\mu/h) = o(\mu\sqrt{N_s})$

In order to balance the squared error in Equation (16), all components are requested to have at least the same dimensions, that are the ones of the squared equation of equilibrium, $(\mu N_s)^2$. The other weights, following this principle, are:

$$\alpha_{inc} = C_1 N_s \quad \alpha_{dir} = C_2 N_s^2 \quad \alpha_{neum} = C_3 N_s \quad (21)$$

where C_1 , C_2 , and C_3 are constants that, in a first approximation, we can consider unitary.

4 Solution of the Stokes problem on a quarter of annulus under body loads

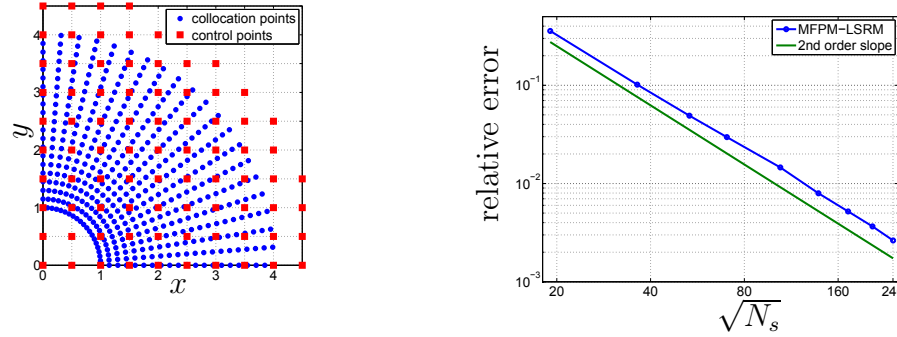
In the following we solve the problem of a Stokes flow in a quarter of annulus, clamped on all its boundary, under a polynomial body load. The problem has been studied in [17] using a stream line formulation and isogeometric analysis for the spatial discretization, exploiting the high regularity of isogeometric shape-functions, and also the possibility of reproducing exactly the geometry of the domain. The analytical solution of this problem is

$$\begin{cases} u = 10^{-6} x^2 y^4 (x^2 + y^2 - 16)(x^2 + y^2 - 1)(5x^4 + 18x^2y^2 - 85x^2 + 13y^4 + 80 - 153y^2) \\ v = -2 \cdot 10^{-6} xy^5 (x^2 + y^2 - 16)(x^2 + y^2 - 1)(5x^4 - 51x^2 + 6x^2y^2 - 17y^2 + 16 + y^4) \end{cases} \quad (22)$$

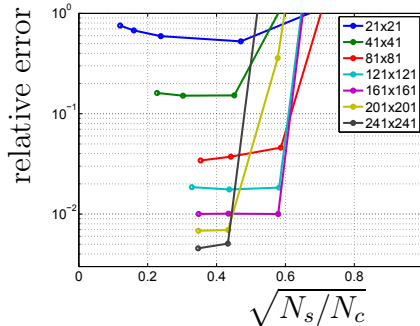
The internal body loads are obtained using the manufactured solution (22).

In Figure 1(a) we show an example of distribution of collocation points and field nodes. In particular we underline the fact that collocation points are distributed in the physical domain, whereas control points are distributed on a regular, Cartesian grid.

For this problem the expected second-order accuracy is achieved, as shown in Figure 1(b) we remark that on the horizontal axis of Figure 1(b) we plot the square root of the number of control nodes used for the approximation, since they are directly proportional to the needed computational effort.


Figure 1: Quarter of annulus under body loads

A numerical test has been performed in order to understand what is the best ratio between the number of field nodes and the number of collocation points. In particular, for each amount N_s of control nodes, different analyses have been performed varying the number of collocation nodes. The results are shown in Figure 2 where we notice that, as expected, on the right side of the diagram (that is, when the number of collocation points equals the number of field nodes) the error is great because of the pressure instability. However, for most of the field node densities, a minimum of the error can be appreciated around the value of $\sqrt{N_s/N_c} = 0.5$.


Figure 2: Quarter of annulus under body loads: relative error versus the ratio between the number of field nodes and collocation points

5 Stationary Navier-Stokes Equations

In the present section we recall the stationary Navier-Stokes Equations, obtained from Equation (11) cancelling the term $\rho\partial\mathbf{u}/\partial t$.

$$\begin{cases} \rho\mathbf{u} \cdot \nabla\mathbf{u} + \nabla p = \mu\Delta\mathbf{u} + \mathbf{b} \\ \nabla \cdot \mathbf{u} = 0 \end{cases} \quad (23)$$

The main difficulty of Equations (23), in addition to the need of satisfying the inf-sup condition, is the handling of the non linear term, which complicates the solution algorithm. A strategy for its solution is the linearization according to the Newton-Raphson algorithm. Unfortunately, despite the fast rate of convergence of this method, convergence is achieved when suitable initial guess solution is given. A guess solution for the Newton-Raphson algorithm is suitable when it is comprised in a bubble with radius proportional to $1/Re$, where Re is the Reynold numbers, defined as the ratio between inertial and viscous forces. This means that the solution of the complete Navier-Stokes equations is more and more difficult when approaching problems with high Reynolds numbers.

A strategy to reduce this difficulty is the use of the Picard linearization, which consists in a “partial” linearization of the convective terms. This strategy exhibits a sub-optimal rate of convergence to the solution, the bubble for the initial guess solution is larger and it is more easily found (see [18] for details).

In both cases of Picard or Newton-Raphson linearization, the discrete problem can be rewritten in the form

$$\mathbf{K}^k \Delta \hat{\mathbf{d}}^k = \mathbf{R}^k \quad (24)$$

where \mathbf{K}^k is the tangent (in the case of Newton Raphson) or secant (in the case of Picard) stiffness matrix, that is suitably assembled using the MFPM discrete differential operators; $\Delta \hat{\mathbf{d}}^k = [\Delta \hat{\mathbf{u}} \quad \Delta \hat{\mathbf{v}} \quad \Delta \hat{\mathbf{p}}]^T$ is the vector of the nodal increment, and \mathbf{R}^k is the residual of the discretized Navier-Stokes system. In all cases, the superscript k reminds that we are performing an iterative process, and therefore k is the iteration number.

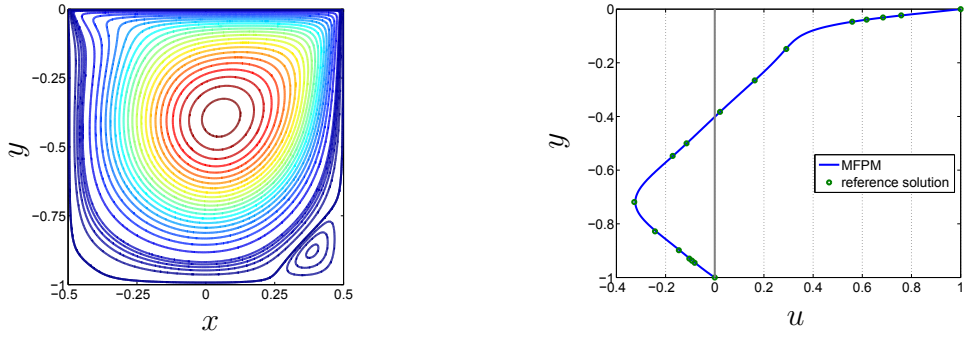
We again discretize equations using the MFPM and adopting $N_c > N_s$, therefore at each iteration we obtain a rectangular, overdetermined system, that again can be solved using the LSRM procedure. Therefore, at each iteration a weighted error is computed, with expression

$$\|e^2\| = (\mathbf{K}^k \Delta \hat{\mathbf{d}}^k - \mathbf{R}^k)^T \mathbf{A}^k (\mathbf{K}^k \Delta \hat{\mathbf{d}}^k - \mathbf{R}^k) \quad (25)$$

and then we minimize with respect to the control variable increment $\Delta \hat{\mathbf{d}}^k$

$$(\mathbf{K}^k)^T \mathbf{A}^k \mathbf{K}^k \Delta \hat{\mathbf{d}}^k = (\mathbf{K}^k)^T \mathbf{A}^k \mathbf{R}^k \quad (26)$$

The main difference with the linear case is that now we are weighting residual equations, so the dimensions of each equation is not depending on the differential operators, or on



(a) Streamlines solution using MFPM and LSRM

(b) Velocity profile in the x -direction along the axis $x = 0$ and comparison with the reference solution by [19].**Figure 3:** Lid-driven cavity problem ($Re = 400$)

the material properties; therefore we propose, as weights:

$$\alpha_i^k = \left(\frac{3N_i}{\sum_{j=1}^{N_i} K_{ij}^k} \right)^2 \quad (27)$$

in order all equations to be of the same order of magnitude. N_i is the number of supporting nodes of the collocation points to which the i -th row of \mathbf{K}^k is referred.

Once the weights have been established, we only have to solve Equation (26), update the solution, and then repeat until the norm of the weighted residual is less than a pre-established tolerance.

6 Solution of the Navier-Stokes Equations on the lid-driven cavity flow

In the following we apply what we have discussed in the previous section to the problem of the lid-driven cavity flow. The domain of the problem is a square of side $L = 1m$. On all boundary, Dirichlet boundary condition are assigned, in particular all sides have no velocity, while the top side is given a tangential velocity $U = 1m/s$.

We solved this problem using $\mu = 1/400 kg/m\ s$ and $\rho = 1kg/m^3$, obtaining a Reynolds number $Re = \rho LU/\mu = 400$. The results, in terms of stream-lines, are shown in Figure 3(a). In absence of analytical solution, we compare the results obtained in the present work with those published in [19] for the same Reynolds number in terms of horizontal velocity profile at the middle vertical axis (Figure 3(b)) and notice a substantial agreement between our results and the reference solution.

7 Conclusion

In the present work, we introduce an extension of the Modified Finite Particle Method that allows the decoupling between collocation points and control nodes. With this modi-

fication, the method is suitable for a Least Squares Residual Method. The present formulation, in combination with the Least Square Residual Method, shows some advantages with respect to other collocation methods: the matrix to invert in order to find the discrete solution of partial differential problems is symmetric, allowing the use of appropriate and faster solvers; the quality of the solution is minimally dependent on the distribution of collocation points, and also extremely random node distributions are permitted. This characteristic, in particular, permits the solution also on more complicated geometries, such as a quarter of annulus, also showing a correct second-order accuracy, when proper weights are assigned to the different equations. A discussion about weights is conducted, as well as the best possible ratio to impose between the number of collocation points and control nodes.

In the final part of the paper we attack the solution of non-linear Navier-Stokes equations and extend the use of LSRM also to non-linear problems. The comparison between the solution found in the present paper and the one given in the reference literature show good agreement, confirming the robustness of the present methodology.

References

- [1] Franco Brezzi and Michel Fortin. *Mixed and hybrid finite element methods*. Springer-Verlag New York, Inc., 1991.
- [2] E.J. Kansa. Multiquadratics - A scattered data approximation scheme with applications to computational fluid-dynamics - II solutions to parabolic, hyperbolic and elliptic partial differential equations. *Computers & Mathematics with Applications*, 19:147 – 161, 1990.
- [3] Edward J Kansa. Multiquadratics - A scattered data approximation scheme with applications to computational fluid-dynamics I surface approximations and partial derivative estimates. *Computers & Mathematics with applications*, 19(8):127–145, 1990.
- [4] J. G. Wang and G. R. Liu. A point interpolation meshless method based on radial basis functions. *International Journal for Numerical Methods in Engineering*, 54(11):1623–1648, 2002.
- [5] C. Franke and R. Schaback. Solving partial differential equations by collocation using radial basis functions. *Applied Mathematics and Computation*, 93(1):73 – 82, 1998.
- [6] L. Wang, F. Chu, and Z. Zhong. Study of radial basis collocation method for wave propagation. *Engineering Analysis with Boundary Elements*, 37:453–463, 2013.
- [7] G Demirkaya, C Wafo Soh, and OJ Ilegbusi. Direct solution of navier–stokes equations by radial basis functions. *Applied Mathematical Modelling*, 32(9):1848–1858, 2008.

- [8] HY Hu, JS Chen, and W Hu. Weighted radial basis collocation method for boundary value problems. *International Journal for Numerical Methods in Engineering*, 69(13):2736–2757, 2007.
- [9] S.-W. Chi, J.-S. Chen, and H.-Y. Hu. A weighted collocation on the strong form with mixed radial basis approximations for incompressible linear elasticity. *Computational Mechanics*, 53(2):309–324, 2014. cited By (since 1996)0.
- [10] D. Asprone, F. Auricchio, G. Manfredi, A. Prota, A. Reali, and G. Sangalli. Particle Methods for a 1d Elastic Model Problem: Error Analysis and Development of a Second-Order Accurate Formulation. *Computational Modeling in Engineering & Sciences*, 62:1–21, 2010.
- [11] D. Asprone, F. Auricchio, and A. Reali. Novel finite particle formulations based on projection methodologies. *International Journal for Numerical Methods in Fluids*, 65:1376–1388, 2011.
- [12] D Asprone, F Auricchio, and A Reali. Modified finite particle method: applications to elasticity and plasticity problems. *International Journal of Computational Methods*, 11(01), 2014.
- [13] D Asprone, F Auricchio, A Montanino, and A Reali. A modified finite particle method: Multi-dimensional elasto-statics and dynamics. *International Journal for Numerical Methods in Engineering*, 2014.
- [14] Robert L Sani, J Shen, Olivier Pironneau, and PM Gresho. Pressure boundary condition for the time-dependent incompressible navier–stokes equations. *International Journal for Numerical Methods in Fluids*, 50(6):673–682, 2006.
- [15] Philip M. Gresho and Robert L. Sani. On pressure boundary conditions for the incompressible navier-stokes equations. *International Journal for Numerical Methods in Fluids*, 7(10):1111–1145, 1987.
- [16] Weinan E and Jian-Guo Liu. Gauge method for viscous incompressible flows. *Communications in Mathematical Sciences*, 1(2):317–332, 2003.
- [17] F. Auricchio, L. Beirao da Veiga, A. Buffa, C. Lovadina, A. Reali, and G. Sangalli. A fully locking-free isogeometric approach for plane linear elasticity problems: a stream function formulation. *Computer methods in applied mechanics and engineering*, 197(1):160–172, 2007.
- [18] Howard Elman, David Silvester, and Andy Wathen. *Finite elements and fast iterative solvers: with applications in incompressible fluid dynamics*. Oxford University Press, 2014.

- [19] UKNG Ghia, Kirti N Ghia, and CT Shin. High-re solutions for incompressible flow using the navier-stokes equations and a multigrid method. *Journal of computational physics*, 48(3):387–411, 1982.

THE ALGORITHM FOR 3D VORTEX SHEET INFLUENCE COMPUTATION IN MESHLESS VORTEX METHOD

ILIA K. MARCHEVSKY AND GEORGY A. SHCHEGLOV

Bauman Moscow State Technical University (BMSTU)
2-nd Baumanskaya st., 105005 Moscow, Russia
E-mail: iliarchelevsky@mail.ru

Key words: Vortex Element Method, Vorticity Flux, Integral Equation, Quadrature Formula, Singularity Exclusion

Abstract. Vortex element method (VEM) is very suitable when solving FSI-problems, especially two-way coupled hydroelastic problems, when it is important to simulate unsteady body motion in incompressible flow [1]. Pure Lagrangian modifications of vortex methods don't require mesh generation in the fluid domain and its reconstruction at every time step due to body's motion. Vortex methods need much less computational resources (time of computations, memory and disk space) in comparison with most popular mesh methods.

Flow simulation using VEM requires the solution of two main problems: vortex wake evolution simulation and vorticity flux on the body surface computation, which are solved sequentially, step by step at every time step. In order to simulate vortex wake evolution there are developed number of approaches: vortex wake approximation with vortex filaments, vortex lattices, vortex points (vortons) of different types etc. The vortex fragmenton model is developed by authors and it has been applied to some FSI-problems [2]. As to vorticity flux simulation, one of the most important problems is vortex sheet intensity computation. There are two fundamental approaches, which are based on elimination of the limit values of normal or tangential velocity components on the body surface [3].

The accuracy of 'normal' approach in some FSI-applications is not enough for practice. In 2D-case 'tangent' approach allows to obtain much more accurate results, but it requires more precise discretization and integration schemes usage [3]. Such schemes are constructed and investigated by authors for 2D-case [4].

In the present research 3D-case is considered. The discretization scheme for 'tangent' approach is presented. The body surface is triangulated using arbitrary mesh generator and vortex sheet intensity assumed to be piecewise constant on the cells. 'Tangent' approach includes calculation of two surface integrals: the integral over the 'influence' cell and the integral over the 'control' cell. For arbitrary triangular mesh 'influence' integral can be calculated analytically. Numerical calculation of the 'control' integral using Gaussian points leads to significant errors for neighbor cells. The quadrature formula with

analytical singularity integration is derived. Non-singular part is integrated numerically by using Gaussian quadratures. All necessary formulae are obtained in invariant form and can be applied for arbitrary triangular cells.

The original algorithm which is based on the developed approach for vortex influences computation is developed.

1 INTRODUCTION AND PROBLEM STATEMENT

The problem of 3D incompressible flow simulation around bluff body is considered. The governing equations are Navier — Stokes equations

$$\nabla \cdot \mathbf{V} = 0, \quad \frac{\partial \mathbf{V}}{\partial t} + (\mathbf{V} \cdot \nabla) \mathbf{V} = \nu \nabla^2 \mathbf{V} - \frac{\nabla p}{\rho_\infty},$$

with boundary conditions

$$\lim_{r \rightarrow \infty} \mathbf{V} = \mathbf{V}_\infty, \quad \lim_{r \rightarrow \infty} p = p_\infty, \quad \mathbf{V}(\mathbf{r}, t) \Big|_{\mathbf{r} \in K} = 0,$$

where \mathbf{V} is flow velocity; p — pressure; $\rho_\infty = \text{const}$ — density; ν — kinematic viscosity coefficient; \mathbf{V}_∞ and p_∞ are parameters of the incident flow; K is body's surface.

The viscosity assumed to be small, so according to L. Prandtl's theory it is possible to take its influence into account only as a cause of vorticity generation on body surface. The flow can be considered inviscid, with vorticity flux from the surface.

The immovable streamlined body is simulated by vortex sheet $\boldsymbol{\gamma}(\mathbf{r}, t)$ influence, which is placed on the body surface, $\mathbf{r} \in K$. The vorticity flux can be simulated if this vortex sheet is free; that means that at every time step this sheet is split into separate vortex elements which form vortex wake around the body.

Vortex wake evolution can be simulated by using one of Lagrangian vortex element methods [1, 2].

As to vorticity flux simulation, one of the most important problems is vortex sheet intensity computation. There are two fundamental approaches, which are based on elimination of the limit values of normal or tangential velocity components on the body surface [3]. These approaches are denoted as ‘normal’ and ‘tangent’.

The accuracy of ‘normal’ approach, especially in FSI-applications, when streamlined bodies are movable and deformable, sometimes is not enough for practice. In 2D-case ‘tangent’ approach allows to obtain much more accurate results, but it requires more precise discretization and integration schemes usage [3]. Such schemes are constructed and investigated by authors for 2D-case [4].

The aim of the present research is development of the corresponding numerical schemes for 3D case.

2 INTEGRAL EQUATION FOR VORTEX SHEET INTENSITY

Due to vortex sheet on the body surface, velocity field has the discontinuity, and its limit value from body side is

$$\begin{aligned} \mathbf{V}_-(\mathbf{r}, t) = \mathbf{V}_\infty + \frac{1}{4\pi} \int_{S(t)} \frac{\boldsymbol{\Omega}(\boldsymbol{\xi}, t) \times (\mathbf{r} - \boldsymbol{\xi})}{|\mathbf{r} - \boldsymbol{\xi}|^3} d\xi + \\ + \frac{1}{4\pi} \int_K \frac{\boldsymbol{\gamma}(\boldsymbol{\xi}, t) \times (\mathbf{r} - \boldsymbol{\xi})}{|\mathbf{r} - \boldsymbol{\xi}|^3} d\xi - \frac{\boldsymbol{\gamma}(\mathbf{r}, t) \times \mathbf{n}(\mathbf{r})}{2}, \quad \mathbf{r} \in K. \end{aligned}$$

Here $S(t)$ is vortex wake region; $\mathbf{n}(\mathbf{r})$ is unit outer normal vector on body surface K .

In order to satisfy the boundary condition on the body surface, vortex sheet intensity should satisfy the integral equation $\mathbf{V}_-(\mathbf{r}, t) = 0$, $\mathbf{r} \in K$.

As it proved in [3], it is enough to satisfy this equation only for tangent component of the velocity:

$$\mathbf{n}(\mathbf{r}) \times (\mathbf{V}_-(\mathbf{r}, t) \times \mathbf{n}(\mathbf{r})) = 0.$$

It leads to Fredholm-type integral equation of the 2-nd kind

$$\frac{\mathbf{n}(\mathbf{r})}{4\pi} \times \left(\int_K \frac{\boldsymbol{\gamma}(\boldsymbol{\xi}, t) \times (\mathbf{r} - \boldsymbol{\xi})}{|\mathbf{r} - \boldsymbol{\xi}|^3} \times \mathbf{n}(\mathbf{r}) d\xi \right) - \frac{\boldsymbol{\gamma}(\mathbf{r}, t) \times \mathbf{n}(\mathbf{r})}{2} = \mathbf{f}(\mathbf{r}, t), \quad \mathbf{r} \in K, \quad (1)$$

where

$$\mathbf{f}(\mathbf{r}, t) = -\mathbf{n}(\mathbf{r}) \times \left(\mathbf{V}_\infty + \frac{1}{4\pi} \int_{S(t)} \frac{\boldsymbol{\Omega}(\boldsymbol{\xi}, t) \times (\mathbf{r} - \boldsymbol{\xi})}{|\mathbf{r} - \boldsymbol{\xi}|^3} d\xi \right) \times \mathbf{n}(\mathbf{r})$$

is known vector function.

3 INTEGRAL EQUATION DISCRETIZATION

In order to find approximate solution of hypersingular integral equation (1), the following assumptions can be made:

1. Body surface is triangulated into N flat cells K_i with areas A_i and normal vectors \mathbf{n}_i , $i = 1, \dots, N$.
2. The unknown vortex sheet intensity on the i -th cell is constant vector $\boldsymbol{\gamma}_i$, $i = 1, \dots, N$, which lies in the plane of the i -th cell, i.e. $\boldsymbol{\gamma}_i \cdot \mathbf{n}_i = 0$.
3. The integral equation (1) is satisfied on average on the cells.

According to these assumptions the discrete analogue of equation (1) can be derived:

$$\frac{1}{4\pi A_i} \sum_{j=1}^N \int_{K_j} \left(\int_{K_i} \mathbf{n}_i \times \left(\frac{\boldsymbol{\gamma}_j \times (\mathbf{r} - \boldsymbol{\xi})}{|\mathbf{r} - \boldsymbol{\xi}|^3} \times \mathbf{n}_i \right) d\xi \right) dr - \frac{\boldsymbol{\gamma}_i \times \mathbf{n}_i}{2} = \frac{1}{A_i} \int_{K_i} \mathbf{f}(\mathbf{r}, t) dr, \quad i = 1, \dots, N. \quad (2)$$

To write down (2) in form of linear algebraic system we should choose local orthonormal basis on every cell $(\boldsymbol{\tau}_i^{(1)}, \boldsymbol{\tau}_i^{(2)}, \mathbf{n}_i)$, where tangent vectors $\boldsymbol{\tau}_i^{(1)}, \boldsymbol{\tau}_i^{(2)}$ can be chosen arbitrary and $\boldsymbol{\tau}_i^{(1)} \times \boldsymbol{\tau}_i^{(2)} = \mathbf{n}_i$. So $\boldsymbol{\gamma}_i = \gamma_i^{(1)} \boldsymbol{\tau}_i^{(1)} + \gamma_i^{(2)} \boldsymbol{\tau}_i^{(2)}$ and we can project (2) for every i -th panel on directions $\boldsymbol{\tau}_i^{(1)}$ and $\boldsymbol{\tau}_i^{(2)}$:

$$\begin{aligned} \frac{1}{4\pi A_i} \boldsymbol{\tau}_i^{(1)} \cdot \left(\sum_{j=1}^N \gamma_j^{(1)} \boldsymbol{\nu}_{ij}^{(1)} + \sum_{j=1}^N \gamma_j^{(2)} \boldsymbol{\nu}_{ij}^{(2)} \right) - \frac{\gamma_i^{(2)}}{2} &= \frac{b_i^{(1)}}{A_i}, \\ \frac{1}{4\pi A_i} \boldsymbol{\tau}_i^{(2)} \cdot \left(\sum_{j=1}^N \gamma_j^{(1)} \boldsymbol{\nu}_{ij}^{(1)} + \sum_{j=1}^N \gamma_j^{(2)} \boldsymbol{\nu}_{ij}^{(2)} \right) + \frac{\gamma_i^{(1)}}{2} &= \frac{b_i^{(2)}}{A_i}. \end{aligned} \quad (3)$$

Here

$$\boldsymbol{\nu}_{ij}^{(k)} = \int_{K_i} \left(\int_{K_j} \frac{\boldsymbol{\tau}_j^{(k)} \times (\mathbf{r} - \boldsymbol{\xi})}{|\mathbf{r} - \boldsymbol{\xi}|^3} d\xi \right) dr, \quad b_i^{(k)} = \int_{K_i} \boldsymbol{\tau}_i^{(k)} \cdot \mathbf{f}(\mathbf{r}, t) dr, \quad k = 1, 2; \quad i, j = 1, \dots, N.$$

Algebraic system (3) has infinite set of solutions; in order to select the unique solution we should satisfy additional condition

$$\int_K \boldsymbol{\gamma}(\mathbf{r}, t) dr = \mathbf{0},$$

which can be written down in the following form:

$$\sum_{i=1}^N A_i \left(\gamma_i^{(1)} \boldsymbol{\tau}_i^{(1)} + \gamma_i^{(2)} \boldsymbol{\tau}_i^{(2)} \right) = \mathbf{0}. \quad (4)$$

System (3)-(4) is overdetermined, it should be regularized, for example, by introducing the 3D-vector $\mathbf{R} = (R_1, R_2, R_3)^T$:

$$\begin{aligned} \frac{1}{4\pi A_i} \boldsymbol{\tau}_i^{(1)} \cdot \left(\sum_{j=1}^N \gamma_j^{(1)} \boldsymbol{\nu}_{ij}^{(1)} + \sum_{j=1}^N \gamma_j^{(2)} \boldsymbol{\nu}_{ij}^{(2)} \right) - \frac{\gamma_i^{(2)}}{2} + \mathbf{R} \cdot \boldsymbol{\tau}_i^{(2)} &= \frac{b_i^{(1)}}{A_i}, \\ \frac{1}{4\pi A_i} \boldsymbol{\tau}_i^{(2)} \cdot \left(\sum_{j=1}^N \gamma_j^{(1)} \boldsymbol{\nu}_{ij}^{(1)} + \sum_{j=1}^N \gamma_j^{(2)} \boldsymbol{\nu}_{ij}^{(2)} \right) + \frac{\gamma_i^{(1)}}{2} + \mathbf{R} \cdot \boldsymbol{\tau}_i^{(1)} &= \frac{b_i^{(2)}}{A_i}, \\ \sum_{j=1}^N A_j \left(\gamma_j^{(1)} \boldsymbol{\tau}_j^{(1)} + \gamma_j^{(2)} \boldsymbol{\tau}_j^{(2)} \right) &= 0, \quad i = 1, \dots, N. \end{aligned} \quad (5)$$

Numerical computations show that system (5) is well-conditioned; its dimension is $2N+3$.

4 MATRIX COEFFICIENTS CALCULATION

The main problem for practical use of the suggested approach is coefficients $\boldsymbol{\nu}_{ij}^{(k)}$ calculation for system (5):

$$\boldsymbol{\nu}_{ij}^{(k)} = \boldsymbol{\tau}_j^{(k)} \times \int_{K_i} \left(\int_{K_j} \frac{\mathbf{r} - \boldsymbol{\xi}}{|\mathbf{r} - \boldsymbol{\xi}|^3} d\xi \right) dr = \boldsymbol{\tau}_j^{(k)} \times \mathbf{I}_{ij}, \quad k = 1, 2, \quad i, j = 1, \dots, N$$

Integral \mathbf{I}_{ij} is calculated over triangular cells K_i and K_j , where i -th cell we call ‘control’, j -th cell — ‘influence’ cell.

The simplest way for integrals \mathbf{I}_{ij} numerical computation is Gaussian quadrature formula usage. But this approach has high computational cost and leads to numerical calculation of improper integral when influence and control cells are neighbor (if they has common edge or common vertex).

The other way is to use some semi-analytical approaches. Firstly, the inner integral over the influence cell K_j can be calculated exactly:

$$\mathbf{J}_j(\mathbf{r}) = \int_{K_j} \frac{\mathbf{r} - \boldsymbol{\xi}}{|\mathbf{r} - \boldsymbol{\xi}|^3} d\xi \quad (6)$$

Secondly, the outer integral over the control cell

$$\mathbf{I}_{ij} = \int_{K_i} \mathbf{J}_j(\mathbf{r}) dr \quad (7)$$

can be calculated using Gaussian dots in non-neighbor case. If the cells have common edge, we need to exclude the singularity from the $\mathbf{J}_j(\mathbf{r})$ and write down it in form

$$\mathbf{J}_j(\mathbf{r}) = \mathbf{J}_j^{\text{reg}}(\mathbf{r}) + \mathbf{J}_j^{\text{sing}}(\mathbf{r}).$$

where $\mathbf{J}_j^{\text{reg}}(\mathbf{r})$ has no singularities and can be easily integrated numerically with high accuracy, while the integral

$$\int_{K_i} \mathbf{J}_j^{\text{sing}}(\mathbf{r}) dr$$

can be calculated exactly in analytic form.

There is well-known way for analytical calculation of integral (6) via considering of the integral from $|\mathbf{r} - \boldsymbol{\xi}|^{-1}$ with respect to $\boldsymbol{\xi}$ over the triangle K_j :

$$\mathbf{J}_j(\mathbf{r}) = \int_{K_j} \frac{\mathbf{r} - \boldsymbol{\xi}}{|\mathbf{r} - \boldsymbol{\xi}|^3} d\xi = \int_{K_j} \nabla_{\boldsymbol{\xi}} \frac{1}{|\mathbf{r} - \boldsymbol{\xi}|} d\xi = - \int_{K_j} \nabla_{\mathbf{r}} \frac{1}{|\mathbf{r} - \boldsymbol{\xi}|} d\xi = - \nabla_{\mathbf{r}} \left(\int_{K_j} \frac{1}{|\mathbf{r} - \boldsymbol{\xi}|} d\xi \right).$$

The last integral is very usual in potential theory, analytical expression for it can be found, for example, in [5]. However, that expression is cumbersome and it also should be differentiated with respect to components of vector \mathbf{r} .

Using computational software of symbolic mathematics *Wolfram Mathematica* and Handbook of integrals [6] it is possible to integrate (6) straightforwardly if vectors $\mathbf{s}_k = \mathbf{r}_k^{(j)} - \mathbf{r}$, $k = 1, 2, 3$, are only known, where \mathbf{r} is point for which integral (6) is calculated, $\mathbf{r}_k^{(j)}$ are vertices of K_j triangular cell. Denoting

$$\mathbf{e}_k^{(j)} = \frac{\mathbf{s}_{k+1} - \mathbf{s}_k}{|\mathbf{s}_{k+1} - \mathbf{s}_k|} = \frac{\mathbf{r}_{k+1}^{(j)} - \mathbf{r}_k^{(j)}}{|\mathbf{r}_{k+1}^{(j)} - \mathbf{r}_k^{(j)}|}, \quad \boldsymbol{\sigma}_k = \frac{\mathbf{s}_k}{|\mathbf{s}_k|}, \quad k = 1, 2, 3,$$

and assuming all the indices to be calculated using a modulus of 3, we obtain

$$\mathbf{J}_j(\mathbf{r}) = \Theta_j \mathbf{n}_j + \Psi_j \times \mathbf{n}_j, \quad j = 1, \dots, N,$$

where

$$\Psi_j = \sum_{k=1}^3 \ln \left(\frac{|\mathbf{s}_k|}{|\mathbf{s}_{k+1}|} \frac{1 + \mathbf{e}_k^{(j)} \cdot \boldsymbol{\sigma}_k}{1 + \mathbf{e}_k^{(j)} \cdot \boldsymbol{\sigma}_{k+1}} \right) \mathbf{e}_k,$$

Θ_j is solid angle subtended by triangular cell K_j which can be calculated, for example, by using the formula [7]

$$\Theta_j = 2 \arctan \left(\frac{|\mathbf{s}_1 \mathbf{s}_2 \mathbf{s}_3|}{|\mathbf{s}_1| \cdot |\mathbf{s}_2| \cdot |\mathbf{s}_3| + (\mathbf{s}_1 \cdot \mathbf{s}_2)|\mathbf{s}_3| + (\mathbf{s}_2 \cdot \mathbf{s}_3)|\mathbf{s}_1| + (\mathbf{s}_3 \cdot \mathbf{s}_1)|\mathbf{s}_2|} \right),$$

here $\mathbf{s}_1 \mathbf{s}_2 \mathbf{s}_3$ denotes the scalar triple product of the vectors.

The procedure of numerical calculation of the integral (7) depends on relative position of cells K_i and K_j . Three different cases should be considered: when the cells don't have common edges and vertices (non-neighbouring case), when cells have common edge (and two common vertices) and, finally, when they have common vertex only.

4.1 Non-neighbouring cells case

Calculation of the integral (7) when cells K_i and K_j don't have common edges and vertices, is provided numerically by using Gaussian quadrature formula:

$$\mathbf{I}_{ij} = \int_{K_i} \mathbf{J}_j(\mathbf{r}) d\mathbf{r} \approx A_i \sum_{p=1}^{N_{GP}} \omega_p \mathbf{J}_j(\boldsymbol{\eta}_p),$$

where N_{GP} is number of Gaussian points; ω_p are weight coefficients; $\boldsymbol{\eta}_p$ are positions of Gaussian points. Values of ω_p and $\boldsymbol{\eta}_p$ for different values of N_{GP} can be found, for example, in [8].

4.2 Neighbouring cells with common edge case

If cells K_i and K_j have common edge with directing unit vector \mathbf{e}_c , for example as it is shown on fig. 1, we should apply Gaussian integration to regular part $\mathbf{J}_j^{\text{reg}}(\mathbf{r})$, which has the form

$$\mathbf{J}_j^{\text{reg}}(\mathbf{r}) = \mathbf{J}_j(\mathbf{r}) - \left(\mathbf{e}_c \ln\left(\frac{|\mathbf{a}| \cdot |\mathbf{c}| - \mathbf{a} \cdot \mathbf{c}}{|\mathbf{b}| \cdot |\mathbf{c}| - \mathbf{b} \cdot \mathbf{c}}\right) + \mathbf{e}_1^{(j)} \ln\left(\frac{\mathbf{a} \cdot \mathbf{c}}{|\mathbf{c}|^2}\right) + \mathbf{e}_2^{(j)} \ln\left(-\frac{\mathbf{b} \cdot \mathbf{c}}{|\mathbf{c}|^2}\right) \right) \times \mathbf{n}_j,$$

or, the same written down in the other way,

$$\mathbf{J}_j^{\text{reg}}(\mathbf{r}) = \mathbf{J}_j(\mathbf{r}) - \left(\mathbf{e}_c \ln\left(\frac{|\mathbf{a}|(1 - \cos \alpha)}{|\mathbf{b}|(1 - \cos \beta)}\right) + \mathbf{e}_1^{(j)} \ln\left(\frac{|\mathbf{a}|}{|\mathbf{c}|} \cos \alpha\right) + \mathbf{e}_2^{(j)} \ln\left(\frac{|\mathbf{b}|}{|\mathbf{c}|} \cos \beta\right) \right) \times \mathbf{n}_j.$$

Where

$$\begin{aligned} \mathbf{e}_c &= \frac{\mathbf{c}}{|\mathbf{c}|} = \mathbf{e}_3^{(j)}, & \mathbf{c} &= \mathbf{r}_1^{(j)} - \mathbf{r}_3^{(j)}, & \mathbf{a} &= \mathbf{r}_1^{(j)} - \mathbf{r}, & \mathbf{b} &= \mathbf{r}_3^{(j)} - \mathbf{r}, \\ \cos \alpha &= \frac{\mathbf{a} \cdot \mathbf{c}}{|\mathbf{a}| \cdot |\mathbf{c}|}, & \cos \beta &= -\frac{\mathbf{b} \cdot \mathbf{c}}{|\mathbf{b}| \cdot |\mathbf{c}|}. \end{aligned}$$

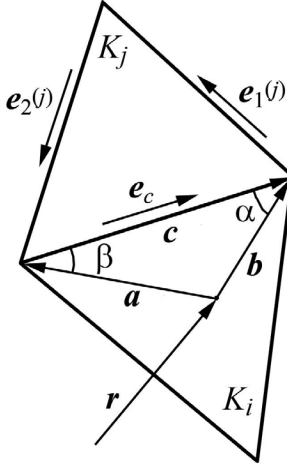


Figure 1: Cells K_i and K_j in case of having common edge

Denoting

$$\Psi_j^{\text{sing}} = \mathbf{e}_c \ln\left(\frac{|\mathbf{a}|(1 - \cos \alpha)}{|\mathbf{b}|(1 - \cos \beta)}\right) + \mathbf{e}_1^{(j)} \ln\left(\frac{|\mathbf{a}|}{|\mathbf{c}|} \cos \alpha\right) + \mathbf{e}_2^{(j)} \ln\left(\frac{|\mathbf{b}|}{|\mathbf{c}|} \cos \beta\right),$$

we finally obtain

$$\mathbf{J}_j^{\text{reg}}(\mathbf{r}) = \Theta_j \mathbf{n}_j + (\Psi_j - \Psi_j^{\text{sing}}) \times \mathbf{n}_j, \quad \mathbf{J}_j^{\text{sing}}(\mathbf{r}) = \Psi_j^{\text{sing}} \times \mathbf{n}_j.$$

All scalar multipliers of Ψ_j^{sing} can be integrated analytically over the cell K_i :

$$\begin{aligned} q_c &= \int_{K_i} \ln\left(\frac{|\mathbf{a}|(1-\cos\alpha)}{|\mathbf{b}|(1-\cos\beta)}\right) dr = \\ &= \frac{|\mathbf{c}|^2}{2} \left(\sin\alpha \ln \frac{|\mathbf{c}|^2 \cos^2(\frac{\alpha_i}{2}) \sin\beta_i}{2A_i \cos^2(\frac{\alpha_i+\beta_i}{2})} + \sin\beta \ln \frac{|\mathbf{c}|^2 \cos^2(\frac{\beta_i}{2}) \sin\alpha_i}{2A_i \cos^2(\frac{\alpha_i+\beta_i}{2})} \right) - A_i \ln \left(\tan \frac{\alpha_i}{2} \tan \frac{\beta_i}{2} \right), \\ q_1 &= \int_{K_i} \ln\left(\frac{|\mathbf{a}|}{|\mathbf{c}|} \cos\alpha\right) dr = -\frac{A_i}{2} \left(3 - 2 \frac{\tan\beta_i}{\tan\alpha_i} \ln \left(1 + \frac{\tan\alpha_i}{\tan\beta_i} \right) \right), \\ q_2 &= \int_{K_i} \ln\left(\frac{|\mathbf{b}|}{|\mathbf{c}|} \cos\beta\right) dr = -\frac{A_i}{2} \left(3 - 2 \frac{\tan\alpha_i}{\tan\beta_i} \ln \left(1 + \frac{\tan\beta_i}{\tan\alpha_i} \right) \right). \end{aligned}$$

Here α_i and β_i are angles of the triangle K_i , which adjoin the common edge of the cells K_i and K_j . Finally,

$$\mathbf{I}_{ij} = \int_{K_i} \mathbf{J}_j^{\text{reg}}(\mathbf{r}) dr + \int_{K_i} \mathbf{J}_j^{\text{sing}}(\mathbf{r}) dr \approx \left(A_i \sum_{p=1}^{N_{GP}} \omega_p \mathbf{J}_j^{\text{reg}}(\boldsymbol{\eta}_p) \right) + \left(\mathbf{e}_c q_c + \mathbf{e}_1^{(j)} q_1 + \mathbf{e}_2^{(j)} q_2 \right) \times \mathbf{n}_j.$$

4.3 Neighbouring cells with common vertex case

If cells K_i and K_j have common vertex, for example as it is shown on fig. 2, the regular part $\mathbf{J}_j^{\text{reg}}(\mathbf{r})$ has the following form (the previous denotation is used):

$$\mathbf{J}_j^{\text{reg}}(\mathbf{r}) = \mathbf{J}_j(\mathbf{r}) - \ln\left(\frac{|\mathbf{a}|}{\sqrt{A_j}}\right) \left(\mathbf{e}_1^{(j)} + \mathbf{e}_3^{(j)} \right) \times \mathbf{n}_j$$

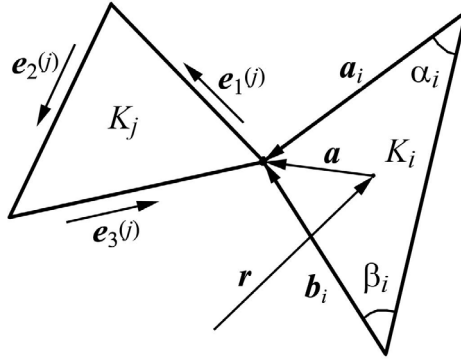


Figure 2: Cells K_i and K_j in case of having common vertex

Again, denoting

$$\Psi_j^{\text{sing}} = \left(\mathbf{e}_1^{(j)} + \mathbf{e}_3^{(j)} \right) \ln\left(\frac{|\mathbf{a}|}{\sqrt{A_j}}\right),$$

we obtain

$$\mathbf{J}_j^{\text{reg}}(\mathbf{r}) = \Theta_j \mathbf{n}_j + (\Psi_j - \Psi_j^{\text{sing}}) \times \mathbf{n}_j, \quad \mathbf{J}_j^{\text{sing}}(\mathbf{r}) = \Psi_j^{\text{sing}} \times \mathbf{n}_j.$$

The scalar multiplier in Ψ_j^{sing} can be integrated analytically over the cell K_i :

$$\begin{aligned} q &= \int_{K_i} \ln\left(\frac{|\mathbf{a}|}{\sqrt{A_j}}\right) dr = \\ &= \frac{1}{4} \left(2A_i \left(\ln \frac{A_i}{A_j} - 3 \right) + 2(\pi - \alpha_i - \beta_i) |\mathbf{a}_i| \cdot |\mathbf{b}_i| \sin \alpha_i \sin \beta_i + \right. \\ &\quad \left. + |\mathbf{a}_i|^2 \sin 2\alpha_i \ln \frac{|\mathbf{a}_i|^2}{A_i} + |\mathbf{b}_i|^2 \sin 2\beta_i \ln \frac{|\mathbf{b}_i|^2}{A_i} \right). \end{aligned}$$

Here α_i and β_i are angles of the triangle K_i , which don't adjoin the common vertex of the cells K_i and K_j . Finally,

$$\mathbf{I}_{ij} = \int_{K_i} \mathbf{J}_j^{\text{reg}}(\mathbf{r}) dr + \int_{K_i} \mathbf{J}_j^{\text{sing}}(\mathbf{r}) dr \approx \left(A_i \sum_{p=1}^{N_{GP}} \omega_p \mathbf{J}_j^{\text{reg}}(\boldsymbol{\eta}_p) \right) + q \left(\mathbf{e}_1^{(j)} + \mathbf{e}_3^{(j)} \right) \times \mathbf{n}_j.$$

5 CONCLUSIONS

The dirived formulae for \mathbf{I}_{ij} make it possible to construct numerical procedure for solving of the discrete analogue of the integral equation for vortex sheet intensity calculation in the framework of ‘tangent’ approach. The analogue formulae can be easily obtained for vortex element upon boundary cells influence calculation as well as cells upon vortex element calculation. It allows to use arbitrary triangular mesh on body surface and to refine mesh near sharp edges, that is especially important for flow around 3D wings simulation.

REFERENCES

- [1] Cottet, G.-H. and Koumoutsakos, P.D. *Vortex Methods: Theory and Practice*. CUP (2000).
- [2] Marchevsky, I.K. and Shcheglov, G.A. 3D vortex structures dynamics simulation using vortex fragmentons, *ECCOMAS 2012, e-Book Full Papers*, Vienna (2012), 5716–5735.
- [3] Kempka S.N., Glass M.W., Peery J.S. and Strickland J.H. Accuracy considerations for implementing velocity boundary conditions in vorticity formulations, *SANDIA REPORT SAND96-0583*, UC-700 (1996).

- [4] Kuzmina, K.S. and Marchevsky, I.K. On Numerical Schemes in 2D Vortex Element Method for Flow Simulation Around Moving and Deformable Airfoils, *Advanced Problems in Mechanics: Proceedings of the XLII Summer School-Conference*, St.Petersburg (2014), 335–344.
- [5] Antonov, V.A., Nikiforov, I.I. and Kholshevnikov, K.V. *Elements of the theory of the gravitational potential, and some instances of its explicit expression*. St.-Petersburg University Press (2008).
- [6] Gradshteyn, I.S., Ryzhik, I.M., Jeffrey, A. (Ed.) and Zwillinger, D. (Ed.) *Gradshteyn and Ryzhik's Table of Integrals, Series, and Products*. Elsevier (2007).
- [7] Van Oosterom, A. and Strackee, J. The Solid Angle of a Plane Triangle. *IEEE Trans. Biom. Eng. BME-30* (1983) **2**:125–126.
- [8] Zienkiewicz, O.C., Taylor, R.L. and Zhu, J.Z. *The Finite Element Method: Its Basis and Fundamentals*. Elsevier (2013).

THE MODIFIED NUMERICAL SCHEME FOR 2D FLOW-STRUCTURE INTERACTION SIMULATION USING MESHLESS VORTEX ELEMENT METHOD

KSEНИЯ С. КУЗМИНА¹ AND ИЛЯ К. МАРЧЕВСКИЙ¹

¹ Applied Mathematics dep., Bauman Moscow State Technical University (BMSTU)
2-nd Baumanskaya st., 105005 Moscow, Russia
E-mail: kuz-ksen-serg@yandex.ru, iliامarchevsky@mail.ru

Key words: Vortex Element Method, 2D Viscous Incompressible Flow, Flow-Structure Interaction, Integral Equation, Numerical Scheme

Abstract. The modification of the meshless Vortex Element Method based on the Viscous Vortex Domain Method and non-classical approach to boundary conditions satisfaction is developed for numerical simulation in 2D FSI-problems for incompressible flows. The developed approach preserves all advantages of meshless lagrangian vortex methods, however the accuracy of vortex layer computation is much higher than in ‘classical’ realizations of vortex methods. No-slip boundary condition is satisfied through limit value of tangential velocity vanishing on the airfoil surface while in ‘classical’ approach normal components of velocity are used. These approaches lead to Fredholm-type integral equation of the second kind and Hilbert-type singular integral equation of the first kind correspondingly.

The developed method allows to simulate flow around fixed, movable and deformable airfoils while the computational cost of the algorithm remains nearly the same. The discretization scheme is constructed in such a way that it provides exactly the same results in direct and inversed motion of the airfoil (i. e. when the rigid airfoil moves translationally in still media and when the airfoil is fixed in the unbounded incident flow).

In addition to number of model problems which shows advantages of the developed approach and its accuracy order, the well-known two-way coupled problem of vortex induced vibrations and wind resonance phenomenon simulation is considered. The obtained dependency of the oscillations amplitude on the eigenfrequency of linear visco-elastic mechanical system (including hysteresis phenomenon) is in good agreement with experimental data and other known numerical simulations. It is shown that meshless vortex method allows to provide numerical simulation in such problems with sufficiently small requirements to memory and computational time and small numerical viscosity.

1 INTRODUCTION

Vortex element method [1, 2, 3] is a well-known meshfree lagrangian CFD method for 2D flow simulation around airfoils. Firstly it had been developed for numerical simulation of inviscid flows, but later it was generalized to newtonian viscous flows. There are several approaches for taking viscosity influence into account: particle strength exchange method, combined mesh and meshfree methods et al. We use ‘Viscous Vortex Domain’ (VVD) method developed by G.Ya. Dynnikova [4, 5] since this approach is purely lagrangian and due to its high accuracy which proved in number of researches.

When using vortex element method the flow around the fixed airfoil is simulated by a thin vortex layer on the airfoil surface while for the flow simulation around moving or deformable airfoil in general case not only vortex layer but also source layer should be introduced on the airfoil surface. Their intensities depend on time, so they should be computed every time step. If airfoil motion law is known, source layer intensity and the so-called ‘attached’ vortex layer intensity can be found explicitly as normal and tangent projections of airfoil surface velocities. At the same time ‘free’ vortex layer intensity is a priori unknown. The accuracy of the vortex layer intensity computation defines the accuracy of the boundary condition satisfaction on the airfoil surface and consequently the accuracy of vortex wake simulation around the airfoil. However, the existent well-known numerical schemes (Discrete Vortex Method), normally being used in vortex element method, sometimes lead to significant errors.

The aim of this paper is to develop modern numerical scheme for vortex element method based on alternative approaches to boundary condition satisfaction for movable and deformable airfoil and to compare its accuracy in case of flow simulation around smooth airfoils and airfoils with sharp edge.

2 GOVERNING EQUATIONS

Viscous incompressible flow is described by Navier — Stokes equations

$$\nabla \cdot \vec{V} = 0, \quad \frac{\partial \vec{V}}{\partial t} + (\vec{V} \cdot \nabla) \vec{V} = \nu \Delta \vec{V} - \frac{\nabla p}{\rho},$$

where $\vec{V}(\vec{r}, t)$ is flow velocity, $p(\vec{r}, t)$ — pressure, $\rho = \text{const}$ — density of the flow, ν — kinematic viscosity coefficient.

No-slip boundary condition on the movable airfoil surface and boundary conditions of perturbation decay on infinity should be satisfied:

$$\vec{V}(\vec{r}, t) = \vec{V}_K(\vec{r}, t), \quad \vec{r} \in K, \quad \vec{V}(\vec{r}, t) \rightarrow \vec{V}_\infty, \quad p(\vec{r}, t) \rightarrow p_\infty, \quad |\vec{r}| \rightarrow \infty.$$

Here \vec{V}_∞ and p_∞ are constant velocity and pressure of the incident flow.

Navier — Stokes equations can be written down in Helmholtz form [6]:

$$\frac{\partial \vec{\Omega}}{\partial t} + \nabla \times (\vec{\Omega} \times \vec{U}) = 0. \quad (1)$$

Here $\vec{\Omega}(\vec{r}, t) = \nabla \times \vec{V}(\vec{r}, t)$ is vorticity field; $\vec{U}(\vec{r}, t) = \vec{V}(\vec{r}, t) + \vec{W}(\vec{r}, t)$, $\vec{W}(\vec{r}, t)$ is the so-called ‘diffusive velocity’, which is proportional to viscosity coefficient [4]:

$$\vec{W}(\vec{r}, t) = \nu \frac{(\nabla \times \vec{\Omega}) \times \vec{\Omega}}{|\vec{\Omega}|^2}.$$

Equation (1) means that vorticity which exists in the flow moves and its velocity is \vec{U} . ‘New’ vorticity is being generated only on airfoil surface, so we can consider that the vorticity distribution in the flow $\Omega(\vec{r}, t)$ is always known.

The streamlined airfoil influence is equivalent to superposition of the attached vortex $\gamma_{att}(\vec{r}, t)$ and source $q_{att}(\vec{r}, t)$ layers influences and free vortex layer $\gamma(\vec{r}, t)$ influence:

$$\gamma_{att}(\vec{r}, t) = \vec{V}_K(\vec{r}, t) \cdot \vec{\tau}(\vec{r}, t), \quad q_{att}(\vec{r}, t) = \vec{V}_K(\vec{r}, t) \cdot \vec{n}(\vec{r}, t), \quad \vec{r} \in K,$$

where $\vec{n}(\vec{r}, t)$ and $\vec{\tau}(\vec{r}, t)$ are normal and tangent unit vectors on the airfoil surface.

Using generalized Helmholtz decomposition ideas [7] flow velocity can be computed using Biot — Savart law:

$$\begin{aligned} \vec{V}(\vec{r}, t) &= \vec{V}_\infty + \frac{1}{2\pi} \int_{S(t)} \frac{\vec{\Omega}(\vec{\xi}, t) \times (\vec{r} - \vec{\xi})}{|\vec{r} - \vec{\xi}|^2} dS + \frac{1}{2\pi} \oint_{K(t)} \frac{\vec{\gamma}(\vec{\xi}, t) \times (\vec{r} - \vec{\xi})}{|\vec{r} - \vec{\xi}|^2} dl_K + \\ &+ \frac{1}{2\pi} \oint_{K(t)} \frac{\vec{\gamma}_{att}(\vec{\xi}, t) \times (\vec{r} - \vec{\xi})}{|\vec{r} - \vec{\xi}|^2} dl_K + \frac{1}{2\pi} \oint_{K(t)} \frac{q_{att}(\vec{\xi}, t)(\vec{r} - \vec{\xi})}{|\vec{r} - \vec{\xi}|^2} dl_K. \end{aligned} \quad (2)$$

Here $S(t)$ is current flow region, $K(t)$ is current airfoil surface; attached and free vortex layer intensities vectors are $\vec{\gamma}_{att} = \gamma_{att} \vec{k}$ and $\vec{\gamma} = \gamma \vec{k}$ and by analogy $\vec{\Omega} = \Omega \vec{k}$, where \vec{k} is unit vector orthogonal to the flow plane; on the airfoil surface $\vec{n}(\vec{r}, t) \times \vec{\tau}(\vec{r}, t) = \vec{k}$.

We assume velocity of the airfoil surface $\vec{V}_K(\vec{r}, t)$ to be known function which is continuous, so vortex layer intensity $\gamma(\vec{\xi}, t)$ can be found from no-slip boundary condition on airfoil surface:

$$\vec{V}(\vec{r}, t) = \vec{V}_K(\vec{r}, t), \quad \vec{r} \in K.$$

If the velocity field $\vec{V}(\vec{r}, t)$ is considered not only in the flow region, but in the whole two-dimensional space, it has discontinuity on the airfoil surface. It can be shown [1] that the limit value of flow velocity from the airfoil side on the airfoil surface is

$$\vec{V}_-(\vec{r}, t) = \vec{V}(\vec{r}, t) - \frac{\gamma(\vec{r}, t) - \gamma_{att}(\vec{r}, t)}{2} \vec{\tau}(\vec{r}, t) + \frac{q_{att}(\vec{r}, t)}{2} \vec{n}(\vec{r}, t). \quad (3)$$

Free vortex layer intensity $\gamma(\vec{\xi}, t)$ can be found from no-slip boundary condition on airfoil surface:

$$\vec{V}_-(\vec{r}, t) = \vec{V}_K(\vec{r}, t), \quad \vec{r} \in K.$$

3 NUMERICAL SCHEMES FOR VORTEX LAYER INTENSITY COMPUTATION

When solving problem using Vortex Element Method, vortex wakes normally are being simulated by discrete vortex-type singularities (vortex elements):

$$\Omega(\vec{r}, t) = \sum_{i=1}^n \Gamma_i \delta(\vec{r} - \vec{r}_i(t)). \quad (4)$$

Here n is number of vortex elements, Γ_i and \vec{r}_i are intensities and positions of vortex elements correspondingly, δ is Dirac delta function. Taking into account (4) we obtain

$$\begin{aligned} \vec{V}_-(\vec{r}) &= \vec{V}_\infty + \sum_{w=1}^n \frac{\Gamma_w}{2\pi} \frac{\vec{k} \times (\vec{r} - \vec{\xi}_w)}{|\vec{r} - \vec{\xi}_w|^2} + \frac{1}{2\pi} \oint_K \frac{\vec{\gamma}(\vec{\xi}) \times (\vec{r} - \vec{\xi})}{|\vec{r} - \vec{\xi}|^2} dl_\xi + \frac{1}{2\pi} \oint_K \frac{\vec{\gamma}_{att}(\vec{\xi}) \times (\vec{r} - \vec{\xi})}{|\vec{r} - \vec{\xi}|^2} dl_\xi + \\ &+ \frac{1}{2\pi} \oint_K \frac{q_{att}(\vec{\xi})(\vec{r} - \vec{\xi})}{|\vec{r} - \vec{\xi}|^2} dl_\xi - \frac{\vec{\gamma}(\vec{r}) - \vec{\gamma}_{att}}{2} \times \vec{n}(\vec{r}) + \frac{q_{att}(\vec{r})}{2} \vec{n}(\vec{r}), \quad \vec{r} \in K. \end{aligned} \quad (5)$$

3.1 *N*-scheme, based on equality between normal components of velocities

Classical approach which is normally being used in Discrete Vortex Method [1], presupposes that the unknown function $\gamma(\vec{r})$ should be found from the equality between *normal* components of the flow velocity limit value and the airfoil surface velocity:

$$\vec{V}_-(\vec{r}) \cdot \vec{n}(\vec{r}) = \vec{V}_K(\vec{r}) \cdot \vec{n}(\vec{r}), \quad \vec{r} \in K. \quad (6)$$

This equation leads to singular integral equation and the principal value of the corresponding integral should be understood in Cauchy sense.

The equation (6) has infinitely many solutions; to select the unique solution this equation should be solved together with the following equation:

$$\oint_K \gamma(\vec{\xi}) dl_K = \Gamma. \quad (7)$$

Total circulation Γ of the vorticity layer on the airfoil can be found from problem statement; it depends on angular velocity and angular acceleration of the airfoil [8].

In order to find numerical solution of equations (6), (7) the so-called ‘Discrete Vortex-type’ quadrature formula is used, which allows to compute numerically Cauchy principal values but it imposes strong constraints on airfoil discretization: polygon legs (hereinafter we call them ‘panels’) which approximate curvilinear airfoil surface should have nearly the same lengths, integral equation is satisfied only in ‘collocation’ points \vec{k}_i placed precisely at centers of panels. All the vorticity from vortex layer assumed to be concentrated in vortex elements with circulations Γ_j placed in vertices \vec{c}_j of the polygon (i. e., at the ends of panels).

Such an approach is hereinafter called N -scheme. It should be noted that vortex wake influence at collocation points can be computed straightforward, however, attached vortex and source layers influences computation is not a trivial procedure.

Systematic studies of the N -scheme accuracy were carried out for the case of a fixed rigid (non-deformable) airfoil. Numerical calculations show that this scheme doesn't allow to obtain high accuracy of free vortex layer intensity calculation. Moreover, significant errors were obtained not only for airfoils with sharp edges (it can be explained easily), but also for circular airfoil when there are vortex elements in the wake near the airfoil — this situation quite typical. Taking into account these disadvantages and restrictions, we can admit that N -scheme has limited applicability, and its accuracy can be not sufficient for correct flow simulation around airfoil. These disadvantages can become unacceptable in case of movable and deformable airfoils.

3.2 T -scheme, based on equality between tangent components of velocities

In order to solve problems, described in previous subsection, another approach can be implemented. It is shown [7] that ‘boundary condition’ (6) is equivalent from mathematical point of view to the following condition

$$\vec{V}_-(\vec{r}) \cdot \vec{\tau}(\vec{r}) = \vec{V}_K(\vec{r}) \cdot \vec{\tau}(\vec{r}), \quad \vec{r} \in K, \quad (8)$$

which corresponds to the equality between *tangent* components of the flow velocity limit value and the airfoil surface velocity.

The equation (8) in association with (5) leads to the following integral equation

$$\begin{aligned} \frac{1}{2\pi} \oint_K \left(\frac{\vec{k} \times (\vec{r} - \vec{\xi})}{|\vec{r} - \vec{\xi}|^2} \cdot \vec{\tau}(\vec{r}) \right) \gamma(\vec{\xi}) dl_\xi - \frac{\gamma(\vec{r})}{2} = \\ = - \left(\left(\vec{V}_\infty - \vec{V}_K(\vec{r}) \right) \cdot \vec{\tau}(\vec{r}) + \sum_{w=1}^n \frac{\Gamma_w}{2\pi} \frac{\vec{k} \times (\vec{r} - \vec{\xi}_w)}{|\vec{r} - \vec{\xi}_w|^2} \cdot \vec{\tau}(\vec{r}) + \right. \\ \left. + \frac{1}{2\pi} \oint_K \left(\frac{\vec{k} \times (\vec{r} - \vec{\xi})}{|\vec{r} - \vec{\xi}|^2} \cdot \vec{\tau}(\vec{r}) \right) \gamma_{att}(\vec{\xi}) dl_\xi + \frac{1}{2\pi} \oint_K \frac{(\vec{r} - \vec{\xi}) \cdot \vec{\tau}(\vec{r})}{|\vec{r} - \vec{\xi}|^2} q_{att}(\vec{\xi}) dl_\xi + \frac{\gamma_{att}(\vec{r})}{2} \right) \end{aligned} \quad (9)$$

It should be noted that in case of smooth airfoils the equation (9) is Fredholm-type integral equation with bounded kernel. The equation (9) as well as the singular equation which follows from (6) has infinitely many solutions; in order to select the unique solution the same equation (7) should be solved together with it.

This approach doesn't have restrictions of N -scheme. Nevertheless, if we use nearly the same ideas as in Discrete Vortex Method, the accuracy will remain very low. So it seems to be rationally to use some other approach: firstly, not to concentrate vorticity into vortex elements and secondly solve integral equation (9) in weak formulation (i. e., on average along the panels) instead of its satisfying at certain collocation points.

Vortex layer intensity is supposed to be piecewise constant function, we denote its unknown value γ_i on the i^{th} panel and intensities of attached vortex and sources layers are similarly should be approximated by piecewise constant functions $\gamma_{att,i}$ and $q_{att,i}$ correspondingly. So the integral equation (9) is approximated by the following algebraic equations:

$$\begin{aligned} & \frac{1}{L_i} \left(\int_{K_i} \sum_{j=1}^N \frac{\gamma_j}{2\pi} \left(\int_{K_j} \frac{\vec{k} \times (\vec{r} - \vec{\xi})}{|\vec{r} - \vec{\xi}|^2} dl_\xi \right) dl_r \right) \cdot \vec{\tau}_i - \frac{\gamma_i}{2} = \\ & = -\frac{1}{L_i} \left(\int_{K_i} \sum_{w=1}^n \frac{\Gamma_w}{2\pi} \left(\frac{\vec{k} \times (\vec{r} - \vec{r}_w)}{|\vec{r} - \vec{r}_w|^2} \right) \cdot \vec{\tau}_i dl_r + \int_{K_i} \sum_{j=1}^N \frac{\gamma_j^{att}}{2\pi} \left(\int_{K_j} \frac{\vec{k} \times (\vec{r} - \vec{\xi})}{|\vec{r} - \vec{\xi}|^2} \cdot \vec{\tau}_i dl_\xi \right) dl_r + \right. \\ & \quad \left. + \int_{K_i} \sum_{j=1}^N \frac{q_j^{att}}{2\pi} \left(\int_{K_j} \frac{(\vec{r} - \vec{\xi}) \cdot \vec{\tau}_i}{|\vec{r} - \vec{\xi}|^2} dl_\xi \right) dl_r \right) - (\vec{V}_\infty - \vec{V}_{K,i}) \cdot \vec{\tau}_i - \frac{\gamma_i^{att}}{2}, \quad i = 1, \dots, N. \quad (10) \end{aligned}$$

Here L_i is the i^{th} panel length which denoted as K_i ; Γ_w and \vec{r}_w are circulations and positions of vortex elements which simulate vortex wake, $w = 1, \dots, n$; $\gamma_{att,j}$ and $q_{att,j}$ are average values of attached vortex and sources layers along the j^{th} panel correspondingly; $\vec{V}_{K,i}$ is average velocity of the airfoil surface along the i^{th} panel.

Average values in (10) should be calculated by using the following formulae:

$$\gamma_i^{att} = \frac{1}{L_i} \int_{K_i} \gamma_{att}(\vec{\xi}) dl_\xi, \quad q_i^{att} = \frac{1}{L_i} \int_{K_i} q_{att}(\vec{\xi}) dl_\xi, \quad \vec{V}_{K,i} = \frac{1}{L_i} \int_{K_i} \vec{V}_K(\vec{\xi}) dl_\xi,$$

but in practical calculations approximate equalities are used:

$$\gamma_i^{att} \approx \gamma_{att}(\vec{k}_i), \quad q_i^{att} \approx q_{att}(\vec{k}_i), \quad \vec{V}_{K,i} \approx \vec{V}_K(\vec{k}_i).$$

We will call the proposed approach T -scheme. For fixed rigid airfoil this approach is developed in [9]. Coefficients of system (10) can be computed analytically; formulae for all integrals in this system are also derived in [9].

The equation (7), which allows to obtain the unique solution, in case of using T -scheme is approximated by equation

$$\sum_{i=1}^N \gamma_i L_i = \Gamma^*.$$

The T -scheme allows to obtain much more accurate results in comparison with N -scheme when simulating flows around fixed rigid airfoils, so it is preferable to use T -scheme for numerical flow simulation around movable and deformable airfoils.

4 NUMERICAL EXPERIMENTS

Now we compare numerical results which can be obtained by using N - and T -schemes. We consider airfoils to be installed at a certain angle of incidence and we assume that they move in the flow with constant horizontal velocity $V = 1$ (direct motion) as well as the same airfoils being immovable in the horizontal constant incoming flow $V_\infty = 1$ (inverse motion); stationary solutions of these problems are the same. Two possible ways of airfoils splitting into panels are considered.

4.1 The numerical scheme with splitting using conform mapping

The simplest implementation is to split the airfoil into panels using the conformal mapping.

Simple shape of some airfoils (circular, elliptical and Zhukovsky airfoils) makes it possible to construct conformal mapping $\xi = \hat{\zeta}(z)$ of the airfoil exteriority on the circle exteriority, that satisfies the necessary conditions at infinity, and the inverse mapping $z = \zeta(\xi)$, transforming the circle exteriority to the airfoil exteriority.

For elliptical and Zhukovsky airfoils these mappings are the following:

$$\hat{\zeta}(z) = \frac{1}{R} \left(z + \sqrt{z^2 - a^2} - H \right), \quad \zeta(\xi) = \frac{1}{2} \left(R\xi + H + \frac{a^2}{R\xi + H} \right). \quad (11)$$

For elliptical airfoils $a = \sqrt{a_1^2 - b_1^2}$, $R = a_1 + b_1$, $H = 0$, a_1 and b_1 are major and minor semiaxes of the ellipse. For Zhukovsky airfoil $R = \sqrt{(a + d \cos \phi)^2 + (h + d \sin \phi)^2}$, $\phi = \arctan \frac{h}{a}$, $H = ih - de^{-i\phi}$, a , d and h are arbitrary parameters, which correspond to length, width and curvature of the airfoil.

Therefore the circle with radius R is approximated with regular n -gon with vertices $\xi_i = Re^{\frac{2\pi i}{N}}$, $i = 0, \dots, (N-1)$, so, vertices of the n -gon which approximates the airfoil are $z_i = \zeta(\xi_i)$. Ends of panels are considered as points of vortices birth \vec{c}_i , collocation points \vec{k}_i are placed at centers of the panels.

Using these conformal mapping we obtain panels with different lengths, and lengths of panels are smaller near ends of the major axis of the elliptical airfoil and near forward part and sharp edge of Zhukovsky airfoil. Significant difference between the lengths of the largest and the smallest panels (almost exactly equal to the ratio of the semiaxes of the ellipse) is not essential, because lengths of neighbor panels differ slightly. Therefore, according to the formal criteria for N -scheme applicability, both N -scheme and T -scheme can be used for vortex layer intensity calculation.

When flow around Zhukovsky airfoil simulating the lengths ratio of the largest panel to smallest increases almost proportionally to the number of panels, and there are always panels (near sharp edge) with significantly different lengths, which are neighbors (for Zhukovsky airfoil with parameters $a = 3.5$, $d = 0.4$, $h = 0.3$ this ratio is about 3. Therefore, N -scheme is unusable for the flow simulation around Zhukovsky airfoil: near the sharp edge there will be significant error. T -scheme for this problem is preferred.

Model problems of vortex layer intensity calculation for elliptical airfoil ($a_1/b_1 = 10$) and Zhukovsky airfoil ($a = 3.5$, $d = 0.4$, $h = 0.3$) have been solved. Both airfoils were installed at the angle of incidence $\beta = \pi/6$. Computations were performed for different number of panels N in cases of direct motion (the airfoil moves in a stationary media) and reversed motion (stationary airfoil in the incoming flow).

If there is no vortex wake near the airfoil these problems can be solved analytically using conformal mappings technique. Using the formulae [9], we can obtain the exact solution $\gamma_{exact}(\vec{r})$ for the vortex layer intensity.

For error estimation in case of using N -scheme we calculate the value

$$\|\Delta\Gamma\|_N = \max_i |\Gamma_i^{ex,c} - \Gamma_i^*|, \quad \Gamma_i^{ex,c} = \int_{K_{i-1}}^{K_i} \gamma_{exact}(\vec{\xi}) dl_\xi. \quad (12)$$

Here Γ_i^* is calculated circulation of vortex elements, $\Gamma_i^{ex,c}$ is circulation obtained from the exact value of the vortex layer intensity on the panels around i^{th} point of birth \vec{c}_i .

When using T -scheme for error estimation we use the following formula:

$$\|\Delta\Gamma\|_T = \max_i [(|\gamma_i^{exact} - \gamma_i|) L_i], \quad \text{where} \quad \gamma_i^{exact} = \frac{1}{L_i} \int_{K_i} \gamma_{exact}(\vec{\xi}) dl_\xi. \quad (13)$$

The results of flow simulation around elliptical airfoil in cases of direct and reversed motion using N -scheme are shown on fig. 1 on double logarithmic scale.

It is seen that in case of elliptical airfoil N -scheme provides second-order accuracy by increasing the number of panels in both forward and inverse motion; at the same time for inverse motion (fixed airfoil in the flow) the error is larger. If we use conformal mapping for splitting Zhukovsky airfoil into panels calculated error $\|\Delta\Gamma\|_N$ of N -scheme is unacceptably high.

When using T -scheme it is possible to obtain results quite close to the exact solution for both elliptical and Zhukovsky airfoils. The errors $\|\Delta\Gamma\|_T$ of vortex layer intensity calculations for elliptical and Zhukovsky airfoils using T -scheme are shown on fig. 2 on double logarithmic scale.

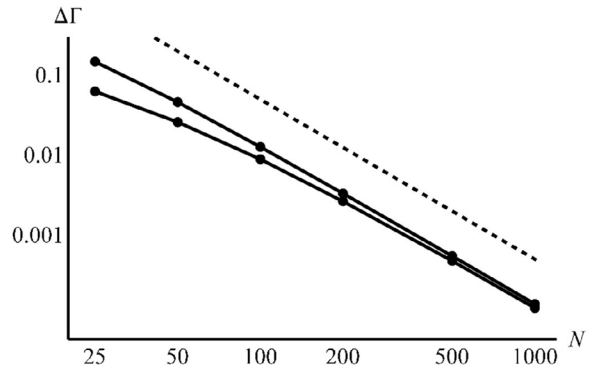


Figure 1: Error $\|\Delta\Gamma\|_N$ of flow simulation around elliptical airfoil (on double logarithmical scale) using N -scheme with different number of panels; dashed line corresponds to $O(N^{-2})$ error

4.2 The numerical scheme with equal lengths of panels

An alternative approach to splitting airfoil into panels assumes that all panels have equal (or nearly equal) lengths.

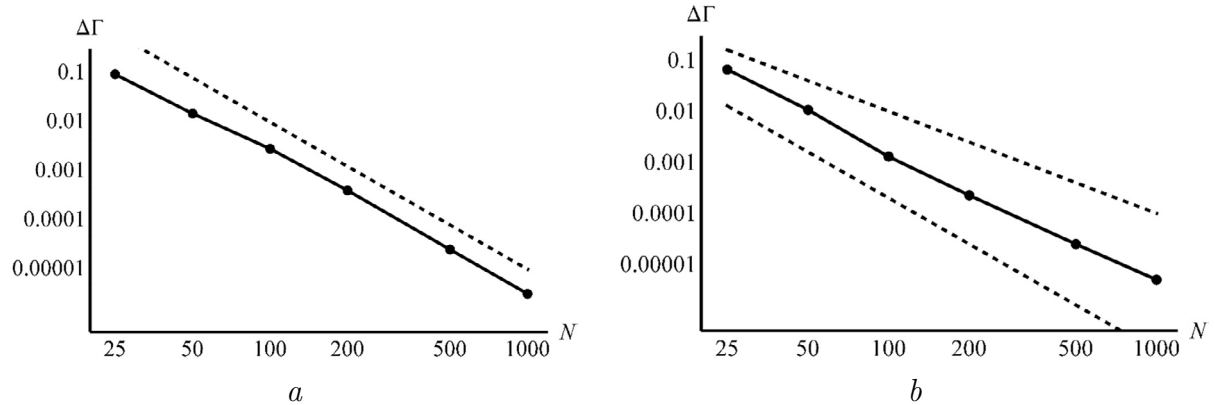


Figure 2: Error $\|\Delta\Gamma\|_T$ of flow simulation around airfoil (on double logarithmical scale) using T -scheme with conformal mapping usage for airfoil splitting: *a* — elliptical airfoil, dashed line corresponds to $O(N^{-3})$ error; *b* — Zhukovsky airfoil, dashed lines correspond to $O(N^{-2})$ and $O(N^{-3})$ errors

As before, in case of using N -scheme the results of the calculation are different for direct and inverse motion, in case of using T -scheme solutions coincide.

The dependence of error of flow simulation around an elliptical airfoil using schemes with equal lengths of panels is shown in fig. 3. It is seen that simulation for direct motion using N -scheme allows to obtain the second accuracy order, and for reversed motion — the third order (fig. 3, *a*). For large number of panels the simulation of the flow around an elliptical airfoil using T -scheme allows to get the third accuracy order (fig. 3, *b*).

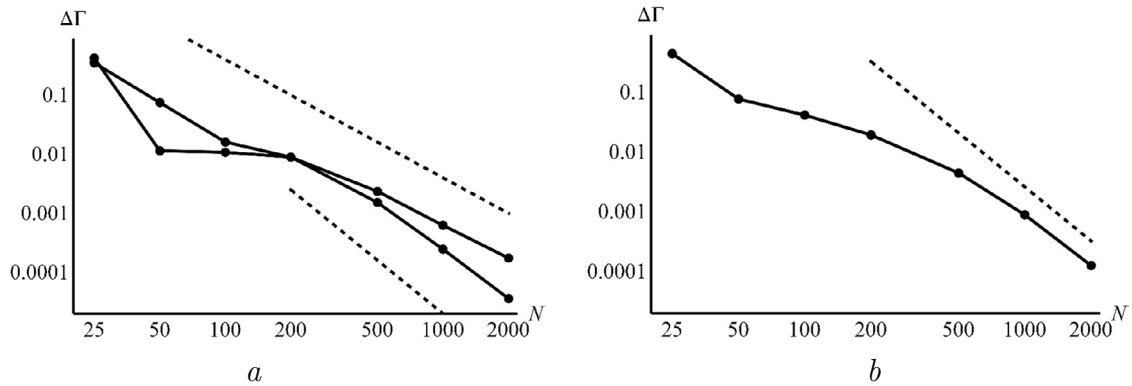


Figure 3: Errors of flow simulation around elliptical airfoil (on double logarithmical scale) using schemes with equal lengths of panels: *a* — N -scheme, dashed lines correspond to $O(N^{-2})$ and $O(N^{-3})$ errors; *b* — T -scheme, dashed line corresponds to $O(N^{-3})$ error

When simulating of the flow around Zhukovsky airfoil using N -scheme with uniform splitting into panels it is possible to obtain correct approximate solution, but only for inverse motion (fig. 4, *a*); and the error decreases very slowly ($O(N^{-0.5})$). In case of direct motion, the error is unacceptably high and it isn't decrease with increasing of N .

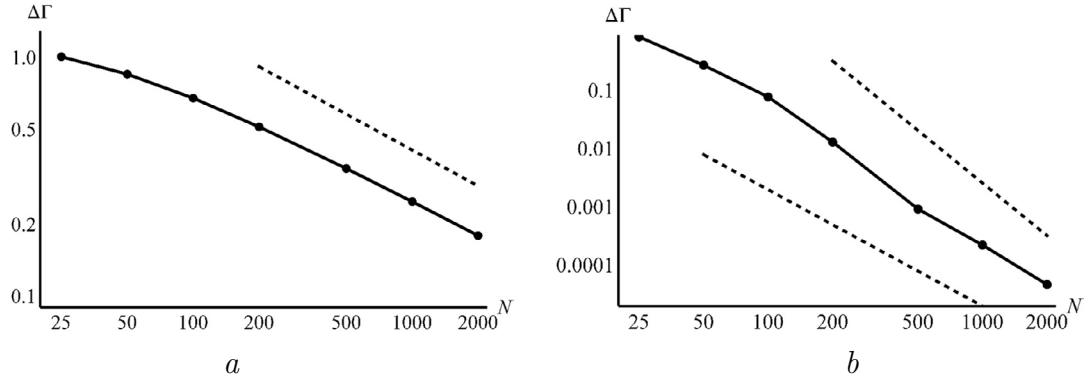


Figure 4: Errors of flow simulation around Zhukovsky airfoil (on double logarithmical scale) using schemes with equal lengths of panels: *a* — *N*-scheme, dashed line corresponds to $O(N^{-0.5})$ error; *b* — *T*-scheme, dashed lines correspond to $O(N^{-2})$ and $O(N^{-3})$ errors

It is seen that the *T*-scheme with uniform splitting of airfoil into panels in case of flow calculation around Zhukovsky airfoil ensures a close to second order accuracy for sufficiently large number of panels.

4.3 Wind resonance phenomenon simulation

For verification of the developed scheme for movable airfoils we consider the motion of the circular airfoil with diameter D across the stream (with one degree of freedom) [10]. Constrain of airfoil assumed to be linear viscoelastic Kelvin — Voigt-type (fig. 5) and its motion is described by the following equation:

$$m\ddot{y}_* + b\dot{y}_* + ky_* = F_y. \quad (14)$$

Here m is the airfoil mass, b is small damping factor, k is the elasticity coefficient of the constraint, F_y is lift force, y_* is the deviation from the equilibrium. The natural frequency of the system $\omega \approx \sqrt{k/m}$ can be changed by varying of the coefficient k .

In all numerical simulations with the following values of dimensionless parameters have been chosen: $\text{Re} = 1000$, $V_\infty = 3.0$, $m = 39.15$, $b = 0.731$. The dimensionless natural frequency of the system is in the following range:

$$\text{Sh}_\omega = \frac{\omega}{2\pi} \cdot \frac{D}{V_\infty} = 0.150 \dots 0.280. \quad (15)$$

About 80 computations have been produced by using the developed *T*-scheme for different values of the dimensionless frequency and the unsteady process have been simulated.

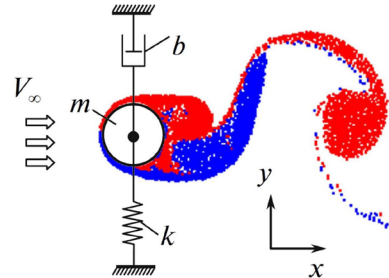


Figure 5: The circular airfoil with Kelvin — Voigt viscoelastic constraint and vortex wake behind it

At the initial time there were still flow and the airfoil in equilibrium position. Time step Δt was equal to 0.01, number of panels which approximates the airfoil $N = 200$. Then the velocity of the incident flow became greater; at time moment $t = 1.0$ (after 100 time steps) it was equal to $V_\infty = 3.0$ and then remained constant. After the transient mode oscillation of airfoil in all cases became close to periodical, their amplitudes dependency on the natural frequency Sh_ω is shown on fig. 6, *a* (dots connected by line).

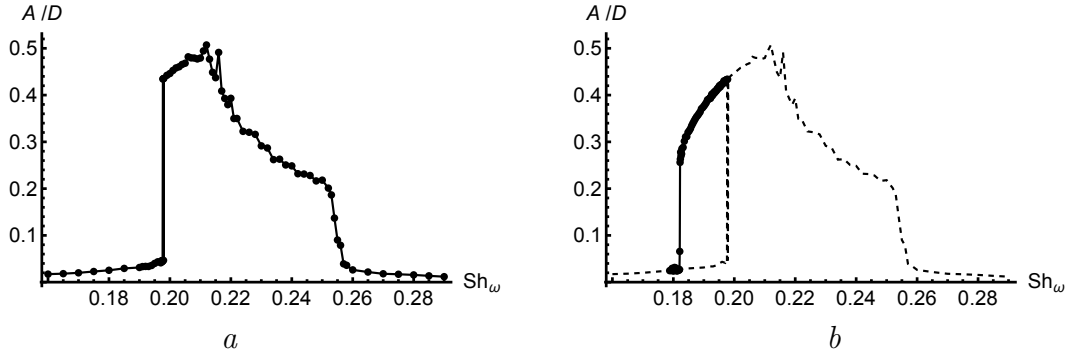


Figure 6: Maximum amplitude of the circular airfoil oscillations simulated using vortex element method: *a* – initial state of airfoil in equilibrium position, *b* — initial state of airfoil is close to resonance oscillations

The fig. 6, *a* shows that there is a sharp increase in the amplitude of oscillations at $Sh_\omega \approx 0.198$. It's well known that there is hysteresis-type phenomenon [11] and in order to simulate it the following computations were performed: from $t = 0$ to $t = 100$ (10 000 time steps) Sh_ω was equal to 0.21; at this time the oscillations become steady with amplitude $A/D \approx 0.47$, then the elasticity coefficient of the constraint was changed abruptly to the values which correspond to Sh_ω from 0.178 to 0.198 with step 0.00025. In each case after the transient mode new steady oscillations were generated, and their amplitudes are shown on fig. 6, *b* (dots connected by solid line).

The obtained results for maximum amplitude of oscillation, the resonance frequency and hysteresis properties are in good agreement with the results given in [11, 12].

5 CONCLUSIONS

The problem of numerical simulation of flow around moving and deformable airfoils is considered. Two different numerical schemes can be used: classic *N*-scheme and developed *T*-scheme. They differ from each other in approaches to boundary condition satisfaction on the airfoil surface: equality of normal and tangential velocity components of the flow and airfoil respectively.

The algorithms suitable for the solution of practical problems are developed based on *T*-scheme.

It is shown that *T*-scheme allows to obtain the solution for wider class of problems in comparison with *N*-scheme, it also provides higher accuracy. An important features of

the developed T -scheme is its ‘symmetry’ — in case of translational motion of the airfoil in the flow, it allows to obtain the same solution in direct and inverse motions.

The model problem of wind resonance of the circular airfoil is considered. The developed approach allows to simulate this phenomenon (including hysteresis) with high accuracy and small computation cost.

Acknowledgements

The work was supported by Russian Federation President’s Grant for young PhD-scientists [proj. MK-3705.2014.8].

REFERENCES

- [1] I. K. Lifanov, S. M. Belotserkovskii. Methods of Discrete Vortices. CRC Press, 1993.
- [2] R. I. Lewis. Vortex Element Methods For Fluid Dynamic Analysis Of Engineering Systems. Cambridge University Press, 2005.
- [3] G.-H. Cottet, P. D. Koumoutsakos. Vortex Methods: Theory and Practice. Cambridge University Press, 2008.
- [4] G. Ya. Dynnikova. Vortex Motion in Two-Dimensional Viscous Fluid Flows // Fluid Dynamics. 2003. Vol. 38/5. P. 670–678.
- [5] G. Ya. Dynnikova. The Lagrangian Approach to Solving the Time-Dependent Navier — Stokes Equations // Doklady Physics. 2004. Vol. 49/11. P. 648–652.
- [6] P. G. Saffman. Vortex Dynamics. Cambridge University Press, 1993.
- [7] S. N. Kempka, M. W. Glass, J. S. Peery, J. H. Strickland. Accuracy Considerations for Implementing Velocity Boundary Conditions in Vorticity Formulations. SANDIA REPORT SAND96-0583 UC-700, 1996.
- [8] P. R. Andronov, S. V. Guvernyuk, G. Ya. Dynnikova. Vortex Methods for Unsteady Hydrodynamic Loads. Moscow, MSU, 2006. [in Russian]
- [9] I. K. Marchevsky, V. S. Moreva. Vortex Element Method for 2D Flow Simulation with Tangent Velocity Components on Airfoil Surface // ECCOMAS 2012 — European Congress on Computational Methods in Applied Sciences and Engineering, e-Book Full Papers. 2012. P. 5952–5965.
- [10] I. K. Marchevsky, V. S. Moreva, V. V. Puzikova. The Efficiency Comparison of the Vortex Element Method and the Immersed Boundary Method for Numerical Simulation of Airfoil’s Hydroelastic Oscillations // COUPLED PROBLEMS 2015 — VI International Conference on Computational Methods for Coupled Problems in Sciences and Engineering, e-Book Full Papers. 2015. P. 800–811.
- [11] Klamo, J.T., Leonard, A. and Roshko, A. The effects of damping on the amplitude and frequency response of a freely vibrating cylinder in cross-flow. *J. of Fluids and Struct.* (2006) **22**: 845–856.
- [12] Klamo, J.T., Leonard, A. and Roshko, A. On the maximum amplitude for a freely vibrating cylinder in cross flow. *J. of Fluids and Struct.* (2005) **21**: 429–434.

USING THE DIPOLE PARTICLES FOR SIMULATION OF 3D VORTEX FLOW OF A VISCOUS INCOMPRESSIBLE FLUID

DMITRII A. SYROVATSKII¹, GALINA YA. DYNNIKOVA¹,
SERGEY V. GUVERNYUK^{1,2}, AND GURGEN ARUTUNYAN²

¹Research Institute of Mechanics, M. V. Lomonosov Moscow State University
Michurinskii pr. 1, Moscow, 119192, Russia
[sd, dyn, guv]@imec.msu.ru, guv@imec.msu.ru

² T-Services,
Leninskii pr. 113/1, 117198 Moscow, Russia
gurgen.arutunyan@t-services.ru

Key words: Meshfree numerical method, three dimensional flow, dipole particles, impuls formulation, incompressible flow.

Abstract. A fully lagrangian numerical method for simulation of 3D nonstationary flow of viscous and ideal incompressible fluid is developed in this work. This method is based on the representation of a vortex field as a set of dipole particles [1]. The introduced vector-function D describes density of dipole momentum. The equation for this function is in accordance with Navier-Stokes equations [2]. The vorticity is equal to curl of dipole momentum density. Thus vortex field is always solenoidal. The dipole particles are generated at a body surface and are moving interacting. The region where function D is essentially non-zero approximately coincides with the vortex region. Each dipole particle induces the velocity field which is equal to field of a point dipole at large distance from the particle. But near a particle the induced velocity field is another taking into account the particle volume and viscosity of the liquid. The method can be applied for simulation of an ideal and viscous flows.

1 INTRODUCTION

Simulation of 3D vortex flow in 3-D space has the problem of the representation of three-dimensional vortex field by discrete elements. This field must be divergence-free as a curl of velocity field. But when the discrete vortex particles are used, this property can be destroyed. The velocity field which the vortex particle induces in accordance with Biot-Savart formula has non-zero vorticity in the whole space but not only in the localization of the particle. If the set of the vortex particles does not form a divergence-free vector field then the rotor of the induced velocity field does not coincide with this vector field. This leads to errors in the calculation if special measures are not taken. Therefore hybrid methods are often applied with combination of the Eulerian and Lagrangian approaches [3]. After the particles have been moved, their intensities are recalculated at Euler mesh for recovering the solenoidality at each step. This procedure returns to the need to build grids, and can increase the numerical viscosity.

In this work the dipole particles are used for simulating of the 3-D vortex field. This

representation provides a solenoidality of the vortex field. The fully lagrangian method of Dipole Domains (DD) is developed in [1]. Dipole distributions are widely used in hydrodynamics to calculate the potential flows (double-layer potential). The idea to construct a numerical method based on the dipole particles was suggested by Yanenko, Veretentsev and Grigoriev [4]. However, numerical realization has not been performed. Chefranov [5] used the point dipoles to model the vorticity in an ideal fluid for analyzing the mechanisms of turbulence and turbulent viscosity. It has been shown that interaction of the point dipoles in an ideal fluid can lead to explosive growth of localized vorticity. The vortex dipoles were applied in papers [6,7,8] for the simulation of the inviscid vortex flow and analyzing of the turbulence.

In the method DD the smooth dipole particles are used. Viscous interaction of the particles can be taken into account.

2 GOVERNING EQUATIONS

We use a vector function \mathbf{D} , which is described by the equation

$$\frac{\partial \mathbf{D}}{\partial t} = \mathbf{V} \times (\nabla \times \mathbf{D}) + \nu \nabla^2 \mathbf{V} - \nabla (\mathbf{V} \cdot \mathbf{D} - \nu \nabla \cdot \mathbf{D}) \quad (1)$$

\mathbf{V} is the divergence-free function with the same curl as \mathbf{D} , i.e. $\nabla \cdot \mathbf{V} = 0$, $\nabla \times \mathbf{V} = \nabla \times \mathbf{D}$.

Applying rotor to equation (1) one obtains the equation

$$\frac{\partial (\nabla \times \mathbf{D})}{\partial t} = \nabla \times (\mathbf{V} \times (\nabla \times \mathbf{V}) + \nu \nabla^2 \mathbf{V}). \quad (2)$$

It is evident that if in the infinite space in initial moment the function \mathbf{V} is equal to the flow velocity with undisturbed conditions at infinity then the equality will be held further because the equation (2) for vector function $\nabla \times \mathbf{D}$ is identical with equation for $\Omega = \nabla \times \mathbf{V}$ following from Navier-Stokes equation.

Equation (1) can be transformed as following

$$\frac{\partial \mathbf{D}}{\partial t} + (\mathbf{V} \nabla) \mathbf{D} = \nu \nabla^2 \mathbf{D} - (\mathbf{D} \nabla) \mathbf{V} - \mathbf{D} \times (\nabla \times \mathbf{V}). \quad (3)$$

This equation is equivalent to the equation which was used in [6,7] where it was written in the next form

$$\frac{\partial \mathbf{D}}{\partial t} + (\mathbf{V} \nabla) \mathbf{D} = \nu \nabla^2 \mathbf{D} - (\nabla \mathbf{V})^T \mathbf{D}.$$

Function \mathbf{V} can be expressed via \mathbf{D} with help of Biot-Savart formula. In infinite space τ it has the form

$$\mathbf{V}(\mathbf{R}) = \frac{1}{4\pi} \int \frac{\mathbf{r} - \mathbf{R}}{|\mathbf{r} - \mathbf{R}|^3} \times (\nabla \times \mathbf{D}) d\tau + \mathbf{V}_\infty, \quad \mathbf{r} \in \tau. \quad (4)$$

Expression (4) can be transformed to following

$$\mathbf{V}(\mathbf{R}) = \frac{2}{3} \mathbf{D}(\mathbf{R}) + \frac{1}{4\pi} \int \left(-\frac{\mathbf{D}}{|\mathbf{r} - \mathbf{R}|^3} + \frac{3(\mathbf{r} - \mathbf{R})(\mathbf{r} - \mathbf{R}) \cdot \mathbf{D}}{|\mathbf{r} - \mathbf{R}|^5} \right) d\tau.$$

Here the integral is taken in the principal value. The integrand is the velocity which the point dipole located in \mathbf{r} induces in the point \mathbf{R} . That is why we call function \mathbf{D} as dipole density.

Equation (3) can be solved in Lagrangian coordinates. Just as in the method VVD, the flow region with nonzero dipole density is simulated by the set of the small regions (domains). The dipole moment of each domain is $\zeta_i = \mathbf{D} \tau_i$, where τ_i is the volume of the domain. Such domain can be considered as the particle which moves and its moment changes in accordance with equation (3). In the case of ideal fluid all dipoles move at velocity \mathbf{V} , and variation of the vector ζ_i is described by the equation

$$\begin{aligned} \frac{d\zeta_i}{dt} &= -(\zeta_i \nabla) \mathbf{V} - \zeta_i \times (\nabla \times \mathbf{V}) = -\nabla(\zeta_i \mathbf{V}), \\ \frac{d\mathbf{r}_i}{dt} &= \mathbf{V}. \end{aligned}$$

In the case of viscous fluid, the diffusion velocity can be added to the fluid velocity \mathbf{V} or/and redistribution of the dipole moments can be applied.

3 TESTING THE METHOD

3.1 Simulation of a vortex ring motion in an unbounded space of ideal fluid

The following distribution function \mathbf{D} was used for simulation of the vortex ring at the initial time: the components D_x and D_y are zero everywhere, D_z is equal to h^{-1} in the region where $x^2 + y^2 < 1 \cap z > z_1 \cap z < z_1 + h$, i.e. in the disk of unique radius and thickness h . \mathbf{D} is zero outside this region. This corresponds to the thin vortex layer with the annular vortex lines at the end surface of the disc. Circulation of this vortex ring is equal to 1. In the discrete representation the disk volume is divided into domains, with dipole particles located at the nodes of a cubic grid with step $\Delta l = 0.05$ (see Figure 1. Dipole moment of every domain is $D_z = \Delta l^3/n$ where $n = 5$ is number of rows, $h = n\Delta l = 0.25$. All the particles are identical. Particles near the end surface are highlighted with a darker color. Vorticity is located near these particles and move with them, because the dipole particles and vortex tubes move in ideal fluid at velocity \mathbf{V} . Each particle is smoothed by function

$$\mathbf{D}_i(\mathbf{r}) = \frac{\zeta_i}{8\pi\varepsilon_i^3} \exp\left(-\frac{|\mathbf{r} - \mathbf{r}_i|}{\varepsilon_i}\right),$$

Hence the distribution of vorticity is

$$\boldsymbol{\omega} = \nabla \times \mathbf{D} = \sum_i \frac{\zeta_i}{8\pi\varepsilon_i^4} \times \frac{\mathbf{r} - \mathbf{r}_i}{|\mathbf{r} - \mathbf{r}_i|} \exp\left(-\frac{|\mathbf{r} - \mathbf{r}_i|}{\varepsilon_i}\right).$$

Distribution of vorticity in the cross section at initial moment is shown in Figure 1d.

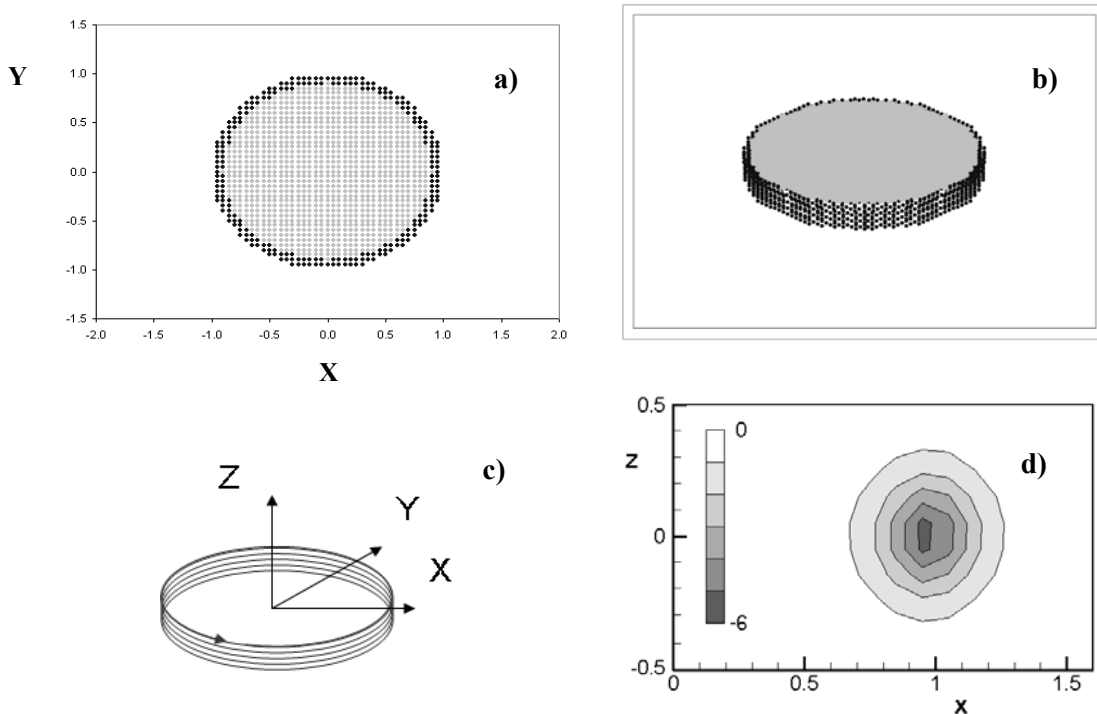


Figure 1. The initial distribution of the dipole particles (a, b); vortex lines (c); vorticity distribution in cross section (d)

In Figure 2 is presented comparison of the translation velocity of the ring with experimental and theoretical data from other researchers. There are shown the velocity calculated from Kelvin and Hicks formulas. Kelvin formula for a thin cored ring with uniform circulation is [9]

$$U = \frac{\Gamma}{4\pi R_0} \left[\ln\left(\frac{8R_0}{\varepsilon_0}\right) - \frac{1}{4} + O\left(\frac{\varepsilon_0}{R_0}\right) \right] \quad (5)$$

where R_0 is ring radius and ε_0 is core radius ($\varepsilon_0/R_0 \ll 1$). Here $\varepsilon_0/R_0 = 0.3$. In formula of Hicks the coefficient 1/4 in (5) is replaced by 1/2. This formula is derived for stagnant fluids inside of the core [10]. Also there are shown the numerical results of Kudela and Kossior [11], who used the Euler-Lagrange method for the ring with uniform circulation inside the core at $\varepsilon_0/R_0 = 0.3$. It should be noted that in inviscid fluid the velocity of the vortex ring with equal geometric characteristics is a linear function of the circulation. If the integration step is inversely proportional to the circulation then a linear relationship must be in accordance with the similarity laws. Deviation from linearity of the results [11] is due to the numerical viscosity probably. Our result is shown by the marker “+”.

Evolution of the distribution of dipoles near plane XZ ($-0.1 < Y < 0.1$) at successive times is presented in Figure 3. Dipole moments are shown by arrows.

The main difficulty of the dipole method is the providing the stability of the numerical scheme. Chefranov (1987) showed when two point dipoles interact, the infinite growth of the dipole moments can occur. The spread of the particles inhibits this process but it adds the numerical viscous. This question should be studied.

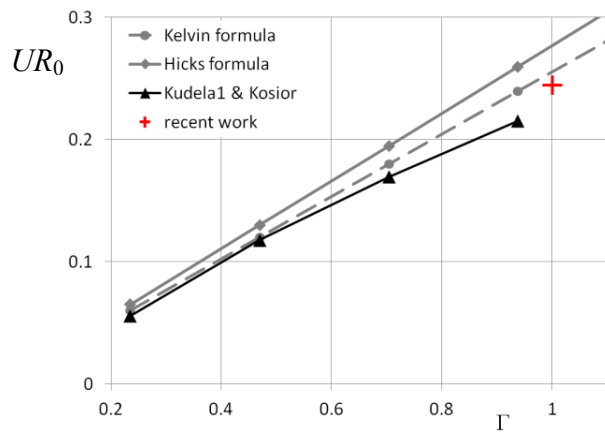


Figure 2. Comparison of theoretical and numerical velocities of vortex ring

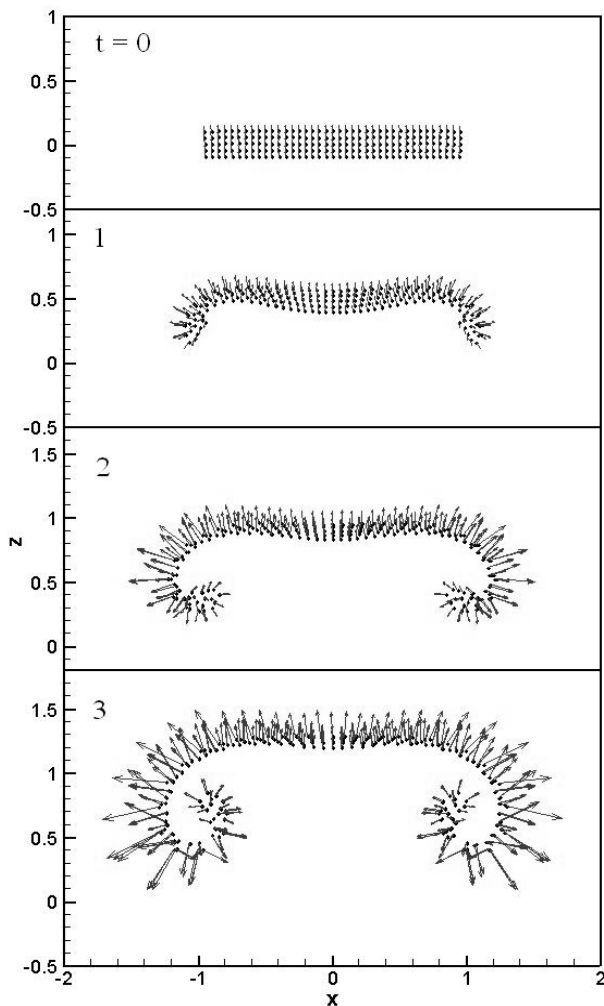


Figure 3. Evolution of the distribution of dipoles near plane XZ ($-0.1 < Y < 0.1$)

3.2 Flow of ideal fluid around the thin rectangular plate at attack angle

The classical task was used for testing the method. As well as it is done by the method of Discrete Vortices, the plate is modeled by the set of discrete elements – dipole particles. The boundary condition at the plate is nonpenetration. The free dipoles are shed from the trailing edge of the plate. The attack angle varies from 1 to 5 degree. The span varies from 2 to 12.

In Figure 4 the lift coefficient dependence on the span at different attack angles is shown.

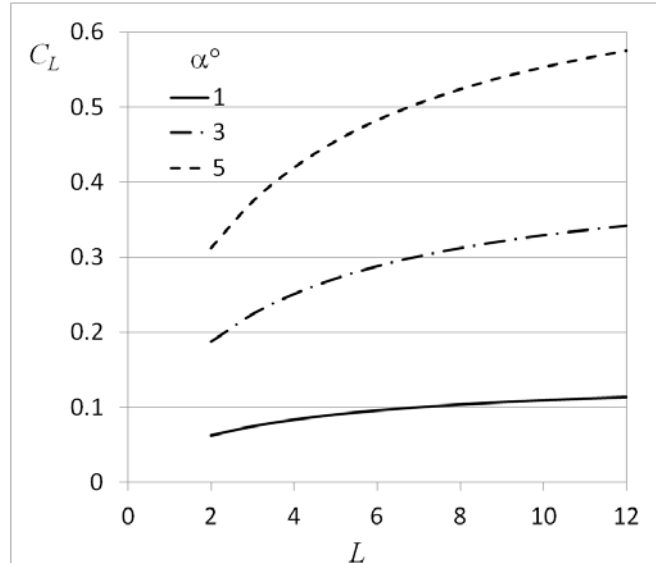


Figure 4. The lift coefficient dependence on the span at different attack angle

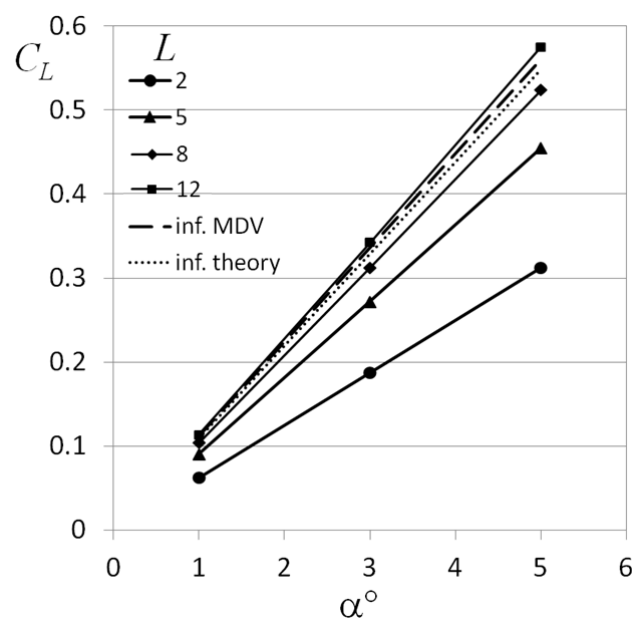


Figure 5 The lift coefficient dependence on the attack angle at different span L

In Figure 5 the lift coefficient dependence on the attack angle at the different span L is shown. The dashed line is obtained by method of discrete vortex (MDV) for 2D flow. The dotted line represents the theoretical curve, obtained by S.A. Chaplygin (1910) for the potential flow.

The number of discrete elements simulating the 3D plate in Figure 4 is equal to N^2L where N is the Number of particles along the horde, $N = 41$. In the case of the 2D plate simulated by MDV the number of elements along the horde is the same.

The convergence of the result with growth of the number N is shown in Figure 6 for the case $L = 6$, $\alpha = 3^\circ$.

One can see that the values of C_L in the case $L = 12$ slightly higher than the values predicted for $L = \infty$. But as it seen at the Figure 6 the increasing of N leads to decreasing these values. Hence the accuracy can be improved by the increasing the number of discrete elements.

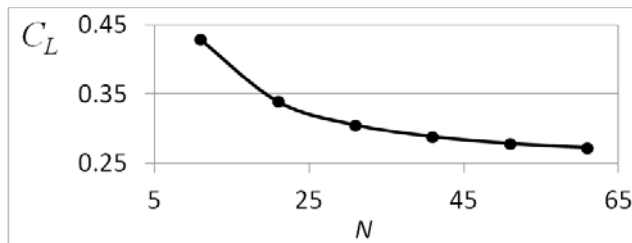


Figure 6. Convergence of the result with growth of the number of points.

4 SOME PRELIMINARY RESULTS

In this section the flow pictures without data of forces are presented as the first results obtained at the personal computer with not enough numbers of the dipole particles.

4.1 The flow of viscous fluid around the sphere

In Figure 7 the formation of the separated flow around the sphere after the instant start is shown. Positions and speed of the dipoles near the plane XY passing through the center of the sphere are drawn. The Reynolds number $Re = 100$.

4.2 The ideal fluid flow generated by the propeller with one blade

The one-blade propeller starts rotation in a stationary medium. It generates the flow which carries away dipole particles generated by the blade. The scheme of the propeller is drawn in Figure 8a. The shape of the blade is depicted in Figure 8b. It consists of isosceles triangle and a semicircle. The dipole particles are shed from the trailing edge of the blade (highlighted in red). Angle of attack of the blade is 7° .

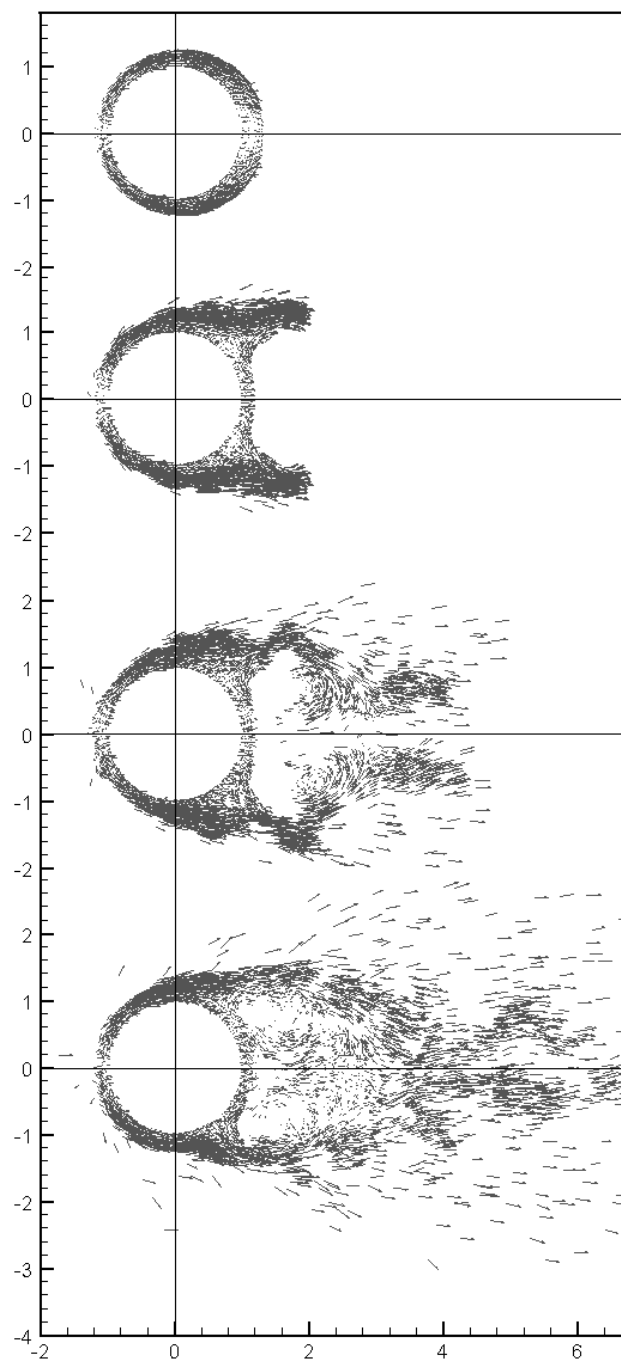


Figure 7. Formation of the separated flow around the sphere after the instant start

4.3 Oscillating plate in a flow of ideal fluid

The horizontal plate which has the form of Cassini oval performs the vertical oscillations in a horizontal flow of ideal fluid directed perpendicularly to the long axis of the oval (see Figure 9a). The Strouhal number $St = fa/U = 0.45$, where f is the frequency of the

oscillations, a is the length of the short axis of the oval. The amplitude of oscillations related to a is equal to 0.085.

The dipole particles are shed from the trailing edge which is highlighted in red in Figure 9a. In Figure 9b the position of the dipole particles is depicted. The color corresponds to the height of the point.

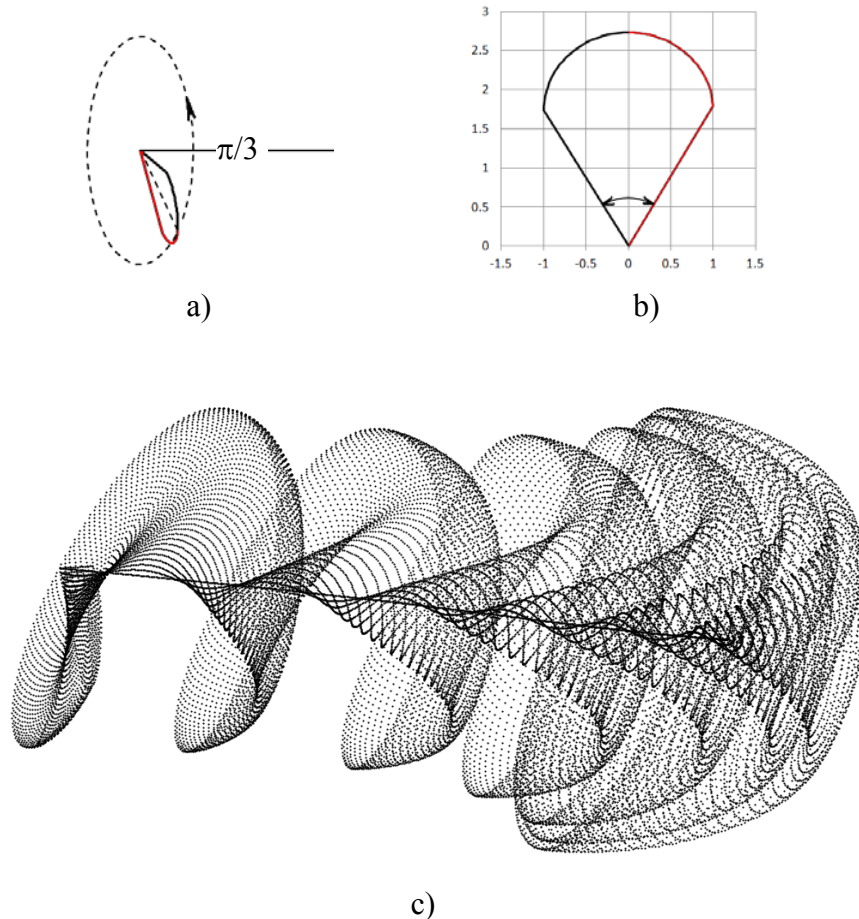


Figure 8. Propeller with one blade: a) scheme of propeller, b) shape of the blade, c) position of the dipole particles

5 CONCLUSIONS

The method of Dipole Domains is perspective method for meshfree simulating 3D flow of ideal and viscous incompressible fluid. The method provides solenoidality of the vortex field and is fully lagrangian. The most important advantages of DD-method has its basis in modeling of essentially non stationary interactions of deformable bodies with the fluid.

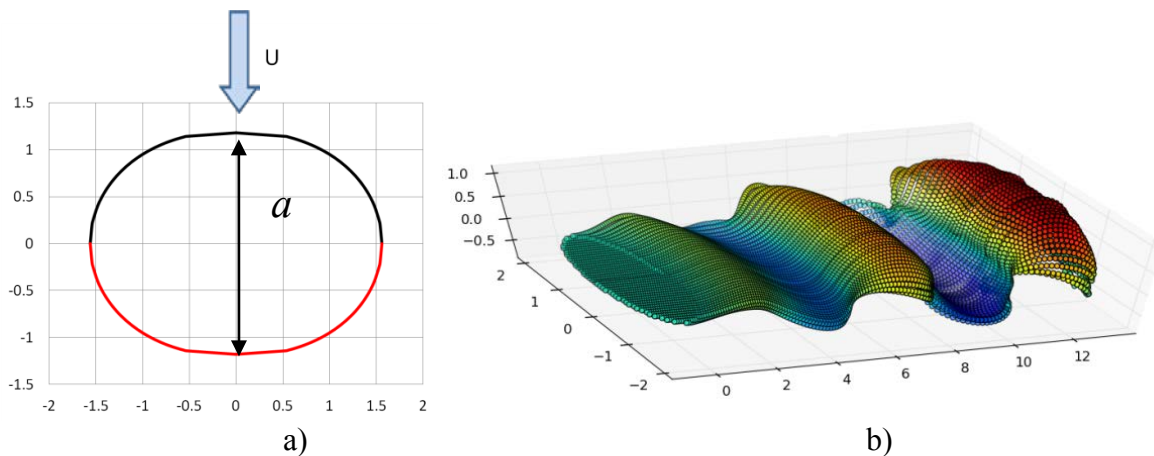


Figure 9. Oscillating plate in a flow of ideal fluid

6 SUPPORT

The work was supported by the Ministry of Education and Science of the Russian Federation (Agreement No. 14.576.21.0079, project id RFMEFI57614X0079).

REFERENCES

- [1] Dynnikova, G.Ya. *Calculation of three-dimensional flows of an incompressible fluid based on a dipole representation of vorticity*. Doklady Physics, **56**, 3, 163-166 (2011).
- [2] Oseledets, V.I., *On a new way of writing the Navier-Stokes equation. The Hamiltonian formalism*, Russ.Math.Surveys, **44** 210-211 (1989).
- [3] Cottet, G.H. and Koumoutsakos, P.D. *Vortex Methods: Theory and Practice*. Cambridge University Press, (2000).
- [4] Yanenko, N.N., Veretentsev, A.N. and Grigoryev, Yu.N., In: *Numerical methods of Mechanics of continuous medium*. Novosibirsk, Vol. 10, p. 144, (1979), in Russian.
- [5] Chefranov, S.G., *The dynamics of point vortex dipoles and spontaneous singularities in three-dimensional turbulent flows*. Journal of Exp. And Theor. Phys. (ISSN 0044-4510), Vol. 93, pp. 151-158, (1987), in Russian.
- [6] Buttke, T.F. and Chorin, A.J., *Turbulence calculations in magnetization variables*, Appl. Numer. Math., 12 (1993), pp. 47–54.
- [7] Cortez, R., *On the accuracy of impulse methods for fluid flow*. SIAM J. Sci. Comput. Vol. 19, No. 4, pp. 1290–1302, July (1998).
- [8] Newton, P.K., *The dipole dynamical system*. Discret and continuous dynamical systems. Supplement Volume (2005) pp. 692-699.
- [9] Green, S. I., *Fluid Vortices*, Springer, (1995).
- [10] Saffman, P. G., *Vortex Dynamics*, Cambridge University Press, (1992).
- [11] Kudela, H. and Kosior, A. *Modeling vortex rings dynamics with vortex in cell method*, Journal of Physics: Conference Series, 318, 062014, doi:10.1088/1742-6596/318/6/062014, 2011.

MODELLING THE FORMATION AND BREAKUP OF PARTICLE CLUSTERS IN METAL MELT SUBJECTED TO EXTERNAL FIELDS

ANTON MANOYLOV¹, VALDIS BOJAREVICS¹, KOULIS PERICLEOUS¹

¹ Centre of Numerical Modelling and Process Analysis, University of Greenwich
30 Park Row, London, UK, SE10 9LS
A.Manoylov@gre.ac.uk, http://cnmpa.gre.ac.uk/group_cseg.html

Key words: Adhesion of particles, CFD-DEM, metal-matrix nano-composites

Abstract. Aluminium and magnesium based metal matrix nano-composites (MMNC) with ceramic nano-reinforcements promise low weight with high durability and superior strength, desirable properties in aerospace, automobile and other applications. However, due to the small size of the particles, adhesion force between becomes significant which leads to particle agglomeration. Large clusters of nano-particles are detrimental for the final properties of the MMNC. To prevent agglomeration and to break up clusters, ultrasonic processing is used via an immersed sonotrode, or alternatively via electromagnetic vibration. The collapse of the cavitation bubbles as a result of ultra-sonication is believed to be the main mechanism of breaking up the clusters of nano-particles. The complex interaction of flow and co-joint particles subjected to the shockwave induced by cavitation is addressed in detail using a discrete-element method (DEM) code. Adhesive, elastic and frictional forces between the particles are incorporated and various models of adhesion are compared.

1. INTRODUCTION

Metal matrix composites (MMC) form a class of advanced materials typically based on light metals such as Al and Mg and ceramic reinforcements including but not limited to Al₂O₃, AlN, SiC etc. Combining the light weight and ductility of Al and Mg with high strength and high modulus of ceramic materials makes MMC desirable for applications in aerospace and automotive industries. A good review of the development of MMCs is given in [1]. Metal matrix nano-composites (MMNC) is a recently developed subclass of MMCs based on nano-particle reinforcements.

MMNCs are manufactured by mixing the nano-particles into the metal melt. Recent papers showed a clear increase in the Young's modulus (by up to 100%) and in hardness (by up to 50%) of the matrix metal with the addition of carbon or ceramic nano-particles [[2]-[4]]. These studies however indicate that the nano-particles tend to form large clusters and that an even distribution of nanoparticles is needed to achieve the beneficial properties of MMNCs. The effect of the distribution of particles on the final properties of MMNCs is explained by the fact that large-size clusters no longer act as dislocation anchors, but instead become defects.

The agglomeration of particles in MMNCs is related to the fact that nano-sized inclusions have a larger ratio of surface area to the volume than e.g. micro-sized particles. This causes surface forces such as van der Waals interaction and adhesive contact to dominate over the volume forces such as e.g. inertia or elastic repulsion in the case of nano-particles.

Various mechanisms of detachment of adhered particles have been reported in the literature [5], which includes turbulent flow. It is expected that drag and shear forces in turbulent flow can improve separation of the particles and thus contribute to de-agglomeration. However, the drag force alone is not sufficient to de-agglomerate the nano-particles. This can be qualitatively illustrated by comparing the Stokes equation for the drag force with the force required to break two spherical particles apart, known as the pull off force, given by e.g. Bradley [5]:

$$6\pi\mu_f R u_f = 4\pi R_p \gamma_{sl} \quad (1)$$

where μ_f and u_f are the velocity and dynamic viscosity of the melt, and γ_{sl} is the solid-liquid interfacial energy. For the case of aluminium melt the dynamic viscosity is $\mu_f=0.0013$ Pa·s. Assuming the interfacial energy $\gamma_{sl}=0.2-2.0$ J/m², equation (1) yields $u_f=100-1000$ m/s. Such fluid velocity values can be locally achieved as a result of the collapse of cavitation bubbles induced by ultrasonic field. Indeed, applying an electro-magnetic stirring in combination with ultrasonic vibrations was found beneficial for nano-particle dispersion in metal melt [[2][5], [8]-[8]].

This paper concerns the investigation of forces causing the agglomeration of nano-particles and the conditions favouring breaking up of these agglomerations. A numerical model has been developed that simulates the response of the cluster of nano-particles to the shockwave induced by the collapse of cavitation bubbles. The collisions of the particles are treated individually using the DEM approach, as opposed to the population balance methods where collisions are using the kinetic theory of granular flow as in e.g. [8]. It is proposed to investigate the behaviour of NPs in metal melts subjected to electro-magnetic [8] and other external fields using a coupled CFD-DEM model similar to that developed by Goniva et al [9] and Hager et al [11]. Whilst a fully coupled CFD-DEM solver is under development, this paper presents results obtained at the scale of a single nano-particle. Authors of this paper reported the results earlier [12], however some theoretical aspects of the modelling are explained in more details in this paper.

2. REVIEW OF ADHESION THEORIES

Bradley [5] first described the van der Waals force acting between two rigid spheres in contact and calculated the pull off force as $P_c=4\pi\gamma R$, where γ is interfacial energy of the contacting materials ¹ and R is the radius of the sphere.

Derjaguin [13] pointed out that elastic deformations of the spheres need to be accounted for as well as the adhesive interactions. He presented the first attempt to consider the problem of adhesion between elastic spheres: calculating the deformations of the spheres using Hertzian contact theory, he evaluated the work of adhesion assuming only the pair-wise interactions of the closest surface elements. The interaction energy between small elements of curved surfaces was assumed the same as for parallel planes which is known as the Derjaguin approximation.

On the other hand, Johnson [14] made an attempt to solve the adhesive contact problem by combining the Hertzian spherical contact problem and the problem of a rigid flat-ended punch. Johnson et al. [15] applied Derjaguin's idea to equate the work done by the surface attractions against the work of deformation in the elastic spheres to Johnson's [14] combined stress superposition. This resulted in the creation of the famous **JKR** (Johnson, Kendall, and Roberts)

¹ The formulae for the pull off force of adhered particles are often used with the notation $\Delta\gamma$ which is the *work of adhesion*. For spheres of the same material $\Delta\gamma \approx \gamma/2$, therefore $P_c=2\pi\Delta\gamma R$

theory of adhesive contact. According to them the attractive adhesion force is acting only over the contact area and significantly affects the shapes of the contacting spherical bodies. The pull off force calculated using JKR model is $P_c=3\pi\gamma R$. The contact area is a circle with radius a , defined as follows:

$$a^3 = \frac{3R}{4E} [P + 6\pi\gamma R + \sqrt{12P\pi\gamma R + 36\pi^2\gamma^2R^2}], \quad (2)$$

where P is the applied normal load and E is the combined Young's modulus. Hertzian theory evaluates the contact radius simply as $a^3=3PR/4E$, therefore JKR theory is reduced to Hertzian if adhesion is neglected, i.e $\gamma=0$.

Derjaguin et al [16] developed a contact theory (**DMT** – Derjaguin, Müller, Toporov) that combined Bradley's adhesion force with Hertz elastic contact theory. The attractive intermolecular force is assumed applicable in the contact area as well as in the surrounding annulus zone. The resulting profile of the deformed spheres remains Hertzian and the pull off force is equal to the one derived by Bradley, $P_c=4\pi\gamma R$. The contact radius is then given by

$$a^3 = \frac{3R}{4E} [P + 4\pi\gamma R] \quad (3)$$

Qualitative analysis of both JKR and DMT models performed by Tabor [17] as well as more detailed analysis based on the Lennard-Jones potential conducted by Muller et al [18] showed that the contradiction between the models lies in the physical principles of adhesive contact assumed by the authors. Both Tabor and Muller concluded that the adhesive contact of larger, softer bodies with stronger surface interaction can be described by the JKR model, while the DMT model is applicable to the smaller, harder bodies with weaker surface interaction. Parameters τ, μ were introduced in [17] and [18] to determine which model is more appropriate:

$$\tau \cong \left[\frac{R\gamma^2}{E^2 z_0^3} \right]^{1/3}, \quad \mu = \frac{32}{3\pi} \left[\frac{2R\gamma^2}{\pi E^2 z_0^3} \right]^{1/3}, \quad (4)$$

where z_0 is the equilibrium separation distance, typically 0.16-0.4 nm [19]. According to Muller if $\mu < 1$ then DMT is applicable whereas if $\mu > 1$ it is JKR.

Maugis [20] suggested a smooth transition model between JKR and DMT approaches which exploits the principles of fracture mechanics. For simplicity, Lennard-Jones interaction potential is replaced by the step-function, which is known as Dugdale approximation. Greenwood and Johnson [21] suggested an alternative model to Maugis based on a combination of two Hertzian profiles that also connect both the JKR and DMT models in one general theory. These two models use a parameter, which defines the area where the adhesion force is applicable. The necessity to evaluate this parameter at every time step during particle collision makes it impractical to use either Maugis [20] or Greenwood and Johnson [21] theories in a DEM solver. Therefore in the present paper the JKR and DMT models are implemented and the Müller parameter μ is used to determine which one is more applicable.

3. CONTACT MECHANICS

3.1. Oblique loading without adhesion.

The most commonly used particle contact model was first introduced by Cundall and Strack [22] in attempt to predict the complex behaviour of sand specimens under loading and unloading. They suggested treating sand particles as spheres which can move individually and

interact only at the contact spots. The contact model consisted of linear spring elements as well and viscous damping elements in both normal and tangential directions, as shown schematically in Figure 1a. The modifications of this model are reviewed in e.g. [23] [24]. The developments of this approach can include addition of rolling and twisting resistance [25] which are neglected in this paper.

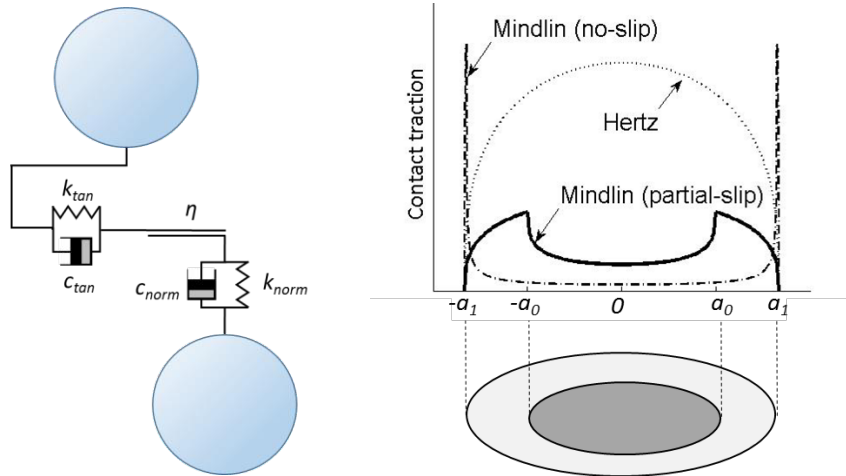


Figure 1 (a) Commonly used spring-dashpot and sliding element model; **(b)** contact traction distribution of two contacting spherical bodies according to the Mindlin and Deresiewicz model. ■ - indicates circular zone with radius a_0 where elastic tangential force is applicable, □ - indicates the ring-shaped micro-slip area with external radius a_1 .

While being extensively used in CFD-DEM simulation codes such as developed by Goniva, Kloss, Hager, Wierink and colleagues [9], [11], this model has a number of disadvantages. Firstly, accurate description of the contact between spherical bodies given by Hertz predicts non-linear normal elastic stiffness as $k_n=2E^*a$, where E^* is the combined Young's modulus and a is the radius of the (circular) contact area. It is noted in [25] that for small deformations Cundall and Strack model works well, although it is not obvious how to correlate the constant elastic stiffness values k_{norm} , k_{tan} and viscous damping coefficients c_{norm} , c_{tan} with properties of the materials involved. In addition to that, this paper considers nano-particles of sizes 50 nm to 1 μm , and therefore adhesion force must be incorporated. All of the adhesion models mentioned in the Section 2 of this paper are based on Hertz elastic theory. For these reasons, Hertz theory is used in this paper to evaluate the relationships between normal force and displacement as well as contact area.

The tangential contact forces are implemented in this paper by means of the Mindlin and Deresiewicz theory [26]. It is assumed that two elastic spheres in tangential contact experience a partial-slip, where the total force is a combination of elastic tangential force in the circular area in the centre of the contact zone and sliding friction force in the ring shaped exterior of the contact zone. Once the partial-slip tangential force exceeds the total sliding friction force, the bodies slide relative to each other. The tangential force in this case is then equivalent to the sliding friction force $F_s=\eta P$, where η is the friction coefficient, P is the normal load. The distribution of contact traction is illustrated in Figure 1b.

Thornton and Yin [27] combined all the major cases of the loading/unloading conditions described by Mindlin & Deresievicz [26] and derived the following expression for the tangential stiffness during oblique loading:

$$k^t = 8G^*a\theta \pm \eta(1 - \theta) \frac{\Delta P}{\Delta \delta_t} \quad (5)$$

where G^* is the combined shear modulus, a is the contact radius, η is the friction coefficient, ΔP is the increment of the normal load, $\Delta \delta_t$ is the increment of the tangential displacement and θ is a parameter defining the ratio of the elastic force to the micro slip friction force. The parameter θ depends on the loading history and is defined as follows:

$$\begin{aligned} \theta^3 &= 1 - \frac{T + \eta\Delta P}{\eta P}; & \theta^3 &= 1 - \frac{T^* - T + 2\eta\Delta P}{2\eta P}; & \theta^3 &= 1 - \frac{T - T^{**} + 2\eta\Delta P}{2\eta P}, \\ \text{for loading} & & \text{for unloading} & & \text{for reloading} & \end{aligned} \quad (6)$$

where T is current value of the tangential force and T^* and T^{**} are the load reversal points. Normal elastic stiffness is defined as $k^n = 2E^*a$ according to Hertz theory; see [27] for details.

3.2. Oblique contact with JKR adhesion

Savkoor and Briggs [28] extended the JKR contact theory to consider the effect of adhesion in the case of oblique loading. It was suggested that applying the tangential force reduces the potential energy by an amount of $T\delta_t/2$. Adding this term to the JKR energy balance equation modified the contact radius (1) as:

$$a^3 = \frac{3R}{4E} \left[P + 6\pi\gamma R \pm \sqrt{12P\pi\gamma R + 36\pi^2\gamma^2R^2 - \frac{T^2E}{4G}} \right] \quad (7)$$

It was concluded that in the presence of tangential force, the contacting spheres peel off each other thus reducing the contact area. The peeling process continues until T reaches the critical value of

$$T_c = 4\sqrt{(3P\pi\gamma R + 9\pi^2\gamma^2R^2)G/E}. \quad (8)$$

For the normal load Thornton and Yin [21] have adopted the JKT theory. The stiffness is then evaluated as

$$k^n = 2E^*a \left[3 - 3 \left(\frac{a_c}{a} \right)^{\frac{3}{2}} \right] / \left[3 - \left(\frac{a_c}{a} \right)^{\frac{3}{2}} \right] \quad (9)$$

where $a_c = 9\pi\gamma R^2/4E$ is the JKR contact radius at the moment of separation (pull off radius).

In the case of oblique loading Thornton and Yin [27] followed [28] in what concerns the peeling process. They however assumed that once the peeling process is complete, the contacting bodies operate in the partial slip regime as described before with the difference that the normal force P is replaced with $P + 6\pi\gamma R$.

3.3. Oblique contact with DMT adhesion.

In this paper it is suggested to combine the Thornton and Yin [27] partial slip no adhesion model with DMT adhesion. The DMT theory assumes that the deformed shapes of the contacting bodies remain within Hertzian elastic theory. Therefore a no-adhesion model [27]

was adopted where the normal force P is replaced with $P+4\pi\gamma R$ to account for the adhesion force. This approach considers instantaneous separation of the particles, as opposed to the JKR theory, where particles stretch elastically prior to pulling off. The maximum stretching in the JKR case is evaluated as $\delta_c = \left(\frac{3\pi^2\gamma^2R}{16E^2}\right)^{1/3}$ whereas $\delta_c=0$ in the DMT case. The effect of the stretching prior to separation is illustrated in the results section.

4. VISCOUS DRAG

The momentum of the fluid is transferred on the particles via the drag force. Di Felice's [29] theory is used to account for the effect of presence of other particles. Drag force on a single particle in a flow with relative velocity $v = v_f - v_p$, where v_f, v_p are the velocities of the fluid and the particle, can be evaluated as follows:

$$\begin{aligned} F_d &= \frac{1}{2} \rho_f v^2 C_d \pi R_p^2 \varepsilon^{-\beta} \\ C_d &= \left(0.63 + \frac{4.8}{\sqrt{Re_p}} \right)^2 \\ Re_p &= \frac{\rho_f}{\mu_f} \alpha_f R_p |v_f - v_p| \end{aligned} \quad (10)$$

where Re_p is the particle Reynolds number, μ_f and ρ_f are dynamic viscosity and density of the fluid, ε is the void fraction value, C_d is the drag coefficient for spherical particles, and function $g(\varepsilon) = \varepsilon^{-\beta}$ is a measure of how much the drag force is affected by the presence of other particles. Empirical parameter β was evaluated to fit the experimental data for a wide range of Reynolds numbers (10^{-2} to 10^4) and void fraction values (0.4 to 1):

$$\beta = 3.7 - 0.65e^{-0.5(1.5 - \log_{10} Re_p)^2} \quad (11)$$

In the literature, modifications of $g(\varepsilon)$ are used, such as $g(\varepsilon) = \varepsilon^{1-\beta}$ [24], $g(\varepsilon) = \varepsilon^{2-\beta}$ [9][11], [23], or $g(\varepsilon) = \varepsilon^{-1-\beta}$ [30]. Di Felice noted however that in the case of the flow through random packed spheres ($\varepsilon \approx 0.4$), Ergun's equation predicts $g(0.4) = \frac{14.6}{C_d} \left(1 + \frac{51.4}{Re_p} \right)$. For a wide range of Reynolds numbers $g(0.4)$ is best predicted by $g(\varepsilon) = \varepsilon^{-\beta}$. In e.g. [25] Stokes drag formula is used multiplied by $g(\varepsilon) = \varepsilon^{-\beta}$.

The void fraction value ε is typically evaluated based on the density of particles in a mesh cell (see e.g. [9], [9][11]). In the present model the CFD mesh is not defined, therefore the void fraction is evaluated based on the cubic cell $10R_p \times 10R_p \times 10R_p$ centred at the particle centre.

5. MODELLING THE BREAKING UP OF NANO-PARTICLE AGGLOMERATES

Two-dimensional densely packed agglomerates of 36 and 37 mono-sized spherical particles were considered as shown in Figure 2. For simplicity, all the forces were assumed acting in the X and Z direction only, and the problem was modelled in two dimensions. Mass, volume, void fraction and contact area were however evaluated assuming that particles are spherical rather than circular. Both normal and tangential contact forces were modelled based on [27] and both JKR and DMT models of adhesion were adopted. The particle material properties are those of SiC and fluid properties are those of liquid aluminium. These and other parameters used in the simulations are provided in Table 1.

Table 1 Particle and fluid properties used in the simulations

Property		Value(s)	Units
Radius	R	50 to 1000	nm
Young's modulus	E	450	GPa
Poison's ratio	v	0.185	-
Particle density	ρ_p	3160	kg/m ³
Friction coefficient	η	0.3	-
Fluid density	ρ_f	2375	kg/m ³
Dynamic viscosity	μ_f	0.0013	Pa·S
Interfacial energy	γ	0.02 to 2.0	J/m ²

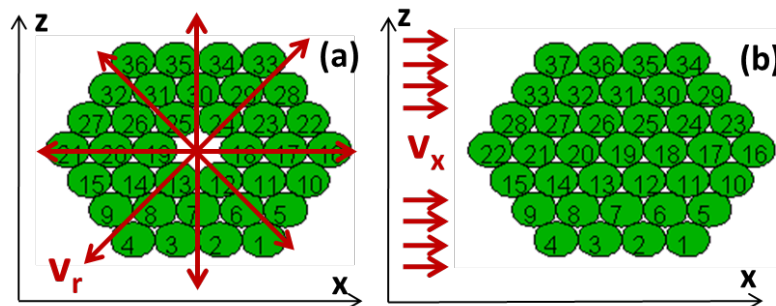


Figure 2 (a) Cluster of 36 particles subjected to the spherical velocity pulse V_r originating in the centre of the cluster. (b) Cluster of 37 particles subjected to lateral velocity pulse V_x .

5.1. Collapsing of Gas Bubbles.

It is known from various sources that ultrasound has a beneficial effect on de-agglomeration of the nano-particle clusters [[2][5], [8]-[8]]. This is explained by the phenomenon of acoustic cavitation, which includes the formation, growth, pulsation and collapse of gas bubbles. These processes are accompanied by the creation of “hotspots” – zones of high temperature and pressure which explain the beneficial effect of ultrasonic vibrations on breaking the clusters and the dispersing of nano-particles [4]. As a result of the implosive collapse of the bubbles high amplitude shockwaves are generated. In [7] authors compare the pressure peak occurring as a result of the collapse with the pressure required to separate two individual nano-particles held together by van der Waals and capillary forces. It is however expected that due to complex pair-wise contact interactions between the particles in a cluster, it is more difficult to de-agglomerate a cluster of particles rather than two individual particles. For this reason the behaviour of a cluster of nano-particles subjected to the shockwave is investigated in this paper.

5.2. Lateral And Spherical Pulses.

In this paper a possibility is also investigated that the agglomerates of nano-particles contain gas bubbles inside (typically hydrogen), originating due to poor wettability of the nano-particles and the specifics of the manufacturing process. In the case of collapsing of a bubble inside of the agglomerate a spherical shockwave is considered radiating from the centre of the cluster as shown in Figure 2a. In [12] authors have also considered lateral pulse originating on the side of the cluster Figure 2b. It was however shown, that lateral pulse causes the cluster to move as a whole, which makes it more difficult to study the de-agglomeration mechanisms.

The behaviour of the gas bubbles in the presence of the ultrasonic waves is a complex problem depending on multiple parameters, and is not studied in this paper. For simplicity it is assumed that the shockwave generated by the collapse of a gas bubble can be described as a rapidly decaying disturbance of the local velocity with an exponential time dependency. Expressing the shockwave as a velocity pulse allows the concentration of the particles to be

$$F_d = \frac{1}{2} \rho_f v^2 C_d \pi R_p^2 e^{-\beta}$$

taken into account using di Felice's approach (equation $C_d = \left(0.63 + \frac{4.8}{\sqrt{Re_p}}\right)^2$)
 $Re_p = \frac{\rho_f}{\mu_f} \alpha_f R_p |v_f - v_p|$

(10)). The details of the behaviour of the gaseous-fluid interface during the bubble collapse are not studied in this paper; therefore the duration τ of the pulse is covering a wide range from 5 ns to 5 μ s in order to investigate a potential effect of the pulse duration. The magnitude of the pulse is defined by the maximum value v_0 which in this paper is ranging from 1-1000 m/s. In [7] authors estimated the cavitation pressure peak as $6 \cdot 10^7$ Pa if a bubble of initial size 100 μ m collapses, and $1.5 \cdot 10^{10}$ if initial size is 1 μ m. Using Bernoulli's equation, these peak pressure values can be correlated with the peak velocities of 225 m/s and 3575 m/s respectively.

5.3. Interfacial Energy.

The interfacial energy γ of the contacting particles can be evaluated from the van der Waals attraction force acting between two flat surfaces separated by an equilibrium distance z_0 :

$$\gamma = \frac{A}{24\pi z_0^3} \quad (12)$$

where A is the Hamaker constant of the material. If particles are interacting in a medium, then Hamaker constant must be modified according to the rule:

$$A_{121} = (\sqrt{A_1} - \sqrt{A_2})^2 \quad (13)$$

where A_1 and A_2 are the properties of the particles and the medium respectively [19]. The average separation distance z_0 for contacting solids with close packed atomic structure can be evaluated as $\sigma/2.5$, where σ is the interatomic distance. The typical value of $\sigma=4$ Å yields $z_0=0.165$ nm (see [19], page 277). Equations (12, 13) can be used to compute the interfacial energy for most solids and liquids. This theory is however not applicable to the system that involves liquid metals or other highly conducting fluids due to short-range non-additive electron exchange interaction. For this reason, a series of the interfacial energy values 0.02, 0.2 and 2.0 J/m² to cover a wide range of interfacial energies. In another paper by authors [12] the interfacial energy values 2.1 J/m² and 2.6 J/m² corresponding to aluminium oxide and silicon carbide particles in aluminium melt are used.

6. RESULTS AND DISCUSSION

6.1. The Effect Of The Contact Model.

In this section the effect of the adhesion model on breaking up of the nano-particles cluster via the spherical shockwave is investigated. Figure 3 shows the positions of the particles after

the incidence of the velocity pulse. The pulse duration is 50 ns, amplitudes 1 to 50 m/s, particles radius is 50 nm and interfacial energy $\gamma_{\text{sl}}=0.2 \text{ J/m}^2$. Here and henceforth the particles belonging to the same sub-cluster are coloured and numbered for convenience. Individual particles are coloured red and have unique numbers. As expected, the no adhesion model (3rd row in Figure 3) predicts that all of the particles become isolated, since particles interact only via friction and elastic forces. As for adhesion models, it can be visually observed that particles tend to form chains of particles in the JKR case (2nd row in Figure 3) and more compact sub-clusters when the DMT model is used (1st row in Figure 3). This can be explained by, firstly, a lower pull off force of the JKR model and, secondly, by the JKR assumption that bodies do not separate instantaneously, but stretch while maintaining contact until the stretching becomes critical and pull off force is reached. This stretching extends the duration of the contact between the particles thus allowing them to re-agglomerate due to collisions with other particles. The analysis of the adhesion models clearly demonstrates that choice of the model may significantly affect the prediction of de-agglomeration.

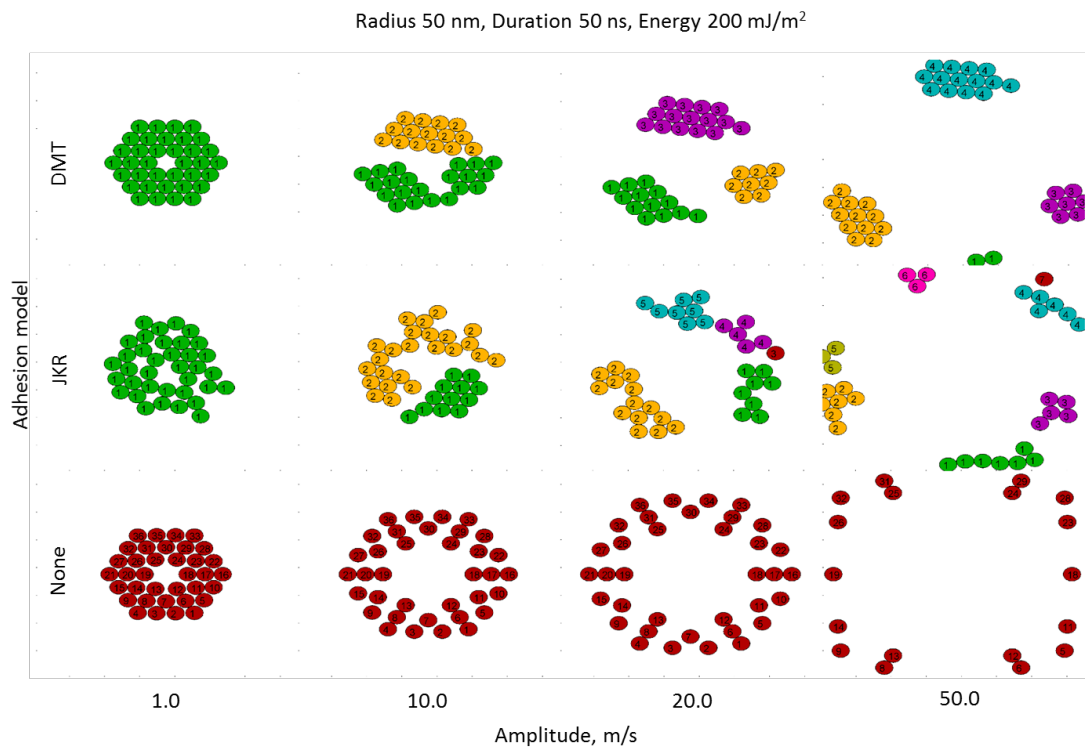


Figure 3 The effect of the adhesion model on breaking up of nano-particle clusters via spherical shockwave.

6.2. The Effect Of The Interfacial Energy.

In this section the results are shown for particles of radius 500 nm with interfacial energy values 0, 0.02, 0.2 and 2.0 J/m². The pulse duration is 500 ns and amplitudes 1.0 to 50.0 m/s. It can be observed from e.g. 3rd row in Figure 4 that particles with higher interfacial energy tend

to form large sub clusters during de-agglomeration. Particles with lower interfacial energy (see e.g. 2nd row in Figure 4) form smaller sub-clusters or individual particles. Same effect has been reported by authors [12] and terms “local” and “global” de-agglomeration were introduced. It was noticed that although global de-agglomeration may separate pieces further apart, the locally de-agglomerated particles can be dispersed by turbulent fluctuations or Brownian motion. For this reason global and local de-agglomeration should be evaluated separately.

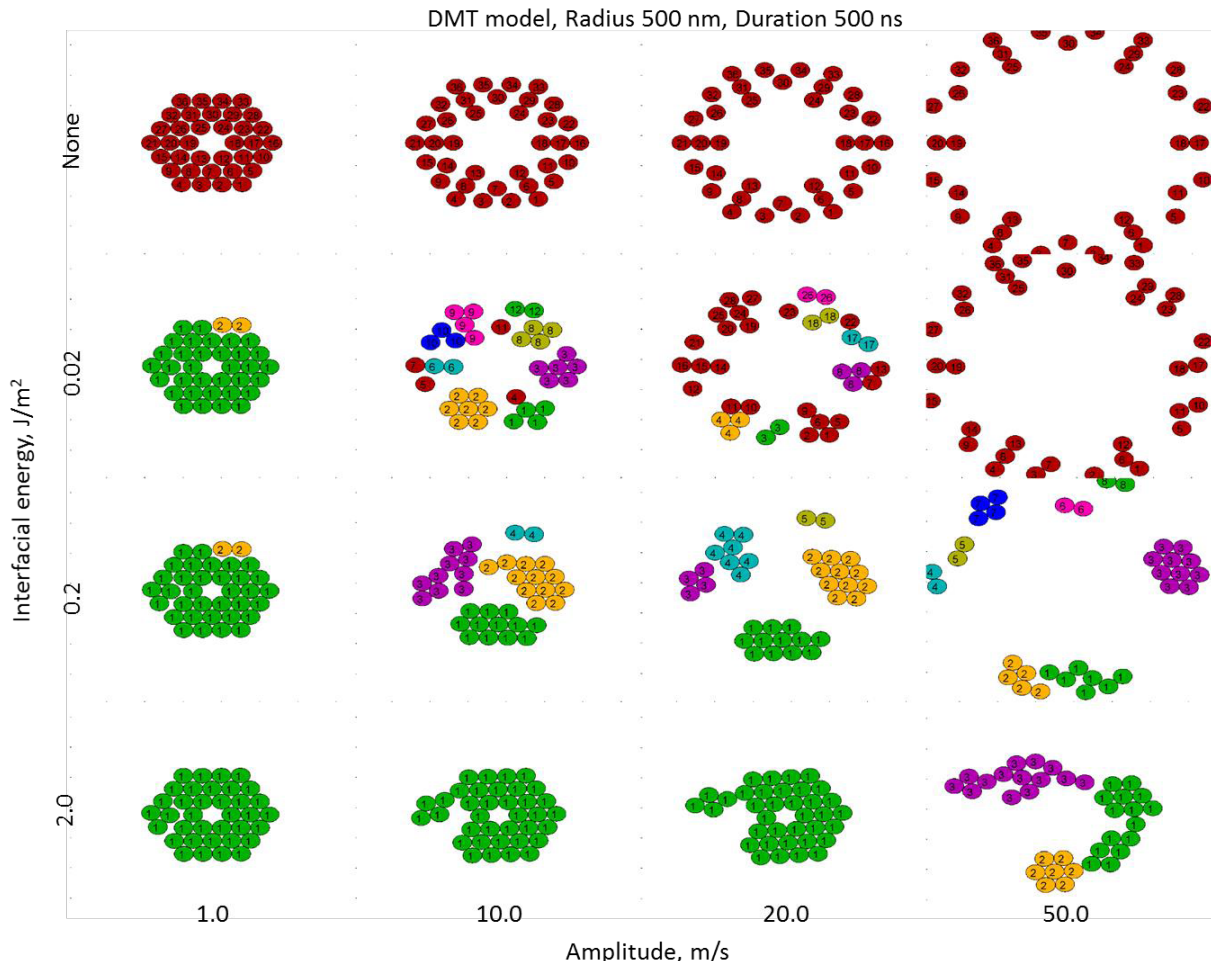


Figure 4 The effect of the interfacial energy on breaking up of nano-particle clusters via spherical shockwave.

7. CONCLUSIONS

A DEM model was developed in order to study the behaviour of a cluster of nano-particles subjected to the shockwave originating in the centre of the cluster. The model incorporates Mindlin and Deresiewicz partial-slip tangential contact theory and both JKR and DMT adhesion force theories. Drag force is implemented using di Felice approach based on the local concentration of particles. The effect of the adhesion model choice was studied and it was shown that JKR model predicts catenulate, chain-like structures whereas in the case of DMT model compact sub-clusters are formed. The behaviour of particles with various interfacial energies was compared, and it was found, that de-agglomerating particles with lower energies

result in smaller sub-clusters and more isolated particles, while under similar conditions particles with higher energies form larger sub-clusters. It is suggested that the effectiveness of the local and global de-agglomeration must be evaluated separately.

This study of the particle-particle interaction forces under various conditions is a part of an ongoing investigation of the mechanisms of de-agglomeration and is expected to help optimizing the electro-magnetic stirring and the ultrasonic processing of the metal melt with added nano-particles.

8. ACKNOWLEDGMENTS

The authors acknowledge financial support from the ExoMet Project (co-funded by the European Commission (contract FP7-NMP3-LA-2012-280421), by the European Space Agency and by the individual partner organizations).

9. REFERENCES

- [1]. Ibrahim, I.A., Mohamed, F. A. and Lavernia, E. J. Particulate reinforced metal matrix composites – a review, *Journal of Material Science* (1991) 26:1137-1156.
- [2]. Vorozhtsov S. et al. Physico-mechanical and electrical properties of aluminium-based composite materials with carbon nanoparticles *Light Metals* (2014), TMS, John Grandfield (Ed.), TMS, Warrendale, PA, 2014
- [3]. Tamayo-Ariztondo, J. et al. Nanoparticles distribution and mechanical properties of aluminium MMNC treated with external fields. *Light Metals* (2014), TMS, John Grandfield (Ed.), TMS, Warrendale, PA, 2014
- [4]. Yang, Y., Lan, J. and Li, X. Study on bulk aluminium MMNC fabricated by ultrasonic dispersion of nano-sized SiC particles in molten aluminium alloy. *Materials Science and Engineering A*, (2004) 380:378–383.
- [5]. Soltani, M. and Ahmadi, G. On particle adhesion and removal mechanisms in turbulent flow. *Journal of Adhesion Science and Technology* (1994) 8(7):763-785.
- [6]. Bradley, R. S. The Cohesive force between Solid Surfaces and the Surface Energy of solids *Phil. Mag.* (1932) 13:853–62,
- [7]. Li, X., Yang, Y., Weiss, D. Ultrasonic cavitation based dispersion of nanoparticles in aluminium melts for solidification processing of bulk aluminium matrix nano-composite: Theoretical study, fabrication and characterization”, *AFS Transactions, American Foundry Society*, Schaumburg, IL, USA (2007)
- [8]. Zhang, D., Nastac, L. , Numerical modelling of the dispersion of ceramic nanoparticles during ultrasonic processing of aluminium-based nano-composites. *Journal of Materials Research and Technology* (2014) 3(4):296-302
- [9]. Djambazov, G. et al. Contactless Acoustic Wave Generation in a Melt by Electromagnetic Induction *Light Metals* (2014), TMS, John Grandfield (Ed.), TMS, Warrendale, PA, 2014
- [10]. Goniva C., et al., “A MULTI-PURPOSE OPEN SOURCE CFD-DEM APPROACH” 8th International Conference on CFD in Oil & Gas, Metallurgical and Process Industries, SINTEF/NTNU, Trondheim Norway, 21-23 June 2011
- [11]. Hager, A et al. Parallel Resolved Open Source CFD-DEM: Method, Validation and Application. *The Journal of Computational Multiphase Flows*, (2014) 6(1):13-27.
- [12]. Manoylov, A., Bojarevics, V., Pericleous, K. A. Modeling the Break-up of Nano-

- particle Clusters in Aluminium- and Magnesium-Based Metal Matrix Nano-Composites. *Metallurgical and Materials Transactions. A* (2015) 46(7): 2893-2907
- [13]. Derjaguin, B. Untersuchungen über die Reibung und Adhäsion, IV. 1. Theorie des Anhaftens kleiner Teilchen. *Kolloid-Zeitschrift* (1934) 69:155-164.
- [14]. Johnson, K. L. A note on the adhesion of elastic solids. *British Journal of Applied Physics* (1958) 9:199-200.
- [15]. Johnson, K.L., Kendall, K. and Roberts, A.D. Surface Energy and the Contact of Elastic Solids. *Proceedings of the Royal Society A*. (1971)324:301–13
- [16]. Derjaguin, B.V., Muller, V.M. and Toporov, Y.P. Effect of Contact Deformations on the Adhesion of Particles. *Journal Colloid and Interface Science* (1975):53(2)
- [17]. Tabor, D. Surface Forces and Surface Interactions. *Journal Colloid and Interface Science* (1977) 58(1)
- [18]. Muller, V.M., Yushenko V. S. and Derjaguin, B.V. On the Influence of Molecular Forces on the Deformation of an Elastic Sphere and Its Sticking to a Rigid Plane. *Journal Colloid and Interface Science*. (1980) 77(1)
- [19]. Israelachvili, J. N., *Intermolecular and Surface Forces*, Academic Press, New York, (1985).
- [20]. Maugis, D. Adhesion of Spheres: The JKR-DMT Transition Using a Dugdale Model. *Journal Colloid and Interface Science*. (1992) 150(1)
- [21]. Greenwood, J. A., Johnson, K. L. An alternative to the Maugis model of adhesion between elastic spheres. *J. Phys. D: Appl. Phys.* (1998) 31:3279–3290
- [22]. Cundall, P. A., Strack, O. D. L. A discrete numerical model for granular assemblies. *Geotechnique* (1979) 20(1): 47-65.
- [23]. Zhou, Z. Y., Kuang, S. B., Chu, K. W., Yu, A. B. Discrete particle simulation of particle–fluid flow: model formulations and their applicability. *J. Fluid Mech.* (2010) 661: 482–510.
- [24]. Zhu, H.P., Zhou, Z.Y., Yang, R.Y., Yu, A.B. Discrete particle simulation of particulate systems: Theoretical developments. *Chemical Engineering Science* (2007) 62:3378 – 3396
- [25]. Marshall, J. S., Discrete-element modelling of particulate aerosol flows. *J. Comp. Physics* (2009) 228:1541-1561
- [26]. Mindlin R. D. and Deresiewicz H. Elastic Spheres in Contact Under Varying Oblique forces. *J. Appl. Mech., Trans. ASME* (1953) 20:327.
- [27]. Thornton, C., Yin, K. K. Impact of elastic spheres with and without adhesion. *Powder Technology* (1991) 65:153-166
- [28]. Savkoor A.R. and Briggs, G. A. D. The Effect of Tangential Force on the Contact of Elastic Solids in Adhesion. *Proc. Roy. Soc. A* (1977) 356:103
- [29]. Di Felice, R. The voidage function for fluid-particle interaction systems. *Int. J. Multiphase Flow*(1994) 20(I):153-159
- [30]. Kafui, K.D., Thornton, C., Adams, M. J. Discrete particle-continuum fluid modelling of gas-solid fluidised beds. *Chem. Eng. Science* (2002) 57:2395-2410

RESOLVING LATERAL SEGREGATION EFFECTS OF STATIC BLENDERS

BRAM T. TON¹, RICHARD J. FARNISH² AND STEFAN ZIGAN³

¹ The Wolfson Centre for Bulk Solids Handling Technology
University of Greenwich
Central Avenue, Kent ME4 4TB, United Kingdom
b.t.ton@gre.ac.uk - www.bulksolids.com

² The Wolfson Centre for Bulk Solids Handling Technology
University of Greenwich
Central Avenue, Kent ME4 4TB, United Kingdom
r.j.farnish@gre.ac.uk - www.bulksolids.com

³ Mechanical, Manufacturing & Design Engineering
University of Greenwich
Central Avenue, Kent ME4 4TB, United Kingdom
s.zigan@gre.ac.uk - www.gre.ac.uk

Key words: static blender, segregation

Abstract. To date static blenders have mainly been used for mixing fluids, but recent research has shown the potential of static blenders for blending powders and granular materials as well. A problem when using a static blender in conjunction with powders and granular materials is trajectory induced segregation at the output of the blender. In order to evaluate the blending process two granular materials exhibiting extreme particle densities and sizes have been discharged into a static blender. The blend is collected in a radially compartmentalised receiving container and the blend composition of each compartment is then analysed. This paper presents a simple counter measure to reduce the effect of trajectory induced segregation. In addition this research has shown that, contrary to expectations, an increased number of blending stages does not necessarily bring improvements in homogeneity of the output stream. The results presented in this paper are of special interest to anyone blending powders and granular materials in an industrial environment.

1 INTRODUCTION

The benefits of using static blenders are numerous for industry; low energy consumption, continuous operation, reduced blender wear when handling abrasive materials and potentially higher time averaged throughput. Despite the numerous benefits, static

blenders are not yet widely used in conjunction with powders and granular materials. This lack of technology uptake is attributed to a lack of thorough understanding of the mechanisms of the static blending process. Static blenders usually consist of several identical blending stages arranged above one another with alternating orientations. Each stage contains one or more baffles such that the descending particulate material is encouraged to interact and blend. There are many design parameters to be considered when analysing a static blender; the spatial arrangement of the baffles, the number of stages, the height of each stage, the relative orientation of consecutive stages, the material bulk properties, material feeding rate and the discharge location of the feed relative to the first blending stage. One of the issues which arises when using a static blender in conjunction with binary mixtures exhibiting extreme particle densities and sizes is trajectory induced segregation at the output of the blender. Trajectory induced segregation occurs when particles have different energies and/or different drag coefficients. To overcome this issue this paper proposes a simple counter measure and has analysed the influence of the number of blending stages on the homogeneity of the output. The presented results are an outcome of an industrial feasibility study to determine the potential of a static blender used in conjunction with a binary mixture of granular materials exhibiting extreme particle densities and sizes.

This research made use of a custom designed static blender which has the flexibility to easily alter the number of blending stages. In order to analyse the lateral homogeneity at the output of the blender the granular material is collected in a radially compartmentalised receiving container. After each test run, the blend composition of each individual compartment is analysed. In addition to varying the number of blending stages a combination of funnels is employed at the output of the blender in an attempt to homogenise the blend. The results show that by using a combination of a conventional funnel and a slotted funnel together with two blending stages the best results are obtained. Surprisingly it was found that having two blending stages instead of four blending stages produced the best results in terms of homogeneity around the discharge area.

2 METHOD

Two granular materials which differ extremely in density and size are used in this research. The first granular material (X) has a density of $0.9 \text{ g} \cdot \text{cm}^{-3}$ and the second granular material (Y) has a density of $4.6 \text{ g} \cdot \text{cm}^{-3}$. The respective size distributions are tabulated in Table 1. The tables clearly indicate there is no overlap between both size distributions which means both granular materials can easily be separated again by using a single sieve for analysis. Unfortunately due to confidentiality restrictions no further information about the granular materials can be provided. According to the specifications of the industrial collaborator a blend composition of 20% of material X and 80% of material Y in terms of weight is used. In terms of volume this roughly relates to equal parts of both materials.

Both granular materials are discharged into the static blender from a split feed pipe

Table 1: Size distributions as % retained

(a) Granular material X

Sieve size	Retained (%)
Fines	1
250 μm	2
355 μm	36
500 μm	29
630 μm	11
710 μm	18
850 μm	3
1.18 mm	0

(b) Granular material Y

Sieve size	Retained (%)
Fines	0
1.40 mm	0
1.70 mm	7
2.00 mm	93
2.80 mm	0
3.35 mm	0

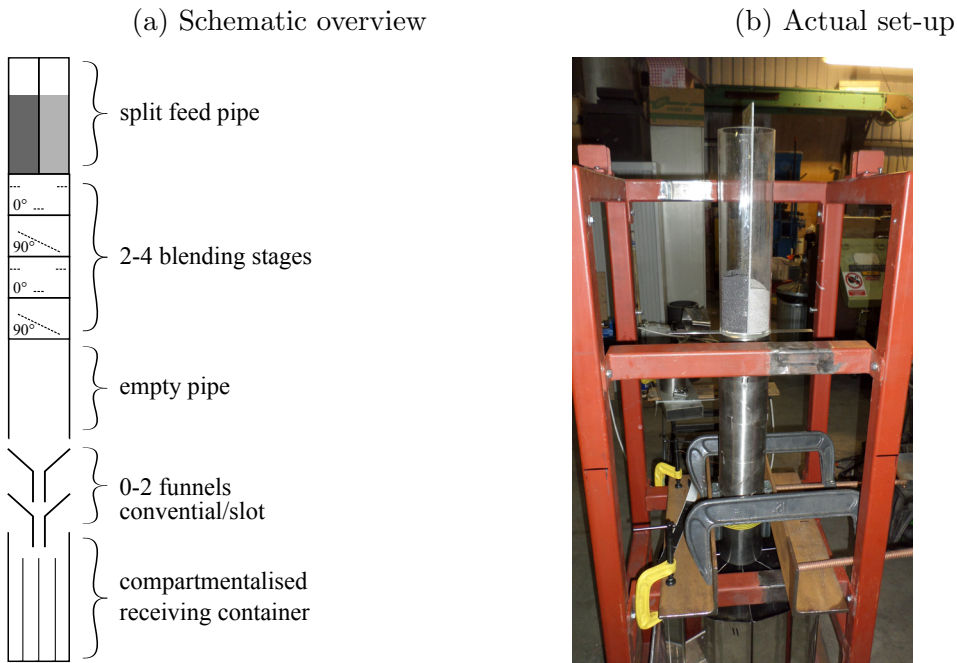
and are collected in a radially compartmentalised receiving container with eight compartments. The split feed pipe has two calibrated orifices at the bottom which are uncovered simultaneously at the beginning of each test run. The orifices are calibrated such that an approximate 20/80% weight flow occurs. The contents of each individual compartment are sieved and the weight ratio as a percentage of granular material X is determined. A schematic overview of the experimental set-up and the actual realisation can be seen in Figure 1. The photograph of the actual set-up does not show the funnels but it does show the compartmentalised receiving container at the bottom.

To influence the blend quality the number of blending stages is varied and a combination of funnels is used at the output of the blender. Two funnel types are considered, a conventional funnel and a slot type funnel. The test conditions are given in Table 2, note that test 1 and 2 are the same and that test 6 and 7 are the same, this is to validate the repeatability and consistency of the results. All testing is undertaken at ambient laboratory conditions.

Table 2: Test conditions

Reference	Blending stages	Conventional funnel	Slot type funnel
1	4	-	-
2	4	-	-
3	4	X	-
4	4	X	X
5	3	X	X
6	2	X	X
7	2	X	X

Figure 1: Experimental set-up



The static blender used in this research has been previously applied in a PhD study at the Wolfson Centre [3]. Each blending stage has an internal diameter of 103 mm and a height of 100 mm. The static blender has a modular set-up such that the number of blending stages can be altered easily. Each blending stage contains three baffles in a configuration similar to the Sulzer [4] type of static liquid blenders. During the tests the blending stages are stacked with alternating orientations of 0° and 90°. Two identical blending stages can be seen in Figure 2. The figure shows the configuration of the three baffles, a central finger protruding at an oblique angle and two perpendicular ridges attached to the walls.

The outlets of the feed pipe are obscured before completely emptying the feed pipe, this is to avoid potential granular material collapsing at the end which could lead to a disrupted flow. Separating both granular materials again is done by using an Endecotts woven wire laboratory test sieve with an aperture of 1.7 mm. After separation both granular materials are weighed using a Sartorius MSU14202P-000-D0 balance.

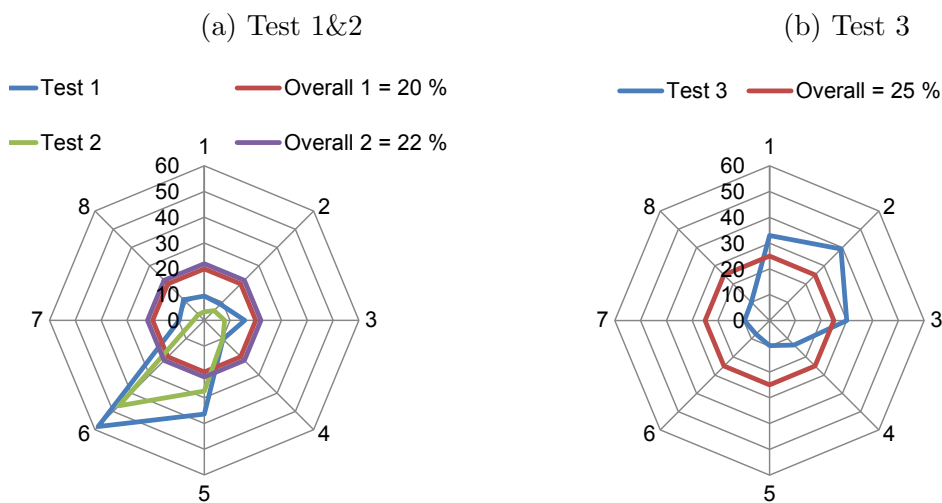
3 RESULTS

The data of each test runs is visualised using a radar graph, each point on the graph corresponds to the blend composition of granular material X as %wt of one of the eight compartments. Each radar graph also shows the overall blend composition. The weight of granular material X discharged during the experiments ranged between 0.8 kg and 1.0 kg and for granular material Y this range was between 2.5 kg and 3.7 kg. The radar

Figure 2: Two identical static blending stages

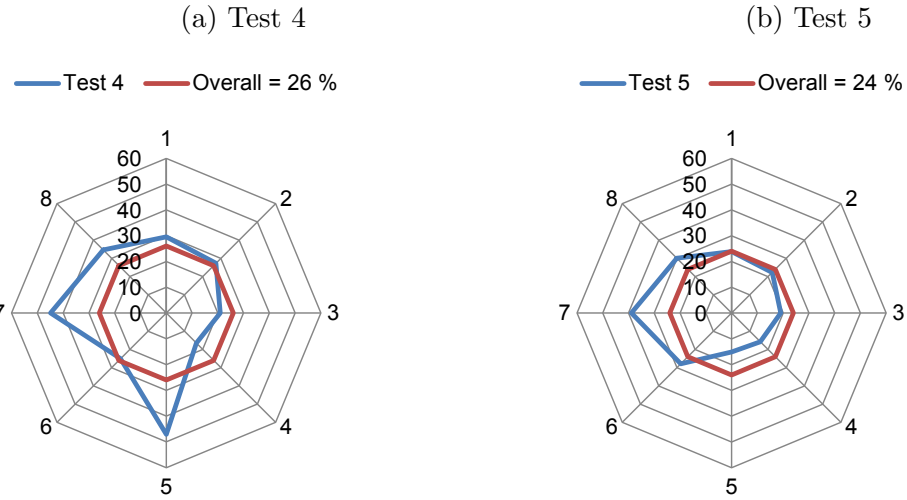


Figure 3: Content (% wt) of granular material X



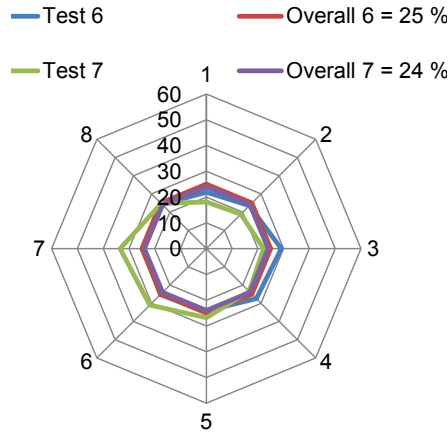
graph in Figure 3a show a strong lateral deviation from the average composition. This can partially be attributed to the final trajectory imparted by the last blending stage. As a counter measure, a regular funnel was installed below the static blender to centralise the deposition of the material. The result can be seen in Figure 3b and shows a slight improvement compared to the initial condition. It can be seen that the blend composition has shifted by 180° which means the material flow is highly susceptible to the rebound effect. To further limit the rebound effect, it was decided to interpose a slotted funnel above the regular funnel. The result of this modification can be seen in Figure 4a, it shows a slight improvement, but still the blend composition was very inconsistent around

Figure 4: Content (% wt) of granular material X



the deposition area. Next it was decided to reduce the number of blending stages from

Figure 5: Content (% wt) of granular material X



four to three, which gave a more controlled deposition as can be seen in Figure 4b. The number of blending stages was finally reduced to just two, which gave the results shown in Figure 5. Using this final configuration the composition around the discharge area is consistent.

4 DISCUSSIONS

The results presented in this paper are preliminary and give rise to many more research questions. One of the issues with the results presented in this paper is that due to time

constraints some of the test runs have not been repeated. Currently the feeds operate in core flow which might cause disruptions during discharge due to wall friction [1]. To obtain more reliable results a feed which operates in mass flow could be used, in addition the feed rates need to be better controlled as the blend composition varied between 20% and 26%. Another issue regarding the feed is the location where the granular materials will be discharged relative to the first blending stage. It can be expected that by discharging materials directly above the protruding finger of the static blender the contribution of the first blending stage will be small.

The design and geometry of the static blender used in this research is rather arbitrary, no valid motivation can be provided as why this specific blender has been chosen other than the fact a similar blender has been used in a previous study [3]. There are a large number of parameters governing the performance of the blender such as the diameter of the blender and the configuration of the baffles inside the blender. More research is needed on how to incorporate these parameters in the design process of a static blender.

The issue of trajectory induced segregation has been noticed in a previous study by Salter et al. [2]. His paper mentions a diffusive stage to radially homogenise the discharging mixture stream. In future work it would be interesting to see if this diffusive stage can also be used in conjunction with extreme particulate blends. Another aspect worth investigating is the contribution to the blending performance caused the arrangement of funnels, this can be done by omitting the static blender from the set-up. The research presented here has focused on a single binary blend of granular materials, further research is needed to verify if the results obtained are also applicable to other blends of particulates. It can be argued that by having smaller differences in density of the granular materials entering the blender the effects of trajectory induced segregation will be smaller.

5 CONCLUSIONS

This paper has shown that the issue of trajectory induced segregation occurring at the output of a static blender can be controlled using a simple combination of funnels. In addition this research has shown that, contrary to expectations, an increased number of blending stages does not necessarily bring improvements in homogeneity of the output stream. The results presented in this paper are relevant for any industry that blends powders or granular material as part of their process. The presented method to analyse the homogeneity around the discharge area is a valuable contribution to enhance the uptake of static blenders in industrial processes.

As the nature of this research is preliminary there are still many open research questions, such as:

- Is the design and geometry of the static blender used an optimal one ?
- Are the results presented also applicable to blending other particulate materials ?
- How does the material feed rate influence the blend quality ?

- How does the material discharge location influence the blend ?

Finally the effect of material properties such as size, cohesiveness and density on the blend quality and blending performance should also be considered in future research.

REFERENCES

- [1] Jenike, A.W. *Storage Flow of Solids*. Utah Engineering Experiment Station, Bul. 123, University of Utah (1964)
- [2] Salter, G.F. and Pittman, A.N. and Reed, A.R. and Barnes, R.N. *Mixing of Particulate Solids Using Static Mixers*. 5th International Conference on Bulk Materials Storage, Handling and Transportation. (1995)
- [3] Salter, G.F. *Investigations into the segregation of heaps of particulate materials with particular reference to the effects of particle size*. PhD thesis, University of Greenwich (1999)
- [4] Sulzer. www.sulzer.com (Accessed May 5th 2015)

SIMULATING MIXING PROCESSES WITH WATER ADDITION USING DEM – FROM BULK MATERIAL TO SUSPENSION

DIPL.-INF. KNUT KRENZER*, PROF. DR.-ING. VIKTOR MECHTCHERINE¹ AND
DR.-ING. ULRICH PALZER²

* IAB – Institut für Angewandte Bauforschung Weimar gGmbH (IAB)
Über der Nonnenwiese 1, 99428 Weimar, Germany
e-mail: K.Krenzer@IAB-Weimar.de, web page: <http://www.iab-weimar.de>

^{†1} Technische Universität Dresden (TUD), Institute of Construction Materials
01062 Dresden, Germany
mechtcherine@tu-dresden.de

^{†2} IAB – Institut für Angewandte Bauforschung Weimar gGmbH (IAB)
Über der Nonnenwiese 1, 99428 Weimar, Germany
Kontakt@IAB-Weimar.de

Keywords: DEM, moisture transfer, user defined contact model, mixing, liquid bridge, suspension.

Abstract. This paper introduces a model in the Discrete Element Method to simulate the mixing processes of dry materials with major water addition more realistically. The presented model covers the representation of liquid transfer from fluid particles or moist particles to dryer ones including increase in volume. Depending on the moisture content of the particles in contact, the adequate interaction model (friction, liquid bridge or suspension) and its parameters are applied.

1 INTRODUCTION

Optimising mixing processes of dry granular materials with major water addition (e.g. concrete mixing) is a challenging task. Reaching the main objective i. e. a homogeneous distribution of all constituents including the liquid phase is not a straight forward process since the material behaviour changes dramatically during the mixing. The mixer must handle first dry material and subsequently moist material and finally suspensions. In all stages, an adequate movement of the constituents has to be ensured to reach their homogeneous distribution; otherwise, as an extreme case, some dry materials may not be mixed properly and can remain in the mixer (

Figure 1). The experimental evaluation of the mixing quality is a time-consuming and complex task. The estimation of the dry materials' distribution can only be performed by a combination of washing, sieving and weighing and is limited to the inherent components with bigger grain sizes. The distribution of the small size components and the liquid phase can only be tested indirectly by the comparison of the overall behaviour of the material. Therefore the optimization of the mixing equipment and the parameter setup is tedious and difficult, especially for new high viscous material mixes, for which no handling expertise exists.



Figure 1: Example of an inadequate mixing, some dry constituents remain in the mixer

An alternative analysis tool is numerical process simulation enabling a process-accompanying evaluation of the distribution of all components in all areas of the mixer. Such tools are already successfully applied for optimising mixing processes. Both fluids and bulk materials can be modelled using Computational Fluid Dynamics (CFD) or the Discrete Element Method (DEM). Currently, however, dry and fluid phases combined in a mixing process can be replicated only to a limited extent, particularly if both phases represent high volume fractions. The approach outlined in this paper aims to simulate this type of mixing process, reflecting the transition from dry to moist bulk material and eventually to a suspension whilst considering changes in material behaviour at each of the intermediate stages. A parametric contact model is necessary for each of the material states and the related state-transitions in order to represent the specific conditions in a process-oriented manner. Such a model was developed with focus on fresh concrete using the DEM approach. One of the key steps of this model replicates how moisture is transferred to and absorbed by, the individual solid particles.

At the moment of inter-particle contact, the contact model is selected depending on the moisture variables of the particles and the overlap. A friction model is used for dry particles, whereas additional liquid bridge forces are considered for moist particles. In the case of a high portion of liquid phase, a specific model is needed to adequately simulate the suspension behaviour. For this purpose, particles are represented by a two-layer model, and interact according to a Bingham model.

The targeted application of the model at hand is the analysis and optimization of complex wet-mixing processes within a wide range of consistencies, e.g. the concrete production process. The model shall enable the evaluation of the liquid distribution and the overall mixing quality with much less effort compared to the experimental approach to detect critical areas within the mixer and to reveal possible options for improvements.

2 APPROACH

During the mixing process of wet mixing processes like in concrete fabrication, the source bulk materials pass several phases, from dry, to wet, ending up as a suspension (Figure 2). To simulate the mixing process, each of these stages has to be represented in the model and especially the transition of the water causing the stage changes must be implemented. Therefore a user defined model has to be implemented, representing the transition from the

early dry state to the final suspension state. The modeling of the transition is based on the results of experimental investigations and known theoretical models.

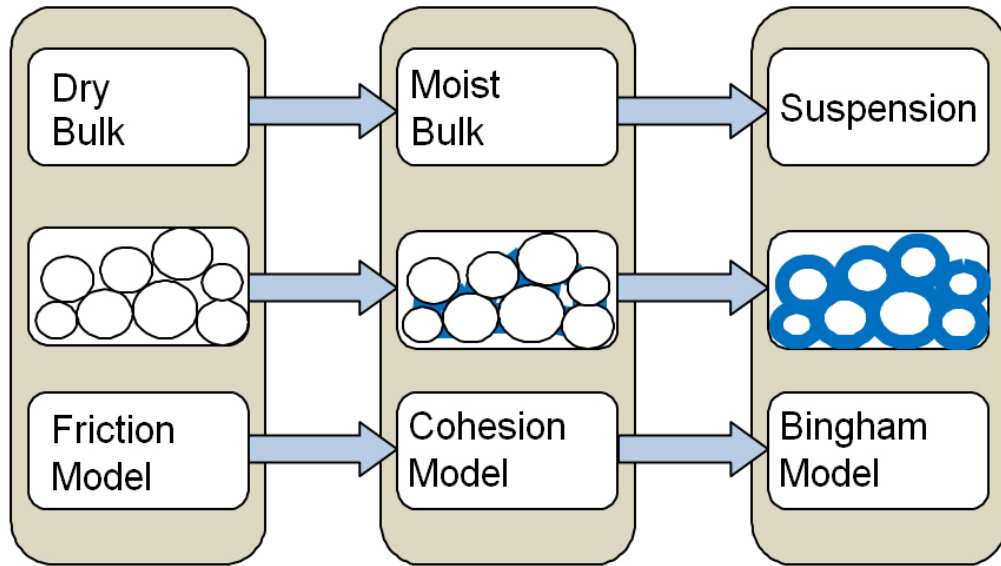


Figure 2: Different moisture states of bulk material during wet mixing and associated contact model

The representation of these states for a single particle in the simulation is introduced by an additional moisture variable. Each particle therefore has its own moisture content. Also the kind of liquid, present at the particle is noted, whether it is water or an already mixed cement paste or mortar. Depending on the moisture variable of two contacting particles, the contact model is chosen at the time of the particle contact. For dry particles a friction model is used, while for wet particles additional liquid bridge forces are integrated. For the suspension state a complete new model has been developed at the IAB, on the base of the Bingham model. The transition between these stages in simulation is triggered by the adsorption and absorption of moisture by the solid particles. At the beginning water is added as particles. When they get into contact with dry material, a time and state dependent transfer of the moisture is calculated and the moisture content of the former dry particle and its volume increases over time, while the water particle loses volume. The process dependent implementation of the moisture content also enables simulating different stages of concrete mixing. Since various particles come in contact with water at various moments in time, also heterogeneity of the mixture and its transition to a homogenous one can be simulated.

The characteristics of the liquid thereby influence the contact model parameters like viscosity and surface tension and therefore affect the contact model calculation e.g. for the liquid bridge force. Thus a smooth transition between all stages is provided.

3 SIMULATING WATER TRANSFER

One of the key issues of the suggested model is to replicate how moisture is transferred between individual particles. For this purpose additional moisture variables are assigned to each particle to simulate the moisture content, type of liquid, (i. e. water, cement paste or mortar) and its exact composition. Initially, water is added as spherical particles. A time- and

state-dependent transfer of moisture occurs upon contact between water and dry particles. The volume and moisture content of the initially dry particles increase over time, whereas the volume of the water particles is decreased (Figure 3). In the first step, the dry particles become wet and build up a two-layer particle with a solid core and an outer liquid film. When small particles absorb a sufficient amount of liquid, they will turn to a suspension and can also be considered as liquid particles. In the concrete mixing process this approach is used to create suspension particles that simulate mortar or cement paste, which can be adsorbed by the bigger aggregate particles. This results in new fluid transition regimes. A general overview of the transfer scenarios is displayed in Figure 4.

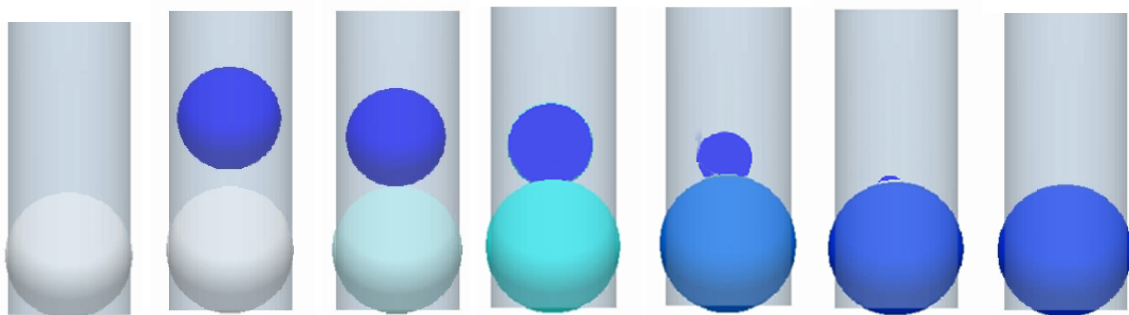


Figure 3: Contact of a water particle (top) and a dry particle (bottom), leading to a volume increase and a moisture transfer. The color of solid particles corresponds to the absolute water content

	t_0	t_1	t_2
Union with equalization (water and suspension particle)	○ ●	○ ●	●
Union with double layer creation (fluid and dry particle)	○ ●	○ ○ ●	○ ○
Exchange with equalization (two suspension particles)	○ ●	○ ○	○ ○

Figure 4: Different water transfer scenarios depending on the contacting particles

The transfer is based on the models by Darcy used in [8] and Washburn [9], depending on the real particle size of the absorbing material and the constitution of the absorbed liquid.

$$v_f = \frac{K}{\eta} * \left(\frac{2\gamma}{rs(t)} - \frac{h}{l} \rho g \right) \quad (1)$$

where K is the permeability, η the viscosity, γ the surface tension, $\frac{h}{l}$ the ratio between the height difference and the distance of the particle centres, ρ the fluid density, g gravitational constant, $s(t)$ the current penetration depth of the fluid. To keep $s(t) \neq 0$ fulfilled at all times the dry starting condition is set $s(t_0) = s_0 = 5e^{-4}m$, accordingly to the initial wetting layer

thickness defined in the model. The real particle size thereby has to be implemented as a particle attribute, because for fine materials like cement the particle size in the simulation is larger by several magnitudes in comparison to the real particle size. One simulation particle models a representative volume of cement.

If a liquid and a dry particle get in contact the first time, an additional amount of liquid is transferred to the dry particle. This models the fluid part that sticks to the surface of the dry particle no matter how long the particle contact was. This is essential for liquids with high viscosity, since they pass liquid by the described model very slowly. For the mixing process there exists also another aspect of. A faster relative movement of the particles leads to a stronger mixing and therefore a faster liquid exchange. To take this effect into account an additional liquid exchange volume was implemented in the simulation using a heuristic formula in the following form is used

$$V_{exchange} = V_{min} \left(\frac{\dot{\gamma}}{\dot{\gamma}_{ref}} \right) \Delta t x \quad (2)$$

where V_{min} is the minimum volume of the interacting particles, $\dot{\gamma}$ is the local shear rate, Δt is the timestep and x is the percentual portion of the liquid exchange per second.

Besides the speed of the liquid exchange, also the maximum amount of liquid a single particle can adsorb is of interest. This depends mainly on the particle size, surface condition (roughness, wettability) and the type of liquid. A series of experimental tests were performed to estimate the maximum liquid amount for several dry material and liquid combinations. Figure 5 shows exemplarily the dependency of the maximum water adsorption by gravel depending on the grain size in a complex structure.

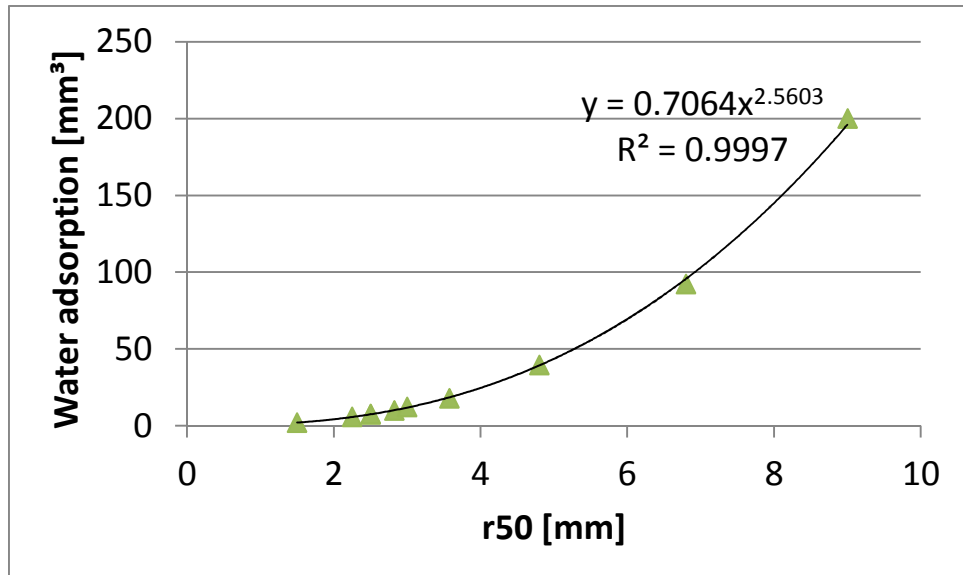


Figure 5: Maximum volume of adsorbed water as a function of average grain radius in a complex structure

4 CONTACT MODELS

At the moment of inter-particle contact, a contact model is selected depending on the moisture variables (Figure 2) of the particles and the degree of overlap (Figure 6). A friction

model is used for dry particles, whereas additional liquid bridging forces are considered for moist particles and a suspension model is used for the suspension state. The friction model is based on the standard models of the DEM and therefore is not presented in detail here.

Particle double layer model

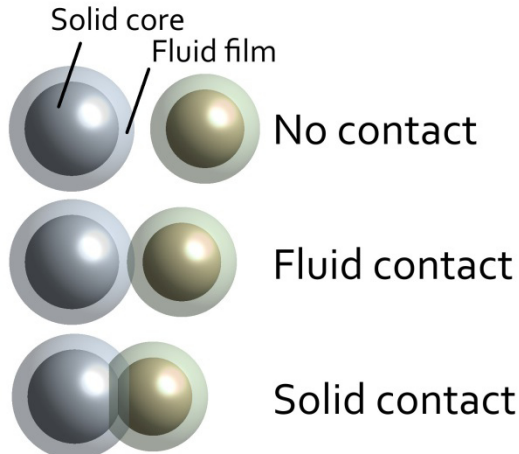


Figure 6: Contact types for the interactions of two double-layer particles

4.1 Liquid Bridge Model

The liquid bridge model is chosen when two particles are in contact and the liquid volume of the contact is in pendular or funicular state or a wet particle interacts with a wall of the mixer. In this case, an additional cohesion force acts on particles. The liquid bridge forces depend on the size of particles, liquid volume, surface tension of liquid, liquid type and the distance between the particles. The model is based on an approach suggested by Mikami [1]:

$$F = 2\pi r_{harm} \gamma F^* \quad (3)$$

The model was verified with experimental data (the experimental setup is shown in Figure 7) and showed a good agreement for low liquid volumes (Figure 9). Furthermore the model was tested on a simple angle of repose test as shown in Figure 8. Additional experiments were performed to get data for higher liquid volumes and various liquid viscosities to widen the range of the model.

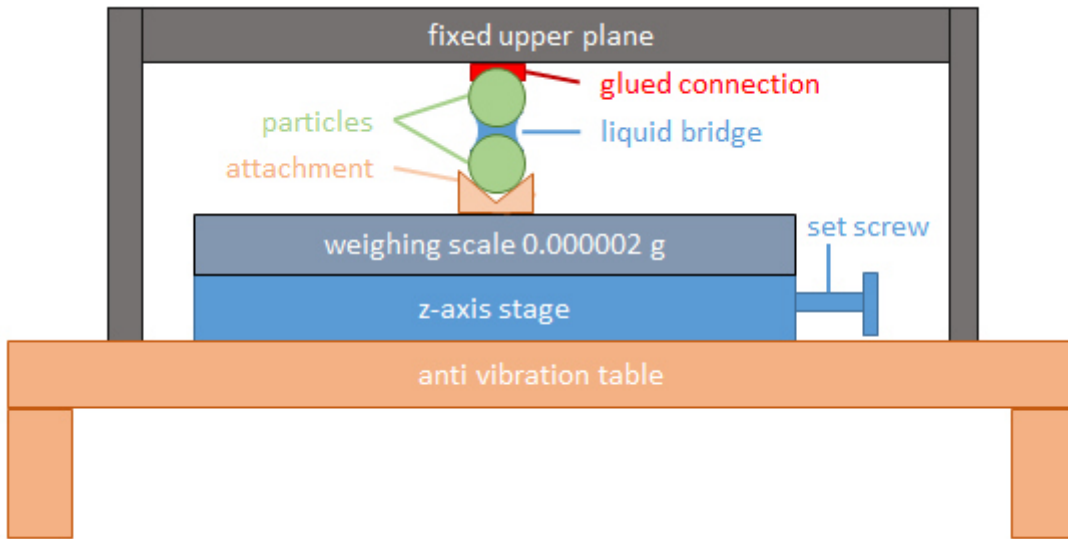


Figure 7: Schematic view of the setup for measuring liquid bridge forces

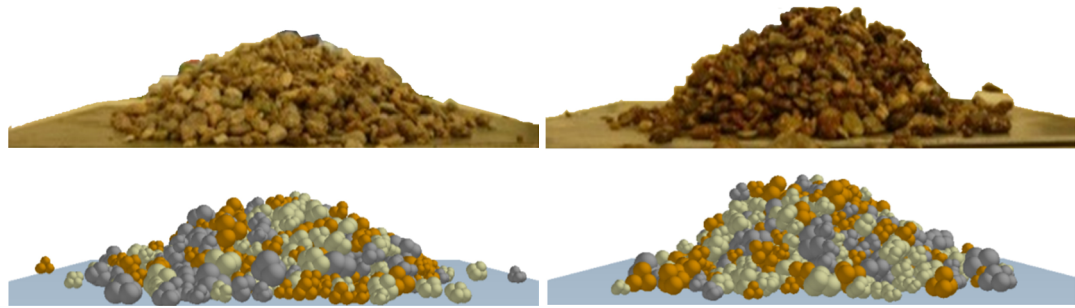


Figure 8: Comparison of dry (left) and wet (right) angles of repose for gravel in the experiment (top) and in the simulation (bottom)

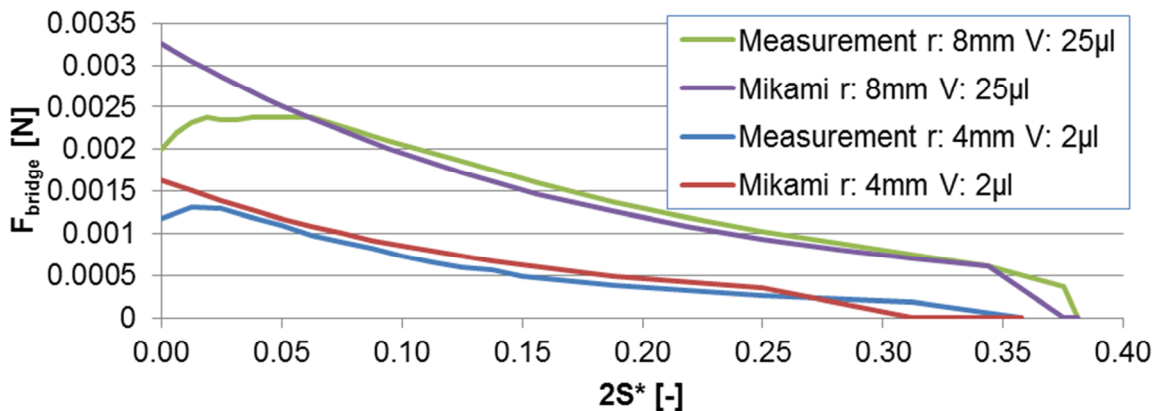


Figure 9: Comparison of the liquid bridge forces of glass spheres with various radii and water volumes computed by the theoretical model by Mikami and measured in the experiment

4.2 Suspension Model

In the case of a high liquid volume at the contact spot of two interacting particles, a specific model is needed to adequately simulate the suspension behaviour. Modeling suspensions like concrete in DEM is not trivial and this is not the typical field of application for this simulation method. Suspensions often have a non-Newtonian material behavior so has fresh concrete. It is usually abstracted by Bingham-Model or the more general Herschel Bulkley model [3]. In CFD simulations these models can be used directly neglecting the phenomena occurring by the direct influence of the granular phase [4]. In the DEM different approaches are needed due to the discrete manner of modelling heterogeneous materials like fresh concrete [6], [7]. Most of the existing DEM models developed for concrete use double layer models to represent the solid aggregates uniformly covered by an imaginary layer of fluid fine mortar. Figure 6 shows the schematic structure of a two-layer particle as used in the present approach.

The constitutive relations used in this paper are based on the Bingham model as described in [2]. Since Bingham model is valid for the continuum mechanics only, it must be adapted to the DEM approach by several heuristics, for example an approximated contact area and shear rates (see Figure 10) as well as transformations to extract the contact force from the shear stress. The basic idea is to approximate the local shear rates by the relative velocity of the particles and the liquid layer in between. From the consistency of the liquid in the contact region the rheological Bingham parameters yield stress and viscosity are derived and the shear stress can be calculated. The shear stress is approximated to a contact force based on equation (4) from [5]:

$$\sigma = \frac{\phi k}{4\pi r^2} F \quad (4)$$

Thereby k is the coordination number and ϕ the solid volume concentration.

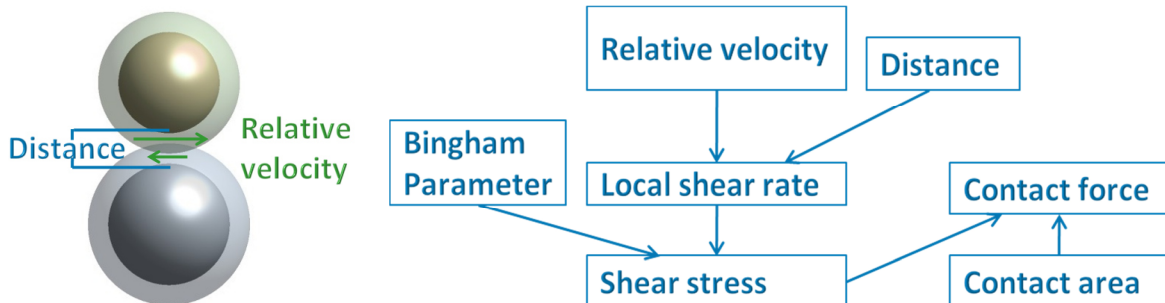


Figure 10: Schematic view of the compensational Bingham model in DEM

5 RESULTS

The developed model was tested on a two phase system of cement and water within a typical mortar mixer. After a mixing phase of one minute the liquid was mostly equally distributed within the mixer. There was a dry area at the lower bottom of the tank (Figure 11) where the mixing tool does not directly interact with the material. This observation is congruent with the experience from the experimental testing.

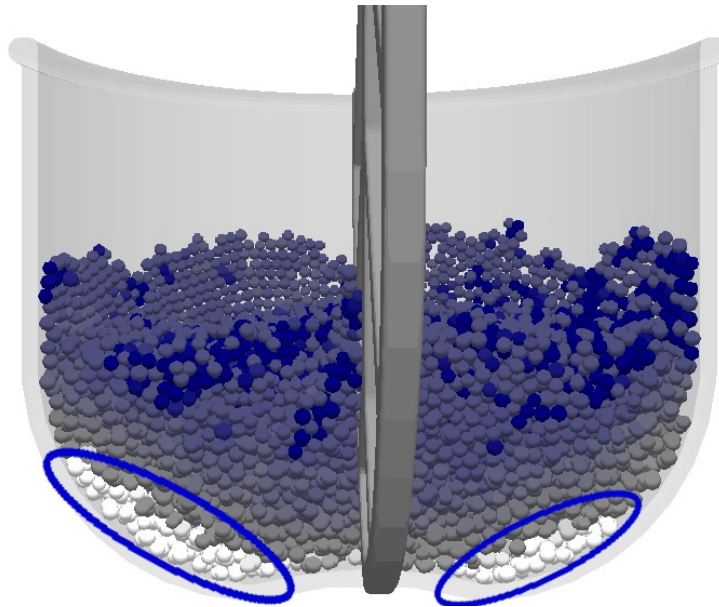


Figure 11: Moisture distribution in a DEM simulation of a cement-water mixing process after one minute of mixing. The color represents the moisture states from dry (white) to completely wetted (blue). The dry parts at the bottom are highlighted

Furthermore, another mixing process was simulated using gravel as an additional third phase. After the water addition, the power consumption derived from the total torque showed the typical curve that can be observed during mixing of concrete (Figure 12). First, an increase of the power consumption occurs, caused by the additional cohesive forces from the liquid bridges. After some time the power consumption drops because of the starting liquefaction of the mixture.

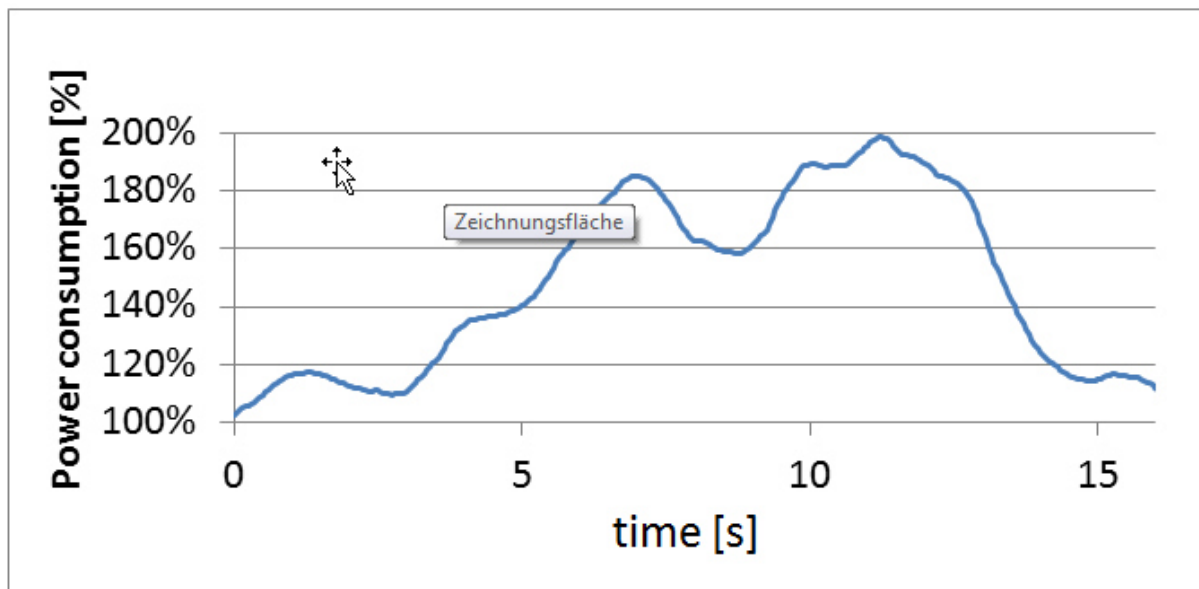


Figure 12: Relative power consumption starting from a dry mix of cement and gravel adding water (time zero)

6 CONCLUSIONS

A new DEM model was suggested to simulate the mixing process of dry granular materials with a massive liquid addition. The model includes the transfer of liquid between particles as a function of their size, moisture state and the liquid's properties. Depending on the particular moisture state adequate contact models are chosen using frictional, cohesive or Bingham-like behavior. The representation of the particles is based on a double layer approach and additional particle variables storing information related to the liquid. The general applicability of the model was demonstrated on two examples of mixing. This offers a basis for investigating more complex mixing processes.

REFERENCES

- [1] Mikami, T., Higehiro, K. and Masayuki, H. *Numerical simulation of cohesive powder behavior in a fluidized bed.* (E. Science, Hrsg.) Chemical Engineering, (1998), p. 1927-1940.
- [2] Krenzer, K., Mehiri, K., David, M., Dehadt, S. and Palzer, U.. *Optimization of Fibred Concrete Mixing.* CPI – Concrete Plant International,(2014) p. 18-21.
- [3] Wüstholtz, Timo: *Experimentelle und theoretische Untersuchungen der Frischbetoneigenschaften von Selbstverdichtendem Beton,* (2005)
- [4] Roussel, Nicolas; Geiger, Mette; Dufour, Frederic; Thrane, Lars; Szabo, Peter: *Computational Modeling of concrete Flow: State of the art*
- [5] Restagno, F., Bocquet, L., and Charlaix, E.. *Where does a cohesive granular heap break.* The European Physical Journal E (2004) p. 177-183.
- [6] Mechtcherine, V. und Shyshko, S.: *Simulating the behaviour of fresh concrete using distinct element method,* (2007).
- [7] Mechtcherine, V., Gram, A., Krenzer, K., Schwabe, J.-H. and Shyshko, S. *Simulation of fresh concrete flow using Discrete Element Method (DEM) - Theory and applications.* Material an Structures (2012) **47**, p. 615-630
- [8] Li, X., Chu, X., and Sheng, D. A saturated discrete particle model and characteristic-based SPH method in granular materials. International Journal for Numerical Methods in Engineering (2007) **72**, p. 858-882.
- [9] IMETER Intelligente Messtechnik für Stoffeigenschaften.. Von Washburn-Gleichung (Theorie): <http://www.imeter.de/imeter-methoden/kapillaritaet-kontaktwinkel-sorptivitaet/washburn-gleichung.html> (2014)

ACTIVE-SET BASED QUADRATIC PROGRAMMING ALGORITHM FOR SOLVING INNER OPTIMIZATION PROBLEMS WITH INEQUALITIES IN GRANULAR DYNAMICS SIMULATIONS

Lukáš Pospíšil¹, Zdeněk Dostál¹ and David Horák¹

¹ VSB-Technical University of Ostrava,

Tr 17. listopadu 15,

CZ-70833 Ostrava, Czech Republic

e-mail: lukas.pospisil@vsb.cz, zdenek.dostal@vsb.cz, david.horak@vsb.cz

web page: <http://industry.it4i.cz/>

Key words: Granular Materials, Contact Problems, DVI, MPRGP

Abstract. Active-set algorithm for solving inner optimization problem in multi-body dynamics is presented. The efficiency of our algorithm is demonstrated on the solution of simple simulation with thousands of moving spherical particles and static box obstacles. We discuss the solvability and the uniqueness of solution of the problem and the influence of solution to resulting velocity during time-stepping schema.

1 Introduction

In this paper, we are interested in granular dynamics problems; in particular, namely simple multibody dynamics problems. These problems that may deal with from hundreds to billions of discrete rigid bodies interacting through contact, impact, or mutual constraints, such as simulation of the movement of granular matter, are one of the most challenging issue in computer-aided kinematics and dynamics of mechanical systems. Many real-world systems contain or interact with granular material, as granular material belongs among the most manipulated materials. For instance, such a material is utilized in a variety of fields, from sand, gravel, or nanoscale powders to large boulders in the civil industry. Devices consisted of rigid bodies interacting through frictional contacts and mechanical joints pose numerical solution challenges because of the discontinuous nature of their motion, see Pfeiffer and Glocker [1].

Usually, these simulations are performed using discrete element method (DEM, see for instance Cundall [2], Avci and Wriggers [3]; a penalty method where the computation of interaction force is based on the kinematics of the interaction, some representative parameters, and an empirical force law.

From our point of view, another method is more interesting. It is more similar to the solution of linear elasticity contact problems, because the problem is consisting of a differential variational inequality (DVI, see Pang and Stewart [4], Renouf and Alart [5], Heyn [6]). The method is sometimes referred to the Lagrange multiplier approach. It enforces non-penetration of rigid bodies via a constraint-based approach. In the DVI method, a linear inequality constrained quadratic optimization problem with symmetric positive semidefinite Hessian matrix must be solved at each time step of the simulation. The unknowns in the problem are the normal contact forces between interacting bodies. The efficient solution of inner optimization problem in DVI brings us to the development of Quadratic programming (QP) algorithms. Our research in the solution of particle dynamics simulations is motivated by the results achieved by Heyn et al. [7].

Authors used our Modified Proportioning with Reduced Gradient projection algorithm (MPRGP) to solve DVI efficiently in spite of the fact that all theoretical results supporting the convergence of MPRGP were valid only for the strictly convex cost functions. Only recently, we successfully extended the theory and explained the convergence of the MPRGP for the problems with more general convex quadratic cost function, see Dostál and Pospíšil [8].

In the paper, we are interested in simple simulations with sphere and box particles, but our algorithms can be easily generalized to particle problems with general geometry.

The first subsection consists of short review of the numerical solution concept and time-stepping scheme. The aim of the paper is not to develop new simulations techniques or to modify the mathematical modelling process. However, we are interested in numerical aspect of the inner QP optimization problem and our proofs of the solvability are based on the object structures. Therefore, we decided to present short review. We present the formulation of the problem and derivation of optimization problem. The presented theory and ideas in these subsections can be considered as a short review of Heyn [6].

In the second section we present own new results in the mathematical aspect of the optimization problem solvability.

In the next section, we present our active-set based algorithm Modified Proportioning with Reduced Gradient Projection (MPRGP). This algorithm was successfully used to solve a linear elasticity contact problems with up to more than 40 million of nodal variables, see Dostál et. al [9]. This method combines the conjugate gradient steps with the reduced gradient projection steps and adaptive precision control of the solution of the auxiliary problems. Special attention is paid in the discussion of the solvability of optimization problem. The performance of the algorithm is demonstrated by the solution of a 3D particle dynamics problem.

The last subsection includes the numerical experiments and results. We have implemented algorithms in C programming language with CUDA library, and we performed simulations on GPU card. The problem of granular dynamics is suitable for solving on such a massively parallel architectures. However, the aim of the paper is not to develop

optimal implementation, but the development of algorithms. Much more efficient implementation was presented by the team from Simulation-Based Engineering Lab (SBEL) University of Wisconsin-Madison in Chrono::Engine software [10].

2 Time-stepping schema and formulation of optimization problem

In this short section, we review the basic of multi-body simulations. For more informations see, for instance, Haug [11] and Heyn [6].

Let us consider the system of $n_b \in \mathbb{N}$ rigid bodies (*particles*) in vector space $\{(x, y, z) \in \mathbb{R}^3\}$. Each particle has 6 degrees of freedom - location of centre of gravity $[r_x, r_y, r_z]^T$ and unit quaternion of rotation $[e_0, e_1, e_2, e_3]^T$. For every body $T_{(i)}, i = 1, \dots, n_b$ in the system in given time t , let us denote $q_{(i)}^t \in \mathbb{R}^7$ as a *vector of generalized position* and $v_{(i)}^t \in \mathbb{R}^6$ as a *vector of generalized velocities*. In our simulations, the rotation of the body is represented by the unit quaternion of rotation and the angular velocity is represented by Euler angles. The position of bodies in the next time-step can be evaluated using time-stepping schema

$$q^{(t+h)} = q^{(t)} + h.Qv^{(t)},$$

where h is *sufficiently small* time step. Here, Q denotes the matrix of linear mapping between derivative of position vector and vector of velocities, see Haug [11]. This equation can be considered as a discretized numerical solution of the first Newton law using Euler method.

The same method is also used for the computation of velocities. The increment in the next time-step depends on the mass of each body, affecting external forces $F_{ext}(t, q, v)$, and contacts and other limiting conditions. This situation is described by second Newton law, i.e.

$$v^{(t+h)} = v^{(t)} + hM^{-1}(F_{ext} + F_C), \quad (1)$$

where M is generalized mass matrix, F_C is a vector of forces induced by contact constraints, and F_{ext} is a vector of external forces. In our simple simulation, the vector of external forces represents the gravity force affecting each body.

The contact between two bodies T_A and T_B constitutes forces and torques

$$\begin{aligned} F_A &= -\tilde{\gamma}n_A(C), & F_B &= \tilde{\gamma}n_A(C), \\ M_A &= C^A \times F_A, & M_B &= C^B \times F_B, \end{aligned}$$

where $n_A(C)$ is outward unit normal to the body T_A at the contact point $C = [C_x, C_y, C_z]^T \in \mathbb{R}^3$ in global coordinate system, and $\tilde{\gamma} \geq 0$ is unknown size of the force. Force F_B causes the change of the position of the body T_B (the components of the generalized velocity vector corresponding to the position of gravity center). The change of rotation of the body T_B (the components of the generalized velocity vector corresponding to the rotation) is effected by associated torque M_B . Analogically, forces F_A and M_A change the position

and rotation of body T_A . All forces can be expressed by one vector

$$F_C = \begin{bmatrix} F_A \\ M_A \\ F_B \\ M_B \end{bmatrix} = \begin{bmatrix} -\tilde{\gamma}n_A(C) \\ C^A \times F_A \\ \tilde{\gamma}n_A(C) \\ C^B \times F_B \end{bmatrix} = \underbrace{\begin{bmatrix} -\tilde{\gamma}n_A(C) \\ -\tilde{\gamma}\tilde{C}^A n_A(C) \\ \tilde{\gamma}n_A(C) \\ \tilde{\gamma}\tilde{C}^B n_A(C) \end{bmatrix}}_{=:D \in \mathbb{R}^{12,1}} = \begin{bmatrix} -n_A(C) \\ -\tilde{C}^A n_A(C) \\ n_A(C) \\ \tilde{C}^B n_A(C) \end{bmatrix} \tilde{\gamma}, \quad (2)$$

where we used the matrix representation of the vector product

$$\tilde{C}^B = \begin{bmatrix} 0 & -C_z^A & C_y^A \\ C_z^A & 0 & -C_x^A \\ -C_y^A & C_x^A & 0 \end{bmatrix}, \quad \tilde{C}^B = \begin{bmatrix} 0 & -C_z^B & C_y^B \\ C_z^B & 0 & -C_x^B \\ -C_y^B & C_x^B & 0 \end{bmatrix}.$$

The unknown size of the force $\tilde{\gamma}$ is constrained by the non-penetration conditions of the bodies, which can be described by *gap function* $\Phi : \mathbb{R}^{7+7} \rightarrow \mathbb{R}$. It holds

- $\Phi([q_A, q_B]) = 0, \tilde{\gamma} \geq 0$ if the bodies are in contact,
- $\Phi([q_A, q_B]) > 0, \tilde{\gamma} = 0$ if the bodies are not in contact,
- $\Phi([q_A, q_B]) < 0$ if the bodies penetrate each other.

Merging these observations, we obtain the *complementarity condition*

$$\begin{aligned} \Phi(q) &\geq 0, \\ \tilde{\gamma} &\geq 0, \\ \Phi(q) &\perp \tilde{\gamma}. \end{aligned}$$

Instead of these conditions, we can consider more numerically stable conditions (see Ańtescu [12])

$$\begin{aligned} \tilde{\gamma} &\geq 0, \\ \frac{1}{h}\Phi(q) + D^T v^{(t+h)} &\geq 0, \\ \frac{1}{h}\Phi(q) + D^T v^{(t+h)} &\perp \tilde{\gamma}. \end{aligned} \quad (3)$$

This problem can be reformulated to the quadratic programming problem with bound constraints, see next theorem. For simplicity we denote $\gamma = t.\tilde{\gamma}$.

Lemma 1. *The solution of the optimization problem*

$$\min_{\gamma \geq 0} \frac{1}{2} \gamma^T N \gamma + r^T \gamma, \quad (4)$$

where

$$N = D^T M^{-1} D, \quad (5a)$$

$$r = \frac{1}{h} \Phi + D^T M^{-1} k, \quad (5b)$$

$$k = M v^{(t)} + h.F_{ext}, \quad (5c)$$

is equivalent to the solution of original problem

$$M(v^{(t+h)} - v^{(t)}) = hF_{ext} + D^T\gamma, \quad (6a)$$

$$\frac{1}{h}\Phi(q) + D^T v^{(t+h)} \geq 0, \quad (6b)$$

$$\frac{1}{h}\Phi(q) + D^T v^{(t+h)} \perp \gamma, \quad (6c)$$

$$\gamma \geq 0. \quad (6d)$$

Proof. The proof is based on the Karush-Kuhn-Tucker optimality conditions. See Heyn [6]. \square

The algorithm in every time-step has the form of Algorithm 1.

Algorithm 1: Time-stepping schema.

Given $t, h, q^{(t)}, v^{(t)}$.

find contacts

if there is a contact

set up N, r from contacts

solve the problem

$$\gamma = \arg \min_{\gamma \geq 0} \frac{1}{2} \gamma^T N \gamma + r^T \gamma$$

$$v^{(t+h)} = v^{(t)} + M^{-1}(hF_{ext} + D\gamma)$$

else

$$v^{(t+h)} = v^{(t)} + hM^{-1}F_{ext}$$

endif

$$q^{(t+h)} = q^{(t)} + h.Qv^{(t)}$$

Return $q^{(t+h)}, v^{(t+h)}$.

3 The solvability and uniqueness of the solution

In this section, we prove that the inner optimization problem has always solution. However, since kernel of Hessian matrix is non-trivial, it can have infinite number of solutions. We show that the resulting velocity is independent of the choice of the solution of inner optimization problem.

Lemma 2. Let $A \in \mathbb{R}^{n,n}$ be a symmetric positive definite matrix and let $B \in \mathbb{R}^{n,m}$ be a rectangular matrix.

Then

$$\text{Ker } B^T AB = \text{Ker } B, \quad (7a)$$

$$\text{Im } B^T AB = \text{Im } B^T. \quad (7b)$$

Proof. See Laub [13] or Dostál [14]. \square

Lemma 3. *The optimization problem (4) is a quadratic programming problem with symmetric positive semidefinite Hessian matrix and right-hand side vector from the image of Hessian matrix, i.e.*

$$\forall x \in \mathbb{R}^{n_c} : \langle Nx, x \rangle \geq 0 \quad (8a)$$

$$r \in \text{Im } N \quad (8b)$$

Proof. At first, we prove (8a). It is necessary to show that $\forall x \in \mathbb{R}^{n_c} : \langle Nx, x \rangle \geq 0$. We use that $M \in \mathbb{R}^{6n_b, 6n_b}$ is symmetric positive definite. Therefore, the inverse is also symmetric positive definite and it induces the norm in \mathbb{R}^{6n_b} . Furthermore, we can write

$$\langle Nx, x \rangle = \langle D^T M^{-1} Dx, x \rangle = \langle M^{-1} Dx, Dx \rangle = \|Dx\|_{M^{-1}}^2 \geq 0.$$

If we take a look into the formula for the right-hand side vector

$$r = \frac{1}{h} \Phi + D^T M^{-1} k,$$

we can use Lemma 2 and simplify the proof of (8b) into the proof of

$$\Phi \in \text{Im } D^T. \quad (9)$$

At first, let us define the vector spaces $\mathcal{V}, \mathcal{W} \subset \mathbb{R}^{n_c}$

$$\mathcal{V} = \text{span} \left\{ \begin{bmatrix} 1 \\ -1 \\ 0 \\ 0 \\ \vdots \\ 0 \\ 0 \end{bmatrix}, \begin{bmatrix} 0 \\ 0 \\ 1 \\ -1 \\ \vdots \\ 0 \\ 0 \end{bmatrix}, \dots, \begin{bmatrix} 0 \\ 0 \\ 0 \\ 0 \\ \vdots \\ 1 \\ -1 \end{bmatrix} \right\}, \quad \mathcal{W} = \text{span} \left\{ \begin{bmatrix} 1 \\ 1 \\ 0 \\ 0 \\ \vdots \\ 0 \\ 0 \end{bmatrix}, \begin{bmatrix} 0 \\ 0 \\ 1 \\ 1 \\ \vdots \\ 0 \\ 0 \end{bmatrix}, \dots, \begin{bmatrix} 0 \\ 0 \\ 0 \\ 0 \\ \vdots \\ 1 \\ 1 \end{bmatrix} \right\}.$$

We take a better look into the structure of matrix $D \in \mathbb{R}^{6n_b, n_c}$ whose blocks are given by (2). This matrix always consists of the pairs of contacts - the contact between the body T_A and the body T_B (denoted by contact AB) as well as the contact between body B and A (denoted by contact BA). For the sake of simplicity we consider the construction

of matrix $D \in \mathbb{R}^{6n_b, n_c}$ with consecutive collocation of the contact pairs. Then each pair of columns corresponds to the pair of contacts and the nonzero rows corresponding to the indexes of the bodies in this contact is given by (2). The submatrix for one pair of contacts AB and BA has the structure

$$D_{\mathcal{R}, \mathcal{C}} = \begin{bmatrix} -n_A(C_{AB}) & n_B(C_{BA}) \\ -\tilde{C}_{AB}^A n_A(C_{AB}) & \tilde{C}_{AB}^A n_B(C_{BA}) \\ n_A(C_{AB}) & -n_B(C_{BA}) \\ \tilde{C}_{AB}^B n_A(C_{AB}) & \tilde{C}_{BA}^B n_B(C_{BA}) \end{bmatrix}, \quad (10)$$

$$\mathcal{R} = \{\text{indexes of } v_A, \text{ indexes of } v_B\},$$

$$\mathcal{C} = \{\text{index of contact } AB, \text{ index of contact } BA\}.$$

The key ingredient of the proof is a small observation – the contact forces in the contact points $C_{AB} = C_{BA}$ have opposite directions and the outward unit normals of the bodies in the contact are also opposite. Thus $n_A = -n_B$ and the submatrix (10) can be written in simpler form

$$D_{\mathcal{R}, \mathcal{C}} = \begin{bmatrix} -n_A & -n_A \\ -\tilde{C}^A n_A & -\tilde{C}^A n_A \\ n_A & n_A \\ \tilde{C}^B n_A & \tilde{C}^B n_A \end{bmatrix},$$

where we used notations $n_A = n_A(C_{AB}) = -n_B(C_{BA})$, $C^A = C_{AB}^A = C_{BA}^A$, and $C^B = C_{AB}^B = C_{BA}^B$.

Using this structure, it is easy to check that

$$\begin{aligned} \forall v \in \mathcal{V} : \quad & Dv = 0, \\ \forall w \in \mathcal{W} \setminus \{0\} : \quad & Dw \neq 0. \end{aligned}$$

Furthermore, we proved that $\mathcal{V} \subset \text{Ker } D$ and $\mathcal{W} \cap \text{Ker } D = \{0\}$. Using this and $\text{Im } D^T \perp \text{Ker } D$, we can write

$$\left. \begin{array}{l} \text{Ker } D \supset \mathcal{V} \perp \mathcal{W} \\ \mathcal{W} \cap \text{Ker } D = \{0\} \end{array} \right\} \Rightarrow \mathcal{W} \perp \text{Ker } D \Rightarrow \mathcal{W} \subset \text{Im } D^T.$$

To prove (9), notice that $\Phi \in \mathcal{W}$ because the gap function has the same value for both contacts AB and BA (the distance between bodies T_A and T_B is the same as distance between bodies T_B and T_A). \square

The previous lemma proves that the cost function is bounded from below. Using the classical results given by Frank and Wolfe [15], we can conclude that the optimization problem (4) has always solution.

Lemma 4. *The velocity in the next time-step $v^{(t+h)}$ given by Algorithm 1 is independent of the choice of the solution of the optimization problem (4).*

Proof. Let $\bar{\gamma}_1, \bar{\gamma}_2$ denote different solutions of optimization problem (4). Then the velocity in the next time-step given by Algorithm 1 is given by

$$\begin{aligned} v^{(t+h)}(\bar{\gamma}_1) &= v^{(t)} + M^{-1}(hF_{ext} + D\bar{\gamma}_1), \\ v^{(t+h)}(\bar{\gamma}_2) &= v^{(t)} + M^{-1}(hF_{ext} + D\bar{\gamma}_2). \end{aligned}$$

Thus the difference of these velocities reads

$$v^{(t+h)}(\bar{\gamma}_1) - v^{(t+h)}(\bar{\gamma}_2) = M^{-1}D(\bar{\gamma}_1 - \bar{\gamma}_2).$$

Since the solutions of quadratic programming problem differ by the vector from the kernel of Hessian matrix, see Dostál [14] and $\text{Ker } N = \text{Ker } D$ (see Lemma 2), we can write

$$v^{(t+h)}(\bar{\gamma}_1) - v^{(t+h)}(\bar{\gamma}_2) = M^{-1}0 = 0.$$

□

4 Modified Proportioning with Reduced Gradient Projection

For solving problem (5), we are using an active-set based algorithm. This algorithm is based on the decomposition of the set of indices of all constraints $\mathcal{M} = 1, \dots, n_c$ into two disjoint subsets subject to the value of the constraint function

$$\mathcal{F}(\gamma) := \{j \in \mathcal{M} : \gamma_j > 0\}, \quad \mathcal{A}(\gamma) := \{j \in \mathcal{M} : \gamma_j = 0\}.$$

Using this decomposition, we decompose the gradient of the cost function $g(\gamma) = \nabla f(\gamma) = N\gamma + r$ in every iteration γ^k into *free* and *chopped* gradient

$$\begin{aligned} \varphi_j(\gamma^k) &= g_j \quad \text{for } j \in \mathcal{F}(\gamma^k), & \varphi_j(\gamma^k) &= 0 \quad \text{for } j \in \mathcal{A}(\gamma^k), \\ \beta_j(\gamma^k) &= 0 \quad \text{for } j \in \mathcal{F}(\gamma^k), & \beta_j(\gamma^k) &= \min\{g_j, 0\} \quad \text{for } j \in \mathcal{A}(\gamma^k). \end{aligned}$$

Modified Proportioning with Reduced Gradient Projection (MPRGP, see Algorithm 2) is an efficient algorithm for the solution of convex quadratic programming problems with simple bounds. The basic version was proposed independently by Dostál [16] and Friedlander and Martínez [17]. It can be considered as a modification of the Polyak algorithm. Dostál and Schöberl in [18] combine the proportioning algorithm with the gradient projections [19]. They use the constant $\Gamma > 0$, the test to decide about leaving the face, and three types of steps to generate the sequence of iterates γ^k that approximate the solution.

The precision of the solution of auxiliary problems is controlled by norm of violation of Karush-Kuhn-Tucker condition in each inner iterate γ^k by

$$\Gamma \|\varphi(\gamma^k)\| \geq \|\beta(\gamma^k)\|,$$

while $\Gamma > 0$ and γ^k satisfying this inequality is called as *proportional*. If $\gamma \in \Omega$, i.e. $\gamma \geq 0$, we call γ *feasible*.

Algorithm 2: Modified Proportioning with Reduced Gradient projection (MPRGP).

```

Step 0 {Initialization of parameters}
 $\gamma^0 \in \Omega, \bar{\alpha} \in (0, \|N\|^{-1}], \Gamma > 0$ 

Step 1 {Proportioning step - removes indices from  $\mathcal{A}(\gamma^k)$ }
If  $\gamma^k$  is not proportional then define
 $\gamma^{k+1} = \gamma^k - \alpha_{CG}\beta(\gamma^k)$  by proportioning,
 $\alpha_{CG} = \frac{\beta^T(\gamma^k)g(\gamma^k)}{\beta^T(\gamma^k)A\beta(\gamma^k)}$  minimizes  $\phi(\gamma^k - \alpha\beta(\gamma^k))$  with respect to  $\alpha$ 

Step 2 {CG step}
If  $\gamma^k$  is proportional then generate
 $\gamma^{k+1} = \gamma^k - \alpha_{CG}p^k$  by trial cg step,
 $p^{k+1} = \varphi(\gamma^k) - \beta_{CG}p^k, \beta_{CG} = (\varphi^T(\gamma^k)Ap^k)/((p^k)^T Ap^k)$ 

Step 3 {Expansion step - expands  $\mathcal{A}(\gamma^k)$ }
If  $\gamma^k \in \Omega$  then accept it else generate
 $\gamma^{k+1} = P_+(\gamma^k - \bar{\alpha}\varphi(\gamma^k)) = \gamma^k - \bar{\alpha}\tilde{\varphi}(\gamma^k)$  by projection to feasible set

```

Every solution $\bar{\gamma}$ of auxiliary problem satisfies the Karush-Kuhn-Tucker conditions expressed by the relation

$$\varphi(\gamma) = 0 \quad \wedge \quad \beta(\gamma) = 0,$$

hence as a stopping criteria, we are using the Euclidean norm of the *projected gradient*

$$g^P(\gamma) = \varphi(\gamma) + \beta(\gamma) = \frac{1}{\alpha}(\gamma - P_+(x - \alpha g(\gamma))),$$

where P_+ is the projection to set of feasible vectors defined as

$$P_+(\gamma)_i = \max\{\gamma_i, 0\}.$$

More details about implementation of the algorithm may be found in [18]. A short review of optimal QP algorithms can be found in Dostál and Pospíšil [20].

5 Numerical experiment

In this section, we present the numerical results showing the efficiency of our algorithm on the simulation of 32810 spherical particles. During the first stage of the simulation, small particles are poured into box represented by five walls. The initial position of the particles and final position can be found in Fig. 3. Afterwards, in $t = 0.3$ s, we add large

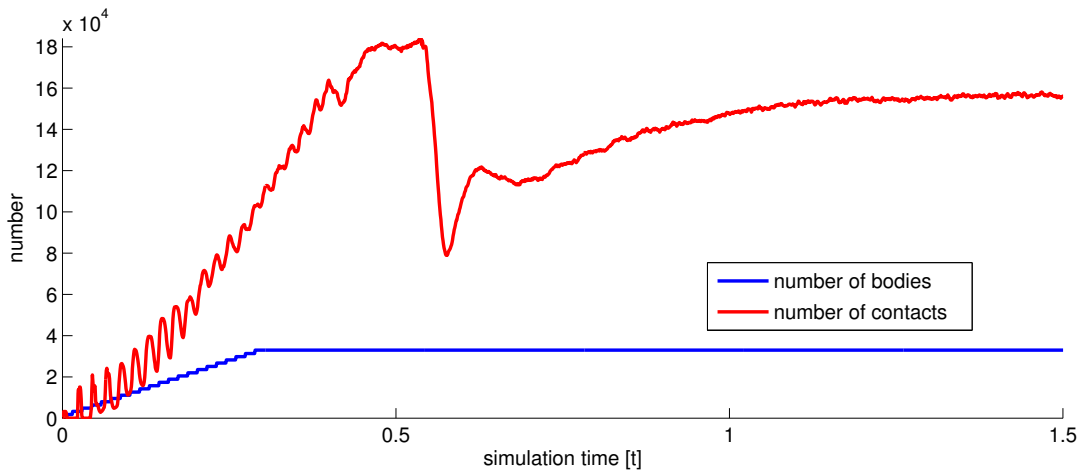


Figure 1: The number of bodies and contacts in the system during the simulation.

spherical particle to study the behaviour of the impact. The material of the bodies is represented by density $\rho = 2800 \text{ kg} \cdot \text{m}^{-3}$. Small particles have radius $r = 0.011 \text{ m}$ and the large one $r_2 = 0.15 \text{ m}$. The stepsize of the time-stepping scheme is $h = 8 \cdot 10^{-4} \text{ s}$.

Algorithm was implemented in C programming language in CUDA environment [21]. For contact detection, we are using our own implementation of the Moving Bounding-Box algorithm [22]. We demand the relative stopping tolerance

$$\|g^P(\gamma)\| \leq 10^{-4} \cdot \|r\|.$$

The number of bodies in the system and the number of contacts can be found in Fig. 1. The number of iterations and the Hessian matrix multiplications (the most time-consuming operation) depends on the dimension of the inner problem, see Fig. 2.

6 Conclusion

In our paper, we proved the solvability of inner optimization problem in multi-body dynamics and presented the results of our active-set algorithm for the solution of optimization problem in particle dynamics. Our numerical experiment shows the efficiency of the algorithm.

REFERENCES

- [1] Pfeiffer, F. and Glocker, C. *Multibody Dynamics with Unilateral Contacts*. John Wiley & Sons, Inc., (2008).
- [2] Cundall, P.A. *A Computer Model for Simulating Progressive Large Scale Movements in Blocky Rock Systems*. Proceedings of the Symposium of the International Society of Rock Mechanics, (1971) 2,8.

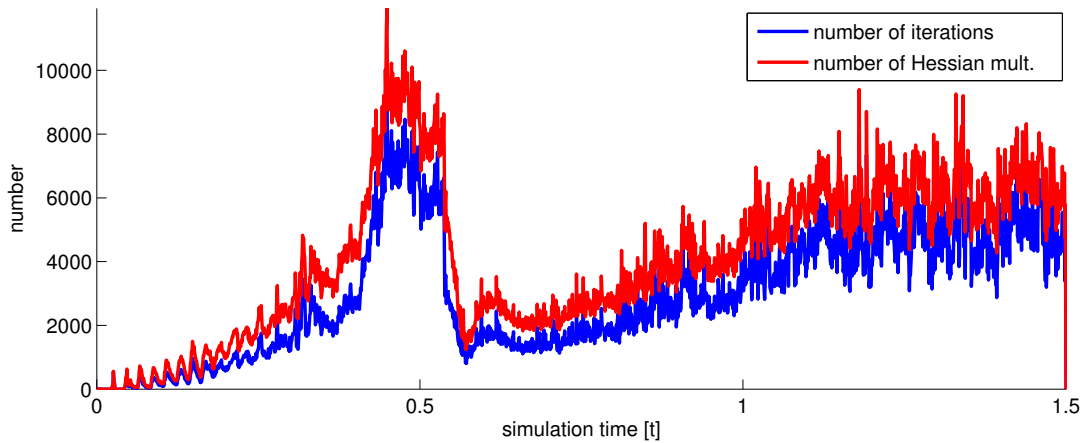


Figure 2: The number of iterations and Hessian multiplications during the simulation.

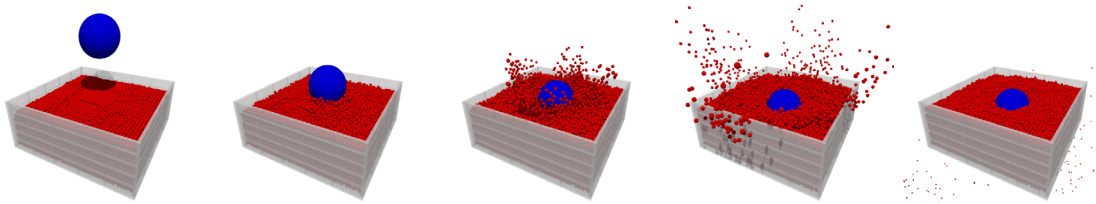


Figure 3: The state of the benchmark simulation in $t = 0.4$ s, 0.56 s, 0.64 s, 0.8 s, 1.44 s.

- [3] Avci, B. and Wriggers, P. *A DEM-FEM Coupling Approach for the Direct Numerical Simulation of 3D Particulate Flows*. Journal of Applied Mechanics, (2011) **79**.
- [4] Pang, J. and Stewart, D. E. *Differential variational inequalities*. Mathematical Programming, (2008) **113**:345–424.
- [5] Renouf, M. and Alart, P. *Conjugate gradient type algorithms for frictional multi-contact problems: applications to granular materials*. Computer Methods in Applied Mechanics and Engineering, (2005) **194**:2019–2041.
- [6] Heyn, T. D. *On the Modeling, Simulation, and Visualization of Many-Body Dynamics Problems with Friction and Contact*. University of WisconsinMadison, PhD Thesis, (2013).
- [7] Heyn, T. D., Anitescu, M., Tasora A. and Negrut, D. *Using Krylov Subspace and Spectral Methods for Solving Complementarity Problems in Many-Body Contact Dynamics Simulation*. International Journal for Numerical Methods in Engineering, (2013) **7/95**:541–561

- [8] Dostál Z. and Pospíšil, L. *Minimization of the quadratic function with semidefinite Hessian subject to the bound constraints*. submitted to Elsevier, (2015).
- [9] Dostál, Z., Kozubek, T., Markopoulos, A., Brzobohatý, T., Vondrák, V. and Horyl P. *A theoretically supported scalable TFETI algorithm for the solution of multibody 3D contact problems with friction*. Computer methods in applied mechanics and engineering, (2012) **205-208**:110–120.
- [10] ProjectChrono - a set of open-source tools for mechanical simulations. <http://chronoengine.info/>
- [11] Haug, E.J. *Computer-Aided Kinematics and Dynamics of Mechanical Systems*. Prentice-Hall, Englewood Cliffs, New Jersey, (1989), Vol I.
- [12] Anitescu, M. *Optimization-based simulation of nonsmooth rigid multibody dynamics*. Mathematical Programming, (2006) **105**:113–143.
- [13] Laub, A. J. *Matrix Analysis For Scientists And Engineers*. Philadelphia, PA, USA, Society for Industrial and Applied Mathematics, (2014).
- [14] Dostál, Z. *Optimal Quadratic Programming Algorithms, with Applications to Variational Inequalities*. SOIA, Springer, New York, US, Vol 23., (2009).
- [15] Frank, M. and Wolfe, P. *An algorithm for quadratic programming*. Naval Research Logistics Quarterly, (1956) **3**:95–110.
- [16] Dostál, Z. *Box constrained quadratic programming with proportioning and projections*. SIAM Journal on Optimization, (1997) **7**:871–887.
- [17] Friedlander, A. and Martínez, J. M. *On The Maximization Of A Concave Quadratic Function With Box Constraints*. SIAM Journal on Optimization, (1994) **4**:177–192.
- [18] Dostál, Z. and Schöberl, J. *Minimizing quadratic functions subject to bound constraints*. Computational Optimization and Applications, (2005) **30**:23–43.
- [19] Schöberl, J. *Solving the Signorini Problem on the Basis of Domain Decomposition Techniques*. Computing, (1998) **60/4**:323–344.
- [20] Dostál, Z. and Pospíšil, L. *Optimal iterative QP and QPQC algorithms*. Annals of Operations Research, (2013).
- [21] NVIDIA: CUDA Programming Guide, <http://docs.nvidia.com/cuda/index.html>, (2015).
- [22] Schinner, A. *Fast algorithms for the simulation of polygonal particles*, Granular Matter, (1999) **2**:35–43.

A GENERAL METHOD FOR MODELLING DEFORMABLE STRUCTURES IN DEM

A. EFFEINDZOUROU¹, K. THOENI¹, B. CHAREYRE² AND A. GIACOMINI¹

¹Centre for Geotechnical and Materials Modelling
The University of Newcastle Callaghan, NSW 2308, Australia
<http://www.newcastle.edu.au>

²Laboratoire 3SR
Domaine Universitaire BP53, 38041 Grenoble Cedex 9, France
<http://www.3sr-grenoble.fr>

Key words: DEM, Cylinder, Grid, Membrane, Arbitrary shape, Minkowsky sum

Abstract. The discrete element method was originally designed to handle rigid spherical particles. In this work, the method is extended to model arbitrary deformable structures, such as membrane and container structures. The paper focuses on the implementation of a deformable discrete element called PFacet (particle facet) in the open-source framework YADE. A PFacet element is geometrically constructed by the Minkowsky sum of a triangular facet and a sphere. Contact detection is based on the three primitives: sphere, cylinder and facet. It allows the representation of arbitrary deformable structures by using the standard contact models for spheres. Finally, the model is validated and an example is presented illustrating the capabilities of the model to simulate arbitrary deformable structures.

1 INTRODUCTION

The discrete element method (DEM) is broadly used to simulate granular materials. The method originally considers the interaction between rigid spheres. The modelling of rounded non-spherical particles allows to take into account the shape of the particles. Indeed, grains in nature and many important phenomena cannot be reproduced just using spherical particles. The simplest method for modelling non-spherical particles is to either bond or clump spheres together [1]. In the first case spheres belonging to the same aggregate interact via a bond where attractive forces are allowed and bonds can brake. In the case of a clump, the aggregate is rigid and the forces on all the spheres making up the clump are added together to obtain the total force. Another way of modelling rounded non-spherical particles is by superquadratic ellipsoids [2] or rounded polyhedra

and spheropolytopes [3]. The latter are discussed more in detail in the following section since a similar concept will be used in the present work. Spheropolytopes are generated from the Minkowski addition of a polytope by a sphere, which is nothing more than the object resulting from sweeping a sphere around a polytope. The idea appeared in [4] for flexible objects and in [5] for convex non-spherical particles. In the latest, a linear triangulation-based contact detection method based on a weighted Delaunay triangulation was used in order to improve the performance. Numerical experiments indicated that the overall complexity of the contact detection is proportional to the number of particles. An extension of the method was published in [6] for simulating non-convex non-spherical particles in 2D. The particle shape was represented by the classical concept of a Minkowski sum, which permits the representation of complex shapes without defining the object as a sum of spherical or convex particles. A well-defined conservative and frictional interaction between these bodies was derived. The method was then extended to 3D by [3].

Starting from the modelling of deformable chained cylinders in 3D [7], this paper presents a general method for modelling deformable non-convex structures with the DEM as published in [8] and implemented into the open-source framework YADE [9]. Firstly, the three primitives used in the model and their implementation are discussed. Then the model is validated and some examples are presented.

2 GENERAL FORMULATION

The contact model of two interacting spheres is presented herein since all possible interactions considered in this work are based on it. The constitutive model used for the sphere–sphere interaction links the relative displacement and relative rotation to the contact force \vec{F} and contact moment \vec{M} acting at the contact between two interacting bodies.

The normal contact force \vec{F}_n and the incremental shear force $d\vec{F}_s$ are calculated as:

$$\vec{F}_n = k_n \vec{u}_n \quad (1)$$

$$d\vec{F}_s = k_s \dot{\vec{u}}_s dt \quad (2)$$

where k_n and k_s are the contact stiffnesses associated to the normal and shear force, \vec{u}_n is the normal distance (or overlap) between the two spheres, $\dot{\vec{u}}_s$ is the relative shear velocity, and dt is the time step.

Considering two spheres S_1 and S_2 , the normal and tangential stiffness of the sphere–sphere contact are defined as follows:

$$k_n = \frac{2E_1 R_1 E_2 R_2}{E_1 R_1 + E_2 R_2} \quad (3)$$

$$k_s = \frac{2E_1 R_1 \nu_1 E_2 R_2 \nu_2}{E_1 R_1 \nu_1 + E_2 R_2 \nu_2} \quad (4)$$

where E_i is the Young's modulus, R_i the radius and ν_i the Poisson's ratio associated to sphere i with $i \in \{1, 2\}$.

The relative rotation of the spheres is used to define the twisting moment \vec{M}_t and the bending moment \vec{M}_b . By adopting a vector representation $\vec{\Omega}_{12}$ of the relative rotation, the moments can be calculated as:

$$\vec{M}_t = k_t \vec{\Omega}_{12}^t \quad (5)$$

$$\vec{M}_b = k_b \vec{\Omega}_{12}^b \quad (6)$$

where k_t and k_b are the contact stiffness associated to the twisting and bending moment respectively, and $\vec{\Omega}_{12}^t$ and $\vec{\Omega}_{12}^b$ are the twisting and bending components of the relative rotation associated to the two spheres.

Plastic deformation is taken into account via the following elastic limits:

$$\begin{aligned} \|\vec{F}_n\| &\leq \sigma_n^l A \\ \|\vec{F}_s\| &\leq F_n \tan \varphi + \sigma_s^l A \\ M_t &\leq \frac{\sigma_n^l I_b}{R} \\ M_b &\leq \frac{\sigma_s^l I_t}{R} \end{aligned} \quad (7)$$

where σ_n^l and σ_s^l are the tensile and shear strengths, $\varphi = \min(\varphi_1, \varphi_2)$ is the friction angle, $A = \pi R^2$ is the reference surface area, $I_t = \pi R^4/4$ and $I_b = \pi R^4/8$ are the reference polar and bending moments of inertia respectively, and $R = \min(R_1, R_2)$ is the reference radius of the contact.

3 CYLINDER ELEMENTS

The cylinder element was introduced in [7]. It is the basic entity for the deformable element described in this paper and, hence, it is summarised in this section.

A cylinder is composed of two nodes and a tube. Geometrically it corresponds to the Minkowski sum of a sphere and a polyline. The deformation of a cylinder is characterised by the positions and orientations of its two nodes. The mass of the cylinder element is lumped into its two nodes.

Three types of interactions are considered: sphere–sphere, sphere–cylinder and cylinder–cylinder. The sphere–sphere contact model is used to calculate the sphere–cylinder and cylinder–cylinder interactions. In order to compute the sphere–cylinder interaction, a virtual sphere is introduced. The virtual sphere is centred at the position of the projection of the contact point between the sphere and the cylinder on the segment connecting its nodes. The cylinder and virtual sphere have the same radius. The displacements at the surface of the cylinder are assumed to vary linearly between its nodes. The translational and rotational velocities of the virtual sphere are linearly interpolated between the cylinder’s nodes. Then, the forces and moments are distributed on the two nodes.

In [7] chained cylinders (or interconnected cylinders) were used. This allows the modelling of elastic perfectly plastic beams that can withstand normal, shearing, bending

and twisting loadings. For a cylinder element with two nodes, N_1 and N_2 , the contact stiffnesses are defined as:

$$\begin{aligned} k_n &= \frac{E_t A}{L} \\ k_t &= \frac{G_t I_t}{L} \\ k_s &= \frac{12E_b I_b}{L^3} \\ k_b &= \frac{E_b I_b}{L} \end{aligned} \quad (8)$$

where E_t and E_b are the tensile and bending moduli of the material respectively, G_t is the shear modulus associated with the twisting moment and $L = \|N_1 - N_2\|$ is the length of the beam element.

4 GRIDS

A grid can be generated using a series of nodes connected to an arbitrary number of cylinders. The modelling of a grid involves the implementation of the interaction between non-adjacent cylinders (no common nodes). In order to handle cylinder–cylinder interactions, the contact forces between two cylinders C_1 and C_2 are determined. The distance between two cylinders C_1 and C_2 is calculated as the distance between two segments (Fig. 1), bearing in mind that each cylinder is geometrically represented by the Minkowski sum of a sphere and a segment.

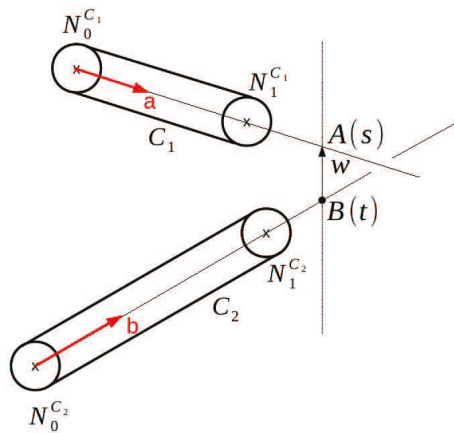


Fig. 1. Distance between two cylinders.

The segments associated to the cylinder C_1 and C_2 are $A = [N_0^{c_1} N_1^{c_1}]$ and $B = [N_0^{c_2} N_1^{c_2}]$ respectively, where $N_j^{c_i}$ correspond to the position of the nodes j of cylinder C_i with

$i \in \{1, 2\}$ and $j \in \{1, 2\}$. The parametric equations of the segments A and B are:

$$A(s) = N_0^{c_1} + s \vec{a} \quad \forall s \in [0, 1] \quad (9)$$

$$B(t) = N_0^{c_2} + t \vec{b} \quad \forall t \in [0, 1] \quad (10)$$

with \vec{a} and \vec{b} being the direction vectors of the segments A and B . The vector w between A and B can then be calculated as:

$$w(s, t) = A(s) - B(t) \quad \forall s, t \in [0, 1] \times [0, 1] \quad (11)$$

The objective is to find $(s_C, t_C) \in [0, 1] \times [0, 1]$ such that:

$$\vec{w}_C = w(s_C, t_C) = A(s_C) - B(t_C) = \min_{(s,t) \in [0,1] \times [0,1]} w(s, t) \quad (12)$$

The segment $[A_C B_C]$ is uniquely defined as simultaneously perpendicular to both lines if the segments A and B do not intersect or are not parallel. This implies that the vector $\vec{w}_C = w(s_C, t_C)$ is uniquely perpendicular to the segment vector of the directions of \vec{a} and \vec{b} and the conditions $\vec{a} \cdot \vec{w}_C = 0$ and $\vec{b} \cdot \vec{w}_C = 0$ are satisfied. Hence, the following system of equations can be written:

$$\begin{cases} \vec{w}_C = A(s_C) - B(t_C) \\ \vec{a} \cdot \vec{w}_C = 0 \\ \vec{b} \cdot \vec{w}_C = 0 \end{cases} \quad (13)$$

The solution of Eq. (13) is given by:

$$\begin{cases} s_C = \frac{(\vec{a} \cdot \vec{b})(\vec{b} \cdot \vec{w}_0) - \|\vec{b}\|(\vec{a} \cdot \vec{w}_0)}{\|\vec{a}\| \|\vec{b}\| - (\vec{a} \cdot \vec{b})^2} \\ t_C = \frac{\|\vec{a}\|(\vec{b} \cdot \vec{w}_0) - (\vec{a} \cdot \vec{b})(\vec{a} \cdot \vec{w}_0)}{\|\vec{a}\| \|\vec{b}\| - (\vec{a} \cdot \vec{b})^2} \end{cases} \quad (14)$$

where $\vec{w}_0 = N_0^{c_1} - N_0^{c_2}$.

For a cylinder–cylinder contact each cylinder is associated to a virtual sphere at the contact point. This approach is similar to the sphere–cylinder contact. The virtual spheres S_{C_1} and S_{C_2} are centred respectively in $A(s_c)$ and $B(t_c)$. Contact laws can then be inherited, and the force and moment linearly distributed on each cylinder node.

5 PFACET ELEMENTS

The grid model described in Section 4 is extended to model arbitrary deformable objects. To achieve this objective a new element is introduced, the so-called PFacet (particle

facet). The PFacet element is geometrically constructed by the Minkowsky sum of a triangular facet and a sphere. It is composed of 3 nodes (spheres) and 3 connections (cylinders). The deformation is defined by the set of positions and orientations of its nodes. The constitutive behaviour of the PFacet element is simulated via an ordinary interaction law acting between the 3 nodes. The mass of the PFacet is equally lumped into the 3 nodes. The introduction of the PFacet element involves the consideration of the following three interactions: sphere–PFacet, cylinder–PFacet and PFacet–PFacet.

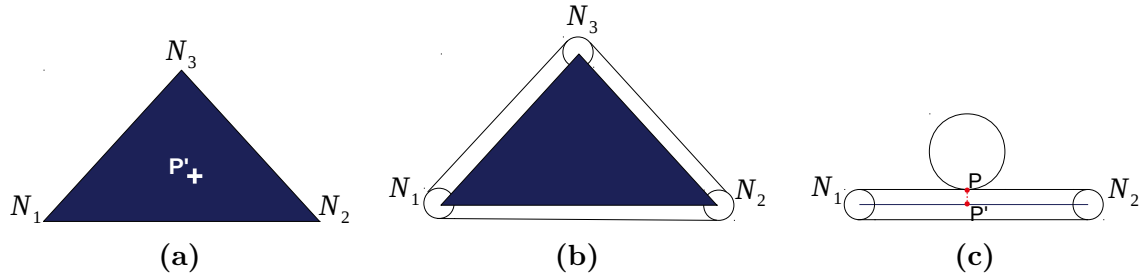


Fig. 2. (a) Triangular skeleton with the nodes, (b) PFacet geometry where the blue zone corresponds to the inside of the PFacet element and (c) P' projection of the contact point P on the plane that contains the PFacet nodes.

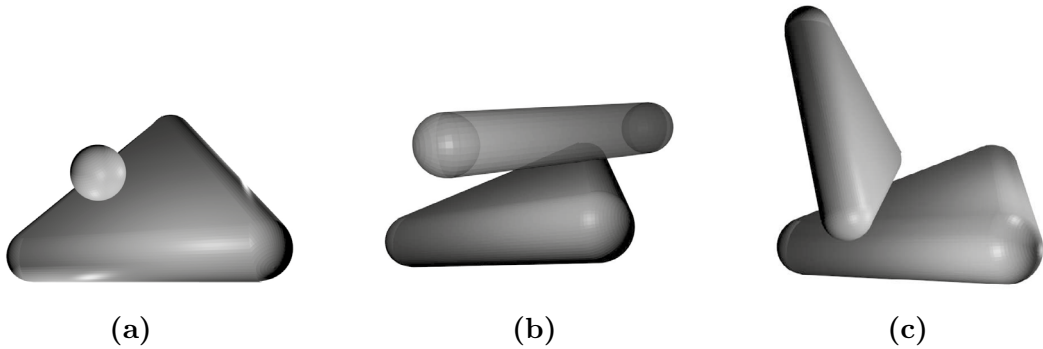


Fig. 3. (a) Sphere–PFacet interaction, (b) Cylinder–PFacet interaction, and (c) PFacet–PFacet interaction.

For a sphere–PFacet interaction (Fig. 3a), the coordinates of the contact point P are characterised by the position of the 3 PFacet nodes. The point P' is the projection of the contact point P (Fig. 2c) on the plane containing the nodes of the PFacet element. The barycentric coordinates (p_1, p_2, p_3) of the point P' (Fig. 2a) are defined as:

$$\begin{aligned}
p_1 &= \frac{\|\overrightarrow{N_1 N_3}\|(\overrightarrow{N_1 N_2} \cdot \overrightarrow{N_1 P'}) - (\overrightarrow{N_1 N_2} \cdot \overrightarrow{N_1 N_3})(\overrightarrow{N_1 N_3} \cdot \overrightarrow{N_1 P'})}{\|\overrightarrow{N_1 N_2}\| \|\overrightarrow{N_1 N_3}\| - (\overrightarrow{N_1 N_2} \cdot \overrightarrow{N_1 N_3})(\overrightarrow{N_1 N_2} \cdot \overrightarrow{N_1 N_3})} \\
p_2 &= \frac{\|\overrightarrow{N_1 N_2}\|(\overrightarrow{N_1 N_3} \cdot \overrightarrow{N_1 P'}) - (\overrightarrow{N_1 N_2} \cdot \overrightarrow{N_1 N_3})(\overrightarrow{N_1 N_2} \cdot \overrightarrow{N_1 P'})}{\|\overrightarrow{N_1 N_2}\| \|\overrightarrow{N_1 N_3}\| - (\overrightarrow{N_1 N_2} \cdot \overrightarrow{N_1 N_3})(\overrightarrow{N_1 N_2} \cdot \overrightarrow{N_1 N_3})} \\
p_3 &= 1 - p_1 - p_2
\end{aligned} \tag{15}$$

The barycentric coordinates of P' are used to distinguish if the contact is inside the PFacet element (the blue zone in Fig. 2b) or not. If $p_1 \geq 0$ and $p_2 \geq 0$ and $p_3 < 1$, the contact is characterised as inside the PFacet element otherwise a sphere–cylinder interaction is considered. The virtual sphere s'_P is positioned in P' . Both, the virtual sphere and the PFacet element have the same radius. The PFacet element radius is defined as the radius of the PFacet node located at the ends of each cylinder. The virtual sphere’s displacement and rotation are linearly interpolated between the 3 nodes of the PFacet N_1 , N_2 and N_3 .

The translational (\vec{v}'_P) and rotational ($\vec{\omega}'_P$) velocities are then calculated from the translational (\vec{v}_{N_1} , \vec{v}_{N_2} and \vec{v}_{N_3}) and rotational ($\vec{\omega}_{N_1}$, $\vec{\omega}_{N_2}$ and $\vec{\omega}_{N_3}$) velocities of the three nodes:

$$\begin{aligned}
\vec{v}'_P &= p_1 \vec{v}_{N_1} + p_2 \vec{v}_{N_2} + p_3 \vec{v}_{N_3} \\
\vec{\omega}'_P &= p_1 \vec{\omega}_{N_1} + p_2 \vec{\omega}_{N_2} + p_3 \vec{\omega}_{N_3}
\end{aligned} \tag{16}$$

Introducing a virtual sphere s'_P allows the use of the contact model for a classical sphere–sphere interaction. The contact force, \vec{F} , is calculated for the virtual sphere and then the force is distributed over the nodes as follows:

$$\vec{F}_{N_i} = p_i \vec{F} \tag{17}$$

where \vec{F}_{N_i} is the force applied at the node N_i with $i \in \{1, 2, 3\}$.

A cylinder–PFacet contact (Fig. 3b) is decomposed into a node–PFacet (i.e. sphere–PFacet) contact between the nodes of the cylinder and the PFacet, and a cylinder–cylinder contact between the cylinder and PFacet cylinders.

A PFacet–PFacet interaction (Fig. 3c), is a combination of node–PFacet and cylinder–cylinder interactions. All these types of interactions have been described above.

6 VALIDATION

A tube of length l (Fig. 4a) is subjected to a bending moment. The cylinder is fixed at one end, precisely the nodes initially positioned at $x = 0$ are only fixed along the x-axis. The bending moment M_b is applied at the other end ($x = l$). A distribution of forces $\{f_1 \dots f_{N_l}\}$ such that $\sum_{k=1}^{k=N_l} f_k = 0$ and $\sum_{k=1}^{k=N_l} x_k f_k = M_b$ is applied on each nodes which

are initially positioned at $x = l$. The forces f_k are linear in y in the initial configuration. The forces are updated constantly during the deformation to reflect the positions x_k in the deformed state. M_b is increased progressively in order to plot the load–displacement relation. The changes of M_b are sufficiently slow to maintain a quasi-static regime of deformation.

The hollow cylinder is potentially able to buckle in bending. For the boundary conditions presented above, the relevant buckling limit is defined in [10]. It corresponds to an ovalisation of the cross section. The maximum bending moment is calculated as:

$$M_b^{max} = \frac{2\sqrt{2}K_n}{9(1-\nu^2)}d \quad (18)$$

where K_n is the stiffness of the beam in tension, ν is the Poisson’s ratio of the wall, and d is the thickness of the wall. This expression is used for comparison in Fig. 4e. In the calculation of M_b^{max} , the values of K_n and ν are obtained from a simulated tension test on the same tube.

When a non-linear displacement is detected in the simulation, the applied moment is kept constant. The buckling is identified when, for a given moment M_b , the deformation of the cylinder increase with time. During the buckling phenomenon, the cylinder enters a dynamic mode of deformation. Finally, the tube reaches an equilibrium via a winding mechanism (Fig. 4d). In the simulation, buckling is reached for a moment value close to the theoretical limit. One can observe that the final state involves self-interaction in the tube (Fig. 4d). It shows that the method developed allows to investigate complex post-buckling behaviours. In addition, the capability of solving problems involving self interacting structures and large deformations is as well demonstrated.

7 EXAMPLE

In the following section a potential application of the developed discrete model is presented. The ability to simulate deformable objects is investigated by simulating a impact of a sphere on a tube. The tube is deformable and composed of 640 PFacet elements with a radius of 2 mm. The tube has a radius of $R = 0.1$ m and a length of 0.8 m. The material parameters used for the tube are: Young’s modulus $E_t = 1$ MPa and Poisson’s ratio $\nu_t = 0.3$.

The impacting sphere is first modelled by a solid sphere (Fig. 5a) and then by a hollow deformable sphere represented by 128 PFacet elements with a radius of 2 mm (Fig. 5a). The material parameters of the sphere are: Young’s modulus $E_s = 100$ MPa and Poisson’s ratio $\nu_s = 0.3$. The sphere has a radius $R = 0.1$ m and an impact velocity of $v = 2$ m/s. To focus on the deformation of the impact gravity was not applied during the simulation.

Fig. 5b and Fig. 5c illustrate the final state of the tube after impact of the solid sphere. The tube is deformed and the sphere is stopped with the creation of a crater. The deformation of the tube almost corresponds to its radius. Fig. 6b and Fig. 6c show

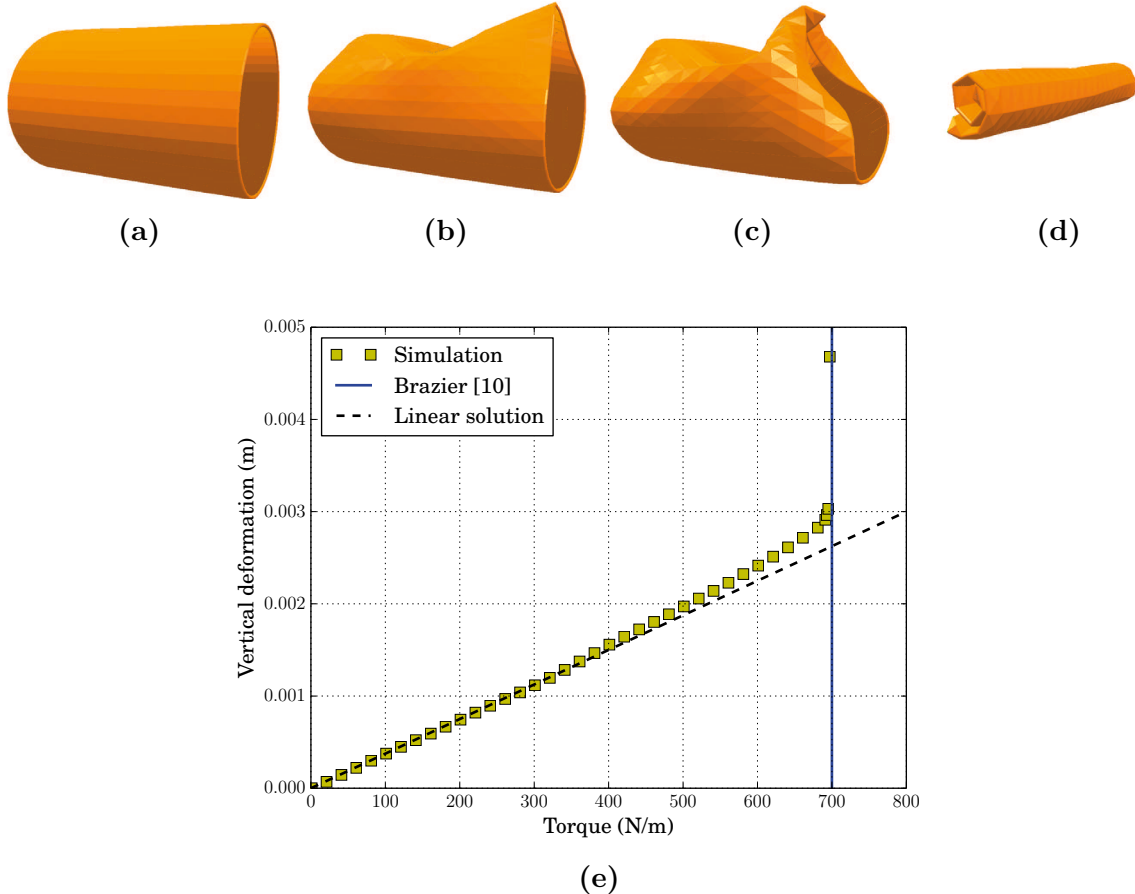


Fig. 4. Buckling of a tube subjected to an end bending moment: (a)–(d) deformation and (e) comparison with theoretical limit.

the final state of the tube after impact of the deformable sphere. It can be seen that the tube is not as deformed as in the previous case and the impacting sphere deforms itself.

8 CONCLUSIONS

The paper presents a method for the simulation of arbitrary deformable objects. The model is an extension of the flexible cylinder element described in [7]. A new element is introduced into the open-source framework YADE [8]. The so-called PFacet (particle facet) is an element geometrically constructed by the Minkowsky sum of a triangular facet and a sphere. Contact detection is based on the three primitives: sphere, cylinder and facet. It allows the representation of arbitrary deformable structures by using the standard contact models for spheres. The ability of the model to reproduce the behaviour of a structure under bending is validated. A tube subjected to an end bending moment is investigated and an excellent agreement with the theoretical buckling limit is observed.

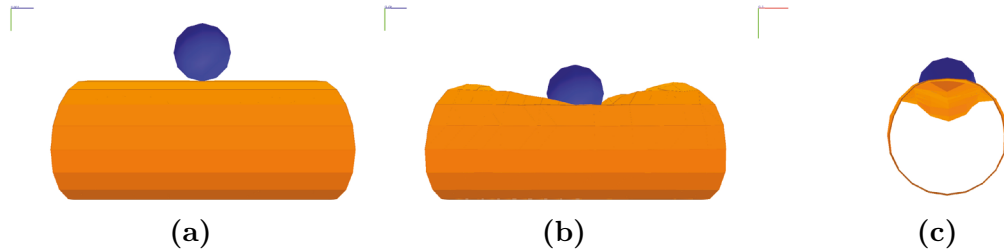


Fig. 5. Solid sphere impacting on tube: (a) initial state before impact, and (b) front view and (c) side view of final state.

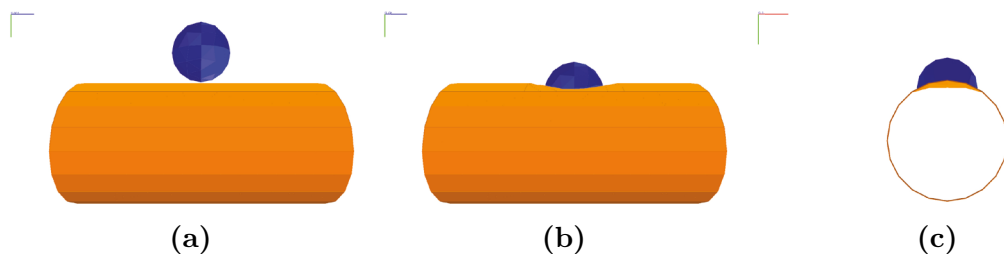


Fig. 6. Hollow deformable sphere impacting on tube: (a) initial state before impact, (b) front view and (c) side view of final state.

Finally, an example of a sphere (solid and hollow) impacting on a tube is presented. Results show that the model is capable of capturing large deformations and to efficiently simulate complex deformable shapes and soil inclusion problems.

REFERENCES

- [1] Radja, A., Dubois, F., (editors). *Discrete-element Modeling of Granular Materials*. ISTE Ltd, London; (2011).
- [2] Donzé, F., Richefeu, V., Magnier, S.. Advances in discrete element method applied to soil, rock and concrete mechanics. *Electronic Journal of Geotechnical Engineering* (2009) **8**:1–44.
- [3] Galindo-Torres, S., Alonso-Marroquín, F., Wang, Y., Pedroso, D., Muñoz Castaño, J.. Molecular dynamics simulation of complex particles in three dimensions and the study of friction due to nonconvexity. *Physical Review E* (2009) **79**:060301–1–4.
- [4] Chareyre, B., Villard, P.. Dynamic spar elements and discrete element methods in two dimensions for the modeling of soil-inclusion problems. *Journal of Engineering Mechanics* (2005) **131**(7):689–698.
- [5] Pournin, L., Liebling, T.. A generalization of distinct element method to tridimen-

- sional particles with complex shape. In: *Powders and Grains 2005*; vol. 2. (2005), p. 1375–1378.
- [6] Alonso-Marroquín, F.. Spheropolygons: A new method to simulate conservative and dissipative interactions between 2D complex-shaped rigid bodies. *Europhysics Letters* (2008) **83**(1):14001–1–14001–6.
 - [7] Bourrier, F., Kneib, F., Chareyre, B., Fourcaud, T.. Discrete modeling of granular soils reinforcement by plant roots. *Ecological Engineering* (2013) **61**:646–657.
 - [8] Effeindzourou, A., Chareyre, B., Thoeni, K., Giacomini, A., Kneib, F.. Modelling of deformable structures in the general framework of the discrete element method. *Geotextiles and Geomembranes* (2015) [under review, submitted on 09/12/2014].
 - [9] Šmilauer, V., Catalano, E., Chareyre, B., Dorofenko, S., Duriez, J., Gladky, A., et al. Yade Reference Documentation. In: Šmilauer, V., (editor). *Yade Documentation*. The Yade Project; 1st ed.; (2010), <http://yade-dem.org/doc/>.
 - [10] Brazier, L.. On the flexure of thin cylindrical shells and other thin sections. *Proceedings of the Royal Society of London Series A* (1927) **116**(773):104–114.

A MOLECULAR DYNAMICS STUDY ON THE EFFECTS OF WALL-FLUID INTERACTION STRENGTH AND FLUID DENSITY ON THERMAL RESISTANCE OF GRAPHENE/ARGON INTERFACE

AHMAD AMANI¹, S.M.H. KARIMIAN¹AND MAHBOD SEYEDNIA²

¹ Department of Aerospace Engineering, Amirkabir University of Technology
424 Hafez Ave., Tehran, Iran, 15875-4413
ahmad.amani@aut.ac.ir, hkarim@aut.ac.ir

² Faculty of New Sciences and Technologies, University of Tehran
North Kargar Ave., Tehran, Iran, 14395-1561
m.seyednia@ut.ac.ir

Key words: Molecular Dynamics, Interface Thermal Resistance, Kapitza Length, Confined Argon Flow.

Abstract. Molecular dynamics simulations of Argon flow confined between two parallel graphene sheets are carried out to investigate the effects of some parameters on heat transfer and thermal properties. These parameters include wall-fluid interaction strength and fluid density where for constant wall temperature simulations, we show that these two parameters have influence on near-wall fluid density. As a result, the heat transfer at wall-fluid interfaces and thus through Argon molecules across the domain will change. To analyze the results, the density and temperature profiles and two other parameters including temperature gradient of the bulk of Argon molecules and the Kapitza length are considered. The Kapitza length represents the thermal resistance at liquid-solid interface. According to the results, the increase of wall-fluid interaction strength leads to greater number of Argon molecules near the walls and consequently, the Kapitza length decreases and an enhancement is observed in temperature gradient and the slope of temperature profile. Furthermore, higher values of fluid density cause that the thermal resistance at wall-fluid interactions increases. Therefore, greater temperature jumps are observed in temperature profiles.

1 INTRODUCTION

Molecular dynamics (MD) simulation of fluid flows in micro/nano sizes has been widely developed to extract detailed information on fluid behavior, especially in medicine, physiology, and nano scale devices [1-4]. Micro-electro-mechanical-systems (MEMS) and Nano-electro-mechanical-systems (NEMS) are such devices which have commercial applications [5] so it is necessary to have a comprehensive perception of thermal transport in these systems. As a result, molecular dynamics approach is implemented to model the heat transfer in nanostructures. In the researches of this field, temperature profile, calculation of heat flux, interface thermal resistance (ITR), thermal conductivity, and thermal efficiency of

various structures are subjected to study [6-13]. Most analyses of these results treat conduction as a diffusion process which can be described by Fourier's law and confirm that the interface thermal resistance strongly affects the heat transfer.

Two theoretical models lead the interpretation of this phenomenon. Acoustic mismatch model (AMM) was proposed by Little [14] which predicted the thermal resistance by treating the phonons as plane waves with assumption that no scattering occurs at the interface. Swartz and Pohl [15] proposed diffusive mismatch model (DMM) which assumes that diffuse scattering destroys acoustic effects at interface. In a solid/liquid interface, two parameters of temperature and near-surface structure of liquid affect the ITR.

Nano scale Poiseuille flows have been subjected to investigate the effects of different parameters on Interface thermal resistance. Shi et al. studied thermal resistance at argon-graphite and argon-silver interfaces [16]. Barisik and Beskok investigated the interface thermal resistances and represented a range for interface thermal resistance of argon-silver interface [17] and also investigated the effect of different silicon-water interaction strength values on the Kapitza length [18]. According to Murad and Puri reports, increase of the fluid pressure or fluid molecule layers will decrease the Kapitza length [19]. In spite of a wide range of knowledge in the discussed field, the affecting parameters on interface thermal resistance of argon flow confined between graphene [20] sheets is not clear.

In this paper, two different parameters including wall-fluid interaction strength and fluid density which have influence on the heat transfer and the thermal properties of an Argon flow confined between two parallel graphene sheets are investigated. We are interested to find out how these parameters affect the thermal properties. The effects of them are represented by plotting the density and temperature profiles. Heat flux, temperature gradient and the Kapitza length will be studied to compare the results and make a conclusion. In the following part, the simulation and the parameters considered in this paper are described and in chapter 3, the results are presented.

2 MOLECULAR DYNAMICS SIMULATION DETAILS

A liquid Argon flow confined between two parallel graphene sheets is simulated. Using LAMMPS solver [21], the mono atomic noble gas molecules of Argon are located in the domain in a way that the particle density [22] is 0.85. However it will be changed for more analysis in 3.2. The particle density is calculated as:

$$\rho^* = \frac{N}{L_1 L_2 L_3} \quad (1)$$

where N is the number of molecules and L is the dimensionless length. It is noteworthy that the particle density can be calculated for the bins and the whole domain.

Total dimensions of the domain are 3.40, 3.46 and 4.34 nm in X, Y and Z directions respectively. Periodic boundary conditions are applied on X and Y directions and Z direction is limited by the graphene sheets. As wall structure, the graphene sheets consist of 448 carbon atoms arranged in Hexagonal lattice with separation of 0.142 nm. In order to avoid the escape of the fluid molecules, the wall molecules are attached to their initial positions by a linear spring with the stiffness of $500\epsilon/\sigma^2$. Using VMD [23], the initial placement of the molecules is depicted in figure 1.

The motions of the molecules are determined by Newton's second law using Verlet's integrating schemes [24-25] with a time step of 1 femtosecond. The intermolecular interactions of Carbon-Carbon molecules are calculated using Adaptive Intermolecular Reactive Empirical Bond Order (AIREBO) potential. AIREBO potential includes three different potentials; REBO, Lennard-Jones and TORSION. The REBO term is a hydrocarbon potential describing the short-range interactions of carbon-carbon molecules. The longer-ranged interactions of carbon-carbon molecules are calculated by The Lennard-Jones term and the TORSION is a 4-body potential which describes the dihedral angle preferences in graphene structure. Implementing Lennard-Jones (L-J) 6-12 potential function, the intermolecular forces between the fluid-fluid molecules are calculated as below [26]:

$$U_{ij} = 4\epsilon \left(\left(\frac{\sigma}{r_{ij}} \right)^{12} - \left(\frac{\sigma}{r_{ij}} \right)^6 \right) \quad (2)$$

where U_{ij} is L-J potential, σ is the distance characteristic length, ϵ is the energy scale and r_{ij} is the distance between two interacting molecules i and j. The derivation of the above equation respect to r_{ij} is applied to calculate the intermolecular forces. The energy scale, ϵ , for Argon is 0.0103403 ev. The wall-fluid interactions are calculated by Lennard-Jones as well as fluid-fluids. Nevertheless, it is noteworthy that the energy scale and the distance characteristic length must be changed to appropriate values. Implementing mixing rule, the distance characteristic length and the energy scale for wall-fluid interactions are 3.268 Å and 0.00557256 ev respectively. This value of ϵ will be referred as ϵ_b in the next sections.

Initial temperature of 130 K is set for Argon molecules. Applying Maxwell-Boltzmann distribution function on the Argon molecules, the initial thermal velocities are randomized. To reach thermal equilibrium, we let the system iterate for 10^6 times (1 ns) while Canonical (NVT) ensemble with Nose-Hoover thermostat is applied on the whole molecules keeping the temperature of the system at 130 K. Afterward, in order to induce a heat flux through the domain, top and bottom wall temperatures are assigned 150 and 110 K, respectively using Nose-Hoover thermostat while NVE ensemble is applied to the water molecules for 2×10^6 iterations (2 ns) to ensure that the system attains equilibrium with the new heat flux conditions. Then, 3×10^6 iterations (3 ns) are considered for averaging to obtain macroscopic properties. The sampling is performed in 29 and 59 slab bins parallel to the graphene sheets to attain temperature and density profiles respectively. The Lennard-Jones potential predicts repulsive forces as the distance between two molecules decreases less than the potential minimum length. Hence, the bins adjacent to the graphene sheets would be unoccupied by the Argon molecules or the number of Argon molecules is not sufficient for sampling. Therefore the adjacent bins are left out in local temperature averaging whereas there would be no omission in the density bins. In other bins with low number of molecules, the results would not be reliable. So for such a bin, a linear interpolation of temperature between the corresponding adjacent bins is implemented to make the temperature profiles continuous. The interpolated temperatures for these bins are calculated and they are marked with a box around in temperature profiles.

Different temperatures for graphene sheets will lead to a thermal gradient in Z direction. As a result, this gradient generates heat flux between the parallel sheets. The rate of heat transfer can be calculated as below:

$$\vec{j} = \frac{1}{V} \left(\sum_i e_i v_i + \sum_{i < j} (f_{ij} \cdot v_j) r_{ij} \right) \quad (3)$$

where V is the volume of the domain and e_i and v_i denote the total energy per atom and the velocity of particle i while f_{ij} and r_{ij} represent the force caused by molecule j which acts on molecule i and the distance between two interacting molecules respectively.

In order to calculate the Kapitza length at the liquid-solid interfaces, an extrapolation is performed on temperature profile from liquid into the solid where the wall temperature is reached. The Kapitza length can be calculated using:

$$\Delta T = L_K \left. \frac{\partial T}{\partial n} \right|_{liquid} \quad (4)$$

where $\frac{\partial T}{\partial n}$ is the temperature gradient on the liquid side and $\Delta T = T_{liquid} - T_{wall}$. In order to analyze thermal properties, Kapitza lengths, the heat flux generated between the walls and the temperature gradient of argon molecules across the domain are studied. In each case, the particles are distributed uniformly over the simulation domain with the corresponding particle density. Two parameters of ε_{C-O}^{LJ} and r_{cut} are the major sources of uncertainties in the system analyzed in this paper. More information about these parameters could be found in Ref [27].

3 RESULTS AND DISCUSSION

In this paper, two different parameters are investigated to study their influences on thermal properties of the mentioned Argon flow. These parameters include wall-fluid interaction strength and fluid density. Temperature and density profiles, temperature gradient plots and Kapitza lengths are utilized to analyze the thermal properties in each case.

3.1 Effect of wall-fluid interaction strength

To investigate the effect of wall-fluid interaction strength, five different interaction strength values including 1, 2, 4, 6, 8 and $10 \times \varepsilon_b$ are considered. The density profiles of each case are depicted in figure 2. Using equation (1), the dimensionless densities are calculated in all the bins for each case. Although it cannot be seen in the figure 2, the density profiles across the channel are not totally symmetric. The particle density of the bins near the upper wall (with higher temperature) is slightly greater than that of the bins adjacent to the lower wall (with lower temperature). It represents the influence of wall temperature on distribution of Argon molecules. This is due to the fact that the molecular motions in the upper layers are greater than those of in the lower layers. Higher molecular motions cause a partial reduction in number of Argon molecules occupying a bin. So the upper bins contain fewer Argon molecules rather than the corresponding lower bins.

According to the Carbon-Argon interactions and their interaction strength, the Argon molecules are repelled or attracted by the Carbons. As a result, different density profiles are obtained for different values of wall-fluid interaction strength. The fluctuations in density profiles are caused by density layering of the Argon molecules near the walls. Getting away from the walls, the fluctuations are decaying and the density is approaching to the initial value of 0.85. Increase of wall-fluid interaction causes more attraction of Argon molecules in near-wall bins. Different density profiles for different interaction strengths affect the thermal properties such as temperature profile, Kapitza length and heat flux of the bulk of Argon molecules.

The temperature profiles obtained using the mentioned slab bins are plotted in figure 3. It is noticeable that different values of wall-fluid interaction strength result in different temperature plots and in all cases, temperature jump can be seen at liquid-solid interfaces. These jumps can be associated with phonon mismatch at the interfaces. The increase of interaction strength leads to more concentration of Argon molecules near the walls and consequently better coupling between the Argon and Carbon molecules. As a result, the temperature of the near-wall Argon molecules would be closer to the corresponding wall temperature and thus the temperature gradient of Argon molecules across the channel increases. The increase in the slope of the temperature profile is the evidence of this phenomenon. The curvature of the profiles can be attributed to thermal conductivity as a function of temperature. It was mentioned in section 2 but it is worth pointing out again that the temperatures marked in a box are the bins with insufficient number of molecules where their temperatures are obtained by linear interpolation.

For more accurate analysis of the temperature profiles, we consider the other parameters mentioned above. The results are extracted from the simulations to make a better study of thermal properties. The temperature gradient of Argon molecules across the channel is plotted in figure 4 for different values of interaction strength. The temperature gradient is obtained by calculation of the slope of the temperature profile. The method of least squares is implemented for curve fitting and the calculation of the slope. The square residuals for all cases are less than 2.5%. According to figure 4, the increase of ε_{Ar-C} enhances the temperature gradient of the bulk of Argon molecules. This is because of the enhancement in the slope of temperature profile which was explained before. Another parameter studied for thermal properties investigation is the heat flux transported between Argon molecules. The amounts of heat flux between the walls are also depicted in figure 4. It is noticeable that the heat flux increases by higher interaction strength as well as the temperature gradient.

As mentioned in section 1, Kapitza length is a parameter representing thermal resistance. For all cases of different interaction strengths, this length has been calculated for two liquid-solid interfaces and the results are plotted in figure 5. Clearly from this figure, there is an inverse relationship between ε_{Ar-C} and Kapitza length. The increase of ε_{Ar-C} reduces the Kapitza length and therefore the thermal resistance at the interfaces as well. Higher amount of ε_{Ar-C} induces more interactions between the Argon and Carbon molecules at the interfaces. Hence, better coupling and heat transfer between these molecules occur. Moreover, it is obvious that the Kapitza length for the upper wall (with higher temperature) is less than that of the lower wall. This is due to the fact that higher temperature dominates the interface thermal conductivity and consequently the Kapitza length.

3.2 Effect of density

The influence of density on thermal properties is investigated in this part. Different values of particle density including 0.65, 0.75, 0.85 and 0.95 have been considered to study if particle density affects thermal properties.

A dimensionless particle density is utilized to plot the number of atoms in each bin across the channel. To investigate the distribution of Argon molecules due to different densities and compare density profiles, the number of Argon molecules in each bin for all cases has been calculated. By dividing the number of particles in each bin by the total number of Argon molecules, we can compare the density profiles. The resultant value is multiplied by 100 and hence the result indicates the percentage of Argon molecules that each bin contains in each case of particle density. Now it would be possible to study the effect of density in the bins across the channel. Figure 6 illustrates the percentage of Argon molecules across the channel for different particle densities.

As it was mentioned earlier, the distribution and the concentration of fluid molecules near the walls affect the temperature jump at the interface of wall and fluid. From figure 6, it is self-evident that increasing density leads to decrease in the percentage of Argon molecules near walls. In other words, higher fluid density increases the concentration of molecules in the middle of the domain rather than near the walls. Therefore lower slope of temperature profile across the domain is expected for higher densities which represents decreasing in temperature gradient of Argon molecules between the walls and the Kapitza length as well. The temperature profiles for different values of particle density are plotted in figure 7. The results for the temperature profiles confirm the fact that increasing fluid density decreases the temperature slope and temperature gradient.

It was mentioned in previous part that the temperature gradient of Argon molecules corresponding to each particle density is obtained by the slope of the temperature profiles. The temperature gradients for different particle densities are depicted in figure 8. As evident from this figure, higher density accompanies by lower temperature gradient. Furthermore, increasing the density enhances the Kapitza length at the interface of the fluid and the walls. Figure 9 shows the variations Kapitza length with particle density. The enhancement in Kapitza length can interpret as increase in interface thermal resistance between the fluid and the walls. The reason of the difference between the Kapitza lengths at two interfaces was mentioned in 3.1.

The amounts of heat flux generated across the channel through Argon molecules for different particle density are shown in figure 10. According to figure 10, the heat flux through Argon molecules has a direct relationship with fluid density. This can be interpreted by using the one-dimensional model of heat conduction, Fourier's law. Below is the one-dimensional form of the Fourier's law:

$$Q_z = -kA_c \frac{dT}{dz} \quad (5)$$

Where Q_z is the heat flux induced in the Z direction, k is thermal conductivity, A_c is cross-sectional area of the heat flux and $\frac{dT}{dz}$ is applied temperature gradient. Due to this equation,

the two parameters, k and $\frac{dT}{dz}$, have influence on heat flux. According to the temperature profiles, the temperature gradients and the Kapitza lengths presented above, as fluid density increases, the interface thermal resistance increases as well. Hence, the temperature gradient of the bulk of Argon molecules decreases. Nonetheless, the induced heat flux through Argon molecules increases which is attributed to the enhancement of thermal conductivity of the bulk of Argon molecules.

4 CONCLUSION

In this paper, we showed that heat transfer and thermal properties at wall-fluid interfaces are as function of near-wall fluid density and wall temperatures. To prove this claim, two parameters including wall-fluid interaction strength and fluid density were considered to analyze the thermal properties of an Argon flow through two parallel graphene sheets. We showed that the these two parameters have influence on fluid density at near wall regions and consequently the thermal properties

The results clearly showed that increase of wall-fluid interaction strength raises the number of fluid molecules near the walls. Higher interaction strength creates better coupling between the Argon and Carbon molecules and thus the slope of temperature profile increases. As a result, the Kapitza length decreases and the temperature gradient of Argon molecules across the system rises.

The studies on the effect of fluid density on thermal properties also indicated that increasing fluid density will change the distribution of fluid molecules near the walls in a way that the interface thermal resistance increases. As a result, the interface thermal conductivity decreases and the temperature jump between the wall and the fluid is enhanced. However higher fluid densities cause an increase in fluid-fluid interactions and thermal conductivity in the bulk of Argon molecules as a consequence.

REFERENCES

- [1] Cruz-Chu, E.R., Malafeev, A., Pajarskas, T., Pivkin, I.V. and Koumoutsakos, P., Structure and Response to Flow of the Glycocalyx Layer, *Biophysical Journal*, (2014) **106**:232-243
- [2] Bresme, F. and Römer, F., Heat transport in liquid water at extreme pressures: A non equilibrium molecular dynamics study, *Journal of Molecular Liquids*, (2013) **185**:1-7
- [3] Castillo-Tejas, J., Castrejón-González, O., Alvarado, J.F.J. and Manero, O., Prediction of excess pressure drop in contraction-expansion flow by molecular dynamics: Axisymmetric and planar configurations, *Journal of Non-Newtonian Fluid Mechanics*, (2014) **210**:1-11
- [4] Adelman, J.L., Sheng, Y., Choe, S., Abramson, J., Wright, E.M., Rosenberg, J.M. and Grabe, M., Structural Determinants of Water Permeation through the Sodium-Galactose Transporter vSGLT, *Biophysical Journal*, (2014) **106**:1280-1289
- [5] Karniadakis, G.E., Beskok, A., and Aluru, N., *Micro flows and Nano flows*, Springer, (2002) New York, 1-9.
- [6] Zhang, G. and Li, B., Thermal Conductivity of Nanotubes Revisited: Effects of Chirality, Isotope Impurity, Tube Length, and Temperature, *J. Chem. Phys.* (2005) **123**:114714.
- [7] Yao, Z., Wang, J.S., Li, B. and Liu, G.R., Interface thermal resistance and thermal

- conductivity in composites, *Phys. Rev. B* (2005) **71**:085417.
- [8] Wu, G. and Li, B., Thermal rectification in carbon nanotube intramolecular junctions: Molecular dynamics calculations, *Phys. Rev. B* (2007) **76**:085424.
- [9] Donadio, D. and Galli, G., Thermal Conductivity of Isolated and Interacting Carbon Nanotubes: Comparing Results from Molecular Dynamics and the Boltzmann Transport Equation, *Phys. Rev. Lett.* (2007) **99**:255502.
- [10] Jiang, J.W., Wang, J.S. and Li, B., Topology-induced thermal rectification in carbon nanodevice, *Europhys. Lett.* (2010) **89**:46005.
- [11] Hu, J., Ruan, X. and Chen, Y.P., Thermal Conductivity and Thermal Rectification in Graphene Nanoribbons: A Molecular Dynamics Study, *Nano Lett.* (2009) **9**:2730.
- [12] Zhang, G.P. and Qin, Z.J., Crossover of the conductivity of zigzag graphene nanoribbon connected by normal metal contacts, *Phys. Lett. A* (2010) **374**:4140.
- [13] Murad, S. and Puri, I.K., Interface thermal resistance and thermal conductivity in composites – an abrupt junction thermal diode model, *Phys. Lett. A* (2010) **374**:4242.
- [14] Little, W.A., The transport of heat between dissimilar solid at low temperature, *Can. J. Phys* (1959) **37**:334±349.
- [15] Swartz, E.T. and Pohl, R.O., Thermal boundary resistance, *Reviews of Modern Physics* (1989) **61**:605±668.
- [16] Shi, Z., Barisik, M. and Beskok, A., Molecular dynamics modeling of thermal resistance at argon-graphite and argon-silver interfaces, *International Journal of Thermal Sciences*, (2012) **59**:29-37
- [17] Barisik, M. and Beskok, A., Boundary treatment effects on molecular dynamics simulations of interface thermal resistance, *J. Comput. Phys.*, (2012) **231**:7881-7892
- [18] Barisik, M. and Beskok, A., Temperature dependence of thermal resistance at the water/silicon, (2014) **77**:47-54
- [19] Murad, S. and Puri, I.K., Thermal transport across nanoscale solid-fluid interfaces, *Applied Physics Letters*, (2008) **92**:133105
- [20] Novoselov, K.S., Geim, A.K., Morozov, S.V., Jiang, D., Zhang, Y., Dubonos, S.V., et al., Electric field effect in atomically thin carbon films, *Science*, (2004) **306**:666-669
- [21] Plimpton, S., Fast Parallel Algorithms for Short-Range Molecular Dynamics, *J Comp Phys*, (1995) **117**:1-19
- [22] Karimian, S.M.H. and Amani, A., A proposal for the implementation of symmetry boundary condition In molecular dynamics simulation, *Proceedings of the third European Conference on Microfluidics, Heidelberg, Germany, December* (2012), 246.
- [23] Humphrey, W., Dalke, A. and Schulten, K., VMD - Visual Molecular Dynamics, *J. Molec. Graphics*, (1996) **14**:33-38
- [24] Allen, M.P. and Tildesley, D.J., *Computer Simulation of Liquids*, Clarendon Press, (1989)
- [25] Swope, W.C., Andersen, H.C., Berens, P.H. and Wilson, K.R., A computer simulation method for the calculation of equilibrium constants for the formation of physical clusters of molecules, *The Journal of Chemical Physics*, (1982) **76**:637-649
- [26] Che, J.W., Cagin, T. and Goddard, W.A., Thermal conductivity of carbon nanotubes, *Nanotechnology*, (2000) **11**:65-69
- [27] Angelopoulos, P., Papadimitriou, C. and Koumoutsakos, P., Data Driven, Predictive Molecular Dynamics for Nanoscale Flow Simulations under Uncertainty, *The Journal of Physical Chemistry B*, (2013), **117**:14808–14816.

FIGURES

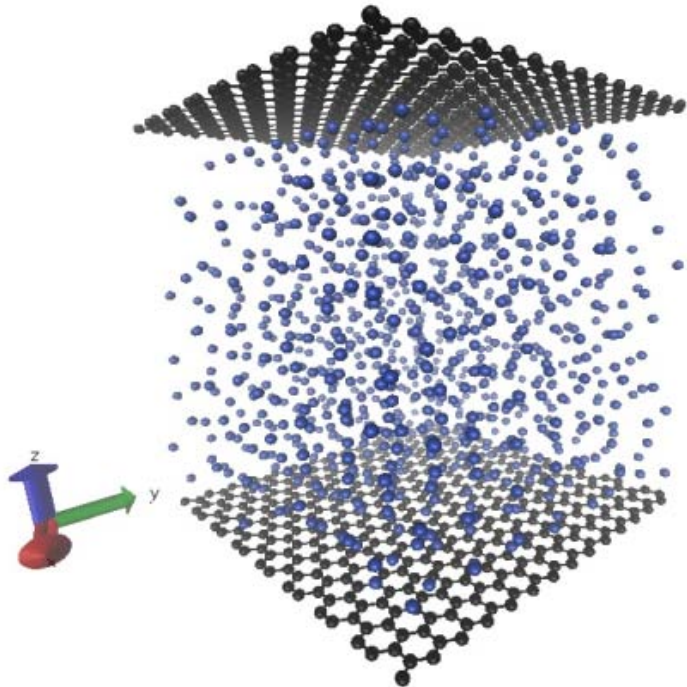


Figure 1: Schematic of initial molecules positions

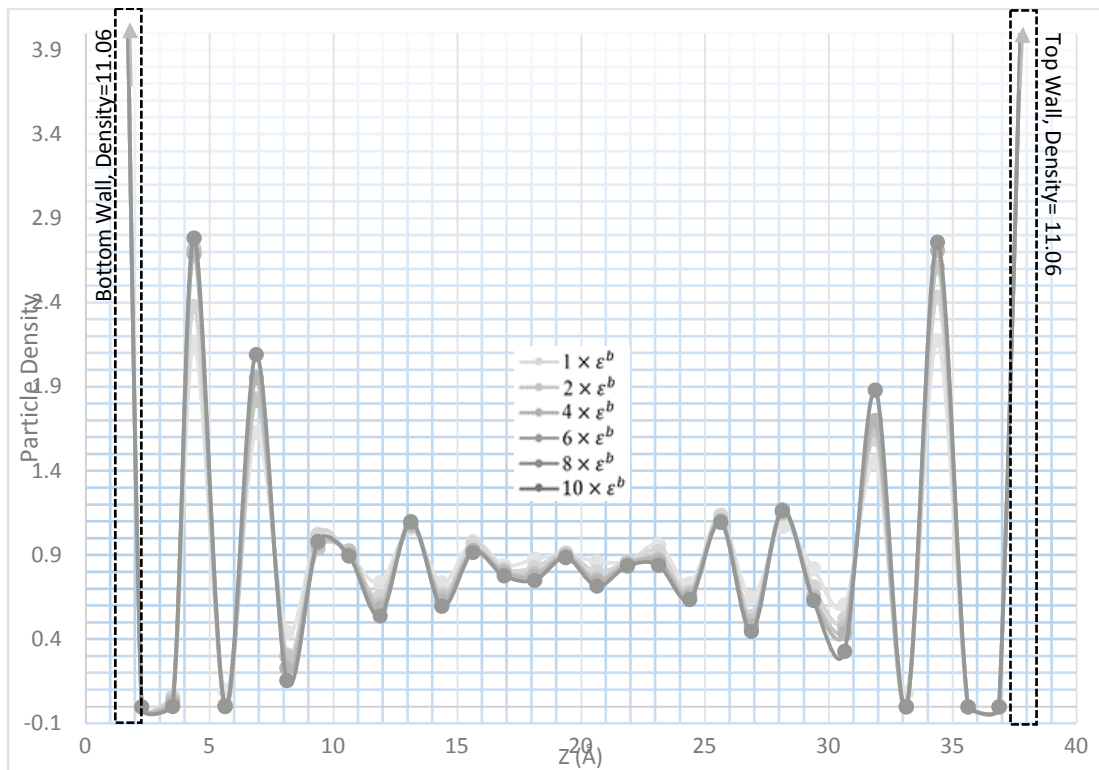


Figure 2: Particle density profiles of different values of wall-fluid interaction strength

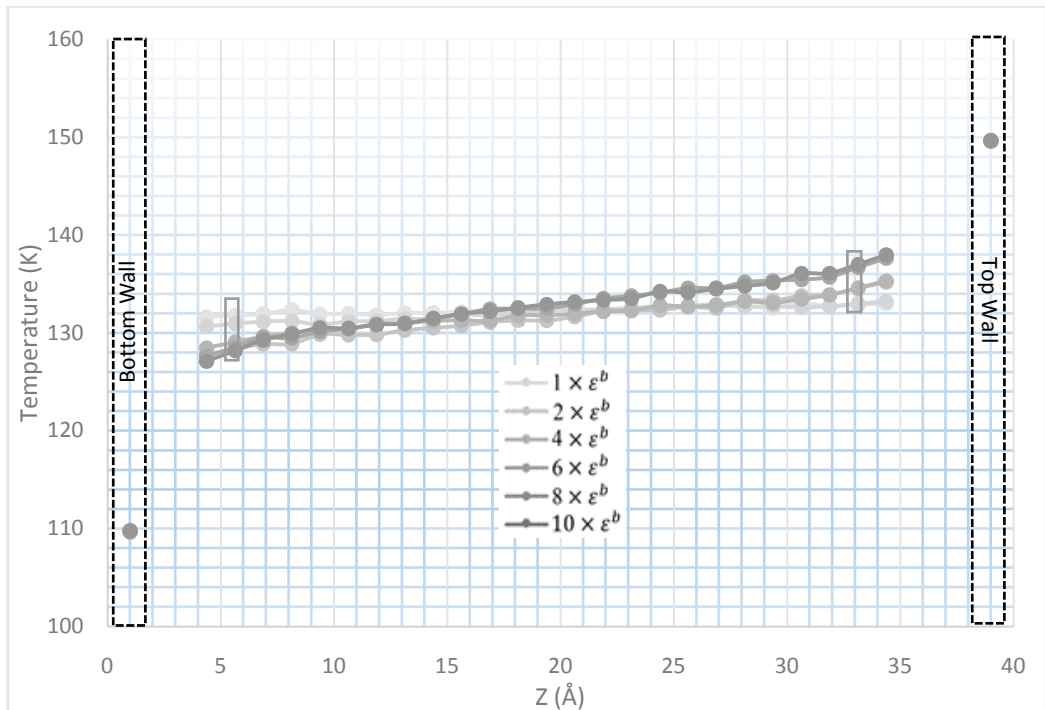


Figure 3: Temperature profiles of different values of wall-fluid interaction strength

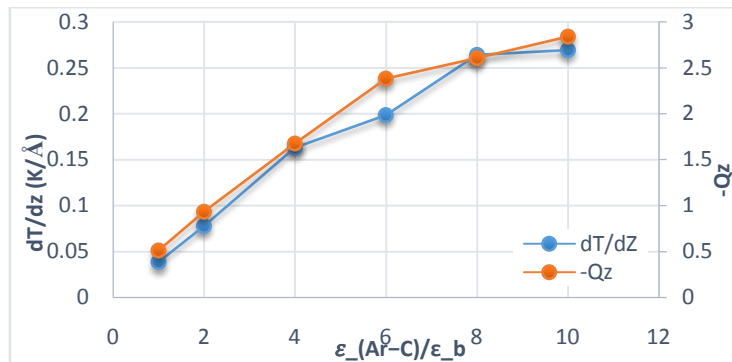


Figure 4: Temperature gradient of the bulk of Argon molecules and heat flux transferred between the walls for different values of wall-fluid interaction strength

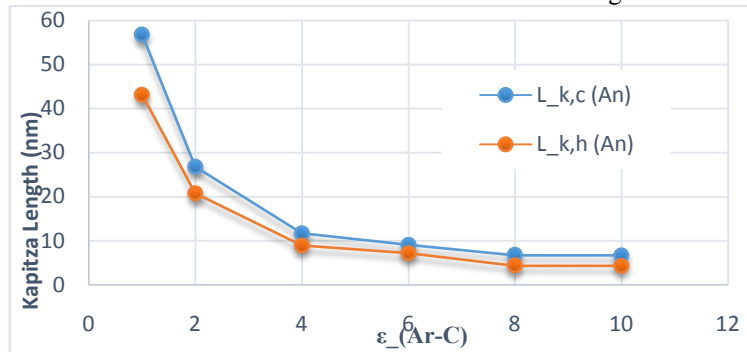


Figure 5: Kapitza length at liquid/solid interfaces for different values of wall-fluid interaction strength

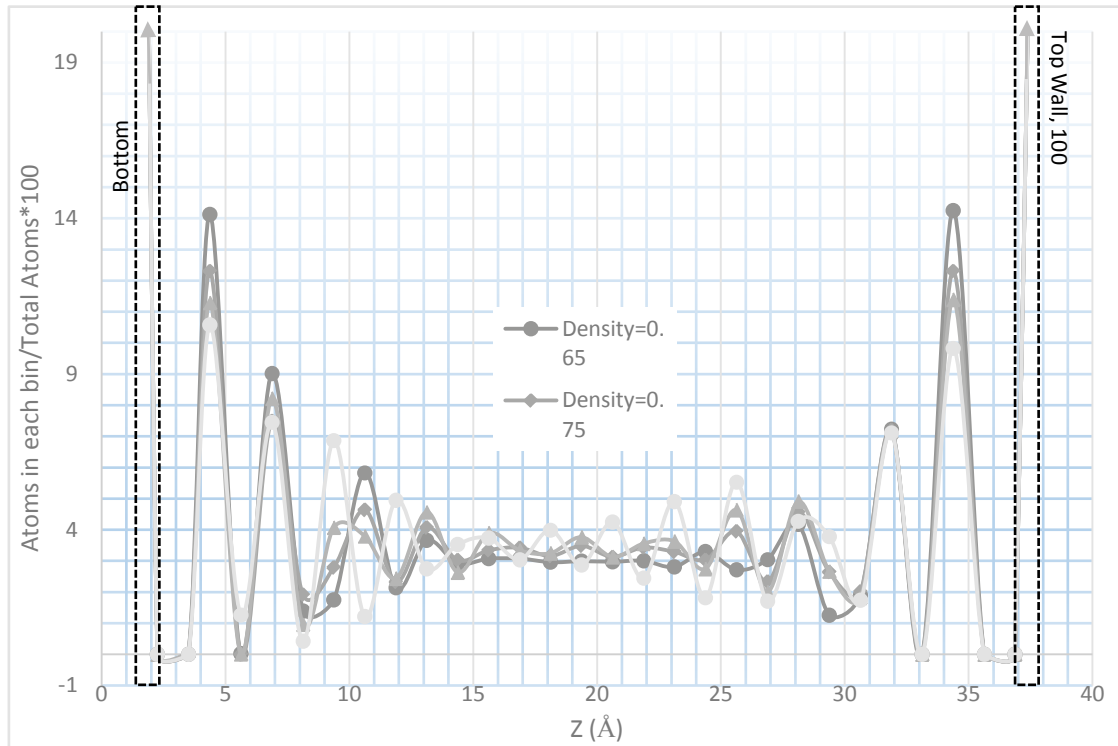


Figure 6: Proportion of the number of molecules in each bin to the total number of molecules for different particle densities

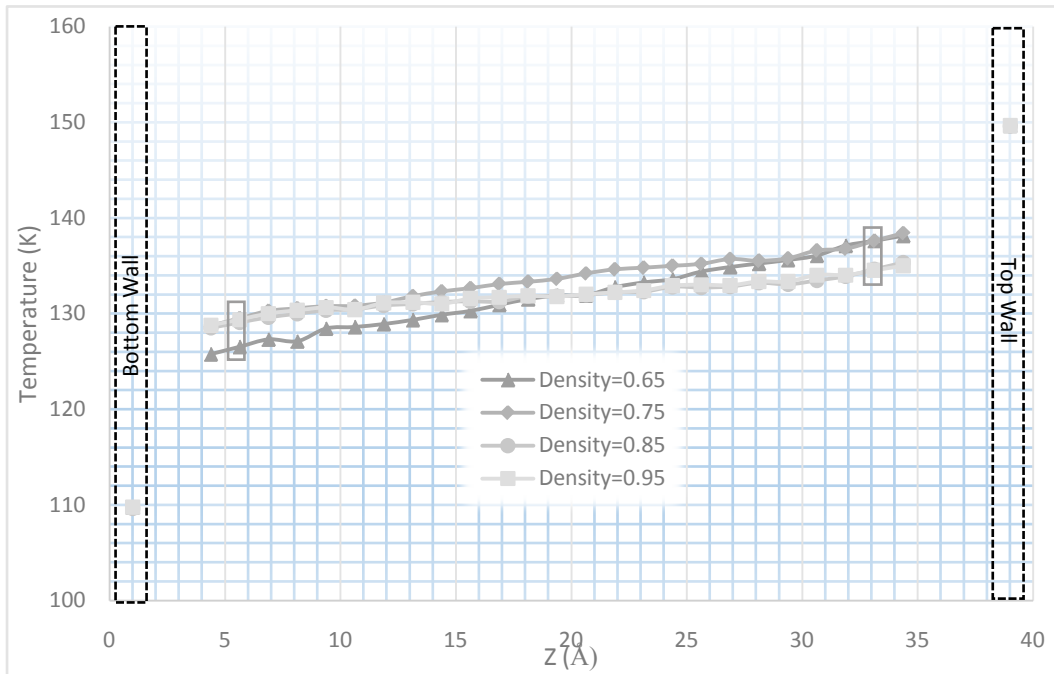


Figure 7: Temperature profiles of different values of particle densities

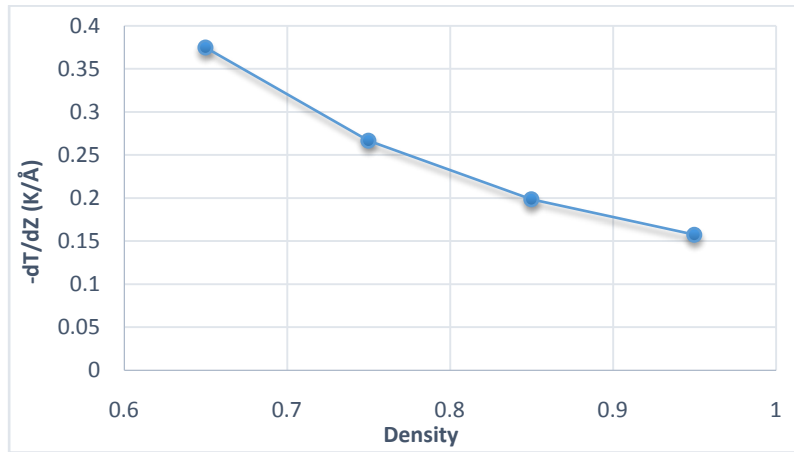


Figure 8: Temperature gradient of the bulk of Argon molecules for different fluid densities

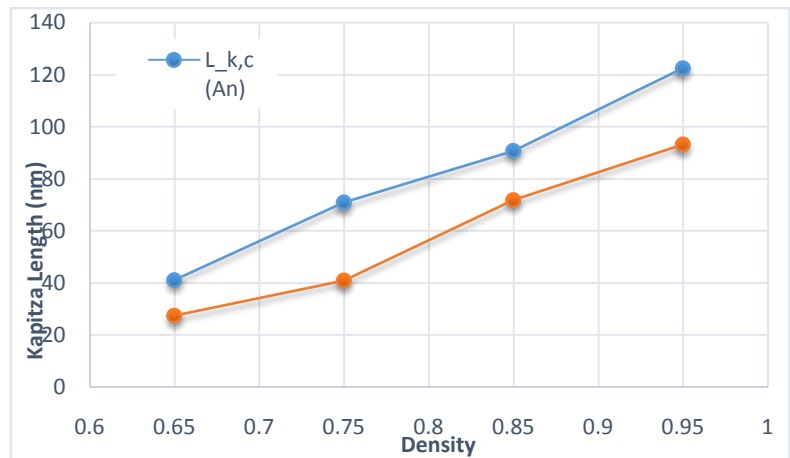


Figure 9: Kapitza length at liquid/solid interfaces for different fluid densities

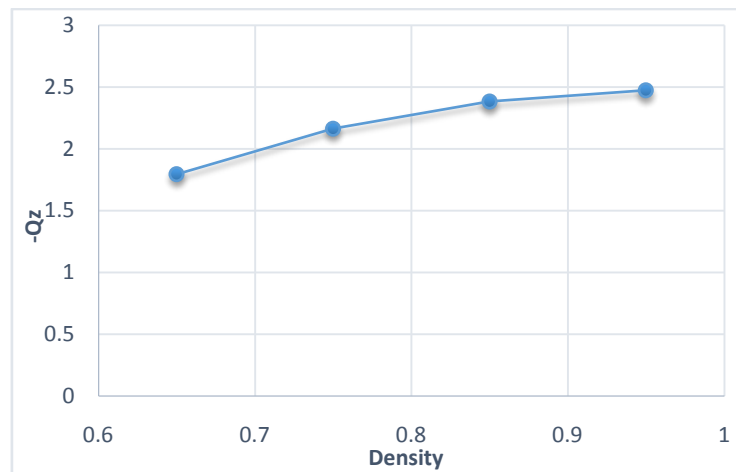


Figure 10: Heat flux generated between the walls for different fluid densities

AN INVESTIGATION INTO THE EFFECT OF PARTICLE PLATYNESS ON THE STRENGTH OF GRANULAR MATERIALS USING THE DISCRETE ELEMENT METHOD

M. POTTCARY¹, A. ZERVOS¹ AND J. HARKNESS¹

¹ Infrastructure Research Group, Faculty of Engineering and the Environment, University of Southampton
University Rd, Southampton, SO17 1BJ
M.Potticary@soton.ac.uk

Key words: Granular Materials, DEM, Contact Problems, Ballast

Abstract. It has long been recognised that the macroscopic mechanical behaviour of a granular material depends, to differing extents, on micro-mechanical properties such as the particle size distribution, the particle shape, the inter-particle friction angle and the particle strength. However, a systematic investigation of some of these effects is still lacking. In this paper we focus on particle shape, which is one of the fundamental characteristics of a granular material.

We build on previous work that used the axes of an equivalent scalene ellipsoid to characterise particle form, one of the three aspects that define particle shape. (The other two being angularity and roughness.) We use DEM simulations to investigate the effect of particle form, and in particular of particle platyness, on the friction angle of a granular material at critical state. It is found that a deviation of particle shape from that of a sphere leads to higher angles of friction; quantities such as fabric, average rates of particle rotation and interparticle sliding are used to provide insights into the underlying micromechanics.

1 Introduction

The shape of its particles is one of the fundamental properties of a granular material. To quantify it, three (assumed) independent aspects of shape are generally considered, each describing geometrical properties of a particle at a different scale of observation. These are particle form, angularity and roughness. Form quantifies the overall shape of a particle, angularity describes the number and sharpness of angles on its perimeter/surface, and roughness relates to the microscopic variations of the particle surface that are to some extent responsible for interparticle friction.

Particle form in particular is generally quantified using the longest (L), intermediate (I) and shortest (S) dimensions of the particle. Whilst a number of different measures

have been proposed to describe form, generally involving combinations of S , I and L , no consensus exists on whether one has a clear advantage over the others [8].

Here we propose a new way of describing form on the basis of an equivalent scalene ellipsoid with axes equal to the dimensions S , I and L of the particle. In this framework, particle form is uniquely defined by two parameters: particle *elongation* and *platyness*. We then perform DEM simulations of triaxial compression on granular assemblies of the same particle size distribution, each consisting of particles of a single form, to investigate the effect of particle platyness. We use the method of potential particles, which allows modelling of particles with (almost) arbitrary shape. Particle size distributions consistent with those of railway ballast are used, while the number of particles in each simulation is consistent with the number of ballast particles present in the specimens of corresponding physical tests.

2 Particle Form

Over the years many different ways to describe particle form have been presented, with many authors contributing to the debate [2, 13, 7, 27, 26, 25, 24, 23, 17, 16]. One of the most common methods is to use a simple solid to represent the particle, and assume that the form of the particle can be determined with reference to the geometry of that solid. The simplest such solid that can be defined in 3D is a sphere.

The definition of form that we use in this study is detailed in [20]. A scalene ellipsoid is used as reference solid; such an ellipsoid is the simplest smooth shape that allows three independent radii, corresponding to a particle's longest (L), intermediate (I) and shortest (S) dimensions. If we consider S , I and L to be coordinates in a three dimensional space, any particle can be represented by a vector \mathbf{f} linking the origin of the axes to point (S, I, L) . Clearly the shape (form) of the particle is represented by the orientation of \mathbf{f} , whereas the length of \mathbf{f} merely quantifies the size of the particle.

To quantify form we consider the intersection F of \mathbf{f} with the $S + I + L - 1 = 0$ “deviatoric” plane, which is normal to the spherical axis $S = I = L$ along which all spherical particles plot. The form of each particle is then uniquely defined by the two in-plane coordinates of F in a frame of reference centered at the intersection P of the spherical axis. In this way particle form is essentially quantified as the deviation of a particle's shape from that of a sphere. These two independent parameters of form, normalised in the $[0, 1]$ interval for ease of use, are given by Equations 1 and are referred to as *platyness* (α) and *elongation* (ζ) respectively.

$$\alpha = \frac{2(I - S)}{L + I + S}, \quad \zeta = \frac{L - I}{L + I + S} \quad (1)$$

Ellipsoids that share the same values for both α and ζ are geometrically similar, i.e. they differ only in size but not shape. All possible scalene ellipsoids plot, on the α - ζ plane, within the triangle shown in Figure 1. The edges and corners of the triangle correspond to degenerate cases where some of the dimensions are equal and/or zero.

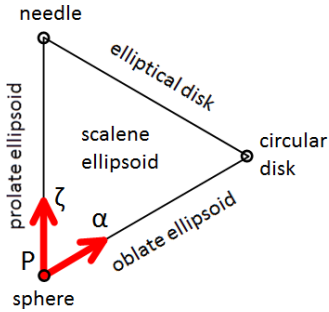


Figure 1: Elongation and Platyness space with description of forms

In [22, 21, 12, 11, 9, 5, 4, 3, 18] the authors showed that any deviation in particle form from a sphere leads to an increase in the strength of the granular material. Preliminary results presented in [20] showed that increases in strength are more sensitive to increases in particle elongation than particle platyness.

In this paper we focus on the effect that particle platyness has on the strength of a granular material at critical state. To isolate this effect, in the analyses reported here elongation was kept constant by setting $L = I$ and therefore $\zeta = 0$. Platyness on the other hand was varied by decreasing S between $S = 1$ (for $L = I = S$, a sphere) and $S = 0$ ($L = I$ and $S = 0$, a circular disk). The particle forms considered have dimensions $L = I \geq S$; a summary is given in Table 1.

Form	$L : I : S$	Platyness α	Elongation ζ
1	1 : 1 : 1	0	0
2	1 : 1 : 0.8	0.14	0
3	1 : 1 : 0.73	0.2	0
4	1 : 1 : 0.6	0.3	0
5	1 : 1 : 0.5	0.4	0
6	1 : 1 : 0.3	0.6	0

Table 1: Table of particle forms considered in the analyses reported here.

3 DEM Modelling

As physical tests on a granular material of a single particle form are very difficult to carry out, the Distinct Element Method (DEM) is used here to simulate triaxial tests. DEM has been used extensively in the field of soil mechanics due to its ability to provide micro-mechanical information on the material at the particle scale. For this paper an in house DEM code was used, detailed in [14], that can accommodate smooth, convex particles of arbitrary shape. Hertzian interparticle contact is assumed.

Models were created using particles of a single form and a particle size distribution

(PSD) representative of that of railway ballast. They were then used to simulate triaxial compression conditions. To determine the PSD, 5 different sizes between the maximum and minimum gradation curves for railway ballast as defined in [1] were created for each model, keeping I equal to the respective sieve size.

To help constrain the models and ensure comparability of results, the total volume contained within each model was kept as close to $0.2m^3$ as possible. As a result the number of grains contained within each model varied with particle shape, however this is also the case with specimens of fixed dimensions used in physical tests.

To create a model, a number of particles were randomly dispersed within 3D space to a target initial void ratio of 2.0. The particles themselves were given random orientation to remove any bias in the initial conditions that could affect results.

The model was then subjected to isotropic compression using periodic boundaries, zero gravity forces and zero inter-particle friction. Once a void ratio of 0.65 was reached, isotropic stress of $100kPa$ was applied to the boundaries and the model was allowed to reach equilibrium. At that point inter-particle friction was reintroduced and the model was subjected to triaxial loading, where the lateral boundaries were stress controlled at a constant $100kPa$. The top boundary was strain controlled and moved downwards at a constant axial strain rate.

Table 2 shows the different model parameters that were used.

Properties	Value
Particle Density	$2700Kg/m^3$
Interparticle Friction Angle	30 degrees
Particle Bulk Modulus	50 GPa
Particle Poisson's Ratio	0.3

Table 2: Material Properties

4 Results

4.1 Shear Strength

Mobilisation of shear strength of a granular material can be described by the mobilised angle of friction ϕ_{mob} , given by Equation 2.

$$\phi_{mob} = \sin^{-1} \left(\frac{\sigma_1 - \sigma_2}{\sigma_1 + \sigma_2} \right) \quad (2)$$

where σ_1 and $\sigma_2 = \sigma_3$ are the principal stresses. Figure 2 plots the mobilised angle of friction against vertical strain for each model. Whilst peak friction angles differ widely, these are not directly comparable because they may correspond to different initial relative densities of the granular materials modelled. (Although it could be argued that, due to the preparation procedure, all models were prepared at or near the densest state possible for

each material and therefore at or near unit relative density, this discussion is reserved for a future publication.) Due to the presumed difference in relative density among models, some reach a very dense packing that results to an almost immediate mobilisation of a very high angle of friction. Other models exhibit a delayed mobilisation of a rather lower peak.

The difference in relative density arises because varying the shape of the particles varies the minimum and maximum achievable void ratio. Therefore, even if two models are sheared from the same initial void ratio, their initial relative densities will most likely differ, precluding meaningful comparisons of peak friction. We note that theoretical estimation of the minimum and maximum void ratios is very difficult; research in the field of particle packing of different shapes does exist, however this is currently limited to mono-dispersed particles [15, 10].

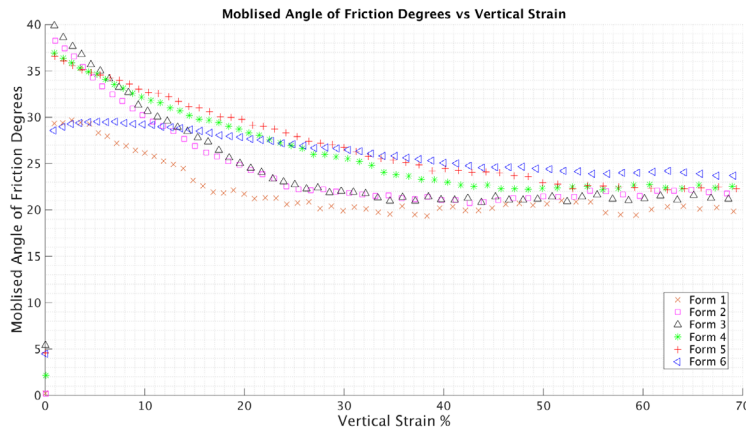


Figure 2: Mobilised angle of Friction against Vertical strain

On the other hand, the friction angle at critical state ϕ'_{crit} is independent of the initial void ratio, allowing valid comparisons. Figure 3 shows that as the shape of the particles becomes more platy, critical state strength increases roughly linearly with platyness.

4.2 Particle Orientation Fabric

At the start of the test, particles have a random orientation. However, as shearing takes place, particles will generally reorient themselves and may do so along some preferred direction. The orientation of each (ellipsoidal) particle can be described by a local system of orthogonal vectors in the directions of its three radii (L , I and S .) The average particle orientation with respect to the global model axes can be quantified by a fabric tensor such as that given by Equation (3) [19]. This describes the average orientation of a set of n unit vectors V^k . For randomly oriented vectors the diagonal of G_{ij} will be equal to $\frac{1}{3}$ and off-diagonal values will be zero, indicating lack of a preferential direction.

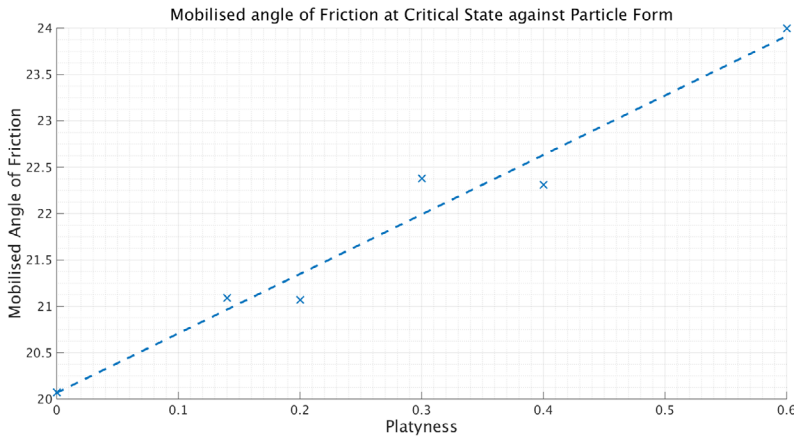


Figure 3: Friction angle at critical state against Platyness

$$G_{ij} = \frac{1}{n} \sum_{k=1}^n V_i^k V_j^k \quad (3)$$

As there is no single vector that describes the orientation of an ellipsoid, this fabric tensor can be calculated for the direction of each one of the three radii. Figure 4 shows how the G_{33} component of the fabric tensor corresponding to the S -direction of each particle varies with vertical strain. G_{33} essentially quantifies the prevalence of particles choosing to reorient their S -axis parallel to the global z -axis, i.e. with their flatter face normal to the maximum principal stress.

All tests started off with random particle orientation, shown by a value of $G_{33} \approx 0.33$ in Figure 4. As shear strains increased, however, so did G_{33} , showing that on average particles re-oriented their flatter face normal to the maximum principal stress in the course of shearing. Also, the rate of reorientation progressively decreases as the model approaches critical state, presumably because a configuration that can accommodate further shearing is reached. This general behaviour is observed even for relatively small values of platyness. In contrast, spherical particles do not show any tendency to re-orient and $G_{33} \approx \text{const.}$ throughout.

4.3 Particle Rotation and Sliding

As a specimen is strained, the particles will displace and rotate to accommodate this by rearranging the structure of the granular skeleton. It is expected that, during this process, particles of different forms will need to translate and rotate in different ways or proportions. Previous numerical studies of 2D assemblies have shown a link between particle rotations and sliding contacts; inhibiting rotation led to larger amounts of sliding and a higher mobilised angle of friction by increasing the amount of energy necessary to distort the skeleton [6].

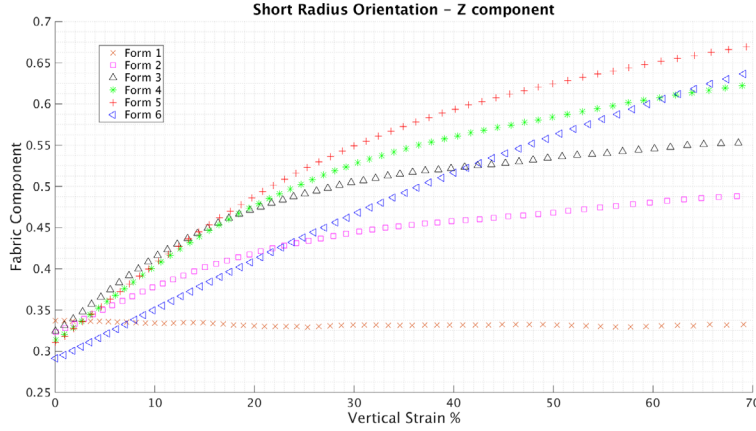


Figure 4: Vertical fabric orientation for the particle's S radius against Vertical Strain

Quantifying rotations and rotation increments in 3D in a meaningful way is more challenging, but can be simplified using the algebra of quaternions: rotation can be considered a quaternion whose real part quantifies the amount of rotation and its three imaginary parts the direction of the axis about which that rotation takes place. Here we focus on differences of the real part between relatively closely spaced time-steps, so that the axis of rotation can be considered unchanged, and divide rotation by the corresponding true vertical strain increment to produce a rate of rotation with strain given by Equation 4.

$$\theta = \frac{d\theta_{quat}}{d\epsilon_z} \quad (4)$$

Figure 5 plots the mean rate of particle rotation against the proportion of sliding contacts for the different particle forms at critical state. Spherical particles rotate much more compared to platy particles; the rate of rotation decreases with increased platyness. Also, as particle platyness increases there is a reduction in the proportion of sliding contacts at critical state. An inverse relationship is seen between rate of rotation and the proportion of sliding contacts at critical state. Therefore to some extent the higher critical state strength exhibited by platy particles is due to platyness suppressing particle rotation and leading to increased interparticle sliding, a mechanism that in comparison requires more energy to be expended.

4.4 Contact Distribution

Contact between two ellipsoids can be any one of six types, depending on which side of one ellipsoid comes into contact with which side of the other. Figure 6 shows the different types. The type of any given contact in a DEM simulation can be determined using the geometry of the contacting particles, the location of the contact point on their surfaces and geometrical arguments. For degenerate cases of ellipsoids, where some of the radii

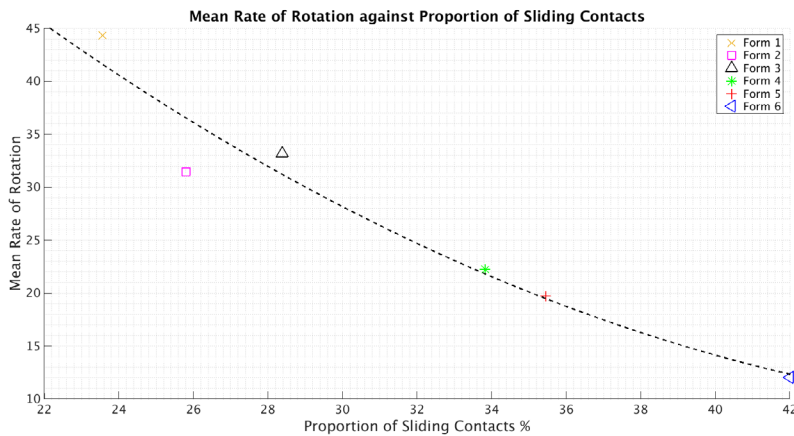


Figure 5: Mean proportion of sliding contacts against mean rate of rotation

are equal, the independent contact types are fewer: for example only one type of contact is possible between two spheres, where $L = I = S$.

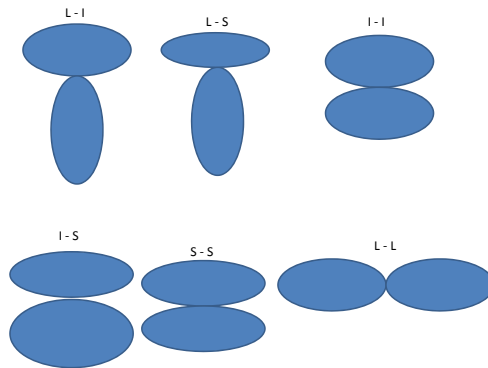


Figure 6: Different contact types for ellipsoidal particles

Figure 7 shows how the number of $S-S$ (“flat-to-flat”) as a percentage of the total number of contacts develops over time for each model. (For spherical particles the difference between L , I and S is simply operational and the data merely confirm that all “types” of contacts occur with the same probability as expected.) As the particle shape becomes platier the proportion of $S-S$ type contacts increases, to some extent reflecting the increasing area of “flat” particle surfaces available for contact. However, although for near-spherical (Form-2) particles the proportion of $S-S$ contacts remains relatively constant (i.e. oscillating around the same value between 10% and 50% strain), for the platter shapes of Form-3, but especially Forms-4, 5 and 6, $S-S$ contacts become even more

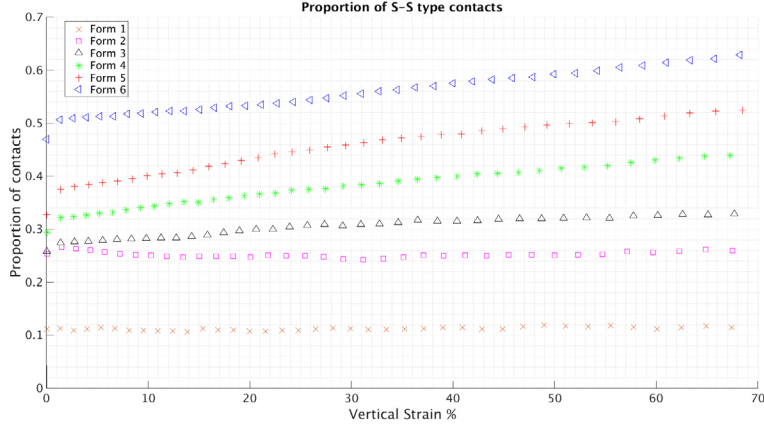


Figure 7: Distribution of contact type *S-S* against Vertical Strain

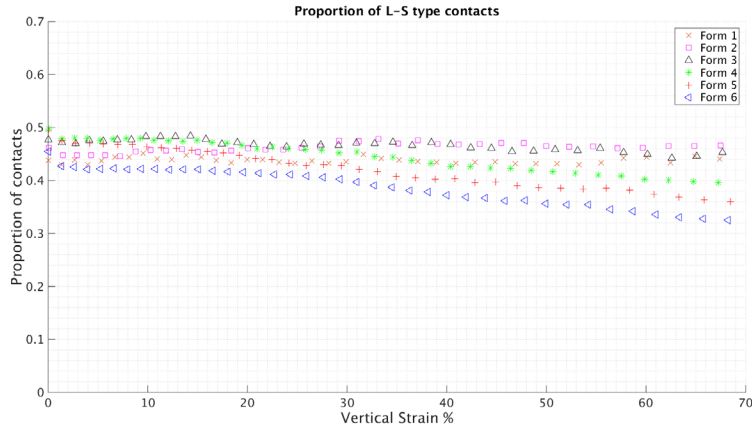


Figure 8: Distribution of contact type *L-S* against Vertical Strain

prevalent as the specimen is strained (e.g. varying by 7% over the same strain range for Form-6). This continuing formation of such contacts coincides with a more pronounced reorientation of particle flats normal to the maximum principal stress, as seen in Figure 4.

Figure 8 plots the proportion of *L-S* (“side-to-flat”) contacts over time for all models. Similarly to *S-S*, it remains relatively constant for near-spherical particles (Form-2 but also 3.) In contrast to *S-S*, however, the proportion of *L-S* contacts for the platier particles (Form-4, 5 and 6) reduces with straining. The proportion of *L-L* (“side-to-side”) type contacts, on the other hand, remains relatively constant throughout for all models; it is plotted in Figure 9.

The data suggest that, as the model is strained, platier particles promote a conversion of less stable *L-S* to inherently more robust *S-S* contacts that are less likely to subsequently break. Finally, there appears to be a threshold value $0.2 \leq \alpha_{cr} \leq 0.3$ of platyness, where a

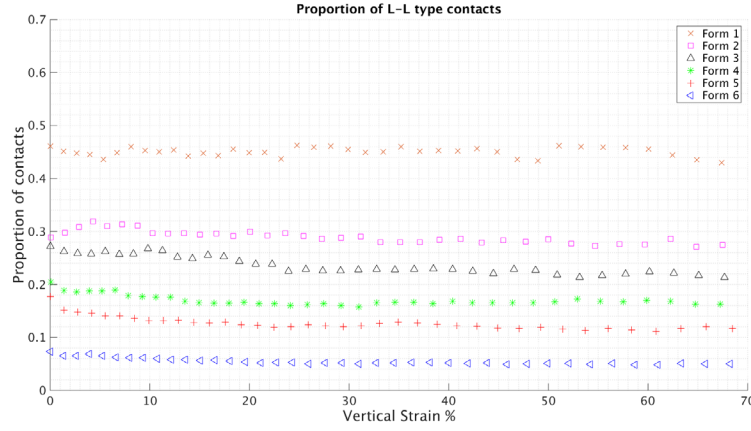


Figure 9: Distribution of contact type *L-L* against Vertical Strain

transition takes place to this type of “platy” behaviour for $\alpha \geq \alpha_{cr}$, from “near-spherical” behaviour for $\alpha \leq \alpha_{cr}$.

5 Conclusion

In this paper we used DEM to investigate the effect of particle platyness on granular material strength.

It was found that as particle platyness increases, so does the strength of the aggregate at critical state. This is accompanied, or rather is the result of, a reduction of particle rotation, which is inhibited by particle platyness, and a corresponding increase in the prevalence of interparticle sliding as the micro-mechanism that accommodates macroscopic straining.

Platier particles also showed a preference for aligning their flatter faces normal to the major principal stress and for forming “flat-to-flat” contacts, both of which arguably increase stability. A critical platyness value $0.2 \leq \alpha_{cr} \leq 0.3$ exists, governing the transition to “platy” behaviour, where more stable ”flat-to-flat“ contacts continue to develop during straining at the expense of other types, from ”near-spherical“ behaviour where this is not the case.

These observations are consistent with particle platyness promoting a more stable configuration of the granular skeleton, thus explaining the increased strength of the aggregate as measured macroscopically.

Acknowledgements

We gratefully acknowledge support from Network Rail (Strategic Partnership with the University of Southampton) and EPSRC Track21 Programme Grant, EP/H044949/1. Use of the IRIDIS High Performance Computing Facility and associated support services at Southampton are also acknowledged.

REFERENCES

- [1] *BSI Standards Publication Aggregates for railway ballast BS EN 13450:2013 BSI*. BSI Standards Limited 2013, 2013.
- [2] BC Aschenbrenner. A new method of expressing particle sphericity. *Journal of Sedimentary Research*, 1956.
- [3] E Azéma and Farhang Radjaï. Stress-strain behavior and geometrical properties of packings of elongated particles. *Physical Review E*, 81(5):1–17, April 2010.
- [4] E Azéma and Farhang Radjaï. Force chains and contact network topology in sheared packings of elongated particles. *Physical Review E*, 85(3):031303, March 2012.
- [5] E Azéma, Farhang Radjaï, Baptiste Saint-Cyr, Jean-Yves Delenne, and Philippe Sornay. Rheology of three-dimensional packings of aggregates: Microstructure and effects of nonconvexity. *Physical Review E*, 87(5):052205, May 2013.
- [6] J.P. P Bardet. Observations on the effects of particle rotations on the failure of idealized granular materials. *Mechanics of Materials*, 18(2):159–182, July 1994.
- [7] P J Barret. The shape of rock particle, a critical review. *Sedimentology*, 27:291–303, 1980.
- [8] SJ Blott and K Pye. Particle shape: a review and new methods of characterization and classification. *Sedimentology*, pages 31–63, September 2007.
- [9] Bernard Cambou, Michel Jean, and Farhang Radjaï. *Micromechanics of granular materials*, volume 77. John Wiley & Sons, 2010.
- [10] A Donev, FH Stillinger, PM Chaikin, and S Torquato. Unusually dense crystal packings of ellipsoids. *Physical review letters*, 2004.
- [11] Nicolas Estrada, E Azéma, Farhang Radjaï, and Alfredo Taboada. Identification of rolling resistance as a shape parameter in sheared granular media. 011306:1–5, May 2011.
- [12] Nicolas Estrada, Alfredo Taboada, Farhang Radjaï, Masami Nakagawa, and Stefan Luding. Shear strength and fabric properties in granular media with interlocked particles. *AIP Conference Proceedings*, 1145(2009):373–376, June 2009.
- [13] Robert L. Folk. Student Operator Error in Determination of Roundness, Sphericity, and Grain size. *Journal of Sedimentary Research*, 25(4), 1955.
- [14] J Harkness. Potential particles for the modelling of interlocking media in three dimensions. *International Journal for Numerical Methods in Engineering*, 80:157315(June):1573–1594, 2009.

- [15] S. Heitkam, W. Drenckhan, and J. Fröhlich. Packing Spheres Tightly: Influence of Mechanical Stability on Close-Packed Sphere Structures. *Physical Review Letters*, 108(14):148302, April 2012.
- [16] JE Dobkins Jr and RL Folk. Shape development on Tahiti-nui. *Journal of Sedimentary Research*, 1970.
- [17] William Christian Krumbein. Measurement and Geological Significance of Shape and Roundness of Sedimentary Particles. *SEPM Journal of Sedimentary Research*, Vol. 11(2):64–72, August 1941.
- [18] Duc-Hanh Nguyen, E Azéma, Philippe Sornay, and Farhang Radjaï. Effects of shape and size polydispersity on strength properties of granular materials. *Physical Review E*, 91(3):032203, March 2015.
- [19] Masanobu Oda. Initial fabrics and their relations to mechanical properties of granular material. *Soils and Foundations*, 12(1):17–36, February 1972.
- [20] M Potticary, A Zervos, and J Harkness. A numerical investigation into the effect of particle form on the strength of granular materials. In *Proceedings of the 22nd UK Conference of the Association for Computational Mechanics in Engineering*, number April, 2014.
- [21] Farhang Radjai and Emilien Azéma. Shear strength of granular materials, 2009.
- [22] Farhang Radjai, Stephane Roux, and Jean Jacques Moreau. Contact forces in a granular packing. *Chaos (Woodbury, N.Y.)*, 9(3):544–550, September 1999.
- [23] ED Sneed and RL Folk. Pebbles in the lower Colorado River, Texas a study in particle morphogenesis. *The Journal of Geology*, 1958.
- [24] Hakon Wadell. Volume, Shape, and Roundness of Rock Particles. *The Journal of Geology*, Vol. 40(No. 5 (Jul. - Aug., 1932)):pp. 443–451, 1932.
- [25] CK Wentworth. The shape of beach pebbles, 1922.
- [26] EM Williams. A Method of Indicating Pebble Shape with One Parameter: NOTES. *Journal of Sedimentary Research*, 1965.
- [27] Theodor Zingg. *Beitrag zur Schotteranalyse*. PhD thesis, 1935.

CORRECTION OF THE GAS FLOW PARAMETERS BY MOLECULAR DYNAMICS

V. PODRYGA¹ AND S. POLYAKOV¹

¹ Keldysh Institute of Applied Mathematics, Russian Academy of Sciences (KIAM RAS)
Miusskaya sq., 4, 125047 Moscow, Russia
e-mail: pvictoria@list.ru, web page: <http://keldysh.ru/index.en.shtml>/

Key words: Molecular Dynamics, Nitrogen, Macroparameters of Gas Area, Compressibility, Heat Capacity, Enthalpy, Pressure, Internal Energy.

Abstract. This work is devoted to the molecular dynamics calculations of real gases and mixtures thereof macroparameters at room and low temperatures. Necessity of such calculations is caused by both the lack of experimental data on the gases properties in selected parameters ranges and problems of multiscale modeling of technically complex microsystems that use gas medium as transport agents. In work modern molecular dynamic approach to calculation of gas macroparameters is set out in a concentrated form, as well as its approbation is carried out by the example of the calculation of nitrogen macroparameters at room and lower temperatures. In numerical experiments the temperature dependences of pressure, kinetic, potential, and total energies, enthalpy, coefficients of compressibility and heat capacity at constant volume are obtained, which agree well with the theoretical and experimental data. Further development of the methodology will be related to calculation of the coefficients of viscosity and thermal conductivity, as well as a generalization to the case of a gas mixture.

1 INTRODUCTION

The current stage of scientific evolution is characterized by a large number of studies carried out for the development and implementation of nanotechnology in the production. Nanotechnology implies a good knowledge of the properties of materials and media used in industrial processes. One way to obtain information about the properties of the medium is a molecular modeling.

This paper deals with the calculation of the properties of gaseous media used as transport agents in installations of supersonic cold gasdynamic sputtering nanoparticles on the surface of various materials [1, 2]. Modern computer technology allows to calculate the properties of the gaseous medium at a molecular level, which makes it possible to determine the macroscopic parameters of gases from first principles.

The problem of gaseous media macroparameters calculating by molecular dynamics simulation arises when either no experimental data on the parameters of a real gas or gas mixture in a range of temperatures and pressures, or when a precise calculation of the gaseous medium state in a multiscale is required. In this paper, there is the motivation of both types as the results of numerical experiments are planned to be used as a database for subsequent multiscale computations of supersonic flows of gas mixtures in installations of supersonic

cold gasdynamic sputtering of nanoparticles on the substrate. As part of this big theme present work is a preparatory step for the joint calculation by continuum mechanics and molecular dynamics of all stages of deposition.

In the work by the method of molecular dynamics [3-7] macroparameters calculation of real gas (nitrogen) is performed. The first step is to bring the gas dynamic computing system in equilibrium at the selected temperature, and then from molecular dynamics calculations of the equation of state of pressure and energy (coefficients of compressibility and heat capacity), the internal energy of the system and enthalpy are determined. The results are compared with known experimental data.

2 MATHEMATICAL STATEMENT OF A PROBLEM

Consider a system of nitrogen molecules N_2 , enclosed in a microvolume V , which is a cube with sides $Lx = Ly = Lz$. The total amount of gas particles depends on the microvolume's size, gas density ρ and particles mass m : $N = \rho \cdot V/m$, $V = Lx^3$.

The dynamics of particles in a microvolume is described by equations of Newton.

$$m \cdot \frac{d^2 \mathbf{r}_i}{dt^2} = \mathbf{F}_i, \quad i = 1, \dots, N, \quad (1)$$

where i – particle's number, N – the amount of particles, m – the mass of a single particle (molecule), $\mathbf{r}_i(r_x, r_y, r_z)$ – the radius vector of the i -th particle, $\mathbf{F}_i(F_x, F_y, F_z)$ – the total force acting on the particle i .

The interaction forces of the particles are expressed through the gradient of the potential energy $U = \sum_{i=1}^N u_i$. As the potential for interaction between nitrogen molecules u_i a Lennard-Jones potential is [8] in form “n-6” from [9].

$$u_i = \frac{1}{2} \sum_{j \neq i} \varepsilon \frac{n}{n-6} \left(\frac{n}{6} \right)^{\frac{6}{n-6}} \left[\left(\frac{\sigma}{r_{ij}} \right)^n - \left(\frac{\sigma}{r_{ij}} \right)^6 \right], \quad i = 1, \dots, N, \quad (2)$$

where $r_{ij} = |\mathbf{r}_i - \mathbf{r}_j|$ – the distance between i -th and j -th particles, ε – the energy of molecular interaction, σ – the effective radius of interaction.

Initial conditions include starting distribution of particle coordinates and velocities. Starting coordinates distribution of the gas particles is taken uniform and consistent with the density corresponding to the selected temperature T_0 and pressure P_0 . Starting velocity distribution of the particles in modulus is set according to the selected temperature and realizes Maxwell distribution. The velocity distribution of the particles on the solid angle is uniform and such that the total momentum of the system is zero.

Periodicity conditions with periods Lx, Ly, Lz on axes x, y, z are considered as the boundary conditions.

The system of equations (1) is solved using a Verlet method [10] in the velocity form:

$$\mathbf{r}^{n+1} = \mathbf{r}^n + \mathbf{v}^n \Delta t + \frac{\mathbf{F}^n}{m} \frac{(\Delta t)^2}{2}, \quad \mathbf{v}^{n+1} = \mathbf{v}^n + \frac{\mathbf{F}^{n+1} + \mathbf{F}^n}{2m} \Delta t, \quad (3)$$

here Δt – the integration step, n – the step's number, \mathbf{F}^{n+1} – the force value on the current step.

Berendsen thermostat is used to achieve the desired temperature of the gas in thermodynamic equilibrium [11, 12].

The purpose of modeling is to obtain the average values of the gas macroparameters. The set of macroparameters consist of kinetic, potential, thermal, internal, and total energies; temperature and pressure; compressibility factors; enthalpy and heat capacity. Formulas below are for determining these macroparameters.

Kinetic energy of a system E_K and kinetic energy of a thermal moving E_T are calculated as sums of every particle energies the following way:

$$E_K = \sum_{i=1}^N \frac{m|\mathbf{v}_i|^2}{2}, \quad E_T = \sum_{i=1}^N \frac{m|\mathbf{v}_i - \mathbf{v}_m|^2}{2}, \quad \mathbf{v}_m = \frac{1}{N} \sum_{i=1}^N \mathbf{v}_i, \quad i = 1, \dots, N, \quad (4)$$

where $|\mathbf{v}_i|$ – the velocity vector's \mathbf{v}_i length of the i -th particle, \mathbf{v}_m – the velocity of the center of mass.

Internal energy E_I and total energy E represent following sums:

$$E_I = E_T + U, \quad E = E_K + U. \quad (5)$$

The temperature of the system is determined by the thermal energy of the system [9, 10]:

$$T = \frac{1}{3 \cdot N \cdot k_b} \left\langle \sum_{i=1}^N m |\mathbf{v}_i - \mathbf{v}_m|^2 \right\rangle, \quad (6)$$

where $\langle \rangle$ – the average value on system states, k_b – Boltzmann constant.

The system pressure P is determined by the virial theorem [12-14]:

$$P = \frac{N \cdot k_b \cdot T}{V} + \frac{1}{3 \cdot V} \left\langle \sum_{i=1}^N \sum_{j>i} (\mathbf{r}_{ij} \cdot \mathbf{F}_{ij}) \right\rangle, \quad i = 1, \dots, N, \quad (7)$$

where $\mathbf{r}_{ij} = \mathbf{r}_i - \mathbf{r}_j$, \mathbf{F}_{ij} – the interaction force between the i -th and j -th particles.

Compressibility factor Z_C describes the deviation of the thermodynamic properties of a real gas from the ideal gas and is expressed through the calculation result (7):

$$Z_C = \frac{P \cdot V}{N \cdot k_b \cdot T} = 1 + \frac{1}{3 \cdot N \cdot k_b \cdot T} \left\langle \sum_{i=1}^N \sum_{j>i} (\mathbf{r}_{ij} \cdot \mathbf{F}_{ij}) \right\rangle, \quad i = 1, \dots, N, \quad (8)$$

Also in the literature expression describing the deviation of the properties of the gas from the properties of the same gas under normal conditions, is investigated:

$$Z_P = \frac{P \cdot V}{P_0 \cdot V_0}, \quad (9)$$

where P_0 , V_0 – the pressure and the volume of the system under normal conditions.

Enthalpy H is another illustrative macroparameter of real gas, which in case of a real gas depends not only on the temperature, but also the pressure:

$$H = N E_I + P V. \quad (10)$$

To calculate the heat capacity C_V of the gas at constant volume, there are many ways of computing [3, 4, 12-17]. In this work calculations were made for the following variants:

$$C_V = \frac{3 \cdot k_b}{2} \left[1 - \frac{3 \cdot N}{2} \frac{\langle E_K^2 \rangle - \langle E_K \rangle^2}{\langle E_K \rangle^2} \right]^{-1}, \quad (11)$$

$$C_V = \frac{3 \cdot k_b}{2} \left[1 - \frac{3 \cdot N}{2} \frac{\langle T^2 \rangle - \langle T \rangle^2}{\langle T \rangle^2} \right]^{-1}, \quad (12)$$

$$C_V = \frac{3 \cdot N \cdot k_b}{2} \left[1 + \frac{2}{3 \cdot N \cdot (k_b \cdot \langle T \rangle)^2} (\langle E_P^2 \rangle - \langle E_P \rangle^2) \right], \quad (13)$$

$$C_V = \frac{3 \cdot N \cdot k_b}{2} \left[1 + \frac{3}{2 \cdot N} \frac{\langle E_P^2 \rangle - \langle E_P \rangle^2}{\langle E_K \rangle^2} \right]. \quad (14)$$

Equation (11) showed itself the most robust in the above mentioned conditions of the problem, so it was used in the preparation of the main results.

The total calculation algorithm is the following sequence of actions. At the initial time distributions of positions and velocities of all the particles are given, then solved the equations of motion, forces of the potential interaction (2), the new coordinates and velocities of the particles taking into account the boundary conditions and external influences on the system from the thermostat, kinetic (4), the internal and total of energies (5) are calculated at each step. Calculations are carried out before the stationary values of the temperature (6) and the pressure (7) which mean the establishment of the thermodynamic equilibrium. Then the rest macroparameters of the system (8) - (11) are calculated.

3 SIMULATION RESULTS

Among the strategies for calculating the gas macroparameters there are two main. The first and simplest of these is to fix the volume and number of particles. The result is "frozen" gas density. In this situation, you can change the pressure and calculate its temperature and other macroparameters (the first version of calculation), or vice versa, change the temperature and

calculate pressure and other macroparameters (the second version of calculation). As a result we obtain dependences of the fundamental gas macroparameters or on the pressure or on the temperature (below results obtained by the second variant are discussed).

The second strategy is to fix the pressure through the using of the barostat. In this case, with a fixed number of the particles system volume changes, and thus the gas density changes. In this strategy also there are two variants of calculations, either at a given temperature (which is controlled by a thermostat) density and other gas macroparameters are calculated, or at given number of particles density, temperature and other gas macroparameters are calculated.

Obviously, the choice of a strategy is linked with the objective function of calculations. Calculation combining both strategies and the various options will be the most complete. In this work we restricted ourselves to the first strategy and the second option for calculating. In this situation, all the temperature dependences of the gas macroparameters are simply determined.

The method of obtaining the average characteristics within the chosen strategy was as follows. First, we calculated the starting point on the P-T diagram corresponding to normal conditions (when the gas pressure is 1 atm., and the temperature of the gas is equal to 273.15 K). For these conditions, the majority of the gas macroparameters, including nitrogen for example, which was chosen for a numerical experiment is well known. In particular, the density of nitrogen at these conditions is 1.24979 kg/m³.

The calculation of the starting point was performed for 27000 of nitrogen molecules in the volume 1004936 nm³. The calculation was performed in 3 stages. First, the system was equilibrated in the conditions of thermostat using the Berendsen thermostat. Thermostating time was 8 ns. Fluctuations in pressure and temperature are not more than 0.05% from average value. Then, also in regulated temperature conditions for 4 ns first calculation of gas average macroparameters was carried out. Further in conditions off the thermostat for a further 4 ns second calculation of gas average macroparameters was carried out. Comparison of the gas macroparameters in the first and the second calculations confirmed the achievement the gasdynamic equilibrium state of the system.

Further calculations of temperature dependences of the gas macroparameters were carried out. For this purpose, on the temperature scale reference points 273.15, 263.15, 253.15, ..., 93.15 K were selected, which were used for calculations. For each reference point, different from 273.15 K, the calculation started from the system state for 273.15 K at the moment of time 8 ns. At the same time thermostat is at once switched to the reference temperature. This calculation was carried out for 4 ns. Then the thermostat is turned off and for another 4 ns gas average macroparameters were calculated.

Fig. 1-5 shows the resulting temperature dependences of the pressure, kinetic and potential energies and enthalpy, calculated per molecule, the specific heat at constant volume, compressibility coefficient (shows the actual deviation of the equation of state of a real gas on pressure from the ideal gas). Analysis of the obtained dependences showed the following.

First, near the start reference point gas is close to ideal gas, and its parameters are close to the known tabular data.

Secondly, at low temperatures the tendency of gas liquefaction (see. Fig. 5) is clearly visible, as evidenced by qualitative and quantitative experimental data. In particular, the specific heat at constant volume close to the point of liquid nitrogen starts to increase

exponentially and eventually reaches not two, but three or more J/K.

Third, linear character of change of such the macroparameters as pressure, kinetic and total energy, compressibility factor Z_p near the point of liquid nitrogen (77 K), means that the chosen strategy for calculating in this area no longer reflects the state of the gas, and in this case it is necessary to move to the second strategy, that is, to use a barostat.

Thus, it can be noted that in general the presented method allows to calculate gas (or gas mixture) macroparameters in the range of room and low temperatures. At the same time near the point of gas liquefaction, both the above strategy for calculating with thermo- and barostats should be used.

To conclude this section, we should mention another issue. The temperature dependences of two major macroparameters of gas: the viscosity and thermal conductivity are not considered in the work. This is partly due to the additional processing costs of their receipt, but the main thing - with the instability of the known computational algorithms to determine them by using periodic boundary conditions. In connection with this in the future it is supposed to conduct a separate researching on a detailed study of the problem.

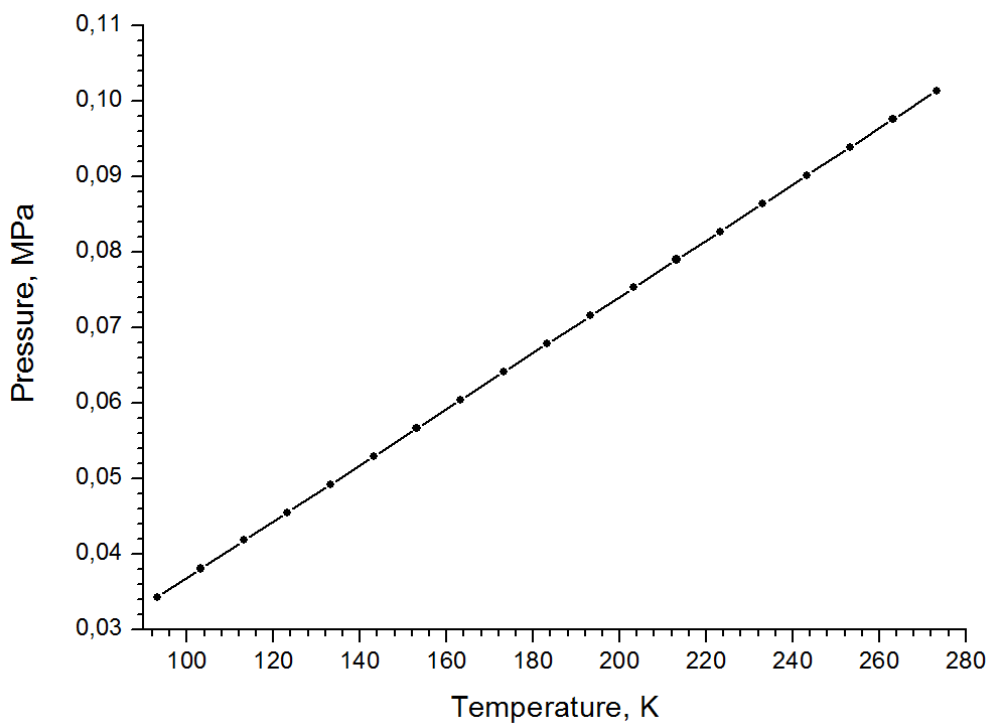


Figure 1: Dependence of pressure from temperature at constant density

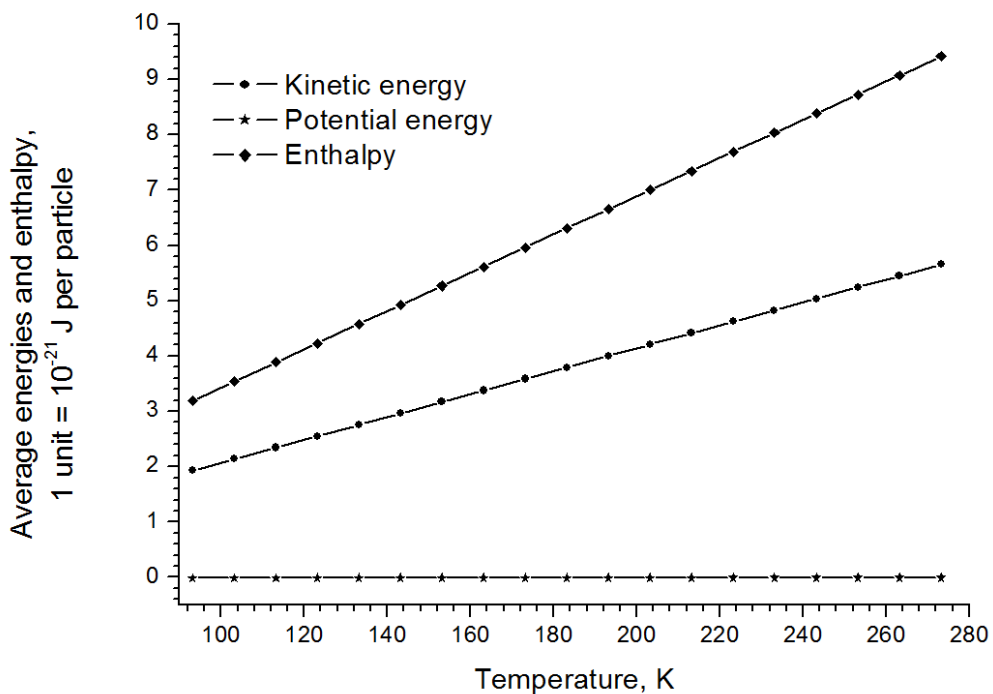


Figure 2: Dependence of average energies and enthalpy (calculated per molecule) from temperature at constant density

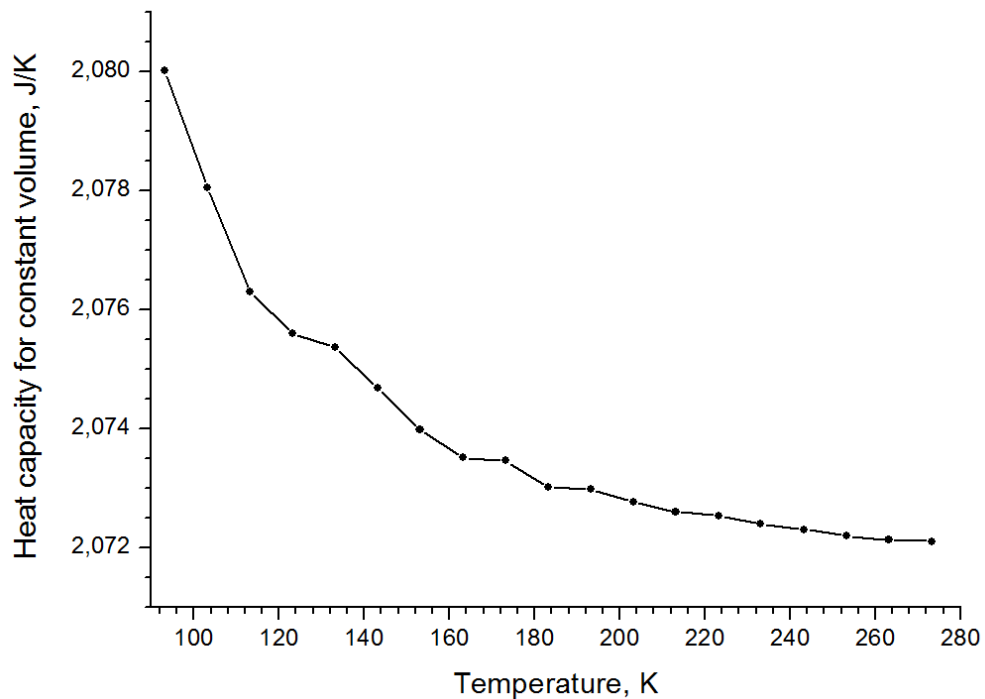


Figure 3: Dependence of heat capacity at constant volume from temperature

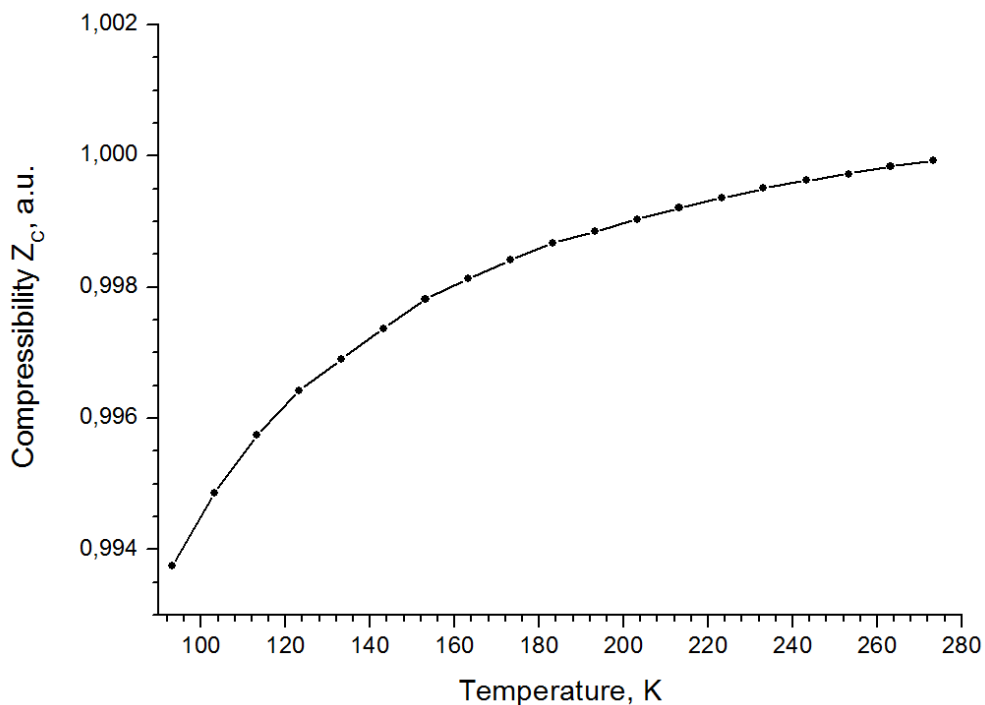


Figure 4: Dependence of compressibility Z_c (deviation from ideal) from temperature

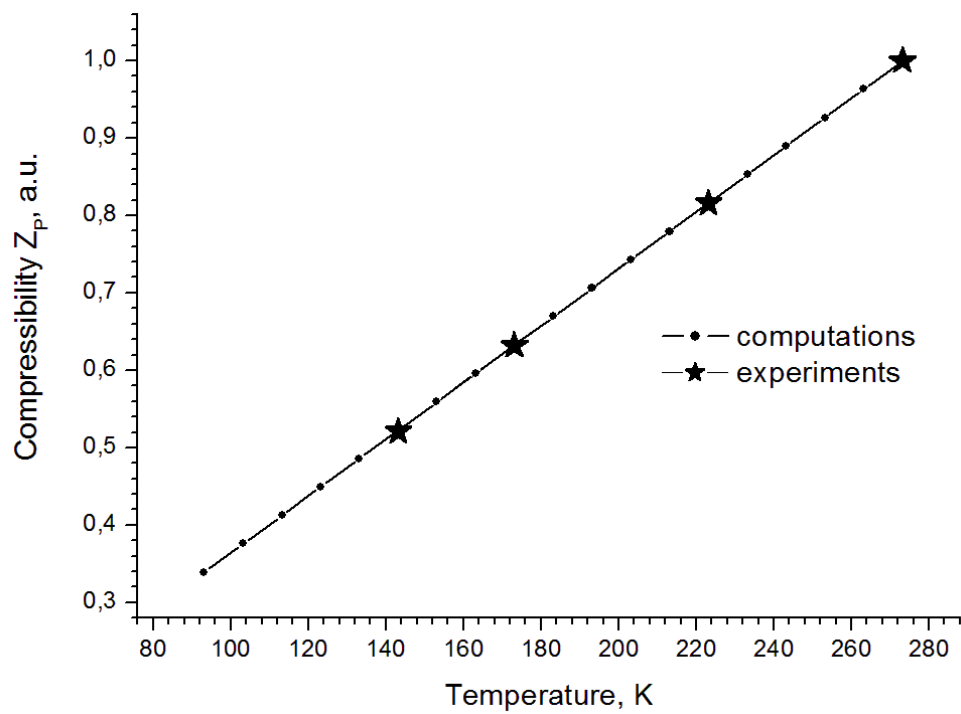


Figure 5: Dependence of compressibility Z_p from temperature

4 CONCLUSIONS

The paper considers the problem of calculating the macroparameters of gas media by molecular dynamics simulation. This issue is relevant for multiscale computing of supersonic flows of gas mixtures in plants sputtering nanoparticles on the surface of various materials. Under this theme, the present work is a preparatory step for the joint calculation of continuum mechanics and molecular dynamics of all stages of sputtering. The results of the work are as a probation of calculation methods of basic gas or gas mixture macroparameters and received specific temperature dependences of the nitrogen macroparameters in the range of room and low temperatures (typical for gaseous media in installations of supersonic cold gasdynamic sputtering). Further development of the technique will be associated with the calculations of the coefficients of viscosity and thermal conductivity of nitrogen, and with the definition of macroparameters for nitrogen and hydrogen mixture in various proportions

REFERENCES

- [1] Resnick D. *Nanoimprint lithography*. / In "Nanolithography. The art of fabricating nanoelectronic and nanophotonic devices and systems" (Edited by Martin Feldman). Woodhead Publishing Limited, (2014).
- [2] Papyrin A., Kosarev V., Klinkov S., Alkhimov A., Fomin V. *Cold Spray Technology*. Amsterdam: Elsevier Science, (2007).
- [3] Frenkel D., Smit B. *Understanding Molecular Simulation. From Algorithm to Applications*. NY: Academic Press, (2002).
- [4] Haile J.M. *Molecular Dynamics Simulations. Elementary Methods*. NY: John Wiley & Sons Inc., (1992).
- [5] Norman G.E., Stegailov V.V. Stochastic theory of the classical molecular dynamics method. *Mathematical Models and Computer Simulations* (2013) **5**(4):305-333.
- [6] Norman G.E., Stegailov V.V. Stochastic and dynamic properties of molecular dynamics systems: Simple liquids, plasma and electrolytes, polymers. *Computer Physics Communications* (2002) **147**:678-683.
- [7] Podryga V. O. Molecular Dynamics Method for Simulation of Thermodynamic Equilibrium. *Mathematical Models and Computer Simulations* (2011) **3**(3):381-388.
- [8] Lennard-Jones J.E. Cohesion. *Proceedings of the Physical Society* (1931) **43**(5):461-482.
- [9] Fokin L.R., Kalashnikov A.N. The transport properties of an N₂-H₂ mixture of rarefied gases in the EPIDIF database. *High Temperature* (2009) **47**(5):643-655.
- [10] Verlet L. Computer «experiments» on classical fluids. I. Thermodynamical properties of Lennard-Jones molecules. *Phys. Rev.* (1967) **159**:98-103.
- [11] Berendsen H.J.C., Postma J.P.M., van Gunsteren W.F. et al. Molecular dynamics with coupling to an external bath. *J. Chem. Phys.* (1984) **81**:3684-3690.
- [12] Rapaport D.C. *The Art of Molecular Dynamics Simulations*. Second Edition. Cambridge University Press, (2004).
- [13] Hockney R.W. Eastwood J.W. *Computer simulation using particles*. McGraw-Hill Inc, (1981).
- [14] Heermann D.W. *Computer Simulation Methods in Theoretical Physics*. Springer-Verlag, (1986).

- [15] Allen M.P., Tildesley D.J. *Computer Simulation of Liquids*. NY: Oxford University Press, (1987).
- [16] Lebowitz J. L., Percus J. K., Verlet L. Ensemble Dependence of Fluctuations with Application to Machine Computations. *Phys. Rev.*, (1967) **153**(1):250-254.
- [17] Lebowitz J. L., Percus J. K. Thermodynamic Properties of Small Systems. *Phys. Rev.*, (1961) **124**(6):1673-1681.

DISCRETE ELEMENT SIMULATION OF WET GRANULAR MATERIALS: PLASTIC COMPRESSION

V.-D. THAN^{1,2}, J.-N. ROUX¹, A.-M. TANG¹ AND J.-M. PEREIRA¹

¹ Université Paris-Est, Laboratoire Navier (UMR 8205), CNRS, ENPC, IFSTTAR,
F77455 Marne-la-Vallée Cedex 2, France
email: vinh-du.than@cermes.enpc.fr

² The University of Danang, College of Technology, Department of Civil Engineering,
48 Cao-Thang St., Hai-Chau Dist., Da Nang, Vietnam

Key words: Plastic compression, Capillary force, Consolidation, DEM

Abstract. We use Discrete Element Method (DEM) simulations in three dimensions (3D) to study the quasistatic response of very loose assemblies of frictional spherical grains to an isotropic compression in the presence of a small amount of an interstitial liquid, which gives rise to capillary menisci and attractive forces. Previous results obtained in 2D [8] are generalized to systems that may be observed in the laboratory. We study the influence of the initial assembling process and of various micromechanical parameters on the plastic compression curves, from very loose states assembled at low P^* to maximally compressed ones in which capillary cohesion is negligible at large P^* . We also show how the plastic response along those compression curves is influenced by rolling resistance in contacts.

1 INTRODUCTION

Many natural and industrial processes involve granular materials, in which grains are bonded, due to a variety of physical effects near intergranular contacts: capillary bridges, solid precipitation, artificial solid bridges. The water menisci joining solid particles in wet granular soils play a key role in the overall behavior studied in geotechnical engineering. Capillary cohesion bestows to these materials specific mechanical features that do not exist with dry grains, such as the ability to form stable structures at very low density, and a strong sensitivity to stress intensity as well as to stress direction. Published studies of bonded granular materials investigate the mechanical properties of cohesive soils (clays and silts) [18, 16], wet beads [6], cohesive powders [7, 8], loessic soils [4, 10], cemented sands [17, 11, 12, 2], or wet sands [15, 3]. The contact networks are hardly accessible to experiments, and intergranular forces are also inaccessible to measurements. Generally, the behavior of materials under a growing external load (oedometric or isotropic tests) is characterized by a compression curve showing an irreversible density increase with pressure.

“Discrete element” simulations, as introduced 35 years ago by Cundall & Strack [5], have become a valuable and efficient tool to investigate the microscopic mechanisms and to classify mechanical properties of granular systems. Cohesive granular materials, especially in loose states, have less frequently been investigated by numerical simulation than cohesionless ones. Inspired by the two-dimensional model for cohesive powders of Gilabert *et al.* [7, 8], a 3D model is developed to investigate the mechanical behavior of a model bonded granular soils (glass beads with capillary bonds in the pendular state). Results are presented for simulations of isotropic compression cycles, both for the macroscopic behaviour (plastic compression curve) and for the evolution of microstructural and micromechanical parameters.

2 MODEL MATERIAL

2.1 Intergranular forces

We consider assemblies of spherical beads of diameter a and mass m , with the elastic properties of glass: Young modulus $E = 70$ GPa, Poisson ratio $\nu = 0.3$. They interact in their contacts by the Hertz law, relating the elastic normal force F_N^E to the normal deflection h as

$$F_N^E = \frac{E}{3(1-\nu^2)} \sqrt{ah^{3/2}}. \quad (1)$$

This corresponds to a force-dependent normal stiffness $K_N = \frac{dF_N^H}{dh} = \frac{E}{2(1-\nu^2)} \sqrt{ah^{1/2}}$. The tangential force model, combining elasticity and friction, is described by [1]. Tangential stiffness K_T (relating increments of tangential elastic force and of tangential elastic displacement is proportional to K_N , $K_T = \frac{2-2\nu}{2-\nu} K_N$). Alternatively, a linear contact elasticity might be implemented, with h -independent stiffness coefficients K_N, K_T . The Coulomb condition $\|\mathbf{F}_T\| \leq \mu F_N^E$, involving the sole repulsive elastic part of the normal force (Fig. 1(b)), is enforced with friction coefficient $\mu = 0.3$.

The attractive capillary force is only present if grains have been in contact and the meniscus has not broken since. A meniscus of volume V_m remains until separation distance reaches its rupture value, $D_r \simeq V_m^{1/3}$ [9]. We use the Maugis approximation [14] for capillary forces:

$$F_N^{cap} = -F_0 \left[1 - \frac{1}{\sqrt{1 + \frac{4V_m}{\pi a D^2}}} \right]. \quad (2)$$

D denotes here the distance between the surfaces of the particles joined by the liquid meniscus. $F_0 = \pi a \gamma \cos \theta$ is the maximum tensile force, involving surface tension γ of the water-air interface (7.27×10^{-2} N/m at 20°C), and θ is the wetting angle, with $\theta = 0$ for a perfectly wetting liquid. Most calculations here are carried out with $V_m/(a^3) = 10^{-3}$, and thus the force range extends to $D_r = a/10$ (corresponding to a very small capillary force). This ratio of meniscus volume V_m to a^3 is one of the dimensionless

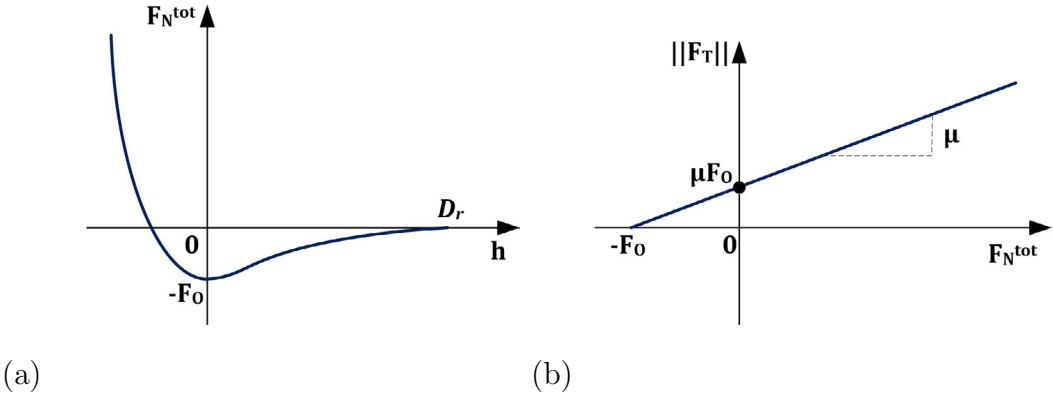


Figure 1: (a) Static normal force, $F_N = F_N^E + F_N^{cap}$, versus deflection h or distance $D = -h$. (b) Coulomb cone limiting the value of the tangential force.

control parameters in the present study, determining the number of liquid bonds and the range of the corresponding capillary attraction. Our work is limited to the pendular state of isolated menisci [15].

The total static normal force combines the elastic normal force (Hertzian force) and the capillary force, $F_N^{tot} = F_N^E + F_N^{cap}$, as shown in Fig. 1(a). A viscous force is added in contacts, opposing the normal relative velocity of grains as in [1], in order to damp the vibrations about equilibrium states – with no notable influence on quasistatic rheology.

Two particles moving away from each other after a collision will only separate if their receding relative velocity is large enough to overcome the capillary force, i.e. larger than a threshold proportional to V^* [7], with

$$V^* = \sqrt{\frac{F_0 D_r}{m}}. \quad (3)$$

The influence of *rolling resistance* (RR) at contacts, as investigated in 2D in [8], is also studied. For simplicity, we only implement this feature with linear contact elasticity. The existence of RR is related to the particle surface roughness, such that contact regions are larger than the ones deduced from contact elasticity. Four additional parameters are necessary: (i) a *rolling spring constant* K_R which expresses the proportion between relative rotation and rolling moment (in the tangential plane), as long as the rolling friction threshold is not reached; (ii) a *pivoting spring constant* K_P (chosen equal to K_R), relating similarly the pivoting moment to the pivoting (i.e., along the normal direction) relative rotation angle; (iii) a *rolling friction coefficient* μ_R with the dimension of a length, setting the maximum norm of the rolling moment $||\Gamma_R||$ to $\mu_R F_N^E$, proportional to the elastic part of the normal force; and (iv) a *pivoting friction coefficient* μ_P (chosen equal to μ_R), requesting similarly the absolute value of the pivoting moment to stay below $\mu_P F_N^E$. In most simulations with RR, we set $\mu_R/a=0.02$, $K_R/(K_N a^2) = 2.5 \times 10^{-5}$ while $K_T/K_N = 1$ and $K_N/a = 4$ GPa.

2.2 Stress control and equilibrium

Numerical samples comprise $N=4000$ equal-sized spherical beads of diameter a and mass m , with no gravity, within a cuboidal cell with periodic boundary conditions. The cell edges are parallel to the coordinate axes $(x_\alpha)_{\alpha=1,3}$. Their lengths $(L_\alpha)_{\alpha=1,3}$ vary simultaneously with the grain positions until a mechanical equilibrium state is achieved for all particles with externally imposed values $(\Sigma_\alpha)_{1 \leq \alpha \leq 3}$ of principal stresses:

$$\sigma_{\alpha\alpha} = \frac{1}{\Omega} \left[\sum_i m_i v_i^\alpha v_i^\alpha + \sum_{i < j} F_{ij}^{(\alpha)} r_{ij}^{(\alpha)} \right]. \quad (4)$$

Here, $\Omega = L_1 L_2 L_3$ is the sample volume, $r_{ij}^{(\alpha)}$ is coordinate α of vector \mathbf{r}_{ij} joining the centers of neighbor beads i and j and $F_{ij}^{(\alpha)}$ the corresponding force coordinate. Velocities \mathbf{v}_i of grain centers comprise, in addition to a periodic field, an affine term corresponding to the global strain rate. Equations of motion for dimensions L_α are written in addition to the ordinary equations for the dynamics of a collection of solid objects, and they drive the system towards an equilibrium state in which conditions $\sigma_{\alpha\alpha} = \Sigma_\alpha$ are satisfied [1]. A typical intergranular force value $F_1 = \max(F_0, Pa^2)$ sets the tolerance levels for individual grain equilibrium, where P is the applied pressure. A configuration is deemed equilibrated when the following conditions are simultaneously satisfied: (i) the net force (the total force) on each spherical grain is less than $10^{-4}F_1$; (ii) the total moment on each sphere is lower than $10^{-4}F_1a$; (iii) the difference between imposed and measured stresses is less than $10^{-4}F_1/a$; and (iv) the kinetic energy per grain is less than $10^{-7}F_1a$.

2.3 Dimensionless control parameters

While calculations are carried out with glass beads of diameter $a = 0.11$ mm, assuming perfect wetting ($\theta = 0$), it is convenient to express dimensionless results as functions of dimensionless input parameters, thereby achieving greater generality. Aside from the friction coefficient, the important dimensionless combinations are the reduced pressure, $P^* = a^2 P / F_0$, comparing the applied pressure to the tensile strength of contacts, and the stiffness parameter $\kappa = [E/P(1 - \nu^2)]^{2/3}$ (for Hertzian contacts), or $\kappa = K_N/P$ (for linear elasticity). $P^* \ll 1$ in cohesion-dominated systems, for which attractive forces may stabilize loose structures. Confining forces dominate for $P^* \gg 1$, and attractive forces become negligible. For the chosen value of a , $P^* = 1$ corresponds to $P = 2$ kPa. κ , on the other hand, sets the typical scale of deflections h under confining forces, as $h/a \sim \kappa^{-1}$ [1]. The simulation parameters are chosen such that P^* reaches large values before κ^{-1} decreases to 10^{-3} . Additional parameters are $\mu_R/a = \mu_P/a$ in systems with RR, as well as the rotation angles for which rolling and pivoting friction thresholds are reached (small enough to be irrelevant in our case).

Table 1: Initial configurations

Φ_0	V_0/V^*	V_m/a^3
0.30	0.2041	1.00×10^{-3} (reference case)
0.30	0.4082	1.00×10^{-3}
	1.2247	
	4.0825	
	12.2474	
	40.8248	
0.30	0.2041	5.00×10^{-4} 2.50×10^{-4}
		1.25×10^{-4} 6.25×10^{-5}
		3.13×10^{-5} 1.56×10^{-5}
		7.80×10^{-6}
0.32	0.2041	1.00×10^{-3}
0.35	0.2041	1.00×10^{-3}
0.40	0.2041	1.00×10^{-3}
0.45	0.2041	1.00×10^{-3}

3 NUMERICAL PROCEDURES

3.1 Specimen preparation

We first use a hard sphere event-driven method to prepare disordered, low density configurations of 4000 grains. All particles are then launched with Gaussian-distributed random velocities with quadratic mean V_0 . They collide and stick to one another within a cell of constant size, forming larger and larger aggregates. Finally, all grains are connected to one another by cohesive contacts and reach an equilibrium position. This initial structure depends on one dimensionless parameter, characterizing the agitation intensity in the assembling stage. It is defined as the ratio of V_0 to the minimum receding velocity V^* introduced in Eq. (3). As in Ref. [7], larger initial agitation levels are observed to produce better connected structures. The initial parameters are listed in Table 1.

3.2 Compaction process

The final packing structures is compacted under growing external isotropic pressure. The main objective of the present paper is the study of the effect of a gradual compression, starting from cohesion-dominated loose states at small P^* , and ending in confinement-dominated denser states at large P^* . A stepwise pressure-controlled loading path is applied. In each compression step, pressure P^* is multiplied by a constant factor $10^{1/4} \simeq 1.7783$, and one waits until the new equilibrium configuration is reached, within the tolerance criteria stated in Sec.2.2. The compression program is pursued until P_{max}^* , well beyond complete plastic collapse is obtained. Then, the effect of P^* back to minimum value from its highest value is also simulated.

4 NUMERICAL RESULTS

4.1 Reference case

A typical test is run with a low initial solid fraction, $\Phi_0 = 0.30$. The results are shown in the form of the conventional compression curve $e - \log(P)$ in Fig. 2. Three regimes

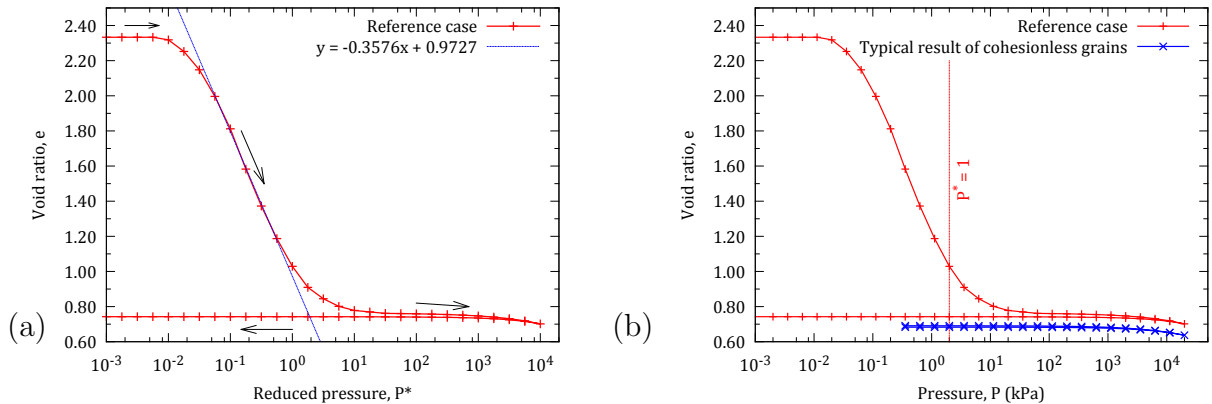


Figure 2: (a) Compression and decompression curves in reference case, with (b) comparison with cohesionless systems.

can be distinguished in the compression curve, for different pressure ranges. A first regime, thereafter called regime **I**, is observed for low reduced pressures P^* , in which the initial structure still sustains the increasing pressure without rearranging, and void ratio e remains nearly constant. In regime **II**, roughly corresponding to interval $0.02 \leq P^* \leq 2$, void ratio strongly decreases, and might be described as linearly varying with $\log P^*$. The loose structures formed at low P^* are no longer able to support the increasing confining pressure, they collapse and restructure. Finally, in regime **III**, e gradually approaches some minimum void ratio e_{min} at the end of the loading process. The slight decrease of e for $P^* \geq 100$ is similar to the cohesionless result, and due to elastic deflections in a stable contact network. The chosen parameters are such that κ remains large enough not to influence the compression process taking place in regime **II**. Upon decompression, e increases slightly, remaining very close to e_{min} : the compaction is essentially irreversible, unlike in the cohesionless granular assembly of Fig. 2(b), for which loading and unloading branches are not distinguishable. The compression curve is similar to the ones obtained by Gilabert *et al.* [8]. An important microstructural characteristic, the coordination number z , defined as the average number of interactions per grain, is the sum of the contact coordination number z_c and the coordination number of distant interactions, through menisci joining non-contacting grains, z_d . Fig. 3 plots z_c , z_d , and z versus P^* in the compression cycle. Initially, one has $z_d = 0$, as the velocities in the aggregation process, in

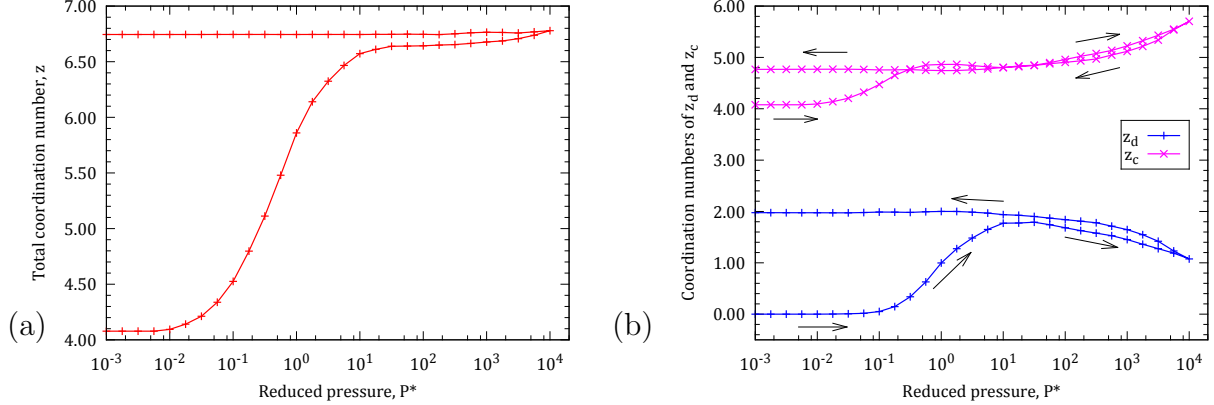


Figure 3: Coordination numbers in reference system subjected to the pressure cycle: z (a); and z_c and z_d (b), versus P^* .

the reference case, are low, and do not allow contact opening. z_c and z_d remain unchanged in regime I. Both coordination numbers start to increase as the structure collapses and reorganizes in regime II. z exhibits little change in regime III, showing that the increase of the number of contacts is mainly due to the closing of narrow gaps between pairs of grains joined by a meniscus, as the structure is further compressed – a moderate effect, partly reversed upon unloading. Further unloading back to small pressures takes place with nearly constant coordination numbers of both types, reflecting the stability of the dense structure formed at high P^* .

4.2 Effect of initial solid fraction

Among the features affected by the assembling process, the competition between compression and aggregation is the most important one. Fig. 4, obtained with standard values $V_0/V^* = 0.2041$, $V_m/a^3 = 10^{-3}$, compares the compression curves of specimens with different initial solid fractions Φ_0 (the red arrow denotes the increase of Φ_0). Denser systems are able to support larger pressures before rearranging, whence larger regime I plateaus (see Fig. 4(a)). However, in regime II, these compression curves start to converge and very nearly coincide in regime III. Coordination numbers z_c and z_d are and remain almost equal whatever the initial Φ_0 (see Fig. 4(b)).

4.3 Effect of initial agitation intensity

Ratio V_0/V^* , characterizing the intensity of initial agitation and its ability to break adhesive contacts, strongly influences the initial assembling process and the resulting coordination number. Fig. 5 shows that this parameter mainly affects the beginning of the compression curve. Six different values of V_0/V^* are used, the difference between

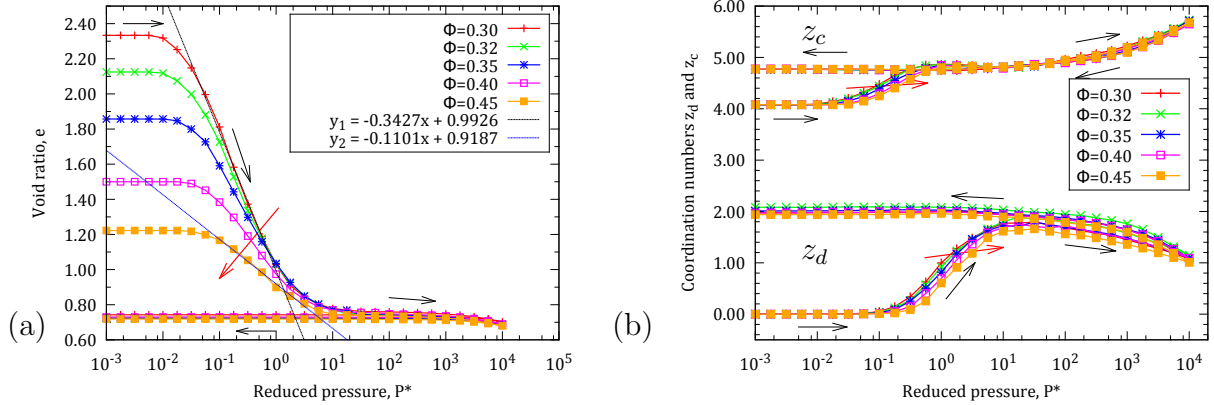


Figure 4: (a) Void ratio e and (b) coordination numbers z_c and z_d versus P^* in compression cycle for different values of Φ_0 .

minimum and maximum values is two-hundredfold. Under low P^* , the wider regime **I** plateaus correspond to the higher initial agitation velocities. If initial velocity V_0 is of the order of V^* , the initial packing structure is strongly perturbed. In other words, the larger the velocity, the stronger the initial structure (see Figure 5(a)), with more contacts – relatively strong increases in initial coordination numbers z_c and z_d are observed at low P^* (see Figure 5(b)). Conversely, with low agitation velocities ($V_0 \leq V^*$), grains stick gently to one another and clusters of aggregated grains are not disturbed. In other words, lower agitation velocities induce more tenuous aggregates.

4.4 Effect of meniscus volume

We now report on investigations of the influence of meniscus volume V_m/a^3 , which is kept low enough for the material (with a saturation hardly exceeding 1%) is maintained in the pendular state. Despite the importance of capillary bridges in the stabilization of loose structures, changing the meniscus volume (or liquid content) seems to have no effect on the macroscopic behaviour of the granular specimens under isotropic compression (no apparent change in the compression curve, e versus $\log P^*$). This is corroborated by the fact that very little change in the coordination number of contacts z_c is observed. Only the coordination number of distant interactions is notably influenced by such a change, especially in regimes **II** and **III**, and in the decompression process, as shown in Fig. 6. As menisci break at larger interparticle distance with larger meniscus volume, more liquid bonds are present.

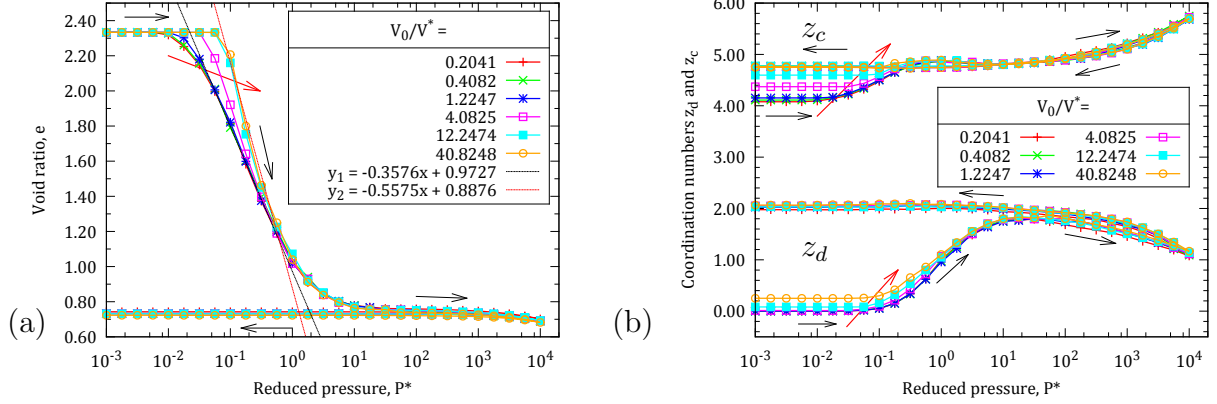


Figure 5: (a) Compression and decompression curves and (b) coordination numbers z_c and z_d for the reference case with different values of V_0/V^* .

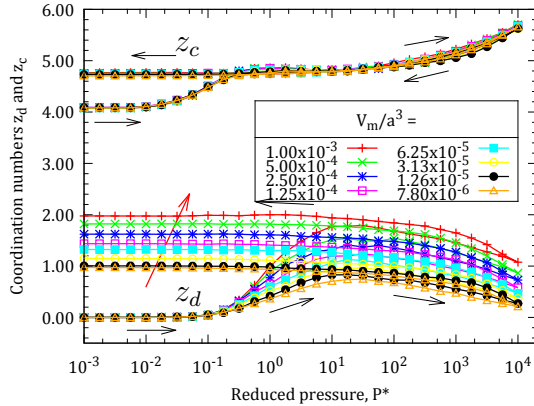


Figure 6: Coordination number z_c , z_d , $z = z_c + z_d$ for standard values $\Phi_0 = 0.30$, $V_0/V^* = 0.2041$ and for different values of V_m/a^3 .

4.5 Effect of rolling resistance

Fig. 7 shows the effect of initial velocities V_0 and rolling/pivoting friction coefficients $\mu_R/a = \mu_P/a = 0.02$ on the initial assembling process and coordination numbers for $\Phi_0=0.30$ and $V_m/a^3 = 10^{-3}$. For the smallest velocities, the appearance of RR in contacts creates denser systems under low P^* , with smaller coordination numbers. Unlike the initial loose structures formed without RR, which can sustain a small non-vanishing pressure in regime I, the compression curve of the tenuously connected (with coordination number approaching 2, i.e., virtually no loop) initially formed with RR, and a low

agitation velocity, responds by some plastic collapse at the first pressure increment, as shown in Fig. 7(a). Its regime I, if it exists, is confined to much smaller pressures. It reappears on the pressure scale of Fig. 7(a) in systems assembled with larger initial agitation velocities, which are better coordinated (Fig. 7(b)), and collapse more abruptly in plastic compression. Interestingly, the system assembled with the lower coordination numbers first react by plastic compression without contact loss, as z_c is constant and z_d remains equal to zero (no contact opening creating a distant interaction). More complete

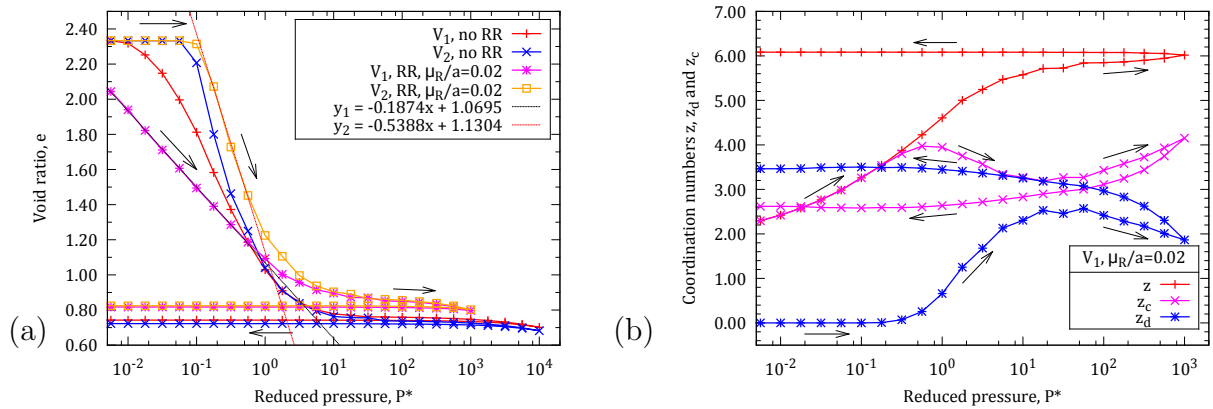


Figure 7: Void ratio e (a) and coordination numbers z_c , z_d and $z = z_c + z_d$ (b) versus P^* in pressure cycle for different systems with or without RR ($V_1 = V_0/V^* = 0.2041$, $V_2 = V_0/V^* = 40.8248$).

analyses of the corresponding structural changes are being carried out, and their results will be published in forthcoming papers.

5 CONCLUSIONS AND OUTLOOK

Our results show that the simple model of wet granular materials implemented in our simulations exhibit the familiar plastic compression properties of cohesive soils or powders, with a well defined limit of gently assembled (minimally coordinated) structures, and low initial densities, such that the behaviour does not depend on dynamical model ingredients. A small level of rolling and pivoting friction is enough to produce strong differences in the plastic behaviour, with the collapse under growing confining pressure becoming notably more gradual.

The research program developed here can be extended in several directions. For example, the quasistatic behavior of a 3D model accounting for the effect of rolling resistance under oedometer and triaxial tests, in pendular state, is a straightforward extension of the present work. The role played by solid bridges instead of capillary bonds could also be investigated.

ACKNOWLEDGMENTS

The first author of the paper is supported by the Scholarship (the Project No 911) of Ministry of Education and Training, the Vietnamese Government to do this work.

REFERENCES

- [1] Agnolin, I. and Roux, J.-N. Internal states of model isotropic granular packings. i. assembling process, geometry, and contact networks. *Phys. Rev. E* (2007) **76**:061302
- [2] de Bono, J., McDowell, G. and Wanatowski, D. Investigating the micro mechanics of cemented sand using DEM. *International Journal for Numerical and Analytical Methods in Geomechanics* (2014) **10**:n/a-n/a
- [3] Bruchon, J.-F., Pereira, J.-M., Vandamme, M., Lenoir, N., Delage, P., Bornert, M. Full 3d investigation and characterization of capillary collapse of a loose unsaturated sand using X-ray CT. *Granular Matter* (2013) **15**:783-800
- [4] Muñoz Castelblanco, J., Delage, P., Pereira, J.-M and Cui, Y.J. Some aspects of the compression and collapse behavior of an unsaturated natural loess. *Géotechnique Letters* (2011) **1**: 17-22
- [5] Cundall, P. and Strack, O. A discrete numerical model for granular assemblies. *Géotechnique* (1979) **29**: 47-65
- [6] Fournier, Z., Geromichalos, D., Herminghaus, S., Kohonen, M., Mugele, M., Scheel, F., Schulz, M., Schulz, B., Schier, C., Seemann, R. and Skudelny, A. Mechanical properties of wet granular materials. *J. Phys.: Condens. Matter* (2005) **17**:S477
- [7] Gilabert, F., Roux, J.-N., Castellanos, A. Computer simulation of model cohesive powders: Influence of assembling procedure and contact laws on low consolidation states. *Phys. Rev. E* (2007) **75**: 011303
- [8] Gilabert, F., Roux, J.-N., Castellanos, A. Computer simulation of model cohesive powders: Plastic compression, structural changes, and elasticity under isotropic states. *Phys. Rev. E* (2008) **78**: 031305
- [9] Herminghaus, S. Dynamics of wet granular matter. *Advances in Physics* (2005) **54**: 221-261
- [10] Jiang, M., Hu, H. and Liu, F. Summary of collapsible behavior of artificially structured loess in oedometer and triaxial wetting tests. *Canadian Geotechnical Journal* (2012) **49**: 1147-1157

- [11] Jiang, M., Yan, H., Zhu, H. and Utili, S. Modeling shear behavior and strain localization in cemented sands by 2D distinct element method analyses. *Computer and Geotechnics* (2011) **38**: 14-29
- [12] Jiang, M., Zhang, W., Sun, Y. and Utili, S. An investigation on loose cemented granular materials via DEM analyses. *Granular Matter* (2013) **15**: 65-84
- [13] Johnson, K. L. *Contact Mechanics*. Cambridge University Press (1985)
- [14] Maugis, D. *Contact, Adhesion and Rupture of Elastic Solids*. Springer Berlin Heidelberg, Springer Series in Solid-State Sciences 130, (2000).
- [15] Mitarai, N. and Nori, F. Wet granular materials. *Advances in Physics* (2006) **55**: 1-45.
- [16] Mitchell, J. and Soga, K. *Fundamentals of Soil Behaviour*. Wiley, New York (2005).
- [17] Wang, Y and Leung, S. Characterization of cemented sand by experimental and numerical investigations. *Journal of Geotechnical and Geoenvironmental Engineering* (2008) **134**: 992-1004.
- [18] Wood, D. M. *Soil Behaviour and Critical State Soil Mechanics*. Cambridge University Press, (1990).

Experimental and numerical investigation of the behaviour of complex shaped particles in a model scale fluidized bed

K. VOLLMARI¹ AND H. KRUGGEL-EMDEN¹

¹Ruhr-University Bochum
Universitätsstr. 150, IC 2/107
Vollmari@leat.rub.de, <http://www.leat.ruhr-uni-bochum.de/>

Key words: DEM, CFD, Experiments, Complex Shaped Particles, Fluidization, Orientations.

Abstract. *In this study a laboratory scale fluidized bed is examined experimentally and numerically through a coupled discrete element method (DEM) and computational fluid dynamics (CFD) approach. Five differently shaped Geldart D particle groups including spheres, cylinders and cuboids are considered. Numerically obtained results for the pressure drop are in good agreement with experiments for most particles. A study on particle orientations is performed which gives valuable insight into deviations between experiments and simulations. The DEM-CFD correctly describes preferred orientations taken up by elongated particles in the fluid flow.*

1 INTRODUCTION

Fluidized beds are widely used in process and energy engineering as they possess favourable characteristics such as fast mixing, uniform temperature distribution and high gas-solid contact. The pressure drop is a key parameter for the characterization of a fluidized bed and is subject to fluctuations. Besides experiments and correlations simulations can be used for the prediction of the pressure drop. With growing computational power numerical simulations with a coupled discrete element method (DEM) and computational fluid dynamics (CFD) approach recently became feasible for the simulation of fluidized systems. Previously most simulations were conducted with spherical particles only, which cannot precisely predict the behavior of real, complex shaped particles like encountered in biomass. With the introduction of new submodels [1, 2] to the DEM-CFD which consider the particle shape and orientation it has become possible to simulate fluidized beds with complex shaped particles [3–5]. As there is an ongoing discussion about the validity of certain submodels, experimental validation is necessary. In this study pressure drops and particle orientations for five differently shaped Geldart D particle groups, including spheres, cylinders and cuboids are experimentally and numerically examined.

2 METHODOLOGY

In the coupled DEM-CFD particles are tracked discretely while the fluid phase is represented through a cell-averaged continuum. In the discrete element method the translational and rotational particle motion is obtained by integrating Newton's and Euler's equations

$$m_i \frac{d^2 \vec{x}_i}{dt^2} = \vec{F}_i^c + \vec{F}_i^{pf} + m_i \vec{g}, \quad (1)$$

$$\hat{I}_i \frac{d\vec{W}_i}{dt} + \vec{W}_i \times (\hat{I}_i \vec{W}_i) = \Lambda_i^{-1} \vec{M}_i, \quad (2)$$

with the particle mass m_i , particle acceleration $d^2 \vec{x}_i/dt^2$, contact force \vec{F}_i^c , particle/fluid force \vec{F}_i^{pf} , gravitational force $m_i \vec{g}$, angular acceleration $d\vec{W}_i/dt$, angular velocity \vec{W}_i , external moment resulting out of contact or particle/fluid forces \vec{M}_i , the inertia tensor along the principal axis \hat{I}_i and the rotation matrix converting a vector from the inertial into the body fixed frame Λ_i^{-1} .

Contact force laws are applied similarly as used for spherical particles [6, 7]. A linear spring damper model is used to provide the normal component of the contact forces

$$\vec{F}^n = k^n \delta \vec{n} + \gamma^n \vec{v}_{rel}^n, \quad (3)$$

where k^n is the spring stiffness, δ the virtual overlap, \vec{n} a normal vector, γ^n a damping coefficient and \vec{v}_{rel}^n the normal velocity in the contact point. Both k^n and γ^n determine the coefficient of normal restitution between particles e_{PP}^n as well as particles and walls e_{PW}^n . For the calculation of the tangential forces a linear spring limited by the Coulomb condition is used

$$\vec{F}^t = -\min(k^t |\vec{\xi}|, \mu_c |\vec{F}^n|) \cdot \vec{t}, \quad (4)$$

where k^t is the stiffness of a linear spring, μ_c is the friction coefficient, $\vec{\xi}$ is the relative tangential displacement and \vec{t} is the tangential unit vector. No rotational friction is considered.

Computational Fluid Dynamics (CFD) in an Eulerian framework is used to describe the fluid phase. The fluid velocity is addressed as a spatially averaged quantity in each cell of a Cartesian grid. The equation of continuity (5) and the equation of momentum (6) are solved

$$\frac{\partial(\varepsilon_f \rho_f)}{\partial t} + \nabla(\varepsilon_f \rho_f \vec{u}) = 0, \quad (5)$$

$$\frac{\partial(\varepsilon_f \rho_f \vec{u})}{\partial t} + \nabla(\varepsilon_f \rho_f \vec{u} \vec{u}) = -\varepsilon_f \nabla p + \nabla(\bar{\tau}) + \varepsilon_f \rho_f \vec{g} + \vec{f}_{int}, \quad (6)$$

where \vec{u}_f , ρ_f and p are the physical fluid velocity, density and pressure. \vec{f}_{int} is the volumetric particle/fluid interaction applied in each CFD cell, ε_f is the local fluid porosity and $\bar{\tau}$ is the fluid viscous stress tensor $\bar{\tau} = \eta_e [(\nabla \vec{u}_f) + (\nabla \vec{u}_f)^{-1}]$ with η_e the effective viscosity determined from the standard k- ϵ turbulent model. The particle/fluid interaction \vec{f}_{int} is given component wise as $f_{int,i} = \bar{\beta}_i (u_i - \bar{v}_i)$, where \bar{v}_i is the fluid cell averaged particle velocity and $\bar{\beta}_i$ is the fluid cell averaged particle/fluid friction coefficient with $i=x, y, z$.

The particle/fluid force \vec{F}_i^{pf} consists of all individual particle/fluid forces including the drag force \vec{F}_i^d and pressure gradient force $\vec{F}_i^{\nabla p}$ acting on a particle i written as $\vec{F}_i^{pf} = \vec{F}_i^d + \vec{F}_i^{\nabla p}$. The approach by Di Felice [1], where the force for an isolated spherical particle is calculated and altered by the influence of surrounding particles is also suitable for non-spherical particles. The respective force reads

$$\vec{F}_i^{pf} = \vec{F}_i^d + \vec{F}_i^{\nabla p} = \frac{1}{2} \rho_f |\vec{u}_f - \vec{v}_i| C_D A_{\perp} \varepsilon_f^{1-\chi} (\vec{u}_f - \vec{v}_i) \quad (7)$$

where C_D is the drag coefficient, A_{\perp} is the cross-sectional area perpendicular to the flow and χ a correction factor. Equation (7) can be rewritten in terms of the particle/fluid friction coefficient as

$$\vec{\beta}_i = \frac{1}{2} \rho_f C_D A_{\perp} \varepsilon_f |\vec{u}_f - \vec{v}_i| (1 - \varepsilon_f)^{\frac{1}{V_i}} \varepsilon_f^{(1-\chi)}. \quad (8)$$

with $\chi = 3.7 - 0.65 \exp(-(1.5 - \log(Re))^2/2)$ as a function of the particle Reynolds-number $Re = \varepsilon_f \rho_f d_e |\vec{u}_f - \vec{v}_i| / \eta_f$. Here d_e describes the diameter of a volume equivalent spherical particle and η_f the fluid viscosity. The drag coefficient C_D of a single particle (including complex shapes) can be derived from correlations such as Hölzer und Sommerfeld [2] which can be written as

$$C_D = \frac{8}{Re} \frac{1}{\sqrt{\phi_{\perp}}} + \frac{16}{Re} \frac{1}{\sqrt{\phi}} + \frac{3}{\sqrt{Re}} \frac{1}{\phi^{3/4}} + 0.42 \times 10^{0.4(-\log(\phi))^{0.2}} \frac{1}{\phi_{\perp}} \quad (9)$$

where ϕ_{\perp} is the crosswise sphericity which is the ratio between the cross-sectional area of the volume equivalent sphere and the projected cross-sectional area of the considered particle perpendicular to the flow.

3 EXPERIMENTAL AND NUMERICAL SETUP

To carry out the experiments a laboratory scale fluidized bed made from antistatic polycarbonate with the dimensions width = depth = 0.11 m and height = 0.41 m, displayed in Fig. 1 was used. The solid matter is placed on a porous plate with an open area of 37%. A pressure tapping point slightly below the porous plate and one in the vessel at h=31 cm are used to measure the differential pressure with a pressure transducer of the type Newport Omega PD41X-V-50 mbar. Images of the experiment were taken with a high speed camera (Optronis CL600x2) at 25 frames per second over a time period of 15 seconds. Geldart-D type beech wood particles including spherical, cylindrical or cuboidal shapes are used, see Table 1.

Table 1 Particle properties including the particle dimensions, the sphericity ϕ , the particle density ρ_p , the initial bed height L_{fb} and the averaged porosity $\bar{\varepsilon}$ of the fixed bed

Shape	Sphere	Ideal Cylinder		Cube			Elongated Cylinder		Elongated Cuboid		
Size [mm]	7.2	6.1	6.2	5.2	6.3	6.3	3.9	14.0	4.2	4.2	11.4
ϕ [-]	1.00		0.87		0.80			0.75			0.73
ρ_p [kg/m³]	772.5		708.5		746.9			764.4			639.7
L_{fb} [mm] / $\bar{\varepsilon}$ [-]	95 0.40		98 0.36		103 0.43			103 0.44			115 0.40

The combination of beech wood and the antistatic polycarbonate of the vessel ensures that no electrostatic effects disturb the experiments. Attrition or breakage do not occur.

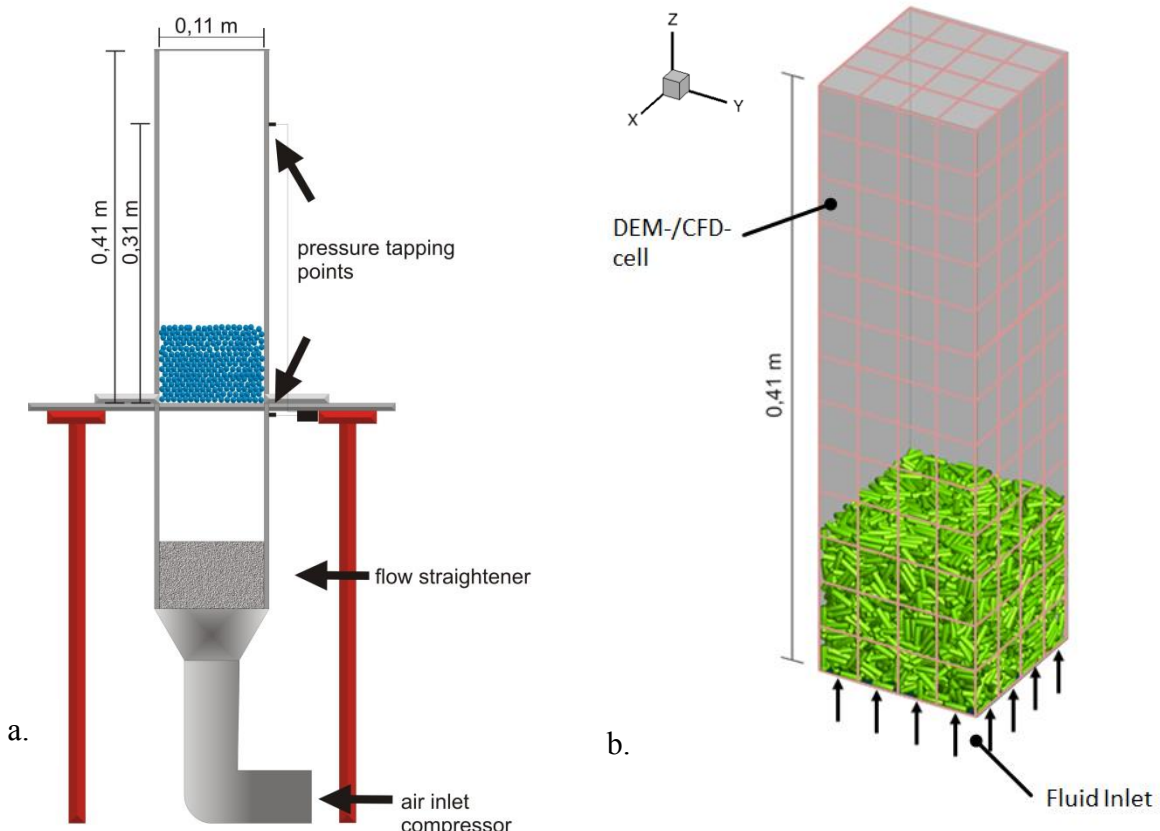


Fig. 1 Experimental (a) and numerical (b) setup and its division into a number of DEM-CFD cells larger than the particle size

The particle mass was kept constant for all experiments at $m = 0.535 \text{ kg}$. The superficial velocity has been increased in steps of 0.1 m/s starting at 0.4 m/s up to 2.4 m/s for all particles. The numerical setup was chosen so that all dimensions and operation conditions remain equal. Cylindrical and cuboidal particles are represented through a polyhedron approximation [8]. The friction and restitution coefficients were determined according to procedures described by Höhner et al. [9] and Hold [10] on the single particle level, respectively.

4 RESULTS AND DISCUSSION

4.1 Pressure drop analysis

Mean pressure drops in experiments and corresponding coupled DEM-CFD simulations are outlined for 5 different particle shapes in Fig. 2. Multiple repetitions have been performed for the experiments and simulations; the error bars show the obtained variations in terms of minimal and maximal values.

Fig. 2a shows the results for $d=7 \text{ mm}$ spherical particles. Good agreement between simulation and experiment can be observed. For velocities $U < 1.4 \text{ m/s}$ there is a mean deviation of $\overline{\Delta p} = 23 \text{ Pa}$, for the fluidized range from $U > 1.4 \text{ m/s}$ onwards an average deviation of

$\overline{\Delta p} = 8 \text{ Pa}$ is obtained. Results for ideal cylinders with the dimensions 6 mm x 6 mm are given in Fig. 2b. Good agreement between experiment and simulation can be seen over the entire velocity range, especially in the fixed bed regime with an average pressure drop difference of only $\overline{\Delta p} = 15 \text{ Pa}$.

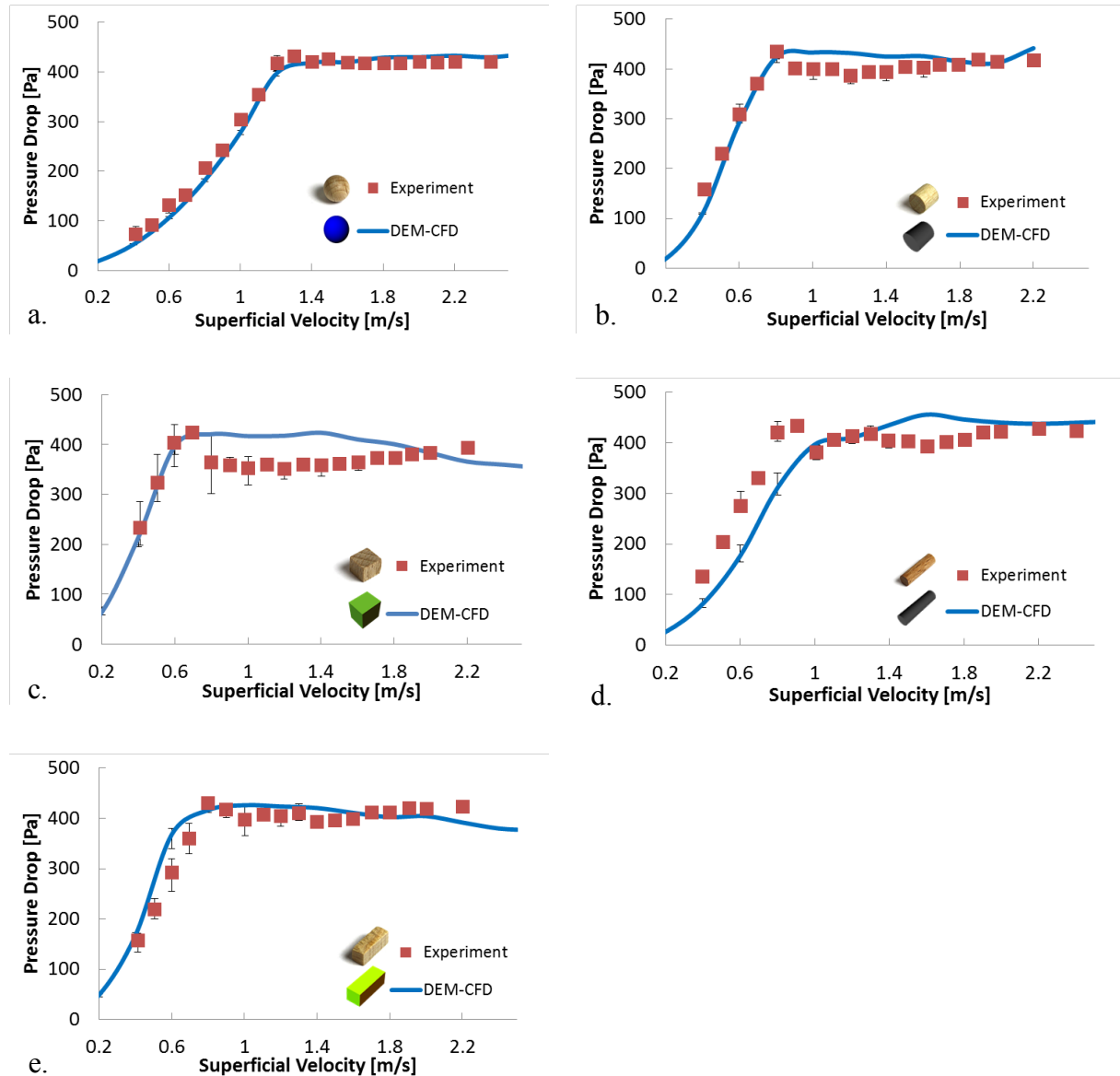


Fig. 2 Pressure drops of five differently shaped particle groups obtained for increasing superficial gas velocities in simulations and experiments for (a) 7 mm spheres, (b) 6 mm x 6 mm ideal cylinders, (c) 5 mm x 6 mm x 6 mm cubes, (d) 4 mm x 14 mm elongated cylinders and (e) 4 mm x 4 mm x 11 mm cuboids

Results for 5 mm x 6 mm x 6 mm cubes are displayed in Fig. 2c. High variations between the minimum and maximum values can be observed in the fixed bed range of the experiments,

nonetheless the simulation is in good agreement with the experimental average value. Different initial bed structures with locally deviating porosities are the reason for the scatter of the experimental values. Opposite to spheres and cylinders, the porosity in packings of cubes can reach values of nearly 0 if the particles align themselves with each other. The deviation of the pressure drop between simulation and experiment increases once the minimum fluidization velocity is passed at $U_{mf} > 0.7$ m/s with $\overline{\Delta p} = 44$ Pa. This is the result of an incomplete fluidization in the experiment, as stacks of particles are not in motion in the corners of the vessel. The same occurs in the simulation at higher velocities, so that the pressure drop declines starting at $U = 1.4$ m/s.

Results for elongated cylinders with the dimensions 4 mm x 14 mm are displayed in Fig. 2d. A deviation between experiment and simulation of $\overline{\Delta p} = 120$ Pa can be observed for the fixed bed regime at $U_{mf} < 0.9$ m/s. Particle shapes that differ strongly from that of a sphere show the tendency to form channels at low superficial velocities, which is the case for 4 mm x 14 mm cylinders for superficial velocities between $0.9 \text{ m/s} < U < 1.6 \text{ m/s}$. The simulation does not reproduce this behavior, as the fluid velocity is only represented through an averaged grid based velocity. Therefore the differences in the velocities, high in the channels and low in the surrounding particle structures, cannot be resolved.

In Fig. 2e the outcome for 4 mm x 4 mm x 11 mm elongated cuboids is given. Experiment and simulation are in good agreement for the entire velocity range with average deviations of $\overline{\Delta p} = 20$ Pa. Deviations between two runs of the same experiment are small with an average deviation of $\overline{\Delta p} = 23$ Pa.

4.2 Particle orientation analysis

As the particle orientation plays an important role for the fluidization behavior and process quality of fluidized beds, the simulations are compared with experiments. Therefore, a Matlab script was written to determine the particle orientations in the experiments based on recorded images. Particle orientations in the simulations are readily available for comparison. To gain statistically relevant data between 50,000 to 250,000 particles have been detected and analyzed per fluid velocity in both DEM-CFD and experiments. Only particles visible through the x-z plane have been analyzed in the simulations to achieve equal conditions for both cases. Particle orientation distributions for four different particle shapes, excluding the spheres, are given in Fig. 3 with numerical results in the left and experimental results being shown in the right column. The error bars in Fig. 3 show the uncertainty of the developed script which is gained from the comparison with manually analyzed samples. As the numerical results have been analyzed based on the calculated data and are therefore exact, no error bars are shown in the left column of Fig. 3.

Orientations for 4 mm x 14 mm elongated cylinders are given in Fig. 3a and Fig. 3b in the range from -89° to 90° of the x-z plane. As -90° and 90° express identical orientations and cannot be distinguished, all affected particles were classified as 90° . An orientation of 0° represents a particle of which the main axis is horizontal to the x-y plane, while values around -89° and 90° represent a particle with its main axis vertical to the x-y plane. The fixed bed shows deviations for the angles that indicate vertical alignment; these are the predominantly occurring orientations in the experiments, but the least occurring in the simulations.

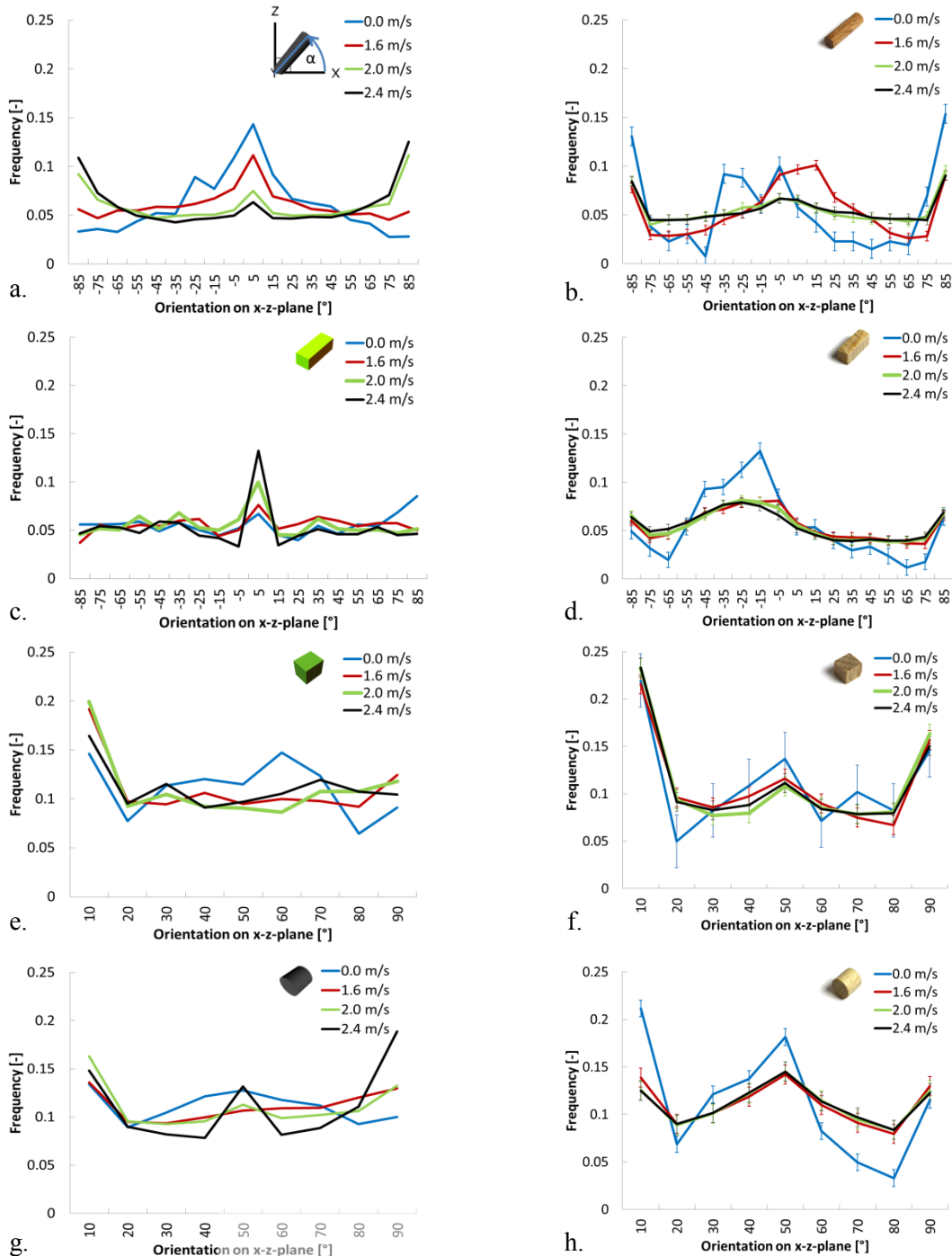


Fig. 3 Frequency distribution of the orientation projected onto the x-z plane for simulations (left column) and experiments (right column) for (a,b) 4 mm x 14 mm elongated cylinders, (c,d) 4 mm x 4 mm x 11 mm elongated cuboids, (e,f) 5 mm x 6 mm x 6 mm cubes and (g,h) 6 mm x 6 mm ideal cylinders

These deviations can explain the differences in the pressure drop of the fixed bed velocity range, which occur despite the comparable bed heights and thereby porosities. With an increase of the superficial velocity the experimental and numerical results fit increasingly

better to each other. Both, simulation and experiment, show that increasing amounts of particles orientate themselves vertically with rising superficial velocities. This finding confirms results indicated in literature [11, 12]. The outcome for 4 mm x 4 mm x 11 mm elongated cuboids is given in Fig. 3c for the DEM-CFD and Fig. 3d for the experiments. For the fixed bed some deviations can be observed between simulation and experiment, this reflects the deviations found in the pressure drop of the fixed bed of the elongated cuboids displayed in Fig. 2e. In the fluidized state the experimental results show only small variations between the three analyzed velocities. The simulations show an increase of horizontally orientated particles with higher velocities, which is the result of particle attachment to the walls as the particles stack up mostly horizontally. Contrary to the 4 mm x 14 mm elongated cylinders, the elongated cuboids do not show an increase of the frequency of the vertical orientations around -89° and 90° with increasing superficial velocities. This confirms the proposition of Cai et al. [11], that particles below a certain elongation ratio behave comparable to equidimensional particles. The DEM-CFD is able to reproduce this behavior. Cuboids with the dimensions 5 mm x 6 mm x 6 mm are displayed in Fig. 3e and Fig. 3f. As the orientation detection is more difficult for equidimensional particles, they are given in the range from 0-90°. The edge of the cube that lies in the range of 0-90° is hereby considered in the analysis. Generally simulation and experiment are in good agreement; both distribution functions remain mostly unchanged for increasing superficial velocities. In Fig. 3g and Fig. 3h the results for the orientations distributions of 6 mm x 6 mm ideal cylinders are displayed. Variations between simulations with different superficial velocities are quite small, and with increasing superficial velocity the orientations become more evenly distributed. Similarly the experimental data shows only small deviations between different superficial fluid velocities.

5 CONCLUSIONS

Pressure drops of 5 differently shaped Geldart-D particle groups have been examined in a laboratory scale fluidized bed, both experimentally and numerically. A combined DEM-CFD approach which considers particle shapes and orientations in the drag force models was used in the simulations. The analysis of the pressure drops showed that DEM-CFD simulations are a useful tool in the description of fluidized systems as the results are in good agreement with the corresponding experiments for most particle types. Minimum fluidization velocities were accurately described by the DEM-CFD except for elongated cylinders which differ strongly from a spherical shape. Particles that differ strongly from a spherical shape show the tendency to form channels for small superficial fluid velocities once the minimum fluidization velocity is passed. These channels result in a lower overall pressure drop as not all particles are fully suspended. The DEM-CFD cannot describe this behavior as the flow is not fully resolved around the particles but only calculated as a cell averaged value. The analysis of the particle orientation showed that differences in the pressure drop of fixed beds at equal bed heights and therefore porosities can be explained through differences in the orientation distributions between experiments and simulations. It was found that elongated cylinders show a tendency to align themselves with the flow with increasing superficial velocities, which confirms findings from the literature [11, 12].

ACKNOWLEDGEMENTS

The financial support by the DFG - KR 3446/6-1 is greatly acknowledged.

REFERENCES

1. Di Felice, R.: *The voidage function for fluid-particle interaction systems*. Int. J. Multiph. Flow. 20, 153–159 (1994).
2. Hölzer, A., Sommerfeld, M.: *New simple correlation formula for the drag coefficient of non-spherical particles*. Powder Technol. 184, 361–365 (2008).
3. Hilton, J.E., Mason, L.R., Cleary, P.W.: *Dynamics of gas–solid fluidised beds with non-spherical particle geometry*. Chem. Eng. Sci. 65, 1584–1596 (2010).
4. Zhou, Z.Y., Pinson, D., Zou, R.P., Yu, a. B.: *Discrete particle simulation of gas fluidization of ellipsoidal particles*. Chem. Eng. Sci. 66, 6128–6145 (2011).
5. Oschmann, T., Hold, J., Kruggel-Emden, H.: *Numerical investigation of mixing and orientation of non-spherical particles in a model type fluidized bed*. Powder Technol. 258, 304–323 (2014).
6. Kruggel-Emden, H., Simsek, E., Rickelt, S., Wirtz, S., Scherer, V.: *Review and extension of normal force models for the Discrete Element Method*. Powder Technol. 171, 157–173 (2007).
7. Kruggel-Emden, H., Wirtz, S., Scherer, V.: *An analytical solution of different configurations of the linear viscoelastic normal and frictional-elastic tangential contact model*. Chem. Eng. Sci. 62, 6914–6926 (2007).
8. Höhner, D., Wirtz, S., Kruggel-Emden, H., Scherer, V.: *Comparison of the multi-sphere and polyhedral approach to simulate non-spherical particles within the discrete element method: Influence on temporal force evolution for multiple contacts*. Powder Technol. 208, 643–656 (2011).
9. Höhner, D., Wirtz, S., Scherer, V.: *Experimental and numerical investigation on the influence of particle shape and shape approximation on hopper discharge using the discrete element method*. Powder Technol. 235, 614–627 (2013).
10. Hold, J.: *Charakterisierung der Mischungs- und Segregationsvorgänge in Modellwirbelschichten mit mono- und bidispersen sphärischen Partikelsystemen: Experimente und gekoppelte CFD / DEM-Modellierung*. , PhD-thesis, Bochum (2013).
11. Cai, J., Li, Q., Yuan, Z.: *Orientation of cylindrical particles in gas-solid circulating fluidized bed*. Particuology. 10, 89–96 (2012).
12. Ku, L.: *Motion and orientation of cylindrical and cubic particles in pipe flow*. J. Zhejian Univ. Sci. 9, 664–671 (2008).

INTERNAL STATES, STRESS-STRAIN BEHAVIOR AND ELASTICITY IN OEDOMETRICALLY COMPRESSED MODEL GRANULAR MATERIALS

M.H. KHALILI, J.-N. ROUX, J.-M. PEREIRA, M. VANDAMME,
S. BRISARD and M. BORNERT

Université Paris-Est, Laboratoire Navier (UMR 8205), CNRS, ENPC, IFSTTAR, F-77455
Marne-la-Vallée

Key words: Granular Materials, DEM, Oedometric compression, Elasticity

Abstract. The behaviour of a model granular material (an assembly of slightly polydisperse spherical beads, with Hertz-Mindlin elastic and frictional contacts) subjected to one dimensional (oedometric) compressions is studied by DEM simulations. We systematically investigate the influence of the (idealized) packing process on the microstructure and stresses in the initial, weakly confined equilibrium state. Such characteristics as density (ranging from maximally dense to moderately loose), coordination number (which might vary independently of solid fraction, especially in dense systems), fabric and stress anisotropies are monitored in oedometric loading cycles in which the major principal stress varies by up to 5 orders of magnitude. The evolution of the solid fraction (or the void ratio) versus the imposed vertical (principal) stress as observed in the loading and unloading paths, like in the case of isotropic compression [2] and unlike laboratory tests on sands, the behaviour shows only very limited plastic strain and is very nearly reversible in dense samples (which tend nevertheless to lose contacts in a loading cycle if the initial coordination number was large). The irreversibility observed in sands should thus be attributed to plasticity or damage within inter granular contacts. The anisotropy of the microstructure is described by the angular distributions of contacts and forces. It is explicitly linked to the stresses in the loading history, by semi-quantitative relations. One of the important characteristics measured during the compression is the ratio of lateral to controlled ('vertical') stress, K_0 . We discuss conditions in which K_0 might be regarded as constant. We calculate, via a static (matrix) method [1], the complete tensor of elastic moduli, expressing response to very small stress increments about the transversely isotropic equilibrium states along the loading path.

1 INTRODUCTION

Granular materials are usually studied in soil mechanics at macroscale as a continuum medium. Recent works tend to investigate more the microstructural mechanism (contact

forces, fabric anisotropy, coordination number...) and relate them to macroscopic behavior. Discrete Element Method (DEM) [4], is a powerful tool to investigate the internal state of packing, and provides relevant variables such as fabric and coordination number [5]. In this paper we propose to study slightly polydisperse spherical beads under uni-axial oedometric compression. The evolution of structural parameters of the different assembly is studied to characterize the internal state during oedometric compression and probe the effect of the initial packing process. Strain reversibility and elasticity are also discussed. Note that other works have covered the oedometric compression by studying the effect of bead size distribution on internal states [6] or stress anisotropy compared to sand experiments [7].

2 DEM MODEL

In this study the sample is modeled by an assembly of 4000 spherical beads slightly polydisperse (from $d_1 = 1$ to $d_2 = 1.2$), which interact through Hertz-Mindlin elastic and frictional contacts. Glass beads were chosen with Young modulus $E = 70$ GPa, Poisson ratio $\nu = 0.3$ and friction coefficient $\mu = 0.3$. Beads are contained in a periodic cuboidal cell. Both grain positions and cell size are simultaneously determined on solving dynamical equations, implemented as in Ref. [1] for isotropic compression. In our case the applied stress and strain tensors describing the oedometric compression are $\sigma_1 = \sigma_0$ and $\varepsilon_2 = \varepsilon_3 = 0$. The strain rate is controlled during the compression and set to a constant value until the desired stress is reached. Then we search for the equilibrium state by allowing the strain rate to vary without exceeding a maximal value. The value of strain rate is set through the inertia parameter $I = \dot{\varepsilon}\sqrt{m/d\sigma_0}$, with m the average particle mass. We also define a stiffness parameter $\kappa = (\tilde{E}/\sigma_0)^{2/3}$, with $\tilde{E} = E/(1 - \nu^2)$, such that the typical contact deflection is of order κ^{-1} .

3 SAMPLE PREPARATIONS

We investigate the effect of the initial state of the bead assembly on the oedometric compression response. Different sample preparation methods provide different microstructures characterized by their density (or solid fraction ϕ), coordination number z and fabric anisotropies. Bead diameters are randomly chosen according to a distribution uniform by volume:

$$p(d) = \frac{(d_1 d_2)^2}{2(d_2^2 - d_1^2)} \frac{1}{d^3}, \quad (1)$$

Random, low density ($\Phi = 0.55$) configurations of non-contacting grains (granular gases) are then subjected to different packing assembly processes, involving either isotropic or oedometric (one-dimensional) compression to a solid state in which contact forces balance the applied stress.

Moderately loose packing. A weakly confined equilibrium state is obtained by applying a stress σ_0 of 10 kPa to the granular gas, until an equilibrium configuration is obtained with contact forces balancing the external load. Samples prepared in these conditions are moderately loose and will be noted Li or Lo according to whether they underwent an isotropic compression (all three principal stresses $\sigma_1 = \sigma_2 = \sigma_3$ set to σ_0) or an oedometric one ($\sigma_1 = \sigma_0$, no strain in directions 2 and 3).

Maximally dense packing with high coordination number. We again confine the granular gas at a confining pressure of 10 kPa. But this time, to maximize density [1], we set the friction coefficient μ to zero. This process gives an unrealistically high initial coordination number (z about 6). In what follows, these configurations will be denoted DHi and DHo, for isotropic and oedometric compression.

Maximally dense packing with low coordination number. To obtain a more realistic coordination number in a dense packing process, we apply a small isotropic dilation to the confined maximally dense sample (the high coordination number one prepared without friction), so that all contacts open, and then confine the dilated configuration under pressure 10 kPa. A mixing step before the final compression phase [1] is necessary in the isotropic case. The final coordination numbers are about 4. We will denote these configurations as DLi (isotropic) and DLo (oedometric).

Tab. 1 characterizes the different initial states, giving values of K_0 , the ratio of “horizontal” stress $\sigma_2 = \sigma_3$ to “vertical” stress σ_1 (σ_1 denotes the applied stress in this paper), fraction x_0 of rattlers (grains carrying no force in equilibrated packs), coordination number z , and coordination number of non-rattler grains, $z^* = \frac{z}{1-x_0}$.

	Loose		Dense High Coordination		Dense Low Coordination	
	oedometric	isotropic	oedometric	isotropic	oedometric	isotropic
K_0	0.72	1.0	0.94	1.0	0.51	1.0
ϕ	0.584	0.589	0.639	0.638	0.634	0.637
z	4.22	4.14	5.98	5.99	4.06	4.17
z^*	4.63	4.63	6.07	6.07	4.54	4.65
$x_0(\%)$	8.8	10.3	1.5	1.3	10.4	10.37

Table 1: Structural parameters of different initial states. Values are averaged over 3 configurations (differences for Φ , z , K_0 lie below given accuracy level).

4 OEDOMETRIC COMPRESSION

4.1 Loading and unloading path

The different preparations of Sec. 3, are subjected to oedometric compressions, in which equilibrium states are obtained at different axial strain σ_1 : 31.62 kPa, 100 kPa,

316.2 kPa, 1 MPa, 3.162 MPa, 10 MPa, 31.62 MPa (equidistant on a logarithmic scale). The calculation involves two steps. First, the system is compressed at a constant strain rate $\dot{\epsilon}_1$, maintaining inertia parameter I to 10^{-5} . Then, once the desired stress level σ_1 is obtained, it is kept constant until equilibrium criteria are satisfied for particles and for internal stress (I is meanwhile requested to stay below 10^{-5}). Upon unloading, the corresponding value of I is set to 10^{-6} .

4.2 Evolution of solid fraction ϕ and coordination number z

Fig. 1 shows the evolution of solid fraction during the oedometric compression of the different sample types. The curves present similar behaviours and curves of samples with the same initial solid fraction almost coincide on this scale – although highly coordinated systems are less deformable in the initial compression stages. Coordination number z

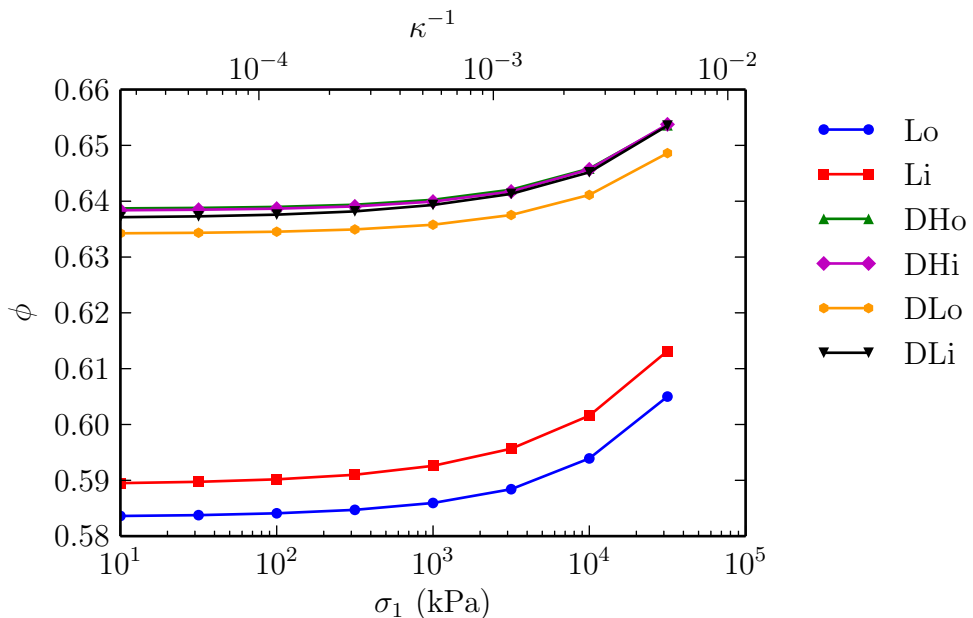


Figure 1: Evolution of ϕ with the vertical stress during the oedometric compression for samples of different preparation routines.

(Fig. 2) slightly decreases in the first compression steps for samples DHi and DHo, for which its initial value is high (~ 6) due to the absence of friction in the assembling process. Friction stabilizes grain packs at lower coordination levels. z increases again at higher pressures, as in all systems: new contacts are formed by closing the gaps between neighbours in denser structures [2]. Under high pressures, coordination numbers increase with density. The evolution of the coordination number depends on its initial value and the value of the solid fraction. Rattler fractions follow the opposite evolution to that of z except for samples DHi and DHo for which the initial decrease of z does not translate

into an increase of x_0 .

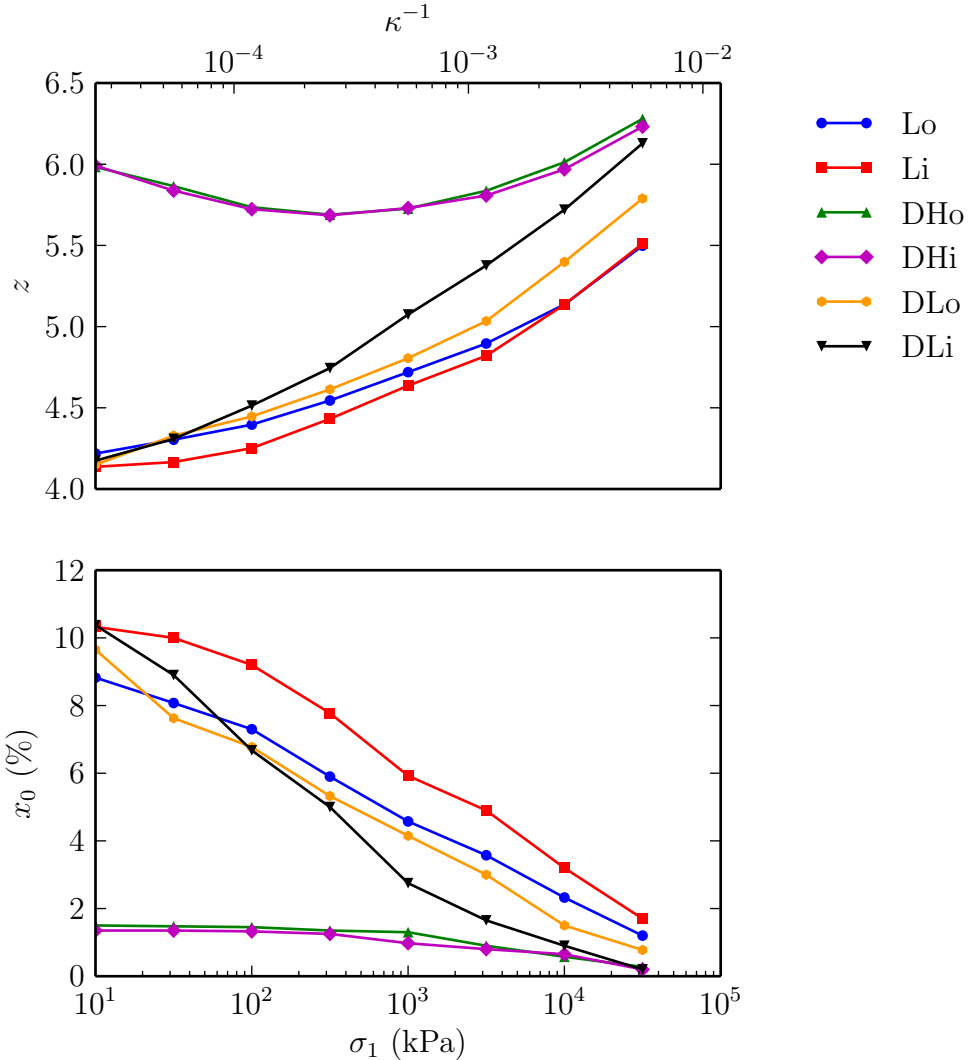


Figure 2: Coordination number z and rattler fraction x_0 versus vertical stress σ_1 along oedometric loading path for the different sample preparations.

4.3 Variation of coefficient of lateral pressure K_0

In experiments on sands [8, 9, 10], K_0 is regarded as constant. As shown in Fig. 3 the variation in K_0 in our simulated bead packings strongly depends on the initial state. Obviously, samples initially confined by an isotropic compression of the granular gas are first devoid of structural anisotropy. Therefore, K_0 varies as the sample becomes anisotropic during the axial compression. This is the case of the samples Li, DHi and

DLi. Within this group, the denser samples reach higher anisotropy, the faster the larger the number of contacts (enabling different force distributions in contact networks).

The samples prepared under oedometric compression of the granular gas (such as DLo and Lo) are anisotropic from the beginning. K_0 is then observed to remain almost constant. As to DHo, prepared with no friction, its very small initial anisotropy is typical of frictionless systems [12]. The anisotropy of contacts and forces also depends on the preparation and will be detailed in the next section.

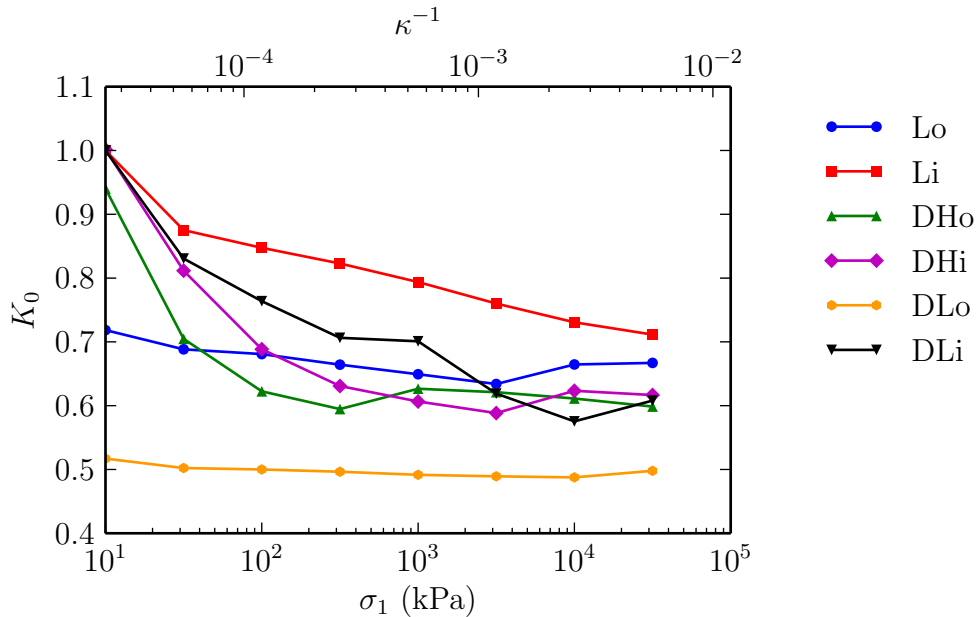


Figure 3: K_0 versus "vertical" stress σ_1 in oedometric compression.

4.4 Anisotropy characterization

K_0 is characteristic of the overall degree of stress anisotropy of the system. At the microscopic level, stresses are determined by contact forces, which may differently contribute to σ_1 and σ_2 , depending on their directions and their amplitudes. Anisotropies of the force network may thus be characterized by the distribution of contact orientations, and also by the angular dependence of the force distribution. We only consider here the normal component of the contact forces, as the tangential force contribution to normal stress components σ_1 , $\sigma_2 = \sigma_3$ is found negligible. We denote as \underline{n} the normal unit vector at contacts.

Contact distribution. Due to rotational invariance about the oedometric compression axis, the density distribution function $P(\underline{n})$ on the unit sphere Σ depends on $|n_1|$ only, and

it and can be expanded in a series of Legendre polynomials of even order. The simplest non-isotropic form is truncated at order 2:

$$P(|n_1|) \simeq 1 + \frac{5}{4} (3c_2 - 1) (3n_1^2 - 1) \quad (\text{with } c_2 = \langle n_1^2 \rangle) \quad (2)$$

Angular distribution of normal force amplitudes. The distribution of the average force amplitude in the contacts with direction \underline{n} depends on $|n_1|$ as well, and its expansion to second order in Legendre polynomials is analogous to (2). We define

$$f_2 = \frac{1}{4\pi} \int_{\Sigma} \mathcal{F}(|n_1|) n_1^2 d^2 \underline{n}$$

with notation $\mathcal{F}(|n_1|) = \langle F_N \rangle(|n_1|)/\langle F_N \rangle$. Here $\langle F_N \rangle$ is the overall average normal contact force and $\langle F_N \rangle(|n_1|)$ is the average normal force among contacts with normal direction \underline{n} .

4.5 Evolution of c_2 and f_2

Fig. 4 is a plot, versus σ_1 , in the oedometric compression, of the second order anisotropy parameters c_2 and f_2 respectively characterizing the contact distribution and the force distribution. c_2 and f_2 , similarly to K_0 , depend on initial state. The large variation of K_0 observed in isotropically assembled samples appears to be due to the evolution of f_2 , rather than that of c_2 . The relation of K_0 to both anisotropy parameters c_2 and f_2 can be made more explicit, as shown in the following section.

4.6 Estimation of K_0 from anisotropy parameters

The normal force contribution to principal stresses is given by:

$$\sigma_{\alpha} = \frac{3z\phi}{\pi} \frac{\langle d \rangle}{\langle d^3 \rangle} \langle F_N \rangle \int_S P(\underline{n}) \mathcal{F}(\underline{n}) n_{\alpha} n_{\alpha} d\Omega \quad (3)$$

Using second order expansion (2), and neglecting the products of anisotropic terms, we get the following approximation

$$\sigma_{\alpha} \simeq \frac{3z\phi}{\pi} \frac{\langle d \rangle}{\langle d^3 \rangle} \langle F_N \rangle \left[\langle n_{\alpha}^2 \rangle + \langle \langle F_N \rangle(|n_{\alpha}|) n_{\alpha}^2 \rangle - \frac{1}{3} \right]. \quad (4)$$

Knowing that $\langle n_2^2 \rangle = \langle n_3^2 \rangle = \frac{1}{2}(1 - \langle n_1^2 \rangle)$, one may finally estimate K_0 as:

$$K_0 = \frac{\sigma_{22}}{\sigma_{11}} \simeq \frac{4 - 3(c_2 + f_2)}{6(c_2 + f_2) - 2}. \quad (5)$$

This estimate of K_0 agrees well with measured values (see Fig. 5).

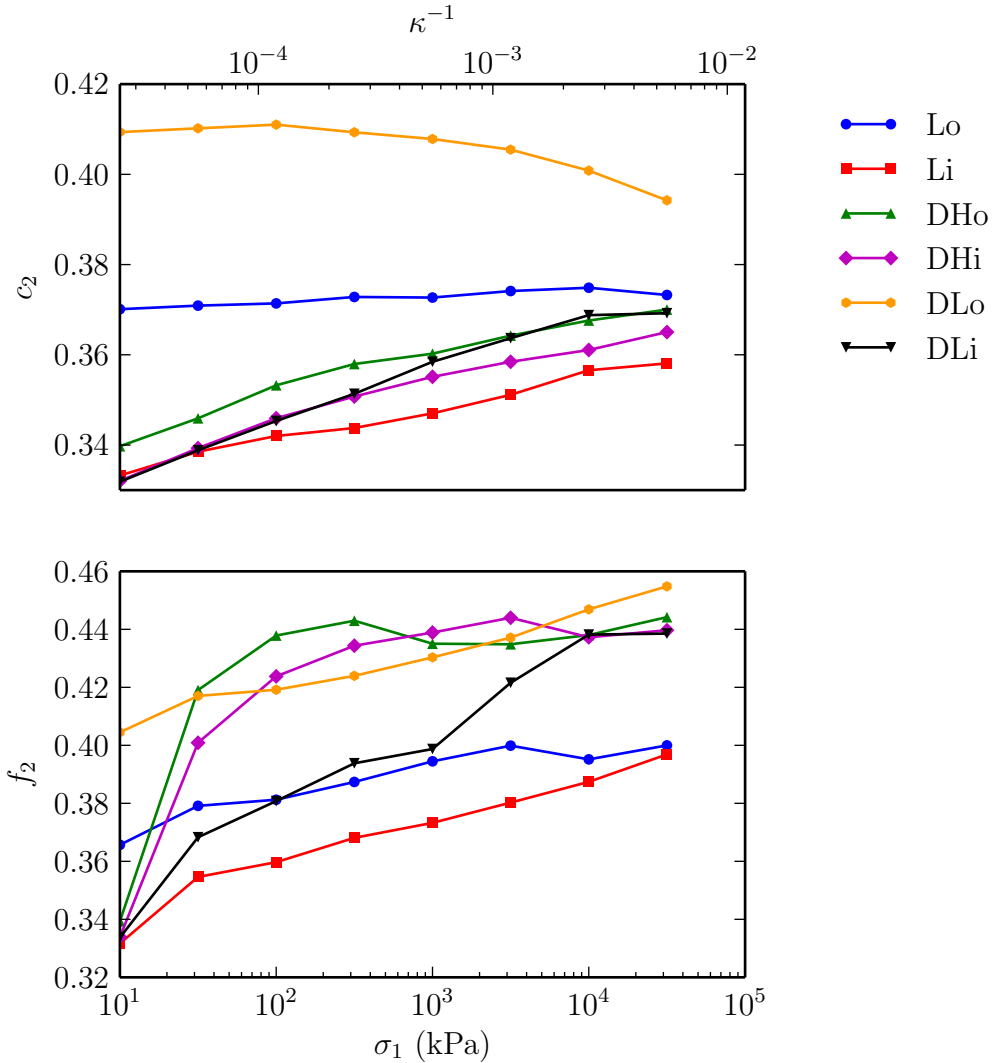


Figure 4: Anisotropy parameters c_2 and f_2 versus applied stress σ_1 .

4.7 Elastic moduli

The elastic moduli are computed in equilibrium configurations via the static method of Ref. [3]. Moduli C_{11} and C_{12} , respectively relating increments of strain ε_1 to increments in stresses σ_1 and σ_2 , are plotted in Fig. 6, as functions of axial stress σ_1 . At low pressure C_{11} depends on both density and coordination number. At high pressure, the coordination tends itself to be determined by the density, and the curves separate in two groups according to solid fraction. For C_{12} only the dependence on the coordination number is observed. The results along unloading paths appear to depend on solid fraction only for C_{11} , and nearly coincide for C_{12} . This is to be correlated to the evolution of coordination

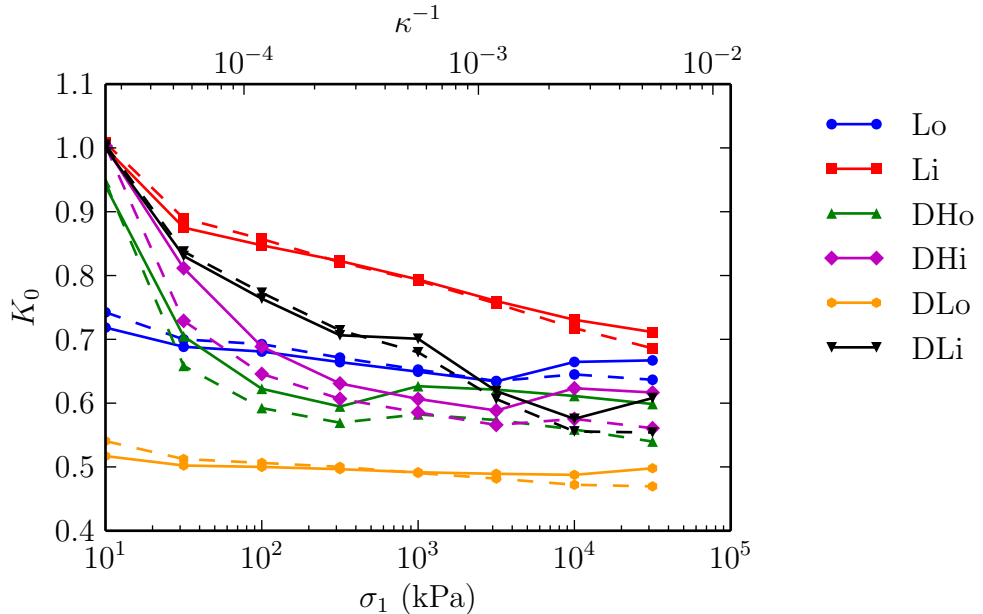


Figure 5: K_0 versus σ_1 . Dots joined by solid line: measured values. Dots joined by dashed line: Eq. 5.

number upon unloading, as shown below in Sec. 5.

5 REVERSIBILITY

5.1 Void ratio

The void ratio $e = -1 + 1/\Phi$, as plotted in Fig. 7 versus axial stress in the compression cycle, appears to be very nearly reversible, especially in dense samples. This behaviour is quite different from the typical experimental ones. In sands, the initial and final values of e in such a cycle is of the order of 0.05, and the final value is almost equal to the lowest one reached in the loading phase [11]. The irreversibility observed in sands should thus be attributed to phenomena (plasticity or damage at contacts) which are not present in the present model. Reversibility, in the simulations, is only apparent, and should not to be confused with elasticity. The right plot of Fig. 7 shows that coordination numbers change irreversibly in the compression cycle: samples with high initial z values end up with much lower final values (as in the isotropic compressions of Ref. [2]). This also justifies the change in the elastic moduli in unloading observed above.

5.2 Elastic strain

From the curves in Fig. 6 we can fit a function $C_{11}(\sigma_1)$ which allows to estimate a total elastic deformation as:

$$\varepsilon^{\text{el}} = \int_{\sigma_{\min}}^{\sigma_{\max}} \frac{d\sigma_1}{C_{11}(\sigma_1)} \quad (6)$$

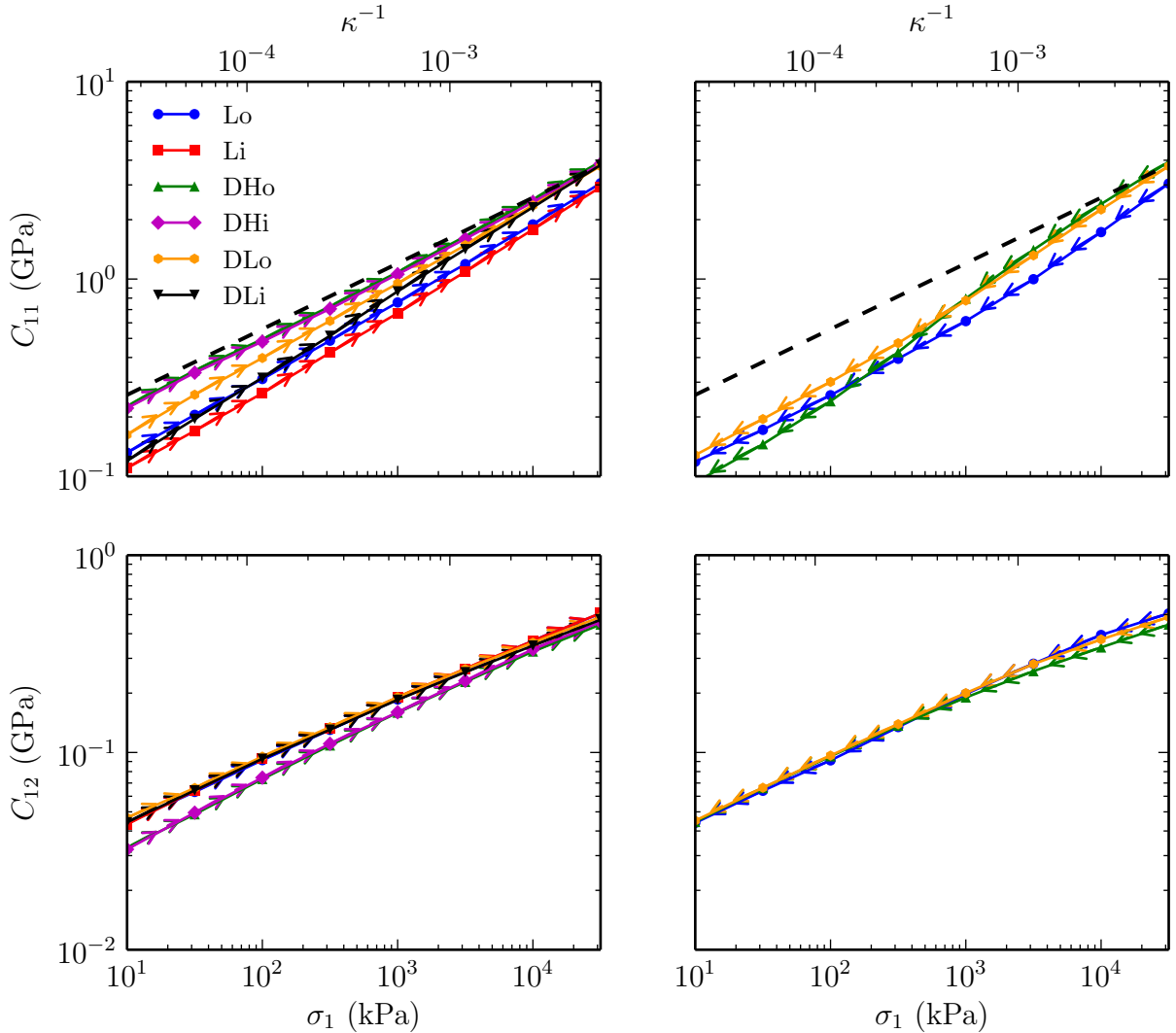


Figure 6: C_{11} (top) and C_{12} (bottom) versus σ_1 in oedometric compression (doubly logarithmic plots), along loading (left graph) and unloading (right graph) paths. Black dashed line has slope $1/3$.

The value of this elastic strain represents the expected strain in the sample if all the occurring evolution were governed by elastic mechanisms. Such elastic strains are smaller than measured strains, as reported in Tab. 2, with larger differences in looser states – thereby providing new evidence of nonelastic strain mechanisms. In the loose case (Lo) the difference between observed and elastic strain is somewhat reduced by considering the unloading stress path, but still of the order as the one obtained in denser systems.

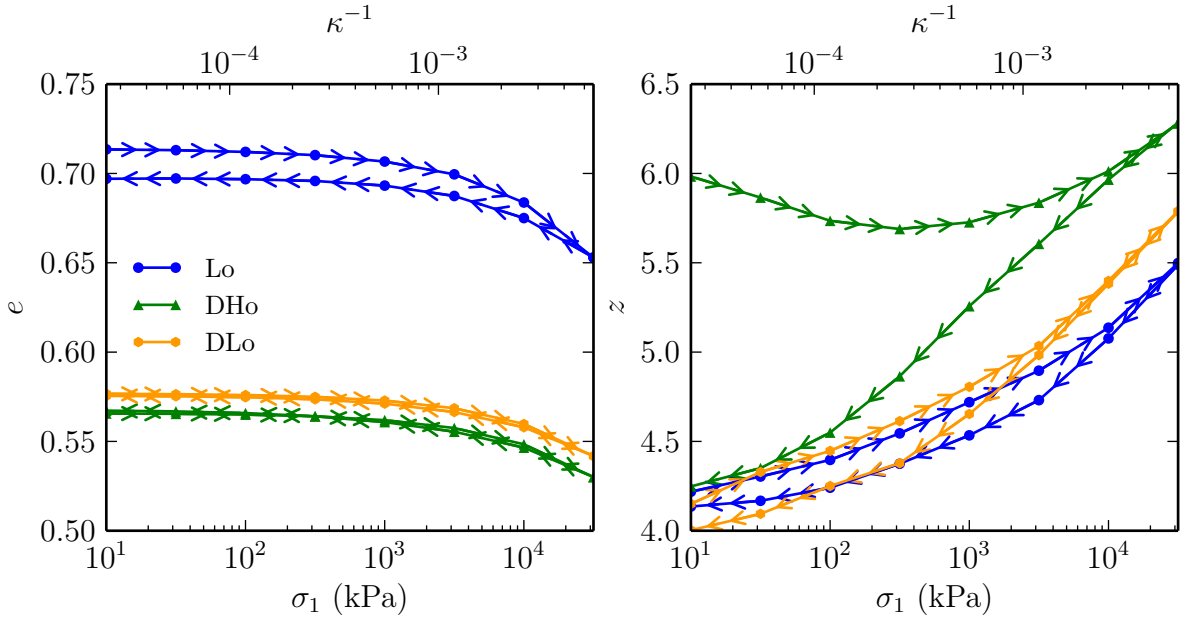


Figure 7: Void ratio e (left) and coordination number z (right) versus σ_1 in oedometric compression cycle.

	ε^{el}	ε^{ld}	ε^{uld}
Lo	1.72 %	3.54 %	2.58 %
DHo	1.27 %	2.28 %	2.38 %
DLo	1.38 %	2.22 %	2.14 %

Table 2: Total strains computed from elastic moduli (ε^{el}) and measured in simulations along loading (ε^{ld}) and unloading (ε^{uld}) paths .

6 CONCLUSION

This numerical study of granular media under oedometric compression shows that the evolution of K_0 depends on the packing process. It was observed that when care is taken to establish an initial anisotropy in the sample (thus mimicking such processes as air pluviation) the coefficient K_0 can be regarded as constant during loading. K_0 can be simply related to fabric (contact orientation) and normal force anisotropy parameters. We also showed that the irreversibility usually obtained for sands in real experiments is not present in our DEM simulations and hence should be attributed to other phenomena that were not included in the model such as grains damage and plasticity.

Acknowledgment: This work has benefited from a French government grant managed by ANR within the frame of the national program Investments for the Future ANR-11-LABX-022-01

REFERENCES

- [1] I. Agnolin and J.-N. Roux (2007) *Internal states of model isotropic granular packings. I. Assembling process, geometry, and contact networks.* Physical Review E, 76(6), 061302.
- [2] I. Agnolin and J.-N. Roux (2007) *Internal states of model isotropic granular packings. II. Compression and pressure cycles.* Physical Review E, 76(6), 061303.
- [3] I. Agnolin and J.-N. Roux (2007) *Internal states of model isotropic granular packings. III. Elastic properties.* Physical Review E, 76(6), 061304.
- [4] P. A. Cundall and O. D. L. Strack (1979) *A discrete numerical model for granular assemblies.* Geotechnique 29,47.
- [5] F. Radjaï and F. Dubois (2011). *Discrete-element modeling of granular materials* (pp. 425-p). Wiley-Iste.
- [6] J. Wiacek and M. Molenda (2014) *Effect of particle size distribution on micro- and macromechanical response of granular packings under compression.* International Journal of Solids and Structures, 51(25), 4189-4195.
- [7] Y. Gao and Y. H. Wang (2014) *Experimental and DEM Examinations of K₀ in Sand under Different Loading Conditions.* Journal of Geotechnical and Geoenvironmental Engineering, 140(5).
- [8] O. Daramola (1980) *On estimating K₀ for overconsolidated granular soils.* Geotechnique, 30(3).
- [9] J. A. Yamamoto, P. A. Bopp and P. V. Lade (1996) *One-dimensional compression of sands at high pressures.* Journal of Geotechnical Engineering, 122(2), 147-154.
- [10] J. Feda (1984) *K₀-Coefficient of Sand in Triaxial Apparatus.* Journal of Geotechnical Engineering, 110(4), 519-524.
- [11] A. Sanzeni and A. Whittle (2012) *Compression and Creep of Venice Lagoon Sands.* Journal of Geotechnical, (October), 1266–1276.
- [12] P.-E. Peyneau and J.-N. Roux (2008) *Solidlike behavior and anisotropy in rigid frictionless bead assemblies.* Physical Review E, 78(4), 041307.

INVESTIGATION OF TIRE-SOIL-INTERACTIONS USING THE DISCRETE-ELEMENT-METHOD

OLIVER ZIEHER¹ AND MARTIN MEYWERK²

¹ Helmut-Schmidt-Universität
Holstenhofweg 85
22043 Hamburg
Germany
Oliver.Zieher@hsu-hh.de

² Helmut-Schmidt-Universität
Holstenhofweg 85
22043 Hamburg
Germany
Martin.Meywerk@hsu-hh.de

Key words: Granular Materials, Discrete Element Method, Soft Soil, Tyre-Soil-Interaction

Abstract. In this article a tyre is investigated which moves in lateral direction, i.e. perpendicular to its regular rolling direction, through sand, which is one representative of a deformable soil. This kind of motion could be a result of skidding of a car where the vehicle slides laterally over the side verge. In order to investigate this motion in the first step the influence of the compliance of the tyre is studied; the result is that an flexible tyre behaves similar to an rigid one. Therefore, in the second step, the simulations and the experimental investigations of the tyre are restricted to a stiff tyre, the results of experiments and simulations with an discrete element method are compared, the influence of some parameters are studied.

1 INTRODUCTION

Different analytical approaches for tyre-soil-interaction are described in literature. Mostly this approaches are used to predict the traction behaviour and the wheel-soil rolling resistance. Extensions of this approaches are capable to predict lateral behaviour and lateral forces during rolling motion with a non-zero slip angle [3].

Often the vertical behaviour of the soil is described by the theory of Bekker [5], whereas the tangential effects are predicted by the approach of Janosi und Hanamoto [4]. In order to describe more complicated cases, where a multi-axial state of stress is important, the Finite Element Method (FEM) can be used. FEM is limited in the case of large deformations or in the case of disruptions. For large deformations and disruptions a

particle method is appropriate, especially in case of non cohesive soils like sand. Therefore, the soil-tyre-interactions we consider in this article is simulated with a particle method, the so-called discrete element method (DEM). In [1, 6] similar situations are simulated with the discrete element method, where plates moving through granular materials. A overview about existing tire-terrain models you can find in [7].

2 EXPERIMENTAL SETUP

For the experimental investigations of the tyre-soil-interaction a modified crash sled test facility is used (cf. Fig. 1(b)). The principal test setup is shown in Fig. 2. The sled 1 with rollers runs on the guide rails ⑤. The guidance ensures only one longitudinal degree of freedom of the sled. The mass of the sled without additional components is 854 kg. On each side of the sled a lever arm ② is mounted with a revolute joint to the sled. The left and the right lever arms are connected by a beam ⑥. The mass of the lever arms and the beam is 702 kg. At one end of each lever arm a wheel (195/65 R15) is mounted. The two wheels interact with sand in two trough fixed on the floor on the right and the left side. That means, that the whole setup is symmetric and nearly no moments with respect to the vertical axis and no lateral forces are acting on the sled. This is an important restriction of the whole construction, because the sled and the guide rails are not designed for large loads of the mentioned kind. The dimensions of the two troughs are: length $l=4000$ mm, width $w=800$ mm, height $h=400$ mm.

The sled is accelerated by several bungee ropes. During acceleration the lever arms are locked by an electromagnet in a horizontal position. Immediately after the wheels are complete over the sand trough at their beginning, the electromagnet is deactivated and the lever arms together with the wheels are accelerated by gravitation. The result is, that the wheels come into contact with the sand and sink into the sand (cf. Fig. 1(a)).

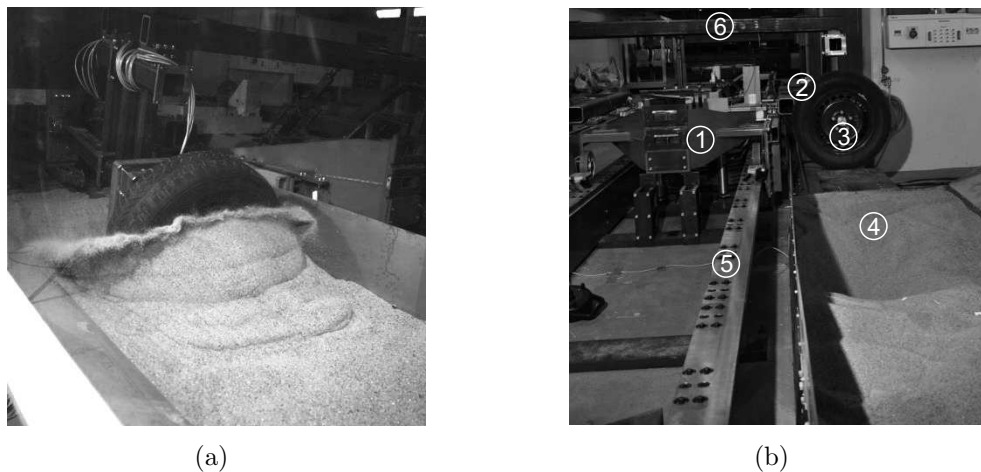


Figure 1: Interaction between wheel and sand (a) and experimental setup (b)

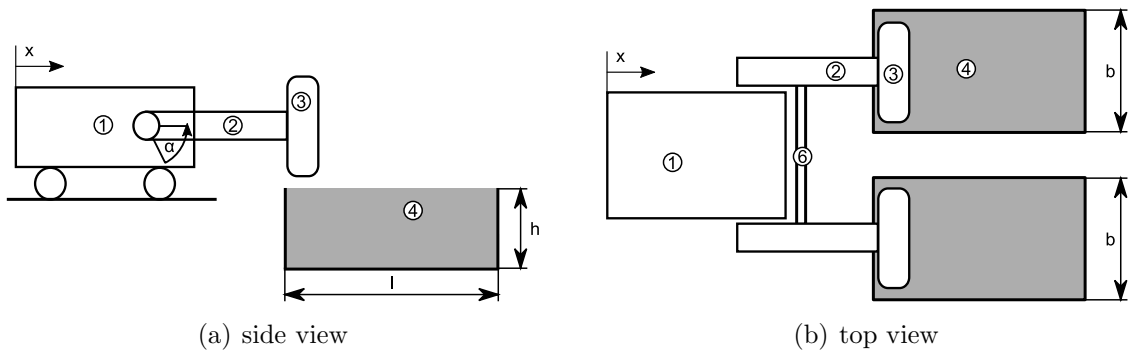


Figure 2: Principal drawing of the experimental setup

3 INFLUENCE OF THE TYRE COMPLIANCE

In a first step the influence of the tyre compliance is experimentally investigated. This is an important aspect for the simulation, because a tyre, which could be assumed rigid in the particle simulation, is easier and needs less resources.

To obtain a comparison between stiff and deformable tyres, the results of two experimental setups are compared: In the first setup an deformable tyre is used, in the second one a stiff surrogate tyre made out of aluminium and polyoxymethylene (cf. Fig. 3). The outer contours of both, deformable and stiff tyre are similar, the tyre patterns are neglected in the surrogate tyre. To obtain similar friction behaviour, the surface of the surrogate tyre is bonded with abrasive paper. Furthermore, the surrogate tyre is completed with an additional mass to obtain the same mass of the tyres.

It is known that the mechanical behaviour of soils depends on the consolidation. Therefore, the sand in the troughs is consolidated by a plate vibrator. This ensures small variations in the experimental results.

To compare the two types of tyre objects (stiff and deformable) we look at the sinkage $h = h(s)$ and the velocity $v = v(s)$ in dependence of the displacement s of the sled. The value $s = 0\text{m}$ is equivalent to that point in time where the arm is horizontal. The sinkage which corresponds of first contact between tyre and sand is between nearly zero sinkage $h = 0\text{ mm}$ and approximately $h = 10\text{ mm}$; the sinkage of first contact depends on the consolidation treatment of the sand. The sinkage h is depicted in Fig. 4(a) for two experiments with a stiff tyre and one with a deformable one. The initial velocities differ slightly in the experiments (cf. Fig. 4(b)). It is obvious, that the sinkage up to a displacement of $s \approx 0.4\text{ m}$ for both tyre objects are nearly the same, differences are the result of differences in the initial velocities, the different tyre types and differences in the characteristics of the soil. Variations in the characteristics of the soil, this means variations between different experiments and spatial variations within the troughs are one of the most challenging aspects in order to obtain reliable experimental results. Oscillations occur in the deformable tyre experiments, whereas no such oscillations can be seen in the stiff tyre experiments.

This experiments show that there are small differences between a stiff and a deformable tyre. This is the reason, that for the characterisation and the simulation of sand with DEM it is sufficient to take the stiff tyre experiments.

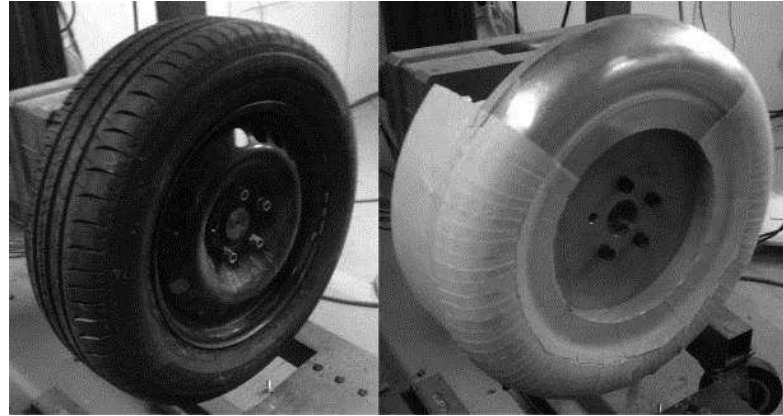


Figure 3: Deformable tyre and stiff surrogate tyre

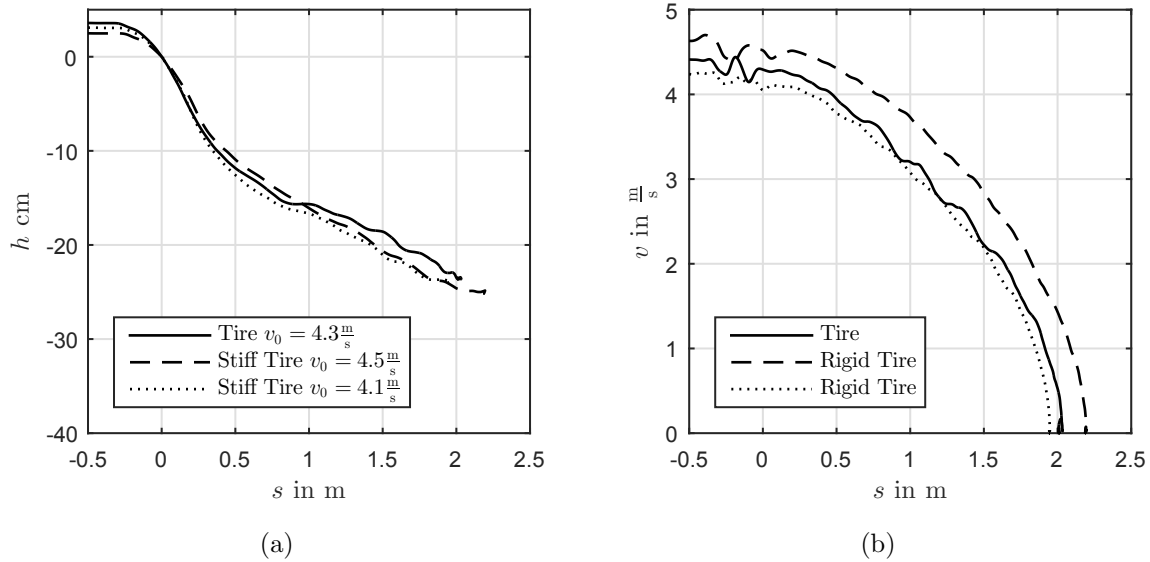


Figure 4: Comparison of two Measurements of a flexible tire and the stiff surrogate tyre

4 SIMULATION

4.1 DEM

One common method to simulate granular media, e.g., sand, is the DEM, particular if the dynamical behaviour including inertia effects are important. In this article the open

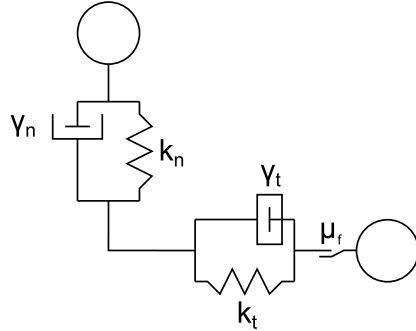


Figure 5: Interaction model of two elements

source software LIGGGHTS is used; the equations of this section are from the user manual of LIGGGHTS. The forces between the elements are calculated by force displacement relations which are illustrated in Fig. 5. The stiffness and damping parameters are given implicitly, for example by Youngs's modulus.

For example the normal contact stiffness

$$k_n = \frac{4}{3} Y^* \sqrt{R^* \delta_n} \quad (1)$$

is dependent on a equivalent Young's modulus Y^* , an equivalent radius R^* of the elements and the penetration δ_n . The parameters Y^* and R^* can be calculated similar to Hertz's contact theory from Youngs's moduli Y_1 , Y_2 , Poisson's ratios ν_1 , ν_2 and the radii R_1 , R_2 , of the two bodies in contact:

$$\frac{1}{Y^*} = \frac{(1 - \nu_1^2)}{Y_1} + \frac{(1 - \nu_2^2)}{Y_2} \quad (2)$$

and

$$\frac{1}{R^*} = \frac{1}{R_1} + \frac{1}{R_2} . \quad (3)$$

The tangential stiffness can calculated by

$$k_t = 8G^* \sqrt{R^* \delta_n} \quad (4)$$

using an equivalent shear modulus

$$\frac{1}{G^*} = \frac{2(2 + \nu_1)(1 - \nu_1)}{Y_1} + \frac{2(2 + \nu_2)(1 - \nu_2)}{Y_2} . \quad (5)$$

The coefficients of damping in normal and tangential direction γ_n and γ_t , resp., can be calculated using the coefficient of restitution β

$$\gamma_n = -2\sqrt{\frac{5}{6}} \beta \sqrt{S_n m^*} \geq 0 \quad (6)$$

where

$$S_n = 2Y^* \sqrt{R^* \delta_n} \quad (7)$$

and

$$\gamma_n = -2\sqrt{\frac{5}{6}} \beta \sqrt{S_t m^*} \geq 0 ; \quad (8)$$

here

$$S_t = 8G^* \sqrt{R^* \delta_n} . \quad (9)$$

Furthermore, it is possible that torques are acting between the grains, which can be included by friction torques

$$\overrightarrow{M_{rf}} = \mu_{roll} k_n \delta_n \frac{\overrightarrow{\omega_{r,scher}}}{|\overrightarrow{\omega_{r,scher}}|} R^* . \quad (10)$$

Here, μ_{roll} is a coefficient of rolling resistance, $\overrightarrow{\omega_{r,scher}}$ is the projection of $\overrightarrow{\omega_r}$ onto the plane, which is tangential to both elements in the point of contact. The vector of the angular velocity $\overrightarrow{\omega_r}$ is the result of the vectors of angular velocities of the two interacting elements.

4.2 Generating the porosity

The porosity η is defined by

$$\eta = \frac{V_v}{V} \quad (11)$$

where V_v is the volume of the voids and V is the total volume of the bulk material.

In the experiments carried out the values of the porosity differ from 0.35 (consolidated) to 0.50 (loose). Therefore, it is essential to adjust the porosity in the simulation, too. To achieve certain values of the porosity the following procedure is applied: In the first step the positions of the elements are generated randomly one by one. If a new element intersects with an already existing one, this new element is refused by the algorithm and a new randomly generated particle is placed (this random generation is repeated until the new element has no intersection to an existing one). With this first step porosities $\eta > 0.7$ can be generated. To reach the goal of smaller porosities $\eta_t \leq 0.7$ a second step is necessary in which the element distribution generated in the first step with $\eta_0 > 0.7$ is modified by increasing the diameters of all particles during a simulation with full consideration of contact conditions and movement of the particles. If an increase factor of

$$\zeta = \sqrt[3]{\frac{1 - \eta_0}{1 - \eta_t}} \quad (12)$$

is reached, the final porosity is η_t .

4.3 Parametrisation

A direct experimental determination of the DEM parameters is not possible (cf. [2]). Therefore, different experiments are used in a parameter identification process, in which the experiments are simulated and the parameters are optimized in order to obtain similar simulation results compared to the experimental results.

The coefficient of friction μ_f is measured in a shear tester, which consists of an upper and a lower box (cf. Fig. 6(a)). The sand in the box is loaded by a normal force F_n . Then the lower box is moved horizontal with a low shear velocity of $v_s \approx 0.08 \frac{\text{m}}{\text{s}}$. The shear force F_s is measured at the upper box. This experimental setup allows the determination of a coefficient of friction μ_f by simulating the shear test. The result is $\mu_f = 0.8$ for the sand investigated in this paper.

A so-called oedometer allows the determination of the Young's modulus. Fig. 6(b) shows a principal sketch of the experimental setup. Since the box is closed in both horizontal directions the vertical load results in a vertical displacement of the load plate, the lateral strain is zero. This experiments yields a Young's modulus of 500 MPa.

The determination of the coefficient μ_{roll} of rolling resistance is possible by investigating experimentally the angle of repose. The angle of repose is the maximum angle between the shoulder of a cone-shaped pile of the sand and the horizontal, where the cone-shaped pile is generated with out slumping of the sand. Fig. 7 shows the pile for the sand used in this investigation (Test) in the background. In the foreground the simulation results of the pile are shown for different values of the coefficient μ_{roll} . For $\mu_{roll} = 0.3$ the experimental pile and the simulated one corresponds good to each other.

The influence of the coefficient of restitution β and Poisson's ratio ν are small, values for β and ν are comprised in Table 1.

Table 1: Simulation Parameters

Description	Symbol	Value	Unit
Young's modulus	Y	500	MPa
Poissons ratio	ν	0.3	-
Coefficient restitution	β	0.3	-
Coefficient of friction	μ_f	0.8	-
Coefficient of rolling friction	μ_{roll}	0.3	-
Element density	ρ	2700	$\frac{\text{m}}{\text{s}}$
Element radius	R	6	mm

4.4 Comparison of experimental results and simulation

The parameters of the DEM are chosen as described in the previous section. The porosity η is a crucial parameter for a good agreement between experimental result and

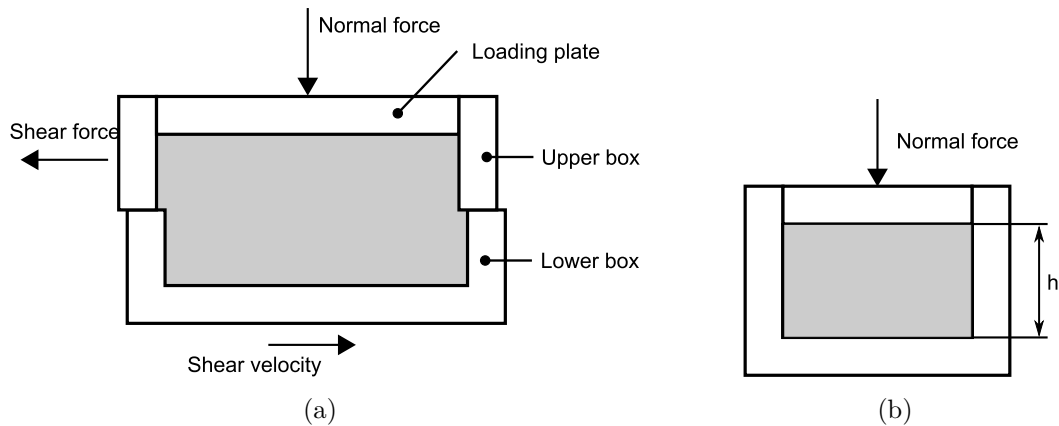


Figure 6: Sketch of the Direct Shear Tester(a) and compression testing device(b)

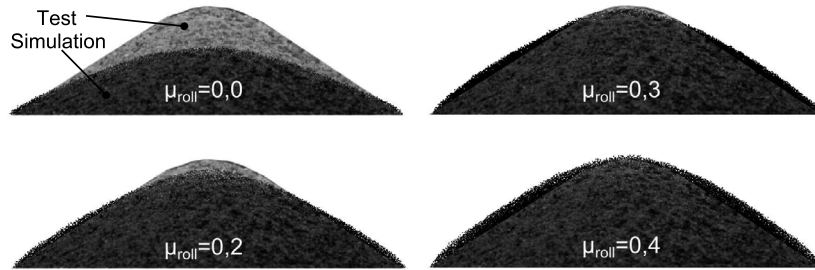


Figure 7: Comparison between a picture of a sand pile and the result of a simulation with different coefficient of rolling friction

simulation, furthermore, the results are highly sensitive on this parameter. The porosity depends strongly on the consolidation of the sand in the trough. Unfortunately, it is very expensive to determine η in the sand. This is the reason for fitting η in order to obtain good agreement between experiments and simulation. Doing this, the sinkage-displacement-function $h(s)$ of the tyre and the velocity-displacement-function $v(s)$ of the sled of the experiment and the simulation is used.

Fig. 8 shows a comparison of $h(s)$ and $v(s)$ for a highly consolidated sand of a porosity of $\eta = 0.59$. A good agreement between the experiments and the simulation is obvious.

More results are shown in Fig. 9 for not highly consolidated sand, the porosity is $\eta = 0.405$. Whereas the agreement of the velocity $v(s)$ is better for $\eta = 0.405$ as for $\eta = 0.59$ shown in 8, the agreement of the sinkage s is better for $\eta = 0.59$ shown in 8.

4.5 Simulations using optimized parameters

Further investigations and comparisons between experiments and simulations show that the agreement can be improved. If the coefficient μ_{roll} of rolling resistance is increased compared to the value which is determined using the experiment for determination of the

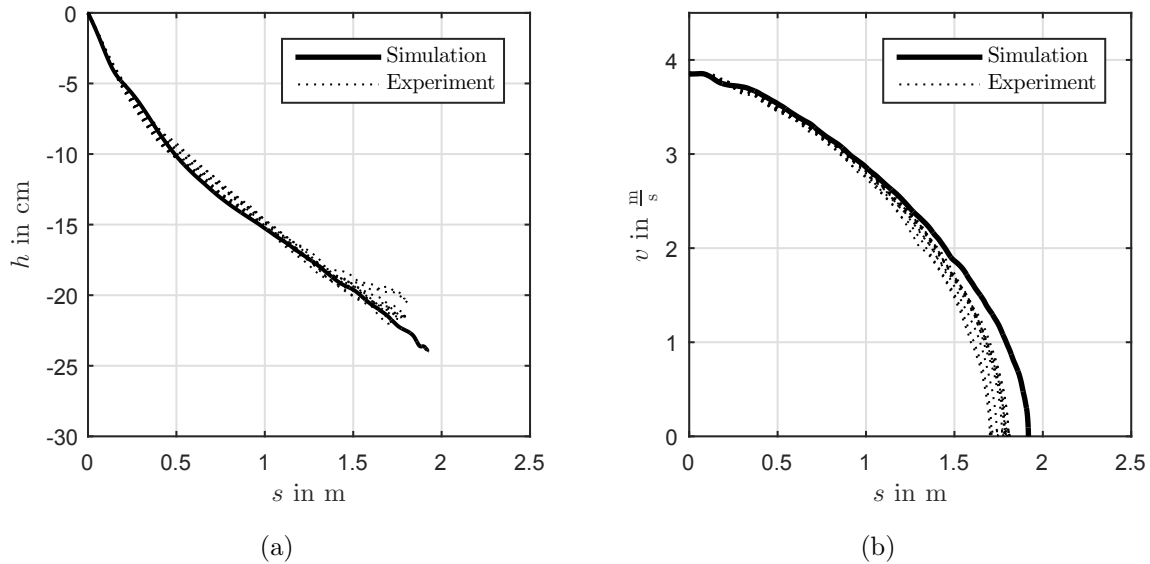


Figure 8: Comparison of experiment and a simulation with a porosity η of 0.59, which is fitted by the sinkage-displacement-function

angle of repose, then a better agreement can be achieved. For an increased value of μ_{roll} the sinkage decreases, which is compensated by an increased porosity. Fig. 10 shows the comparison for $\mu_{roll} = 0.6$ and $\eta = 0.4175$ and good agreement between experiments and simulation.

5 CONCLUSION

It is shown that it is possible to obtain a good agreement between experiments and simulation for the sled test with the rigid tyre. Furthermore, the generation of a specific porosity for the DEM is shown. Optimized parameters which differ from those advised by the simple experiment of the angle of repose are recommended.

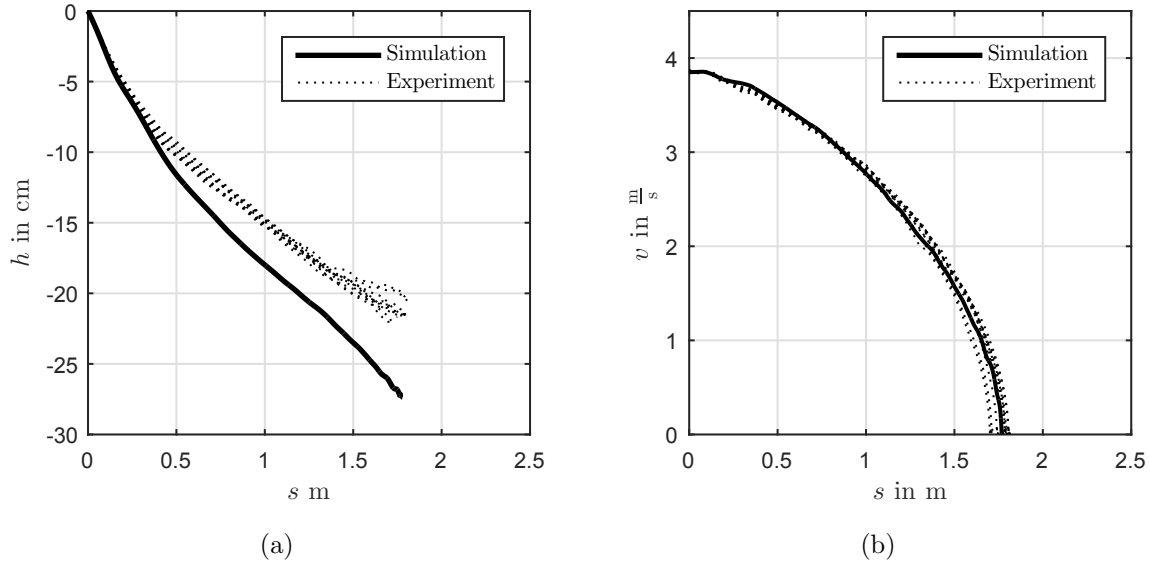


Figure 9: Comparison of experiment and a simulation with a porosity η of 0.405, Which is fitted by the velocity-displacement-function

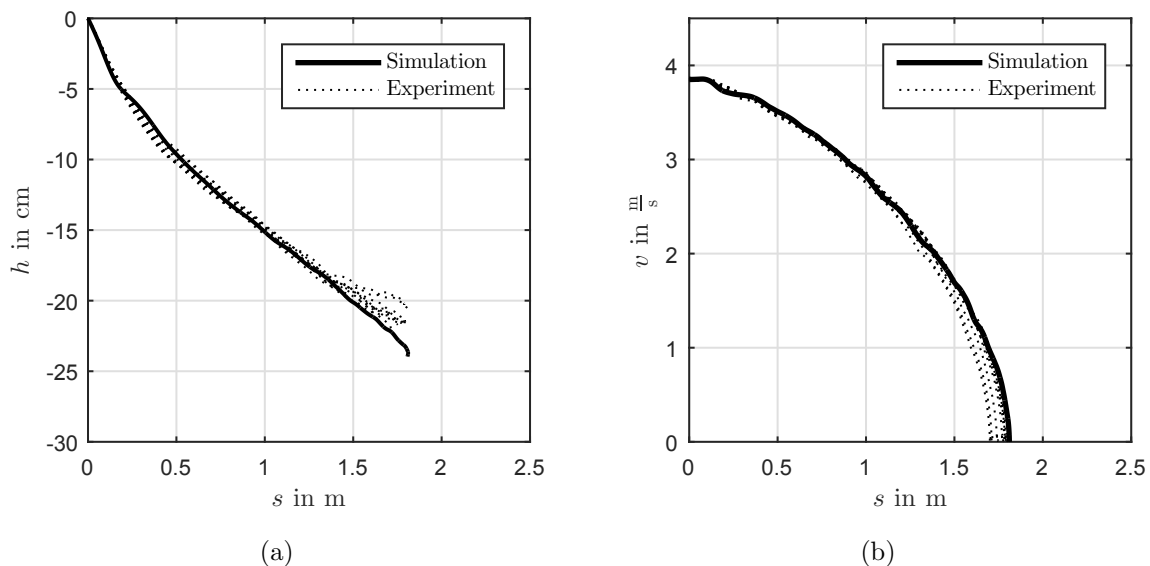


Figure 10: Comparison of experiment and a simulation with optimized parameters: $\eta=0.4175$ and $\mu_{roll}=0,60$

REFERENCES

- [1] Obermayr, M., Dressler ,K., Vrettos ,C. and Eberhard ,P., Prediction of draft forces in cohesionless soil with the Discrete Element Method *Journal Of Terramechanics* (2011) **48**:347–358.
- [2] Huang, Y., Three dimensional simulation of lunar dust levitation under the effect of simulated sphere body *Journal of Terramechanics* (2011) **48**:297–306.
- [3] Harnisch, C., *Dynamische Echtzeitsimulation der Gelndefahrt mehrachsiger Radfahrzeuge* (2001)
- [4] Janosi, Z. and Hanamoto, B., The analytical determination of drawbar pull as a function of slip for tracked vehicles in deformable soils. *First international Conference on Soil Mechanics of Soil-Vehicle Systemst* (1961)
- [5] Bekker, M. G., Introduction to Terrain-Vehicle Systems. *The University of Michigan Press* (1961)
- [6] Tsuji, T., Nakagawa Y., Matsumoto, N., Kadono, Y., Takayama, T., Tanaka, T., 3-D DEM simulation of cohesive soil-pushing behavior by bulldozer blade *Journal of Terramechanics* (2012) **49**:37–47.
- [7] Taheri, Sh., Sandu, C., Taheri, S., Pinto, E. and Gorisch, D., A technical survey on Terramechanics models for tire-terrain interaction used in modeling and simulation of wheeled vehicles *Journal of Terramechanics* (2015) **57**:1–22.

Microdynamic analysis of ellipsoidal particle flow in a shear cell

MUZA HID HOSSAIN¹, HAIPING ZHU¹ AND AIBING YU²

¹School of Computing, Engineering and Mathematics, University of Western Sydney
Locked bag 1797, Penrith, NSW 2751, Australia
18130049@student.uws.edu.au, H.zhu@uws.edu.au

²Faculty of Engineering, Monash University
14 Alliance Lane (Engineering 72), Clayton Victoria 3168, Australia
Aibing.Yu@monash.edu.au

Key words: Granular materials, rheology, discrete element method, shear cell, ellipsoidal particle

Abstract. This paper studies rheological properties of ellipsoidal particles in a model annular shear cell and compares them with the relevant parameters obtained for spherical particles under similar conditions using the discrete element method (DEM). Some important microdynamic variables such as velocity, coordination number, volume fraction and stress were considered. It was found that there are some differences between the spherical and ellipsoidal particles in terms of these properties. The feature was explained by the microscopic structures at particle scale such as those related to particle alignment and inter-particle forces.

1 INTRODUCTION

It is of paramount importance to understand the dynamical behaviour of particle flow due to the fact that it touches our daily lives from all possible directions: from residence materials like rice and sugar to commercial production facilities like pharmaceutical and food processing industry, from natural disasters like avalanches and landslides to artificial activities like transportation of pulverized coals and mixing of gravel with cement. In the earlier stages of the research field of particle flow, the primary focus was on macro-dynamic properties of the flow based on physical experiments (e.g. [1]). But it was expensive, and very much limited to detailed investigation of phenomena. The breakthrough happened with the ingenious development of numerical models.

One of the most popular methods in this area is the so-called Discrete Element Method (DEM) [2]. This method gives the best possible theoretical microdynamic description of ideal mechanical behaviour of particle conglomerate which is either stationary or in flow. The DEM has been applied in various particulate systems [3]. However, it is still far from practical function and much work is needed. Majority of earlier works using the DEM was based on spherical particles. With recent available computational resources, the research objective is

inclining more in the direction of non-spherical particles due to its closeness towards practical application.

In this paper, the shear flow of ellipsoidal particles in an annular shear cell is studied, and compared with that of spherical particles under the similar conditions, in terms of some key physical properties such as particle velocity, coordination number, volume fraction and stresses. Particle alignment of the ellipsoidal particles is also examined and used to explain the difference on these properties for the non-spherical and spherical particles.

2 SIMULATION METHOD AND CONDITIONS

In this work, granular rheological analysis was performed by means of the DEM using spring dashpot model for soft particle simulation. The software package PFC3D 5.0 was utilised to simulate the flows of spherical and ellipsoidal particles in a 3D annular shear cell. The non-linear model based on Hertz-Mindlin and Deresiewicz model [4, 5] was used to calculate the contact forces between particles. The details on the DEM can be seen elsewhere [6].

A rectangular segment of widely studied annular shear cell was considered for both spherical and ellipsoidal particles (Fig. 1) here. For comparison, the cases of spherical and ellipsoidal particles have the same segment, with a dimension of $12d \times 60d \times h$, where d is the diameter of spherical particles. The segment has two periodic boundary planes perpendicular to the x-axis. 320 spherical particles of $1.5d$ diameter were used to constitute each of the upper and lower platens of the segment so that the entire area of the platens was filled. The particles forming the platens possess the same physical properties (such as, density, damping coefficient, friction coefficient and stiffness) as other particles.

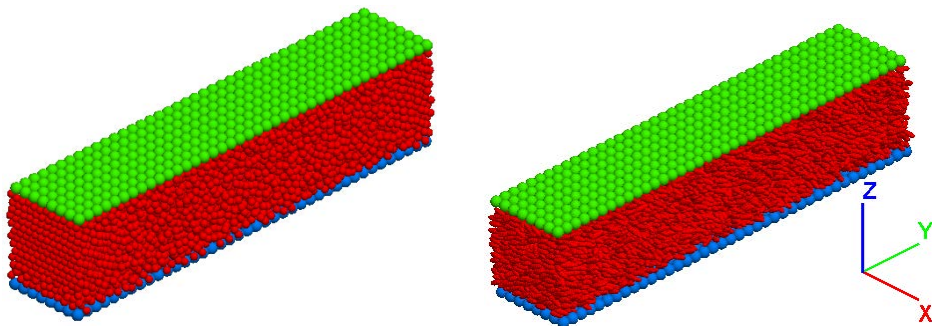


Fig. 1. Model shear cells (left: spherical, right: ellipsoidal)

The ellipsoidal particles considered have an aspect ratio of 2.5:1, and the same volume of the spherical particles. Bubble-pack algorithm [7] was used to construct these particles (Fig.2) in this work. The closed surface of the non-spherical particle was first constructed with triangular meshes of various sizes. Then spherical particles of various sizes were used to fill the space within the surface to obtain a specific volume. These particles were then glued and made immobile relative to each other and thus the particle of desired shape was constructed.

In each simulation, 10000 mono-disperse particles (spherical or ellipsoidal) are first generated randomly between the upper and lower platens with an initial volume fraction of 0.7. The position of the upper platen is then lowered gradually until the desired pressure acting on the particle assembly is applied. While the lower platen remains at the same height, the upper platen height varies to maintain the constant normal pressure. Shear rate is then gradually increased to the pre-set value after the loading has been stabilized. When the system becomes steady, the process of calculating microdynamic properties starts. The particle properties and simulation parameters are given in Table 1.

It is worth noting that the gravity was considered to affect the dynamic behaviours of shear flows and was ignored in some of the previous studies [8]. In this work, the gravity has been included in the simulations. Our simulations indicate that it does not have noticeable effect on granular rheology for the configurations considered. Further work will be conducted to clarify this issue.

3 RESULTS AND DISCUSSION

The results are discussed in terms of particle alignment, velocity profile, coordination number, volume fraction and stress tensor.

3.1 PARTICLE ALIGNMENT

Particle orientation (alignment) is of special interest in the study of non-spherical particles because of its strong influence on the dynamic properties of granular assembly. In this study, we observed that the ellipsoidal particles are approximately aligned with the direction of the shear velocity, as shown in Fig. 3. This means that the major axes of the particles are parallel to the flow. This finding is similar to that obtained in earlier studies (e.g., [9]). It is worth mentioning that the more elongated the particles are, the more they are aligned towards the shear flow. It has also been identified by studying the statistical distribution of the particulate inclination angles along the direction of shear velocity (not included in this paper, for brevity). The sections below will discuss on how this phenomenon affects the characteristics of flow dynamics of ellipsoidal particulate assemblies.

3.2 VELOCITY PROFILE

The velocity profile was studied for assemblies of spherical and ellipsoidal particles. It was observed that being in agreement with the previous studies [8, 10], the velocity components in



Fig. 2. Ellipsoidal particle

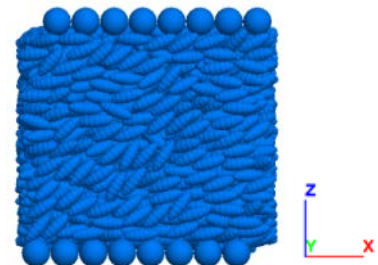


Fig. 3. Particle orientation during flow

the y- and z-axis directions are small and can be ignored. Hence, only the velocities in the x-axis direction (direction of the flow) on the xz-plane are shown in Fig. 4.

Table 1: The particle properties and parameters used in the simulations

Property	Value	Unit
Particle friction coefficient, μ	0.3	(-)
Critical damping ratio, D (normal and shear)	0.3	(-)
Young's modulus, E_y	2.5×10^6	$\pi \rho d g / 6$
Poisson's ratio, ϑ	0.3	(-)
Time step	0.00001	$\sqrt{d/g}$
Normal pressure	1.4×10^6	$\pi \rho d g / 6$
Shear velocity	6.5	$\sqrt{g d}$

It can be clearly seen that for both spherical and ellipsoidal particles, there is a symmetric velocity field with small velocities at the central region, and the velocity gradually increases towards the moving platens with the maximum shear velocity at the regions near the platens. The variation of the velocity is due to the dissipative interaction forces between particles at the adjacent laminar layers. The movements of particles near the platens are mainly driven by the interaction forces between particles and the platens, causing large velocities. The particles in the central region move in the two flow directions, counterbalancing each other there, resulting in negligible velocities.

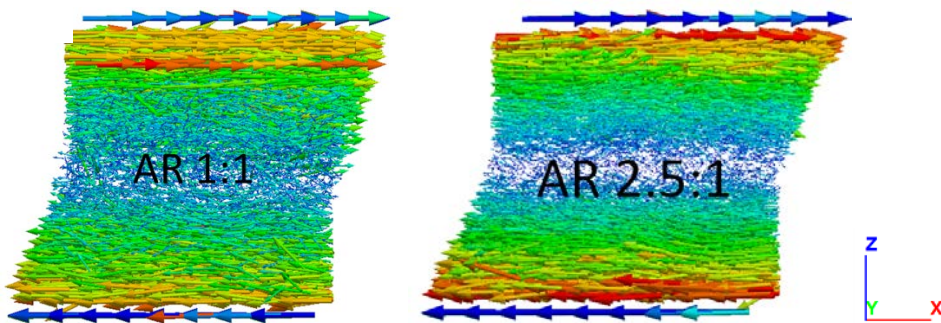


Fig. 4. Velocity fields for assemblies of particles (left: spherical; right: ellipsoidal with aspect ratio 2.5:1)

To have a clearer view, the time-averaged velocities of particles at different layers are analysed in Fig. 5a. Both ellipsoidal and spherical particle assemblies show similar linear velocity gradient with near-zero value at the central plane. The relative velocity is not 1 or -1, which indicates that there is a slip near the platens.

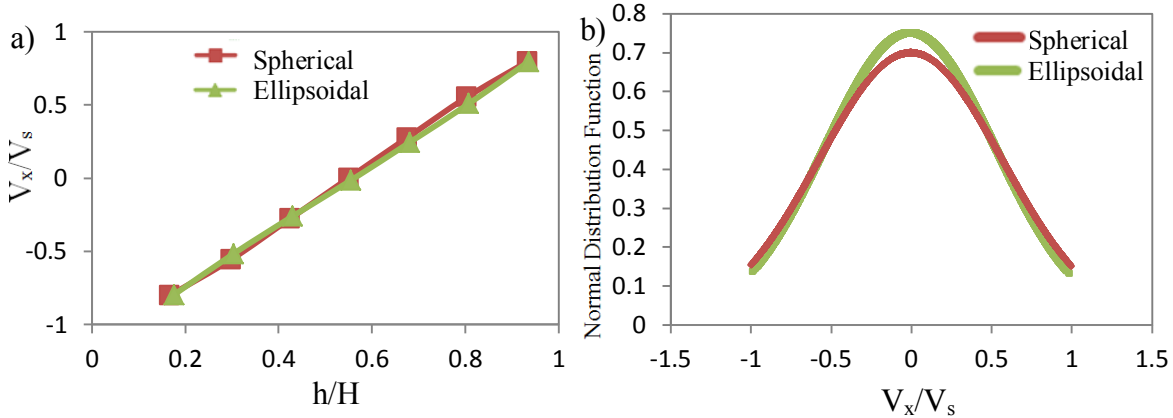


Fig. 5. a) Scaled velocity gradient along scaled height for spherical and ellipsoidal particle assemblies; b) normal distribution of scaled velocities with spherical and ellipsoidal particles. V_x and V_s are the average velocity of particles at a layer and shear velocity of the platens respectively, and h and H are the layer height and segment height respectively.

It is worth mentioning that the velocity gradient for shear cell is still an open question, even for spherical particles. While some studies [8] suggested there was a linear velocity profile, others found the velocity profile was non-linear [10]. It is a subject that needs further work but is beyond the scope of this paper.

Further, the statistical distribution of the particle velocity is shown in Fig. 5b for the two assemblies of particles. A clear symmetric Gaussian distribution of velocity can be seen with its peak at the zero velocity for both cases. In addition, the plot suggests that the velocity distribution of ellipsoidal particles has a higher peak at the mean value (zero) and lower dispersion away from the mean value, which implies that the number of stationary particles is higher for ellipsoidal particles. This phenomenon can be explained by particle alignment. As the particles become aligned with the direction of flow, the more elongated the particles are, the higher is the frictional surface between two laminar layers of the flow. This causes more energy dissipated and hence the peak increases at the mean velocity. In other words, the deviation of individual particle velocities from the mean value reduces with the elongation of particles.

3.3 COORDINATION NUMBER AND VOLUME FRACTION

In granular rheology analysis, coordination number and volume fraction are the two key parameters that are often utilized to understand the flow pattern. In this study, we consider the coordination number and volume fraction on the central plane of the segment perpendicular to the direction of flow. It was found that ellipsoidal particles have much higher coordination number and volume fraction than spherical particles.

The relationship between coordination number and volume fraction is of research interest in the previous studies [10]. The relationship is complex even for spherical particles, and related to particle properties, and operational and geometrical conditions. In general, it is

non-linear in a large range. But for some cases, it is linear in a certain range. To study the feature for the systems considered here, more cases with higher normal pressures have been considered. As shown in Fig. 6, the two properties maintain positive relationship for spherical particles, as well as for ellipsoidal particles in the range of coordination number considered, i.e., between 0.59 and 6.3 for spherical particles, and 10.8 and 12 for ellipsoidal particles. Further comparison indicates that the variation gradient of the coordination number with volume fraction is higher for ellipsoidal particles.

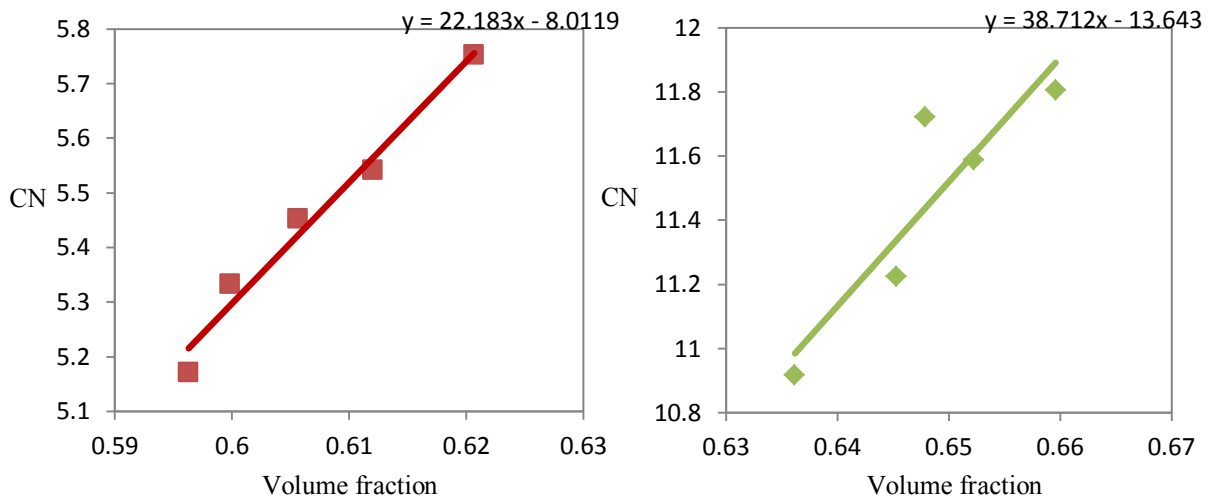


Fig. 6. Relationship between coordination number and particle volume fraction for spherical (left) and ellipsoidal (right) particles.

3.4 STRESS TENSOR ANALYSIS

In this section, stress tensors are microdynamically investigated for both cases of spherical and ellipsoidal particles. Fig. 7 shows the distributions of the stresses along the y axis direction. It can be seen that all stresses vary little along the y axis direction for the two cases. Of all the normal stresses, T_{zz} has the highest magnitudes, while T_{yy} the lowest. These results are similar to the findings in the previous studies of spherical particles [11]. The difference between the magnitudes of T_{yy} and T_{zz} for the two kinds of particles are not significant, due to the fact that the inter-particle forces in the y and z axis directions have similar values for the two cases. It can be clearly observed that T_{xx} for ellipsoidal particles is smaller than that of spherical particles while T_{xz} for ellipsoidal particles is higher than that of spherical particles. This is because the values of stresses are not only related to the values of the forces between particles, but also the directions of the branch vector connecting the mass centers of the particles in contact. Although the inter-particle forces in the x axis direction are larger for the case of ellipsoidal particles, the components of the branch vector in the x axis direction are

much smaller, resulting in smaller stress T_{xx} . The components of the branch vector in the z axis direction are much larger, so the magnitude of the shear stress T_{xz} is higher for ellipsoidal particles.

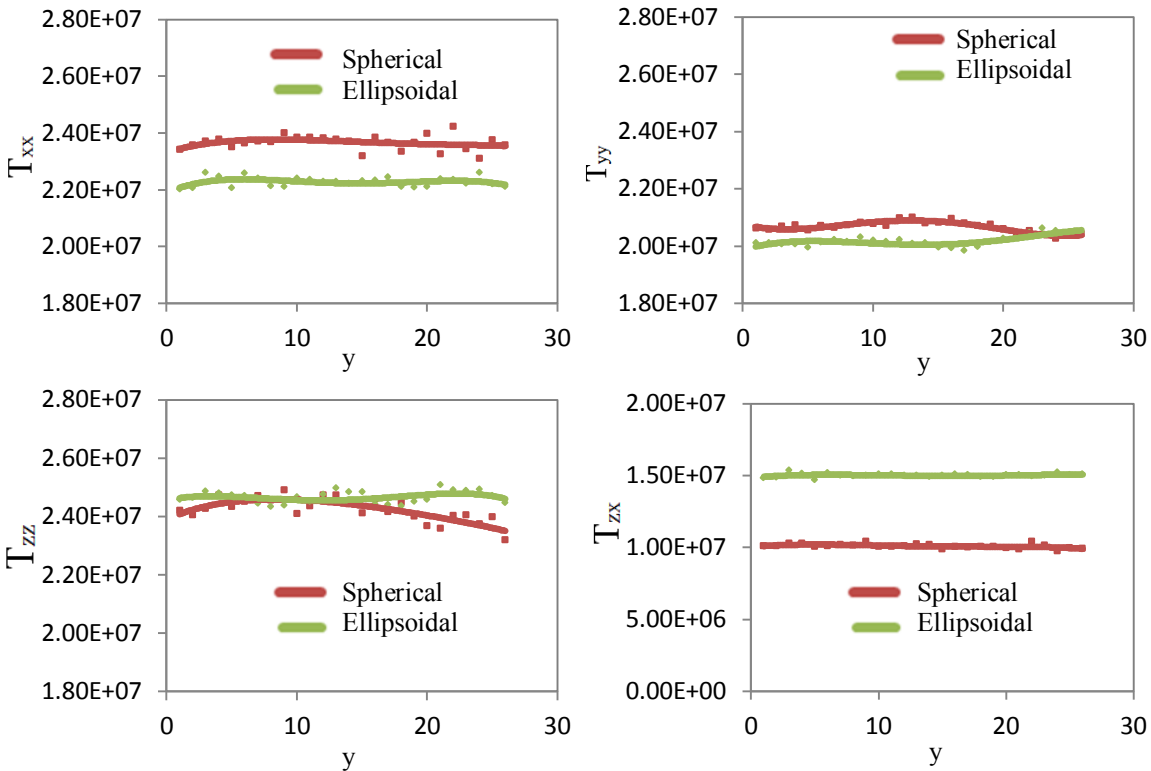
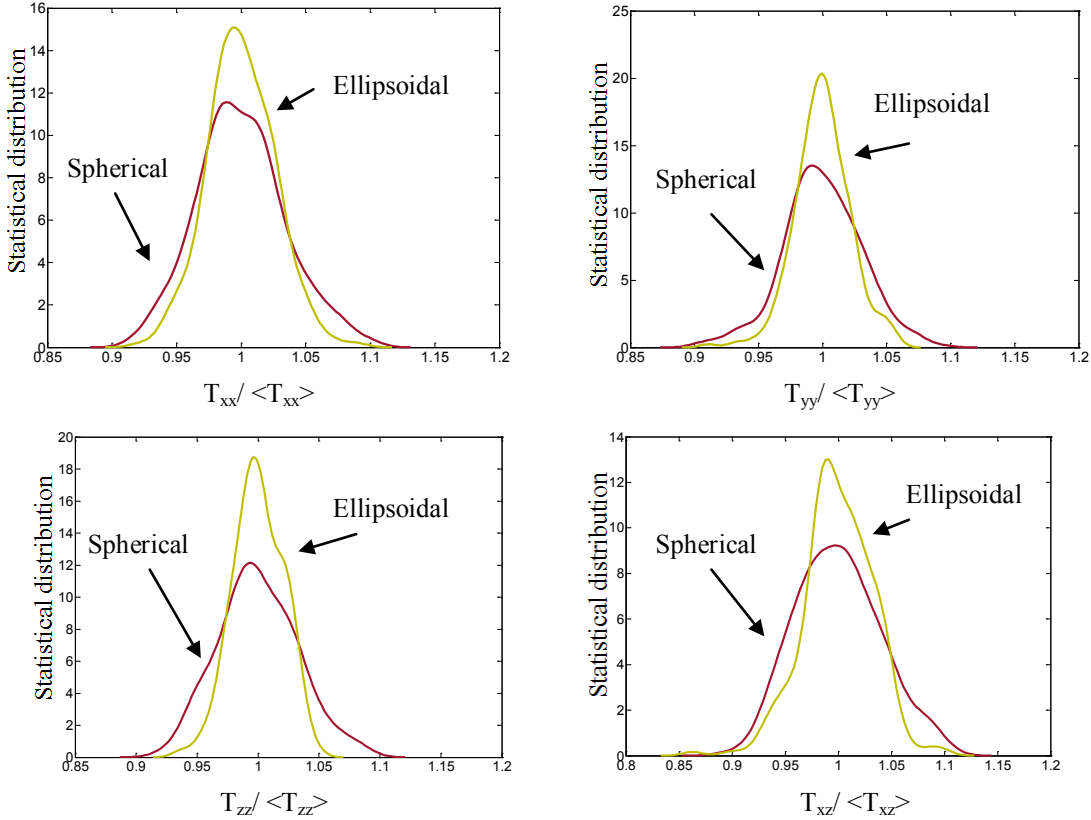


Fig. 7. Distributions of the stress tensor along the y- axis direction.

These stresses can be further analysed through their statistical distributions, as shown in Fig. 8. The trends are qualitatively similar to the result found for cohesive spherical particles in [11]. In all cases, it can be observed that ellipsoidal particle assembly has a higher peak but has less deviation from the mean. This is due to the particle alignment which orderly fashions the flow towards the direction of shear producing uniformity, and the force chains in ellipsoidal particle assembly which are created and destroyed less frequently than spherical particles. Normally, as the particles get more elongated, the weak force chains grow in percentage causing the less dispersion [12].

It is also observed that T_{yy} and T_{zz} for ellipsoidal particles have relatively higher peak while T_{xx} the lowest peak. This results from the fact that ellipsoidal particles are aligned with the flow direction (x-axis direction) and have less movements in the transverse directions (y- and z- axis directions), which causes more uniform distribution of T_{yy} and T_{zz} . On the other hand, the lowest peak of T_{xx} is attributed to the large impact of particles shearing in opposite directions, resulting in more deviation of T_{xx} from its mean value compared to other stresses.


 Fig. 8. Statistic distribution of the scaled stresses T_{xx} , T_{yy} , T_{zz} and T_{xz} in the yz-plane

4 CONCLUSION

While results on spherical particles assembly have been found to be qualitatively in agreement with the well-established knowledge, some interesting points have been identified demarking spherical and ellipsoidal particles. The major axes of ellipsoidal particles are approximately aligned with the direction of shear velocity of the flow, which is consistent with the previous studies. For both spherical and ellipsoidal particles, the linear velocity distributions are discovered. There is no significant difference for the two kinds of particles in terms of the velocity profile. Ellipsoidal particles have larger overall coordination number and volume fraction. Similar to spherical particles, the coordination number for ellipsoidal particles has a linear relationship with volume fraction. The stresses are also influenced by the shape of ellipsoidal particles. Especially, the ellipsoidal particle assembly has a much higher shear stress than spherical particles. Overall, ellipsoidal particle assembly has less dispersion in the distributions of velocity and stresses compared with spherical particles.

5 REFERENCES

- [1] Carr, J. and Walker D. An annular shear cell for granular materials. *Powder Technology* (1968) **1**(6): 369-373.
- [2] Cundall, P. A. and Strack, O. D. A discrete numerical model for granular assemblies. *Geotechnique* (1979) **29**(1): 47-65.
- [3] Zhu, H.P., Zhou, Z.Y., Yang, R.Y. and Yu, A.B. Discrete particle simulation of particulate systems: A review of major applications and findings. *Chemical Engineering Science* (2008) **63**: 5728 - 5770
- [4] Hertz, H. Über die Berührung fester elastischer Körper. *Journal für die reine und angewandte Mathematik* (1881) **92**: 156-171.
- [5] Deresiewicz, H. *Effects of an oscillating torsional couple on the contact surfaces of elastic spheres*. No. CU-TR-5. Columbia University of New York Dept. of Civil Engineering and Engineering Mechanics, (1953).
- [6] Zhu, H.P., Zhou, Z.Y., Yang, R.Y. and Yu, A.B. Discrete particle simulation of particulate systems: Theoretical developments. *Chemical Engineering Science* (2007) **62**: 3378 – 3396
- [7] Guo, Y., Wassgren, C., Hancock, B., Ketterhagen, W. and Curtis, J. Granular shear flows of flat disks and elongated rods without and with friction. *Physics of Fluids* (2013) **25**(6): 063304.
- [8] Campbell, C. S. Stress-controlled elastic granular shear flows. *Journal of Fluid Mechanics* (2005) **539**(-1): 273.
- [9] Taghavi R. Automatic clump generation based on mid-surface. In: D. Sainsbury et al. (eds). *Continuum and Distinct Element Modelling in Geomechanics*. Itasca, Minneapolis (2011) pp. 791-797.
- [10] Wang, X. Zhu, H. P. and Yu, A. B. Microdynamic analysis of solid flow in a shear cell. *Granular Matter* (2012) **14**(3): 411-421.
- [11] Aarons, L. and Sundaresan S. Shear flow of assemblies of cohesive granular materials under constant applied normal stress. *Powder Technology* (2008) **183**(3): 340-355.
- [12] Az'ema E. and Radja'i, F. Stress-strain behaviour and geometrical properties of packings of elongated particles. *Physical Review E* (2010) **81**: 051304.

NON-SMOOTH CONTACT DYNAMIC APPROACH FOR RAILWAY ENGINEERING: INVESTIGATION OF BALLAST BEHAVIOUR UNDER STABILISATION PROCESS

JEAN-FRANCOIS FERELLEC¹, ROBERT PERALES², PIERRE-EMMANUEL LAURENS¹, MICHEL WONE³, JULIA PLU¹ AND GILLES SAUSSINE¹

¹Direction Technique SNCF
6 av. François Mitterrand, 93574 La Plaine Saint Denis Cedex, France
congreso@sncf.fr

²AD'missions
20 rue Brunel, 75017 Paris, France

³ ITG
24-26 rue de la Pépinière, 75008 Paris, France

Key words: Ballast, railway, stabilisation, polyhedron, DEM, NSCD.

Abstract. Railway maintenance procedures include the stabilisation of ballasted tracks. The procedure of dynamic stabilisation which consists in vibrating laterally the rail while applying a vertical load is analysed using a discrete element code based on non-smooth contact dynamics. The ballast stones are modelled realistically using polyhedrons based on real ballast stones scans. The evolution of the compaction level and contact number between particles is analysed during the dynamic stabilisation process. A model is proposed to predict settlement. The results of simulation show the effectiveness of this maintenance procedure. It also points out the relevance of the model to predict settlement.

1 INTRODUCTION

Traffic on railway lines becoming faster, more frequent and with higher loads require very strict maintenance procedures of railway tracks. The compaction or stabilisation of ballasted tracks is essential as it impacts the lateral resistance of the track which counters the buckling force of rails. This is particularly the case of the very common long welded rails along which build up large forces due to temperature variation of up to seventy degrees in French standards.

Procedures to stabilise or compact ballasted tracks rely mainly on models based on empirical observations and the fundamental mechanical phenomena involved in the ballast during these procedures are not fully understood.

Experimental in-situ or laboratory testing campaigns to analyse the mechanical behaviour of the ballast during the different types of maintenance procedures are costly both in terms of time and budget. To avoid these constraints engineers in charge of maintenance have opted for the numerical approach among which the continuous method is the most popular. In the case of ballasted track behaviour analysis, this latter presents however limits in representing

the ballast material as it cannot reproduce the basic mechanics at the scale of the ballast stones which is essential in explaining the global behaviour of the ballast. The discrete element method (DEM) which models a granular material as interacting particles [1] is a more adequate numerical approach to analyse the mechanical behaviour of railway ballast and particularly the phenomena occurring during ballast stabilisation.

DEM has been developed in multiple variants in which the contact between the particles can be treated in different ways and where the shape of the particles is modelled in a more or less realistic way. In this latter the most common shape is the sphere as it facilitates the interaction treating process between the particles easier. Spheres however usually render the behaviour of real granular materials only in a qualitative way because of their simple shape. Efforts have been made to get models giving more quantitatively reliable results leading to some improvement [2-6] but failing to catch the irregular shape of real particles. In the last decade, newer models managed to reproduce the shape of real particles and in particular ballast stones [7-14] but they remained quite demanding in terms of computation time. In parallel of these recent realistic shape models, emerged a class of DEM taking into account the polyhedral shapes of ballast stones and based on an approach called non-smooth contact dynamic (NSCD).

The NSCD method is based on an implicit time integration of the equations of dynamics and a non-smooth formulation of steric exclusion and friction between particles [15-16]. This method requires no elastic repulsive potential and no smoothing of the Coulomb friction law for the determination of the contact forces between the particles as the conventional DEM models mentioned before would. For this reason, the simulations can be performed with large time steps compared to molecular dynamics or explicit DEM approaches.

In this paper, we propose an investigation of the process of ballast stabilisation using NSCD. In this process, the railway sleepers are loaded laterally along their main axis with a cyclic load and vertically with a constant simultaneous load in order to compact the ballasted track. A three-sleeper track section is modelled using LMGC90 an NSCD code where the ballast stones are represented by polyhedrons of irregular shapes based on real ballast particles scans and the sleepers by polyhedrons also based on regular geometry of real sleepers. Two different approaches are used to load the middle sleeper: an analytical vibration model and a sleeper acceleration spectrum measured in situ during a dynamic stabilisation. The dynamic stabilisation is preceded by a tamping process to prepare the ballast as it would on a real track. Finally the evolution of the solid fraction or compaction level of the ballast under the middle sleeper is analysed to verify the efficiency of the whole procedure.

The first section of this paper describes the NSCD approach and the corresponding LMGC90 code used in the analysis. The second part presents the dynamic stabilisation process in details and explains the configuration of the simulation. The final part discussed the results of the simulations in terms of evolution of the solid fraction, settlement and number of contacts between particles below the sleeper before concluding.

2 NON-SMOOTH CONTACT DYNAMIC MODEL

In this study, the simulations were carried out by means of the non-smooth contact dynamics (NSCD) method with irregular polyhedral particles. In this section we present the properties of this numerical method and compare it to the classical numerical approach called

molecular dynamics (MD).

The NSCD method is based on implicit time integration and non-smooth formulation of mutual exclusion and dry friction between particles in case of contact [15-17]. The equation of motion for each particle is written in term of differential inclusions in which velocity jumps replace accelerations. The unilateral contact interactions and Coulomb friction law are represented as set-valued force laws according to convex analysis.

The approach is characterized by a time-stepping approximation, and in this work we use a time integrator like theta-method. The implementation of the time-stepping scheme requires that the contacts taken into account in the considered step are geometrically described: definition of contact normal and contact location.

The contact law is defined by a non-smooth relation between normal force and normal relative velocity and Signorini conditions. The Coulomb friction law friction force and sliding velocity at a contact are not related together via a mono-valued function. The collision law is taken into account by introducing a restitution coefficient which relates the relative velocities before and after contact. In our simulations where we consider a dense packing, we choose normal and tangent restitution coefficients equal to zero.

In an assembly of particles, for each time step, the aim is to solve the core problem in order to find for each contact between particles the local relative velocities and the local reactions. This interaction problem is solved by an iterative solver called non-linear Gauss-Seidel which consists in solving a single contact problem with other contact forces treated as known and consequently updating interaction, until a certain convergence criterion is fulfilled.

At a given step of evolution, all kinematics constraints implied by enduring contacts and the possible rolling of some particles over others are simultaneously taken into account, together with the equations of dynamics, in order to determine all velocities and contact forces in the system. The method is thus able to deal properly with the non-local character of the momentum transfers, resulting from the perfect rigidity of particles in contact. The NSCD method makes no difference between smooth evolution of a system of rigid particles during one time step and non-smooth evolutions in time due to collisions or dry friction effects.

The MD-like methods are based on regularisation schemes where impenetrability is approximated by a steep repulsive potential and Coulomb's law by a viscous or elastic regularised friction law, to which smooth computation methods can be applied. In this case the choice of a viscous parameter or elastic properties is not easy in particular with particles with irregular shape. This regularisation implies the choice of smaller time step in order to preserve the stability of the integration scheme compared to the NSCD approach. The uniqueness is not guaranteed by the NSCD approach for perfectly rigid particles in absolute terms. However, by initialising each step of calculation with the forces calculated in the preceding step, the set of admissible solutions shrinks to fluctuations which are basically below the numerical resolution. In MD-based simulations, this "force history" is encoded by construction in the particle positions.

We used here the NSCD based LMGC90 code which is a multipurpose software developed in Montpellier (France) and capable of modelling a collection of deformable or non-deformable particles of various shapes (spherical, polyhedral, or polygonal) by different algorithms [18].

3 SIMULATION OF DYNAMIC STABILISATION OF BALLASTED TRACK

3.1 Dynamic stabilisation concept

During maintenance, a ballasted track follows a specific sequence of procedures. The first step usually consists of correcting the geometry of the track by tamping. In the tamping process, each sleeper is lifted up before a set of vibrating tampers is inserted into the ballast on each side of the sleeper until their ends are located under the sleeper level. The ballast under the sleeper is then squeezed by these tampers. The tampers are finally retracted and moved to the next sleeper. After tamping the lateral resistance of the track is reduced hence the track requires stabilisation before being operational. This stabilisation can be performed naturally by relying on successive passages of trains of regular traffic at reduced speed leading to a relatively long period before the track is fully operational. This phase can however be speeded up by using the process of dynamic stabilisation.

The dynamic stabilisation is performed using equipment rolling on the rails, vibrating laterally the track and applying a vertical load simultaneously. The degree of stabilisation can be controlled by tuning the vibration frequency, vertical load or rolling speed. The objective of dynamic stabilisation is to reorganise the ballast stones, increase the lateral resistance of the track and homogenise the compaction of the ballast. It constitutes a faster alternative to the natural stabilisation using regular traffic.

3.2 Configuration of simulation

The track section sample used to analyse the dynamic stabilisation process is illustrated in figure 1. It presents a shoulder on one side and a vertical containing wall on the other side as if a contiguous line existed. 90000 ballast particles, which are represented by polyhedrons based on real ballast stone scans, are generated in a parallelepiped volume and settled under gravity. Three sleepers are created inside the ballast at the right positions replacing some of the ballast stones. The shoulder of the track is then created by removing some of the ballast stones. The sample obtained this way is a non-dense state. The middle sleeper is then tamped using a set of sixteen tampers (figure 1) before going through the dynamic stabilisation process. In this case the outside sleepers act as boundary conditions and are not tamped or stabilised. The friction coefficient between the particles and between the particles and sleepers has been determined equal to 0.8, the density of the ballast stone to 2700kg/m^3 .

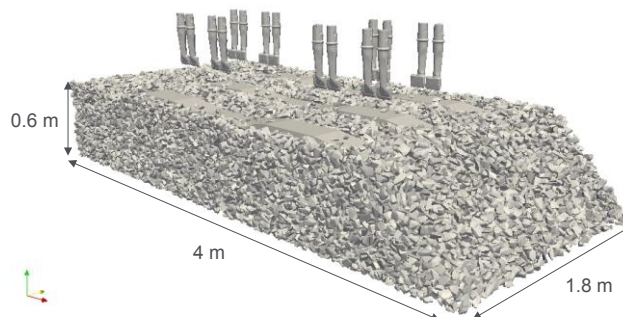


Figure 1: Track section sample configuration

3.3 Loading pattern

Two approaches were used to load the middle sleeper for the dynamic stabilisation. The first consist of exciting the sleeper using a signal based on the specifications of the stabilising equipment (figure 2.a). The lateral velocity of the sleeper oscillates with a sinusoidal amplitude evolution corresponding to the displacement of the stabilising equipment along the track. Two sinusoidal periods are implemented to represent two successive stabilising equipments. Simultaneously two vertical loads shaped in a sinusoidal way are applied corresponding to the displacement of the same two successive stabilising equipments.

The second approach used the lateral acceleration spectrum of a sleeper measured in-situ during a campaign of dynamic stabilisation. The lateral velocity obtained from the acceleration spectrum by simple integration is then applied to the middle sleeper as in the first approach. As for the vertical load, is it similar to the one used in the first approach. For industrial confidentiality reason, the lateral acceleration spectrum is not divulged in this paper.

Both approaches are based on a dynamic stabilisation process with a vibration frequency of 25Hz and amplitude of 2.5mm and a rolling speed of 2000m/h.

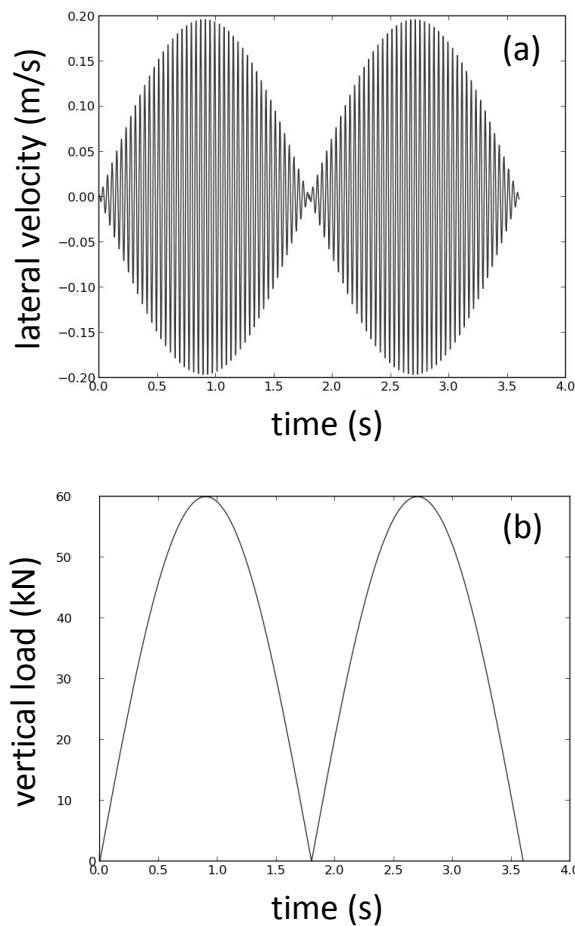


Figure 2: Lateral velocity of sleeper (a) and applied vertical load (b)

4 SIMULATION RESULTS

4.1 Compaction level

Compaction level or solid fraction, that is the fraction of solid phase inside the ballast, is one of the measurable parameters in simulations that help to measure the efficiency of the stabilisation process: a substantial gain in solid fraction is an indicator of a successful stabilisation. Solid fraction evolution is measured here under the middle sleeper for the stabilisation and also the tamping phase beforehand.

Figure 3 shows the evolution of the solid fraction gain during the tamping process. At the beginning of the process the solid fraction presents a slight decrease which is linked to the insertion of the tampers which disturb the ballast stones arrangement. Then during the squeezing phase of tamping, the solid fraction is progressively increased to reach a level of 6% approximately. The simulation clearly shows that tamping improves the compaction of the ballast under the sleeper.

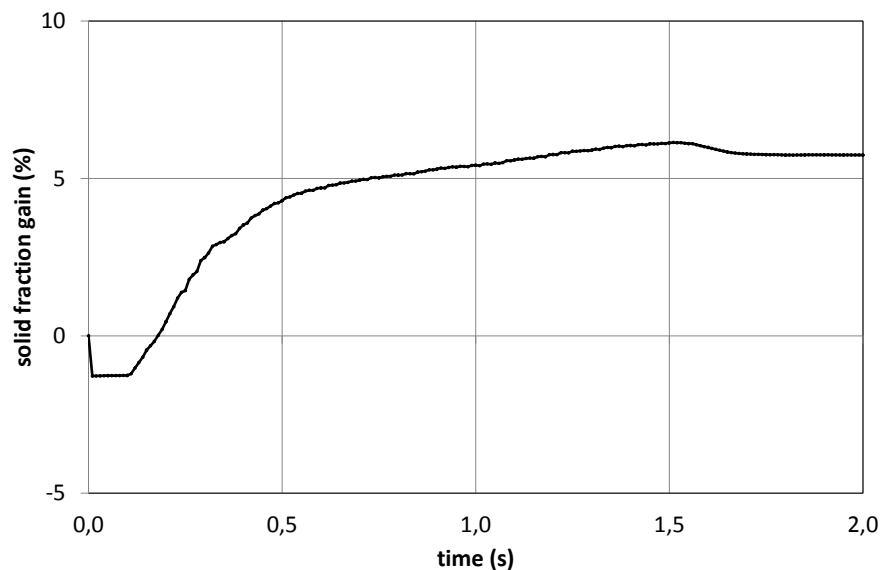


Figure 3: Solid fraction gain evolution during tamping

Figure 4 shows the evolution of the solid fraction in the simulation of the stabilisation using the first approach to model the vibration of the sleeper, the vibration model represented on figure 2. During application of both vibration waves, it shows a progressive gain of solid fraction with a decreasing rate reaching a final gain level of 4%. The first vibration wave offers a 3% gain higher than the second one only equal to 1%. The action of the vibration waves is not linear with time. Any additional wave would probably give a solid fraction gain lower than 1%. These results seems to show that the dynamic stabilisation process as described above, that is using two waves of vibrations, is enough to stabilise the ballasted track. Any additional passage of the equipment would not bring any substantial improvement.

The approach using the sleeper lateral acceleration spectrum presents a similar trend but with slightly lower gains in compaction. Figure 5 shows the evolution of the solid fraction in the simulation of the stabilisation using this second approach. The total gain reaches a

maximum of around 3.3%. This difference can be explained by the fact that the acceleration spectrum was measured with a type of sleeper different from the simulation one. But as for the first approach, the first vibration wave offers a higher gain than the second wave: 2.5% compared to less than 1%. These second simulation results confirm that two waves are enough to stabilise the track.

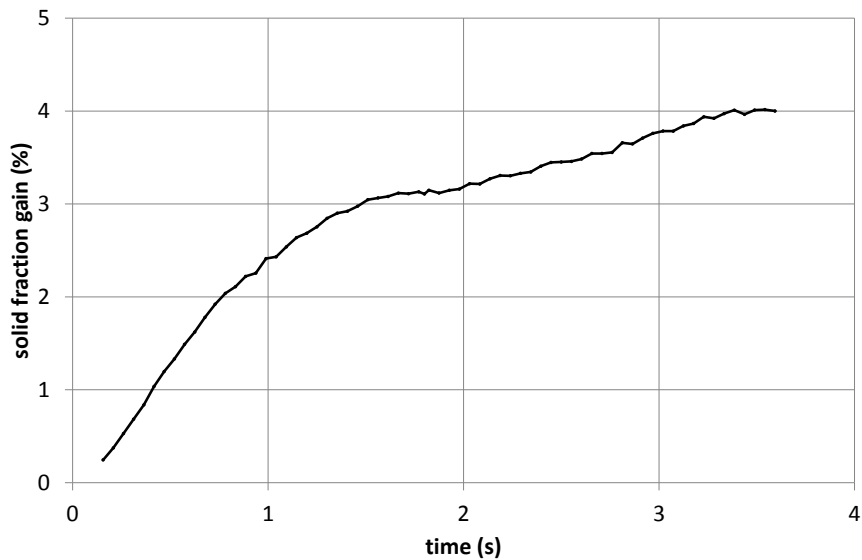


Figure 4: Solid fraction gain evolution during dynamic stabilisation using vibration model

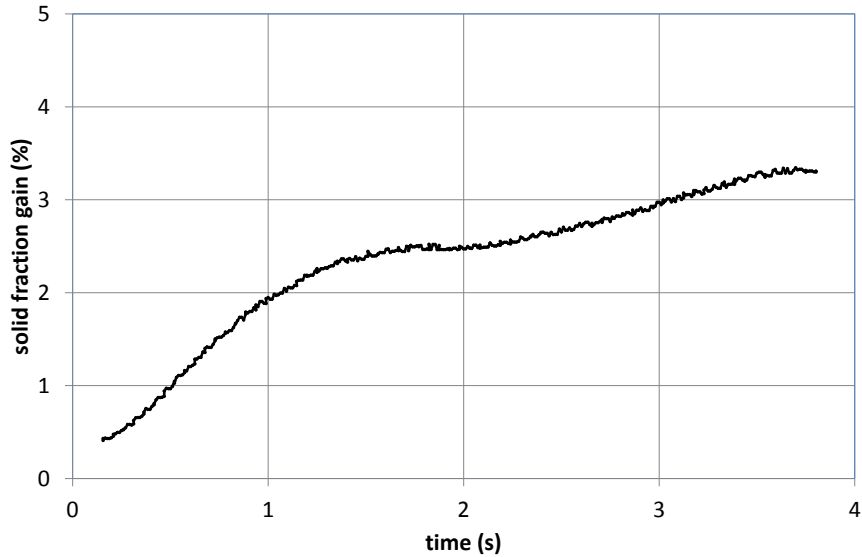


Figure 5: Solid fraction gain evolution during dynamic stabilisation using acceleration spectrum

4.2 Settlement

Figures 6 and 7 respectively show the settlement of the middle sleeper for the analytical

vibration model and the spectrum approach. As expected the first approach, which gives the higher compaction gain, offers a higher final settlement of approximately 35mm while the second approach reaches 28mm. In agreement with the compaction, the first vibration wave gives a higher settlement than the second one. There is a clear correlation between the settlement and the solid fraction gain. The dynamic stabilisation is associated with a settlement of the track.

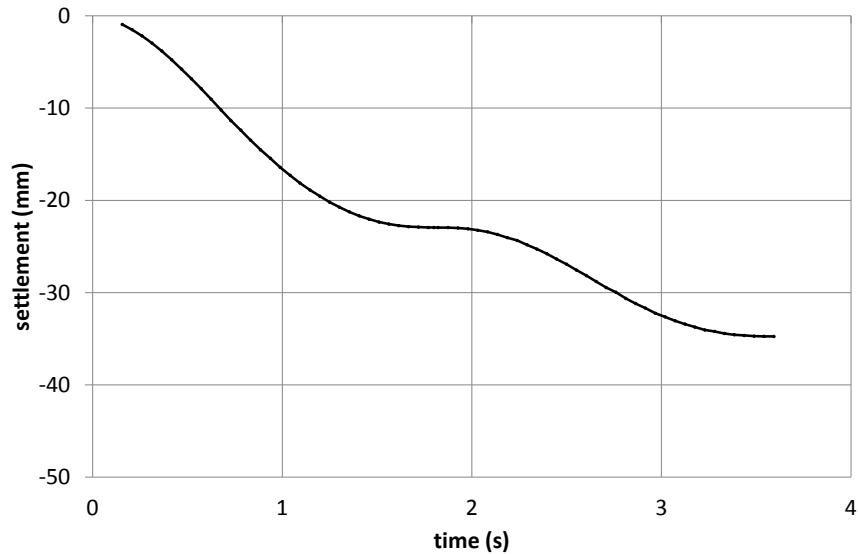


Figure 6: Settlement during dynamic stabilisation using vibration model

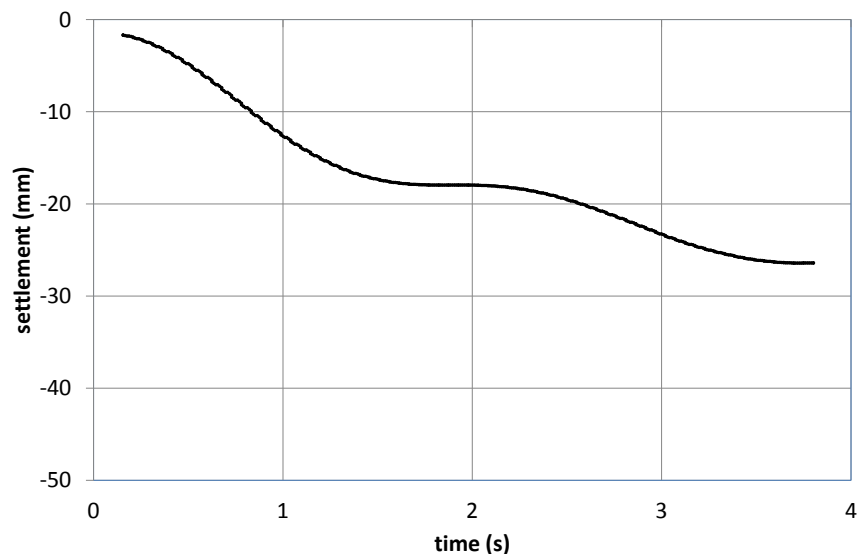


Figure 7: Settlement during dynamic stabilisation using acceleration spectrum

Previous simulations have been performed at SNCF (main railway company in France) to establish a model to estimate the settlement z of a track after a dynamic stabilisation which is based on research performed on pile insertion using vibrations [19]. Under a vertical load F

and lateral vibration of amplitude a and frequency ν , the sleeper settlement z is estimated using the following equation:

$$z^2(t) = k \cdot a \cdot l \cdot t \cdot \nu \cdot 2\pi \frac{F}{m \cdot g} \quad (1)$$

where k is a constant function of the sleeper shape, l the width of the sleeper, t the time and m the mass of ballast below the sleeper. As explained in section 3, the stabilising equipment is moving along the track at a constant speed. Subsequently each sleeper will actually be subject to the lateral vibration and vertical load illustrated on figure 2: a 25Hz lateral vibration and vertical load with varying amplitudes. In the end, the sleeper settlement is actually the combination of successive settlements due to vibrations of different amplitudes a_i and loads of different levels F_i :

$$z^2(t) = \sum_{i=1}^n k \cdot a_i \cdot l \cdot t \cdot \nu \cdot 2\pi \frac{F_i}{m \cdot g} \quad (2)$$

Figure 8 shows a comparison of sleeper settlement during stabilisation obtained from the settlement model and from the simulation using the analytical lateral vibration and vertical load models of figure 2. Both curves present very similar trends pointing out the relevance of the settlement model proposed. It shows that this settlement model can be used to estimate track settlement assuming parameter k is known for the type of sleeper used on the track.

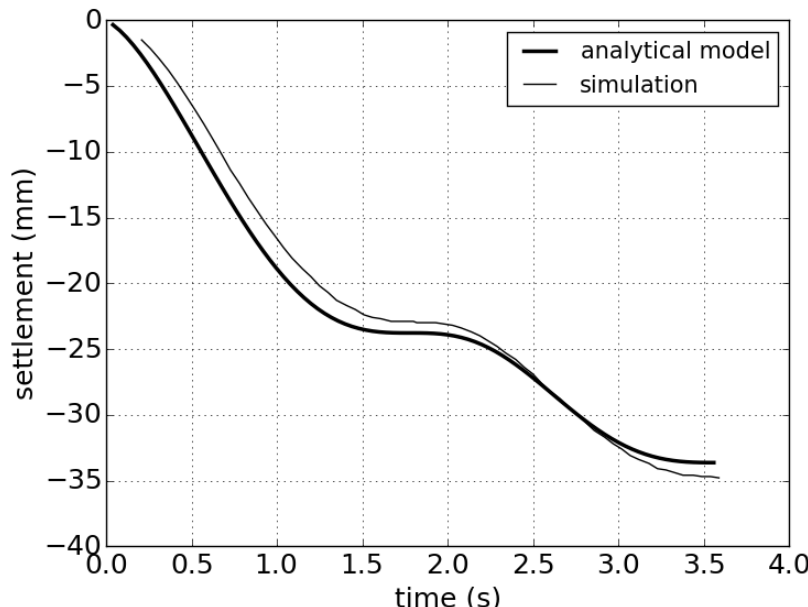


Figure 8: Comparison of settlement during dynamic stabilisation obtained from settlement model (—) and from simulation with analytical vibration model (—)

4.3 Number of contacts

The evolution of the number of contact per ballast stone, or coordination number, helps

understanding the phenomena occurring during the dynamic stabilisation process. Figures 9 and 10 show the evolution of the coordination number during the stabilisation for both vibration models for the ballast located under the middle sleeper. Each vibration wave clearly decreases the coordination number from 4 to 3.5. Each wave actually fluidises to a certain extent the ballast hence reducing the number of contacts between ballast stones. As a vertical load is applied simultaneously, this fluidised phase promotes the compaction of the ballast vertically. The rearrangement of the ballast stones is facilitated. The fluidisation temporarily reduces the resistance to shear of the ballast as a granular material. After stabilisation the coordination number returns to its initial value of 4. In its final more compacted state, the ballast has hence probably reached a higher level of shear strength which in turn translates into a higher lateral resistance of the sleeper.

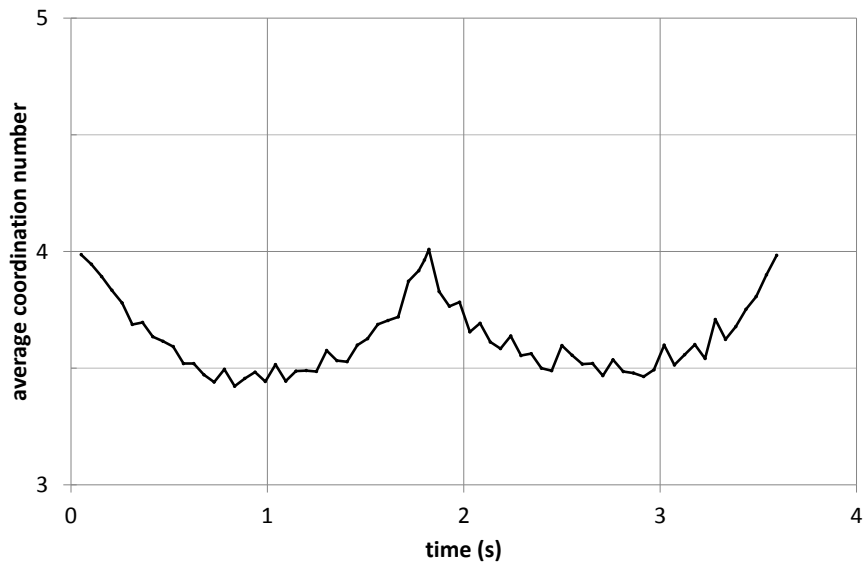


Figure 9: Evolution of coordination number during dynamic stabilisation using vibration model

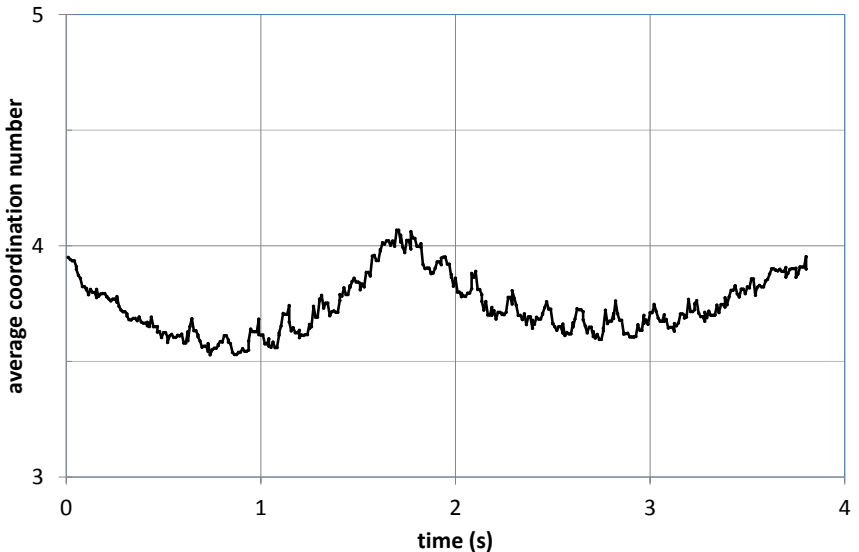


Figure 10: Evolution of coordination number during dynamic stabilisation using acceleration spectrum

5 CONCLUSIONS

- Simulations of the procedure of dynamic stabilisation of ballasted railway tracks have been performed using a DEM code based on NSCD approach which represents the ballast stones as realistic polyhedrons. The gain in compaction level showed that dynamic stabilisation is an adequate procedure to stabilise track. The evolution in compaction gain, settlement and average contact number between ballast stones, also showed that two waves of lateral vibrations, associated with a vertical load, are sufficient to fully compact the ballast and that any additional wave does not bring any substantial improvement.
- A sleeper settlement model for dynamic stabilisation is proposed. A comparison with the simulation settlement shows its relevance for estimation of settlement during dynamic stabilisation process.
- Further simulations are underway to analyse the effect of the stabilisation speed on the compaction. Additional simulations will also be undertaken to check the effect of this method of stabilisation on the lateral resistance of the track in order to establish a model for lateral resistance gain for dynamic stabilisation.

REFERENCES

- [1] Cundall, P.A. and O.D.L. Strack, A discrete numerical model for granular assemblies. *Geotechnique*, 1979. 29(1): p. 47-65
- [2] Williams, J.R. and A.P. Pentland, Superquadric and model dynamics for discrete elements in interactive design. *Eng. Comput.*, 1992. 9: p. 115-127.
- [3] Lin, X. and T.T. Ng, A three-dimensional discrete element model using arrays of ellipsoids. *Geotechnique*, 1997. 47(2): p. 319-329.
- [4] Mustoe, G.G.W. and M. Miyata, Material flow analyses of non-circular-shaped granular media using discrete element methods. *J. Eng. Mech.*, 2001. 127(10): p. 1017-1026.
- [5] Cleary, P.W., Large scale industrial DEM modelling. *Engineering Computations*, 2004. 21(2-4): p. 169-204.
- [6] Pournin, L., et al., Three-dimensional distinct element simulation of spherocylinder crystallisation. *Granular Matter*, 2005. 7(2-3): p. 119-126.
- [7] Hart, R., P.A. Cundall, and J. Lemos, Formulation of a three-dimensional distinct element method - Part II : Mechanical calculations for motion and interaction of a system of many polyhedral blocks. *Int. J. Rock Mech. Min. Sci. Geomech. Abstr.*, 1988. 25(3): p. 117-125.
- [8] Matsushima, T., et al., Discrete element simulation of an assembly of irregularly shaped grains: quantitative comparison with experiments, in 16th ASCE Engineering Mechanics Conference, 2003: University of Washington, Seattle.
- [9] Abou-Chakra, H., J. Baxter, and U. Tuzun, Three-dimensional particle shape descriptors for computer simulation of non-spherical particulate assemblies. *Advanced Powder Technology*, 2004. 15(1): p. 63-77.
- [10] Wang, L.B., J.Y. Park, and Y.R. Fu, Representation of real particles for DEM simulation

- using X-ray tomography. *Construction and Building Materials*, 2007. 21(2): p. 338-346.
- [11] Price, M., V. Murariu, and G. Morrison, Sphere clump generation and trajectory comparison for real particles, in Discrete Element Methods Conference 2007: Brisbane, Australia.
- [12] Lee, Y., et al., A packing algorithm for three-dimensional convex particles. *Granular Matter*, 2009. 11(5): p. 307-315.
- [13] Ferellec, J.-F. and G.R. McDowell, A method to model realistic particle shape and inertia in DEM. *Granular Matter*, 2010. 12(5): p. 459-467.
- [14] Ferellec, J.-F. and G.R. McDowell, Modelling realistic shape and particle inertia in DEM. *Geotechnique*, 2010. 60(3): p. 227-232.
- [15] J.J. Moreau, An introduction to unilateral dynamics in Novel approaches in civil engineering, Lecture Notes in Applied and Computational Mechanics, Frémond,M. and Maceri,F., Springer-Verlag 1-46.
- [16] J. Moreau, Some numerical methods in multibody dynamics: application to granular materials. *European J. Mech. A Solids*, 13(4, suppl.), pp. 93-114, 1994. Second European Solid Mechanics Conference (Genoa, 1994).
- [17] G. Saussine, C. Cholet, P.E. Gautier, F. Dubois, C. Bohatier, J.J. Moreau, Modelling ballast behaviour under dynamic loading. Part 1: A 2D polygonal discrete element method approach, *Comput. Methods Appl. Mech. Eng.* 195 (2006) 2841 - 2859.
- [18] F. Dubois and M. Renouf Numerical strategies software architecture to the modelling of dynamical systems in interaction. Application to multibody dynamics, in Multibody 2007 proceedings, 25-28 June 2007 - Politecnico di Milano, Milano, Italy
- [19] E. Azema, Etude numérique des matériaux granulaires à grains polyédriques: rhéologie quasi-statique, dynamique vibratoire, application au procédé de bourrage du ballast. PhD thesis, university of Montpellier 2, France, October 2007.

PARAMETRIC EVALUATION FOR POWDER FLOWABILITY USING A FREEMAN RHEOMETER: A DISCRETE ELEMENT METHOD STUDY

Z. YAN, S. K. WILKINSON, S. A. TURNBULL, E. H. STITT, AND M. MARIGO

Johnson Matthey Technology Centre
PO Box 1, Belasis Avenue, Billingham, Cleveland, TS23 1LB, UK
E-mail: Michele.Marigo@matthey.com; web page: <http://www.matthey.com>

Key words: FT4 rheometer, Powder Flow, Discrete Element Method, Multisphere,

Abstract. A discrete element method (DEM) using the Hertz-Mindlin and JKR models was used to model the flowability measurement on a cohesive particulate material in the Freeman FT4 powder rheometer. An assessment of DEM parameters was carried out to understand the operation of this equipment and to study the correlation between inter-particle properties and flowability. Simulation results indicate that the static and rolling friction coefficients, and JKR cohesion energy density are all negatively correlated with powder flowability, meaning that an increase in any of these parameters results in a decrease in powder flowability. At higher level friction, the force and torque have a larger measurement deviation, which is possibly due to local jamming in the particle bed. The powder flowability decreases as particle size increases for the current coarse grained system. Particles size distribution width has very little effect on the flowability changes. Particles with lower sphericity tend to have lower flowability possibly due to particle interlocking. It was demonstrated that rolling friction has a large effect on flowability for a give non-spherical particle shape.

1 INTRODUCTION

Flowability is the ability of granular media and powders to flow, and can influence the process performance during powder handling, including hopper discharge, powder feeding, blending, mixing, and die filling. Additionally, this can influence product quality. Flowability depends on multiple physical properties (for example: particle size, particle size distribution, shape factors, and surface texture) and environmental variables (temperature, humidity, pressure, etc.) [1, 2]. Recently, the Freeman FT4 powder rheometer (Freeman Technology, Malvern, UK) has become an increasingly popular device for measuring the flow energy of particulate materials. The characterisation consists of a dynamic test regime, in which the flow resistance encountered for an impeller moving within a powder bed is assessed.

Currently, the FT4 is commonly used for comparative studies and ranking of powder flow properties, but not yet as a quantitative support tool for process design or a possible calibration tool for DEM simulation [3]. Bharadwaj et al. [4] studied the effects of particle size, shape, size distribution and friction on force and torque on the impeller in the FT4. In this work non-cohesive glass beads were used to understand the operation of the FT4 in conjunction with a discrete element method (DEM). Hare et al. [5] showed in DEM simulations for cohesive salinized glass beads that measured torque had the biggest impact on flow energy measurement in the FT4. Following this literature precedent, the objectives of this paper are thus:

- (1) To carry out a broader investigation using DEM for a better understanding on the FT4

operation.

- (2) To investigate how input DEM interparticle properties govern the bed bulk response during the downward cycle for the dynamic test. This includes:
- Particle-particle properties such as static and rolling friction coefficients and cohesion energy density.
 - Particle geometrical factors such as particle size, particle size distribution (PSD), shape.

2 METHODS AND PROCEDURES

2.1 Discrete Element Method (DEM)

In this work, the soft-sphere DEM approach developed by Cundall and Strack [6] using the Hertz-Mindlin contact model [7, 8] was utilised to calculate the normal and tangential contact forces. Cohesion of particles was modelled with the Johnson-Kendall-Roberts (JKR) model [9]. An additional term $F_{coh} = kA$ was added to normal contact force, where A is the particle contact area; k is the cohesion energy density in J/m³ [10].

The FT4 DEM simulations were carried out using the open source DEM code, LIGGGHTS [11].

2.2 Description of the FT4

The FT4 measures the axial force and torque on the impeller blade that is rotated and moved downwards and upwards through the powder bed [12]. The force and torque reflect the resistance to powder flow.

The total flow energy is defined as the sum of the work done by both the axial and rotational motions of the impeller, given by [5],

$$\text{Flow Energy} = \int_0^h \left(\frac{T}{R \tan \alpha} + F \right) dh \quad (1)$$

where T is the torque on impeller blade; R is the radius of the impeller and α is the helix angle of impeller movement; F is the downward force acting on the blade; h is the vertical travel distance of impeller through the powder bed. The flow energy measured during the downward movement was utilised for the comparisons whereas it is assumed that low energy represents good flowability and conversely a high energy value represents poor flowability.

2.3 DEM input parameters

The FT4 equipment has the vessel made of borosilicate glass while the impeller blade was made of stainless steel. The DEM material property inputs for these were selected from the literature and are listed in the Table 1. While interaction between particle and walls such as restitution and friction between particles and the walls (blade and vessel) may have an effect on the bulk flow behaviour, the other material and wall properties were held constant and assigned with nominal ‘guessed’ values. This was done in order to reduce the numbers of varied parameters and consequently, simulations. In support of this assertion it is noted that Bharadwaj et al. [4] reported that the static and rolling friction between particle and wall have a much weaker impact compared with inter-particle friction in the DEM simulations of the FT4 using glass beads. Inter-particle properties such as inter-particle particle static (μ_{s-pp}) and rolling (μ_{r-pp}) friction coefficients, and cohesion energy density (k_{pp}) were varied to investigate their effect on the powder flow.

Table 1: DEM input parameters. Underlined the ones varied in this study.

Material parameters	Symbols	Values	Refs.
Young modulus vessel (GPa)	E_v	64	[4]
Young modulus blade (GPa)	E_b	190	[13]
Young modulus particle (GPa)	E_p	0.02	
Poisson's ratio vessel (-)	ν_v	0.25	[4]
Poisson's ratio blade (-)	ν_b	0.30	[13]
Poisson's ratio particle (-)	ν_p	0.2	
Particle density (kg/m^3)	P	2500	
Coefficient of restitution particle-blade (-)	ε_{pb}	0.7	
Coefficient of restitution particle-vessel (-)	ε_{pv}	0.7	
Coefficient of restitution particle-particle (-)	ε_{pp}	0.85	
Static friction coefficient particle-blade (-)	μ_{s-pb}	0.30	
Static friction coefficient particle-vessel (-)	μ_{s-pv}	0.30	
Static friction coefficient particle-particle (-)	μ_{s-pp}	<u>0.05-0.50</u>	
Rolling friction coefficient particle-blade (-)	μ_{r-pb}	0.05	
Rolling friction coefficient particle-vessel (-)	μ_{r-pv}	0.05	
Rolling friction coefficient particle-particle (-)	μ_{r-pp}	<u>0.05-0.45</u>	
Cohesion energy density particle-blade (J/m^3)	k_{pb}	50	
Cohesion energy density particle-vessel (J/m^3)	k_{pv}	50	
Cohesion energy density particle-particle (J/m^3)	k_{pp}	<u>10-10⁵</u>	

Due to the computational power limitations, a grain-coarsening scheme was used to reduce particle number and increase time step in this study, in the same manner as reported by other researchers [4]. Spheres ranging from 0.6 to 3mm were used in this study.

2.4 Multi-sphere (MS) approach

It is commonplace in DEM simulations to represent non-spherical shapes using the multi-sphere method wherein the non-spherical particles are approximated by conjoining multiple spheres and integrating them as one rigid body [14]. In this study the effect of particle shapes was investigated by looking at particle sphericity. Sphericity (Φ_s) is defined as $\Phi_s = \pi^{1/3}(6V_p)^{2/3}/A_p$, where V_p is the volume of the object, A_p is its surface area [15]. Table 2 reports the details about the MS clumps used in this investigation.

They consist of monosized small spheres, with the same volume equivalent diameter ($d_v = 3$ mm), but differing in sphericity values. V_p and A_p were calculated by assuming that a MS clump has an ideal shape. V_p and A_p were calculated by assuming that a MS clump has an ideal shape. For example, for a cube clump $V_p=a^3$ and $A_p=6a^2$.

Table 2: Characteristics of the MS clumps. N is the total number, and d_0 is the diameter of the constituent spheres.

Shapes	Geometry (ideal shape)	MS clumps	Size (mm)	N	d_0 (mm)	Φ_s
Sphere			$d = 3.0$	1	3.0	1.0
Cylinder			$l = 2.620$ $H = 2.620$	27	0.874	0.87
Cube			$a = 2.418$	64	0.644	0.81
Tetrahedron			$c = 4.932$	56	0.940	0.67

2.5 DEM simulation procedures

Prior to a test in the FT4, a conditioning preparation was conducted to ensure the particle bed have a reproducible initial condition [12]. Several repeat tests on monosized spherical particles at $\mu_{s\text{-pp}} = 0.50$, $\mu_{r\text{-pp}} = 0.45$, and $k_{\text{pp}} = 10^5 \text{ J/m}^3$ were carried out first. This test condition was expected to have the worst powder flowability for the parameter range selected (shown in the following sections), and might experience particle-bridging during natural packing under gravity. Additionally, a flow energy change due to particle rearrangement was expected after conditioning. However, it was shown that the conditioning stage has a negligible effect on the calculation for the flow energy. Therefore for all simulations with spherical particles, the conditioning step was ignored to reduce the central processing unit (CPU) time cost; a decision corroborated by other publications [4]. For simulations with non-spherical particles, the clumps consist of too many fine constituent particles, which make the computation even more CPU and time consuming. Thus the conditioning stage was also ignored. During the test cycle, the impeller moves downwards whilst being rotated anticlockwise with a helix angle of 5° and a tip speed of 100 mm/s.

3 PARAMETRIC STUDIES

3.1 Effect of static and rolling friction

Fig. 1 plots the force (Fig.1a) and torque (Fig.1b) on the blade, and the resultant flow energy (Fig.1c) via Eq. (1) for different friction levels. It is seen that, compared with the baseline test ($\mu_{s\text{-pp}} = 0.05$, $\mu_{r\text{-pp}} = 0.05$), an increase in rolling friction coefficient ($\mu_{s\text{-pp}} = 0.05$, $\mu_{r\text{-pp}} = 0.45$) seems to have very little effect on the force, but a very significant effect on the torque. Therefore torque, compared with force, is more sensitive to rolling friction, which implies that flow resistance to rotational motion of blade is larger than to axial motion [4]. An increase in static friction coefficient ($\mu_{s\text{-pp}} = 0.50$, $\mu_{r\text{-pp}} = 0.05$) has a significant effect on both the force and torque, resulting in an increase in flow energy. Force and torque at a high level of static friction show larger deviation than at a high level of rolling friction, possibly due to the local jamming of the powder as the blade is subject to higher flow resistance. On an average basis, static friction has a major contribution to flow resistance, and rolling friction has a lesser one. A more rigorous method combining Design of Simulations (DoS) and

Principal Component Analysis (PCA) is currently being developed to study the parameter sensitivity in greater detail.

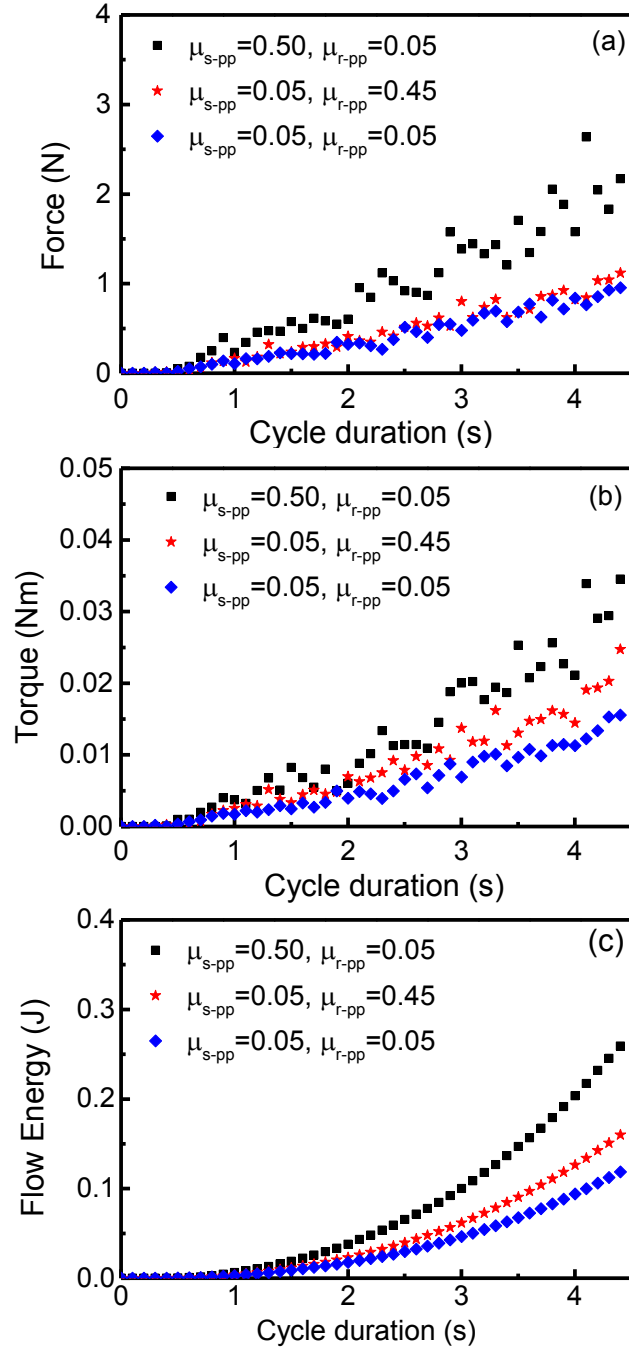


Figure 1: The force, torque on blade and flow energy during test cycle with spherical monosized particles (2mm in diameter). Conditions: $E_p=0.02\text{GPa}$, $\varepsilon_p=0.85$, and $k_{\text{pp}}=10^5\text{ J/m}^3$

3.2 Effect of cohesion energy density

Fig. 2 shows the effect of the cohesion energy density. It is seen that at the low level of static and rolling friction, the effect of cohesion energy density is small on calculated flow energy, while its effect is more significant at a high level of static and rolling friction. This suggests that cohesion energy and the friction are positively cross-correlated. The interaction

of these parameters is something which will require further scrutiny through design of simulations (DoS) and sensitivity analysis approaches.

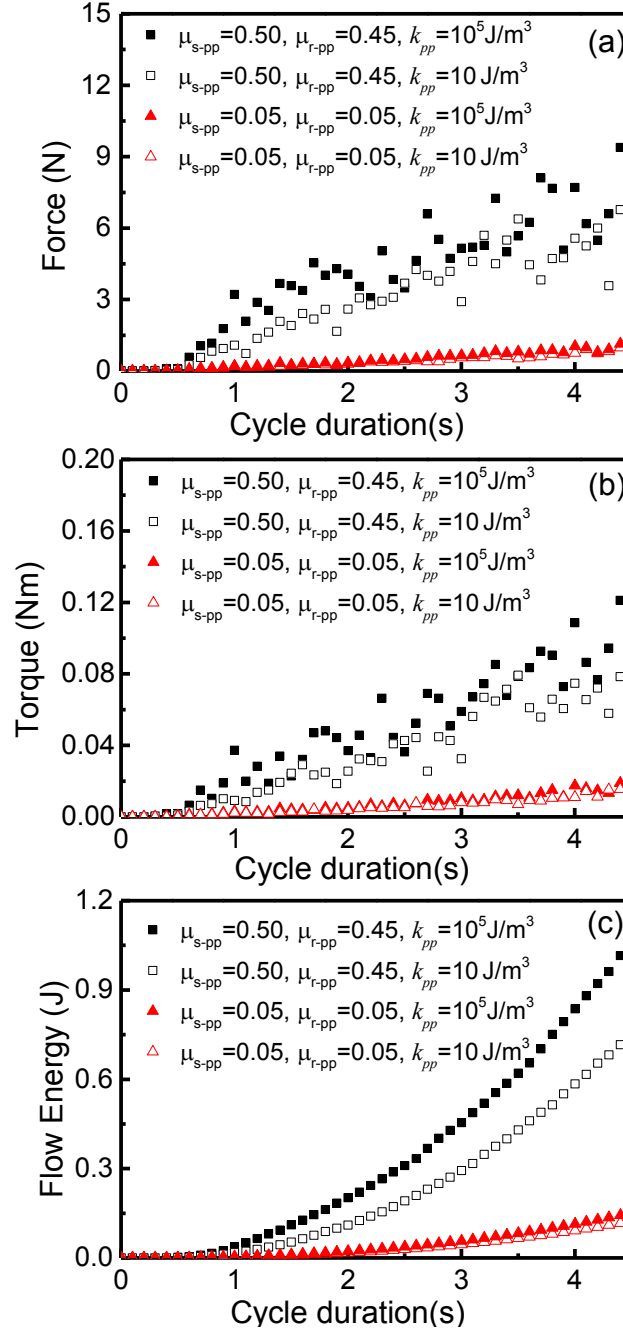


Figure 2: The force, torque on blade and flow energy during test cycle with spherical monosized particles (2mm in diameter). Conditions: $E_p=0.02\text{GPa}$, and $\varepsilon_p=0.85$.

3. 3 Effect of particle size

Fig. 3 shows the effect of particle size on the force, torque and flow energy measurement. It shows that the force and torque increase as the particle size increases. Bharadwaj et al. [4] found the same trend with non-cohesive glass beads in DEM simulations. Experimental data in [16] shows that, for a cohesive powder, cohesivity increases as particle size decreases. This

is due to smaller sized powders having larger contact areas, resulting in lower flowability. Other inter-particle forces such as van der Waals and electrostatic forces also contribute to the size dependency of flowability for fine powder. However, the role of such forces was not considered in this study. Thus, the simulations in this study are not comparable with experimental observations of fine, cohesive materials. In this coarse-grained cohesive system, the flowability of powder decreases as the particle size increases. This is possibly because the effect of the cohesion energy density, at the chosen value in this study, was not prominent in a coarse-grained system. Liu et al. [17] found the flowability of pulverised coal (40-240 μm) decreased as its mean size increased in the FT4 basic flow energy. However, in their measurement the cohesivity of the coal was unknown. Fine particles need to be considered and more comprehensive contact models should be included.

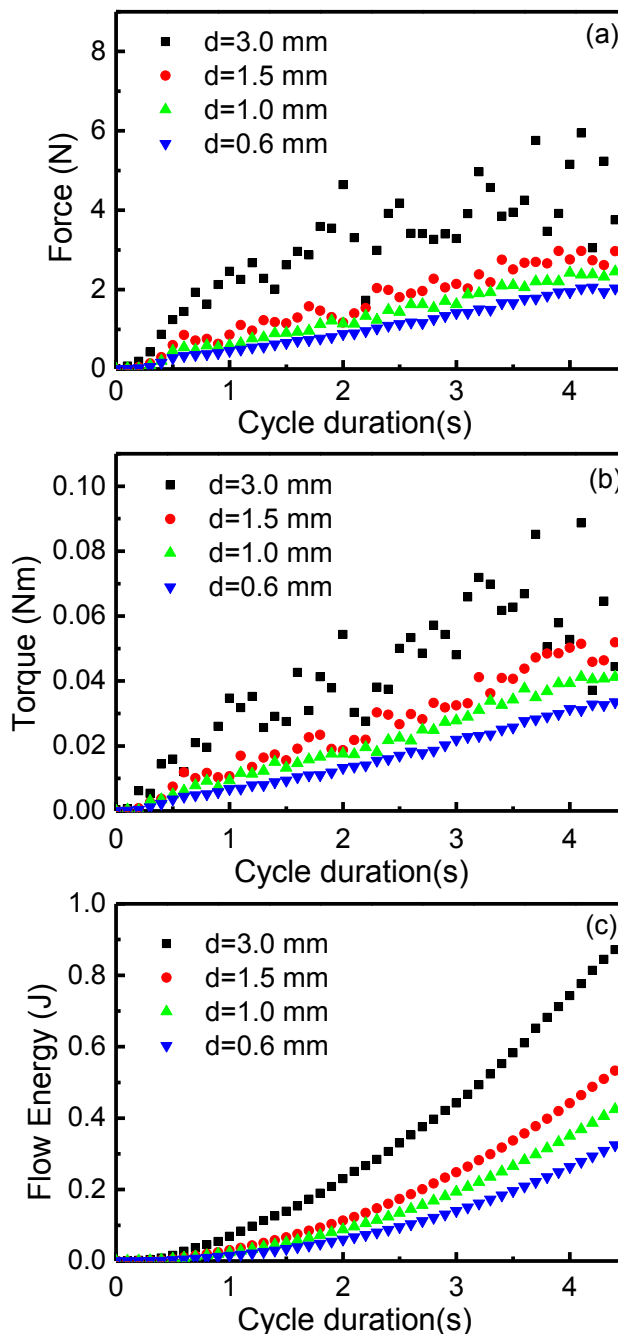
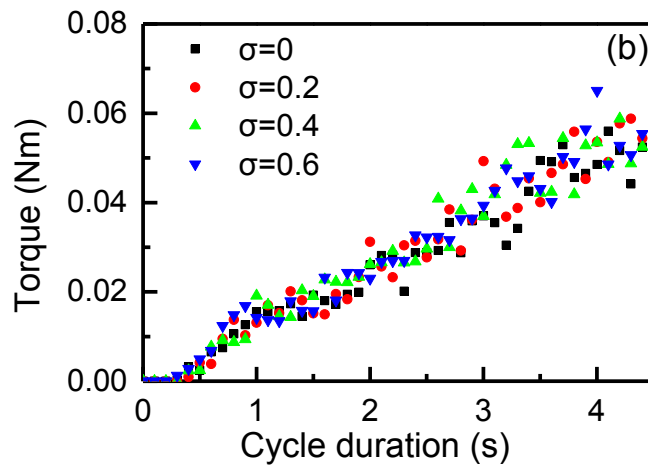


Figure 3: Effect of particle size on the force, torque and flow energy. Conditions: $E_p=0.02\text{GPa}$, $\varepsilon_p=0.85$, and $k_{pp}=10^5 \text{ J/m}^3$

3. 4 Effect of particle size distribution (PSD)

Powders with PSD (number based) in a normal distribution $f(d)=\frac{1}{\sigma\sqrt{2\pi}}\exp(-\frac{(d-d_0)^2}{2\sigma^2})$

were modelled in this study. The powders have the same mean size $d_0=2 \text{ mm}$ but with different distribution standard deviation ($\sigma=0, 0.2, 0.4$ and 0.6). Smaller σ value means a narrower PSD (specially, $\sigma=0$ for monosized powder). Particles under $600 \mu\text{m}$ (diameter) were cut off as presence of a lot of fine particles is CPU and time costly. Fig. 4 shows the PSD effect on force, torque and flow energy during the test cycle. It seems in this study, the particle size distribution width has a very small effect on flow resistance. This indicates that the uncertainties in the PSD within the current range would not significantly affect the force, torque and flow energy. For cohesive powders, a broader PSD will impede flowability. This is due to the fact that a powder with differently sized particles enables more efficient particle packing. A higher packing density leads to an interlocking effect as the small particles fill in the gaps between larger ones. Also the higher contact surface area is expected to contribute larger cohesive force [18]. For particles with a number based normal distribution, the volume fraction of the small particles is rather low. Furthermore, the fine particles (under $600\mu\text{m}$) were discounted for the aforementioned reason. For these two reasons, the difference in total contact the surface area is not prominent for different σ values, explaining an insignificant of effect of PSD on flowability. However, for the sample with monosized particles, force, torque and flow energy were slightly lower than for samples having a normal distribution in particle size.



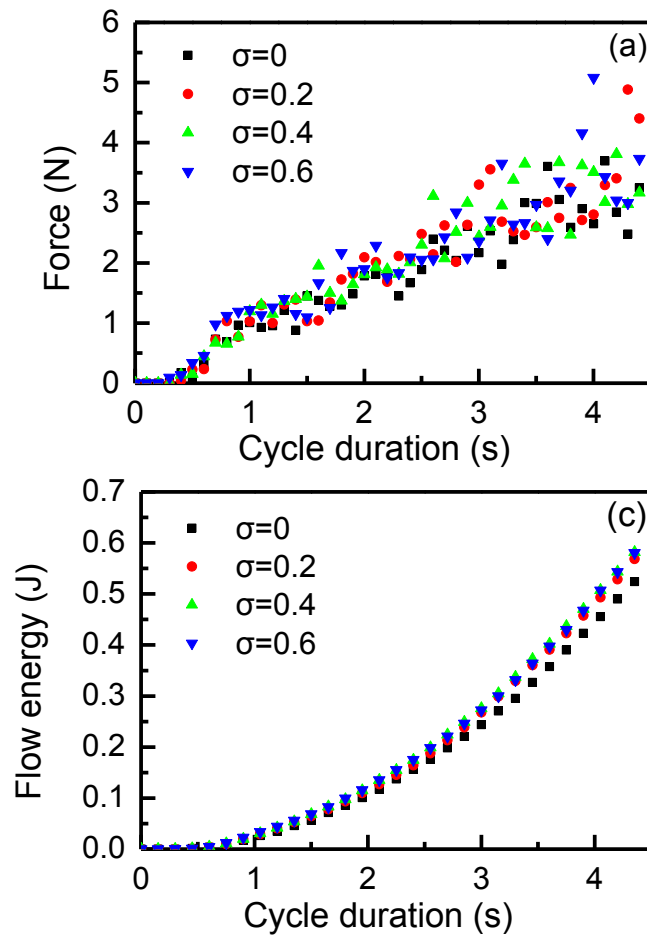


Figure 4: Effect of particle size distribution on the force, torque and flow energy. Conditions: $E_p=0.02\text{GPa}$, $\varepsilon_p=0.85$, and $k_{pp}=10^5 \text{ J/m}^3$

3.5 Effect of shape factors

Fig. 5 plots the results for the bed material consisting of different shaped clumps (see Table 2); showing the increase in force, torque and flow energy as the sphericity of the clumps decreases. Considering that the clumps have the same volume equivalent size d_v , it was presumed that the difference in measurements is not due to the difference in clump size (as shown in Section 3.3 where particle size has an effect) but in the sphericity. Generally, the sphericity of the particles represents the rolling resistance of the particles; the more angular the clump, the larger the rolling resistance, and hence the lower the flowability of the powder. Cleary et al. [19] and Santos et al. [20] both found a lower sphericity of irregular shaped particles led to lower flowability of powders. Furthermore, when the rolling friction was also considered for the clumps, it was seen that the presence of rolling friction can play an extra contribution to the decrease of flowability. Markauskas et al. [21] found both the shape factor and rolling friction should be considered to model the flow behaviour of the irregular shaped powders in a hopper.

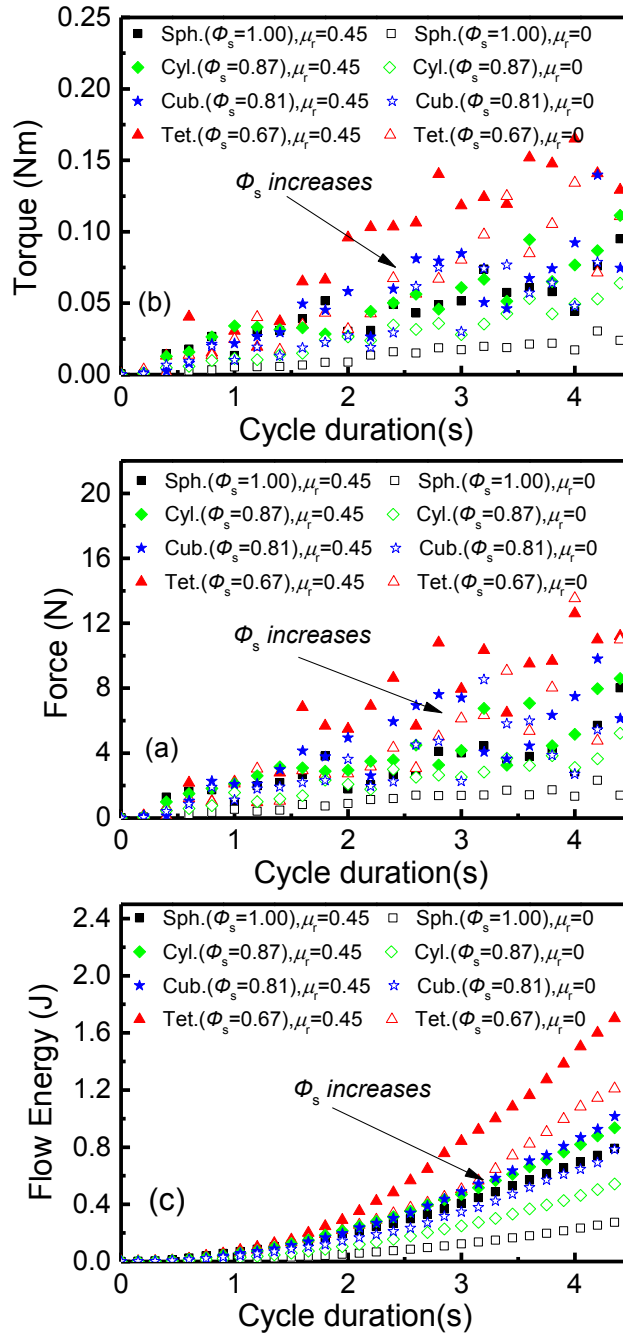


Figure 5: Effect of sphericity of non-spherical particles on the force, torque and flow energy. Conditions: $E_p=0.02\text{GPa}$, $\varepsilon_p=0.85$, and $k_{pp}=10^5 \text{ J/m}^3$

4. CONCLUSIONS

A DEM approach was used to model the flowability of a cohesive powder in the FT4 powder rheometer. A parametric study was carried out to investigate the effect of inter-particle properties such as inter-particle static and rolling friction coefficients, cohesion energy density, particle size, size distribution, and shape factors on flowability in a coarse-grained system. The important findings are as follows:

- An increase of the particle-particle static or rolling friction coefficients, or cohesion energy density, leads to increase of the force and torque on the blade and flow energy,

indicating a decrease of the flowability of powder. At a high level of friction, the force and torque have larger measurement deviation, possibly because of local jamming the material bed. Friction coefficients and the cohesion energy density are positively cross correlated.

- In the current coarse-grained system, the flowability of particles decreases as particle size increases. Conversely, a lower flowability for finer powders was observed in experiments from the cited literature. This is due to the fact that other interparticle force effects, playing a role for finer real particles, are not considered in this DEM model.
- Particle with a normal distribution in particle size shows lower flowability than that with monosized particles; however, it seems that the particle distribution width has a very small effect on flowability change. This might be due to the volume fraction of smaller particles is rather low for a number based normal PSD in all the simulations and the contribution of the increased surface area is not prominent.
- A multisphere approach was used to account for the irregular shape of particles by approximating them as rigid clumps. A powder whose particles have lower sphericities tends to have lower flowability due to a mechanism of particle interlocking. It is also shown that rolling friction should be also incorporated to better predict the flowability of a powder with irregular shapes.

The current proposed DEM has been used to investigate the operation for the FT4 rheometer during the downward cycle. Further work is being carried out to understand:

- The effect of input parameter sensitivity and interactions by using a more rigorous method combining Design of Simulations (DoS) and Principal Component Analysis (PCA) similarly to the one developed in Ref. [22].
- The inclusion of fine particles and experimental validation to verify the current DEM and grain coarsening scheme.
- The effect of segregation due to particle size effects.

5. ACKNOWLEDGMENTS

This work is supported by the IPROCOM Marie Curie initial training network, funded through the People Programme (Marie Curie Actions) of the European Union's Seventh Framework Programme FP7/2007-2013/ under REA grant agreement No. 316555.

6. REFERENCES

- [1] Ganesan, V., Rosentrater, K.A., and Muthukumarappan, K. Flowability and handling characteristics of bulk solids and powders - a review with implications for DDGS. Biosyst. Eng. (2008)101:425-435.
- [2] Yang, S., and Evans, J.R.G. Metering and dispensing of powder; the quest for new solid freeforming techniques. Powder Tech. (2007)178:56-72.
- [3] Pantaleev S, Yordanova S, Ooi J., and Marigo M. Powder Mixing - an Experimentally Validated DEM Study Joint 5th UK-China & 13th UK Particle Technology Forum, 13rd-15th 2015, Leeds, UK.
- [4] Bharadwaj, R., Ketterhagen, W.R., and Hancock, B.C. Discrete element simulation study of a Freeman powder rheometer. Chem. Eng. Sci. (2010) 65:5747-5756.

- [5] Hare, C., Zafar, U., Ghadiri, M., Freeman, T., Clayton, J., and Murtagh, M. Analysis of the Dynamics of the FT4 Powder Rheometer. *Powder Tech.* (2015) doi:10.1016/j.powtec.2015.04.039
- [6] Cundall P.A, Strack O.D.L. A discrete numerical model for granular assemblies. *Geotechnique* (1979) 29:47-65.
- [7] Hertz H. Ueber die Berührungs fester elastischer Körper. *J. Reine Angew Math.* (1881) 92: 156-171.
- [8] Mindlin R.D. Compliance of elastic bodies in contact. *ASME Trans. J. Appl. Mech.* (1949) 16: 259-268.
- [9] Johnson, K.L., Kendall, K., and Roberts, A.D. Surface energy and the contact of elastic solids. *Proc. Math. Phys. Eng. Sci.* (1971) 324:301-313.
- [10] Grima, A.P., and Wypych, P.W. Development and validation of calibration methods for discrete element modelling. *Granul. Matter* (2011)13:127-132.
- [11] Kloss, C., Goniva, C., Hager, A., Amberger, S., and Pirker, S. Models, algorithms and validation for opensource DEM and CFD-DEM. *Prog. Comput. Fluid Dy.* (2012) 12:140-152.
- [12] <http://www.freemantech.co.uk>
- [13] An, Z., Ying, A., and Abdou, M. Application of discrete element method to study mechanical behaviors of ceramic breeder pebble beds. *Fusion Eng. Des.* (2007) 82:2233-2238
- [14] Amberger, S., Friedl, M., Goniva, C., Pirker, S., and Kloss, C. Approximation of objects by spheres for multisphere simulations in DEM. In *ECCOMAS 2012*, 10-14 Sept., 2012, Vienna, Austria
- [15] Wadell, H. Volume, Shape and Roundness of Quartz Particles. *J. Geology* (1935) 43: 250-280.
- [16] Hou, H., and Sun, C.C. Quantifying effects of particulate properties on powder flow properties using a ring shear tester. *J. Pharma. Sci.* (2008) 97:4030-4039.
- [17] Lu, H., Guo, X., Liu, Y., and Gong, X. Effect of Particle Size on Flow Mode and Flow Characteristics of Pulverized Coal. *KONA Powder Part J.* (2015) 32:143-153
- [18] Xu X., Yao, S., Han, N. and Shao B. Measurement and influence factors of the flowability of microcapsules with high-content β -carotene. *Ch. J. Chem. Eng.* (2007) 15:579-585.
- [19] Cleary, P.W., and Sawley, M.L. DEM modelling of industrial granular flows: 3D case studies and the effect of particle shape on hopper discharge. *Appl. Math. Model* (2002)26:89-111.
- [20] Dos Santos, E.G., da Silva Carvalho, L.C., Mesquita, A.L.A., Mesquita, A.L.A., and Gomes, L.M. A study about the particle shape effect using the discrete element method (DEM). *15th Brazilian Congress of Thermal and Engineering*, 10-13, Nov., Belem, PA, Brazil
- [21] Markauskas, D., and Kačianauskas, R. Investigation of rice grain flow by multi-sphere particle model with rolling resistance. *Granul. Matter* (2011)13(2):143-148.
- [22] Yan Z., Wilkinson S.K., Stitt E.H., and Marigo M., Discrete Element Modelling (DEM) input parameters: understanding their impact on model predictions using statistical analysis, *Computational Particle Mechanics* (2015) (under review).

POWDER COMPACTION WITH POLYGONAL PARTICLES BUILT FROM RADIALLY EXTENDING ONE-DIMENSIONAL FRICTIONAL DEVICES

FRITZ ADRIAN LÜLF¹, PETER WRIGGERS

¹ Institute for Continuum Mechanics
Leibniz University of Hannover
Appelstr. 11, D-30167 Hannover, Germany
luelf@ikm.uni-hannover.de, <http://www.ikm.uni-hannover.de/>

Key words: Granular Materials, powder compaction, DEM, Contact Problems, Prandtl bodies

Abstract. Powder compaction is a major ingredient in a wide range of production techniques for objects of every day importance. Diverse applications – from pharmaceutical tablets to metallic and ceramic parts, where compaction is usually a part in the sintering process – are covered by current technology. The aim of cold compaction is to increase the relative density of the part.

Due to the granular nature of the powder material compaction is random process which requires careful mastering and comprehensive understanding. The experimental access to compaction processes, even as simple ones as uniaxial compaction, are limited. Therefore simulation of compaction processes offers the opportunity to improve understanding of powder compaction.

The Direct Element Method (DEM) simulates the powder as individual particles. These particles are distinct from each other and the forces applied to the entire powder are equilibrated by the contacting force between the particles. Usually, an explicit time integration, with or without considering dynamic effects, allows the particles to move and the powder to be compacted.

Especially for metallic powders the plastic deformation of individual particles plays an important role and has a perceptible influence up to the macroscopic scale of the whole part. This leads to efforts to formulate a DE method in which individual particles are discretized as distinct FE models. Yet, such approach is deemed too costly for the simulation entire parts.

Therefore a new approach for plastic particle deformation has been devised. The particles are simulated as 'hedgehogs' of one-dimensional frictional devices. The frictional devices form spikes that extend in a radial way from the center of the particle. The tips of the spikes are connected and the connections form the edges of the polygonal particles. The contacts between the particles are found by geometric means as intersections

of the spikes of one particle with the edges of the particle's contact partner. This indents the spike and its frictional device generates forces that act on the two particles. Multiple contacts between two particles are allowed and concave particles can be treated intrinsically.

Preliminary results indicate that this new approach to model plastic particles might bridge the gap between sufficiently realistic behaviour of the plastic particles and low computational effort. However, for now, the results are based on two-dimensional proof-of-concept simulations and, for the sake of simplicity, the springs in the spikes are linear and the friction is rate-independent and perfectly plastic. These model assumption already offer considerable liberties to tune the plastic behaviour of the particles to experimental results.

1 INTRODUCTION

In the simulation of the compaction of metal powder the defining factor is the inter-particle contact. Ideally it has to capture the entire physics of real-world particle interaction. It can be easily imagined that the contact involves elastic and plastic behaviour of the particles and both responses are likely to be highly non-linear.

A feasible concept is based on capturing of the elastic/plastic responses on the level of contact, as e.g. done by [1]. He uses rigid particles and contacts between them as separate entities. In fact the paradigm of object oriented programming promotes this view [2]. Whenever two, otherwise rigid particles come into contact a contact object between those two particles is constructed. This contact object stores all information relevant to the interaction between the particles. In particular, this could be information on the plastic deformation.

Obviously a problem arises once the powder changes its topology. Such topology changes are more present in uniaxial compaction than in isostatic compaction [3]. Supposing that two particular particles detach, the contact object is deleted and all information on contact is lost. Should these particles come into contact again, they would start over unaffected from the previous contact states. Even if the contact object for this particular pair of particles is stored for the case that the two particles should reconnect at a later time, the plastic deformation in the contact remains exclusive to these two particles. Should one of the two particles come into a contact with a third particle this would be a contact between two pristine particles, unaffected by the plastic deformation of the first particle.

This problem is usually solved by assuming that while new contacts are established, especially during the early phases of compaction when there is still rearrangement, the contacts on one particle are not mutually influencing each other [4]. This assumption will fail when e.g., later during the compaction, sliding planes occur in the powder [5]. Then the particles are already deformed to an extent that the different contacts acting on

one particle are interacting while new contacts are established between already deformed particles.

The solution of this problem is obviously that the history of contacts has to remain at the level of the particles, and not at the level of the contacts. Outside the framework of DEM it is possible to eliminate the particles and to concentrate on the contacts alone. This can be achieved by introducing beam networks, see [6]. But inside the framework of DEM a particle is the central and only entity.

One possible approach is the Meshed Discrete Element Method (MDEM), where each particle is defined by a distinct finite element mesh [7, 8]. This approach offers the possibility for each particle to deform and remain in a deformed state after the resolution of a contact if plastic deformation occurred during the contact. Furthermore different contacts can interact at one particle. Depending on the mesh-size, the chosen material model, and the contact behaviour between the finite elements of two discrete meshed particles nearly every imaginable behaviour can be simulated.

However, there is a considerable drawback to the MDEM. Due to the required number of finite elements per particle and the contact search between the finite elements, the overall number of particles that currently can be simulated in a powder with the MDEM is counted in dozens rather than hundreds or even thousands. Therefore the MDEM is at the moment no feasible alternative to rigid particles whose plastic deformations are treated at the levels of the contacts.

This paper presents a novel approach that combines plastic deformation at the level of the particles at relatively modest computational costs. In this method polygonal particles are built from radially extending one-dimensional frictional devices or, for short, from hedgehog particles.

IN the following the concept of hedgehog particles is explained. Starting with a brief motivation for polygonal particles and it will be described how the frictional devices are arranged inside the particle. In the next steps the contacts between particles and the dynamics of the particles are described. In a closing section a proof-of-concept simulation is presented.

For the time being the hedgehog particles are limited to two dimensions. Thus one can focus on the main ingredients without the complexity of three-dimensional geometry. The aim of presenting a proof-of-concept simulation also supports the decision of remaining in two dimensions. The long term aim is to simulate powder compaction with topology changes and plastic deformation of the particles.

2 POLYGONAL PARTICLES BUILT FROM RADIALLY EXTENDING ONE-DIMENSIONAL FRICTIONAL DEVICES

2.1 Polygonal particles

The basic idea of deformable polygonal particles goes back to at least [3]. He and his co-workers observed experimentally that spherical copper particles deform to become

Polyhedra if compacted. Recently [9] revived the concept by formulating a repulsive force between rigid polygonal shapes. The force is formulated based on a potential in the overlapping area between two polygonal shapes. This presented work is based on these investigations and extends rigid polyhedra to deformable, polygonal shaped particles.

2.2 Perfectly plastic spring-friction-element

The spring-friction-elements form the spikes of the “hedgehog”. They determine the deformation behaviour of the particle. The perfectly plastic spring-friction-element is also known as Prandtl-body. It can be implemented as a function that returns a force f for a prescribed displacement ϑ . Its internal state is described by the total deformation ϵ and the plastic deformation ϵ_p . The mechanical properties are determined by Young’s modulus E , the yield stress σ and the flow variable γ . The reader is referred to the introductory chapter of [10] for more information. The geometrical properties of the spring-friction-element are described by the initial length $l^{(0)}$ and the area of the cross section A . Thus the force f can be expressed as $E A \epsilon$. The current length is $l = \epsilon l^{(0)}$ at any given time. The spring-friction element for the “hedgehog” particle includes in its implementation some additional checks to allow a force-less detachment from another particle during the resolution of a contact.

2.3 Hedgehog particles

The particle is defined as a “hedgehog” of n spring-friction-elements, each element forming a “spike”. Figure 1 displays such a particle. The center of the particle is positioned at x_{part} and y_{part} . This point is common to all spikes of the particle. The whole particle can be rotated by an angle of ϕ_{part} against the x -axis.

Each spring-friction-element is positioned with its own angle ϕ_i against the unrotated position of the particle. The position angle of a spring-friction-element in the global coordinate frame is $\phi_{\text{part}} + \phi_i$. This facilitates the description of the tips of the spikes for a contact search, because the global coordinate frame is common for all particles. Each spring-friction-element has its own properties, like e.g. undeformed length $l^{(0)}$ and mechanical properties.

For the following contact search, all spikes must lie within the polygon of the particle. But the polygon does not have to be convex.

3 CONTACTS

The contact between two particles, as it is described in the following, will take place between the spike of a particle P_a and an edge of the particle P_b . For the special case of a spike-spike-contact a similar approach can be formulated. The methodology consists in finding an overlap ϑ between the edge and the spike. Then the spring-friction-element that is forming the spike is subjected to the overlap ϑ . The spike then returns a force as described in section 2.2. Finally this force is applied to the two particles that are in

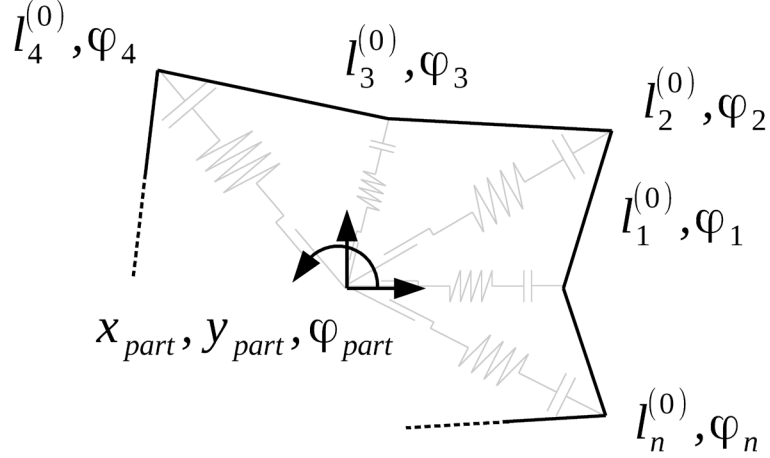


Figure 1: The prototypical, undeformed particle

contact.

3.1 Interparticle contact

As an example, the intersection is calculated between the i -th spike of P_a and the edge of P_b that spans between the spikes j and $j + 1$. In order to compute possible overlaps with simple algebra, the spike and the edge are expressed as 2-tuples of points in the global coordinate frame, which is common for all particles.

This leads for the spike to

$$\vec{s} = \left\{ \begin{bmatrix} x_{\text{part}}^{(a)} + l_i^{(0)(a)} \cos(\phi_{\text{part}}^{(a)} + \phi_i^{(a)}) \\ y_{\text{part}}^{(a)} + l_i^{(0)(a)} \sin(\phi_{\text{part}}^{(a)} + \phi_i^{(a)}) \end{bmatrix}, \begin{bmatrix} x_{\text{part}}^{(a)} \\ y_{\text{part}}^{(a)} \end{bmatrix} \right\}, \quad (1)$$

It is important to note that the undeformed length of the spike is used. This allows a direct computation of the overlap ϑ .

For the 2-tuple of the edge the deformed length of the spikes is taken, because the particle P_b can be deformed. This yields

$$\vec{e} = \left\{ \begin{bmatrix} x_{\text{part}}^{(b)} + l_j^{(b)} \cos(\phi_{\text{part}}^{(b)} + \phi_j^{(b)}) \\ y_{\text{part}}^{(b)} + l_j^{(b)} \sin(\phi_{\text{part}}^{(b)} + \phi_j^{(b)}) \end{bmatrix}, \begin{bmatrix} x_{\text{part}}^{(b)} + l_{j+1}^{(b)} \cos(\phi_{\text{part}}^{(b)} + \phi_{j+1}^{(b)}) \\ y_{\text{part}}^{(b)} + l_{j+1}^{(b)} \sin(\phi_{\text{part}}^{(b)} + \phi_{j+1}^{(b)}) \end{bmatrix} \right\}. \quad (2)$$

The overlaps are calculated by solving

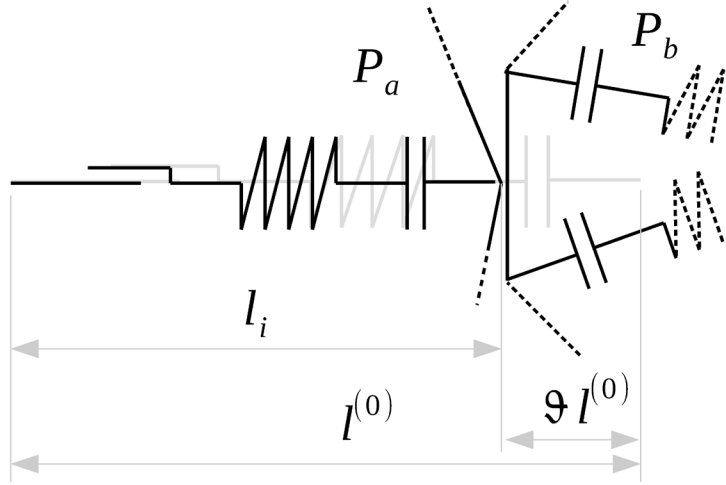


Figure 2: The prototypical spike-edge contact

$$\begin{bmatrix} \vec{s}_{2,x} - \vec{s}_{1,x} & \vec{e}_{1,x} - \vec{e}_{2,x} \\ \vec{s}_{2,y} - \vec{s}_{1,y} & \vec{e}_{1,y} - \vec{e}_{2,y} \end{bmatrix} \begin{bmatrix} \vartheta_a \\ \vartheta_b \end{bmatrix} = \begin{bmatrix} \vec{e}_{1,x} - \vec{s}_{1,x} \\ \vec{e}_{1,y} - \vec{s}_{1,y} \end{bmatrix} \quad (3)$$

for ϑ_a and ϑ_b .

If $0 < \vartheta_b < 1$ a contact might exist and ϑ_a is passed to the i -th spike to obtain a force f . This overlap is treated internally by the spring-friction-element. If the returned force is zero, the contact search is continued with other edges, spikes and particles, depending on the level the contact search algorithm is currently operating on. If, on the other hand, the force has a non-zero value $f \neq 0$, the spike i of P_a is indented accordingly in order to avoid a penetration into P_b . The force that is returned from the indentation of the spike is aligned along the direction of the spike

$$\vec{f} = f \begin{bmatrix} \cos(\phi_{\text{part}}^{(a)} + \phi_i^{(a)}) \\ \sin(\phi_{\text{part}}^{(a)} + \phi_i^{(a)}) \end{bmatrix}. \quad (4)$$

This force can be applied directly to P_a , because the spike passes through the center of the particle and no moment is generated.

For the particle P_b the force \vec{f} is also applied to the center, but in addition a moment has to be calculated, because the force is applied at the intersection point of the undeformed spike and the edge. This intersection point is calculated as

$$\vec{i} = \begin{bmatrix} \vec{s}_{1,x} \\ \vec{s}_{1,y} \end{bmatrix} + \vartheta_a \begin{bmatrix} \vec{s}_{2,x} - \vec{s}_{1,x} \\ \vec{s}_{2,y} - \vec{s}_{1,y} \end{bmatrix}. \quad (5)$$

The generated moment is calculated as

$$m = \left\| \begin{bmatrix} \begin{bmatrix} x_{\text{part}}^{(b)} \\ z_{\text{part}}^{(b)} \\ 0 \end{bmatrix} - \vec{i} \\ \vec{f} \\ 0 \end{bmatrix} \right\|. \quad (6)$$

This moment is applied to P_b .

It should be noted, that, with this procedure, no spike of the particle P_b is indented. The reason for this is phenomenological. If a sharply pointed spike of a particle is pressed against the flat edge of another particle, it is safe to assume that the spike is indented, deformed and bent, while the edge receives only a local indentation mark, a scratch, so to speak, which does not affect the nearby spikes. This assumes similar materials.

3.2 The contact search algorithm

The above procedure is repeated for all n_a spikes of particle P_a with all n_b edges of particle P_b . Then the roles of P_a and P_b are inverted and the procedure is repeated for all n_b spikes of particle P_b with all n_a edges of particle P_a . During these calculations the deformed and undeformed lengths of the particles' spikes are frozen. The indentations of the spikes are only applied once the contact calculations are finished. This ensures that no particle is preferred and all overlaps that stem from the preceding integration step are duly treated. Also, with this process, all overlaps are resolved.

On global level the possibilities of contacts between particles are checked with a primitive n^2 contact search and the longest spikes of each particle as radius of the enveloping circle. This approach is taken for the sake of simplicity and has to be abandoned for large particle assemblies.

4 PARTICLE DYNAMICS

The dynamics of the particles are adapted to the quasistatic nature of the compaction process. [11] argues that simulations including dynamical effects are better suited to rapid granular flows, like e.g. pouring, than for quasistatic processes, like e.g. compaction. [12] proposes an approach which is used for the simulation of Brownian motion. By eliminating the superposition of the underlying flow, the dynamic model can be formulated as

$$\vec{x}(t + \Delta t) = \vec{x}(t) + \mathbf{R}^{-1} \vec{F} \Delta t. \quad (7)$$

In this algorithm - based on an explicit Euler integration - the vector \vec{x} combines the translational and rotational degrees of freedom of the particle, the vector \vec{F} the forces acting on these three degrees of freedom and \mathbf{R} is a resistance term, which can be different for each degree of freedom. The dynamic model neglects the inertia of the particles and is thus suitable for a quasistatic process.

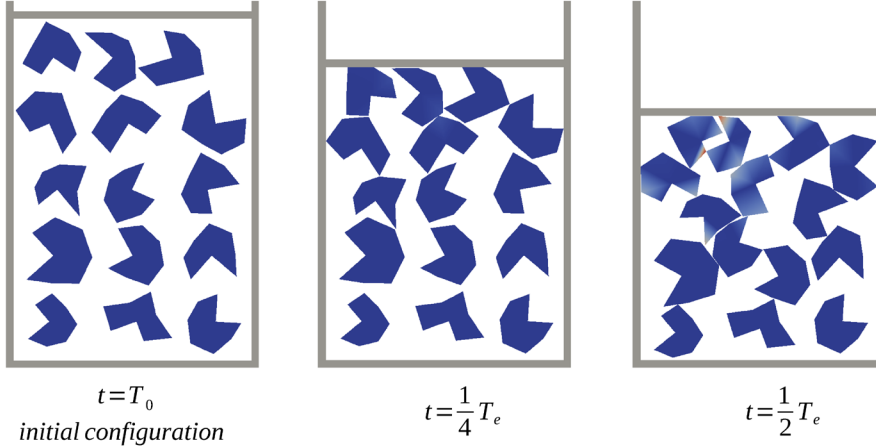


Figure 3: The initial configuration and the first two states of the proof-of-concept simulation

5 PROOF-OF-CONCEPT

The proof-of-concept simulation aims at establishing a multi-particle simulation. The main focus is set on contacts between multiple particles at the same time.

For the simulation 15 hedgehog particles are compressed uniaxially in a 2-dimensional die. The particles are randomly placed and do not contact each other at the beginning.

The figures 3 and 4 show the initial setup and four stages of compaction. The plastic deformation ϵ_p of the spikes is shown in colour.

The die consists of rigid walls. The contacts between particles and walls are treated the same way as the particle-particle contact, see section 3. In case of particle-wall contacts the walls are treated as edges and the particles' spikes deform due to contact with the wall. All contacts are considered as frictionless.

The forces exerted by particles on the walls are summed up. Figure 5 shows the force histories related to contact with the lower horizontal and the left vertical wall. The forces at the lower wall depict that the "powder" actually resists the compaction. The increase of the forces at the vertical wall shows that the powder produces a lateral pressure due to the compaction.

The force histories display a great deal of jittering. This jittering is introduced by the freezing mechanism during the contact search. If a spike comes into contact with an edge - which might also be a wall - the spike is indented. Then the particle is moved depending on the force returned from the spike. This can lead to a gap and thus the contact state is lost. If the amplitude of the force is large enough, the particle might move far enough, such that the contact is not reestablished for several time steps. Hence the force drops to

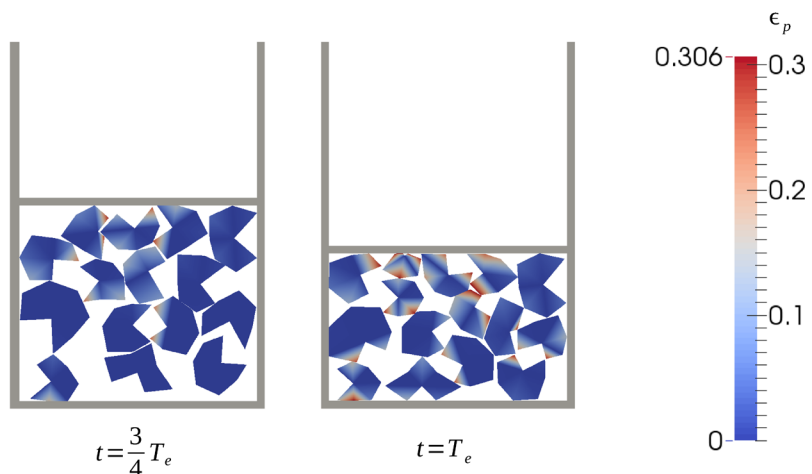


Figure 4: The last two states of the proof-of-concept simulation

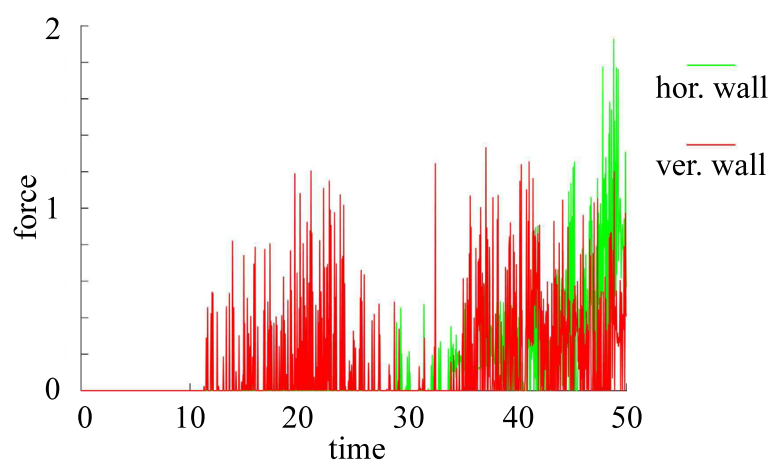
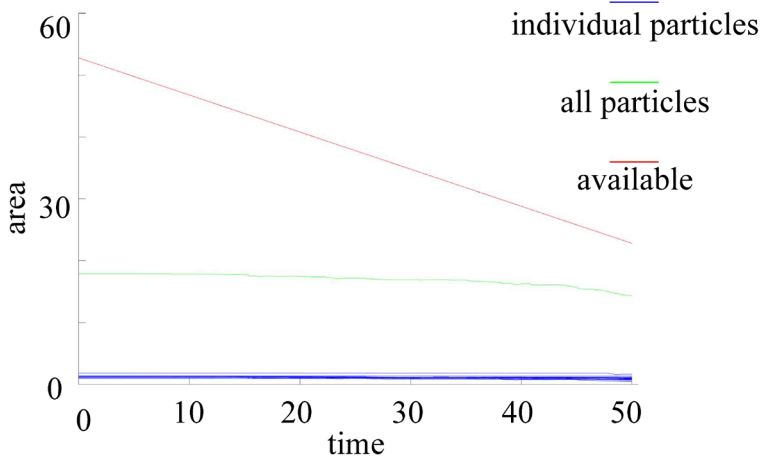


Figure 5: The vertical and horizontal forces on the wall

**Figure 6:** The areas involved

zero. If the contact partners reestablish their contact, the force returns to a high level. For the movement of particles, which happens generally in a smooth way, this can be neglected, but for the forces, that are recorded at every time-step, this jittering becomes very visible.

The transfer from vertical to horizontal forces proves that hedgehog particles can transfer a pressure. This transfer of a pressure is a feature of real powder compaction and is intuitively understandable. Naturally the curves of vertical and lateral stress obtained with this simulation do not match the ones obtained from experiments, like e.g. the ones performed by [13], because the hedgehog particles are not calibrated. But these curves could be applied to calibrate the properties of the hedgehog particles with respect to the experimental data. This would then enable the use of hedgehog particles for simulations with more realistic geometries than a simple die. However, this is beyond the aim of this proof-of-concept simulation.

6 CONCLUSION AND OUTLOOK

The presented work offers the hedgehog particle as a novel approach that combines the plastic deformation of particles with a probably acceptable computational cost. This should allow for a simulation of powder compaction with topology changes in which the particles retain their individual plastic deformation. The hedgehog particles consist of radially extending frictional devices and possess a quasi static behaviour. The contacts between the particles are defined as intersections of spikes with edges. This allows an intrinsic treatment of non-convex particles as long as the spikes remain inside the particle.

The hedgehog particles are subjected to a uniaxial compaction as a proof-of-concept simulation. This simulation demonstrates that the properties of the hedgehog particles

can be calibrated against experiments.

Furthermore, the simulation illustrates the property of the particles of loss of area, which is not physical. This effect is shown in figure 6. If the area of the particles is linked by density to a mass, this effect would correspond to a loss of mass. This is neither desirable nor physically correct. Therefore an an isochoric condition - like $\det J = 1$ - has to be introduced at particle level. If a spike gets indented, the other spikes should extend to compensate for the loss of area. This part is however ongoing research, because it is not easily determined how this isochoric condition could be formulated, especially considering that for some configurations all spikes of a particle could be indented at the same time. For this proof-of-concept simulation the loss of area is considered to be on the edge of being negligible on the powder level. However, for individual particles it can be rather significant and the loss of area is definitely an issue that has to be addressed during the further development of the hedgehog particles.

Also the absence of friction in the proof-of-concept simulation has to be considered as a major problem, because, as [14] argues, friction is the dominating mechanism in rather dense, static packing. Also, a slight friction might remedy the effects of resolving and reestablishing contacts which cause the observed jittering.

In the far future an extension of the concept to 3 dimensions should follow. There, the contacts would be the insertion of a spike of one particle with the triangle spanned between the tips of three spikes of the particle's contact partners. While the calculation of intersections in 3 dimensions is more complex.

In conclusion the prospect of simulating powder compaction with plastically deformable particles, that deform under high stress states and offer a modest computational effort, warrants the pursuit of the development of hedgehog particles in 2 and ultimately in 3 dimensions.

REFERENCES

- [1] Wellmann, C. and Wriggers, P. A two-scale model of granular materials *Computer Methods in Applied Mechanics and Engineering* (2012) **205-208**:46–58.
- [2] Balagurusamy, E. *Object oriented programming with C++*. McGraw Hill, Sixth Edition, (2013)
- [3] Fischmeister, H. F.; Arzt, E. and Olsson, L. R. Particle deformation and sliding during compaction of spherical powders: a study by quantitative metallography *Powder Metallurgy* (1978) **21**:179–187.
- [4] Fischmeister, H. F. and Arzt, E. Densification of Powders by Particle Deformation *Powder Metallurgy* (1983) **26**:82–88.
- [5] DAddetta, G. A., Kun, F. and Ramm E. On the application of a discrete model to the fracture process of cohesive granular materials *Granular Matter* (2002) **4**:77–90.

- [6] Redanz, P. and Fleck, N. A. The compaction of a random distribution of metal cylinders by the discrete element method *Acta Materialia* (2001) **49**:4325–4335
- [7] Harthong, B.; Jérier, J.-F.; Dorémus, P.; Imbault, D. and Donzé, F.-V. Modeling of high-density compaction of granular materials by the Discrete Element Method *International Journal of Solids and Structures* (2009) **46**:3357–3364.
- [8] Jérier, J.-F.; Harthong, B.; Richefeu, V.; Chareyre, B.; Imbault, D.; Donzé, F.-V. and Dorémus, P. Study of cold powder compaction by using the discrete element method *Powder Technology* (2011) **208**:537–541.
- [9] Feng, Y.; Han, K. and Owen, D. Energy-conserving contact interaction models for arbitrarily shaped discrete elements *Computer Methods in Applied Mechanics and Engineering* (2012) **205-208**:169–177.
- [10] Simo, J. and Hughes, T. *Computational Inelasticity*, (eds.) Marsden, J. Sirovich, L. and Wiggins, S. (Eds.) Springer-Verla (1998).
- [11] Bagi, K. A quasi-static numerical model for micro-level analysis of granular assemblies *Mechanics of Materials* (1993) **16**:101–110.
- [12] Ball, R. and Melrose, J. A simulation technique for many spheres in quasi-static motion under frame-invariant pair drag and Brownian forces *Physica A: Statistical Mechanics and its Applications* (1997) **247**:444–472.
- [13] Bier, W.; Dariel, M.P.; Frage, N.; Hartmann, S. and Michailov, O. Die compaction of copper powder designed for material parameter identification *International Journal of Mechanical Sciences* (2007) **49**:766–777.
- [14] Luding, S. Collisions and contacts between two particles. *H.J. Hermann et al. (eds.) Physics of dry granular media* Kluwer Academic publishing (1998).

TRIBOLOGICAL EFFECTS IN GRANULAR MATERIALS AND THEIR IMPACT ON THE MACROSCOPIC MATERIAL BEHAVIOUR

Bettina Suhr¹ and Klaus Six¹

¹ Virtual Vehicle Research Center
Inffeldgasse 21/A, A-8010 Graz, Austria
bettina.suhr@v2c2.at, klaus.six@v2c2.at, <http://www.v2c2.at>

Key words: Tribology, Direct Shear Test, Granular Materials, DEM, Friction

Abstract. In the discrete element simulation of granular materials, the modelling of contacts is crucial for the macroscopic material behaviour. From the tribological point of view, friction at contacts needs to be modelled carefully, as it depends on several factors, e.g. contact normal load or temperature to name only two. In discrete element method (DEM) simulations the usage of Coulomb's law of friction is state of the art. It reduces all tribological effects to only one constant coefficient of friction. Motivated by research on wheel-rail contacts, a pressure dependency of the interparticle coefficient of friction is introduced in a new DEM model. Direct shear tests are conducted on steel spheres of a certain size distribution. The strong influence of interparticle friction on the bulk friction is shown via a variation of the constant interparticle friction coefficient. Simulations with constant and pressure dependent interparticle friction are compared. For the pressure dependent interparticle friction a pressure dependency of the bulk friction is seen which matches qualitatively the behaviour known from testing reported in literature.

1 INTRODUCTION

Solid like granular materials generally comprise a high number of particle-particle and particle-environment contacts. The frictional behaviour of these contacts has a high influence on the macroscopic behaviour of the material. In the sense of a tribological system friction is influenced by several parameters like contact normal load, relative motion, surface roughness, contact temperature and contact conditions (dry, wet, lubricated contact conditions, etc.).

The discrete (distinct) element method (DEM) was introduced by Cundall and Strack, see [1], and has become a widely used tool for modelling the mechanical behaviour of solid-like granular materials. While there are several topics of active research regarding DEM, it is state of the art to consider the frictional behaviour of contacts by application of Coulomb's law. At a contact the resulting contact force is decomposed in normal

and tangential direction, F_n and F_t , and contact laws for their calculation are chosen. In tangential direction the force which can be transferred is bounded. This bound has a high influence on the behaviour of the granular material and generally consists of a part depending on the normal force and a part representing cohesion (independent of the normal force). Coulomb's law is the simplest way to model the normal force dependent part of this bound. A constant interparticle friction coefficient, μ , is introduced, which describes the maximal allowed ratio between tangential and normal force. While the contact sticks, the ratio is strictly less than the coefficient of interparticle friction. When the ratio of tangential and normal force grows and equality is reached, the contact slides. During sliding the ratio remains constant. For cohesionless materials Coulomb's law can be written as follows:

$$F_t = \min(\mu F_n, \tilde{F}_t) , \quad (1)$$

where \tilde{F}_t is the pre-sliding shear force calculated using the contact constitutive model. Coulomb's law can also be stated using the internal friction angle, ϕ , which is connected to the interparticle friction coefficient by $\mu = \tan(\phi)$.

Frequently used tests for the investigation of the shear behaviour of granular materials are the triaxial test and the direct shear (or shear box) test. Usually the Mohr-Coulomb failure criterion is used which reads as:

$$\tau_f = \tan(\Phi)\sigma_n + c , \quad (2)$$

where τ_f is the final shear stress, Φ is the bulk friction angle and c is a material parameter representing cohesion of the granular material, i.e. $c = 0$ for cohesionless materials. The bulk friction angle of a granular material is an important characteristic for its shear behaviour. Alternatively the peak friction angle can be determined, where the maximal shear stress instead of the final one is used in equation (2).

In the literature there exist several works which state a strong influence of the interparticle friction on the bulk friction angle, see e.g. [2, 3, 4] who simulated direct shear tests and compared the results to experiments.

It is frequently stated that the bulk/peak friction angle of a granular medium is constant, i.e. independent of the normal stress. This result can be found e.g. in [3] or [4] who considered equi-sized steel balls and glass beads respectively. Direct shear test with different normal stresses were conducted. In the regime of applied normal stresses, in both works a linear relation between the measured shear stress and normal stress was found. Thus the application of the Mohr-Coulomb criterion was justified and the bulk friction angle was constant.

On the contrary, [4] states a clearly non-linear relation, i.e. pressure dependency, when the shear test is performed on paired glass beads instead of single glass beads. Here the applied normal stress ranges from 3 kPa to 24 kPa and a dependency of the bulk friction angle on these pressures can be seen. In [5] the same experimental results are

compared to DEM simulation. The pressure dependency of the bulk friction angle found in the experimental results could not be reproduced in the DEM simulations which used a constant interparticle friction coefficient for all load cases.

Similar experimental results regarding a pressure dependency of the bulk friction angle are found in [6] where railway ballast is investigated in direct shear tests. The normal stress is varied between 15 kPa and 75 kPa and a nonlinear dependency between shear stress and normal stress is shown. Here also several works on rock-fill materials are cited which state a non-linear relationship which is significant at low normal stresses and gradually reduces as the normal stress increases.

This description matches well with the results of [7]. A pressure dependent coefficient of friction between smooth silo walls and particles was found for small normal stresses. It seems that depending on the considered material and particle shape a non-linear relation between bulk friction angle and normal stress can be observed for low normal stresses.

Motivated by the above experimental findings on granular media and results obtained on the wheel-rail contact for steel, the authors will use a non-constant coefficient of friction in DEM simulations. In simulations of direct shear tests, the application of this law will result in a non-linear dependency of the bulk friction angle on the normal stress.

2 PRESSURE DEPENDENT FRICTION COEFFICIENT

Investigations on the frictional behaviour of wheel-rail contacts (steel-steel) showed that the assumption of a constant coefficient of friction is not sufficient to reproduce results observed at experiments, see e.g. [8]. In Figure 1 results of High Pressure Torsion tests (HPT) are shown. In a HPT test two steel discs are rotated against each other, while the normal stress, σ_n and the shear stress, τ , are measured. In this case the ratio between τ and σ_n is the coefficient of friction. From Figure 1(a) to 1(b) the maximum normal stress σ_n is doubled. If the coefficient of friction was constant, then $\frac{\tau}{\sigma_n}$ would be constant and thus τ would be doubled. In Figure 1(b) it can be seen that the τ is clearly

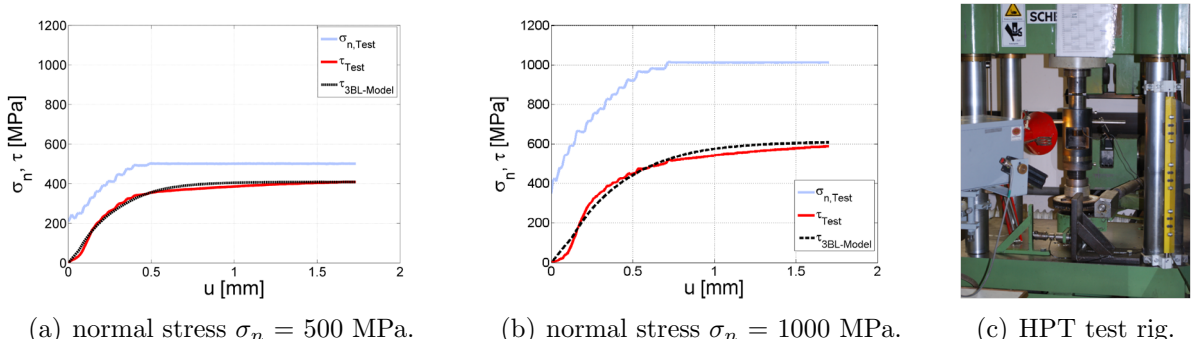


Figure 1: High Pressure Torsion (HPT) tests where two steel-discs are rotated against each other; measurement of normal stress (σ_n) and shear stress (τ) over displacement u ; increasing normal stress reduces ratio τ/σ_n , comparison to results from model [8].

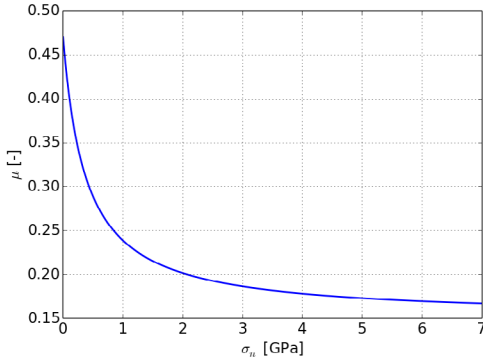


Figure 2: Graph of the pressure dependent coefficient of friction as defined in Equation (3).

lower and therefore a significant dependency of the coefficient of friction on the normal load can be concluded from the experiments.

Similar results as in [8] are also obtained in [9] from Popov et. al. With the method of Movable Cellular Automata (MCA) the wheel-rail contact is modelled (steel-steel) and from simulation results a normal pressure dependent coefficient of friction is derived:

$$\mu(\sigma_n) = 0.15 + \frac{0.3243}{1 + 0.00212 \frac{\sigma_n E}{\sigma_0}}, \quad (3)$$

where σ_n is the applied normal stress, E is the Young modulus, $E = 206 \text{ GPa}$, and σ_0 is the ultimate strength and was varied between 92 and 552 MPa. The graph of the above function is plotted in Figure 2 for $\sigma_0 = 400 \text{ MPa}$.

This pressure dependent coefficient of friction will be used in the following DEM simulations. For the contact forces the frequently used Hertz-Mindlin no slip contact model will be used, compare e.g. [10]. In normal direction of the contact the Hertz model is as follows:

$$F_n = \frac{4}{3} \hat{E} \sqrt{\hat{R}} \sqrt{u_n^3}, \quad (4)$$

where \hat{E} is the equivalent Young modulus of the contact, \hat{R} is the equivalent contact radius and u_n is the overlap in normal direction. In the Hertzian contact model the area of contact is circular (sphere-sphere contact), therefore an averaged pressure, $\bar{\sigma}_n$ can be calculated by dividing the contact force by the contact area.

$$\bar{\sigma}_n := \frac{F_n}{a^2 \pi} = \frac{F_n}{\pi} \left(\frac{4 \hat{E}}{3 F_n \hat{R}} \right)^{\frac{2}{3}}, \quad (5)$$

where $a = \left(\frac{3 F_n \hat{R}}{4 \hat{E}} \right)^{\frac{1}{3}}$ is the radius of the contact patch. In the tangential direction of the contact the Mindlin no slip model is applied. The trial or pre-sliding shear force is denoted by $F_{t,t}$ and can be calculated as:

$$F_{t,t} = 8a\hat{G}u_s, \quad (6)$$

where \hat{G} is the equivalent shear modulus and u_s the shear displacement. Using the constant coefficient of friction, the shear force is given by:

$$F_t = \begin{cases} F_{t,t} & \text{if } F_{t,t} \leq \mu F_n \\ \mu F_n & \text{otherwise} \end{cases}. \quad (7)$$

For the use of the pressure dependent friction coefficient, we now change Equation (7) to:

$$F_t = \begin{cases} F_{t,t} & \text{if } F_{t,t} \leq \mu(\bar{\sigma}_n)F_n \\ \mu(\bar{\sigma}_n)F_n & \text{otherwise} \end{cases}, \quad (8)$$

where $\bar{\sigma}_n$ is given by Equation (5) and $\mu(\bar{\sigma}_n)$ by Equation (3).

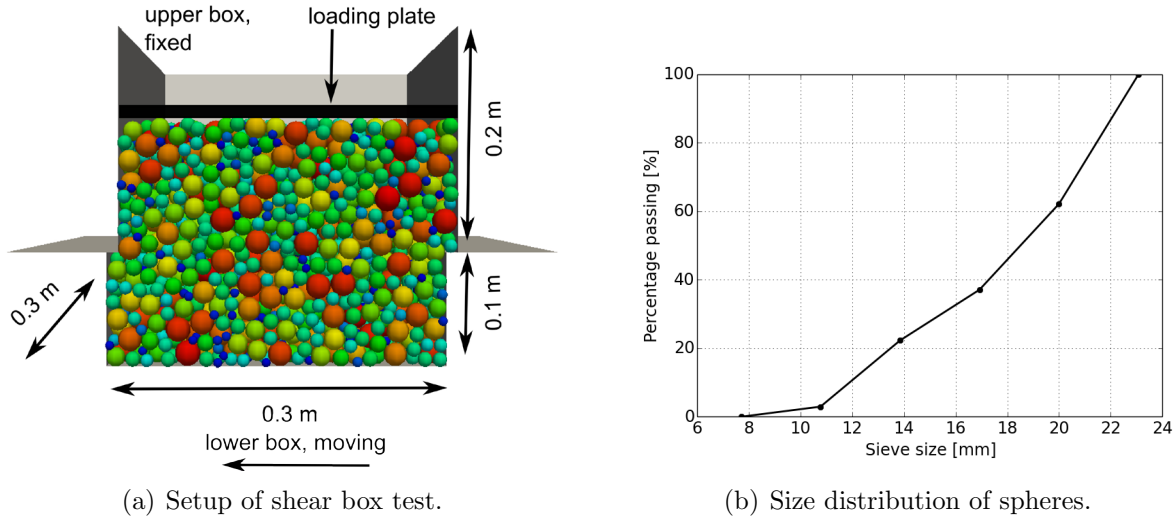
3 DEM SIMULATION OF DIRECT SHEAR TESTS

The influence of interparticle friction on the macroscopic behaviour will be investigated via simulation of direct shear tests. Results of a variation of the constant friction coefficient will be compared to those obtained with the above introduced pressure dependent friction coefficient.

All simulations are conducted with the DEM software Yade, [11]. In this software the soft contact approach is used together with explicit discretization in time. As already mentioned the main focus of this work is the modification of the tangential contact law, regarding the friction coefficient. The basis for this work is the Hertz-Mindlin no-slip contact model as given in Equations (4, 7). If the modified contact law, (4, 8), is used, it will be stated explicitly.

The setup of a direct shear test is shown in Figure 3(a). The lower box has the dimensions $0.3 \text{ m} \times 0.3 \text{ m} \times 0.1 \text{ m}$ and the upper box $0.3 \text{ m} \times 0.3 \text{ m} \times 0.2 \text{ m}$. For all shear tests non-uniform sizes of steel spheres are used. These sphere samples all share the same size distribution, which can be seen in Figure 3(b). The material of the spheres and the walls of the shear box is assumed to be equal. The material parameters of steel used in the DEM simulation are summarized in Table 1.

For sample generation 6000 spheres of the mentioned size distribution are randomly placed in a box above the shear box. Then the spheres fall under the influence of gravity and are allowed to come to rest in the shear box. To achieve a dense packing the friction coefficient is set to 0 in this initial phase of the simulation. For a reduction of computational time the gravity force is enlarged by factor 5. When the spheres came to rest, a steel plate is inserted above the spheres, the friction coefficient is increased to 0.2 and gravity force is set to its original value. Now the normal load is applied on the spheres using a servo control mechanism (P-control). After the specified normal load is reached and the spheres are at rest, the shearing phase starts by imposing a velocity on the lower

**Figure 3:** Details on shear box test and size distribution of spheres.

shear box. Variations of the shear velocity showed that shearing with $1 \frac{mm}{s}$ yielded results which can be considered quasi-static, i. e. a lower shearing rate yielded the same result.

The direct shear test will be simulated with three different levels of applied normal stress, $\sigma_n = 75$ kPa, 225 kPa and 375 kPa. At first the interparticle friction coefficient is constant, $\mu = 0.2$, and the Hertz-Mindlin no slip contact model (4, 7) is used. In Figure 4(a) the shear stress over the shear path is shown in the upper plot. For the calculation of the shear stress, all contact forces belonging to the lower box and the bottom are summed; then only the component in shear direction is divided by the cross-sectional area of the shear box 0.09 m^2 . In the lower part of Figure 4(a) the porosity of the samples is plotted over the shear path. At the beginning of all three tests there is a short phase where the samples are compressed, while dilation occurs for the rest of the simulation. Due to problems with the control of the applied normal stress at the beginning of the simulations sometimes kinks in the shear stress can be seen. As the duration of these problems is usually very small, the effect on the overall response of the bulk material is negligible.

To check the influence of the spheres' initial configuration on the simulation results, five different configurations were generated with the above described procedure. The results

Table 1: Parameters used in DEM simulations.

Parameter	Diameter	Density	Young modulus	Poisson's ratio	friction coefficient
Value	8 - 24 mm	$7833.34 \frac{kg}{m^3}$	200 GPa	0.28	0.2

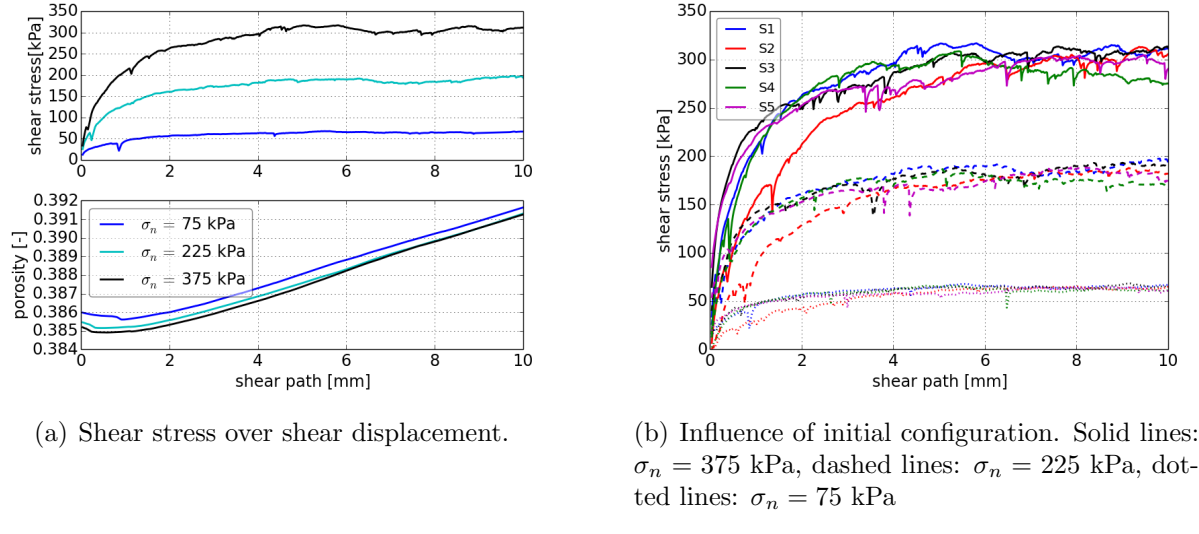
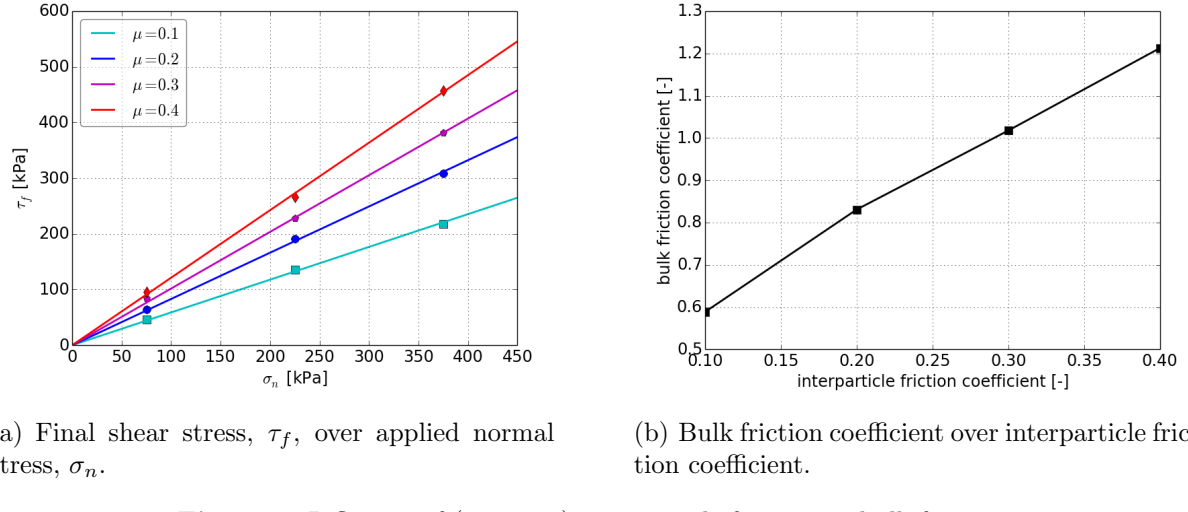


Figure 4: Simulation results for direct shear tests with constant interparticle friction $\mu = 0.2$.

can be seen in Figure 4(b). The different initial settings are named S1 till S5. It can be seen that S2 has a lower initial slope than the other settings and S4 has the smallest final shear stress for all three levels of applied normal stress. It seems that for the chosen size distribution of the spheres the sample generation method can not ensure similar initial packings. Also differences in the initial porosity of the settings occur, which lie between 0.383 and 0.386. The maximal deviations in the final shear stress are 3 % for $\sigma_n = 75$ kPa, 11 % for $\sigma_n = 225$ kPa and 9 % for $\sigma_n = 375$ kPa. Obviously, to some extent the same problems would occur if tests in the lab were conducted. Nevertheless the reduction of these deviation via a different method for sample generation will be future work. For the time being, influences off the different initial settings will be reported, where they are of interest.

3.1 Influence of constant interparticle friction coefficient

It is well known that interparticle friction is a key factor for the shear behaviour of granular materials. In the following the interparticle friction coefficient will be varied between 0.1 and 0.4 to investigate its influence on the bulk friction angle for one considered initial setting. From the conducted simulations the final shear stress is calculated as the median of the last hundred readings of the shear stress (over a shear path of 2 mm). Here the median instead of the mean value is chosen due to its insensitivity with respect to outliers. Figure 5(a) shows the resulting final shear stresses, τ_f , over the applied normal stress, σ_n , for the different values of the interparticle friction coefficient. The already mentioned Mohr-Coulomb criterion for cohesionless material is used and the least squares fit for each value of interparticle friction is shown. The slope of these lines is the tangent of

(a) Final shear stress, τ_f , over applied normal stress, σ_n .

(b) Bulk friction coefficient over interparticle friction coefficient.

Figure 5: Influence of (constant) interparticle friction on bulk friction.

the bulk friction angle and will be denoted here as bulk friction coefficient. In Figure 5(b) this bulk friction coefficient is plotted over the interparticle friction coefficient.

The Mohr-Coulomb criterion states a linear relation between normal stress and final shear stress. The obtained bulk friction coefficient shows no pressure dependency. The simulation results obtained with constant interparticle friction coefficients agree well with the linear Mohr-Coulomb criterion. Thus, it can be concluded that constant interparticle friction can not be used to obtain a pressure dependency in bulk friction.

The strong influence of interparticle friction on the bulk friction coefficient is well shown with the presented results.

3.2 Usage of pressure dependent interparticle friction

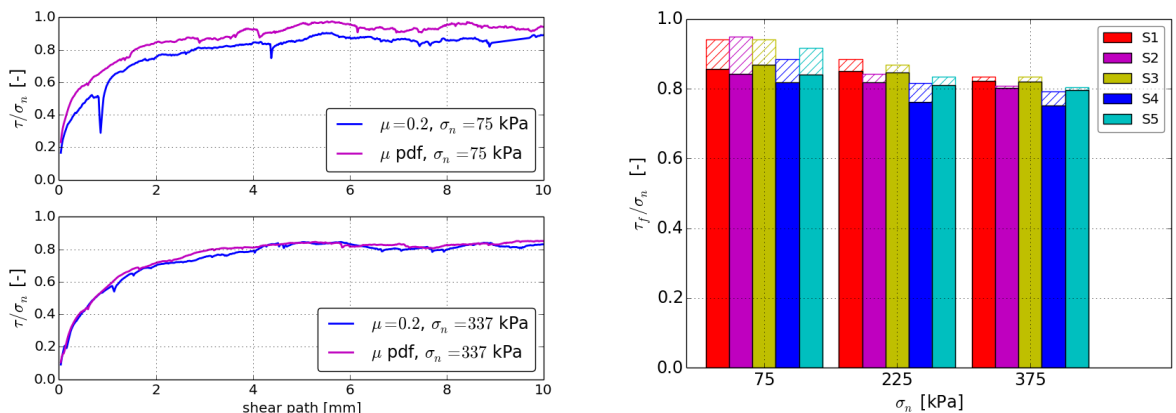
As a next step simulations with the pressure dependent interparticle friction coefficient, (3) from [9], together with the modified shear force law (8) are presented. The results will be compared to simulations using $\mu = 0.2$. In the model of pressure dependent interparticle friction, the Young modulus is set to $E = 200$ GPa. For the ultimate strength, σ_0 , the interval of 92 to 552 MPa is specified in [9]. In this work $\sigma_0 = 400$ MPa is used. In Figure 6(a) the normalized shear stress $\frac{\tau}{\sigma_n}$ is plotted over the shear path for $\mu = 0.2$ and the pressure dependent friction coefficient, μ pdf. Considering $\sigma_n = 375$ kPa in the lower plot, then the simulation results for $\mu = 0.2$ and pressure dependent μ coincide (calibration of the model via σ_0). In the upper plot, where $\sigma_n = 75$ kPa, $\frac{\tau_f}{\sigma_n}$ is about 10 % larger for for pressure dependent μ than for $\mu = 0.2$. For the pressure dependent μ the bulk friction coefficient decreases with increasing σ_n until it coincides at $\sigma_n = 375$ kPa with the value obtained with $\mu = 0.2$, compare Figure 6(a). Thus, the pressure dependency which is introduced in interparticle friction is also seen in the resulting bulk friction coefficient.

This behaviour of the bulk friction coefficient qualitatively agrees with observations from direct shear experiments reported in literature.

The pressure dependency in bulk friction, caused by the pressure dependency in interparticle friction, is in a similar range than the scatter of results caused by the different initial settings, compare Figure 4(b). A comparison of the simulations using $\mu = 0.2$ and pressure dependent μ for all five initial settings is done. In Figure 6(b) the bulk friction coefficient is calculated for each simulation individually. The solid bars show the bulk friction for the simulations with $\mu = 0.2$ and shaded bars belong to pressure dependent μ . While the extent of pressure dependency of the bulk friction coefficient varies between the initial settings it is present in all cases.

The authors would like to emphasize that it is not possible to use a higher (constant) friction coefficient and to obtain the same results as with pressure dependent μ . While it would be possible to chose a lower value for interparticle friction such that the final shear stress for $\sigma_n = 75$ kPa is met, then the final shear stress for $\sigma_n = 225, 375$ kPa would be too high.

For the simulation with pressure dependent μ and $\sigma_n = 75$ kPa the normal forces at the end of the test are plotted in Figure 7(a). For improved visibility only contacts with $F_n \geq 70$ N are displayed. With this threshold 10 % of all contact are plotted. On the same contacts the pressure dependent μ is shown in Figure 7(b). The friction coefficient lies between 0.189 and 0.23 at contacts with $F_n \geq 70$ N. As it can be seen in the plot, most contacts have larger friction coefficients than the value of 0.2 which was used for the comparison simulation. If all contacts are considered, then the maximal friction coefficient is 0.46.



(a) Normalized shear stress over shear displacement. Comparison for $\sigma_n = 375$ kPa and $\sigma_n = 75$ kPa.

(b) Final shear stress divided by normal stress over applied normal stress for five different initial settings. Solid bars: $\mu = 0.2$, shaded bars: $\mu = \text{pdf}$.

Figure 6: Comparison of constant interparticle friction and pressure dependent friction (pdf).

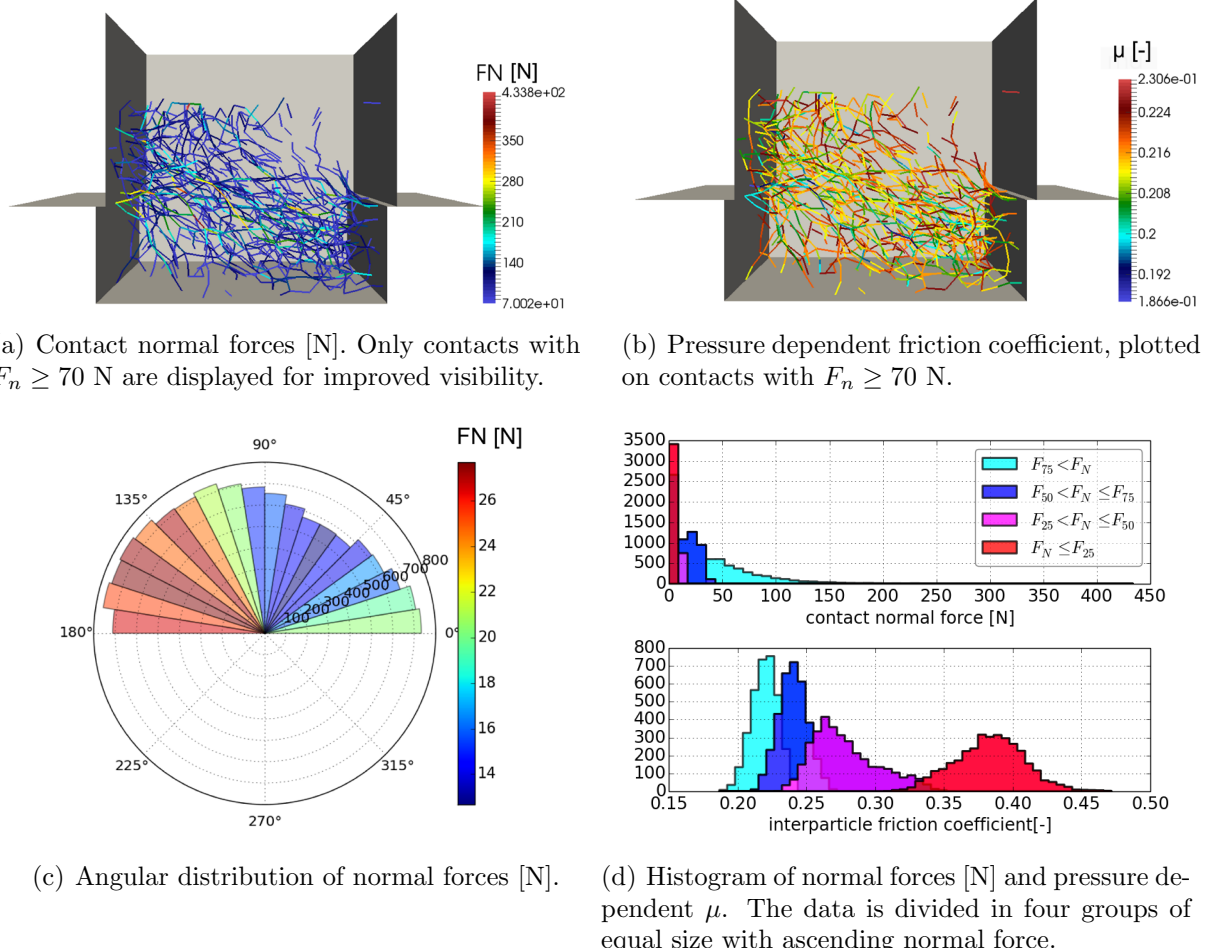


Figure 7: Fabric analysis of simulation with pressure dependent friction coefficient and $\sigma_n = 75$ kPa at shear displacement 10 mm

The angular distribution of normal forces at sphere-sphere contacts is shown in Figure 7(c). The length of each bar represents the number of contacts in the corresponding direction and the colour of each bar stands for the averaged normal force. Note that the average forces are low as many contacts have very small normal forces. It can be seen that the contacts which carry the largest load are clearly directed.

In Figure 7(d) two histograms of the contact normal force and the pressure dependent μ are shown. The data is divided in four groups of equal size with ascending normal force. Each group contains 25 % of all contacts, so in the first group $F_n \leq F_{25}$, where F_{25} denotes the 25 % quantile of the data and so on. The upper histogram shows the normal force. Note that nearly half of the data (the first two groups) lies in the first bin, which illustrates the huge amount of contacts which carry nearly no load. In the lower histogram the corresponding values of the interparticle friction coefficient are plotted.

Low contact forces belong to high values of interparticle friction, as can be seen for the red and magenta data group. High contact forces result in lower interparticle friction. The values of the cyan data group lie in the same interval as those plotted in Figure 7(b). Note that overlaps between the data groups of the interparticle friction coefficient exist, as the contact's equivalents radius also enters its calculation.

4 CONCLUSIONS

In this contribution simulations of direct shear tests are conducted. The samples consist of steel spheres of a certain size distribution and are loaded at three different levels of normal stress, $\sigma_n = 75, 225, 375$ kPa. The influence of the spheres' initial configuration is rather strong. Comparing five different initial settings deviations in the final shear stress up to 11 % occur. To some extent this problem would also occur when experiments were conducted in the lab. The reduction of these deviations via a modification of the method for sample generation will be future work.

The strong influence of interparticle friction on the bulk friction of the granular material is shown via a variation of a constant interparticle friction coefficient. Motivated by results on the whee-rail contact of steel a newly developed pressure dependency of interparticle friction is introduced. Direct shear tests with pressure dependent interparticle friction and constant $\mu = 0.2$ are compared. The pressure dependency introduced in interparticle friction is clearly seen in the resulting bulk friction coefficient. Considering one initial setting and $\sigma_n = 75$ kPa, then the bulk friction coefficient is about 10 % larger for pressure dependent μ than for $\mu = 0.2$. For the pressure dependent μ the bulk friction coefficient decreases with increasing σ_n until it coincides at $\sigma_n = 375$ kPa (where the model was calibrated) with the value obtained with $\mu = 0.2$. Due to the scatter of results with different initial configurations it is difficult to quantify the effect on the bulk friction coefficient in general. Nevertheless the pressure dependency in bulk friction is – to different extent – seen for all five initial settings. Qualitatively these results matches the behaviour observed in testing reported in literature.

ACKNOWLEDGMENTS

The authors gratefully acknowledge funding of the Austrian Science Fund (FWF) for the project P 27147-N30: Short- and Long-Term Behaviour of Solid-Like Granular Materials.

VIRTUAL VEHICLE Research Center is funded within the COMET – Competence Centers for Excellent Technologies – programme by the Austrian Federal Ministry for Transport, Innovation and Technology (BMVIT), the Federal Ministry of Science, Research and Economy (BMWFW), the Austrian Research Promotion Agency (FFG), the province of Styria and the Styrian Business Promotion Agency (SFG). The COMET programme is administrated by FFG.

REFERENCES

- [1] P. A. Cundall and O. D. L. Strack. A discrete numerical model for granular assemblies. *Gotechnique*, 29(1):47–65, 1979.
- [2] Q. Ni, W. Powrie, X. Zhang, and R. Harkness. *Effect of Particle Properties on Soil Behavior: 3-D Numerical Modeling of Shearbox Tests*, chapter 4, pages 58–70. Numerical Methods in Geotechnical Engineering. 2000.
- [3] L. Cui and C. O’Sullivan. Exploring the macro- and micro-scale response of an idealised granular material in the direct shear apparatus. *Geotechnique*, 56:455–468(13), 2006.
- [4] Johannes Härtl and JinY. Ooi. Experiments and simulations of direct shear tests: porosity, contact friction and bulk friction. *Granular Matter*, 10(4):263–271, 2008.
- [5] Johannes Härtl and Jin Y. Ooi. Numerical investigation of particle shape and particle friction on limiting bulk friction in direct shear tests and comparison with experiments. *Powder Technology*, 212(1):231–239, Sep 2011.
- [6] Buddhima Indraratna, Ngoc Trung Ngo, and Cholachat Rujikiatkamjorn. Behavior of geogrid-reinforced ballast under various levels of fouling. *Geotextiles and Geomembranes*, 29(3):313 – 322, 2011.
- [7] U Tuzun and O R Walton. Micro-mechanical modelling of load dependent friction in contacts of elastic spheres. *J. Phys. D: Appl. Phys.*, 25(1A):A44, 1992.
- [8] K. Six, A. Meierhofer, G. Müller, and P. Dietmaier. Physical processes in wheel–rail contact and its implications on vehicle–track interaction. *Vehicle System Dynamics*, 2015. article in press.
- [9] V.L. Popov, S.G. Psakhie, E.V. Shilko, A.I. Dmitriev, K. Knothe, F. Bucher, and M. Ertz. Friction coefficient in rail–wheel contacts as a function of material and loading parameters. *Physical Mesomechanics*, 5(3):17–24, 2002.
- [10] Chiara Modenese. *Numerical Study of the Mechanical Properties of Lunar Soil by the Discrete Element Method*. PhD thesis, University of Oxford, 2013.
- [11] V. Šmilauer, E. Catalano, B. Chareyre, S. Dorofeenko, J. Duriez, A. Gladky, J. Kozicki, C. Modenese, L. Scholtès, L. Sibille, J. Stránský, and K. Thoeni. Yade documentation, 2010. The Yade Project, 1st ed., 2010.

USING DELAUNAY TRIANGULATIONS TO INVESTIGATE THE EFFECT OF INTERPARTICLE FRICTION ON CRITICAL-STATE DEM SIMULATIONS

KEVIN J. HANLEY¹, XIN HUANG² AND CATHERINE O’SULLIVAN³

¹ Institute for Infrastructure and Environment, School of Engineering,
The University of Edinburgh, Edinburgh EH9 3JL, UK
k.hanley@ed.ac.uk

² Department of Geotechnical Engineering, School of Civil Engineering
& Key Laboratory of Geotechnical Engineering,
Tongji University, Shanghai 200092, China
xhuang@tongji.edu.cn

³ Department of Civil and Environmental Engineering,
Imperial College London, London SW7 2AZ, UK
cath.osullivan@imperial.ac.uk

Key words: Critical-state soil mechanics, Triaxial shearing, Contact network, Strong force chains, Delaunay triangulation.

Summary. *It is now broadly accepted that failure in a granular material is dominated by buckling failure of strong force chains oriented in the direction of the major principal stress. In this paper, Delaunay triangulation is used to explore the role of the interparticle friction coefficient (μ) in stabilising these strong force chains. An isotropic numerical sample was created in 3D which contains 20,164 polydisperse spherical particles inside a periodic cell. μ was changed to 0.0, 0.1, 0.25, 0.5, 0.75 or 1.0 to create six samples, each of which was sheared triaxially until critical state was attained. The contact network was obtained at the end of each simulation by joining the centroids of the contacting particles. The Voro++ software library was used to compute two types of periodic Voronoi tessellation of the particle centroids: the conventional unweighted tessellation and the radical tessellation which is weighted by particle diameter. These were converted to their Delaunay duals to facilitate direct comparison with the associated contact networks. The numbers of edges (i.e., contacts) that are in the contact networks decrease consistently as μ is increased towards 1. This contrasts with the numbers of edges, faces or tetrahedra in the Delaunay triangulations, all of which increase with increasing μ up to $\mu = 0.25$ and become approximately constant thereafter. Two quantities were defined: the percentage of faces in the triangulation comprising three contacts (P_{fc}) and the percentage of tetrahedra comprising six contacts (P_{tc}). P_{fc} shows a linearly-decreasing trend with increasing angle of shearing resistance and both P_{fc} and P_{tc} decrease continuously as μ is increased. This indicates that triangular motifs become less widespread as friction increases and that the weak supporting network which is present at low μ values is effectively absent at high μ .*

1 INTRODUCTION

The stress distribution within any granular material subjected to load is highly heterogeneous. Strong force chains, consisting of contacting particles aligned with the major principal stress orientation, form upon loading to transmit the majority of the load and carry the deviatoric stress during shear deformation. These strong force chains are supported by a weak orthogonal contact network. The formation of strong force chains has been observed experimentally using image analysis [1], tomography [2] and photoelasticity [3]. The development of strong force chains supported by a weak orthogonal network has often been observed in discrete element method (DEM) simulations, e.g., [4-6]. Over the last 15 years, it has become increasingly widely accepted that the dominant failure mechanism in a granular material is buckling failure of the strong force chains. Evidence supporting this hypothesis has been provided by a range of complementary investigation tools such as DEM simulation [7], photoelasticity experiments [8] and analytical modelling [9-11].

A parametric study was conducted recently [12] in which three-dimensional numerical samples were sheared triaxially to a critical state using different values of the interparticle friction coefficient (μ). This was an extension of previous DEM studies on the same subject [13,14]. It was found that the stability of the strong force chains increases with increasing μ while the supporting weak contact network has greatest importance for stabilising the strong force chains at low values of μ [12]. In this paper, the same data set is analysed using Delaunay triangulation of the particle centroids. The principal aim of this short study is to investigate whether triangular motifs become less common and linear structures more so as μ is increased: [15] found this to be the case for two-dimensional packings of disks but this finding has not been observed in 3D, to the best of the authors' knowledge.

2 DEM SIMULATIONS

A 3D numerical sample was created by randomly placing 20,164 polydisperse spherical particles within a periodic cell. These boundary conditions were chosen to avoid inhomogeneities at the periphery of the sample [16]. The periodic cell was initially cubical, consisting of three pairs of mutually-orthogonal periodic boundaries. The particle size distribution of the numerical sample, shown in Figure 1, is representative of Toyoura sand with a ratio of maximum to minimum particle diameters of around 3.6. A simplified Hertz-Mindlin contact model was used. The particle shear modulus and Poisson's ratio were set at 29 GPa and 0.12, respectively, to match experimentally-measured properties of quartz [17]. The particle density was set at 2650 kg/m³: a realistic value for a quartz sand. Gravity was inactive throughout the simulations. A stable isotropic assembly was created at a confining pressure of 100 kPa by moving opposing pairs of periodic boundaries closer together using a stress-control algorithm. The interparticle friction coefficient was 0.0 at this stage. Following isotropic compression, the interparticle friction coefficient was changed to 0.0, 0.1, 0.25, 0.5, 0.75 or 1.0. Each of these six samples was subjected to drained triaxial shearing to an axial strain of around 54%. This strain level was sufficient to reach the critical state in all simulations. All of these simulations were run using a version of the open-source LAMMPS code [18] which has been modified by the authors to include a stress-control algorithm for periodically-bounded samples and contact models which have been revised substantially to correspond to those in [19,20].

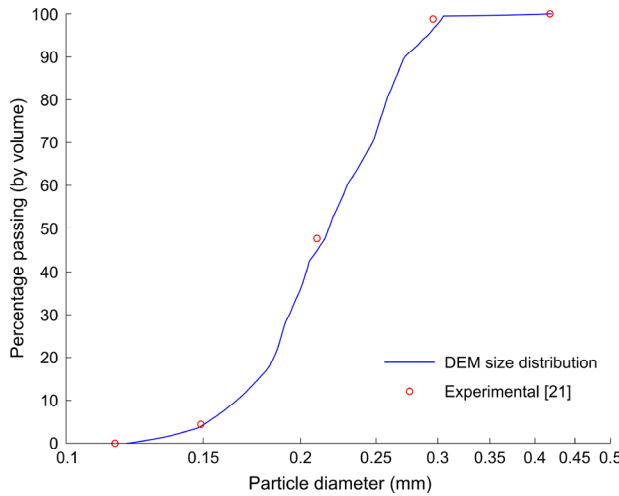


Figure 1: Particle size distribution of the numerical sample compared with a digitised size distribution of a real Toyoura sand measured by sieve analysis [21]

3 DATA ANALYSIS

The six samples were compared only at the end of the triaxial simulations, at around 54% axial strain, once critical state had been attained. Critical state is characterised by the continued deformation of a sample under shear without a change in either volume or stress state. The contact networks were easily obtained by joining the centroids of the contacting particles. Each interparticle contact corresponds to an edge in the contact network. In addition, Voronoi tessellations were computed based on the particle centroids. Voro++ [22] was chosen for this analysis as it is capable of doing periodic tessellations with non-cubical cells. In these simulations, the samples are almost cubical at the end of isotropic compression but become highly non-cubical during shearing. Two types of periodic Voronoi tessellation were computed: the conventional unweighted tessellation which does not take particle diameter into account and the radical (or Laguerre) tessellation which is weighted by particle diameter. These were converted to their Delaunay duals using MATLAB [23]. This conversion facilitated a direct comparison between the edges of the Delaunay tessellations and the edges of the associated contact networks.

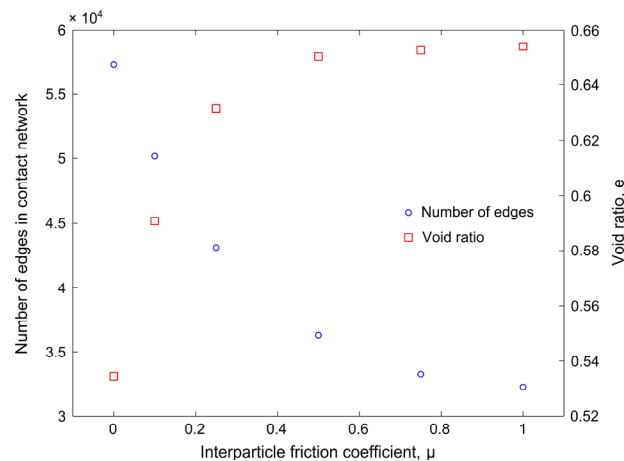
4 RESULTS AND DISCUSSION

Figures showing the macro-scale response of five of the six samples (excluding the frictionless simulation) are provided in [12]. Table 1 summarises the key macro-scale results at the critical state of each simulation. In Table 1, φ'_{cv} is the angle of shearing resistance and e is the void ratio, defined according to the soil mechanics convention as the volume of voids divided by the volume of solids. $q = \sigma'_1 - \sigma'_3$ is the deviatoric stress and $p' = \frac{\sigma'_1 + 2\sigma'_3}{3}$ is the mean effective stress where σ'_1 , σ'_2 and σ'_3 represent the major, intermediate and minor principal effective stresses, respectively. $\sigma'_2 = \sigma'_3$ for these axisymmetric triaxial simulations.

Table 1: Macro-scale data at the end of the six simulations after the attainment of critical state

μ	q (kPa)	p' (kPa)	φ'_{cv} ($^{\circ}$)	e
0.0	23.951	107.99	4.98	0.5344
0.1	61.885	120.63	13.54	0.5909
0.25	87.794	129.27	18.17	0.6317
0.5	99.514	133.18	19.97	0.6504
0.75	90.418	130.14	20.19	0.6527
1.0	100.49	133.50	20.98	0.6542

The number of particles is constant throughout these simulations; therefore, the coordination number is directly proportional to the number of edges in a contact network. Figure 2 shows that the number of edges (or equivalently the coordination number) decreases with increasing μ from around 57,000 at $\mu = 0.0$ to 32,000 when $\mu = 1.0$. The opposite trend is observed in the void ratio which increases with increasing μ as shown on the secondary vertical axis on Figure 2. As μ decreases, particles are packed together more closely and so a corresponding increase in the number of contacts is unsurprising.

**Figure 2:** The variations in the number of contacts and the void ratio at the critical state with the interparticle friction coefficient

Although the number of contacts decreases with increasing μ , Figure 3 shows the opposite trend for the number of edges in the Delaunay triangulations which increases with μ up to $\mu = 0.25$ and remains approximately constant thereafter. This is the case for both the conventional, unweighted tessellation based solely on the particle centroids and for the radical tessellation which is weighted by particle diameter.

The numbers of faces or tetrahedra in the Delaunay triangulations also increase with increasing μ up to $\mu = 0.25$ as shown in Figures 4 and 5. Further increases in μ beyond 0.25 do not affect the numbers of faces or tetrahedra in the triangulations. This is perhaps expected from Figure 3 as each face comprises three edges and each tetrahedron comprises six edges. The existence of a threshold beyond which the system shows little sensitivity to μ is reported by [12] who found that the critical-state loci were almost identical for $\mu = 0.5$, 0.75 and 1.0. However, [12] observed substantial differences between $\mu = 0.25$ and $\mu = 0.5$, exemplified by

the differences in void ratio in Table 1. Based on Figures 3-5, it seems that triangulations of the particle centroids ‘saturate’ at lower values of μ than conventional macro-scale measures such as q , p' or e .

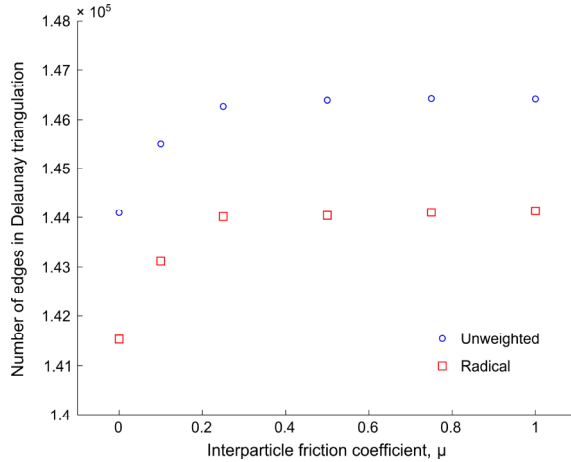


Figure 3: The number of edges in the Delaunay triangulations against the interparticle friction coefficient at the critical state

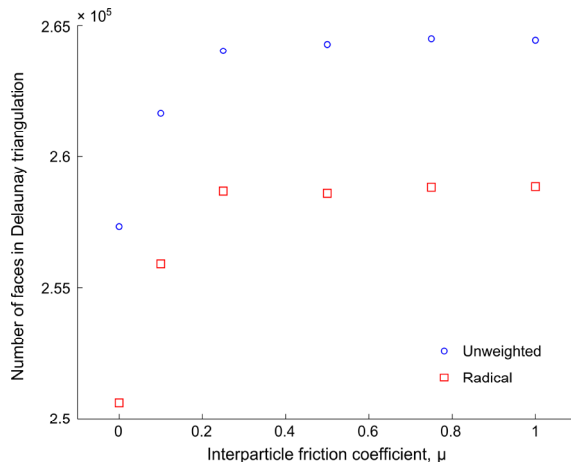


Figure 4: The number of faces in the Delaunay triangulations against the interparticle friction coefficient at the critical state

Two distinct sets of edges connecting particle centroids are available for each simulation: one set of interparticle contacts and one set of Delaunay triangulation edges. These may be compared as some edges are common to, or absent from, both sets, while some edges appear only in the Delaunay set. Every single interparticle contact is present among the associated Delaunay triangulation edges; hence the interparticle contacts may be regarded as a subset of the Delaunay triangulation edges. By comparing Figures 2 and 3, it is apparent that there are between 2.4 and 4.6 times more edges in any Delaunay triangulation than there are in the corresponding contact network. Figure 6 shows the percentage of triangulation edges which are contacts for each simulation. These results are very similar for both types of Voronoi tessellation. As the number of contacts decreases with increasing μ and the number of

Delaunay edges increases with increasing μ , Figure 6 exhibits a sharp decrease as μ increases.

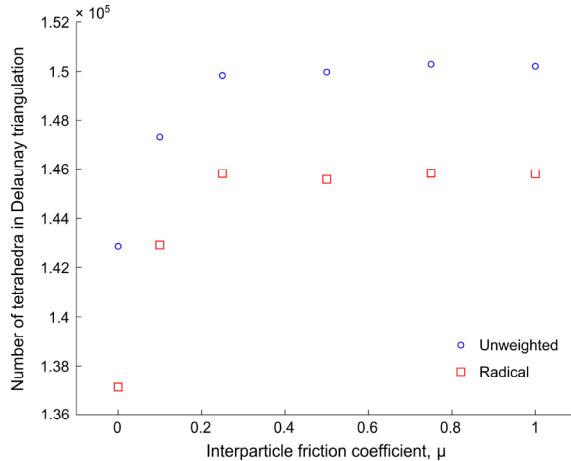


Figure 5: The number of tetrahedra in the Delaunay triangulations against the interparticle friction coefficient at the critical state

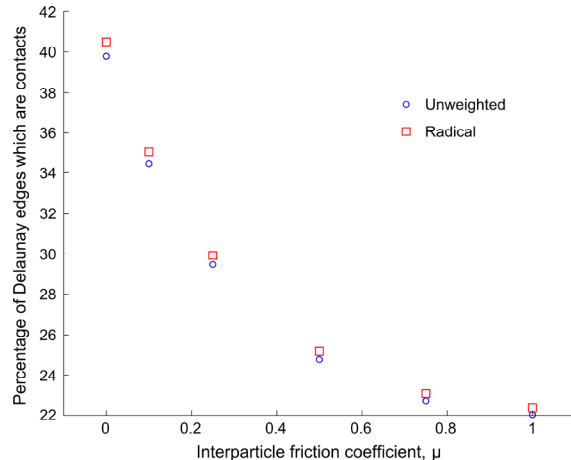


Figure 6: The percentage of Delaunay triangulation edges which are interparticle contacts for each simulation against the interparticle friction coefficient

Two quantities were defined: the percentage of faces in the triangulation comprising three interparticle contacts (P_{fc}) and the percentage of tetrahedra comprising six contacts (P_{tc}). P_{fc} and P_{tc} are respectively plotted against the interparticle friction coefficient on Figures 7 and 8. Both P_{fc} and P_{tc} decrease monotonically as μ is increased. These two figures support the hypothesis of Smart and Ottino [15] that triangular motifs become less widespread as friction increases. Furthermore, these figures also provide additional evidence for the observation that a weak supporting network develops during shearing only at low μ values [12]: the support provided to a strong force chain by weak contacts necessarily creates many triangular arrangements of particles which are far less prevalent at high μ than at low μ values.

Many DEM simulations have shown that there is a non-linear relationship between the angle of shearing resistance, φ'_{cv} , and the interparticle friction coefficient, μ , or equivalently the interparticle friction angle, $\varphi'_p = \arctan \mu$ [7,12-14]. The reason for this non-linear

relationship remains the subject of some debate and is often poorly captured by analytical models [24-26]. One explanation is the interplay between rolling and sliding at the particle contacts [12]; this is not captured correctly by existing analytical models which neglect the effect of buckling. Prior research has shown that the critical buckling load has a non-linear relationship with μ and there exists a threshold value of μ beyond which the critical buckling load becomes invariant, as is the case for φ'_{cv} [12].

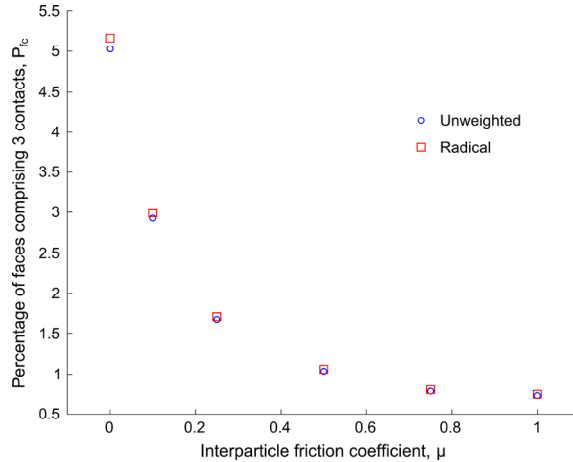


Figure 7: The percentage of Delaunay triangulation faces which are composed of three interparticle contacts against the interparticle friction coefficient at the critical state

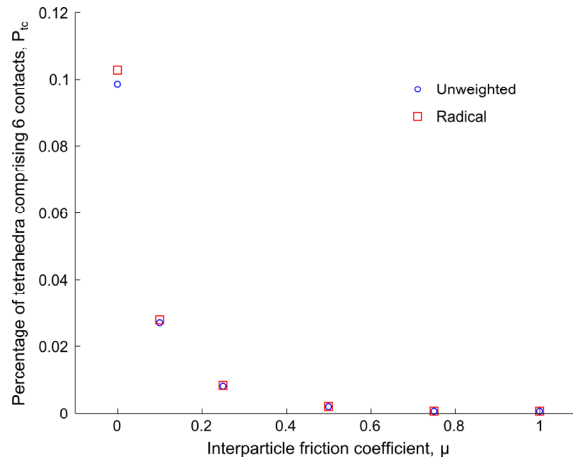


Figure 8: The percentage of Delaunay triangulation tetrahedra which are composed of six interparticle contacts against the interparticle friction coefficient at the critical state

Figure 9 shows that increasing μ reduces P_{fc} (Figure 7) but increases φ'_{cv} . The regressions on Figure 9 show that the relationship between P_{fc} and φ'_{cv} is almost linear. Interestingly, the shear resistance increases when the proportion of triangular structures is reduced. This is somewhat counter-intuitive: triangular structures tend to be more robust and tolerant to variations in the loading direction than columnar structures which are strong only when subjected to an axial load. It seems that the effect of μ on strength is much more significant than the proportion of triangular structures; having a relatively large proportion of triangular

structures at low μ does not noticeably affect φ'_{cv} . Another way of looking at these results is that the contribution to strength due to interparticle friction is dominant compared with the contribution to strength due to micro-scale particle geometry.

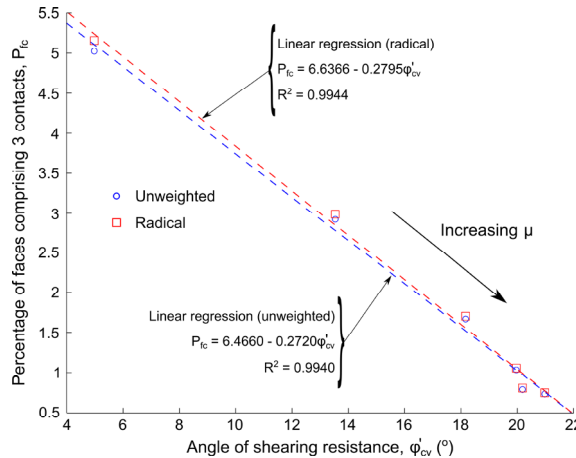


Figure 9: The percentage of Delaunay triangulation faces which are composed of three interparticle contacts against the angle of shearing resistance ($^{\circ}$)

5 CONCLUSIONS

Six polydisperse numerical samples with differing interparticle friction coefficients were sheared triaxially to critical state. Contact networks were obtained and periodic Delaunay tessellations were computed at the end of each simulation using the particle centroids. The numbers of edges that are in the contact networks decrease consistently as μ is increased. This contrasts with the numbers of edges, faces or tetrahedra in the Delaunay triangulations, all of which increase with increasing μ up to $\mu = 0.25$ and become approximately constant thereafter. The existence of a threshold beyond which the system shows little sensitivity to μ is also reported by [12]. Two quantities were defined, both of which decrease monotonically as μ is increased: the percentage of faces in the triangulation comprising three contacts (P_{fc}) and the percentage of tetrahedra comprising six contacts (P_{tc}). These results provide additional evidence for the observations that triangular motifs become less widespread as friction increases [15] and that a mechanically-stable, weak supporting network has greatest importance for stabilising the strong force chains at low values of μ [12]. P_{fc} shows a linearly-decreasing trend with increasing angle of shearing resistance, i.e., the shear resistance increases when the proportion of triangular structures is reduced. This implies that the effect of having a relatively large proportion of triangular structures at low μ is insignificant compared to the effect of μ on the rolling/sliding behaviour [12].

REFERENCES

- [1] Rechemacher, A., Abedi, S. and Chupin, O. Evolution of force chains in shear bands in sands. *Géotechnique* (2010) **60**(5): 343-351.
- [2] Hasan, A. and Alshibli, K.A. Experimental assessment of 3D particle-to-particle

- interaction within sheared sand using synchrotron microtomography. *Géotechnique* (2010) **60**(5): 369-379.
- [3] de Josselin de Jong, G. and Verruit, A. Étude photo-élastique d'un empilement de disques. *Cah. Grpe fr. Etud. Rheol.* (1969) **2**: 73-86.
 - [4] Rothenburg, L. and Bathurst, R.J. Analytical study of induced anisotropy in idealized granular materials. *Géotechnique* (1989) **39**(4): 601-614.
 - [5] Barreto, D. and O'Sullivan, C. The influence of inter-particle friction and the intermediate stress ratio on soil response under generalised stress conditions. *Granul. Matter* (2012) **14**(4): 505-521.
 - [6] Radjai, F., Wolf, D.E., Jean, M. and Moreau, J.-J. Bimodal character of stress transmission in granular packings. *Phys. Rev. Lett.* (1998) **80**(1): 61-64.
 - [7] Thornton, C. Numerical simulations of deviatoric shear deformation of granular media. *Géotechnique* (2000) **50**(1): 43-53.
 - [8] Behringer, R.P., Daniels, K.E., Majmudar, T.S. and Sperl M. Fluctuations, correlations and transitions in granular materials: statistical mechanics for a non-conventional system. *Philos. Trans. A Math. Phys. Eng. Sci.* (2008) **366**: 493-504.
 - [9] O'Sullivan, C., Wadee, M.A., Hanley, K.J. and Barreto, B. Use of DEM and elastic stability analysis to explain the influence of the intermediate principal stress on soil strength. *Géotechnique* (2013) **63**(15): 1298-1309.
 - [10] Tordesillas, A. and Muthuswamy, M. On the modeling of confined buckling of force chains. *J. Mech. Phys. Solids* (2009) **57**: 706-727.
 - [11] Hanley, K.J., O'Sullivan, C., Wadee, M.A. and Huang, X. Use of elastic stability analysis to explain the stress-dependent nature of soil strength. *Roy. Soc. Open Sci.* (2015) **2**: 150038.
 - [12] Huang, X., Hanley, K.J., O'Sullivan, C. and Kwok, C.Y. Exploring the influence of interparticle friction on critical state behavior using DEM. *Int. J. Num. Anal. Met.* (2014) **38**(12): 1276-1297.
 - [13] Peña, A.A., Lizcano, A., Alonso-Marroquin, F. and Herrmann, H.J. Biaxial test simulations using a packing of polygonal particles. *Int. J. Num. Anal. Met.* (2008) **32**(2): 143-160.
 - [14] Yang, Z.X., Yang, J. and Wang, L.Z. On the influence of inter-particle friction and dilatancy in granular materials: a numerical analysis. *Granul. Matter* (2012) **14**(3): 433-447.
 - [15] Smart, A.G. and Ottino, J.M. Evolving loop structure in gradually tilted two-dimensional granular packings. *Phys. Rev. E* (2008) **77**: 041307.
 - [16] Huang, X., Hanley, K.J., O'Sullivan, C. and Kwok, F.C.Y. Effect of sample size on the response of DEM samples with a realistic grading. *Particuology* (2014) **15**: 107-115.
 - [17] Simmons, G. and Brace, W.F. Comparison of static and dynamic measurements of compressibility of rocks. *J. Geophys. Res.* (1965) **70**: 5649-5656.
 - [18] Plimpton, S. Fast parallel algorithms for short-range molecular dynamics. *J. Comput. Phys.* (1995) **117**(1): 1-19.
 - [19] Thornton, C., Cummins, S.J. and Cleary, P.W. An investigation of the comparative behaviour of alternative contact force models during elastic collisions. *Powder Technol.* (2011) **210**(3): 189-197.
 - [20] Thornton, C., Cummins, S.J. and Cleary, P.W. An investigation of the comparative

- behaviour of alternative contact force models during inelastic collisions. *Powder Technol.* (2013) **233**: 30-46.
- [21] Yang, J. and Sze, H.Y. Cyclic behavior and resistance of saturated sand under non-symmetrical loading conditions. *Géotechnique* (2011) **61**(1): 59-73.
 - [22] Rycroft, C.H. Voro++: A three-dimensional Voronoi cell library in C++. *Chaos* (2009) **19**: 041111.
 - [23] The MathWorks Inc. MATLAB version 7.13 R2011b [computer software] (2011). Natick, Massachusetts, US.
 - [24] Horne, M.R. The behaviour of an assembly of rotund, rigid, cohesionless particles. III. *P. Roy. Soc. A-Math. Phy.* (1969) **310**(1500): 21-34.
 - [25] Caquot, A. *Équilibre des massifs à frottement interne: stabilité des terres, pulvérulentes ou cohérentes*. Gauthier-Villars, Paris (1934).
 - [26] Bishop, A.W. Discussion on ‘Shear characteristics of a saturated silt, measured in triaxial compression’. *Géotechnique* (1954) **4**(1): 43-45.

ANALYSIS OF AIRBORNE FINES IN CYLINDRICAL BIOMASS STORAGE SILOS

L. L. LULBADDHA WADUGE¹ AND S. ZIGAN²

1 The Wolfson Centre for Bulk Solids Handling Technology

2 Mechanical Manufacturing and Design Engineering

University of Greenwich, Central Avenue, Chatham Maritime, Kent ME4 4TB

e-mail: L.L.LulbaddhaWaduge@greenwich.ac.uk, web page: www.bulksolids.com/

e-mail: s.zigan@gre.ac.uk, web page: www.gre.ac.uk

Key words: Air-current segregation (ACS), biomass storage silos

Abstract. Biomass handling industries are transporting and storing huge quantities of biomass materials. During transportation, wood pellets can be subject to attrition (a process that generates additional fines and dust). When filling large volume storage silos the fines tend to concentrate in certain areas within the silo, depending upon the size of the particles and their sensitivity to the method of filling (Zigan et al. 2008). These particles are easily made airborne when discharged from the storage and can represent an increased health related hazard as well as dust explosion hazards. The risk of dust explosions increases with the size of storage. Previous researchers have developed dust explosion models in order to assist practitioners from industry to minimise the health and safety risks for their plants[1].

This research studies the significance of airborne fines concentration in different silo locations. The fines concentrations will be evaluated according to analysis approach described first in Zigan et al. 2008. The experimental silo is cylindrical and a mixture fines and coarse particles will be fed by gravity centrally into the silo.

It was found that fines tended to accumulate near the silo wall. This can partly be explained by a segregation phenomenon called air current segregation (ACS). ACS is present in the silo as an effect of both circulating air currents generated by the falling particle jet. The fines reach the terminal velocity before the coarse particles then the fines follow the dominant air flow direction.

This research shows the importance of including a consideration of the fines concentration in any modelling approach developed to indicate the propagation and mobilisation of fugitive particulate material during filling operations.

1 INTRODUCTION

Transporting and storing large quantities of bulk materials is common to most of the industries related to bulk-solids handling. (i.e. Drax Power Station which produces 7% of the UK electricity and burns ~12m tonnes of wood pellets annually). Among them, the biomass handling industries are very common. One of the most hazardous incidents which occurs in biomass industry are dust explosions.

Fines are generated due to breakage of wood pellets during transportation and filling processes. During handling dust gets airborne and creates a dust cloud in silos and other enclosed vessels. The creation of the dust is very hazardous in many aspects. One of the main hazards is the health issues the operators can face as a cause of inhaling the dusty air[2]. And the other issue is that concentrated dust can create dust explosions at certain levels of dust concentration.

Although some protection and safety overalls can be worn in order to avoid the health hazard, the risk of dust explosions remains the same. critical levels of dust concentrations have been found through a number of experiments and software calculations[3]. Thus the remaining necessity is to predict the concentrations of dust at different locations in silos and the other filling vessels.

Therefore this paper introduces an experiment of locating the airborne dust/fines concentrations through investigating the dust settlement at the bottom of silo. In addition to that there are findings relating to the behaviour of air-currents in the vessel during the filling process.

The main focus of this paper is on the amount of dust generated due to the air current segregation during the filling process of biomass storage silos.

There are a number of researches [1] which have focused on investigating the segregation of fine particles along with the air-currents in silos during the filling procedure which can be referred to as air current segregation. But most of the researches focused on materials which have less diversity in terms of particle size.

According to Zigan et al. alumina powder segregates at higher filling rates [1]. Alumina powder requires a higher filling rates as alumina powder has the characteristics which shows less separation of fines from the main particle jet during the filling. That experiment shows it is required to use a mixture of materials with a good diversity of particle sizes.

Therefore this paper is particularly focused on using a mixture of saw dust and wood pallets consisting of two known particle sizes which have a good diversity of particle sizes.

1.1 Concepts

This experiment is designed on two arguments.

- Concentration of the fines in the collectors at the edge depends on the air flow patterns created by the falling particle jet.
- As this mixture is consists of particles with two different sizes, a constant flow of the falling particle jet cannot be expected. Instead a particle jet with a spiral shape can be expected. This is due to the separation of the fine particles form the coarse particles.
- This effect might depend on size of the opening. Which is not focused in this paper.

Furthermore, the expected settlement of dust at the end of experiment should be a vertical fall under the terminal velocity. The reason is there should be no interactions or trajectories between particles.

2 METHODOLOGY

2.1 The rig

A rig has been built previously for the purpose of investigating the scaling rule of air-current segregation of alumina powder [1]. It has been preliminary identified that the rig is ideal for the current experiment after some minor modifications. The modifications that have been added are:

- Modified feeding mechanism: The current feeder has been designed for use with alumina powder. But as the mixture of saw dust with wood pallets (broken) that has been used in this experiment has the characteristics of a mass flow. Therefore the feeding mechanism has been rebuilt with a gravity feeder designed for a mass flow[4].
- Air extractors: The rig has been originally built with four air extractors and flow meters attached. In this particular experiment the air extraction has been adjusted to extract 10.575 Litres per minute, which is equal to the volumetric feeding rate of the material. Material collectors (sample pouches) at the bottom of the rig: As the original design of the rig was for alumina power, which had the flowability of a core flow could easily flow through the bottom orifice of collectors. Because the new material a mass flow like behaviour a set of bags has been used instead of the orifices at the bottom.



Figure 1 : Bottom
(collectors) of the rig

2.2 Sample Preparation

The aim of the experiment was to investigate the effect of the dust generation due to air-current segregation when using materials which have different sized particles to fill a silo. Therefore this experiment has been conducted with a material consisting of two different sized particles of the same material. Broken wood pellets which have a size range between 3.15 mm to 4.75 mm have been used as the coarse particles of the mixture. These coarse particles were mixed with the fines of the same material with a size range of 0.1 μm to 500 μm . The mixture consists the ratio (weight) of 1: 10 between the fines and the coarse material.



Figure 2 : Materials combination

The final mixture which has been used for the experiments had a weight of 1100 grams with 100 grams of fines and 1000 grams of coarse materials.

2.3 Experimental

The mixture has been fed into the rig from the top opening with the aid of a gravity feeder. Then the air extractors were activated while the filling process to extract the air inside the rig. The extractors were calibrated to extract air in the same feeding (volumetric) flow-rate as the biomass mixture. Simultaneously a high-speed video with 224 fps and a resolution of 224x160 of the flow has been captured. The experiment was stopped after feeding 1100 grams of materials. Then the settled dust at the bottom of the silo has been analysed.

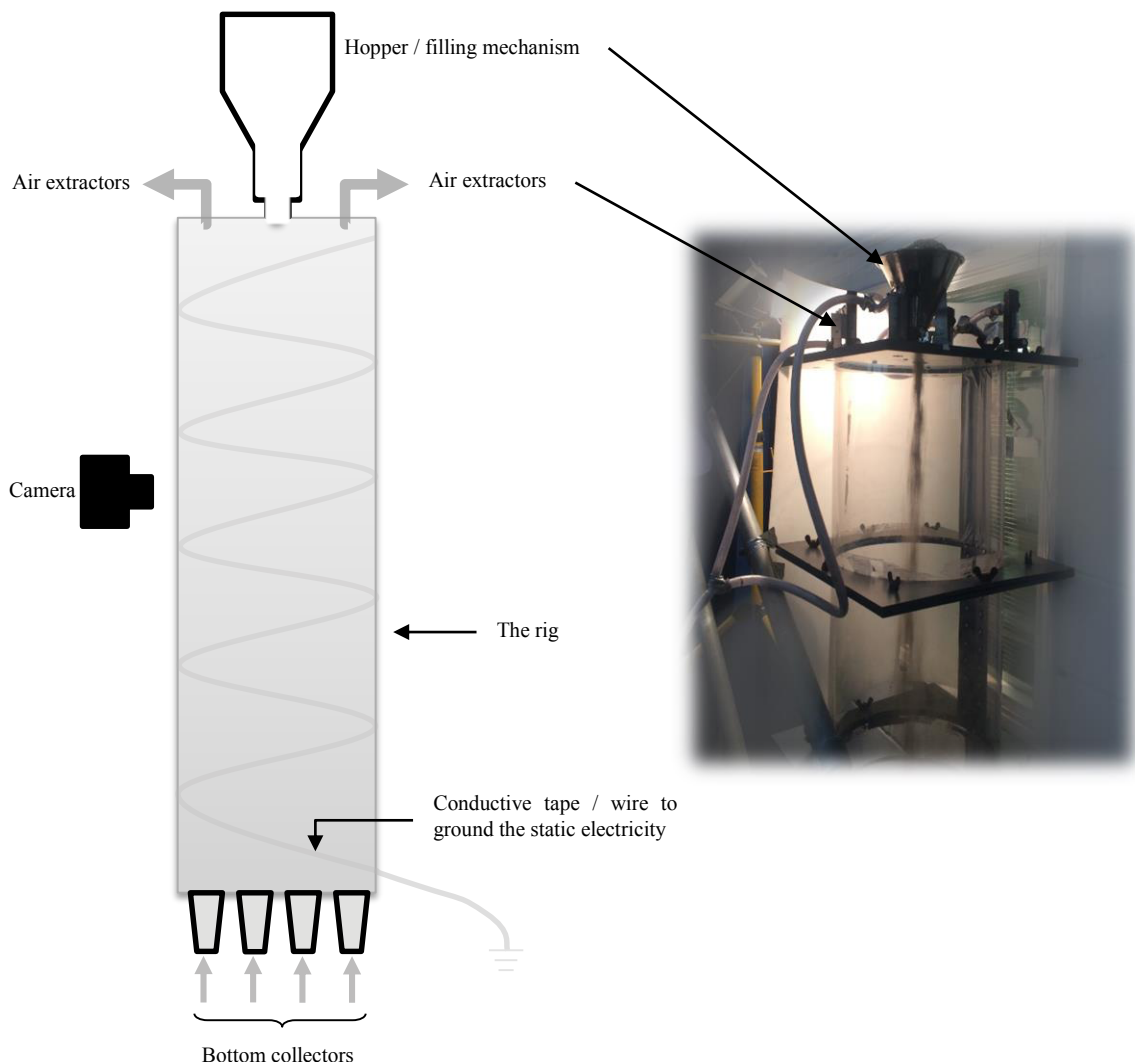


Figure 3 : Schematic overview of the rig and the actual rig

3 RESULTS AND DISCUSSION

3.1 Mass distribution

The total mass distributions are presented in Figure 4 and 5. The weight distribution of the settled dust was centred in to the middle of the collectors.

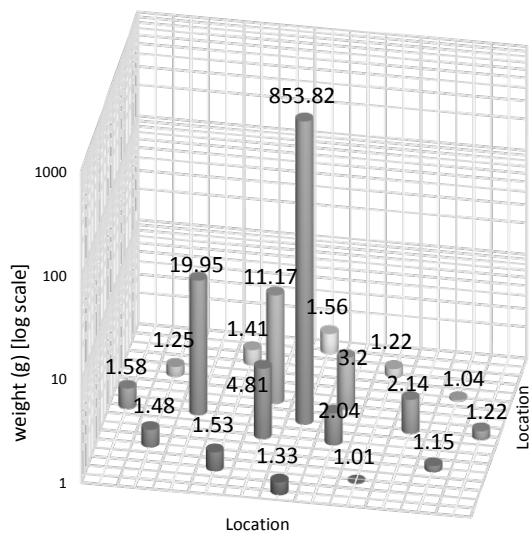


Figure 5 : mass distribution of Test 1

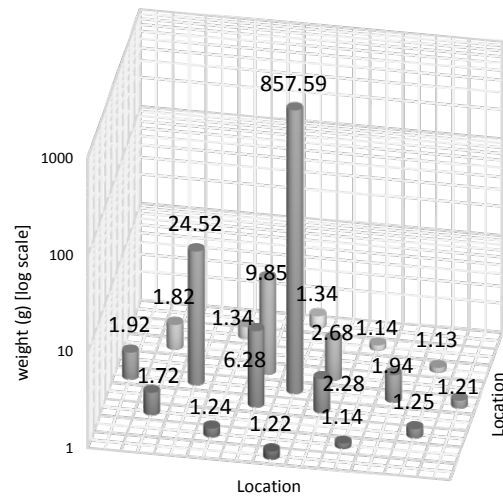


Figure 4 : mass distribution of Test 2

Figure 4 and 5 show the mass distribution is slightly off-centred and the distribution at the compartment 13 to 17 is very low. Furthermore it is clear that there are more materials dropped towards to the left side of the collectors. But still the results can be considered as an almost symmetrical distribution. It shows that the most of the coarse materials dropped straight on the bottom of silo.

3.2 Particle size distribution

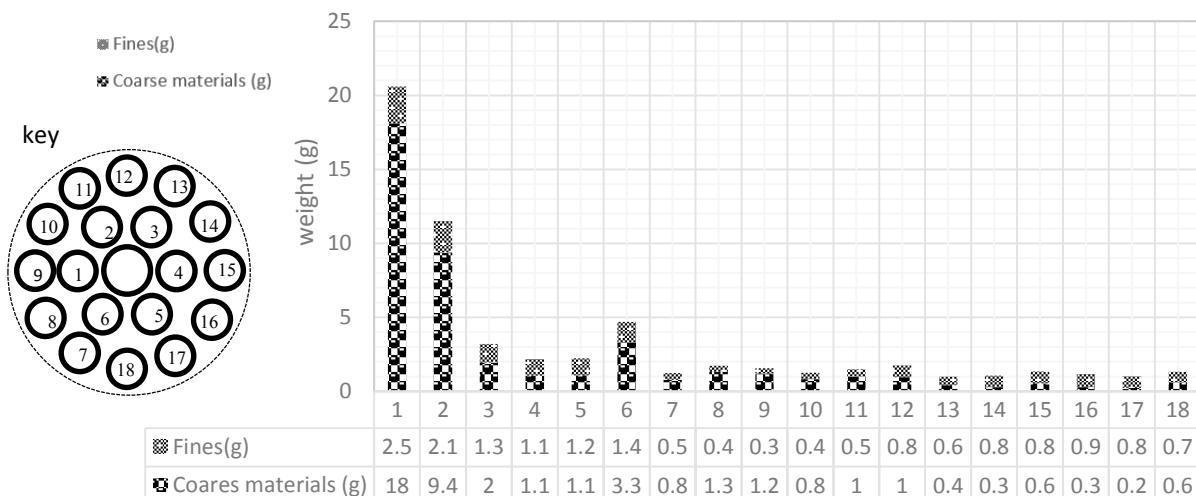


Figure 6 : Distribution of individual components for Test 1

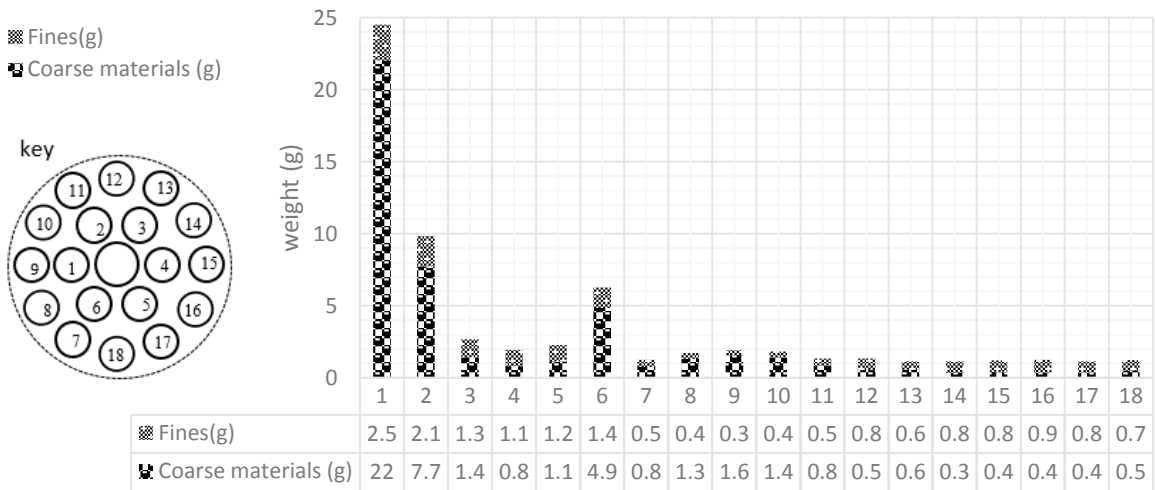


Figure 7 : Distribution of fines for Test 2

The centre compartment contains 786.06 grams of the coarse materials and 49.76 grams of fines. As a percentage 5.74% of middle compartment contains fines. Which is a significantly lower than the initial 10% (something like this...).

Figure 8 shows a higher percentage of fines from collector number 12 to 18 and figure 9 shows similar results from test 2. From that it is clear that the air currents carried fines away from the main particle jet to the edge of the silo. Even though the particle jet is slightly off centred a considerable amount collected at the centre collector.

3.3 Dust concentrations

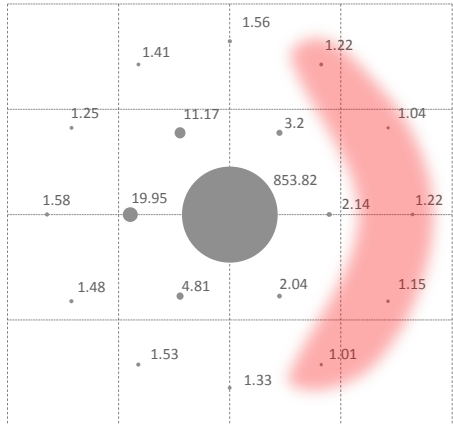


Figure 9 : Mass distribution and potentially explosive areas (red). (Test 1)

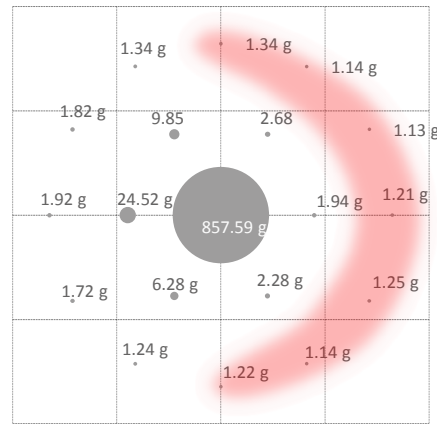


Figure 8 : Mass distribution and potentially explosive areas (red). (Test 2)

Figures 8 and 9 show that there are areas with higher dust concentrations. According to Eckhoff et al. the range of explosive dust concentration is between 100 g/m^3 to few kg/m^3 [5]. Figures 6 and 7 shows that collectors 14 to 17 have more than 50% dust from the total of both coarse and fines. Therefore there will be a risk of explosion when filling a large scaled silo.

3.4 Segregation index

The segregation index introduced by Zigan et al. [1] has been used to calculate as shown in the equation (1).

$$I_s = \sqrt{\sum_i \left(\frac{M_i}{M_L} \times \left[\frac{c_i - c_L}{c_L} \right]^2 \right)} \quad (1)$$

c_i Mass fraction of fines in compartment i
 M_i Mass of powder in compartment i
 c_L Mass fraction of fines over all compartments.
 M_L Total mass of all compartments.

The segregation index has been calculated for both test 1 and test 2 in order to have an idea about the segregation.

Segregation index of test 1 = 0.2795

Segregation index of test 2 = 0.3210

(The above results were taken at the discharge rate of 4.91 kg/min (10.57 Liter per minute). The air extraction rate was the same value as the filling rate.)

4 CONCLUSIONS

It was observed that the fine particles of the material comes to the terminal velocity quickly while the coarse particles remain under the gravitational acceleration for a longer time. The air-currents inside the silo take fine particles away from the main jet. This observation was very clear in the video footage as well as in the pictures, for example (refer to the figure 3).

Therefore it is necessary to do a simulation with two way coupling method. Which will show this phenomena and it will be useful in further understanding.

The experiment confirms the prediction mentioned in the beginning. Which is the concentration of fines in the outside compartment depends on the patterns of the air-currents created by the falling particle jet.

Particle stream is falling slightly off the centre. And the flow shows a spiral pattern consisting of coarse particles. This can only be examined through a simulation or high speed video footage. A simulation with two way coupling will help to better understand the physics behind these observations. Finally it is necessary to focus about shape of falling particle jet.

5 REFERENCES

- [1] S. Zigan, R. B. Thorpe, U. Tuzun, G. G. Enstad, and F. Battistin, "Theoretical and experimental testing of a scaling rule for air current segregation of alumina powder in cylindrical silos," *Powder Technology*. Elsevier B.V., 18-Mar-2008.
- [2] K. Reinhold, M. Järvis, and P. Tint, "Practical tool and procedure for workplace risk assessment: Evidence from SMEs in Estonia," *Saf. Sci.*, vol. 71, no. PC, pp. 282–291, Jan. 2015.

- [3] C. J. Coffey and D. W. Price, "Probabilistic risk assessment in combination with CFD modelling of biomass dust explosions within large bulk storage volumes," in *Institution of Chemical Engineers Symposium Series*, 2012, no. 158, pp. 520–526.
- [4] V. Thayalan and R. G. Landers, "Regulation of Powder Mass Flow Rate in Gravity-Fed Powder Feeder Systems," *J. Manuf. Process.*, vol. 8, no. 2, pp. 121–132, Jan. 2006.
- [5] R. K. Eckhoff, "Understanding dust explosions. The role of powder science and technology," *J. Loss Prev. Process Ind.*, vol. 22, no. 1, pp. 105–116, Jan. 2009.

BACK FROM THE SOLID TEMPERATURE TO KINETIC ENERGY OF ITS MACRO-MOLECULES

Sergey V. Arinchev

Moscow Bauman State Technical University
107005, 2-ya Baumanskaya street, 5/1, Moscow, Russian Federation
arinchev@inbox.ru

Key words: Solid, Macro-molecule, Temperature, Kinetic Energy

Summary. *For solving the solid heat-conduction problem, the “temperature” concept is replaced with the original “macro-molecule kinetic energy” concept. The heat-conduction problem is considered as the solid forced-vibration problem with the transient taken into account.*

The macro-molecules are point particles. Their contact is not available. Interaction of macro-molecules is determined by their force characteristic. Macro-molecule models of the solid bars made of different materials (steel, fluoroplastic, aluminium alloys) are tested for tension, compression and torsion in the laboratory [1-3] and proved their right of existence. For solving the test problems, the required number of macro-molecules is relatively small (about a hundred) and there is no need in a supercomputer.

The fact is that the available particle-based methods reveal the contradiction between their principle finite character and the classic continuous infinitesimal approach. For example, in the work [4] we see the attempt to combine the finite particles and the point-stress concept. The work [5] presents the same attempt to combine the finite particles and the concepts of point temperature and point heat flux. There is even the attempt to approximate the 2nd-order spatial derivative of the heat-conduction equation. Let's take another way. It is time to overcome the available indecision and hesitate and to meet the original discreet particle-based challenge. We know from the secondary school: there is no temperature, there is kinetic energy of separate molecules. So, using the well-known proportionality law

$$\bar{E} = \frac{3}{2} kT \quad (1)$$

let us go right-to-left back home from the solid temperature to (averaged) kinetic energy of its macro-molecules.

It is better to take the relative values (2) to dispense with the dimensional quantities like

the Boltzmann conversion factor k . H_j is the j -th macro-molecule hotness degree, $j = 1, \dots, n$.

$$\frac{T_j}{T_{\max}} = \frac{\bar{E}_j}{\bar{E}_{\max}} \approx \frac{H_j}{H_{\max}} \quad (2)$$

It is obtained by averaging (3) kinetic energy of the macro-molecule in the integration time interval t . The hotness-degree calculation procedure is specified below (see Figure 9).

$$H_j = \frac{\int_0^t E_j(\tau) d\tau}{t} \quad (3)$$

The considered $0.01 \times 0.01 \times 0.03$ (m) solid bar is specified in Figure 1. The bar material

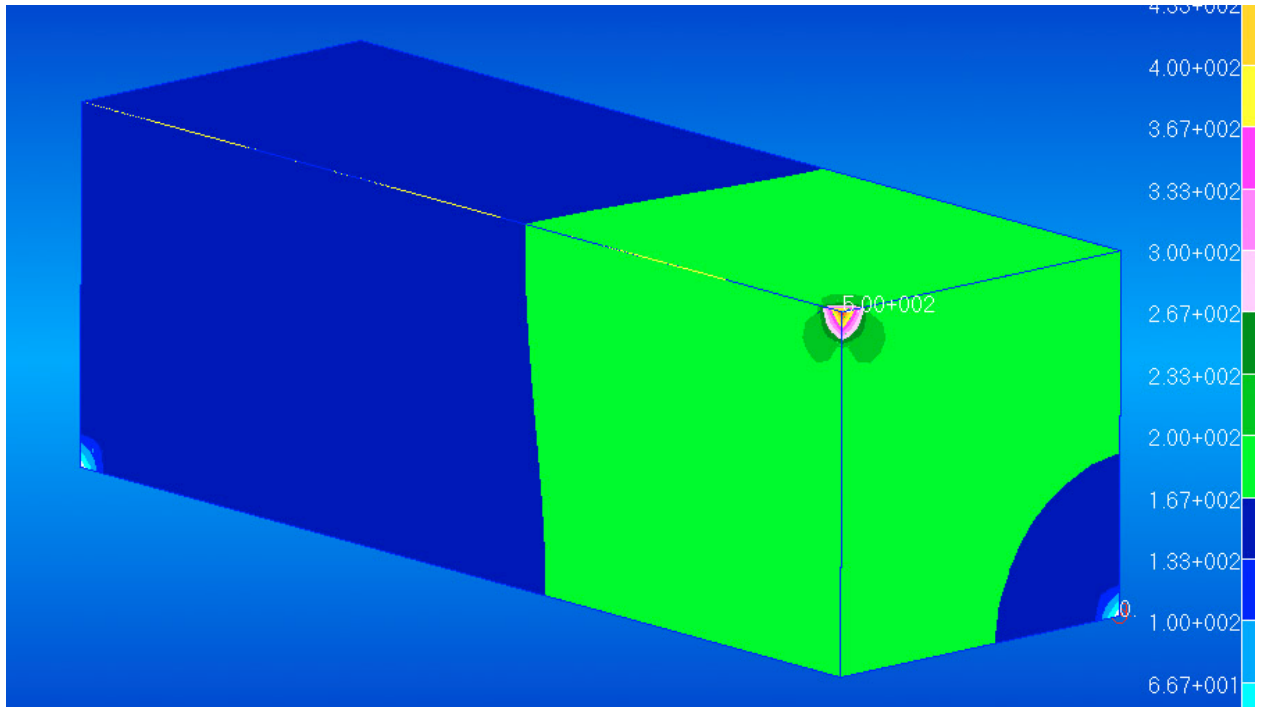


Figure 1: Bar reference temperature field (exact solution) obtained using MSC.Nastran.Thermal

is isotropic. The bar is loaded by applying the three point temperatures to its vertices: the two 0 °K (frozen) vertices are in the bottom face, the 500 °K (maximum temperature) vertex is in the front edge. Figure 1 presents the reference (exact) FEM solution of the steady-state heat-conduction problem obtained using MSC.Nastran.Thermal software. This exact temperature field is compared below with the determined distribution of the established macro-molecule hotness degree.

There are two important features of the obtained exact FEM solution:

- 1) **uniformity** of the temperature field. The colour change is available. But it is not a

temperature drop. It is just the vicinity of the (167 °K) temperature-scale level specified in the Figure 1 right side. Except for the immediate loaded-vertex vicinity, the bar volume temperature varies by a dozen °K. That is why the Figures below compare the exact FEM reference temperature distribution and the obtained macro-molecule hotness-degree distribution only 1) along the bar front upper edge (containing the maximum-temperature vertex) and 2) along the bar back lower edge (containing the frozen vertex). Approximate ratio of the bar volume temperature and the bar maximum temperature is 1/3. The ratio is 1.0 in the maximum-temperature point. It is 0.0 in the frozen point. The fact is that these values do not depend on the applied maximum temperature. It is the characteristic estimate of the (2) ratios.

2) **independence** of the obtained temperature field on thermal properties (specific heat, density, thermal conductivity factor) of the material. The fact is that the problem is a steady-state one, internal heat sources are not available, material is isotropic. So, the heat-conduction equation [5] is the homogeneous Laplace equation reduced by the temperature-conductivity factor. Likewise, this temperature field does not depend on mechanical properties (stiffness factor) of the material. So, the specified material properties of the macro-molecule model may be selected arbitrarily in compliance with the established calculation requirements.

The considered macro-molecule model is specified in Figure 2. It is developed using MSC.Adams software. The macro-molecules are arranged in the nodes of the design lattice.

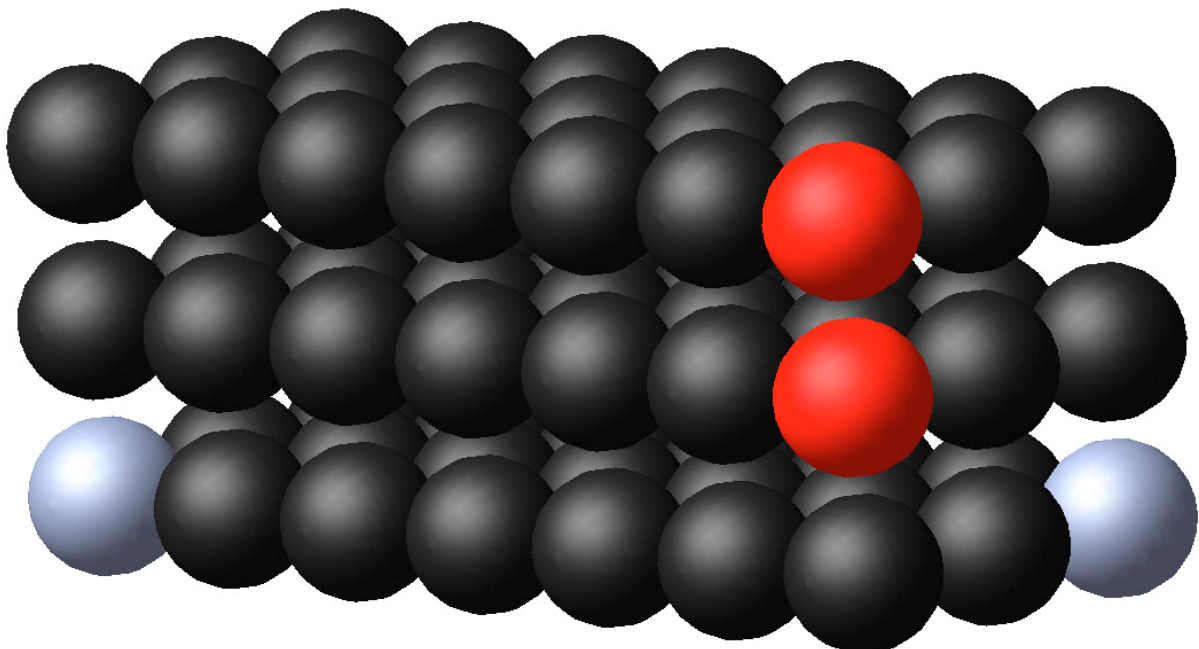


Figure 2: Bar macro-molecule model made of $3 \times 3 \times 7 = 63$ molecules

Their interaction is determined by their force characteristic (specified below). If the macro-

molecule is hot, then it oscillates in the vicinity of its equilibrium state. The macro-molecules are fixed (slate-blue ones), if they are frozen. Heating load is applied to the two red points. It is the internal kinematic excitation. It means that these points move in relation to each other with the given intensity. This internal excitation may not be a noise one. Mono-harmonic excitation is sufficient. The 3D transient takes place. It finally converges to a steady-state kinetic-energy distribution. This distribution is compared with the exact FEM temperature field specified above.

It is important to trace convergence of the specified distribution in the model macro-molecule number. The bar edge ratio is 1:1:3. So, there are three options: $2 \times 2 \times 4 = 16$ macro-molecules, $3 \times 3 \times 7 = 63$ macro-molecules (see Figure 2) and $4 \times 4 \times 10 = 160$ macro-molecules.

The main feature of the obtained exact FEM solution is distribution **uniformity**. The uniformity origin is understandable, if the particles contact with each other and exchange their impacts. But the macro-molecules do not contact with each other. They just oscillate in the vicinity of the lattice nodes. To solve the problem, let's consider the beam oscillation modes.

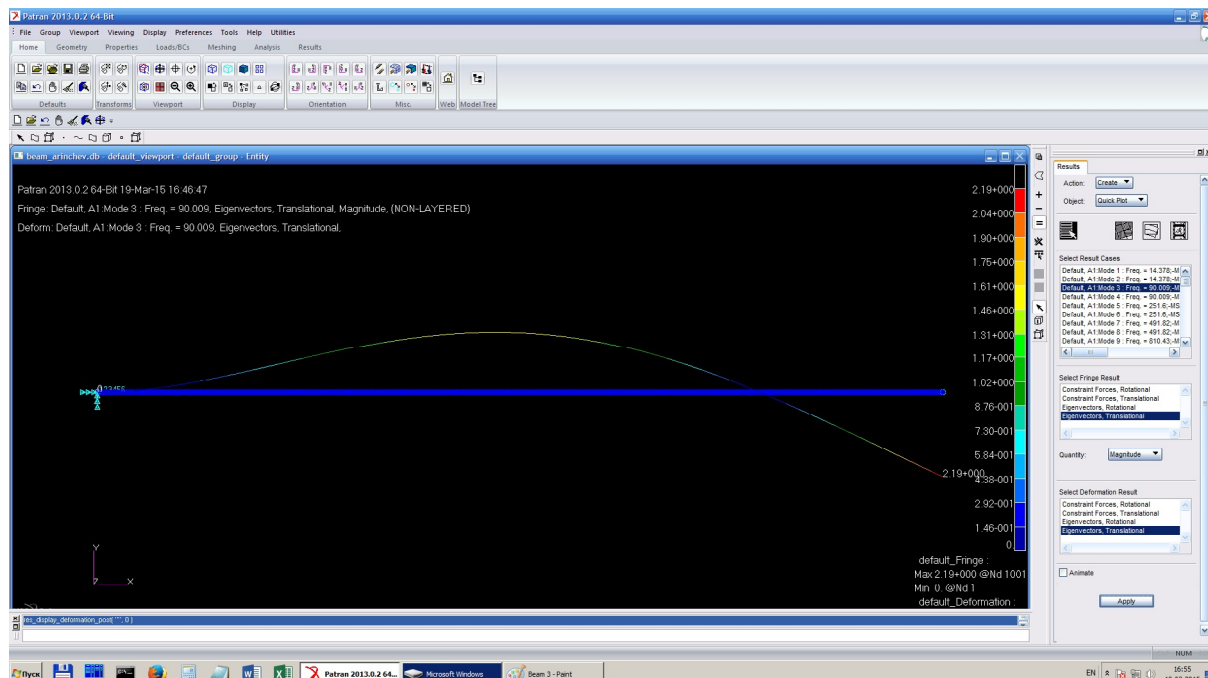


Figure 3: Beam oscillation mode No. 2

Figure 3 specifies the beam oscillation mode No. 2. Figure 4 specifies the beam oscillation mode No. 100. It is evident that the higher the mode No., the more uniform is the mode distribution. The conclusion is: only higher (molecular) harmonics shall be available in the heating excitation response. Lower harmonics (bending ones, torsion ones, tension ones, etc.) shall not be available. Figure 5 illustrates one of the bar lower bending oscillation modes. Figure 6 illustrates one of the bar higher molecular oscillation modes.

But there is the difficulty. Frequencies of the required molecular harmonics make hundreds

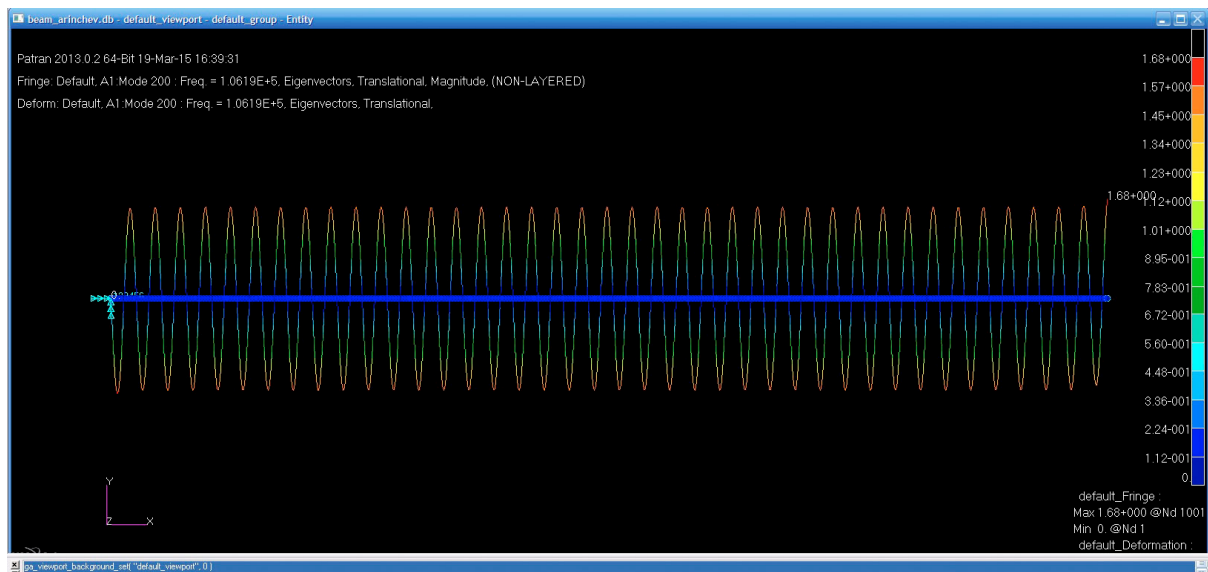


Figure 4: Beam oscillation mode No. 100

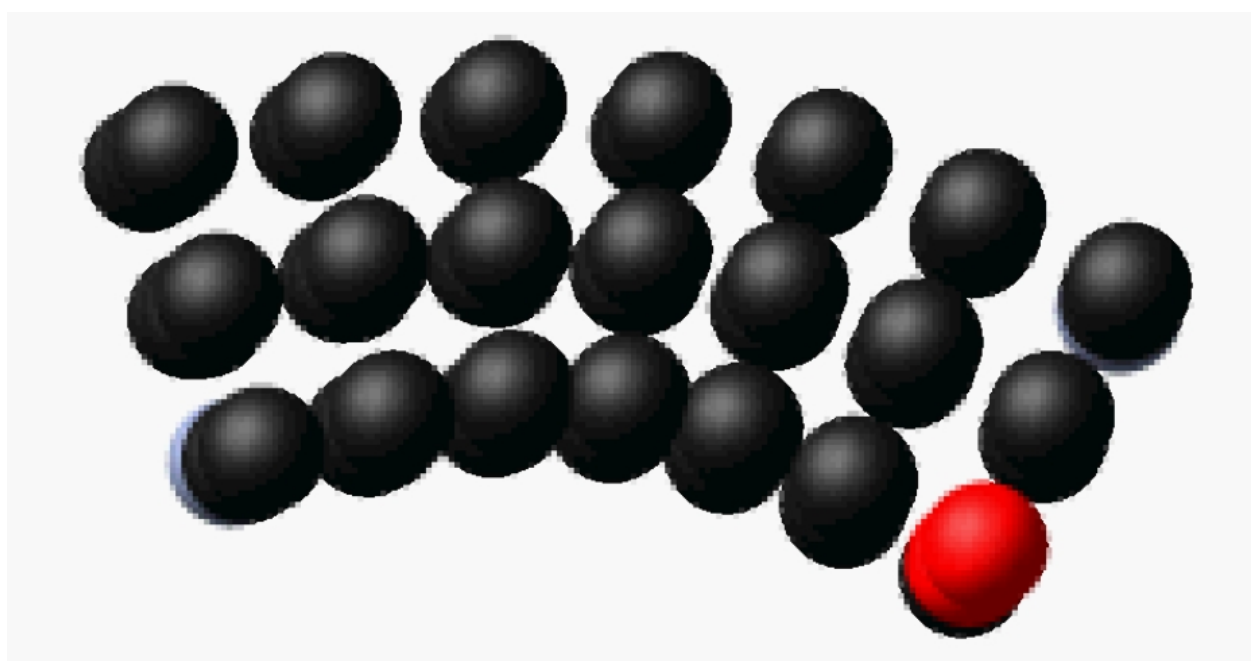


Figure 5: Bending oscillation mode of the bar made of $3 \times 3 \times 7 = 63$ molecules (top view)

of thousands of Hz. It is really impossible to integrate such a transient. The outcome is to take into account the second important feature of the exact FEM solution: **independence** of the

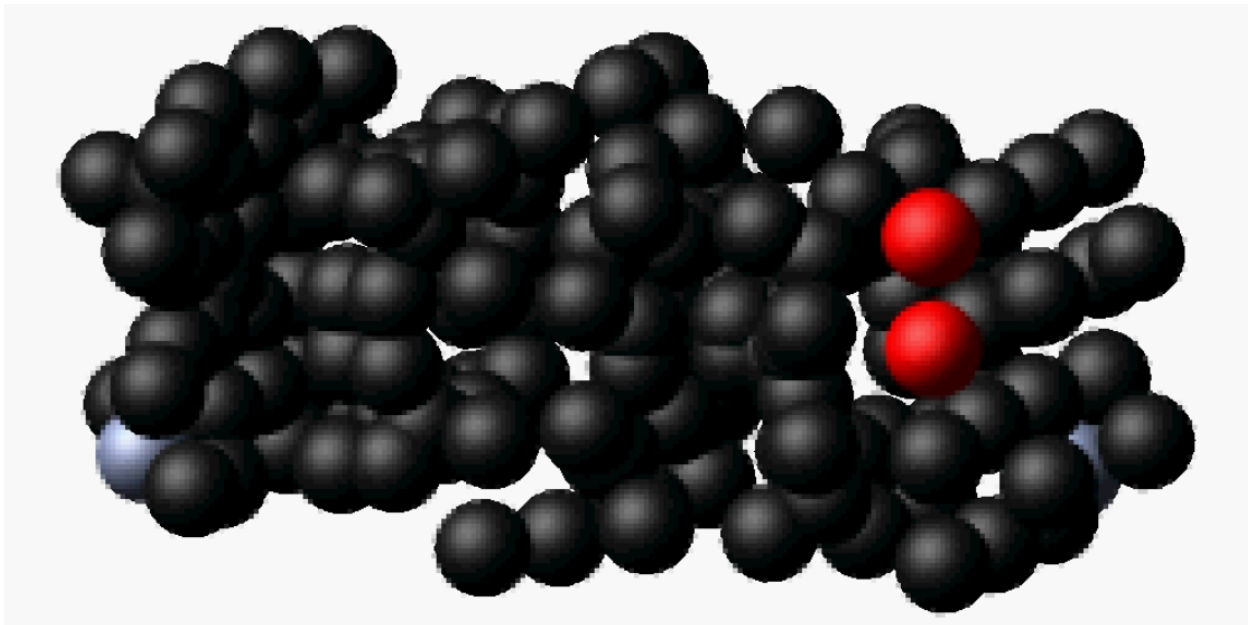


Figure 6: Molecular oscillation mode of the bar made of $4 \times 4 \times 10 = 160$ molecules

solution on the material properties. So, let's lower the model stiffness factor (A , see below) to get down the available molecular frequency range and to provide the comfortable integration conditions. This assumption has the drawback. It makes impossible to solve the coupled problem of heat-conduction analysis and thermal-stress analysis at the same time for the same model. It is assumed that the comfortable upper frequency level is 50 Hz.

The macro-molecule interaction mode is "each one with each one except for itself". Interactions of the model containing $2 \times 2 \times 4 = 16$ macro-molecules are illustrated in Figure 7 using thin lines in the MSC.Adams interface. The available number of combinations is significant. It requires developing a special program using the built-in MSC.Adams language.

The interactions are determined by the macro-molecule force characteristic. The macro-molecules are arranged in the lattice nodes. The material is an isotropic one, 3D central-symmetry interaction is available. There are many equilibrium positions. Potential of the Lennard-Jones type provides a single equilibrium position (root) and does not fit here. The multi-root macro-molecule force characteristic is developed in [2]. It is arranged within the envelope of the Lennard-Jones type. The required number of roots of the macro-molecule force characteristic is determined by the number of the macro-molecule essential neighbors specified in Figure 8. Let the red one be the given macro-molecule and the yellow ones be its neighbors. Let's assume that the force characteristic is set to zero, if the distance between the interacting macro-molecules exceeds $2a$, where a is the lattice spacing parameter. (It is the so called short-range interaction and the most simple one.)

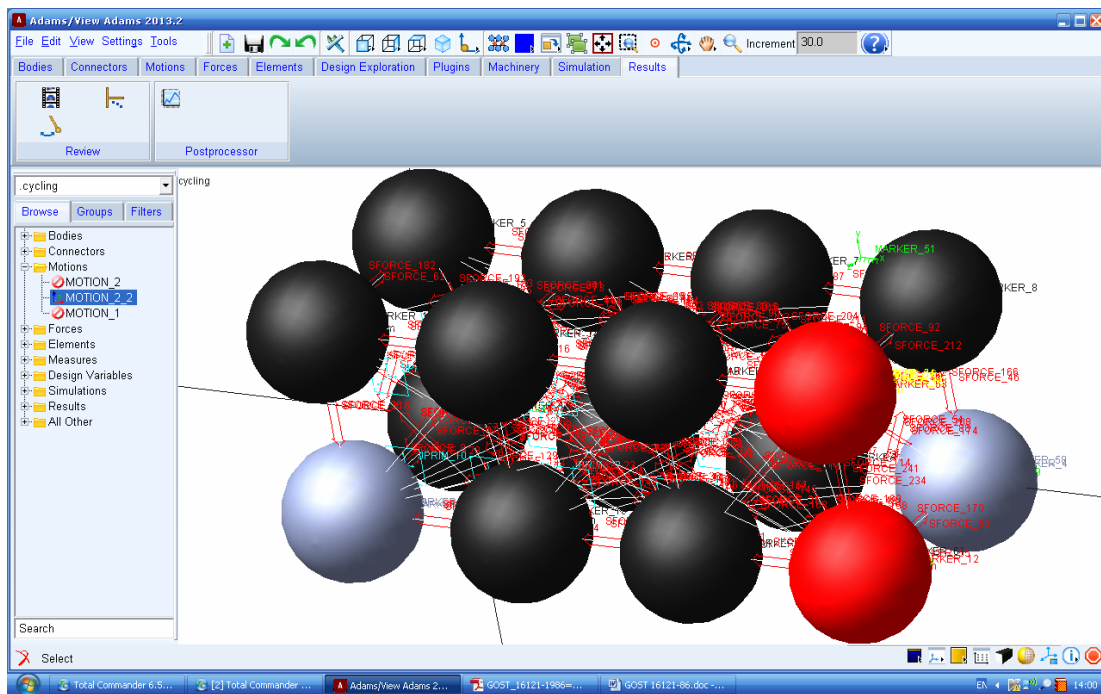


Figure 7: Bar macro-molecular model made of $2 \times 2 \times 4 = 16$ molecules in MSC.Adams

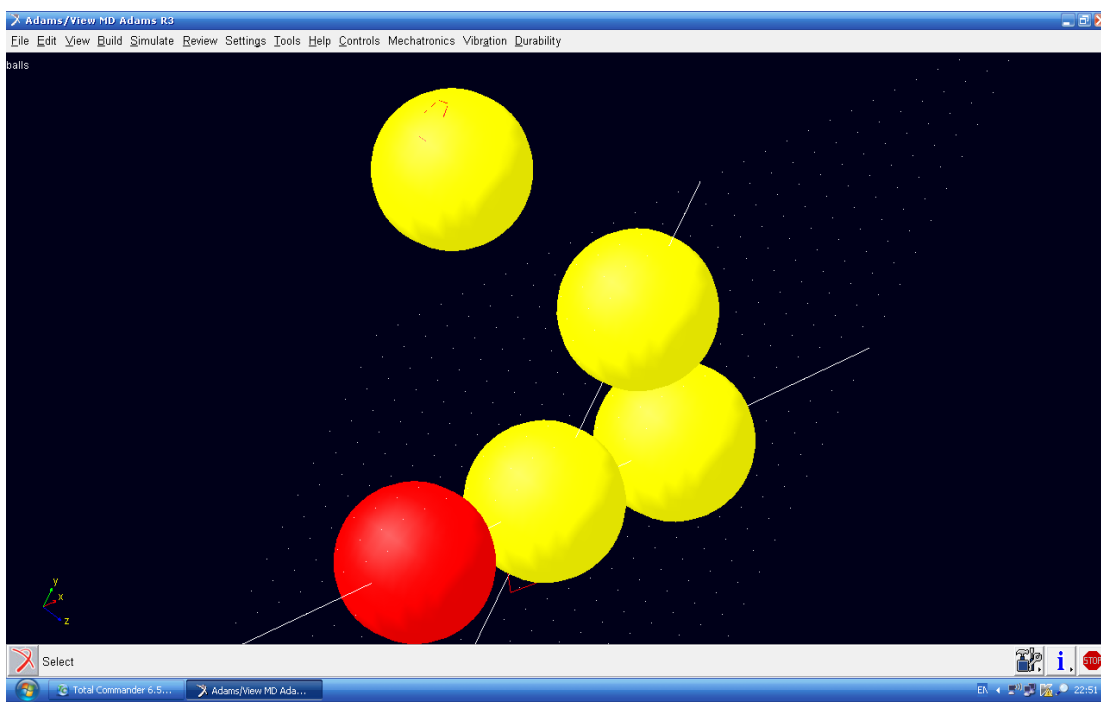


Figure 8: Four essential neighbors (yellow) of the given macro-molecule (red)

In this case, all the neighboring interacting macro-molecules may be subdivided into four groups. Within each group, distance between the given (red) macro-molecule and the selected group member is the same. So, the whole group of the neighboring macro-molecules may be represented by a one of them. This is the essential neighbor. Figure 8 presents four essential neighbors. So, at least four roots shall be available in the macro-molecule force characteristic.

But that is not all. The required equilibrium state shall not be just available. It shall be stable as well, and derivative of the force-characteristic curve shall be positive in the equilibrium point. To obtain the positive derivatives in the two neighboring roots, the curve shall go up, then go down and then again go up between them. That is why, an additional root between each pair of the specified ones takes place, and the following seven-root force characteristic is taken into account for the short-range macro-molecule interaction [2]:

$$F_{jk}(r_{jk}, \dot{r}_{jk}) = A(r_{jk} - a_1)^p [\prod_{i=1}^7 (r_{jk} - a_i)] step(r_{jk}, 2sa, 1.0, 2a, 0.0) + \delta \dot{r}_{jk} \quad (4)$$

where:

F_{jk} – interaction force between the j -th and the k -th macro-molecules;

r_{jk} - distance between the j -th and the k -th macro-molecules;

\dot{r}_{jk} - relative radial velocity of the j -th and the k -th macro-molecules;

A – stiffness factor;

$a_i, i = 1, \dots, 7$ – seven roots of the force-characteristic curve;

p – exponent of the increasing component of the curve envelope;

$step(\dots)$ – standard (cubic-parabola) function of the built-in MSC.Adams view-command language (decreasing component of the curve envelope);

s – decrease factor of the curve envelope;

a – lattice spacing parameter;

δ – damping factor.

Formula (4) has two components: positional component with the stiffness factor A and the damping component with the damping factor δ . A is the factor that shall be lowered (see above) to get down the available molecular frequency range and to provide the comfortable integration conditions. δ is the factor providing numerical stability of the available integration procedure. It may affect the obtained solution of the considered heat-conduction problem.

Thermo-dynamic equations of the considered macro-molecule model (5) are dynamic

$$-m_j \ddot{r}_j - \sum_{\substack{k=1 \\ k \neq j}}^n \bar{F}_{jk} = 0 \quad , j = 1, \dots, n \quad (5)$$

equations for point masses m_j . The equations include inertia forces and the interaction forces between macro-molecules determined by their force characteristic (4). Rotations are forbidden. If time $\tau = 0$, then the entire model rests (is frozen). Two molecules (see slate-blue ones in Figure 2) remain frozen during the entire integration process in compliance with the imposed freezing conditions:

$$\bar{r}_i = \bar{r}_{i0} ; \bar{r}_l = \bar{r}_{l0} \quad (6)$$

The red molecules (see Figure 2) move in relation to each other in the vertical direction in compliance with the imposed heating conditions:

$$(\bar{r}_m - \bar{r}_q) \cdot \bar{e}_2 = a + D \sin(2\pi f \tau) \quad (7)$$

where:

a – lattice spacing parameter;

\bar{e}_2 - unit vector of the vertical (Y -coordinate) axis;

D – heating excitation intensity (not exceeding $0.1a$);

f – heating excitation frequency (is selected arbitrarily in the 50 Hz vicinity).

So, the problem of the solid heat conduction is reduced to the problem of forced vibrations of the system of point masses with the transient taken into account. In this system the temperature concept is replaced with the concept of the macro-molecule hotness degree.

Figure 9 specifies the hotness-degree calculation procedure in compliance with formula (3). The red curve is kinetic energy of the macro-molecule No. 157 depending on time τ .

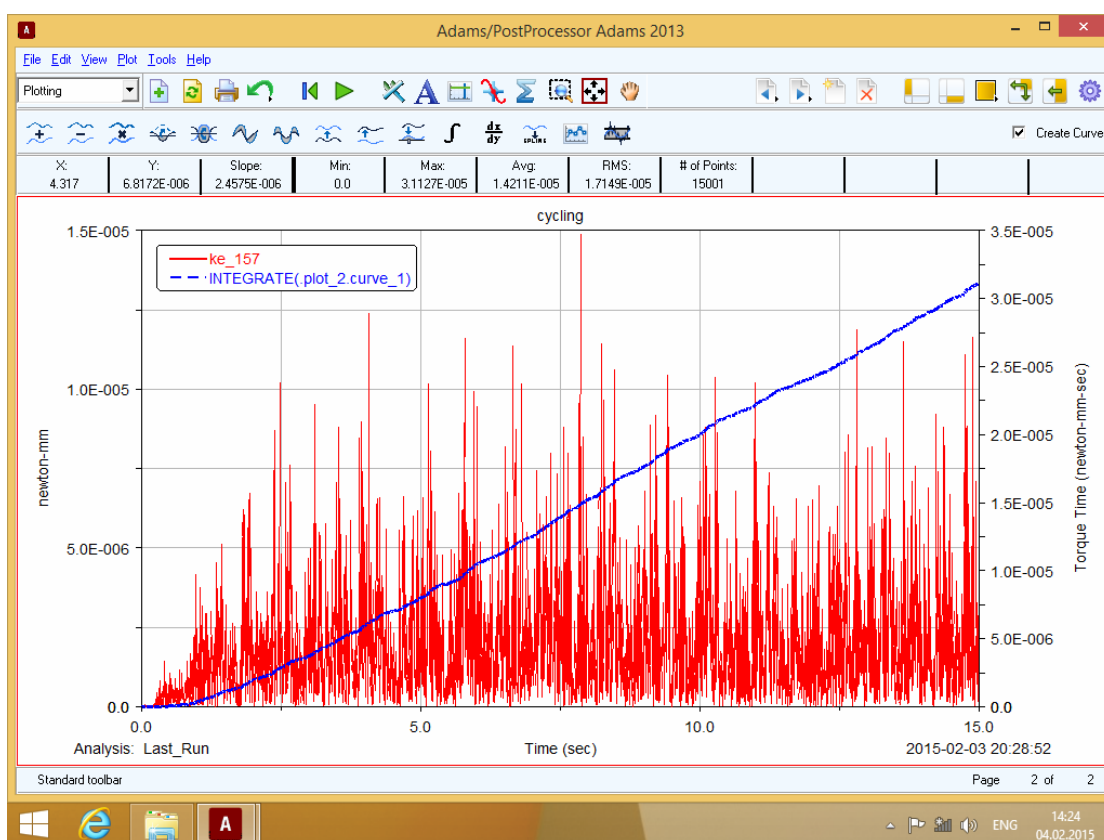


Figure 9: Macro-molecule hotness-degree calculation procedure

Heating excitation is mono-harmonic (7). But the response is a poly-harmonic one. Integration time interval is $t = 15$ s. It is long enough to cope with the transient and to obtain the steady-state process. The blue curve is the integral substituted in the numerator of the fraction (3). This integral is close to a straight line denoting that the steady-state heating process is obtained.

The Figures 10-12 present the obtained calculation results. They characterize the macro-molecule hotness degree distribution within the solid bar. This distribution has the uniform character. That is why the results specify only the upper front edge of the bar (see Figures 1-2) and its lower back edge. Convergence in the number of molecules is important. That is why there are three options: 16 molecules (Figure 10), 63 molecules (Figure 11) and 160 molecules (Figure 12). Damping factor δ is varied approximately two times in the vicinity of the obtained solution. Red continuous lines specify the exact finite-element relative-temperature (2) solution obtained using MSC.Nastran.Thermal software (see Figure 1). Polyline specifies the corresponding macro-molecule approach using relative hotness degree. There are 4 macro-molecules in the Figure 7 edge. That is why there are four vertices in the

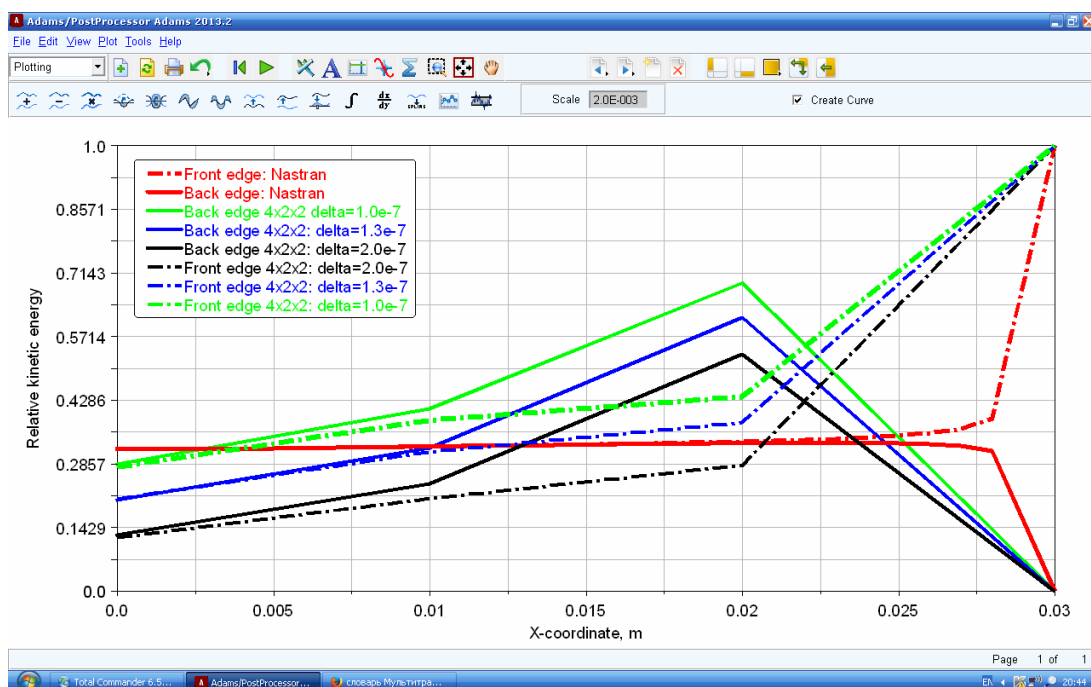


Figure 10: Macro-molecule relative hotness degree distributed along the edges of the model made of $2 \times 2 \times 4 = 16$ molecules

Figure 10 polyline. The dash-dot lines refer to the upper front edge. The solid lines refer to the lower back edge.

It is evident that the obtained macro-molecule result and the exact finite-element result are sufficiently close to each other. The higher the number of macro-molecules of the considered model, the smoother the polylines, the lower the influence of the damping factor.

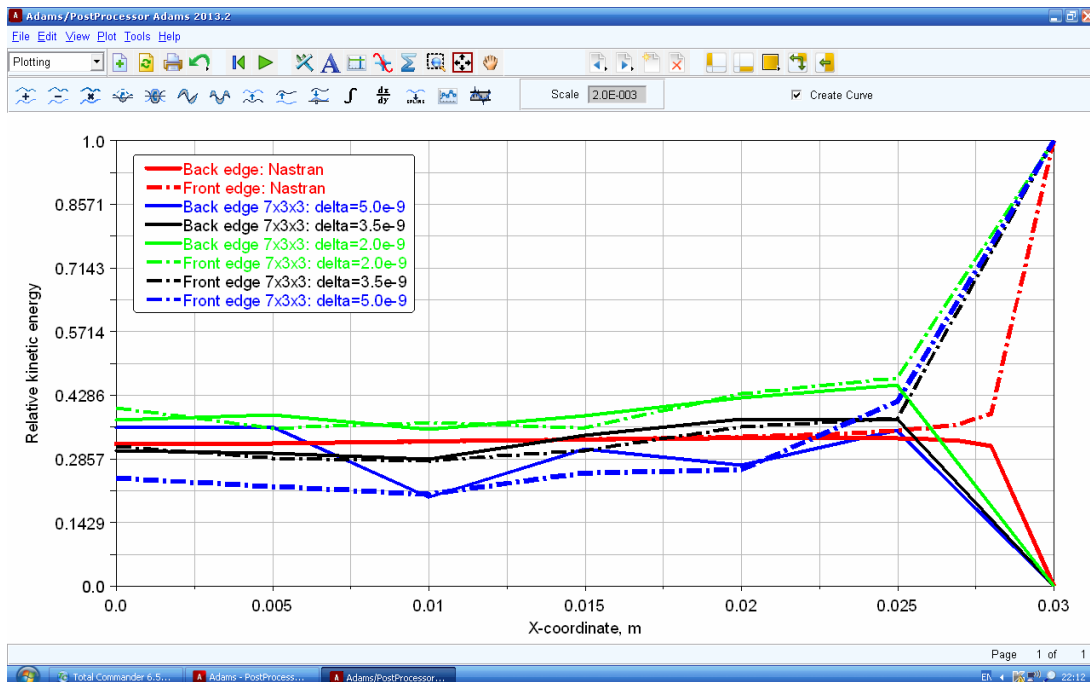


Figure 11: Macro-molecule relative hotness degree distributed along the edges of the model made of $3 \times 3 \times 7 = 63$ molecules

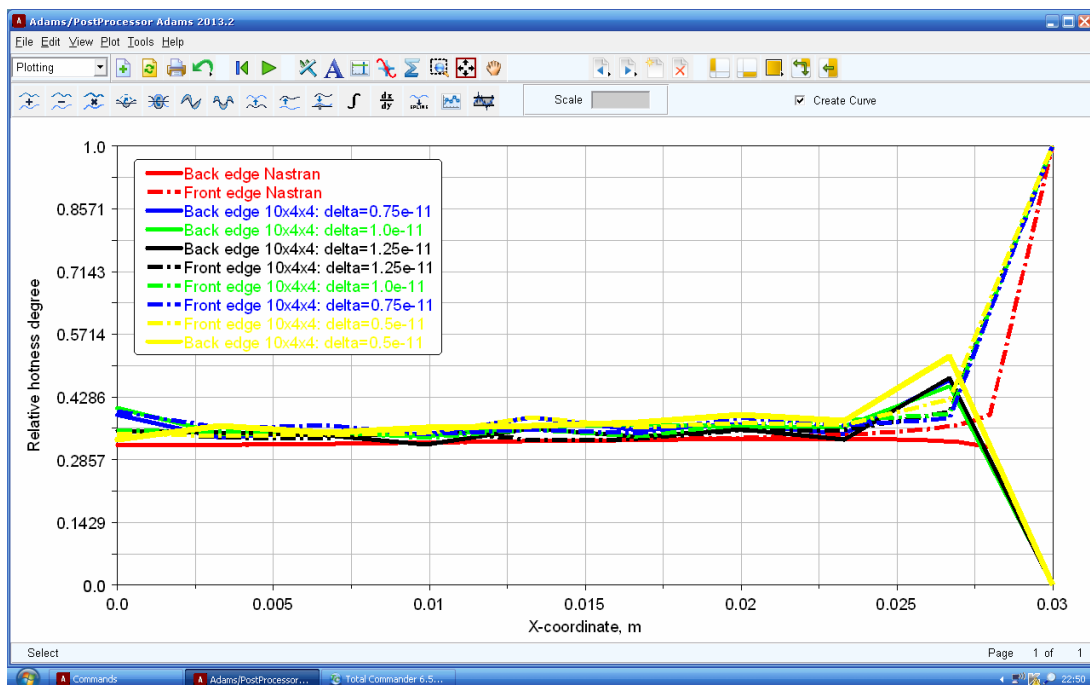


Figure 12: Macro-molecule relative hotness degree distributed along the edges of the model made of $4 \times 4 \times 10 = 160$ molecules

CONCLUSIONS

- Solution of the considered heat-conduction problem may be obtained by replacing the concept of temperature with the original “macro-molecule kinetic energy” concept.
- The approach has a drawback: it can not be used for solving the coupled problem of heat-conduction analysis and thermal-stress analysis at the same time for the same model.

REFERENCES

- [1] Аринчев С.В., Yuri Sillano. Моделирование процесса разрыва стального бруска методом частиц в среде MSC.Adams // *Russian Federation, Известия ВУЗов Машиностроение* (2012)6:39-45.
- [2] Sergey V. Arinchev. Simulation of high-ratio compression of a parallelepipedal duralumin bar using the particle-based method and MSC.Adams software // *CIMNE. Proceedings of the III International Conference on Particle-based methods. – Fundamentals and Applications. University of Stuttgart (Germany), 2013, 18-20 September, Ebook*: p. 670-680.
- [3] Аринчев С.В., Букеткин Б.В. Моделирование процесса кручения стержня из фторопласта методом «частиц» // *Russian Federation, Известия ВУЗов, Машиностроение* (2014)4:38-43.
- [4] Fabian Spreng, Alexandra Mueller and Peter Eberhard. The introduction of a bi-adaptive smoothed particle hydrodynamics formulation beneficial for machining process simulation // *CIMNE. Proceedings of the III International Conference on Particle-based methods. – Fundamentals and Applications. University of Stuttgart (Germany), 2013, 18-20 September, Ebook*: p. 602-613.
- [5] Patrick H. Peacock, David W. Holmes Development and verification of a particle number density variant of SPH to robustly incorporate energy and heat transfer // *CIMNE. Proceedings of the III International Conference on Particle-based methods. – Fundamentals and Applications. University of Stuttgart (Germany), 2013, 18-20 September, Ebook*: p. 949-960.

AN APPLICATION OF THE FINITE-DISCRETE ELEMENT METHOD IN THE SIMULATION OF CERAMIC BREAKAGE: METHODOLOGY FOR A VALIDATION STUDY FOR ALUMINA SPECIMENS

A. FARSI¹, J. XIANG¹, J. P. LATHAM¹, A. D. PULLEN^{1†},
M. CARLSSON², E. H. STITT², M. MARIGO²

¹Applied Modelling and Computation Group (AMCG),
Department of Earth Science and Engineering

^{1†}Department of Civil and Environmental Engineering
Imperial College London, South Kensington Campus,
London SW7 2AZ, United Kingdom

²Johnson Matthey, P.O. Box 1, Belasis Avenue,
Billingham, Cleveland, TS23 1LB, United Kingdom

Key words: Ceramics, Fracture, FEMDEM, Multi-body systems

Abstract. Alumina (aluminum oxide, Al_2O_3) particles are pelletised and fired to produce high porosity catalyst pellets of complex shapes. These pellets fill cylindrical reactor columns with particulate packing structures that are key to the in-service performance, but will suffer breakages which impact on catalyst performance. The combined Finite-Discrete Element Method (FEMDEM) is ideally suited to the simulation of both the multi-body pellet dynamic packing and quasi-static interactions as well as the stress field of each individual pellet, its deformations and fragmentation. The application of FEMDEM fracture modelling to a fine-grained brittle and porous material is novel. This paper presents a methodology for a validation study through comparison with three point-bending and Brazilian tests and discusses FEMDEM's potential in modelling multi-body fragile systems.

1 INTRODUCTION

The combined Finite-Discrete Element Method (FEMDEM) [1] has been widely employed in computational modelling in the last decade, mostly for geomechanical applications. Recently some validation studies have been carried out for both rock fragmentation [2] and multi-body interactions [3]. The application of FEMDEM simulations to describe the behaviour of porous ceramics is novel and its employability needs to be assessed. The methodology for a validation study is now presented. The specimens selected for the validation work are fired at three different temperatures to obtain the three grades of porosity

in the range 0.15-0.36. Their associated properties are characterised by Vickers indentations, and three-point bending tests for the purpose of model calibration. The specimens are also analysed by Field Emission Scanning Electron Microscopy (FESEM) to investigate the type of porosity and the pore size distribution within the sample cross sections to evaluate the homogeneity of their microstructure. Laboratory test load-displacement curves and high-speed video images are compared to the numerical results obtained from FEMDEM. Digital image correlation and tracking methods are employed to compare the fracture path and the displacement of the fragments during the experiment with the numerical results. The numerical model describes the entire experimental apparatus as a multi-body problem with the cross-head impacting on the specimen. This enables more realistic modelling of the effects of compliant rig components where the sample interacts with the lower constraint supports and the axial driving punch above and therefore of the actual forces and displacements during the experiment. The code is fully dynamic and can represent dynamic effects such as strain waves propagating through the specimens and the testing apparatus. This paper presents the intriguing post-failure behaviour as observed in the experiments and as captured by the simulation and discusses the potential for this methodology to model multi-body fragile systems.

2 SAMPLES

Prismatic and cylindrical specimens have been selected for the validation work. All the specimens are sintered with a reference alpha-alumina powder, which is compacted at an initial porosity of 0.45 and then fired at 1200°C, 1300°C and 1400°C respectively to obtain three sets of bars and pellets with final porosity of 0.36, 0.26 and 0.15. The 0.36 porosity specimens are shown in Figure 1. Porosimetry and densitometry tests are employed to assess the pore size distribution and density of the specimens for the different firing temperatures. The specimens are also analysed by field emission scanning electron microscope to investigate the type of porosity and the pore size distribution within the sample cross sections to evaluate the homogeneity of their microstructure. The porosity of the ceramic specimens does not present important variations along the cross section, allowing them to be considered homogeneous and isotropic. The specimens of each set are then tested with Vickers indentations and three-point bending tests to infer the Young's modulus and tensile strength. The mechanical properties are then compared with the values for porous alumina ceramics found in literature [4] and [5] and the energy release rate is calculated on the basis of correlation curves presented in literature.

3 THREE-POINT BENDING AND BRAZILIAN TESTS

Two different experiments have been selected for the validation work on ceramic breakage. The three-point bending test consists of placing a specimen on two supports and applying a vertical load in the middle of the two supports by means of a punch. Before failure, according to the Euler-Bernoulli beam theory, a homogeneous bar experiences the

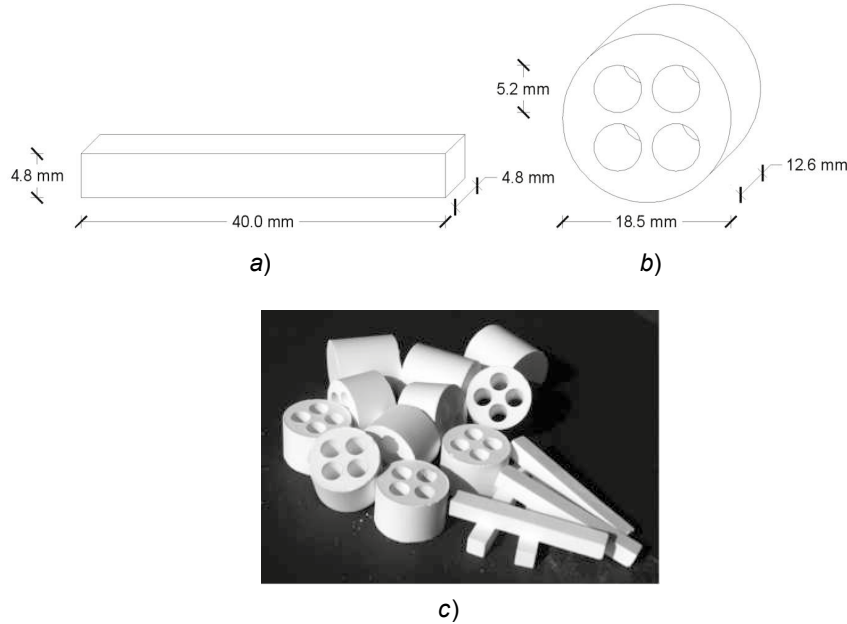


Figure 1: Final geometry of the 0.36 porosity a) bars and b) cylinders with holes. c) Photograph of the tested materials.

maximum tensile and compressive stress respectively in its bottom and top surfaces, in the exact middle of the two supports. Since the tested material fails under tensile stress before it fails under compression, a fracture will initiate from the bottom side when the tensile stress reaches the value of the tensile strength of the tested material. By solving the Euler-Bernoulli differential equation it is possible to express the maximum tensile stress experienced by the specimen as a function of the applied load and moreover infer the tensile strength (f_t) and the Young's modulus (E) from the maximum force (F) and deflection (w) applied to the beam before failure.

$$f_t = \frac{3Fs}{2H^3} \quad (1)$$

$$E = \frac{Fs^3}{4wH^4} \quad (2)$$

In equations (1) and (2) s is the span between the two supports and H is the height and width of a bar with a square cross-section. As mentioned before, the stress field induced in the specimen by the controlled boundary conditions not only restricts the area where the fracture can initiate, but also constrains the opening mode when the fracture is propagating. In fact, neglecting the possible effects of microscale inhomogeneities and anisotropies, the material points that are failing experience a pure horizontal extension,

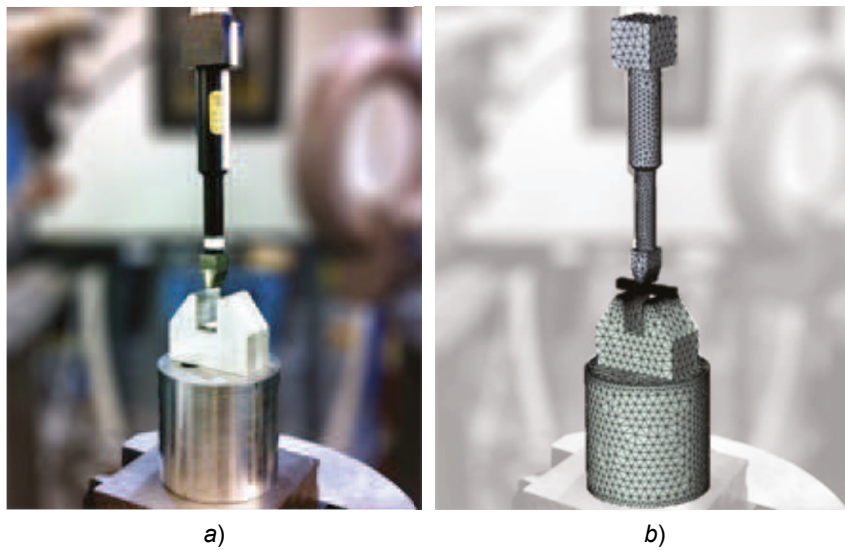


Figure 2: a) Photograph of the real three-point flexural test apparatus and b) tetrahedral mesh in its 3D numerical simulation.

which is normal to the plane of the crack, in a mode I opening fashion. The apparatus in Figure 2 is the one used in the experiments. A metal support with a 20 mm span is fixed to a steel cylinder. The punch is a steel cross-head instrumented with a load cell and attached to an actuator. The experiment is executed in displacement control, with a cross-head velocity of 0.5 mm/min.

The three-point bending apparatus is mounted on actuators of different size, depending on the velocity of the test. The testing machine can record forces and displacements during the experiment. A second data logger is connected to the force transducer that has been fixed on the cross-head. This makes it possible to record the force at a higher frequency and to have a more consistent set of measurements, for example when the experiment is performed with different actuators. The experiment is also recorded with a high-speed camera, which enables the correction of errors in the force-deflection curve resulting from possible rig compliances and localised plastic deformation at the points of contact. The deflection is set to zero where the linear extension of the curve intersects the horizontal axis. The corrected deflection of the beam before failure is then calculated by subtracting the average of the two displacements in the points of contact with the supports from the displacement of the midpoint as illustrated in Figure 3. The high-speed video is also employed to determine the fracture path and velocity of the fragments.

The experiment is modelled with 2D and 3D FEMDEM simulations. The boundary conditions and the 2D triangular mesh are illustrated in Figure 4. The top of the punch is constrained with constant velocity. To reduce the run time of the numerical simulation, the velocity of the constraint is set to 0.1 m/s. Although this loading rate is significantly higher than the one in the laboratory experiment, it induces a quasi-static response in

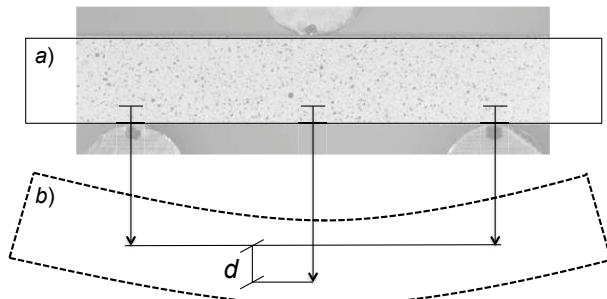


Figure 3: a) Beam before contact with no deformation and b) immediately before failure with deflection d calculated as the difference between the displacement of the midpoint and the average of the two displacements of the points of contact with the supports.

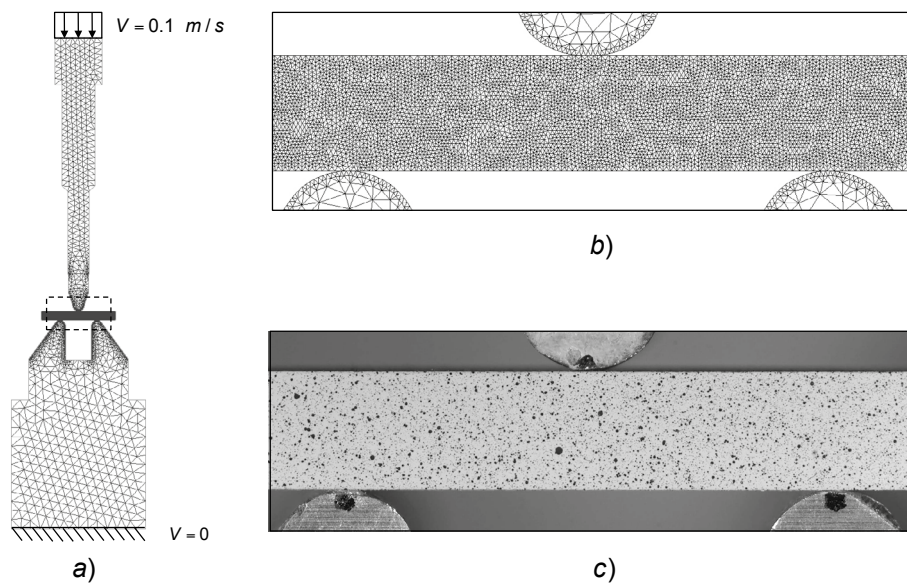


Figure 4: a) Boundary conditions for the three-point flexural experiment and triangular mesh of its 2D numerical simulation. b) Detail of the specimen discretisation and c) corresponding frame from the high-speed video.

the bar as there is no significant difference between the force applied by the punch and the one applied by the two constraints. To further reduce the calculation time, when the simulation starts, the punch is in contact with the specimen and for this reason an initial velocity equal to the one applied to the constraint is imposed to the whole punch. The discretisation of the punch and constraints is refined only where the contact occurs so as to better represent the geometry of their contours without considerably increasing the computational burden. The specimen is discretised with an unstructured fine mesh to correctly represent both the de-bonding stress during the opening of the crack and the fracture path along the element boundaries. The total number of elements employed in the model is around 20,000. The material properties used to describe the three-point bending apparatus are $E_s=210$ GPa, $\nu_s=0.3$ and $\rho_s=7850$ kg/m³, where E_s is the Young's modulus, ν_s is the Poisson's ratio and ρ_s is the density. The material properties used for the specimens vary depending on the porosity of the tested sample: the reported results refer to the 0.36 porosity set with $E_c=60$ GPa, $\nu_c=0.22$, $\rho_c=2560$ kg/m³ and $f_t=78$ MPa. The interaction between the steel and the alumina sample is modelled using a Coulomb coefficient of friction equal to 0.01.

$$\sigma_h = \frac{6EH}{s^2}w \quad (3)$$

The mean and horizontal stress fields in the apparatus and in the tested specimen respectively at different time lapses are reported in Figure 5. The simulated stress field in the bar sample before failure agrees with the theoretical predictions of Euler-Bernoulli beam theory. Equation (3) represents the relation between beam deflection and the horizontal stresses experienced by the material point between the two supports in the bottom side of the beam before failure. In Figure 6a this analytical solution is compared with the horizontal stress calculated in the corresponding FEMDEM simulation. In accordance with the analytical solution, the horizontal stress extrapolated from the simulation increases linearly until it reaches the value of the tensile strength (78 MPa) and then, when the fracture starts to propagate, it drops to zero. The numerical model slightly overestimates the displacements (and thus underestimate the stiffness) due to the joint element discretisation [6]: this leads to a slightly lower gradient for the numerical curve. In Figure 6b the force-deflection curve calculated in the numerical simulation is compared with three experimental results. The maximum value for the contact force is slightly higher in the numerical results than in the theoretical prediction: this can be because the mesh elements are not all perfectly aligned across the vertical plane where the stress field develops its maximum tension. The fracture path produced in the numerical simulations is close to the one observed in the experiments as shown in Figure 5b.

The second experiment used to validate the simulation is a Brazilian disc test on alumina catalyst supports. The test consists of placing a cylindrical pellet between two plates and diametrically compressing it to failure. This type of experiment is often used as an indirect

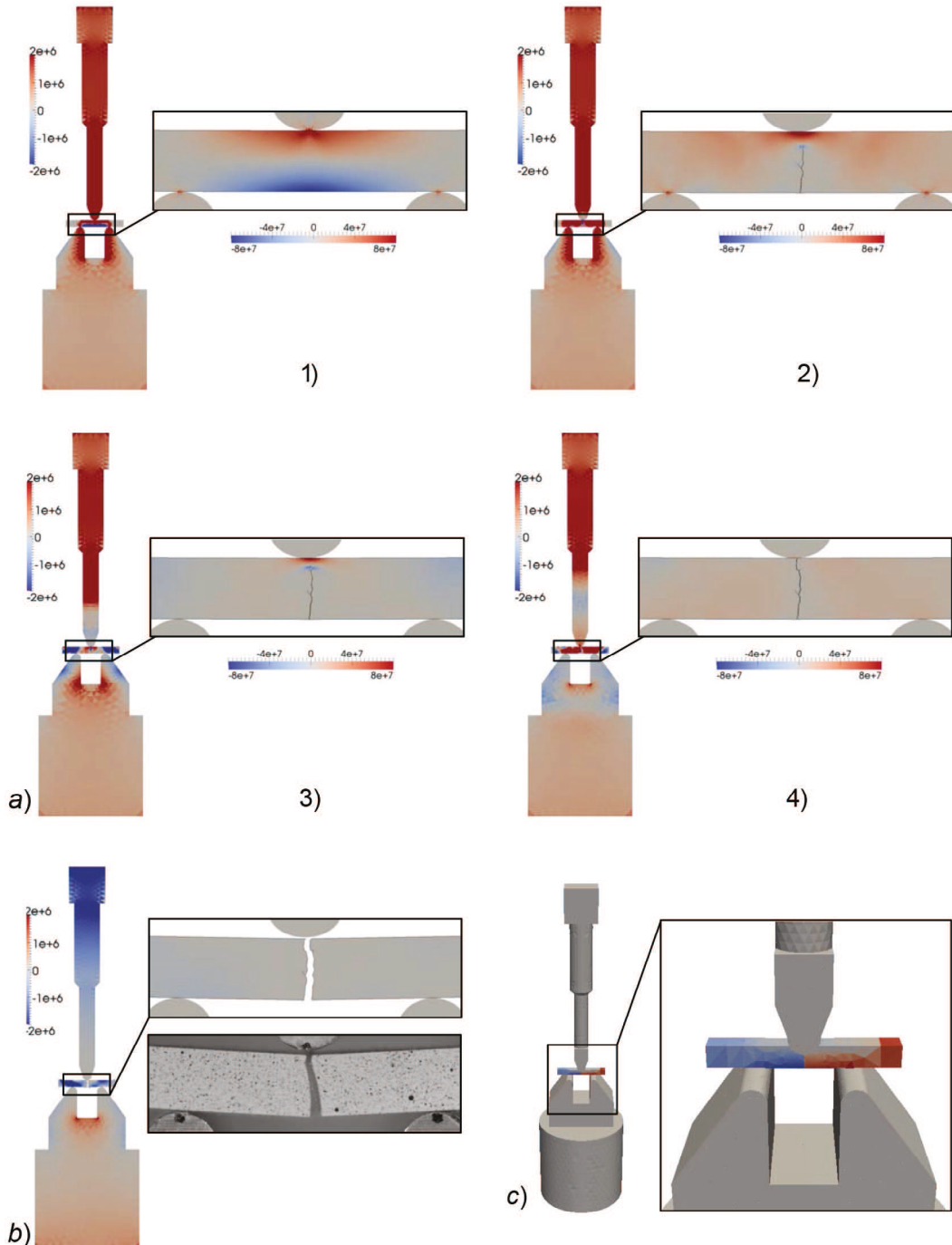


Figure 5: a) Stress field in a 2D numerical model showing a crack propagating at different times during a three-point flexural test: the mean stress for each time lapse is shown on the image of the apparatus on the left and the horizontal stress is shown on the magnified beam on the right. b) Comparison between the model of the specimen after failure in the 2D numerical simulation and a frame from the high-speed video recording of the actual experiment. c) Horizontal displacement field in a 3D numerical model.

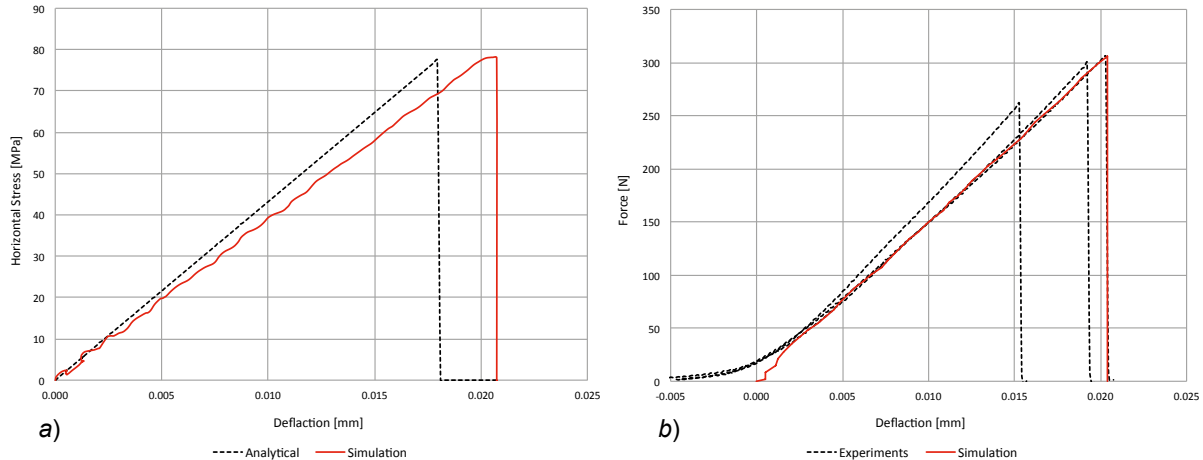


Figure 6: a) Comparison of the vertical displacement and the horizontal stress experienced by the material point between the two supports in the bottom side of the beam in a 2D numerical model and in the analytical solution. b) Force-deflection curves calculated in the numerical simulation and obtained from three experiments.

testing method to evaluate the tensile strength of brittle materials such as concrete, rock, and ceramics. The compression induces a stress field with horizontal tensile stress which according to a linear elastic model has its highest value in the centre of the disc. The tensile strength can be calculated based on the two-dimensional elastic solution for a disc with two concentrated forces applied to its vertical extremes. It is then possible to express the horizontal tensile stress experienced by the specimen in the centre of the disc as a function of the applied load (F) and of the geometry of the sample.

$$f_t = \frac{2F}{\pi Dt} \quad (4)$$

Assuming that failure occurs at the point of maximum tensile stress, i.e. at the centre of the disc, the Brazilian test formula (4) gives an estimate of the indirect tensile strength (f_t), where D is the diameter of the disc and t its width [7]. Similarly to the three-point bending experiment, the first material point that is failing experiences a horizontal extension, normal to the plane of the crack, in a mode I opening fashion. However, this equation does not take into account defects, local crushing and plastic deformations at the points of contact, which might affect the stress field induced in the cylinder. The presence of holes in the disc, such as in a catalyst support, has the effect of generating a more complex stress field that cannot be precisely described by the equation above. At failure, the opening mode can also be affected, producing a shear crack. A FEMDEM simulation is capable not only of representing the stresses and deformations of a disc with holes before failure, but also of replicating the fracture propagation in a mixed mode

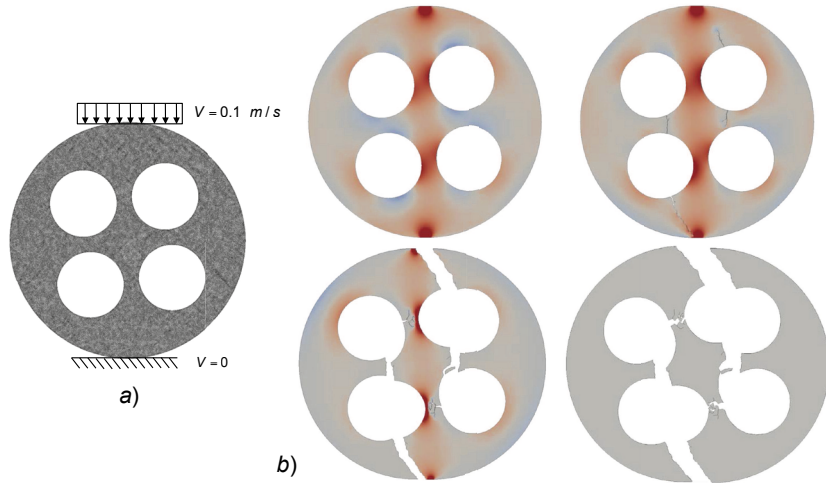


Figure 7: a) Boundary conditions for the Brazilian test of a ceramic pellet with four holes diametrically compressed against two steel plate and triangular mesh of its 2D numerical simulation. b) Time-lapse numerical results immediately before failure and after failure.

opening fashion, as shown in Figure 7b, where the test is modelled with a 2D simulation. The boundary conditions and the triangular mesh are shown in Figure 7a. The top plate is constrained with a constant vertical velocity of 0.1 m/s. Similarly to the three-point bending model, the specimen is discretised with an unstructured fine mesh to correctly represent both the de-bonding stress during the opening of the crack and the fracture path along the boundaries of elements. The total number of elements employed in the model is around 70,000. The methodology proposed for this validation work consists of repeating the test for different orientations of the axes of symmetry defined by the hole positions and for each of the three porosity sets and then comparing the force displacement curves, fracture paths and fragment sizes against the numerical results. More precisely, the pellets are compressed not only in their weak and strong orientations, but also in the other mixed configurations: the numerical results for the 0.36 porosity set are shown in Figure 8a.

4 MULTI-BODY CERAMIC SYSTEMS

Numerical analyses similar to those presented above can be applied to any type of pellet geometry and results can be employed for the evaluation of its mechanical performance. An example could be the shape and porosity analysis for the evaluation of the performance of catalyst supports, i.e. the ceramic pellets where the actual catalytic metal is dispersed, employed in fixed bed reactors. On the one hand a support needs to be highly porous to maximise the total surface area and therefore its catalytic activity, but on the other a high porosity can make the support too weak and unsuitable for the loading and operating conditions (Figure 8b). Also, during the standard lifecycle of the plant some of the ceramic pellets are crushed to fragments due to the thermal contractions of the reactors, reducing their service life and their efficiency. In particular, the accumulation of fine frag-

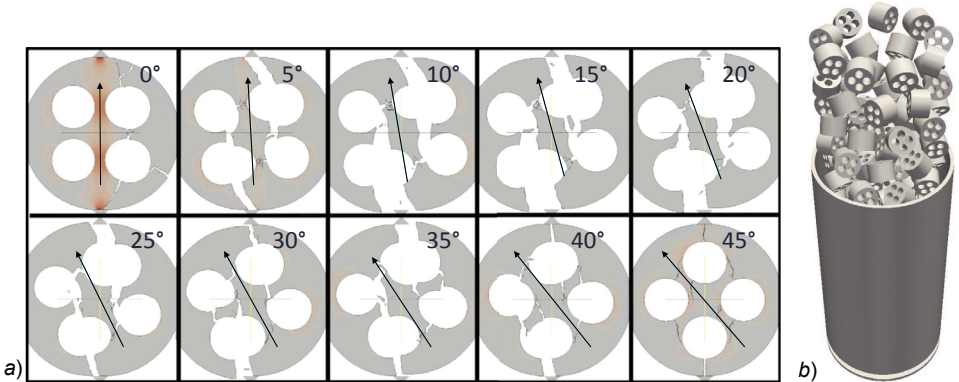


Figure 8: a) Pellet fragmentation during compression in different orientations and b) numerical simulation of the loading of alumina cylindrical pellets in a steel tube.

ments may produce localised reductions of permeability in the reactor, causing pressure drops and potentially reducing the lifetime of the reactor itself. FEMDEM simulations can be employed for the evaluation of the mechanical performance of catalysts to improve their strength, reduce the number of fine fragments at failure while meeting the required geometric surface area. Ultimately more realistic loading conditions, such as the compression applied by neighbouring catalysts due to the thermal shrinkage of the reactor, can be modelled for an even more precise evaluation of mechanical performances. To do this the operating conditions need to be replicated by modelling the packed structure of the fixed bed reactor. The problem of simulating the packing of cylindrical pellets in a tube has been approached with various computational techniques illustrated in literature. In [8] the packing process is simulated with both a semi-stochastic approach, where the particle path is randomly determined on the base of the overlapping of voxels, and a deterministic approach, where the repulsive forces and torques applied to the particles are calculated by measuring the number of their overlapping voxels and their voxel-level contact forces. In [9] these voxel-based methods are compared to discrete element simulations where the contact forces are calculated between pairs of spheres and the pellets are represented with clusters of spheres clumped together. A 3D FEMDEM simulation can be employed to simulate the pellets being cast into a reactor: pellets of any complex shape can be represented with a tetrahedral mesh and their contact forces are calculated with a penalty method and a Coulomb model of friction. An example is shown in Figure 9. A tube of 100 mm in diameter is filled with 220 ceramic pellets. Each particle is a cylinder of 18.5 mm diameter and 12.6 mm in width with 4 holes. As shown in Figure 9a, each pellet is discretised with 784 tetrahedra. The container is meshed with around 64,000 tetrahedra for a total of approximately 240,000 elements for the whole model. The geometries of the container and pellets have been imported from CAD drawings. All the particles are introduced in the domain above the container with a random orientation and a zero initial velocity. This process is completely automated through a pre-processing tool (POSITIT) that facilitates the control of filling conditions and avoids the need for a manually defined

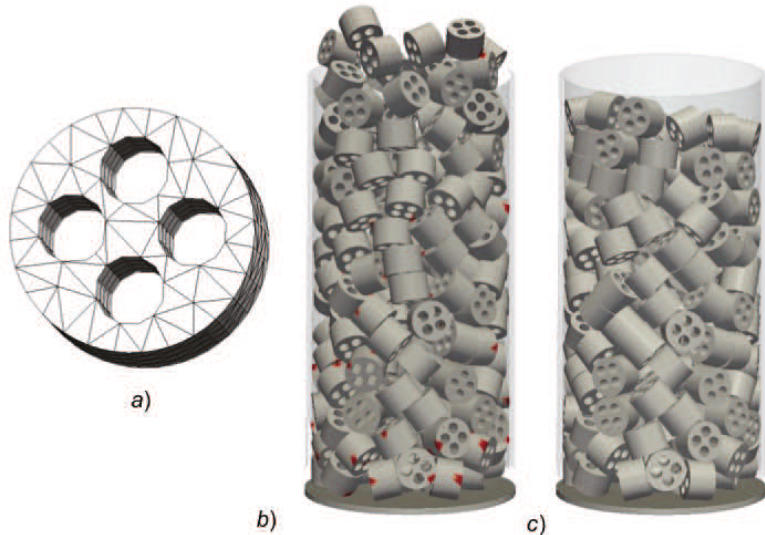


Figure 9: a) Tetrahedral mesh of a ceramic pellet with 4 holes, b) numerical results of pellet settlement simulation within a cylindrical container, with contact forces represented in red, and c) final packed structure after the filling process.

3D space for the initial conditions of each single pellet. In the numerical simulation in Figure 9b the pellets are modelled as rigid bodies with a density $\rho_c=2560 \text{ kg/m}^3$ and the interaction between them is computed employing a Coulomb coefficient of friction equal to 0.4. Both the forces transmitted between the pellets and their points of contact can be extracted and visualised for each time step. The simulation runs in parallel on 10 cores in less than 24 hours. Alternatively, the same model can also be run in parallel employing deformable bodies to simulate not only the contact forces transmitted between the catalysts but also the stresses inside each particle.

5 CONCLUSIONS

Codes based on the combined Finite-Discrete Element Method (FEMDEM) are now widely applied in research: for industry applications more validation work needs to be done to demonstrate their robustness and accuracy in simulating complex dynamic fracture processes, especially in the context of porous ceramics. A novel methodology for the verification and validation of FEMDEM simulations has been the object of this paper. Some of the advantages of FEMDEM in modelling complex fragmentations by diametrical compression and multi-body interactions for ceramic materials have been presented. These include the explicit representation of fractures during the fragmentation process and the potential to represent complex-shaped bodies. Experimental and numerical results have been compared, confirming that a FEMDEM numerical simulation of mode I fracture in ceramic bars matches the experimental results of a three-point bending test. These results give a first confirmation that a FEMDEM code can be used for the evalua-

tion of catalyst mechanical performance. More confirmation can be obtained in the near future both by comparing the results obtained above for a Brazilian test simulation with the results from actual experiments and by employing the data extrapolated from more complex multi-body simulations of the packed structure inside the reactor.

ACKNOWLEDGEMENTS

The authors would like to thank Dogan Ozkaya for providing us with data from FESEM analysis and Daniel Curry for his help with sample preparation. This research is sponsored by EPSRC and the Johnson Matthey Technology Centre.

REFERENCES

- [1] A. Munjiza, *The Combined Finite-Discrete Element Method*. Wiley, 2004.
- [2] E. Rougier, E. Knight, S. Broome, a.J. Sussman, and a. Munjiza, “Validation of a three-dimensional Finite-Discrete Element Method using experimental results of the Split Hopkinson Pressure Bar test,” *International Journal of Rock Mechanics and Mining Sciences*, vol. 70, pp. 101–108, Sept. 2014.
- [3] J. Xiang, A. Munjiza, J.-P. Latham, and R. Guises, “On the validation of DEM and FEM/DEM models in 2D and 3D,” *Engineering Computations*, vol. 26, no. 6, pp. 673–687, 2009.
- [4] D. Lam, F. Lange, and A. Evans, “Mechanical properties of partially dense alumina produced from powder compacts,” *Journal of the American Ceramic Society*, vol. 77, no. 8, pp. 2113–2117, 1994.
- [5] J. Magdeski, “The porosity dependence of mechanical properties of sintered alumina,” *Journal of the University of Chemical Technology and Metallurgy*, vol. 45, no. 2, pp. 143–148, 2010.
- [6] E. Lorentz, “A mixed interface finite element for cohesive zone models,” *Computer Methods in Applied Mechanics and Engineering*, vol. 198, no. 2, pp. 302–317, 2008.
- [7] International Society for Rock Mechanics, “Suggested Methods For Determining Tensile Strength of Rock Materials,” in *International Society for Rock Mechanics Commission on Standardization of Laboratory and Field Tests*, vol. 15, pp. 99–103, 1978.
- [8] R. Caulkin, X. Jia, and C. Xu, “Simulations of structures in packed columns and validation by X-ray tomography,” *Industrial & Engineering Chemistry Research*, pp. 202–213, 2008.
- [9] R. Caulkin, W. Tian, M. Pasha, A. Hassanpour, and X. Jia, “Impact of shape representation schemes used in discrete element modelling of particle packing,” *Computers and Chemical Engineering*, vol. 76, pp. 160–169, 2015.

DEVELOPMENT OF HIGHER ORDER PARTICLE DISCRETIZATION SCHEME FOR ANALYSIS OF FAILURE PHENOMENA

Mahendra Kumar Pal¹, Maddegedara L.L. Wijerathne², Muneo Hori²,
Tsuyoshi Ichimura² and Seizo Tanaka²

¹ Department of Civil Engineering, The University of Tokyo
7-3-1 Hongo, Bunkyo-ku, Tokyo 113-8656 Japan
e-mail: mahendra@eri.u-tokyo.ac.jp

² Earthquake Research Institute, The University of Tokyo
1-1-1 Yayoi, Bunkyo-ku, Tokyo, 113-0032, Japan
e-mails: lalith@eri.u-tokyo.ac.jp, hori@eri.u-tokyo.ac.jp, ichimura@eri.u-tokyo.ac.jp,
tanaka.seizo@gmail.com

Key words: Higher order PDS, PDS-FEM, Local polynomial expansion, Conjugate tessellation, Mode-I crack

Abstract. This paper presents the higher order extension of Particle Discretization Scheme (PDS) and its implementation in FEM framework (PDS-FEM) to solve boundary value problems of linear elastic solids, including brittle cracks. Higher order PDS defines an approximation $f^d(\mathbf{x})$ of a function $f(\mathbf{x})$, defined over domain Ω , as the union of local polynomial approximation of $f(\mathbf{x})$ over each Voronoi tessellation elements of Ω . The support of the local polynomial bases being confined to the domain of each Voronoi element, $f^d(\mathbf{x})$ consists of discontinuities along each Voronoi boundaries. Considering local polynomial approximations over elements of Delaunay tessellation, PDS define bounded derivatives for this discontinuous $f^d(\mathbf{x})$. Utilizing the inherent discontinuities in $f^d(\mathbf{x})$, PDS-FEM proposes a numerically efficient treatment for modeling cracks. This novel use of local polynomial approximations in FEM is verified with a set of linear elastic problems, including mode-I crack tip stress field.

1 INTRODUCTION

Particle based numerical methods have been very popular and widely accepted in solid mechanics and computational fluid mechanics. A salient feature of particle methods is that they provide relatively simple treatments for modeling crack propagation, which is one area particle methods are widely used. The movements of crack tip singularity is highly sensitive to even the minor heterogeneities in materials, external loading, etc., and

makes the crack path to produce wide range of behaviours like branching, bending, etc. Hence, it is essential to perform probabilistic analysis of crack-path variability, based on methods like statistical model[1] or Monte-Carlo simulation[2]. Construction of probability density function (PDF) of crack paths for a given problem requires a large number of simulations, skyrocketing the required computational resources. Hence, numerical methods with efficient failure treatments are necessary for realizing the need of constructing crack path PDF for practical applications.

Particle based numerical tool such as smooth particle method (SPH)[3], element free Galerkin method (EFGM)[4], reproducing kernel particle method (RKPM)[5] are efficient methods for failure analysis. Accuracy of these methods is improved by introducing some additional nodes in domain, where more refinement (*h-adaptivity*) is needed. However, these methods are not capable of incorporating the Poisson's effect and encounter problems in enforcing the essential boundary conditions. While FEM has well established mathematical foundation, it is not numerically efficient in modeling crack propagation; requires complex treatments like introduction of new nodes, adaptive mesh refinements, etc. Recent advancement such as element free Galerkin method (EFGM)[4], partition of unity method (POU)[6], eXtended finite element method and other mesh-less methods enable accurate modeling of crack tip stress singularity, which is a function of \sqrt{r} , θ ; (r, θ) is a polar coordinate system at the crack tip. In-spite of higher accuracy, these enhancements are complex to implement and introduce a hefty computational overhead. In nutshell, particle methods and finite element method have their own positive and negative features.

Considering the merits of finite element methods and particle methods, Particle Discretization Scheme (PDS) had been proposed[7, 8], and implemented into FEM framework (PDS-FEM). We refer this original work as 0^{th} -order PDS. PDS-FEM provides a numerically efficient failure treatment which allows one to construct PDF of 3D crack paths in large scale problems. This paper presents the higher order extension of PDS and PDS-FEM to simulate brittle elastic cracks. Just as in 0^{th} -order PDS, the higher order extension also uses the tessellations pair Voronoi and Delaunay, of a domain Ω , to approximate functions and their derivatives defined over Ω . Higher order PDS extension defines an approximation $f^d(\mathbf{x})$ of a function $f(\mathbf{x})$, defined over Ω , as the union of local polynomial approximation of $f(\mathbf{x})$ over each Voronoi tessellation elements. The support of the local polynomial bases being confined to the domain of each Voronoi element, $f^d(\mathbf{x})$ consists of discontinuities along each Voronoi boundaries. Considering local polynomial approximations over elements of Delaunay tessellation, PDS define bounded derivatives for this discontinuous $f^d(\mathbf{x})$. Further, exploiting the inherent discontinuities in $f(\mathbf{x})$ PDS-FEM propose a numerically efficient treatment for modeling cracks. This paper presents the higher order extension PDS-FEM and its numerically efficient treatment for modeling brittle elastic cracks. Some benchmark problems, including a mode-I crack tip problem, are presented to verify the higher order PDS-FEM.

This paper is consist of four other sections along with introduction. The second section

emphasis on the concept of higher order PDS. Implementation of PDS into finite element framework has been explained in third section. Numerical examples with the results are discussed in fourth section. Final section includes the concluding remark.

2 HIGHER ORDER PDS

A unique feature of PDS is the use of conjugate tessellations to approximate functions and their derivatives. In this paper, we use Voronoi and Delaunay tessellations pair for approximating functions and derivatives, respectively [7, 8]. PDS is not inherently bound to the tessellation pair Voronoi and Delaunay, and should work with any other conjugate domain tessellation pair.

Let $f(\mathbf{x})$ be a target function in an analysis domain V ; Voronoi and Delaunay tessellations for V be $\{\Phi^\alpha\}$ and $\{\Psi^\beta\}$; \mathbf{y}^α and \mathbf{z}^β be the mother points of Φ^α and the center of gravity of Ψ^β , respectively. Denoted by $\phi^\alpha(\mathbf{x})$ and $\psi^\beta(\mathbf{x})$ are the characteristic functions of Φ^α and Ψ^β , respectively. Here, the characteristics function of $\{\Phi^\alpha\}$ is defined such that $\phi^\alpha(\mathbf{x}) = 1$ if $\mathbf{x} \in \Omega^\alpha$ and $\phi^\alpha(\mathbf{x}) = 0$ if $\mathbf{x} \notin \Omega^\alpha$; $\psi^\alpha(\mathbf{x})$ follows similar definition.

Higher order PDS approximates a function $f(\mathbf{x})$ and its derivatives $f(\mathbf{x}),_i$ as

$$f(\mathbf{x}) \approx f^d(x) = \sum_{\alpha=1}^{N^\alpha} \sum_{n=0}^{|P^\alpha|} f^{\alpha n} P^{\alpha n}, \quad (1)$$

$$f(\mathbf{x}),_i \approx g_i^d(x) = \sum_{\beta=1}^{N^\beta} \sum_{m=0}^{|Q^\beta|} g_i^{\beta m} Q^{\beta m}, \quad (2)$$

where, $P^{\alpha n}(\mathbf{x} - \mathbf{y}^\alpha) \in P^\alpha = \{1, (\mathbf{x} - \mathbf{y}^\alpha), \dots, (\mathbf{x} - \mathbf{y}^\alpha)^r, \dots\} \phi^\alpha(\mathbf{x})$ and $Q^{\beta m}(\mathbf{x} - \mathbf{z}^\beta) \in Q^\beta = \{1, (\mathbf{x} - \mathbf{z}^\beta), \dots, (\mathbf{x} - \mathbf{z}^\beta)^r, \dots\} \psi^\beta(\mathbf{x})$. N^α is a number of Voronoi elements and N^β is a number of Delaunay elements.

The coefficients $f^{\alpha n}$'s and $g_i^{\beta m}$'s are found by minimizing the errors $E^f = \int (f(\mathbf{x}) - f^d(\mathbf{x}))^2 dv$ and $E^g = \int \|g^d(\mathbf{x}) - \nabla f^d(\mathbf{x})\|^2 dv$, respectively. $\|\cdot\|$ is the norm of a vector (\cdot) . Minimization of E^f and E^g produce following pair of linear sets of equations, each of which can be solved to find $f^{\alpha n}$'s and $g_i^{\beta m}$'s

$$\sum_m |P^\alpha| I^{\alpha nm} f^{\alpha m} = \int_{\Phi^\alpha} f(\mathbf{x}) P^{\alpha n}(\mathbf{x} - \mathbf{y}^\alpha) dv \quad (3)$$

$$\sum_m |Q^\beta| A^{\beta nm} g_i^{\beta m} = \sum_{\alpha, l} f^{\alpha l} \int_{\Psi^\beta} Q^{\beta n} (P^{\alpha l}(\mathbf{x} - \mathbf{z}^\beta)) ,_i dv. \quad (4)$$

$I^{\alpha nm}$ and $A^{\beta nm}$ are defined as $I^{\alpha nm} = \int_{\Phi^\alpha} P^{\alpha n} P^{\alpha m} dv$ and $A^{\beta nm} = \int_{\Psi^\beta} Q^{\beta n} Q^{\beta m} dv$. According to above formulations, it is straightforward to include the higher order polynomials

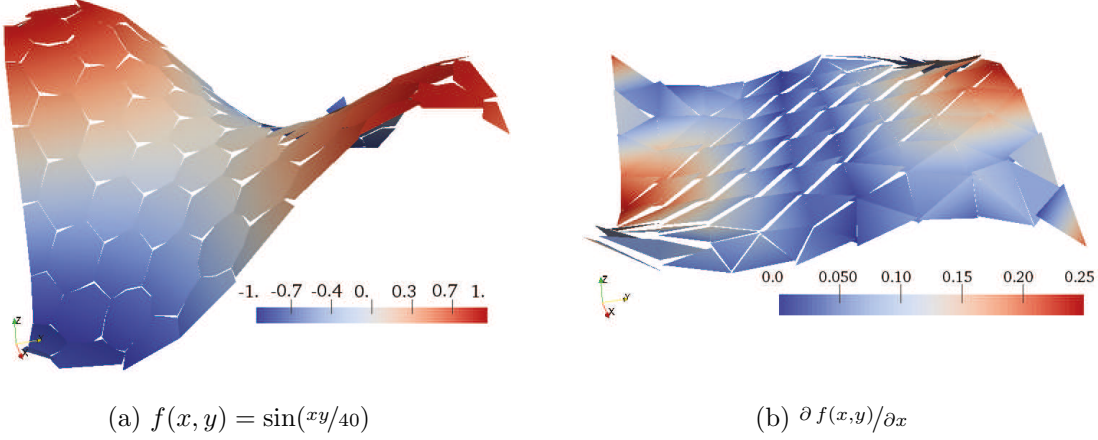


Figure 1: $f(x,y) = \sin(xy/40)$ and $\partial f(x,y)/\partial x$ approximated with higher order PDS; $P^\alpha = \{1, (x - x^\alpha), (y - y^\alpha)\} \phi^\alpha(\mathbf{x})$ and $Q^\beta = \{1, (x - x^\beta), (y - y^\beta)\} \psi^\beta(\mathbf{x})$.

in the original PDS[7, 8] that uses the characteristic functions as the basis functions of discretization.

As seen in Fig. 1(a), an approximation of a function obtained with higher order PDS contains discontinuities along the boundaries of Φ^α (i.e. $\partial\Phi^\alpha$'s). Hence PDS gets its particle nature. Nevertheless of the discontinuities, PDS defines bounded derivatives, smoothly connecting the discontinuous function approximation over the conjugate tessellation Ψ^β (see Fig. 1(b)). This allows one to use PDS in solving boundary value problems. As shown in the latter half of the next section, the discontinuities in $f^d(\mathbf{x})$ also contribute to derivative $g_i^d(x)$, which is conveniently exploited to implement an efficient treatment for modeling cracks in solids.

Numerical experiments show that the error of approximation diminish at a second order rate for both the function and derivatives as discussed in previous work [9]. Further, higher accuracy and convergence rates can be obtained by including higher order polynomials to the sets P^α and Q^β .

3 HIGHER ORDER PDS-FEM

3.1 Formulation

Consider standard Boundary Value Problem (BVP) of infinitesimal deformation of a linearly elastic body occupying the space V . We ignore body forces for the sake of simplicity. This section presents the implementation of higher order PDS in FEM framework to solve this BVP. We use the following standard Lagrangian as the weak form for this BVP.

$$\mathcal{L}(\boldsymbol{\epsilon}, \mathbf{c}) = \frac{1}{2} \int \boldsymbol{\epsilon} : \mathbf{c} : \boldsymbol{\epsilon} dv \quad (5)$$

We approximate the displacement field \mathbf{u} and $\nabla \mathbf{u}$ as

$$u_i \approx \sum_{\alpha} u_i^{\alpha} = \sum_{\alpha} \sum_m^{|\mathcal{P}^{\alpha}|} u_i^{\alpha m} P^{\alpha m} \quad (6)$$

$$u_{i,j} \approx \sum_{\beta} g_{ij}^{\beta} = \sum_{\beta} \sum_n^{|\mathcal{Q}^{\beta}|} g_{ij}^{\beta n} Q^{\beta n} \quad (7)$$

The unknown $g_{ij}^{\beta n}$'s can be found by minimizing the error $E^{\mathbf{g}} = \sum_{\beta} \int_{\Psi^{\beta}} \left\| g_{ij}^{\beta} \mathbf{e}_i \otimes \mathbf{e}_j - \nabla \mathbf{u}^{\alpha} \right\|^2 dv$ with respect to $g_{ij}^{\beta n}$.

$$g_{ij}^{\beta n} = \left(B^{\beta nn'} \int_{\Psi^{\beta}} Q^{\beta n'} (P^{\alpha m})_{,j} dv \right) u_i^{\alpha m} \quad (8)$$

$$= b_j^{\beta n \alpha m} u_i^{\alpha m}. \quad (9)$$

where $[B^{\beta nn'}] = [A^{\beta n' n}]^{-1}$. For the sake of brevity, the above tensor equations can be expressed as

$$\mathbf{g}^{\beta n} = \mathbf{b}^{\beta n \alpha m} \otimes \mathbf{u}^{\alpha m} \quad (10)$$

With Eq. 10, and approximation scheme of PDS, strain: $\boldsymbol{\epsilon}$ can be approximated as $\boldsymbol{\epsilon} \approx \sum_{\beta, n} \boldsymbol{\epsilon}^{\beta n} Q^{\beta n}$, where

$$\boldsymbol{\epsilon}^{\beta n} = \text{sym} (\mathbf{b}^{\beta n \alpha m} \otimes \mathbf{u}^{\alpha m}) \quad (11)$$

and *sym* stands for symmetric part of the second order tensor. Further, $\boldsymbol{\sigma}$ is determined as $\boldsymbol{\sigma}^{\beta} = \mathbf{c}^{\beta} : \boldsymbol{\epsilon}^{\beta}$, where \mathbf{c}^{β} is the constitutive tensor for Ψ^{β} .

With the above definitions, implementation of PDS in FEM framework is straightforward. Substituting Eq. 11 into Eq. 5 and setting its first variation $\delta \mathcal{L} = 0$, following linear set of equations can be obtained

$$\sum_{\alpha' m'} \sum_{n, n'} A^{\beta nn'} \left(\mathbf{b}^{\beta n \alpha m} \cdot \mathbf{c} \cdot \mathbf{b}^{\beta n' \alpha' m'} \right) \cdot \mathbf{u}^{\alpha' m'} = \mathbf{0}.$$

In the above set of governing equations, the stiffness matrix for a Delaunay tessellation Ψ^{β} can be readily recognized as

$$\mathbf{k}^{\beta} = \sum_{n, n'} A^{\beta nn'} \left(\mathbf{b}^{\beta n \alpha m} \cdot \mathbf{c} \cdot \mathbf{b}^{\beta n' \alpha' m'} \right),$$

where \mathbf{k}^{β} is a matrix of size $(6 |\mathcal{P}^{\alpha}|) \times (6 |\mathcal{P}^{\alpha}|)$ or $(12 |\mathcal{P}^{\alpha}|) \times (12 |\mathcal{P}^{\alpha}|)$ with triangular element in 2D or tetrahedral elements in 3D, respectively.

3.2 Modeling brittle fracture with PDS-FEM

As mentioned, a major advantage of PDS-FEM is the simple and numerically efficient treatment for modelling discontinuities. PDS approximation $f^d(\mathbf{x})$ of a function $f(\mathbf{x})$ inherently consists of discontinuities along each edge of Voronoi elements $\partial\Phi^\alpha$'s, which are clearly visible in Fig. 1(a). When PDS defines bounded derivatives for $f^d(\mathbf{x})$ over Ψ^β , contribution from these discontinuities along $\partial\Phi^\alpha$'s are also taken in to account (Eq. 4). In PDS-FEM, a brittle crack along a segment of a given $\partial\Phi^\alpha$ is modeled by dropping those contributions from an infinitesimal neighbourhood of the relevant $\partial\Phi^\alpha$. As explained below, this failure treatment requires nothing more than recalculation of a single element stiffness matrix.

According to the definition, $P^{\alpha n}$ can be written as $P^{\alpha n} = F^{\alpha n}(\mathbf{x} - \mathbf{y}^\alpha) \phi^\alpha(\mathbf{x})$, which allows to express $b_j^{\beta n \alpha m}$ in Eq. 9 as

$$b_j^{\beta n \alpha m} = \sum_{n'}^{|Q^\beta|} B^{\beta n n'} \int_{\Psi^\beta} Q^{\beta n'} \left(F_{,j}^{\alpha m} \phi^\alpha + F^{\alpha m} \phi_{,j}^\alpha \right) dv \quad (12)$$

$$= \sum_{n'}^{|Q^\beta|} B^{\beta n n'} \left(\int_{\Psi^\beta} Q^{\beta n'} F_{,j}^{\alpha m} \phi^\alpha dv + \int_{\partial\Phi^\alpha} Q^{\beta n'} F^{\alpha m} n_j ds \right), \quad (13)$$

where, n_j^α is the unit outward normal along $\partial\Phi^\alpha$. In Eq. 13, the term $\int_{\partial\Phi^\alpha} Q^{\beta n'} F^{\alpha m} n_j ds$ is responsible for including the contribution to ϵ_{ij}^β from the discontinuities along $\partial\Phi^\alpha$ in the approximated displacement field.

What is required to model a brittle crack along a segment of Voronoi boundary, $\partial\Phi^\alpha$, is dropping this contribution $\int_{\partial\Phi^\alpha} Q^{\beta n'} F^{\alpha m} n_j ds$ from the corresponding segment of $\partial\Phi^\alpha$, when evaluating $\mathbf{b}^{\beta n \alpha m}$. As an example, to model a crack along the boundary AG creating a crack surfaces AG and GA' in Fig. 2(b), all it needs is to exclude the contributions $\int_{AG} Q^{\beta n'} F^{\alpha_1 m} n_j^{AG} dl$ and $\int_{A'G} Q^{\beta n'} F^{\alpha_2 m} n_j^{A'G} dl$, when evaluating $\mathbf{b}^{\beta n \alpha m}$, and recalculate the element stiffness matrix of corresponding Delaunay element. The integration $\int_{\partial\Phi^\alpha} Q^{\beta n'} F^{\alpha m} n_j ds$ can easily be evaluated with numerical integration over lines/planes in 2D/3D settings, respectively.

Compared with the treatments used in other methods to model propagating cracks, this treatment is simple and numerically efficient. Most existing numerical methods which requires introduction of new nodes, enrichment involving complex integration and introduction of new DOFs, etc., while above PDS-FEM treatment require only recalculation of an element stiffness matrix. Especially, in simulating large scale problems utilizing high performance computing, this simple crack treatment has a clear advantage over the existing methods.

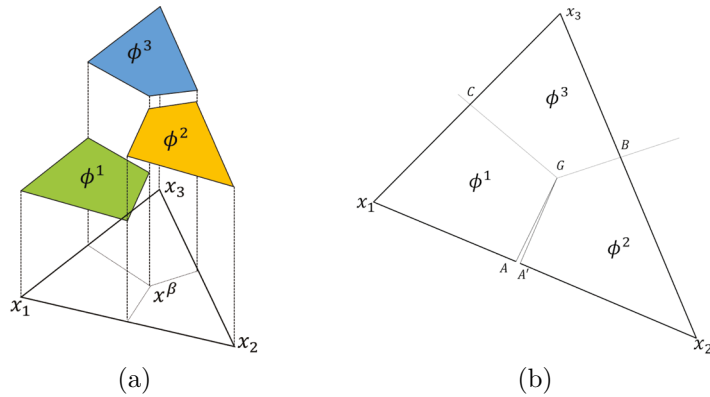


Figure 2: Simulation of crack; (a) existing discontinuities in the displacement field approximated with PDS, (b) modeling a crack by dropping contribution from infinitesimally thin neighborhood of the Vorono boundary to be broken.

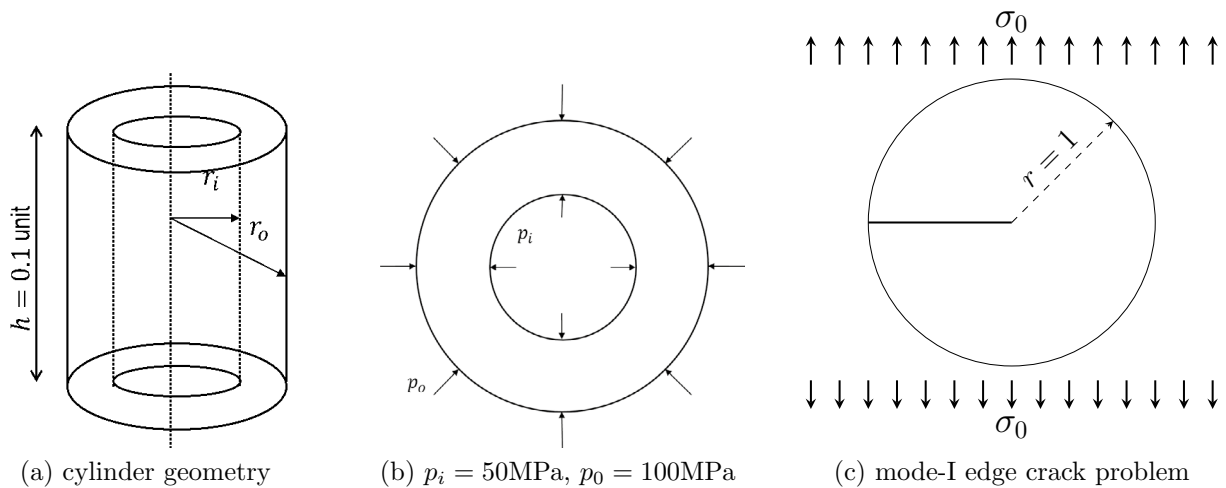
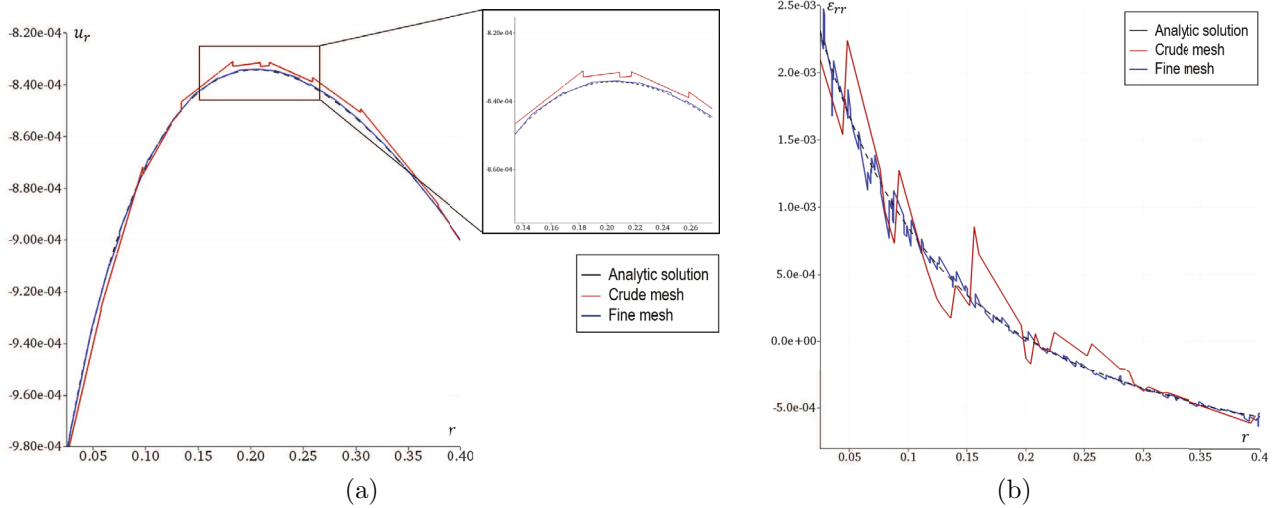


Figure 3: Settings of the thick cylinder and mode-I edge crack problems.


 Figure 4: (a) Displacement: u_r and (b) strain: ϵ_{rr} along radial direction

4 NUMERICAL EXAMPLES

In this section, we present some numerical results to verify the of higher order extension of PDS-FEM. Specifically, the analytic solutions and numerical results are compared for the problem of thick cylinder subjected internal and external pressure, and mode-I crack subjected to far field loading.

4.1 Thick cylinder under internal and external pressure

A thick cylinder subjected to internal and external pressure, which is a classical problem, is considered to verify the 3D implementation of PDS-FEM. The problem settings are illustrated in Fig. 3(a) and (b). The boundary conditions at the cylinder ends are set to reproduce plain strain conditions. The set of polynomial bases used are

$$\begin{aligned} P^\alpha &= \{1, (x - x^\alpha), (y - y^\alpha), (z - z^\alpha)\} \\ Q^\beta &= \{1, (x - x^\beta), (y - y^\beta), (z - z^\beta), (x - x^\beta)^2, (y - y^\beta)^2, (z - z^\beta)^2, (x - x^\beta)(y - y^\beta), \\ &\quad (x - x^\beta)(z - z^\beta), (y - y^\beta)(z - z^\beta)\} \end{aligned}$$

Figure 4 compares the analytic solutions and numerical results of radial displacement u_r and strain component ϵ_{rr} , along a radial line. A quick comparison advocates the improvement in solution with the mesh refinement, and that the numerical solutions are in good agreement with analytic solution. For this specific setting, u_r reaches its maximum at $r = 0.2$. Figure 5 shows the error of u_r and ϵ_{rr} at $r = 0.2$, for several tessellations with different element sizes. As is seen, the error diminishes at a second order rate with respect to the number of degrees of freedoms, which is the expected.

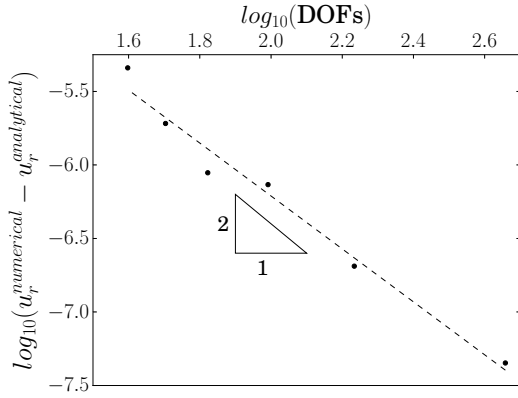


Figure 5: Error in u_r at $r = 0.4$ for the thick cylinder problem with 1st-order PDS-FEM; obtained with tessellations of different element sizes.

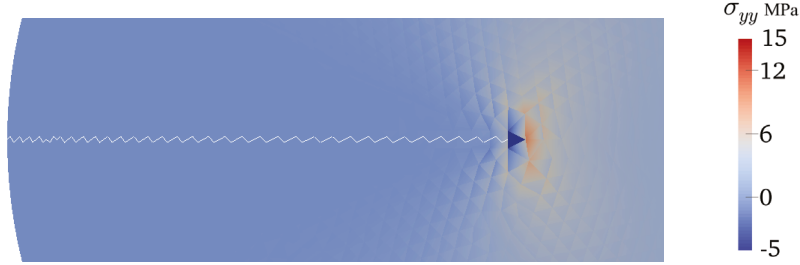


Figure 6: σ_{yy} in the crack tip neighborhood. White lines are broken Voronoi boundaries.

4.2 Stress singularity at a mode-I crack tip

In order to verify the crack treatment proposed in section 3.2, the classical 2D mode-I edge crack in an infinite domain is considered. Far field tensile stress $\sigma_0 = 10\text{MPa}$ is applied in y -direction, and plane stress state is assumed. The Youngs modulus and the Poisons ratio of the plate is assumed to be 1GPa and 0.33, respectively. 3(c) shows the simulated circular domain; displacement boundary conditions along the circular boundary is set according the analytic solution. The set of polynomial bases used are given below. This setting is referred as 1st-order PDS-FEM.

$$\begin{aligned} P^\alpha &= \{1, (x - x^\alpha), (y - y^\alpha)\} \\ Q^\beta &= \{1, (x - x^\beta), (y - y^\beta), (x - x^\beta)^2, (y - y^\beta)^2, (x - x^\beta)(y - y^\beta)\} \end{aligned}$$

Figure 7 shows σ_{yy} in the vicinity of the crack tip. It is found that except at a small neighbourhood of the crack tip, the stress component are accurate and the error diminishes at a second order rate. However, there is a significant error within the crack tip

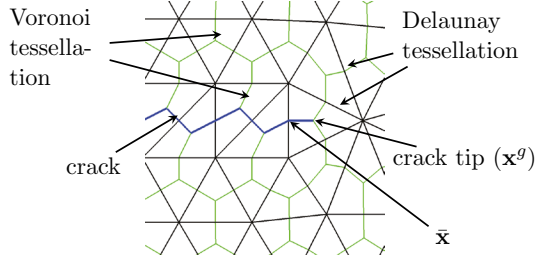


Figure 7: Change of mother point for the polynomial bases of crack tip element

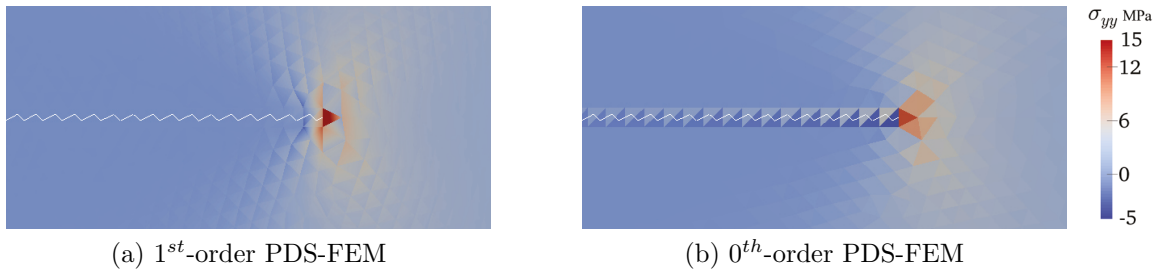


Figure 8: σ_{yy} in the vicinity of the crack tip, with polynomial mother points moved to \bar{x} .

element (i.e. element containing the crack tip). This deviation is not unexpected since crack tip singularity of $\sigma = f\left(\frac{1}{\sqrt{r}}, \sin\frac{\theta}{2}, \cos\frac{\theta}{2}\right)$ cannot be accurately approximated with polynomials. Judicious selection of bases function would be most appropriate approach to restore the stress singularity.

It is of interest to investigate the effect of the location of the mother point \mathbf{x}^{β_c} of base polynomial set P^{β_c} , where Ψ^{β_c} is the Delaunay element containing the crack tip. As mentioned, mother points (i.e. center of area \mathbf{x}^g) of Ψ^β 's are used as \mathbf{x}^β in P^β . Polynomial bases with \mathbf{x}^g may have negative effects in approximating singular stress field. To investigate the effect of setting \mathbf{x}^β of the crack tip element to be outside of Ψ^{β_c} , a set of simulations are conducted with setting $\mathbf{x}^{\beta_c} = \bar{\mathbf{x}}$, where $\bar{\mathbf{x}}$ is the mid of broken edge as shown in Fig. 7(b).

Figure 8 shows σ_{yy} in the vicinity of crack tip with 0th-order PDS-FEM and 1st-order PDS-FEM. As is seen in Fig. 8(a) that choosing $\bar{\mathbf{x}}$ as polynomial mother point for Ψ^{β_c} rectifies the above problem in the crack tip element. Further, 1st-order PDS-FEM has significant improvement in reproducing traction free condition along the crack surface, compared to 0th-order. This is clearly visible in Fig. 9.

J-integral along a set of closed paths are evaluated for different sets of tessellation in order to verify the crack tip stress singularity of 1st-order PDS-FEM. According to Fig. 10 the error of J-integral diminishes at a rate of 1.4, while 0st-order has first order rate [8].

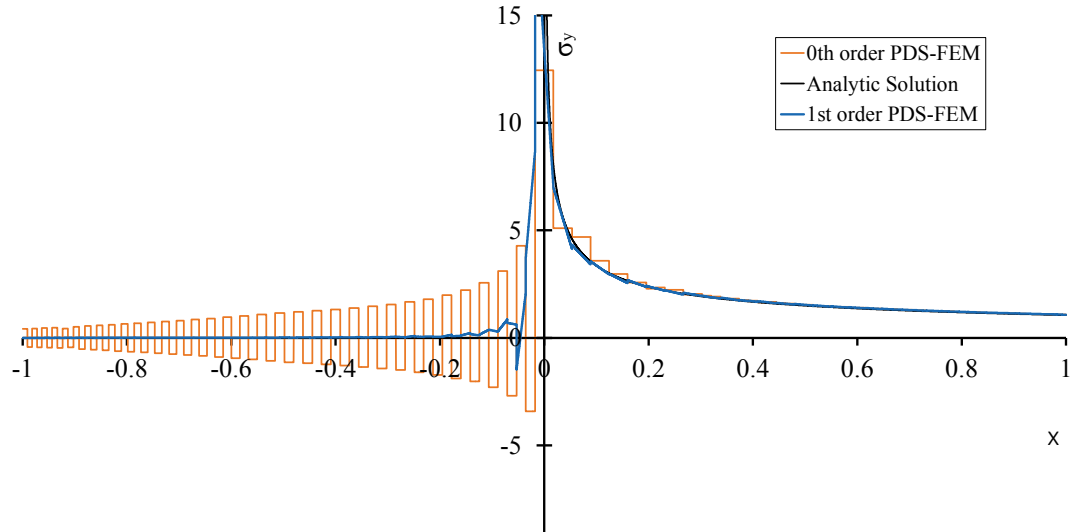


Figure 9: σ_{yy} along a section passing through the upper crack surface.

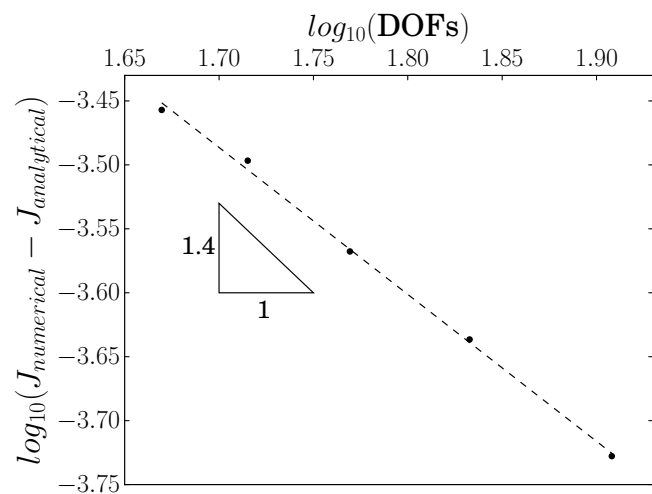


Figure 10: Convergence rate of J-Integral of mode-I edge crack problem with 1st-order PDS-FEM.

5 CONCLUDING REMARKS

Higher order extension of PDS and PDS-FEM are presented. The verification tests indicates that second order convergence rate for displacement, strain and stress can be attained with first and second order polynomial sets for P^α and Q^β , respectively. While crack tip singularity also has higher accuracy, higher order PDS-FEM shows a significant improvement in reproducing traction free condition along the crack surface, compared to 0^{th} -order PDS-FEM.

REFERENCES

- [1] S. Rahman, J.S. Kim,: Probabilistic fracture mechanics for nonlinear structures, Int. J. of Pressure Vessels and Piping, 78, pp. 261-269, 2001.
- [2] Morsaleen Shehzad Chowdhury, Chongmin Song, Wei Gao,: Probabilistic fracture mechanics by using Monte Carlo simulation and the scaled boundary finite element method, Engineering fracture mechanics, 78, pp. 2369-2389, 2011.
- [3] Benz W,: Smooth particle hydrodynamics: a review. In: Numerical Modeling of Non-linear Stellar Pulsation: Problems and Prospects, Kluwer Academic, Boston, 1990.
- [4] Belytschko T, Lu YY, and Gu L,: Element free galerkin methods. Int. J. Numer. Methods Eng. 37, pp. 229-256, 1994.
- [5] Liu WK, Adee J, and Jun S,: Reproducing kernel and wavelets particle methods for elastic and plastic problems, In: Advanced Computational Methods for Material Modeling, AMD 180/PVP 268 ASME, pp. 175-190, 1993.
- [6] Babuska I and Melenk JM,: The partition of unity method, Int. J. Numer. Methods Eng. 40, pp. 727-758, 1997 .
- [7] Muneo Hori, Kenji Oguni, Hide Sakaguchi,: Proposal of FEM implemented with particle discretization scheme for analysis of failure phenomena, J. of Mech. and Phys. of Solids, Vol.53, pp. 681-703, 2005.
- [8] M.L.L. Wijerathne, Kenji Oguni, Muneo Hori,: Numerical analysis of growing crack problem using particle discretization scheme, Int. J. for Numerical Methods in Engineering, Vol.80, pp. 46-73, 2009.
- [9] Mahendra Kumar Pal, Lalith Wijerathne, Muneo Hori, Tsuyoshi Ichimura, Seizo Tanaka,: Implementation of Finite Element Method with higher order Particle Discretization Scheme, J. of Japan Society of Civil Engineers, Ser.A2 (Applied Mechanics(AM)),70(2), pp. 297-305, 2014.

INCLUSION OF PORE PRESSURE EFFECTS IN DISCRETE ELEMENT MODELING OF ROCK CUTTING

RUDY L.J. HELMONS¹, SAPE A. MIEDEMA² AND C. VAN RHEE²

¹ Delft University of Technology
Mekelweg 2, 2628 CD Delft, Netherlands
r.l.j.helmons@tudelft.nl

² Delft University of Technology
Mekelweg 2, 2628 CD Delft, Netherlands

Key words: Rock Cutting, DEM, SPH, poromechanics

Abstract. Many rock excavation processes occur in a marine environment, like in drilling for oil/gas, dredging, trenching and deep sea mining. The presence of a fluid in and surrounding the rock can have a significant influence on the cutting process, through differences in the ambient (confining) and pore pressure. The cutting motion deforms the rock matrix, and as a result, local fluid pressure differences will occur. The magnitude of these pressure differences, and thus its effect on the cutting process, increases with larger water depths and/or higher cutting velocities. The apparent strength of the rock matrix increases with higher confining pressures, resulting in a higher cutting force.

The Discrete Element Method is used successfully to simulate the rock cutting process of dry rock for various applications. In this paper, the authors extend DEM with a fully coupled fluid pressure model to simulate the mechanics of saturated rock. This is done by solving a pore pressure diffusion equation with a Smoothed Particle (SP) method. By using the SP, it is possible to convert the discontinuum properties of the DEM to a continuum, in which the fluid pressure is modeled and applied as an additional force in the DEM.

Qualitative results show that the model is able to capture the increase in cutting force with increasing confining pressure, as well as deformation rate effects applied on saturated rocks.

1 INTRODUCTION

An important factor in future oil and gas reserves are the costs to drill a well. These costs are influenced by the rate of penetration (ROP). The ROP becomes increasingly susceptible to the hydrostatic pressure when drilling holes at larger depths. This transition is likely to occur in the range where the hydrostatic pressure is of the same order of magnitude as the strength of the rock. Proper modeling and understanding of the phenomena

that occur when drilling rock at large depths can help in improving the performance of the drilling process.

The combination of high pressure and high deformation makes it complicated to model the cutting of rock. Several empirical and analytical models [1], [2], [3] have been developed to describe the rock cutting process. However, most of these models are specifically designed for practical purposes and are less suitable for research purposes. Knowledge about effects like the shape and size of cuttings, the amount and kind of damage to the virgin (uncut) rock, lay-out of the cutting structure on the drill bit is desired to further optimize the cutting process. The Discrete Element Method (DEM) is a powerful tool that can help to give a more detailed analysis of the rock cutting process. This has already been done for various applications: Tunneling [4], [5], dredging/alluvial mining [6], [7], [8] and (oil/gas) drilling [8], [9], [10], [11].

It is generally accepted that the drilling specific energy (amount of energy required to drill unit volume of rock), depends on the differential pressure, i.e. on the difference between the bottom-hole pressure and the virgin pore pressure. However, it has also been recognized early on that such a conceptual model is probably not applicable to low-permeability dilatant rocks because the fluid cannot be supplied rapidly enough to the failed regions, causing the pore pressure in the failed zones to drop or even vanish, as discussed by Detournay and Atkinson [2]. Results of single cutter experiments by Zijssling [12] support this view.

The existing DEM models for drilling are thus far based on application of the differential pressure, automatically assuming dry rock [9], [10], [11]. Therefore, these models lack the influence of a changing pore pressure. In this paper, an approach that considers the dynamically changing pore pressures is presented. This paper is a further improvement of the work presented in [6].

2 PRESSURE EFFECTS

The influence of the fluid pressure on the cutting process can be estimated through the pore Peclet number, which can be interpreted as the ratio of deformation rate over the pore pressure dissipation rate. According to Detournay and Atkinson [2], the pore Peclet number ζ_{Pe} is given by

$$\zeta_{Pe} = \frac{v_c t_c}{4D} = \frac{v_c t_c n \mu C_f}{4\kappa} \quad (1)$$

with cutting velocity v_c , cutting thickness t_c , pore pressure diffusivity coefficient D , dynamics fluid viscosity μ , porosity n , fluid compressibility C_f and intrinsic permeability κ in m^2 . In general, it can be assumed that when $\zeta_{Pe} < 1$, the dynamic pore pressure changes are negligible and that the process can be considered as drained. In case $\zeta_{Pe} > 1$, the effect of the pore pressure changes can significantly influence the cutting process, this regime is often referred to as the undrained regime. The most profound phenomena that are observed in uni-axial and tri-axial tests with varying axial strain rates are:

1. Dilative strengthening [13], [14].

2. Compactive weakening [14].
3. Cavitation (complete loss of pore pressure, as observed in Mancos shale [12]).

3 METHOD

3.1 Discrete element method - Rock

In DEM, the solid material is represented as a collection of particles (these can be any arbitrarily shape, most often spheres in 3D or discs with unit thickness in 2D are used for the sake of simplicity) that have mutual interactions in normal and tangential directions. This paper gives the description and results in 2D. The translational and rotational motion of a particle is governed by the standard equations of rigid body mechanics

$$m_i \vec{a}_i = \vec{F}_i \quad (2)$$

$$I_i \vec{\alpha}_i = \vec{T}_i \quad (3)$$

\vec{F} and \vec{T} are the sums of all forces and moments applied to the particle i due to external loading, contact interactions with neighboring objects and from damping in the system. The interaction force between a pair of particles can either consist of a collision type or a bond type of interaction. In both cases the force is decomposed into normal and tangential components, with

$$\vec{F} = \vec{F}_n + \vec{F}_t = \vec{n} F_n + \vec{t} F_t \quad (4)$$

where \vec{n} is the unit vector normal to the particle surface at the point of interaction. The contact forces F_n and F_t are determined with a constitutive model for the interaction. At the beginning of each simulation, a bond is installed between neighboring particles. These bonds are defined by a linear elastic perfect brittle model (see figure 1), meaning that a bond breaks immediately when its strength is exceeded. Note that a bond can break either in normal (tension) or in tangential (shear) direction and not in compressive direction (macroscopic compressive failure is considered as a localization of many micro-shear and tensile failures). After a bond is broken, the bond will be removed from the simulation. Broken bonds and new interactions are considered as collisions between two particles. For stability, numerical damping as in [15] has been applied.

The DEM can be regarded as a micro-mechanical model, with the contact and bond model parameters being micro-parameters. It is assumed that with the adequate micro-mechanical parameters macroscopic rock properties are obtained, of which the Young's modulus E , Poisson ratio ν , and compressive and tensile strengths σ_c and σ_t are the most relevant. These properties will be used in calibrating the micro-mechanical model to sufficiently mimic the macroscopic rock mechanics.

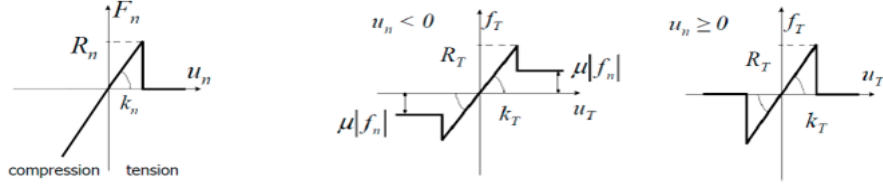


Figure 1: Linear elastic perfect brittle bond model: (left) normal direction, (middle) shear direction with contact after failure and (right) shear direction without contact after failure

3.2 Smoothed particle approach - fluid pressure

The effect of a rapidly changing effective stress is modeled with the use of a pore pressure diffusion equation, as in [16]. This equation is based on the combination of mass conservation, Darcy flow and a constitutive equation for the compressibility of the pore fluid, given respectively by

$$\frac{D\zeta}{Dt} + \nabla \cdot \vec{u} = 0 \quad (5)$$

$$\vec{u} = -\frac{\kappa}{\mu} \nabla p \quad (6)$$

$$p = M(\zeta - \alpha \epsilon_v) \quad (7)$$

which through substitution results in the pore pressure diffusion equation given by

$$\frac{Dp}{Dt} - M \nabla \cdot \left(\frac{\kappa}{\mu} \nabla p \right) = -\alpha M \frac{D\epsilon_v}{Dt} \quad (8)$$

with pressure p , fluid bulk modulus M , intrinsic permeability κ , dynamic fluid viscosity μ , effective stress coefficient α and volumetric strain ϵ_v . The coupling of the discrete data obtained from the DEM computations with the pore pressure diffusion equation (3.2) is obtained by using a Smoothed Particle (SP) approach. DEM and SP work in a co-located fashion, meaning that both methods use the same discretisation points.

In the DEM-SP model, the discretized particles are taken from a particle size distribution and randomly stacked together. The unstructured positions and random size (and thus mass) of the particles can easily result in numerical instabilities and inaccuracies. To adjust for the random size and positioning of the particles, the Corrective Smoothed Particle Approach (CSPM) is used ([17]).

In CSPM, the kernel interpolation of a field quantity A (which can be any arbitrary parameter) is calculated by

$$A(\vec{r}_i) = \frac{\sum_j A_j m_j W(\vec{r}_i - \vec{r}_j, h)}{\sum_j m_j W(\vec{r}_i - \vec{r}_j, h)} \quad (9)$$

with particle mass m , kernel function W , position r , smoothing length h , index i for particle under consideration and index j for neighboring particles (including particle i).

In a similar fashion, the first order derivative of a function A is determined by

$$\nabla_i A(\vec{r}_i) = \frac{\sum_j (A_i - A_j) m_j \nabla W(\vec{r}_i - \vec{r}_j, h)}{\sum_j (\vec{r}_i - \vec{r}_j) m_j \nabla W(\vec{r}_i - \vec{r}_j, h)} \quad (10)$$

where ∇_i is the gradient with respect to particle i . Higher order derivatives cannot be calculated directly. The first derivative is necessary to determine the volumetric strain rate in equation (3.2),

$$\dot{\epsilon}_v = \nabla \cdot \vec{v} = \frac{\partial v_x}{\partial x} + \frac{\partial v_y}{\partial y} \quad (11)$$

Here the Wendland C2 kernel function is used [18]

$$W = \begin{cases} \frac{7}{\pi^2} (1 - R)^4 (4R + 1) & \text{if } R \leq 1 \\ 0 & \text{if } R > 1 \end{cases} \quad (12)$$

where

$$R = \frac{\|\vec{r}_i - \vec{r}_j\|}{h} \quad (13)$$

To calculate the diffusive term in (3.2), we make use of the results of [19]:

$$\nabla \cdot \kappa \nabla p = \sum_j \frac{m_j (\kappa_i + \kappa_j)}{\rho_i} (p_i - p_j) \frac{\vec{n}_{ij} \cdot \nabla W(\vec{r}_i - \vec{r}_j, h)}{\|\vec{r}_i - \vec{r}_j\|} \quad (14)$$

where \vec{n}_{ij} is the normal unit vector of the neighboring particle centers. Note that here κ is a property of the particles and thus that it can differ throughout the rock sample. In our case, it is assumed that κ is constant.

Two way coupling is applied every timestep. DEM is advanced half a timestep, based on the intermediate velocities the volumetric strain rate is calculated with SP. This is then used to advance the pore pressure diffusion one timestep in a forward Euler scheme. The local pressure gradient of the fluid is calculated based on the new pore pressure distribution. The pressure gradient is then added as an interaction force to the sum of forces acting on the particles through

$$\vec{F} = -\nabla p \frac{\pi d_p^2}{4} w \quad (15)$$

with particle diameter d_p and unit thickness w . Finally the DEM is advanced the second half timestep.

It is possible that the fluid pressure drops below the vapor pressure during simulations. When this happens, the liquid will vaporize and as a result, the compressibility of the fluid increases with several orders of magnitude. In the simulations, this is modeled through a simplified approach. When the pressure drops below the pressure minimum, the pressure value is fixed at the minimum pressure. From thereon it is only possible to increase the pressure by having fluid flow towards the cavitated zone, so if

$$p_i < p_{min} \quad \text{then} \quad p_i = p_{min} \quad \text{and} \quad \frac{\partial p_i}{\partial t} = \max \left(\frac{\partial p_i}{\partial t}, 0 \right) \quad (16)$$

3.3 Boundary conditions

In DEM-SP, boundary conditions have to be applied for both the rock and fluid phase. For rock this is done by restricting or prescribing the motion of specific particles or walls. In case of the fluid pressure, the boundary conditions are somewhat harder to set. The SP discretisation of (3.2) in itself automatically applies Neumann boundary condition (zero gradient), meaning that it allows no fluid flow across the boundaries of the rock. This is applicable in the case where equipment is moving through the rock (cutting teeth, compressive tests, splitting tests, etc.). In case of a rock boundary that is in contact with clear fluid, like the top layer of the seabed, a Dirichlet boundary condition (fixed value, such as hydrostatic pressure) is applied. However, the boundaries of the rock may change during the simulation. Therefore it is necessary to use a method to determine what particles are part of the rock boundary. To determine this, we make use of the divergence of position, as suggested by [20].

$$\nabla \cdot \vec{r} = \frac{\partial x}{\partial x} + \frac{\partial y}{\partial y} = 2 \quad (17)$$

This is applied to the standard Smoothed Particle approach of [21], because otherwise the CSPM in equation (3.2) automatically corrects for the particle deficiency, always setting at a value of 2.

$$\nabla_i A(\vec{r}_i) = \sum_j m_j \frac{A_j}{\rho_j} \nabla W(\vec{r}_i - \vec{r}_j, h) \quad (18)$$

In the interior domain of the rock, equation (3.3) is valid. However, at the boundaries this value differs due to particle deficiency, see figure 2. Here, particles with $\nabla \cdot \vec{r} \leq 1.5$ are considered to be part of the boundary. With this technique, the particles that require a Dirichlet boundary condition can now be identified.

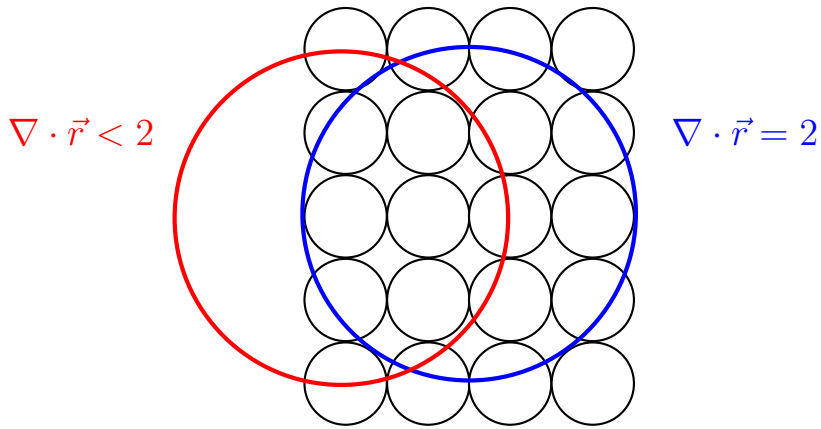


Figure 2: Schematic overview of particle deficiency

4 RESULTS

We compare the results of our approach with the experiments of Kaitkay and Lei [22]. They performed rock cutting experiments on Carthage marble. The model is calibrated to match the Youngs' modulus and the compressive strength of the rock. The used material properties are shown in table 1. A uniform particle size distribution with sizes ranging from 0.125 to 0.163 mm is used. In our approach, we used point contact bonds.

Table 1: Properties of Carthage marble and simulation specimen

Property	Carthage marble [22]	DEM-SP
E [GPa]	44.8	41.9
ν [-]	0.24	0.22
σ_c [MPa]	103	97
σ_c at $p_c = 34.5$ [MPa]	186	160
σ_{BTS} [MPa]	not published	6.3

The model for the cutting experiments is 50 mm in length and 16 mm in height. The bottom and sides of the specimen are constrained with walls to represent the surrounding rocks. The top layer is exposed to a hydrostatic pressure and flow of pore fluid through the top layer to the surrounding (clear) fluid is allowed.

Cutting simulations were performed for three pressure states (0.1, 3.5 and 34.5 MPa) and two rake angles ($\alpha = -15$ and $\alpha = -25$ deg) with cutting speed and depth of cut kept at 1 m/s and 0.8 mm, respectively.

The averaged cutting forces of our approach are compared with the experimental data of [22] in figure 3. The calculated cutting forces in our simulations are scaled with the length of the perimeter of the cutter that is in contact with the virgin rock, which is estimated as 11.3 mm for the experiments of [22].

In figure 5, it is shown what the influence of the pore Peclet number (here scaled by adjusting the pore pressure diffusion coefficient) on the cutting forces will be. An impression of the amount of damage that occurs during cutting is shown in figures 6 and 7. Note that damage here is defined as $D = \frac{\text{nr of broken bonds}}{\text{total initial bonds}}$. Lastly, snapshots of the pressure distribution during the same cutting experiments are shown in figures 8 and 9.

suggest: is apparent from a comparison of figure 3 and 4.

5 DISCUSSION

The trend of the simulated cutting force matches well with the cutting forces measured in the experiments is apparent from a comparison of figures 3 and 4. However, it must be noted that the horizontal forces show much better resemblance than the vertical components.

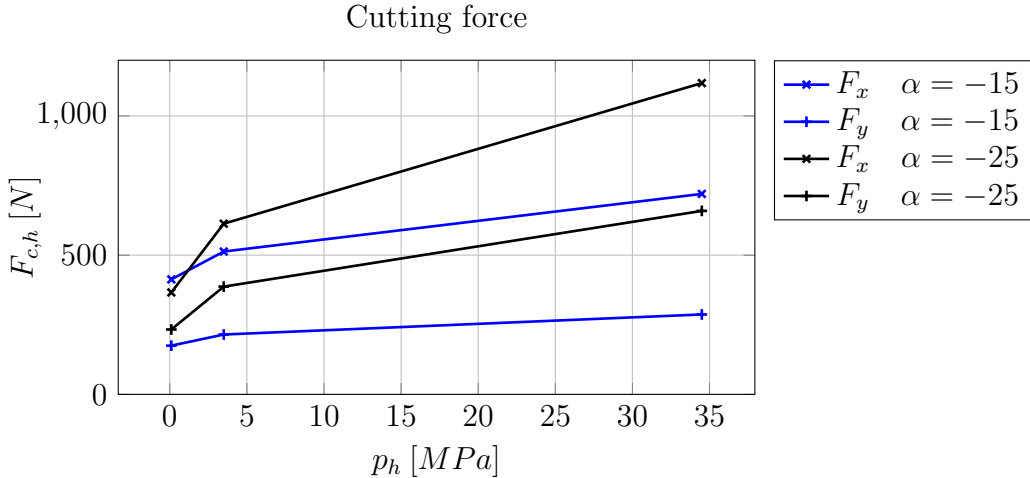


Figure 3: Cutting force vs hydrostatic pressure, simulations with DEM-SP.

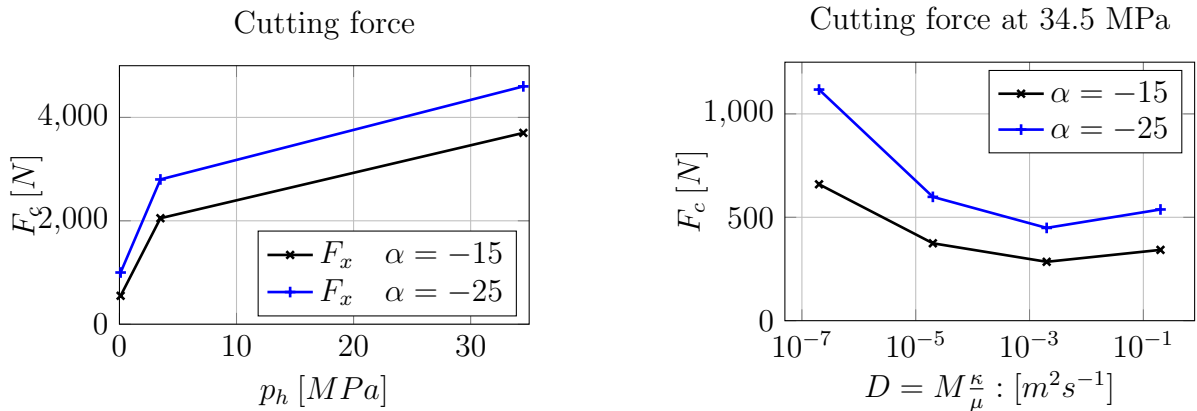


Figure 4: Cutting force vs hydrostatic pressure, experiments [22].

Figure 5: Cutting force vs pore pressure diffusivity.

In both the experiments and in our approach, a distinction can be noticed between brittle cutting at low hydrostatic pressures and ductile cutting at high hydrostatic pressures. This transition is also noticeable when comparing the amount of damage that occurs to the DEM particles during cutting. The amount of damage and the number of fully damaged particles is significantly higher at high hydrostatic pressures, which can be observed by comparing figures 6 and 7. It also seems that after the material has been cut, some sort of filter cake is being left. The shape of the filter cake is rather smooth, which seems more realistic compared to the 'velcro'-like structures that are obtained by the method of Lei and Kaitkay [9]. Also the size of the filter cake seems to increase with increasing

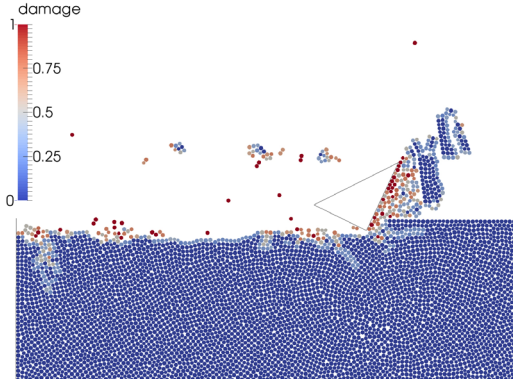


Figure 6: Damage during cutting with bit at $\alpha = -25$ and at $p_h = 0.1$ MPa.

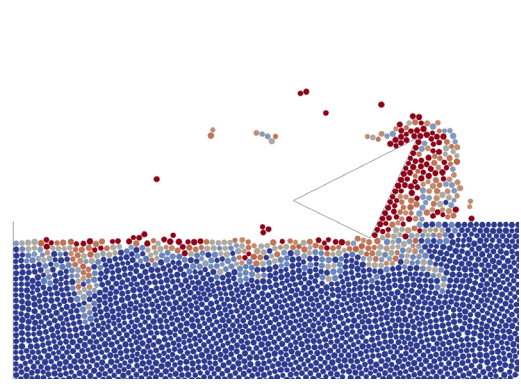


Figure 7: Damage during cutting with bit at $\alpha = -25$ and at $p_h = 34.5$ MPa.

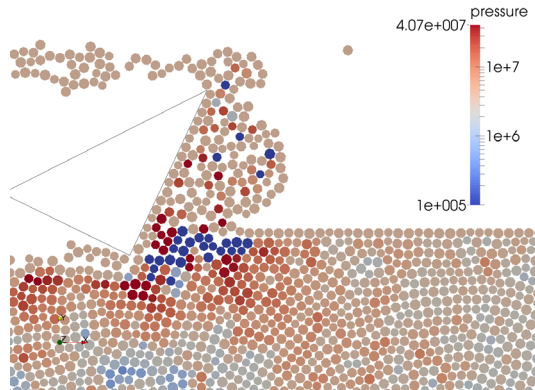


Figure 8: Snapshot of pressure distribution during cutting with bit at $\alpha = -25$ and at $p_h = 3.5$ MPa.

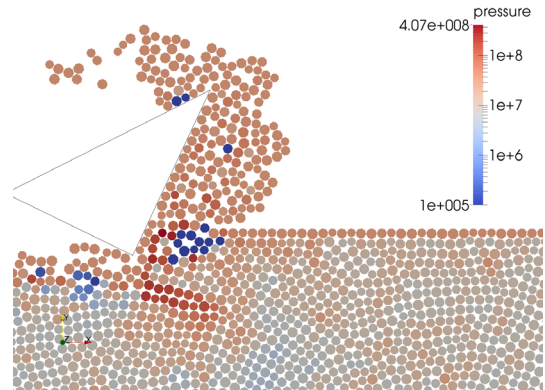


Figure 9: Snapshot of pressure distribution during cutting with bit at $\alpha = -25$ and at $p_h = 34.5$ MPa.

confining pressures.

The occurrence of cavitation is clearly shown in figures 8 ($p_h = 3.5$ MPa) and 9 ($p_h = 34.5$ MPa). These figures show typical snapshots of the cutting process. The cavitating zone is located along the shear failure that occurs between the tip of the drill bit and the surface of the intact rock. Due to dilation of the particles along the shear failure, locally the pore pressure drops. The pressure drop is that large that the fluid will cavitate, which limits the local pressure gradient and effectively also limiting the required cutting force. It should be noted that the cavitating zone is larger at lower hydrostatic pressure.

In figure 5, results are shown where the pore pressure diffusion coefficient $D = M \frac{\kappa}{\mu}$ has been varied. In practice, this can be represented by varying the permeability of the rock (for instance, compare two rocks that have same strength and stiffness, but different

permeability). This is one approach to vary the pore Peclet number. It is also possible to alter the pore Peclet number by changing the pore volume deformation rate in the rock (i.e. many small pores or few bulk pores). An obvious way of changing the pore Peclet number this way is by changing the process parameters: cutting speed and cutting depth (effects for the difference between e.g. rotary drilling and mud motor drilling). A minimum in the cutting force with respect to the pore pressure diffusion coefficient can be observed. This is most likely due to the mutual interaction of compaction weakening and dilatant strengthening, of which both might dominant in a different regime of the pore Peclet number, i.e. dilatant strengthening is especially dominant in the undrained regime, while compaction weakening is more typical for slower processes, as is shown in [14].

Quantitatively, the values calculated by DEM-SP underestimate the measured values. The most profound reasons why the results underestimate the experiments are likely:

- The tensile strength in the simulation might deviate significantly from that of the experiments. However, the tensile strength in the experiments is not known. Based on [23] it is expected that the BTS value in the experiments would be approximately 10 MPa in this case of marble.
- Friction of the particles along the drill bit is underestimated. The disc-shaped particles tend to roll too easily compared to real grains.
- In 2D-DEM it is automatically assumed that the process is plane strain, while in practice the cutting process is 3D. The same effect was noted by [4].
- A different particle size distribution might improve the results. Now a small distribution is used, but a wider PSD might give a less structured rock and a less structured damage pattern.
- A cutting thickness of three particles is quite low, especially for the fluid pressure calculation (three particles thickness is getting close to the minimum number of neighbors that are required for numerical stability).
- By using parallel bonds instead of contact bonds it might be possible to increase the post-failure strength of the rock.
- The poro-mechanical properties of the numerical rock may differ significantly with those of the real rock (e.g. compactant vs. dilative, porosity).

6 CONCLUSION

By using the combination of DEM and SP to simulated the deformation of saturated rock can help in research for cutting processes. The smoothed particle approach is shown to be useful to interpolate discrete information of individual DEM particles to a continuum

field, and again the SP can be used to relate continuum properties (e.g. pore pressure, heat conduction) to the individual DEM particles. Although the results that we have obtained match qualitatively with experiments, quantitative results require further improvement.

7 ACKNOWLEDGMENTS

This research is part of the PhD-project of EXHADERO (Excavation of Hard Deposits and Rock), which is performed with support of Delft University of Technology, Agentschap NL, Royal Dutch Shell, Royal Boskalis Westminster, Van Oord Dredging and Marine Contractors and Royal IHC. The authors are grateful for their support.

REFERENCES

- [1] Nishimatsu, Y. The mechanics of rock cutting. *International Journal of Rock Mechanics and Mining Sciences* (1972) **9**:261-270.
- [2] Detournay, E. and Atkinson, C. Influence of pore pressure on the drilling response in low-permeability shear-dilatant rocks. *International Journal of Rock Mechanics and Mining Sciences* (2000) **37-7**:1091-1101
- [3] Miedema, S.A. and Zijssling, D. Hyperbaric rock cutting. In *OMAE2012*, Rio de Janeiro, Brasil, (2012).
- [4] Rojek, J. and Labra, C. and Su, O. and Onate, E. Discrete element simulation of rock cutting. *International Journal of Rock Mechanics and Mining Sciences* (2011) **48-6**: 996-1010.
- [5] Moon, T. and Oh, J. A study of optimal rock-cutting condition for hard rock TBM using the discrete element method. *Rock Mechanics and Rock Engineering* (2011) **45**: 837-849.
- [6] Helmons, R.L.J. and Miedema, S.A. and van Rhee, C. A New Approach to Model Hyperbaric Rock Cutting Processes. In *OMAE2014*, San Francisco, California, USA, (2014).
- [7] Rojek, J. Discrete element thermomechanical modeling of rock cutting with valuation of tool wear. *Computational Particle Mechanics* (2014) **1-1**:71-84.
- [8] Huang, H. and Lecampion, B. and Detournay, E. Discrete element modeling of tool-rock interaction I: rock cutting. *International Journal for Numerical and Analytical Methods in Geomechanics* (2013) **37-13**: 1913-1929.
- [9] Lei, S. and Kaitkay, P. Distinct element modeling of rock cutting under hydrostatic pressure. *Key Engineering Materials* (2003) **250**: 110-117.

- [10] Ledgerwood, R. PFC modeling of rock cutting under high pressure conditions. In *Rock Mechanics: Meeting Society's Challenges and Demands, Proceedings of the 1st Canada-US Rock Mechanics Symposium*, Vancouver, Canada. (2007)
- [11] Mendoza Rizo, J. *Considerations for discrete element modeling of rock cutting* Diss. University of Pittsburgh, (2013).
- [12] Zijssling, D.H. Single cutter testing-a key for PDC bit development. *Society of Petroleum Engineers*, Richardson, TX, 1987.
- [13] Brace, W. and Martin, R. A test of the law of effective stress for crystalline rocks of low porosity *International Journal of Rock Mechanics and Mining Sciences* (1968) **5**: 415-426.
- [14] Swan, G. and Cook, J. and Bruce, S. and Meehan, R. Strain rate effects in Kimmeridge bay shale *Int. J. Rock Mech. Min. Sci.* (1989) **26-2**: 135-149.
- [15] Potyondy, D.O. and Cundall, P.A.A. A bonded-particle model for rock, *International journal of rock mechanics and mining sciences*, (2004), **41-8**: 1329-1364.
- [16] Coussy, P.O. *Poromechanics* John Wiley and Sons Ltd., (2004).
- [17] Chen, J.K. and Beraun, J.E. and Carney, T.C. A corrective smoothed particle method for boundary value problems in heat conduction. *International Journal for Numerical Methods in Engineering* (1999) **148-1**: 227-264.
- [18] Wendland, H. Piecewise polynomial, positive definite and compactly supported radial functions of minimal degree. *Advances in Computational Mathematics* (1995) **4**: 389-396.
- [19] Cleary, P.W. and Monaghan, J.J. Conduction modelling using Smoothed Particle Hydrodynamics. *Journal of Computational Physics* (1999) **148-1**: 227-264.
- [20] Muhammad, N. and Rogers, B.D. and Li, L. Understanding the behaviour of pulsed laser dry and wet micromachining processes by multi-phase smoothed particle hydrodynamics (SPH) modelling. *Journal of Physics D: Applied Physics* (2013) **46-9**: 095101.
- [21] Lucy, L. A numerical approach to the testing of the fission hypothesis *Astronomical Journal* (1977): 1013-1024.
- [22] Kaitkay, P. and Lei, S. Experimental study of rock cutting under external hydrostatic pressure. *Journal of Materials Processing Technology* (2005) **159-2**: 206-213.
- [23] Hoek, E. and Kaiser, P.K. and Bawden, W.F., *Support of underground excavations in hard rock*. Balkema Rotterdam.(1995)

A PORE-SCALE APPROACH OF TWO-PHASE FLOW IN GRANULAR POROUS MEDIA

C. YUAN¹, B. CHAREYRE² AND F. DARVE³

¹ Grenoble-INP, UJF, CNRS UMR 5521, 3SR Lab.
BP 53, 38041, Grenoble cedex 9, France
chao.yuan@3sr-grenoble.fr

² Grenoble-INP, UJF, CNRS UMR 5521, 3SR Lab.
BP 53, 38041, Grenoble cedex 9, France
bruno.chareyre@3sr-grenoble.fr

³ Grenoble-INP, UJF, CNRS UMR 5521, 3SR Lab.
BP 53, 38041, Grenoble cedex 9, France
felix.darve@3sr-grenoble.fr

Key words: Pore-scale Modeling, Network Models, Two-phase Flow, DEM, Drainage

Abstract. A pore-scale model is presented for simulating two-phase flow in granular materials. The solid phase is idealized as dense random packings of polydisperse spheres, generated with the discrete element method (DEM). The pore space is conceptualized as a network of pores connected by throats, which is obtained by using regular triangulation. Theoretical formulas for calculating geometrical properties and entry capillary pressure for given pores are developed by extending the Mayer and Stowe-Princen (MS-P) theory of drainage. Such relationships are employed in the network for defining local invasion criteria, so that the drainage can be represented by the replacement of W-phase when the threshold value is reached. The events of W-phase entrapment are considered during the coupling procedures. This pore-scale model is verified by comparing simulation results with experimental data of quasi-static drainage experiments in a synthetic porous medium. The simulated $P^c - S^w$ curve in primary drainage is in agreement with the experimental one.

1 INTRODUCTION

Understanding transport properties of multiphase flow in porous media is of great importance for many areas of engineering and science, such as oil recovery, agriculture irrigation and environmental restoration. Although most of these problems describe such flow process at the macro-scale, pore-scale modeling provides an important means to improve our understanding of the insight physical processes. In order to simulate large

domains, one often represent the porous medium by a pore-network, in which the void space of the medium is represented by a lattice of wide pores connected by narrow throats. By using appropriate physical laws that govern the transport and arrangement of fluids in system, network can then be made to replicate experimental measurements at the microscopic scale. The use of network modeling was pioneered by Fatt in the 1950s[9], who derived capillary pressure curves of primary drainage and computed pore size distributions in a network of interconnected pores. Since then, numerous researchers have contributed to our present understanding of multiphase flow in pore-scale with network[16, 19, 2, 14, 17, 11].

The method considered in this study is similarly devoted to the pore-scale modeling of the transport process of multiphase flow, but important differences are also noticeable in the geometrical idealization of the pore space and network modeling. These difference are mainly due to the spherical geometry of the solid particles and to the pore space decomposition technique. This study represents a first step in the direction of developing a fully coupled, computationally efficient model combining two-phase flow and deformation in porous media. In particular, we will focus our effort on the faithful approximation of the capillary pressures applied by the fluid-fluid interface on solid grains and of the arrangements of phases displacements, with the aim of incorporate these pressures and arrangements in the discrete element method (DEM) computation[7].

2 PORE-SCALE NETWORK

We propose a pore-scale network model for simulating two-phase flow in granular materials. The solid phase is idealized as dense random packings of polydisperse spheres, generated with the discrete element method (DEM)[22]. The decomposition of the pore space is obtained in three dimensions by a using Regular Triangulation method, in which the void of porous media is conceptualized as a network of pores connected by throats. A similar network was introduced recently for the so called the Pore-scale Finite Volume scheme (PFV) for one-phase flow. It is able to reflect in a natural way the deformation of the porous material system. Here it will be discussed briefly; a more detailed description can be found in [5] and [3].

Regular Triangulation (or referred as weighted Delaunay triangulation) generalizes classical Delaunay triangulation to weighted points, where weights account for the size of the spheres[8]. The dual Voronoi graph of regular triangulation is entirely contained in voids between solid spheres. Such network scheme can ideally be assigned to solve the flow path problem within the porous sample. A typical network of Regular Triangulation is shown in Fig.1. Based on this decomposition, a “pore” in 3D is bounded by four solid spheres with respective radius $R\{r_1, r_2, r_3, r_4\}$, which are arranged forming a simple tetrahedron packing order. Pore body volume is defined to be the irregular cavity within the tetrahedron(see Fig.2a). The shape of pore throat is considered to be the cross section extending within tetrahedral facets, thus the volume of throat is assumed to be 0. Specifically, the geometry of entry pore throat is a critical cross-sectional area quantified by the multiphase

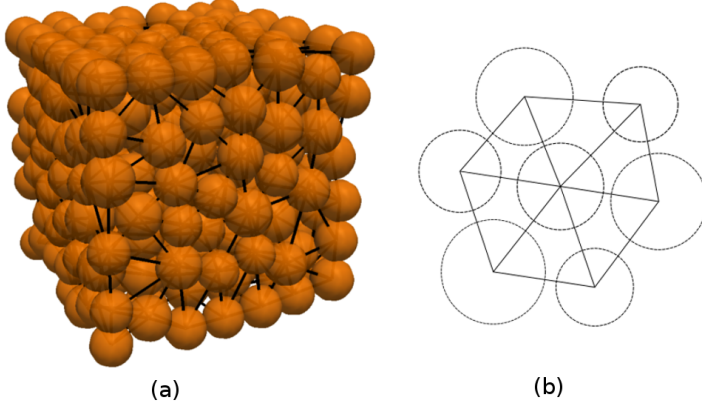


Figure 1: Definition of pore network for packing of spheres, generated by regular triangulation in 3D(a) and 2D(b).

contact lines (shown in Fig. 2b).

Since each pore is a tetrahedron, it has four neighbors, resulting in a lattice of connectivity four. Although the similar network can be found in other models [15, 10], those decomposition techniques are limited by solid particle size, in which the triangulation can only be assigned in packing of equal spheres. In this model, the network definition applies polydisperse sphere packings. The only restriction on this geometrical description is that the center of one sphere should not lie inside another sphere. As such, contact or even moderate overlaps between adjacent spheres are allowed.

3 DRAINAGE MODEL

3.1 Local rules

The phenomena of multiphase flow in porous media can be divided into quasi-static regime and dynamic ones. For two-phase flow, or referred as drainage and imbibition, in the absence of gravity, the conventional immiscible displacement can be described by two dimensionless numbers, the viscosity ratio M and the capillary number C_a ,

$$M = \frac{\mu_{inv}}{\mu}, C_a = \frac{\mu v}{\sigma} \quad (1)$$

where μ_{inv} is the viscosity of invading phase, μ is the viscosity of receding phase, v is the receding phase average or macroscopic velocity and σ is the interfacial tension between two fluid phases ([13, 12]). The limit of “quasi-static” flow is defined by C_a closed to 0.

The model we propose is aiming to simulate the primary drainage phenomenon of air-water system, or typically, more generally nonwetting-wetting (NW-W) systems. We hypothesize the drainage process is in a quasi-static regime, in which dynamic effects is in absent and the flow is dominated by capillary forces. Thus, we can neglect the effects of phases viscosity during the process. The porous within a fluid phase is uniform in every connected domain.

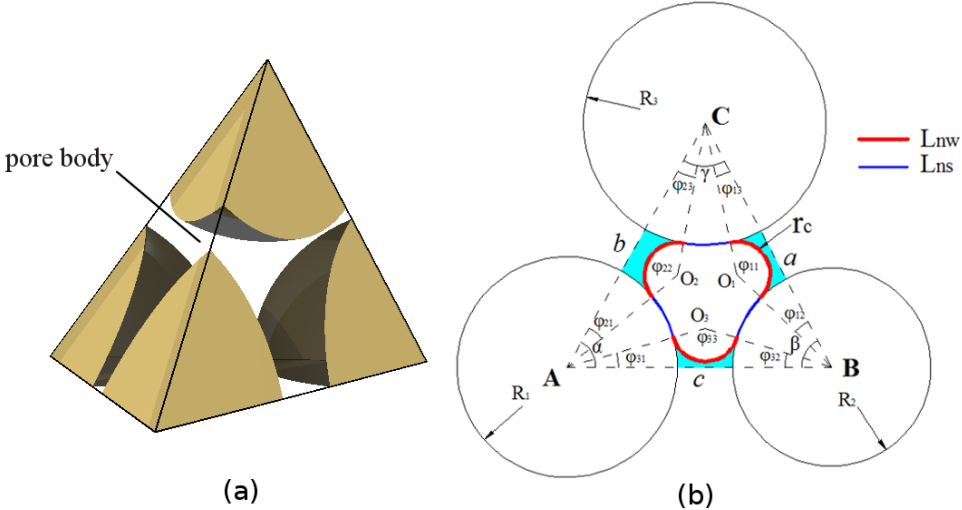


Figure 2: Pore geometry. (a) A pore defined by tetrahedral element of the finite volume decomposition. (b) Definition of pore throat geometry. r_c is the curvature of meniscus; L_{nw} is the length of contact line between nonwetting and wetting phases; L_{ns} is the length of contact line between nonwetting and solid phases.

The drainage process is controlled by the capillary pressure P^c , i.e., the pressure difference between NW-phase and W-phase. The invasion of one pore is controlled by the associated pore throats. Because the entry capillary pressure of pore body is smaller than that of pore throat, after the invasion of throat, the body is filled by NW-phase spontaneously. In principle, the receding W-phase can be present in the involved domain in the form of disconnected pendular rings left behind. The relationship between the capillary pressure and volume of liquid bridge can be found in our previous research[20, 21]. However, in this model, we assume this volume is negligible. So there is no saturation associated with corner W-phase. Thus the state of a local pore unit is in binary condition, i.e., the pore is either filled with W-phase or with NW-phase.

A relationship between capillary pressure P^c , interfacial tension, σ , and curvature of the NW-W interface, C , is given by the Young-Laplace equation,

$$P^c = \sigma C \quad (2)$$

The curvature C is fixed by the boundary conditions of NW-phase, W-phase and solid particle surface. However, in a complex pore geometry, the curvature is difficult to define. So a more clearly knowledge of connection among P^c , C and pore geometry is required.

3.2 Determination of entry capillary pressure

The drainage process is assumed in quasi-static regime, so P^c is applied into porous media to result in from one equilibrium state to another. The NW-phase invasion is locally controlled by entry capillary pressure P_e^c of pore throat. The determination of P_e^c

is based on MS-P (Mayer-Stowe-Princen) method, which follows the balance of forces for NW-W interface of pore throat [16, 18].

$$\sum F = F^p + T^\sigma = 0 \quad (3)$$

where, F^p is the capillary force acting on pore throat section domain; T^σ is the total tension force along multi-phase contact lines. The same strategy for solving P_e^c can also be found in [14] and [11]. For completeness, we recall the generic aspect of the MS-P method hereafter.

As described in the previous section, the geometry of pore throat has a mixed cross-sectional shape extending in the facet of tetrahedral pore. Fig.2b shows the schematic cross section of a local pore throat formed by solid phase surface and NW-W interface. In local drainage of pore unit, when NW-phase invades pore body, W-phase will remain in the corners of throats along the fictitious tube. The longitudinal curvature of the resulting interface inside the tube is zero[11]. The critical curvature of three menisci extending within throat section, i.e., the curvature of contact lines between NW-phase and W-phase, are equal. Let that radius be denoted by entry capillary radius r_c . Then, following Young-Laplace equation, P_e^c can be written:

$$P_e^c = P^n - P^w = \frac{\sigma^{nw}}{r_c} \quad (4)$$

in which, P^n and P^w are pressure of NW-phase and W-phase; σ^{nw} is NW-W interface tension.

According to the geometry of pore throat we defined in Fig.2b, the forces acting on interface can be written:

$$F^p = P_e^c A_n \quad (5)$$

$$T^\sigma = L_{nw}\sigma^{nw} + L_{ns}\sigma^{ns} - L_{ns}\sigma^{ws} \quad (6)$$

where, A_n is the area of pore throat section; L_{nw} and L_{ns} are total length of NW-W contact lines and NW-Solid contact lines, respectively. The multiphase interfacial tensions, σ^{ns} , σ^{ws} and σ^{nw} have a relationship with contact angle θ , defined by Young's equation,

$$\sigma^{ns} - \sigma^{ws} = \sigma^{nw} \cos \theta \quad (7)$$

Then Eq.6 will be read,

$$T^\sigma = (L_{nw} + L_{ns} \cos \theta) \sigma^{nw} \quad (8)$$

In a local pore geometry, Eq.5 and Eq.8 can be expressed by the functions of r_c (see Appendix), so the equilibrium state in Eq.3 can be implicitly described by r_c :

$$\sum F(r_c) = F^p(r_c) + T^\sigma(r_c) = 0 \quad (9)$$

Function of $\sum F(r_c)$ is monotonic; the value boundary of r_c can be obtained by following the geometry of pore throat. Therefore, r_c can be solved by numerical technique. Finally, P_e^c can be determined by Eq.4.

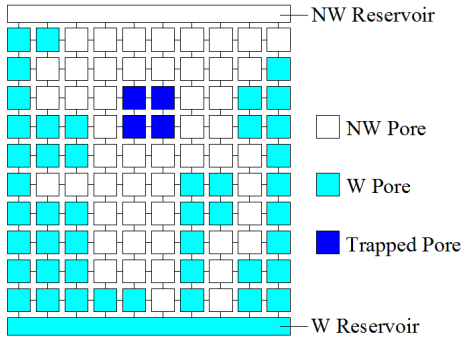


Figure 3: Demonstration of NW-phase invasion and W-phase trapping in network (in 2D mapping for clarify).

3.3 Drainage and entrapment of W-phase

Each tetrahedral pore has four neighboring pores, thus the coordination number in 3-D is four. In order to explain the invasion logic of our model, herein we project the system of 3-D network to a 2-D lattice mapping (see Fig.3). Pore bodies and throats are represented by squares and line bondings respectively. Different flags are assigned to the pores for tracking the flow path, which can dynamically record the pore states and the connectivity of different regions with the reservoirs. A search algorithm is employed for updating those states during invasion.

Initially, the porous media is saturated, and the top and bottom boundaries are connected to NW and W reservoirs, respectively. Drainage starts by increasing the capillary pressure P^c , in which we increase the local pressure of NW reservoir P^n and keep local pressure of W reservoir P^w constant. A search is executed on the pore throats which are connecting with NW reservoir, to locate the easiest entrance for invasion. The first displacement of an interface, also referred to as Haines jump, happens when local P^c surpasses the minimum threshold, e.g. the local entry capillary pressure $P_e^c(i)$ of pore unit i . After pore i being drained, a recursion algorithm check whether the interface may progress further to next adjacent pores. Such NW-phase percolation will be performed until no more pores can be drained. Then a new equilibrium is achieved, and the state flags are updated for next step of drainage. So the Haines jump events maybe not only displace the W-phase pore-by-pore, but could also involve pore clusters. Such discontinuous changes of the W-phase content can also be verified by experimental tests[6]. As the NW-phase is invading, the W-phase may form clusters of pores which are disconnected from the W reservoir. It is assumed that disconnected regions remain saturated by a fixed amount of the W-phase throughout subsequence increase of P^c . In order to identify this entrapment events, a dynamic search rule is employed during each step of drainage by assigning a Trapped Pore flag(as seen in Fig.3).

3.4 Implementation

The network has been implemented in C++[5]. The C++ library CGAL [1] is used for the regular triangulation procedure. Geometry for determination of entry capillary pressure and local drainage rules are also implemented in this model with C++. This pore-scale network is freely available in the open-source software Yade [22].

The CGAL library insures exact predicates and constructions of network. The only nontrivial operation is the computation of entry phase curvature needed to define the NW-W phase contact lines and pore throat areas to determine acting forces in Eq.9.

4 COMPARISON WITH EXPERIMENT

4.1 Numerical setup

In this section, we verify the pore-network model by comparing the simulation results with experimental data of quasi-static drainage experiment in a synthetic porous medium[6]. The medium consisted of packed glass beads, with three size classes, 0.6, 0.85 and 1.0-1.4 mm in diameter. The glass beads are contained in a column of 70 mm in length and 7 mm in diameter, with a porosity of 0.34. Drainage is carried out by pumping water out of the porous medium with a certain flow rate to maintain the system to equilibrate. A 5 mm section of the column is imaged by using X-ray micro-tomography to obtain capillary pressure-saturation ($P^c - S^w$) relationship.

In the simulation, it is unachievable to assign the pore-network (Regular Triangulation) in geometry of circular column, so we compromise by implementing model in cuboid packings. Following the experimental scene, the simulation packing is connected to the NW reservoir on the top, and to the W reservoir at the bottom.

In the research, we couldn't manage to achieve the original positioning data of glass beads in benchmark experiment[6]. But the porous medium with target PSD and porosity can be emulated by using our DEM software by the growth of spheres after randomly positioning, using the radius expansion-friction decrease (REFD) growth algorithm, a dynamic compaction method which lets one control the porosity of dense random packings [4]. So we compromise to simulate a series of repeated test on different randomly positioning packings with the consistent PSD and porosity of the experiment. In order to compare conveniently with all simulation cases, the simulation results and experiment data are both normalized to be dimensionless quantities. We represent the capillary pressure P^c by,

$$P^* = \frac{P^c \bar{D}}{\sigma^{nw}} \quad (10)$$

in which, $\bar{D} = 0.8675$ mm is the average size for PSD, $\sigma^{nw} = 7.28 \times 10^{-2}$ N/m is the W-phase (water) surface tension in contact with NW-phase (air) in 20°C. We also assume the material of solid particles is perfectly wetting, thus the contact angle θ in simulation is 0.

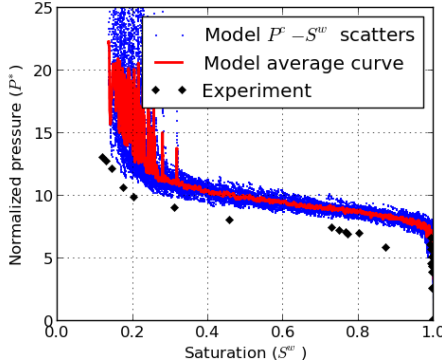


Figure 4: Comparison between simulation and experiment for primary drainage $P^c - S^w$ curves. The No. of observations of simulation is 100.

4.2 Comparison results and discussion

Using the technique described above, we compute the primary drainage process of 100 random dense packings with the same PSD and porosity. Fig.4 presents the results of these simulations, in which we gather all scattered (S^w, P^*) points of each simulation in one image. As shown in Fig.4, although all packings share the same macro-mechanics parameters, the $P^c - S^w$ curves still have a distinct variety because of micro setup, i.e., sphere positioning. Especially, the residual saturation has a great difference. We compare the average results from 100 repeating simulations with the experimental data. It shows satisfactory agreement between predicated capillary curve and obtained experimentally by Culligan et al.[6]. The unremarkable difference is mainly caused by the different specimen shapes, i.e., the simulation using cuboid column packing and experiment using circular column one. A more detailed discussion can be found in [23].

We capture one test from the series of simulation and cut a slice to observe the characteristics of invasion as shown in Fig.5. By increasing P^c , the invasion starts from the pores with larger throat, in which the entry capillary pressure is smaller (see slice-a). By comparing slices-b and c, we can find out that at certain circumstances even a slight changing in P^c can cause a notable NW-W interface movement. So such event, i.e., Haines jump, can involve a cluster of pores, causing a obvious discontinuous decrease of W-phase content. In slice-d showing the finish of test, even under a large P^c , there is no changing in saturation, which means such W-phase is entrapped by NW-phase.

5 CONCLUSIONS

A pore-scale network model of quasi-static two-phase flow in dense sphere packings has been proposed. The model can satisfactorily replicate the phenomenon of primary drainage in synthetic porous medium. The pore space is efficiently represented by means of a Regular Triangulation and the entry pore throat geometry is mathematically determined by the equilibrium of the pore system. The key methods of this model are the calculation

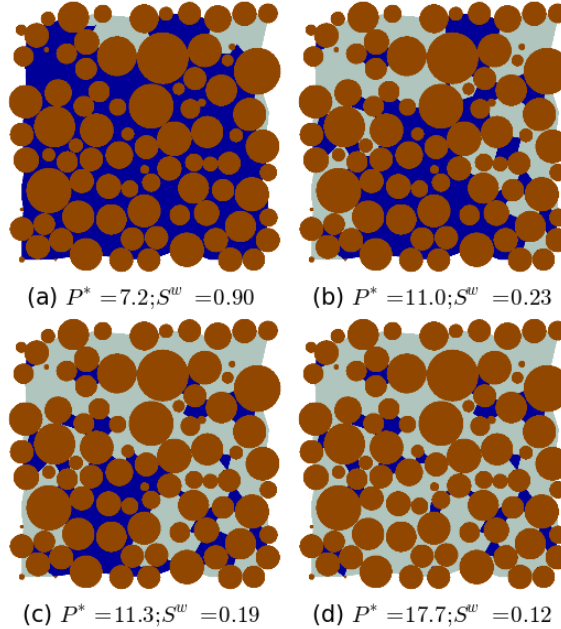


Figure 5: The process of drainage, NW-phase invade from top. Brown (gray) is solid phase, blue (black) is W-phase, and light cyan (white) is NW-phase, see color version of this figure in the HTML.

of the entry capillary pressure applied by the fluids and the prediction of the displacements of phases. Expressions of the local capillary force and tension force induced on the NW-W interface of pore throat have been derived, which are based on Young-Laplace equation and local pore geometry. The definition of entry capillary pressure is based on MS-P (Mayer-Stowe-Princen) method, which follows the balance of forces for NW-W interface in quasi-static regime. The drainage process is represented by the invasion of NW-phase when the threshold value is reached.

The key feature of the model is its capability to entrap the receding W-phase, indicating the residual saturation. A dynamic search algorithm is applied to identify whether local disconnection causes large clusters of wetting pores to get disconnected with wetting phase reservoir. For validation purpose, the model has been used for simulating primary drainage experiments carried out in a glass bead packing. The simulated curve is in agreement with experiment one, which means the capability of the pore-scale network model for simulating a real porous medium can be verified.

6 Appendix: Calculation of capillary force and tension force for a pore throat

In this appendix, we will explicitly solve the capillary force F^p and tension force T^σ acting on pore throat by using pore throat radius.

In a given pore throat (see Fig.2b), the radii and positions of neighboring solid particles are known. Let's denote a possible pore throat radius by r_c and suppose the porous media

being in perfectly wetting condition, i.e., contact angle $\theta = 0$. The contact line between NW and W phases would be tangent with solid surface.

In triangulation domain ΔABC , the area may be written as follows:

$$A_{\Delta ABC} = \frac{1}{2}bc \sin \alpha \quad (11)$$

Using laws of cosines, we can write the following equations to solve α , β and γ in ΔABC ,

$$a^2 = b^2 + c^2 - 2bc \cos \alpha \quad (12)$$

$$b^2 = a^2 + c^2 - 2ac \cos \beta \quad (13)$$

$$c^2 = a^2 + b^2 - 2ab \cos \gamma \quad (14)$$

Likewise, the areas and φ_{ij} in ΔAO_3B , ΔBO_1C and ΔAO_2C can be obtained.

To solve F^p , the total area of liquid bridge A_{lb} within pore throat section can be calculated:

$$\begin{aligned} A_{lb} = & (A_{\Delta AO_3B} - 0.5R_1^2\varphi_{31} - 0.5R_2^2\varphi_{32} - 0.5r_c^2\varphi_{33}) \\ & + (A_{\Delta BO_1C} - 0.5R_2^2\varphi_{12} - 0.5R_3^2\varphi_{13} - 0.5r_c^2\varphi_{11}) \\ & + (A_{\Delta AO_2C} - 0.5R_1^2\varphi_{21} - 0.5R_3^2\varphi_{23} - 0.5r_c^2\varphi_{22}) \end{aligned} \quad (15)$$

The area of pore throat A_n may be written as:

$$A_n = A_{\Delta ABC} - A_{lb} - 0.5R_1^2\alpha - 0.5R_2^2\beta - 0.5R_3^2\gamma \quad (16)$$

Combining Eq.4, 5 and 16, the explicit expression of F^p would be obtained.

Because of the perfectly wetting assumption, T^σ acting on multi-phase contact lines in Eq.8 can be simplified by,

$$T^\sigma(r_c) = (L_{nw} + L_{ns})\sigma^{nw} \quad (17)$$

The contact lines L_{nw} and L_{ns} can be obtained as follows:

$$L_{nw} = r_c\varphi_{11} + r_c\varphi_{22} + r_c\varphi_{33} \quad (18)$$

$$L_{ns} = R_1(\alpha - \varphi_{21} - \varphi_{31}) + R_2(\beta - \varphi_{32} - \varphi_{12}) + R_3(\gamma - \varphi_{13} - \varphi_{23}) \quad (19)$$

Combining Eq.17, 18 and 19, the explicit expression of T^σ would be calculated.

REFERENCES

- [1] J. Boissonnat, O. Devillers, S. Pion, M. Teillaud, and M. Yvinec. Triangulations in cgal. *Computational Geometry: Theory and Applications*, 22:5–19, 2002.
- [2] S. Bryant and M. Blunt. Prediction of relative permeability in simple porous media. *Phys. Rev. A*, 46:2004–2011, Aug 1992.
- [3] E. Catalano. *A pore-scale coupled hydromechanical model for biphasic granular media*. PhD thesis, Grenoble INP, 2012.
- [4] B. Chareyre, L. Briançon, and P. Villard. Theoretical versus experimental modelling of the anchorage capacity of geotextiles in trenches. *Geosynthetics International*, 9(2):97–123, 2002.
- [5] B. Chareyre, A. Cortis, E. Catalano, and E. Barthélemy. Pore-scale modeling of viscous flow and induced forces in dense sphere packings. *Transp. Porous Med.*, 92:473–493, 2012.
- [6] K. Culligan, D. Wildenschild, B. Christensen, W. Gray, M. Rivers, and A. Tompson. Interfacial area measurements for unsaturated flow through a porous medium. *Water Resour. Res.*, 40(12), 2004.
- [7] P. Cundall and O. Strack. A discrete numerical model for granular assemblies. *Geotechnique*, (29):47–65, 1979.
- [8] H. Edelsbrunner and N. R. Shah. Incremental topological flipping works for regular triangulations. *Algorithmica*, 15(6):223–241, 1996.
- [9] I. Fatt. The network model of porous media i, ii, iii. *Trans AIME*, 207:144–181, 1956.
- [10] M. Gladkikh and S. Bryant. Prediction of interfacial areas during imbibition in simple porous media. *Advances in Water Resources*, 26(6):609 – 622, 2003.
- [11] V. Joekar-Niasar, M. Prodanović, D. Wildenschild, and S. Hassanzadeh. Network model investigation of interfacial area, capillary pressure and saturation relationships in granular porous media. *Water Resour. Res.*, 46, 2010.
- [12] R. Lenormand. Liquids in porous media. *Journal of Physics: Condensed Matter*, 2(S):SA79, 1990.
- [13] R. Lenormand, E. Touboul, and C. Zarcone. Numerical models and experiments on immiscible displacements in porous media. *Journal of Fluid Mechanics*, 189:165–187, 1988.

- [14] S. Ma, G. Mason, and N. Morrow. Effect of contact angle on drainage and imbibition in regular polygonal tubes. *Colloids and Surfaces A: Physicochemical and Engineering Aspects*, 117(3):273 – 291, 1996.
- [15] G. Mason and D. Mellor. Simulation of drainage and imbibition in a random packing of equal spheres. *Journal of Colloid and Interface Science*, 176(1):214 – 225, 1995.
- [16] R. Mayer and R. Stowe. Mercury porosimetrybreakthrough pressure for penetration between packed spheres. *Journal of Colloid Science*, 20(8):893 – 911, 1965.
- [17] P. Øren, S. Bakke, and O. Arntzen. Extending predictive capabilities to network models. *SPE Journal*, 3(4):324–336, 1998.
- [18] H. Princen. Capillary phenomena in assemblies of parallel cylinders: II. capillary rise in systems with more than two cylinders. *Journal of Colloid and Interface Science*, 30(3):359 – 371, 1969.
- [19] R.Chandler, J.Koplik, K.Lerman, and J.F.Willemsen. Capillary displacement and percolation in porous media. *Journal of Fluid Mechanics*, 119:249–267, 6 1982.
- [20] L. Scholtes, B. Chareyre, F. Nicot, and F. Darve. Micromechanics of granular materials with capillary effects. *International Journal of Engineering Science*, 47(1112):1460 – 1471, 2009.
- [21] L. Scholtes, P. Hicher, F. Nicot, B. Chareyre, and F. Darve. On the capillary stress tensor in wet granular materials. *Int. J. Numer. Anal. Meth. Geomech.*, 33(10):1289–1313, 2009.
- [22] V. Smilauer, E. Catalano, B. Chareyre, S. Dorofeenko, J. Duriez, A. Gladky, J. Kozicki, C. Modenese, L. Scholtes, L. Sibille, J. Stransky, and K. Thoeni. Yade Reference Documentation. In V. Smilauer, editor, *Yade Documentation*. 2010. <http://yade-dm.org/doc/>.
- [23] C. Yuan, B. Chareyre, and F. Darve. Pore-scale simulations of drainage in granular materials: finite size effects and the representative elementary volume (submitted to journal). *Advances in Water Resources*, 2015.

AERODYNAMIC PROPERTIES OF PARTICLES IN THE GRAVITATIONAL FLOW OF A CHUTED BULK MATERIAL

I.N. LOGACHEV¹, K.I. LOGACHEV¹, O.A. AVERKOVA¹, V.A. UVAROV¹,
A.K. LOGACHEV¹

¹Belgorod State Technological University named after V.G. Shukhov
(BSTU named after V.G. Shukhov),
308012 Belgorod, Russia, Kostukova str., 46
kilogachev@mail.ru, web page: <http://www.bstu.ru>

Key words: Granular Materials, Bulk Material Transfer, Air Suction, Local Exhaust Ventilation.

Abstract. Chutes are a linking element of transportation lines used for transfers of reprocessed materials from one transporting group or equipment to another. The mode of the chuted material motion and the nature of the associated aerodynamic processes are determined by the aggregate physical and mechanical properties of the material being transferred and structural design of chutes. Structurally chutes are subdivided into prismatic, cylindrical and pyramid-shaped (bin) chutes by shape and into vertical, tip and kinked chutes by the bottom slope angle. The most common in practice are tip chutes of a prismatic or a pyramid shape. The purpose of this work was the study of particle movement of granular materials in the sloping chute. In the result of the research, we revealed the following.

1 INTRODUCTION

Chutes are a linking element of transportation lines used for transfers of reprocessed materials from one transporting group or equipment to another. Transfer groups can be technically divided into four groups (Fig.1): conveyer to conveyer loading of material; conveyer to equipment loading of material; equipment to conveyer loading of material; equipment to equipment loading of material.

In all cases the material being transferred is first supplied to the funnel adjacent to the process equipment or mounted at the belt conveyer pulley, and then the material is chuted by gravity to the lower transport conveyer or to the process equipment.

The mode of the chuted material motion and the nature of the associated aerodynamic processes are determined by the aggregate physical and mechanical properties of the material being transferred and structural design of chutes [1].

Structurally chutes are subdivided into prismatic, cylindrical and pyramid-shaped (bin) chutes by shape and into vertical, tip and kinked chutes by the bottom slope angle.

The most common in practice are tip chutes of a prismatic or a pyramid shape.

2 PECULIARITIES OF A BULK MATERIAL MOTION IN CHUTES

A granular material model selected to be used in study of the mechanical properties is a

flow of crushed granite ($\rho_1 = 2750 \text{ kg/m}^3$) which particles being 1.25-2.5 mm ($d_s = 1.56 \text{ mm}$) and 0.625-1.25 mm ($d_s = 0.74 \text{ mm}$) in size are by their shape and aerodynamic properties close to granular materials widely used in the ore preparation industry (crushed iron ore, chalk-stone, agglomerate, fines of agglomerated iron ore concentrate, etc.)

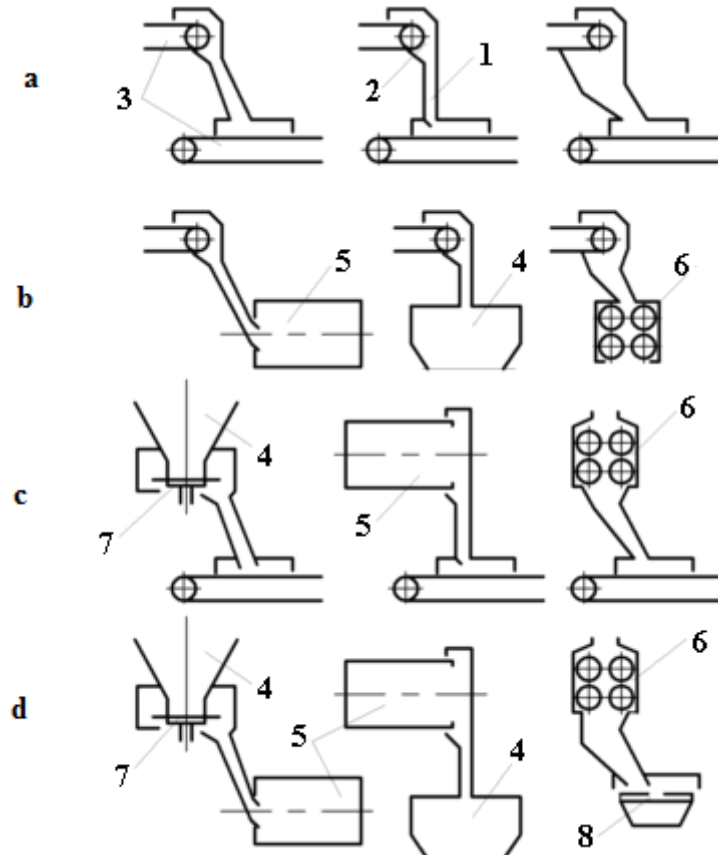


Figure 1: Conveyer to conveyer loading pattern (a), conveyer to equipment loading pattern (b), equipment to conveyer loading pattern (c) equipment to equipment loading pattern (d): 1 - chute; 2 - funnel; 3 - conveyers; 4 - bins; 5 - drums (for the material cooling, mixing etc.); 6 - crushers; 7 – disc feeds; 8 - sieve

The study of modes of crushed granite particles motion and distribution in the tip chute cross-section as well as the measurement of the particles stream velocity was conducted on a test bench the main element of which was 3 m long chute of rectangular cross-section installed at various angles to the horizontal plane. The material was supplied to the chute from the upper bin through pre-tared diaphragms (Fig. 2).

2.1 Modes of Motion

When chuting crushed granite as in the case of grain flows in inclined pipes which for the first time ever were thoroughly studied by P.N. Platonov [2], there were three modes of motion observed: constrained motion mode, intermediate mode and unconstrained motion mode.

The first mode feature is that a material is moved as an indiscrete mass with no noticeable discontinuity of contact among the particles. There is no bulk concentration gradient. The intermediate mode features local discontinuities in the indiscrete mass of particles. The third mode features the total decomposition of the indiscrete mass into separate particles or jets divorced from each other.

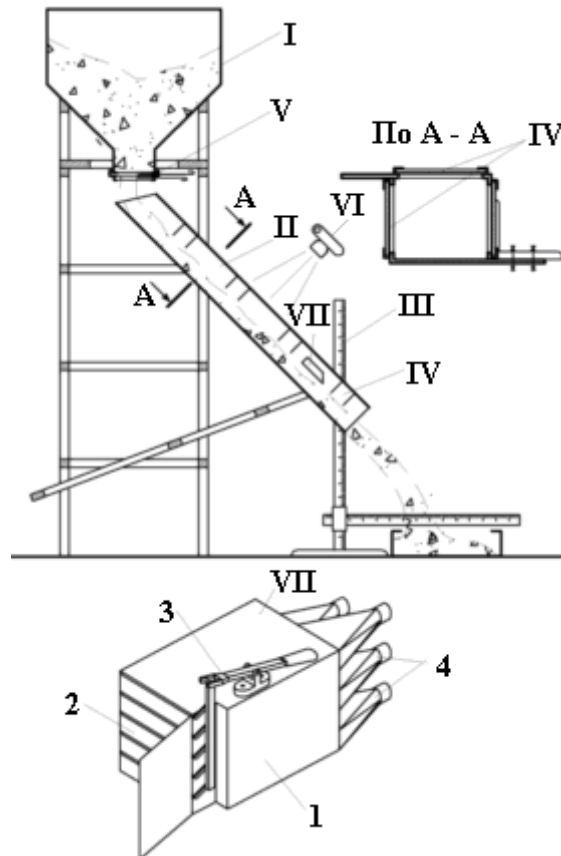


Figure 2: Diagram of the experimental arrangement for the study of physical and mechanical properties of a bulk material stream: I – upper bin; II - chute; III - coordinate spacer; IV - windows; V - diaphragm; VI – photo camera; VII - flow divider (1 – body, 2 - shelves, 3 – valve controller, 4 - bins)

Analyzing the motion of grain under high specific loads P.N. Platonov suggested using a chute inclination angle Θ as the parameter defining the nature of bulk material motion.

For instance, he noticed that the mode of constrained motion takes place if

$$\Theta_h < \Theta < \Theta_e , \quad (1)$$

while the mode of unconstrained motion occurs when

$$\Theta > \Theta_e , \quad (2)$$

where Θ_h, Θ_e are external and internal friction angles respectively.

When studying the stream of crushed granite particles in the tip chute we observed the mode of unconstrained motion at the chute inclination angles less than the internal friction angle. Therefore, an attempt was made to use the Froude number^x describing the stream kinetic movement instead of the chute inclination angle as a criterion for a change in the motion modes: $Fr = gh / v_1^2$, where h is a stream depth, m.

In order to clarify the physical meaning of this criterion for a bulk material motion in a chute under small specific loads we use the similarity of this motion with a motion of water in inclined drop structures. Let us evaluate the energy of particles in a cross section of the stream.

The flow strength of a material moving through surface ds (Fig.3) per unit time with respect to datum 0-0 drawn through the lower point of the cross-section area in question is:

$$d\Theta = \beta_1 \rho_1 v_1 \frac{v_1^2}{2} ds + \beta_1 \rho_1 v_1 g dS \cdot y \cos \Theta. \quad (3)$$

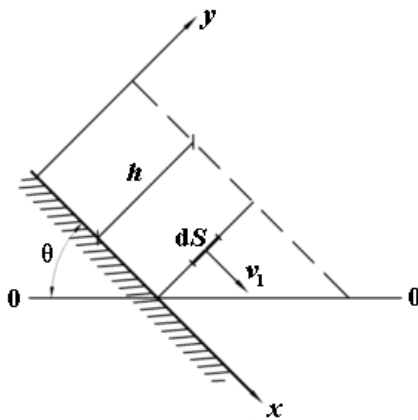


Figure 3: To the definition of a bulk material flow energy in a chute

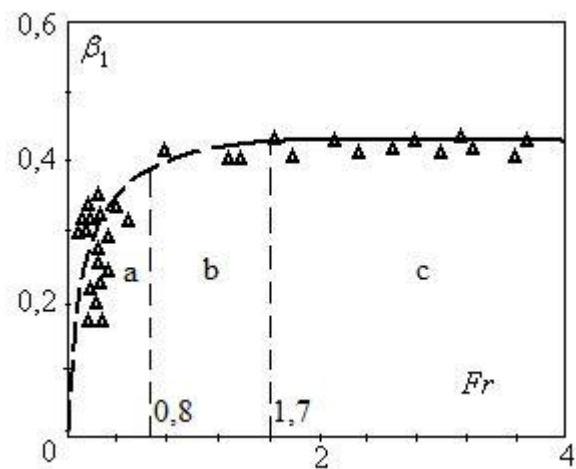


Figure 4: Dependence between a bulk concentration of crushed granite particles and Froude number

Then, the total material flow strength is

$$\Theta = \int_S \beta_1 \rho_1 v_1 \frac{v_1^2}{2} dS + \int_S \beta_1 \rho_1 g v_1 y \cos \Theta \cdot dS. \quad (4)$$

Dividing the flow strength value by the bulk material weight flow rate

$$G_T = \beta_1 \rho_1 g \bar{v}_1 \cdot S. \quad (5)$$

^x There is a good professional practice of applying this criterion in case with a bulk material flow with vertical chutes fully filled. For instance, when studying the motion of crushed graphite in a vertical pipe Z.R. Gorbis [4] defined the area of critical values of Froude numbers $1.65 < Fr_{cp} < 5$ at which one mode is changed to another.

and assuming that there is no bulk concentration gradient throughout the chute cross-section we obtain the energy per weight unit of the material passing through the cross-section area per time unit.

$$\mathcal{E} = \int_S v_i^3 dS / (2gS\bar{v}_i) + \left(\int_S yv_i dS \right) \cdot \cos \Theta / (S\bar{v}_i), \quad (6)$$

where \bar{v}_i is a medium flow speed of the bulk material motion.

For a rectangular chute, when

$$v_i = f(x, y), \quad G_T = \beta_i g \rho_i \epsilon h \bar{v}_i, \quad (7)$$

we have:

$$\mathcal{E} = \frac{\alpha_0 \bar{v}_i^2}{2g} + \frac{k_0 h}{2} \cos \Theta, \quad (8)$$

where ϵ is the chute width, m; h is a bulk material flow depth, m; α_0 is the flow momentum correction factor equal to:

$$\alpha_0 = \left(\epsilon \int_0^h v_i^3 dh \right) / \left(\epsilon \bar{v}_i^3 h \right); \quad (9)$$

k_0 is the flow potential energy correction factor equal to:

$$k_0 = \left(\epsilon \int_0^h v_i y dy \right) / \left(\bar{v}_i \epsilon \frac{h}{2} \right). \quad (10)$$

It is obvious that in case with a gradientless motion of bulk material $\alpha_0 = 1$ and $k_0 = 1$.

The extreme value of specific energy \mathcal{E} in view of (7) occurs in our case when the flow depth $h = h_{kp}$:

$$\frac{d\mathcal{E}}{dh} = -\alpha_0 G_T^2 \cdot (\rho_i g \beta_i \epsilon h_{kp})^2 / (gh_{kp}) + \frac{1}{2} k_0 \cos \Theta = 0 \quad (11)$$

or in the criterion form:

$$Fr_{kp} = \frac{2\alpha_0}{k_0 \cos \Theta}, \quad (12)$$

where Fr_{kp} is the critical Froude number value equal to

$$Fr_{kp} = gh_{kp} / \bar{v}_i^2. \quad (13)$$

When studying inclined drop structures [3] it was noticed that the critical Froude number value describes the transition of a subcritical fluid flow into a rapid flow. The latter is characterized by discontinuity of the fluid jet, especially at its free surface, and by an abundant aeration of the flow. The transition of the constrained motion of bulk material into the unconstrained motion is accompanied with a similar phenomenon: discontinuity of the jet and galloping motion of particles (saltation). Returning to condition (1) we can note that choosing Fr number as the transition criterion it is possible to consider the material flow rate in addition to the chute inclination angle. In other words, Fr criterion provides much information on a bulk material stream.

Let us refer to the experiment. The research data concerning the nature of motion of a stream of crushed granite particles in a chute is shown on Fig. 2.4.

As in the case with the vertical motion of material [4], the dependence diagram $\beta_1 = f(Fr)$ is clearly divided into three areas that correspond to three modes of stream motion. In area $Fr > 1.7$ (c), the bulk concentration is constant and virtually equal to the concentration of material at rest. This area corresponds to the mode of constrained motion. On the interval $0.8 < Fr < 1.7$ (area (b)) the bulk concentration is sharply decreased, the material motion is characterized by local discontinuities among particle groups, and there is a velocity gradient in the flow depth. This area shall be conventionally called the transition area while the numbers within this area shall be the critical numbers. At Froude numbers below 0.8 (area a) dependence $\beta_1 = f(Fr)$ is curvilinear and the lowest Froude number corresponds to the lowest bulk concentration. This area describes the mode of unconstrained motion. Note that according to equation (12) the area of the critical Froude numbers at inclination angles in question is

$$2 < Fr_{cp} \leq 2.5 , \quad (14)$$

which is in line with the experimental data.

Various modes of bulk material motion complicate the analysis of the portrait of aerodynamic interaction of bombarding particles. Particles are flown around with air and the conditions of heat and mass exchange between the material and air change.

2.2 Particle Distribution

Distribution of particles over a chute cross-section in the mode of unconstrained motion is static. The theoretical prerequisites to the study of static regularities were made by L. Boltzman [5] who studied a stream of a large quantity of small elastic balls. He demonstrated that the particles concentration and speed are determined by the F distribution function. This function pattern is defined by the differential equation:

$$\frac{\partial F}{\partial t} + u_x \frac{\partial F}{\partial x} + u_y \frac{\partial F}{\partial y} + u_z \frac{\partial F}{\partial z} + X \frac{\partial F}{\partial u_x} + Y \frac{\partial F}{\partial u_y} + Z \frac{\partial F}{\partial u_z} = \Delta_c F ,$$

where X, Y, Z are external force components; u_x, u_y, u_z are projections of particle velocities on coordinate axes; $\Delta_c F$ is the rate of change of the fixed point distribution function due to collision of particles.

However, the reduced equation in general defies solutions. There are approximate methods of solution known [6] with no regard to external forces that are determinative in our case. Therefore, in order to determine concentrations of particles we conducted experimental tests. There was a flow divider with five synchronized valves installed on the material motion path. Particles caught in the divider during a fixed interval of time were discharged from the divider bins and weighted. The experiments conducted in association with R.N. Shumilov [7] enabled to clarify the following pattern of motion of 0.625-1.25 mm crushed granite particles. A substantial part of particles is moving at the chute bottom. Moreover, the share of "bottom" particles is increased with the increase in the material flow rate (Fig. 5a) and with the decrease in the distance to the stream falling point at the chute bottom (l). This is explained by a superposition of two processes occurring in a stream of airborne particles. The first is saltation process that is a galloping motion of particles resulting from the periodic impact of particles

on the chute bottom, and the second process is the intercollision of particles.

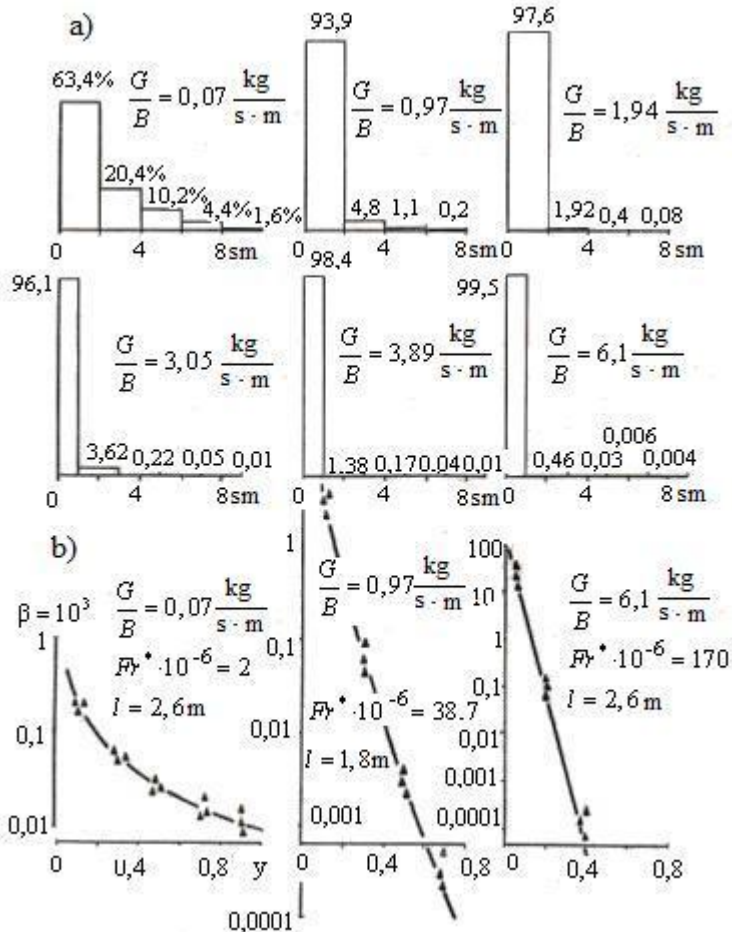


Figure 5: Distribution of crushed granite particles with the chute section height

At small flow rates or at a great distance l , when the concentration of particles is low, there is mostly a galloping motion with virtually no intercollision of particles. The transverse gradient of particles concentration is comparatively low.

At high flow rates, the concentration of particles reaches such values when intercollision of particles becomes so apparent that not every saltating particle having penetrated the thickness of particles flying above it is capable of leaving the stream. The quantity of particles drawn out from the stream and moving above it is small. The concentration gradient is high (Fig.5b)

The following quantitative characteristics were established. Distribution of particles with the channel height is clearly exponential

$$\beta = \beta_0 \exp(-ay^n), \quad (15)$$

and the bulk concentration of particles at the chute bottom is subject to the flow continuity law $\beta_0 = v_{1_H} \beta_n / v_1$, where β_n is a bulk concentration of particles at the point of particles impact on the chute bottom; v_{1_H} is the stream velocity at the chute inlet; v_1 is the stream velocity in

the section in question. Coefficients a and n depend on the material flow rate and the distance to the section in question, i.e. l . The generalized parameter taken was a modified number that

$$Fr^* = \frac{G_1 g}{v_1^3 \rho_1} , \quad (16)$$

(if $v_1 = \bar{v}_1$) is related with the Froude number as follows:

$$Fr^* = \beta_1 F_r . \quad (17)$$

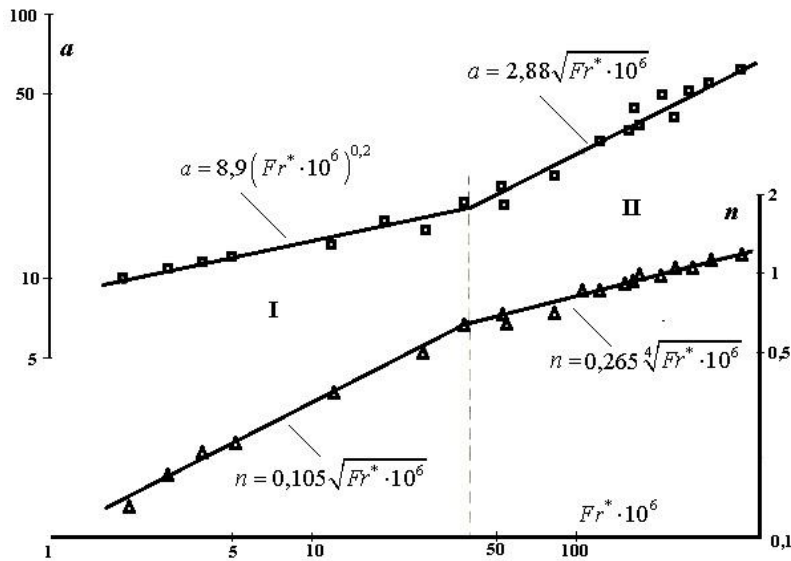


Figure 6: Variation of a and n coefficients with an increase in Fr^*

The plots of a and n coefficients against Fr^* are shown on Fig.6. Here, there are two areas clearly distinguished. The first area at $Fr^* \cdot 10^6 < 40$ which we conventionally call *the area of pseudo-uniform distribution of particles* features a saltating motion and a comparatively low bulk concentration gradient ($n = 0.1-0.67$; $n_{cp} \approx 0.3$).

The second area, that is, *the area of laminar motion*, at $Fr^* \cdot 10^6 > 40$ features a bed in which the most of colliding particles is moving and a small quantity of particles saltating above the bed. The concentration gradient is high ($n = 0.67-1.2$; $n_{cp} \approx 1$).

This peculiarity of the material motion in a tip chute makes the aerodynamic interaction pattern even more complicated and significantly changes the conditions of heat exchange.

2.3 Motion Speed

In industrial conditions a bulk material is typically chuted as a non-dense bed. Here, the effect of solid friction of particles is substituted with the effect of air drag forces, the frictional force resulting from the contact of particles with the chute walls and the gravity forces.

Unlike the gravity and air drag forces, the frictional force of particles contact is transient and very hard to determine. In order to obtain design data concerning the bulk material motion velocities we conducted experimental tests. There was the velocity of a stream of particles measured in various modes of motion in a tip chute of the experimental arrangement

(Fig.2.). The velocity value was determined using two methods: the photographic method and the ballistic one. The first method consisted in measuring of a particle travel path in a time of the photographic shutter opening. Knowing the time of exposure $\Delta\tau$ and measuring the particles path sections obtained on photographic prints it is possible to determine the mean projection of particles velocity on the chute axis: $v_i = \frac{1}{N} \sum_{i=1}^N \frac{\Delta x_i}{\Delta\tau}$.

Section projections Δx_i were determined using a ruler photographed together with airborne particles so that it was not necessary to consider the scale in photographing and photocopying. We used this method at low flow rates of bulk materials when the probability of superposition of paths could be neglected.

At low flow rates of a material the material velocity was determined using the second method which consisted in measuring the path of the material stream at the chute outlet. With the knowledge of the chute inclination angle and coordinates of the stream centerline, the material final velocity was calculated using a reduced dynamic equation of free settling particles. The centerline coordinates were determined using a coordinate spacer which horizontal axis was positioned in the material stream for more accurate measurements.

Solving the dynamic equation for a free-falling body

$$\ddot{v}_i = \bar{g} \quad (18)$$

in XOY coordinate system (Fig.7) with some transformations we obtain the following formula

$$v_k = \frac{x_k}{\cos \Theta} \sqrt{\frac{g}{2(y_k - x_k \tan \Theta)}}, \quad (19)$$

which was used to calculate the velocity of particles at the chute outlet.

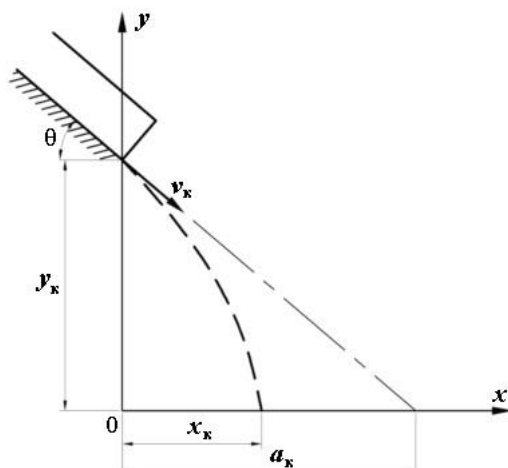


Figure 7: To the definition of a path of bulk material particles poured from a tip chute

Since dynamic equation (18) does not account for the air drag forces relation (19) gives rather excessive results.

Experimental tests showed that a chuted stream of bulk material particles is virtually uniformly accelerated (Fig.8a).

The acceleration rate is:

$$a_T = g \sin \Theta \cdot (1 - f_{mp} \operatorname{ctg} \Theta). \quad (20)$$

Conditional coefficient of the chute walls resistance to particle motion f_{mp} depends on the modes of motion (Fig. 8 b, c).

In case of the unconstrained motion this coefficient is lower than the coefficient of sliding friction f_{ck} , and the relation $\delta = f_{mp} / f_{ck}$ is: $\delta = 0.5$ for the unconstrained motion, $\delta = 1$ for the constrained motion.

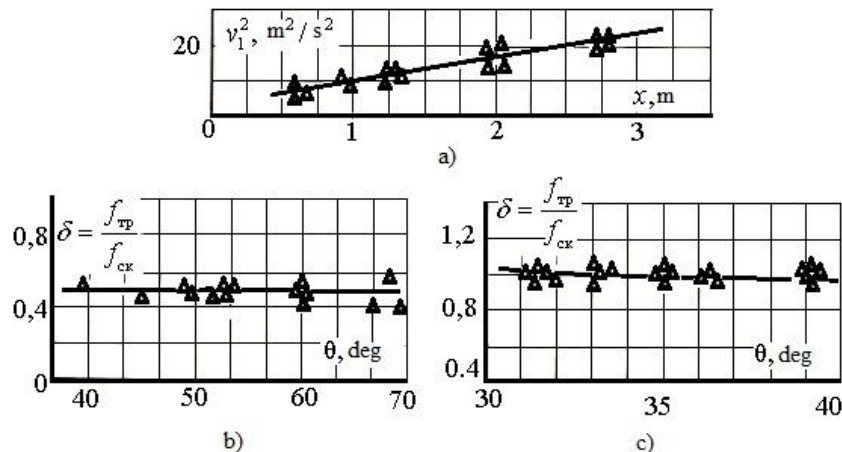


Figure 8: Chute length variation in particle velocity (a) and the relation of the friction coefficient to the chute inclination angle in case of the unconstrained (b) and constrained (c) modes of bulk material motion

Considering the fact that f_{ck} varies over a wide range and depends on many factors (physical and mechanical properties of the transferred material, chute wall surface condition, etc.) practical calculations of local exhausts of transfer groups are recommended to be based on the assumption that $f_{mp} = 0.5$.

Now, let us consider peculiarities of a material motion in kinked chutes. We will calculate the path and velocity of the conveyed bulk material stream (Fig. 9).

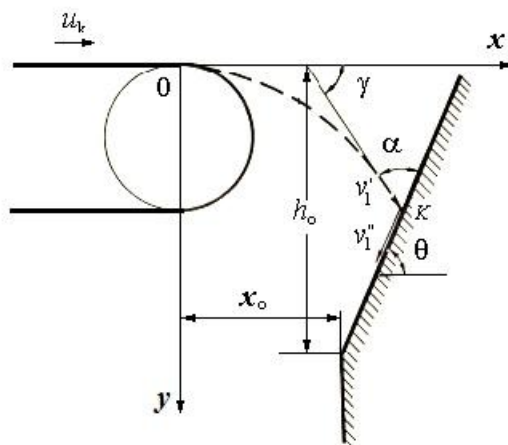


Figure 9: To the definition of the settling velocity of particles in the chute receiving funnel

To this effect we use equation (18). By integrating this equation at the initial conditions $v_1|_{t=0} = u_k$, $x|_{t=0} = 0$, $y|_{t=0} = 0$, we obtain:

a) for a jet trajectory (jet axis equation)

$$x = u_k t, \quad y = gt^2 / 2 \quad (21)$$

or

$$y = 0.5g(x/u_k)^2 ; \quad (22)$$

b) for velocity

$$v_1 = \sqrt{u_k^2 + 2gy} \quad (23)$$

or, in view of (22),

$$v_1 = \sqrt{u_k^2 + (gx/u_k)^2}, \quad (24)$$

where u_k is the forward velocity of particles that is equal to the velocity of the horizontal conveyer belt, m/s.

Based on the chute wall position and the conveyer speed the discharged material flow may either contact the belt wall or not. The first case leads to a sharp change both in the jet trajectory and speed.

The flow-to-wall contact condition as is clear from relation (22) is determined by the following inequation:

$$h_0 > (x_0/u_k)^2 g / 2. \quad (25)$$

In order to find a point of contact (K point having coordinates x_K , y_K) it is necessary to jointly solve path equation (22) and the obstacle surface equation. The latter in our case looks as follows:

$$y = h_0 - (x - x_0) \operatorname{tg} \Theta. \quad (26)$$

Then

$$x_k = \frac{u_k^2}{g} \left(\sqrt{1 + 2g \frac{h_0 + x_0 \operatorname{tg} \Theta}{(u_k \operatorname{tg} \Theta)^2}} - 1 \right) \operatorname{tg} \Theta, \quad y_k = \frac{gx_k^2}{2u_k^2}. \quad (27)$$

If the wall is vertical ($\Theta \rightarrow \pi/2$) it is easy to obtain

$$x_k = x_0, \quad y_k = g(x_0/u_k^2)/2. \quad (28)$$

As soon as the coordinates are available formula (24) can be used to determine the bulk material stream velocity at the moment of contact.

Elastic forces and the wall drag forces make the stream change its direction. An impact of a stream of irregularly-shaped particles is not an elastic impact in the strict sense, and, therefore, the angle of reflection is not equal to the angle of incidence for a stream in general or for single particles within the stream. R.L. Zenkov's studies [8] show that the angle of reflection for a bulk material stream is virtually equal to $\pi/2$. The stream velocity after the impact is: $v'_1 = Kv'_1$, where v'_1 is the stream velocity at the wall contact, m/s; v''_1 is the stream velocity after the wall contact, m/s; K is a correction factor accounting for the reduction in speed at the chute turn.

Chute turn α , deg	0	10	20	30	40	45	50	60
K	1.0	0.97	0.93	0.85	0.75	0.69	0.63	0.45

In our case angle α is an acute angle between the tangent to the jet path in the contact point and the wall plane.

The tangent slope is determined after differentiating equation (22): $\operatorname{tg} \gamma = g x_{\kappa} / u_{\kappa}^2$,

$$\text{Then it is obvious that } \alpha = 180 - \left(\Theta + \operatorname{arctg} \frac{gx_{\kappa}}{u_{\kappa}^2} \right) .$$

The further calculation of the bulk material stream velocity is based on the formula: $v_1 = \sqrt{2a_l l + (v_1'')^2}$.

In case with significant drops of a fine material (when $h > 0.5$) the medium drag force must be considered.

12 CONCLUSIONS

By its physical and mechanical properties, a bulk material stream in chutes features the unbound mode of accelerated motion with exponential distribution of particles by the channel cross-section depth which significantly changes the conditions for the dynamic intercomponent interaction, heat and mass exchange as compared to physically one-dimensional models. By the particles distribution streams may be divided into two classes: streams featuring pseudo-uniform distribution of particles when a saltating motion of particles with a light concentration gradient prevails and streams featuring a laminar motion when the most portion of particles colliding each other is at the chute bottom and a small portion of saltating particles is above the layer of particles with a heavy concentration gradient.

The reported study was partly supported by RFBR, research project No. 14-41-08005r_ofi_m.

REFERENCES

- [1] Logachev, I.N. and K.I. Logachev. *Industrial Air Quality And Ventilation: Controlling Dust Emissions*. CRC Press, Boca Raton, (2014).
- [2] Platonov, P.N.. *Motion peculiarities of grain streams. Thesis ... Doctors of Engineering M* (1969).
- [3] Chertousov, M.L.. *Hydraulics*. M; L: Gosenergoizdat, (1962).
- [4] Gorbis, Z.R. *Heat exchange of dispersed through flows*. M; L: Energiya, (1964).
- [5] Boltsman, L. *Gas theory readings*. Gostekhizdat, (1956).
- [6] Shidlovskiy, V.P. *Introduction to rarefied gas dynamics*. M: Nauka, (1965).
- [7] Logachev, I.N. and Shumilov, R.N. Movement of bulk materials in chutes // *Air ventilation and treatment: Collected papers of NIImetallurgventilyatsiya* (1970). 4: 124-129.
- [8] Zenkov, R.L. *Bulk cargo mechanics*. M: Mashgiz, (1952).

DEFORMATION OF A DROPLET IN COUETTE FLOW SUBJECT TO AN EXTERNAL ELECTRIC FIELD SIMULATED USING ISPH

NIMA TOFIGHI, MURAT OZBULUT AND MEHMET YILDIZ

Faculty of Engineering and Natural Sciences (FENS), Sabanci University,
Orhanli, Tuzla, 34956 Istanbul, Turkey
e-mails: nima@sabanciuniv.edu
ozbulut@sabanciuniv.edu
meyildiz@sabanciuniv.edu

Key words: Smoothed Particle Hydrodynamics, Droplet Deformation, Electrohydrodynamics

Abstract. Incompressible smoothed particle hydrodynamics method has been used to simulate the deformation of a two-dimensional liquid droplet suspended in Couette flow in presence of an external electric field. The results show that the elongation and orientation of the droplet is dependent on permittivity and conductivity ratios.

1 INTRODUCTION

The interaction between liquid droplets with a fluid environment is one of the most common problems arising in nature and industry, particularly in emulsification, mixing and suspensions. Simulation of the behavior of droplets in linear shear has attracted much attention where either of the droplet or the background flow may be Newtonian or non-Newtonian [1–3]. Special attention has been paid to stable rotation of droplets or their breakup. Evolution of a Newtonian droplet in non-Newtonian background fluid is studied in [1, 3] while the effects of an external electric field in a Newtonian-Newtonian case is investigated in [2].

In this study, a two-dimensional Incompressible Smoothed Particle Hydrodynamics (ISPH) scheme is used to simulate the two-phase flow of a droplet in simple shear [4]. Both fluids are modeled as leaky dielectric material [5, 6]. We have carried out numerical simulations of a Newtonian droplet in non-Newtonian background flow in a recent study [3]. Here, we extend that study to evolution of droplets in linear shear while they are exposed to an external electric field. Comparison of results with those without electric field shows that it is possible to manipulate the elongation and orientation of the droplets, as suggested by [2].

2 GOVERNING EQUATIONS

Equations governing an incompressible flow may be written as

$$\nabla \cdot \mathbf{u} = 0, \quad (1)$$

$$\rho \frac{D\mathbf{u}}{Dt} = -\nabla p + \frac{1}{Re} \nabla \cdot \boldsymbol{\tau} + \frac{1}{We} \mathbf{f}_{(s)} + \frac{1}{Ei} \mathbf{f}_{(e)}, \quad (2)$$

where \mathbf{u} is the velocity vector, p is pressure, ρ is density, t is time and $D/Dt = \partial/\partial t + \mathbf{u} \cdot \nabla$ represents the material time derivative. Here, $\boldsymbol{\tau}$ is the viscous stress tensor,

$$\boldsymbol{\tau} = \mu [\nabla \mathbf{u} + (\nabla \mathbf{u})^\dagger], \quad (3)$$

where μ denotes viscosity and superscript \dagger represents the transpose operation. Local surface tension force is expressed as an equivalent volumetric force according to the CSF method [7],

$$\mathbf{f}_{(s)} = \gamma \kappa \hat{\mathbf{n}} \delta. \quad (4)$$

Here, surface tension coefficient, γ , is taken to be constant while κ represents interface curvature, $-\nabla \cdot \hat{\mathbf{n}}$, where $\hat{\mathbf{n}}$ is unit surface normal vector. $\mathbf{f}_{(e)}$ is the electric force vector defined as [5]

$$\mathbf{f}_{(e)} = -\frac{1}{2} \mathbf{E} \cdot \mathbf{E} \nabla \varepsilon + q^v \mathbf{E}. \quad (5)$$

In the above equation, ε denotes electric permittivity, q^v is the volume charge density near the interface while \mathbf{E} is the electric field vector. Assuming small dynamic currents and neglecting magnetic induction effects, the electric field is irrotational [8] and may be represented by gradient of an electric potential ϕ , $\mathbf{E} = -\nabla \phi$. Further assumption of fast electric relaxation time compared to viscous relaxation time leads to the following relations for electric potential and charge density

$$\nabla \cdot (\sigma \nabla \phi) = 0, \quad (6)$$

$$q^v = \nabla \cdot (\varepsilon \nabla \phi), \quad (7)$$

where σ is the electrical conductivity.

Dimensionless values are formed using the following scales

$$\begin{aligned} \mathbf{x} &= \mathbf{x}^*/H, & \rho &= \rho^*/\rho_f, & \mu &= \mu^*/\mu_f & \mathbf{u} &= \mathbf{u}^*/U_w, & t &= t^*U_w/H, \\ \mathbf{E} &= \mathbf{E}^*/E_\infty, & \phi &= \phi^*/E_\infty H, & p &= p^*/\rho_f U_w^2, \\ \mathcal{R} &= \rho_d/\rho_f, & \mathcal{M} &= \mu_d/\mu_f, & \mathcal{P} &= \varepsilon_d/\varepsilon_f, & \mathcal{C} &= \sigma_d/\sigma_f, \end{aligned} \quad (8)$$

leading to Reynolds, Weber and Electroinertial numbers defined as

$$Re = \frac{\rho_f U_w H}{\mu_f}, \quad We = \frac{\rho U_w^2 H}{\gamma}, \quad Ei = \frac{\rho_f U_w^2}{\varepsilon_f E_\infty^2}. \quad (9)$$

Here E_∞ is the undisturbed electric field intensity, H is the distance between electrodes, U_w is the wall velocity (figure 1-a). An asterisk marks dimensional variables whereas subscripts \square_d and \square_f denote droplet and background fluid phases, respectively.

To distinguish between different phases, a color function \hat{c} is defined such that it assumes a value of zero for one phase and unity for the other. The color function is then smoothed out across the phase boundaries as

$$c_i = \sum_{j=1}^{J_n} \frac{\hat{c}_j W_{ij}}{\psi_i}, \quad (10)$$

to ensure smooth transition between the properties of each phase when used for their interpolation. Here, $\psi_i = \sum_{j=1}^{J_n} W_{ij}$, is the number density of SPH particle i , calculated as the sum of interpolation kernel of neighboring particles i and j over all neighbors of particle i , J_n . Interpolation kernel, $W(r_{ij}, h)$, is a function of the magnitude of distance vector, $\mathbf{r}_{ij} = \mathbf{r}_i - \mathbf{r}_j$, between particle of interest i and its neighboring particles j and h , the smoothing length [9, 10]. Interpolation of phase properties is carried out using Weighted Harmonic Mean (WHM),

$$\frac{1}{\chi_i} = \frac{c_i}{\chi_d} + \frac{1 - c_i}{\chi_f}, \quad (11)$$

where χ may denote density, viscosity, permittivity or conductivity [11]. The smoothed color function is also utilized to evaluate $\delta \simeq |\nabla c|$, $\kappa = -\nabla \cdot \hat{\mathbf{n}}$ and $\hat{\mathbf{n}} = \nabla c / |\nabla c|$ in (4). In this formulation, a constraint has to be enforced to avoid possible erroneous normals [12]. In this study, only gradient values exceeding a certain threshold, $|\nabla c_i| \simeq \beta/h$, are used in surface tension force calculations. A β value of 0.08 has been found to provide accurate results without removing too much detail [4].

A predictor-corrector scheme is employed to advance the governing equations of flow in time using a first-order Euler approach with variable timestep according to Courant-Friedrichs-Lowy condition, $\Delta t = C_{CFL}h/u_{max}$, where u_{max} is the largest particle velocity magnitude and C_{CFL} is taken to be equal to 0.25. In predictor step all the variables are advanced to their intermediate form using following relations,

$$\mathbf{r}_i^* = \mathbf{r}_i^{(n)} + \mathbf{u}_i^{(n)} \Delta t + \boldsymbol{\delta} \mathbf{r}_i^{(n)}, \quad (12)$$

$$\mathbf{u}_i^* = \mathbf{u}_i^{(n)} + \frac{1}{\rho_i^{(n)}} \left(\frac{1}{Re} \nabla \cdot \boldsymbol{\tau}_i + \frac{1}{We} \mathbf{f}_{(s)i} + \frac{1}{Ei} \mathbf{f}_{(e)i} \right)^{(n)} \Delta t, \quad (13)$$

$$\psi_i^* = \psi_i^{(n)} - \Delta t \psi_i^{(n)} (\nabla \cdot \mathbf{u}_i^*), \quad (14)$$

where starred variables represent intermediate values and superscript (n) denotes values at the n th time step. Artificial particle displacement vector in (12), $\boldsymbol{\delta} \mathbf{r}_i$, is defined as stated in [3] where a constant value of 0.06 is used.

Using intermediate values, pressure at the next time step is found by solving the Poisson equation which is then followed by corrections in position and velocity of the particles, completing the temporal transition.

$$\nabla \cdot \left(\frac{1}{\rho_i^*} \nabla p_i^{(n+1)} \right) = \frac{\nabla \cdot \mathbf{u}_i^*}{\Delta t}, \quad (15)$$

$$\mathbf{u}_i^{(n+1)} = \mathbf{u}_i^* - \frac{1}{\rho_i^*} \nabla p_i^{(n+1)} \Delta t, \quad (16)$$

$$\mathbf{r}_i^{(n+1)} = \mathbf{r}_i^{(n)} + \frac{1}{2} \left(\mathbf{u}_i^{(n)} + \mathbf{u}_i^{(n+1)} \right) \Delta t + \boldsymbol{\delta} \mathbf{r}_i^{(n)}. \quad (17)$$

Boundary conditions are enforced through MBT method described in [13] while first derivative and Laplace operator are approximated through following expressions

$$\frac{\partial f_i^m}{\partial x_i^k} a_i^{kl} = \sum_j \frac{1}{\psi_j} (f_j^m - f_i^m) \frac{\partial W_{ij}}{\partial x_i^l}, \quad (18)$$

$$\frac{\partial^2 f_i^m}{\partial x_i^k \partial x_i^l} a_i^{ml} = 8 \sum_j \frac{1}{\psi_j} (f_i^m - f_j^m) \frac{r_{ij}^m}{r_{ij}^2} \frac{\partial W_{ij}}{\partial x_i^l}. \quad (19)$$

Here, $a_i^{kl} = \sum_j \frac{r_{ij}^k}{\psi_j} \frac{\partial W_{ij}}{\partial x_i^l}$ is a corrective second rank tensor that eliminates particle inconsistencies. Left hand side of (15) is discretized as

$$\frac{\partial^2 f_i^m}{\partial x_i^k \partial x_i^l} (2 + a_i^{kk}) = 8 \sum_j \frac{1}{\psi_j} (f_i^m - f_j^m) \frac{r_{ij}^k}{r_{ij}^2} \frac{\partial W_{ij}}{\partial x_i^k}. \quad (20)$$

3 RESULTS

In this study, deformation of a neutrally buoyant droplet suspended in plane Couette flow is simulated. The droplet is expected to elongate in the direction of flow, possibly reaching an equilibrium dictated by the balance between the forces acting on the interface [3]. A schematic of this case is provided in figure 1-a. Computational domain consists of an 8×32 rectangle discretized by 39973 particles initially arranged in a Cartesian grid for background fluid and concentric circles for the droplet [14]. A close-up view of the particle arrangement in the vicinity of the droplet is provided in figure 1-b. Initial droplet radius is half of the distance between moving walls, $H/2$, while the droplet is placed at the center of the channel. Top and bottom walls abide by the no-slip condition and are moving in opposite directions at a velocity of $U_w/2$ while applying a potential difference of $\Delta\phi = E_\infty H$. Periodic boundary condition is imposed in streamwise direction. Particles inside the droplet are at rest while background fluid particles are initialized with undisturbed Couette flow velocity. Reynolds, Weber and Electroinertial numbers are set to 1, 0.2 and 50, respectively. The background and droplet fluids have identical density

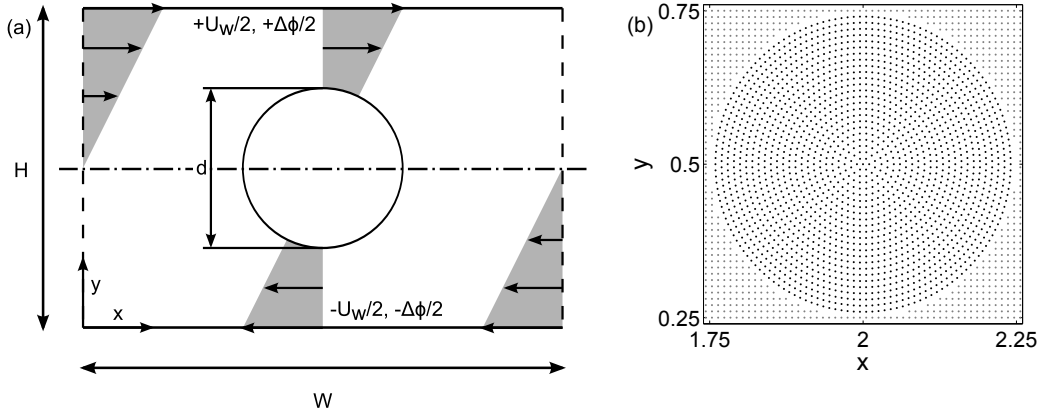


Figure 1: (a) Schematic of the test case. (b) Closeup view of initial particle distribution in the vicinity of the droplet. Black points denote droplet particles whereas gray points are background fluid particles.

and viscosity while permittivity and conductivity ratios are varied according to table 1. Equal permittivity and conductivity ratios are not considered here.

Figure 2 provides droplet deformation factor defined as

$$D_f = \frac{L_{max} - L_{min}}{L_{max} + L_{min}}, \quad (21)$$

where L_{max} and L_{min} denote major and minor axis of an approximated ellipsoid [15]. Denoting the test cases in pairs of permittivity and conductivity ratios as $(\mathcal{P}, \mathcal{C})$, cases $(5.0, 0.2)$ and $(5.0, 0.5)$ do not reach a steady profile during the simulation time. Observing the deformation rate of case $(5.0, 0.2)$, we predict that the droplet will eventually breakup, given sufficient simulation time. Averaged values of D_f are provided in table 1 for better comparison. At constant \mathcal{P} , increasing \mathcal{C} results in larger deformation factors for $\mathcal{P} < 1$ while this trend is reversed for $\mathcal{P} > 1$. Similarly, at constant \mathcal{C} , a larger \mathcal{P} results in larger D_f for $\mathcal{C} < 1$ while increasing \mathcal{P} for $\mathcal{C} > 1$ reduces the deformation factor.

Figure 3 provides a better representation of the interface profile at the end of the simulations. Smoothed color function is used to define the droplet interface by plotting its contour at 0.5 level. The droplets are more slender where deformation factor is larger (refer to table 1). It is notable that the angle between major axis of the elliptic droplet and streamwise direction becomes smaller with increasing conductivity ratio. The shape of case $(5.0, 0.2)$ is immediately distinguishable due to its large deformation. As $f_{(e)}$ increases with \mathcal{P} , the extreme elongation happens as a result of suppression of surface tension forces by electrical forces. It is also notable that the droplet has lost its elliptic shape at this simulation time.

Figure 4 provides snapshots of interface in red, streamlines in blue and electric field lines in black for the case without electric field, case with largest elongation $(5.0, 0.2)$ and two other cases. The last two cases, $(0.2, 2.0)$ and $(2.0, 0.2)$, are chosen based on their

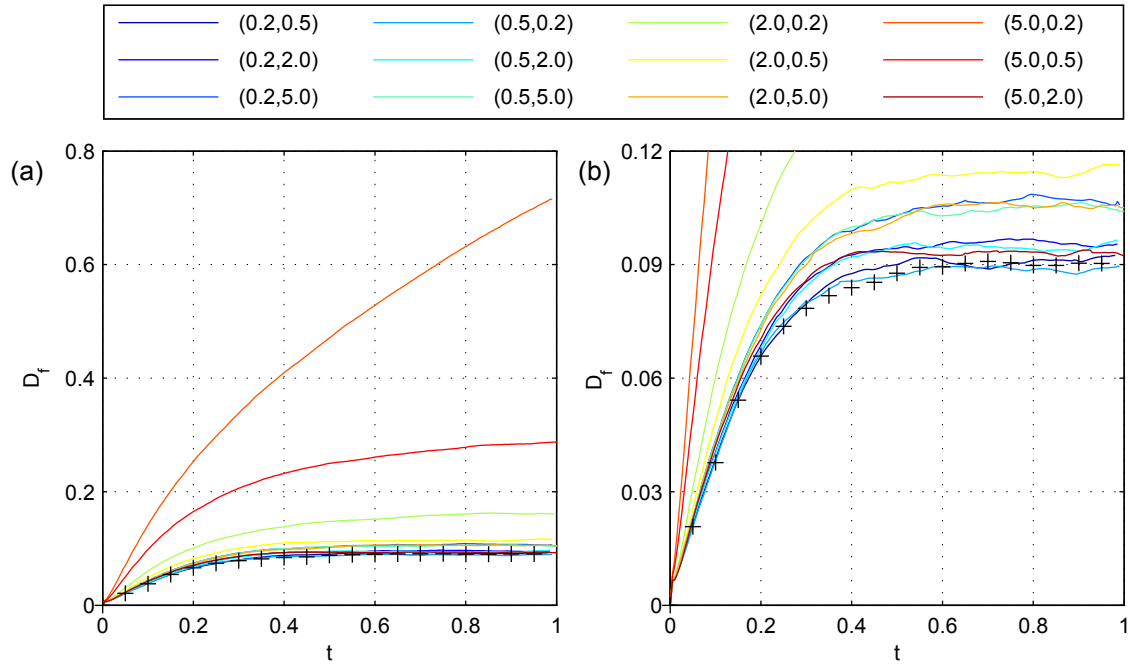


Figure 2: Comparison of the deformation factor for all cases (a) and a close up view of the cases with steady shape (b). Black plus signs denote the case without electric field.

Table 1: Deformation factor for different permittivity and conductivity ratios. Cases with bold numbers did not reach a steady profile during the simulation. Deformation factor without electric field is $D_f = 0.09$.

\mathcal{P}	0.2	0.5	2	5	
\mathcal{C}	0.2	-	0.089	0.162	0.675
	0.5	0.091	-	0.115	0.284
	2	0.096	0.094	-	0.093
	5	0.107	0.105	0.105	-

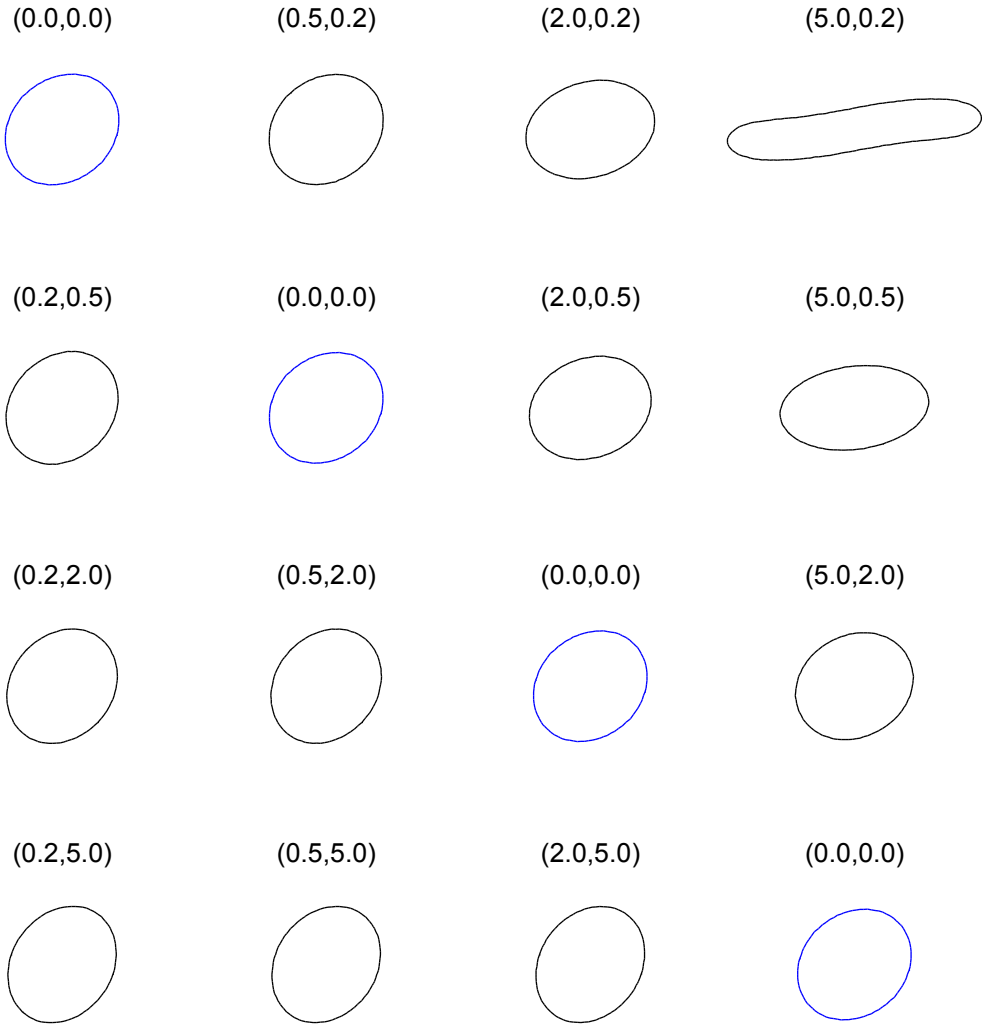


Figure 3: Interface profiles of droplet at the end of the simulation. Permittivity and conductivity pairs $(\mathcal{P}, \mathcal{C})$ are shown above each case. The case with no electric field, shown in blue, is repeated in each row marked as $(0.0, 0.0)$.

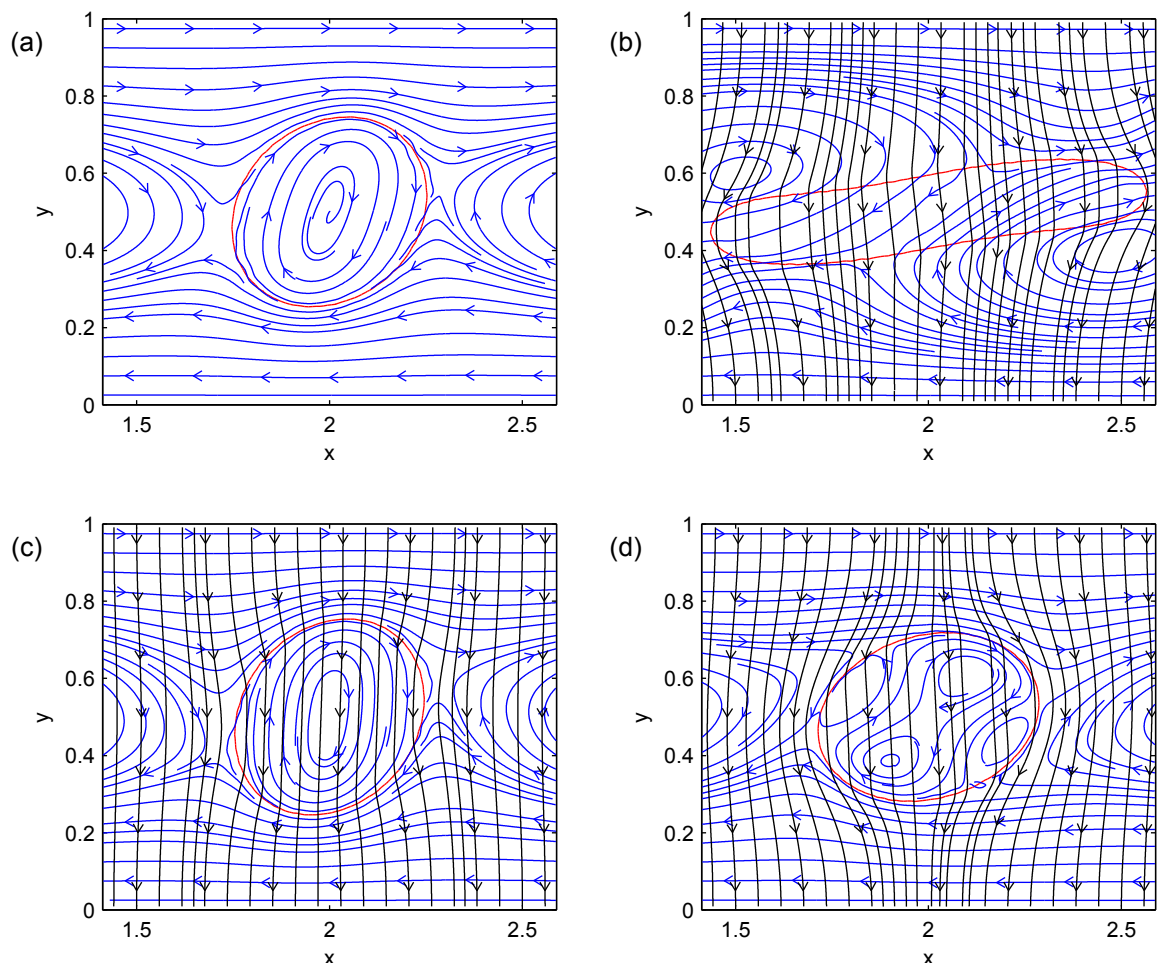


Figure 4: Snapshots of droplet interface in red, streamlines in blue and electric field lines in black at the end of simulation; (a) without electric field; (b) (5.0, 0.2); (c) (0.2, 2.0); (d) (2.0, 0.2).

final orientation when compared to the case without electric field. Case (0.2, 2.0) is more aligned to normal direction whereas (2.0, 0.2) is more aligned to streamwise direction. Case without electric field shows a circulation region inside droplet while two types of streamlines in background fluid are observed. The first type traverses the whole domain while the second type approaches the droplet and then reverses its direction. Case (5.0, 0.2) shows no circulation inside the droplet while two large vortices are observed near trailing edges of the droplet. These vortices encompass both droplet and background fluid and rotate in the direction of imposed shear. Since the droplet is less conductive than the surrounding fluid in this case, the electric field lines diverge from the surface of the droplet. The streamlines in case (0.2, 2.0) resemble those of the case without electric field in general. Electric field lines converge toward the droplet as it is more conductive than surrounding fluid in this case. The streamlines in case (2.0, 0.2) start to show a different pattern than that of the case with no electric field. A pattern similar to the case without shear, that is four vortical structure rotating alternatively in clockwise and counterclockwise rotations [8], is observed here. The vortices rotating in the direction of background flow's vorticity are paired, separating the vortices countering the imposed shear. With a conductivity ratio of $C = 0.2$, the droplet is less conductive than surrounding fluid and the electric field lines diverge from the droplet surface.

4 CONCLUSION

In this paper, we use ISPH to simulate the deformation of a neutrally buoyant droplet in planar Couette flow under external electric field. The deformation factor is compared for different permittivity and conductivity ratios. It is seen that it is possible to overcome the surface tension forces at suitable permittivity and conductivity ratios, resulting in droplet elongations that are likely to end in breakup. The effects of permittivity and conductivity ratios on streamline patterns are also studied. It is seen that the circulation patterns may change for cases with a preference for aligning with the streamwise direction, resulting in patterns resembling those observed in the absence of imposed shear.

5 ACKNOWLEDGMENTS

The authors gratefully acknowledge financial support provided by the Scientific and Technological Research Council of Turkey (TUBITAK) for project number 112M721.

REFERENCES

- [1] Chinyoka, T., Renardy, Y., Renardy, A. and Khismatullin, D. Two-dimensional study of drop deformation under simple shear for Oldroyd-B liquids. *J. Non-Newton. Fluid Mech.* (2005) **130**:45-56.
- [2] Maehlmann, S. and Papageorgiou, D.T. Numerical study of electric field effects on the deformation of two-dimensional liquid drops in simple shear flow at arbitrary Reynolds number. *J. Fluid Mech.* (2009) **626**:367-393.

- [3] Zainali, A., Tofighi, N., Shadloo, M.S. and Yildiz, M. Numerical investigation of Newtonian and non-Newtonian multiphase flows using ISPH method. *Comput. Meth. Appl. Mech. Eng.* (2013) **254**:99–113.
- [4] Tofighi, N. and Yildiz, M. Numerical simulation of single droplet dynamics in three-phase flows using ISPH. *Comput. Math. Appl.* (2013) **66**:525–536.
- [5] Saville, D. Electrohydrodynamics: The Taylor-Melcher leaky dielectric model. *Annu. Rev. Fluid Mech.* (1997) **29**:27–64.
- [6] Shadloo, M., Rahmat, A. and Yildiz, M. A smoothed particle hydrodynamics study on the electrohydrodynamic deformation of a droplet suspended in a neutrally buoyant Newtonian fluid. *Comput. Mech.* (2013) 1-15.
- [7] Brackbill, J., Kothe, D. and Zemach, C. A continuum method for modeling surface-tension. *J. Comput. Phys.* (1992) **100**:335–354.
- [8] Hua, J., Lim, L. and Wang, C. Numerical simulation of deformation/motion of a drop suspended in viscous liquids under influence of steady electric fields. *Phys. Fluids* (2008) **20**:113302.
- [9] Monaghan, J.J. and Lattanzio, J.C. A refined particle method for astrophysical problems. *Astron. Astrophys.* (1985) **149**:135–143.
- [10] Monaghan, J.J. and Kocharyan, A. SPH simulation of multiphase flow. *Comput. Phys. Commun.* (1995) **87**:225–235.
- [11] Tomar, G., Gerlach, D., Biswas, G., Alleborn, N., Sharma, A., Durst, F., Welch, S.W.J. and Delgado, A. Two-phase electrohydrodynamic simulations using a volume-of-fluid approach. *J. Comput. Phys.* (2007) **227**:1267–1285.
- [12] Morris, J.P. Simulating surface tension with smoothed particle hydrodynamics. *Int. J. Numer. Methods Fluids* (2000) **33**:333–353.
- [13] Yildiz, M., Rook, R.A. and Suleman, A. SPH with the multiple boundary tangent method. *Int. J. Numer. Methods Eng.* (2009) **77**:1416–1438.
- [14] Tofighi, N., Ozbulut, M., Rahmat, A., Feng, J.J. and Yildiz, M. An incompressible smoothed particle hydrodynamics method for the motion of rigid bodies in fluids. *J. Comp. Phys.* (2015) **297**:207 - 220.
- [15] Taylor, G. Studies in electrohydrodynamics I. Circulation produced in a drop by an electric field. *Proc. R. Soc. Lon. Ser. A* (1966) **291**:159–166.

NUMERICAL SIMULATION OF WATER AND WATER EMULSION DROPLETS EVAPORATION IN FLAMES WITH DIFFERENT TEMPERATURES

PAVEL A. STRIZHAK, ROMAN S. VOLKOV AND ALENA O. ZHDANOVA

National Research Tomsk Polytechnic University
Lenina Avenue, 30, 634050, Tomsk, Russia
E-mail pavelspa@tpu.ru

Key words: Water Droplet, Evaporation, High-Temperature Gas Environment.

Abstract. The models of heat and mass transfer and phase transition for “water droplet – flame” system have been developed using non-stationary nonlinear partial differential equations. The system of differential equations was solved by the finite-difference method. The locally one-dimensional method was used to solve the difference analogous of differential equations. One-dimensional differential equations were solved using an implicit four-point difference scheme. Nonlinear equations were solved by the iteration method. The evaporation rates of water droplets (with sizes from 0.05 mm to 5 mm) in the flame zone (at the temperatures from 500 K to 1200 K) were determined. Theoretical analysis established essentially nonlinear (close to exponential) form of dependence of the water droplet evaporation rate on the temperature of the external gas area and the temperature of a droplet surface. In particular, the water droplet evaporation rate varies from 0.25 to 0.29 kg/(m²s), when the temperature of external gas area is about 1100 K. On the other hand, the water droplet evaporation rate does not exceed 0.01 kg/(m²s) when the temperature of external gas area is about 350 K. Besides, it has been found out that droplets warm up at different rates depending on their initial temperature and velocity. As a result, the integral characteristics of droplet evaporation can increase substantially, when droplets move through the external gas area at the same temperature. We performed a similar investigation of droplet streams with droplet concentration 0.001–0.005 m³ in 1 m³ of gas area (typical parameters for modern spray extinguishing systems).

1 INTRODUCTION

The study of sprayed water phase transitions during the motion in high-temperature gas environment has been getting more and more attention in recent years [1, 2]. The results of these studies have a large number of practical applications. For example, they can be used in the technologies of polydisperse extinguishing, two-phase gas-vapor coolant formation with the specified parameters, wastewater combustion neutralization, and others [3-5]. Currently, new optical methods have emerged, that enable visualization and video recording of heat and mass transfer fast processes during the evaporation of fine liquid flow in high-temperature gases. Thus, it became possible to develop experimental methods for studying these processes. However, it is still of topical interest to develop numerical models for calculating

the parameters of the system “sprayed liquid – high-temperature gas environment” taking into account the experimental characteristics of liquid spray motion and evaporation (the deformation and entrainment of droplets, the evaporation rate, etc.).

The aim of this work is to develop the numerical model of heat and mass transfer of water droplets during their motion in high-temperature gas environment.

1 PROBLEM STATEMENT

In formulating the problem, it was considered that a water droplet moved (in free fall) in high-temperature gas environment (Figure 1). Under the conditions of phase transition, water vapor was blown into the near-wall part of the droplet and mixed with combustion products. It was believed that mass transfer was implemented by diffusion and convection mechanisms in the external environment. It was assumed that droplet size decreased under the conditions of intensive evaporation. After some time, the droplet evaporated completely. In formulating the problem of heat and mass transfer, a cylindrical droplet (elongated in the direction of its motion) was examined (Figure 1). It was considered that gas environment was binary (“combustion products – water vapor”). It was also assumed that the thermal characteristics of reacting substances do not depend on the temperature.

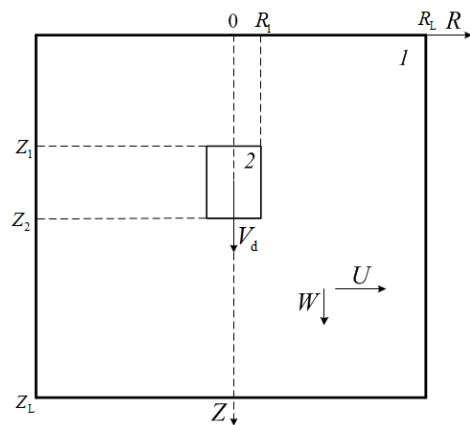


Figure 1: A diagram of the solution area of the problem of heat and mass transfer: 1 – high-temperature gas mixture, 2 – water droplet

1 MATHEMATICAL MODEL AND SOLUTION METHODS

The system of non-stationary nonlinear partial differential equations is derived from the physical model that has been formulated taking into account convective flows in a mixture of combustion products and water vapor. The system is as follows ($0 < \tau < \tau_d$) [6]:

$$0 < R < R_L, 0 < Z < Z_1, Z_2 < Z < Z_L; R_1 < R < R_L, Z_1 < Z < Z_2$$

Poisson's equation:

$$\frac{\partial^2 \Psi}{\partial R^2} - \frac{1}{R} \frac{\partial \Psi}{\partial R} + \frac{\partial^2 \Psi}{\partial Z^2} = -R\Omega \quad (1)$$

vorticity equation:

$$\frac{1}{Sh} \frac{\partial \Omega}{\partial \tau} + U \frac{\partial \Omega}{\partial R} + V \frac{\partial \Omega}{\partial Z} - U \frac{\Omega}{R} = \frac{1}{Re_1} \left[\frac{\partial^2 \Omega}{\partial R^2} + \frac{1}{R} \frac{\partial \Omega}{\partial R} + \frac{\partial^2 \Omega}{\partial Z^2} \frac{\Omega}{R^2} \right] + \frac{\partial \Theta_1}{\partial R} \quad (2)$$

energy equation for the mixture of water vapor and combustion products:

$$\frac{1}{Sh} \frac{\partial \Theta_1}{\partial \tau} + U \frac{\partial \Theta_1}{\partial R} + V \frac{\partial \Theta_1}{\partial Z} = \frac{1}{Re_1 Pr_1} \left[\frac{\partial^2 \Theta_1}{\partial R^2} + \frac{1}{R} \frac{\partial \Theta_1}{\partial R} + \frac{\partial^2 \Theta_1}{\partial Z^2} \right] \quad (3)$$

water vapor diffusion equation:

$$\frac{1}{Sh} \frac{\partial \gamma_w}{\partial \tau} + U \frac{\partial \gamma_w}{\partial R} + V \frac{\partial \gamma_w}{\partial Z} = \frac{1}{Re_1 Sc_1} \left[\frac{\partial^2 \gamma_w}{\partial R^2} + \frac{1}{R} \frac{\partial \gamma_w}{\partial R} + \frac{\partial^2 \gamma_w}{\partial Z^2} \right] \quad (4)$$

balance equation:

$$\gamma_w + \gamma_f = 1 \quad (5)$$

$$0 < R < R_1, Z_1 < Z < Z_2$$

heat equation for the droplet:

$$\frac{1}{Fo_2} \frac{\partial \Theta_2}{\partial \tau} = \frac{\partial^2 \Theta_2}{\partial R^2} + \frac{1}{R} \frac{\partial \Theta_2}{\partial R} + \frac{\partial^2 \Theta_2}{\partial Z^2} \quad (6)$$

$$Sh = \frac{v_m t_m}{z_m}, \quad Re_1 = \frac{V_m z_m}{v_1}, \quad Pr_1 = \frac{v_1 \rho_1 C_1}{\lambda_1}, \quad Sc_1 = \frac{v_1}{D_1}, \quad Fo_2 = \frac{\lambda_2 t_m}{\rho_2 C_2 z_m^2}.$$

Initial ($\tau=0$) conditions (Figure 1): $\Theta=\Theta_0$ at $0 < R < R_1, Z_1 < Z < Z_2$; $\Theta=\Theta_f, \gamma_f=1, \gamma_w=0, \Psi=0, \Omega=0$ at $0 < R < R_L, 0 < Z < Z_1, Z_2 < Z < Z_L; R_1 < R < R_L, Z_1 < Z < Z_2$.

Boundary ($0 < \tau < \tau_d$) conditions (Figure 1): at the interface “liquid – gas” ($R=R_1, Z_1 < Z < Z_2; Z=Z_1, Z=Z_2, 0 < R < R_1$) – IV type of boundary conditions was assumed for energy equations taken into account vaporization, II type of boundary conditions was specified for energy equations taken into account water vapor blowing; at the external borders ($R=0, R=R_L, 0 < Z < Z_L; Z=0, Z=Z_L, 0 < R < R_L$) – the condition of zero gradients of the respective functions was assumed for all equations.

Boundary conditions were specified to emphasize the effect of water vapor blowing on the conditions of heat transfer on all droplet faces for energy equations:

$$R=R_1, Z_1 < Z < Z_2: \frac{\partial \Theta_2}{\partial R} = \frac{\lambda_1}{\lambda_2} \frac{\partial \Theta_1}{\partial R} - Q_e W_e \frac{z_m}{\Delta T \lambda_2} - \rho_3 C_3 v_e (\Theta_{3s} - \Theta_{2s}) \frac{z_m}{\lambda_2},$$

$$Z=Z_1, Z=Z_2, 0 < R < R_1, \frac{\partial \Theta_2}{\partial Z} = \frac{\lambda_1}{\lambda_2} \frac{\partial \Theta_1}{\partial Z} - Q_e W_e \frac{z_m}{\Delta T \lambda_2} - \rho_3 C_3 v_e (\Theta_{3s} - \Theta_{2s}) \frac{z_m}{\lambda_2}.$$

The motion equation of the droplet under the conditions of vaporization taking into account the forces of resistance and gravity:

$$\frac{dv_d}{dt} = \frac{3\rho_3}{4\rho_2 2r_d} c_\chi |v_d - v_e| (v_d - v_e) + g,$$

where $v_d(0)=v_0$.

The following equation was used for the drag coefficient in numerical simulation taking into account the nonsphericity of the droplet, its unsteady motion [7], evaporation on the body surface [8] and movement (of convection flows) inside the droplet:

$$c_\chi = 24.3 k_g \frac{1}{B+1} \frac{1 + \frac{2\mu_2}{3\mu_3}}{1 + \frac{\mu_2}{\mu_3}} (A+1)^{1.2 \pm 0.03} \text{Re}^{-0.635}.$$

The geometric factor k_g characterizes the form deviation from spherical (for cylindrical disks $k_g=1.64$). The ratio $1/(B+1)$ is a coefficient that describes the effect of droplet evaporation on resistance force ($B=C_2(T_{3s}-T_{2s})/(Q_e+q_v/W_e)$) [8]. The ratio $[1+(2\mu_2/3\mu_3)]/[1+\mu_2/\mu_3]$ is the coefficient taking into account possible convective flows inside the droplet. The ratio $(A+1)^{1.2 \pm 0.03}$ characterizes the accelerated body motion (A – dimensionless complex, which describes the relative acceleration ($A = \frac{d}{v_d^2} (\frac{dv_d}{dt})$)) [7].

The following expression was used to determine the mass evaporation rate:

$$W_e = \frac{\beta}{1-k_\beta \beta} \frac{(P^n - P)}{\sqrt{2\pi R_t T_e / M}},$$

where k_β – dimensionless coefficient ($k_\beta \approx 0.4$).

The layer thickness of the evaporating droplet was determined by the formula $l_e = \frac{W_e t}{\rho_2}$.

The following scale variables were used to convert the equations into the dimensionless form: characteristic average droplet size ($z_m=1$ mm); time scale ($t_m=1$ s); temperature scale ($T_m=1000$ K); rate scale ($v_m=1$ m/s).

Where: τ – dimensionless time; τ_d – dimensionless time of droplet existence; Ψ – dimensionless equivalent of the current function; Ω – dimensionless equivalent of vorticity; Θ – dimensionless temperature; U, V – dimensionless velocity components of water vapor and combustion products in the direction of the axis R and Z respectively; γ_f – dimensionless concentration of combustion products; γ_w – dimensionless water vapor concentration; λ –

thermal conductivity, $\text{W}/(\text{m}\cdot\text{K})$; Q_e – thermal effect of liquid evaporation, J/kg ; W_e – evaporation rate, $\text{kg}/(\text{m}^2\cdot\text{s})$; ΔT – temperature difference ($\Delta T=T_m-T_0$); C – specific heat capacity, $\text{J}/(\text{kg}\cdot\text{K})$; v_d – droplet velocity, m/s ; v_e – linear velocity of vapor outflow from the droplet surface, m/s ; c_χ – dimensionless drag coefficient; g – acceleration of gravity, m/s^2 ; β – dimensionless evaporation coefficient; P – water vapor pressure near the boundary of evaporation, N/m^2 ; P^n – saturated water vapor pressure, N/m^2 ; R_t – universal gas constant, $\text{J}/(\text{mol}\cdot\text{K})$; T_e – droplet surface temperature, K ; M – molar mass, kg/kmol ; indexes: 0 – initial state, 1 – high-temperature gases, 2 – water droplet, 3 – water vapor, d – droplet, e – evaporation, f – fuel, m – scale, s – surface, v – vapor, w – water.

The system of non-stationary partial differential equations (1)–(6) was solved by the finite difference method [9]. The difference analogues of differential equations were solved by the local one-dimensional method [9]. One-dimensional differential equations were solved by the sweep method using an implicit four-point difference scheme [9]. Nonlinear equations were solved by the iteration method. Irregular dimensionless steps in time ($10^{-8}\div 10^{-6}$) and in coordinate grid ($10^{-4}\div 10^{-2}$) were used to increase the accuracy when solving the system of non-stationary differential equations (1)–(6). The method for assessing the reliability of the results of numerical studies was performed, based on the verification of applied difference scheme conservativeness, similar to [6].

Numerical studies were carried out at the following parameters [10, 11]: initial temperatures of liquid droplets $\Theta_0=0.3$ and gas $\Theta_f=0.3\div 1.1$; thermal effect of evaporation $Q_e=2.26 \text{ MJ/kg}$; droplet sizes $R_d=0.25$, $Z_d=1$ and solution area $R_L=10$, $Z_L=1000$; initial droplet velocity $V_0=0.5$; water molar mass $M=18 \text{ kg/kmol}$.

3 RESULTS AND DISCUSSION

Table 1 shows the dependence of the mass rate of water droplet evaporation on the temperature of gas environment. Data in the table was obtained as a result of the calculations using the developed model of heat and mass transfer. The essentially nonlinear nature of the relation $W_e=f(\Theta_f)$ was established from the results of theoretical research.

Table 1: The dependence of the mass rate of water droplet evaporation on the temperature of gas environment

Θ_f	0.3	0.5	0.7	0.9	1.1	0.3
$W_e, \text{kg}/(\text{m}^2\cdot\text{s})$	0.005	0.0116	0.065	0.155	0.214	0.005

The values have been obtained that correspond to the mass rate of droplet evaporation during the motion through high-temperature gases. These values correlate well with the results of previous experiments [12]: the evaporation rate was $W_e=0.006 \text{ kg}/(\text{m}^2\cdot\text{s})$ at the temperature of fuel combustion products $T_f=300 \text{ K}$, and $T_f=1100 \text{ K}$, $W_e=0.270 \text{ kg}/(\text{m}^2\cdot\text{s})$.

Figure 2 shows the isotherms at $\tau=0.02$ (correspond to the beginning of the motion) for two schemes considering the mutual disposition of droplets. In the case of two (Figure 2a), and five (Figure 2b) droplets moving consecutively, the parameter L_n varied from 0.01 to 5.

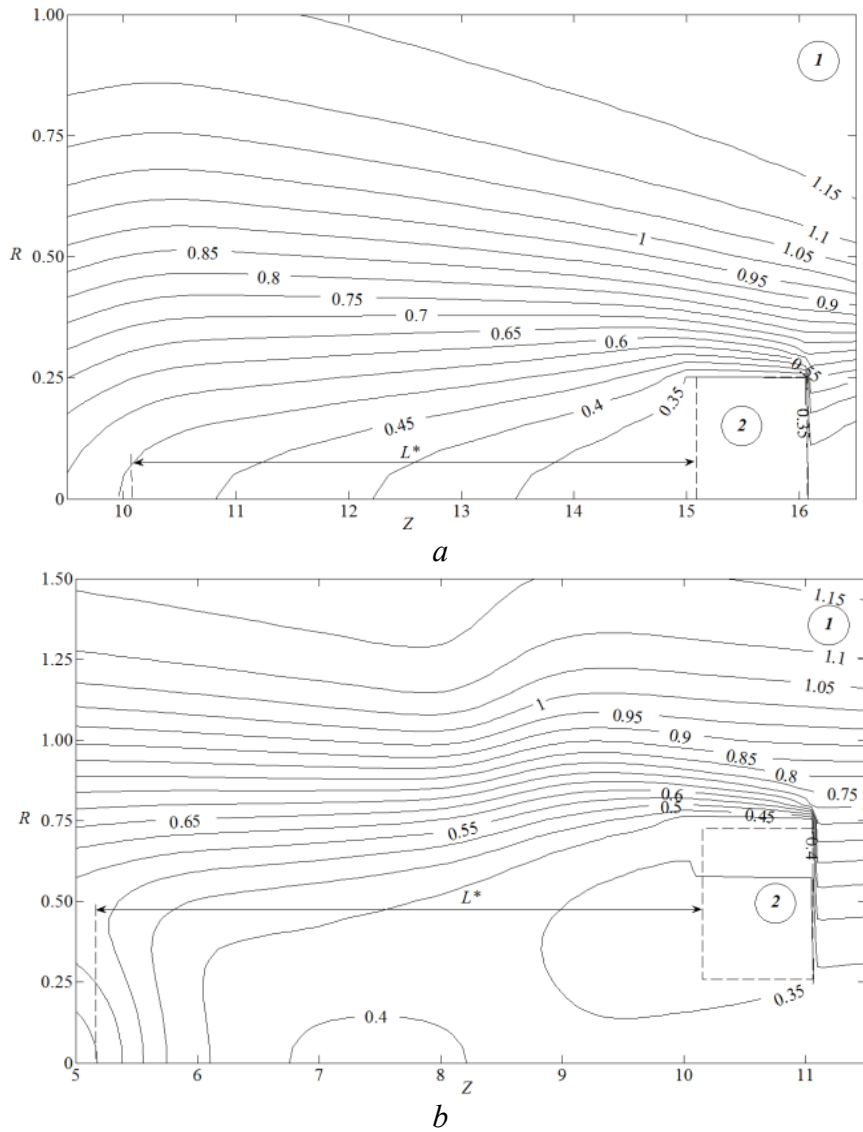


Figure 2: Isotherms (Θ) for the system with two droplets moving consecutively at $\tau=0.02$, $R_d=0.25$, $Z_d=1$, $L_n=1$ (a) and five droplets at $\tau=0.02$, $R_d=0.25$, $Z_d=1$, $L_n=2$ (b):
I – high-temperature gas environment, 2 – water droplet

Figure 2 demonstrates a decrease of the gas temperature in the vicinity of droplets. It can be seen that the temperature in the droplet track varies considerably. This is primarily due to the evaporation of droplets. The trajectory of each droplet also plays a decisive role. The temperature in the track changes slightly (relative to the initial droplet temperature) in contrast to that in a small neighborhood of the line corresponding to the trajectory when varying L_n in a wide range.

Satisfactory compliance with the results of theoretical studies and the data obtained in the experiments allow us to conclude on the adequacy of the developed model of heat and mass transfer during the motion and evaporation of droplets and droplet liquid flow in high-temperature gas environment.

The research results have been obtained using established numerical model; they can be used to develop new and improve existing technologies, providing the implementation of phase transitions in the system “liquid spray – high-temperature gas environment”.

This work was financially supported by the Russian Science Foundation (Project No. 14-39-00003).

REFERENCES

- [1] Maltsev, R.V. and Rebrov, A.K. Gas-dynamic colliders: numerical simulations. *J.Appl. Mech. Tech. Phys.* (2007) **48**:142–151.
- [2] Lebedev, V.P., Lemanov, V.V., Misura, S.Ya. and Terekhov, V.I. Effect of flow turbulence on film cooling efficiency. *Int. J. Heat Mass Transfer* (1995) **38**:2117-2125.
- [3] Rodriguez, B. and Young, G. Development of international space station fine water mist portable fire extinguisher. *in: 43rd International Conference on Environmental Systems, Vail, CO* (2013).
- [4] Nikitin, M.N. Using a gas–vapor mixture at the fuel combustion. *Ind. Energy* (2010) **12**:37-42.
- [5] Ma, J., Liu, D., Chen, Z. and Chen, X. Agglomeration characteristics during fluidized bed combustion of salty wastewater. *Powder Technol.* (2014) **253**:537-547.
- [6] Glushkov, D.O., Kuznetsov, G.V. and Strizhak, P.A. Numerical investigation of water droplets shape influence on mathematical modeling results of its evaporation in motion through a high-temperature gas. *Math. Probl. in Eng.* (2014) **2014**:Article ID 920480.
- [7] Tchen, C.M. *Mean value and correlation problems connected with the motion of small particles suspended in a turbulent fluid*. The Hague. Martinus Nijhoff, (1947).
- [8] Eisenklam, P., Arunachalam, S.A. and Weston, J.A. Evaporation rates and drag resistance of burning drops. *Proc. 11th Symp. On Combustion* (1967) **11**: 715-728.
- [9] Samarskii, A.A. *The Theory of Difference Schemes*. Marcel Dekker, USA, (2001).
- [10] Vargaftik, N.B., Filipov, L. P., Tarzimanov, A. A. and Totskii, E. E. *Handbook of Thermal Conductivity of Liquids and Gases*. CRC Press, Boca Raton, Fla, USA, (1994).
- [11] Vargaftik, N.B. *Tables of Thermophysical Properties of Liquids and Gases*, Hemisphere Publishing, New York, (1975).
- [12] Terekhov, V.I., Terekhov, V.V., Shishkin, N.E. and K.Ch.Bi. Heat and mass transfer in disperse and porous media experimental and numerical investigations of nonstationary evaporation of liquid droplets. *Journ. Eng. Phys. Thermophys.* (2010) **83**:883–890.

PARTICLE CONTACT LAWS AND THEIR PROPERTIES FOR SIMULATION OF FLUID-SEDIMENT INTERACTION WITH COUPLED SPH-DEM MODEL

DAVID F. VETSCH¹, FLORIAN FLEISSNER², ALEXANDRA MUELLER³
AND ROBERT M. BOES⁴

¹ Laboratory of Hydraulics, Hydrology and Glaciology (VAW), ETH Zurich
Wolfgang-Pauli-Str. 27, CH-8093 Zürich, Switzerland
e-mail: vetsch@vaw.baug.ethz.ch, web page: <http://www.vaw.ethz.ch>

² Institute of Engineering and Computational Mechanics, University of Stuttgart
Pfaffenwaldring 9, D-70569 Stuttgart, Germany
e-mail: florian.fleissner@itm.uni-stuttgart.de, web page: <http://www.itm.uni-stuttgart.de>

³ Institute of Engineering and Computational Mechanics, University of Stuttgart
Pfaffenwaldring 9, D-70569 Stuttgart, Germany
e-mail: alexandra.mueller@itm.uni-stuttgart.de, web page: <http://www.itm.uni-stuttgart.de>

⁴ Laboratory of Hydraulics, Hydrology and Glaciology (VAW), ETH Zurich
Wolfgang-Pauli-Str. 27, CH-8093 Zürich, Switzerland
e-mail: boes@vaw.baug.ethz.ch, web page: <http://www.vaw.ethz.ch>

Key words: Contact Laws, DEM, Fluid-Sediment Interaction, SPH

Abstract. The transport of sediment due to the interaction of fluid and solids is a prevalent geophysical process. The detailed modelling of the interaction between the fluid and the sediment particles is still a challenging task. In the present study we model the fluid phase by smoothed particle hydrodynamics (SPH) using the classical approach where the fluid is assumed to be weakly compressible. The sediment, in terms of solid spheres made of granite, is modelled by the discrete element method (DEM). Both of them are meshfree particle methods but SPH is a continuum approach and DEM describes the motion and interaction of discrete solid objects. The interaction between SPH and DEM particles is modelled as particle-to-particle contact in combination with a boundary condition at the solid interface. Therefore, a contact law is used to capture the collision process and to ensure balancing of collision forces. In doing so, two contact types have to be modelled, i.e. sediment-sediment and fluid-sediment. The approach and properties these contact types are presented in detail. Advantages and drawbacks of the approaches are discussed based on examples.

1 INTRODUCTION

Sediment transport due to the interaction between fluid and sediment particles is a prevalent process in the environment as occurring in rivers for example. Common modelling approaches are mainly based on empirical closure conditions for the estimation of the transport rate. Numerical simulations for the investigation of the underlying processes in

detail are rather seldom [1]. This is mainly because of the difficulties that arise from the fluid-sediment interaction, especially when complex object geometries and moving boundaries have to be considered. For fluid-structure interaction, particle methods became a promising approach that may also be suitable for the simulation of sediment transport. The main advantage of meshfree particle methods is that there is no need for costly grid generation and interface tracing or capturing techniques. In the present study we model the fluid phase by smoothed particle hydrodynamics (SPH) using the classical approach where the fluid is assumed to be weakly compressible. The sediment, in terms of solid spheres made of granite, is modelled by the discrete element method (DEM). The interactions between the particles are modelled as particle-to-particle contacts, whereas three different contact types may be distinguished: sediment-sediment, fluid-sediment and fluid-fluid. The first is the basis of DEM, where contact laws are used to capture the collision process and to ensure balancing of collision forces. The latter corresponds to the SPH discretization. For the modelling of the fluid-sediment interaction, the combination of DEM and SPH is not straight forward, since SPH is a continuum approach and DEM is based on discrete force models. Thus, the interaction is considered as SPH-DEM particle contact in combination with a boundary condition for the SPH particle at the solid interface.

In this contribution the sediment-sediment and fluid-sediment interaction are presented in detail. The advantages and drawbacks of the approaches are discussed based on three examples: the collision of two sediment particles, the buoyancy force acting on a sediment particle and the settling of a sediment particle. It will be shown for the sediment-sediment interaction that the error of the interaction force strongly depends on time step size and material properties. For the fluid-sediment interaction the importance of an appropriate parametrisation of the contact law is pointed out.

2 MODELLING APPROACH

The governing equations used for modelling of the fluid flow are the Euler equations in Lagrangian form, whereas energy conservation is omitted (isothermal fluid). The simulation of the sediment particles is based on Newton's second law and the dynamic Euler equations that describe the conservation of linear and angular momentum, respectively. For simplification purposes, the sediment particles are considered to be spherical.

3.1 Smoothed Particle Hydrodynamics

The idea behind SPH can be described as replacing the fluid by a set of points that follow the motion and carry information about the properties of the fluid. These points can be seen either as interpolation points for the discretization of the governing equations or as real material particles [2]. For the present work, the standard SPH method is used that is also termed “weakly compressible SPH”, where the computation of the pressure is based on an equation of state for water.

For the discretization of the governing equations, the fluid continuum is approximated by particles, whereas any quantity or function $A_r(\vec{r})$ at location \vec{r} can be obtained by interpolation based on a kernel function $W(r_{ab}, h)$, where $r_{ab} = |\vec{r}_a - \vec{r}_b|$ is the distance between two particles a and b , and h is the smoothing length. For the present work the Gaussian kernel with a cut-off at distance $2h$ is used..

Considering particles with mass m , density ρ and position \vec{r} identified by indices a and b , where a identifies the particle of interest and b the neighboring particles within cut-off distance with masses according to a volume element of the fluid $m_b = \rho_b(\vec{r}_b) d\vec{r}_b$ and $A_b = A_r(\vec{r}_b)$, the summation interpolant can be written as

$$A_a(\vec{r}_a) = \sum_b m_b \frac{A_b}{\rho_b} W(r_{ab}, h) . \quad (1)$$

The derivative of A_a can be obtained by ordinary differentiation of the kernel function. Consequently, the Euler equations can be discretized for particles according to this concept. The conservation of mass in its discretized form reads

$$\frac{d\rho_a}{dt} = \rho_a \sum_b \frac{m_b}{\rho_b} (\vec{u}_a - \vec{u}_b) \cdot \vec{\nabla}_a W_{ab} , \quad (2)$$

and the conservation of momentum reads

$$\frac{d\vec{u}_a}{dt} = - \sum_b m_a \left(\frac{p_a}{\rho_a^2} + \frac{p_b}{\rho_b^2} + \Pi_{ab}(\alpha, \beta) \right) \vec{\nabla}_a W_{ab} + \vec{f}_e , \quad (3)$$

where $\Pi_{ab}(\alpha, \beta)$ is the artificial viscosity term [3], \vec{u}_a is the velocity, p_a is the pressure (similar for neighboring particles with index b). The particles are moved by

$$\frac{d\vec{r}_a}{dt} = \vec{u}_a . \quad (4)$$

The equation system is closed by an appropriate equation of state for the pressure p :

$$p_a = B \left(\left(\frac{\rho_a}{\rho_f} \right)^{\gamma_p} - 1 \right), \quad B = \frac{c_s^2 \rho_f}{\gamma_p} , \quad (5)$$

where ρ_f is the reference density of the fluid and usually $\gamma_p = 7$. The choice of B determines the speed of sound. Since the time-step size of the simulation may depend on the speed of sound c_s , a rather small value compared to its effective value of ~ 1500 m/s is preferred to gain a faster simulation progress. In order to limit density variations to a maximum of 1%, the sound velocity is chosen so that the Mach number of the flow is 0.1 or less [3]; this yields $c_s = 10u_{ref}$. The reference velocity u_{ref} depends on the problem, e.g. the wave propagation velocity in the case of free surface flow.

For time integration a predictor-corrector method based on the leapfrog scheme is used [4]. The size of the time step Δt is determined based on three characteristic time scales: the CFL-condition with $u_{max} = \max(|\vec{u}|_{max}, c_s)$ and the maximum of acting internal as well as external forces, i.e. the viscous forces and the applied forces in terms of the maximum particle acceleration a_{max} , whereas the former is only relevant for flows with low Reynolds numbers. For SPH, the relevant length scale is the smoothing length h . According to these considerations, the size of a time step can be obtained by the assignment

$$\Delta t = \alpha_s \min \left(\frac{h}{u_{\max}}, \frac{h^2}{\nu}, \sqrt{\frac{h}{a_{\max}}} \right), \quad (6)$$

where α_s is a safety factor in the range of 0.125 and 0.5 (see e.g. [5]). More recent and advanced considerations about the maximum time step are given in [6].

3.2 Discrete Element Method

The original concept of the DEM [7] is to allow for a usually small but non-physical interpenetration of colliding rigid bodies. The interpenetration is regarded to be an equivalent for the surface deformation and contact forces are related to the displacement or the amount of interpenetration δ in general. With regard to a pair of colliding particles, the penetration continues until the forces exerted by the particles are balanced by the contact force, i.e. when maximum penetration is reached. This can be modelled by a spring-damper system (Figure 1), where the collision force is expressed as the sum of a penalty and a damping force:

$$\vec{F}_c = \vec{F}_n(k(\delta)) + \vec{F}_d. \quad (7)$$

The penalty force $\vec{F}_n(k(\delta))$ acts in the direction of the surface normal and is discussed in the next section. A simple approach for modelling dissipation is the application of a viscous damper that depends on the collision velocity $\dot{\delta} = |\vec{v}_i - \vec{v}_j|$ in the direction of the spring-damper system axis. The damping force is $\vec{F}_d = -d\dot{\delta}\vec{e}_{sd}$ where d is the viscous damping coefficient. With the depicted spring-damper system tangential forces such as fiction may be considered. For a general formulation of a nonlinear spring-damper model see [8].

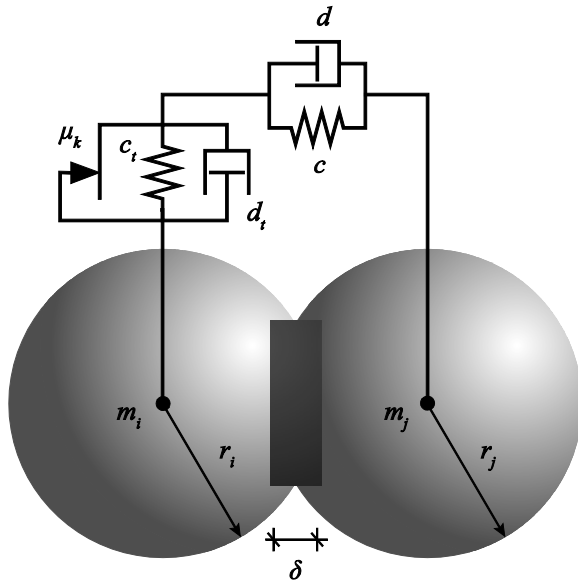


Figure 1: Spring-damper system for the modelling of penalty forces due to overlapping including friction.

The time dependent motion of sediment particles is simulated according to Newton's second law that describes the conservation of linear momentum (here for constant mass)

$$m \frac{d\vec{v}}{dt} = \vec{F}_a , \quad (8)$$

where \vec{v} is the velocity and m is the mass of the particle, and the solution of the dynamic Euler equations for the conservation the angular momentum

$$\mathbf{I} \cdot \frac{d\vec{\omega}}{dt} + \vec{\omega} \times (\mathbf{I} \cdot \vec{\omega}) = \vec{M}_a \quad (9)$$

where $\mathbf{I} = \mathbf{I}^T$ is the tensor of moment of inertia in the fixed principal frame of the particle and $\vec{\omega}$ the angular velocity. For the solution of equation (9) using quaternions see e.g. [9]. The applied force \vec{F}_a acting on a particle is the sum of contact forces \vec{F}_c and external forces, i.e. due to gravity. Consequently, the applied torque \vec{M}_a is the sum of torque due to contact- and external forces.

For the time integration of a dissipative DEM the Newmark- β schemes are appropriate [9]. However, in combination with SPH the same scheme with identical parameters is also used for the DEM to avoid asynchronism. The size of a time step can be obtained by similar conditions as for the SPH method. The relevant length scale is the radius of the smallest sphere r_{\min} . Furthermore, the maximum velocity u_{\max} and maximum acceleration a_{\max} are taken into account. Including a safety factor α_s , this leads to the following conditions for the time-step size

$$\Delta t = \alpha_s \min \left(\frac{r_{\min}}{u_{\max}}, \sqrt{\frac{r_{\min}}{a_{\max}}} \right) . \quad (10)$$

3 CONTACT LAWS

According to the previously introduced spring-damper system, the contact forces act either in normal or tangential direction. In normal direction the penalty force $\vec{F}_n(k(\delta))$ can be determined using different approaches, either linear or nonlinear depending on $k(\delta)$, i.e. material properties. In tangential direction different kinds of friction may be considered but in the current scope only the friction between fluid and sediment particles is discussed (see section 3.2).

3.1 Sediment-sediment interaction

Linear Force Model

Considering a perfectly elastic spring with stiffness c [N/m], the force to obtain a displacement δ [m] in the direction of the spring-damper system axis \vec{e}_{sd} is

$$\vec{F}_s(\delta) = -c\delta\vec{e}_{ij} = \vec{F}_n(k(\delta)) , \text{i.e. } k(\delta) = c\delta . \quad (11)$$

Hertz Force Model

A more physically motivated approach for modelling the interaction of two perfectly elastic spheres with frictionless surfaces is based on the contact theory of Hertz [10]. The nonlinear force law is written as

$$\vec{F}_n(k(\delta)) = -K\delta^n \vec{e}_{ij}, \text{ i.e. } k(\delta) = K\delta^n, \quad (12)$$

where K is the generalised stiffness constant and $n = 1.5$ [10]. For two colliding spheres i and j , the stiffness parameter depends on the radii and the material properties,

$$K = \frac{4}{3(\sigma_i + \sigma_j)} \left[\frac{r_i r_j}{r_i + r_j} \right]^{\frac{1}{2}}, \quad (13)$$

with material parameters σ_i and σ_j :

$$\sigma_k = \frac{1 - \nu_k^2}{E_k}, \quad (k = i, j), \quad (14)$$

where ν_k is Poisson's ratio and E_k is Young's modulus. An in-depth description of the Hertz contact theory is given by [11], for example.

3.2 Fluid-sediment interaction

Introduction

Universal and robust boundary conditions for the simulation of fluid-structure interaction with SPH are still an unsolved problem and part of ongoing research, see e.g. [12-14]. There are different solutions that include the creation of virtual boundary particles to avoid incomplete SPH interpolants: ghost particles, repulsive particles and dynamic particles [15]. The approach applied in this work is a combination of the first two concepts; thereby the main goal is to avoid penetration of the solid boundary by fluid particles.

Modified Lennard-Jones Potential

The use of a Lennart-Jones (LJ) potential allows modelling of the interaction of fluid particles with a rigid body in a similar manner as molecular interaction. Other than the original LJ potential that leads to an infinitely large force for a particle distance towards zero, [16] propose a force law with a finite value k of the force at the boundary ($|\vec{F}_n(r_{ij})| = k$ where r_{ij} is the distance between two particles). The maximum force value k at the boundary may be also denoted as stiffness of the boundary. Furthermore, the influence of the potential is limited to a given distance R , i.e. $|\vec{F}_n(r_{ij})| = 0$ for $r_{ij} \geq R$. The point where the force changes from repulsion to attraction can be set equal to r_0 . For the investigation of wall bounded flows, an approach depending on the particle distance to the boundary δ_w is preferable.

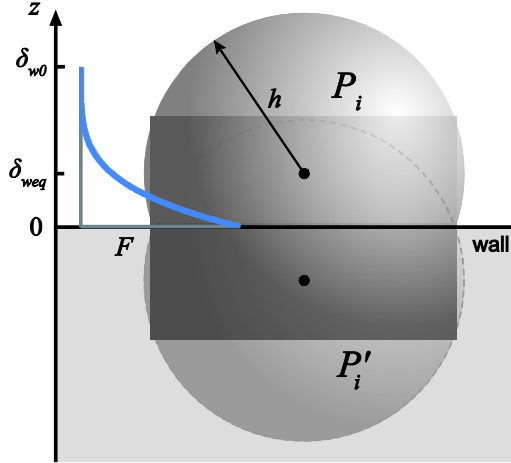


Figure 2: SPH particle P_i with smoothing length h close to the solid surface of a sediment particle (indicated by “wall”) at equilibrium position $\delta_{w_{eq}}$. The mirrored particle P'_i is used to obtain appropriate boundary for pressure and density.

For the interaction of a fluid particle with a sphere of radius r_s the following definitions are introduced:

$$\delta_w := r_{ij} - r_s, \delta_{w0} := r_0 - r_s, D_w := R - r_s . \quad (15)$$

Consequently, the force exerted by the modified Lennard-Jones (MLJ) potential within a maximum distance to the solid surface is

$$\vec{F}_n(\delta_w) = \begin{cases} k \frac{(\delta_w - D_w)^2 (\delta_w - \delta_{w0})(\delta_w - 2D_w + \delta_{w0})}{(D_w + r_s)^2 (2D_w - \delta_{w0} + r_s)(\delta_{w0} + r_s)} \vec{e}_{ij}, & \text{if } \delta_w < D_w, \\ 0 & \text{otherwise.} \end{cases} \quad (16)$$

Considering only repulsive forces (Figure 2), i.e. $D_w = \delta_{w0}$, equation (16) becomes

$$\vec{F}_n(\delta_w) = k \left(\frac{\delta_{w0} - \delta_w}{\delta_{w0} + r_s} \right)^4 \vec{e}_{ij}, \quad \delta_w \leq \delta_{w0} . \quad (17)$$

To balance a given external force of amount F the equilibrium distance to the wall is

$$\delta_{w_{eq}} = \delta_{w0} - (\delta_{w0} + r_s) \left(\frac{F}{k} \right)^{1/4} \quad (18)$$

If a certain equilibrium distance to the wall is preferred, the appropriate stiffness could be obtained by rearranging equation (18),

$$k = F \left(\frac{\delta_{w0} + r_s}{\delta_{w0} - \delta_{w_{eq}}} \right)^4 . \quad (19)$$

Ghost particle

For an SPH particle in contact with a sediment particle, an incomplete interpolant at the boundary has to be avoided. This is rudimentary done by creation of a ghost particle P_i' with the same properties as the original particle P_i (Figure 2). Indeed, this leads to slip conditions at the boundary. Thus, a fiction law has to be introduced to consider wall effects.

Friction

The tangential force $\vec{F}_t(\delta_w)$ that acts on a fluid particle in contact with a sediment particle is actually a viscous shear force $\vec{F}_v(\delta_w)$ plus effects due to the character of the surface. The tangential force can be written as

$$\vec{F}_t(\delta_w) = \begin{cases} -\left|\vec{F}_v(\delta_w)\right| \tanh(\eta\{v_t\}) \vec{e}_t, & \text{if } \delta_w < D_{visc}, \\ 0 & \text{otherwise,} \end{cases} \quad (20)$$

where $\{v_t\}$ is the value of relative tangential velocity v_t and D_{visc} is the influence distance of the force with respect to the surface. The viscous shear force can be expressed as $\vec{F}_v(\delta_w) = \mu_v(\Delta s)^2 \vec{v}_t / \delta_w$, where Δs is the initial spacing of SPH particles and μ_v is a coefficient that is related to the viscosity of the fluid and the surface roughness. To prevent numerical instabilities, the hyperbolic tangent of the relative tangential velocity is used, i.e. $\eta\{v_t\}$, where η is the friction slope.

4 EXAMPLES

4.1 Role of material properties

The parameters of the Hertz law, i.e. Poisson's ratio ν_k and Young's modulus E_k , are material properties commonly used in engineering practice. However, this connection to real materials has to be used with care, since the used approaches for the interaction forces are approximations that balance momentum but they do not render the contact of real material in detail. Although, the Hertz law is a reasonable model for the latter, the size of the time step would be very small already for moderate accuracy when it comes to very stiff materials such as granite. Thus, use of modified material properties which allow for larger time steps while still maintaining the accuracy requirements seems to be a useful approach. However, in such a case a larger penetration, i.e. a larger displacement of the sphere, has to be accepted. To illustrate this, consider the collision of two identical spheres with opposite velocity. The Hertz force model is applied as contact law. For varying Young's modulus E the maximum penetration depth δ_{max} can be estimated based on the conservation of energy [17] and thus the correct penalty force is known. The ratio of δ_{max} and the sphere radius r_s , $a = \delta_{max}/r_s$, can be used as a measure of displacement. For the present example, a is varied between 0.09% ($E = 6.0 \cdot 10^{10} \text{ N/m}^2$) and 5% ($E = 3.44 \cdot 10^6 \text{ N/m}^2$). In Figure 3 the standard deviation of the penalty force against the size of the time step is depicted. For the present example it is shown, that for the same level of accuracy, an approximately five times larger penetration has to be accepted to gain a magnitude in time-step size. For fluid-sediment simulations this aspect might be relevant, because the time-step size of SPH is usually larger than that of the DEM.

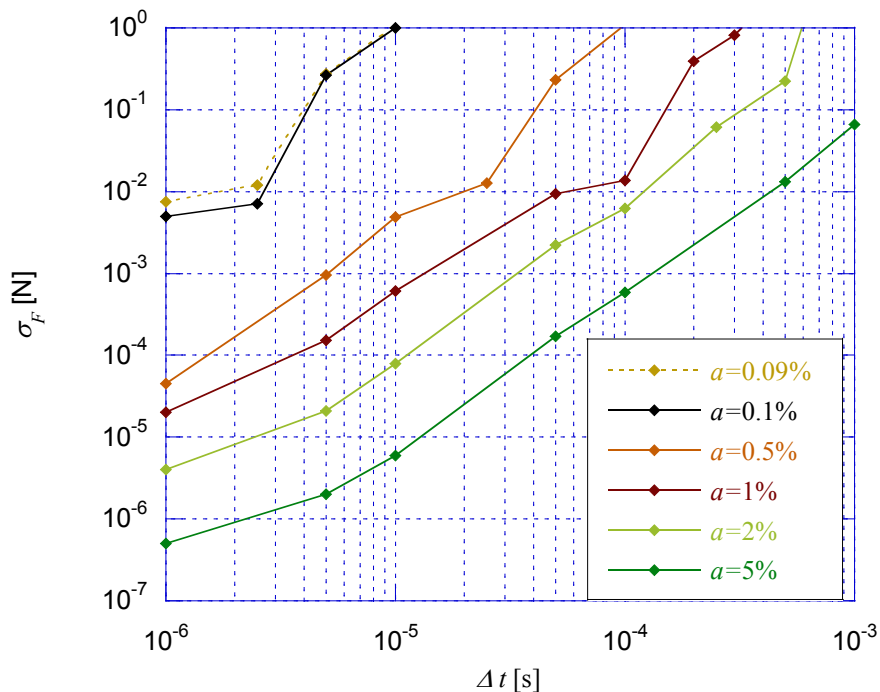


Figure 3: Standard deviation of the penalty force against the time-step size for the given example.

4.2 Buoyancy

Improper representation of the buoyancy force may lead to an incorrect weight of the submerged body. Thus, the resistance of the body against acting fluid dynamic forces may be misleading as well. To illustrate the influence of the contact law parameters, a simple experiment is carried out, where a sediment particle with radius $r_s = 0.015$ m is initially located in the middle of a small tank of water at height $z_s = 0.5h_f$, with $h_f = 0.1$ m.

The interaction of the fluid particles with the sphere is modelled by the MLJ potential. The distance to the sphere surface where the penalty force is zero is set equal to the smoothing length, i.e. $\delta_{w0} = h$, which corresponds to an active penalty force as soon as interaction takes place. The stiffness of the potential is obtained by evaluating a slightly modified form of equation (19), namely⁴

$$k = F \left(\frac{h + r}{h(1 - \psi_{eq})} \right)^4, \quad (21)$$

where $\psi_{eq} = \delta_{w0}/h$ and the amount of the force is equal to the median pressure acting on the sphere, i.e. at the middle of the sphere $F = (h_f - z_s) \rho_f g \Delta s^{\sigma-1}$, where σ is the dimension of the problem and g the gravitational acceleration. The parameter ψ_{eq} actually determines the characteristics of the potential and thus the gradient of the repulsive force. For the given case with almost no fluid motion other force laws would also work, but they may not be able to prevent particle penetration with the estimated parameters when it comes to dynamic problems with larger flow velocities.

For this example, different resolution of fluid particles in terms of the initial particle distance $\Delta s = [0.01, 0.005, 0.0025] \text{ m}$, hereafter referred to as particle resolution, are considered and the parameter ψ_{eq} is varied until the difference of the exact and simulated submerged weight is within a few per cent. According to equation (21) the force law depends on the parameter ψ_{eq} which actually defines the equilibrium distance between the fluid particles and the sphere by $\delta_{w_{eq}} = h\psi_{eq}$. Thus, the parameter ψ_{eq} indirectly controls the amount of displaced fluid and, consequently, the buoyancy force. Furthermore, the mass of the fluid particles is set according to $m_a = \rho_0(\Delta s)^\sigma$ wherein the term $(\Delta s)^\sigma$ corresponds to a finite volume of fluid and ρ_0 to the initial density. Hence, it could be expected that $\delta_{w_{eq}}$ converges to $\Delta s/2$ for decreasing values of Δs and $\psi_{eq} \rightarrow 1/3$ for the present case with $h = 1.5\Delta s$. This tendency was quite well reproduced by the experiments.

4.3 Settling of sphere

The influence of the scaling of the contact law on the terminal settling velocity of a sphere in a water tank with water depth h_f is exemplified here. The force law is scaled by varying d_{w0} . Besides the standard configuration with $d_{w0} = h$, three different setups are studied: $d_{w0} = 2h$ and $d_{w0} = 3h$, resulting in a boundary condition with a smaller maximum repulsive force and slower increase for decreasing particle distance, and $d_{w0} = 0.5h$, which has the opposite effect.

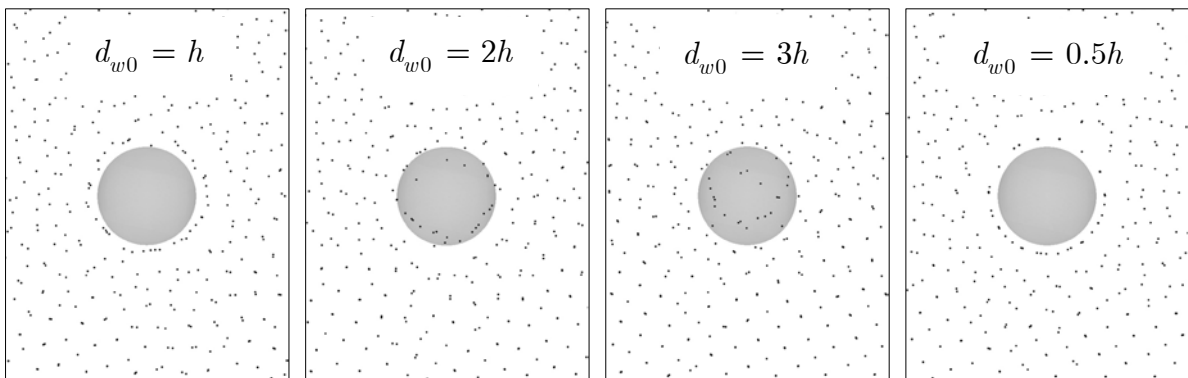


Figure 4: Positions of fluid particles for different scaling of the MLJ force law. The pictures show the sphere at a position of approximately $0.5h_f$.

The reference for the MLJ is assumed to be equal to the maximum dynamic pressure $F = 0.5\rho_f w_s^2 \Delta s^{\sigma-1}$, where w_s is an estimate for the terminal settling velocity. However, the total pressure acting on the sphere is actually larger, because the a priori unknown ambient pressure is not considered.

For the case with the standard configuration, $d_{w0} = h$, and the case with $d_{w0} = 0.5h$, the difference of the reference force and the total effective pressure is less important, since the deviation is compensated by the force law in terms of a slightly smaller wall distance than the supposed equilibrium distance. For this configuration, the majority of the fluid particles do not penetrate the sphere surface, as depicted in Figure 4. In the two cases where $d_{w0} > h$, the increase of the repulsive force is slower than for the standard configuration and the deviation

mentioned before becomes more apparent. The fluid particles are now able to penetrate the surface of the sphere. This has the effect, that the buoyancy force of the sphere is reduced and the terminal settling velocity becomes larger than for the standard configuration, i.e. the measured terminal velocity increases from 0.475 m/s ($d_{w0} = h$) to 0.593 m/s ($d_{w0} = 3h$).

12 CONCLUSIONS

The combination of two meshfree particle methods, namely SPH and DEM, are considered for the simulation of fluid flow and sediment transport. Thereby, the sediment-sediment and fluid-sediment interaction is modelled by contact laws.

For the sediment-sediment interaction the Hertz force law is used that relates material properties to a repulsive contact force depending on penetration. It is shown by the example of two colliding spheres, that the accuracy of the contact force is strongly related to the material properties and the time-step size. Maintaining the level of accuracy, the time-step can be increased while reducing the stiffness of the material. However, the displacement of the particles also increases. This may become an issue (damping) in the case of simulations where small variations play a role, e.g. motion and forces due to turbulence quantities.

The proposed contact law for fluid-sediment interaction is computationally efficient, easy to implement for arbitrary geometries and allows for the creation of multiscale models. However, the choice of model parameters is not straight forward, since the reference force for the contact law may not be known a priori. Furthermore, physical properties of the sediment particles are affected by the contact law such as the buoyancy. For the used approach, this implies that the contact law depends on the particle resolution and the problem at hand. For this the adjustment of the repulsive force according to local fluid dynamic properties, e.g. the local flow depth [18], may be an improvement. However, this approach is limited to situations where flow conditions are more or less steady.

ACKNOWLEDGEMENTS

The simulation software used for this work is called PASIMODO (“PArticle SImulation and MOlecular Dynamics in an Object oriented fashion”) which is a multi-purpose particle simulation tool, see [9] and [19].

REFERENCES

- [1] Schmeeckle MW. Numerical simulation of turbulence and sediment transport of medium sand. *Journal of Geophysical Research: Earth Surface*. 119 (2014) 1240-62.
- [2] Monaghan JJ. Theory and Applications of Smoothed Particle Hydrodynamics. in: JF Blowey, AW Craig, (Eds.). *Frontiers of Numerical Analysis*. Springer Berlin Heidelberg2005. pp. 143-94.
- [3] Monaghan JJ. Simulating free-surface flows with SPH. *Journal of Computational Physics*. 110 (1994) 399-406.
- [4] Monaghan JJ, A Kos, N Issa. Fluid motion generated by impact. *Journal of Waterway Port Coastal and Ocean Engineering-Asce*. 129 (2003) 250-9.
- [5] Lee ES, C Moulinec, R Xu, D Violeau, D Laurence, P Stansby. Comparisons of weakly compressible and truly incompressible algorithms for the SPH mesh free particle method.

- Journal of Computational Physics.* 227 (2008) 8417-36.
- [6] Violeau D, A Leroy. On the maximum time step in weakly compressible SPH. *Journal of Computational Physics.* 256 (2014) 388-415.
- [7] Cundall PA, ODL Strack. Discrete numerical-model for granular assemblies. *Geotechnique.* 29 (1979) 47-65.
- [8] Luding S. Collisions & contacts between two particles. *Physics of Dry Granular Media.* 350 (1998) 285-304.
- [9] Fleissner F. Parallel Object Oriented Simulation with Lagrangian Particle Methods. Shaker, Aachen, 2010.
- [10] Hertz H. Ueber die Berührung fester elastischer Körper. *Journal für die reine und angewandte Mathematik* (Crelles Journal). 1882 (1882) 156-71.
- [11] Popov VL. Contact Mechanics and Friction : Physical Principles and Applications. Berlin : Springer, 2010.
- [12] Mayrhofer A, M Ferrand, C Kassiotis, D Violeau, F-X Morel. Unified semi-analytical wall boundary conditions in SPH: analytical extension to 3-D. *Numerical Algorithms.* 68 (2015) 15-34.
- [13] Adami S, XY Hu, NA Adams. A generalized wall boundary condition for smoothed particle hydrodynamics. *Journal of Computational Physics.* 231 (2012) 7057-75.
- [14] Marrone S, M Antuono, A Colagrossi, G Colicchio, D Le Touzé, G Graziani. δ -SPH model for simulating violent impact flows. *Computer Methods in Applied Mechanics and Engineering.* 200 (2011) 1526-42.
- [15] Gomez-Gesteira M, BD Rogers, RA Dalrymple, AJC Crespo. State-of-the-art of classical SPH for free-surface flows. *Journal of Hydraulic Research.* 48 (2010) 6 - 27.
- [16] Muller M, S Schirm, M Teschner, B Heidelberger, M Gross. Interaction of fluids with deformable solids. *Computer Animation and Virtual Worlds.* 15 (2004) 159-71.
- [17] Vetsch D. Numerical Simulation of Sediment Transport with Meshfree Methods. *VAW Mitteilung Nr. 219.* VAW ETH Zurich, Zürich, 2012.
- [18] Rogers BD, RA Dalrymple. SPH modeling of Tsunami waves. *Advanced Numerical Models for Simulating Tsunami Waves and Runup.* 10 (2008) 75-100.
- [19] Lehnart A. Ein Smoothed Particle Hydrodynamics-Verfahren zur Behandlung der Eulergleichungen. *MSc Thesis.* Stuttgart: Universität Stuttgart; 2008. (in German)

PARTICLE TRACKING NUMERICAL METHODS FOR NANOPARTICLE TRANSPORT IN HETEROGENEOUS POROUS MEDIA

DIMITRIOS V. PAPAVASSILIOU^{1,2}, AND NGOC PHAM²

¹ National Science Foundation (NSF)
Division of Chemical, Bioengineering and Environmental Transport Systems
4201 Wilson Blvd, Arlington, VA 22230, USA
e-mail: dpapavas@nsf.gov, web page:
<http://www.ou.edu/content/coe/cbme/people/faculty1/papavassiliou.html>

² University of Oklahoma
School of Chemical, Biological and Materials Engineering
100 East Boyd St. T335, Norman, OK 73019, USA
e-mail: ngocpham@ou.edu, web page: <http://www.semni.org>

Key words: Lattice Boltzmann methods, Lagrangian particle tracking, porous media.

Abstract. A single-phase flow, lattice Boltzmann method (LBM) is utilized with a Lagrangian particle tracking (LPT) method for the simulation of flow and transport of nanoparticles in a porous medium. The 3D pore matrix is obtained either as a randomly packed with spheres porous medium or from images of segments of rock (sandstone) through micro-computed tomography (μ -CT). The particles are assumed to be passive. When the particles collide with the solid matrix, they can either adsorb or continue their motion, based on the assumption that the deposition process is a pseudo-first order process. Furthermore, the solid-fluid interface is assumed to be heterogeneous, so that the simulated nanoparticles can adsorb at different rates at different sites of the interface. Simulations are validated with theoretically expected results, based on macroscopic filtration equations.

1 INTRODUCTION

Charge heterogeneity of the pore surfaces has been found to be important for colloidal transport in porous media. In such conditions, the presence of surface charge heterogeneity generates patchy surface areas, which can be favourable for particle attachment [1, 2]. It is widely admitted that the surface charge heterogeneity in natural porous media, like rocks in hydrocarbon reservoirs, originates from metallic oxides (such as iron, aluminum, and manganese oxide) being present at the porous matrix surface. Naturally, these oxides are randomly distributed across the porous medium (often called the collector) surfaces, yet they are usually grouped into patches in mathematical models. This type of modeling results in the assumption of a patchy distribution of surface charge heterogeneity [3]. It has been claimed so far in the literature that the pattern of the patchy distributions plays no role in colloidal retention, yet the fraction of favorable surface, λ , caused by heterogeneity is important [4].

In this work, we use lattice Boltzmann methods in conjunction with Lagrangian particle tracking (LBM/LPT) simulations to numerically study the effect of different patterns of surface charge heterogeneity in packed-sphere beds. We created four different patterns of surface charge heterogeneity, and conduct parametric investigation of λ and probability of attachment associated with the heterogeneous surfaces under different pore velocities.

2 LATTICE BOLTZMANN METHOD AND LAGRANGIAN PARTICLE TRACKING

To simulate the velocity field in the packed-sphere beds, we adopted the lattice Boltzmann method (LBM), a class of computational fluid dynamics methods with second-order accuracy. This method has been widely adopted to simulate flow of single phase and multi-phases over a wide range of Reynolds number flows. Details about the method can be found elsewhere [5, 6], and are not presented herein. The use of the LBM begins with choosing the number of directions in space and the number of velocity lattice vectors, typically denoted as $DmQn$, where m is the former and n is the later. We employ a D3Q15 scheme with a bounce back boundary condition in this study. The packed-sphere beds were numerically generated by packing rigid and impermeable spheres in simulation boxes following a modified Lubachevsky-Stillinger algorithm [7]. Water with a viscosity of 0.001 Pa.s was used as the working fluid.

Table 1. Simulation parameters

Sphere diameter, d_s	250 μm
Porosity, ϕ	0.46
Pore velocity, u_p	0.02, 0.065, and 0.13 cm/s
Fraction of attachable surface ($p_a \neq 0$), λ	0.2, 0.5, and 0.8
Deposition probability, p_a	0.001, 0.005, 0.01, and 0.05
Number of injected pore volume, PV	5
Particle diameter, d_p	10 and 53 nm

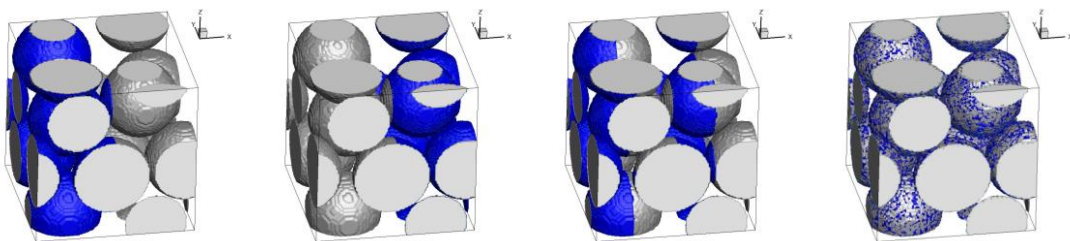


Figure 1. Different spatial distributions of surface charge heterogeneity. Assuming flow from left to right, the blue surface areas indicate surfaces where deposition can occur (i.e., $p_a \neq 0$), whereas those in gray are non-depositable ($p_a = 0$). From left to right: *Entry*, *Exit*, *Stripes*, and *Mixture*.

In association with the LBM, the Lagrangian particle tracking (LPT) algorithm is employed to advance passive particles through the packed-sphere beds. This method allows one to follow the particles and track their trajectories in the Lagrangian framework. As long as dilute particle solutions are considered in this study, the particles are assumed to be monodisperse with no particle-particle interactions. At each simulation time step, the particles are propagated by convection and Brownian motion. When colliding with the solid wall, the particles can either be returned to their original positions at the previous time step or attached to the wall with a pre-defined probability of attachment, p_a . A particle is retained if the pre-defined p_a is larger than or equal to a random number between 0 and 1, generated at the time of collision. Notice that irreversible attachment is assumed in the attachment implementation. Details of the mathematical formulation of the LPT is available in our previous works [8-10].

In this study, we generated four different packed-sphere beds with four different patterns of surface charge heterogeneity, named Entry, Exit, Stripes, and Mixture (see Figure 1). To simulate the heterogeneous surface charge, p_a was non-zero at λ fraction of the surface area, and was zero otherwise. The particle injection strategy consisted of 5 pore volume (PV) of passive particles in each simulation. Other simulation parameters are available in Table 1.

3 RESULTS AND DISCUSSION

3.1 Validation

The precision of the LBM/LPT in conjunction with the probabilistic approach of particle deposition checking in the presence of chemically heterogeneous collector is validated by matching simulation results with that predicted from patch-wise model. Due to irreversible attachment, the patch-wise model is formulated as follows

$$\begin{cases} \frac{\partial C}{\partial t} = D \frac{\partial^2 C}{\partial x^2} - u \frac{\partial C}{\partial x} - \frac{\rho_b}{\phi} \frac{\partial S}{\partial t} \\ \frac{\partial S}{\partial t} = \frac{\phi}{\rho_b} k_a C, \quad k_a = \lambda k_{a-\text{high}} + (1-\lambda) k_{a-\text{low}} \end{cases} \quad (1)$$

where C is the concentration of particles, D is the effective diffusivity of the particles in the porous media, u is the pore velocity, ρ_b is the bulk density of the column, ϕ is the porosity of the column, S is the adsorbed particle concentration, k_a is the average attachment coefficient. Figure 2 presents breakthrough data, obtained from simulation along with prediction from Equation (1). Simulation conditions can be found in the figure caption. It is evidenced from Figure 2 that the simulation results are in excellent agreement with the prediction, confirming the precision of the simulation approach.

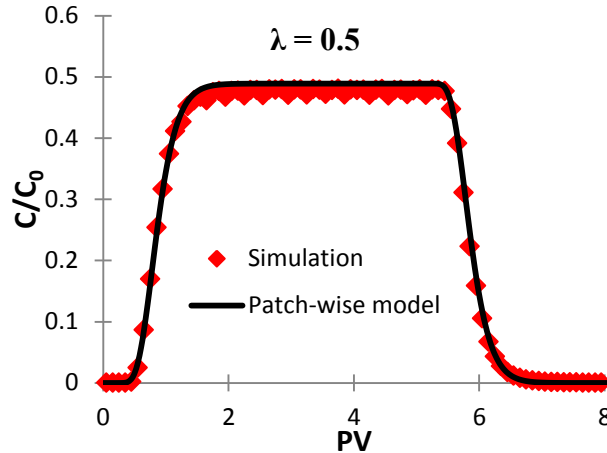


Figure 2. Comparison of particle breakthrough curves obtained from simulation and patch-wise model. Simulations was done with $d_s = 150 \mu\text{m}$, $d_p = 100 \text{ nm}$, $\phi = 0.35$, $u_p = 0.0028 \text{ cm/s}$, $k_{a-\text{high}} = 0.105 \text{ 1/s}$, $k_{a-\text{low}} = 0.01 \text{ 1/s}$, and $D = 7 \times 10^{-6} \text{ cm}^2/\text{s}$.

3.2 Effect of probability of attachment, p_a

To look into the effect of p_a on particle retention, we isolate the contribution of λ by fixing its value at 0.5 while pore velocity was varied from 0.02 to 0.13 cm/s. Also, p_a took four different values of 0.001, 0.005, 0.01, and 0.05. In our simulation, p_a is proportional to the favorable level of the collector surface, and is correlated to the nominal deposition rate as follows

$$k_0 = \frac{1}{\Delta t} \ln \left(\frac{1}{1 - p_a} \right) \quad (2)$$

where Δt is the simulation time step. Figure 3 shows the average attachment coefficient, k_a , as a function of $Da \times Pe$. Note that k_a was obtained by fitting simulation data with Equation (1), and Da is the Damkohler number and Pe is the Peclet number, which are dimensionless. It is apparent from Figure 3 that the pattern effect is noticeable at $Da \times Pe$ equal to 400 and beyond, as k_a of the four different heterogeneous patterns start going apart. The difference between k_a is more pronounced at higher $Da \times Pe$, inferring the role of the heterogeneous pattern at high p_a . The fact that the divergence of k_a is only visible at a certain $Da \times Pe$, a threshold of $Da \times Pe$ beyond which the pattern effect is notable might exist. Among the four heterogeneous pattern, beyond the diverging point, k_a of the *mixture* is always the highest.

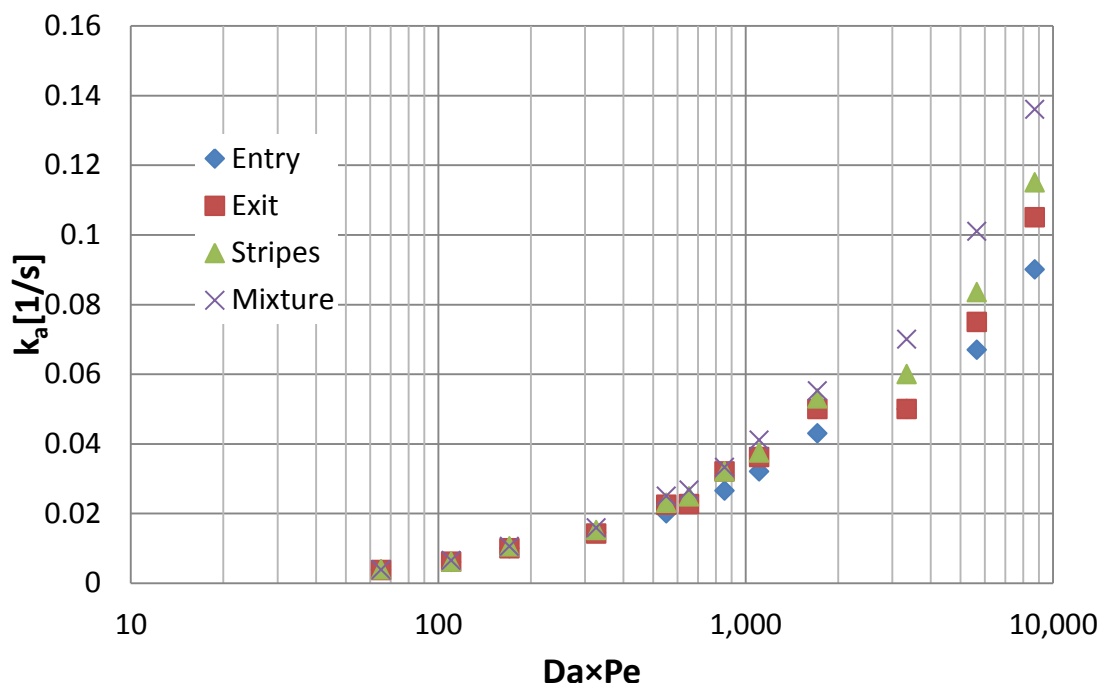


Figure 3. Particle deposition rate as a function of the product of Damkohler and Peclet number at different p_a and pore velocities. Other simulation parameters included $d_p = 10$ nm and $\lambda = 0.5$. p_a were 0.001, 0.005, 0.01, and 0.05, u_p was varied at 0.02, 0.065, and 0.13 cm/s.

12 CONCLUSIONS

- Our findings have shown that the effect of surface charge heterogeneity pattern play an important role in colloidal retention in packed beds. At high deposition rate, the effect becomes more pronounced.
- On the other hand, it diminishes as the deposition rate decays.
- At a particular λ , there exists a threshold of $Da \times Pe$ beyond which the pattern effect should be taken under consideration.

REFERENCES

- [1] Tufenkji, N. and Elimelech, M. Breakdown of colloid filtration theory: role of the secondary energy minimum and surface charge heterogeneities. *Langmuir*. (2005) **21**:841-852.
- [2] Song, L., Johnson, P.R. and Elimelech, M. Kinetics of colloid deposition onto heterogeneously charged surfaces in porous media. *Environ. Sci. Technol.* (1994) **28**:1164-1171.
- [3] Vaidyanathan, R. and Tien, C. Hydrosol deposition in granular media under unfavorable surface conditions. *Chem. Eng. Sci.* (1991) **46**:967-983.

- [4] Chen, J.Y., Ko, C.H., Bhattacharjee, S. and Elimelech, M. Role of spatial distribution of porous medium surface charge heterogeneity in colloid transport. *Colloids Surf., A.* (2001) **191**:3-15.
- [5] Sukop, M.C. and Thorne, D.T. *Lattice Boltzmann Modeling: An Introduction for Geoscientists and Engineers*. 1st ed. NewYork: Springer; 2006.
- [6] Chen, S. and Doolen, G.D. Lattice Boltzmann Method for Fluid Flows. *Annu. Rev. Fluid. Mech.* (1998) **30**:329-364.
- [7] Skoge, M., Donev, A., Stillinger, F.H. and Torquato, S. Packing hyperspheres in high-dimensional Euclidean spaces. *Phys. Rev. E.* (2006) **74**:041127.
- [8] Pham, N.H., Swatske, D.P., Harwell, J.H., Shiau, B.-J. and Papavassiliou, D.V. Transport of nanoparticles and kinetics in packed beds: A numerical approach with lattice Boltzmann simulations and particle tracking. *Int. J. Heat Mass Transfer.* (2014) **72**:319-328.
- [9] Voronov, R.S., VanGordon, S.B., Sikavitsas, V.I. and Papavassiliou, D.V. Efficient Lagrangian scalar tracking method for reactive local mass transport simulation through porous media. *Int. J. Numer. Methods Fluids.* (2010) **67**:501-517.
- [10] Papavassiliou, D.V. Scalar dispersion from an instantaneous line source at the wall of a turbulent channel for medium and hight Prandtl number fluids. *Int. J. Heat Fluid Flow.* (2002) **23**:161-172.

THE AERODYNAMICS OF A JET OF PARTICLES IN A CHANNEL

I. N. LOGACHEV¹, K. I. LOGACHEV¹, O. A. AVERKOVA¹, V. A. UVAROV¹,
 A. K. LOGACHEV¹

¹Belgorod State Technological University named after V.G. Shukhov
 (BSTU named after V.G. Shukhov),
 308012 Belgorod, Russia, Kostukova str., 46
 kilogachev@mail.ru, web page: <http://www.bstu.ru>

Key words: Granular Materials, Bulk Material Transfer, Air Suction, Local Exhaust Ventilation.

Abstract. The main cause for dust discharge is ejection, i.e. formation of directional air flows in a stream of a bulk material due to the dynamic interaction of bombarding particles with air. Discovery of induced air flow occurrence regularities enables both forecasting the level of air pollutions with aerosol emission and choosing the optimum engineering solutions of air containment and dedusting. So far we have studied solid particles flowing in a chute and a jet of loose matter. Both situations represent extreme cases of the more general problem of material flowing through a duct with different distances between flow boundaries and duct walls. Without detriment to generality of the problem we shall consider a flat flow limited by vertical walls.

1 INTRODUCTION

So far we have studied solid particles flowing in a chute and a jet of loose matter [1]. Both situations represent extreme cases of the more general problem of material flowing through a duct with different distances between flow boundaries and duct walls. Without detriment to generality of the problem we shall consider a flat flow limited by vertical walls. The flow would be symmetrical with respect to centerline axis OX with positive direction of the axis corresponding to the direction of flowing particles. Owing to the symmetry of aerodynamic field, we shall only study the airflow pattern in the first quadrant, XOY , of the coordinate system chosen by us. Basic relations for studying aerodynamic processes will be provided by dimensionless dynamics equations that could be expressed as follows provided that $N_t \gg N$:

$$u_x \frac{\partial u_x}{\partial x} + u_y \frac{\partial u_x}{\partial y} = F_x - \frac{\partial \mathbf{P}}{\partial x} + N_t \frac{\partial^2 u_x}{\partial y^2}, \quad u_x \frac{\partial u_y}{\partial x} + u_y \frac{\partial u_y}{\partial y} = F_y - \frac{\partial \mathbf{P}}{\partial y} + \frac{\partial}{\partial x} \left(N_t \frac{\partial u_x}{\partial y} \right), \quad \frac{\partial u_x}{\partial x} + \frac{\partial u_y}{\partial y} = 0. \quad (1) - (3)$$

2 PLANE-PARALLEL FLOW

In case of a plane-parallel motion of solid particles the airflow initiated by them inside the duct could as well be represented by plane-parallel motion ($u_y = 0$). Combined equations (1) – (3) are thereby greatly simplified. Owing to the continuity equation it holds that $\frac{\partial u_x}{\partial x} = 0$ i.e. the velocity u_x while remaining constant over the flow line depends only on the ordinate

$$u_x = f_u(y). \quad (4)$$

The first two of the combined equations thus will assume the following form:

$$\frac{\partial \mathbf{P}}{\partial x} = F_x + N_\tau \frac{d^2 u_x}{dy^2}; \quad \frac{\partial \mathbf{P}}{\partial y} = F_y. \quad (5)$$

Considering that the projection of inter-component interaction force against on OY axis equals zero ($v_y = 0; u_y = 0$), it follows that $\frac{\partial \mathbf{P}}{\partial y} = 0$ and the pressure only changes along the duct

$$\mathbf{P} = f_p(x). \quad (6)$$

Then the first of combined equations (5) would transform into an ordinary second-order differential equation

$$\frac{d\mathbf{P}}{dx} = F_x + N_\tau \frac{d^2 u_x}{dy^2}, \quad (7)$$

that, as required by (4) and (6), is equivalent to the following combined equations

$$\frac{d\mathbf{P}}{dx} = \Pi; \quad F_x + N_\tau \frac{d^2 u_x}{dy^2} = \Pi, \quad (8)$$

where Π is a constant equal to $\Pi = (\mathbf{P}_k - \mathbf{P}_h)/l$, $\mathbf{P}_h, \mathbf{P}_k$ is the pressure at the beginning and at the end of a duct of length l .

It should be noted that, generally, $v = f(x)$ and the projection of the vector of inter-component interaction force onto OX depends on x and y . This fact contradicts the initial requirement (4). Hence, there is no sense in the supposition about plane-parallel character of injected airflow inside the duct with accelerated movement of material particles.

Uniform movement of particles should be supposed in order to eliminate this inconsistency. As that would significantly restrict the application of findings, let's consider just one special case where material velocity $v = v_0 - \text{const}$ greatly exceeds air velocity, and or generalized exponential distribution of particles results in

$$F_x \approx \beta_0 e^{-\left(\frac{y}{b}\right)^t} \cdot v_0^2 \quad (9)$$

and the equation (8) becomes

$$N_\tau \frac{d^2 u_x}{dy^2} = -\beta_0 v_0^2 e^{-\left(\frac{y}{b}\right)^t} + \Pi. \quad (10)$$

Under boundary conditions

$$u_x(b_0) = 0; \quad \left. \frac{du_x}{dy} \right|_{y=0} = 0 \quad (11)$$

the solution has the form

$$u_x = B_k \int_y^{b_0} \left(\int_0^y e^{-\left(\frac{y}{b}\right)^t} dy \right) dy - \Pi_k \frac{b_0^2 - y^2}{2}, \quad (12)$$

where b_0 is a dimensionless duct breadth variable; B_k, Π_k are dimensionless complexes

$$B_k = \frac{\beta_0 v_0^2}{N_\tau}; \quad \Pi_k = \frac{\Pi}{N_\tau}. \quad (13)$$

In particular, with particles uniformly distributed inside duct ($t \rightarrow \infty$)

$$u_x = (B_k - \Pi_k) \frac{b_0^2 - y^2}{2}. \quad (14)$$

In this case the airflow direction, being the same across the entire duct, is determined with a summation sign $B_k - \Pi_k$. $\Pi_k > B_k$ gives rise to a counterflow while $\Pi_k < B_k$ corresponds to a direct flow. A perfect analogy could be observed in this case with one-dimensional movement of material in a chute.

Air flow rate in this case would be determined by an obvious relation

$$q_s = 2 \int_0^{b_0} u_x dy = 2(B_k - \Pi_k) \frac{b_0^3}{3}. \quad (15)$$

When concentration of material is not constant throughout its cross-section but rather varies (e.g. according to exponential law, $t = 1$), at a certain Π_k the airflow could delaminate so that some air would flow downward (along the centerline with its greater concentration of particles) and the remainder would be displaced upward. Indeed, the solution for (14) at $t = 1$ would assume the form

$$u_x = B_k b(b_0 - y) - \Pi_k \frac{b_0^2 - y^2}{2} - B_k b^2 \left(e^{-\frac{y}{b}} - e^{-\frac{b_0}{b}} \right). \quad (16)$$

with

$$\frac{\Pi_k}{B_k} < 2 \left(\frac{b}{b_0} \right)^2 \cdot \left(\frac{b_0}{b} - 1 + e^{-\frac{b_0}{b}} \right) \quad (17)$$

the velocity $u_x(0) > 0$ along the centerline, corresponding to a direct flow zone.

Along the straight line $y = y_0$ where y_0 is the ordinate meeting the equation

$$B_k b(b_0 - y_0) = \Pi_k \frac{b_0^2 - y_0^2}{2} + B_k b^2 \left(e^{-\frac{y_0}{b}} - e^{-\frac{b_0}{b}} \right), \quad (18)$$

the velocity u_x becomes equal to zero. Finally, the $y_0 < y < b_0$ area manifests countercurrent airflow ($u_x < 0$).

In this case the straight line $y = y_0$ becomes a dividing line between direct flow and counterflow. The equality condition determining the first type of airflow is

$$q_s^\downarrow = \int_0^{y_0} u_x dy = B_k b \frac{2b_0 y_0 - y_0^2}{2} - \Pi_k \frac{3b_0^2 y_0 - y_0^3}{6} + B_k b^3 \left(e^{-\frac{y_0}{b}} - 1 + \frac{y_0}{b} e^{-\frac{b_0}{b}} \right), \quad (19)$$

while, for the second type, it would be

$$q_s^\uparrow = \int_{y_0}^{b_0} u_x dy = B_k b \frac{(b_0 - y_0)^2}{2} - \Pi_k (b_0 - y_0) \frac{2b_0^2 - b_0 y_0 - y_0^2}{6} + B_k b^3 \left[e^{-\frac{b_0}{b}} \left(1 + \frac{b_0 - y_0}{b} \right) - e^{-\frac{y_0}{b}} \right]. \quad (20)$$

3 ONE-DIMENSIONAL FLOW

Plane-parallel flow pattern considered before is extremely unlikely to appear in practice. Transverse overflow of air – the key necessary condition for such currents – is hardly conceivable. Solving the generalized problem analytically would pose insurmountable difficulties at $u_y \neq 0^*$. Nor is it easy to solve hydromechanics equations numerically due to nonlinearity [2]. A possible alternative approach may involve equations that bind cross-sectional averages of various flow parameters. As illustrated earlier, one-dimensional problems yield satisfactory outcomes often enough. Thus we could formulate a one-dimensional problem for a jet of loose matter confined to a duct with its wall set apart by the distance b_0 from the centerline. Let's denote the half-breadth of such a jet as b_n . Consequently, there would be two flows: air moving together with material inside a band $0 \leq y \leq b_n$ corresponding to an inner dual-component flow and air flowing through a gap between the wall and jet boundary surface corresponding to an outer single-component flow.

Let's suppose that falling particles are distributed uniformly across the jet

For the inner flow ($0 \leq y \leq b_n$) the equation would appear as

$$\frac{\partial}{\partial x} \int_0^{b_n} u_x^2 dy + u_y u_x \Big|_0^{b_n} = \frac{D}{\sqrt{2}\nu} \int_0^{b_n} (\nu - u_x)^2 dy - \frac{\partial}{\partial x} \int_0^{b_n} P dy + N_\tau \frac{\partial u_x}{\partial y} \Bigg|_{b_n}^{b_0} \quad (21)$$

For the outer flow ($b_n \leq y \leq b_0$) the equation would appear as

$$\frac{\partial}{\partial x} \int_{b_n}^{b_0} u_x^2 dy + u_y u_x \Big|_{b_n}^{b_0} = - \frac{\partial}{\partial x} \int_{b_n}^{b_0} P dy + N_\tau \frac{\partial u_x}{\partial y} \Bigg|_{b_n}^{b_0}. \quad (22)$$

To perform the averaging, suppose that pressure remains constant throughout the cross-section of the duct. Thus,

$$\int_0^{b_n} P dy \approx P b_n; \quad \int_{b_n}^{b_0} P dy = P(b_0 - b_n). \quad (23)$$

Air velocity in the inner flow, averaged by flow rate, will be designated using u while that in the outer flow will be designated using ω (positive direction matching the direction of OX axis):

$$\int_0^{b_n} u_x dy = b_n u; \quad \int_{b_n}^{b_0} u_x dy = (b_0 - b_n) \omega. \quad (24)$$

Positing that

$$\int_0^{b_n} u_x^2 dy \approx b_n u^2; \quad \int_{b_n}^{b_0} u_x^2 dy \approx (b_0 - b_n) \omega^2, \quad (25)$$

$$\int_0^{b_n} (\nu - u_x)^2 dy \approx b_n (\nu - u)^2 \quad (26)$$

and assuming normal admission of air on the boundary between inner and outer streams i.e.

* Due to presence of vertical boundaries along the flow this problem could not be reduced to studying self-similar airflow.

$$u_x(x, b_n) = 0; \quad \left. \frac{\partial u_x}{\partial y} \right|_{y=b_n} = 0, \quad (27)$$

further considering the consequence to flow symmetry,

$$u_y(x, 0) = 0; \quad \left. \frac{\partial u_x}{\partial y} \right|_{y=0} = 0, \quad (28)$$

and accounting for a frictional shear stress at the duct wall,

$$-\bar{\tau}_{cm} = N_\tau \left. \frac{\partial u_x}{\partial y} \right|_{y=b_0}; \quad \bar{\tau}_{cm} = \frac{\tau_{cm}}{\rho_2 c^2}, \quad (29)$$

integral relations (21) and (22) would lead us to the following system of ordinary differential equations:

$$\frac{du^2}{dx} = \frac{D}{\sqrt{2}\nu} (\nu - u)^2 - \frac{d\mathbf{P}}{dx} \text{ at } 0 \leq y \leq b_n, , \quad (30)$$

$$\frac{d\omega^2}{dx} = -\frac{d\mathbf{P}}{dx} - \varepsilon_\tau \text{ at } b_n \leq y \leq b_0, , \quad (31)$$

$$u + \omega(r-1) = u_0 + \omega_0(r-1) = u_m - \text{const}, \quad (32)$$

where

$$r = b_0 / b_n; \quad \varepsilon_\tau = \bar{\tau}_{cm} / (b_0 - b_n), , \quad (33)$$

The latter equation expresses a cross-sectional flow rate conservation law in a duct with impervious walls.

The equation (30) in view of (31) and (32) could be expressed in the following form, making it easier to integrate:

$$\frac{du^2}{dx} + \frac{2(u_m - u)}{(r-1)^2} \cdot \frac{du}{dx} - \varepsilon_\tau = \frac{D}{\sqrt{2}\nu} (\nu - u)^2, \quad (34)$$

or

$$\left[\frac{2r(r-2)}{(r-1)^2} u + \frac{2u_m}{(r-1)^2} \right] \frac{du}{dx} = \frac{D}{\sqrt{2}\nu} (\nu - u)^2 + \varepsilon_\tau. \quad (35)$$

This equation could be applied for analyzing the simplest case when $\nu = \nu_0 - \text{const}$ and forces of friction against duct walls are negligibly small. Equation (34) would thus become

$$\frac{du}{dx} = \frac{D(\nu_0 - u)^2}{\sqrt{2}\nu_0 \cdot R(r, u)}; \quad (36)$$

$$R(r, u) = 2[r(r-2)u + u_m]/(r-1)^2, \quad (37)$$

and resolve at initial conditions as follows: $u = u_h$ at $x = x_h$ would assume the form

$$\left[\frac{2r(r-2)}{(r-1)^2} v_0 + \frac{2u_m}{(r-1)^2} \right] \cdot \frac{u - u_n}{(v_0 - u)(v_0 - u_n)} + \frac{2r(r-2)}{(r-1)^2} \ln \frac{v_0 - u}{v_0 - u_n} = \frac{D}{\sqrt{2}v_0} (x - x_n). \quad (38)$$

Let's analyze the behavior of u and ω along the duct with different b_0/b_n ratios characterizing restriction of flow by duct walls. The following values will be assumed as known initial data:

$$u_n = u_0; \quad \omega_n = \omega_0 \quad \text{at } x_n = 0. \quad (39)$$

The relation (38) could be transformed into

$$\frac{D}{\sqrt{2}v_0} x = \left[\frac{2r(r-2)}{(r-1)^2} v_0 + \frac{2u_m}{(r-1)^2} \right] \cdot \frac{u - u_0}{(v_0 - u)(v_0 - u_0)} + \frac{2r(r-2)}{(r-1)^2} \ln \frac{v_0 - u}{v_0 - u_0} \quad (40)$$

or

$$\bar{x} = \left[\frac{2r(r-2)}{(r-1)^2} + \frac{2\bar{u}_m}{(r-1)^2} \right] \cdot \frac{\bar{u} - \bar{u}_0}{(1-\bar{u})(1-\bar{u}_0)} + \frac{2r(r-2)}{(r-1)^2} \ln \frac{1-\bar{u}}{1-\bar{u}_0}, \quad (41)$$

where

$$\bar{u}_m = u_m / v_0 = \bar{u}_0 + \bar{\omega}_0 (r-1); \quad \bar{u}_0 = u_0 / v_0; \quad \bar{\omega}_0 = \omega_0 / v_0; \quad \bar{u} = u / v_0; \quad \bar{x} = xD / (\sqrt{2}v_0). \quad (42)-(43)$$

The distance between the duct origin and a cross-section where the inner air flow velocity becomes equal to zero

$$u = u_m, \quad (45)$$

will be expressed using x_m . This cross-section will henceforth be named critical, and x_m will be regarded as initial run of the duct. In the critical section the continuity equation (32) would make the outer flow velocity equal to zero. Due to the equality condition (41) the relative length of the initial run will be

$$\bar{x}_m = \left[\frac{2r(r-2)}{(r-1)^2} + \frac{2\bar{u}_m}{(r-1)^2} \right] \cdot \frac{\bar{u}_m - \bar{u}_0}{(1-\bar{u}_m)(1-\bar{u}_0)} + \frac{2r(r-2)}{(r-1)^2} \ln \frac{1-\bar{u}_m}{1-\bar{u}_0}. \quad (46)$$

Fig.1 plots the dependence of this length on r in various initial conditions. As it can be seen, the value \bar{x}_m will rise both when the flow centerline is moved away from duct walls (with increasing r) and when initial velocities \bar{u}_0 and $\bar{\omega}_0$ are increased. Additional air volume is necessary to ensure increased air velocities.

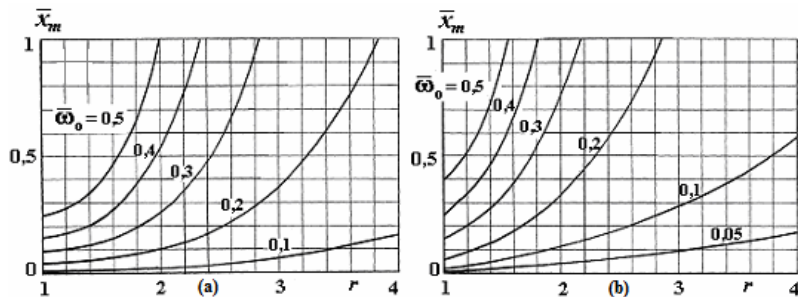


Figure 1: Relative length of the initial run as a function of flow restriction at $\bar{u}_0 = 0$ (a) and $\bar{u}_0 = 0.2$ (b)

Beyond the critical section lies a zone of upward outer flow ($\omega < 0$). As air moves further away from the critical section, the upward outer flow will experience increasing flow rates until a maximum is reached at a certain spot that will be named the extreme cross-section. As the equation (37) hints, the presence of an extreme cross-section is conditional on

$$R(r, u_e) = 0 \quad (47)$$

or

$$u_e = -u_m / (r(r-2)), \quad (u_e \leq v_0). \quad (48)$$

As we can see, in case of a downward initial flow in the duct it would only be possible at restriction degrees

$$r < 2. \quad (49)$$

The length of the zone $x_e - x_m$, (let's name it the initial eddy run length) is determined with the relation (41)

$$\bar{l}_u \equiv \bar{x}_e - \bar{x}_m = \left[\frac{2r(r-2)}{(r-1)^2} + \frac{2\bar{u}_m}{(r-1)^2} \right] \cdot \frac{\bar{u}_e - \bar{u}_m}{(1-\bar{u}_e)(1-\bar{u}_m)} + \frac{2r(r-2)}{(r-1)^2} \ln \frac{1-\bar{u}_e}{1-\bar{u}_m}. \quad (50)$$

The equality condition (41) determines changes in velocity on this run. Further velocity increases u become impossible because the function $R(r, u)$ turns negative and, therefore,

$$\frac{du}{dx} < 0, \quad (51)$$

i.e. air begins to escape the inner flow. Air flow rate in the outer counterflow decreases to zero in the next critical section.

The differential equation (36) in this case would be rewritten as

$$\frac{du}{dx} = -\frac{D(v_0 - u)^2}{\sqrt{2}v_0 |R(r, u)|}, \quad (52)$$

and its in the initial condition $u = u_e$ at $x=x_e$ would become

$$\bar{x}_e - \bar{x}_m = \left[\frac{2r(r-2)}{(r-1)^2} + \frac{2\bar{u}_m}{(r-1)^2} \right] \cdot \frac{\bar{u}_e - \bar{u}_m}{(1-\bar{u}_e)(1-\bar{u}_m)} + \frac{2r(r-2)}{(r-1)^2} \ln \frac{1-\bar{u}_e}{1-\bar{u}_m}. \quad (53)$$

The length $\bar{x}_m - \bar{x}_e$, to be named the final eddy run length, is determined with the relation

$$\bar{l}_\kappa \equiv \bar{x}_m - \bar{x}_e = \left[\frac{2r(r-2)}{(r-1)^2} + \frac{2\bar{u}_m}{(r-1)^2} \right] \cdot \frac{\bar{u}_m - \bar{u}_e}{(1-\bar{u}_m)(1-\bar{u}_e)} + \frac{2r(r-2)}{(r-1)^2} \ln \frac{1-\bar{u}_m}{1-\bar{u}_e}. \quad (54)$$

As it could be seen from a comparison of the result with the equality condition (447),

$$\bar{l}_u = \bar{l}_\kappa, \quad (55)$$

that could be explained by a constant velocity of falling particles. The total length of an eddy, resulting from an obvious relation

$$\bar{l} = 2\bar{l}_u = 2\bar{l}_\kappa, \quad (56)$$

decreases with decreasing initial airflow velocity in inner and outer flows (Fig.2) with relative duct size kept constant. Lower values of r would produce more eddies in the outer flow (Fig.3). Absolute velocity in a flow of particles fluctuates around average value. At the limit $r \rightarrow 1$ it becomes equal to u_0 . We have a case of a one-dimensional problem for a chute. The other extreme case could be observed with increasing r . Increasing distances between the flow and duct wall reduces the occurrence of eddies until counterflow could only be observed near the end of the duct. Finally, further increases of r result in exclusively direct flow of air along the entire duct with increasing velocities in the inner flow and decreasing velocities in the outer flow. The limit case of $r \rightarrow \infty$ corresponds to a free flow of particles whose air injection at $v = v_0 - \text{const}$ could be described in view of (36) and (37) by the equation

$$\frac{du}{dx} = \frac{D}{\sqrt{2}v_0} \cdot \frac{(v_0 - u)^2}{2u}, \quad (57)$$

that resolves at $u = u_0$ at $x = 0$ as

$$\frac{v_0}{v_0 - u} - \frac{v_0}{v_0 - u_0} + \ln \frac{v_0 - u}{v_0 - u_0} = \frac{D}{2\sqrt{2}v_0} x. \quad (58)$$

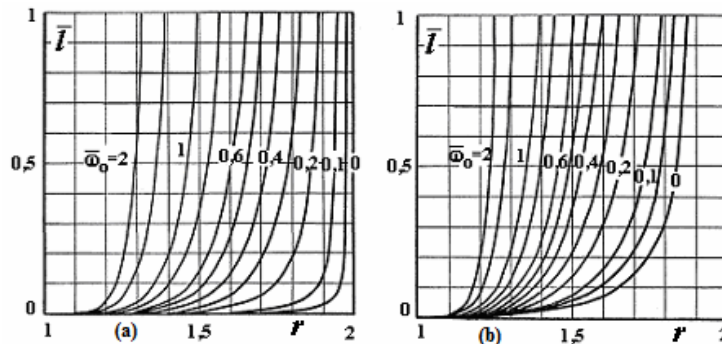


Figure 2: Variation in relative eddy length as a function of restricting the flow of loose matter at $\bar{u}_0 = 0$ (a) and $\bar{u}_0 = 0.2$ (b)

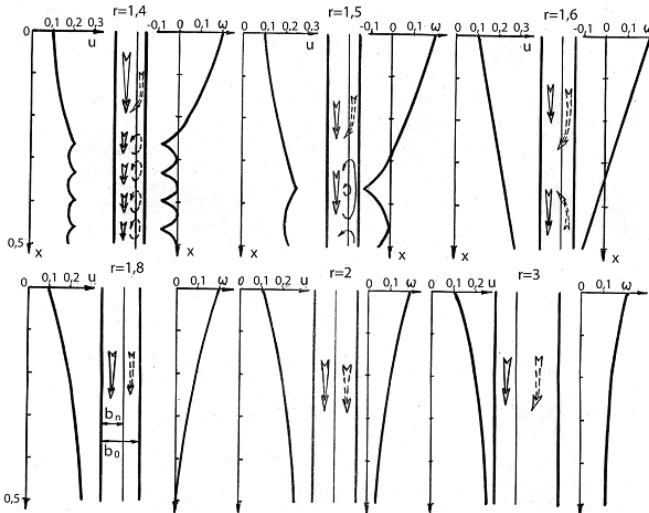


Figure 3: Variation in relative air velocity inside duct for uniformly distributed falling particles of loose matter ($D = \sqrt{2}$; $v_0 = 0.5$; $u_0 = 0.1$ and with $\omega_0 = 0.2$)

Fig.4 shows how duct breadth may change final velocity of material injected from the duct with the flow. This change is notably asymptotic in nature. Velocity almost stabilizes when duct walls become spaced by $5 \div 7 b_n$. Walls produce no braking effect on the velocity of injected air. As material becomes closer to the flow, the quantity of injected air noticeably drops. This happens due to impaired conditions for air overflowing from the outer into the inner flow.

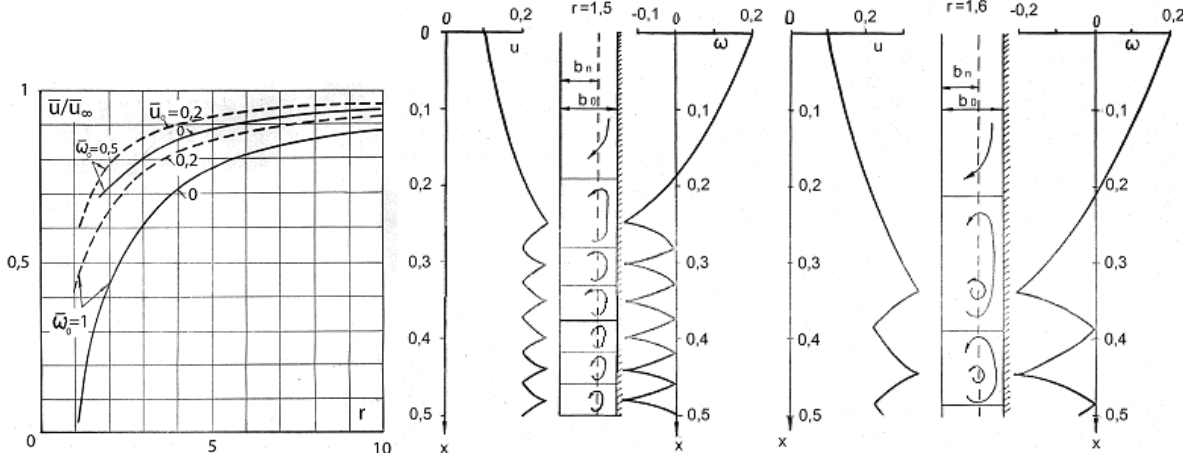


Figure 4: Variation in relative velocity of injected air at the end of the duct ($\bar{x} = 0,5$) as a function of flow restriction (\bar{u}_∞ is the injected airflow velocity at the end of the jet at $r \rightarrow \infty$)

Figure 5: Variation in relative air velocity inside duct for linearly accelerated falling particles of loose matter ($D = \sqrt{2}$; $v_0 = 0.5$; $u_0 = 0,1$; $\omega_0 = 0,2$)

A similar flow pattern could be observed in case of linearly accelerated particles of loose matter. The differential equation (46) describing changes in air velocity in the inner flow at negligibly small frictional forces at duct walls could be rewritten as

$$(a_1 u + b_1) \frac{du}{dv} = \frac{D}{\sqrt{2}} (v - u)^2, \quad a_1 = 2r(r-b)/(r-1)^2; \quad b_1 = 2u_m/(r-1)^2. \quad (59)-(60)$$

Substituting for variables

$$\hat{v} = D(v a_1 + b_1) / (\sqrt{2} a_1^2); \quad \hat{u} = D(u a_1 + b_1) / (\sqrt{2} a_1^2), \quad (61)$$

the equation (59) could be reduced to the form

$$\hat{u} \frac{d\hat{u}}{d\hat{v}} = (\hat{v} - \hat{u})^2, \quad (62)$$

considered by us when solving the problem of air injection with a free jet.

As an example we can plot calculated ratios using the approximation

$$(v - u)^2 \approx v^2 \left(1 - \frac{u}{v}\right)^2, \quad \left(1 - \frac{u}{v}\right)^2 \approx \left(1 - \frac{u}{v}\right)^2, \quad (63)$$

producing satisfactory results for a free jet. The equation (59) would be easy to integrate in view of this approximation. At initial conditions $u = u_h$, $v = v_h$ at $x = x_h$ it holds that

$$a_1 \frac{u^2 - u_h^2}{2} + b_1 (u - u_h) = \gamma_a \frac{D}{\sqrt{2}} \cdot \frac{v^3 - v_h^3}{3v^2} (v - u)^2, \quad \gamma_a = \pm 1. \quad (64)$$

Whence we can determine

$$u = \frac{B}{2A} \left(\sqrt{1 + \frac{4AC}{B^2}} - 1 \right), \quad (65)$$

where

$$A = a_1 / 2 - z; B = b_1 + 2vz; \quad C = a_1 u_n^2 / 2 + b_1 u_n + v^2 z; \quad z = \gamma_a D \cdot (v^3 - v_n^3) / (\sqrt{2} \cdot 3v^2); v = \sqrt{2x + v_0^2}. \quad (66)-(68)$$

Calculation should proceed as follows. The change in injected air velocity on the initial run is determined:

$$x_n = 0; x_m \geq x \geq x_n; \gamma_a = 1; u_n = u_0; v_n = v_0. \quad (69)$$

The formula (65) is used to calculate velocity u . Its value grows on this section from u_0 to u_m . By further increasing x we transition into the initial run of the first eddy. Without changing initial values of u_n, v_n, x_n we end up with $x_m \leq x \leq x_e, u_m \leq u \leq u_e = -u_m / [r(r-2)]$, if $r < 2$ (the center of the eddy will not be reachable with $r \geq 2$). Further increases of x lead to a transition into the final run of the first eddy. Changes in velocity u are determined by the same relation (65) with different initial values

$$v_n = v_{ne} = \sqrt{2x_e + v_0^2}; \quad u_n = u_e; \quad \gamma_a = -1. \quad (70)$$

In this area the velocity u decreases from u_e down to u_m (as x increases from x_e to x'_m). The initial run of the second eddy occurs here. Changes in the velocity u on this spot could be determined using the formula (65), adjusted for different initial conditions

$$x_n = x'_m; \quad v_n = \sqrt{2x'_m + v_0^2}; \quad u_n = u_m; \quad \gamma_a = 1. \quad (71)$$

Velocity increases again from u_m to u_e . After that, the final run of the second eddy begins, so that initial conditions must be adjusted again in order to calculate velocities.

$$x_n = x'_e; \quad v_n = \sqrt{2x'_e + v_0^2}; \quad u_n = u_e; \quad \gamma_a = -1. \quad (72)$$

The calculation procedure is repeated. As it can be seen, $\gamma_a = +1$ should be posited at initial runs of eddies while $\gamma_a = -1$ should be posited at final runs. These runs differ in length owing to equal acceleration of the particle flow. Unlike the case of uniform motion considered earlier, the initial run is longer than the final run and the second eddy is longer overall than the first one. This becomes evident on Fig.5 showing calculated flow patterns for a jet in a duct using the same initial parameters that were used to produce the flow pattern for a uniformly moving flow of loose matter (Fig.3).

For airflows inside a cylindrical duct where a stream of falling particles is located coaxially, integral dynamics equations could be written based of relations (72), (33) as follows:

$$\frac{\partial}{\partial x} 2\pi \int_0^{r_n} u_x^2 r dr + 2\pi r u_r u_x \Big|_0^{r_n} = \frac{D}{\sqrt{2}v} 2\pi \int_0^{r_n} (v - u_x)^2 r dr - \frac{\partial}{\partial x} \int_0^{r_n} 2\pi P r dr + N_\tau 2\pi r \frac{\partial u_x}{\partial r} \Big|_0^{r_n} \text{ at } 0 \leq r \leq r_n; \quad (73)$$

$$\frac{\partial}{\partial x} 2\pi \int_{r_n}^{r_0} u_x^2 r dr + 2\pi r u_r u_x \Big|_{r_n}^{r_0} = -\frac{\partial}{\partial x} 2\pi \int_{r_n}^{r_0} P r dr + N_\tau 2\pi r \frac{\partial u_x}{\partial r} \Big|_{r_n}^{r_0} \quad (74)$$

at $r_n \leq r \leq r_0$, where r_n, r_0 are dimensionless radii of particles and duct boundaries.

Based on the same assumptions for simplification, namely that the static pressure is constant throughout the cross-section of the duct

$$\int_0^{r_n} \mathbf{P} r dr = \mathbf{P} \frac{r_n^2}{2}; \quad \int_{r_n}^{r_0} \mathbf{P} r dr = \mathbf{P} \frac{r_0^2 - r_n^2}{2}; \quad (75)$$

air admission at the boundary of outer and inner channels occurs radially

$$u_x(x, r_n) = 0; \quad \left. \frac{\partial u_x}{\partial r} \right|_{r=r_n} = 0; \quad (76)$$

owing to axial symmetry of currents and impermeability of duct walls

$$u_r(x, 0) = 0; \quad \left. \frac{\partial u_x}{\partial r} \right|_{r=0} = 0; \quad u_r(x, r_0) = 0; \quad (77)$$

in presence of shearing stress at duct walls

$$-\bar{\tau}_w = N_\tau \left. \frac{\partial u_x}{\partial r} \right|_{r=r_0}, \quad \bar{\tau}_w = \tau_w / (\rho_2 c^2). \quad (78)$$

by introducing averages over cross-sections of the inner and outer flows

$$2\pi \int_0^{r_n} u_x r dr = \pi r_n^2 u; \quad 2\pi \int_{r_n}^{r_0} u_x r dr = \pi (r_0^2 - r_n^2) \omega, \quad 2\pi \int_0^{r_n} u_x^2 r dr \approx \pi r_n^2 u^2; \quad 2\pi \int_{r_n}^{r_0} u_x^2 r dr \approx \pi (r_0^2 - r_n^2) \omega^2, \quad (79)-(80)$$

$$2\pi \int_0^{r_n} (v - u_x)^2 r dr \approx \pi r_n^2 (v - u)^2. \quad (81)$$

integral relations are reduced to differential equations of one-dimensional streams

$$\frac{du^2}{dx} = \frac{D}{\sqrt{2}\nu} (v - u)^2 - \frac{d\mathbf{P}}{dx} \text{ at } 0 \leq r \leq r_n, \quad \frac{d\omega^2}{dx} = -\frac{d\mathbf{P}}{dx} - \varepsilon_\tau \text{ at } r_n \leq r \leq r_0, \quad (82)-(83)$$

$$u + \omega(n^2 - 1) = u_0 + \omega_0(n^2 - 1) = u_m, \quad (84)$$

where n is the ratio between radii of boundaries surrounding the jet of material

$$n = r_0 / r_n; \quad \varepsilon_\tau = \bar{\tau}_w 2r_0 / (r_0^2 - r_n^2) \dots \quad (85)-(86)$$

Therefore, combined equations for an axially symmetric flow would differ from similar equations of a plane problem only in the equation for airflow (84) that depends on relative duct size, squared. The resulting numerical relationships of the planar problem are valid for axially symmetric problem as well. In this case it is just enough to replace r with n^2 in formulations.

These findings are in a qualitative and quantitative agreement with experimental data. Indeed, the described turbulent flows were observed for the first time by A.S. Serenko who researched currents in a sand layer moving along the bottom wall in a one-meter long square pipe [3]. It was noted that air countercurrents occurred not always but only at certain position of the upper (with respect to flowing material) duct wall.

With a clearance height of 40 mm unidirectional current of injected air was observed in the duct. In this case flowing particles fill the entire cross-section of the duct ($r \rightarrow 1$). Countercurrents arise when duct clearance height is increased. Notably, air moves in line with particle layer at the beginning but reverses into a counterflow toward the end of the duct. A similar pattern was reported by O.D. Neykov and Ya.I. Zilberberg researching aerodynamics of streams of iron powder in a tilted chute [4].

A.S. Serenko's experiments have shown that the distances from duct inlet to the point where air countercurrent arises could be brought down virtually to zero by obstructing the

inlet with a gate valve. In other words, the initial run becomes shorter as the original flow rate of outer flow diminishes – this agrees comfortably with our findings.

It should be noted that circulation inside a duct filled with flowing material throughout the entire cross-section (such circulation could be named “natural”) is likely only in exceptional cases. Natural circulation is hindered by a number of factors. First of all, when lumpy and grainy are handled, particles occupy virtually the entire clearance area of ducts, and the inherent transverse gradient of particle concentration deforms longitudinal velocity profile of injected air rather slightly. When aspiration develops in a descending pattern in a hollow duct area not filled with material, there is an outside positive gradient precluding the occurrence of a countercurrent. An opposite effect would be observed when handling heated material: a thermal head produced by inter-component heat exchange will promote formation of natural circulation.

4 CONCLUSIONS

It was demonstrated that when a free stream of particles is enclosed with impenetrable walls air inflow is hindered and, hence, closed circulation flows occur in $1 < r < 2$. As far as the distance between the walls and the stream surface becomes shorter ($r \rightarrow 1$) the length of these whirls and the velocity variation amplitude in the external stream is reduced to zero while flow velocity in a stream of particles tends to a constant value equal to the initial velocity. As far as the distance to the channel walls becomes longer the whirls become longer too and with $r >$ there is only an external reverse flow which area is decreased inversely as r .

It was demonstrated that when the channel section is partially filled with a stream of particles averaged integral equations for a boundary layer may be used as a basis for making one-dimensional equations that describe the motion of two-component stream (internal flow) and the air flow in a cavity limited to the stream surface and the channel walls (external flow). The general solutions of these equations may be used to derive particular solutions for one-dimensional problems regarding a chute with the pseudo-uniform distribution of particles and regarding a free jet of freely-falling particles which creates the base for development of a universal methodology of computation of the induced air volumes.

The reported study was partly supported by RFBR, research project No. 14-41-08005r_ofi_m and the President of the Russian Federation, project MK-103.2014.1.

REFERENCES

- [1] Logachev, I.N. and K.I. Logachev. *Industrial Air Quality And Ventilation: Controlling Dust Emissions*. CRC Press, Boca Raton, (2014).
- [2] Roach, P. Computational fluid dynamics. M: Mir, 1980. p. 616.
- [3] Serenko, S. Dust control of the main flows of solid material reprocessing: Abstract Thesis ... Cand.Sc. (Engineering) Kiev (1952).
- [4] O.D. Neykov, Ya.I. Zilberberg. Study of air mechanics of closed chutes with powder materials gravity flow. *Prevention of a sudden combustion of powders and explosions of gas-dispersion systems*. Kiev: Naukova dumka (1975), pp: 196-203.

A MASTER EQUATION FOR FORCE DISTRIBUTIONS IN POLYDISPERSE FRICTIONAL PARTICLES

Kuniyasu Saitoh¹, Vanessa Magnanimo¹, and Stefan Luding¹

¹ Faculty of Engineering Technology, MESA+, University of Twente
Drienerlolaan 5, 7522 NB, Enschede, The Netherlands

Key words: Friction, Granular Materials, Force Chains, Quasi-static Deformations, Stochastic Model, DEM

Abstract. An incremental evolution equation, i.e. a Master equation in statistical mechanics, is introduced for force distributions in polydisperse frictional particle packings. As basic ingredients of the Master equation, the conditional probability distributions of particle overlaps are determined by molecular dynamics simulations. Interestingly, tails of the distributions become much narrower in the case of frictional particles than frictionless particles, implying that correlations of overlaps are strongly reduced by microscopic friction. Comparing different size distributions, we find that the tails are wider for the wider distribution.

1 INTRODUCTION

Quasi-static deformations of soft particles, e.g. glasses, colloids, and granular materials, have been widely investigated because of their importance in industry and science. However, their macroscopic behaviors are still not fully understood due to disordered configurations and complex dynamics [1]. At the microscopic scale, their mechanical response is probed as a reconstruction of the force-chain network [2], where non-affine displacements of particles cause a complicated restructuring of the network including also opening and closing contacts. If a macroscopic quantity, e.g. stress tensor, is defined as a statistical average in the force-chain, its response to quasi-static deformations is governed by the change of probability distribution function (PDF) of forces. Therefore, the PDFs in soft particle packings have practical importance such that many theoretical studies [3, 4] have been devoted to determine their functional forms observed in experiments [5] and simulations [6].

Recently, we have proposed a Master equation for the PDFs as a stochastic approach towards a microscopic theory for quasi-static deformations of two-dimensional bidisperse frictionless particles [7]. The Master equation can reproduce stochastic evolution of the PDFs under isotropic (de)compressions, where the conditional probability distributions (CPDs) for the Master equation fully encompass the statistics of microscopic changes

of force-chain networks. In addition, any changes of macroscopic quantities constructed from the moments of forces can be predicted by the Master equation.

In this paper, we generalize our stochastic approach towards wider four-disperse size distributions and include friction in the contacts. We determine the CPDs from MD simulations and compare them with the cases of polydisperse frictionless and bidisperse frictionless particles. First, we explain our MD simulations in Sec. 2. Then, we show our results in Sec. 3 and conclude in Sec. 4.

2 METHOD

We use MD simulations of two-dimensional four-disperse mixtures of frictional soft particles. The number of constituents (N_1 , N_2 , N_3 , and N_4) and the size distribution are the same with those used in the experiments of wooden cylinders [8] as listed in Table 1, where the mass, m , is identical in simulations to be used for the unit of mass. The normal force between the particles in contact is given by $f_{ij}^n = k_n x_{ij} - \eta_n \dot{x}_{ij}$ with a normal stiffness, k_n , and normal viscosity coefficient, η_n . Here, an overlap between the particles i and j is introduced as

$$x_{ij} = R_i + R_j - d_{ij} \quad (1)$$

with an interparticle distance, d_{ij} , and the particles' radii, R_i and R_j . Thus, the relative speed in the normal direction is given by its time derivative, \dot{x}_{ij} . The tangential force is introduced as $f_{ij}^t = k_t y_{ij} - \eta_t \dot{y}_{ij}$ which is switched to the sliding friction, $f_{ij}^s = -\mu |f_{ij}^n|$, when the tangential force exceeds the critical value, i.e. if $|f_{ij}^t| > \mu |f_{ij}^n|$, where $k_t = k_n/2$, $\eta_t = \eta_n/4$, and μ are a tangential stiffness, tangential viscosity coefficient, and friction coefficient, respectively. Here, y_{ij} and \dot{y}_{ij} are a relative displacement and speed in the tangential direction, respectively (see the details in Ref. [9]).

To make static packings of $N (= N_1 + N_2 + N_3 + N_4) = 1872$ particles, we randomly distribute them in a $L \times L$ square periodic box, where no particle touches others and the friction coefficient is set to zero, $\mu = 0$ (i.e. we use frictionless particles during the preparation of static packings). Then, we rescale every radius as $R_i(t + \delta t) = [1 + \{\bar{x} - x_m(t)\}/\lambda] R_i(t)$ ($i = 1, \dots, N$), where t , δt , \bar{x} , and $x_m(t)$ are time, an increment of time, a target value of averaged overlap, and the averaged overlap at time t , respectively. Here, we use a long length scale $\lambda = 10^2 \bar{\sigma}$ with the mean diameter in the final state, $\bar{\sigma}$, to rescale each radius gently¹. During the rescaling, each radius increases if the averaged overlap is smaller than the target value, $x_m(t) < \bar{x}$, and vice versa, so that the averaged overlap will finally converge to \bar{x} . Note that neither particle masses nor the ratios between different diameters change during the rescaling, i.e. $\sigma_i(t + \delta t)/\sigma_j(t + \delta t) = \sigma_i(t)/\sigma_j(t)$. We stop the rescaling when every acceleration of particles drops below a threshold, $10^{-6} k_n \bar{\sigma}/m$, and assume that the system is static.

¹We confirmed that static packings prepared with longer length scales, $\lambda = 10^3 \bar{\sigma}$ and $10^4 \bar{\sigma}$, give the same results concerning their power-law behaviors, i.e. *critical scaling*, near jamming [10], while we cannot obtain the same results with a shorter length scale, $\lambda = 10 \bar{\sigma}$.

Figure 1(a) is a snapshot of our simulation, where the system is static with the averaged overlap, $\bar{x} = 3 \times 10^{-6} \bar{\sigma}$, and each color corresponds to each constituent as listed in Table 1. Figure 1(b) shows the complete Delaunay triangulation (DT) of the same packing in Fig. 1(a), where the red solid lines represent force-chain networks, while the blue solid lines connect the nearest neighbors without contacts. In our simulations, the distances from jamming are determined by the critical scaling of averaged overlap, $\bar{x} = A(\phi - \phi_J)$ [10], where the critical amplitude is found to be $A \simeq 0.25\bar{\sigma}$ as shown in Fig. 2(a). We also confirm other critical scalings of the static pressure divided by the normal stiffness (Fig. 2(b)) and the first peak value in radial distribution function of scaled distance (Fig. 2(c)), where we find that the power law dependence on the distance from jamming are given by $p/k_n = 1.25 \times (\phi - \phi_J)^{1.04}$ and $g_1 = 0.31(\phi - \phi_J)^{-1}$, respectively² [10].

Then, we switch the friction coefficient to $\mu = 0.5$ and apply an isotropic compression to the prepared packings by multiplying every diameter by $\sqrt{1 + \delta\phi/\phi}$ such that the area fraction increases from ϕ to $\phi + \delta\phi$. After compression, we relax the system until every acceleration of particles drops below the threshold again.

Table 1: The number of particles per species, N_s , diameters, σ_s , and masses, m_s , of the four kinds of particles ($s = 1, 2, 3, 4$) resembling values used in experiments with wooden cylinders in Ref. [8]. Each color in Fig. 1 are also listed in the last column.

s	N_s	σ_s/σ_4	m_s/m_4	colors
1	807	0.3	1.0	green
2	434	0.6	1.0	red
3	414	0.8	1.0	blue
4	217	1.0	1.0	gray

3 RESULTS

In this section, we introduce a Master equation for the PDFs of forces as a stochastic description of microscopic changes of force-chain networks. First, we study microscopic responses of force-chain networks to isotropic compressions (Sec. 3.1), where we describe mean values and fluctuations of overlaps in terms of applied strain increments and distances from jamming (Sec. 3.2). We then introduce a Master equation (Sec. 3.3) and determine transition rates for the Master equation (Sec. 3.4).

3.1 Microscopic response

At the microscopic scale in soft particle packings, the mechanical response to quasi-static deformations is probed as reconstruction of force-chain networks, where complicated

²Here, p/k_n is dimensionless in two-dimension and the scaled distances in radial distribution functions are defined as $r \equiv d_{ij}/(R_i + R_j)$.

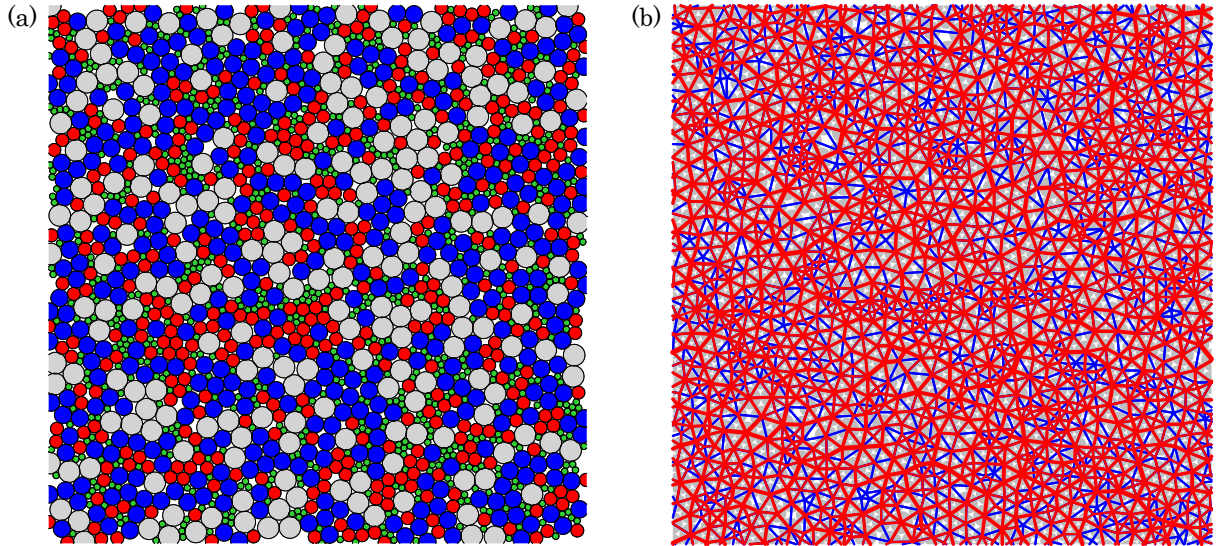


Figure 1: (Color online) (a) A static particle packing with an averaged overlap, $\bar{x} = 3 \times 10^{-6} \bar{\sigma}$, where the total number of particles is $N = 1872$. (b) The complete Delaunay triangulation (DT) of the static packing in (a): The red solid lines are equivalent to force-chains, where their widths are proportional to the magnitudes of contact forces. The blue solid lines connect the nearest neighbors without contacts. The gray circles represent the particles.

particle rearrangements cause the recombination of force-chains including also opening and closing contacts. To take into account such changes in structure, we employ the complete Delaunay triangulation (DT) of static packings as shown in Fig. 1(b), where not only the particles in contacts, but also the nearest neighbors without contacts, i.e. *virtual contacts*, are connected by Delaunay edges. We then generalize the definition of “overlaps” from Eq. (1) to

$$x_{ij} \equiv R_i + R_j - D_{ij} , \quad (2)$$

where D_{ij} is the Delaunay edge length and the overlaps between particles in virtual contacts ($R_i + R_j < D_{ij}$) are defined as negative values. Because the DT is unique for each packing, contacts and virtual contacts are uniquely determined.

If we apply an isotropic *affine* compression to the system, every generalized overlap, Eq. (2), (not only contacts, but also virtual contacts) changes to

$$x_{ij}^{\text{affine}} = x_{ij} + \frac{D_{ij}}{2\phi} \delta\phi , \quad (3)$$

where we neglected the higher order terms proportional to $x_{ij}\delta\phi$ and $\delta\phi^2$. However, the particles are randomly arranged and the force balance is broken for each particle by the affine deformation. Therefore, the system relaxes to a new static state, where non-affine displacements of particles cause complex changes of contacts including opening and closing contacts. After the relaxation, overlaps change to new values, $x'_{ij} \neq x_{ij}^{\text{affine}}$, that is *non-affine responses* of overlaps.

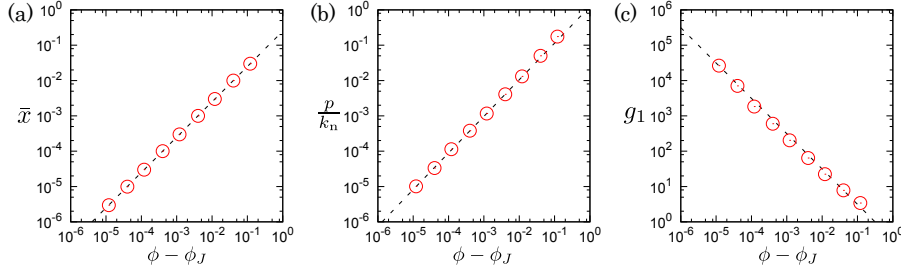


Figure 2: (Color online) Double logarithmic plots of the (a) averaged overlap, \bar{x} , (b) static pressure scaled by the normal stiffness, p/k_n , and (c) first peak of radial distribution function for scaled distance, g_1 , where the dotted lines are power law fittings, (a) $\bar{x} = 0.25\bar{\sigma}(\phi - \phi_J)$, (b) $p/k_n = 1.25 \times (\phi - \phi_J)^{1.04}$, and (c) $g_1 = 0.31(\phi - \phi_J)^{-1}$, respectively.

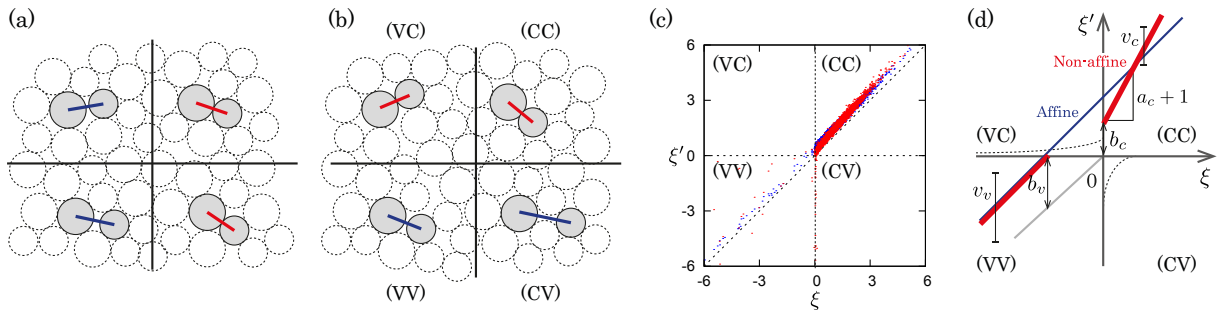


Figure 3: (Color online) (a) and (b): Sketches of static packings (a) before and (b) after (de)compression, where the red and blue solid lines represent contacts and virtual contacts, respectively. The four kinds of transitions, (CC) contact-to-contact, (VV) virtual-to-virtual, (CV) contact-to-virtual, and (VC) virtual-to-contact, are displayed. (c) A scatter plot of scaled overlaps, where the red and blue dots are ξ' and ξ^{affine} plotted against ξ , respectively. (d) A schematic picture of affine and non-affine responses of scaled overlaps, where the blue and red solid lines represent ξ^{affine} (in average) and the linear functions, $m_s(\xi)$, respectively. The slope in (CC), a_c , and all the dimensionless lengths, b_s and v_s , are proportional to γ , while the slope in (VV) is negligible, $a_v \simeq 0$.

As shown in Figs. 3(a) and (b), there are only four kinds of transitions from x_{ij} to x'_{ij} : A positive overlap, $x_{ij} > 0$, remains as positive, $x'_{ij} > 0$, or a negative overlap, $x_{ij} < 0$, stays in negative, $x'_{ij} < 0$, where they do not change their signs and thus contacts are neither generated nor broken. We call these changes “*contact-to-contact (CC)*” and “*virtual-to-virtual (VV)*”, respectively. The other cases are that a positive overlap changes to a negative one and a negative overlap becomes positive, where existing contacts are broken and new contacts are generated, respectively. We call these changes opening and closing contacts, or in analogy to the above, “*contact-to-virtual (CV)*” and “*virtual-to-contact (VC)*”, respectively.

In the following, we scale the generalized overlaps by the averaged overlap before compression such that scaled overlaps before compression, after affine deformation, and after relaxation are introduced as $\xi \equiv x_{ij}/\bar{x}$, $\xi^{\text{affine}} \equiv x_{ij}^{\text{affine}}/\bar{x}$, and $\xi' \equiv x'_{ij}/\bar{x}$, respectively

(we omit the subscript, ij , after the scaling). From Eq. (3) and the critical scaling, $\bar{x} = A(\phi - \phi_J)$, the scaled overlap after affine deformation is found to be

$$\xi^{\text{affine}} = \xi + B_a \gamma \quad (4)$$

which is a *linear function* of ξ with an offset, $B_a \gamma \equiv (D_{ij}/2A\phi) \gamma$, proportional to the scaled strain increment, $\gamma \equiv \delta\phi / (\phi - \phi_J)$. However, the scaled overlap after non-affine deformation, ξ' , fluctuates around mean due to complicated particle rearrangements during the relaxation.

3.2 Mean and fluctuation

To describe scaled overlaps after non-affine deformation, ξ' , we measure their mean and fluctuations through scatter plots. Figure 3(c) displays the scatter plot, where the four different transitions under compression are mapped onto four regions: (CC) $\xi, \xi' > 0$, (VV) $\xi, \xi' < 0$, (CV) $\xi > 0, \xi' < 0$, and (VC) $\xi < 0, \xi' > 0$, respectively. In this figure, overlaps after affine deformation are described by the *deterministic* equation (4), while those after non-affine deformation distribute around *mean values* with finite *fluctuations*. The differences between affine and non-affine responses are always present, but not visible if the applied strain is small or the system is far from jamming, i.e. if $\gamma \ll 1$, while ξ' deviates more from ξ^{affine} and data points are more dispersed if $\gamma \gg 1$.

In the same way as affine response, Eq. (4), we describe the mean values of ξ' in (CC) and (VV) regions by linear functions of ξ ,

$$m_s(\xi) = (a_s + 1)\xi + b_s , \quad (5)$$

where the subscripts, $s = c$ and v , represent the mean values in (CC) and (VV), respectively. We also introduce standard deviations of ξ' from their means as v_s (which are almost independent of ξ). Then, the systematic deviation from the affine response is quantified by the coefficients, a_s , b_s , and v_s , as summarized in Fig. 3(d). Note that the affine response, Eq. (4), is obtained if $a_s = v_s = 0$ and $b_s = B_a \gamma$. Except for $a_v \simeq 0$, all the coefficients *linearly* increase with the scaled strain increment (Fig. 4), where all data with a wide variety of $\delta\phi$ and $\phi - \phi_J$ collapse onto linear scalings,

$$a_s = A_s \gamma , \quad b_s = B_s \gamma , \quad v_s = V_s \gamma , \quad (6)$$

between the fitting range, $10^{-6} \leq \gamma \leq 5 \times 10^{-3}$, with the scaling amplitudes, A_s , B_s , and V_s , listed in Table 2. We observe that $a_v \simeq 0$ and $B_v \approx B_a$ ($\simeq 1.3$ in average) such that virtual contacts almost behave affine in average except for their huge fluctuations ($V_v \gg V_c$). In contrast, B_c is always smaller than B_a such that $m_c(\xi)$ intersects ξ^{affine} at $\xi^* = (B_a - B_c)/A_c \simeq 1.3$, which is independent of γ . This leads to small responses, $\xi' < \xi^{\text{affine}}$, of small overlaps, $\xi < \xi^*$, and vice versa, implying preferred tangential and hindered normal displacements as a sign of non-affine deformations [11].

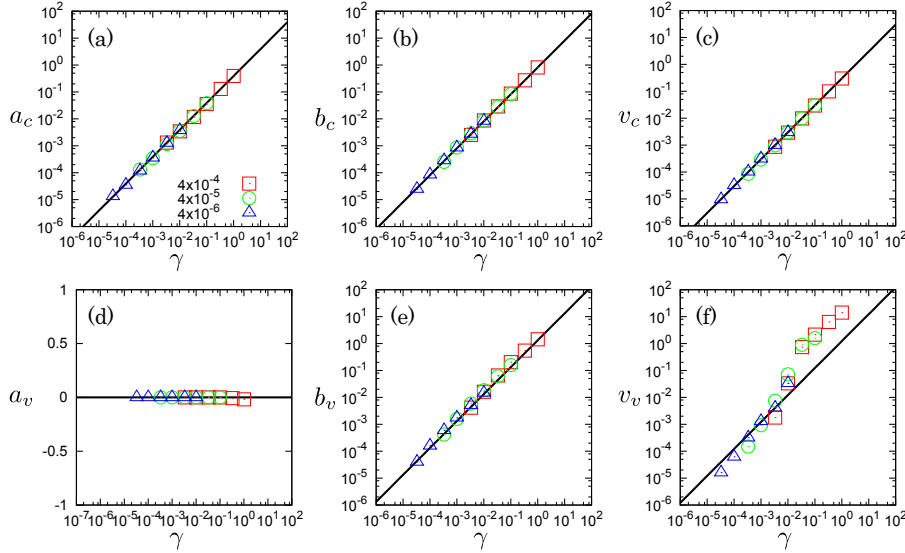


Figure 4: (Color online) Double logarithmic plots of the coefficients for mean values and fluctuations of scaled overlaps as functions of the scaled strain increment, (a) a_c , (b) b_c , (c) v_c , (e) b_v , and (f) v_v , and a semi-logarithmic plot of (d) a_v , where we apply strain increments $\delta\phi = 4 \times 10^{-4}$, 4×10^{-5} , and 4×10^{-6} (as indicated by the different symbols in the legend of (a)) to the static packings with $\phi - \phi_J = 1.2 \times 10^{-1}$, 4×10^{-2} , 1.2×10^{-2} , 4×10^{-3} , 1.2×10^{-3} , and 4×10^{-4} . The solid lines represent the linear scalings, Eq. (6), between the fitting range, $10^{-6} \leq \gamma \leq 5 \times 10^{-3}$.

In contrast to (CC) and (VV), the data of ξ' in (VC) and (CV) are concentrated in narrow regions (the inside of the dashed lines in Fig. 3(d)), whereas ξ^{affine} linearly increases with ξ in (VC) and there is no data of ξ^{affine} in (CV), i.e. affine responses do not generate opening contacts.

Table 2: Scaling amplitudes in Eq. (6), A_s , B_s , and V_s , for polydisperse frictional particles. The q -indices for the CPDs in (CC) and (VV), where q_s^{BL} , q_s^{PL} , and q_s^{PN} are the q -indices for bidisperse frictionless particles [7], polydisperse frictionless particles, and polydisperse frictional particles, respectively.

s	A_s	B_s	V_s	q_s^{BL}	q_s^{PL}	q_s^{PN}
c	0.39	0.81	0.30	1.13	1.72	1.19
v	0.00	1.32	1.22	1.39	1.96	1.09

3.3 Master equation

The reconstruction of force-chain networks attributed to the changes, (CC), (VV), (CV), and (VC), is well captured by the PDFs of scaled overlaps. Here, we introduce the PDF as $P_\phi(\xi)$ with the subscript, ϕ , representing the area fraction in the system. Because the total number of Delaunay edges is conserved during deformations, the PDFs

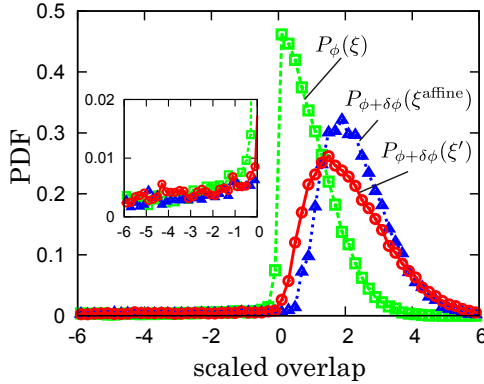


Figure 5: (Color online) The PDFs of scaled overlaps before compression, $P_\phi(\xi)$ (the squares), after affine deformation, $P_{\phi+\delta\phi}(\xi^{\text{affine}})$ (the triangles), and after non-affine deformation, $P_{\phi+\delta\phi}(\xi')$ (the circles), where the inset is a magnification of the PDFs of negative scaled overlaps.

are normalized as $\int_{-\infty}^{\infty} P_\phi(\xi) d\xi = 1$.

In our previous study of bidisperse frictionless particles [7], we found that the affine deformation, Eq. (4), just shifted the PDF to the positive direction, while the non-affine deformation broadened the PDF in positive overlaps and generated a discontinuous “gap” around zero³. We also find that the PDF of negative overlaps after non-affine deformation is comparable with that after affine deformation. In our simulations of polydisperse frictional particles ($\mu = 0.5$), we observe similar results to our previous study. Figure 5 displays the PDFs for polydisperse frictional particles, where the PDF before compression, $P_\phi(\xi)$, has a discontinuous gap around zero. The affine deformation pushes the PDF towards the positive direction as $P_{\phi+\delta\phi}(\xi^{\text{affine}})$, where the discontinuity is smoothed out because of the polydispersity in the system. After non-affine deformation, the PDF widens in positive overlaps as $P_{\phi+\delta\phi}(\xi')$, while there is no significant difference between $P_{\phi+\delta\phi}(\xi^{\text{affine}})$ and $P_{\phi+\delta\phi}(\xi')$ in negative overlaps (the inset in Fig. 5).

To describe such the non-affine evolution of the PDFs, we connect the PDF after non-affine deformation to that before compression through the Chapman-Kolmogorov equation [13],

$$P_{\phi+\delta\phi}(\xi') = \int_{-\infty}^{\infty} W(\xi'|\xi) P_\phi(\xi) d\xi , \quad (7)$$

assuming that transitions between overlaps (from ξ to ξ') can be regarded as *Markov processes*. On the right-hand-side of the Chapman-Kolmogorov equation (7), the conditional probability distribution (CPD) of scaled overlaps, ξ' , which were ξ before compression, is introduced as $W(\xi'|\xi)$. By definition, the CPD is normalized as $\int_{-\infty}^{\infty} W(\xi'|\xi) d\xi' = 1$. Then, the Master equation for the PDFs is derived from Eq. (7) as [13]

³Such a discontinuity is specific to static packings, where a corresponding gap has been observed in a radial distribution function of glass with zero-temperature [12].

$$\frac{\partial}{\partial \phi} P_\phi(\xi') = \int_{-\infty}^{\infty} \{T(\xi'|\xi)P_\phi(\xi) - T(\xi|\xi')P_\phi(\xi')\} d\xi \quad (8)$$

with the transition rate defined as $T(\xi'|\xi) = \lim_{\delta\phi \rightarrow 0} W(\xi'|\xi)/\delta\phi$. The first and second terms on the right-hand-side of the Master equation (8) represent the gain and loss of new overlaps, ξ' , respectively. Therefore, the transition rates or the CPDs fully determine the statistics of microscopic responses of force-chain networks.

3.4 Conditional probability distributions

We determine the CPDs of scaled overlaps as the distributions of ξ' around their mean values, $m_s(\xi)$. For example, the CPD for affine deformation is given by a delta function, $W_{\text{affine}}(\xi'|\xi) = \delta(\xi' - \xi^{\text{affine}})$, which just shifts the PDF by $B_a\gamma$, i.e. $P_{\phi+\delta\phi}(\xi) = P_\phi(\xi - B_a\gamma)$. However, non-affine deformations generate fluctuations of scaled overlaps around their mean values so that the CPDs must have finite widths. In the following, we determine the CPDs for *polydisperse frictionless particles* and those for *polydisperse frictional particles* to examine the effect of particle friction (characterized by the friction coefficient, μ) on the statistics of microscopic responses of force-chain networks. We also compare our results with our previous work of *bidisperse frictionless particles* [7] to study the influence of size distributions.

Figures 6(a) and (c) show the CPDs for polydisperse frictionless particles ($\mu = 0$) in (CC) and (VV), respectively. As can be seen, all data are *symmetric* around the mean values, $m_s(\xi)$, and are well collapsed if we multiply the CPDs and the distances from the mean values defined as $\Xi_s \equiv \xi' - m_s(\xi)$ by γ and $1/\gamma$, respectively. In these figures, the solid lines are given by $\gamma W_{CC}(\xi'|\xi) = f_c(\Xi_c/\gamma)$ and $\gamma W_{VV}(\xi'|\xi) = f_v(\Xi_v/\gamma)$ with the *q-Gaussian distribution* [14],

$$f_s(x) = \frac{1}{c(q_s)} \left[1 + \frac{x^2}{n(q_s)V_s^2} \right]^{\frac{1}{1-q_s}}, \quad (9)$$

where the functions are defined as $n(t) = (t-3)/(1-t)$ and $c(t) = V_s \sqrt{n(t)} B(1/2, n(t)/2)$ with the beta function, $B(x, y)$. In Table 2, we list the *q-indices* which characterize shapes of the CPDs. Note that the *q*-index must be in the range between $1 < q_s < 3$, where the normal (Gaussian) distribution corresponds to the limit, $q \rightarrow 1$. Figures 6(b) and (d) are semi-logarithmic plots of Fig. 6(a) and (c), respectively, where the dotted lines are the CPDs obtained from our previous study on bidisperse frictionless particles [7]. From these results, we observe that the basic properties of CPDs, i.e. their symmetry and self-similarity for different γ , are not affected by the size distribution. However, we find that the CPDs for polydisperse particles have much wider tails than those for bidisperse particles, i.e. $q_s^{\text{BL}} \ll q_s^{\text{PL}}$ in Table 2, implying that the spatial correlation of scaled overlaps increases with the increase of polydispersity [15].

Figures 7(a) and (c) display the CPDs for polydisperse frictional particles ($\mu = 0.5$) with the same polydispersity as in Fig. 6 for (CC) and (VV) cases, respectively. Note

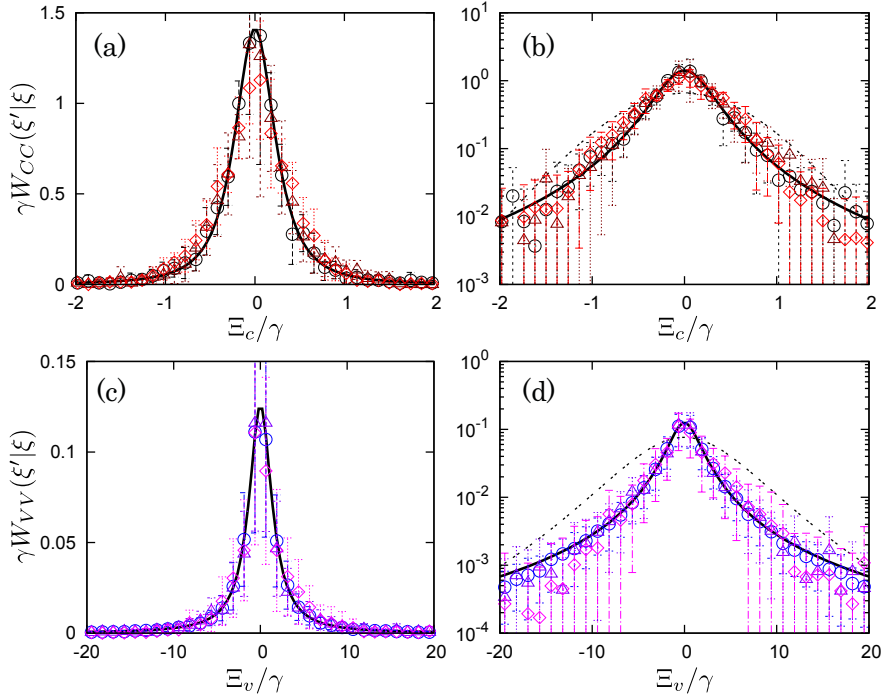


Figure 6: (Color online) The CPDs for *polydisperse frictionless particles* multiplied by γ in (a) (CC) and (c) (VV) plotted against scaled distances from mean values, Ξ_s/γ ($s = c, v$). (b) and (d) are semi-logarithmic plots of (a) and (c), respectively. The solid lines are the q -Gaussian distributions with the q -indices, (b) $q_c^{\text{PL}} = 1.19$ and (d) $q_v^{\text{PL}} = 1.09$, respectively. The dotted lines are the CPDs obtained from our previous study of two-dimensional *bidisperse frictionless particles* [7], where the q -indices are given by (b) $q_c^{\text{BL}} = 1.13$ and (d) $q_v^{\text{BL}} = 1.39$, respectively.

that all data are symmetric around their mean values and well collapse after the same scaling as in Fig. 6. Figures 7(b) and (d) are semi-logarithmic plots of Fig. 7(a) and (c), respectively, where the dotted lines are the CPDs for bidisperse frictionless particles [7]. Comparing the results in Figs. 6 and 7, we confirm that the basic properties, i.e. symmetry and self-similarity, of the CPDs do not change by particle friction, while the tails of CPDs for frictional particles are much narrower than those for frictionless particles, i.e. $q_s^{\text{PN}} \ll q_s^{\text{PL}}$ in Table 2. Therefore, the microscopic friction at the contact drastically decrease the spatial correlations of scaled overlaps.

4 SUMMARY

We have introduced a Master equation for the PDFs of forces in two-dimensional polydisperse frictionless and frictional particle packings. We find that the microscopic response to isotropic compression increasingly deviates from the affine prediction with the increase of the scaled strain increment, γ , in agreement with our previous study of bidisperse frictionless particles [7]. The scaling amplitudes for mean values of scaled overlaps are almost the same as those for bidisperse frictionless particles [7], implying

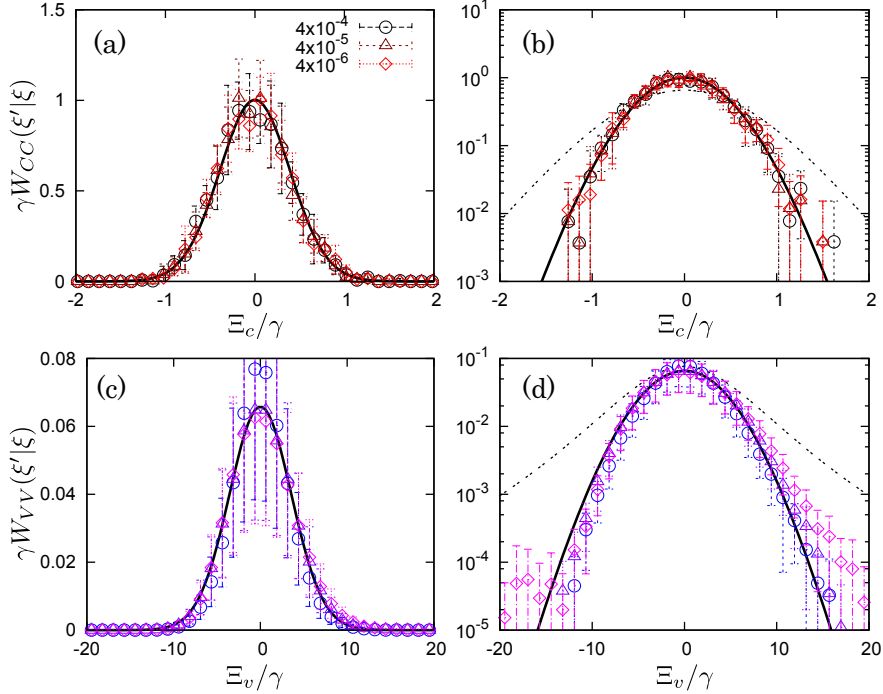


Figure 7: (Color online) The CPDs for *Polydisperse frictional particles* multiplied by γ in (a) (CC) and (c) (VV) plotted against scaled distances from mean values, Ξ_s/γ ($s = c, v$). (b) and (d) are semi-logarithmic plots of (a) and (c), respectively. The solid lines are the q -Gaussian distributions with the q -indices, $q_c^{\text{PN}} = 1.19$ and $q_v^{\text{PN}} = 1.09$, respectively. The dotted lines are the CPDs obtained from our previous study of two-dimensional *bidisperse frictionless particles* [7], where the q -indices are given by (b) $q_c^{\text{BL}} = 1.13$ and (d) $q_v^{\text{BL}} = 1.39$, respectively.

that the degree of non-affinity depends on neither particle friction nor size distribution in average. In addition, symmetry and self-similarity of the CPDs, which govern the statistics of microscopic changes of the force-chain network, are not affected by friction and size distribution. In contrast, the shapes and widths of the CPDs are different for different systems: By using the q -indices to describe their shapes in all cases, we observe that the q -index for polydisperse particles is larger than bidisperse particles, which means that the spatial correlation of scaled overlaps increases with polydispersity (the q -index not equal to one means a non-Gaussian distribution). On the other hand, the q -index becomes nearly equal to one if microscopic friction is considered, implying a dramatic decrease of spatial correlation.

In conclusion, the basic properties of the Master equation, i.e. linear scalings of mean values and fluctuations of scaled overlaps, and the symmetry and self-similarity of the CPDs, are insensitive to particle friction and size distributions, in the cases tested in this paper, while the shape of CPDs depends on both friction coefficient and polydispersity, implying different spatial correlations of scaled overlaps for different material properties.

Acknowledgment

This work was financially supported by the NWO-STW VICI grant 10828. A part of numerical computation was carried out at the Yukawa Institute Computer Facility, Kyoto, Japan.

REFERENCES

- [1] J. Lemaitre and J.-L. Chaboche, *Mechanics of Solid Materials* (1990). Cambridge University Press, Cambridge, UK.
- [2] T. S. Majmudar, M. Sperl, S. Luding, and R. P. Behringer, *Phys. Rev. Lett.* (2007) **98**, 058001.
- [3] S. Henkes and B. Chakraborty, *Phys. Rev. E* (2009) **79**, 061301.
- [4] J. H. Snoeijer, T. J. H. Vlugt, M. van Hecke, and W. van Saarloos, *Phys. Rev. Lett.* (2004) **92**, 054302.
- [5] E. I. Corwin, H. M. Jaeger, and S. R. Nagel, *Nature* (2005) **435**, 1075.
- [6] L. E. Silbert, G. S. Grest, and J. W. Landry, *Phys. Rev. E* (2002) **66**, 061303.
- [7] K. Saitoh, V. Magnanimo, and S. Luding, *Soft Matter* (2015) **11**, 1253.
- [8] G. Combe, V. Richefeu, and G. Viggiani, *Geomechanics from Micro to Macro*, Soga *et al.* (Eds). Taylor & Francis Group, London, ISBN 978-1-138-02707-7 (2015).
- [9] S. Luding, *J. Phys.: Condens. Matter* (2005) **17**, S2623.
- [10] M. van Hecke, *J. Phys.: Condens. Matter* (2010) **22**, 033101.
- [11] W. G. Ellenbroek, M. van Hecke, and W. van Saarloos, *Phys. Rev. E* (2009) **80**, 061307.
- [12] L. Berthier, H. Jacquin, and F. Zamponi, *Phys. Rev. E* (2011) **84**, 051103.
- [13] N. G. van Kampen, *Stochastic Processes in Physics and Chemistry*, 3rd edition (2007). Elsevier B. V. Amsterdam, The Netherlands.
- [14] C. Tsallis, *J. Stat. Phys.* (1988) **52**, 479.
- [15] V. Ogarko and S. Luding, *Soft Matter* (2013) **9**, 9530.

MODELING OF ELASTO-PLASTIC BEHAVIOUR OF GRANULAR MATERIALS USING MULTI-PARTICLE FINITE ELEMENT SIMULATIONS

Nouha ABDELMOULA^{1*}, Barthélémy HARTHONG¹, Didier IMBAULT¹
and Pierre DORÉMUS¹

¹ Université Joseph Fourier/INPG/CNRS, UMR 5521 3SR
Domaine Universitaire, BP 53, 38041 Grenoble cedex 9, France
*abdelmoula.noouha@gmail.com

Key words: Granular Materials, Multi-Particles Finite Element Method, Yield Surface, Flow Rule, Elasto-plasticity, Multi-scale Modelling

Abstract. The method of multi-particle finite element involving assemblies of meshed particles interacting through finite-element contact conditions is adopted to study the plastic flow of a granular material with highly deformable elastic-plastic grains. In particular, it is investigated whether the flow rule postulate applies for such materials. Using a spherical stress probing method, the influence of incremental stress on plastic strain increment vectors was assessed for numerical samples compacted along two different loading paths up to different values of relative density. Results show that the numerical samples studied behave reasonably well according to an associated flow rule, except in the vicinity of the loading point where the influence of the stress increment proves to be very significant. The influence of relative density and initial loading path is discussed.

1 INTRODUCTION

Powder metallurgy includes several processes for the shaping of ductile metal powder. Among these, cold compaction of powders followed by sintering is one of the most commonly used in the industry, allowing the manufacturing of complex shaped engineering components and substantial cost savings. This paper is concerned with the cold compaction stage. During this step, powders undergo large deformation accompanied by a significant densification. For instance, the initial volume after die filling for iron powder (initial density is about $3.3g/cm^3$) is reduced by about half (final density is about $7.1g/cm^3$) at the end of the compaction step [1].

During compaction, failure can occur as a result of a locally highly deviatoric loading close to singularities of complex-shaped parts. This failure mechanism is poorly understood, such that manufacturers currently undertake long and costly trials and errors campaigns to obtain defectless parts. There is a need for numerical modelling of the cold

compaction process involving reliable failure criteria for powder materials. But before getting a failure criterion it is necessary to have a constitutive model for powders so as to reproduce the evolution of stresses and strains throughout compaction.

Currently available models are variants of the Drucker-Prager Cap model [2] that is available in commercial finite-element codes, and has been proved to be reliable in the average sense. But Drucker-Prager Cap model is based on persistent isotropy, which has been proved to be clearly wrong for powder materials by several experimental studies involving triaxial experiments, such as [3]. Yet, taking compaction-induced anisotropy into account is necessary to correctly reproduce the evolution of stresses and strains for singular loading paths, precisely where failure might occur.

The Drucker-Prager Cap model [2] and its variants are based on so-called classical elasto-plasticity, i.e., on the concepts of yield surface and flow rule based on plastic potential. Experimental studies such as [1, 3, 4] have given enough data to model the shape of yield surfaces, but very few of them [4] have given insight about plastic potential, which requires to separate incremental plastic strain and elastic strain.

To obtain more data about plastic deformation mechanisms in powder materials, the Discrete Element Method (DEM) was introduced for the modeling of granular media in the fields of geomechanics and granular flow, and were then applied to hard and ductile powder materials [5, 6]. But this approach is not appropriate to describe grain deformations and use simplified contact formulations that become highly questionable for ductile particles when the relative density reaches a significant value [7], because deformable particles undergo a drastic change in shape.

Following [8, 9, 10], the present work uses the Multi-Particle Finite Element Method (MPFEM) which is based on finite element simulations of the mechanical behaviour of an assembly of meshed particles in contact. The use of finite element discretization and continuum mechanics modelling at particle scale in MPFEM combines discrete behavior of granular materials with the ability to accurately reproduce large contact deformation so as to simulate compaction from low (0.5) to high relative densities (0.98). This method is limited by its computational cost related to the large number of degrees of freedom required to simulate a relatively small number of particles. Despites this limitation, recent studies [11, 12] have proved the power of this method. The present paper applies MPFEM to the study of incremental plastic flow in powder materials.

2 METHOD

2.1 Numerical model

MPFEM simulations of the compaction of an assembly of particles under quasi-static loading conditions were carried out using an explicit integration scheme (commercial finite element program ABAQUS/Explicit). The use of this resolution scheme is adopted due to its capability to solve problems involving complex contact configurations and nonlinear constitutive behaviour including large strains kinematics. In this study, a polydisperse

assembly of 50 spherical particles was used (Fig. 1). The assembly was obtained using an algorithm accompanying open source DEM code YADE [13], consisting in generating 50 randomly disposed particles in a 1x1x1 (mm) cubic cell and growing their radii. When the particles start to touch each other, contact forces are created with respect to classical DEM algorithms. Particles rearrange and the procedure is stopped when stresses on the cell walls stabilise.

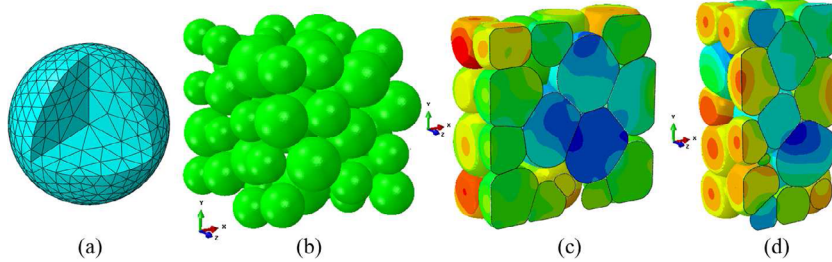


Figure 1: (a) Mesh for one particle. (b) Assembly of 50 undeformed particles. A section along the z plane: (c) after isotropic straining and (d) after closed die compaction by the MPFEM.

The model is then built in ABAQUS in the form of 50 meshed spherical particles surrounded by six rigid planes forming a cubic box of 1x1x1 (mm). Particles were meshed using approximately 3300 quadratic tetrahedral elements per particle. The mesh is made up of small elements at the boundary of the particle and larger elements in the center of the particle (Fig. 1.a). This configuration allowed optimising simulation time while maintaining a reasonable accuracy in the description of contact surfaces.

Individual particles were assigned a constitutive model associating linear, isotropic elasticity (with elastic modulus $E = 10$ GPa and Poisson coefficient $\nu = 0.435$) and Mises plasticity with an isotropic power-law strain-hardening:

$$\sigma = k(\varepsilon^{pl})^n \quad (1)$$

Where $k = 20.5$ MPa and $n = 0.24$ are material parameters, and σ and ε^{pl} are, respectively, the Mises stress and the equivalent plastic strain. These parameters were calibrated on a lead alloy corresponding to the experimental tests performed by [10]. Particle/particle and particle/plane contact interactions were modeled by means of a penalty contact algorithm and a classical Coulomb friction law with a friction coefficient $f = 0.1$. No contact cohesion was introduced.

In the present study, the numerical assembly was compacted using either isotropic straining (referred to as isotropic compaction, Fig. 1.c) and uniaxial straining along x direction (referred to as closed die compaction, Fig. 1.d). Table 1 shows the order of magnitude of calculation time required for the two loading paths and three assemblies involving a different number of particles, up to a relative density $D = 0.9$. All simulations were run using parallel computing on four Intel Xeon E7450 CPUs with 2.4 GHz using domain-level parallelisation.

Table 1: Calculation time using parallel computing with 4 CPUs

Samples	Loading paths	Calculation time
9 particles	Isotropic	6 hours
	Closed die	9 hours
15 particles	Isotropic	10 hours
	Closed die	12 hours
50 particles	Isotropic	19 hours
	Closed die	22 hours

Closed die compaction required more time than isotropic compaction due to larger displacements involved.

An important feature of the present work is that the numerical sample was limited to 50 particles to improve computational efficiency. An assembly of 50 particles is not sufficient to obtain a good representativeness of real powder materials in terms of averaged response. But it provides a large amount of qualitative but relevant information on the incremental plastic deformation mechanisms in real materials.

2.2 Probing of yield surfaces

In the present work, the numerical sample is compacted by means of the six rigid planes translating along their normal, so that initially parallel planes remain parallel throughout the loading. As a result, distortional strains are all kept to zero. Boundary conditions are either stress-driven (the total normal force on each plane is controlled to reach desired stress values) or strain-driven (normal displacements are imposed so that desired elongational strains are controlled). Using such boundary conditions, it can be checked that tangent force components on the rigid planes are negligible compared to normal components, meaning that no stress or strain rotation is applied. As a result, the numerical sample being initially isotropic, stress and strain principal directions are assumed to remain coaxial throughout the simulation. The consequence of such an approach is that the behaviour of the sample is only observed in the 3D principal stress space instead of the general 6D stress space.

Yield surfaces of the numerical sample were obtained as follows:

Step 1 The sample is compacted with a defined loading path (closed die compaction or isotropic compaction) up to a defined value of relative density D (Fig. 2.a). This step involves large deformations.

Step 2 The deformed sample is elastically unloaded to low (compressive) stress values to avoid any loss of contact between the planes and the sample (Fig. 2.b).

Step 3 The sample is reloaded with a proportional loading path in a defined direction of the stress space until the onset of plasticity is detected (Fig. 2.c).

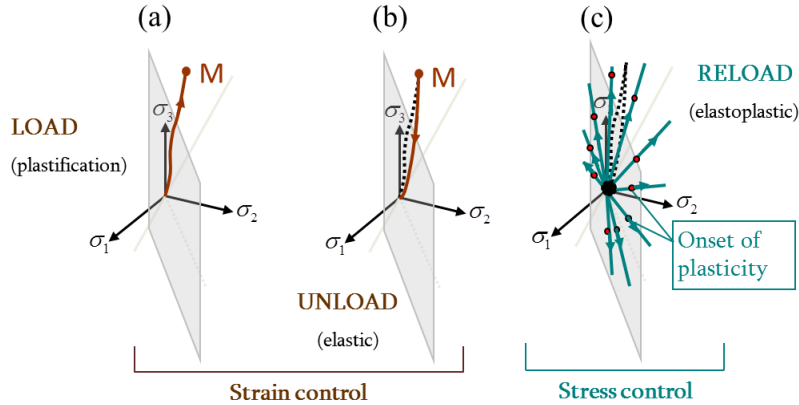


Figure 2: Method for probing yield surfaces: (a) First loading (Step 1), (b) unloading (Step 2), (c) reloading in various directions (Step 3).

For each reloading path (Step 3), this procedure gives one point of the yield surface of the sample corresponding to the strain-hardening state resulting from the initial loading (Step 1). To get the yield surface, Step 3 is repeated with a different loading direction, restarting simulations from Step 2. In the present study, the probing of yield surfaces is limited to the Rendulic plane of equation $\sigma_2 = \sigma_3$.

Step 1 is strain-driven so that rigid body motion of particles in the early rearrangement stage does not lead to huge displacement values for small applied stresses. Spherical stress probing simulations need to be conducted using stress control in the subsequent steps, as will be explained further. Transition from strain control to stress control is made between Step 2 and Step 3 so that small stress variations that might occur remain within the elastic range.

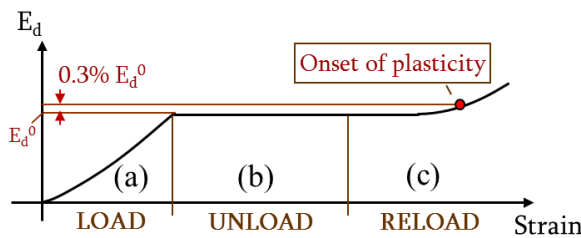


Figure 3: Determination of the onset of plasticity during (a) first loading, (b) unloading, and (c) reloading

Following [11], the detection of yield points during Step 3 is based on the total dissipation E_d , equal to the sum of plastic and frictional dissipation within the numerical model.

The onset of plasticity is defined as the point where the total dissipation in the assembly reaches a threshold value equal to $E_d^0 + 0.3\%E_d^0$, E_d^0 being the value of the total dissipation at the end of Step 1. Fig. 3 illustrates the evolution of the total dissipation between Step 1 and Step 3. Upon unloading, the total dissipation remains constant within a very good approximation (Fig. 3.b).

Fig. 4 shows the yield surfaces in a deviatoric stress/mean stress diagram with various values of final relative density D for the same assembly (50 particles) that was submitted to isotropic and closed die compaction. The results were qualitatively similar to known experimental [3] and numerical [12] results. As pointed out by [12], the evolution of yield surfaces on a monotonic loading path such as isotropic and closed die compaction was an approximately homothetic growth. Also, yield surfaces were oriented in the direction of the loading paths, which differed from the hydrostatic axis in the case of closed die compaction (Fig. 4.b) as a result of compaction-induced anisotropy.

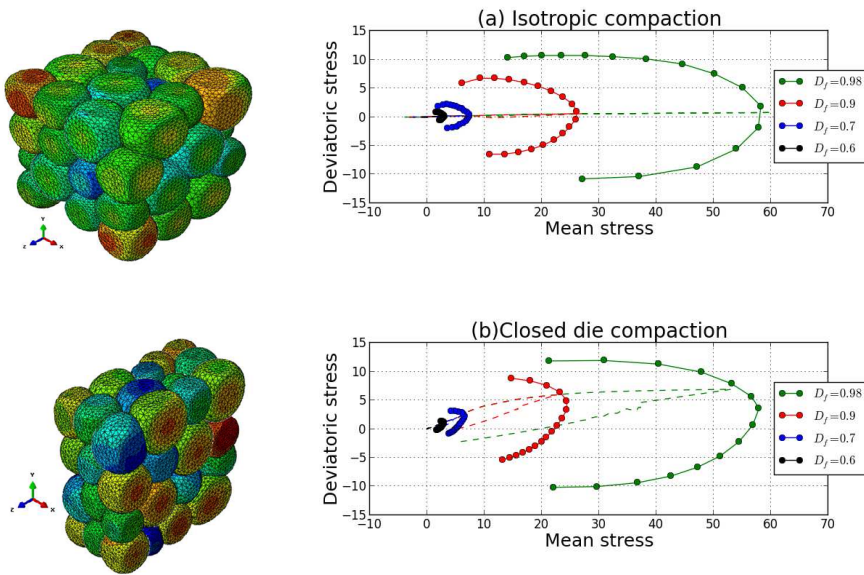


Figure 4: Evolution of yield surfaces from initial to various final relative density values, $D = 0.6, 0.7, 0.9$ and 0.98 , with a monotonic loading: (a) isotropic compaction and (b) closed die compaction. The dotted line is the initial loading/unloading path.

2.3 Spherical stress probing method

In classical elasto-plasticity, the incremental plastic strain obeys the flow rule equation:

$$d\boldsymbol{\varepsilon}_{ij}^{pl} = \lambda \frac{\partial g(\boldsymbol{\sigma}, \chi)}{\partial \sigma_{ij}} \quad (2)$$

where $d\boldsymbol{\varepsilon}^{pl}$ is the increment of plastic strain, $\boldsymbol{\sigma}$ the stress tensor, χ the strain-hardening variables, g the plastic potential and λ the plastic multiplier. Assuming g is regular,

equation (2) states that for a given state of stress and strain-hardening, the direction of the incremental plastic strain $d\boldsymbol{\varepsilon}^{pl}$ is unique.

In the present work, the existence of a plastic potential, and more generally, the incremental plastic flow could be studied on the numerical sample by using a spherical stress probing method [14, 15]. This method first consists in loading the numerical sample to a given state of stress $\boldsymbol{\sigma}_0$ on the yield surface (i.e. at the elastic limit, this corresponds to Step 3 as previously stated). Then, the two following steps are applied (Fig. 5):

Step 4 A small stress increment of magnitude $\Delta\sigma$ in a given direction is applied.

Step 5 The sample is unloaded back to $\boldsymbol{\sigma}_0$.

Assuming that no plastic dissipation occurs during the unloading phase conducted in Step 5, the incremental plastic strain $d\boldsymbol{\varepsilon}^{pl}$ was defined as the difference in total strain between the end of Step 3 and the end of Step 5.

Repeating Step 4 and Step 5 for different directions of the stress increment gives the incremental plastic strain vectors corresponding to the response of the sample to different stress increments $\Delta\sigma$ of same magnitude but different directions. The response of the sample were represented by the plastic strain response envelope, which is a closed surface containing the tips of all the plastic strain response vectors (such a surface for the stress increments would be a sphere). In the present paper, only stress increments in the Rendulic plane were applied.

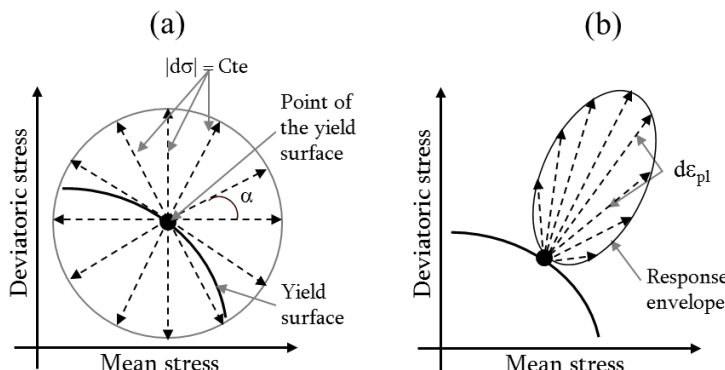


Figure 5: Method for detect the potential: (a) stress probes and (b) plastic strain response

Referring back to equation (2), if the flow rule applies and if a potential function exists, the plastic strain increment $d\boldsymbol{\varepsilon}^{pl}$ does not depend on the direction of $d\boldsymbol{\sigma}$. In such a case, the plastic strain response envelope is a line segment (Fig. 6.a), since the direction of $d\boldsymbol{\varepsilon}^{pl}$ is unique and entirely defined by $\boldsymbol{\sigma}$ and χ . If the response envelope of the plastic strain is not a straight line, then $d\boldsymbol{\varepsilon}^{pl}$ depends on the direction of $d\boldsymbol{\sigma}$, which means that the flow rule equation (2) is not valid (Fig. 6.b).

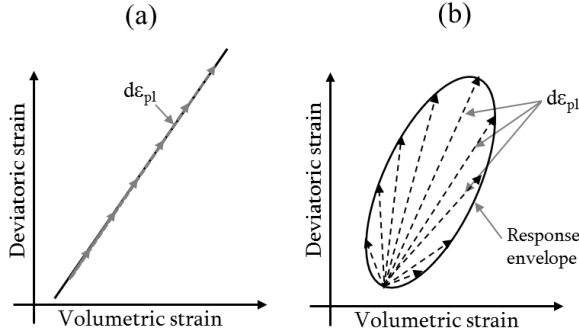


Figure 6: Plastic strain response envelope: (a) according to the flow rule postulate, (b) if the flow rule postulate is not valid.

3 RESULTS

In this section, plastic strain response envelopes are plotted in deviatoric strain/volumetric strain graphs in arbitrary units and superimposed to deviatoric stress/mean stress graphs with respect to the yield point they are associated to.

In order to preserve the aspect ratio of yield surfaces and plastic strain response envelopes, so as to visually assess normality of the flow rule, invariants of stress and strain were defined in a slightly unconventional way:

$$\begin{aligned} \sigma_M &= \frac{1}{\sqrt{3}} (\sigma_1 + \sigma_2 + \sigma_3); & \sigma_D &= \sqrt{2/3} [\sigma_1 - \frac{1}{2}(\sigma_2 + \sigma_3)]; \\ \varepsilon_V &= \frac{1}{\sqrt{3}} (\varepsilon_1 + \varepsilon_2 + \varepsilon_3); & \varepsilon_D &= \sqrt{2/3} [\varepsilon_1 - \frac{1}{2}(\varepsilon_2 + \varepsilon_3)]; \end{aligned} \quad (3)$$

where σ_M , σ_D , ε_M , ε_D are the mean stress, deviatoric stress, volumetric strain and deviatoric strain, respectively; σ_1 , σ_2 , σ_3 , ε_1 , ε_2 , ε_3 are principal Cauchy stresses and Hencky strains, respectively. Using definitions (3), yield points represented on following figures form the intersections of the 3D yield surfaces in the principal stress space and the Rendulic plane, without any scaling.

Fig. 7.a,c shows plastic strain response envelopes for isotropic and closed die compaction of the sample for a constant stress increment magnitude $\Delta\sigma$. The value of $\Delta\sigma$ had to be tuned through a trial and error procedure and it is different for each initial loading path. It was chosen as small as possible, but large enough so that the incremental plastic strain response was significantly larger than numerical noise. As expected, the magnitude of plastic strain increment vectors increases with deviatoric stress such that, keeping a constant value of $\Delta\sigma$ for all the yield points, it is not possible to see all plastic response envelopes on the same graph. For this reason, plastic strain envelopes were normalised and represented in Fig. 7.b,d. Note that in the case of the closest yield point to the loadig point, underlined in Fig. 7.a, plastic strain increment vectors were too small to be detected. This is the reason why no normalised plastic strain envelope was plotted for this yield point in Fig. 7.b.

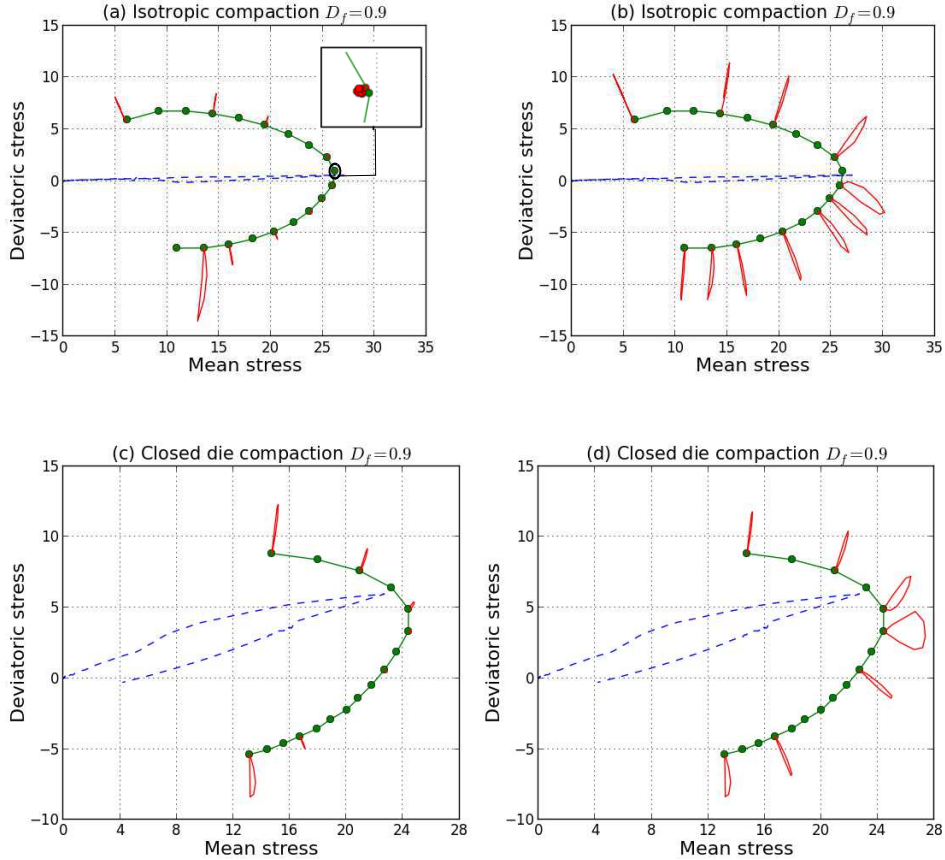


Figure 7: Plastic strain response envelopes for some points of the yield surface with final relative density $D = 0.9$. (a) and (b) Isotropic compaction. (c) and (d) Closed die compaction. In (b) and (d), plastic strain response envelopes have been normalised. The dotted line is the initial loading/unloading path.

Fig. 7.b,d show that most plastic strain increment vectors are close to line segments, and are approximately normal to the yield surface, suggesting the validity of an associated flow rule for such materials. This observation was made in the deviatoric stress (strain)/mean stress (strain) plane, and it is possible that 3D plastic strain response envelopes were planar surfaces, obviously different from line segments when plotted in the deviatoric plane, as it was observed for granular assemblies of rigid particles [14].

However, in the vicinity of the tip of the yield surfaces, plastic strain response envelopes can no more be assimilated to line segments. Such singular behaviour is confirmed by results presented in Figures 8 and 9. For low values of the final relative density D , plastic strain response envelopes suggest a highly non-associated behaviour close to the tips of closed-die-compaction yield surfaces, which becomes very striking at $D = 0.6$ (Fig.

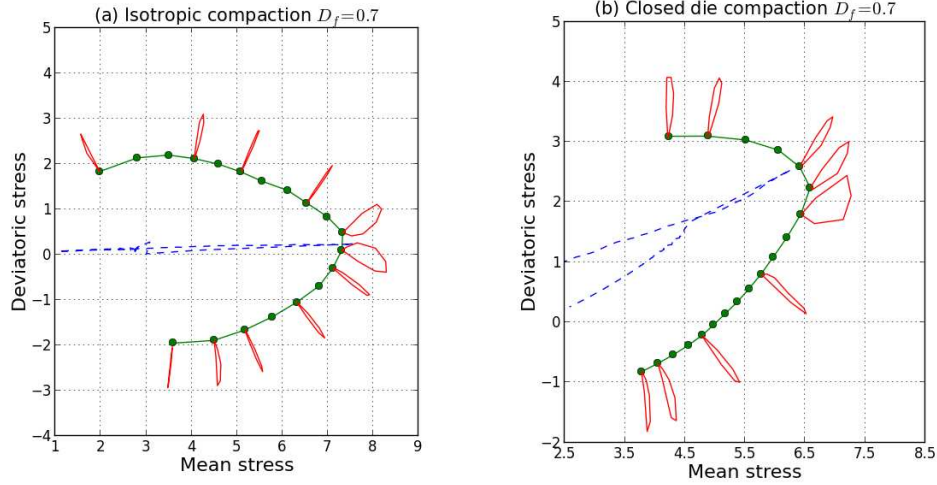


Figure 8: Normalized plastic strain response envelopes for some points of the yield surface with final relative density $D = 0.7$ for (a) isotropic and (b) closed die compaction. The dotted line is the initial loading/unloading path.

9.d). Results for $D = 0.9$ (Fig. 7.b,d) are closer to an associated-flow-rule material, which is probably the consequence of the sample becoming denser and thus, closer to the associated, Mises elastic-plastic constitutive model of the particles.

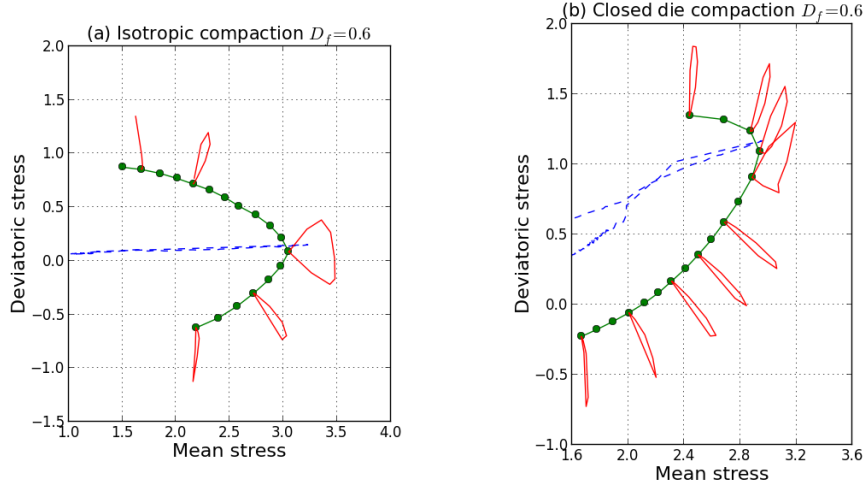


Figure 9: Normalized plastic strain response envelope for some points of the yield surface with final relative density $D = 0.6$ for (a) isotropic and (b) closed die compaction. The dotted line is the initial loading/unloading path.

[12] also showed using MPFEM simulations, that in a large deformation context, con-

tact surfaces between particles are created normal to the direction joining two particles, this direction remaining more or less constant during a monotonic loading such as isotropic or closed die compaction. As a result of this very special contact configuration, contact surfaces that increase in size during densification oppose an increasing resistance to normal stresses; and the particular loading that created the contact structure is precisely a loading for which contact surfaces essentially undergo normal loading. In the present case, this phenomenon results in plastic strain increment vectors being very small in magnitude.

The singular behaviour observed on plastic strain response envelopes could be related to the particular stress state corresponding to the loading point. Fleck et al. [5] obtained yield surfaces in the context of powder densification through a micromechanical modelling approach. In their results, loading points correspond to singular points of the yield surfaces, as a result of all the contacts experiencing purely normal loading, so that the direction of slip is undetermined. In the present case, it is not obvious that slip is the main mechanisms for plastic strains, but the increased resistance to normal loading of contacts might block plastic strains resulting from the stress state, leading to an increased significance of the role played by small stress increments in plastic deformation mechanisms.

4 CONCLUSIONS

This paper is concerned with the incremental plastic behaviour of ductile powder materials, i.e., granular materials with highly deformable elastic-plastic grains. Based on MPFEM simulations involving an assembly of meshed, deformable particles, the incremental plastic strain response of numerical samples to stress states on the plastic limit was studied. It was observed that such materials present a singular, highly non-associated behaviour in the vicinity of loading points, which is an original feature of the behaviour of ductile powders. In a small region of the principal stress state surrounding the loading points, the direction of the plastic strain increment vector shows a very significant dependency on the direction of the stress increment. This singular behaviour was attributed to the effect of contact surfaces resulting from grain deformation.

REFERENCES

- [1] Brewin, P.R., Coube, O., Doremus, P. and Tweed, J.H. *Modelling of Powder Die Compaction*. Springer-Verlag London Limited. (2008) **374**.
- [2] Drucker, D.C. and Prager, W. *Soil mechanics and plastic analysis or limit design*. Quarterly journal of mechanics and applied mathematics. (1952) **10**:157–175.
- [3] Schneider, L.C.R. and Cocks, A. C. F. *Experimental investigation of yield behaviour of metal powder compacts*. Powder Metallurgy. (2002) **345**:237–245.
- [4] Pavier, E. and Dorémus, P. *Triaxial characterisation of iron powder behaviour*. Powder Metallurgy. (1999) **42**:345–352.

- [5] Fleck, N. A., Kuhn, L. T. and McMeeking, R. M. *Yielding of metal powder bonded by isolated contacts*. Journal of the Mechanics and Physics of Solids. (1992) **40**:1139–1162.
- [6] Martin, C. L. *Elasticity, fracture and yielding of cold compacted metal powders*. Journal of the Mechanics and Physics of Solids. (2004) **52**:1691–1717.
- [7] Harthong, B., Jérier, J.-F., Richefeu, V., Chareyre, V., Dorémus, P., Imbault, D., Donzé, F.-V. *Contact impingement in packings of elastic-plastic spheres, application to powder compaction*. International Journal of Mechanical Sciences. (2012) **61**:32-43.
- [8] Gethin, D. T., Lewis, R. W. and Ransing, R. S. *A discrete deformable element approach for the compaction of powder systems*. Modelling and Simulation in Materials Science and Engineering. (2003) **11**:101–114.
- [9] Procopio, A. T. and Zavaliangos, A. *Simulation of multi-axial compaction of granular media from loose to high relative densities*. Journal of the Mechanics and Physics of Solids. (2005) **53**:1523–1551.
- [10] Chen, Y., Imbault, D., Dorémus, P. *Numerical simulation of cold compaction of 3d granular packings*. Materials Science Forum. (2006) **534-536**:301–304.
- [11] Schmidt, I., Kraft, T. and Wonisch, A. *Simulation of the material behavior of metal powder during compaction*. Proceedings of the Institution of Mechanical Engineers, Part E: Journal Process Mechanical Engineering. (2010) IMechE Vol. 224.
- [12] Harthong, B., Imbault, D. and Dorémus, P. *The study of relations between loading history and yield surfaces in powder materials using discrete finite element simulations*. Journal of the Mechanics and Physics of Solids. (2012) **60**:784–801.
- [13] Šmilauer, V., Catalano, E., Chareyre, B., Dorofeenko, S., Duriez, J., Gladky, A., Kozicki, J., Modenese, C., Scholtès, L., Sibille, L., Stránský, J., Thoeni, K., *Yade Documentation*. V. Šmilauer, ed., The Yade project, 1st ed. (2010). <http://yade-dem.org/doc/>.
- [14] Calvetti F., Viggiani G. and Tamagnini C. *A numerical investigation of the incremental behavior of granular soils*. Italian Geotechnical Journal. (2003) **3**:11–29.
- [15] Darve, F., and Nicot, F. *On flow rule in granular media: phenomenological and multi-scale views (Part II)*. International Journal for Numerical and Analytical Methods in Geomechanics. (2005) **29**:1411–1432.

VORTEX PARTICLE METHOD FOR AERODYNAMIC ANALYSIS: PARALLEL SCALABILITY AND EFFICIENCY

K. Ibrahim¹, G. Morgenthal²

¹ Bauhaus-University Weimar
Marienstrasse 13, 99423 Weimar, Germany
khaled.ibrahim.tolba@uni-weimar.de

² Bauhaus-University Weimar
Marienstrasse 13, 99423 Weimar, Germany
guido.morgenthal@uni-weimar.de

Key words: Vortex Particle Method, Wind Structure Interaction, Bluff Body Aerodynamics, Aero-elastic Response.

Abstract. This paper presents an analysis of the scalability and efficiency of a simulation framework based on the Vortex Particle Method (VPM). The code is applied for the numerical aerodynamic analysis of line-like structures. The numerical code runs on multi-core CPU and GPU architectures using OpenCL framework. The focus of this paper is the analysis of the parallel efficiency and scalability of the method being applied to an engineering test case, namely the aero-elastic response of a long-span bridge girder. The target is to assess the optimal configuration and the required computer architecture, such that it becomes feasible to efficiently utilize the method within the computational resources available for a regular engineering office. The simulations and the scalability analysis are performed on a regular gaming-type computer.

1 Introduction

The Vortex Particle Methods (VPM) uses a grid free formulation in order to solve the Navier-Stokes equations of an incompressible fluid flow. The VPM models vortical flows typical for aerodynamic applications especially around bluff bodies i.e. moderate to high Reynolds number via solving the vorticity transport equations in Lagrangian form [1, 2]. Vortex sheets are modelled as particles with invariant strength which are transported downstream by convection and diffusion due to the induced velocity field and the free stream velocity. The vorticity field can be computed as superposition of the local vorticity created by each particle. Based on the Bio-Savart law the induced velocity field is computed and accordingly the particles are convected through a suitable time integration scheme.

Different algorithms are available in literature [3] for solving the Bio-Savart integral. For N particles discretisation of the domain, the naive particle-particle interaction method scales as $O(N^2)$. Alternatively, within the current implementation of the VPM method, an enhanced algorithm termed the Particle-Particle-Particle-Mesh (P3M) algorithm is used [4]. This algorithm requires an intermediate correction step that can be efficiently computed in parallel, for which Graphical Processing Units (GPUs) were used in a thread-per-particle implementation. Here, in parallel fashion each thread calculates the contributions on its local particle due to all the other particles at a given point in time [5].

2 Modelling and Simulation

The simulations of the structural aero-elastic response can be divided into two intertwined aspects. Namely, the structural dynamics problem modelled by the interaction between the wind induced forces and the dynamic characteristics of the structure. And the fluid dynamics problem representing the wind flow, modelled by the Navier-Stokes (N-S) equations. For an incompressible viscous flow N-S equations are given by,

$$\frac{\partial \mathbf{u}}{\partial t} + (\mathbf{u} \cdot \nabla) \mathbf{u} = -\frac{1}{\rho} \nabla p + \nu \nabla^2 \mathbf{u}, \quad (1)$$

$$\nabla \cdot \mathbf{u} = 0. \quad (2)$$

Where for time $t \in (0, \infty)$ the vector velocity field \mathbf{u} in three spatial dimensions is $\mathbf{u}(\mathbf{x}, t) : \mathbb{R}^3 \times [0, t] \rightarrow \mathbb{R}^3$, while the scalar pressure field is $p(x, t) : \mathbb{R}^3 \times [0, t] \rightarrow \mathbb{R}$ and ν is the kinematic viscosity.

Equation [1] represents the conservation of momentum, where to the left hand side is the material derivative i.e. the rate of change of momentum and to the right hand side are the pressure and viscous forces. Due to the incompressibility condition, the conservation of mass implies that velocity u is a solenoidal field i.e divergence free.

The N-S equations in the form presented above, constitutes four equations of the primitive variables \mathbf{u} and p . Analytical solution of the N-S equations exists only for rare simplified test cases [6]. Hence, simulation of flow phenomena is based primarily on numerical methods.

2.1 Vortex Particle Method

For solving the N-S equations there are multitude of numerical schemes that differ in their formulations as well as their underlying computational schemes. The choice of the suitable scheme is essential for an accurate modelling of the underlying physics, while efficiently using the computational resources. The Vortex Particle Method is proposed as an efficient numerical technique for simulations of high Reynolds number, incompressible flows around bluff bodies e.g. in the context of wind engineering. This mesh-less numerical technique provides an alternative to classical mesh based Eulerian methods such as finite volume and spectral methods. The formulation and the discretisation of

the N-S equations in the VPM, reflect the natural representation in dominantly vortical flow, which is inherent in flows around bluff bodies. Additionally, the method accounts for free-space boundary conditions, thus providing a robust approach for flows around structures such as towers, masts and bridges [5].

The VPM method is derived based on describing the fluid dynamic events in the flow in terms of the evolution of the vorticity field ω [1] such that,

$$\omega(\mathbf{x}, t) = \nabla \times \mathbf{u}(\mathbf{x}, t). \quad (3)$$

For three dimensional space $x \in \mathbb{R}^3 \rightarrow \mathbf{u} \in \mathbb{R}^3 \wedge \omega \in \mathbb{R}^3$. Whilst in two dimensional domain $x \in \mathbb{R}^2 \rightarrow \mathbf{u} \in \mathbb{R}^2 \wedge \omega \in \mathbb{R}$ where the vorticity has only one component namely the orthogonal component to the \mathbb{R}^2 .

The motion of an incompressible fluid governed by the momentum and mass conservation equations [1] and [2] might as well be represented in terms of the vorticity transport equation. By considering equation [3] and applying the curl operator to equation [1] it becomes,

$$\frac{\partial \omega}{\partial t} + \nabla \times [(\mathbf{u} \cdot \nabla) \mathbf{u}] = -\frac{1}{\rho} \nabla \times \nabla p + \nu \nabla \times [\nabla^2 \mathbf{u}]^0. \quad (4)$$

The pressure term vanishes, because the curl of the gradient of any scalar field is always zero. Similarly, for the left hand side using the vector identity $(\mathbf{u} \cdot \nabla) \mathbf{u} = \frac{1}{2} \nabla \mathbf{u} \cdot \mathbf{u} - \mathbf{u} \times (\nabla \times \mathbf{u})$ it follows,

$$\nabla \times [(\mathbf{u} \cdot \nabla) \mathbf{u}] = \nabla \times (\omega \times \mathbf{u}).$$

For the right hand side of equation [4], Considering the vector identity for the Laplacian of \mathbf{u} , where $\nabla^2 \mathbf{u} = \nabla(\nabla \cdot \mathbf{u}) - \nabla \times (\nabla \times \mathbf{u})^0$ and considering the vanishing term due to the incompressibility condition in equation [2] it follows,

$$\nu \nabla \times [\nabla^2 \mathbf{u}] = -\nu \nabla \times [(\nabla \times \omega)]. \quad (5)$$

Thus, the continuity equation $\nabla \cdot \mathbf{u} = 0$ is now implicitly included. Following the same vector identity for the Laplacian of ω , where $\nabla \times (\nabla \times \omega) = \nabla(\nabla \cdot \omega)^0 - \nabla^2 \omega$ and since the divergence of the vorticity ω is always zero. The vorticity transport equation can be written as,

$$\frac{\partial \omega}{\partial t} + \nabla \times (\omega \times \mathbf{u}) = \nu \nabla^2 \omega. \quad (6)$$

Since $\nabla \times (\omega \times \mathbf{u}) = \omega(\nabla \cdot \mathbf{u})^0 \mathbf{u}(\nabla \cdot \omega)^0 - (\omega \cdot \nabla) \mathbf{u} + (\mathbf{u} \cdot \nabla) \omega$, the vorticity transport equation for $x \in \mathbb{R}^3, t \in [0, t_\infty]$ can be written such that,

$$\frac{\partial \omega}{\partial t} + (\mathbf{u} \cdot \nabla) \omega = \nu \nabla^2 \omega + (\omega \cdot \nabla) \mathbf{u}. \quad (7)$$

In the left hand side the first term is the rate of increase of vorticity by time and the second term is the convection of vorticity. In the right hand side the viscous diffusion of vorticity and the rate of vorticity deformation i.e. vortex stretching respectively [1].

2.2 Simulation framework

The simulation framework is based on a two dimensional cross sectional analysis. In analogy to section model wind tunnel testing, such approach is particularly used in predominantly two dimensional flow simulations as in line-like structures e.g. bridges and high-rise buildings. Nevertheless, as an extension to the concept and to capture the three dimensional flow phenomenon, Pseudo Three-Dimensional simulation proposed by Morgenthal [5] is implemented in the current framework. Which is a numerical approach, where multiple two-dimensional simulations are carried out such that they are linked together via the dynamical properties of the structure.

In the current framework rewriting equation [7]. Since $x \in \mathbb{R}^2 \rightarrow u = \langle u_x, u_y, 0 \rangle \wedge \omega = \langle 0, 0, \omega_z \rangle$, therefore the term corresponding to the vortex stretching $(\omega \cdot \nabla) \mathbf{u}$ vanishes. The vorticity transport equation becomes,

$$\frac{\partial \omega}{\partial t} + (\mathbf{u} \cdot \nabla) \omega = \nu \nabla^2 \omega. \quad (8)$$

Two benefits of this formulation are the absence of pressure term and the automatic satisfaction of the continuity equation [2]. The equations are now only dependent on vorticity and velocity field. Thus for solving the vorticity field an analytic expression connecting vorticity and velocity at each specific point in time and space is essential.

Based on Helmholtz Theorem [1, 4], the velocity field $\mathbf{u}(x, t)$ can be resolved into the sum of an irrotational i.e curl-free vector field u_p and a solenoidal i.e divergence free vector field u_w i.e. $u = u_p + u_w$. Assuming a given potential function ϕ for the irrotational field and, a divergence free function ψ for the rotational field, u could be written as,

$$\mathbf{u} = \nabla \phi + \nabla \times \psi. \quad (9)$$

Using the definition of vorticity in equation [3], the vorticity becomes,

$$\omega = \cancel{\nabla \times \nabla \phi}^0 + \nabla \times (\nabla \times \psi) = \cancel{\nabla(\nabla \cdot \psi)}^0 - \nabla^2 \psi. \quad (10)$$

Since, the curl of the gradient of the potential function is zero and ψ is defined to be a divergence free function, the vorticity yields to be the laplacian of the stream function i.e. Poisson equation.

Considering that, as the domain boundaries extend to infinity the solenodial stream function ψ decays to zero. Hence, the irrotational component becomes $u_p = u_\infty$. And

using the Green's function solution to the above mentioned Poisson equation [10], this yields the velocity field in terms of the so-called Biot-Savart law. Such that,

$$\mathbf{u}(\mathbf{x}) = \mathbf{U}_\infty - \frac{1}{2\pi} \int_{\mathcal{D}} \frac{\omega(\mathbf{x}_0) \times (\mathbf{x}_0 - \mathbf{x})}{|\mathbf{x}_0 - \mathbf{x}|^2} d\mathcal{D}_0, \quad (11)$$

where $\mathcal{D} \in \mathbb{R}^2$ and the velocity $\mathbf{u}(\mathbf{x})$ at point x in space is the superposition of all the contributions from the vorticity field in the domain.

2.2.1 Discretisation

The vorticity can be discretized in numerous ways e.g. particles or segments in 2D and filaments or sheets in 3D [1]. In this implementation by Morgenthal [4], particles are used for discretisation and are convected with the flow such that the strength of each particle τ_p is the local circulation. whereby circulation is a quantity closely related to vorticity, it is defined as the line integral of the velocity around a closed contour, such that

$$\tau = \oint \mathbf{u} \cdot d\mathbf{x}. \quad (12)$$

Due to this discretisation the vorticity field created by N_p vortex particles (circulation particles) becomes,

$$\omega(\mathbf{x}, t) = \sum_{p=1}^{N_p} \delta(\mathbf{x} - \mathbf{x}_p(t)) \Gamma_p, \quad (13)$$

where δ is the Dirac delta function and x_p is the position of particle τ_p contributing to the vorticity field based on the separation distance. Whereby the strength of each particle $\tau_p = \tau_p ez$ remains constant. The velocity at point x in space is thus the superposition of the contributions from all particles in the domain

$$\frac{\partial \mathbf{x}}{\partial t} = \mathbf{U}_\infty - \sum_{p=1}^{N_p} \mathbf{K}_\sigma(\mathbf{x}_p - \mathbf{x}) \Gamma_p. \quad (14)$$

Singularities arise when two particles are at very small separation to each other, those are mollified by using a smooth function $K_\sigma(\mathbf{x})$, in the current implementation Gaussian mollification kernel is applied [4].

2.2.2 Fluid Structure Interaction

Using Boundary Element Method (BEM), the structural cross section is discretised in \mathbb{R}^2 . Generally the BEM uses a given boundary conditions to fit boundary values into an integral equation, rather than values throughout the space defined by a partial differential equation e.g. the Poisson equation equation [10]. Accordingly, the the velocity boundary

conditions of equation [11] are satisfied as well its corresponding surface vorticity. The local vorticity at each panel is calculated and released to the domain at every time step.

For computation of the resultant integral forces on a rigid body, the pressure gradient is computed through,

$$\nabla p = \nu \rho \nabla^2 u \quad (15)$$

where ν is the kinematic viscosity, ρ is the density and u is the velocity field. By integrating the surface pressures the aerodynamic section forces can be directly calculated, based upon which the static wind coefficients are calculated. For drag coefficient,

$$C_D = \frac{F_D}{1/2 \rho D U_\infty^2}, \quad (16)$$

where F_D is the drag force and D is the characteristic depth of the cross section. Similarly the coefficients of lift and moment are calculated from the lift force and the moment respectively.

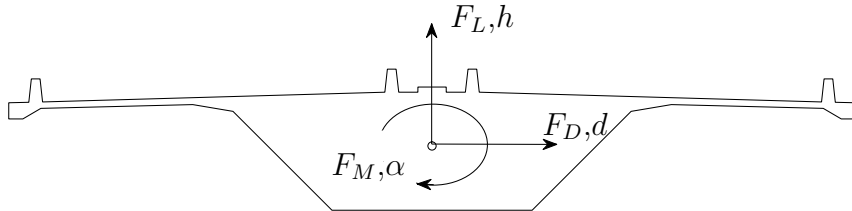


Figure 1: Schematic of a two dimensional bridge cross section with three degrees of freedom; h for vertical motion due to lift force F_L . d for lateral motion due to drag force F_D and rotation α due to moment F_M .

The two dimensional structural displacement response is achieved by solving the equation of motion for each degree of freedom. For the vertical response,

$$m\ddot{h} + 2m\xi_h\omega_h\dot{h} + m\omega_h^2 h = F_h(t), \quad (17)$$

where m is the mass, ξ_h is the damping ratio and ω_h is the natural frequency. Similarly, the equation of motion is solved for the lateral and rotational degrees of freedom with their corresponding damping, natural frequency and mass or inertia.

3 Reference Object

In the following section, the presented numerical method is compared to results from wind tunnel tests provided from an industrial test case. The dimensions of the cross section are presented in figure [2].

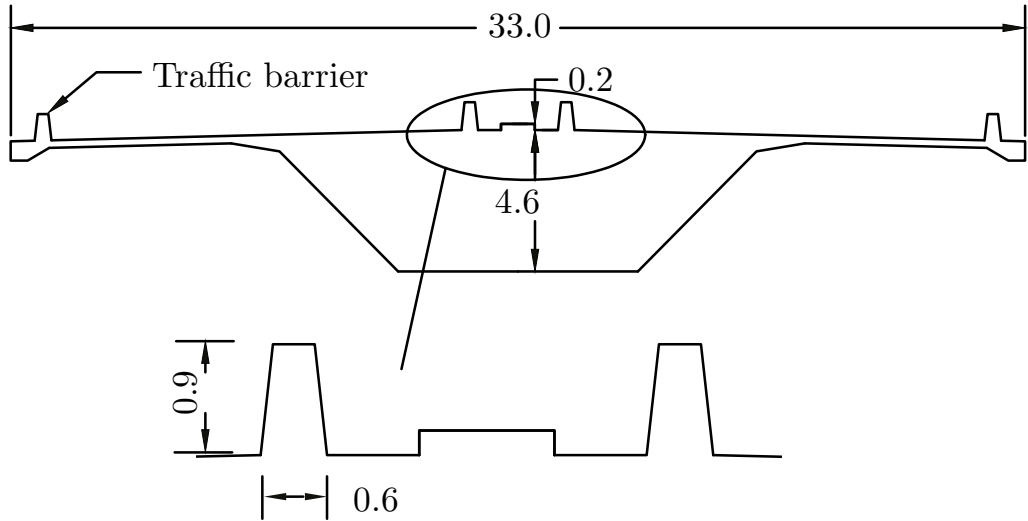


Figure 2: Bridge cross section, dimensions in meter.

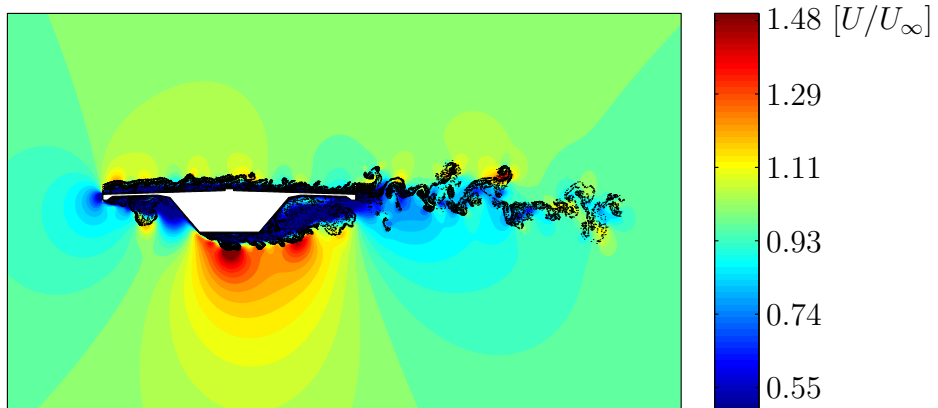


Figure 3: A snapshot of flow field around a bridge cross section using Vortex Particle Method.

3.1 Static wind coefficients

Before pursuing the dynamic response simulations, static section simulations were performed for validation of the basic aerodynamic behaviour e.g. for laminar flow see figure [3]. The static cross section model of the bridge was simulated for varying wind incidence angles α in the range of -7 to +7 degree with 1 degree steps. The static wind coefficients are compared with good agreement against the corresponding wind tunnel results, as in figure [4].

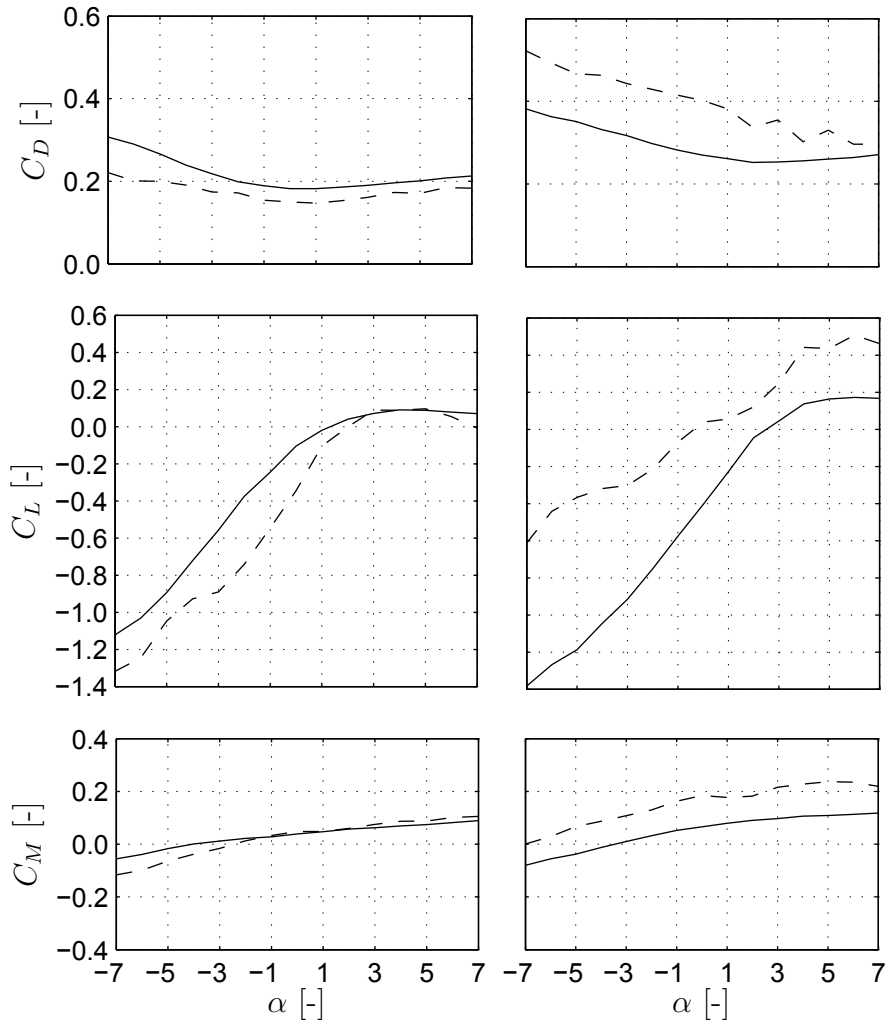


Figure 4: Comparison of static wind coefficients (C_D , C_L , C_M) for different incidence angles α ; continues line for wind tunnel results and dotted line for numerical simulation results. To the left smooth wind; to the right turbulent wind with Isotropic Turbulence intensity $I = 10\%$. The simulations were performed at full scale size. The wind tunnel tests for the static cross section were done at the scale of 1:80.

3.2 Aero-elastic response

An aero-elastic model of the bridge at the construction stage of a 216 m long cantilever i.e. 108 m from each cantilever side is modelled and simulated by a set of six two dimensional simulation slices. The vibration modes of the structure were computed using commercial Finite Element software. The four natural modes used in the analysis (two vertical and two lateral deck modes) are depicted in figure [5].

Simulations of 600s real time were performed for the bridge aero-elastic response due to turbulent inflow wind configuration. The simulations were performed based on two

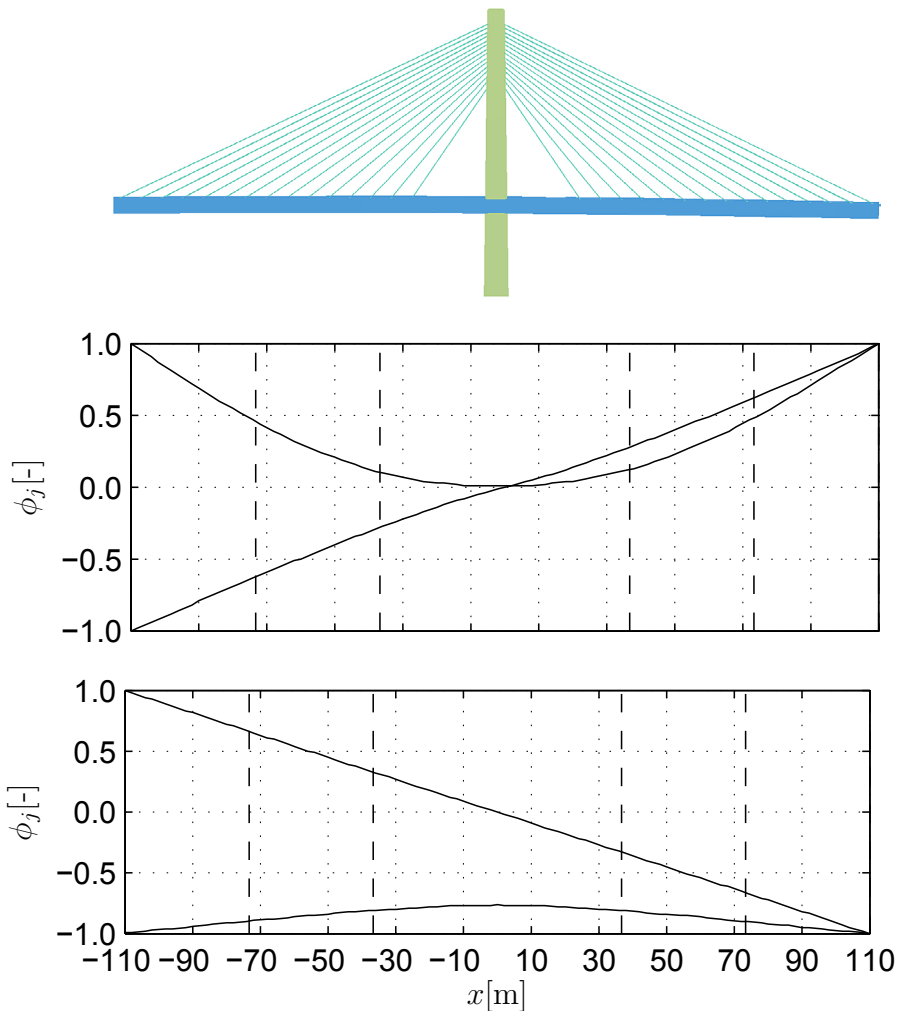


Figure 5: Finite Element model; corresponding vertical and lateral mode shapes, from top to bottom.

methods,

1. CFD using VPM as presented in section [2.2] coupled with modal superposition.
2. For validation, the structural response is computed using a commercial software based on FEM with time variant forces and admittance function to account for the turbulence wind effect on the structure, the turbulence admittance function is presented in [7, 8]. As an input to calculate the wind induced time variant forces, the wind coefficients as function of incidence angle α are provided. Those coefficients, are obtained from previous static CFD simulations e.g. as in figure [4] or from wind tunnel test results.

Model	Lateral [m]	Vertical [m]	rotation [rad]
FEM	0.10	0.39	0.0006
CFD + FSI	0.08	0.25	0.0002

Table 1: Peak displacements at the tip. Comparison between CFD simulation coupled with modal superposition for Fluid Structure Interaction (FSI) Vs. FEM model with time variant forces and admittance function to account for turbulent wind induced forces.

The maximum cantilever tip displacement in vertical, lateral and rotation for both cases is shown as a comparison with the two different methods in Table [1]. The results shows a very reasonable agreement. It is crucial to mention that the commercial FEM software based on modelled wind forces tends to be more conservative (upper estimation of displacements) in comparision to CFD simulation. Since, as a substitute to resolving the complete physics of fluid structure interaction as done in the CFD model, it uses the concept of admittance [7] of the fluctuation spectrum on the structure. A visualisation of three slices used in the CFD simulation is shown in figure [6]

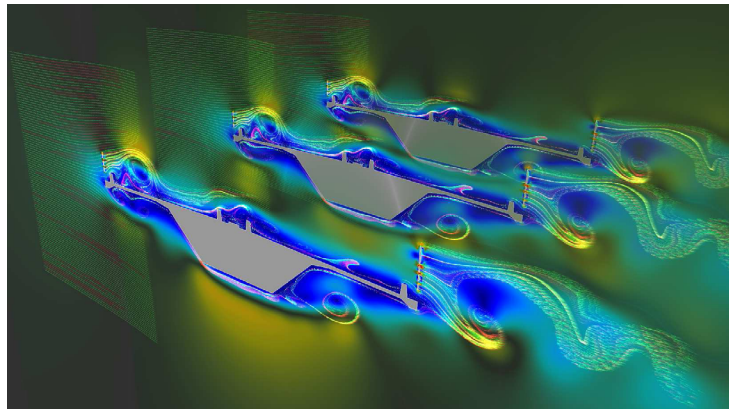


Figure 6: Three slices CFD simulation of the left cantilever side in figure [5]; Pseudo Three-dimensional simulation under turbulent wind.

4 Scaling and Parallel Efficiency

Recalling the concept of pseudo three-dimensional simulation, since each slice could be simulated independently at each time step OpenMP parallelisation is used to compute each slice in parallel. A synchronization point at the end of the time step is essential for coherence between the CFD solutions and the structural dynamics solution [5, 9]. For the local particles interaction computations, Graphical Processing Unit (GPU) is used in a thread per particle manner to compute the heavy arithmetic workload share of the algorithm. The implementation was realised by Morgenthal, Corriols and Bendig using Open Computing Language (OpenCL), allowing to execute the code on different

hardware architectures namely Central Processing Units (CPU) as well as GPU's. The memory fetching tasks and less arithmetic intensive operations are done on CPU, whilst the arithmetic computations are done in parallel using the GPU threads. The OpenMP strategy is designed such that each simulation slice utilizes one CPU core while the GPU kernel resources are shared between the different cores.

This section is concerned with evaluating the scalability and parallel efficiency of the simulation framework. Scalability is the ability of the algorithm to handle a growing amount of work based on a given parallelisation strategy [10]. Generally in high performance computing two common scalability measurements are used. Namely,

- Weak scaling, as a metric to how the solution time varies with the number of cores for a fixed problem size per CPU core.
- Strong scaling, as a metric to how the solution time varies with the number of cores for a fixed total problem size i.e. as the number of CPU cores increase, the load per core decreases.

In order to normalise the absolute run time for different problem size, MPUPS (Million Particle Updates Per Second) is defined as a measuring quantity. Such that,

$$MPUPS = \frac{nParticles \times nIterations}{Calc.Time \times 10^6} \quad (18)$$

Where *nParticles* is the total number of particles, *nIterations* is the number of computational iterations over the simulation kernel and *Calc.Time* is the wall clock time for each simulation run. The number of iterations is kept constant as 1000 steps for all problem sizes and processor counts.

4.1 Weak Scaling

For a fixed problem size per CPU core, namely 2.5×10^5 particle per core. The weak scaling is done for number of CPU cores (Computing slices) from one to four. Corresponding to 2.5×10^5 up to 1×10^6 particles. It is shown in figure [7] a nearly ideal weak scaling where the performance almost stay constant for a constant problem size per node. The slight drop in the performance starting from three cores, can be explained due to the serialization time that is introduced when the CPU'S share the GPU unit for the particle update computations. This idealisation time happens because after 5×10^5 particles the GPU needs to be shared in serial manner between the different CPU cores. Using GPU with more threads and/or Multi GPU's would postpone the occurrence of the serialization instance to a higher number of cores i.e. simulation slices, because the increase of the capacity would allow sharing the GPU kernel for more number of particles.

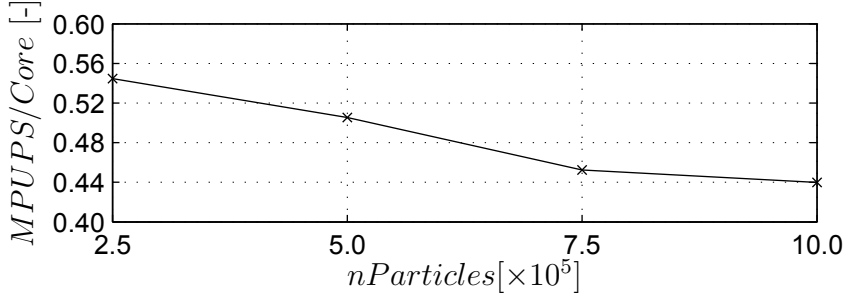


Figure 7: Weak scaling of simulation framework; representing variation in the computational efficiency per CPU core ($MPUPS/Core$) versus total number of particles ($nParticles$). As the number of particles increase the number of cores increase as well i.e. fixed problem size per CPU core.

4.2 Strong Scaling

The strong scaling is performed for a total problem size of 5×10^5 particles. Using this approach the GPU resources have to carry the same computation once requested by one CPU core and later on requested by two, three and four cores. It is seen from figure [8] that the total computation efficiency is increased between one and two cores, later on slightly reducing. This can be explained by the time spent in moving the data between

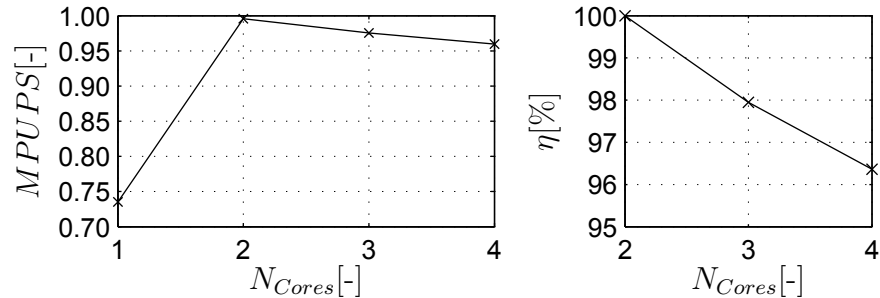


Figure 8: Strong scaling (left) and Parallel efficiency η (right) of simulation framework; Strong scaling represents the total computational efficiency ($MPUPS$) as the a problem with a fixed size is distributed on different number of cores (N_{cores}) i.e. for increasing number of cores the load per core is decreasing. Computational efficiency is calculated relative to the optimal number of cores for a given problem size, for this case optimal N_{cores} is 2 for $nParticles = 5 \times 10^5$.

the hosting CPU core and the GPU device memory. As the number of cores increase even for the same number of particles it is expected that the performance would drop due to the time cost of the data transfer.

4.3 Parallel Efficiency

Considering two simulation slices i.e. CPU cores as the reference point to evaluate the computation efficiency with relation to the drop down due to the data transfer. The parallel efficiency as shown in figure [8] is computed from the strong scaling, showing a very slight drop as the number of cores increase. It is crucial to remark that strong scaling as well as the parallel efficiency was done for a problem size 5×10^5 particles, the value previously concluded from the weak scaling to be optimal before the effect of the serial sharing of the GPU resources takes place. Hence, Strong scaling and Parallel efficiency measurements could be used to analyse the computation versus data transfer efficiency.

5 Summary and Conclusion

Vortex method has been presented along with its formulations and assumptions reaching to the vortex transport equation and the two dimensional Particle Vortex Method for CFD simulations. Based upon this numerical approach a simulation framework efficiently parallelised for CPU's and GPU's using OpenCL was used to simulate a test case the aeroelastic response of a bridge in the construction stage. The results were compared versus wind tunnel as well as other simulation approach.

Finally, the scaling and the parallel efficiency of the utilised simulation framework has been presented. The simulation approach presents a computationally very efficient yet accurate method that can be used to study numerous wind engineering problems related to the behaviour of line-like structures of complex geometries exposed to natural wind conditions.

REFERENCES

- [1] Cottet, G.-H., and Koumoutsakos, P. Vortex Methods: Theory and Practice. Cambridge University Press, New York, 2000.
- [2] Walther, J.H., Larsen, A., 1997. Discrete vortex method for application to bluff body aerodynamics. *J. Wind Engng. and Industrial Aerodynamics* 6768, 1831
- [3] Appel, A.W., 1985. An efficient program for many-body simulation. *SIAM J.Sci. Stat. Comput.* 6, 85103
- [4] Morgenthal, G., 2002. Aerodynamic Analysis of Structures Using High-resolution Vortex Particle Methods. Ph.D. thesis. University of Cambridge.
- [5] Morgenthal, G., Corriols, A.S., Bendig, B., 2014. A gpu-accelerated pseudo-3d vortex method for aerodynamic analysis. *Journal of Wind Engineering and Industrial Aerodynamics* 125, 69–80
- [6] Von Wendt, J.F. (Ed.). Computational Fluid Dynamics: An Introduction. New York: Springer-Verlag, 1996.

- [7] Xu, You-Lin. Wind effects on cable-supported bridges. John Wiley & Sons, 2013.
- [8] Rasmussen, J., Hejlesen, M., Larsen, A., Walther, J., 2010. Discrete vortex method simulations of the aerodynamic admittance in bridge aerodynamics. Journal of Wind Engineering and Industrial Aerodynamics 98, 754–766.
- [9] Morgenthal, G., Kovacs, I., Saul, R., 2005. Analysis of Aeroelastic Bridge Deck Response to Natural Wind. Structural Engineering International (IABSE) 15, 232235.
- [10] Hill, Mark D. (1990). "What is scalability?". ACM SIGARCH Computer Architecture News 18 (4): 18

NUMERICAL MODELING OF METAL CUTTING PROCESSES USING THE PARTICLE FINITE ELEMENT METHOD (PFEM) AND A PHYSICALLY BASED PLASTICITY MODEL

RODRÍGUEZ J.M.¹, JONSÉN, P.² AND SVOBODA, A.³

¹ Division of Mechanics of Solid Materials

Department of Engineering Sciences and Mathematics. Lulea University of Technology
E-mail rodjua@ltu.se

² Division of Mechanics of Solid Materials

Department of Engineering Sciences and Mathematics. Lulea University of Technology
E-mail par.Jonsen@ltu.se

³ Division of Mechanics of Solid Materials

Department of Engineering Sciences and Mathematics. Lulea University of Technology
E-mail ales.svoboda@ltu.se

Key words: Particle Finite Element Method, Dislocation density constitutive models, Metal cutting.

Abstract. Metal cutting is one of the most common metal shaping processes. Specified geometrical and surface properties are obtained by break-up of material and removal by a cutting edge into a chip. The chip formation is associated with large strain, high strain rate and locally high temperature due to adiabatic heating which make the modeling of cutting processes difficult. Furthermore, dissipative plastic and friction work generate high local temperatures. These phenomena together with numerical complications make modeling of metal cutting difficult. Material models, which are crucial in metal cutting simulations, are usually calibrated based on data from material testing. Nevertheless, the magnitude of strain and strain rate involved in metal cutting are several orders higher than those generated from conventional material testing. Therefore, a highly desirable feature is a material model that can be extrapolated outside the calibration range. In this study a physically based plasticity model based on dislocation density and vacancy concentration is used to simulate orthogonal metal cutting of AISI 316L. The material model is implemented into an in-house Particle Finite Element Method software. Numerical simulations are in agreement with experimental results, but also with previous results obtained with the finite element method.

1 INTRODUCTION

Cutting tool designs and cutting process parameters may be optimized by experimental measurements or by numerical analysis. In deformation zones in front of the tool and beneath the cutting edge, the material is deformed plastically by simultaneous action of large compressive and shearing stresses. The friction forces and dissipative plastic work generate high temperatures. This makes direct observation in the cutting zone during machining difficult.

In this study, the particle finite element method (PFEM) using a physical based dislocation density model is compared with a set of numerical simulations carried out using the finite element method (FEM).

2 THE PARTICLE FINITE ELEMENT METHOD

Let us consider a domain containing a fluid. This domain is characterized by a set of points, hereafter called *particles*. The particles contain all the information for defining the geometry and the material and mechanical properties of the underlying domain.

Summary of the steps

The PFEM is conceived for the solution of fluid-dynamics problems using a Lagrangian approach based on the formulation of the Navier–Stokes equations in material coordinates[3]. The PFEM, typically, consists of the following steps

1. Fill the fluid domain with a set of points referred to as ‘particles’. The accuracy of the numerical solution is clearly dependent on the considered number of particles.
2. Generate a finite element mesh using the particles as nodes. This is achieved using a Delaunay triangulation.
3. Identify the external boundaries to impose the boundary conditions and to compute the domain integrals.
4. Solve the non-linear Lagrangian form of the governing equations finding velocity and pressure at every node of the mesh.
5. Update the particle positions using the computed values of velocity and pressure.
6. Go back to step 2 and repeat for the next time step.

In this solution scheme, not only is the numerical solution of the equations critical from the computational point of view, but so are the generation of a new mesh and the identification of the boundaries. To this purpose a Delaunay triangulation scheme is adopted together with the boundary identification method presented in the following section.

Identification of the boundaries

In a Lagrangian framework the external boundary and the reference volume are defined by the position of the material particles. Every time the mesh is regenerated, the particles belonging to the boundary may change and the new boundary nodes (and therefore the particles) have to be identified. The Delaunay triangulation generates the convex hull of the set of particles. Moreover, the convex hull may not be conformal with the external boundaries. A possibility to overcome this problem is to correct the generated mesh using the so-called α -shape method to remove the unnecessary triangles from the mesh using a criterion based on the mesh distortion. The α -shape method can also be used for the identification of the fluid particles which separate from the rest of the domain.

2.1 The particle finite element method in the numerical simulation of metal cutting processes

The standard PFEM presents some weaknesses when applied in orthogonal cutting simulation. For example, the external surface generated using α -shape may affect the mass conservation, the chip shape and sometimes generates an unphysical welding of the workpiece and the chip.

To deal with this problem, in this work we propose the use of a constrained Delaunay algorithm. Furthermore, addition and remotion of particles are the principal tools, which we employ for sidestepping the difficulties, associated with deformation-induced element distortion, and for resolving the different scales of the solution.

In the numerical simulation of metal cutting process, despite the continuous Delaunay triangulation, elements arise with unacceptable aspect ratios; for this reason, the mesh is also subjected to laplacian smoothing. Laplacian smoothing is an algorithm to smooth a mesh. For each node in a mesh, a new position is chosen based on the position of neighbors and the node is moved there. In the case that a mesh is topologically a rectangular grid then this operation produces the Laplacian of the mesh.

3 PHYSICAL BASED MODELS

Physical based models are models where the physical mechanisms are underlying the deformation in contrast to empirical models which are of a more curve-fitting nature. However, due to the need for averaging and also limited knowledge about some of the relations making up the model, physical based models need also be calibrated. Two different types of physical based models exist. One option is to explicitly include variables from physics as internal state variables. The other possibility is to determine the format of the constitutive equation based on knowledge about the physical mechanisms causing the deformation. The latter is a so-called “model- based-phenomenology” Some advantages of physical based models is the possibility to link effects from other scales, e.g. via parameters for grain size or models for microstructure evolution that extends the model validity to a larger domain. This may extrapolated the validity of the model outside their range of calibration. This requires that the physical mechanisms implemented in the models still dominate the deformation in the extended range.

The dislocation density model consider dislocation glide and climb processes contributions to the plastic straining. The yield limit in this approach is separated into two components according to

$$\sigma_y = \sigma_G + \sigma^* \quad (1)$$

σ_G and σ^* are the long-range athermal component and the short-range contributions to the flow stress, respectively. The first component σ_G , is the stress needed to overcome the long-range interactions lattice distortions due to the dislocation substructure. The second component, σ^* , is the stress needed for the dislocation to pass through the lattice and to pass short-range obstacles. Thermal vibrations will then also assist the dislocation when passing an obstacle. The long-range stress component is commonly written as;

$$\sigma_G = m\alpha Gb\sqrt{\rho_i} \quad (2)$$

where m is the Taylor orientation factor, α is a proportionality factor, G is the temperature dependent shear modulus, b is the magnitude of Burgers vector and ρ_i is the immobile dislocation density. The short-range stress components may be written as,

$$\sigma^* = \hat{\tau}G \left\{ 1 - \left[\frac{kT}{\Delta F b^3 G} \ln \left(\frac{\dot{\varepsilon}_{ref}}{\dot{\varepsilon}^p} \right) \right]^{\frac{1}{q}} \right\}^{\frac{1}{p}} \quad (3)$$

where ΔF denote the required free energy needed to overcome the lattice resistance or obstacles without assistance from external stress, τ denote the athermal flow strength required to move the dislocation past barriers without assistance of thermal energy, $\dot{\varepsilon}_{ref}$ denote the reference strain rate. The exponent p and q characterize the barrier profiles and usually have values between $0 \leq p \leq 1$ and $0 \leq q \leq 2$ respectively.

3.1 Structure evolution

The evolution of the structure is considered to consist of a hardening and a recovery process. The used model assumes that the mobile dislocation density is stress and strain independent and much smaller than the immobile ones. Hence the evolution equation is written;

$$\dot{\rho}_i = \dot{\rho}_i^{(+)} - \dot{\rho}_i^{(-)} \quad (4)$$

where index i denotes the immobile dislocations. The increase in immobile dislocation density is assumed to be related to the plastic strain rate and may therefore be written according to

$$\dot{\rho}_i^{(+)} = \frac{m}{b} \frac{1}{\lambda} \dot{\varepsilon}^p \quad (5)$$

where λ denote the mean free path which is a function of the size of the grains and the dislocation sub-cell diameter. The recovery may occur by dislocation glide and/or climb. The former is described by

$$\dot{\rho}_i^{(-)} = \Omega \rho_i \dot{\varepsilon}^p \quad (6)$$

where Ω is a recovery function which depends on the temperature and strain rate. Recovery by climb is describe by

$$\dot{\rho}_i^{(-)} = 2c_\gamma \frac{D_v}{c_v^{eq}} \frac{Gb^3}{kT} (\rho_i^2 - \rho_{eq}^2) c_v \quad (7)$$

where c_v is the vacancy fraction, c_v^{eq} is the thermal equilibrium vacancy concentration, D_v is the diffusivity and c_γ is a calibration parameter. More details are found in (Lindgren et al).

4 NUMERICAL MODELING OF METAL CUTTING PROCESSES USING PFEM AND A PHYSICAL BASED CONSTITUTIVE MODEL

The orthogonal cutting process has been analyzed utilizing an in-house particle finite element method code. This software is based on a Lagrangian formulation combined with an implicit time integration scheme. A staggered method for coupled transient mechanical and heat transfer analysis is used. A mixed displacement-pressure linear finite element with one integration point was used. A continuous Delaunay triangularization of the particle in its updated configuration facilitates the analysis facing large excessive deformations and shear localization. The insertion of particles at different deformation zones occurs through a plastic power error estimator. The physical based material model was implemented inside the code as a new material model. This was based on a thermo-elasto-plastic model with isotropic hardening using a multiplicative decomposition plasticity formulation which takes account high strain rates.

An orthogonal cutting operation was employed to mimic 2D plain strain conditions. The depth of cut, used for all the test cases, was equal to 3mm. The dimension of the workpiece was 8*1.6 mm. A horizontal velocity corresponding to the cutting speed was applied to the particles at the right side of the tool. The particles along the bottom and the left sides of the workpiece were fixed. Cutting data used for the numerical simulations are the same used in Svoboda et al (2010).

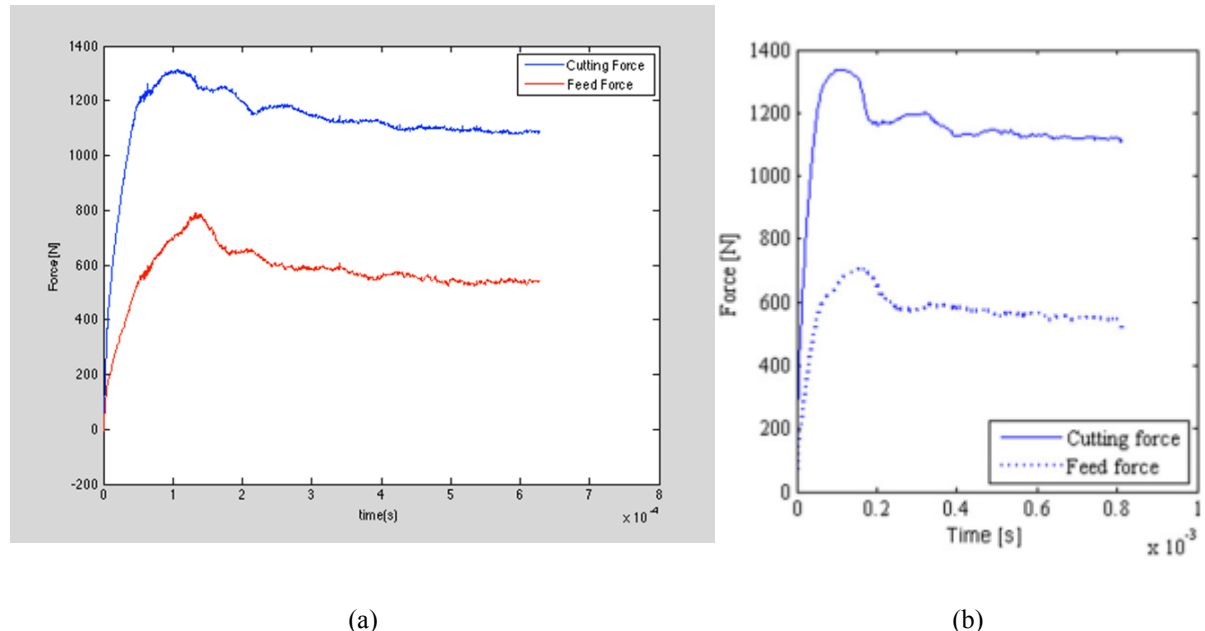


Figure 1: Comparison of cutting and feed force PFEM-FEM. In (a) results predicted by PFEM and in (b) results predicted by FEM.

The loading histories of simulated forces (see figure above), were evaluated at the tool chip interface. Figure 1 on the left presents the results using PFEM and the figure on the right present the results using FEM (Svoboda et al 2010). The force time curves are very similar for both numerical simulations. Average values of the computed forces in the steady state region are compared with experimental results and numerical results obtained using FEM presented in Svoboda et al (2010) in the following table.

The table 1 shows that the cutting force was overestimated in all tests by about 15%. Meanwhile, the feed force was underestimated by about 5%. The results presented in the table above were compared with the results in Svoboda et al (2010), showing that PFEM is able to predict results to those obtained using (FEM). Literature overview (Lindgren, 2009) show that in the industrial production of nominally identical cutting tool as well as variations in material properties of nominally the same material can cause variations around the 10% in forces.

Table 1: Simulated cutting and feed forces

Table 4. Measured and simulated cutting forces.

Test no	Measured		Simulated JC				Simulated DD			
	F_c (N)	F_f (N)	F_c (N)	e (%)	F_f (N)	e (%)	F_c (N)	e (%)	F_f (N)	e (%)
1	446	437	425	-4.7	350	-19.9	485	8.7	400	-8.5
2	960	592	1065	10.9	515	-13.0	1100	14.6	545	-7.9
3	442	439	440	-0.5	355	-19.4	480	8.6	390	-11.2
4	929	560	1050	13.0	510	-8.9	1075	15.7	530	-5.4

Test no	F_c (N)	E(%)	F_f (N)	E(%)
1	513.6	15.1	427.6	-2,15
2	1100	14.5	557	-5,91
3	507	14.7	411	-6,38
4	1094	17.7	549	-1,96

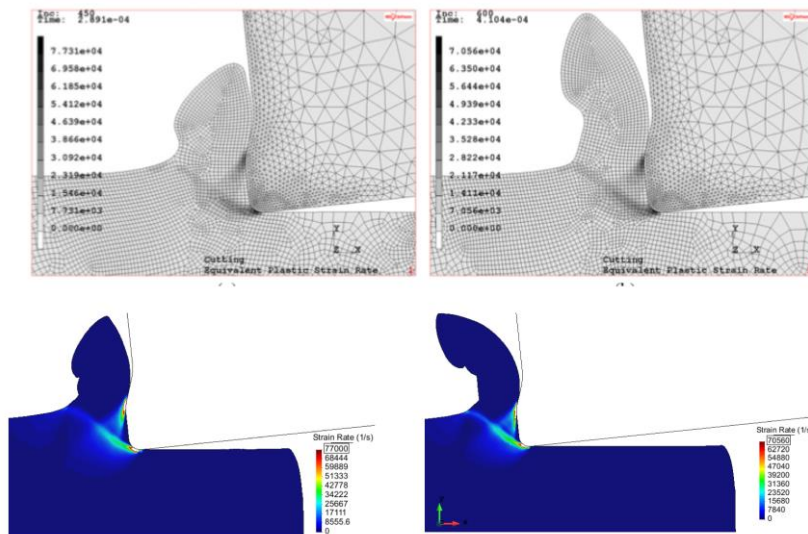


Figure 2: Effective plastic strain rate. FEM and FEM

Figure 2 illustrates distribution of plastic strain rates in the primary and the secondary shear zones. A comparison of the predicted chip shape using PFEM (below) and FEM (above) shows that the numerical strategies predict similar chip shapes, although the chip tool contact length predicted by PFEM a little lower than FEM.

CONCLUSIONS

In this work a dislocation density model have been used together with PFEM to virtually reproduce orthogonal cutting of AISI 316L steel. Numerical results obtained using PFEM have been compared with both experimental results and numerical results. The PFEM based numerical model can also predict similar strain rate distribution and chip shape as the FEM model. Also, the numerical model developed within this work is in agreement with experimental results and can predict forces near the wanted precision.

REFERENCES

- [1] Svoboda A, Wedberg D and Lindgren L-E 2010 Simulation of metal cutting using a physically-based plasticity model. *Modelling Simul. Mater. Sci. Eng.* 18 1–19Idelsohn, S.R. and Oñate, E. Finite element and finite volumes. Two good friends. *Int. J. Num. Meth. Engng* (1994) **37**:3323-3341.
- [2] Rodriguez, J. M. 2014. Numerical modeling of metal cutting processes using the Particle Finite Element Method (PFEM). <http://hdl.handle.net/10803/145692>
- [3] S. R. Idelsohn, E. Oñate, and F. D. Pin, "The particle finite element method: a powerful tool to solve incompressible flows with free-surfaces and breaking waves," *International Journal for Numerical Methods in Engineering*, vol. 61, pp. 964-989, 2004

NUMERICAL SIMULATION OF PENETRATION PROBLEMS IN GEOTECHNICAL ENGINEERING WITH THE PARTICLE FINITE ELEMENT METHOD (PFEM)

LLUÍS MONFORTE¹, JOSEP MARIA CARBONELL^{1,2},
MARCOS ARROYO¹ AND ANTONIO GENS¹

¹ Universitat Politècnica de Catalunya - BarcelonaTech
Campus Norte UPC, 08034 Barcelona, Spain
e-mail: antonio.gens@upc.edu

² Centre Internacional de Mètodes Numèrics en Enginyeria (CIMNE)
Universitat Politècnica de Catalunya
Campus Norte UPC, 08034 Barcelona, Spain

Key words: PFEM, Porous media, soil mechanics, penetration tests.

Abstract. This paper highlights a computational framework for the numerical analysis of saturated soil-structure interaction problems. The variational equations of linear momentum and mass balance are obtained for the large deformation case. These equations are solved using the Particle Finite Element Method. The paper concludes with a benchmark test and the analysis of a penetration test.

1 INTRODUCTION

Penetration tests -such as cone penetration test (CPT), T-Bar, and others- are widely used in geotechnical engineering to determine soil properties. Using a realistic description of the soil behavior (e.g. elasto-plastic effective stress response) increases both the range of conditions for and the precision of test interpretation. The downside is that a number of material non-linearities are added to a problem that already features a severe geometric non-linearity.

Finite element method is well suited to include all sort of non-linearities. However, when a Lagrangian formulation is employed -typically when a path dependent material model is used- the mesh may experience severe distortion, leading to numerical inaccuracies and even rendering the calculation impossible. In order to alleviate this problem several numerical techniques based on FEM have been proposed (adaptive methods, Arbitrary Lagrangian-Eulerian,...).

In this work, the Particle Finite Element Method (PFEM) is employed to simulate the penetration of a rigid probe into the soil. The method is characterized by a particle

discretization of the domain: every time-step a finite element mesh -whose nodes are the particles- is build using a Delaunay's tessellation and the solution is evaluated using well shaped, low order finite elements [1, 2].

The soil-water mixture is modeled as a two-phase continuum employing a finite deformation formulation. The linear momentum and mass balance equations are written following the movement of the solid skeleton, where the unknown fields are the solid skeleton displacements and the fluid pressure ($u - p_w$ formulation). The water flow is assumed to obey a generalization of the Darcy's Law whereas a multiplicative hyperelastic-plastic constitutive response is assumed for the solid skeleton. The proposed model differs slightly from previous approaches [3, 4] in the definition of the reference configuration, in the Darcy's law and the working unknowns.

The proposed approach is assessed against a numerical benchmark example, an oedometer test, showing a good agreement with the analytical solution. Finally, the effect of the penetration rate of the CPT on the cone resistance and the excess pore pressure in a Modified Cam Clay soil is evaluated.

2 GOVERNING EQUATIONS

In this section, the governing equations of the porous media are highlighted. First, the strong form of the mass and momentum balance equations are obtained. After briefly describing the constitutive equations, the weak form of the residual is presented.

2.1 Strong form

The mass of each phase of the porous media -solid skeleton, m_s , and water, m_w - in an arbitrary deformed domain Ω_i^{n+1} may be expressed as:

$$\begin{aligned} m_s &= \int_{\Omega_i^{n+1}} \rho_s (1 - \varphi) d\Omega^{n+1} \\ m_w &= \int_{\Omega_i^{n+1}} \rho_w \varphi d\Omega^{n+1} \end{aligned} \quad (1)$$

where φ is the porosity and ρ_s and ρ_w are the solid and water density respectively.

Since the mass on the control volume is conserved, the material derivative of the integral is null; therefore:

$$\begin{aligned} \frac{d(m_s)}{dt} = 0 &\implies \int_{\Omega_i^{n+1}} \left(\frac{\partial(\rho_s(1 - \varphi))}{\partial t} + \frac{\partial(\rho_s(1 - \varphi)v_i)}{\partial x_i} \right) d\Omega^{n+1} = 0 \\ \frac{D(m_w)}{Dt} = 0 &\implies \int_{\Omega_i^{n+1}} \left(\frac{\partial(\rho_w \varphi)}{\partial t} + \frac{\partial(\rho_w \varphi \bar{v}_i)}{\partial x_i} \right) d\Omega^{n+1} = 0 \end{aligned} \quad (2)$$

where $\frac{d}{dt}$ and $\frac{D}{Dt}$ are the material derivatives with respect to the solid and fluid phase and v and \bar{v} are the solid and fluid velocities.

After some algebraic manipulation and summing both expressions, an equation for the conservation of mass in the mixture is obtained:

$$\frac{-\varphi}{K_w} \frac{dp}{dt} - \frac{v^d}{K_w} \cdot \nabla p + \nabla \cdot v + \nabla \cdot v^d = 0 \quad (3)$$

where the Darcy's velocity, v^d , has been introduced: $v^d = \varphi(\bar{v} - v)$, p is the water pressure and K_w is the water compressibility.

The problem definition is completed with the balance of linear momentum of the mixture. Excluding inertial effects, the strong form can be expressed as:

$$\nabla \cdot \sigma + \rho g = 0 \quad (4)$$

where σ is the total Cauchy stress tensor and $\rho = (1 - \varphi)\rho_s + \varphi\rho_w$ is the density of the mixture.

According to the principle of effective stress, the total stress tensor is equal to the sum of the pore pressure and the effective stress, σ' :

$$\sigma_{ij} = \sigma'_{ij} + p\delta_{ij} \quad (5)$$

2.2 Constitutive relations

A multiplicative elasto-plastic constitutive response is assumed for the solid skeleton. The integration of stresses is performed with an explicit integration scheme with adaptive sub-stepping and a correction for the yield surface drift is applied [5].

A large deformation generalization of the Darcy's Law, excluding inertial effects, may be written as:

$$v^d = \frac{K}{\rho_w g} \cdot (\nabla p + \rho_w g) \quad (6)$$

where K is the spatial permeability tensor and g is the gravity; compressions in the water pressure are considered negative. In this work, this constitutive law is stated in a spatial setting; that is, the spatial description of the permeability tensor is assumed to be constant. On the other hand, the permeability may be considered as a material property (then, the principal directions of the tensor rotate with the deformation) [4].

2.3 Residual form

The weak form of the mass conservation expression, equation (3), is expressed in the current deformed configuration; a fully implicit time-marching scheme is used:

$$R = \int_{\Omega^{n+1}} q \left(\frac{\partial \Delta u_i^{n+1}}{\partial x_i} - \frac{\Delta p^{n+1}}{K_w} \right) \frac{1}{J_0^{n+1}} d\Omega^{n+1} - \int_{\Omega^{n+1}} \frac{\partial q}{\partial x_i} \frac{K_{ij}}{\rho_w g} \left(\frac{\partial p^{n+1}}{\partial x_j} + \rho_w g_j \right) \frac{\Delta t}{J_0^{n+1}} d\Omega^{n+1} \quad (7)$$

where q is the virtual Cauchy water pressure, $\Delta u^{n+1} = u^{n+1} - u^n$ and $\Delta p^{n+1} = p^{n+1} - p^n$.

In the other hand, the residual of the mechanical problem, equation (4), is:

$$R = \int_{\Omega^{n+1}} \frac{\partial w_i}{\partial x_j} \sigma_{ji} d\Omega^{n+1} + \int_{\Omega^{n+1}} w_i g_i \rho d\Omega^{n+1} \quad (8)$$

where w is the virtual displacement.

The tangent matrices of the problem are derived performing a pull-back of the residual to the initial configuration and all large-strains terms are considered. It is worth noting that the usual small strains equations of computational geomechanics may be obtained from the presented formulation by neglecting second order terms of the residual and tangent matrices.

In the present implementation, both equations are solved in a monolithic approach; the space is discretized with linear triangles and the same shape functions are used both for displacements and water pressure. This type of element may produce spurious oscillations in the pore pressure field when the fluid is almost incompressible and in the nearly impermeable situation as a result of failure to satisfy the inf-sup condition. In order to alleviate these oscillations, a Fluid Pressure Laplacian stabilization term is added to the mass balance equation [6].

The problem is completed with the contact constraints, that are imposed with a penalty method.

3 NUMERICAL METHOD

A typical solution algorithm with the Particle Finite Element Method involves the following steps:

1. Discretize the domain with a Finite Element mesh. Define the shape and movement of the rigid structure.
2. Identify the external boundaries. Search the nodes that are in contact with the rigid structure and initialize the contact conditions.
3. Compute some time-steps of the coupled hydro-mechanical problem using a monolithic solver.
4. Construct a new mesh. This step may include introducing new particles on the domain in areas with large plastic dissipation, generate a new Delaunay's tessellation and perform some mesh smoothing; then, state variables are interpolated from the previous mesh to the new one.
5. Go back to step 2 and repeat the solution process for the next time-steps.

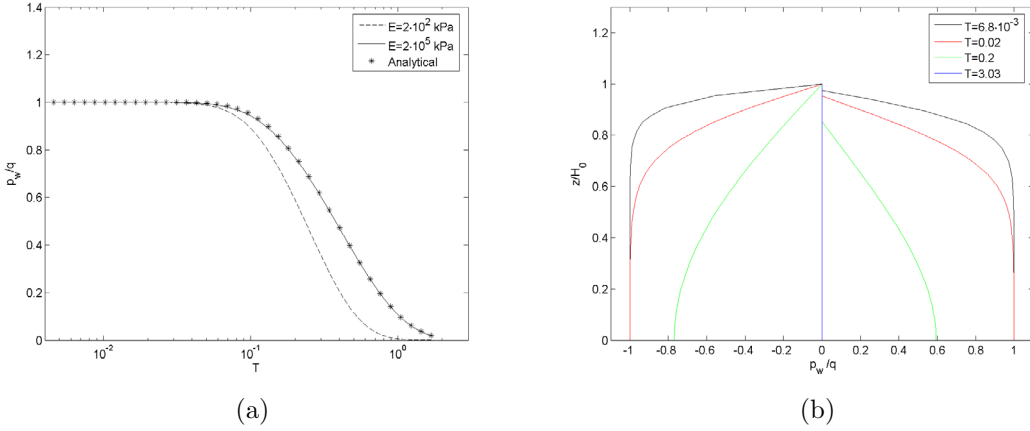


Figure 1: Oedoemeter test. Dissipation curves for two sets of parameters at the center of the oedoemeter and (b) isochrones: vertical profiles of the water pressure for $E = 2 \cdot 10^5$ kPa (left) and $E = 2 \cdot 10^2$ kPa (right).

4 NUMERICAL EXAMPLES

In this section, first a benchmark example is presented to assess the implementation; then, some results on the influence of the penetration velocity of CPT on some geotechnical quantities of interest are presented.

4.1 Oedometer test

The first example corresponds to an oedometer test in a weightless soil. This test consists on applying a vertical load to a soil sample whose lateral displacements are prevented; drainage is only allowed through the top of the sample. Small strains analytical solutions states that the key constitutive parameter that controls the pore pressure dissipation is the coefficient of consolidation, $c_v = \frac{E(1-\nu)}{(1+\nu)(1-2\nu)} \frac{K}{\rho_w g}$.

Figure 1(a) shows the variation of the water pressure at the bottom of the sample as a function of time for two sets of parameters (Young's modulus and permeability) maintaining constant the coefficient of consolidation $c_v = 2.7 \cdot 10^{-3} \text{ m}^2/\text{s}$. In the larger Young's modulus case, both displacements and deformations are small and the solution agrees well with the small strains analytical solution. The other case is different due to the severe geometric non-linearity: as consolidation takes place the height of the domain decreases; thus, the draining path length reduces, see Figure 1(b).

4.2 Penetration test

The last numerical example consists on the penetration of a smooth CPT in a Modified Cam Clay soil; the geometry and constitutive soil parameters try to mimic the example reported by Sheng et al [7].

Figure 2(a) shows the evolution of the net cone resistance in terms of penetration depth

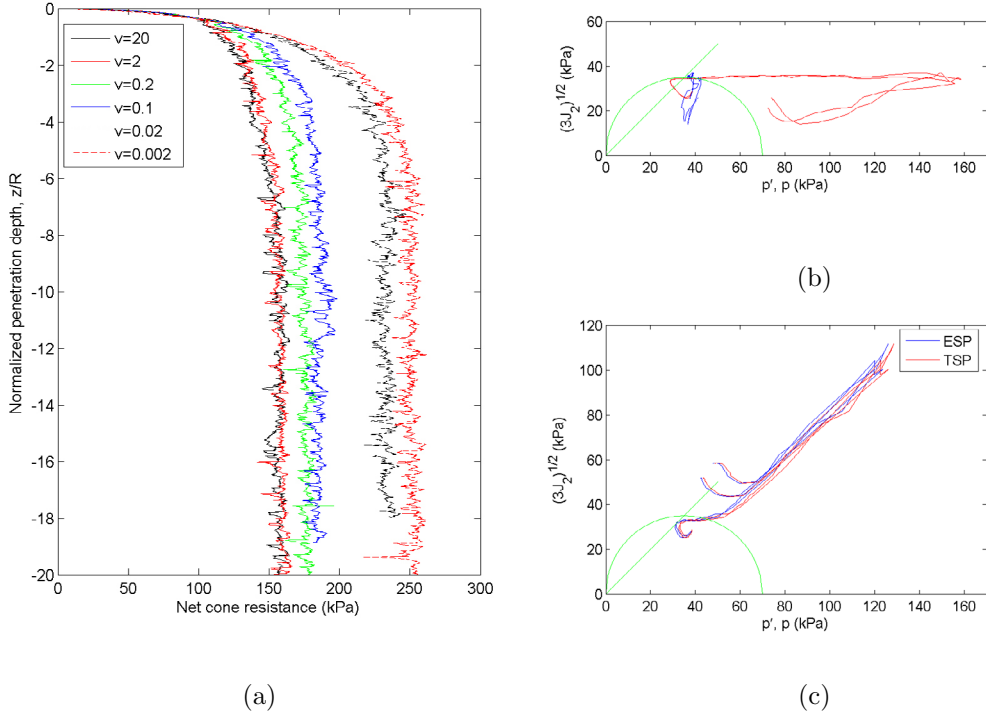


Figure 2: CPT test. Variation of the net cone resistance in terms of the penetration depth for different penetrations rates, (a). Effective stress path (ESP) and total stress path (TSP) at an horizontal distance of $\frac{R}{3}$ to the CPT shaft and a depth of 7 and 9.5 radii below the cone initial position for a penetration velocity of 20 m/s, (b), and 0.002 m/s, (c), along with the initial yield surface and the critical state line, in green. Compressions are assumed positive.

for various penetration velocities. Although these curves present some oscillations due to the numerical method, in all cases a steady state is achieved approximately at 6 radii. These results are in good agreement with the reference solution.

The computed cone resistance varies between two limiting values; the smallest one coincides with the larger penetration rates whereas the largest one coincides with the smaller penetration rates. Figures 2(b) and 2(c) show the stress path of two typical points for a penetration velocity of 20 m/s and 0.002 m/s respectively. It can be seen that in the larger penetration velocity the effective mean stress remains approximately constant whereas large excesses of water pressure are generated; this response may be idealized as representing undrained conditions. The fact that the mean effective stress is not constant in the elastic phase is mostly due to the hyperelastic constitutive model, that couples the volumetric and deviatoric behavior, although some numerical issues (the interpolation between evolving meshes and the use of a stabilized form) may also play a role. On the other hand, for a penetration velocity of 0.002 m/s the total and effective

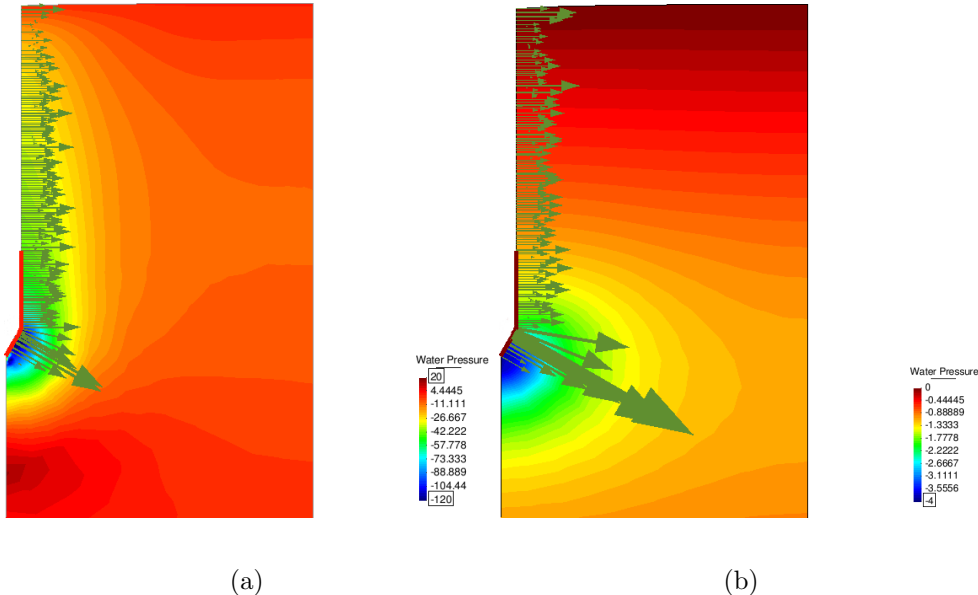


Figure 3: CPT Test. Contours of the Cauchy water pressure and contact force after a penetration of 20 radii for a velocity of 20 m/s, (a), and 0.002 m/s, (b). Compression in the water pressure field are depicted with negative values.

stress path practically coincide since a limited variations on the water pressure takes place; thus, this simulation may be interpreted as the drained limit.

The water pressure profile for the larger rate, after a penetration of 20 radii, is depicted in Figure 3(a). This field exhibits its maximum value near the edge of the tip and the shaft of the CPT; from this point, it sharply decreases in the horizontal direction and below the tip; some tractions in the water pressure occur below the cone tip. Large water pressures are also encountered at the cone shaft, where shearing continues.

In the other hand, for a penetration rate of 0.002 m/s, Figure 3(b), the water pressure contour hardly varies from the initial state; the maximum (4 kPa) is observed below the cone tip.

5 CONCLUSIONS

In this work, a numerical framework for the analysis of saturated porous media undergoing large deformations has been presented. The basic balance equations and its linearized form have been described. By means of the analysis of the oedometer test it has been shown that the obtained results are accurate. Indeed using a large deformation theory may reflect results that are artificially excluded by the linear theory. Finally, a parametric analysis of the penetration velocity of a rigid probe into a Modified Cam Clay soil has been performed.

ACKNOWLEDGMENTS

The support of the Ministry of Education of Spain through research grant BIA2011-27217 is gratefully acknowledged.

REFERENCES

- [1] Carbonell, J.M., Oñate, E. and Suárez, B. Modeling of ground excavation with the particle finite-element method *Journal of Engineering Mechanics* (2010) **136**:(4) 455–463
- [2] Carbonell, J.M., Oñate, E. and Suárez, B. Modelling of tunelling processes and rock cutting tool wear with the particle finite element method *Computational Mechanics* (2013) **52**(3):607–629
- [3] Borja, R.I. and Alarcón, E. A mathematical framework for finite strain elastoplastic consolidation. Part I: Balance laws, variational formulation, and linearization *Comput. Methods Appl. Mech. Engrg.* (1995) **122**(1):145–171
- [4] Larsson, J. and Larsson, R. Non-linear analysis of nearly saturated porous media: theoretical and numerical formulation *Comput. Methods Appl. Mech. Engrg.* (2002) **191**:3885–3907
- [5] Monforte, L., Arroyo, M., Gens, A. and Carbonell, J.M. Explicit finite deformation stress integration of the elasto-plastic constitutive equations *Computer Methods and Recent Advances in Geomechanics - Proceedings of the 14th Int. Conf. of IACMAG* (2014) 267–272
- [6] Preisig, M. and Prévost, J.H. Stabilization procedures in coupled poromechanics problems: A critical assessment *Int. J. Numer. Anal. Mesh. Geomech.* (2011) **35**:1207–1225
- [7] Sheng, D., Kelly, R., Pineda, J. and Lachlan, B. Numerical study of rate effects in cone penetration test *3rd International Symposium on Cone Penetration Testing* (2014) 419–428

ON SOME DRAWBACKS AND POSSIBLE IMPROVEMENTS OF A LAGRANGIAN FINITE ELEMENT APPROACH FOR SIMULATING INCOMPRESSIBLE FLOWS

MARCO LUCIO CERQUAGLIA¹, GEOFFREY DELIEGE¹, ROMAIN
BOMAN¹, LUC PAPELEUX¹, VINCENT TERRAPON¹ AND
JEAN-PHILIPPE PONTHOT¹

¹ Department of Aerospace and Mechanical Engineering
University of Liège
Quartier Polytech 1, Allée de la Découverte 9, 4000 Liège (Belgium)
marcolucio.cerquaglia@ulg.ac.be; <http://www.ltas.ulg.ac.be/>

Key words: Particle finite element method, free surfaces, sloshing, dam break

Abstract. In this paper a Lagrangian finite element approach for the simulation of incompressible flows is presented, based on the so-called Particle Finite Element Method (PFEM). The spatial discretization and the definition of the boundary terms are discussed in detail with a specific focus on free-surface flows. Additionally, some problems that can arise from the use of such a method are pointed out. Some numerical examples are given and discussed in the last section of the paper.

1 INTRODUCTION

In the past decades numerical simulation of fluid flows has been mostly limited to Eulerian approaches, mainly due to the difficulty to treat extremely large deformations in a Lagrangian framework. On the other hand, the simulation of free-surface or multi-phase flows can become very difficult using an Eulerian description, due to the presence of interfaces, even if some techniques, such as the Volume Of Fluid (VOF) [4], have been developed in order to take the presence of interfaces into account. Up to a certain extent, these problems can be solved thanks to the Arbitrary Lagrangian-Eulerian (ALE) formulation [2]. Nevertheless, when it comes to problems involving complex free-surface flows, including mixing and separation, and possibly interacting with solid bodies, all the former approaches reach their limit, especially for industrial applications.

In this paper, we focus on the case of free-surface incompressible flows using a Lagrangian approach based on the Particle Finite Element Method (PFEM) [11]. In the first part of the paper a general description of the PFEM method is given. In the second part different

expressions of the governing equations are discussed, and spatial and time discretization are analyzed in more detail, together with some implementation issues. Finally, in the last part, some numerical examples are given.

2 THE PFEM METHOD

In the PFEM method the fluid is discretized using a set of points, referred to as *particles* hereafter, which actually represent material points of the body. In order to evaluate the forces acting on each particle, a new mesh is built at each time step, based on an Extended Delaunay Triangulation (EDT) [5], in such a way that the computational cost needed to evaluate nodal connectivity grows almost linearly with the number of particles [6]. At each remeshing the contours of the body are identified using the so-called α -shape technique [3]. Based on the new mesh, the Meshless Finite Element Method (MFEM) shape functions [7] can be defined in order to solve the corresponding weak form of the governing equations. The main steps of the PFEM method can be summarised as follows:

1. at a given time step, discretize the domain using a set of particles;
2. define the particle connectivity through an Extended Delaunay Triangulation (EDT);
3. identify the domain boundaries using the α -shape technique;
4. solve the governing equations using the MFEM shape functions;
5. use the solution obtained at the end of step 4 to update particles positions;
6. go back to step 2 and repeat the process for the next time step.

For a complete description of the method, refer e.g. to [11].

In the present implementation of the method, limited to 2D, a simple Delaunay triangulation is used, together with classical linear Finite Element shape functions, instead of MFEM ones.

3 GOVERNING EQUATIONS

The Navier-Stokes equations (momentum balance and mass conservation) for an incompressible Newtonian fluid in the current and reference configuration can be written, in Lagrangian form, as

$$\rho \frac{D\mathbf{u}}{Dt} = -\text{grad}(p) + \mu \text{div}(\text{grad}(\mathbf{u})) + \mu \text{div}(\text{grad}(\mathbf{u})^T) + \rho \mathbf{b} \quad \text{in } \Omega \quad (1)$$

$$\text{div}(\mathbf{u}) = 0 \quad \text{in } \Omega \quad (2)$$

and

$$\begin{aligned} \rho \frac{D\mathbf{U}}{Dt} = & -\frac{1}{J} \text{Div}(J p \mathbf{F}^{-T}) + \frac{1}{J} \mu \text{Div}\left(J \text{Grad}(\mathbf{U}) \mathbf{F}^{-1} \mathbf{F}^{-T} + \right. \\ & \left. J \mathbf{F}^{-T} \text{Grad}(\mathbf{U})^T \mathbf{F}^{-T}\right) + \rho \mathbf{b} \quad \text{in } \Omega_0 \end{aligned} \quad (3)$$

$$\operatorname{Div} (J\mathbf{F}^{-1}\mathbf{U}) = 0 \quad \text{in } \Omega_0 \quad (4)$$

respectively, where Ω and Ω_0 are the volumes occupied by the fluid in the current and reference configuration, $\rho(\mathbf{x}, t)$ is the density, $\mu(\mathbf{x}, t)$ is the viscosity, $\mathbf{u} = \mathbf{u}(\mathbf{x}, t)$ is the velocity vector, $p(\mathbf{x}, t)$ is the pressure, and $\rho\mathbf{b}(\mathbf{x}, t)$ is a body force, such as gravity for instance. $D(\cdot)/Dt$ is the Lagrangian, or material, derivative of the quantity (\cdot) , $\mathbf{F} = \frac{d\mathbf{x}}{d\mathbf{X}}$ is the deformation gradient and $J = \det(\mathbf{F})$. Capital letters are used to denote quantities defined in the reference configuration.

These equations have to be complemented with Dirichlet and Neumann boundary conditions:

$$\mathbf{u}(\mathbf{x}, t) = \bar{\mathbf{u}}(\mathbf{x}, t) \quad \forall \mathbf{x} \in \Gamma_D \quad (5)$$

$$\boldsymbol{\sigma}(\mathbf{x}, t) \cdot \mathbf{n} = \bar{\mathbf{t}}(\mathbf{x}, t) \quad \forall \mathbf{x} \in \Gamma_N, \quad (6)$$

where $\bar{\mathbf{u}}(\mathbf{x}, t)$ and $\bar{\mathbf{t}}(\mathbf{x}, t)$ are imposed velocities and surface tractions respectively, $\boldsymbol{\sigma} = \boldsymbol{\sigma}(\mathbf{x}, t)$ is the Cauchy stress tensor, \mathbf{n} denotes the unit outward normal to the boundary, $\Gamma_D \cup \Gamma_N = \partial\Omega$ and $\Gamma_D \cap \Gamma_N = \emptyset$.

3.1 Weak form and spatial discretization

For further developments, only the forms corresponding to Equations (3) and (4) will be discussed, the developments related to the current configuration being the same. Introducing the following spaces for trial and test functions

$$\begin{aligned} S &= \left\{ \mathbf{U} \in \mathbf{H}^1(\Omega) \mid \mathbf{U} = \bar{\mathbf{U}} \quad \text{on } \Gamma_D \right\}, \\ S_0 &= \left\{ \mathbf{W} \in \mathbf{H}^1(\Omega) \mid \mathbf{W} = \mathbf{0} \quad \text{on } \Gamma_D \right\}, \\ Q &= \left\{ q \in L^2(\Omega) \right\}, \end{aligned}$$

the weak form of Equations (3) and (4) can be established by multiplying Equation (3) by a vector test function $\mathbf{W} \in S_0$ and Equation (4) by a scalar test function $q \in Q$. Integrating over the reference volume and using Green theorem, the weak form finally reads

$$\begin{aligned} \int_{\Omega_0} \rho_0 \frac{D\mathbf{U}}{Dt} \cdot \mathbf{W} d\Omega_0 &= \int_{\Omega_0} J p \mathbf{F}^{-T} : \operatorname{Grad}(\mathbf{W}) d\Omega_0 \\ - \int_{\Omega_0} \mu J \left[\operatorname{Grad}(\mathbf{U}) \mathbf{F}^{-1} \mathbf{F}^{-T} : \operatorname{Grad}(\mathbf{W}) + \mathbf{F}^{-T} \operatorname{Grad}(\mathbf{U})^T \mathbf{F}^{-T} : \operatorname{Grad}(\mathbf{W}) \right] d\Omega_0 &\quad (7) \\ + \int_{\Omega_0} \rho_0 \mathbf{b} \cdot \mathbf{W} d\Omega_0 + \int_{\Gamma_N} \mathbf{W} \cdot \bar{\mathbf{t}} d\Gamma_N \quad \forall \mathbf{W} \in S_0, \end{aligned}$$

$$\int_{\Omega_0} \operatorname{Div}(J\mathbf{F}^{-1}\mathbf{U}) q d\Omega_0 = 0 \quad \forall q \in Q. \quad (8)$$

Equations (7) and (8) can be discretized using linear isoparametric finite elements, leading to the following system of semi-discrete equations:

$$\mathbf{M} \frac{D\mathbf{V}}{Dt} + \mathbf{K}\mathbf{V} + \mathbf{D}^T \mathbf{P} = \mathbf{B}, \quad (9)$$

$$\mathbf{D}\mathbf{V} = \mathbf{0}, \quad (10)$$

where \mathbf{M} is the mass matrix (that can be lumped if needed), \mathbf{K} the matrix containing the viscous terms, \mathbf{D} the discrete version of the divergence operator, and \mathbf{B} a vector containing the contribution of body forces and surface tractions. Spatial integration can be performed using classical Gauss integration (1 Gauss point per linear triangle in 2D).

3.2 Pressure stabilization and boundary terms

Pressure stabilization The selected discretization, i.e. linear velocity and pressure, is known to violate the Ladyzhenskaya-Babuška-Brezzi (LBB) condition. To circumvent this problem a Petrov-Galerkin pressure stabilization procedure has been preferred over a fractional step method as it shows better mass conservation properties, as discussed in [1].

The approach used here is the one adopted by Tezduyar *et al.* [13] and consists in adding to the mass conservation equation an integral term defined as the product of a stabilizing parameter τ_{PSPG}^e (see [13]) and the residual of the momentum equation.

The stabilized version of Equation (8) is then

$$\int_{\Omega_0} \text{Div} (J\mathbf{F}^{-1}\mathbf{U}) q d\Omega_0 + \sum_{e=1}^{N_{el}} \int_{\Omega_0} \tau_{\text{PSPG}}^e \frac{1}{\rho_0} \text{Grad}(q) \left(\rho_0 \frac{D\mathbf{U}}{Dt} + \frac{1}{J} \text{Div}(Jp\mathbf{F}^{-T}) - \frac{1}{J} \mu \text{Div} \left(J\text{Grad}(\mathbf{U}) \mathbf{F}^{-1}\mathbf{F}^{-T} + J\mathbf{F}^{-T} \text{Grad}(\mathbf{U})^T \mathbf{F}^{-T} \right) - \rho_0 \mathbf{b} \right) = 0 \quad \forall q \in Q. \quad (11)$$

By neglecting the higher-order term $\text{Div} (J\text{Grad}(\mathbf{U}) \mathbf{F}^{-1}\mathbf{F}^{-T} + J\mathbf{F}^{-T} \text{Grad}(\mathbf{U})^T \mathbf{F}^{-T})$, the equations to be solved can be finally summarized as follows

$$\mathbf{M} \frac{D\mathbf{V}}{Dt} + \mathbf{K}\mathbf{V} + \mathbf{D}^T \mathbf{P} = \mathbf{B}, \quad (12)$$

$$\mathbf{C} \frac{D\mathbf{V}}{Dt} + \mathbf{D}\mathbf{V} + \mathbf{L}\mathbf{P} = \mathbf{H}. \quad (13)$$

Boundary terms A further important remark has to be made regarding the form of the equations proposed in the present work and in particular the treatment of boundary terms.

When dealing with incompressible Newtonian fluids the Navier-Stokes equations are often written in so-called *Laplace form*, since the term $\mu \text{div} (\text{grad}(\mathbf{u})) + \mu \text{div} (\text{grad}(\mathbf{u})^T)$ in

Equation (1) simplifies to $\mu \operatorname{div}(\operatorname{grad}(\mathbf{u})) = \mu \Delta \mathbf{u}$. Even if this is correct from a physical point of view, it has some consequences for the expression of the weak form of the equations.

In particular, the correct natural boundary condition for the Laplace weak form of the Navier-Stokes equations is

$$\int_{\Gamma_N} \mathbf{W} \cdot \bar{\mathbf{t}} d\Gamma_N - \int_{\Gamma_N} \mathbf{W} \cdot [\mu \operatorname{grad}(\mathbf{u})^T] \cdot \mathbf{n} d\Gamma_N. \quad (14)$$

Therefore, the ‘physical’ boundary condition $\int_{\Gamma_N} \mathbf{W} \cdot \bar{\mathbf{t}} d\Gamma_N$, containing the surface tractions, is *not* the natural boundary condition that derives from the Navier-Stokes equations written in Laplace form.

Some authors do not account for this subtlety, even if it leads to a violation of the objectivity principle, as discussed in [10], and neglect the second term appearing in Equation (14).

In this work the Navier-Stokes equations are written in *divergence form* so that the boundary term $\int_{\Gamma_N} \mathbf{W} \cdot \bar{\mathbf{t}} d\Gamma_N$ represents simultaneously both a ‘physical’ and a natural boundary condition.

3.3 Time integration

Time integration is performed using an implicit backward-Euler scheme. Positions at time t^{n+1} are computed as

$$\mathbf{X}^{n+1} = \mathbf{X}^n + \mathbf{V}^{n+1} \Delta t, \quad (15)$$

which leads to the system of fully-discrete equations

$$\begin{bmatrix} \frac{1}{\Delta t} \mathbf{M}^{n+1} + \mathbf{K}^{n+1} & \mathbf{D}^{Tn+1} \\ \frac{1}{\Delta t} \mathbf{C}^{n+1} + \mathbf{D}^{n+1} & \mathbf{L}^{n+1} \end{bmatrix} \begin{Bmatrix} \mathbf{V}^{n+1} \\ \mathbf{P}^{n+1} \end{Bmatrix} = \begin{Bmatrix} \mathbf{B}^{n+1} + \frac{1}{\Delta t} \mathbf{M}^{n+1} \mathbf{V}^n \\ \mathbf{H}^{n+1} + \frac{1}{\Delta t} \mathbf{C}^{n+1} \mathbf{V}^n \end{Bmatrix}. \quad (16)$$

Due to the implicit time integration, Equations (16) are non-linear so that an iterative algorithm has to be used to find the solution at time t^{n+1} . As discussed in [8] a Picard algorithm is preferable to a Newton-Raphson algorithm in this case.

3.4 Problems related to remeshing

In the present approach a problem can arise due to the continuous remeshing of the domain. In particular, since for quantities that are not defined at the nodes, such as stresses, no proper projection is made from the old mesh to the new one, perturbations of the solution can appear after a remeshing. In other words, the solution is no longer C^0 continuous in time.

To the best of our knowledge, this is the first time in the literature that this problem related to the PFEM method is addressed. We will first try to give some justification of what happens and then suggest some ideas on how to alleviate the problem.

Problem description Let us suppose that the equilibrium at time n has been reached: nodes are moved to the new position $\bar{\mathbf{X}}^{n+1}$ and a remeshing takes place, leading to an unequilibrated configuration.

There are two contributions to this new out-of-balance configuration: the first one comes from the fact that the physical problem is not at equilibrium anymore and the second one from the fact that the equilibrium at time n was computed on a different mesh and there is no guarantee that the same equilibrium solution would have exactly held on the new mesh. The latter can introduce some perturbations in the velocity and pressure fields: we will denote these perturbations on velocity and pressure as $\delta\mathbf{V}^{n+1}$ and $\delta\mathbf{P}^{n+1}$, respectively.

The momentum equation that has to be verified at time $n + 1$ becomes

$$\mathbf{M} \left(\frac{\bar{\mathbf{V}}^{n+1} + \delta\mathbf{V}^{n+1} - \mathbf{V}^n}{\Delta t} \right) + \mathbf{K} (\bar{\mathbf{V}}^{n+1} + \delta\mathbf{V}^{n+1}) + \mathbf{D}^T (\bar{\mathbf{P}}^{n+1} + \delta\mathbf{P}^{n+1}) = \mathbf{B}, \quad (17)$$

where $\bar{\cdot}$ quantities are solution to the physical (unperturbed) equilibrium. If physical equilibrium is satisfied, then Equation (17) becomes

$$\underbrace{\mathbf{M} \frac{\delta\mathbf{V}^{n+1}}{\Delta t}}_{(a)} + \underbrace{\mathbf{K} \delta\mathbf{V}^{n+1}}_{(b)} + \underbrace{\mathbf{D}^T \delta\mathbf{P}^{n+1}}_{(c)} = \mathbf{0}. \quad (18)$$

Term (b) is directly defined by the velocity field perturbation $\delta\mathbf{V}^{n+1}$ and for dynamic problems, if this perturbation is finite but small, this term is small with respect to the other two. On the contrary, term (a) is amplified by the presence of the time step Δt . If one wants Equation (18) to be satisfied, the only contribution that can counter-balance the first term comes from term (c), which therefore results in oscillations of the pressure field. Evidence of this phenomenon is given in section 4.

Possible remedies The amplitude of pressure oscillations is proportional to the extra inertial force (a). Term (a) is proportional to the velocity jump $\delta\mathbf{V}^{n+1}$ (which itself depends on the problem and on the mesh size) and inversely proportional to time step Δt . Thus, in general, pressure oscillations decrease for finer meshes and larger time steps.

4 NUMERICAL EXAMPLES

In this section some numerical applications of the present approach are presented.

4.1 Sloshing problem

In this example the free sloshing of an incompressible Newtonian fluid in a rigid reservoir is considered, as depicted in Figure 1. This problem has already been studied in

the literature (see for instance [1, 12]), so it represents a good benchmark to validate our code.

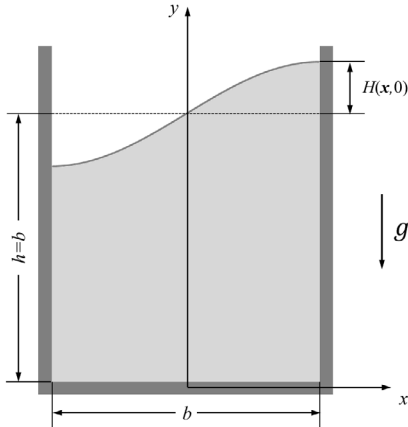


Figure 1: Sloshing problem. A fluid is placed in a reservoir and an initial out-of-balance configuration is enforced through the free-surface profile definition.

The initial free-surface profile is defined as

$$H(\mathbf{x}, 0) = a \sin\left(\pi \frac{x}{b}\right), \quad (19)$$

where b is the width of the reservoir, H denotes the free-surface height with respect to the average level and a is the initial amplitude. In this case values of $a = 0.01$ m and $b = 1.0$ m, as well as fictitious values of fluid viscosity $\mu = 0.01$ kg/ms, density $\rho = 1.0$ kg/m³ and gravity $g = 1.0$ m/s² are considered. For the calculation, an initial discretization of 1166 nodes and 2330 triangles and a constant time step of 0.01 s are used. A free-slip condition is enforced on the container walls.

Figure 2 presents the time evolution of the free surface at $x = \pm b/2$. Circles denote values obtained from [12] and triangles from [1]. Very good agreement is observed, especially with the solution provided by Radovitzky and Ortiz [12]. For this problem a maximum relative error of $5 \cdot 10^{-4}\%$ on mass conservation is obtained.

Remeshing issues A numerical example is proposed to illustrate the problems described in section 3.4, related to continuous remeshing.

The example is again a sloshing problem, as presented above, but this time a very coarse mesh is employed, in order to better highlight the issue. Moreover values of $\rho = 1000$ kg/m³ and $g = 9.81$ m/s² are used. The initial mesh is depicted in Figure 3. During the simulation, if remeshing is performed at each time step, four possible configurations exist, as depicted in Figure 4. Results are shown in Figures 5 and 6. All the analyses are performed with a time step of 0.001 s.

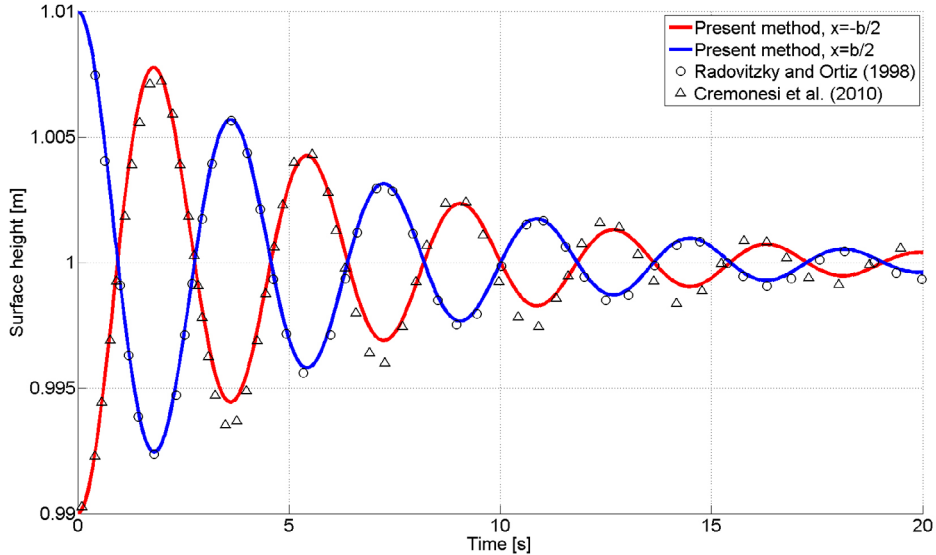


Figure 2: Sloshing problem. Time evolution of the position of the free-surface at $x = -b/2$ and $x = b/2$: very good agreement with other authors' results is found, especially the one obtained by Radovitzky and Ortiz [12].

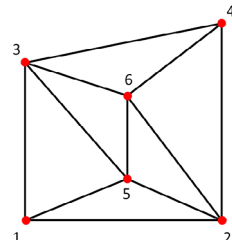


Figure 3: Remeshing issues: initial mesh. An extremely coarse mesh (with only 6 nodes) is used in order to better understand the influence of remeshing on the results.

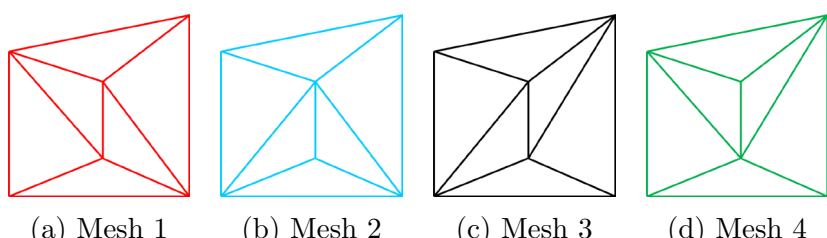


Figure 4: Remeshing issues. Four different configurations can be obtained during the simulation due to remeshing: they correspond to meshes 1, 2, 3 and 4.

In Figure 5 the velocity along the y -direction of node 5 for the case with continuous remeshing is displayed and compared to results obtained for meshes 1-4 without remeshing. Colored images are used to symbolize the configuration of the remeshing case that corresponds to a given portion of the simulation.

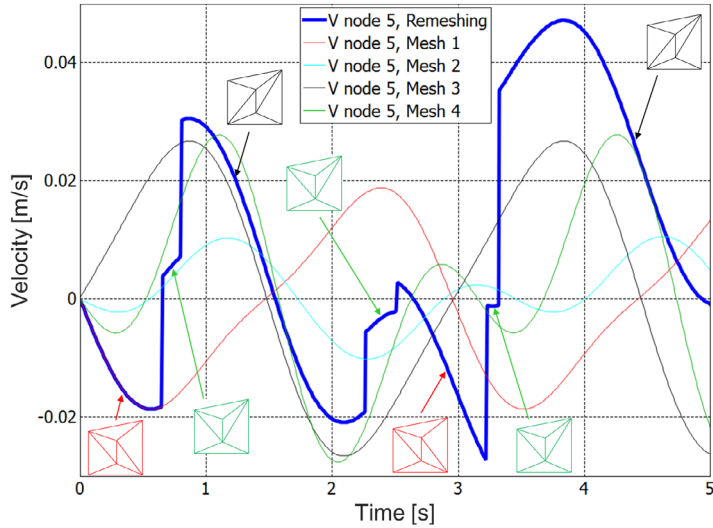
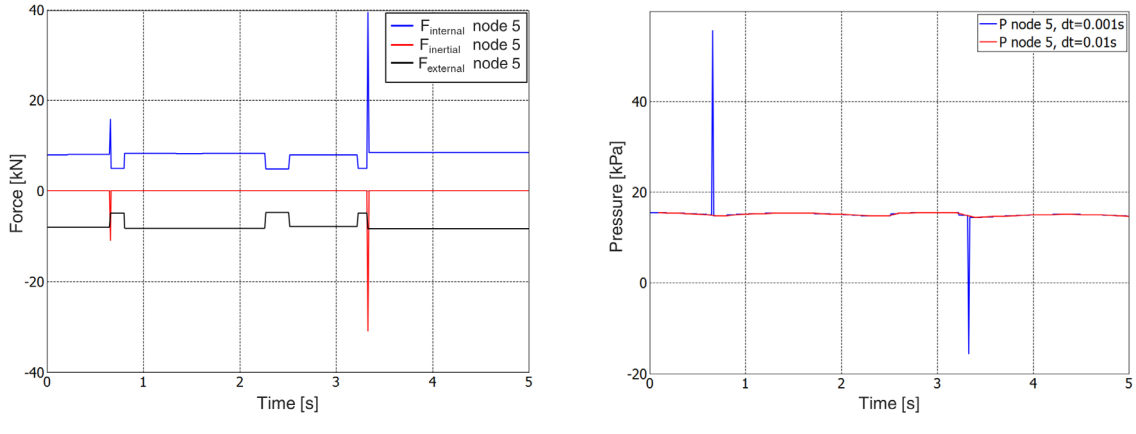


Figure 5: Remeshing issues: node 5 velocity along the y -direction. The thick blue line represents the case where a remeshing is performed at each time step, while thin lines are the results obtained for meshes 1-4 (see Figure 4) without remeshing. Colored images indicate the configuration of the continuous remeshing case that corresponds to a given part of the simulation. Whenever the configuration changes, discontinuities appear in the velocity field due to the fact that the discrete solution can be different from one mesh to another.

First of all, as it could be expected for such a coarse mesh, four different results are obtained for the four meshes. Moreover, for the continuous remeshing case, it can be seen that remeshing can introduce discontinuities in the velocity field. This can be expected in view of the very different solutions the four configurations without remeshing can lead to. To better understand the implications of this observation on the results, Figure 6(a) shows the evolution of inertial, internal and external forces along the y -direction at node 5. Inertial forces represent the term $\mathbf{M} \frac{D\mathbf{V}}{Dt}$ in Equation (12), internal forces the term $\mathbf{K}\mathbf{V} + \mathbf{D}^T \mathbf{P}$ and external forces the term \mathbf{B} .

As discussed in section 3.4 jumps of inertial forces can be observed after remeshing (corresponding to the larger velocity jumps), to which correspond discontinuities in the internal forces, which, in this case, basically corresponds to the pressure gradient.

In Figure 6(b) one can observe the strong discontinuities appearing in the pressure field, due to the perturbations introduced by the remeshing. As previously discussed, it can be observed that for a larger time step, i.e. 0.01 s, the pressure peaks are strongly attenuated.


(a) Forces along the y -direction at node 5

(b) Pressure at node 5

Figure 6: Remeshing issues. Perturbations induced by the remeshing in the velocity field cause strong discontinuities in the inertial term, that have to be counter-balanced by internal forces (a), in particular by the pressure gradient. Strong oscillations in the pressure field (b) correspond to discontinuities in the velocity field induced by remeshing (peaks in the blue curve). A larger time step reduces them, since smaller accelerations are induced by velocity perturbations.

Again, this phenomenon will also become less and less visible for finer and finer meshes.

4.2 Dam break

The dam break problem is a classical benchmark for the analysis of free-surface flows. The problem is depicted in Figure 7 and consists in a column of water in a container, initially held by a rigid wall. The wall is instantaneously removed and the motion of the water is studied.

In this case a length $L = 0.146$ m is considered. Classical values for water properties are chosen, that is a density $\rho = 1000$ kg/m³ and a dynamic viscosity $\mu = 0.001$ kg/ms. An initial mesh of 1650 nodes and 3171 elements, and a time step of 0.02 s are used. A no-slip condition is enforced on container walls. The solutions obtained at different time steps are shown in Figure 8 and compared to experimental results obtained by Koshizuka and Oka [9]. Again, a good agreement is observed.

5 CONCLUSIONS

A Lagrangian finite element approach for the study of incompressible flows, based on the PFEM method, has been presented.

Particular attention has been devoted to the mathematical formulation of the method and to the correct definition of the weak form, in particular concerning boundary terms. The validity and robustness of the approach have been assessed on some simple examples.

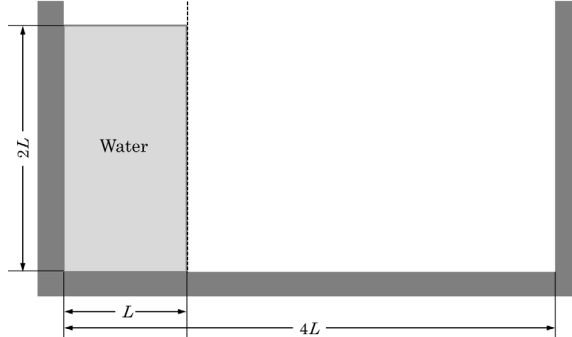


Figure 7: Dam break problem. The water column is initially held by a rigid wall. The wall is suddenly removed and the motion of the fluid is regarded.

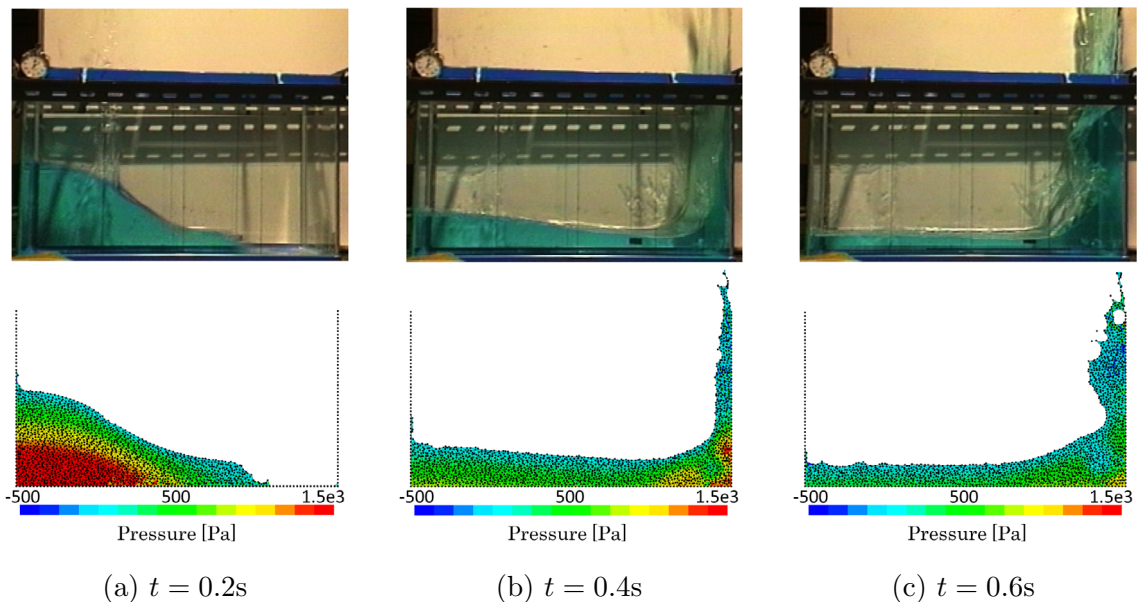


Figure 8: Dam break problem. Comparison between experimental results taken from [9] (top) and numerical ones (bottom). The evolution of the water column is displayed at times $t = 0.2\text{ s}$ (a), $t = 0.4\text{ s}$ (b) and $t = 0.6\text{ s}$ (c): good agreement with experimental results can be seen. Pressure field is also shown for the numerical solution.

Finally, some problems related to the continuous remeshing procedure used in the present method have been pointed out. It was shown that some perturbations are introduced by the remeshing in the velocity field: these perturbations can be amplified by a small time step, leading to large accelerations that have to be compensated by the pressure gradient, resulting in large oscillations in the pressure field, if the mesh is not fine enough. No

solution to this problem has been found so far, but it is a perspective for future works.

REFERENCES

- [1] Cremonesi M., Frangi A. and Perego U. A Lagrangian finite element approach for the analysis of fluid-structure interaction problems. *Int. J. Num. Meth. Engng.* (2010) **84**:610–630.
- [2] Donea J., Huerta A., Ponthot J.P. and Rodríguez-Ferran A. *Encyclopedia of Computational Mechanics, Stein E., de Borst R., Hughes T.J.R. (eds)*. John Wiley & Sons (2004).
- [3] Edelsbrunner H. and Mücke E.P. Three dimensional alpha shapes. *ACM Transaction on Graphics* (1994) **13**(1):43–72.
- [4] Hirt C.W., Nichols B.D. Volume of fluid (VOF) method for the dynamics of free boundaries. *J. Comput. Physics* (1981) **39**:201–225.
- [5] Idelsohn S., Calvo N. and Oñate E. Polyhedrization of an arbitrary 3D point set. *Comput. Methods Appl. Mech. Engrg.* (2003) **192**:2649–2667.
- [6] Idelsohn S. and Oñate E. To mesh or not to mesh. That is the question... *Comput. Methods Appl. Mech. Engrg.* (2006) **195**:4681–4696.
- [7] Idelsohn S., Oñate E., Calvo N. and Del Pin F. The meshless finite element method. *Int. J. Num. Meth. Engng.* (2003) **58**:893–912.
- [8] Idelsohn S., Oñate E., Del Pin F., Calvo N. Fluid–structure interaction using the particle finite element method. *Comput. Methods Appl. Mech. Engrg.* (2006) **195**:2100–2123.
- [9] Koshizuka S. and Oka Y. Moving particle semi-implicit method for fragmentation and incompressible fluid. *Nuclear science and engineering* (1996) **123**:421–434.
- [10] Limache A. and Idelsohn S. Laplace form of Navier-Stokes equations: a safe path or a wrong way? *Mecánica Computacional* (2006) **25**:151–168.
- [11] Oñate E., Idelsohn S., Del Pin F. and Aubry R. The particle finite element method. An overview. *Int. J. Comput. Methods* (2004) **61**:964–989.
- [12] Radovitzky R. and Ortiz M. Lagrangian finite element analysis of Newtonian fluid flows. *Int. J. Num. Meth. Engng.* (1998) **43**:607–619.
- [13] Tezduyar T.E., Mittal S., Ray S.E., Shih R. Incompressible flow computations with stabilized bilinear and linear equal-order-interpolation velocity-pressure elements. *Comput. Methods Appl. Mech. Engrg.* (1992) **95**(2):221–242.

VERTICAL NATURAL MODES OF THE GRAVEL AGGREGATE IN THE BALLASTED RAILWAY TRACK

AKIRA AIKAWA

PhD, Senior Researcher, Railway Dynamics Division,
Railway Technical Research Institute
Hikari-cho, Kokubunji, Tokyo, 185-8540 Japan
E-mail: aikawa.akira.11@rtri.or.jp, web page: <http://www.rtri.or.jp/>

Key words: Ballasted Track, Natural Frequency, Large-scale Parallel Computing, FEM.

Abstract. This research investigates the natural vibration characteristics of the ballast layer by using field measurement, full-scale experiments and large-scale finite element analysis. The results indicate that the natural frequency of the vertical elastic vibration of the ballast layer is numerically detected at around 310 Hz at which the whole ballast aggregate repeats the vertical expansion and shrinkage elastically, and that the rigid-body natural vibration numerically occurs approximately at 120 Hz at which the mass of the track structure vibrates simultaneously up and down as depending on the stiffness of the ballast layer. The stress acting on an angularity part of the ballast gravel is inferred to be about 1100 times greater than the average stress on the bottom surface of the sleepers.

1 INTRODUCTION

The dynamic loads by trains are transmitted to the ballasted layer as an elastic wave through the inside of gravel and consequently induce the natural vibration modes in the ballast layer, specific to the ballast structures, which will trigger the ballast degradation. Therefore, the ballasted track requires periodic maintenance work, which is an important subject of technical research. However, the dynamic characteristics of the ballast layer have not yet been sufficiently elucidated. The dynamic loads are roughly divided into two major factors. One is dynamic load exerted by the passing axle load of a train. The frequency characteristics depend on the number of axes passing per unit of time, and are limited to a low-frequency domain, ranging from only several Hertz to approx. 20 Hz. The other is the impact load generated by the rolling contact mechanism between the wheels and rails. When the sharp-pulse-shaped waveform of the impact load is transformed into a frequency domain, it has many vibration components with broadband characteristics ranging between a low frequency and several kilohertz frequencies. This paper presents the field measurement of the dynamic responses of the ballasted track with a train passing, at a sampling frequency of 10 kHz without low-pass filters, using the special sensing sleepers and sensing stones, which were developed by the authors (Aikawa, 2012); (Urakawa & Aikawa et al, 2009). Moreover, by introducing the finite element transient response analysis of large-scale parallel-computing by FrontISTR (Okuda) based on a fine ballast aggregate model, both of the elastic natural vibration and the rigid-body natural vibration of the granular ballasted layer can be numerically simulated.

2 IDENTIFICATION OF NATURAL VIBRATION MODES THROUGH FULL-SCALE TESTING

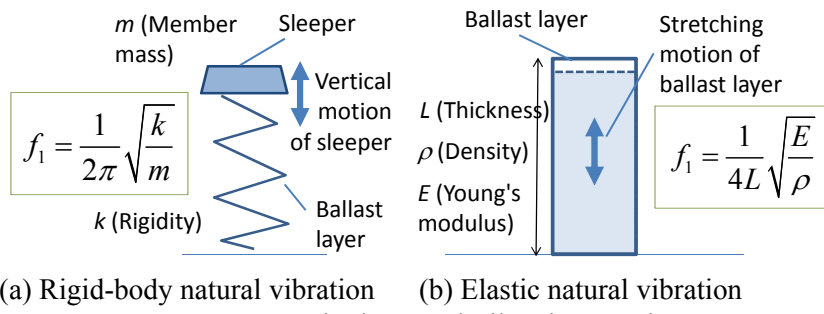
2.1 Vertical natural vibration motions

Figure 1 shows the characteristics of the principal natural vibration motions in the vertical direction of the ballast layer. One is the rigid-body natural vibration and the other is the elastic natural vibration. The structure of the ballasted track can be regarded as a single degree of freedom system consisting of sleepers, rails, etc., which constitute the mass of the track structure and also the stiffness of the ballast layer and road bed. The rigid-body vibration is the motion in which this single degree of freedom system vibrates vertically and rigidly under the dynamic load of a train. There are six kinds of rigid-body natural vibration in total: Translational and rotational along each of three axes. However, the translational vibration components in the vertical direction are dominant both in the dynamic loads applied to the ballast layer and in the responses of the ballast layer. Therefore, this research focuses on the translational behavior in the vertical direction. It has been said that this mode exists approx. at 100 Hz (Grassie et al, 1993).

On the other hand, the elastic vibration is the motion in which the whole ballast layer expands and contracts vertically as an elastic body. This natural vibration is considered not to occur in a normal-state ballast layer but to occur when the ballast layer is under high confining pressure generated by the train's weight applied to the ballast layer. So far no research has been done to capture this mode, i.e. ballast motion in the frequency domain related to this mode. It should be added that on a real track natural vibration that entails the bending deformation and torsional deformation of the members occurs.

2.2 Vibration test of a full-scale mockup of a ballasted track

The author built a full-scale mockup of a ballasted track structure and investigated the natural vibration characteristics of a ballasted track by performing an experimental modal analysis based on the impulse excitation test (Sakai & Aikawa et al, 2012); (Aikawa et al, 2011). Figure 2 shows the profile/plane of the mockup and the sensor positions. To build the full-scale mockup, the author employed new ballast using hard Andesite which complies with the same standard for the real track and they were compacted sufficiently. For the mockup, type-3 pre-stressed concrete (PC) mono-block sleepers were used, which are widely used for the meter-gauge (1067 mm wide) conventional railway lines of Japan Railway Companies. The test was performed by vibrating (by hitting) the end of the sleeper with an impulse hammer in three different directions: vertically, laterally and longitudinally. The test record includes the acceleration responses at 22 points on the top surface of the sleeper and several points in the ballast layer. The author then obtained the accelerances, which are the transfer



(a) Rigid-body natural vibration (b) Elastic natural vibration

Figure 1: Vertical natural vibration motions

functions of the acceleration responses to the excitation force in the frequency domain, conducted an experimental modal analysis in consideration of the location relationship of measuring points, and thus identified the natural vibration frequencies and their modal shapes of the ballasted track between the low frequency domain and 1 kHz.

Figure 3 shows the natural vibration frequencies and the specific modal shapes of the ballasted track. Though there are 6 rigid-body vibration modes as stated above, the figure shows only the rigid-body translational mode in the vertical direction and indicates that the vertical, translational rigid-body vibration is generated at 98 Hz, which almost agrees with the previous research results. Besides, 6 types of dominant natural vibration entailing the bending and torsional deformations of sleepers are identified. However, the author was not able to capture any vertical elastic natural vibration of the ballast layer in this test. That is probably because the elastic vibration modes of the whole ballast layer would occur only when continuity in the ballast layer is sufficiently satisfied according to the train loads on the ballast layer.

2.3 Field measurement and spectral analysis

The dynamic responses were measured on an actual ballasted track of a main conventional railway line in Japan. The track structure at the measurement site, consisting of continuous welded rail weighing 60 kg/m and type-3 PC sleepers, was designed based on the Japanese standard (Railway Bureau, MLIT, Japan & RTRI, 2012) that allows a running speed higher than 130 km/h and the measurement site was located on a solid embankment in a straight section. For spacing between the sleepers, 41-42 sleepers are positioned over a distance of 25 m. The ballast layer at the measurement site is made of relatively new Andesite hard gravel with clear-cut edges, and the ballast layer is approx. 30 cm thick. This paper focuses on the measured responses for a train at a traveling speed of approx. 120 km/h with the sampling frequency is 10 kHz. The details of the measurement are described in Reference (Aikawa, 2012).

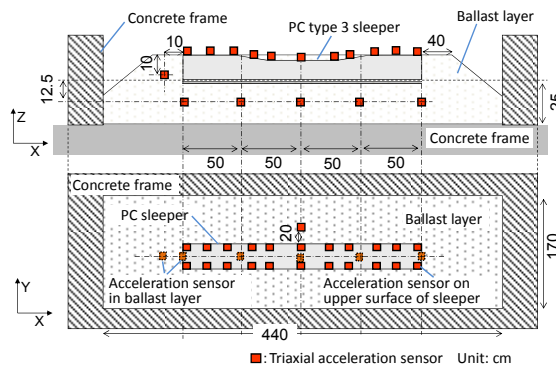


Figure 2: Overview of full-scale test

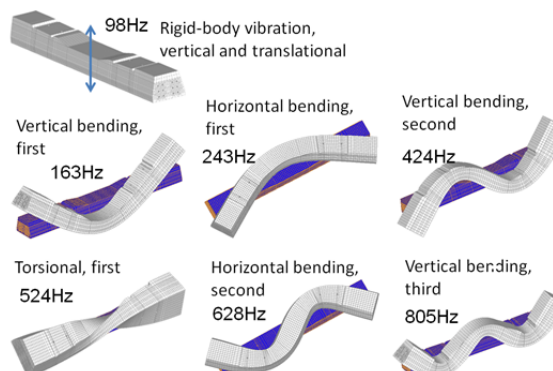


Figure 3: Mode shapes of natural vibration

Figure 4 shows the response acceleration amplitude spectrum and the response displacement amplitude spectrum of the ballast at a depth of 10 cm by applying the fast Fourier transformation of the time history response waveforms, and smoothing them at a bandwidth of 20 Hz. The acceleration spectrum indicates that the high-frequency components above 100 Hz as well as the low-frequency components contribute greatly to the ballast response. When focusing on the ballast displacement, its amplitude is extremely small in the high-frequency domain. For instance, the displacement amplitude is only 1/1000 μm at a frequency of approx. 800 Hz, which is equivalent to the natural frequency of the ballasted track entailing the third mode of the vertical bending of the sleeper. This means that the vibration components in the high-frequency domain are not transmitted by rigid-body vibrations around the center of gravity of the ballast gravel, but the dynamic loads are transmitted through the elastic undulation propagation attributable to the local and minute deformation behavior and sliding behavior at the tips of the edges at the contact points between the ballast stones. On the other hand, the displacement amplitude in the low-frequency domain from several Hertz to 20 Hz is several thousand times larger than those in the high-frequency domain. Consequently, the loads in the low-frequency domain are mainly transmitted through the rotational and/or translational rigid-body vibrations of the individual ballast gravel. This figure also shows the peak profiles of the responses related to the natural vibration modes of the ballasted track, which are shown in the preceding paragraph. These curves identify the rigid-body resonance vibration of the ballast layer around 100 Hz and indicate another large peak profile of the resonance mode around 300 Hz.

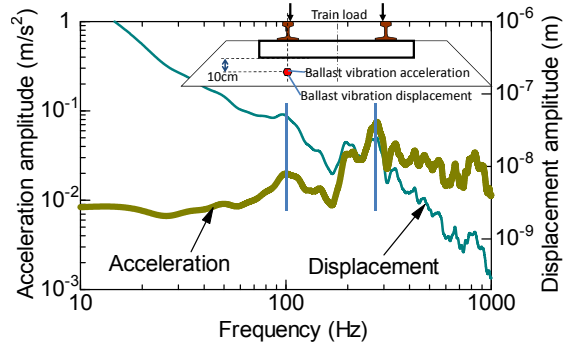


Figure 4: Acceleration and displacement amplitude spectrum of the ballast

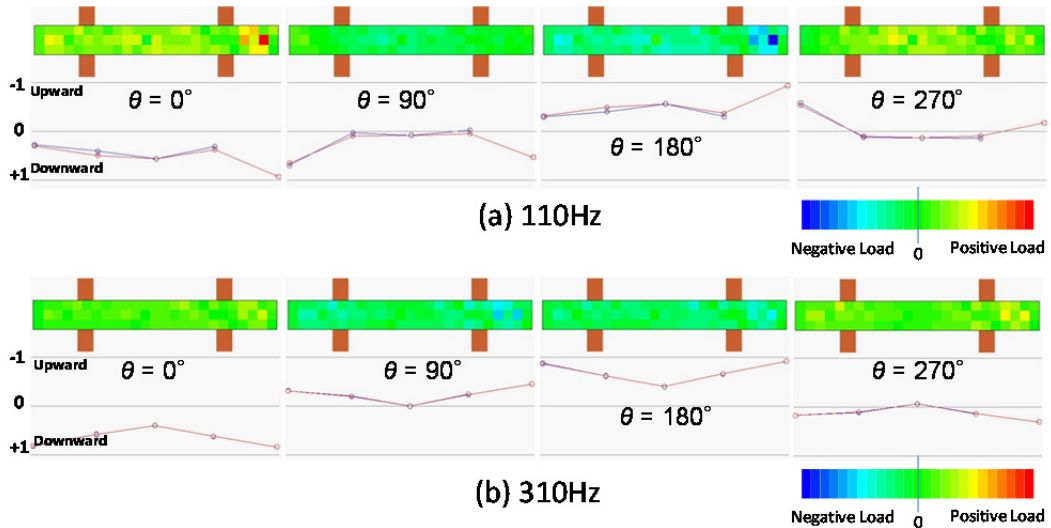


Figure 5: Distribution of the vertical loading at the bottom of the sensing sleeper and the normalized displacement at the top of the sleeper (measured)

Figure 5 shows the relationship between the vertical loading on the bottom surface of the sleeper and the normalized vertical displacement of the sleeper in cases of two different frequencies (110 Hz and 310 Hz). In the figures, θ denotes the relative phase angles. Regarding the sleeper motion, the downward direction indicates the downward behavior of the sleeper and the upward direction indicates the upward behavior of the sleeper. Both the figures (a) and (b) show that the sleeper repeats a vertical periodic movement at these frequencies, with entailing the bending deformations of the sleeper in the high frequency regions, in synchronization with the phase angles.

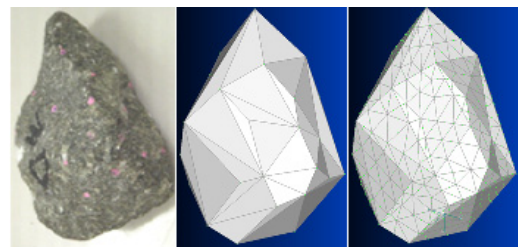
3 LARGE-SCALE FINITE ELEMENT TRANSIENT RESPONSE ANALYSIS REGARDING THE ELASTIC VIBRATION MODE OF THE BALLASTED TRACK

3.1 Finite element modelling of the ballast aggregate

The three-dimensional shape measurement was performed to determine the three-dimensional vertex coordinates of the ballast gravel. Based on the measured coordinates, each shape was expressed using a polyhedron rigid-body discrete model and converted into an aggregate, with the same size and shape, of tetrahedron secondary elastic finite elements. The details of the measurement are described in reference (Aikawa, 2012).

Figure 6 shows exemplary pictures of a piece of ballast gravel and its numerical discrete element and finite element models. A sufficiently fine mesh size of 1 cm was adopted to support the precise representation of natural frequencies of individual ballast gravel up to several 10 kHz. Table 1 presents the physical property values of the ballast. As the density of the ballast gravel, the laboratory experimental value obtained from specific gravity tests was provided. Young's moduli and Poisson's ratio were derived from the previous reports in the literature. Regarding the structural damping coefficient, the author adopted the general values of a concrete structure.

Figure 7 shows the procedure for the creation of a ballast aggregate by both of the discrete element and finite element modelling. First, about 100 pieces of the ballast polyhedron discrete element models were placed randomly in the air above rectangular box frames. The gravel was then dropped freely by the gravity and compressed vertically with a loading plate



(a) Ballast (b) DEM Model (c) FEM Model
Figure 6: Exemplary pictures of existing ballasts and the digitized models

Table 1: Physical property values

Item	Ballast
Density ρ	2700 (kg/m ³)
Young's modulus E	30 (GPa)
Poisson's ratio ν	0.2
Structural damping parameters η	0.01

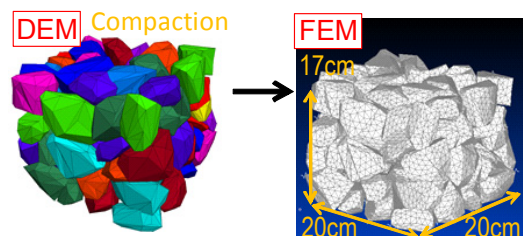


Figure 7: Modelling of the ballast aggregate

using the discrete element software. Next, all individual polyhedron discrete element models were converted into assemblages consisting of the small finite element tetrahedron second-order elastic solid elements, split into 1-cm meshes with geometry and contact-point information maintained. Each polyhedron discrete element model was divided into approximately one thousand tetrahedron finite elements. The finished rectangular block model is 20 cm in width/length and 17 cm in height, and has more than 90 000 tetrahedron finite elements.

In this procedure, the contact-points were connected to one another through Multi-Point Constraints (MPCs), which connected the nodes of elements in three axial directions related to the contact pair of blocks at each contact point. The provided contact-connectivity exhibits no expansion or contraction because its stiffness is several ten thousand times harder than that of ballast pieces. Accordingly, the spring functions around the contact points are represented by the elastic deformation of ballast angularities, which are composed of assemblages of several tetrahedron-finite-elements adjacent to the contact points.

Regarding the modelling of the contact structure, three types of connections were employed according to the mechanism of the connection obtained by the discrete element analysis. The ballast grains touching one another at a single point were linked through one contact location on each stone, and this type of connection allows the rotational behaviors of ballast grains around the contact points. The ballast grains touching one another with their edges were linked through two points at both ends of the side on each stone, and these types of connection between ballast grains allow the rotational behavior of hinge mechanism like a door hinge. The ballast grains touching one another with their faces were linked through three or more points around the contact surface of each stone and these types of connections contribute to the stability of the structure and the propagation of elastic-waves.

Figures 8 show the finite element model of a type-3 PC sleeper, which is developed by the authors (Sakai & Aikawa et al, 2012) and which consists of 51 146 nodes and 51 944 solid elements. The sleeper model has an ability to make the precise representation of all natural frequencies and their response values up to 1 kHz within 5% deviation. Its physical weight is 161.40 kg and its volume is 0.0677 m³.

A large-scale finite element model was constructed, with multi-point constraints (MPCs), by assembling 48-units of the above-mentioned rectangular unit block models of the ballast and the type-3 PC sleeper model. Figure 9 shows

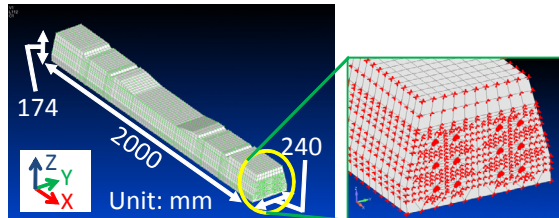


Figure 8: Model of a type 3 PC sleeper

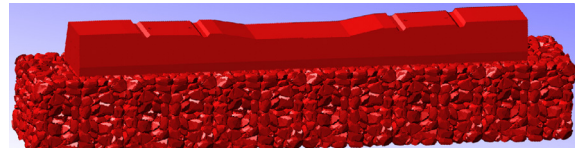


Figure 9: Assembly of ballasted track model

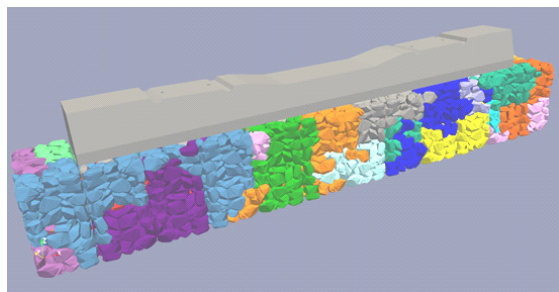


Figure 10: Domain segmentation

the finished analysis model of the sleeper-ballast layer system, which consists of 7.05 million nodes and 4.15 million 2nd order solid elements. The degree of freedom exceeds 21 million. Figure 10 shows the domain segmentation. The whole model is divided into 24 sub-domains for large-scale parallel computing of FrontISTR, by introducing the direct solver MUMPS. By adopting the finite element analysis regarding the modeling of the ballast layer having a complicated structure, it is possible to reproduce the phenomena such as the stress-concentration and the wave-propagation within the ballast layer fast, easily and exactly.

The time-history response waveforms were calculated numerically by inputting measured loading waveforms to the top surface of a sleeper model when a passenger train moved over the top surface of the previously described ballasted track model. Figure 11 shows the actual waveforms of vertical loading (measured in the cross-sectional area 14 cm in width and 18 cm length on the bottom surface of the rails) applied by the first axles of a lead coach bogie when the passenger train moved through the test section at about 120 km/h. In the finite element analysis, the waveforms were uniformly input to the whole points located within the bottom area of the rails on the top surface of the sleeper model. The calculation time interval was set at $\Delta t = 0.1$ (ms) and total calculating steps are 800 times. The specifications about the various parameters of each model are shown in Table 2.

3.2 Nodal displacement distribution in the ballast aggregate and the sleeper system

Figure 12 shows the distribution of the nodal displacement in the ballast aggregate and the sleeper system at $t = 55.0$ (ms) when the load peaks appear as the first axle of the lead coach bogie passed above the sleeper center. It can be seen that the dynamic displacement induced by a passing train on the ballast is not distributed uniformly throughout the ballast aggregate and the sleeper. Significant displacement is concentrated locally around the rail positions. The analytical results show that the 30 μm maximum downward displacement occurred.

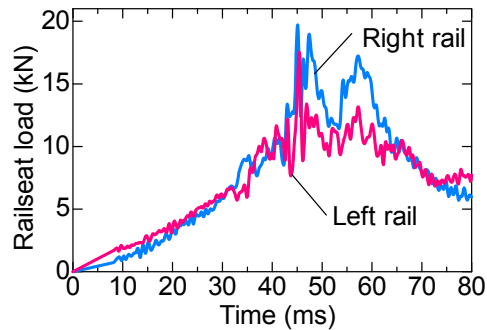


Figure 11: Measured waveform

Table 2: Calculation parameters

Item	Young's modulus (GPa)	Poisson's ratio	Density (kg/m^3)
Ballast	30	0.200	2 700
Concrete	45	0.167	2 350
Steel	210	0.290	7 820

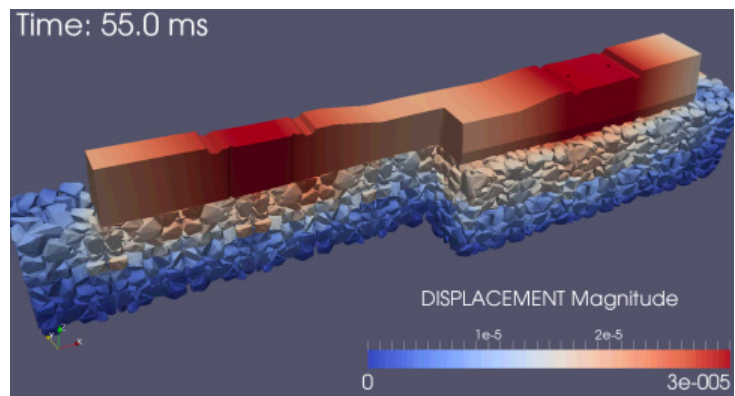


Figure 12: Nodal displacement ($t = 55.0$ ms)

3.3 Time history of von Mises stress

Figure 13 shows the time history waveforms of response of von Mises stress on the cross-section inside the gravel angularity acting on three different contact points, each with an angularity, of the ballast gravel placed at different depths below the loading point of the left rail location. From the figure, the stresses in the gravel increase gradually, with repeating alternately the minute upward (compression) and downward (tension) motions at the frequency of approximately 300 Hz, according to the inputted loads. In this case, the maximum stresses of approximately 50 MPa after the elapse of about 45 ms to 53 ms are observed near the ballast surface beneath the sleeper bottom. It can be seen that the rise in the peak response value becomes gentler as the measurement point becomes farther (i.e. deeper) from the loading point, and that there is a tendency for waveforms to become smoother along with the steep decrease in high-frequency vibration included in the wave. Although the investigation reported here involves elastic body analysis without the use of any constitutive equations, the diminishing trend of energy inside the ballast is closely reproduced by simulating the actual structure of the ballast aggregate in detail. This means that the ballast aggregate structure featuring angularity parts has the mechanism of energy attenuation.

Figure 14 shows the linear amplitude spectra of response of von Mises stress, on the cross-section inside the gravel angularity acting at different depths below the loading point of the left rail, which are obtained by conducting by the fast Fourier transformation of these time history response waveforms and smoothing them at a bandwidth of 20 Hz. From the figure, these spectra curves identify the 1st order elastic vibration resonance mode of the ballast layer at around 337 Hz, where the whole ballast layer stretches vertically as an elastic body.

In this analysis, significant stresses up to 80 MPa are observed in tetrahedral elements near the contact part while the average maximum pressure on the ballast surface is 74 kPa. In this case, the stress acting on the angularity part is approximately 1100 times greater than the average loading stress on the ballast surface. Assuming that the unconfined compressive strength is 60 MPa at the angularity part of the ballast gravel, the application of a dynamic load of 55 kPa or more to the ballast-layer surface would cause minute fracturing or breakage around locations where the stress acting on the angularity part of the ballast gravel converges.

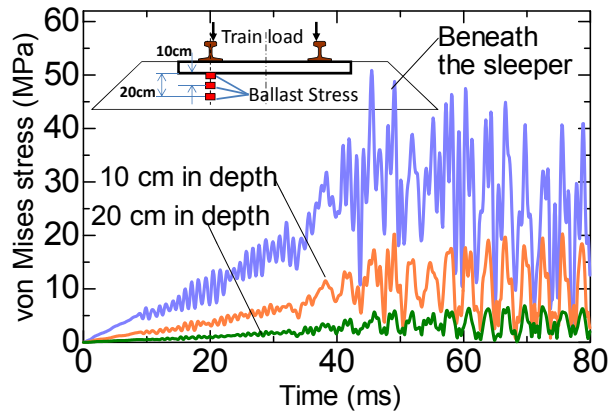


Figure 13: Time history of von Mises stress

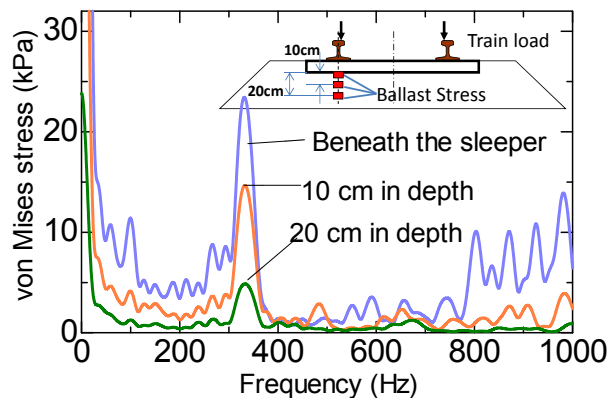


Figure 14: Spectra of von Mises stress

1100

3.4 Amplitude spectrum of the vertical displacement regarding impact loading

To detect the exact frequency of the elastic vibration mode of the ballast layer, the author performed a numerical experiment (simulation) which simulates the impulse loading experiment by using a transient response analysis of the aforementioned large-scale ballast aggregate model. Figure 15 shows the amplitude spectra of the vertical displacement of the sleeper by applying a 0.1-ms square impulse loading waveform. The impulse loading to the left and right rails totals 100 kN. According to the impact loading numerical experiment, the results indicate that the rigid-body natural vibration mode occurs at around 310 Hz. The results indicate that the analytical natural frequency of the elastic vibration mode of the ballast layer fairly coincides with the above-mentioned measured one and that the frequency corresponds to 3-times the value of the measured natural frequency of the rigid-body mode.

4 LARGE-SCALE FINITE ELEMENT TRANSIENT RESPONSE ANALYSIS REGARDING THE RIGID-BODY VIBRATION MODE

To examine the dominant rigid-body resonance motion observed at around 100 Hz, this chapter describes the large-scale finite element transient response analysis of the ballasted track by using the bilinear contact springs in place of the MPCs. According to the above-mentioned drop-weight test results, it is inferred that the ballast jumping motion, that is a rigid body bounce mode, causes large displacement. Therefore, regarding the aforementioned large-scale finite element ballasted track model, the contact-point information between the ballast pieces and the sleeper nodes is modeled with bilinear springs, that is, with tensionless contact. Table 3 shows the calculation parameters regarding contact points. In this analysis, the tension spring factors are

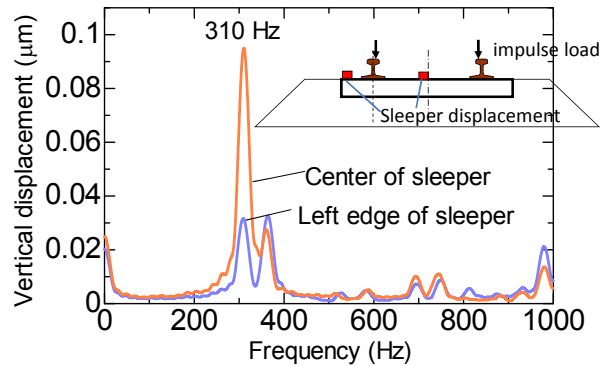


Figure 15: Response spectrum of vertical displacement regarding impulse loading

a 0.1-ms square impulse loading waveform. The impulse loading to the left and right rails totals 100 kN. According to the impact loading numerical experiment, the results indicate that the rigid-body natural vibration mode occurs at around 310 Hz. The results indicate that the analytical natural frequency of the elastic vibration mode of the ballast layer fairly coincides with the above-mentioned measured one and that the frequency corresponds to 3-times the value of the measured natural frequency of the rigid-body mode.

Table 3: Parameters of bilinear springs

Item	Compression spring factor (GN/m)	Tension spring factor (GN/m)
Ballast - Ballast	30	0.0003
Sleeper - Ballast	10	0.0001

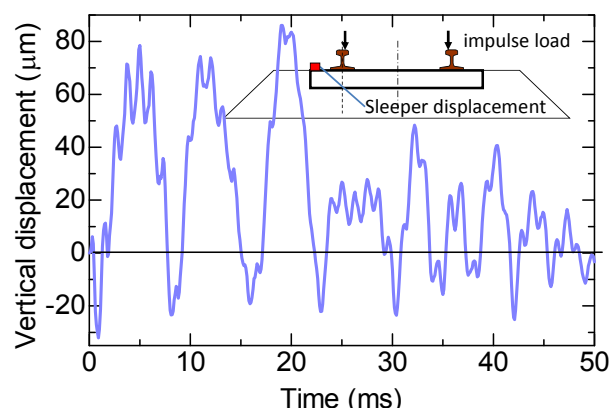


Figure 16: Time history of sleeper displacement

set at 1/100000 values of the compression spring factors.

Figure 16 shows the time history responses of the vertical displacement at the left edge of the sleeper immediately after the 0.1-ms square impulse loading waveforms of 100 kN. In this figure, the downward displacement means the downward motion of the sleeper (that is, the compression of the ballast layer), and the upward displacement means the upward motion of sleeper (that is, the extension of the ballast layer). According to the figure, when an impact load is applied, the ballast layer instantaneously deforms elastically due to compression and then returned to the pre-loading position. Thus, it takes only about 1 ms for the ballast layer to be compressed and be restored. Following the compression and restoration of the ballast layer, sleeper-jumping occurs. The cause for this sleeper-jumping is the strain energy stored in the ballast being released abruptly.

Figure 17 shows the amplitude spectrum of the vertical displacement of the sleeper. The results indicate that the rigid-body natural vibration occurs at 120 Hz. The value is approximately 10 - 20% larger than the experimental one. However, that is almost 1/3 of the elastic natural vibration frequency. According to the large-scale finite element analysis with nonlinear contact springs indicates that the rigid body natural vibration mode occurs almost at 1/3 of the elastic natural vibration frequency. It is inferred that the rigid-body natural vibration mode may occur at frequencies which are equal to the ones obtained by dividing the frequency of the elastic natural vibration mode by odd numbers.

5 Discussion

When the contact-point information between the sleeper bottom and ballast pieces is modelled with MPCs, the vertical elastic natural vibration mode of the ballast layer numerically occurred at about 310 Hz. On the other hand, when the contact-point is modeled with nonlinear contact springs, that is, with tensionless contact, the rigid-body natural vibration mode is numerically detected approximately at 120 Hz. These analytical results coincide substantially with the ones obtained by the in-situ measurement and the full-scale experiment. Accordingly, the natural mode which occurs when an impact load is applied is mainly determined by the contact condition on the sleeper bottom.

As shown in aforementioned Figure 5, the amplitude of displacement of the ballast gravel decreases in inverse proportion to the squares of frequency according to the physical theory. Therefore, the occurrence of the rigid-body natural vibration at 1/3 of the elastic natural vibration frequency is expected to induce 9 times larger amplitude of displacement within the ballast structure than the elastic natural frequency. Therefore, the occurrence of the rigid-body natural vibration largely contributes to progress the deterioration of the ballasted structure. That is, in theory, the improvement of the contact condition between the sleeper bottom and

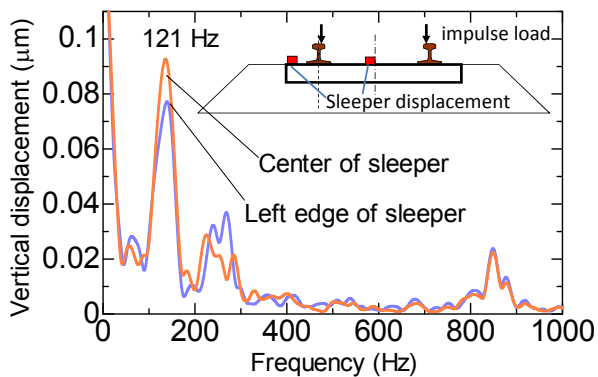


Figure 17: Vertical displacement regarding impulse loading

ballast layer can reduce the amplitudes of displacement to 1/9 compared with that in the current status of the ballasted track.

Figure 18 shows the structural damping coefficient on the sleeper bottom in vertical direction regarding a 30-cm-thick ballast layer, which has been identified by the experimental modal analysis using the full-scale mockup and precise finite element analysis according to the reference (Sakai and Aikawa, 2012). The figure shows that the damping factor of ballasted layer has extremely strong frequency dependency. The ballast layer, in the high-frequency domain over 200 Hz, provides extremely high damping functions for reducing the impact energy. However, the ballast layer is almost non-resistant subject to the low-frequency wave components of dynamic loads. The low-frequency load components are not damped, unless the ballast aggregate is fully constrained by an appropriate amount of uniform pressure from the surrounding area.

Based on the above-mentioned mechanisms, the improvement of the contact condition adjacent to the sleeper bottom contributes to restrain occurrence of the rigid-body natural vibration resulting in a reduction of the ballast degradation.

6 CONCLUSIONS

In this paper, the author dealt with the vertical natural vibration modes of the ballast layer which lead to the phenomena of ballast deterioration, based on the precise field measurement, the full-scale experiments and the large-scale numerical analysis based on high performance parallel computing. The results can be summarized as follows:

- (1) The impact loads by running trains induce the natural vibration modes within the ballast layer specific to the structure and consequently propagate within the ballast layer through motion in the natural vibration modes.
- (2) The analytical results indicate that the stress acting on the angularity part of the ballast gravel is approximately 1100 times greater than the average loading stress on the ballast surface, and that the minute fracturing or breakage, around locations where the stress acting on the angularity part of the ballast gravel converges, occurs at any time due to regular train passage.
- (3) The normal frequency of the vertical elastic vibration mode is numerically detected at around 310 Hz. The rigid body vibration occurs almost at 1/3 of the elastic vibration mode frequency. The result coincides substantially with the field measurement results. It is inferred that the rigid body vibration modes easily occur at frequencies which are equal to the ones obtained by dividing the frequency of the elastic vibration mode by odd numbers according to the amount of the overburden mass.

- (4) The occurrence of the rigid-body modes of the ballast layers plays an important role in the progress of the ballast deterioration. Therefore, the improvement of the contact condition near the sleeper bottom contributes to reduce the displacement amplitude of ballast gravel resulting in a reduction of the ballast degradation.

REFERENCES

- [1] Aikawa, A.: "Application of a Special Sensing Sleeper for Dynamic Interaction within the Boundary Layer between a Sleeper and Ballasts," *The 11th International Conference on Computational Structures Technology*, Paper No. 130, Civil-Comp Press, (2012).
- [2] Aikawa, A., Urakawa, F., Abe, K., Namura, A.: "Dynamic Characteristics of Railway Concrete Sleepers using Impact Excitation Techniques and Model Analysis," *The 9th World Congress on Railway Research*, (2011).
- [3] Aikawa, A.: "Assessment of the Dynamic Characteristics of a Ballasted Railway Track subject to Impact Excitation using Three-Dimensional Composite Finite Element - Discrete Element Modelling," *The 11th International Conference on Computational Structures Technology*, Paper No.137, Civil-Comp Press, (2012).
- [4] CERFACS, ENS Lyon, INPT(ENSEEIHT)-IRIT, Inria and University of Bordeaux, "MULTIFRONTAL Massively Parallel Solver (MUMPS 5.0.0) Users' guide", <http://graal.ens-lyon.fr/MUMPS/>, (2015).
- [5] Grassie, S.L., Gregory, R.W., Harrison, D., Johnson, K.L.: "Modelling of railway track and vehicle/track interaction at high frequencies," *Vehicle System Dynamics*, 22 (3-4), pp.209-262, (1993).
- [6] Okuda, H.: "Structural Analysis for Large Scale Assembly: Research and Development of Innovative Simulation Software," <http://www.ciss.iis.u-tokyo.ac.jp/>
- [7] Railway Bureau, MILT (Ministry of Land, Infrastructure, Transport and Tourism, and Railway Technical Research Institute, Japan) and RTRI: "Design Standards for Railway Structures and Commentary (Track Structures)," Maruzen Publishing Co., Ltd., (2012), (in Japanese).
- [8] Sakai, H. and Aikawa, A.: "Three-Dimensional Finite Element Analysis of Sleeper Vibration with the Influence of Ballast," *The 1st International Conference on Railway Technology: Research, Development and Maintenance*, Civil-Comp Press, (2012).
- [9] Sakai, H. and Aikawa, A.: "Finite Element Vibration Analysis of Sleepers including Ballast Damping Characteristics," *International Journal of Railway Technology*, 1(3), pp.37-59, Civil-Comp Press, (2012).
- [10] Urakawa, F., Aikawa, A., et al.: "Development of Remote Automatic Measuring System for Long-term Measurement of Dynamic Responses of Tracks," *Proceedings of Railway Mechanics*, No. 13, pp. 23-28, JSCE, (2009), (in Japanese).
- [11] A. Aikawa, "Determination of the Natural Modes of a Ballast Layer", *Proceedings of the Ninth International Conference on Engineering Computational Technology*, Civil-Comp Press, No.19, (2014).

REGULAR OR RANDOM: A DISCUSSION ON SPH INITIAL PARTICLE DISTRIBUTION

J. YOUNG, I. ALCÂNTARA, F. TEIXEIRA-DIAS, J. OOI AND F. MILL

School of Engineering
The University of Edinburgh
The King's Buildings, Edinburgh EH9 3JL, UK
E-mail: james.young@ed.ac.uk (corresponding author), URL: <http://www.eng.ed.ac.uk/>

Key words: Smooth particle hydrodynamics, Initial particle distribution, Random particle distribution, Lid driven cavity, Flow

Abstract. Smoothed Particle Hydrodynamics (SPH) has been used to model a variety of objects and for a number of applications in engineering and science. These have ranged from astrophysics to fluid and solid mechanics problems. Much research has been dedicated to forming a better understanding of the SPH method. As a consequence, new numerical techniques have been developed in order to overcome some of its difficulties and limitations. Nonetheless, there is still a gap in information concerning the impact of the initial particle distribution on the effectiveness of the SPH method. With this in mind, a review of existing recommendations for SPH initial configurations has been conducted in this paper. In addition to this, a numerical example is presented which is based on the classical 2-D lid driven cavity problem, wherein the upper boundary exerts a horizontal shear force on the fluid inside the cavity. The velocity of the lid is $v = 10^{-3}$ m/s and the cavity is square with length $l = 1 \times 10^{-3}$ m. The fluid was modelled with a density $\rho = 1000$ kg/m³, a viscosity $\mu = 10^{-3}$ kg/ms (Re = 1). These parameters were held constant for all consequent comparisons. The number of particles is varied from (20 × 20) to (80 × 80). The initial distribution is modelled in three different ways: (i) regular, (ii) pseudo-random (with a 30% random deviation from the regular grid) and (iii) fully random. The effectiveness of each initial particle distribution is assessed according to the field velocities and horizontal and vertical centreline velocity profiles. The impact of the initial particle distribution is highlighted and compared against a reference CFD result, and recommendations and conclusions are drawn for the SPH method.

1 INTRODUCTION

In recent years, new numerical techniques have been developed in order to overcome some of the difficulties and limitations inherent to the SPH method. Despite this progression, there is still a gap in information concerning the impact of initial particle distribution. A literature review highlighted that most SPH simulations implement a completely regular initial particle

distribution. With this in mind, a review of existing methods in SPH initial configurations has been conducted.

Idelshon et al. [1] discussed various essential issues concerning meshless methods and, in particular, what is meaningful when opting for a non-mesh-based method over a mesh-based one. However, the authors don't focus specifically on the impact of initial particle distribution in meshless methods.

Diehl et. al. [2] present a novel, and perhaps the most comprehensive, study on the effect of initial particle spacing on SPH. In comparing initial particle distributions the authors highlight that a cubic lattice arrangement is prone to artefacts due to the alignment of particles along grid axes although it does display very little noise and is simple to implement. They do not recommend this method. Similarly, random initial configurations are not recommended as the lattice effects are not fully understood and the configuration results in high levels of noise. The authors propose an initial configuration based on Weighted Voronoi Tessellations (WVTs), which has been implemented in a variety of astrophysics problems. They further present a new method for setting up SPH simulations with arbitrary, spatially varying resolution requirements in 2, 3 or N dimensions. While discussing the difficulties in estimating the errors in the SPH equations from first principles, Monaghan [3] states that these errors depend on the dynamics of the simulation. He further states that one approach to estimate these errors involving initially distributing the particles on a regular grid and then shifting them randomly by some distance, as investigated by Colagrossi [4]. Monaghan goes on to state that if the particle spacing is small relative to the dominant length scales, then the disorder resulting from the initial shifting of particles is not relevant.

Monaghan [5] later wrote a paper addressing the claims by Imaeda et al. [6] that the SPH method contains a fundamental flaw which is highlighted by shear flow simulations. Monaghan's paper stated that, provided that the initial particles configuration was in an equilibrium state, the results obtained were independent of initial distribution. Monaghan also highlights how, for simulations with a low Mach number and stiff equations of state, the initial particle distribution equilibrium condition is of paramount importance. If this condition is not respected and particles are placed at random, Monaghan states that "violent fluctuations in the pressure will drive the fluid out of the region of interest".

While discussing the importance of local conservation, Price [7] states how a random initial distribution will result in errors which are proportional to $1/\sqrt{N}$, where N is the number of particles in the simulation. Price continues to demonstrate that, in a Hamiltonian system, the particles will rearrange until a minimum energy state is achieved, thus leading to an inherent remeshing of particles. Cartwright et al. [8] investigated the effect of Poisson noise on simulations involving rings of particles in Keplerian rotation. This Poisson noise was a product of using a random number algorithm in the initial placement of particles, which is commonly found in simulations involving spiral galaxies. This investigation highlighted that gravity calculations are not affected by Poission noise. Density was found to be much more susceptible and the effect increased with the total number of particles. The pressure calculations were found to be the most influenced by noise where the effect was found to scale with \sqrt{N} . Hubber et al [9]

confirm the Poissonian errors given by both Price and Cartwright. They further state that as the minimum energy state, as discussed previously, is formed, the errors in the corresponding lattice distribution scales with $1/(N \log N)$.

Controlling the initial particle distribution appears to fundamentally conflict with the philosophy of the SPH method. A large number of authors agree that best results are achieved when avoiding a fully random initial particle distribution, provided they are not relaxed prior to running the simulation.

A numerical example based on a 2D shear driven cavity problem is examined in the present paper in order to highlight the effect of initial particle distribution. The numerical example uses a variety of initial particle distributions including; completely random, pseudo-random and regular distributions. The aim of the numerical example is to aid in determining some generic conclusions about the influence of initial particle distribution on the SPH method.

2 SMOOTHED PARTICLE HYDRODYNAMICS

Initially devised to solve astrophysical problems in three-dimensional open space [10, 11], smoothed particle hydrodynamics is considered to be a truly meshfree particle method and one of the oldest of its kind. Since its initial formulation, SPH has been extended to a range of physical problems including fluid and solid mechanics. The collective movement of the particles resembles the movement of a liquid or a gas flow and it can be modelled using equations from classical Newtonian hydrodynamics. A basic SPH formulation is presented below. A more detailed formulation can be found in [12, 13, 14].

2.1 General SPH formulation

In SPH, a system is represented by a set of particles which are distributed throughout the continuum. These particles possess material properties and interact with each other depending on their range of influence which is controlled by a weighting or smoothing function. The particles require no connectivity. Field functions are first converted into their integral representation. This also known as the kernel approximation. The kernel approximation of a function $f(x)$ is represented by the integration of the multiplication of that function by the smoothing kernel function.

$$\langle f(x) \rangle = \int_{\Omega} f(x') \nabla W(x - x', h) dx' \quad (1)$$

Within the smoothing kernel function, or smoothing function, h is the smoothing length which is used to define the area of influence of the smoothing function W . This smoothing function should fulfil some basic requirements [15, 16]. The approximation for the spatial derivative $\langle \nabla \cdot f(x) \rangle$ is obtained by substituting $f(x)$ with $\langle \nabla \cdot f(x) \rangle$ in equation 1 and applying the divergence theorem along with the knowledge that the surface integration can be neglected inside the problem domain, which gives

$$\langle \nabla \cdot f(x) \rangle = - \int_{\Omega} f(x') \cdot \nabla W(x - x', h) dx' \quad (2)$$

The kernel approximation is then further estimated through particles, which is known as the particle approximation. This is achieved by replacing the integration in the representation of the field function and its derivatives with summations over all the correlating values at the neighbouring particles in a local domain called the support domain. The particle approximation of a field function is given as

$$\langle f(x) \rangle = \sum_{j=1}^N \frac{m_j}{\rho_j} f(x_j) \cdot \nabla W_{ij} \quad \text{where} \quad \nabla W_{ij} = \frac{x - x'_j}{r_{ij}} \frac{\delta W_{ij}}{\delta r_{ij}} = \frac{x_{ij}}{r_{ij}} \frac{\delta W_{ij}}{\delta r_{ij}} \quad (3)$$

N is the total number of particles within the influence area of the particle i . Similarly, the particle approximation of the derivative of a field function is given by

$$\langle \nabla \cdot f(x) \rangle = - \sum_{j=1}^N \frac{m_j}{\rho_j} f(x_j) \cdot \nabla W_{ij} \quad (4)$$

The values of the particle approximations are calculated at every time step. Therefore, the distribution of particles may initially influence the results. The formulation described is applied to field functions in the form of partial differential equations (PDEs) and results in ordinary differential equations (ODEs) in a discretized form which is dependent on time. The ODEs are solved through an explicit integration algorithm in order to achieve fast time stepping.

2.2 SPH formulation of the Navier-Stokes equations

The SPH formulation of the Navier-Stokes equations is derived by firstly discretising the equations. This leads to a set of ODEs which evolve with time. This set of ODEs can then be solved through time integration and are based on three fundamental physical laws of conservation: conservation of mass, conservation of momentum and conservation of energy. By implementing the general formulation given above, the Navier-Stokes equations can be written as [12, 14]

$$\begin{cases} \frac{D\rho_i}{Dt} = \sum_{j=1}^N m_j v_{ij}^\beta \cdot \frac{\partial W_{ij}}{\partial x_i^\beta} \\ \frac{Dv_i^\alpha}{Dt} = - \sum_{j=1}^N m_j \left(\frac{\sigma^{\alpha\beta}_i}{\rho_i^2} + \frac{\sigma^{\alpha\beta}_j}{\rho_j^2} \right) \frac{\partial W_{ij}}{\partial x_i^\alpha} \\ \frac{De_i}{Dt} = \frac{1}{2} \sum_{j=1}^N m_j \left(\frac{p_i}{\rho_i^2} + \frac{p_j}{\rho_j^2} \right) v_{ij}^\beta \frac{\partial W_{ij}}{\partial x_i^\beta} + \frac{\mu_i}{2\rho_i} \epsilon_i^{\alpha\beta} \epsilon_i^{\alpha\beta} \\ \frac{Dx_i^\alpha}{Dt} = v_i^\alpha \end{cases} \quad (5)$$

where σ is the total stress tensor made up of isotropic pressure and viscous stress such that $\sigma^{\alpha\beta} = -p\delta^{\alpha\beta} + \tau^{\alpha\beta}$ and $\tau^{\alpha\beta} = \mu\epsilon^{\alpha\beta}$, where μ is the dynamic viscosity and ϵ is the shear strain

rate. The relative velocity between particles, $v_{ij} = v_i - v_j$. The Greek subscripts α and β denote coordinate directions and summations in the discretised equations are taken over repeated indices.

3 NUMERICAL MODEL

The numerical example presented is based on a 2D lid driven cavity problem, where the upper boundary exerts a horizontal shear force on the fluid in the cavity. The purpose of this example was to highlight and compare the impact of initial particle distributions. The example is a derivation of that which is presented by Liu [14].

A square ($l = 1 \times 10^{-3}$ m) cavity is filled with water. The bottom and side walls of the cavity are rigid. The top wall, or lid, slides in its plane from left to right at a velocity of 1×10^{-3} m/s exerting a shear force on the fluid within the cavity. The fluid was modelled with a density $\rho = 1000$ kg/m³ and a viscosity $\mu = 10^{-3}$ kg/ms yielding $Re = 1$. In addition to these properties, the particles which simulated the fluid were also initialised with zero velocity and pressure. Gravity was neglected.

Three different particle distributions were investigated. These included a completely random distribution, a pseudo-random distribution and a completely regular distribution. Through varying the number of particles in the domain of each test, the sensitivity of the simulation to the number of particles was explored in addition to the impact of initial particle distribution. With this in mind, a total of four different domain particle densities was implemented. The following 12 tests were carried out: three different initial particle distributions, each with four different number of particles. Particle distributions varied from completely random to pseudo-random to regular. The number of particles varied from 400 (20×20) to 1600 (40×40), 3600 (60×60) and 6400 (80×80), excluding virtual or boundary particles. The same number of particles was used for the random and partly random configurations to model the fluid.

The pseudo-random configuration was created by shifting each particle in the regular grids randomly by up to 30% of the spacing between particles. This ensured that an element of disorder was incorporated into the initial distribution whilst preventing the particles from clumping together.

The cavity walls and lid were modelled using virtual particles that exert a repulsive boundary force on the inner particles to prevent them from escaping the domain, also known as type 1 particles. The repulsive force was scaled with the particle spacing [14]. For each type of distribution and number of particles, the particles used to model the fluid were offset from the boundary by half the spacing between particles used in the corresponding regular grid. This was done to prevent the simulation exploding due to the repulsive force exerted from the boundary. The boundary particles themselves were separated by half the spacing used for the particles modelling the fluid in the regular grids. The same configuration of boundary particles was used for each type of distribution and scaled accordingly with the total number of particles used to model the fluid. The boundary particles modelling the lid were initialised with a velocity of 1×10^{-3} m/s. The properties and position of the boundary particles did not evolve with time but are used in the approximations carried out at the internal particles. Further exterior boundary

particles which can be used to ensure that particle deficiency does not occur near the boundary were not used in these simulations, which may have resulted in some inaccuracy. Figure 1 shows the 12 different initial configurations and highlights the boundary and internal particle configurations discussed. The smoothing length of each particle was set as the initial distance between particles in the regular grid in the horizontal direction, which equals the distance in the vertical direction. The mass of each particle was set to the density times the particle spacing in the horizontal and vertical direction in the regular grid. These smoothing lengths and masses were used for the corresponding pseudo-random and random simulations. Although it was appropriate to assume that the mass of the particles in the regular grid was the density of the particle times the discretized volume of space it influences, applying this mass directly to the pseudo-random and random simulation will have resulted in some non-physical initial density distributions. A constant time step of 2.0×10^{-5} was used. All twelve simulations were ran for 7500 time steps, as this was when the most volatile of them was deemed to have reached a steady state solution.

4 RESULTS AND DISCUSSION

A benchmark was required in order to validate the results obtained using the SPH method. With this in mind, a simulation was run on the Computational Fluid Dynamics (CFD) package STAR-CCM+. This simulation was chosen for comparative purposes as the velocity vectors, vorticity contours and locations of primary vortex it produced were in good agreement with those from previous studies [17, 18]. Figure 2 displays the absolute velocity magnitude difference between the SPH simulations and the the STAR-CCM+ reference case while Figure 3 displays the relative difference. These figures are displayed in increasing number of particles (top to bottom) and increasing the element of randomness (left to right). The first column shows the simulation results for the initially regular distribution, the second for the pseudo-random distribution and the last for the completely random distribution. Figures 4 and 5 show the non-dimensional vertical velocity profile along the horizontal centreline and the non-dimensional horizontal velocity profile along the vertical centreline, respectively.

Figures 4 and 5 highlight that the results produced from the SPH and CFD methods generally agree. It is clear that for the lower particle distributions, the SPH results deviate as compared to the reference solution. Additionally, these figure show how the initially random and pseudo-random distributions produced noisy curves with large fluctuations. These plots appear to indicate that the high density and structured distribution produces the overall best results

Due to the adaptive nature of the SPH method it should not, supposedly, be affected by the arbitrary distribution of particles. Therefore it was expected that the results may have favoured a specific number of initial particles but would not have been heavily influenced by the type of distribution. However, this was clearly not the case as the results showed that a regular distribution produced the most favourable results for the parameters measured. Due to the repulsive force between particles, random distributions were expected to quickly move to their minimum energy state. Although this repositioning of particles inevitably causes some spurious velocities, it was expected that these would quickly dampen out and not impact the overall

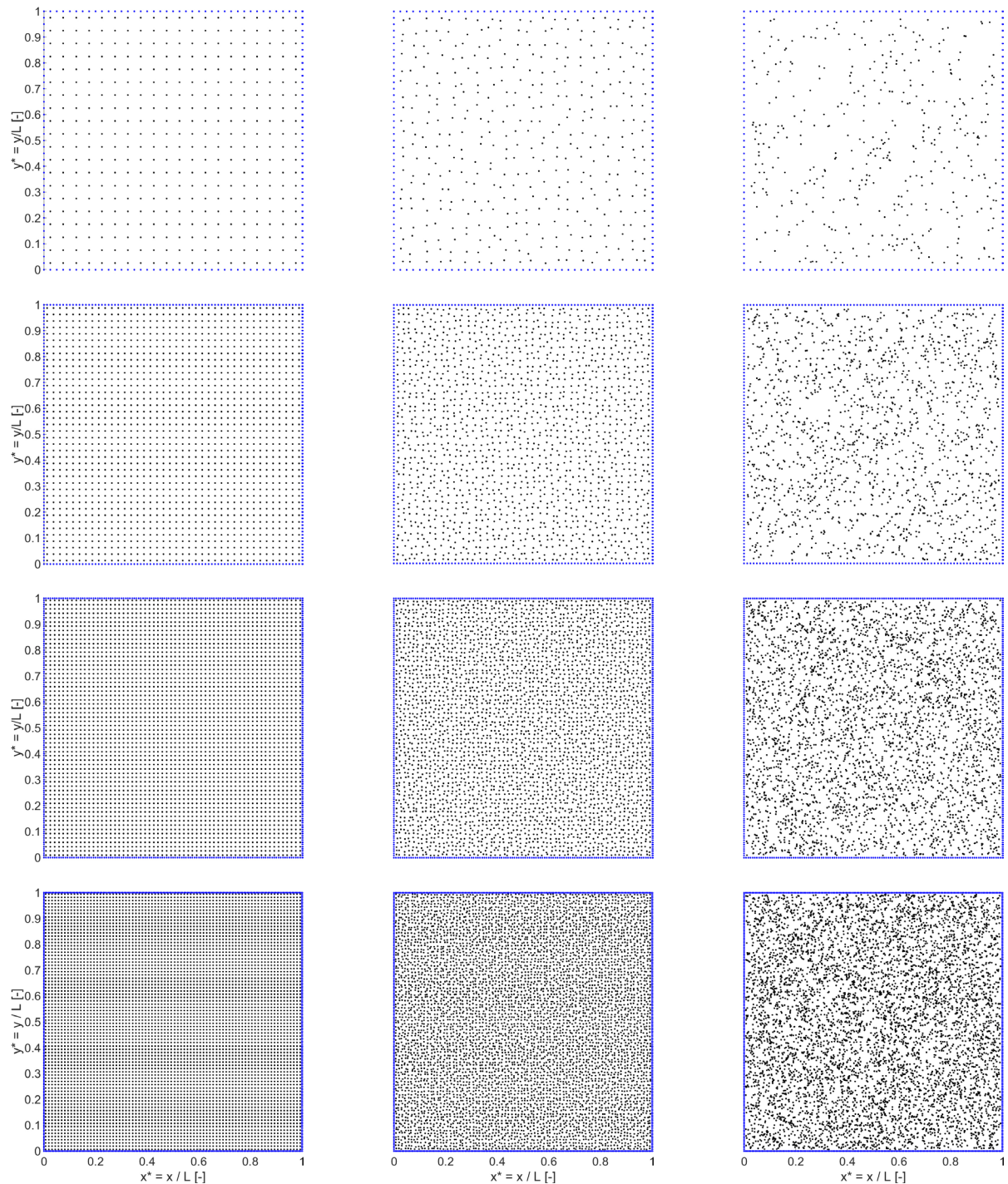


Figure 1: Different particle density for each initial particle distribution: Top to bottom: 20×20 , 40×40 , 60×60 and 80×80 ; left to right: regular distribution, pseudo-random distribution and random distribution. Figures 2 and 3 follow this arrangement.

quality of the results.

Figures 2 to 5 clearly highlight that the 20×20 particle distributions simply do not contain a sufficient quantity of particles to accurately capture the physics of the shear cavity. Therefore, when attempting to draw conclusions from the simulation results, these distributions were discarded. The literature review highlighted that a random configuration should not be used unless the distribution is allowed to reach equilibrium prior to imposing external forces. It was predicted that the effects caused by the initially random configuration would be damped out in the early stages of the simulations. This was checked for the 60×60 random initial configuration which was allowed to reach equilibrium prior to being exposed to the shear force. The results of this simulation did not highlight an improvement over the corresponding simulation which was not allowed to reach equilibrium prior to imposing the shear force.

5 CONCLUDING REMARKS

From the results obtained some general remarks can be made about the influence of the initial particle distribution. The regular distribution produced the least noisy results which were the most easily interpreted. The random distributions were the noisiest of the three which is clearly highlighted by the vertical and horizontal velocity curves around the corresponding centrelines. Although the choice of particle distribution is situational, a regular distribution is recommended. When investigating the number of particles to be used, there is clearly a minimum below which the method cannot capture the physics of the simulation. In the case of this lid-driven shear cavity, that amount was between 400 (20×20) and 1600 (40×40) particles. The results also highlighted that there may also be a recommended maximum number of particles as the transition from 3600 (60×60) to 6400 (80×80) particles resulted in a decrease in the quality of the results obtained, especially for the random configuration. One should also bear in mind the computational costs involved in the simulations. Simulations involving higher number of particles would require more CPU time, while simulations involving lower number of particles would require less CPU time. Additionally, the time used to generate the initial particle configuration should also be accounted for. All the additional factors ought also to be considered when trying to extrapolate conclusions about either to opt for a regular or random distribution, with more or less particle density.

REFERENCES

- [1] Idelsohn, S. R. and Oñate, E. To mesh or not to mesh. That is the question... *Comput. Methods in Appl. Mech. Eng.* (2006) **195**(37-40):4681–4696.
- [2] Diehl, S. et al. Generating Optimal Initial Conditions for Smooth Particle Hydrodynamics Simulations. *Mon. Not. R. Astron. Soc.* (2012)
- [3] Monaghan, J. J. Smoothed particle hydrodynamics. *Rep. Prog. Phys.* (2005) **68**(8):1703–1759.

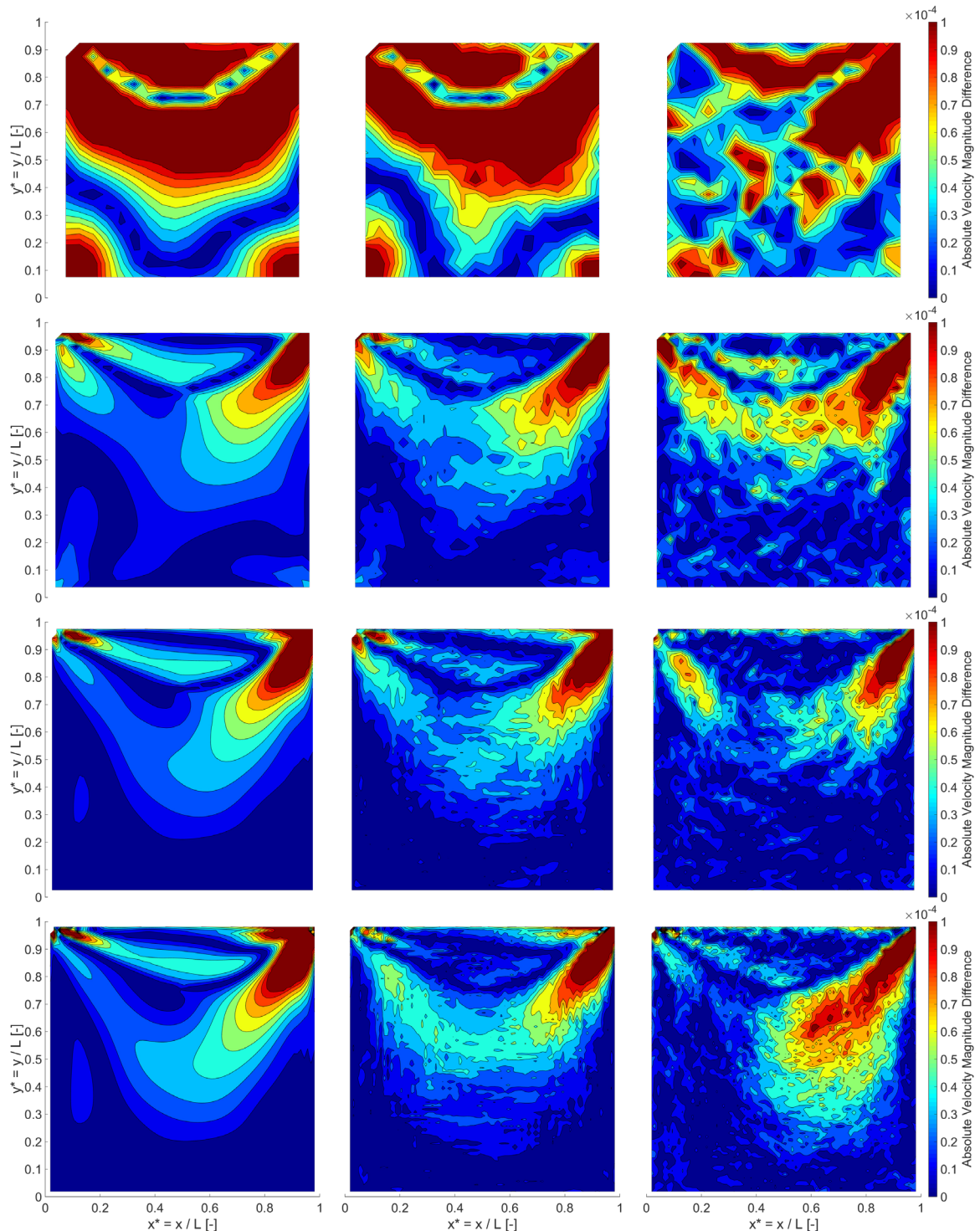


Figure 2: Absolute velocity magnitude difference between SPH results and Star-CM++.

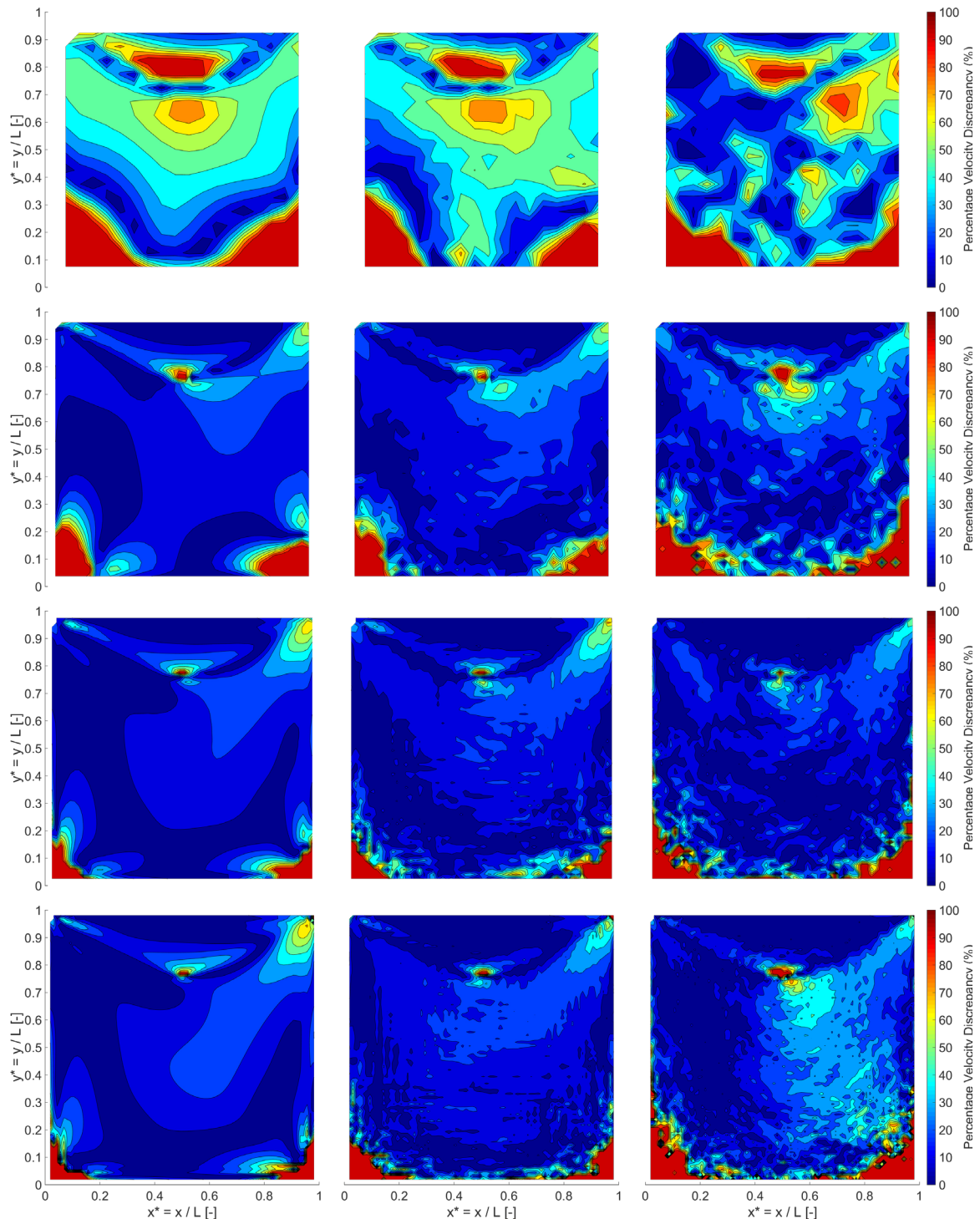


Figure 3: Relative velocity magnitude difference between SPH results and Star-CM++.

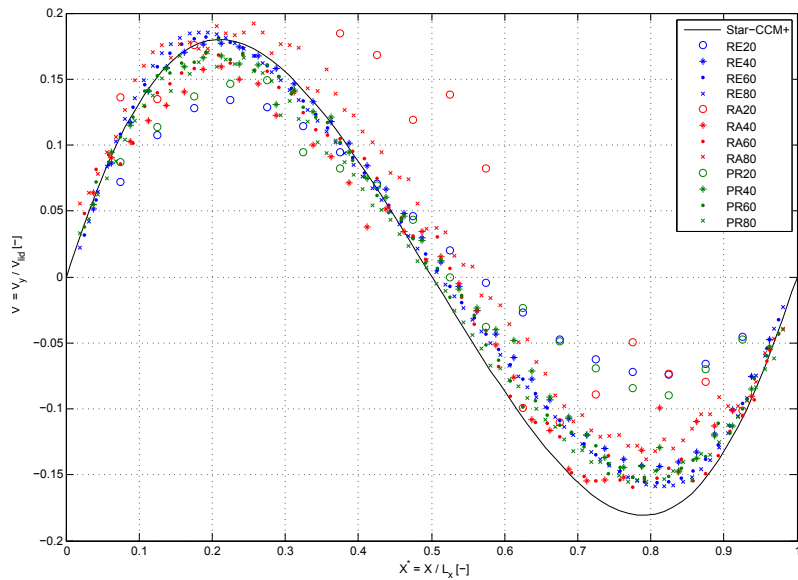


Figure 4: Non-dimensional vertical velocities along the horizontal centreline of the cavity: regular (RE), pseudo-random (PR) and random (RA).

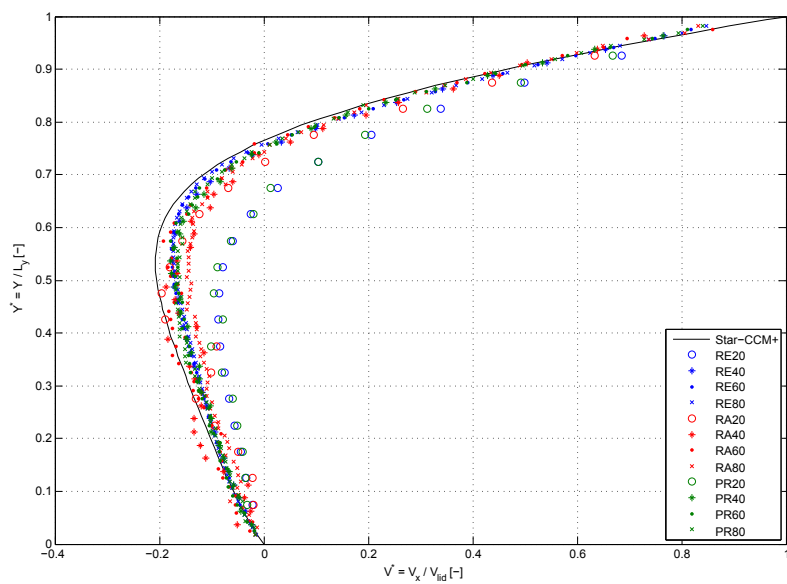


Figure 5: Non-dimensional horizontal velocities along the vertical centreline of the cavity: regular (RE), pseudo-random (PR) and random (RA).

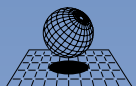
- [4] Colagrossi, A. *A Meshless Lagrangian Method for Free-Surface and Interface with Fragmentation*. Ph.D. Thesis. Università di Roma La Sapienza, Rome (2003).
- [5] Monaghan, J. J. Smoothed particle hydrodynamic simulations of shear flow. *Mon. Not. R. Astron. Soc.* (2006) **365**(1):199–213.
- [6] Imaeda, Y. and Inutsuka, S.-I. Shear Flows in Smoothed Particle Hydrodynamics. *Astrophys. J.* (2002) **569**(1):501–518.
- [7] Price, D. J. Smoothed particle hydrodynamics and magnetohydrodynamics. *J. Comput. Phys.* (2012) **231**(3):759–794.
- [8] Cartwright, A., Stamatellos, D. and Whitworth, A. P. The effect of Poisson noise on SPH calculations. *Mon. Not. R. Astron. Soc.* (2009) **395**(4):2373–2380.
- [9] Hubber, D. A., Falle, S. A. E. G. and Goodwin, S. P. Convergence of AMR and SPH simulations - I. Hydrodynamical resolution and convergence tests. *Mon. Not. R. Astron. Soc.* (2013) **432**:711–727.
- [10] Lucy, L. B. A numerical approach to the testing of the fission hypothesis. *Astron. J.* (1977) **82**(12).
- [11] Gingold, R. A. and Mon, J. J. Smoothed particle hydrodynamics: theory and application to non-spherical stars. *Mon. Not. R. Astron. Soc.* (1977) **181**:375–389.
- [12] Liu, M. B. and Liu, G. R. Smoothed Particle Hydrodynamics (SPH): An Overview and Recent Developments. *Arch. Comput. Methods Eng.* (2010) **17**:25–76.
- [13] Galagali, N. *Algorithms for Particle Remeshing Applied to Smoothed Particle Hydrodynamics*. MA Thesis. Massachusetts Institute of Technology (2009).
- [14] Liu, G. R. and Liu, M. B. *Smoothed Particle Hydrodynamics — A Meshfree Particle Method*. World Scientific Publishing (2003).
- [15] Liu, M. B., Liu, G. R. and Lam, K. Y. Constructing smoothing functions in smoothed particle hydrodynamics with applications. *J. Comput. Appl. Math.* (2003) **155**:263–284.
- [16] Monaghan, J. J. Why Particle Methods Work. *SIAM J. Sci. Comput.* (1982) **3**(4):422-433.
- [17] Kim, J and Moin, P. Application of a fractional-step method to incompressible Navier Stokes equations. *J. Comput. Phys.* (1985) **59**(2):308–323.
- [18] Schreiber, R and Keller, H. Driven cavity flows by efficient numerical techniques. *J. Comput. Phys.* (1983) **49**(2):310–333.

AUTHORS INDEX

Abdelmoula, N.	1040	Deliége, G.	1081
Abdelraheem, A.	451	Dimaki, A.V.	442
Abriak, N-E.	81	Djelal, C.	497
Aigner, A.	117	Dmitriev, A.I.	248, 612
Aikawa, A.	1093	Dorémus, P.	1040
Alcântara, I.	1105	Dostal, Z.	732
Altus, E.	355	Dubina, R.	34
Aman, Z.	171	Dynnikova, G.	692
Amani, A.	755	Eberhard, P.	308, 333
Antonyuk, S.	567	Effeindzourou, A.	744
Arinchev, S.V.	909	El Cheikh, K.A.	497
Arroyo, M.	1073	Eliáš, J.	34, 320
Arutunyan, G.	692	Eremina, G.M.	255
Asai, M.	403, 451	Farnish, R.J.	714
Asprone, D.	657	Farsi, A.	921
Astafurov, S.V.	442, 612	Fatemizadeh, S.	635
Auricchio, F.	657	Ferellec, J-F.	842
Averkova, O.A.	969, 1016	Fernandes, D.T.	590
Barakos, G.N.	263	Fleissner, F.	998
Baroudi, D.	646	Forgber, T.	105, 117
Beck, F.	333	Fraser, K.A.	275
Bellezi, C.A.	590	Fukumoto, Y.	537
Ben-Shmuel, Y.	355	Furen, M.	171
Benahmed, N.	519	Gens, A.	1073
Benvenuti, L.	93	Ghobakhloou, M.	646
Berzins, M.	202	Giacomini, A.	744
Boes, R.M.	998	Glushkov, D.O.	287
Bojarevics, V.	702	Govender, N.	81
Boman, R.	1081	Gritton, C.	202
Bonelli, S.	519, 558	Guarnieri, M.	579
Bornert, M.	810	Guvernyuk, S.	692
Brisard, S.	810	Hamad, F.	635
Brunier-Coulin, F.	519	Hanley, K.J.	890
Bustanchy, M.	623	Harkness, J.	767
Cao, T.D.	140	Harthong, B.	1040
Carbonell, J.M.	1073	Helmons, R.L.J.	945
Carlsson, M.	921	Hidalgo, R.C.	71
Cerquaglia, M.L.	1081	Ho, H.	214
Chalak, C.	161	Horak, D.	732
Chareyre, B.	60, 161, 744, 957	Hori, M.	933
Chauchat, J.	60	Hossain, M.	833
Chen, W.	41, 602	Hsiao, F.P.	214
Cheng, H.	485	Hu, H.	308
Cheng, L-Y.	590	Huang, C-H.	226
Chircota, Y.	275	Huang, X.	890
Colonia, S.	263	Ibrahim, K.	1052
Cuéllar, P.	519, 558	Ichimura, T.	933
Curbach, M.	367	Idris, N.A.B.	403
Dahl, P.I.	105	Imbault, D.	1040
Darve, F.	161, 957	Ishimoto, J.	410
Del Cid, L.I.	237	Janda, A.	71
Delenne, J-Y.	519, 558	Jing, L.	474

Jonsén, P.	1066	Mustoe, G.	237
Kakogiannou, E.	128	Ngoma, J.	519, 558
Karimian, S.M.H.	755	Nicot, F.	419
Khalili, M.H.	810	Niklasch, C.	460
Kirby, R.M.	202	Nikonov, A.Y.	248, 612
Kiss, L.I.	275	Nishimoto, K.	590
Kloss, C.	93, 117	Nitka, M.	343, 507
Kolubaev, E.A.	612	Nogami, T.	451
Konietzky, H.	41	Ochiai, N.	410
Korkiala-Tanttu, L.	646	Ohtsuka, S.	537
Koumousis, V.	53	Ooi, J.Y.	1105
Krenzer, K.	722	Ou, Y.C.	214
Kruggel-Emden, H.	801	Ouhbi, N.	545
Kuzmina, K.S.	680	Ozbulut, M.	981
Kwok, F.C.Y.	474	O'Sullivan, C.	890
Latham, J.P.	921	Pal, M.K.	933
Laurens, P-E.	842	Palzer, U.	722
Lazari, M.	149	Papavassiliou, D.V.	1010
Leung, A.Y.F.	474	Papeleux, L.	1081
Lichtenheldt, R.	430	Peng, C.	529
Lin, B-C.	226	Peng, F.	602
Logachev, A.K.	969, 1016	Perales, R.	842
Logachev, I.N.	969, 1016	Pereira, J-M.	789, 810
Logachev, K.I.	969, 1016	Pericleous, K.	702
Lohman, W.J.A.	391	Perrin, G.	545
Lora, M.	128	Peters, B.	419
Luding, S.	1028	Pham, N.	1010
Lulbadda Waduge, L.L.	900	Philippe, P.	519, 558
Lülf, F.A.	866	Picano, F.	579
Maggiolo, D.	579	Pirker, S.	93
Magnanimo, V.	1028	Pizette, P.	81, 497
Manoylov, A.	702	Plu, J.	842
Marchevsky, I.K.	670, 680	Podryga, V.	779
Marigo, M.	854, 921	Polyakov, S.	779
Marion, A.	579	Ponthot, J-P.	1081
Marzougui, D.	60	Popov, V.L.	22
Mayer, P-M.	460	Pospisil, L.	732
Maza, D.	71	Potticary, M.	767
Mechtcherine, V.	722	Psakhie, S.G.	22, 255, 442, 612
Meywerk, M.	822	Pullen, A.D.	921
Michael, M.	419	Radjaï, F.	519, 558
Miedema, S.A.	945	Radl, S.	105, 117
Milani, D.	379	Reali, A.	657
Mill, F.	1105	Reischl, D.S.	367
Miyagawa, Y.	403	Rémond, S.	497
Mohammadi-Amin, M.	623	Rodríguez, J.M.	1066
Monforte, L.	1073	Roux, J-N.	545, 789, 810
Montanino, A.	657	Rubio-Largo, S.M.	71
Moermann, C.	635	Saitoh, K.	1028
Morgenthal, G.	379, 1052	Salomons, E.	391
Mueller, A.	998	Sanavia, L.	128, 140, 149
Murakami, A.	537	Saussine, G.	842

Scherer, V.	298
Schrefler, B.A.	140, 149
Seyednia, M.	755
Shcheglov, G.A.	670
Shilko, E.V.	22, 442, 612
Six, K.	878
Smolin, A.Y.	255
Sofianos, C.	53
Solowski, W.T.	646
Song, E.	192
St-Georges, L.	275
Steijl, R.	263
Stitt, E.H.	854, 921
Strizhak, P.A.	287, 991
Suhr, B.	878
Sun, Y.	192
Svoboda, A.	1066
Syrovatskiy, D.	692
Tanaka, S.	933
Tang, A-M.	789
Teixeira-Dias, F.	1105
Tejchman, J.	343, 507
Terrapon, V.	1081
Than, V-D.	789
Thoeni, K.	744
Thommes, M.	567
Thäte, D.	567
Tofighi, N.	981
Tolchard, J.R.	105
Ton, B.T.	714
Tsukamoto, M.M.	590
Turnbull, S.A.	854
Uvarov, V.A.	969, 1016
van Rhee, C.	945
Vandamme, M.	810
Vanhove, Y.	497
Vetsch, D.F.	998
Voivret, C.	545
Volkov, R.S.	991
Vollmari, K.	801
Vysokomornaya, O.V.	287
Wang, C.	529
Wang, R-Z.	214, 226
Wang, X.	460
Wang, Y.	140
Weis, D.	567
Wiese, J.	298
Wijerathne, L.	933
Wilke, D.N.	81
Wilkinson, S.K.	854
Wirtz, S.	298
Wissing, F.	298
Wone, M.	842
Wriggers, P.	866
Wu, W.	529
Xiang, J.	921
Xu, Z.	602
Yamamoto, H.	485
Yamamoto, Y.	410
Yan, Z.	854
Yang, J.	192
Yildiz, M.	981
Young, J.	1105
Yu, A.	833
Yu, H-S.	529
Yuan, C.	957
Zaabout, A.	105
Zervos, A.	767
Zhang, D.	602
Zhdanova, A.O.	991
Zhifan, Z.	171
Zhou, G.	183
Zhou, H.	391
Zhu, H.	833
Zieher, O.	822
Zigan, S.	714, 900
Zuriguel, I.	71



CIMNE
International Center
for Numerical Methods in Engineering